Handbook on the Physics and Chemistry of Rare Earths volume 5

Edited by: Karl A. Gschneidner, Jr. and LeRoy Eyring
ISBN: 978-0-444-86375-1

North Holland Publishing Company (1982)

PREFACE

Karl A. GSCHNEIDNER, Jr., and LeRoy EYRING

These elements perplex us in our rearches [sic], *baffle us in our speculations, and haunt us in our very dreams. They stretch like an unknown sea before us – mocking, mystifying, and murmuring strange revelations and possibilities.*

Sir William Crookes (February 16, 1887)

This lament of Sir William Crookes which introduced the preface to the first four volumes of this series still beckons hauntingly for satisfaction. Although many of the greatest mysteries he contemplated have been satisfactorily solved, there still remains the need for voyages of discovery on the "unknown sea".

We anticipated the need for other volumes to follow the first four, both to cover topics already mature but not included and others whose time had not yet come. We underestimated both aspects of this need. There is a time for a review of past work when the review itself promotes understanding and stimulates new lines of research. In response to this the publisher will continue the series to assure an evolving authoritative and comprehensive *Handbook on the Physics and Chemistry of Rare Earths*. Volume 5 contains new topics concerning thin films of alloys and compounds, transport properties of intermetallic compounds, catalytic behavior of metallic and non-metallic surfaces, defects and transformations in oxides, physical and chemical properties of fluorides, and spectroscopic properties of lanthanide ions in a variety of ionic hosts.

It is our intent that the handbook will continue to serve as a chronicle, charts, and navigational aids to those who would explore the mysteries of this unknown sea, the rare earths.

CONTENTS

CONTENTS OF VOLUMES 1–4

VOLUME 1: METALS

VOLUME 2: ALLOYS AND INTERMETALLICS

VOLUME 3: NON-METALLIC COMPOUNDS – I

VOLUME 4: NON-METALLIC COMPOUNDS – II

Handbook on the Physics and Chemistry of Rare Earths, edited by K.A. Gschneidner, Jr. and L. Eyring

Chapter 41

RARE EARTH ALLOYS AND COMPOUNDS AS THIN FILMS

M. GASGNIER
Centre National de la Recherche Scientifique,
Laboratoire des Elements de Transition dans les Solides, E.R. No. 210,
1 Place A. Briand, 92190 Meudon Bellevue, France

Contents

Symbols and abbreviations

A	= exchange stiffness constant
AES	= Auger electron spectroscopy
e	= thickness
e-gun	= electron beam gun
EELS	= electron energy loss spectroscopy

EPR = electron paramagnetic resonance
ESR = electron spin resonance
fL = foot Lamberts
FMR = ferromagnetic resonance
g = Landé spectroscopic splitting factor
g_{eff} = effective Landé factor
H_c = coercive force or coercivity
H_{coll} = collapse field
H_{int} = internal magnetic field
$H_k^{(*)}$ = effective anisotropy field
$H_k'^{(*)}$ = anisotropy field
$H_u^{(*)}$ = uniaxial anisotropy field
IR = infrared
ISS = ion scattering spectroscopy
K_u = uniaxial magnetic anisotropy
l = characteristic length
LEED = low energy electron diffraction
$4\pi M_0$ = magnetization
$4\pi M_s$ = saturation magnetization
$4\pi M_{eff}$ = effective saturation magnetization
M–H = characterization of hysteresis curves
N-type = voltage controlled
OLCP = orbit–lattice coupling parameter
Q = magnetic quality factor
R_0 = reflectivity
R_s = Hall coefficient
RDF = radial distribution function
R–TM = rare earth–transition metal
S-type = current controlled
SAS = small angle scattering
S.C. = semiconductor
S.C.→M. = semiconductor to metal
SIMS = secondary ion mass spectroscopy
SQID = superconducting quantum interface device
STEM = scanning transmission electron microscopy
T_c = Curie temperature
T_{comp} = compensation temperature
TEM = transmission electron microscopy
V_b = bias voltage
V_H = Hall voltage
w_s = stripe width
XPS = X-ray photoelectron spectroscopy
XRF = X-ray fluorescence
θ = paramagnetic value (Weiss constant)
θ_F = Faraday rotation
θ_K = Kerr rotation
ρ = electrical resistivity
ρ_H = Hall resistivity
σ_w = wall energy density

(*)The definition of H_k, H_k' and H_u may vary from one author to another.

Equations

Amorphous magnetic films, main relations between the parameters:

$K_u = \frac{1}{2} M_s H_k$

$K_u > 2\pi M_s^2$ favorable condition for bubble domains

$K_{eff} = K_u - 4\pi M_s$

$l = \sigma_w / 4\pi M_s^2$

$\sigma = 4(AK_u)^{1/2}$

$Q = K_u / 2\pi M_s^2$

$4\pi M_s^{eff} = 4\pi M_s - 2K_u / M_s$

$H_k = 3\lambda\sigma / M_s$ (λ and σ being the magnetostriction and stress coefficient, respectively)

or

$H_k = \frac{3}{2}\lambda\sigma$ (λ and σ being the longitudinal saturation magnetostriction and isotropic stress constant, respectively)

$H_k' = H_k - 4\pi M_s$

1. Introduction

It is well known that metallic thin films of pure elements, and above all of the transition elements, are complex subjects. This comes in part from the "natural gettering effect" of gases which are present in the system during the preparation or in the course of the determination of the physico-chemical properties (transfer into a new atmosphere; bombardment by electrons, neutrons, ions, . . .; annealing; . . .). Such a situation has been observed for rare earth, Cr, Mo, W, Ta and Bi metals for instance. One notes this is also time for the sulfurization of Au and Ag thin films in an ambient atmosphere. Many times this influences the physical properties of the materials, and often numerous discrepancies are found in the results described in the literature (Gasgnier, 1980).

In the case of binary or ternary rare earth systems as thin films, which are either amorphous (alloys) or crystalline (compounds), the problems of preparation, of characterization, of crystallization (and/or recrystallization) and above all of determination of the basic physico-chemical laws, are acute. Our survey of the literature will give clear evidence that an ideal reproducibility of two or three identical samples is difficult. In the numerous preparations we have studied there is always at least one parameter which varies. Such a variation induces, generally, drastic changes in the properties. A typical example has been reported by Winters et al. (1969) for GdFe films prepared by sputtering. Therefore, as early as this date these authors had observed that film composition strongly depends on vapor pressure, sputtering rate, atomic size, system geometry, sticking probabilities and sputtering coefficients (V_b is important). This assertion is chiefly true for amorphous materials and for crystallization (and/or recrystallization) phenomena in the course of film annealing.

We insist that amorphous materials, because they are especially delicate, should be treated with great care. In order to explain the magnetic and the microstructural configurations of these films numerous experimental methods and models have been used. Some review papers have shown the different characteristics of these configurations. One should notice that models have evolved or have been transformed, through the use of more refined measurement techniques, chiefly during the last years. We mention the following review papers: Cargill (1975, 1978a), Cargill and Mizogushi (1978), Grundy (1977, 1980), Chaudari et al. (1977), Coey (1978) and Leamy and Dirks (1978, 1979). From all the results which have been reported it is possible to advance an hypothesis: there may be room for several models, magnetic as well as microstructural, for the same sample. Grundy (1980) clearly defines this problem in his conclusion: "It would seem that interesting *variations* in *magnetic properties* can be obtained by marrying the wide compositional ranges with the *different microstructures* that can be obtained experimentally .... It is known that the details of *film nucleation* and *growth differ* in the *deposition techniques* .... There would seem, therefore, to be a fruitful field of research in further study of the preparation-dependent properties of amorphous magnetic films." He shows that some results reported in his paper support this view. Cargill (1978b), for

amorphous GdCo alloys prepared by sputtering or evaporation, concludes "... the possible sensitivity of microstructure to preparation conditions. Effects of deposition conditions on microstructure are well known for crystalline materials, and they are now being more widely recognized and studied in amorphous solids .... Some important physical properties can be very sensitive to quite subtle aspects of structure on both atomic and microstructural scales." This permits the introduction of the largely fluctuating results reported for the magnetic properties. Various authors have tried a partial synthesis of these results, and in particular they have tentatively explained the origin of one of the most discussed parameters, i.e., the uniaxial magnetic anisotropy (K_u). We refer the reader to the following papers: Gambino et al. (1974b), Cargill (1975), Heiman et al. (1978), Leamy and Dirks (1979), Mizoguchi and Cargill (1979), Fert and Azomoza (1979), Biesterbos (1979) and above all Eschenfelder (1980). Heiman et al. (1978) conclude, after carrying out a large investigation of the magnetic properties of various alloys such as R–Fe, R–Co, R–CoMo or Au or Cu, that "The *fundamental mechanisms responsible* for K_u and the effects of annealing are not *understood*" (see section 2.1.5.1). Other authors have mentioned similar situations. About the coercivity (H_c) Buravikhin et al. (1975a) write: "The investigation of H_c is very difficult because it is a structure-sensitive parameter and a *slight change* in the *film preparation* technology causes *abrupt changes* in H_c." On the other hand the concept of thin films cannot be entirely understood if we exclude the role of the gases either absorbed, adsorbed or enclosed in the course of the preparation. So, argon (by the sputtering method) and oxygen (whatever the evaporation method) have been recognized as the more important poisons for amorphous materials. Müller et al. (1977) conclude that "It is not possible to speculate about the influence of structure fluctuations on magnetic properties without a *precise characterization* of the *chemical sample composition*". Schneiger and Brunsch (1978) report: "FeGd films are *extremely sensitive* not only to minute *contaminations* of the vacuum by *oxygen* contamination but also to the *prefabricational conditioning* of the vacuum system. This will *impose* extremely *tight control* demands on any *fabrication process* of FeGd films with *reproducible properties.*" Such an assertion reveals the great importance of the chemical analysis of the materials. In this way it seems natural to determine the atomic percent ratio of the gases inside the films (Ar, O_2, H_2, N_2, H_2O, CO, ...) and of magnetic and non-magnetic impurities. Now, in fact, few papers do present such results. Frisch and Reuter (1979) study the gas evolution during the heat treatment of amorphous GdCo films rf-sputter-deposited in a Kr atmosphere. Between 300 and 1 000 K they observe that only Kr and H_2 are released. They conclude that "It is clearly seen that the H_2 desorption precedes the evolution of Kr". This result is very important because the exact role of H_2 has been rarely studied. It is well known that it is difficult to obtain absolutely pure metals, above all of the transition elements. Therefore the formation of a small amount of a chemical compound or the addition at faint concentrations of different elements as impurities, can induce changes in magnetic and structural properties. These changes can also come from the apparatuses used for the measurement,

which are becoming more and more sensitive. For instance, a SQID apparatus (Josephson effect) can detect some ppm of magnetic impurities included in a borosilicate or in a float-glass support.

So, the systematic bibliography presented in this review, had led us to present the results not by way of formulae, curves and tables which most of the time would have been valid for a special sample only, but by the much better possible comparison of well defined properties. This choice has been determined by the complexity of the results. The treatment of one magnetic property can lead to the report of many curves, the presentation of many large tables, or finally to the exposition of many different models (formulae, hypotheses, . . .) such that a clear classification will be difficult, if not impossible. Such a situation comes from the fact that numerous papers do not give precisely all the many experimental parameters: chemical analysis of the starting bulk material, residual gas analysis in the vacuum, cleanness of the substrates, thickness and composition of the films, presence of a possible sublayer at the film–substrate or at the film–air interfaces, X-ray and electron diffraction patterns, ... Likewise the exact possibilities of the apparatus are not always determined, and rarely are the computed systematic errors given, or else not *all* the physical properties are measured which does not permit comparisons between the results.

In a philosophical way, our own impression, in a general manner, is that the results and the conclusions developed in numerous papers are only the ideas of the authors and do not lead to a complete comprehension of the problems. There is in fact a lot of polemics between the authors. And the situation for R–TM alloys as thin films seems alarming. Indeed, the future of these alloys, as industrial or commercial materials, now seems to lead to an impasse, whereas garnet films have been used in the past few years, as memories and other devices. This can be described in a simple way: from the first papers of Chaudari et al. (1973a,b) and Herd and Chaudari (1973) about GdCo films as future magnetic bubble devices, there has been an increase of the number of papers up to about 1976. As shown in fig. 1, since this year there has been a net decrease in this field of research not only on the fundamental side but also on the technological one. These two themes are clearly demonstrated by the following observations:

1) At the last Intermagnetic Congress in Boston (1980), only 9 papers out of about 250 communications were devoted to amorphous or crystalline rare earth systems, and no special Session was attributed to this subject. However, a new class of materials such as GdFeB or FeB alloys seems to be a future development.

2) In his survey of the technological properties of amorphous R–TM films, Eschenfelder (1980b) concludes that "The net result is that the cost advantages possible from amorphous materials are not likely to be realized until the technology has advanced to the point where we are using bubbles smaller than 0.5 μm and probably not even then unless we find ways to achieve greater anisotropies"!

From various pertinent conclusions and numerous considerations about R–TM

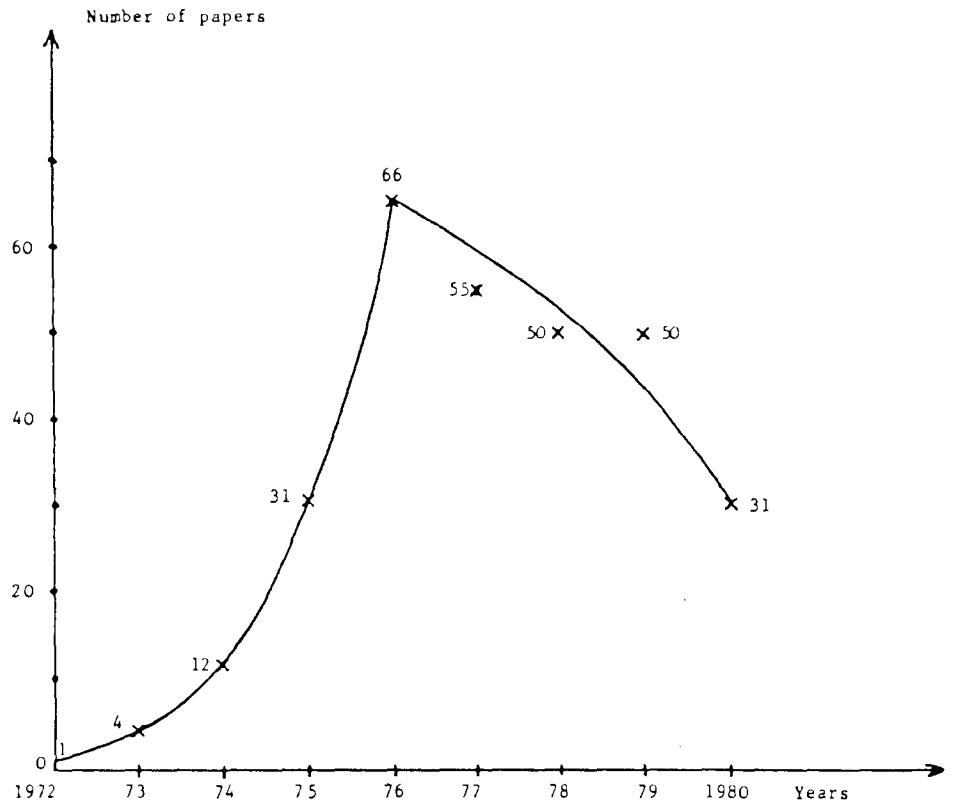

Fig. 1. The distribution of the 245 papers published on R–TM amorphous films from 1972 to 1980.

thin films, we have tentatively demonstrated the complexity of the investigation of their physical properties and of their industrial technology. Other problems such as ageing, porosity and annealing behavior, for instance, are not yet resolved; all these parameters induce the phenomenon of crystallization of the amorphous alloys. (In the bulk state the thermal stability of some R–Mn, Fe, Co or Ni alloys has been reported by Buschow and Dirks (1980).)

One must assume that the remarks made for R–TM systems are often also valid for the other rare earth systems. To explore the largest range of information we have compiled the largest possible bibliography. This has brought to the forefront contradictory, diversified and original results and conclusions. To expose more or less the whole of the data in the absence of clear-cut criteria for selection, we have chosen a triple classification. The first one is reported in the Contents. The second and third ones are enclosed in the subsections. They consist in establishing the list of alloys and compounds with the following criteria: first the rare earths are classified as their natural series, that is Sc, Y, La to Lu; secondly the other components are classified, as much as possible, according to their atomic number. Additionally, the R–Co–X (X = Fe, Ni, Mo,

Cu and Au) systems are classified in R–X paragraphs. This classification scheme has the difficulty that each physical-chemical property is not located in one place. (When it was possible we have made some correlations in special paragraphs.) This permits one to obtain a good idea of the work which has been done. Thus the reader will be informed on the subjects which have been of greatest interest, the ones which have not, or have little, been studied, and the ones which may be developed in the future.

Finally, our purpose is two-fold. First we will note the discrepancies, the contradictions and the affirmations more or less hazardously published in the literature; the complexity of various problems which are not yet controlled or resolved, such as the interpretation of some physical parameters; the annealing behaviour; and the possible industrial applications. Secondly we will analyze in as much detail as possible all the papers which have been compiled.

Remarks:

1) We have excluded from our classification halides and boron. For the last element, this is perhaps a mistake, because, as mentioned above, it may be one of the components in amorphous alloys in future developments.

2) We have also excluded the work which has been carried out with such materials as ribbons, thinned single crystals and very thick films.

3) Except in definite cases, we have rarely studied the problems of doping and of implantation.

4) Comparisons with the bulk state are rarely mentioned, because the bibliography would become too extended.

2. Rare earth–transition metal systems

2.1. *Rare earth–(3d)–3d transition metal systems*

2.1.1. *Gadolinium–titanium alloys*

Some magnetic properties of numerous ferromagnetic amorphous gadolinium alloys such as Gd_x(Mg, Ti, V, Cr, Nb, Ge, Si or Au)$_{1-x}$ prepared by sputtering or evaporation have been reported by McGuire and Gambino (1980). The main features relative to each element will be described in the following subsections. The authors have studied more particularly the transport properties such as spontaneous Hall effect and resistivity, and also magnetization ($4\pi M$), T_c and θ. They observe wide variations in the recorded data and notice that they cannot be compared to the ones relative to the crystalline state. From their results they propose a model for the spontaneous Hall effect which includes both the total spin of the Gd ion and a factor which contains the exchange interaction. The Hall effect increases with the paramagnetic θ. All the samples have a negative ρ_H.

By comparison with the other alloys, Gd_xTi_{1-x} alloys exhibit the lowest resistivity at 4.2 and 293 K, i.e. 142 and 167 $\mu\Omega$ cm, respectively, of all the alloys studied to date.

2.1.2. *Gadolinium–vanadium alloys*

Magnetic properties of Gd_xV_{1-x} alloys have been reported by McGuire and Gambino (1980) as mentioned above. By comparison with the other samples, these alloys exhibited as the main characteristic a high T_c (105 K).

2.1.3. *Gadolinium–(cobalt)–chromium alloys*

For binary Gd_xCr_{1-x} alloys, McGuire and Gambino (1980) have studied the same properties as noted in section 2.1.1. By comparison with the other systems, GdCr shows a high resistivity (200 $\mu\Omega$ cm).

To obtain bubble domain devices, Chaudari and Gambino (1975) have studied ternary amorphous alloys as GdCo (Au, Cu, Mo or Cr) prepared by sputtering. Their samples are richer in Co because Gd resputters along the deposit. The addition of a third element in GdCo layers has been made to obtain better materials in bubble devices.

These authors have noticed that chromium addition leads to a lower cobalt moment as a consequence of d-band filling. But, as reported in section 2.2.2.1, they conclude that Mo is a better element for bubble materials than GdCoX amorphous alloys. Schneider (1975) has investigated the magnetic properties of alloys such as GdCoCr prepared by rf bias sputtering to obtain bubble magnetic devices. He compares the results obtained with two samples with different Cr content, and he determined at 293 K the paramagnetic–ferrimagnetic transition. Samples with 22 at% Cr have a T_c of about 630 K and a T_{comp} of 120 K. By slight reduction of the Cr content (22 to 10 at%) magnetization increases by a factor of three. Treatments such as annealing or radiation damage do not change the magnetic anisotropy. These films are good getters for oxygen. An amount of 3 to 13 at% O_2 increases H_c by a factor of ten compared to oxygen-free films. However, numerous problems have not yet been solved, such as the dependence of $4\pi M_s$ on Cr content or the temperature dependence of the bubble domain related to properties such as K_u and bubble collapse field. The author concludes that such materials with low H_c in oxygen-free films will be attractive for bubble devices. But to our knowledge no further experiments have been done.

2.1.4. *Gadolinium, holmium, yttrium–(cobalt)–manganese alloys*

Lee and Heiman (1975a) have prepared, by thermal evaporation, some alloys such as Gd(and Ho)Mn_2 and Gd(and Ho)$_6Mn_{23}$. They observe that they are not magnetically ordered, and that the Mn–Mn exchange is reduced in amorphous film compared to crystalline ones.

McGuire et al. (1977) have prepared, by rf sputtering, a $Gd_{20}Mn_{80}$ sample. The magnetic and transport properties show that this sample has a negative Hall angle and a high resistivity ($\approx$250 $\mu\Omega$ cm). The authors establish a model to explain the Hall effect, and assigned a negative Hall angle close to $-1°$ to Mn.

McGuire and Taylor (1979) have studied GdMn, Gd(Co)Mn and YMn films deposited by two or three e-guns. Amorphous GdMn alloys are ferrimagnetic while GdMn compounds in the crystalline state are ferromagnetic. The magnetic moment of Mn depends on the concentration, but in contrast with both Fe and

Co, for which the magnetic moment increases with increasing content, the one for Mn decreases when the Mn content increases. As reported by McGuire et al. (1977) GdMn alloys have a behavior similar to GdNi alloys. McGuire and Taylor (1979) report the $4\pi M_s$ and T_c variations versus composition and the Hall effect and Hall resistivity as main data. They observe: a) the decrease of Mn moment in GdMn is difficult to interpret because of the decrease of T_c and the fact that magnetization saturation may not occur; b) the Gd and Mn or (CoMn) moments are antiparallel; c) T_c is relatively constant (205 K) versus at% Gd (from 10 to 22 at%, T_c increases from 100 to 205 K and remains constant up to 100 at%) and that induces strong Gd–Gd and Gd–Mn interactions and weaker negative Mn–Mn interactions; d) the Hall effect is large and proportional to the magnetization as required for an anomalous Hall effect and ρ_H/ρ is negative; this effect is difficult to analyze in GdCoMn alloys; in contrast a $Y_{19}Mn_{81}$ alloy presents a positive ρ_H/ρ, ratio, and the authors conclude to a possible magnetic moment for Y which contributes to ρ_H (perhaps induced by impurities?).

2.1.5. *Rare earth–iron systems*

2.1.5.1. *Binary amorphous alloys*

2.1.5.1.1. Introduction

Heiman et al. (1975a), Heiman and Lee (1975) and Heiman et al. (1976) have reported the magnetic properties of R(Gd to Lu)–Fe alloys in order to explain the dependence of the data on the concentration and on the R species. They have chiefly studied the variations of T_c and of the internal magnetic field (from Mössbauer data). They propose a mean-field theory model and show that three features are required to obtain agreement between calculations and data:
- the Fe spin must decrease with the R concentration;
- the decreasing rate must vary with the R species;
- the magnitude of the exchange constant, Fe–Fe and R–Fe, must increase with the R concentration.

The results are sensitive to the spin of the Fe atoms. T_c and H_{int} decrease from Gd to Lu, and the shape of the magnetization versus temperature curves can be reproduced for a wide range of composition and of R species (YFe—and also LuFe—present some peculiarities, see sections 2.1.5.1.2 and 10). In the amorphous state T_c is much lower than in the bulk. Mimura et al. (1978a) for (Gd to Er)–Fe alloys have obtained such results for T_c and T_{comp} measurements.

Before the analysis of results and theories for R–Fe alloys (R = Y, La, Nd, Gd to Lu) one must deal with a basic problem which depends on all the parameters involved in film fabrication. Obviously a slight change in the experimental procedures can induce drastic changes in the physico-chemical properties. So, Winters et al. (1969), who were the first authors, to our knowledge, to prepare Gd_3Fe_5 films by sputtering, concluded that "*film composition* is a *strong function* of vapor pressure, sputtering rate, atomic size, system geometry, sticking probabilities and sputtering coefficients". These authors also pointed to the problem of gas incorporation (Ar, O_2, ...) throughout the films; surprisingly, this parameter was only studied again some years afterwards.

2.1.5.1.2. Yttrium–iron alloys

Lee and Heiman (1975a), Heiman and Lee (1975, 1976) and Heiman and Kazama (1979) have reported the magnetic properties, for films prepared either by sputtering or by thermal evaporation. They conclude from T_c measurements, Mössbauer effect data and temperature dependence of the magnetization, that YFe alloys cannot be related to other heavy rare earth–Fe alloys. This is because they observe an anomalous and strange behavior for the recorded values. They show that Y can be compared in fact to Lu (see section 2.1.5.1.10) (these elements exhibit a lower H_{int}, as deduced from Mössbauer data). Heiman and Kazama (1979) have attributed to these alloys a spin-glass characteristic which makes it difficult to assign values to the usual magnetic properties. Other salient results show that T_c is not defined, that magnetization decreases with temperature, that T_{comp} does not exist, and that there are strong fluctuations in the Fe–Fe exchange coupling resulting from the absence of a well-defined ferromagnetic state. In addition they compared these data with results from crystalline state alloys. McGuire and Gambino (1978) have studied the transport properties of these alloys; they noted a positive Hall effect.

Chappert (1979) has studied the Mössbauer spectra of Y_xFe_{1-x} films prepared by ion sputtering. He shows the variations of the spectra at 1.6 K for various compositions and at 4.2 K for different applied longitudinal fields. His results show that Y_xFe_{1-x} do not exhibit a quadrupole interaction, the magnetic structure being governed by the Fe–Fe exchange force; there is no ferromagnetic saturation and the results can be derived from speromagnetic or asperomagnetic structures. "The magnetic structures are described in detail by Chappert (1979), Coey (1978) and Asomoza (1980). The reader should also consult the references listed by these authors. For each alloy these structures depend on the components. They differ, for instance, for YFe, GdCo and DyNi alloys. Some of the structures have been discussed but they are still not well defined." Biesterbos et al. (1977), for samples prepared by e-gun, report from T_c measurements and temperature dependence of the magnetization, that the alloys with high Fe content (>64 at%) are ferromagnetic, and those with low Fe content (<59 at%) are not ferromagnetic. At low temperature (<20 K) they observe a high value of H_c(≈800 Oe), which is believed to be due to the existence of narrow Bloch lines or by a network of small domains. They report that their samples with high Fe content show a thermomagnetic history effect as for spin-glasses of mictomagnets (ferrimagnetic clusters). Sylvester et al. (1978) study the magnetoelastic excitations (microwave resonance and phonon pulse-echo procedure) of YFe_2 films prepared by thermal evaporation (W crucibles). They compare the amorphous and crystalline states (the transition temperature is close to 870 K). They conclude that *crystalline* YFe_2 samples present a strong magnetoelastic coupling associated to the Fe ions. They think, from neutron measurements, that it will be possible that Y exhibits a finite magnetic moment (such a result should be due also to small magnetic impurities inside the materials) and conclude that the alloys may be ferrimagnetic (no conclusions were presented for the amorphous state). Biesterbos et al. (1976) have studied the variations of T_c and of mag-

netization as a function of the applied pressure for different compositions and temperatures. In a general way T_c and M_s decrease when pressure increases, and decrease when Fe content and temperature increase. The authors show that T_c is lower in amorphous (20–300 K) than in crystalline materials, like Y_2Fe_{17} for instance. They suggest that the magnetic properties are governed mainly by the itinerant 3d electrons.

2.1.5.1.3. Lanthanum–iron alloys

Heiman and Lee (1976) and Heiman and Kazama (1979) have studied LaFe samples by the same method and experimental procedures as used for the YFe alloys. They conclude that such materials have a well-defined T_c (determined from magnetization measurements) which increases from 275 to 300 K as the at% Fe increases, and that they are ferromagnetic with large exchange fluctuations. By comparison with other rare earths they have a larger H_{int} (Mössbauer effect). However, there are some difficulties to explain some results. T_c, measured by the Mössbauer effect, is about 200 K, and the ratio μ_B/Fe atom obtained by this method is larger ($\approx$30%) than the ratio μ_B/Fe atom obtained from magnetization. All their samples are easily saturated. Baghat et al. (1978) have reported some spin resonance measurements. They demonstrate that films as $La_{24}Fe_{76}$, prepared by coevaporation, show a ferromagnetic resonance, even at 300 K.

2.1.5.1.4. Neodymium–iron alloys

Heiman and Lee (1976), in their comparison of elements, have noticed that Nd_xFe_{1-x} alloys (Fe-rich samples) exhibit a high T_c (375 K) and a large H_{int}.

Taylor et al. (1978) made an extensive survey of the magnetic properties of Nd_xFe_{1-x} alloys ($0.08 \leq x \leq 0.71$) prepared by two e-guns. They report magnetization versus composition, temperature and perpendicular applied field; Hall angle versus composition; K_u versus temperature; H_c and T_c versus at% Nd; and Mössbauer spectra as a function of temperature. From these results the authors establish that the magnetic structure is sperimagnetic with Nd and Fe moments coupled in the same sense, that the iron subnetwork is not collinear, and that the Nd subnetwork is disordered. They report also from mean-field analysis that the exchange constant, as for Gd–Fe, is positive, indicating a ferromagnetic coupling. They compare their results to the ones obtained for GdFe and DyFe alloys.

2.1.5.1.5. Gadolinium–iron alloys

Several experimental procedures have been used to prepare GdFe amorphous films. By *sputtering* Winters et al. (1969) have deposited Gd_3Fe_5 samples (see subsection 2.1.5.1.1 for their conclusions). Chaudari et al. (1973a) have first studied the magnetic properties of such materials by *rf sputtering*. Afterwards other procedures have been used, such as ion beam, magnetron, dc, ac, diode or triode apparatus; the evaporation method can be done either by cosputtering or simple sputtering (buttons) onto various substrates at 293 K or heated, with or without bias voltage. By *e-gun*, Orehotsky and Schröder (1972) were the first to prepare GdFe amorphous samples by coevaporation. Other techniques, such as scanning e-gun and unique target, have been also used. By *thermal evaporation* (Joule effect) Mimura and Kobayashi (1975) and Lee and Heiman (1975) have

prepared by coevaporation technique amorphous films; Gasgnier and Caro (1977) have obtained such materials by evaporation of a Gd_xFe_y conglomerate onto glass substrates at 293 K. Numerous magnetic, magneto-optical and microstructural properties of these alloys have been described in detail in the literature. But the results are complex and often contradictory, the greatest problem being the origin of the magnetic perpendicular anisotropy.

2.1.5.1.5.1. The uniaxial magnetic anisotropy. The explanation of the origin of this parameter is still the subject of numerous polemics and discussions. Various models have been advanced in order to determine the origin:

- atomic pair ordering (involving dipolar and perpendicular interactions);
- short-range (or long-range) ordering;
- stress contributions;
- columnar microstructure;
- magnetoelastic effect of microstructure;
- oxygen contamination or adsorption;
- argon clustering.

It is not possible to choose one or other model, but it is clearly evident, as shown in sections 2.1.6.1, 2.2, 3.1 and 3.3, that the results are not easily comparable. The experimental procedures and the film compositions are so diverse that the samples can exhibit a wide range of different intrinsic properties. In this way, Eschenfelder (1980a,b) and Grundy (1980) call for new refined experiments in order to understand the mechanisms responsible for the uniaxial anisotropy. Two other problems, not yet clear, may also be considered: the change of sign of K_u and the comparison of the properties of GdFe and GdCo films.

As reported and detailed by Eschenfelder (1980b), it seems that atomic pair ordering and microstructural characteristics may be more fundamental. The mean-field theory calculation reported by Heiman et al. (1975a), Heiman et al. (1976) and Gangulee and Taylor (1976) for sputtered films, has shown, however, some limits to the explanation of the magnetic properties. Gangulee and Taylor (1976) and Taylor and Gangulee (1976) have noted, for films prepared by e-gun, that other mechanisms may be responsible for the uniaxial anisotropy. They suggest for instance long-range structural ordering, like Taylor (1976a) who suggests a large influence of this phenomenon. However, Roberts et al. (1977), using this technique, concluded that a pair ordering (dipolar interaction) mechanism was responsible. They add that K_u increases monotonically with increasing at% TM, and that like pairs induce perpendicular anisotropy, while unlike pairs induce in-plane anisotropy. They report sublattice magnetization from the molecular field analysis.

Zwingman et al. (1976), Katayama et al. (1977a, 1979), Mimura et al. (1978a), Tsunashima et al. (1979), Dirks and Leamy (1978), Leamy and Dirks (1979) and Takagi et al. (1979), have introduced the concept of stress contributions due to the substrate constraints. Katayama et al. (1977a) study K_u variations versus V_b, rf voltage, Ar pressure, focusing field and annealing at 570 K for a $Gd_{28}Fe_{72}$ specimen prepared by rf sputtering. They observe that K_u is positive (as for

thermally evaporated films) except for high V_b (> -50 V) where it is negative. Heiman et al. (1978) report a similar result for K_u versus V_b for a $Gd_{24}Fe_{76}$ sample, but with greater magnitude changes for the K_u values; their results are conflicting with those of Zwingman et al. (1976).

Katayama et al. (1977a, 1979) explain that the negative K_u is due to the resputtering effect of isolated Gd atoms. From annealing studies they found a rapid decrease of internal stress and atomic pair ordering, but the stress caused by the film–substrate mismatching remains. Their conclusions and those of Nishihara et al. (1978) about GdCo films are not the same (see section 2.1.6.1). Tsunashima et al. (1978), from a study of the magneto-elastic contribution, estimated it to be 10 to 30% of the total of the perpendicular anisotropy. They think that argon inclusions are an important contribution to the internal stress in sputtered films, because they observe that K_u is sensitive to V_b. But recently, Konishi et al. (1980), for films prepared by e-gun, have shown that their samples were sensitive to external stress but not affected by internal stress; they conclude that anisotropy has its origin mainly in other sources and suggest a magnetostriction effect. Gasgnier and Colliex (1978) have observed that thick films (more than 5000 Å) prepared by thermal evaporation from W crucibles are cracked and rolled up when they are deposited onto float-glass substrates. Such a phenomenon is not apparent when a thin chromium film is predeposited.

From X-ray scattering Cargill (1974), and from X-ray patterns Covault et al. (1976) support the short-range ordering model for $GdFe_2$ and $Gd_{26}Fe_{74}$ films prepared by sputtering. Covault et al. (1976) rule out stress and conclude a similarity between GdFe and GdCo films, whereas Heiman et al. (1978) show that the coupling of magnetization to any structural anisotropy for GdFe evaporated or sputtered films, is the inverse of that in GdCo. Besides, they report that a correlation between X-ray diffraction profiles and K_u is unfortunately coincident and misleading.

Another problem has been reported as the influence of oxygen on the uniaxial anisotropy for thermally evaporated films. Schneider and Brunsch (1978) and Brunsch and Schneider (1978) have shown a decrease of K_u by O_2 contamination, explained by the increasing amount of non-magnetic material, i.e., the inclusions of iron or gadolinium amorphous oxides. The films behave as a "sponge-like" configuration with small magnetic volumes. Shinoda et al. (1979) and Tsunashima et al. (1980) report that adsorbed O_2 destroys perpendicular anisotropy. Brunsch and Schneider (1978) report also film contamination by H_2 and N_2 gases. They observe for K_u a similar dependence for these gases as for O_2. Lastly, the annealing effect has been the object of some studies. Katayama et al. (1977a) report that GdFe films, heated at 570 K for four hours, do not change, K_u remaining nearly constant and positive. Heiman et al. (1978), for sputtered and evaporated (e-gun) films, and Gangulee and Taylor (1978), for evaporated films (e-gun), note a K_u decrease by a factor of two. Such a phenomenon has been observed by Katayama et al. (1978) after annealing at 420, 470 and 520 K.

From all these results and from all these models, one must conclude that few authors have really confronted the basic problem, i.e. the experimental pro-

cedure, as reported by Grundy (1980) and Heiman et al. (1978). So, for GdFe, GdCo, GdCoMo, GdCoCu and GdCoAu alloys, Heiman et al. (1978) give the following pertinent conclusions from their numerous data: "The fundamental mechanisms responsible for K_u, and the effects of annealing are not understood. In fact, it appears that none of the models advanced thus far are in agreement with all the data. One is tempted to suggest that more than one mechanism is responsible for K_u . . . . We suggest that any mechanism (or mechanisms) which purports to explain the origin of K_u in R–TM alloys must be consistent with the results presented in this paper." In the following sections this complex problem will be also pointed out. Another problem which has been scarcely studied concerns the chemical analysis of the films. Indeed, if some papers mentioned the percent ratio of gases throughout the samples, many others disregard this parameter. It is now known that rare earths are excellent getters for hydrogen (Gasgnier, 1980) and that transition metals are rapidly oxidized. On the other hand, the film–substrate interface is also rarely studied and possible compound nucleation with adsorbed gases at the substrate surface cannot be neglected—Wandelt et al. (1977), Brunsch and Schneider (1978) and Schneider and Brunsch (1978) have all commented upon this subject.

2.1.5.1.5.2. Other magnetic properties. Chaudari et al. (1973a) have first reported some magnetic properties of $Gd_{1-x}Fe_x$ alloys prepared by *rf sputtering*. They study the dependence on thickness and the characteristic length (obtained from stripwidth and thickness measurements). For thicknesses of more than 2000 Å the films present a perpendicular anisotropy and for smaller thicknesses it is in-plane. Later, Heiman et al. (1975a), Heiman et al. (1976, 1978), Mimura et al. (1976a,b,c 1978b,c), Imamura et al. (1976a), Zwingman et al. (1976), McGuire et al. (1977), Katayama et al. (1977a, 1978, 1979), Tsumashima et al. (1978), Takagi et al. (1979) and Bochkarev et al. (1979), have reported numerous data for the main properties of such materials like: K_u, $4\pi M_s$, H_c, H_k, T_c, T_{comp}, w_s, σ_w, l, A and magneto-elastic constants ... versus composition, temperature, bias voltage, saturation magnetization .... These works present comparisons with various other binary systems [(Tb to Lu)Fe, Gd(Co or Ni) and Gd(Cu or Au) alloys] or ternary systems [GdCo(Fe or Ni), GdCo(Mo, Cu or Au) alloys] and other experimental procedures such as e-gun and thermal evaporation. As for K_u, the results and the models described are different from one paper to another, and the explanation of the magnetic properties are again the subject of discussions and polemics.

Magnetic configurations such as bubble, stripe and spark-like domains have been exhibited by Imamura et al. (1975, 1976a, 1977), Mimura et al. (1976a,b,c, 1978a,b) and Katayama et al. (1977a, 1978). Mimura et al. (1976c) have studied the static bubble properties for device applications. Katayama et al. (1977a, 1978) show the effect of annealing at 520 K and of film–substrate mismatching upon stripe configuration changes. Imamura et al. (1976b, 1977) and Mimura et al. (1976b, 1978) have shown that GdFe films can be used for thermomagnetic recording (contact printing with various magnetic materials and thermomagnetic writing by use of a laser). They discuss their results in order to obtain the best

values of T_c, H_c, θ_k and thickness. So, for possible applications of films with high density bits, they report that the magnetic properties must be characterized by a small demagnetizing field, a low T_c and a large H_c. Addition of yttrium seems to enhance the last two parameters (Mimura et al., 1978b). Biesterbos (1979) has reviewed the main properties (advantages and disadvantages) and the principal thermomagnetic techniques (writing, reading and erase process) for sputtered and evaporated films.

Other magneto-optic properties such as the Kerr effect were studied by Imamura and Mimura (1976) and Mimura et al. (1976b, 1978c). They discuss the variations of the Kerr rotation angle and of the Kerr hysteresis loop versus the film composition and the iron sublattice magnetization. Shirakawa et al. (1976) show by the polar Kerr effect that the sign of the hysteresis loops is reversed $(+\rightarrow -)$ as the temperature increases; besides, the sign of the polar Kerr effect coefficient of iron above T_{comp} is also negative (the TM moment is therefore dominant). The same conclusions are obtained for R–Co alloys. On the other hand, Imamura et al. (1975, 1976a), and Mimura et al. (1976a, 1978a) have studied the M–H hysteresis loops as a function of film composition and of magnetizing field; and as a function of applied field, which shows the mechanism of the reversed domain magnetic patterns.

Shikarawa et al. (1976), Mimura et al. (1976b) and Onishi et al. (1979) have reported the EHE of rf sputtered films. Shikarawa et al. (1976) report a change of polarity $(-\rightarrow +)$ at T_{comp} with increasing temperature and note that the sign of the EHE coefficient of Fe is positive, suggesting the contribution of Fe to EHE. For R–Co alloys they observe the same effect, but it is reversed with respect to R–Ni alloys. Mimura et al. (1976b) find an inverse polarity for M–H curves and EHE curves for a film with a dominant Gd moment. They also report Hall voltage and saturation magnetization versus film composition; the Hall voltage is reversed as the compensation (26 at% Gd). V_H becomes negative and saturation magnetization is minimum (close to 0) for high Gd contents. EHE is similar for GdCo films but drastically different for GdNi samples. Onishi et al. (1979) have used EHE for a new apparatus used to measure the velocity of a straight domain wall (when a domain wall is parallel to the current the Hall voltage increases linearly with wall position). They note that the geometry of the substrate affects the positional dependence of the Hall voltage. McGuire et al. (1977) have studied galvanomagnetic effects (spontaneous Hall effect, magnetization, ρ, ρ_H and ρ_H/ρ data) for $Gd_{20}Fe_{80}$ films prepared by sputtering or evaporation. They report ρ_H as a function of applied field for Fe-rich and Gd-rich films and the $|\rho_H/\rho|$ (%) dependence on the atomic fraction of Fe in Gd. For Fe-rich samples the contribution of Fe is 6%, whereas it is only 2% for Gd-rich specimens. These authors offer a model to explain the Hall effect, and conclude that the Gd and Fe moments are antiparallel, and the Hall effect is negative for Gd and positive for Fe.

Another procedure, such as Mössbauer effect measurements, has been used to determine the magnetic properties. Heiman and Lee (1975) presented a Mössbauer spectrum at 300 K for a $Gd_{23}Fe_{77}$ film prepared by evaporation and which exhibited a uniaxial magnetic anisotropy. The spectrum differs in shape and in

peak intensity from the one reported by Katayama et al. (1979) at 292 K, for a film prepared by rf sputtering, but with no reported composition. Heiman and Lee (1975) deduce the H_{int} and show that it is higher than for the other heavy rare earths. Katayama et al. (1979) deduce the average hyperfine field and observe an anomalous increase of this value which they attribute to a local inhomogeneity in the Fe concentration in the film as suggested by Nishihara et al. (1978). Heiman et al. (1975a) have also reported Mössbauer spectra (see section 2.1.5.1.1).

Orehotsky and Schröder (1972) were the first to study amorphous films prepared by *e-gun* evaporation. For numerous alloys (from pure Gd and pure Fe) they report the change of the magnetic moment versus the applied field, composition and temperature. It decreases from 1600–1700 emu cm^{-3} at 4.2 K to 10–100 emu cm^{-3} at 296 K for a Gd-rich film, and from 500–800 emu cm^{-3} at 4.2 K to 350–500 emu cm^{-3} at 295 K for a Fe-rich film, but increases with increasing applied field. From saturation magnetization measurements, they remark that Gd-rich films do not saturate in fields of 18 000 Oe, this phenomenon being attributed to the perpendicular anisotropy. They conclude that their alloys are ferrimagnetic with an antiferromagnetic coupling, and that the amorphous and the crystalline states appear to have the same magnetization values. Besides, they note from their experimental procedure that deposition procedures must be done carefully because of the likely contamination by *hydrogen gettering* and the formation of gadolinium hydride as a consequence. But, later on, no other papers reported this phenomenon. The comparison of amorphous and crystalline states was undertaken more recently by Vittoria et al. (1978) for $GdFe_2$ materials. They have used the e-gun procedure in order to minimize the imperfection due to thermal evaporation. They conclude that the magnetic state is quite different in the amorphous and crystalline states, because it appears that a reduction of magnetization occurs due to a reduction in crystal density. Besides, the net magnetic moments of Gd and Fe appear to remain constant in the two states. They observe a behavior of the magnetic moment for amorphous films identical to the one reported by Orehotsky and Schröder (1972). Their studies of amorphous, mixed amorphous–crystalline and crystalline films from FMR measurements, permit the determination at 5 and 293 K of sublattice magnetizations (similar in the amorphous and the crystalline states); the g-value, the FMR linewidth, the A/M value and the magnetic damping parameter are higher (by a factor of two) for crystalline films; the FMR linewidth shows broadening inhomogeneities induced by variations in the local magnetic anisotropy.

Taylor (1976a), Taylor and Gangulee (1976) and Gangulee and Taylor (1978) have studied a) room-temperature saturation magnetization ($4\pi M_s = 0$, for 26 at% Gd) and saturation magnetization versus temperature ($4\pi M_s$ is minimum at about 320 K for 26 at% Gd; a second minimum is observed at the crystallisation temperature at about 500 K); b) H_k and K_u variations with Gd content (H_k is maximum at the compensation point (more 9000 Oe), K_u decreases slowly as Gd content and temperature increase); c) Fe spin and Gd–Fe exchange energy versus Gd content. They have observed stripe domains

and show that films with thicknesses of more than 500 Å exhibit a perpendicular anisotropy. They think that Gd–Fe pairs contribute to the in-plane anisotropy and Fe–Fe and Gd–Gd pairs contribute to the perpendicular anisotropy, the latter being dominant. By comparison with Gd–Co alloys, Gangulee and Taylor (1978) conclude that Gd–Fe samples are better materials for bubble domain devices. Other properties such as $4\pi M_0$, and l values versus the concentration were measured by Roberts et al. (1977). Urner-Wille et al. (1978) reported Kerr-effect enhancement of Gd–Fe films (Fe-rich alloys) with CeO_2 coatings. They observed that the Kerr rotation increases as the reflectivity, for normal incidence of linearly polarized light, decreases. They discuss the efficiency parameter which is proportional to the sine square of the Kerr rotation. Urner-Wille and Witter (1979), while discussing magneto-optic storage materials, report that the most important parameter is the film homogeneity. They used a rotating substrate. They demonstrate the existence of a compensation point switching in a homogeneous specimen, and writing, erase and reading processes are investigated from an analysis of the magneto-optical Kerr signal. Prinz et al. (1979, 1980) have studied the complex index of refraction and the complex magneto-optical coefficient by ellipsometer measurements at 293 K for various RFe and RCo films. For GdFe specimens they observe that the second coefficient varies smoothly with composition.

By *thermal coevaporation*, Lee and Heiman (1975) report, from magneto-optic measurements (polar Faraday and Kerr rotation), the determination of T_c, T_{comp} and H_c. For various GdFe alloys, they show that T_c is lower for amorphous than for crystalline samples, that T_{comp} decreases with increasing Fe content, that the Gd–Gd and/or the Gd–Fe exchange is reduced in amorphous materials, and that the orbital moment of Gd strongly affects H_c. They compare their results to several alloys and compounds such as: (Gd, Ho)Mn; (Y, Tb, Ho)Fe; (Y, Gd, Tb, Ho)Co and (Gd, Ho)Ni. By the same method of preparation, Lubitz et al. (1976b) have obtained $GdFe_2$ samples studied by FMR and with a vibrating sample magnetometer in the temperature range 90–500 K at 9.23 GHz. They report variations of $4\pi M$, $2K_u/M$, g-value and linewidth versus the temperature. They conclude that their samples are inhomogeneous. This has also been observed by Vittoria et al. (1976) for $Gd_{1-x}Fe_x$ films. They used higher frequencies, and show that for Fe-rich samples (>65 at%) the Fe–Fe exchange predominates, and suggest that for lower concentrations the materials are disordered ferromagnets. Lubitz et al. (1976b) and Vittoria et al. (1976) conclude that the temperature dependence of the linewidth is proportional to frequency in agreement with the Landau–Lifshitz mechanism (damping parameter). Imamura and Kobayashi (1975) have shown that their films exhibit a perpendicular anisotropy for thicknesses of more than 500 Å. They report simple M–H loops and M_s variations versus Gd content, and magnetic domain patterns. Amatsu et al. (1977), through the polar Kerr effect, have observed anomalous hysteresis loops (presence of outer loops in addition to the usual ones) and domains. They explain such a behavior and the relation between the effective anisotropy field and the coercive field by the double-layer model, assuming the compensation

wall is inclined with respect to the axis normal to the film plane. They present a model which shows the magnetization and spin signs and conclude it is related to the imperfections caused by the evaporation method. The same model has been reported by Imamura and Kobayashi (1975). Tagirov and Glazer (1978) have reported, for films prepared from "explosive evaporation" of powders, the volume and surface hysteresis loops at different temperatures. They propose a remagnetized multi-layer model with exchange interaction between layers, and suggest that their specimens exhibit three main layers: surface top, volume and surface bottom. Buravikhin et al. (1976) have studied the magnetic domains as a function of the annealing process. Close to the compensation point a few structure variations occur, which vanish at the compensation point (470 K), and above it the initial magnetic axis rotates by $\pi/2$ and new domains appear. At 570 K the films become polycrystalline, with formation of $GdFe_5$ at 670 K, indicating that the samples are Fe-rich.

Bochkarev et al. (1976a) have evaluated the best magnetic properties needed to obtain optimal materials for thermomagnetic applications. To do this they determined the plane polarization angle rotation of the incident light, the absorption coefficient and the magneto-optic quality factor which was found to be the larger at 22 at% Gd. They observe a maximum for H_c at 320 K for 26 at% Gd.

Some transport properties (EHE, ρ, ρ_H) have been reported by Gasgnier and Colliex (1978) and Gasgnier et al. (1979). At 293 K some samples prepared from a GdFe agglomerate exhibit a EHE with a square shape. In a study of the temperature dependence they found that the loops tilt up at 256 K over a temperature range of 1 K. Such samples, as shown by Bitter patterns, have nearly regular stripe domains of about 1 μm, perhaps with bubble nucleation. Przyluski et al. (1979) have studied the effect of composition and temperature on the resistance, the resistivity, the stability with temperature of resistance and the microhardness of thin films. They observe a maximum of the resistivity for films with 35 at% Fe, and a maximum of the TCR (temperature coefficient of resistance), which change sign ($- \rightarrow +$) at about 56 at% Fe. They suggest that samples with a TCR of zero can be used for resistors (films of high stability). The hardness of their samples increased with increasing Fe content. Few results have been reported so far in this field of investigation. Orehotsky and Schröder (1972) observe that the space "in-situ" resistance presents no anomalies with thermal cycling between 77 and 298 K. This indicates that films deposited at 77 K remain structurally stable when heated to 293 K. Brunsch and Schneider (1978) and Schneider and Brunsch (1978) report a strong increase of resistivity with increasing O_2, H_2 and N_2 partial pressures.

2.1.5.1.5.3. Characterization: microstructure and chemical analysis. Dirks and Gijsbers (1979a,b) have shown, according to the conclusions of Leamy and Dirks (1978), that in particular GdFe and in general RFe and RCo *evaporated* thin films deposited on NaCl substrates exhibit a *columnar microstructure.* The films consist of columnar regions, having their axis nearly perpendicular to the substrate, with a subnetwork of material possessing a lower density. Gill et al. (1978), for ion-beam *sputtered* films deposited on carbon-coated copper grids,

observed, by high-resolution dark field electron microscopy, coherent scattering regions which are interpreted as *clusters* of atoms with random positions. The films exhibit an in-plane magnetization with no long-period structures such as compositional fluctuations or columnar growth. However, their samples are inhomogeneous in thickness of composition. In electron diffraction patterns two diffuse halos appear which represent amorphous phase separation which comes from Gd and Fe ion (or atom) resputtering. The conclusion of these two papers are quite different, but the two experimental procedures are also different and it is difficult to make a reasonable comparison.

Gill et al. (1978) have deduced from their AES spectra that their samples are inhomogeneous. The inhomogeneities come from gas incorporation (O_2, Ar, H_2), from substrates (C, Cu) and from surface roughening. AES depth profile shows a large O_2 contamination at the free surface of the film, and quite different profiles for rf sputtered and in-situ ion-beam sputtered samples; the last one shows strong variations in the Gd/Fe concentration ratio. Gasgnier et al. (1979), for films prepared by scanning e-gun, have observed, through electron energy loss spectroscopy measurements, wide compositional variations for neighboring areas (below 1 μm in extension). This method has allowed Gasgnier and Colliex (1978) and Gasgnier et al. (1979) to determine the film composition. The plasmon loss profile, of the energy loss spectra, shift and change from 15 eV for a Gd-rich film to 23 eV for a Fe-rich sample: therefore the effective number of valence electrons includes 3d electrons and a small fraction of 4f electrons. The core-loss signals of Gd and Fe are useful to estimate the compositions. This permits the derivation of the thickness with an accuracy of $\pm 10\%$. The electron diffraction patterns for Gd- or Fe-rich films always exhibit two diffuse halos as shown by Gasgnier et al. (1978) and Gasgnier (1981). This can be interpreted by an amorphous phase separation as explained by Gill et al. (1978).

In terms of characterization of the films XPS studies have been done for sputtered and evaporated (e-gun) samples. Guntheroldt and Shevchik (1976) have made XPS spectra for numerous compositions. They found evidence for the existence of a Gd$\rightarrow$Fe and of a Fe (s$\rightarrow$d) charge transfer. The Gd$\rightarrow$Fe charge transfer (smaller than the one for the crystalline state) increases with decreasing Fe concentration. This assertion has been challenged by Wandelt et al. (1977) who have shown, from XPS measurements on cosputtered films, that the samples of Güntheroldt and Shevchik (1976) were a mixture of Gd_2O_3 and pure Fe. In fact, as demonstrated by Terzieff and Lee (1979), for films prepared by e-gun, the charge transfer, if it exists at all, must be smaller than one electron per Gd atom. From their XPS binding energy values obtained as a function of the Fe content, they conclude that the core levels of amorphous GdFe are not sensitive to a change in the chemical environment. They suggest for the charge transfer the possibility of an intraband mechanism. Katayama et al. (1978), for sputtered films, have not observed shifts of the 4f band during annealing up to 510 K, but they do not present spectra, and their results cannot be compared to the above-mentioned ones.

The problem of the contamination is important. Brunsch and Schneider (1978)

and Schneider and Brunsch (1978) have studied the influence of the adsorption of O_2, H_2 and N_2 gases on the magnetic properties. They conclude that their samples have a nearly *identical sensitivity* to a gas model of a film as a "sponge tissue" due to O_2 contamination, which can explain the decrease of $4\pi M_s$, K_u and H_c, the increase of ρ and the occurrence of superparamagnetism above a critical O_2 content. Such GdFe porous films have been reported by Gill and Judy (1979) from their studies of the atomic diffusion by AES, for rf sputtered samples overlayered by a polycrystalline Co film. (The atomic diffusion is induced by annealing.) They conclude that GdFe films show a liquid-like phase behavior and form a porous matrix. Earlier, Gill et al. (1978) had observed the formation of Gd_2O_3, FeO, ... for O_2 contaminated samples. Wandelt et al. (1977) show that the films are overlayered with Gd_2O_3, Fe_3O_4 and Fe_2O_3 compounds when they are exposed to the air. Dirks and Gijsbers (1979a,b) have heated their films in a first state to about 740 K and show the formation of Gd_2O_3 and of α-Fe. The initial electron diffraction pattern, which is characterized by one halo, evolves and changes to two distinct rings. The structure does not change after annealing up to 970–1120 K, and above this temperature there is a sudden recrystallisation, with the disappearance of the columnar microstructure and of the oxide network. Crystallization studies at some other temperatures have been reported by Gill and Judy (1979) who observe at 570 K a microcrystallization of Fe in an amorphous matrix, and by Gangulee and Taylor (1978) who note that GdFe alloys crystallize at about 500–530 K before reaching T_c which, consequently, cannot be measured.

Remark. For bulk alloys, Buschow and van Diepen (1976), Buschow (1976, 1977b) and Buschow and Dirks (1980) have reported the influence of hydrogen on the magnetic properties and the crystallization behaviour of several RFe alloys (R = Y, Ce, Sm, Gd, Tb, Ho and Er).

2.1.5.1.6. Terbium–iron alloys

The main magnetic properties for materials such as Tb_xFe_{1-x}, prepared by sputtering, were reported by Mimura and Imamura (1976a) and Mimura et al. (1978a). They have studied in particular the Curie temperature, coercivity and domain patterns in view of thermomagnetic recording applications using the Curie point. They note that the low T_c ($\approx$390 K) and the large H_c (1–5 kOe) are potentially appealing for such applications. Mimura et al. (1976d,e) have shown domain configurations and bits written with different laser powers on films of various concentrations and having a good perpendicular anisotropy. In the same way Mimura et al. (1978b) have obtained high resolution visual display of magnetic information recorded on magnetic tape or disc by thermomagnetic contact printing. They give magneto-optical properties (T_c, H_c, θ_K, R_0) versus composition. They report the readout signal-to-noise ratio as a function of the incident light: it is maximum for Tb(and Dy)Fe alloys as compared with other RFe systems. They discuss their values and interpret the reduction of θ_K in terms of the decrease.of the Fe sublattice magnetization with increasing temperature in the readout region. Matsushita et al. (1976, 1977), Sunago et al. (1976) and Hishii et al. (1977) have also studied these properties. T_c is a sensitive

parameter. Heiman et al. (1975a) have reported that its value is much lower in the amorphous state than in the crystalline state (section 2.1.5.1.1). Lee and Heiman (1975a), for $TbFe_2$ amorphous films, report a value for T_c equal to the one of Mimura et al. (1976d), that is 390 K. However, Matsushita et al. (1976) give a value of 310 K for a $Tb_{37}Fe_{63}$ alloy, Sunago et al. (1976) report a value of 350 K.

According to Matsushita et al. (1977) thermal annealing reduces M_s, H_c and T_c. T_c decreases by 65% by heating to 470 K ($T_c \approx 370$ K). Such a reduction is suitable for thermomagnetic writing applications. Printer patterns from magnetic tape and a plated digital computer disc are presented.

Chen et al. (1980), for samples such as Tb_xFe_{1-x} ($0.16 < x < 0.35$), prepared by rf cosputtering, with a perpendicular uniaxial anisotropy, have examined the magneto-optic properties for memory applications. They observe that magnetization and coercivity change dramatically with target composition and thickness. At the compensation composition (22.3 at% Tb), such materials present a high hysteresis loop, squareness and a coercivity appropriate for magneto-optic recording. Under a laser beam, the films have a high writing sensitivity and a high reading contrast for bit sizes of 1 μm.

Ohashi et al. (1979, 1980) have shown that samples such as $Tb_{17-27}Fe_{83-73}$, prepared by rf sputtering at 293 K, have a compensation point at 21 at% Tb. They study, through Kerr effect, the after-effect due to the slow coefficient, the applied field and the temperature. Prinz et al. (1979, 1980), for films prepared by e-gun coevaporation, have reported some magneto-optic properties such as $4\pi M_s$, complex magneto-optic coefficient and complex index of refraction. They show that the complex magneto-optic coefficient and $4\pi M_s$ vary so strongly for TbFe alloys that they are difficult to analyse.

Forester et al. (1978) and Takagi et al. (1979) have studied the magnetostriction of films prepared either by e-gun or by rf sputtering. Forester et al. (1978) report that their samples are magnetically hard and that magnetostriction varies with the composition point (22 at% Tb), and reaches a maximum for 40 at% Tb as in bulk material. This magnetostriction is relatively large and the authors conclude that the terbium single-ion magnetostriction mechanism, active in crystalline materials, always plays a strong role in the amorphous ones. Takagi et al. (1979) have determined the magnetoelastic coupling constant, the saturation magnetostriction and the saturation versus composition. They observe a high magnetoelastic coupling constant which reaches a maximum for 32 at% Tb. This composition is near $TbFe_2$ and the value obtained in the amorphous state is smaller than in the crystalline one. Yamaguchi et al. (1980) have used this large magnetostriction coupled to the large stiffened elastic constant effect for the propagation of surface acoustic waves in a delay line consisting of amorphous $TbFe_2$ films deposited onto $LiNbO_3$ substrates. The samples are heated at 510 K in order to relieve internal stresses. They observe a large surface acoustic wave velocity change in the delay line. They conclude that such systems may be used for variable delay lines and tunable surface acoustic wave oscillators. They also show that for $(HoTbDy)Fe_2$ films the calculations agree with experimental results. Lubitz et al. (1976b) have made FMR measurements on $TbFe_2$ amor-

phous films prepared by thermal evaporation; at low temperature they observe large linewidths, which suggest inhomogeneous broadening with magnetostrictive origin.

Shirakawa et al. (1976), Mimura et al. (1976b) and Onishi et al. (1979) show that TbFe films prepared by rf sputtering present an extraordinary Hall effect. They report the hysteresis loops, the Hall voltage and the saturation magnetization versus temperature and composition. Heiman and Lee (1975, 1976) and Heiman and Kazama (1979) show the variations versus Fe content, of the internal magnetic field (Mössbauer effect). Biesterbos et al. (1979) have investigated the influence of oxygen on the microstructure and magnetic properties of films prepared by vapor deposition. By electron microscopy they observe a columnar microstructure in the Fe-rich area, and the formation of Tb_2O_3 in O_2 atmosphere. They report the T_c, $4\pi M_s$ and H_c variations with partial O_2 pressures. For high O_2 contents T_c and H_c decrease rapidly, while $4\pi M_s$ increases abruptly. They also study the dependence of T_c and T_{comp} on O_2 pressure and Fe content. They explain the variation by assuming an Fe enrichment of the amorphous matrix, which is also demonstrated by the change from perpendicular to in-plane magnetization when partial O_2 pressures increase. (Magnetic domains are described in section 2.3.) Dirks and Gijsbers (1979a,b) have studied the crystallization behavior of amorphous films; they report identical electron microscope observations as given by Biesterbos et al. (1979).

2.1.5.1.7. Dysprosium–iron alloys

In a general manner DyFe alloys present characteristics close to the ones for TbFe. They were reported by Mimura et al. (1976b,d,e, 1977, 1978a,b,c) and Mimura and Imamura (1976b), for magnetic properties and Curie point writing applications; by Heiman et al. (1975a) for T_c and T_{comp} variations versus Fe content; by Heiman and Lee (1975) from H_{int} measurements; by Lubitz et al. (1976b) from FMR measurements which indicate that $DyFe_2$ alloys are ordered well above 293 K and exhibit little temperature dependence; by Dirks and Gijsbers (1979a,b) for microstructure and the amorphous–crystalline transition by heating. Chappert (1979) has reported Mössbauer spectra at 4.2 K for amorphous $Dy_{21}Fe_{79}$ and crystalline $DyFe_3$ films for both ^{161}Dy and ^{57}Fe resonances. He reports ^{161}Dy hyperfine field values and Fe saturation moments for $DyFe_3$ alloys; he concludes that such materials are sperimagnetic, with Fe moments scattered in a cone. Katayama et al. (1979) studied Mössbauer spectra and hyperfine field distributions at ^{57}Fe resonance at 293 K for films with positive and negative K_u. They show that the magnetic properties of their samples prepared by rf sputtering with and without V_b vary and they attribute such variations to local inhomogeneity of the Fe content. They think that Fe moments are distributed over all directions within a narrow cone. On the other hand, they study the variations of K_u versus V_b: for a V_b increase, K_u decreases and becomes negative near $V_b = -70$ V. The authors explain this phenomenon as due to microscopic changes in atomic arrangements caused by the resputtering effect of isolated Dy atoms.

2.1.5.1.8. Holmium–iron alloys

Heiman and Lee (1974) have studied HoFe films with uniaxial anisotropy prepared by thermal evaporation. They report the variations of T_c and T_{comp} versus Fe concentration. With increasing Fe content T_c increases from 120 to 300 K, while T_{comp} decreases. Compared to the crystalline state these parameters are drastically lowered in the amorphous state, and the T_c increase with Fe content decreases in the crystalline state. This can be explained by a charge-transfer model. These results have been also obtained by Heiman and Lee (1975a), Heiman et al. (1975a), Lee and Heiman (1975a,b) and Mimura et al. (1978a). Lee and Heiman (1975a) have reported the temperature dependence of the polar Kerr and Faraday rotation, they show the hysteresis loops, and concluded that such materials will be interesting for bubble devices. A sample as $Ho_{33}Fe_{67}$ has a low T_c (270 K). Heiman and Lee (1975) have reported internal magnetic field measurements. Lubitz et al. (1976b) report, from FMR measurements, the g-values of $HoFe_2$ alloy; this parameter increases at low temperature which induces an increase of the Ho moment; as for $TbFe_2$ this alloy presents large linewidths at low temperature. They report Landau–Lifshitz relaxation rates near 293 K and observe additional contributions which decrease with annealing: for $HoFe_2$ they are important and may be the result of non-uniform strains which couple to the magnetostriction.

2.1.5.1.9. Erbium–iron alloys

Mimura et al. (1978a) have shown the variations of T_c and T_{comp} versus the concentrations. Their samples have a large magnetization.

2.1.5.1.10. Lutetium–iron alloys

To our knowledge no systematic data have been reported for Tm and Yb alloys (see section 2.1.5.1.1). The $Lu_{1-x}Fe_x$ alloys, as mentioned above, have been studied in general for comparison with YFe or LaFe systems. Heiman and Lee (1976) present the T_c variations versus concentration. They observe strange properties as for YFe. Heiman and Kazama (1979) report that materials such as YFe have spin-glass characteristics. As compared to YFe, they state that the magnetization, T_c and H_{hf} (magnetic hyperfine field) are slightly lower and that exchange fluctuations are larger in LuFe alloys. Heiman and Lee (1975) show that this material presents a lower H_{int}, a fact which confirms their theory. As for YFe, Bhagat et al. (1978) discuss the results of Heiman and Lee (1976) and report identical results from spin resonance measurements as for YFe, i.e. a ferromagnetic resonance even at 300 K.

2.1.5.2. *Ternary amorphous alloys*

2.1.5.2.1. Gadolinium–(cobalt)–iron systems

In the course of a study of the anisotropy of Gd(Fe or Co) alloys, prepared either by sputtering or by evaporation, Taylor (1976b) reports some results relative to $Gd_xFe_yCo_z$ alloys prepared by evaporation. In such materials K_u, H_k and $4\pi M_s$ vary according to the Gd content and the value of the Co/Fe ratio. For instance, for 24 at% Gd, $4\pi M_s$ increases as the Co/Fe ratio increases from 0 to 1, but K_u and H_k decrease. Thus, H_k decreases from 6000 to 1000 Oe. With regard to the dependence on the x, z and z/y values, he shows that for $x > 21$ and $z = 45$

the anisotropy is in-plane (strong negative influence of GdCo (unlike pairs) on the perpendicular anisotropy) and for $x = 8$ the anisotropy remains perpendicular (negative influence of Fe–Co pairs on the perpendicular anisotropy). From his results he concludes the possibility of preferential atomic ordering of like species in the growth direction during deposition because like pairs (Fe–Fe, Gd–Gd, . . .) contribute to the perpendicular anisotropy.

Taylor and Gangulee (1977) have prepared alloys such as $Gd_x(Fe_{1-y}Co_y)_{1-x}$ by co-evaporation from three e-guns. They describe their specimens as pseudo-binary GdFe–GdCo alloy systems. They report essentially the variations of the K_u dependence with the concentration of each element and also the concentration dependences of $4\pi M_s$ and H_k. They explain the anisotropy data by a dipolar equation which involves the contribution of the dipolar coupling constant for each pair and the sublattice magnetizations. They attribute the anisotropy to pair ordering in which pairs like Gd–Co and Gd–Fe contribute to the in-plane anisotropy and pairs like Gd–Gd and TM–TM contribute to the perpendicular anisotropy, the Fe–Co pairs being the strongest contributor. (The TM–TM pairs contribute in the same sense to the anisotropy in FeCo polycrystalline alloys.) Chen et al. (1978) have studied such alloys, but they have used bias sputtering to prepare their samples. They report the effects of changing the Co and Fe amounts of magnetic properties. Mainly they observe that K_u is quite insensitive to the Fe and Co content, and conclude that this is not a determining factor in the mechanism giving rise to K_u. They contradict the above-mentioned results of Taylor and Gangulee (1977) and claim that the K_u variation is due to mechanisms in the deposition process. From their data they observe that increasing the Fe content reduces the exchange between the rare earth and the transition metal sublattices and shifts the compensation point towards increased Gd content. McGuire et al. (1977) have reported the Hall resistivity ratio for two samples, $Gd_{25}Fe_{60}Co_{15}$ and $Gd_{22}Fe_{30}Co_{48}$; these ratios are positive and decrease when the Co content increases.

2.1.5.2.2. Gadolinium–(nickel)–iron systems

McGuire et al. (1976) have reported some magnetic and transport properties for alloys such as $Gd_{18}Fe_{82-x}Ni_x$ ($12 < x < 68$) prepared by co-evaporation. They study the magnetization and the Hall resistivity versus temperature and composition and the specific resistivity versus temperature. As for Gd_xNi_{1-x} alloys they conclude that the sign of the Hall resistivity for Ni is negative (McGuire et al., 1977). They show that the Ni and Fe moments are parallel in the FeNi sublattice and that the Ni moment goes to zero as the Fe concentration goes to zero. Compared to the crystalline form Gd and Ni have a negative spontaneous Hall resistivity, whereas the one for Fe is positive.

2.1.5.2.3. Gadolinium–(yttrium)–iron systems

Mimura et al. (1978c) have prepared, by rf co-sputtering, some samples with various Y contents. To obtain magneto-optical storage media they have studied the change in H_k and T_c in GdFe films by Y addition. The GdYFe films have a perpendicular anisotropy with a rectangular hysteresis loop. T_c decreases and H_k increases with increasing Y content. The low T_c and the high H_k permitted them to write stable small bits ($\approx 6\ \mu m$) with a laser beam.

2.1.5.2.4. Gadolinium–(neodymium)–iron systems

Heiman et al. (1979) have studied such alloys as $(Gd_{1-y}Nd_y)_{1-x}Fe_x$ prepared either by e-gun or sputtering. They report numerous results relative to $4\pi M_s$, T_c, H_c, nucleation field and K_u. They compare these results with theory. The mean-field theoretical analysis described the temperature-independent magnetic behavior and showed that Nd couples ferromagnetically to the TM moment. They observe that K_u is largest in evaporated films. It is positive and low by sputtering and negative with $V_b < 0$, but since the films have a too high H_c, they are not attractive for bubble devices. By annealing up to 470 K they observe that $4\pi M_s$ does not change and that K_u and H_c are reduced.

2.1.5.2.5. Gadolinium–(terbium, dysprosium, holmium)–iron systems

Some properties have been reported for alloys rich in Fe content (77 at%). Values and variations of K_u, H_c and θ_K have been studied relative to their application in thermomagnetic and optomagnetic computer devices (Netherlands Patent, 1977).

2.1.5.3. *Crystalline systems*

2.1.5.3.1. Gadolinium–iron systems

In order to provide a historical point of view, we refer here to some papers in which the crystallographic state is unfortunately poorly defined. They come from a Russian scientific team in Irkutsk, who since 1965 have reported numerous magnetic properties for GdFe films. A large number of these papers have not been translated or received by our scientific organizations; for a survey of these works (more than 50 titles) one must turn to "Chemical Abstracts", which gives the summaries of a Conference Series as "Sbornik Fizika Magnit. (or Magnet.) Plenok, Irkutsk" from 1967 to 1979. The ambiguity is due, on the one hand, to the experimental procedure: the films are generally deposited onto heated substrates by thermal evaporation, and on the other hand to the fact that until 1973, to our knowledge, no diffraction patterns were reported. Buravikhin et al. (1975a) described their films as a "soft dispersion crystalline structure similar to the amorphous state". So, apart from some results obtained by annealing, as mentioned below, we have not been able to classify the as-deposited films as pure amorphous materials. From our partial bibliography some results can be reported. Nedelko (1965), Buravikhin and Nedelko (1965), Kurenskii et al. (1965), Nedelko and Buravikhin (1966), Buravikhin et al. (1967), Voskobojnik et al. (1967), and Buravikhin et al. (1971), have studied the coercive force, the electrical resistance, the hysteresis loops, the domain structures, the thickness, the temperature (annealing, cooling) and the ageing. The hysteresis loops have a rectangular shape and also are straight lines; the domain patterns present various configurations versus film concentration and applied magnetic field. Buravikhin and Nedelko (1965) conclude that a uniaxial anisotropy normal to the surface may develop at a critical thickness. Buravikhin et al. (1975a) have studied the magnetization which decreases to 0 at 80 at% Gd, the magnetization which is near zero for $GdFe_2$ samples and the coercive force which is high at the magnetic compensation point (films of $Gd_{30}Fe_{70}$ composition). In addition they observed magnetic domains for $GdFe_2$ and $GdFe_5$ specimens. (The authors also report a magnetostriction—near 0—for $SmFe_2$ films.) Domyshev et al. (1974)

have reported, for $GdFe_2$ crystalline films, a T_c of 780 K, and magnetostriction, magneto-elastic parameters, Young modulus, anisotropy field, magnetization and coercive force. They compare their values for $GdMn_2$, $GdCo_2$, $GdNi_2$ and $GdCu_2$ compounds, and discuss their results in terms of exchange interactions, of atomic radius size of the 3d elements and of grain size variations after annealing. They conclude that it is possible to establish a correlation between the magneto-elastic, magnetic and structural properties for these Laves phase compounds, and that the anisotropic internal stresses are the major factor in the magnetic anisotropy.

Taylor (1966a), for Gd_8Fe_{92} polycrystalline films prepared by e-gun, observed a lower H_k and a higher K_u than for amorphous ones. Lubitz et al. (1976a) and Prinz et al. (1977) have studied, by microwave magnetic resonance, the magnetic properties of crystallized films prepared by thermal evaporation (W crucibles) deposited onto heated substrates (520 K). Lubitz et al. (1976a) report numerous quantities such as: $4\pi M_0$, g_{eff}, A, conductivity, ferrimagnetic resonance, magnetic damping parameter and surface anisotropy parameters, for $Gd_{1-x}Fe_x$ samples ($0 \leqslant x \leqslant 1$). From the variation of A versus the Fe content, they suggest that the Gd–Gd exchange is small compared to the Fe–Fe one. The authors conclude that GdFe is similar to permalloy systems in that spin waves are readily excited and that $4\pi M_0$, the damping parameter, g, and the surface anisotropy constants are similar; but show an important difference, in that eddy current losses and exchange conductivity linewidth broadening at high frequencies are much lower. Such materials should be suitable for cross-tie memory applications, but their magnetic properties vary considerably by a slight alteration of the composition. For a $Gd_{86}Fe_{14}$ sample Prinz et al. (1977) have found a large resonance linewidth which is due to a random distribution of crystallites. The linewidth should broaden as the temperature is lowered, since the magnetic anisotropy increases. The main magnetic properties of $GdFe_2$ films described by Vittoria et al. (1978) have been reported in section 2.1.5.1.5.2. By annealing at 570 K their as-deposited amorphous samples crystallize and are degraded at 620 K. Gangulee and Taylor (1978) report a crystallization temperature of about 500–530 K.

Other work has been done in order to define the compounds obtained by annealing. Nedelko and Buravikhin (1966), Buravikhin et al. (1971, 1976), Egorov et al. (1974) and Bocharev et al. (1974) have determined the following compounds: Gd_2Fe_{17}, $GdFe_5$, $GdFe_4$, $GdFe_7$, $GdFe_2$ and $GdFe_3$. Bocharev et al. (1974) have tentatively established a relation between the evaporation rate and the compounds obtained by thermal evaporation. Fitzgerald and May (1974) have prepared Gd_3Fe_5 films by e-gun. After annealing at 1000 K they observe the coexistence of Gd_2O_3 and α-Fe_2O_3, and above 1370 K they claim to have obtained $Gd_3Fe_5O_{12}$ and $GdFeO_3$ crystals. But one of their electron diffraction patterns could be indexed according to the B-Gd_2O_3 structure. Gasgnier (1981) has tentatively prepared pure crystalline Gd_xFe_y structures. But annealing amorphous films at low temperature with an electron beam one induces complex transformations. Fig. 2 presents an electron diffraction pattern which shows the coexistence of several phases which cannot be indexed easily. Even by com-

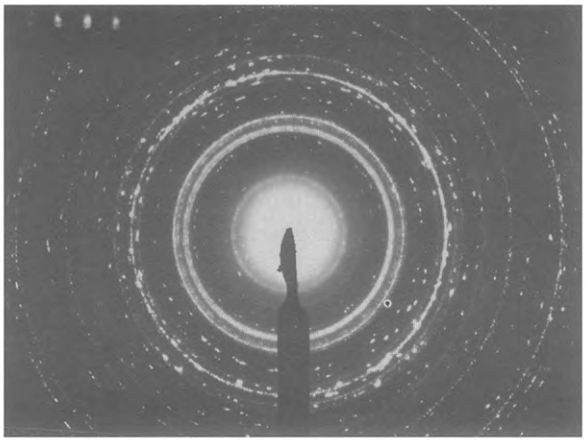

Fig. 2. Complex electron diffraction pattern of a GdFe film, initially amorphous, after annealing by means of an electron beam.

parison with the numerous known bulk structures it was not possible to entirely resolve this pattern. The C-Gd_2O_3 and α-Fe structures are sometimes observed, as reported by Dirks and Gijsbers (1979a,b). Besides, from one sample to another the crystallization mode changes. The same observations were made for other R–TM systems such as YFe, CeFe and DyFe films. Upon annealing at high temperature some GdFe samples crystallize with the $GdFeO_3$ or $Gd_3Fe_5O_{12}$ structures; Gill et al. (1978) have observed the formation of Gd_2O_3, FeO, ... by heating their films; Gill and Judy (1979) report that after annealing at 570 K their samples exhibit a microcrystallization of iron imbedded in an amorphous matrix. Wandelt et al. (1977) observe the formation of Gd_2O_3, Fe_3O_4 and Fe_2O_3 at the surface of samples exposed to ambiant atmosphere.

2.1.5.3.2. Terbium–iron systems

Donoho et al. (1973), McLane (1974) and McLane et al. (1975) have studied electric wave generation and magneto-elastic ultrasonic generation in polycrystalline $TbFe_2$ films prepared by thermal evaporation (W crucibles) by deposition onto heated substrates (490–670 K). They observe that ultrasonic generation and magnetic anisotropy are strongly dependent on the thickness and on the substrate temperature: the peak-signal amplitude is maximum at 590 K for a thickness of 1 μm, and above 590 K the films exhibit a strong perpendicular magnetic anisotropy. The authors had thought of applications in the field of ultrasonic transducer materials and of bubble devices, but, as described in section 2.1.5.1.6, amorphous films seem to be more appropriate. By means of a new apparatus Luzgin (1975), for $TbFe_2$ samples, has measured the magneto-elastic parameter at various temperatures. Buravikhin et al. (1971) have reported the planar Hall effect and the magnetization of TbFe films. After annealing at 720 K they observe the formation of $TbFe_5$ and Tb_2O_3 compounds. They conclude, as for the $GdFe_5$ compound, that the RFe_5 phase is antiferromagnetic and responsible for the magnetic compensation. Dirks and Gijsbers (1979a,b) have studied, as for GdFe amorphous films, the crystallization behavior of TbFe

samples. Upon annealing at 740 K they observe the formation of Tb_2O_3 and α-Fe; the microstructure does not change by heating up to 970–1120 K, and above these temperatures there is a sudden recrystallization with the disappearance of the columnar structure (see sections 2.1.5.1.5 and 2.1.6.1). They have also studied Gd, Dy and Ho alloys and conclude that the amorphous–crystalline transition, for R_xFe_{1-x} ($0.1 < x < 0.7$) with an initial columnar microstructure, is similar for all of the alloys. Buravikhin et al. (1976b) have observed a similar phenomenon by annealing of poorly crystallized Tb_xFe_{1-x} films; they report the formation of Tb_2O_3 and α-Fe.

2.1.6. *Rare earth–cobalt systems*

2.1.6.1. *Binary amorphous alloys*

2.1.6.1.1. Introduction

Heiman and Kazama (1978) studied YCo and LaCo alloys. They concluded that, in contrast with RFe alloys, the size of the R atom does not play a significant role in the properties of RCo materials, but that rather the charge state of the R-type atom does. They report that the differences which appear between amorphous and crystalline states are due to a reduction of the charge transfer from R atom to Co atom in the amorphous state. This indicates that Co moments are quite localized. Tao et al. (1973, 1974) and Roberts et al. (1977) confirm the existence of a charge transfer. Terzieff and Lee (1979) conclude from XPS measurements that, as for GdFe, the charge transfer must be smaller than one electron per Gd atom. They do not agree with the results of Heiman and Kazama (1978) and Taylor and Gangulee (1976) which give charge-transfer values of 1.41 and 1.86, respectively. Jouve et al. (1976) conclude to the absence of charge transfer.

RCo films have been the subject of a large number of analyses. As for RFe alloys, the large spread of results is mainly linked to the preparation conditions.

2.1.6.1.2. Yttrium–cobalt alloys

Suran et al. (1977, 1978, 1979), Krishnan et al. (1978a,b) and Le Dang et al. (1980) investigated the magnetic properties of YCo_3 samples prepared by dc sputtering. The films are ferromagnetic with an in-plane magnetization. By FMR, static and spin-echo measurements they study the influence of V_b, temperature, Ar and O_2 absorption on K_u, H_c and resonance linewidth. They observe the existence of a thin surface layer formed at the initial stage of the deposition and studied its magnetic characteristics. They show that Co has an ionic character in this layer while it is covalent in the bulk film; the layer has in-plane magnetization induced either by Ar inclusions or by small clusters of Co atoms. They observe that the bulk film has a strong negative in-plane anisotropy after annealing at about 500 K in Ar, which should be attributed to a columnar structure with Co pairs formed within the specimen thickness. They suggest that K_u is related to deposition parameters and that strain (magnetostriction) is a secondary effect. However, at the surface the sign of K_u is opposite to that in the bulk film. Asomoza et al. (1977) and Asomoza (1980) show that YCo_3 specimens are sperimagnetic and that, as Y is non-magnetic, the films have no

T_{comp} and consequently no EHE, and the saturation Hall resistivity versus temperature remains constant between 60 and 300 K. McGuire et al. (1977) observe, for a YCo_2 sputtered film, that $\rho_H(4.2\text{ K})$ changes sign $(-)\rightarrow(+)$ with the applied field, in the range from -5 to $+5$ kOe. They noted, by comparing two samples with identical compositions, that ρ differs by a factor of two and ρ_H by a factor of four. But they were unable to explain such discrepancies. Their samples are saturated at 6000 G. Bhagat et al. (1978) reported spin resonance measurements on YCo_x co-evaporated films. They observe strongly different magnetic properties between low and high Y concentrations. So, $4\pi M_s = 0$ at high content (x) and has positive values for low content. McGuire et al. (1977) obtain for $4\pi M_s$ values of 4300 and 5700 G. Furthermore, Bhagat et al. (1978) note that for $Y_{20}C_{80}$ samples A is about 1/4 of that in pure crystalline Co and diminishes with increasing Co content. Heiman and Lee (1975a) show that T_c and the magnetic moment increases with increasing Co content, T_c being higher than for GdCo alloys.

Heiman and Kazama (1978) studied the Co moment and the Co–Co exchange in YCo_x films prepared by e-gun. They compare their results with the crystalline state. The Y concentration at which the Co moment disappears is much higher in amorphous samples than in crystalline ones. So, the YCo_2 compound is not magnetically ordered, while the amorphous films present a net magnetization.

2.1.6.1.3. Lanthanum–cobalt alloys

Only Heiman and Kazama (1978) studied $LaCo_x$ alloys. They concluded that these alloys exhibit no significant difference with the YCo_x alloys.

2.1.6.1.4. Neodymium–cobalt alloys

Taylor et al. (1978), for Nd_xCo_{1-x} $(0.08 < x < 0.70)$ films prepared by e-gun, have made a large survey, of the magnetic properties, as for NdFe films. (Their samples become partially crystalline at $x > 0.5$.) From measurements of magnetization versus composition they show that the Co moment drops to zero for $x = 0.5$, in agreement with the results reported for YCo and LaCo (Heiman and Kazama, 1978). From $4\pi M_s$, K_u, H_c and ρ_H/ρ measurements and from the mean field analysis, they determined exchange contents and subnetwork magnetizations and concluded from a large reduction of the Nd–Co exchange coupling, that a Nd dispersion in a cone reduces the net moment to 77% of the free-ion value. Therefore the NdCo alloys are sperimagnetic structures, the Co subnetwork being ferromagnetic. Besides, they report K_u variations versus temperature and composition. K_u exhibits a sharp maximum at all temperatures from 4 to 300 K for 20 at% Nd, and is proportional to the square of the Nd subnetwork magnetization; H_c changes with the Nd at% at 4.2 K: it increases up to about 6000 Oe with increasing Nd content ($x = 0.5$); T_c decreases versus Nd concentration from 700 K ($x = 0.25$) to 150 K ($x = 0.50$) and is always higher than for crystalline materials as shown previously for other RCo alloys by Lee and Heiman (1974).

2.1.6.1.5. Samarium–cobalt alloys

Prinz et al. (1979, 1980) studied the complex index of refraction and the complex magneto-optic coefficient versus Sm content of films prepared by e-gun.

The coefficient decreases as the Sm concentration increases; this is interpreted as the result of the filling of the Co d-bands by the Sm electrons. Larsen and Livesay (1978, 1979a,b) report the magnetic properties of rf sputtered $SmCo_5$ films activated by hydrogen (30–100 atm) at 420–870 K. They observe that thicker films (>500 Å) have properties similar to the bulk. The thickness, the nature of the substrate (NaCl, sapphire, glass) and the H_2 pressure influence such magnetic quantities as M_s, K_u and the rotational hysteresis energy. The surface of the films shows alterations after annealing at 870 K under a pressure of H_2 as high as 100 atm. AES spectra show the presence of O_2 and Sm segregation. The properties of the surface, and also perhaps the stresses, play a large role in the hydriding phenomenon. The authors have investigated the hydriding–dehydriding cycles and their rate constants. By addition of small amounts of N_2 (1–4%) this rate is greatly reduced. They suggest that their experiments provide a way to monitor hydriding–dehydriding rates in $SmCo_5$ alloys. Zhang et al. (1980) prepared by dc diode sputtering SmCo and SmRR'Co films. Their targets have as nominal composition $SmCo_5$ and $Sm_{0.5}(RR')_{0.5}Co_5$ (R, R' = La, Ce, Nd, Pr), but they do not give any information on their film compositions. From their annealing results it is doubtful that they kept the same elemental concentration ratios as they had in their target (other than the $SmCo_5$ compound). However, the as-deposited films are amorphous and they report some magnetic properties such as T_c, M_s (both higher in amorphous than in crystalline form), K_u, which is negative, V_H and hysteresis loops. Kumar and Das (1978) and Kumar et al. (1978) obtained $SmCo_5$ amorphous films by arc-plasma spraying (see section 2.1.6.2.2).

2.1.6.1.6. Gadolinium–cobalt alloys

2.1.6.1.6.1. Composition and homogeneity. For dc and rf sputtered films, Cronemeyer (1974), Cuomo and Gambino (1975), Bourne et al. (1975), Funakoshi (1975), Covault et al. (1976), Katayama et al. (1977b), Heiman et al. (1978), Burilla et al. (1978), Leamy and Dirks (1978), Knappe et al. (1978) and Ohkoshi et al. (1980) studied the film *composition* versus V_b, target voltage and target composition. Cronemeyer (1974) notes that $GdCo_2$ and $GdCo_3$ targets induce differences in film properties, and that by increasing V_b the Co content increases. Cuomo and Gambino (1975) show that the Co/Gd ratio deviates, by increasing V_b, more rapidly from stoichiometry with $GdCo_5$ targets than with $GdCo_3$ ones. Bourne et al. (1975) report large variations of the composition for V_b up to −100 V and variations in composition due to small changes of the parameters during deposition. Heiman et al. (1978) observe changes in composition for V_b up to −400 V. As V_b increases the Gd content decreases, the Co content decreases to a minimum at −200 V and then increases. Ohkoshi et al. (1980) observe that the Gd content decreases with increasing V_b. Knappe et al. (1978) present a model to describe the film composition and noticed differences for dc and rf bias sputtering. From all these results emerges as the main conclusion: when V_b increases, Gd atoms are preferentially resputtered from the growing film. For evaporated films (single source e-gun), Taylor (1974) studied their composition and compared it with that of the target, freshly prepared or partially consumed. He concluded that the evaporation must consume no more than 1% of the source material in order to obtain

films with compositional variations of 1% or less. The problem of *homogeneity* is complex. The intrinsic structure of the film can vary widely with changes in: a) the Co/Gd ratio; b) the inclusion of Ar (or other rare gases); c) the incorporation of O_2 (or other gases: H_2, N_2, . . .). Shirakawa et al. (1974) observe a change in the Co/Gd ratio in different areas of the films. They notice that at low deposition rate the Co content is not constant through the samples. Bourne et al. (1975) find a similar result by measurement of the variation of the stripe period observed by the Kerr effect. Tsunashima et al. (1977) obtain anomalous torque curves which are due to subtle changes of preparation conditions during the film growth. This phenomenon has been observed by Tarnoczi et al. (1976), Nagy et al. (1976a), Lutes et al. (1977), Chung et al. (1979) and Maksymowicz et al. (1979). Prasad et al. (1979), from FMR measurements, report the existence of inhomogeneities which increase when V_b increases. They conclude that the inhomogeneities are randomly distributed in the whole volume of the film. Hafner and Hoffmann (1979) report the influence of the thickness on magnetic properties. The inclusion of rare gases (Ar, Ne and Kr) during sputtering is linked, in a general manner, to V_b. Esho and Fujirawa (1976) show that the Ar content increases with increasing V_b, which leads to a decrease in film density and a rapid film deterioration. Togami et al. (1980) report similar results from AES and electron microprobe analysis. They report that films under low Ar pressures are less sensitive to background contamination than at high pressures where they become porous and therefore more easily contaminated. Cuomo and Gambino (1977) notice that metastable compositions exist, with a high degree of stability, with concentrations of Ar, Ne and Kr varying from a few to 30 at% Co. Surprisingly Heiman et al. (1978) observe that the Ar content increases to about 15 at% for $V_b = -200$ V and decreases to a few at% for $V_b = -400$ V. Prasad et al. (1979) investigated the effect of annealing in vacuum and in argon. They conclude that Ar annealing leads to a homogenization of the films, while vacuum heating up to 560 K does not. To our knowledge only Ohkoshi et al. (1980) conclude that Ar content is independent of V_b. Frisch and Reuter (1979) studied the release of Kr, for amorphous rf sputtered films, by annealing treatments up to about 1000 K. During heating there is firstly the formation of crystalline $GdCo_2$ which permits grain boundary diffusion and secondly a reaction with the substrate which induces a second release mechanism. The incorporation of oxygen has been investigated in several papers. Ohkoshi et al. (1980) notice a drastic decrease of O_2 contamination with increasing V_b. Kobayashi et al. (1980) investigate the influence of O_2 on the uniformity of their samples and observe an increase of the O_2 concentration from the center to the edge of the film. Togami et al. (1980) conclude that O_2 is the more important contaminant. The consequence of O_2 contamination for magnetic properties has been investigated by Brunsch and Schneider (1977a,b, 1978), Maksymowicz et al. (1979), Herd (1977), Hafner and Hoffmann (1979), and Tsunashima et al. (1980). Terzieff and Lee (1979) gave evidence for the contamination by O_2 after ageing and annealing. From XPS measurements they observe the formation of Gd_2O_3, which is indicated by a shift of the Gd 4f peak, and an increase of the O 1s peak.

Other studies have been carried out with other gases such as N_2 and H_2. Esho

(1979) observes that films sputtered under partial N_2 pressure exhibit a Co/Gd ratio which increases when the partial pressure increases. Brunsch and Schneider (1978) report changes in magnetic properties of films contaminated by H_2 and N_2. Frish and Reuter (1979) notice that H_2 desorption precedes the desorption of Kr, during annealing.

Another important problem arises from the film–air and film–substrate interfaces. Esho (1976), Lutes et al. (1977) and Chung et al. (1979) report a change in magnetic properties due to these interfaces. Suran et al. (1980) and Ohkoshi et al. (1980) showed by FMR measurement and AES analysis, the existence of either one interface or two interfaces, respectively; they are induced by oxygen contamination and therefore lead to the formation of Gd_2O_3. Suran et al. (1980) demonstrate its presence by chemical etching. Such a reactivity is due, on the one hand, to O_2 adsorbed inside the substrate surface or gettered in the first stage of the deposition, and on the other hand to free O_2 as traces in the vacuum or in the atmosphere. Venturini et al. (1976) show the existence of a sublayer with a depletion in Gd content (2 at%) after bombardment by Ar ions.

Therefore, as shown by Maksymowicz et al. (1979) argon and oxygen may control the magnetic properties. One must conclude: a) that argon can be regarded as a third component and change the magnetic interactions, and b) that the formation of Gd_2O_3 leads to a decrease of the Gd content and therefore of the sublattice magnetization.

2.1.6.1.6.2. Ordering temperatures. Tao et al. (1973) notice that T_c is higher (565 K) for a $Gd_{33}Co_{67}$ rf sputtered film than for the corresponding crystalline ($GdCo_2$) compound (395 K). Lee and Heiman (1975a) report that T_c is always higher for amorphous alloys than for crystalline compounds such as $GdCo_3$, Gd_2Co_7 and $GdCo_5$. Tao et al. (1974) add that this result is true in the composition range 0.6–0.8 at% Co, and notice that for a $Gd_{60}Co_{40}$ alloy T_c is quite close to that for the compound. Jouve et al. (1976), for $GdCo_3$ alloys, report $T_c = 880$ K. In a study of the pressure dependence (up to 27 kbar) Biesterbos et al. (1976) show that for $GdCo_x$ alloys ($x \leqslant 60$), T_c decreases slightly. They notice that $Gd_{40}C_{60}$, $Gd_{55}Co_{45}$ and $Gd_{65}Co_{35}$ alloys have $T_c = 320$, 220 and 160 K, respectively. Müller et al. (1977) made a comparison of some previous data. They studied the T_c dependence on x and y in the $(Gd_{1-x}Co_x)_{1-y}A_y$ system (A = Ar or O_2) and concluded that the results are not reproducible due to the presence of impurities.

Chaudari et al. (1973b) and Tao et al. (1974) show that T_{comp} decreases from 500 K ($Gd_{35}Co_{65}$ alloy) to 50 K ($Gd_{18}Co_{82}$ alloy). Lee and Heiman (1975) observed a decrease of T_{comp} from 510 to 80 K for the $GdCo_2$ to $GdCo_5$ alloys. Visnovski et al. (1976), Bochkarev et al. (1976b) and Dirks et al. (1977) report T_{comp} as 370 and 420 K for $Gd_{24}Co_{76}$ sputtered films and $Gd_{20}Co_{80}$ evaporated films, respectively. Venturini et al. (1976) notice a $T_{comp} = 140$ K for a $Gd_{19}Co_{81}$ alloy. Venturini and Richards (1976) give T_{comp} as 103 K and 140 K for other samples and studied the process of reverse magnetization at these temperatures. For $GdCo_3$ alloys, Jouve et al. (1976) find $T_{comp} = 230$ K. For $GdCo_x$ films, Suran et al. (1980) give $T_{comp} = 100$ K. The results therefore vary. This can come from the film homo-

geneity and from inclusion of impurities. Shirakawa et al. (1974) observe a ΔT_{comp} as large as 60 K for different lateral areas on the film. Lutes et al. (1977) report a ΔT_{comp} of 100 K over the thickness, Kobayashi et al. (1980) notice a decrease in T_{comp} for the more contaminated areas of the film. Matsushita et al. (1978) observe shift of T_{comp} (of about 5 K) for GdCo films coated with a permalloy layer. But, as demonstrated by Müller et al. (1977) and Müller (1978) the non-reproducibility of the values comes either from impurities (O_2 atoms statistically distributed), or from the reduction of the number of magnetic nearest neighbours due to Ar inclusions (change in the short-range ordering). Maksymowicz et al. (1979), Müller et al. (1977), Esho (1979), Gron and Stobiecki (1979), Suran et al. (1980) and Kobayashi et al. (1980) observe a decrease of T_{comp} with increasing gas impurities (Ar, O_2 and N_2). (Twarowski and Lachowicz (1979) noticed a shift in compensation composition (77 at% Co) and interpreted this as evidence for Gd_2O_3 formation and/or Ar inclusion.)

2.1.6.1.6.3. Anisotropy. As for GdFe, the problem of the anisotropy (origin, sign and variations) remains complex. As explained by Heiman et al. (1978), Cargill (1978a,b), Müller and Perthel (1978) and Müller et al. (1978), this complexity comes from the numerous preparation parameters and deposition conditions. The influence of composition changes, of inhomogeneities, of V_b, of Ar, O_2, N_2 and H_2 as absorbed gases, of ion irradiation and of annealing lead to various interpretations. Moreover, the mode of preparation as sputtered (dc or rf, with and without bias) or thermally evaporated films, increases the discrepancies and it is difficult to compare the results. Müller and Perthel (1978) and Müller (1978) examined in detail the well known resputtering effect. For sputtered films it is promoted by V_b or ion bombardment in the course of the deposition. They built a model which includes two types of resputtering processes which come from either adatoms or inner atoms and take part to a degree depending on the surface roughness and the energies of the sputtering ions. They calculate the atomic pair distribution formed by resputtering. For evaporated films they report that mainly adatoms will be re-evaporated, and that the sign of the anisotropy is different in evaporation and sputtering. They add that stress or column growth can induce anisotropy. They conclude that sign and magnitude of the anisotropy depend strongly on the surface configurations, on the binding energies assumed for the different pairs (small shifts in the binding energy of a Gd–Co pair can change the sign of the anisotropy) and on the preparation conditions. Katayama et al. (1976) give numerous details on the resputtering effect. Mizoguchi and Cargill (1978) investigated in details the magnetic dipolar interactions which involve an anisotropically distributed atomic moment or anisotropic microstructures. They conclude that the spatial scale of magnetically important structural anisotropies is probably different in sputtered and evaporated films.

The same hypothesis as for GdFe (see section 2.1.5.1.5.1) can be used in order to explain the anisotropy. They are a source of controversies and conflicts as shown in the following paragraphs (review papers were mentioned in the introduction).

For sputtered films studied by electron microscopy, Herd (1977, 1978, 1979)

supports the model of anisotropically shaped Co-rich clusters and rules out the stress model; Leamy and Dirks (1978a,b) and Dirks and Leamy (1978a, 1979) support the model of inhomogeneous anisotropic microstructure (columnar structure) and of stress effects; Hoffmann et al. (1979) proposed the pair-ordering model; and Wang et al. (1979) considered the predominance of Gd–Co pairs. For evaporated films, Nandra and Grundy (1977a) suggest a growth induced anisotropy (atomic arrangements) and rule out shape or physical growth features. The experiments of Nandra and Grundy (1976) on evaporation at oblique incidence support a stress-induced orientation of the spin moments.

For sputtered films studied by X-ray diffraction, Onton et al. (1976) and Covault et al. (1976) support the short-range ordering model and rule out the pair-ordering model and the stress contributions. For evaporated samples, Onton and Lee (1976) report a magneto-structural model and rule out the shape anisotropy. Heiman et al. (1975b) report that anisotropy is most likely associated with the Co sublattice, and that it is more likely due to a preferred pseudo-crystalline coordination (anisotropic local coordination) than to pair ordering.

In a study of the dependence on the resputtering effect, Katayama et al. (1976a, 1977a,b), Hirano et al. (1977), Nishihara et al. (1978, 1979) and Gambino and Cuomo (1978) show that a positive K_u is closely related to this phenomenon, and its origin is supposed to be atomic pair ordering. Hafner et al. (1979) conclude that this mechanism is unique. Lee and Heiman (1975b) argue for a preferential arrangement of the Gd atoms and rule out pair ordering. Nagy et al. (1976) support a shape anisotropic effect, and Esho (1979) a microstructural defect in the atomic order caused by Gd resputtering, and conclude that K_u may result from the change in the exchange constant.

The dependence of the anisotropy on absorbed Ar inside the films has been studied by some authors. Katayama et al. (1977a,b), and Burilla et al. (1978) report variations of K_u as a function of Ar partial pressures. Esho and Fujiwara (1976) and Ohkoshi et al. (1980) suggest a shape anisotropy mechanism based on Ar clustering in shaped voids. Tsunashima et al. (1978) find that Ar inclusions play an important role in the internal stresses and this leads to magneto-elastic contributions. Burilla et al. (1978) report that absorbed gases have some direct influence on the short-range order by some unknown mechanism. In the area of sputtering condition preparations, Katayama et al. (1977a,b), Heiman et al. (1978), Jouve et al. (1979), Burilla et al. (1978) and Suran et al. (1980) show that K_u depends on V_b. (Bourne et al. (1975) observed no correlation for films of similar composition.)

Another field of investigation is the study of the effects of ion-radiation damage on the anisotropy. Gambino et al. (1974a,b) and Hasegawa et al. (1974) support that the source of anisotropy for sputtered films is atomic pair ordering, with an excess of Co–Co pairs. Cronemeyer (1974) reports that this phenomenon is enhanced by rf bias and that rare gas ion damage encourages pairing. Gambino et al. (1974a) and Ali et al. (1976) observe that ion irradiation destroys the anisotropy. Grundy et al. (1977) conclude that some particular atomic arrangements (pair ordering or other correlations) account for the anisotropy and rule

out shape or physical growth features. Kosicik et al. (1978), for evaporated films, report a negative K_u. After ion bombardment K_u becomes less negative and this cannot be explained by O_2 contamination, as supported by Brunsch and Schneider (1977a,b). They suggest that a positive contribution to K_u is created during irradiation.

Other hypotheses have been developed. Taylor and Gangulee (1976), for evaporated films, determined a) that unlike pairs contribute to the in-plane anisotropy, while like pairs contribute to the perpendicular anisotropy; b) that Gd–Co pairs are dominant; c) that pair ordering is not the only mechanism for anisotropy; and d) that the shape effect and long-range ordering may be taken into account. For sputtered films Twarowski and Lachowicz (1979a,b) support the stress induced anisotropy model and argue that RKKY interactions contribute to the magnetostriction.

The contamination by O_2 which leads to the formation of Gd_2O_3 (deactivation of Gd moments) has been studied by several authors. Cargill (1978a,b) and Cargill and Mizoguchi (1979) report a detailed model relative to the oxidation mechanism. They conclude that magnetic dipolar interactions associated with such anisotropic inhomogeneities may be responsible for the anisotropy either of doped evaporated films or zero-bias sputtered films. Brunsch and Schneider (1977a,b) conclude that oxide inclusions generate an anisotropic stress situation which leads to a perpendicular anisotropy via magnetostriction. Brunsch and Schneider (1978) observe that K_u decreases with increasing partial H_2 and N_2 pressures. (Esho (1979), for rf sputtered films evaporated under a Ar–N_2 pressure, reports that K_u decreases with increasing partial N_2 pressure.) Brunsch and Schneider (1978) conclude that, in order to generate a positive K_u a certain amount of incorporated non-magnetic materials is necessary which holds 10 at% magnetically deactivated Gd. Hafner and Hoffmann (1979) and Hafner et al. (1979) observe that excess O_2 decreases or destroys the anisotropy pair ordering by activating Co pairs. They conclude that partial O_2 pressures can be used just in the right concentration to induce anisotropy. Dirks and Leamy (1978a,b) report that films prepared by e-gun and deposited onto rotation substrates under partial O_2 pressure, have a positive K_u. Their as-deposited samples possess a high tensile stress, which is reduced to a compressive stress in an O_2 atmosphere. This coincides with the development of a perpendicular anisotropy. Shinoda et al. (1979) and Tsunashima et al. (1980) report, for evaporated films with an in-plane magnetization, that a positive K_u is induced after annealing at 470–570 K under partial O_2 pressure. Hoffmann and Winkler (1979a) show that, after annealing at 490 K, O_2 reacts with Gd atoms and this causes a positive K_u. They assume that voids or density inhomogeneities do not contribute to the uniaxial anisotropy. Herd (1977) observes a change from in-plane to perpendicular anisotropy with slight to moderate O_2 contamination. One must notice that Visnovski et al. (1976), for GdCo films coated with a SiO layer, observed an increase of a positive K_u.

The problem of annealing behavior is complex, as noticed by Heiman et al. (1978), who report a decrease of K_u by a factor of 2.5 after annealing. Katayama

et al. (1977a, 1978) and Perthel et al. (1977) observed, after annealing at various temperatures up to 570 K, a net decrease of K_u. When studied as a function of annealing time they show that K_u becomes negative at both 520 and 470 K. Katayama et al. (1978) concluded that this change in K_u is due to atomic rearrangements and the destruction of the Co–Co pairs. Perthel et al. (1977) added that they do not observe a decrease of K_u near T_{comp} in contrast to Cronemeyer (1974), Heiman et al. (1976) and Venturini and Richards (1976). They rule out the shape anisotropy model and support a possible coupling to the Co sublattice. Chaudari and Cronemeyer (1975) report that K_u decreases with increasing temperature which they believe is due to a dominant Gd–Co coupling. Prasad et al. (1979) report a similar behavior and suggest that Co pairs are destroyed by atomic diffusion. Kosicik et al. (1978) observe a decrease of K_u during annealing. Herd (1977) report that K_u increases after annealing from 620 to 670 K. Müller et al. (1978) report negative K_u values between 100–320 K and then positive values after annealing above 350 K. They conclude that short-range order and stresses induce anisotropy. Some other observations have been made concerning the dependence of the anisotropy on concentration. Bochkarev et al. (1979) show that positive K_u is minimum close to 19.5 at% Gd. Maksymowicz et al. (1979) report that K_u exists for a Co content range of 72–80 at% and a Ar content range of 3–14 at%. Bourne et al. (1975) observed considerable scatter of the K_u values versus composition.

Lastly, the film–substrate and the film–air interface are now studied in more detail. Tsunashima et al. (1978), from torque measurements, observed a negative K_u at the film–substrate interface and a positive one at the free surface. Chung et al. (1979), from magnetic ripple theory, support the same result. Hafner and Hoffmann (1979) added that K_u is higher at the film–substrate interface than at the free interface. Suran et al. (1980) observe, after annealing, that the free surface (as an oxide) possesses a negative K_u.

Therefore, as for GdFe, and for the GdCoMo, GdCoCu and GdCoAu alloys, the origin of K_u is always unknown. The reader is referred to the results reported in each of the sections relative to these alloys in order to have a better idea of the complexity of the problem. Moreover the large discussion about as-deposited and annealed binary and ternary alloys given by Heiman et al. (1978) shows that a clear conclusion is not possible. Müller et al. (1979) notice that the temperature dependence of K_u is widely sensitive to the preparation conditions. They conclude, as Heiman et al. (1978), that more than one mechanism is responsible for the anisotropy.

2.1.6.1.6.4. Saturation magnetization. The saturation magnetization has been studied as a function of composition in relation to several other factors. Chaudari et al. (1973a) and Cuomo et al. (1974) show that $4\pi M_s$ can vary from several thousand to a few hundred Oersteds, being minimum at the compensation point (78 at% Co). For $Gd_{14}Co_{86}$, $Gd_{18}Co_{82}$ and $Gd_{29}Co_{80}$ alloys, Cronemeyer (1974) reports $4\pi M_s$ values of 2800, 1100 and 0 Oe. Tao et al. (1974) noticed for the compensation point a shift up to 84 at% Co, and show that at 4.2 K, $4\pi M_s = 0$ for this composition. Jouve et al. (1976) observed for $GdCo_3$ films

an increase of $4\pi M_s$ from negative to positive values, with a zero value at 78 at% Co. Taylor and Gangulee (1976) noticed few differences in $4\pi M_s$ for sputtered and evaporated films. Nagy et al. (1976, 1977) and Frait et al. (1976), observed a minimum at 81 at% Co for evaporated films. Imamura and Kobayashi (1975) report a different $4\pi M_s$ behavior for evaporated alloys (W crucibles): it decreases abruptly from 100 to 83 at% Co, then increases up to 78 at% Co and then again decreases down to zero for 60 at% Co.

As a function of V_b, Katayama et al. (1977a, 1977b) report for a $Gd_{24}Co_{76}$ alloy a nearly linear increase of $4\pi M_s$ from negative values to zero (−45 V) and to positive values. They attribute this effect to the resputtering of Gd atoms. Ohkoshi et al. (1980) observe first an increase from negative to positive values, then a maximum at −40 V and a decrease to negative values for $V_b > -75$ V. Heiman et al. (1978) reported for $Gd_{28}Co_{72}$ and $Gd_{22}Co_{78}$ alloys that $4\pi M_s$ is always positive for V_b from +50 to −400 V. For the first alloy they noticed a minimum value near 0 for −100 V; but for the higher values, and also for the second alloy, $4\pi M_s$ increases linearly. This is interpreted to be due to the increase of the Gd/Co ratio. Prasad et al. (1979) showed that $4\pi M_s$ varies, not only with V_b, but also with the film thickness, and reaches a maximum at 5000 Å. Suran et al. (1980) noticed positive values for $4\pi M_s$ and a large increase versus V_b (4600 Oe at −200 V). Tsunashima et al. (1977) reported that $4\pi M_s$ varies along the film thickness, and that a large magnetization appears at the first deposition stage.

The influence of temperature on the saturation magnetization has been studied by many authors. Chaudari et al. (1973b) for sputtered films, and Lubitz et al. (1976b) for evaporated films as $GdCo_3$, reported nearly similar profile curves, with a minimum at 400 K. Bochkarev et al. (1979) noticed a slight decrease from 290 to 490 K; upon addition of Y, and of Sm and Ho, they noticed that $4\pi M_s$ remains constant in the same range of temperature. By *annealing* at 450 and 470 K, Hasegawa et al. (1974) and Hasegawa (1974), for a $Gd_{20}Co_{80}$ alloy, observed an increase of $4\pi M_s$ from 800 to 1000 Oe; for increasing *ion irradiation* they report a similar phenomenon. Katayama et al. (1978) observed an increase of $4\pi M_s$ upon annealing up to 570 K; in the first stage of the annealing the rate of change is large. Heiman et al. (1978) reported no significant changes even at temperatures removed from T_{comp}. Esho (1979) noticed no change after annealing at 720 K.

Magnetization is also influenced by *absorbed gases* throughout the films. Cuomo et al. (1977) showed that, for GdCo and GdCoMo films, incorporation of a large amount of Ar (or Kr) leads to a decrease of $4\pi M_s$. Gron and Stobiecki (1979) observed an increase for stronger Ar dilution. Katayama et al. (1977a) observed with increasing Ar pressure that $4\pi M_s$ decreases from positive to negative values and then increases rapidly and becomes positive. This is interpreted by a shift in film composition towards the Co-rich side. Katayama et al. (1977b) present an identical curve but it is reversed and now exhibits a maximum; the interpretation, however, is the same. Venturini et al. (1976) after Ar ion implantation, observed the formation of a thin surface layer with a

non-uniform $4\pi M_s$. Kosicik et al. (1978) reported that ion bombardment decreases $4\pi M_s$. Hafner and Hoffmann (1979), for non-contaminated films, and Visnovski et al. (1976), for GdCo films coated with a SiO layer, observed that magnetization values are higher. Brunsch and Schneider (1977a,b) show that larger and larger O_2 contaminations shift the compensation point, and that $4\pi M_s$ versus Gd concentration exhibits nearly identical variation for all partial pressures and a minimum ($\approx$450 Oe) at the compensation point. Esho (1979) studied the $4\pi M_s$ dependence on V_b and the partial N_2 pressure. The films deposited at $V_b = 0$ and under a partial N_2 pressure exhibited a higher magnetization than those deposited with $V_b = 0$ and a zero partial N_2 pressure. From FMR measurements Frait et al. (1976), Nagy et al. (1977), Lubitz et al. (1976b), Maksymowicz et al. (1977), Prasad et al. (1979) and Suran et al. (1980) investigated $4\pi M_s^{eff}$. Nagy et al. (1977) report that this value is minimum for evaporated films at the compensation point. Lubitz et al. (1976b) observed a decrease from 2500 Oe to 0 Oe in the temperature range 100–300 K. Maksymowicz et al. (1977) reported changes for varying film composition. Before annealing the spectra of perpendicular resonance exhibit four lines, and after annealing (570–670 K) only one broad line. These results show that, except for a small Gd content $4\pi M_s^{eff}$ is enhanced after annealing. Prasad et al. (1979) reported a maximum of this value for thicknesses as large as 5000 Å and $V_b = 150$ V. Suran et al. (1980) studied the properties of this parameter in more detail. They assume the existence of a film–air interface. For as-deposited films, $4\pi M_s^{eff}$ decreases with decreasing temperature. After annealing in argon, this parameter is enhanced (by a factor of 2 in the surface layer). They suggest that Ar annealing leads to an atomic reconstruction of this layer.

Linked to $4\pi M_s$ and $4\pi M_s^{eff}$, studies of H_u, H_k, H_k', net magnetization, K_{eff} (effective anisotropy constant) and saturation field, have been made by Cronemeyer (1974), Frait et al. (1976), Nagy et al. (1976b, 1977), Onton and Lee (1976), Venturini et al. (1976), Venturini and Richards (1976), Taylor and Gangulee (1976), Maksymowicz et al. (1979), Prasad et al. (1979), Hafner and Hoffmann (1979), Bochkarev et al. (1979), Chung et al. (1979), Taylor (1980) and Suran et al. (1980). A determination of H_{coll} has been done by Brunsch and Schneider (1977a) and Bochkarev et al. (1979).

2.1.6.1.6.5. Coercive force and other properties. Shirakawa et al. (1974) show that, for different lateral areas of the film, H_c varies as a function of the deposition rate and the temperature, and exhibits different maxima (200 to 500 Oe). The relationship betwen H_c and composition exhibits a sharp maximum (1 kOe) near 79 at% Co, and low values at each end of the composition range 78.5–79.3 at% Co. Esho (1975) observes that H_c is maximum (1.5 kOe) at 312 K. He notes the presence of a sublayer at the film–air interface and shows that, after etching of this layer, H_c increases by a factor of two. These changes indicate that the magnetization varies over the film thickness. Hasegawa et al. (1974) and Hasegawa (1974) report low H_c values (between 0.5 and 6 Oe) and observe that film annealing leads to a drastic decrease by a factor of 2. This reduction is higher for compositions near the compensation point. They discuss

the changes in H_c in terms of the formation of Gd_2O_3 for annealing films and of fluctuations in A and K_u for irradiated films. Cuomo et al. (1974) report H_c values from 0.5 up to 5000 Oe. Tarnoczi et al. (1977) studied the magnetic configurations near a domain such as a "compensation line" and domain wall movements. They discuss the structures in terms of magnetic subnetworks. They show that H_c is dependent upon the distance from the "compensation line" after both saturation and demagnetization. The curves are asymmetric, and H_c has a sharp maximum at zero. They conclude that the domain wall reaches the compensation line from one side at 300 Oe, and that on the other side this field is even higher. Brunsch and Schneider (1977a,b, 1978) report that H_c increases when the films are more and more contaminated by O_2 and H_2. Gron and Stobiecki (1979) observe that the H_c maximum is enhanced with increasing Ar content inside the film. Matsushita et al. (1978) noted a decrease of H_c for GdCo films coated with a permalloy or a metallic layer; below T_c this situation is reversed. *Other magnetic parameter* such as g, A, l, σ_w, w_s, Q and θ_K were studied by Chaudari et al. (1973b), Hasegawa (1974), Hasegawa et al. (1974), Cronemeyer (1974), Lubitz et al. (1976b), Brunsch and Schneider (1977a), Nagy et al. (1977), Dirks et al. (1977), Katayama et al. (1978), Tsunashima et al. (1978), Bochkarev et al. (1979) and Suran et al. (1980). *Susceptibility* measurements are reported by Hasegawa (1974), Stobiecki et al. (1978), Chung et al. (1979) and Hafner and Hoffmann (1979). *Magnetostrictive* properties are studied by Twarowski and Lachowicz (1979a,b,c). They show magnetostrictive hysteresis loops and saturation magnetostriction versus composition (which is maximum in the vicinity of the compensation point) for sputtered films.

2.1.6.1.6.6. Kerr and Hall effects. Another field of investigation of the magnetic properties was developed by recording the magnetic hysteresis loops obtained by the Kerr and Hall effects and by in-plane magnetization. The ones which come from the *polar Kerr effect* present different shapes and magnitudes according to the authors. Such a phenomenon is not surprising because it is associated with the magnetic domain configurations (Bourne et al., 1975). Shirakawa et al. (1974) show that film composition, deposition rates and temperature induce various forms for the loops and their polarity. Their M–H loops (from association of the polar Kerr effect and of the transverse Hall effect) show at 360 K (T_{comp}) a rectangular shape and reverse in polarity above this temperature. Shirakawa et al. (1976) show that the polarity reverses from (+)→(−) at T_{comp} and that the sign of Co is negative. They concluded that the polar Kerr effect is associated with the Co sublattice. Bochkarev et al. (1976b) obtain nearly identical results. Visnovsky et al. (1976) interpret their Kerr spectra as a sum of the two contributions of the magnetic moments of Gd and Co. Tsujimoto et al. (1980), for films overlayered either by a TbFe or by a NiFe film, report different shapes and polarities of the loops, at T_{comp}, according to the coating alloy. They remark that for TbFe the change in polarity depends on a critical thickness, 340 Å. They conclude that it is due to the exchange coupling between each film. Ogawa et al. (1976) report briefly that the Kerr rotation is mostly due to the contribution of the Co content, and accounts for the polarity reversal at T_{comp}. Müller et al. (1976),

Esho (1975) and Lutes et al. (1977) present loops with strange shapes such as asymmetrical or with several steps or partial reversals of the magnetization. The samples were prepared by sputtering and studied versus the temperature. These anomalous loops are interpreted as magnetization changes throughout the films, i.e., by the existence of different magnetic sublayers at the film–glass or the film–air interfaces or inside the film. These sublayers are described in terms of the Co and Gd moments of spin orientation. Müller et al. (1976) establish a detailed model. Esho (1976) concludes that the magnetization gradient results from the changes in the amount of residual gases inside the film. Lutes et al. (1977) associate their loops to the presence of two interfaces, and identify the bias field, measured from the loops, as the effective exchange field between the coupled Gd-rich and Co-rich layers. They also calculated the wall energy density. Hasegawa et al. (1974) studied the changes of the loops versus the temperature, the applied field and the ion irradiation. The found that an irradiation of 10^{14} ions cm^{-2} destroys the uniaxial anisotropy, and the characteristic loop exhibits a net in-plane anisotropy.

GdCo films present a characteristic EHE. Okamota et al. (1974), for rf sputtered films, studied the transverse and the planar Hall effect. They showed hysteresis loops relative to the transverse Hall effect (some have a rectangular shape) and reported the reversed polarity effect at T_{comp} (520 K). They concluded that the transverse Hall effect is large, that the EHE plays a dominant role in this effect, that the planar Hall effect is much smaller and that the geometry of the Hall sample affects the Hall output voltage. Okamoto et al. (1975) show also that the transverse Hall voltage loops are rectangular near T_{comp} and linear in other temperature ranges. They report that this effect is a function of the total area of the reversed magnetic domains with applied field. Shirakawa et al. (1976) report that the polarity of the EHE hysteresis loops (with a rectangular shape near T_{comp}) and the sign of the EHE of Co are reversed in comparison to the ones obtained from the polar Kerr effect. They observe that ρ_H reverses from (−) to (+) at T_{comp}, and varies according to the Gd content: 110 and 320 K for 17 and 21.5 at% Gd, respectively. For a sample such as $Gd_{21.5}Co_{78.5}$, ρ remains constant (250 $\mu\Omega$ cm). They conclude that the EHE is associated with the Co sublattice moment. Asomoza et al. (1977) and Asomoza (1980) report for $GdCo_3$ sputtered films a T_{comp} of 250 K. They observe that the shape of the loops can vary widely from sample to sample and with temperature, particularly near T_{comp}. They conclude as for other RCo_3 alloys (R = Dy, Er and Ho) that the EHE is essentially associated with the Co moment. They demonstrate such a phenomenon by the decrease in magnitude of the EHE for a $Gd(Co_{25}Ni_{75})_3$ alloy. Ogawa et al. (1975, 1976) report ρ_H as a function of the temperature and observe a change in polarity at T_{comp} ($\approx$240 K) for a $Gd_{19}Co_{81}$ sputtered film. They conclude, from the increase of ρ_H with increasing Gd content, that ρ_H depends essentially on Gd. They notice that two other samples with 10 and 26 at% Gd do not present the polarity reversal for temperatures up to 310 K. McGuire et al. (1977a,b) investigated the Hall effect properties of GdCo films and compared their results with results reported for various other binary and ternary alloys.

They discussed the results of Shirakawa et al. (1976) and of Ogawa et al. (1975, 1976). They noticed that only Shirakawa et al. (1976) give the resistivity for one sample, and conclude that it is difficult to make a comparison between their conclusions, because the ratio ρ_H/ρ is not defined. McGuire et al. (1977b) propose a new model which includes the sum of each magnetic sublattice moment, with a greater contribution for Gd. They show that a small change in the film content can drastically change ρ_H. For example, two samples with 16 and 18 at% Gd, have a Hall resistivity of 4.1 and $-4.6\,\mu\Omega\,\text{cm}$, respectively. They conclude that non-magnetic impurities (O_2, Ar, ...) enclosed in the film raise ρ and not ρ_H. A better knowledge of the resistivity will lead to a more quantitative analysis. (Przyluski et al. (1979) report, as for GdFe films, the variations of ρ between 0 to 100 at% Co. They noticed a maximum ($\approx 350\,\mu\Omega\,\text{cm}$) near 25 at%. But they give no analysis of their sample. They also report resistance, temperature coefficient of the resistance and microhardness of the films versus at% Co.) Brunsch and Schneider (1977b) observe an exponential increase of ρ with increasing O_2 pressure. Gron and Stobiecki (1979) show the influence of Ar on the resistivity of $Gd_{23}Co_{77}$ films prepared by sputtering: ρ increases with increasing Ar at%. But when studied as a function temperature they do not observe a change of polarity at T_{comp} for the ρ_H/ρ ratio, which remains positive. This fact seems surprising and may be induced by an error in the experimental procedure.

Some papers report the determination of R_s from EHE: Ratajczak et al. (1977) give a value of $5500 \times 10^{-12}\,\Omega\,\text{cm}\,\text{G}^{-1}$ for a $Gd_{19}Co_{81}$ sample; Stobiecki et al. (1978) studied the variation of R_s versus the Co concentration: below 80.5 at% it is positive and it becomes infinite at this composition; above this concentration it is negative (the two curves are symmetrical). Okamoto et al. (1974), for a film with an unknown composition, report a value of $4400 \times 10^{-12}\,\Omega\,\text{cm}\,\text{G}^{-1}$. Some anomalous Hall hysteresis loops have been reported. Gron and Stobiecki (1979) observed changes for these loops as a function of the Ar concentration; Lutes et al. (1977) interpreted their hysteresis loops as a function of the presence of magnetic sublayers. From the transverse Hall effect and in-plane loops Nagy et al. (1976a) built a model of inhomogeneous magnetic layers in the direction of the film thickness. They observed strong changes in shape and magnitude of the loops versus temperature; their in-plane loops possess satellite loops which reflect magnetization inhomogeneity. Tarnoczi et al. (1976), by successive deposition of two films, one without V_b and the other with V_b, observed anomalous hysteresis loops and transverse Hall effect, which demonstrate the change in magnetization for each layer. Imamura and Kobayashi (1975) show that in-plane loops change shape and amplitude depending upon the film composition.

In the field of galvanomagnetic effects, Okamota et al. (1975) and Berger (1976) report a negative magnetoresistance for GdCo sputtered films with a uniaxial magnetic anisotropy. They show that it is associated with the removal, by a field, of domain walls crossed by a current. Berger (1976) proposes a model which relates the sense of the dc current to the domain wall position and shows that the magnetoresistance is equal to $-\beta^2$ (β being the tangent of the Hall angle).

2.1.6.1.6.7. Magnetic domains and applications. The observation of *magnetic domains* has been the subject of various papers (see subsection 2.3). The polar Kerr effect and the Bitter technique have been used by Chaudari et al. (1973a,b), Cuomo et al. (1974), Gambino et al. (1974b), Shirakawa et al. (1974), Okamota et al. (1974, 1975), Esho (1975), Bourne et al. (1975), Visnoski et al. (1976), Bochkarev et al. (1976b), Ratajczak et al. (1977), Grundy et al. (1977), Tarnoczi et al. (1977), Matsushita et al. (1978) and Tsujimoto et al. (1980). The change of shape of the domains has been studied as a function of various effects such as ion or electron irradiation, temperature, composition, deposition rate, applied or demagnetizing fields and coating with another film. Gambino et al. (1974a) and Grundy et al. (1977) show that damaging by a flux of $5\text{–}7 \times 10^{15}$ Ar ions cm^{-2} destroys the stripe domains. Gambino et al. (1974a) investigated this effect versus the composition and the thickness of the films. They note that after application of an applied field and ion bombardment a film with an initially in-plane magnetization changes to a perpendicular magnetization. Bochkarev et al. (1976b) report annealing and demagnetizing effects on the stripe domain width; their patterns are as maze configurations. For a $Gd_{24}Co_{76}$ sample they observe, by increasing the temperature, an increase of the width; at 370 K the maze pattern vanishes and reappears at 377 K. The domains are stable between 293 and 333 K. Okamota et al. (1975) show the change of domain shape versus annealing and applied film; Shirakawa et al. (1974) report such changes versus composition and deposition rate; Matsushita et al. (1978) studied this change as a function of temperature after coating GdCo films with permalloy or metallic layers. Tsujimoto et al. (1980) show that the direction of the stripe domains can be controlled easily by coating the GdCo films with a NiFe layer. Gambino et al. (1974a) and Cuomo et al. (1974) observe a stripe width increase after ion bombardment or with increasing Co concentration; Ratajczak et al. (1977) and Hasegawa (1974) report a decreasing width after annealing. Bourne et al. (1975) noticed a variation in stripe width within the same film and for different samples as the composition varied. Their stripe domains are more irregular near the magnetic compensation. Freiser (1980) studied other configurations of magnetic domains such as zig-zag walls (saw-teeth) and "static magnetically charged walls" for films prepared by evaporation. He explains this shape by a compromise between the magnetostatic energy and the anisotropy energy. Taylor (1980) presents identical domains for evaporated and sputtered Co-rich films. He notices a change in their configurations versus the thickness and M_s. He concludes that such materials can exhibit bubbles with a much greater range of sizes than garnet layers. Ratajczak et al. (1977) showed bubbles domains for a $Gd_{19}Co_{81}$ film.

With regard to magnetic domains, other studies have been devoted to the *dynamic properties*. Cuomo et al. (1974) showed that bubbles can reach a mobility and velocity higher than 1000 cm/s. Miyama et al. (1978, 1980) studied the effects of applied driving fields, of the temperature and of a permalloy film coating. They noticed a wall velocity as high as 15 000 cm/s for samples with high H_c. Their sputtered films had an orthorhombic anisotropy. They found a non-

linear dependence of the wall velocity on the driving field, and a suppression of the saturation wall velocity with an overlayered permalloy film. They performed an analysis of their results by taking in account the subnetwork moments. Hasegawa (1974) and Hasegawa et al. (1974) report that thermal annealing (450 K) and an ion radiation of 10^{12} ions cm^{-2} are sufficient to lower the wall-motion coercivity for samples with 77–80 at% Co. Onishi et al. (1979, 1980) devised a new method in order to measure the domain wall velocity: they used the Hall effect, and showed that V_H and the position of straight domain walls are dependent upon the geometry of the film. Their films, which were prepared by sputtering or thermal evaporation (W crucibles), exhibited a large EHE.

Thermodynamic recording has first been reported by Chaudari et al. (1973b); they describe a method to write and erase spots, by use of a laser and of an external magnetic field. Matsushita et al. (1975a) obtain nearly identical phenomena for samples exhibiting rectangular hysteresis loops with large H_c values at T_{comp}. The domains are circular, closer in shape and stable, their diameter can vary according to the applied field and the laser pulse width. Wieder (1974) studied the dynamic magnetization reversal which occurs during laser-induced thermomagnetic recording. Togami (1978, 1979a,b) analyzed the characteristics of $Gd_{25}Co_{75}$ sputtered films according to their dependence on the homogeneity, the thickness, the temperature and H_c; he found that these films have a good writing sensitivity and stability even after many write–erase cycles with a laser beam. The stability is perhaps due to an increase of the wall coercivity. Mimura et al. (1976c) rule out GdCo films for thermomagnetic writing because they claim that T_c is too high for such alloys. (Lee and Heiman (1975a) report T_c is higher than 500 K for $GdCo_2$ and $GdCo_5$ alloys.)

2.1.6.1.6.8. Characterization by X-ray and electron diffraction. Correlation between magnetic properties and X-ray diffraction and electron diffraction or electron imaging has been investigated by several authors. From changes in *X-ray diffraction* patterns Onton et al. (1976), Wagner et al. (1976), Onton and Lee (1976), Covault et al. (1976) and Heiman et al. (1978) have tentatively explained the mechanism of K_u. Their main conclusions are derived from X-ray spectrum profiles. Thus changes in the patterns have been found according to the experimental procedures: sputtering with and without bias and different values of V_b and thermal evaporation. Without bias the spectra present only one large diffraction peak (at about 20°). With V_b up to −200 V there is simultaneously a shift of this peak towards 22–25° and the appearance of a shoulder (at about 15°). Covault et al. (1976) do not observe this shoulder. Heiman et al. (1978) notice that it vanishes for high V_b values (−400 V). The position of these peaks vary slightly from one experiment to another. Onton and Lee (1976) and Esho (1979) conclude that thermally evaporated and bias sputtered films are similar. Heiman et al. (1978) rejected the "correlation between X-ray diffraction profiles and K_u" (see section 2.1.6.1.5.1). They base this conclusion on the facts that X-ray profiles of ternary alloys are independent of bias and anisotropy effects and that the annealing effect reduces K_u with no change in the diffraction profiles. Esho (1979) observed the influence of N_2 and Ar gas on the X-ray

diffraction spectra. He notes that N_2 does not affect the pattern, and that an increase in Ar content is correlated with a peak shift towards higher angles. Cargill (1978a,b) and Mizoguchi and Cargill (1979) characterize the effects of deposition conditions on microstructure by SAS and large-angle scattering. They discuss the effects of V_b, of O_2, of annealing and of ion bombardment on the SAS characteristics for GdCo and GdCoMo films. Thus with increasing ion bombardment the intensity of the SAS increases, and the peak shifts to smaller scattering angle. They present SAS data for a zero-bias sputtered $Gd_{82}Co_{18}$ film and conclude that the scattering pattern probably reflects a microstructure of aligned voids of rod or platelet shape. Moreover they explain the O_2 contamination, by building a model of magnetization near a rod shaped void at which Gd_2O_3 is being precipitated. The corresponding SAS is attributed to phase separation involving the formation of Gd_2O_3 clusters. They discuss the anisotropic and isotropic SAS in terms of microstructural inhomogeneities and make a large survey of the results reported previously.

The first *electron microscopy* studies have been made by Herd and Chaudari (1973). They report that their as-deposited sputtered films exhibit coherent scattering regions which are smaller than 15 Å. After annealing at 670 K they notice a sharpening of the diffuse haloes. From the profile of the low-angle scattering they conclude that a columnar structure develops in the film with no evidence for the formation of voids. Herd (1977, 1978, 1979) studied the microstructure with a higher resolution microscope. The main results, for O_2 contaminated and uncontaminated films, confirm the columnar structure and show the existence of a void network structure. The columnar structure disappears either for deposition with −50 V bias or after annealing at 520 K for thermal evaporation. At this temperature a glass transition is induced and above 520 K a considerable plastic flow occurs. Many electron diffraction patterns are given for different film compositions, different O_2 contamination and after annealing. These patterns can present either a single broad peak or split peaks. A single broad peak indicates a larger homogeneity of the films and this state is more likely to be found in thermally evaporated films. The presence of two types of SAS, one associated with voids and one perhaps due to mass density variations, indicates phase separation. Leamy and Dirks (1977), Dirks and Leamy (1977a,b) and Leamy and Dirks (1978) show that vapor and sputter films possess an anisotropic microstructure which consists of columnar regions surrounded by a network of lower density material. The columns are oriented according to the direction of incidence of the vapor from the source. This structure is produced by self-shadowing of the incident vapor atoms during film growth. They discuss their observations in detail and present structural models for normal- and oblique-incidence deposition. In addition SAS electron patterns are presented to verify the columnar nature of the microstructure. Hoffmann et al. (1979) report a closely identical model, with a columnar structure perpendicular to the film plane. Nandra and Grundy (1976) noticed this configuration. Graczyk (1976, 1978) studied the scattered electron intensity, SAS intensity profiles and reduced RDF for sputtered thin films of different thicknesses and

compositions. He compares his results to that obtained by X-ray diffraction as mentioned above. In his first paper he concludes that the initial layers have a modified structure as compared to the thicker film. This modification is induced by the initial transients in the sputtering process and the high reactivity of Gd with O_2; this leads to a smaller density of Gd–Co pairs and an increasing of Gd–O pairs. In the second paper he observes the presence of voids and compositional fluctuations in the films, and discusses the problem of porosity and roughness. He finds that phase separation occurs as rod and sheet shaped configurations with a direction perpendicular to the film plane. For sputtered films of different compositions deposited at different bias, Wang et al. (1979) report scattered intensity and reduced RDF curves, some of them being near identical to the ones of Graczyk (1978). Cargill (1975), Nandra and Grundy (1977), Graczyk (1978), Wang et al. (1979) and Urner-Wille and Winkler (1979a) investigated the atomic arrangements. Nandra and Grundy (1977) report the interference function for different compositions and compare it to the ones obtained in the microcrystalline state. Their RDF exhibits either a shoulder relative to the Gd–Co distance, or a splitting of the first peak relative to the Co–Co and Gd–Gd distances. This is in disagreement with the RDF obtained by Graczyk (1976) from electron diffraction and by Cargill (1975) from X-ray diffraction for such an alloy as $Gd_{18}Co_{82}$. Urner-Wille and Winkler (1979) reported on the electron diffraction intensity, elastically scattered intensity and reduced RDF. The effect of annealing (up to 850 K) on the peak position and the effect of O_2 were discussed. As Graczyk (1976), they observed the formation of Gd–O and Gd–O–Gd bonds. They confirm that GdCo films have columnar structures and are sensitive to O_2 contamination (diffusion). Two other results were noted: the Co–Co and Gd–Co pair distances are equal to the ones reported by Graczyk (1976), and after annealing at 730 K the film crystallizes. Hoffmann and Winkler (1979) report identical results, and confirm by AES measurements the O_2 diffusion during annealing. Therefore new experiments must be carried out to refine the structural order; in this way, Herd (1977) and Nandra and Grundy (1977) propose high resolution electron microscopy as the most appropriate technique.

2.1.6.1.7. Terbium–cobalt alloys

Lee and Heiman (1975a) studied the magnetic properties of *evaporated* films with different compositions. They found that T_c is greater than 600 K, T_{comp} decreases with increasing Co content and H_c is greater than 20 kOe at 293 K. They noticed that some samples are difficult to saturate. Heiman et al. (1975) report that K_u has a value sufficient to induce a perpendicular magnetization. Prinz et al. (1979, 1980) show that TbCo films possess the same characteristics as SmCo and GdCo alloys for magneto-optic experiments. Dirks et al. (1977) determined the values of T_{comp}.

2.1.6.1.8. Dysprosium–cobalt alloys

Jouve et al. (1976) compared $DyCo_{3.5}$ alloys with (Gd, Ho or Er)$Co_{3.5}$ ones. They noticed that T_c (900 K) and T_{comp} (200 K) are close to those of Gd. Roberts et al. (1977) find a strong reduction of the moment for $DyCo_x$ (and $HoCo_x$) films

prepared by e-gun with more than 15 at% R. They studied the variations of $4\pi M_0$, l and K_u with composition, and noted that K_u increases with increasing R content. In contrast, Jouve et al. (1976) claim that K_u is independent of the R concentration. Coey et al. (1976) and Chappert (1979) gave the magnetic properties as deduced from Mössbauer spectra for sputtered $DyCo_{3,4}$ alloys. They determined the hyperfine interactions and concluded that this alloy has a sperimagnetic structure and that the Co moment is ferromagnetic. They report T_c and T_{comp} to be 900 and 300 K, respectively. Luzgin and Domyschev (1977) found that evaporated $DyCo_3$ alloys deposited onto hot substrates (350 K) are ferrimagnetic materials. They observed the presence of cylindrical magnetic domains and studied the elastic stresses.

Asomoza et al. (1977) and Asomoza (1980) investigated ρ_H of $DyCo_3$ alloys. They did not observe the reversal of the magnetic moment of Dy in the temperature range of 200–350 K; therefore T_{comp} is higher than 350 K. Ogawa et al. (1976) reported T_{comp} to be near 240 K for $DyCo_x$ sputtered films. They claim that the Dy moment predominates in ρ_H, while Asomoza et al. (1977) concluded that it is the Co moment that predominates.

2.1.6.1.9. Holmium–cobalt alloys

The first magnetic properties of evaporated HoCo films were investigated by Heiman and Lee (1974) by polar Faraday rotation and magnetic measurements. They observed that with increasing Co content T_c increases (150 to 600 K), T_{comp} decreases (300 to 120 K) and that T_c is higher and T_{comp} is lower than in the crystalline state. The results are explained in terms of charge transfer. They support the origin of K_u as due to the orbital moment of the Ho atoms, and rule out stress-induced, shape anisotropy and Co pair-ordering mechanisms. In later papers, Lee and Heiman (1975a,b) and Heiman et al. (1975b) report identical conclusions and add that the easy axis of magnetization is related to the incident vapor beam and that such materials can sustain bubble domains. Roberts et al. (1977) note the important role of charge transfer. They claim that the origin of K_u comes from the vital role of Co atoms (dipolar mechanism), and another significant contribution may be due to a slight growth-induced preferential orientation of the local crystal field anisotropy. For $Ho_{20-40}Co_{80-60}$ alloys Dirks et al. (1977) observed that T_{comp} increases with decreasing Co content, and reaches 80 K for a $Ho_{20}Co_{80}$ alloy. (Lee and Heiman (1975a) give T_{comp} as 150 K for a $HoCo_3$ alloy.) By comparison with a GdCo alloy they conclude that, for $HoCo_x$ (and $ErCo_x$) alloy, T_{comp} is considerably reduced and suggest that the effect of the local crystal field is strong. Grundy et al. (1977) find that the origin of K_u for $HoCo_4$ samples is the same as for $GdCo_4$ alloys.

Ratajczak and Labedzka (1977) and Ratajczak and Goscienska (1979, 1980) studied the anomalous Hall hysteresis loops in the vicinity of T_{comp} for flash-evaporated films. They showed the relation between magnetic domain structures and hysteresis loops at T_{comp}. They explained the anomalous configurations in terms of film homogeneity and the magnetization reversal process. They propose a model of change in film composition and reject the one of magnetic

compensation interface proposed by Esho (1976). Ratajczak et al. (1979) study EHE near T_{comp} for films with an unknown composition. They observe that ρ_H is always positive with a sharp cusp at T_{comp}. They conclude that the Hall effect arises from Ho. Such results are surprising, because the reversal of the magnetic moment of R at T_{comp} is not observed. Asomoza et al. (1977) and Asomoza (1980), for $HoCo_3$ alloys, observe a change of sign $(-)\rightarrow(+)$ at T_{comp} (220 K) for the ρ_H variation versus temperature. They conclude that the Hall effect is associated essentially with the Co moment. Matsushita et al. (1975b) studied the thermomagnetic writing properties using a laser beam on evaporated HoCo films. They give hysteresis loops, H_c and saturation force results. The last one is large and allows one to write spots at a temperature lower than T_c. They report that the diameter of the spots change when the applied external magnetic field is increased. As for GdCo films, Leamy and Dirks (1977, 1978, 1979) and Dirks and Leamy (1978a) observed the same anisotropic microstructure for Ho_xCo_{1-x} films. They note that K_u is almost stress independent (weakly positive values for magnetostriction) in $HoCo_x$ materials and support the correlation between the orientation of K_u and the vapor beam direction (Heiman et al., 1975b). Nandra and Grundy (1977a,b) find from the electron diffraction pattern that the interference functions for vapor quenched $HoCo_x$ films are dependent on the concentration. They remark that the peak position moves to lower values as the at% Ho increases; for the composition $Ho_{54}Co_{46}$ this decrease is surprisingly large. They compare their results to microcrystalline models. They discuss RDF and determine the nearest distances between Co–Co, R–Co and R–R atoms. They observed that, when the Ho content increases, the first peak exhibits a shoulder (due to Ho–Co correlations) and that a third peak appears (due to Ho–Ho correlations). These results indicate definite atomic spacings and short-range order. For $Ho_{20}Co_{80}$ alloys the stripe domains appear for thicknesses above 1400 Å and change in configuration with increasing film thickness. They conclude that strong uniaxial magnetic anisotropy can coexist with the disordered atomic arrangement. Hoffmann et al. (1979) studied the mechanism of this anisotropy by means of high-resolution wide-angle and low-angle electron diffraction in $HoCo_x$ films prepared by e-gun. The as-deposited films have an in-plane magnetization, which becomes perpendicular at about 650 K (the appearance of stripe domains), and exhibit a columnar microstructure. They conclude that K_u is due to anisotropic pair ordering generated by deactivation of Ho moments due to O_2 diffusion.

2.1.6.1.10. Erbium–cobalt alloys

Blades (1968) studied some properties of ErCo films prepared by fast quenching covaporization. An alloy such as $Er_{16}Co_{84}$ exhibited no metastable homogeneous crystallographic systems and has magnetic properties similar to those of Co. Jouve et al. (1976) report for $ErCo_{3.5}$ alloys that T_c is 940 K and T_{comp} is 94 K—this value is close to the one obtained by Dirks et al. (1977). Asomoza et al. (1977) and Asomoza (1977) observed a T_{comp} near 50 K for $ErCo_3$ from a study of the ρ_H variation versus temperature.

2.1.6.2. *Crystalline compounds*

2.1.6.2.1. RCo_2 compounds

Some magnetic, magneto-elastic and crystalline properties of films such as RCo_2 which are either well crystallized or not in a well-defined amorphous state (see section 2.1.5.2) were studied by Domyshev et al. (1974), Buravikhin et al. (1975) and Luzgin and Domyshev (1975). Domyshev et al. (1974) report that $GdCo_2$ exhibits the same properties as $GdMn_2$ and $GdFe_2$ films. However, $GdCo_2$ samples exhibit the highest H_c, H_k, $4\pi M_0$ and internal microstresses. Buravikhin et al. (1975) give the magnetization and magnetostriction as a function of the Gd concentration. Comparing this with $SmCo_2$ and $TbCo_2$ specimens they observe an abrupt decrease to zero of the magnetostriction in the sequence Tb, Sm and Gd. These compounds display a change in magnetic domain structure with varying temperature and applied field. They report that H_c increases abruptly from 600 to 700 K for $GdCo_2$ as well as for $SmCo_2$ films. They discuss their results in terms of grain size. One must remark that the films seem well crystallized about 600 K, while pure amorphous films have a transition temperature at about 780 K. Luzgin and Domyshev (1975) have reported the magnetic and magneto-elastic properties of RCo_2 films (R = Y, Nd, Pr, Sm, Gd, Tb and Dy) prepared by thermal evaporation. They give the variation of H_c, H_k, M_0, T_c and magnetostriction as a function of the element R and the temperature. For thick SmCo films, prepared by co-evaporation (crucibles) Hardt (1966) reported that the formation of the $SmCo_2$ compound was associated with one or more structures. (Buschow (1977a), for bulk $GdCo_2$, showed the influence of H_2 absorption on the magnetic properties.)

2.1.6.2.2. RCo_5 and other cobalt-rich compounds

RCo_5 compounds generally exhibit a high H_c or intrinsic coercivity (H_{ci}). Stoffel (1968) obtained H_c values of 600 Oe at 170 K and 535 Oe at 293 K for evaporated $NdCo_5$ films, and after annealing at 910 K. For sputtered $SmCo_5$ films deposited onto hot substrates (600 K) Theuerer et al. (1969) observed H_c values as high as 20 kOe (1 kOe in the bulk). This value decreases rapidly when the temperature increases (1 kOe at 1170 K). Upon addition of Cu, H_c reaches values as high as 30 kOe. Allen et al. (1974) and Allen and Nelson (1974), for high-rate sputtered thick films such as $SmCo_5$ single-phase, obtain H_{ci} values of 35–40 kOe after annealing at 870–970 K. The dependence on the substrate temperature, the thickness, the evaporation rate and the vacuum were studied and H_c values up to 17 kOe were found by Beloussov et al. (1976) for flash evaporated $SmCo_5$ and $GdCo_5$ films. Bendson and Judy (1973), for dc triode sputtered $Sm_{22}Co_{78}$ and $Gd_{12}Co_{88}$ films, obtained a H_c of 4 kOe and 1.2 kOe, respectively. (Their samples are crystallographically poorly defined.) Kumar and Das (1978) and Kumar et al. (1978) obtained for arc plasma sprayed $SmCo_5$ films a high H_c (5.4 kOe) and H_{ci} (67.5 kOe) after annealing of the near amorphous initial samples at 1200 K. Above this temperature the films recrystallize and H_{ci} decreases. This decrease is observed when the films contain both the $SmCo_5$ and Sm_2Co_{17} phases. The authors suggest that this method is efficient to produce magnetic materials. For flash-evaporated $SmCo_5$ and $Gd_{10}Co_{90}$ films deposited onto hot substrates (470 K)

Shelkovnikov et al. (1976) reported low H_c values like 10–100 Oe. Hardt (1966) found that evaporated films with a fine microstructure had H_c values from 30 to 340 Oe depending on the Co/Sm ratio, the annealing temperature (760–940 K) and the presence of a magnetic field. The only conclusion he can draw is that H_c decreases for higher Co concentrations (above the $SmCo_5$ stoichiometry).

Stoffel and Strnat (1965) studied for the first time some magneto-optical characteristics of RCo_5 films (R = Y, Nd, Sm and Gd). Stoffel (1969) measured the index of refraction and the magneto-optic properties of the Nd_2Co_5 and Nd_2Co_{17} compounds. By comparison between the R elements, he shows that the absolute value of the magneto-optic effect, for RCo_5 compounds, decreases with increasing R content and that it is proportional to the total magnetization and not to a sublattice magnetization. Benson and Judy (1973) studied $(Sm, Gd)_{5-35}Co_{95-65}$ films as a function of composition and grain size, the moment density, squareness, rotational hysteresis loss and domain pattern as ripple configurations. Their films are isotropic with an in-plane magnetization. They discuss the phenomenon of wall motion reversal. Damba et al. (1974), for films deposited onto hot substrates (470 K) by co-evaporation (W crucibles), studied the magnetization as a function of the Co content and annealing at 670–720 K. They observed the formation of ferromagnetic Gd_2Co_{17} and of $GdCo_5$ which exhibit a large magnetization. Shelkonikov et al. (1976) noticed large magnetic after effects, which may be due to change in the magneto-elastic interaction between domain boundaries and lattice defects in their $SmCo_5$ films. They studied the magnetization reversal phenomenon which involves pronounced after effects. Zhang et al. (1980) report hysteresis loops, T_c, M_s and H_c values for amorphous samples annealed up to 1170 K. Their films such as SmCo or RR'Co (undetermined composition) show a decrease of T_c with increasing (RR') content, low H_c values ($\approx$500 Oe) and large relative magnetization values after annealing above 1170 K, which is interpreted as a signal of the presence of β-Co crystallites. Their materials do not have large magnetic properties because of the absence of the $SmCo_5$ compound. Bochkarev et al. (1973) investigated the resistivity, the Hall emf, and the thermo-emf of $DyCo_5$ films prepared by thermal evaporation. Their initial deposits are nearly amorphous. After annealing at 773 K they observe the formation of the $DyCo_5$ compound, and after extended annealing at this temperature the Dy_2Co_7 and Dy_2Co_{17} structures. From the Hall emf, Hall constant and Hall emf isotherm, they showed that $DyCo_5$ is ferromagnetic with a T_{comp} of 480 K. This temperature decreases with the formation of the other compounds. Besides, the change in sign of the Hall emf and Hall constant ($(-)\rightarrow(+)$) with increasing temperature (from 300 K ($DyCo_5$) to 200 K ($DyCo_5 + Dy_2Co_7 + Dy_2Co_{17}$)), is explained by reorientation of the magnetic sublattice magnetizations. The phenomena of amorphous–crystalline transitions and of structural transformations were described for (Sm, Gd and Dy)Co_5 and for mischmetal such as the $Sm_{0.5}(RR')_{0.5}Co_5$ or $RR'Co_5$ (R, R' = La, Ce, Nd and Pr) compounds. Buravikhin et al. (1975b, 1979) and Yegorov et al. (1977) report $SmCo_5$ phase transformations for films annealed up to 1070 K. They observe in a general manner the formation of Sm_2Co_7 and Sm_2Co_{17}; the same nominal

compounds have been observed for Gd and Dy by Damba et al. (1974) and Bochkarev et al. (1973), respectively. Yegorov et al. (1977) and Buravikhin et al. (1975b) claim that two isostructural $SmCo_5$ phases should coexist. Buravikhin et al. (1979) showed that the vacuum quality and the rate of condensation can influence the different structures which are obtained. Their as-deposited films exhibit $SmCo_5$, Sm_2Co_{17}, β-Co and Sm_2O_3 phases. Kumar and Das (1978) and Kumar et al. (1978) found an amorphous–crystalline transition temperature in the range of 770–970 K, with formation of $SmCo_5$ and sometimes of Sm_2Co_{17}. They discussed a method to obtain pure $SmCo_5$ films. Allen et al. (1974) and Allen and Nelson (1974), after annealing their $SmCo_5$ specimens at 1270 K, observed grain growth up to about 1 μm. Hardt (1966), for thin films with a small grain size ($\approx$50 Å), observed no change of the microcrystalline structure after annealing up to 970 K in a vacuum of 10^{-7} Torr. Inside an electron microscope and by beating with the electron beam, Herd and Chaudari (1973) and Herd (1977, 1978) have observed, for rf sputtered GdCo films, various compounds such as $GdCo_3$, $GdCo_5$, Gd_2O_3, α-Co, CoO and/or GdH_2, according to the temperature and the annealing method (slow heating or pulse annealing). The formation of the $GdCo_3$ and $GdCo_5$ compounds is only observed for films which are not contaminated by O_2, and by flash annealing. The formation of Gd_2O_3 and of Co phases is obtained after heating at about 780 K or in O_2 atmosphere. Nandra and Grundy (1977a,b), for $(Gd, Ho)_{20}Co_{80}$ amorphous metastable films prepared by e-gun, reported the beginning of crystallization of α-Co at about 620 K and an obvious crystallization above 870 K. Above 870 K several phases appear and these are identified as microcrystals (small clusters) of RCo_2, RCo_3, R_2Co_7, RCo_5 and R_2Co_{17}, and also α-Co, CoO and R_2O_3 crystallites. The electron diffraction patterns are complex and difficult to index; however, it seems that the RCo_5 and R_2Co_7 compounds are observed more often. Hoffmann et al. (1979) show that

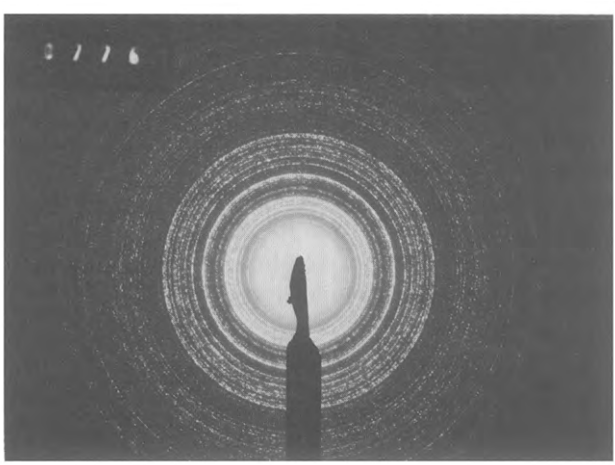

Fig. 3. Complex electron diffraction pattern of a GdCo film, initially amorphous, after annealing by means of an electron beam.

$GdCo_x$ and $HoCo_x$ films crystallize at 770 and 900 K, respectively; the columnar structure vanishes, with formation of various structures such as $GdCo_5$, Gd_2O_3, Co and Gd; and $HoCo_3$, Ho_2Co_{17}, Ho_2O_3, Co and Ho. Gasgnier (1981) showed for $GdCo_x$ films after heating at high temperature, the formation of complex coexistent structures, as reported in fig. 3. Jain and Subbarao (1975) investigated the crystallization phenomenon of their $RR'Co_5$ films. After annealing in air at 570 K no structural order appears at 720 K, and then at 870 K they observed the coexistence of various phases such as $RR'Co_5$, Co_2O_3 and Co_3O_4. Inside an electron microscope and after annealing with the electron beam there is formation of $RR'Co_5$ and of Co_2O_3. Zhang et al. (1980), after annealing $SmCo_x$ and $Sm(RR')Co_x$ samples up to 1170 K, reported the formation of β-Co crystals but not any of RCo_5. They showed that the addition of RR′ in mischmetal films decreases the amorphous–crystalline transition temperature (below 720 K). At 1170 K the authors claim the observation of an unknown oxide and a larger β-Co crystal. These conclusions are doubtful because the interpretation of the electron diffraction patterns is not clear and the film compositions are not reported.

2.1.7. *Rare earth–nickel systems*

2.1.7.1. *Binary amorphous alloys*

2.1.7.1.1. Yttrium–nickel alloys

McGuire and Gambino (1978) studied some magnetic and transport properties of sputtered $Y_{1-x}Fe_x$ ($x > 82$) films. They report a decrease of ρ and ρ_H as the Y content increases, a T_c of 360 K for low Y content, a negative ρ_H in contrast to the one of YFe and YCo alloys, and a positive ρ_H/ρ ratio. Asomoza et al. (1979) and Asomoza (1980) claim that YNi_3 alloys are not magnetic and do not exhibit EHE. The resistivity of $YNi_{3.5}$ films shows a minimum at 14 K and then increases until 300 K. They have a low isotropic and anisotropic magnetoresistance which can be induced by impurities.

2.1.7.1.2. Gadolinium–nickel alloys

Lee and Heiman (1975) reported a T_c of 38 K for $GdNi_2$ films which compares to 85 K for the bulk or crystalline compound and noticed an enhancement of the Ni–Ni exchange for such materials. Imamura and Kobayashi (1975) showed that evaporated films possess a perpendicular anisotropy for thicknesses above 1000 Å. Depending on the Gd content they observed a rapid decrease of $4\pi M_s$ from 450 Oe to zero for 0 to 10 at% Gd. Important studies were made in the field of transport properties such as EHE and ρ. Shirakawa et al. (1976) reported EHE and polar Kerr effect hysteresis loops for sputtered and evaporated Ni-rich films. They observed a reversal of the EHE loops with increasing temperature (77 to 127 K) for sputtered samples. The direction of the sign reversal ((+) to (−)) is opposite to the one for Gd–Fe and Gd–Co alloys. They suggested an identical behavior for the Kerr effect, and conclude, as McGuire et al. (1977), that Ni contributes a negative sign. Mimura et al. (1976b), for rf sputtered Ni-rich films (85 and 95 at%) with perpendicular magnetization, reported hysteresis loops at 293 and 77 K. They observe a negative polarity of the EHE with no reversal

effect. For a $Gd_{15}Ni_{85}$ alloy they reported a T_{comp} of 130 K. They discussed their results in terms of the moments and the signs of V_H for Gd and Ni, and conclude that Ni plays a dominant role. McGuire and Gambino (1978) reported that sputtered Gd_xNi_{1-x} films are ferrimagnetic with Gd and Ni coupled antiparallel. Depending on the composition they showed that the Ni moment decreases with increasing Gd content, and that T_c is minimum (40 K) for 20 at% Gd. They investigate $4\pi M_s$, $4\pi M_0$, ρ, ρ_H and ρ_H/ρ variations as functions of the composition and temperature. They observed a decrease for ρ_H/ρ as the Gd content increases, and above 40 at% Gd this ratio becomes negative. They assigned to Ni a large negative Hall effect, and explain their results using a model like that for GdCo. But for $Gd_{1-x}Co_x$ alloys the Co moment goes to zero at $x \approx 0.5$, while for $Gd_{1-x}Ni_x$ alloys the Ni moment is small at $x \approx 0.2$, but does not completely vanish until $x > 0.57$. They conclude that it is difficult to evaluate Ni contributions and that their model is surely not the best.

Asomoza et al. (1979a) and Asomoza (1980) have studied magnetic and transport properties of $GdNi_z$ alloys ($2.4 \leq z \leq 3.6$) $GdNi_3$ samples exhibit a Curie–Weiss behavior in the paramagnetic regions. Depending on the Ni content T_c is slightly composition dependent ($37 \leq T_c \leq 43$ K). $GdNi_3$ is like a soft ferromagnet. The resistivity of $GdNi_3$ and $GdNi_{4.5}$ alloys exhibit a complex behavior. Each sample has a sign reversal of the isotropic magnetoresistance: negative for $GdNi_3$ and positive for $GdNi_{4.5}$. $GdNi_3$ specimens show a positive EHE between 1.2 and 40 K, and a decrease of the spontaneous ρ_H, which is equal to zero at 50 K.

2.1.7.1.3. Dysprosium, holmium, erbium–nickel systems

Asomoza et al. (1977), Fert et al. (1977), Fert and Asomoza (1979), Asomoza et al. (1979a,b) and Asomoza (1980) reported numerous magnetic and transport properties relative to (Dy, Ho or Er)Ni_3 alloys. The main results show that such materials have a paramagnetic susceptibility which does not deviate from the free ion susceptibility at low temperature. Their resistivities exhibit a minimum for temperatures between 11 and 24 K. This minimum decreases from Dy to Er and it is also dependent on the applied field. For $HoNi_3$ alloys, as the applied field increases the minimum shifts towards higher temperature (11 to 22 K). The three materials show a positive isotropic magnetoresistance and moment, and possess an anisotropic magnetoresistance due to the rare earth quadrupole. It is positive for (Dy, Ho)Ni_3 and negative for $ErNi_3$ (change of sign in the middle of the heavy rare earth series). $DyNi_3$ and $HoNi_3$ have a positive Hall effect. Asomoza et al. (1979a) conclude that the magnetic measurements can be interpreted on the basis of a phenomenological random axial crystal field model, and that entirely new aspects of the influence of the amorphous structure appear in the transport properties, i.e., increase of resistivity on ordering and associated positive magnetoresistance, which can be ascribed to coherent exchange scattering by neighbouring ions. Lee and Heiman (1975a) reported on some magnetic properties of Ho_xNi_y alloys. They found a T_c greater than 400 K for Ho_2Ni_{17} and $HoNi_5$ films and a $T_c = 15$ K for $HoNi_2$ specimens. Lee and Heiman (1975b) show that HoNi films, with more than 85 at% Ni are magnetic near 293 K.

2.1.7.2. *Ternary amorphous gadolinium–(cobalt)–nickel alloys*

Hasegawa and Taylor (1975) determined the spin and magnetic moments versus temperature and composition of co-evaporated (3 e-guns) $Gd_{1-x}(Co_{1-y}Ni_y)_x$ alloys. They observed for their ferrimagnetic films a magnetization behavior described as a pseudo-two-lattice model, the two transition metals forming one sublattice which interacts antiferromagnetically with the Gd one. These sublattices are coupled less strongly than in GdCo or GdCoMo systems (small intersublattice exchange interaction). Their films crystallize at about 500 K. Gangulee and Kobliska (1978) reported from spin and exchange interaction, $4\pi M_s$, g and T_c measurements that Ni and Co are separate constituents with the Co atom being the magnetically dominant one in $Gd_{21}Nd_{50}Co_{29}$ alloys. They obtain a T_{comp} of 255 K. They concluded by comparison of the mean-field analysis model with their results, that it is difficult to obtain reliable values of the exchange interaction energies with three or more magnetic constituents, unless complete magnetization data up to T_c are available. Meyer et al. (1975) studied the change of T_c, T_{comp}, $4\pi M_s$, AQ and l values by substitution of Co by Ni in dc sputtered GdCo films. Samples such as $Gd_{21}Co_{79}$ have a T_c and T_{comp} of 880 and 230 K, respectively; with addition of Ni (20 and 50 at%) T_{comp} increases up to 265 K and T_c decreases to 750 K. In the same way, $4\pi M_s$ decreases from 1600 to 800 G (50 at% Ni), and the AQ value decreases by a factor of four, whereas l remains constant. They conclude that their alloys are constituted from Gd atoms and "fictitious" 3d atoms which have an atomic moment intermediate between Co and Ni. Asomoza and Campbell (1977) found the saturation Hall resistivities versus temperature for Gd $Gd(Co_{25}Ni_{75})_3$ alloys change sign at $T_{comp} \approx 220$ K. By comparison with the other RCo_3 alloys the ternary alloys show a lower magnitude of the Hall effect, corresponding to the lower average transition metal moment. McGuire et al. (1977) obtained a ρ_H/ρ value near 1 for two different samples.

Taylor (1980) observed, using a ferrofluid method, the existence of charged walls with a saw-tooth configuration for sputtered and evaporated films such as $Gd_x(Co_yNi_{1-y})_{1-x}$ $(0.25 \leq y \leq 0.50)$. These domains vary with thickness and magnetization. By substitution of Ni for Co in GdCo films a strong decrease occurs for the $4\pi M_s$ and H_c values. These films have their hard axis perpendicular to the surface. He studied wall motion and bubble rotation.

2.1.7.3. *Crystalline compounds*

2.1.7.3.1. Lanthanum–nickel systems

Gasgnier (1981) prepared LaNi films by thermal evaporation. Electron diffraction measurements of the as-deposited samples show the coexistence of small crystallites of Ni and an amorphous alloy. After annealing with the electron beam, Ni recrystallizes, and a second ring pattern appears which can be indexed according to a hexagonal structure with: $a = 3.95$ and $c = 6.90$ Å. By further annealing, new ring patterns appear, but they are complex. Only one of them was indexed as a fcc lattice with $a \approx 7$ Å (bulk $LaNi_2$ is fcc with $a =$ 7.35 Å). So, it was not possible to link the thin film structures to ones in the bulk state. Also for CeNi films unknown structures were observed.

2.1.7.3.2. Samarium–nickel systems

As mentioned previously for GdFe and GdCo, the films studied by Buravikhin et al. (1975a) are not strictly amorphous. They reported the magnetization as a function of Sm content—it decreases rapidly to zero for 22 at% Sm—and magnetostriction (near 0) for $SmNi_2$.

The formation of a number of crystal structures were observed as the Sm concentration varied for SmNi samples deposited at 470 K, and annealed at 740 K: Ni and Sm (15%), Ni, Sm_2Ni_{17}, $SmNi_2$ and $SmNi_5$ (15–40%), Ni and $SmNi_2$(40–60%) and $SmNi_2$ and SmNi (60–70%) have been observed by Buravikhin et al. (1973). They reported $4\pi M_s$ before and after annealing and gave some hysteresis loops. They showed that Sm_2Ni_{17} has a higher magnetization than Gd_2Ni_{17}. They conclude that Sm is less active than Gd in forming intermetallic compounds (see references listed by these authors). Kameneva et al. (1976) studied the magnetic properties of SmNi films as a function of the Ni content and temperature. They showed that such materials can have a superparamagnetic behavior.

2.1.7.3.3. Gadolinium–nickel systems

Buravikhin et al. (1975a) observed a more rapid decrease of the magnetization for GdNi than for SmNi—it reaches zero at ≈16 at% Gd; the magnetostriction of GdNi is lower than for GdFe and GdCo and decreases rapidly to zero for 32 at% Gd as in $GdNi_2$.

Egorov et al. (1974), by simultaneous thermal evaporation (tungsten crucibles), studied the formation of various compounds in GdNi films deposited at 470 K and heated at 720 K. They observed, depending on the Gd content, the presence of several phases such as Gd_2Ni_{17}, $GdNi_4$, Gd_2Ni_7, $GdNi_3$, $GdNi_2$ and GdNi. Domyshev et al. (1974) reported the magnetic, magnetostriction and magnetoelastic properties for $GdNi_2$ compounds. They measure a T_c of 140 K, and low magnetostriction, $4\pi M_s$, H_c and H_k values compared to bulk $GdCo_2$. As mentioned above, Kamena et al. (1976) attributed a superparamagnetic behavior to GdNi films. They reported numerous data such as H_c, $4\pi M_0$, hysteresis loops and magnetic domains as a function of the Gd content, the annealing temperature and the Ni grain size. They observed that the magnetic domains vanish when the Gd content increases. This may be due either to a decreasing magnetization or to a more strongly superparamagnetic behavior. After annealing they noticed a higher magnetization which is interpreted by an increase of the Ni grain sizes.

2.2. *Rare earth–(3d)–4d transition metal systems*

2.2.1. *Gadolinium–niobium alloys*

To our knowledge McGuire and Gambino (1980) are the only ones to have reported some magnetic properties for such systems. (For a comparison with other elements see sections 2.1, 3.3, 7.1, 7.2 and 7.3.) They have shown that these alloys have lower T_c (48 K), θ (90) and ρ_H/ρ (−0.012) values.

2.2.2. *Gadolinium–cobalt–molybdenum alloys*

2.2.2.1. *Main magnetic properties*

As mentioned by Hasegawa et al. (1975a) and Chaudari and Cronemeyer (1976), the addition of Mo to GdCo amorphous alloys decreases the magnitude and temperature dependence of the magnetic moment. This metal has a low density of states at the Fermi level, behaves like a nonmagnetic metal, and strongly reduces the moment of the Co sublattice. The preparation of ternary alloys has been done to produce bubble domain devices; other diluents like Au and Cu have been proposed (see sections 3.2 and 3.3). It should be recalled that Eschenfelder (1980) has reported numerous data about magnetization and bubble properties for these materials.

Ferrimagnetic alloys such as $(Gd_{1-x}Co_x)_{1-y}Mo_y$ prepared by rf sputtering have been studied and discussed by Hasegawa (1975), Hasegawa et al. (1975a,b), Chaudari et al. (1975), Cuomo and Gambino (1975), Argyle et al. (1975) and Kobliska et al. (1975a). They have reported the main magnetic data and suggested several models to explain the film properties. Several authors have shown that sputtering parameters and geometry influence the film uniformity and that substrate temperature and nature influence the film properties (Cuomo and Gambino, 1975; Chaudari et al., 1975; Kobliska et al., 1975b; Bajorek and Kobliska, 1976). Heiman et al. (1978) have studied the effects of substrate bias and observed that Mo is largely unaffected by V_b (the Mo content remains constant).

Some other results can be reported. Hasegawa et al. (1975a) have shown the variation of T_c and T_{comp} versus the Mo content and temperature, and have offered a band model based on a simple molecular field analysis of their magnetization data. They also gave some experimental results obtained by the polarization Kerr effect. Argyle et al. (1975) have concluded that Kerr rotation is due mostly to Co atoms. McGuire et al. (1977) have reported the transport properties (Hall resistivity, Hall coefficient, resistivity) and the magnetic properties (magnetization) for an alloy such as $Gd_{72}Co_{15}Mo_{11}$ versus temperature. Above T_{comp} ($\approx$230 K), ρ_H and R_s are positive. The authors discuss the results in terms of inhomogeneities and of impurities (O_2, argon, ...) which can increase the sample resistivity. Mizoguchi et al. (1978) have studied the in-plane susceptibility near T_{comp} ($\approx$200 K) for two different samples. The susceptibility presents a minimum value at T_{comp}. They developed a theory of the in-plane susceptibility in terms of an antiferromagnetic or a columnar susceptibility. They discussed the K_u and remanent magnetization dependence on temperature. They compared experimental and theoretical results in an attempt to explain the origin of the susceptibility, and indicate the influence oxygen can have upon the antiferromagnetic susceptibility. They conclude that the in-plane susceptibility appears to rule out the possibility of a micromagnetic columnar anisotropy and that the films are highly uniform except for a thin surface layer. They observe that K_u is 1.7 times higher when a low evaporation rate is used than that obtained at in high rates; this result is due to a lower Mo content. They noticed that argon has no effect on K_u. By comparison with evaporated films the authors noted a larger

in-plane anisotropy than by bias-sputtering which is thought to be due to inhomogeneities.

Such materials are convenient to support bubble domains. In order to produce suitable devices numerous experiments have been done. Kryder et al. (1974, 1975, 1976a,b, 1977), Chaudari et al. (1975), Hasegawa (1975), Bajorek and Kobliska (1976), Hafner and Humphrey (1977), Kobliska et al. (1977) and De Luca et al. (1978) have studied the bubble mobility (propagation, expansion, velocity) dependence on an overlayered permalloy film such as NiFe, or on an in-plane driving field or on a pulsed current, or on laser impact, for different kinds of structured devices (T–I and Y–I bars and chevrons). Chaudari et al. (1975) have observed that for a well-defined temperature dependence of the bubble device the magnetization should be as nearly constant as possible near the operating point of the device and T_c and T_{comp} must be far from 293 K; for GdCoMo alloys the best behaviour versus temperature is obtained on the Co-rich side with 12–15 at% Mo. They showed that Mo lowered the Co moment, and determined the magnetic properties of these specimens. One of the main characteristics is reached for a content of 16 at% Mo: the product $AQ\alpha$ $4\pi M_s$ has the smallest value. Kryder et al. (1976b, 1977) have reported a bubble velocity of 500 m/s; Hafner and Humphrey (1978) give an instantaneous velocity of 400 m/s. De Luca et al. (1978) have studied the propagation of magnetic domains (stripe domains and bubble raft as a hexagonal array of bubbles) with a current pulsed directly through the film; they discuss the propagation dependence on the Gd content. Such bubble raft configurations and stripe domains have been observed by Chaudari and Herd (1976) and Herd (1976) by Lorentz microscopy (see section 2.3).

2.2.2.2. *Effect of rare gas incorporation*

Bajorek and Kobliska (1976) have reported that excess Ar and Mo influence the magnetization. They concluded that this primarily depends on film composition whereas the anisotropy energy density exhibits a more complex behavior. Cuomo and Gambino (1977) have shown that large rare gas (Ne, Ar, Kr) concentrations induce metastable quaternary alloys such as GdCoMoAr. They believe that the amorphous alloys can accommodate relatively high concentrations of large interstitial voids in the disordered materials. Their samples are stable from 293 K to the crystallization point. They conclude that the magnetic dilution provided by the gas produces a low $4\pi M_s$; therefore these alloys are suitable for bubble domain applications. Kobliska et al. (1977) have studied the change in magnetic properties for alloys with two different Ar contents inducing bubbles with either 2 μm or 1 μm diameter sizes. They discussed and computed the optimum values of Q and w_s and the optimum composition with saturation magnetization at 290 K for acceptable temperature sensitivity. They deduced that an ideal material should have Gd/Co = 0.095, $4\pi M_s = 1500$ G and $T_c =$ 450 K. They concluded that the degree of temperature insensitivity improves with decreasing bubble diameter and is satisfactory only for sub-half-micron bubble materials.

Mizoguchi et al. (1977a) have studied such alloys of various compositions obtained by bias voltage variations. They showed how Ar^+ ion implantation can damage the magnetic properties and noted that K_u decreases almost linearly with doses up to 10^{14} Ar^+/cm^2 and decreases more slowly at higher doses. They used a short-range atomic ordering model to explain the anisotropy. Gangulee and Kobliska (1978a) investigated the temperature dependence on the saturation magnetization of $(GdCoMo)_{91}Ar_9$ films in terms of the mean-field theory. They gave spin and exchange interaction energy values for different Ar and Gd/Co contents, subnetwork magnetization, g, A and K_u variations versus temperature. They observed an increase of the dipolar coupling constant with increasing Ar content, while it appears that no correlation with the magnitude of K_u exists. They concluded that K_u does not only depend on the composition but also on the manufacturing parameters, and that the temperature dependence of the anisotropy energy can be described in terms of a dipolar model. The same authors (1978b) compared the same magnetic properties for two specimens with different Ar contents. They observed a change in saturation magnetization, a decrease for T_c and T_{comp} with increasing Ar content (T_{comp} went from 360 K to 155 K, for amounts of Ar increasing from 2 to 9 at%). They noted that the exchange coupling constants values do not vary, except the Gd–Co one, which decreases with increasing Ar content. Nishida et al. (1979) report K_u and $4\pi M_s$ variations at 293 K versus at% Mo and V_b, and the K_u and A dependence after annealing at 500 K on the heating time. They suggested that a distribution of atomically ordered pairs in ternary alloys accounts for this behavior. As Heiman et al. (1978), Cuomo and Gambino (1975) and Gangulee and Kobliska (1978a,b) showed that the Mo atoms are hardly resputtered from the film (this leads to a rapid decrease of K_u) and such materials have a good thermal stability of the anisotropy. Nishida et al. (1979) suggested that a Mo atom is strongly tied to its neighboring atoms and suppresses movement of Co atoms and this changes the direction of the Co–Co pair axis (see section 3.1 for a comparison with GdCoCu alloys).

Mizoguchi and Cargill (1979) give many details about K_u which arises from magnetic dipolar interactions involving anisotropically distributed atomic moments or anisotropic microstructures. They describe also anisotropy arising from pseudo-dipolar anisotropic exchange; they demonstrate that classical dipolar interactions can produce magnetic anisotropy for $Q > 1$, and compared the structural anisotropies for both sputtered and evaporated samples.

2.2.2.3. *Effect of oxygen and hydrogen incorporation*

Argyle et al. (1975) have determined the total magnetization and Co sublattice magnetization dependence on temperature from Kerr rotation measurements, for alloys prepared by rf sputtering. They observed anomalous polarization Kerr loops due to interface effects relative to the Gd oxidation at the surface. They concluded that the formation of a Gd_2O_3 layer results in an enrichment of Co in the top (film–air interface) with a thickness of 50–100 Å. In order to have a

complete magnetic analysis they removed this layer or protected the as-deposited films by SiO_2.

Malozemoff et al. (1977), by using polar Kerr effect (as θ) and ellipticity (as ϵ) measurements of the reflected light which arises from magnetic circular dichroism, concluded to the formation of a surface layer due to oxidation. It gives a contribution which adds to the bulk θ but subtracts from the bulk ϵ. They removed this surface by etching. The film–substrate interface showed that θ and ϵ values are different from the bulk. With increasing Mo content θ and ϵ both drop, while with increasing Gd and O content θ does not change but ϵ increases. They discussed the degree of surface oxidation.

More recently Hafner and Hoffmann (1979), Hafner et al. (1980) and Stobiecki et al. (1980) have studied, either by ageing or by annealing with and without oxygen (or hydrogen), the magnetic properties and the depth magnetic profiles of their samples prepared by rf sputtering. As for Gd–Co films, they have established a columnar model to explain the film growth, and O_2 diffusion along the boundaries of the columns. In this way there is formation of Gd_2O_3. They proposed two models for the magnetization behavior before and after annealing of films with different compositions. From susceptibility measurements they determined $4\pi M_s$, H_k, H_k' and K_u changes at the free surface and at the film–substrate interface. These values depend also on the thickness: they are larger for thicker films. On the other hand they have observed that the effect of annealing with an O_2 partial pressure destroyed the perpendicular anisotropy while annealing at 570 K in a 10^{-6} Torr vacuum leads to a stable perpendicular anisotropy. With a partial pressure of oxygen or of hydrogen the magnetization increased. These experiments show that H_k and K_u increase with annealing and that Q has a maximum at 570 K.

Stobiecki and Hoffmann (1980) have reported the influence of oxygen on the transport properties for two kinds of films, one with T_{comp} above 293 K and one with T_{comp} below 293 K. From ρ, EHE, and T_{comp} measurements they concluded that two effects are observed: ordering, especially in the Gd sublattice, and oxidation. Below 520 K usually ordering effects dominate. Above 520 K oxygen diffuses (along column boundaries, as mentioned above) into the film and decreases the net Gd sublattice magnetization. The Co and Gd sublattices contribute then to the Hall effect. In this way they refute the results of Shirakawa et al. (1976) who suggested a dominant effect of the Co sublattice magnetization from their experiments on EHE and polar Kerr rotation by annealing from 4 to 525 K; but they fit in with those of McGuire et al. (1977).

2.2.2.4. *Effects of annealing*

The temperature dependence of the magnetic properties of these alloys has been studied by different authors but they have not determined the role of oxygen. Kobliska and Gangulee (1975) have shown that a sample such as $Gd_{15}Co_{70}Mo_{15}$ retained all functional magnetic properties even after annealing at 620 K. However, some changes are accounted for, particularly a shift of T_{comp} from 230 to 250 K after annealing from 420 to 620 K. These are believed to be due to structural and/or stress changes. Chaudari and Cronemeyer (1976) have

reported the variations of H_u, $4\pi M_s$, K_u and the g-factor from 80 to 570 K. Their rf sputtered samples have a T_{comp} below 293 K. They noticed the presence of a strong surface mode removed by ion milling. They described a model to determine the subnetwork moments which are related to the anisotropy energy. They concluded that K_u may be made to fit a pseudo-dipolar variation of the subnetwork magnetization. But the values of the coupling constants (Gd–Co being dominant) and their surprising behavior with Mo additions (large variations) do not readily explain the anisotropy in a real physical situation.

Cuomo and Gambino (1977) have reported $4\pi M_s$ variations versus temperature from 4 to 580 K for two different alloys with Ar and Kr incorporation. Both samples show the same T_{comp} (190 K) and the same T_c (500 K), but at 0 K, $4\pi M_s$ is lowered from 1550 to about 1300 Oe for the specimen with the higher gas content. Heiman et al. (1978) found no significant change in $4\pi M$ or K_u by annealing. They concluded that Mo stabilizes the films against the annealing effects. By comparison with Cu or Au additions for which increases are found (see sections 3.1 and 3.3) they suggest that the differences are due to the chemical bonding: Cu and Au are insoluble in Co, while Mo forms many compounds with Co. Katayama et al. (1978) have shown changes of M_s and K_u with annealing time at a temperature of 500 K and for different Mo contents. They concluded that Mo improves the chemical stability of the films and that the rates of change of M_s and K_u decrease with increasing Mo concentration. They also reported the following parameters for a sample with 14 at% Mo: A, $2w$, σ_w and l. In XPS studies they did not observe a shift of the 4f band.

Stobiecki et al. (1980) found that annealing at 770 K leads to a crystallization state (microcrystalline structure) which destroys the perpendicular anisotropy. Cuomo and Gambino (1977) reported a crystallization temperature of 1070 K for alloys with 15 at% Mo in a vacuum of 10^{-9} Torr. Hafner et al. (1980) showed that proper annealing leads to a magnetization maximum at 570 K and that at these temperatures Gd and Co are oxidized.

Remark. Discussion about K_u has been mentioned for GdCo alloys (see section 2.1.6.1).

2.2.2.5. *Effects of rare earth substitution*

Bochkarev et al. (1979) have pointed out that the magnetic properties of GdCoMo films may be changed by partially substituting Y and Sm for Gd to fabricate bubble domain devices. Their samples were prepared by sputtering. They showed the evolution of $4\pi M_s$, H_{coll} and P_0 (domain structure period) for GdCo, YGdCoMo and YSmGdCoMo films. For the quinternary composition the three parameters do not change with temperature (290 to 420 K). They also reported 4π M_s, H_u, Q, P_0, l and K_u values for different compositions.

2.2.2.6. *Structure determined by electron and X-ray diffraction*

Graczyk (1978) has investigated the short range order structure, microstructure and compositional fluctuations of thin films (such as GdCoMoArO) prepared by bias sputter. From his small angle scattering experiments he reports the presence of one halo which shifts with the rotation angle and decreases in intensity as this parameter increases. This clearly shows the anisotropic scatter-

ing. Bright field electron micrographs indicate both typical atomic adsorption, increasing the surface roughness, as well as the presence of voids. Another micrograph shows inhomogeneities with a cylindrical shape nearly perpendicular to the surface. For this alloy the author has calculated the small angle scattering curves for a low density void model and for a compositional fluctuation model, and he believes that the halo is partially due to interparticle interference. Heiman et al. (1978) have observed that X-ray diffraction patterns exhibit little dependence on V_b and K_u; all their patterns are similar to those observed for GdCo amorphous films prepared with $V_b = -100$ V.

2.3. *Lorentz microscopy: magnetic domains*

The visualization of magnetic domains by electron microscopy is limited by the thickness of the films (about 1200 Å). Grundy (1977, 1980) has written two review articles in which he describes and compares the properties of magnetic materials which are able to support bubble domains. He also gave numerous details relative to the observation of magnetic domains in the electron microscope.

2.3.1. *Binary alloys*

2.3.1.1. *Neodymium–cobalt films*

Zdanowics et al. (1978) have made some observations for Nd–Co amorphous films obtained by vacuum evaporation. The typical domain patterns can change with film enrichment with Co or with Nd. Co-rich films show zig-zag shaped domain walls, Nd-rich films have a weaker magnetic anisotropy.

Nowak and Scharff (1979) have shown the existence of a primary ripple structure due to small crystallite sizes (40 Å) and a large uniaxial anisotropy field in $Nd_{35}Co_{65}$ polycrystalline films deposited by vacuum evaporation. The samples have a columnar structure. In magnetic fields only the ripples rotate as a whole.

2.3.1.2. *Gadolinium–iron films*

Gill et al. (1978), for in-situ ion beam sputtered and rf sputtered amorphous GdFe alloys, have shown that films possess in-plane magnetization ripples, cross-tie walls and stress-induced magnetic anisotropy. Upon heating with the electron beam the domains change and there is formation of a radial cross-tie structure and circularly shaped ripples. Gasgnier and Colliex (1979) and Gasgnier et al. (1979) have shown some magnetic structures such as stripe domains with a possible nucleation of bubbles for a sample with 25 at% Gd (near the compensation point) and of domain walls for as-deposited amorphous films prepared either by thermal evaporation or by e-gun. They have observed that the application of the magnetic field of the objective lens can turn or displace the domains and reverse the contrast of the domains, and that localized annealing as brief "pulse annealing" can create new domains which can develop over the entire area of the film (fig. 4). Buravikhin et al. (1975, 1976) have reported some domain structures for GdFe amorphous and crystalline films prepared by ther-

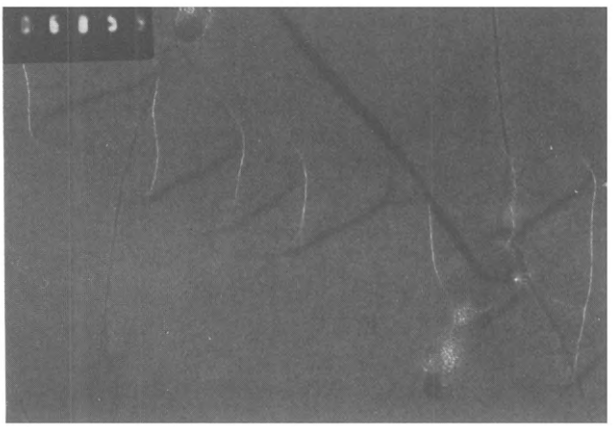

Fig. 4. Magnetic domains of an amorphous GdFe film (Lorentz microscopy).

mal evaporation, and the dependence of the magnetic compensation point on the substrate temperature (between 220 and 590 K) and the annealing conditions. Near the magnetic compensation point few variations of the domains are observed, but they vanish when the magnetic compensation point is reached; at high temperature new structures appear with an easy axis perpendicular to the initial direction. Historically the first observations have been made on $GdFe_2$ and GdFe crystalline films by Voskobojnik et al. (1967). Near the magnetic compensation point they observed the disappearance of the domains and they interpreted this phenomenon as due to an antiferromagnetic interaction between the Fe and Gd atoms.

2.3.1.3. *Gadolinium–cobalt films*

Herd and Chaudari (1973) were the first to study such materials prepared by rf sputtering, near the magnetic compensation point (i.e. 79 at% Co). They annealed their samples at 670 and 720 K and observed the formation of a columnar structure and crystallization of the Co metal. For a Co content lower than 79 at% only domain walls (in-plane magnetization) and in-plane ripples are observed (the compensation point is 393 K). For 80 to 83 at% Co stripe domains appear as well as in-plane domain walls. By cycling the magnetic field of the objective, bubbles are generated equally well in either amorphous or partially crystallized films. At 720 K the in-plane magnetization becomes stronger. Herd (1977, 1978) has reported on the influence of the oxygen contamination, the Gd content and the annealing on the domain configuration and on the anisotropy. This author has shown how the magnetic structures change when they are induced by one or the other of these parameters, and how it is possible to observe the in-plane to perpendicular anisotropy transition. So, for pure GdCo films the net magnetization is in-plane, and with slight to moderate O_2 contamination it is perpendicular; heavy O_2-contaminated samples (Co-rich) heated by pulse annealing present perpendicular domain structures. Stripe domains obtained by heating can transform to bubbles by application of a perpendicular bias field. Numerous

other domain configurations are presented in relation with the microstructural characteristics of the films.

Nandra and Grundy (1976, 1977), in order to explain the perpendicular magnetic anisotropy, have studied stripe domains for such samples as $Gd_{20}Co_{80}$ prepared either by e-gun co-evaporation or by dc bias sputtering. They reported the domain configurations obtained by oblique and normal incidence deposition, the nucleation and the change in domains for as-deposited and annealed (up to 870 K) films. Films deposited at 77 K exhibit in-plane domains with no change after annealing; those deposited at 290 K and heated to 570 K show nucleation of stripe domains; at 870 K the samples appeared to be crystalline and a complete stripe configuration is observed. Hoffmann et al. (1979) have reported, for GdCo films prepared either by e-gun or by bias sputtering, that unannealed specimens exhibit in-plane zig-zag domain walls and ripples with no perpendicular anisotropy. But evaporated films show a perpendicular anisotropy after annealing at 450 K and are characterized by an increase of the contrast of the stripe domain. This perpendicular anisotropy dropped sharply after heating above 770 K and the stripe domains vanished. Leamy and Dirks (1977, 1979) and Dirks and Leamy (1978a,b) have prepared their samples as $Gd_{25}Co_{75}$ either by vapor deposition or by sputtering. The as-deposited films have isotropic in-plane ripples which transform in strong stripe domains by annealing at 520 K (perpendicular anisotropy) or by pulse annealing. They discuss their results versus Q.

Ali et al. (1976) and Grundy et al. (1977) have studied the effect of radiation damage (ion and electron) on the stripe domain structure. Argon ion doses below 10^{15}–10^{16} ions cm^{-2} do not affect the structure; films with a thickness of more than 800 Å have a perpendicular anisotropy and show bubbles after application of a normal bias. Doses of $\approx 10^{16}$ ions cm^{-2} destroy the perpendicular anisotropy.

2.3.1.4. *Holmium–cobalt films*

Nandra and Grundy (1977) have observed stripe domains with various configurations which depend on the thickness for $Ho_{20}Co_{80}$ alloys. The domain configuration changes from weak stripes to a typical maze-like stripe domain structure as the film thickness increases from 1400 to 2500 Å. For co-evaporated HoCo films with a thickness of 1400 Å they observed stripe domains, in contrast to GdCo films prepared by the same technique which do not exhibit such configurations. Annealing of $Ho_{20}Co_{80}$ samples causes a loss of stripe domains at 470–570 K, and the resulting domains are in-plane. The authors concluded that a strong uniaxial magnetic anisotropy and a disordered arrangement coexist in these films. Hoffmann et al. (1979) have observed, for unannealed films, the same configurations as for GdCo samples: by heating at 650 K, $Ho_{32}Co_{68}$ films exhibit stripe domains which vanish after annealing above 900 K. Grundy et al. (1977) have studied the electron radiation damage in a $HoCo_4$ film: the impact of the focused electron beam destroys the stripe domains and an in-plane magnetization appears.

2.3.1.5. *Other rare earth–transition metal films*

Biesterbos et al. (1979) have studied magnetic domains in TbFe alloys contaminated by O_2. Samples prepared by vapor deposition under different partial

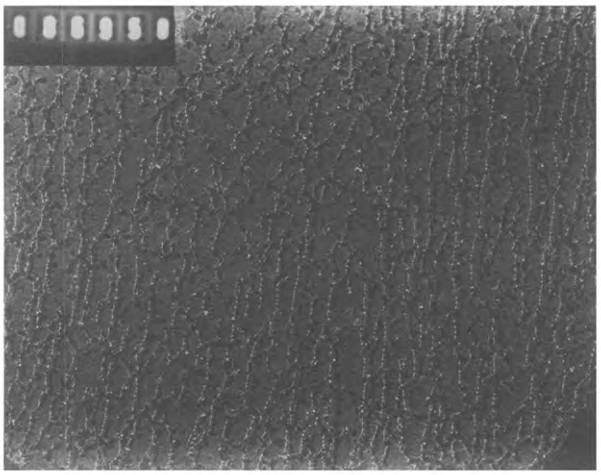

Fig. 5. Magnetic domains of an amorphous YFe film, after annealing at low temperature.

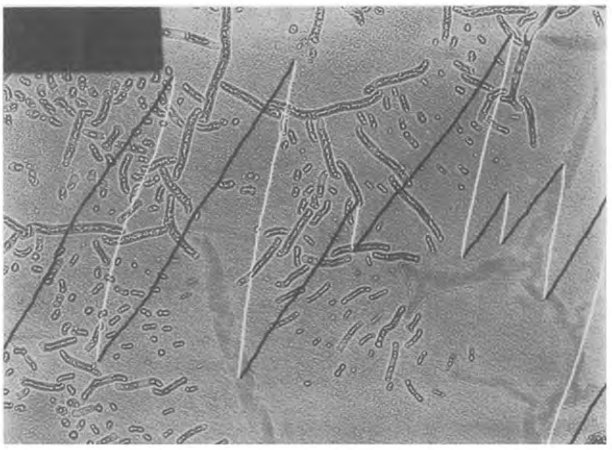

Fig. 6. Magnetic domains of an amorphous YCo film.

oxygen pressures exhibit either a perpendicular component of the magnetization (stripe and single domains) at low O_2 pressure, or in-plane domains and ripples coexisting with domain walls at high O_2 pressure. This suggests a biaxial component anisotropy.

By courtesy of Dr. Colliex (1980) we report some peculiar aspects of magnetic domains in amorphous alloys which have been prepared either by e-gun or by thermal evaporation. Fig. 5 shows nearly aligned Bloch walls with cross-ties observed in YFe films after slow annealing; before heating it appeared as a randomly rippled structure. Figs 6 to 9 show characteristic domains of YCo, TbCo, CeNi and DyNi films. Unfortunately their compositions were not determined.

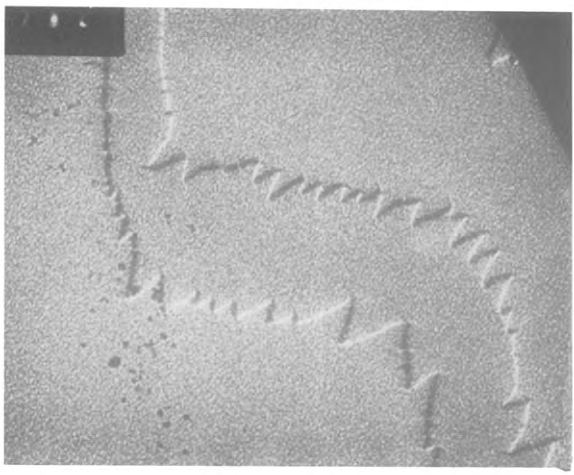

Fig. 7. Magnetic domains of an amorphous TbCo film.

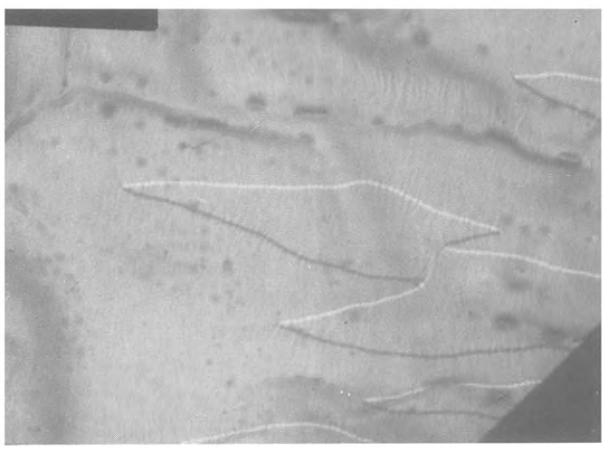

Fig. 8. Magnetic domains of a CeNi film.

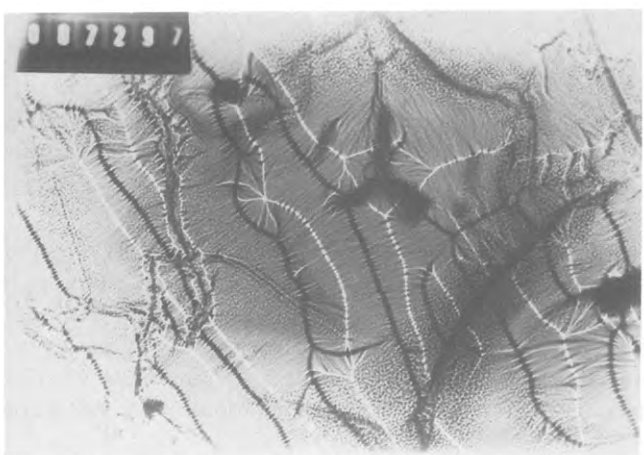

Fig. 9. Magnetic domains of an amorphous DyNi film.

2.3.1.6. *Gadolinium–gold films*

Bostanjoglo and Röhkel (1971) have observed the magnetic domains of GdAu films prepared by evaporation "in situ" in an electron microscope. At 4 K they saw spontaneous structures and observed a change with magnetic switching. The domains varied with temperature (the amorphous–crystalline transition occurs at 160 K) and with applied magnetic field.

2.3.2. *Ternary alloys*

2.3.2.1. *Gadolinium–cobalt–molydenum films*

Such specimens have been studied by Chaudari and Herd (1976) and Herd (1976). They observed stripe and bubble domains and discussed the formation of these with respect to Q and different applied fields (perpendicular bias or pulsed or rotating in-plane fields). They gave details about bubble formation: peculiar bubbles can be created with $Q < 1$ by reduction of a perpendicular field. They found "weak" and "strong" stripe domains: different configurations with $Q > 1$ such as formation of stripe domains from perpendicular saturation and Bloch line motion along wall strips showing bubble formation; and with $Q < 1$ the nucleation of bubbles from saturation with different bias values. As numerous magnetic structures were observed the authors concluded that the type of domain pattern obtained is an interaction of a perpendicular and an in-plane component. These components can vary independently of each other according to the temperature. This leads to a perpendicular anisotropy lying in microscopically small spatially separated regions.

2.3.2.2. *Gadolinium–cobalt–gold films*

In the same way Chaudari and Herd (1976) and Herd (1976) have studied Gd–Co–Au films. For $Q > 1$ they showed strip contrast due to Bloch line walls and the formation of a dense rafter of unichiral bubbles (packing with hexagonal order) with increasing perpendicular to in-plane ratio. For $Q \gg 1$ the films exhibit circular domains with multiple (eight) Bloch lines (materials with lower Q exhibit only two Bloch lines). Herd (1979) has shown that the magnetic domain structures in $Gd_{17}Co_{76}Au_7$ films prepared by bias sputtering exhibit a dependence on the bias voltage.

Hischii et al. (1977) have prepared by rf sputtering a specimen with a perpendicular uniaxial anisotropy. They observed various kinds of bubble domains under a bias field: unichiral bubbles, bubbles with two or four Bloch lines, and also maze domains for thicker films, and white and black bubbles for higher bias field. They discussed the variation of the intensity of the wall image as a function of the angle between the easy axis and the film normal.

3. Rare earth–noble metal systems

3.1. *The copper systems*

3.1.1. *Binary systems*

3.1.1.1. *Amorphous state*

3.1.1.1.1. Gadolinium–copper alloys

The first magnetic properties for such materials have been reported by Heiman and Lee (1976), who prepared samples by sputtering. The measurements on three different compositions show a decrease of T_c (53 to 35 K) with increasing Cu content (0.76 to 0.86 at%). They conclude that the R–R exchange coupling is ferromagnetic with an exchange constant about half as large as that in Gd metal or Gd alloys. Mizoguchi et al. (1977b) and McGuire et al. (1978) have established that alloys deposited by rf sputtering exhibit at low temperature a magnetic phase diagram quite close to that of Gd_xAl_{1-x}. The Gd_xCu_{1-x} system has a spin-glass behavior (with a wide variation of exchange interaction) for $x = 0.21$ and 0.31, and a ferromagnetic behavior for higher concentrations, with intermediate states. The structures are discussed in terms of partially ferromagnetic regions, small ferromagnetic clusters and random anisotropy effects.

Popplewell and Charles (1978) have shown that alloys which are prepared by vapor quenching deposition are metastable and always amorphous after deposition at 77 K and annealing at 293 K. They concluded that these materials are ferromagnetic, and that the added Cu decreases T_c by simply increasing the Gd–Gd distance. Heiman and Kazama (1978) have determined the magnetization and the Curie temperature of alloys prepared by co-evaporation with 30 to 60 at% Gd. As Mizoguchi et al. (1977) and Heiman and Lee (1976) they found that their samples were not saturated at low Gd contents. Except for 40 at% Gd, the magnetization is near the expected value. The calculation of T_c using a percolation model is shown to be consistent with the experimental results, i.e. T_c increases nearly linearly with the Gd content, with the two end values being 0 K at $x = 0.25$ and 200 K for pure amorphous Gd (for crystalline Gd, $T_c = 290$ K).

3.1.1.1.2. Terbium–copper alloys

Heiman and Kazama (1978) have noticed that the magnetization is reduced by local anisotropy effects (such as lack of saturation) for TbCu alloys.

Boucher (1980) has studied amorphous ($Tb_{0.25}Cu_{0.75}$) thick films (20–40 μm), which were prepared by sputtering, using neutron or X-ray small angle scattering. He concluded that magnetic short range ordering occurs at temperatures much higher than the asymptotic Curie temperature, and that there is a microscopic atomic structure as a dense stacking of atoms (the film contained 2 at% Ar).

3.1.1.1.3. Dysprosium–copper alloys

Coey and von Molnar (1978), by rf sputtering deposition, have studied a DyCu alloy with the following composition: $DyCu_{1.44}Ar_{0.05}O_{0.23}$. They observed a sharply defined spin-freezing temperature at 18 K marked by a cusp in the low-field dc susceptibility (as for the Gd–Al system). They developed and discussed a

model to explain the spin-glass behavior. Tissier et al. (1980) also observed the spin freezing transition at 18 K for DyCu amorphous films (41 at% Dy). At 100 mK they recorded the hysteresis loops which show large Barkhausen jumps giving direct evidence of asperomagnetic (random ferromagnetic) domains containing $\approx 10^{18}$ Dy atoms.

Heiman and Kazama (1978), as for terbium, noticed a reduction of the magnetization of DyCu and HoCu samples.

3.1.1.1.4. Magnetic and transport properties

The magnetic moment, spontaneous Hall effect and resistivity of amorphous films such as $Pr_{0.4}Cu_{0.6}$ and $R_{1-x}Cu_x$ (R = Pr, Nd, Gd, Tb, Dy, Ho, Er and Tm) have been studied by McGuire et al. (1977a, 1979). In the later paper the authors conclude that alloys with Nd, Gd, Tb, Dy and Ho are ferromagnetic at 4.2 K, with a Curie temperature below 25 K, except for Gd, for which it is near 77 K. The magnetization is one third to one half of the expected saturation, except again for Gd. The highest resistivity is obtained for GdCu films. The Hall resistivity is positive except for Gd and Tb, and the calculated values have the same sign as those for the pure elements. The ratio ρ_H/ρ at 4.2 K is shifted toward positive values, but the authors can only speculate about this shift, and they think that its origin is due to a polarization of Cu by the rare earth moments.

3.1.1.2. *Crystalline state*

Domyshev et al. (1974) have given some properties (crystalline magnetic and magnetoelastic) for $GdCu_2$ thin films (1000–1500 Å) prepared by thermal evaporation. The films have the $MgCu_2$-type structure. The authors show, by comparison with $GdMn_2$, $GdFe_2$, $GdCo_2$ and $GdNi_2$ thin films, that $GdCu_2$ has the highest Young's modulus, resistivity and density of dislocations.

3.1.2. *Ternary systems*

3.1.2.1. *Amorphous state (gadolinium–(cobalt)–copper alloys)*

Such samples have been studied for magnetic bubble devices and magneto-optic applications.

Chaudari et al. (1974) have prepared GdCoCu amorphous materials by rf sputtering. Their films are richer in Co, because there is a Gd resputtering effect. They have observed that a "drive field" for bubble domain propagation in T-bar devices is proportional to the magnetization. They have studied particularly the magnetic quality factor and the exchange stiffness versus the temperature.

Potter et al. (1976) have measured the bubble velocity as a function of drive field for bubbles in rf sputtered films. They have shown that magnetic annealing lowers the coercivity. They have measured the wall mobility and dynamic coercive force and presented the first conclusive data on the existence of gyrotropic deflection in an amorphous material. Minkiewicz et al. (1976) have shown that for samples prepared by rf sputtering, Cu dilutes the transition metal sublattices much differently than Mo. But overall the static coercivity in as-deposited films is larger than one would desire for device applications, and it is lowered by annealing treatments (Potter et al., 1976).

The influence of the deposition parameters on the properties of the samples have also been studied. Burilla et al. (1976) have used a multiple-target method for sputtered amorphous films. They speculate on the exact mechanism that determines K_u. Albert and Guarnieri (1977) have studied the influence of biased magnetron deposition parameters (target current, sputtering pressure and substrate bias voltage). This technique yields a film composition close to the one of the target. The authors show the dependence of $4\pi M$, K_u and Q on dc target current for different argon sputtering pressures and for 0 and -100 V bias voltage. Their specimens deposited with substrate bias show an increase of K_u without addition of Ar and a composition shift. Such results appear to eliminate a possible Ar incorporation mechanism for the anisotropy. Heiman et al. (1978) have shown that the fundamental mechanisms responsible for K_u and the effects of annealing are not understood. For GdCoCu alloys they have observed that the addition of Cu seems to increase K_u after annealing.

One should notice that Potter et al. (1976) did not observe a significant change in K_u after annealing, but on the other hand, Heiman et al. (1978) have shown a large change in magnetization after annealing. They have tentatively explained their results by the nature of the chemical bonding of Cu with GdCo alloys for the K_u increase, and by the insolubility of Cu in Co for the $4\pi M$ change (see sections 2.2 and 3.3.2 for a comparison with Mo and Au). In the same way Nishihara et al. (1979) have studied the effects of copper on the magnetic uniaxial anisotropy and compared this effect to that induced by molybdenum. These authors have reported that Cu as well as Gd atoms are easily resputtered in bias sputtering of GdCoCu films. So, the anisotropy is larger than that of GdCoMo and changes greatly with annealing. They conclude that the magnetic anisotropy strongly depends on the resputtering probability of copper.

As for R–TM amorphous films, the various authors have given numerous magnetic results relative to GdCoCu materials. But it seems evident that the various experimental procedures used to examine their fundamental properties induce different mechanisms which are responsible for the varying results (Heiman et al., 1978).

3.1.2.2. *Crystalline state ($SmCo_{5-x}Cu_x$ alloys)*

Theuerer et al. (1969) have studied $SmCo_{3.65}Cu_{1.35}$ films deposited by vapor deposition. Unfortunately the authors have only noticed the existence of a fine grained structure, with no mention of the crystalline one. However, their results are interesting because they observe a very high coercive force of 30 000 Oe (12 000 for the bulk) for a thin film (4000 Å) deposited onto glass substrates heated to 770 K. A thick film (5 μm) exhibited a coercive force of 13 350 Oe. They attribute this large value to the magnetic anisotropy and to the fine grained structure.

Shelkovnikov et al. (1976), for $(Sm, Gd)Co_{5-x}Cu_x$ films prepared by flash evaporation onto substrates heated to 470 K, have observed large magnetic after effects. They discuss the origin of such properties and show that these effects are characteristics of high coercivity in the materials.

3.2. *The silver systems*

3.2.1. *Amorphous and crystalline gadolinium–silver alloys*

Bates et al. (1970a,b), Charles et al. (1971, 1973) and Popplewell et al. (1975, 1977, 1978) have studied the properties of ferromagnetic GdAg alloys prepared by vapor-quenched evaporation. They have investigated the alloys series from 0 to 100 at% Gd. In this range they notice that alloys with 76–100 at% Gd are amorphous, and for Gd content less than 66 at% there is formation of a fcc structure with a lattice parameter increasing from 3.94 to 4.04 Å (pure Ag). These authors have studied the amorphous phase by RDF and defined a binary hard-sphere model. From ESR experiments they have studied the variation of T_c with composition. They report various changes (increase or decrease) of this parameter versus the Gd content and the substrate temperature during the deposition. A special feature is observed for 87 at% Gd (also defined by RDF): for such a composition T_c is equal to 40 K. Hauser (1975) has reported that amorphous Gd_xAg_{1-x} ($20 \leqslant x \leqslant 70$) prepared by sputtering onto cold substrates (77 K) are ferromagnets. When the Gd content increases from 20 to 100, T_c linearly increases from 20 to 253 K. The pure Gd films are quasi-amorphous. (Notice that for pure amorphous Gd films, Heiman and Kazama (1978) report a T_c of 200 K, while for polycrystalline Gd $T_c = 290$ K.)

3.2.2. *Amorphous thick films*

3.2.2.1. *Neodymium–silver alloys*

Friederich et al. (1979) have reported the first data obtained by EPR for non-s rare earth ions (Nd^{3+}), e.g. $Nd_{17}Ag_{83}$, which is paramagnetic down to 4.2 K. The experiments were done at 293, 100 and 4.2 K in a magnetic field of 1000 to 5000 G, and showed the presence of some complicated structure. The results are discussed in terms of the g factor. The resonance observed above 100 K indicates the existence of sites having a non-axial crystal field. The authors think that EPR is promising for investigation of the electrical field gradients (or crystal fields) in amorphous rare earth alloys (see next section for transport properties).

3.2.2.2. *Heavy rare earth–silver alloys* (R = *Gd to Er*)

Magnetic properties, such as suceptibility, magnetization, coercive field and Curie temperature, have been compared with the crystalline state properties for such alloys as $Gd_{54}Ag_{46}$, $Tb_{48}Ag_{52}$ and (Dy, Ho or Er)$_xAg_{1-x}$, in the form of sheets (30–100 μm) prepared by diode sputtering (Boucher, 1976, 1977a,b). The amorphous samples show a spontaneous magnetization at low temperatures corresponding to a ferromagnetic state ($T_c = 122$ and 64 K for GdAg and TbAg, respectively), the crystalline state is antiferromagnetic. The absence of anisotropy in GdAg alloys does not permit one to observe the hysteresis effect. For TbAg, DyAg and HoAg alloys such a phenomenon is only observed at temperatures less than 40, 15 and 8 K, respectively. The author interprets the low temperature magnetic properties (magnetic ordering and magnetic after effect) in terms of exchange interaction, anisotropy and applied fields. He believes that a complex amorphous state involving both ferromagnetic and antiferromagnetic

interactions exists. Boucher and Barbara (1979) have made a detailed investigation of the magnetic after effect in $Tb_{52}Ag_{48}$ sheets: this phenomenon exists only in a peculiar range of the magnetization (medium applied fields), is due to the reversal of the moments and can be represented by an activation energy law. Chappert et al. (1980) have done Mössbauer experiments to study the relaxation effects in crystalline and amorphous DyAg alloys. In the amorphous state the magnetic interactions are predominantly positive with $T_c =$ 18 K, but there is no collinear magnetic arrangement. The interpretation of the relaxation effects is discussed in terms of the spin–lattice relaxation, spin-flips between two different spin systems and mutual spin-flip models. Asomoza et al. (1980) have studied the extraordinary Hall effect (EHE) for $R_{50}Ag_{50}$ alloys (R = Pr, Nd, Gd, Tb, Dy and Er), prepared by sputtering. They report numerous data about the resistivity, the Hall resistivity, the magnetization per ion, the normalized Hall resistivity, the magnetic moment at saturation and the normalized Hall angle. They conclude that EHE varies through the rare earth series approximately as for rare earth impurities in silver, and that it is due to orbital exchange and 5d spin–orbit interactions. Ousset et al. (1980) have observed in $(Gd, Dy \text{ or } Er)_{50}Ag_{50}$ an up-turn of the resistivity at low temperature and a negative magnetoresistance. Their results indicate a coherent exchange scattering with a predominant contribution from anti-ferromagnetic pairs. They have tested their results with a ternary alloy such as $Ag_{50}Lu_{50-x}Dy_x$ ($x = 50$ and 35) and shown that the resistivity increase at low temperature is larger for $x = 50$. The magnetoresistance is also larger for the same composition (see also Asomoza, 1980).

3.2.3. *Dilute thin films: dysprosium or erbium–silver system*

Barberis et al. (1977) and Pela et al. (1980, 1981) have studied the stress effects on the electron spin resonance (ESR) spectra (at 1.5 K) of diluted Dy or Er (1 to 2 at%) in epitaxially grown single crystal or microcrystalline oriented Ag thin films. They report that the numerous data about the anisotropic g-value, the line width and lineshape can be explained by the mixing of excited crystalline field levels with the ground state—these admixtures are caused by the planar strain induced by the difference in the thermal expansion coefficients between the film and the substrate. The authors estimate the lower limits for the tetragonal and trigonal second order orbit–lattice coupling parameters. Numerous mathematical results support their conclusions. They discuss the results of Dodds and Sunny (1978) and think that these authors, who studied microcrystalline films, have confused the tetragonal second order OLCP with the trigonal one.

3.3. *The gold systems*

3.3.1. *Binary systems*

3.3.1.1. *Amorphous thin films*

McGuire and Gambino (1979, 1980) have reported numerous data on transport properties for several R_xAu_y (R = Pr to Tm) alloys. They made the following observations: T_c is below 20 K for all the elements, except for Gd ($T_c \approx 100$ K);

only Gd alloys have almost full magnetization, while it is one-third or one-half of the expected saturation for the other alloys; the resistivity ranges between 90 and 230 $\mu\Omega$ cm for HoAu and NdAu, respectively; the spontaneous Hall effect, which is proportional to the paramagnetic θ value, is positive for the Pr to Eu alloys and negative for the heavy rare earth alloys. They propose a model to explain the last parameter by including both the total spin of the rare earth ion and a factor which contains the exchange evergy via the conduction electrons. They have shown that such a model is valid for numerous Gd_xM_{1-x} (M = Mg, Si, Ti, V, Cr, Ge, Nb) alloys, which are ferromagnets (some data are reported in sections 2 and 7). The ratio ρ_H/ρ increases linearly with θ, the only exception being the GdAu alloy. However, there are some discrepancies with the first results given by McGuire et al. (1977a,b) for several pieces of data: for example, they reported for the $Tb_{47}Au_{53}$ alloy a resistivity of 385 $\mu\Omega$ cm, while in their 1979 and 1980 papers it is equal to 190 $\mu\Omega$ cm; the authors do not explain this rather large change.

3.3.1.2. *Terbium–gold alloy*

Boucher (1977c) has reported the magnetic susceptibility, the Curie temperature (32 K) and the hysteresis loops below 15 K for a $Tb_{52}Au_{48}$ sheet alloy prepared by diode sputtering with high deposition rate. The author notices that the first-neighbour R–R interactions are ferromagnetic and predominant, that the second-neighbour ones are antiferromagnetic, and that this explains the spontaneous magnetization of this alloy.

3.3.1.3. *Amorphous and crystalline gadolinium–gold system*

Bostanjoglo and Röhkel (1971) have obtained amorphous samples by evaporation "in situ" in an electron microscope at low temperature (30 K) onto carbon foils. By annealing they observed at 160 K, as a critical temperature, the formation of small crystallites. They discuss their results in terms of ferromagnetic clusters. At low temperature clusters are aligned forming a superferromagnetic state and at the critical temperature they are decoupled forming a superparamagnetic state. Such conclusions are consistent with the magnetic domains observed by Lorentz microscopy (see section 2.3).

3.3.1.4. *Dilute thin films: erbium or ytterbium–gold system*

Suassana et al. (1977), Gandra et al. (1980a) and Pelà et al. (1981) have studied, as for ErAg, the stress effect on the ESR spectra of Er in Au. They report the lower limits for the tetragonal and trigonal second order OLCP. In comparison to silver the first one is $\approx$2.5 times larger and the second one is positive (negative for Ag). There is a maximum anisotropy of the g-factor for films with a thickness of 550 Å. They discuss their results relative to the sticking effect, the nature of the substrates (quartz or NaCl) inducing deformation, and cracking or sliding effects. Gandra et al. (1980b) report for YbAu positive values for tetragonal and trigonal parameters. For such an alloy they show that the Kondo temperature is low.

3.3.2. *Ternary systems*

3.3.2.1. *Amorphous state: gadolinium–cobalt–gold alloys*

As for copper, Chaudari et al. (1974) have reported the magnetic properties of

such samples for bubble domain applications. Cuomo and Gambino (1975) and Heiman et al. (1978) have shown the effects of the sputtering parameters (such as substrate bias, target voltage, pressure, system geometry and target composition) and annealing on changes in magnetization, anisotropy, composition, X-ray diffraction patterns and Ar content in the films. Heiman et al. (1978) interpret their results, in the same way as for copper, by noticing that gold is insoluble in cobalt. Hasegawa et al. (1975b) have studied the magnetic properties of $(Gd_{1-x}Co_x)_{1-y}Au_y$ films prepared by rf sputtering. From magnetization data versus temperature and composition, they discuss the sublattice moments and the spin values of Gd and Co and the exchange constants, and they conclude that the origin of the perpendicular uniaxial anisotropy is due to cobalt atomic pair ordering promoted by a dipolar energy. K_u has larger values in GdCoAu alloys than in GdCoMo alloys. McGuire et al. (1977b) have given some transport data for an alloy such as $Co_{70}Gd_{19}Au_{10}$. They have observed that ρ_H shifts and this can be interpreted by inhomogeneous sample composition, and T_{comp} is not well defined.

Miyama et al. (1978) and Matsushita et al. (1978) have reported numerous magnetic data for GdCoAu films prepared by rf sputtering and coated with a permalloy (NiFe) film. Near T_{comp} (285 K) they determined the dependence of H_c. Miyama et al. (1978) studied the dependence of the domain wall velocity on the presence of an overlayered permalloy film, the temperature and the drive field. They measured wall velocities up to 35 000 cm s^{-1} and showed that the saturation of the wall velocity is suppressed by the permalloy overlay. Matsushita et al. (1978) showed that T_{comp} is lowered by about 5 K by coating of a permalloy film. They also found numerous domain patterns for different magnetized states.

We remind the reader briefly of the work done by Lorentz microscopy: Herd (1976, 1979), Chaudari and Herd (1976), and Hishii et al. (1977) have studied GdCoAu samples in order to observe magnetic bubbles (see section 2.3).

3.3.2.2. *Amorphous and crystalline state: gadolinium–iron–gold alloys*

Gasgnier (1981) has studied the evolution of GdFe amorphous films overlayered by a gold film. In X-ray diffraction two line systems are observed: one for amorphous Gd–Fe alloy (broad haloes) and one for Au. Upon ageing at ambient atmosphere there is no transformation to the crystalline state. Upon heating of different gold films of various thicknesses with an electron beam in an electron microscope, the samples crystallized. In the first stage of the annealing three ring systems which correspond to C–Gd_2O_3, Fe and Au were found. Upon further heating there is recrystallization and the following structures have been defined:

- fcc ($a = 3.60$ Å);
- fcc ($a = 3.75$ Å) (with the thicker Au films);
- primitive cubic ($a = 7.60$ Å) (with the thinner Au films);
- hcp ($a = 3.70$ Å, $c = 6.05$ Å);
- an unknown system with the following interplanar distances: 7.11, 5.69, 5.53, 4.35, 2.97, 2.60 and 2.36 Å.

It is possible to make some remarks by comparison with known bulk alloys: bulk GdAu is CsCl-type (bcc) with $a = 3.60$ Å, while the indexing of the film leads to a fcc structure. Bulk $GdAu_2$ is tetragonal ($MoSi_2$-type) with $a = 3.73$ Å and $c = 9.02$ Å, whereas the indexing leads to a fcc structure with $a = 3.75$ Å and a hexagonal one with $a = 3.70$ Å. The nature of these systems is complex and they can possibly be interpreted as ternary alloys or oxidized compounds.

4. Rare earth–bismuth and tin systems

4.1. *Ternary amorphous gadolinium–iron–bismuth alloys*

Urner-Wille (1979, 1980), Hansen and Urner-Wille (1979) and Heitman et al. (1980) have prepared, by e-gun evaporation onto rotating glass substrates, thin films (300–2200 Å) of $(Gd_{1-x}Fe_x)_yBi_{1-y}$ alloys. They are ferrimagnetic with a perpendicular uniaxial anisotropy. The magnetic and magneto-optic properties have been studied in the temperature range $4.2\ K < T \leq T_c$ for magneto-optical storage applications as a photoconductor sandwich (thermomagnetic switching). The main results show a strong decrease of T_{comp} with increasing Bi content and a constant GdFe content ($T_{comp} \approx 300$ K for $y = 0$ and 0 K for $y = 0.11$), while T_c (which decreases slowly from 480 to 400 K for $y = 0.17$) and the crystallization temperature are much less affected; the Faraday and Kerr rotations are enhanced with increasing Bi content and with decreasing temperature. These two observations suggest a strong influence of the bismuth on the Gd–Fe exchange which increases and on the iron spin value which decreases with increasing Bi content. It is in contrast to other alloys prepared by sputtering, where ternary additions tend to decrease the transition metal moment (Chaudari et al., 1973; Gangulee and Kobliska, 1978); in addition the Gd–Fe and Fe–Fe distances seem to be influenced by the Bi ions as indicated by the slow decrease of T_c and by the tensile stress measurements which present a continuous reduction of about 80% with increasing Bi content from 0 to 18 at%.

The authors give some other data about the temperature variation of the saturation magnetization, the reflectivity and the optical absorption. They compare the Faraday and Kerr rotation ($\lambda = 6330$ Å, $T = 293$ K), for various materials (GdFe, TbFe, DyFe and MnBi) and show that for $(Gd_{0.26}Fe_{0.74})_{0.89}Bi_{0.11}$ samples θ_F and θ_K are higher than those for RFe alloys and are lower than those for MnBi alloys. They also observed that H_c varies with temperature, the nature of the substrates (glass or CdS) and the surface roughness (CdS).

4.2. *Ternary amorphous gadolinium–iron–tin alloys*

Urner-Wille et al. (1980) have also studied ternary $(Gd_{0.26}Fe_{0.74})_{1-x}Sn_x$ ($0 < x \leq 0.2$) alloys prepared by the same method as the GdFeBi alloys. Such samples also have a perpendicular uniaxial anisotropy. The magnetic and the magneto-optic properties of tin alloys are similar to the ones of bismuth alloys: T_{comp}

decreases strongly with increasing Sn content (from 300 K for $x = 0$ to 10 K for $x = 0.2$), T_c is less affected (480 to 400 K), and θ_F and θ_K increase strongly with increasing Sn content. The authors conclude that a strong reduction of the exchange constants and a stronger localization of the Fe spin occurs. On the other hand, they show that addition of Sn tends to improve the thermal stability. They have examined the heat distribution in the sample and the substrate to understand the local reversal of magnetization during thermodynamic switching (they observed the formation of cylindrical domains with heat treatment using a laser and "domain erasure" by cooling-down treatment). The temperature rise for domain nucleation is between 293–373 K. The structural stability of the magnetic samples can be maintained after extensive cycling.

4.3. *Binary crystalline systems*

4.3.1. *Samarium–bismuth system*

Gasgnier (1981) has studied samarium thin films overlayered with a bismuth film by deposition onto float-glass substrates at 77 or 293 K. The X-ray diffraction patterns show the presence of two phases, SmH_2 and Bi. Upon ageing at ambiant atmosphere, or annealing in air at 370 K, the formation of a compound identified as $Sm(OH)_3$ is observed (see fig. 10). This compound is identified by comparison with the well known patterns of the light rare earth hydroxides (Gasgnier, 1980). The crystallographic system is hexagonal with $a = 6.31$ Å and $c = 3.59$ Å. The formation of this compound is surprising. By annealing up to 570 K it disappears and there is formation of C-Sm_2O_3. Inside the electron

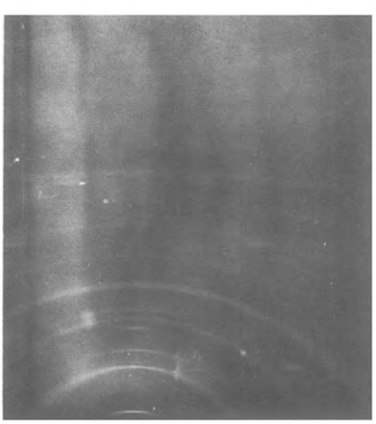

Fig. 10. X-ray diffraction pattern of a SmBi film, after annealing at low temperature. The system of lines corresponds to $Sm(OH)_3$. (The fifth diffraction line, as an elongated spot, corresponds to the (111) of Au.)

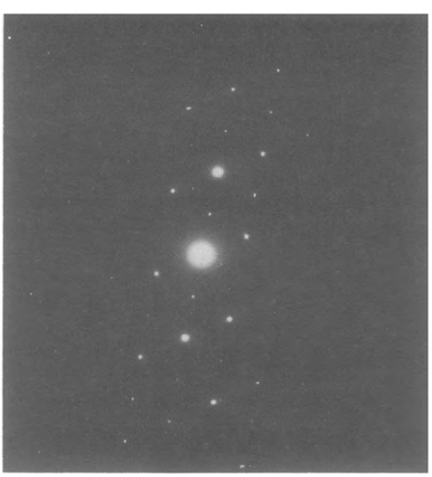

Fig. 11. Electron diffraction pattern of a GdBi film after heating at high temperature. The spot system corresponds to a fcc cell with $a = 6.36$ Å.

microscope, in the first stage of heating of the SmBi films as a C-Sm_2O_3 film forms, the bismuth is simultaneously volatilized as it coalesces into drops.

4.3.2. *Gadolinium–bismuth system*

The samples are prepared as for SmBi films. The X-ray diffraction patterns show the coexistence of Bi and GdH_2. By annealing in air from 470 up to 720 K there is formation of C-Gd_2O_3, and simultaneously there is the appearance and the disappearance of different phases. At 470 K GdH_2 disappears and a fcc structure ($a = 5.54$ Å) appears; it disappears at 520 K and a new compound is then observed with the following interplanar distances: 7.28, 3.64 and 3.40 Å. This phase is also unstable and disappears at 720 K, and a new phase appears with the following interplanar distances: 3.62 and 2.97 Å. Such compounds or alloys cannot be attributed to GdBi alloys or to $GdBiO_3$, because they are too unstable.

It is more likely that they are due to bismuth oxides which are numerous and poorly defined in thin films. In the course of the annealing of the thinner Bi films with the electron beam, there is formation of C- and B-Gd_2O_3. Simultaneously there is formation of little black drops which quickly evaporate at beam impact. These drops are thought to be Bi, because there is no formation of GdBi compounds or of Bi oxides. With a thick bismuth film, the first ring pattern is easily indexable as a fcc structure ($a = 5.55$ Å), the same one as seen by X-ray diffraction. By intense annealing large crystals are formed. These are stable at high temperature (fig. 11), with a fcc structure ($a = 6.36$ Å) which would correspond to the bulk GdBi compound ($a = 6.31$ Å).

5. Rare earth–aluminum systems

5.1. *Amorphous state*

5.1.1. *Experimental procedures*

The studies of amorphous RAl alloy thin films are recent ones. Two modes of evaporation have been used to obtain such samples. They consist either of utilizing a rf sputtering apparatus, or of evaporating from a tungsten crucible an agglomerate such as RAl_x.

The rf sputtering permits one to obtain films with a better defined composition. In this way, Coey et al. (1977), by bombardment of a $GdAl_2$ target, obtained thick films (4 μm) with a composition such as $GdAl_{1.55}Ar_{0.11}Mo_{0.14}$ (as for RFe and RCo films the inclusion of Ar throughout the thickness is not surprising). Malozemoff and Jamet (1977), Mizoguchi et al. (1977b,c), Hart et al. (1979) and Malozemoff and Hart (1980) have obtained compounds with a composition such as $Gd_{0.37}Al_{0.63}$ (near $GdAl_2$). Malozemoff and Jamet (1977), McGuire et al. (1978) and Jamet and Malozemoff (1978) have evaporated numerous alloys such as Gd_xAl_{1-x} ($0.2 < x < 0.81$).

The first experiments done by thermal evaporation (Joule effect) have been

realized by Gasgnier et al. (1976, 1978) and Schiffmacher et al. (1978). In a tungsten crucible small pieces of bulk rare earth metals (such as Gd, Tb, Dy, Ho and Tm) are mixed with bulk, high purity, pieces of aluminum. As the crucible is heated a strong reaction between the two elements is observed, with aluminum projections (as liquid drops) flying out of the crucible into the vacuum. The reaction temperature has not been established. One of the strongest reactions was found for the DyAl alloys. After cooling, the stabilized bulk agglomerate (DyAl) formed in the crucible was crushed to a powder. The X-ray diffraction pattern of this powder is indexable according to $DyAl_3$ rhombohedral lattice. Thin films (300–1200 Å) deposited onto float-glass substrates at 77 and 290 K are mirror-like planes. X-ray and electron diffraction patterns show two large haloes characteristic of an amorphous material. Later, Singh and Srivastava (1979, 1980) have obtained similar results with very few differences.

Tibbets and Egelhoff (1980) have obtained $YbAl_3$ by monolayer deposition of ytterbium onto aluminum crystals.

5.1.2. *Magnetic properties*

The magnetic properties of some RAl alloys have been established for thick amorphous films. By magnetization measurements over a wide range of fields and temperatures (in particular susceptibility measurements) and by microwave magnetic resonance, McGuire et al. (1978) and Jamet and Malozemoff (1978) have shown that the $Gd_{1-x}Al_x$ system exhibits a complex magnetic phase diagram. For $x < 0.4$ the alloys show spin-glass behavior (a metastable magnetic configuration of frozen-in disorder of the spin system within a disordered atomic array); for $0.56 < x < 0.81$ the alloy is ferromagnetic; for $0.4 < x < 0.56$ and $x > 0.81$ there are intermediate states.

Mizoguchi et al. (1977b), Malozemoff and Jamet (1977) and McGuire et al. (1978) have shown that the transition state of Al_xGd_y is below 16 K, and that at 30 K there is predominance of ferromagnetic exchange interactions. It should be noted that for a $GdAl_{1.55}Ar_{0.11}Mo_{0.14}$ film (Coey et al., 1977) the transition state is below 17.5 K. Numerous other magnetic experiments and measurements have been carried out on such samples as a function of the temperature and the composition: magnetization ($4\pi M_\perp, 4\pi M_\parallel$), anisotropy fields, susceptibility (magnetic, static, inverse), volume susceptibility, resonance fields and isothermal remanence signals of the resonance line position, effective g-factors, heat capacity, magnetic specific heat, thermal hysteresis, and relaxation effects. From these results different models and descriptions of such materials have been reported. Mizoguchi et al. (1977b) point out that this is a new class of spin-glass materials because they are not dilute alloys and are amorphous, and the magnetic properties differ markedly from the crystalline form of $GdAl_2$ with $T_c = 170$ K. Mizoguchi et al. (1977c) have discussed their results as not being an artifact. McGuire et al. (1978) have shown that the intermediate states (both ferromagnetic and spin-glass) can be induced by the presence of partially ferromagnetic regions, or by small ferromagnetic clusters, or by random anisotropy effects which could then help to stabilize the spin-glass disorder in the

ferromagnetic regions. Malozemoff and Jamet (1977), Jamet and Malozemoff (1978), Hart et al. (1979) and Malozemoff and Hart (1980) have studied in particular the shift of the resonance line position with decreasing temperature in the vicinity of the freezing temperature (16 K). They have proposed a semiquantitative model, where demagnetized fields are related to the anisotropic dipolar fields of the clusters with additional field-induced columnar magnetic structures. Later they have shown the evolution of local anisotropy fields of an inhomogeneous magnetic system. They have attributed the resonance to partially ferromagnetic clusters, the line shift being due to exchange fields. In the last paper they have shown that for temperatures above the freezing temperature the data are in accordance with an exchange-narrowing model, and below 16 K the frequency dependence is better described by a local field than by a g-shift.

5.2. *Crystalline state: the RAl_3 compounds (R = Gd, Tb, Dy, Tm)*

5.2.1. *$DyAl_3$ system*

5.2.1.1. *Obtaining the crystallized state*

In order to obtain a crystallized state the amorphous films are annealed inside an electron microscope by the electron beam (Gasgnier et al., 1976). By a slow change of the condenser aperture, it is possible to heat the sample gradually. This method leads to the formation of small crystallites, which recrystallize by further annealing and it is possible to observe larger crystals. By the "pulse-annealing" method another phenomenon is observed. Because of the electron beam impact there is, generally, a strong reaction, as in the crucible, and a quasi-instantaneous growth of large crystals, which can be observed over the whole grid area. These crystals are generally isolated from each other and stay on a thin contaminated film (Al_2O_3 and/or carbon). Slight annealing does not change their aspect. Further heating melts and volatilizes them.

The indexing of the electron diffraction patterns shows that the small and large crystals are $DyAl_3$. When no other ring systems are observed (due to Al, Dy and DyH_2), it is possible that during the reaction an excess of R and/or Al inside the film was vaporized.

5.2.1.2. *Structural polytypes*

The more important features of RAl_3, as bulk material, have been described by several authors (see Gasgnier et al., 1976). The results obtained by Gasgnier et al. (1976, 1978), Schiffmacher et al. (1978) and Singh and Srivastava (1979, 1980) during thin films annealing show that the RAl_3 compounds can be described as polytypic substances. For instance, $DyAl_3$ possesses numerous crystallographic phases with three different symmetries (cubic, hexagonal or rhombohedral), which can be associated with polytypic packing of hexagonal atomic planes with the $DyAl_3$ composition. But for this compound, the stacking is not perfectly closed-packed ($c/a = 1.57$), which is explained by the difference between the ionic radii of Dy and Al. Defining the cubic as 3C, hexagonal and nH and rhombohedral as nR (n being an integer) these structures can be identified as hexagonal, with the following properties for the parameters a and c:

- a is nearly constant, independently of the stacking;
- c is equal to nh (n number of sequence planes, h spacing between two layers).

For $DyAl_3$, $a = 6.08$ Å, and the total of the atomic diameters is $d_{Al} + d_{Dy} = 2.86$ Å $+ 3.54$ Å $= 6.40$ Å. The difference between the two values leads to a slight distortion of the ideal stacking sequence. The crystallographical properties of such structures can be illustrated by the reported parameters of two well-known phases of $DyAl_3$

$DyAl_3$(4H): $a = 6.08$ Å, $c = 9.35$ Å (4×2.385 Å);

$DyAl_3$(15R): $a = 6.08$ Å, $c = 35.86$ Å (15×2.385 Å).

5.2.1.3. *Geometrical and structural properties of the crystals*

The small crystallites obtained after annealing of the thin amorphous films have a primitive cubic lattice. It is the b-$DyAl_3$ phase, labeled as 3C, of the structural polytypes. The electron diffraction patterns consist of continuous rings.

The large crystals which appear after strong heating show some peculiar aspects. Three different crystal configurations have been observed. One of them exhibits "pole figures" and "extinction contours" (fig. 12) and it also has a polygonal appearance (Gasgnier et al., 1976). They have the form of thin lamellae for which the c axis of the stacking planes is parallel to the electron beam. Such crystals are found in the thinner films. The second aspect, observed with the thicker films, shows large bent striated crystals with a knee configuration (fig. 13) (the two zones are separated either by a grain boundary or by a twin). The third aspect is characterized by "needle-like" crystals (fig. 14). The structural data will be described in the next section.

5.2.1.4. *Resolution of the electron diffraction patterns*

A large number of electron diffraction patterns have been obtained with the striated crystals. They have been indexed according to different crystallographic structures with cubic, hexagonal and rhombohedral cells. But some are so

Fig. 12. Small polygonal $DyAl_3$ crystals with "pole figures" and "extinction contours".

Fig. 13. Large $DyAl_3$ crystal with a "knee" configuration.

complex that no indexing is possible; indeed, they consist of an alignment of close spot diffractions which are often elongated (fig. 15). This pattern has been obtained by the microdiffraction technique on each part of a "knee". This can be explained by the syntactic intergrowth of polytypes into the same crystal. However, some single phases have been observed from their simple electron diffraction patterns. The explanation and the indexing of these phases have been reported by Gasgnier et al. (1976). Briefly, the crystals generally have either a hexagonal compact cell (denoted as n_1H) or a rhombohedral one (denoted as n_2R, with n_2 being an integer multiple of 3). (The stacking sequence notation is shortened with the Ramsdell notation.) Each of them is distinguished by the presence (hexagonal structures) or the absence (rhombohedral structures) of the (10.0) reflection. The complete indexing of all the films has permitted the determination, in addition to the three well-known bulk structures 3C, 4H and

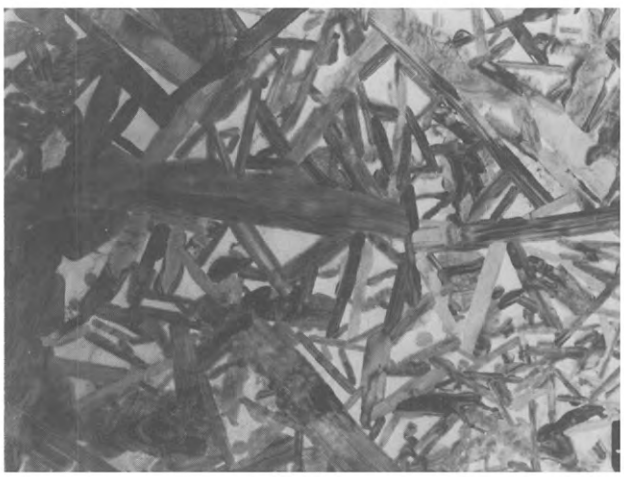

Fig. 14. Small $DyAl_3$ crystals with a "needle" aspect.

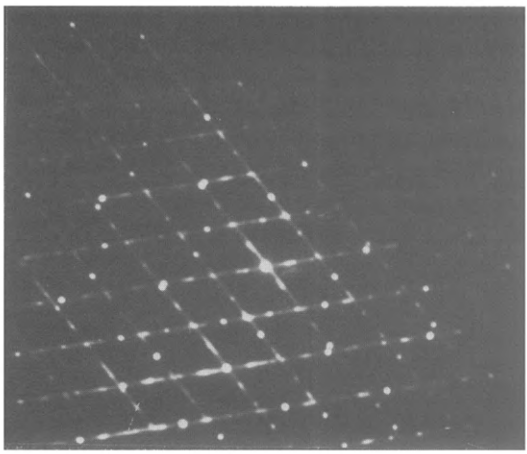

Fig. 15. Microdiffraction pattern obtained from each part of the "knee" shown in fig. 13.

15R, of the following phases: 6H, 8H, 10H, 12H 14H, 9R, 12R and 42R (the 42R structure has $c = 100.2$ Å). This list is not complete because some patterns with small interspot distances (elongated spot configurations) have not been indexed. They induce the formation of large c parameters, larger than the one for 42R. Another special feature has been observed: as seen on fig. 16, the rows of spots are not along a straight line but assume the bent configuration of the corresponding crystal (fig. 17).

5.2.1.5. *Lattice imaging*

With a large magnification and an objective aperture containing a large number of beams, as seen on the electron diffraction pattern shown in fig. 18 (the circle being the aperture projection), it is possible to image the crystal lattice. Thus, a periodic potential imaging inside a crystal can be obtained with a resolution of about 1.4 Å. The TEM presented in fig. 19 shows a succession of lamellar microdomains of polytypic materials. The different structures have been

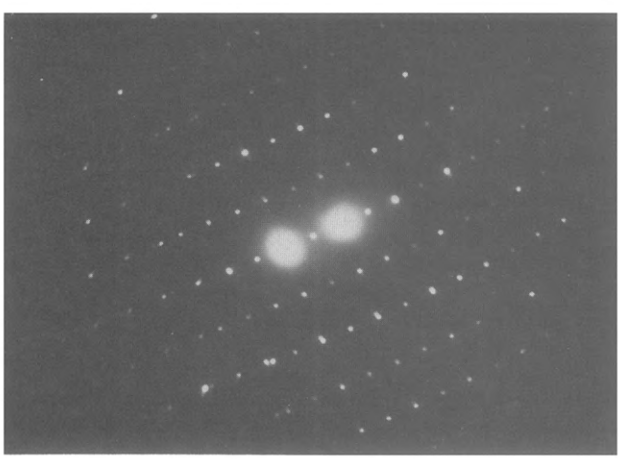

Fig. 16. Electron diffraction pattern showing rows of spots with a bent configuration.

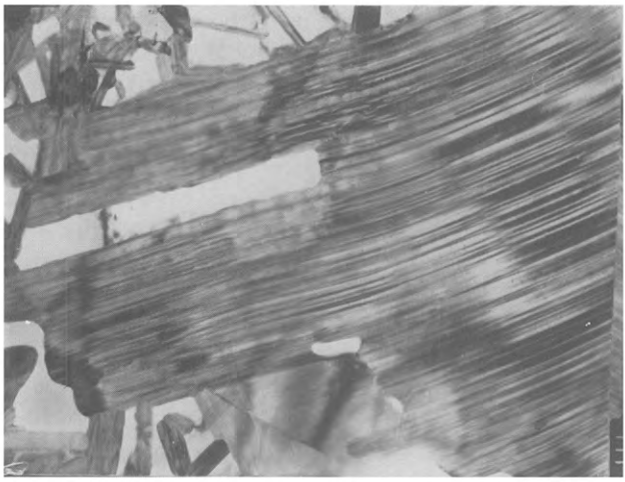

Fig. 17. A micrograph of the crystal of which the electron diffraction pattern is shown in fig. 16. The bend of the crystal corresponds to that of the rows of spots.

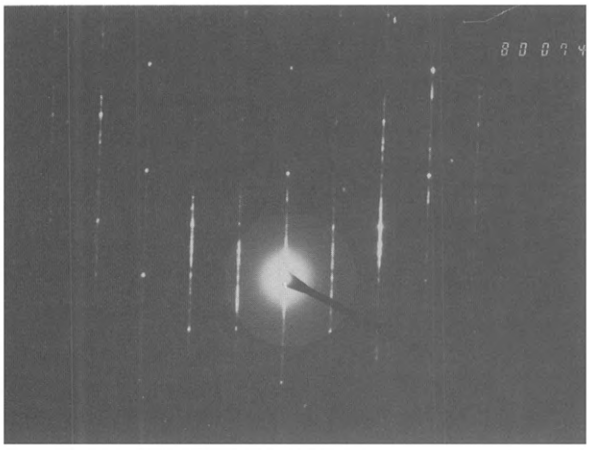

Fig. 18. Complex electron diffraction pattern corresponding to a polytypic syntactic intergrowth (the circle is the projection of the diameter of the aperture).

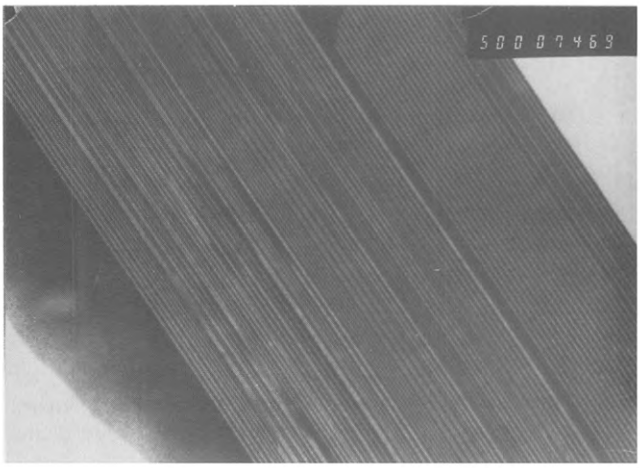

Fig. 19. Transmission electron microscopic photomicrograph of the crystal corresponding to fig. 18. Each space between striae permits one to define a structure.

distinguished by taking into account that the unit plane is the basic hexagonal plane. Some of these phases are sometimes reduced to a few atomic planes (the 3C and 4H ones have a thickness of about 20 Å). Gasgnier et al. (1978) and Schiffmacher et al. (1978) have shown the high resolution lattice imaging of the 6H and 15R structures. The 15R one has been defined according to two stacking sequences as:

/ABCBA/BCACB/CABAC/ (as type I),

/ACBCA/BACAB/CBABC/ (as type II).

In fig. 20 the two zones are reported, with their spatial positions differing by a rotation of $\frac{1}{3}\pi$ or π. There is inversion of the direction for the blocks of each zone.

5.2.2. *$GdAl_3$, $TbAl_3$ and $TmAl_3$ systems*

Gasgnier et al. (1978) have shown that $GdAl_3$ exhibits only the 3C structure ($a = 4.30$ Å). In the bulk such a structure has been observed only for rare earths from Dy to Sc. However, by extrapolation of the curve of a plot of the ionic radius of the R elements versus lattice parameter, the estimated value for $GdAl_3$ is close to the one obtained experimentally. In contrast to this behavior for $GdAl_3$, Singh and Srivastava (1979) have observed, by using the same experimental procedure as Gasgnier et al. (1976), the following structures: 3C, 4H, 5H, 8H, 9R, 15R and 2H (the last one being the only one found in the bulk phase).

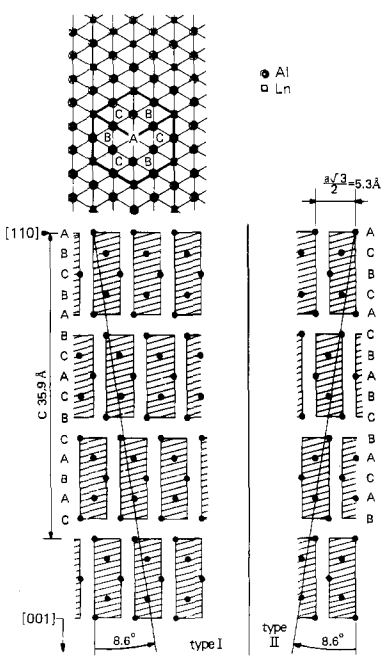

Fig. 20. Disposition of five-layer blocks in a 15R polytype. (The second and third block sequences of type II are interchanged.)

Singh and Srivastava (1980) have determined the following phases for $TbAl_3$: 2H, 3C, 5H, 6H, 10H and 9R (the last one being found in the bulk phase).

Gasgnier et al. (1978) have reported for $TmAl_3$ the formation of the 15R ($a \approx 6$ Å and $c \approx 35.3$ Å) and 3C structures (the last one is the structure of the bulk phase).

5.2.3. *Hypothesis on the polytypic phenomenon*

In a case which is peculiar to the DyAl compounds a highly exothermic reaction has been observed between the two elements. This leads to the formation of large crystals with a polytypic configuration. To our knowledge such a phenomenon has never been described for other amorphous alloy materials. Gasgnier et al. (1976) have suggested that the "wild" experimental procedure may be linked to a thermodynamic state which is highly out of equilibrium at the time of the birth of the alloy. Such a phenomenon can be associated to "dissipative structures", which are characterized by a crystalline structure having a long period in the solid state. This hypothesis is perhaps not the correct one. Thus the role of impurities should be taken into account; in this way the presence of oxygen has been studied in $DyAl_3$ amorphous films by AES. Another explanation can be linked to physical solid-state theories. Thus, Singh and Srivastava (1980) have tentatively explained the amorphous–crystalline transformation of $TbAl_3$ thin films by the nearly free electron approximation. But they claim, first that a Brillouin zone exists in an amorphous material, and secondly that the Fermi surface spanning vector $G(k_f) = 2k_f$ can be defined for such a material. Since it is difficult to describe a Brillouin zone in a disordered material, and as the G value has still not been resolved for alloys with a lanthanide trivalent ion, which induces complex systems, this hypothesis cannot be verified.

RAl_3 alloys are interesting materials, and some questions have not yet been resolved to explain the observed phenomena:

– what process permits these materials to have an amorphous state at room temperature: atomic dissociation, clusters, hybrid R–Al ligands ... ;

– what process permits the formation of polytypic structures from the amorphous state: out-of-equilibrium thermodynamics, impurities, solid-state physics laws ... ?

5.2.4. *A peculiar case: the $YbAl_3$ compound*

Tibbetts and Egelhoff (1980) have studied Yb thin films deposited on monocrystal substrates. By XPS and LEED they controlled the inter-diffusion processes. The pure Yb surface layers are in a divalent state (f_{14}-Yb). Above 420 K the interdiffusion becomes substantial and they observed the formation of a mixed-valence state (f_{13}–f_{14}-Yb). Further annealing at 520 K causes a reversion to the divalent state; such a phenomenon is also produced by slight ion bombardment. By XPS they showed that the peak concentration of (f_{13}-Yb) appears to coincide with the stoichiometric alloy $YbAl_3$. On the other hand they have observed that in a dilute solution of Yb in Al, the rare earth is divalent.

5.3. *Other rare earth–aluminum systems* (R = *Ce, Gd, Dy, Tm*)

This section is devoted to another aspect of the complexity of the amorphous–crystalline phenomenon (Gasgnier, 1982).

5.3.1. *Cerium–aluminum systems*

Upon heating with the electron beam the crystallization modes are quite different, depending on the cerium concentrations.

5.3.1.1. *Films poor in cerium*

X-ray and electron diffraction patterns of the cerium-poor as-deposited films exhibit an aluminum ring system and a large halo relative to an amorphous material. By annealing inside the electron microscope a new ring system appears which is characteristic of small crystallites and can be indexed as a hexagonal structure with $a = 6.92$ Å and $c = 6.28$ Å. No compounds of the CeAl system are related to these parameters. Upon further heating this alloy, which is very unstable, disappears and the formation of large aluminum crystals are observed.

5.3.1.2. *Films rich in cerium*

The as-deposited cerium-rich films show in X-ray diffraction broad haloes characteristic of amorphous materials.

In the first stage of annealing small crystallites appear (white and grey in contrast) as seen in fig. 21. The electron diffraction patterns show that the crystallites correspond to the compound Ce_3Al_{11} (orthorhombic structure) inside an aluminum matrix (fig. 22). After further annealing the aluminum ring system disappears and there is formation of large crystals which have a hexagonal structure with $a = 4.60$ Å and $c = 6.52$ Å. (These parameters are close to those of the $CeAl_3$ compounds, but a and c are reversed.)

Other samples have shown the following phenomena during successive annealings. First, the coexistence of small crystallites of aluminum and of an unknown compound, characterized by two intense rings with interplanar dis-

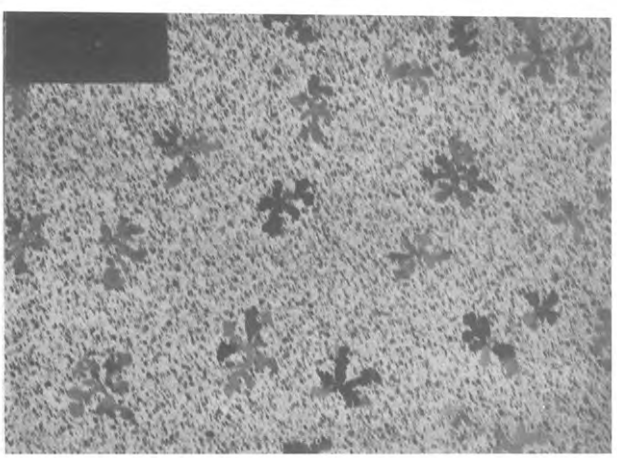

Fig. 21. A CeAl film after annealing at low temperature by means of the electron beam. The small contrasting crystals correspond to the compound Ce_3Al_{11}.

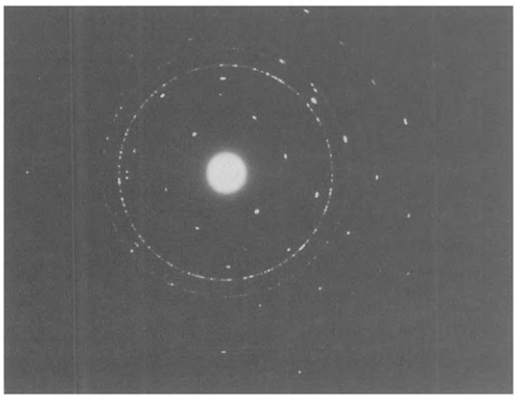

Fig. 22. Electron diffraction patterns corresponding to one of the crystals shown in fig. 21. The electron beam is parallel to the 010 axis. The ring system is that of Al.

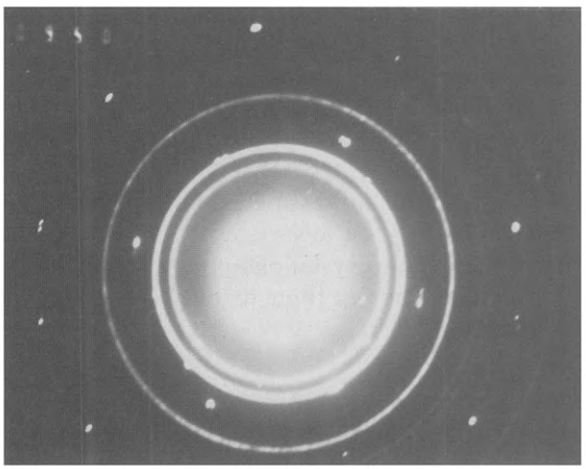

Fig. 23. Complex electron diffraction pattern of a CeAl film after annealing at high temperature. Three structures coexist (see text).

tances of 2.77 and 1.71 Å. Secondly, the disappearance of aluminum, and the presence of a complete ring system, involving the two above-mentioned interplanar spacings. This system can be indexed as a fcc lattice with $a = 4.78$ Å. It coexists with other phases whose diffraction patterns (fig. 23) pertain to CeO_2 and to a tetragonal lattice with $a = 4.57$ Å and $c = 10.90$ Å. According to the annealing mode (pulse annealing or progressive heating) many other complex ring and spot systems appear. One of them has been indexed as a tetragonal cell with $a = 4.18$ Å and $c = 5.52$ Å. It is clear that the CeAl system is complex when it crystallizes or recrystallizes upon heating.

5.3.2. *Gadolinium–aluminum system*

The X-ray diffraction patterns of the as-deposited GdAl films, heated on their substrates at 570 and 720 K, show the coexistence of the aluminum ring system and a broad halo. By annealing inside the electron microscope a number of

TABLE 1
Gd–Al system: crystallographic properties of unknown structures.

		Structures H_1	H_2	H_3	H_4	H_5	C_1	O_1
Parameters	*a*	7.90	7.90	5.40	5.50	5.25	4.90	6.85
	b	—	—	—	—	—	—	9.25
	c	22.40	11.20	11.20	8.60	6.15	—	11.20
Crystal geometry		large and small	large and small	large	large	large	small	large

structures (table 1) appear; generally none have been reported in the bulk state. They are characterized either by small crystallites in the first stage of the heating, or by large crystals in the final stage. The formation of these structures depends on several parameters: film thickness, heating mode (pulse annealing, progressive annealing), and probably the Al/Gd concentration. Different kinds of crystals can coexist within the same sample. Sometimes large aluminum crystals appear. Two remarks can be made concerning the lattice parameters. The orthorhombic structure (O_1) differs from that of bulk Gd_2Al by the parameter *a* ($a = 7.90$ Å in the bulk). The C_1 structure may be associated to Gd_3AlC_x. The results are not so surprising because the bulk crystallographic structures are diversified. Thus, GdAl and Gd_2Al could have two or three distinct orthorhombic lattices, respectively.

5.3.3. *Dysprosium–aluminum system*

Some of the DyAl samples have shown some unusual modes of crystallization, drastically different from those described for $DyAl_3$.

First, inside the amorphous matrix at the beam impact a crystal appears and it grows slowly when the heating increases. By shifting the beam to each side of the initial nucleated crystal it is possible to obtain a large crystal without apparent defects. The corresponding electron diffraction patterns permit one to index a fcc structure with $a = 7.85$ Å, which is probably the $DyAl_2$ compound.

Secondly, some samples exhibit another mode of crystallization and a ring system appears, which can be indexed as a fcc structure with $a = 5.45$ Å.

Thirdly, in coexistence with the polytype $DyAl_3$ crystals, there are some isolated crystals with different structures. Some of them are complex. Only one has been indexed as a primitive cubic ($a = 7.20$ Å) or a bcc one ($a = 10.15$ Å).

5.3.4. *Thulium–aluminum system*

As for the other R–Al system it has been observed that several new phases are formed in the TmAl system. One of them has been defined as Tm_2Al with an orthorhombic cell. The other ones are not always easy to index (spot systems are often isolated or poorly defined). However, from a series of different patterns

relative to large crystals, three structures have been indexed: a hexagonal (a = 7.85 Å, c = 10.25 Å), a tetragonal (a = 10.25 Å, c = 13.64 Å) and a primitive cubic (a = 7.25 Å) structure. Some spot systems are characterized as row spots but are not indexable according to the polytype structures of the RAl_3 compounds.

5.4. *A peculiar case: the Er–Al_2O_3 system*

Sichel and Miller (1976) have deposited by co-sputtering evaporation Er and Al_2O_3 (with the Er content varying from 50 to 100%). From their resistivity and magnetic susceptibility measurements they discuss the formation of ErAl compounds at 300 K. They observed the total dissociation of Al_2O_3 and the appearance of the following compounds: ErAl, $ErAl_2$, $ErAl_3$ and Er_2Al_3.

6. Superconducting systems

6.1. *Binary dilute alloys*

6.1.1. *Lanthanum–gadolinium systems (dilute gadolinium impurities)*

Schwidtal (1962) has shown that lanthanum foils exhibit either a hcp structure with a superconducting transition at 4.9 K or a fcc structure with a superconducting transition at 6.0 K. In thin films, small additions of Gd (up to 0.75 at%) lower the transition temperatures at a rate of 4.4 K per at% Gd, regardless of the method of preparing the films, i.e. quench-condensed or annealed. Korn (1965) has co-evaporated LaGd thin films containing 10 at% Gd. The author found the existence of an antiferromagnetic spin ordering at 4 K.

6.1.2. *Lead, indium, aluminum–rare earth systems (dilute rare earth impurities)*

Schwidtal (1960) has also studied the influence of a paramagnetic impurity like Gd (from 0.2 up to 2.3 at%) on the superconducting properties of Pb. By co-evaporation the sample is condensed on a substrate at low temperature. The superconducting transition temperature decreases linearly with increasing Gd content. In the same manner Hauser et al. (1966) have produced thin films such as Pb–2.9 at% Gd with a transition temperature of 1.52 K. Their results are in good agreement with those of Schwidtal (1960) and Woolf and Reif (1965). Moreover, Hauser et al. (1966) have studied the transition temperature for Pb–Pb: 2.9 at% Gd sandwich films, in order to examine the proximity effect of lead with a dilute magnetic alloy. The two metals are mutually insoluble in the solid state. Woolf and Reif (1965) and Dick and Reif (1969) have studied by conductance and tunnel conductance measurements and by far IR the energy gap properties and the superconducting properties of PbGd dilute alloy. They conclude that all the spins are due to 4f electrons. Lastly Mrstik and Ginsberg (1973) give the transition temperatures and the sensitivity curves versus the Gd content for quench-condensed superconducting Pb films containing 3.1 at% Gd by tunneling

and high-frequency electromagnetic experiments. They compare their results with theoretical views.

Delfs et al. (1975) have obtained quench-condensed PbCe (0–10 at% Ce) films to examine the connection between the superconductivity and the Kondo effect. They have studied the superconducting transition (between 0–7 K) versus the Ce content and shown that the transition temperatures are sensitive to the degree of structural disorder. The samples exhibit changes of the transition temperature and Kondo resistance by annealing at 77 and 20 K, respectively.

The studies of Mrstik and Ginsberg (1973) and of Delfs et al. (1971) also comprised InGd and InCe dilute magnetic alloys.

Craven et al. (1971) have shown the influence of dilute erbium impurities (0.274 to 0.006 at%) on the superconducting transition of aluminum thin films, overlayered by SiO. They have observed that the anomalous excess conductivity in Al films is quenched by the addition of paramagnetic impurities. The transition temperature varied from 1.575 to 1.95 K, but non-linearly with the Er content.

6.2. *Binary non-dilute systems*

Ghosh and Douglass (1977) have prepared by rf sputtering R_xGe_{1-x} ($0.2 < x < 0.9$) films deposited onto hot substrates (1020 K). With R = Y and $x = 0.32$ (i.e. YGe_2) they have observed by resistance measurements a superconducting transition temperature of 3.8 K. With R = La and an alloy of the $LaGe_2$ composition this temperature is 2.6 K.

Savitskii et al. (1974, 1975, 1977) have reported numerous studies on alloy thin films such as (Ti, V, Zr, Nb and Pb)Sm and PbLa, prepared by thermal evaporation or by e-gun. For (Ti, V, Zr and Nb)Sm they have not observed the formation of intermetallic compounds, and (Ti and Zr)Sm were superconducting above 4.2 K For the $PbSm_x$ system they found that for $0 < x < 0.25$ there is a superconducting transition at 7 K as for pure Pb. For $0.25 < x < 0.52$ the superconducting transition is at 6.7 K with the formation of $SmPb_2$ and $Sm_{11}Pb_{10}$ compounds. For $x < 0.52$ an unknown compound with a superconducting transition above 4.2 K has been observed. In the $PbLa_x$ system the transition is observed at 6.5 K for $0 < x < 0.25$, for $0.25 < x < 0.63$ the transition, if it exists, is below 4.2 K and for $x < 0.63$ the transition corresponds to the one of the dhc phase of La (4.9 K). These authors conclude that such results can define superconducting temperature versus composition diagrams.

Manning and Briscoe (1978) have shown that $La_{1-x}Au_x$ ($0 < x \leq 0.32$) amorphous films deposited by vapor condensation have a superconducting transition temperature which decreases as the Au content increases. For pure La it is 4.6 K and for $x = 0.32$ it is 1.6 K. The residual resistivity increases with increasing Au content from 68 $\mu\Omega$ cm (pure La) up to 208 $\mu\Omega$ cm. For $x < 0.26$ the films deposited at 4.2 K and then annealed at up to 293 K crystallize. For $0.26 < x < 0.32$ the samples are stable. The authors think that the amorphous phase may be more homogeneously disordered than liquid-quenched foils.

6.3. *Ternary compounds RRh_4B_4 and RMo_6S_8 (R = Er, La)*

Recently Robinson (1977) has described the properties of RRh_4B_4 (R = Er, Y) and RMo_6S_8 (R = La, Yb) bulk compounds as future superconducting materials. In the literature one notices that RRh_4B_4 can be made with R = Nd, Gd, Ho and Lu.

Christner et al. (1979) and Rowell et al. (1979) have studied the properties of $ErRh_4B_4$ compounds in thin films.

Christner et al. (1979) have prepared their samples by dc sputtering and described their experimental procedure in detail. They have minimized the contamination by oxygen which can influence the physical properties. The X-ray diffraction patterns show the formation of the $ErRh_4B_4$ compound and a small amount of RhB. The composition has been also studied by AES. The superconducting transition temperature varies from 6.0 to 7.8 K, which is somewhat different from the bulk (8.7 K). One film exhibits such a temperature and returned to the normal state at about 1.0 K (in the bulk state the change to the magnetic state is 0.9 K). Another sample, exhibiting the presence of RhB, has a transition temperature of 4.5 K.

Rowell et al. (1979) have evaporated $ErRh_4B_4$ compounds by sputtering. Their superconducting and ferromagnetic transitions are at 7.1 to 8.1 K and 0.84 to 1.05 K, respectively. They show that the two transition temperatures are depressed from 8 to 2 K and 0.95 to 0.45 K by irradiation with 1.8 MeV α-particles. They conclude that all superconductors which are unusually sensitive to damage are cluster compounds such as A15 Chevrel phases. These results raise interesting questions concerning the band structure of cluster compound superconductors, the nature of the magnetic transition and generally about the sensitivity of cluster compounds to damage.

Przyslupski et al. (1979) have prepared by dc sputtering thin films such as $LaMo_6S_8$. They are annealed in the range of temperatures from 290 up to 1320 K. The transition temperatures have been measured as 6.2 and 5.4 K (11.4 K for bulk material). The sample properties have been studied in magnetic fields up to 8 T and in the temperature range 1.7–4.2 K. The curves of the critical current and of the pinning force density show a highest critical current density reached for $B = 0$ and $T = 1.7$ K, with $J_c = 1.7 \times 10^7$ A m^{-2}.

7. Other rare earth systems

7.1. *The rare earth–magnesium system (R = Gd, Sm)*

McGuire and Gambino (1980) have reported magnetic data for amorphous GdMg alloys. Compared to the other Gd alloys studied, these materials possess the highest Curie temperature (130 K), Weiss constant (133 K) and negative ρ_H/ρ ratio (−0.022).

Gasgnier (1981) has tentatively studied SmMg films to try to form hydride materials. A SmMg mixture was preheated at low temperature in a tungsten crucible and then deposited onto glass substrates at a high condensation rate. The as-deposited film was heated at 370 to 500 K and studied step-by-step by X-ray diffraction. At low temperature SmH_2 coexisted with magnesium (this sample exhibited preferential orientation: the (0 . 02) diffraction line of Mg is intense and characterized by a diffraction segment). During annealing some diffraction peaks, which it has not been possible to attribute to any of the known SmMg compounds or to MgH_2, appear and disappear. Between 370 and 420 K two diffraction lines appear at 4.21 and 2.31 Å, which disappear at 430 K; at 450 K a new diffraction line at 5.51 Å is observed and it disappears at 490 K. At about 500 K there is formation of C-Sm_2O_3.

The as-deposited films studied by electron microscopy show the presence of small magnesium crystals, which recrystallize by annealing with the electron beam. Simultaneously new crystals, which cannot be indexed as any of the known SmMg compounds, SmH_2, MgH_2 or C-Sm_2O_3, appear. The electron diffraction patterns are complex. At high temperature new large crystals with unknown structures appear. Only some patterns have led to identification of a fcc structure (a = 8.65 Å) which may be linked to the $SmMg_2$ compounds.

7.2. *The rare earth–silicon system* (R = *La, Ce, Gd*)

Lazorenko et al. (1978) have studied LaSi films prepared by vaporization and observed by electron microscopy. At 290 K the samples are amorphous and by annealing at 720 and 770 K the formation of $LaSi_2$ and La_2Si_3, respectively, occurs. By further annealing at 870 and 1070 K the authors observe the formation of new structures, also related to $LaSi_2$ and La_2Si_3; at higher temperatures other new phases appear but they have not been identified.

McGuire and Gambino (1980) report that amorphous GdSi is ferromagnetic with a high resistivity (12 700 $\mu\Omega$ cm at 4.2 K and 965 $\mu\Omega$ cm at 293 K) which is much higher than that observed in other Gd alloys studied. They give the magnetic data for such an alloy.

Levin (1979) has studied the ternary compound $CeCo_2Si_2$. He reported the dependence of the spontaneous Hall effect and the magneto-resistance on the applied field. He observed anomalous galvanomagnetic effects due to an asymmetric distribution of charge carriers caused by their spin–orbit interaction with magnetic defects (Co clusters).

7.3. *The gadolinium–germanium system*

McGuire and Gambino (1980) have reported the transport properties of GdGe amorphous film. Compared to other Gd alloys, such a sample has a large resistivity (285 $\mu\Omega$ cm) and a low T_c (70 K).

7.4. *The gadolinium–zinc system*

Domyschev et al. (1974) have studied the system GdZn but were unable to produce the $GdZn_2$ Laves phase compound. The authors thought this was due to the low electronegative ratio of these elements.

8. Rare earth–chalcogenide systems

8.1. *Samarium*

8.1.1. *Samarium monosulfide*

In the bulk state this compound presents an isostructural discontinuous transition at 6.5 kbar labeled as

Semiconductor (S.C. SmS) → Metallic (M. SmS).

Some properties of these two phases are reported in table 2. Suryanarayanan (1978) has described almost all of the other properties in a review article.

Between these end members several other phases have been observed with intermediate oxidation states as defined by their lattice parameters which fall between the two extremal values reported.

8.1.1.1. *Preparation and structural properties*

The first paper relative to SmS thin films was that by Holtzberg and Torrance (1971). Their samples were prepared by e-gun from previously synthesized SmS. By deposition onto quartz substrates heated at 620 K, the films crystallized as the (S.C. SmS) phase, with $a = 5.97$ Å.

Later Batlogg et al. (1974) prepared SmS thin films by flash evaporation onto heated quartz substrates (620 K). These films are green in transmission and purple in reflection, and, as reported by Holtzberg and Torrance (1971), are mainly (S.C. SmS). Suryanarayanan and Brun (1976) have used a multi-source multi-substrate evaporator to obtain the (S.C. SmS) phase.

Then Bzhalava et al. (1974) carried out a series of experiments which have led to the understanding of the transition phase in thin films. By evaporation onto sapphire and quartz substrates they have obtained the (S.C. SmS) phase. After *polishing* with a diamond paste they have observed the (M. SmS) phase. Heating this latter phase has resulted in the reverse transition, i.e. the formation of the (S.C. SmS) phase. The cycle polishing–heating reconverted each form. Volkon-

TABLE 2
Properties of the (S.C. SmS) and (M. SmS) phases.

SmS phase	Color	Lattice parameters	Oxidation state
S.C.	black	$a = 5.97$ Å (NaCl type)	+2
M.	gold	$a = 5.62$ Å (NaCl type)	+3

skaya et al. (1975) concluded that the polished phase was identical with the high-pressure phase; the mechanical stresses act like hydrostatic pressures. Bzhalava et al. (1975) and Schul'man et al. (1975) have obtained by deposition onto heated substrates (520 K) a mixture of the two phases. Kaminskii et al. (1975), Petrov et al. (1977) and Sattikulov et al. (1978), using a laser, have observed this phase transition.

By *rubbing* Pohl et al. (1975a,b) and Chenevas-Paule et al. (1977) have also obtained this transition. By evaporation onto glass substrates at 85 or 290 K, Gasgnier and Sénateur (1980) have observed some new phenomena. For the thinner films ($e < 2000$ Å) they have shown that the samples were amorphous. Previously Ivanchenko et al. (1971) and Lashkarev and Ivanchenko (1972) had obtained a similar result. For the thicker films ($e > 2000$ Å), Gasgnier and Sénateur (1980) have shown that it was possible to have either one or the other of the two modifications, or their coexistence, depending on the substrate temperature. By deposition at 290 K the films are (S.C. SmS); by deposition at 85 K and by slowly heating up to 290 K the samples are (M. SmS). They are present as coexisting phases by abrupt heating up to 290 K. In these films it is usual to obtain high pressure phases according to the deposition parameters (deposition rate, substrate temperature, thickness, ...). From X-ray and electron diffraction it has been determined that the lattice parameters were smaller than those given previously. Such a result has been ascribed to the presence of a small amount of oxygen inside the films, and to the formation of a ternary compound such as $SmS_{1-x}O_x$. In table 3 are reported some lattice parameters obtained by different authors.

8.1.1.2. *Optical properties*

8.1.1.2.1. Amorphous state

Ivanchenko et al. (1971) and Lashkorev and Ivanchenko (1971) have reported the absorption spectra, which are characterized by four absorption bands in the range 0.5–2.3 eV. The authors have discussed the electronic transitions in Sm^{2+} and the transition energy differences. They concluded that the optical absorption can be explained by features of the Sm^{2+} ion electron structure and the

TABLE 3
Comparison of the lattice parameters obtained by different procedures.

	Bzhalava et al. (1974)	Bzhalava et al. (1975)	Schul'man et al. (1975)	Gasgnier and Sénateur (1980)
Method	X-ray	X-ray	X-ray (thick films deposited at 520 K)	X-ray and electron diffraction (films deposited at 80 and 290 K)
(S.C. SmS) a_1 (Å)	5.97	5.97	5.94, 5.84	5.91
(M. SmS) a_2 (Å)	5.69	5.66	5.63	5.58 (thick films) 5.47 (thin films)

interaction of the 4f and 5d states with the crystal field environment. They present a scheme of the energy bands and the optical electronic transitions.

8.1.1.2.2. Crystalline state

Many experiments have been done to characterize mainly the transition (S.C. SmS)→(M. SmS) and the different electronic structure of each phase.

Holtzberg and Torrance (1971), Batlogg et al. (1974), Pohl et al. (1975), Pogarev et al. (1976), Suryanarayanan et al. (1976, 1977), Oskotskii (1977), Smirnov et al. (1976, 1978) and Glurdzhidze et al. (1978) have studied the optical absorption in the range 0.4–4.5 eV. Kukhaskii et al. (1977) and Pohl et al. (1975) have reported the transmittance and reflectance curves.

For the (S.C. SmS) phase there are five transitions:

$$4f^6(^7F_0) \rightarrow 4f^5\,(^6H_j)\,5d\,t_{2g}$$
$$4f^5\,(^6F_j)\,5d\,t_{2g}$$
$$4f^5\,(^6H_j)\,5d\,e_g$$
$$4f^5\,(^6P_j)\,5d\,t_{2g}$$
$$4f^5\,(^6F_j)\,5d\,e_g$$

The results obtained by Glurdzhidze et al. (1978) by reflection spectra in the phonon energy range 0.06–2.3 eV have permitted the observation, for the first time, of the fine structure of the absorption and reflection spectra associated with the splitting of the initial and final electron states. The authors conclude that the spin–orbit interactions splits the $4f^5$ (^6H_j), $4f^5$ (^6F_j) and 5d t_{2g} states. Moreover, there is an energy gap of 0.15 eV between the valence and conduction bands.

For the (M. SmS) phase there are two absorption peaks at 1 and 1.8 eV at room temperature (Pogarev et al., 1976), and four at low temperature (8 K) (Smirnov et al., 1976). These last authors conclude that, as the transition Sm^{2+}: $4f^6 \rightarrow 4f^5$ (^6H_j) 5d t_{2g} coincides for the two phases, the samarium is in a mixed valence ground state. Oskotskii (1977) has tentatively interpreted the origin of the different transitions which seems more complex than that of the one in the (S.C. SmS) phase, as also reported by Suryanarayanan et al. (1977).

Kukharskii et al. (1977), who determined the electron effective mass in (M. SmS), report that the reflection spectra of such samples show a bell-shaped absorption at 6000 Å. The authors made an unambiguous separation of the contributions of free carriers and interband transitions, since the bell-shaped maximum is shifted quite definitely relative to the fundamental absorption edge.

Another series of experiments have been carried out to study the properties of such materials for laser writing–reading and holographic storage. In this way Kaminskii et al. (1975), Pohl and Holtzberg (1975), Grachev et al. (1976) and Petrov et al. (1977) have tentatively shown that it is possible to use SmS for optical digital data storage by a laser-induced phase transition. Sattikulov et al. (1978) have used a Q-switched ruby laser as a light source to realize a source of ultrasound with SmS thin films. It is excited in this way when the laser pulse heats the film to the phase-transition temperature (470–570 K).

8.1.1.3. *Transport properties*

Pohl et al. (1975) have reported the dc electrical conductivity, Hall coefficient and "Hall mobility" versus temperature for the (M. SmS) phase. Goncharova et al. (1976) have reported for several (S.C. SmS) and (M. SmS) samples the resistivity and the Hall coefficient versus temperature. From their results they developed a model for the electronic transitions and discuss its temperature dependence.

Chenevas-Paule et al. (1977) have recorded the resistivity versus temperature of the two phases in the range 1–300 K. From their results they estimate the Kondo temperature to lie between 20 and 50 K. They conclude that (M. SmS) is not a Kondo compound similar to $CeAl_3$ and since the resistivity does not increase with temperature they believe in the presence of Sm^{3+}.

8.1.2. *Samarium sesquisulfide*

Batlogg et al. (1974) have prepared some films of Sm_2S_3 (where Sm is only trivalent), and gave some results for optical absorption. Their absorption edge starts at about 2.8 eV, but no pressure shift has been observed. This peak corresponds to the transition $4f_6$ ($^7F_0$) $\rightarrow 4f^5$ (^6H_j) 5d e_g of SmS.

Kehaiov et al. (1979) have prepared Sm_2S_3 thin films by vacuum thermal deposition from two independent sources. By X-ray and electron diffraction they have shown that the films, deposited onto substrates heated at 770–970 K, have the γ-form Sm_2S_3 with $a = 8.41$ Å. By annealing at 1220 K the "β-form" appears.

Suryanarayanan and Brun (1976) have reported for Sm_2S_3 thin films ($a = 8.43$ Å) the optical density at 10 K. They observed two sharp peaks at 2.57 and 2.71 eV, tentatively identified as being due to an f $\rightarrow$ f transition from a localized Sm^{3+} level.

8.1.3. *Samarium ternary monosulfides*

Some optical density studies have been done by Suryanarayanan (1977), Suryanarayanan and Brun (1976) and Suryanarayanan et al. (1977). They have shown that for Tm and Yb as substituted elements the thin films crystallized in the fcc NaCl structure. The optical density of a $Sm_{0.6}Yb_{0.4}S$ film ($a = 5.84$ Å) shows three broad absorption bands due to the transition (Sm^{2+}) $4f^6 \rightarrow 4f^5 4d$ (t_{2g}, e_g), and a maximum which can be attributed to the transition (Yb^{2+}) $4f^{14} \rightarrow 4f^{13}$ ($^2F_{5/2}$) 5d t_{2g} or $4f^{14} \rightarrow 4f^{13}$ ($^2F_{7/2}$) 5d e_g. They conclude that Yb and Sm are both stable divalent ions, and that the S.C. $\rightarrow$ M. transition cannot be observed. Some other results have been described for samples such as $Sm_{0.7}Tm_{0.3}S$, $Sm_{0.4}Tm_{0.6}S$ [for a Tm content <0.3 the optical density spectra are identical to (M. SmS)], and $Sm_{1-x}Yb_xS$. For the last one the lattice parameter of the fcc cell decreases from 5.97 to 5.68 Å with x increasing from 0 to 1. The optical spectra show the first three peaks of Sm^{2+} and another one corresponding to a transition relative to Yb^{2+}, as noted above.

8.1.4. *Samarium selenide and telluride*

Such compounds have a continuous transition from 0 to 50–60 kbar. Like SmS, Ivanchenko et al. (1971) and Lashkarev and Ivanchenko (1972) have studied SmSe and SmTe amorphous thin films.

In the crystalline state the optical absorption and the structural properties have been described by Suryanarayanan and Paparoditis (1970), Holtzberg and Torrance (1971), Bucher et al. (1971), Paparoditis and Suryanarayanan (1972) and Suryanarayanan et al. (1970, 1972). The results show the existence of two large peaks at about 0.95 and 1.8 eV for SmSe, and of 1.20 and 2.05 eV for SmTe, in the range 0.5–2.2 eV. They have been interpreted by the Sm^{2+} transitions:

$$4f^6 \rightarrow 4f^5\,5d\,t_{2g}, \quad 4f^6 \rightarrow 4f^5\,5d\,e_g.$$

Suryanarayanan et al. (1972) have shown that the results obtained by magnetic circular dichroism are in good agreement with those of Holtzberg and Torrance (1971). The lattice parameter of the fcc unit cells are 6.20 Å for SmSe and 6.60 Å for SmTe. Magneto-optical properties have been reported by Paparoditis and Suryanarayanan (1972).

On the other hand, Singh et al. (1976, 1977) have studied SmSe thin films by electron microscopy and electrical resistance. They found a new compound with a hexagonal cell, which was obtained after annealing at 470 K. This lattice, as deduced from electron diffraction patterns, seems quite curious. Indeed, the authors interpret the presence of two rings as (00 . 1) and (00 . 3) by a double diffraction effect. But the rings relative to (00 . 2) or (00 . 4) are not observed, and this destroys their hypothesis. Moreover, the more intense ring of the pattern corresponds to the (222) diffraction of C-Sm_2O_3.

Dumas and Schlenker (1974) have studied $Sm_{1-x}Nd_xSe$ ($x < 0.15$) polycrystalline thin films obtained by thermal evaporation. At 290 K the samples are of S.C. type for $x < 0.11$, and of M. type for $x > 0.11$. Their optical absorption shows the presence of three peaks. Some resistance measurements are given versus temperature and composition.

8.2. *Europium*

8.2.1. *Europium monosulfide*

The various optical and electronic properties of EuS in the bulk state have been reported by Guntherodt (1974) and Schoenes (1975) in two review articles, with 165 and 115 references, respectively.

8.2.1.1. *Thin films: technology and structural properties*

The first paper relative to a EuS thin film evaporated by electron bombardment and grown by epitaxy on (100) or (110) cleavage surfaces of single crystal substrates of different materials (NaCl, CaF_2, . . .), was that by Chen and Zeitman (1965). The films exhibit a fcc, NaCl-type, structure ($a = 5.96$ Å) with a single-crystal configuration. The use of non-oriented substrates (Cu, Si, mica) led to the formation of polycrystalline samples. However, Reichelt and Viehweg (1973) obtained single-crystal films by e-gun evaporation onto mica substrates heated to 670 K. They observe that the films are twinned at 50%, with two twin positions. Tu et al. (1971) also obtained a good epitaxial growth on the cleavage plane of mica and on the (111) plane of MgO and spinel, using e-gun evaporation. In the same way Mitani et al. (1975) observed epitaxial ordering by deposition

onto NaCl substrates. Polycrystalline films have been obtained either by e-gun evaporation, by Ahn and Shafer (1971), Tu et al. (1972), and Campana et al. (1973) or by thermal evaporation, by Palatnik et al. (1971 and 1975), and Suryanarayanan and Brun (1976). For this material no structural transition has been observed.

Other problems relative to such films are described by many authors. These include: non-stoichiometry, inhomogeneities (inclusion of oxygen), lattice defects and internal strains.

Such parameters can induce strong variations in the optical, magnetic and electric properties of the film. It seems that the substrate temperature is one of the parameters responsible for this situation, as noticed by Palatnik et al. (1971), Tu et al. (1972), Mitani et al. (1975), Schienbein et al. (1978), Harpaintner (1978), Mayr et al. (1979) and Köhne et al. (1980) Schienbein et al. (1978) have also shown that the deposition rate and the substrate temperature can be adjusted to obtain Eu or S excess and the absence or presence of oxygen. They noted EuS and Eu_2O_3 formation for substrates heated between 290 and 390 K. At 500 K the formation of a mixture of $EuS + EuS_{1.9}$ occurred, and at 99 K Eu_3S_4 appeared.

8.2.1.2. *Optical properties*

Results have been obtained by optical absorption, Faraday rotation and magnetic circular dichroism. The electronic transitions have been interpreted by Güntherodt et al. (1970) and Schoenes (1975), for instance, as:

$$Eu^{2+}: 4f^7\,(^8S_{7/2}) \rightarrow \begin{matrix} 4f^6\,(^7F_j)\,5d\,t_{2g} \\ 4f^6\,(^7F_j)\,5d\,e_g \end{matrix}.$$

Using magnetic circular and linear dichroism Ferré et al. (1972) obtained similar results by measurements above and below $T_c = 16.5$ K. They observed the presence of three components in the absorption band, two of them due to spin–orbit coupling, and the third perhaps related to a spin forbidden transition, such as 5d t_{2g} with a mixing of $S' = 5/2$ and $S = 7/2$ states.

Palatnik et al. (1971, 1975), Tu et al. (1972), Ahn and Shafer (1971), Ikesawa and Suzuki (1973), Mitani et al. (1975) and Mayr et al. (1979) have studied the dependence of the absorption spectra on the nature and the temperature of the substrate, the impurities and the lattice effects. Ahn and Shafer (1971) have shown that with increasing incorporation of iron in a EuS film, the optical absorption increases. From optical transmission and reflection spectrometry data and the first experiment on light scattering from acoustic spin waves, Mayr et al. (1979) have shown that it is possible to determine stoichiometric variations, lattice defects, oxide formation and magnetic homogeneity.

The reflectance variations have been studied by Paparoditis et al. (1975) by thermoreflection measurements.

8.2.1.3. *Transport properties*

8.2.1.3.1. Magnetic properties

Suryanarayanan and Brun (1976) have observed in the X-band paramagnetic and ferromagnetic resonances in EuS. The Curie temperature is 16.6 K, indicating a good stoichiometry for the film.

Feierabend et al. (1976) have shown the pressure effect by magnetization and Kerr effect measurements versus the temperature. With e-gun evaporation onto a cold substrate (12 K), in a vacuum of 10^{-6} Torr, the Curie temperature is 26.5 K. But in a vacuum of 10^{-5} Torr it is larger and decreases after annealing. These variations indicate that contaminations were present in the film.

Schewe and Hoffmann (1977a,b) and Schewe and Harpaintner (1978) have studied the stray field in dependence on the temperature and the transverse susceptibility; the presence of a large stray field is caused by stoichiometric defects. At low temperature, the temperature dependence of the crystalline anisotropy dominates, and at high temperature the thermal expansion anomaly is responsible for the magnitude of the stray fields. Their samples had an in-plane magnetization. Ahn and Shafer (1971) observed a large Faraday rotation in EuS stoichiometric films with an in-plane magnetization. They reported that stoichiometric and Fe-doped (16 at% Fe) samples are ferromagnetic with T_c varying from 18 up to 45 K. For their Eu-excess films T_c had increased up to 22 K. For pure EuS, the coercive force decreased from 30 Oe (5–2 K) to 0 Oe (15 K).

Changes in the magnetic properties according to the experimental procedures have been reported by several authors. Köhne et al. (1980), who used measurements of the coercive force, the wall mobility and the saturation magnetization versus temperature, have observed the bulk magnetic properties are only partially approached. They discuss the effect of oxygen inclusions on the T_c values. They believe this is due to the formation of chemical bonds such as Eu–O–Eu. They have also observed that the nature of the substrate can change the film properties by a phenomenon linked to lattice and non-stoichiometry defects. From Mössbauer effect studies Maletta and Crecelius (1975) found that the hyperfine interactions and lattice parameters change with lattice defects. Based on spin-polarized photoelectron measurements, Campana and Siegman (1973) suggest that changes in the magnetic photoelectric properties are related to the degree of ionicity of the chemical bonding.

By the same procedure Campana et al. (1973) have shown the existence of a non-saturated surface sheet at a temperature as far below the ordering temperature of the bulk as 16.75 K. Surface spin-exchange scattering due to 4f-electron excitations explains this result. Bush et al. (1969) observed spin polarization, which can be due to impurities, in semiconducting ferromagnetic EuS films. They proposed this occurs because of an exchange interaction of the impurities with the $4f^7$ levels.

On the other hand, Mitani et al. (1975) described, from their magnetic circular absorption results and their Faraday rotation spectra, a magnetic exciton model for the low energy absorption band of EuS.

8.2.1.3.2. Electric properties

A number of papers have reported on the resistivity of EuS films. Ahn and Shafer (1971) noticed a low electrical resistivity in Eu-excess films. Palatnik et al. (1979) showed that the nature of the substrate can change the resistivity, e.g. $10^9\ \Omega$ cm for epitaxial deposition on NaCl and $10^6\ \Omega$ cm for polycrystalline films on glass or mica (the epitaxial films are mechanically unstable). Feierabend et al.

(1976) obtained a value of $10^5\ \Omega$ cm at 290 K. Köhne et al. (1980) measured the resistivity of their Eu_xS_y sample versus the temperature.

Bayer and Zinn (1973), and Bayer (1975) have studied the switching phenomena in polycrystalline films of the type GdS/EuS/GdS and Gd/EuS/Gd. They have shown the characteristics of the S- or N-shaped current-controlled and voltage-controlled at different temperatures and with an external magnetic field. They have discussed the non-linearities of the current transport behavior. Ahn and Shafer (1971) have observed that the switching properties in their films are similar to those of the stoichiometric samples.

8.2.1.4. *Magnetic structures determined by Lorentz microscopy*

Some work has been carried out on EuS films by this method by Pfisterer et al. (1969) and Tischer (1971, 1973). At low temperature (8–16 K) polycrystalline films exhibit ferromagnetic domains. Many are revealed by imaging electron microscopy. The authors have observed two states of demagnetization: the first is due to a thermal effect by intense electron beam annealing and the second to ac demagnetization. Under these conditions a multidomain configuration appears. Generally the samples show a ripple structure, but the magnetic structures are influenced considerably by mechanical stresses. Tischer (1971) has also studied the behavior of the magnetic domains during demagnetization of $Eu_{1-x}Gd_xS$ films.

8.2.2. *Ternary europium monosulfides*

Campana and Siegmann (1973) have studied some $Eu_{1-x}Gd_xS$ films ($0 < x < 0.12$). As mentioned above Tischer (1971) has observed, by Lorentz microscopy, ferromagnetic domains in $Eu_xGd_{1-x}S$ thin films.

The papers of Bayer and Zinn (1971, 1973) and Hackfort and Zinn (1979) gave more results on the properties of such compounds for $0 < x < 0.35$. They described magneto-optical experiments: resistivity, T_c, hysteresis and magnetization measurements, magnetic polarization, and coercive field strength between 4.2 and 300 K. The results are discussed as a function of the Gd and S concentrations. So, when x increases T_c increases up to 150 K and the magnetization strongly decreases (Bayer and Zinn, 1973). By deposition of the compound on quartz glass or MgO substrates heated to 300–810 K, Hackfort and Zinn (1979) found an effective free carrier concentration proportional to x, and an antiferromagnetic Eu–Gd and Gd–Gd spin ordering due to the predominant superexchange between the nearest Gd and Eu neighbours rather than to the long-range RKKY exchange via free carriers. Neither set of results are in agreement with the magnetic impurity state model.

8.2.3. *Europium selenide and telluride*

The first results relative to EuSe thin films were to our knowledge those of Suits and Argyle (1965). Crystalline films obtained by evaporation have a fcc structure (NaCl-type) with $a = 6.19$ Å. Magnetization measurements have shown that the compound is ferromagnetic. The authors present the room-temperature absorption coefficient and Faraday rotation measurements. They observed two

peaks in the absorption curve, one at 4800 Å and one at 8000 Å. Their Faraday rotation strongly depends on the temperature which requires that two paramagnetic transitions of opposite sign are included in the absorption band. The authors give two explanations for the electronic transition: one as $4f^7\ (^8S_{7/2}) \rightarrow 4f^6 5d\ (^8P_5)$ and one as a virtual $4f^7 \rightarrow 4f^7 5d$ transition as a charge transfer.

By magnetic circular dichroism, Suryanarayanan and Paparoditis (1970) have shown that a low temperature EuSe is metamagnetic below T_c. The optical absorption presents two peaks which correspond to the transitions:

$$4f^7\ (^8S_{7/2}) \rightarrow 4f^6 5d\ t_{2g} \text{ and } 4f^6 5d\ e_g.$$

Ferré (1971) and Paparoditis and Suryanarayanan (1972) have confirmed these results. In the same way Busch et al. (1970) have shown through the Faraday effect that the magnetic Brillouin zone of metamagnetic EuSe is half the chemical Brillouin zone. From Faraday rotation versus temperature and optical absorption measurements they propose an exchange splitting of excited states.

EuTe thin films with a NaCl-type structure, $a = 6.58$ Å, have been studied by Briat et al. (1969), Suryanarayanan and Paparoditis (1970), Busch et al. (1970 and 1971), Ferré et al. (1971), Paparoditis and Suryanarayanan (1972) and more recently by Schoenes and Watcher (1977). The electronic transition is determined as:

$$4f^7\ (^8S_{7/2}) \rightarrow 4f^6 5d\ t_{2g} \text{ and } e_g.$$

Busch et al. (1970, 1971) concluded that EuTe presents an antiferromagnetic mode and a ferromagnetic dependence. The latter within the antiferromagnetic structure can be explained by assuming a ferromagnetic superlattice model, relative to the 5d t_{2g} band which gives rise to a magnetic Brillouin zone. The measurements have been done by Faraday rotation, optical absorption and magnetic circular dichroism.

8.3. *Other rare earths (Tb, Er, Tm)*

8.3.1. *Terbium telluride*

To our knowledge this compound has been the subject of only one paper, Chander et al. (1978). The crystalline structure is given as primitive cubic with $a = 3.145$ Å. This result seems unusual in comparison with other rare earth chalcogenides which always exhibit a fcc NaCl-type, structure. (By multiplying the parameter by 2, it becomes 6.29 Å, which is comparable to that of SmTe and TmTe.)

8.3.2. *Erbium telluride*

Vasilkovskii et al. (1977) studied Er_2Te_3 thin films deposited by thermal evaporation onto a heated substrate (up to 370 K). From resistance and Hall emf measurements they obtained a negative temperature coefficient of resistance. They concluded that Er_2Te_3 is a semiconductor with hole conductivity.

8.3.3. *Thulium selenide and telluride*

Suryanarayanan et al. (1975, 1977, 1978) have reported some structural and optical results for these films. For TmSe they showed the existence of a fcc lattice with $a = 5.68$–5.695 Å. By optical absorption they observed a maximum and a minimum indicating a mixed valence state. For TmTe they found either a unique phase (fcc, $a = 6.32$ Å) or two coexisting structures (fcc, $a = 6.29$ Å and $a = 6.10$ Å). Optical absorption at 5.2 and 300 K shows that (S.C. TmTe) has the following transitions:

$$4f^{13} \rightarrow \begin{matrix} 4f^{12}(^3H_6)\,5d\,t_{2g} \\ 4f^{12}(^3H_6)\,5d\,e_g \end{matrix}.$$

(The sample with two phases has a quite different optical absorption.) The authors concluded that Tm is purely divalent, as confirmed by the study of $TmTe_{1-x}S_x$ which has a nonvarying optical density up to $x \approx 0.3$. The lattice cell parameter of this ternary compound varies from 5.88 Å up to 6.15 Å ($x \approx 0.3$).

8.4. *Ytterbium*

The only result concerning YbS has been reported by Lashkarev et al. (1972). The polycrystalline films deposited by thermal evaporation onto heated substrates (470–570 K) present a fcc phase with $a_1 = 5.56$ Å (in the bulk state $a_1' = 5.67$ Å). In the same way these authors have also studied YbSe and YbTe thin films with fcc structures ($a_2 = 5.86$ Å and $a_3 = 6.08$ Å, respectively) (in the bulk state: $a_2' = 5.93$ Å and $a_3' = 6.36$ Å). From their diffuse reflection results they give a scheme for the energy bands, and conclude that ytterbium monochalcogenides differ from europium and samarium by the presence of hole-type conduction.

Suryanarayanan et al. (1970) have shown that YbSe thin films have two fcc phases: one stoichiometric as YbSe with $a = 5.93$ Å and the other rich in Se as $YbSe_{1.5}$ with $a = 5.65$ Å. By optical absorption and magnetic circular dichroism measurements they conclude that YbSe is diamagnetic (as YbTe) and $YbSe_{1.5}$ is paramagnetic with a trivalent state for Yb. The optical absorption shows that the transition in YbSe and YbTe can be attributed to:

$$4f^{14}(^1S_0) \rightarrow \begin{matrix} 4f^{13}(^2F_{7/2})\,5d\,e_g \\ 4f^{13}(^2F_{5/2})\,5d\,e_g \end{matrix}.$$

In another paper Paparoditis et Suryanarayanan (1972) have reported the magneto-optical properties of thin films codeposited on heated substrates (670–770 K). They have shown that the properties depend especially on the Se concentration. Suryanarayanan et al. (1974) have studied YbTe films in more detail by optical absorption and magnetic circular dichroism. They proposed an energy level diagram, and concluded that the f-levels of ytterbium are located between the valence and conduction bands. These optical properties can be linked to a S.C.–M.-type transition, like the one observed at high pressures (150–190 kbar).

Wong and Wood (1971) have shown that YbTe and YbSe single crystal films (0.5 μm) are semiconducting and that the optical absorption is similar to the one in EuS. These compounds are unstable in moist air.

Singh and Srivastava (1977) have observed, as for SmSe, the formation of a curious YbSe compound with a hexagonal cell, with lattice parameters larger than the ones for SmSe.

Vasilkovskii et al. (1977) have studied the magneto-electrical properties of Yb_2Te_3 films, as for Er_2Te_3 (see above, section 8.3.2).

9. Rare earth–pnictide systems

Campana and Siegman (1973) have given some results for GdP, GdAs and GdSb metastable films evaporated by e-gun onto substrates at 4.2 K. Between 20 and 160 K the samples crystallize. The authors conclude, as for EuS, EuSe and EuTe films, that the changes in the magnetophotoelectric properties are related to the degree of ionicity of the chemical bonding.

Wachter and Wallschleger (1972) have studied Eu_3P_2 and Eu_3As_2 films as magnetic semiconductors prepared by e-gun. They present some magneto-optical properties and conclude that Eu pnictides are more covalent than Eu chalcogenides (the 5d state is not identical in these compounds). Campana et al. (1973) have shown, as for EuS, that thin polycrystalline Eu_3P_2 films have a non-saturated surface sheet at a temperature far below the ordering temperature of the bulk which is in the range of 2.82 K.

Yim et al. (1972) have studied ScP and ScAs single-crystal epitaxial layers. Each compound has a fcc lattice (a = 5.31 Å and a = 5.46 Å, respectively). They are n-type conductors, totally miscible in all proportions, and form a continuous series of solid-solution alloys. The optical absorption shows a minimum. The band gaps are 1.1 eV for ScP and 0.76 eV for ScAs.

10. Some oxidized compounds

10.1. *The RMO_3 compounds (R = La, Nd, Y; M = Cr, Al, Sc)*

Some systems, such as $LaCrO_3$, $NdAlO_3$, $YAlO_3$ and $YScO_3$, have been studied. Terao (1973a,b) have studied $LaCrO_3$ thin films prepared by vacuum evaporation of chromium and lanthanum. By electron diffraction and by annealing up to 1770 K he has observed at 610 K the formation of a rhombohedral structure corresponding to $LaCrO_3$, but the lattice parameters can vary from one sample to the other indicating some difference in the stoichiometry. At 1170 K and between 1570 and 1770 K two new modifications appear, which have been indexed on monoclinic cells.

Zaytsev et al. (1975) have studied the evolution by annealing in air up to 1670 K of two-layer and three-layer thin films of CrY and CrYCr produced by

successive vaporizations. They conclude from their electron diffraction patterns that $YCrO_3$, Cr_2O_3 and Y_2O_3 are formed. They have the following crystallographic structures: $YCrO_3$ monoclinic, and Y_2O_3 bcc or hexagonal (A-type) (the initial as-deposited film being a mixture of $Y_2O_3 + Cr + Y$). The Cr_2O_3 compound decomposes at about 1200 K.

Chernobrovkin et al. (1976, 1979) studied the systems $YScO_3$, $NdAlO_3$ and $CrNdAlO_3$ as cermets deposited by e-gun and rf sputtering. They first studied the dielectric properties, and then, by electron diffraction, the cermet films. These as-deposited films are amorphous when prepared by thermal evaporation and form Cr crystallites in the amorphous $NdAlO_3$ matrix by rf sputtering. By annealing at 970 K Cr_2O_3 is formed, the $NdAlO_3$ always being amorphous. The authors discuss the structures so obtained on the basis of the vacuum deposition parameters. Osupov et al. (1976) have also given some dielectric characteristics, versus the thickness and the effect of oxygen, for $NdAlO_3$ thin films. They have shown that the dielectric strengths are fairly high and the dielectric loss tangent is small.

Korotkov et al. (1978) have observed, by heating Y_2O_3–Al_2O_3 films to 1170–1220 K, the formation of $YAlO_3$, which coexists with the compounds Y_2O_3 and $Y_4Al_2O_9$.

10.2. *The R_2O_3–MO_x compounds (R = Y, Nd, Dy; M = Al, Y, Ti)*

As mentioned above, Korotkov et al. (1978) studied the evolution of Y_2O_3–Al_2O_3 thin films and their dependence on the annealing conditions. They observed successively the formation of the following compounds:

$Y_2O_3 + \gamma\text{-}Al_2O_3$ (770–1070 K),

$Y_2O_3 + YAlO_3 + Y_4Al_2O_9$ (1170–1220 K),

$Y_4Al_2O_9$ (dominant) + some Y_2O_3(1270 K),

$Y_3Al_5O_{12}$ (garnet) + Y_2O_3 (1320–1370 K),

this mixture being stable up to 1670 K.

Caro et al. (1974) and Loier et al. (1974) have studied thin films of the Nd_2O_3–Y_2O_3 binary system with 7–10 mole% Y_2O_3 by electron microscopy. The samples were prepared by the thermal co-evaporation technique. They have shown by electron microscopy the influence of the yttrium concentration on the formation of A-, B- and C-type Nd_2O_3, and the epitaxy between them. They have shown that the A-Nd_2O_3 phase is pure, but B-R_2O_3 consists of twinned crystals containing R_2O_3 with a small concentration of yttrium, and C-R_2O_3 has a large amount of yttrium in some areas. However, one should notice a discrepancy in the interpretation of the electron diffraction patterns: the one reported by Caro et al. (1974) as a B-Nd_2O_3 lattice is correct, whereas the one indexed by Loier et al. (1974) cannot be related to the A-Nd_2O_3 phase, because the pattern does not have a hexagonal symmetry.

In another way Yamanaka et al. (1977) have studied thin films in the

system Dy_2O_3–TiO_2 which were deposited by co-sputtering of Dy and Ti. They obtain oxidized compounds which are defined as $Dy_xTi_{1-x}O_2$. For $x > 0.1$ the samples are amorphous. They give as a function of x the absorption threshold energy and the refractive index, which is high in a film such as $Dy_{0.1}Ti_{0.9}O_2$.

Finally, Sichel and Miller (1976) did not observe the formation of erbium–aluminum oxidized compounds by co-sputtering of a deposit of Er and Al_2O_3 (see section 5.4).

10.3. *The R_2O_2S compounds (R = La, Sm, Eu, Gd, Y)*

Maple and Buchanan (1973) and Buchanan (1974) have studied thin films of La_2O_2S, Y_2O_2S and Gd_2O_2S with small additions of Eu, Tb or Tm, which produce, respectively, red, green and blue emission. Their samples were deposited by rf sputtering in an Ar–H_2S gaseous mixture. The as-deposited film composition varies with the H_2S pressure, e.g. in the case of the La–S system the following phases were identified:

$$La_2S_3\text{–}LaS\text{–}La_2O_2S_2\text{–}La_2O_2S\text{–}La_2O_{2+y}S_{1-x}\text{–}La_2O_3.$$

In order to have a performing phosphor they annealed their samples at 1270 K in a mixture of $SO_2 + H_2$. They studied the luminescence versus thickness and beam power density, and obtained a brightness of 40 000 fL. On the other hand they prepared a multilayer sample of La_2O_2S–Tb, La_2O_2S–Eu and La_2O_2S–Tm as a sequence film, and observed multicolor emission.

Sella et al. (1979) have prepared Y_2O_2S, La_2O_2S and Gd_2O_2S thin films evaporated by rf sputtering. They minimized the oxidation effects and reduced the sulfur deficiency in such a way as to obtain pure oxysulfides. Their as-deposited layers are quasi-amorphous, and crystallize after annealing at 870 K for La_2O_2S, and 1120 K for Gd_2O_2S and Y_2O_2S. Calcination in H_2S at elevated temperature (920 and 1170 K, respectively) leads to the formation of R_2S_3 and RS. By heating in an inert atmosphere (1120 K in a mixture of $Ar + H_2$) the oxides and oxysulfides are formed. Such samples can be used in cathodo-luminescent and electro-luminescent devices (Eu was chosen as activator).

Gasgnier and Sénateur (1980), by annealing quasi-amorphous SmS thin films at low temperature with the electron beam of an electron microscope, obtained the pure Sm_2O_2S compound. Upon heating to higher temperature formation of C- and B-Sm_2O_3 occurs, and of unknown structures which are probably oxysulfurides with large lattice parameters (see section 10.4).

Palatnick et al. (1975) have annealed EuS thin films above 570 K. They observed the appearance of a new compound with a bcc lattice (Mn_2O_3-type) with $a = 12.28$ Å. They suggest that this compound is Eu_2O_2S. This interpretation is very surprising, because this structure has never been reported in the literature for Eu_2O_2S, and the reported space group and structure are those of the C-R_2O_3 phase. By further annealing these authors note the following sequence:

$$EuS \rightarrow Eu_2O_2S\ (bcc) \rightarrow Eu_2O_2S \rightarrow Eu_3O_4 + Eu_2O_3.$$

Their conductivity measurements show that the oxidized films have a semiconductor character. At 670 K the absorption spectra show a distinct change of the initial peak relative to EuS (2 eV) which indicates a transition $Eu^{2+} \rightarrow Eu^{3+}$. During the oxidation stages other peaks appear, but the patterns are complex and difficult to interpret because of the coexistence of several compounds. The final product has been determined as B-Eu_2O_3.

10.4. *The gadolinium–gallium system*

Gasgnier (1981) has studied by electron microscopy some samples of GdGa obtained by evaporation of a mixture of these elements. Upon heating with the electron beam small black drops appear and quickly evaporate. Since no compounds are observed, these drops are due to Ga condensation (just as for bismuth, see section 4.3). The only compounds which have been identified are C- and B-Gd_2O_3. At high temperature some unknown crystallographic phases are observed, which have the same characteristics as the ones observed for Sm–S systems. The reported electron diffraction pattern (fig. 24) shows the presence of a diffraction pattern which is not compatible with the B-R_2O_3 structure (Gasgnier and Sénateur, 1980). This method does not appear to be a technique which can be used to obtain garnet films.

10.5. *The lanthanum–samarium system*

Thin film La–Sm samples are prepared from two distinct evaporation sources such as tungsten crucibles. This procedure yields two different sorts of sandwich films: Sm–La and Sm–La–Sm (Gasgnier, 1981). These samples are deposited at room temperature. Upon heating with the electron beam of the electron microscope the thinner lanthanum films of the two sequences show the formation of C- and B-Sm_2O_3 and A-La_2O_3. The thicker lanthanum films of the Sm–La–Sm

Fig. 24. Electron diffraction pattern of a large crystal obtained after annealing of a GdGa film. The two spots in the vicinity of the central spot do not correspond to the B-Gd_2O_3 structure.

sequence exhibit, without annealing, the coexistence of the C-Sm_2O_3 and LaH_2 structures. By further annealing new crystals appear, but the electron diffraction patterns do not correspond to known structures. This is a new case showing the complexity of the recrystallization phenomenon in thin films.

11. Conclusion

Almost all of the materials which have been discussed in this chapter share one main characteristic: their intrinsic properties are closely connected to the numerous parameters of the experimental conditions of the preparation. Compared with pure element thin films, this sensitivity is enhanced by the fact that the samples possess at least two components. We have noticed that for some systems the large variation of the results has not always permitted one to reach a final conclusion. So, some of the physical, chemical and crystallographical properties and other phenomena are difficult to explain. Some of them are characteristic:

- origin and true mechanism for K_u;
- strange magnetic, electrical and optical properties of some systems;
- contamination effect of gases and impurities, and therefore the influence of the chemical bonding;
- obtaining amorphous films prepared by thermal evaporation and deposited onto a substrate at room temperature;
- amorphous–crystalline transition behavior;
- formation of crystalline phases during annealing, which have not been observed in the bulk state.

This list, which is not exhaustive, shows that thin film characterization is an acute problem. This naturally leads to the problem of the reproducibility of the samples, and also has a great bearing on the industrial applications. Thus, the great enthusiasm with which R–TM thin films were greeted has diminished; now a new class of similar materials, superconducting films, seem to have a great future interest. We can then ask the following question: will this new field of research be fruitful? On our part, we think that one should not be pessimistic because thin film characterization now seems to be on the way of progress. Indeed, chemical analysis and observation and measurements of microstructural properties and basic physical properties become more and more accurate. This is due to the appearance of more powerful and sensitive apparatuses such as STEM, and high resolution microscopes, EELS, XPS, SIMS, AES, XRF, SQID, ρ and ρ_H measurements, etc. In parallel, the experimental procedures should become more and more refined: rotating substrates in order to increase film homogeneity, ultra-high vacuum systems to decrease the contamination, great caution about the cleanness of the experiments, fabrication of the purest possible bulk materials, etc. When the greater part of the parameters and the experimental procedures are linked to the film preparation and are controlled in a systematic manner, a great step will be made towards achieving "ideal" thin film materials.

But the evidence of all these experiments will lead to a high cost of the manufactured product and such a situation can limit the possible industrialization and commercialization. However, one sees that more and more research centers and universities have established or are in the process of establishing microstructural analysis laboratories. Their main goal is to bring together some of the various analytical techniques which are now either commercialized or developed by some specific laboratories. We can speculate that the future of thin films lies in these new laboratories. But to reach the best possible understanding of the results a great effort of collaboration between research workers will be necessary. Unfortunately, until now this effort has been scanty. We think in particular of the poor knowledge and even sometimes the ignorance of some physicists of the chemical properties and the chemical reactivities of materials, and conversely of the poor understanding and also the ignorance of some chemists of the physical laws. Such a situation is not always consistent with the research of fundamental properties in such a critical area like thin films where so many difficulties converge and where physics, chemistry, surface science and analytical chemistry merge.

References

Ahn, K.Y. and M.W. Shafer, 1971, IEEE Trans. Mag. MAG **7**, 394.

Albert, P.A. and C.R. Gurnieri, 1977, J. Vac. Sci. Technol. **14**, 138.

Ali, A., P.J. Grundy and G.A. Stephens, 1976, J. Phys. D, Appl. Phys. **9**, L69.

Allen, R.P. and R.D. Nelson, 1974, US Patent 3 856 579.

Allen, R.P., S.D. Dahlgren, H.W. Arrowsmith and J.P. Heinrich, 1974, Techn. Rept. AFML-TR74-87 (AD 785538).

Amatsu, M., S. Honda and T. Kusuda, 1977, IEEE Trans. Mag. MAG **13**, 1612.

Argyle, B.E., R.J. Gambino and K.Y. Ahn, 1975, AIP Conf. Proc. **24**, 564.

Asomoza, R., 1980, Thesis Orsay (France).

Asomoza, R., I.A. Campbell, H. Jouve and R. Meyer, 1977, J. Appl. Phys. **48**, 3829.

Asomoza, R., I.A. Campbell, A. Fert, A. Liénard and J.P. Rebouillat, 1979a, J. Phys. F, Metal Phys. **9**, 349.

Asomoza, R., I.A. Campbell and A. Fert, 1979b, J. Physique **40**, Suppl. C-5, 225.

Asomoza, R., J.B. Bieri, A. Fert, B. Boucher and J.C. Ousset, 1980, J. Physique **41**, Suppl. C-8, 467.

Bajorek, C.H. and R.J. Kobliska, 1976, IBM J. Res. Dev. **20**, 271.

Barberis, G.E., J.F. Suassuna, C. Rettori and C.A. Pelá, 1977, Solid. State Commun. **23**, 603.

Bates, P.A., J. Popplewell and S.W. Charles, 1970a, J. Phys. D, Appl. Phys. **3**, L15.

Bates, P.A., J. Popplewell and S.W. Charles, 1970b, Fizika **2**, Suppl. 2, 11.1.

Batlogg, B., J. Schoenes and P. Wachter, 1974, Phys. Letters **49A**, 13.

Bayer, E., 1975, Physica **80B**, 57.

Bayer, E. and W. Zinn, 1971, Z. Angew. Phys. **32**, 83.

Bayer, E. and W. Zinn, 1973, IEEE Trans. Mag. MAG **9**, 4.

Belousov, A.N., V.I. Krylepov and N.A. Manakov, Russian Patent 1902-76.

Bendson, S.A. and J.H. Judy, 1973, IEEE Trans. Mag. MAG **9**, 627.

Berger, L., 1976, AIP Conf. Proc. **29**, 165.

Bhagat, S.M., J.N. Lloyd and N. Heiman, 1978, J. Appl. Phys. **49**, 1683.

Biesterbos, J.W.M., 1979, J. Physique **40**, Suppl. C-5, 274.

Biesterbos, J.W.M., M. Brouha and A.G. Dirks, 1976, AIP Conf. Proc. **29**, 184.

Biesterbos, J.W.M., M. Brouha and A.G. Dirks, 1977, Physica **86-88B**, 770.

Biesterbos, J.W.M., A.G. Dirks, A.J.P. Farla and P.J. Grundy, 1979, Thin Solid Films **58**, 259.

Blades, J.D., 1968, Rept. F-B, 2361 (AD 681290).

Bochkarev, V.F., V.A. Buravikhin, V.T. Sukhomlin and V.A. Egorov, 1973, Sov. Phys. J. **16**, 1753.

Bochkarev, V.F., O.P. Budanov and G.I. Popova, 1974, Sb. Fiz. Magnit. Plenok **6**, 123.

Bochkarev, V.F., A.E. Gafner, E.C. Chizhik and T.I. Kodintseva, 1976a, Sb. Fiz. Magnit. Plenok **9**, 79.

Bochkarev, V.F., E.C. Chizhik and A.E. Gafner, 1976b, Sb. Fiz. Magnit. Plenok **9**, 56.

Bostanjoglo, O. and K. Röhkel, 1971, Phys. Stat. Sol. a **7**, 387.

Boucher, B., 1976, J. Physique Lettres **37**, L345.
Boucher, B., 1977a, Phys. Stat. Sol. a **40**, 197.
Boucher, B., 1977b, IEEE Trans. Mag. MAG **13**, 1601.
Boucher, B., 1977c, Phys. Stat. Sol. a **42**, K165.
Boucher, B., 1980, J. Physique **41**, Suppl. C-8, 135.
Boucher, B. and B. Barbara, 1979, J. Phys. F, Metal Phys. **9**, 151.
Briat, E., M. Billardon, R. Suryanarayanan and C. Paparoditis, 1969, Phys. Stat. Sol. **35**, 983.
Brunsch, A. and J. Schneider, 1977a, J. Appl. Phys. **48**, 2641.
Brunsch, A. and J. Schneider, 1977b, IEEE Trans. Mag. MAG **13**, 1606.
Brunsch, A. and J. Schneider, 1978, IEEE Trans. Mag. MAG **14**, 731.
Buchanan, R.A., 1974, US Patent 3 825 436.
Bucher, E., V. Narayanaminti and A.A. Jayaraman, 1971, J. Appl. Phys. **42**, 1741.
Buravikhin, V.A. and A.A. Nedelko, 1965, Bull. Acad. Sci. USSR, Phys. Ser. **29**, 697.
Buravikhin, V.A., A.A. Nedelko and V.N. Shelkovnikov, 1967, Sov. Phys. J. **10**, 87.
Buravikhin, V.A., V.F. Bochkarev, V.A. Egorov and V.N. Shelkovnikov, 1971, Sov. Phys. J. **11**, 1530.
Buravikhin, V.A., V.N. Shelkovnikov, G.A. Kameneva, V.A. Egorov and N.A. Manakov, 1973, Sov. Phys. J. **16**, 127.
Buravikhin, V.A., L.V. Ushapovskii and A.A. Kashaev, 1974, Sb. Fiz. Magnit. Plenok **6**, 138.
Buravikhin, V.A., V.N. Shelkovnikov, N.A. Manakov and G.A. Kamenova, 1975a, Acta Phys. Slov. **25**, 241.
Buravikhin, V.A., V.A. Egorov, L.M. Sidorenko, V.B. Apkanov and N.A. Manakov, 1975b, Sb. Fiz. Magnit Plenok **8**, 3.
Buravikhin, V.A., V.F. Bochkarev, O.P. Budanov and V.L. Karabanova, 1976, Sb. Fiz. Magnit. Plenok **9**, 47.
Buravikhin, V.A., V.A. Egorov, L.M. Sidorenko and V.B. Apkhanov, 1979, Russian Metall. **3**, 162.
Burilla, C.T., W.R. Bekebrede and A.B. Smith, 1976, AIP Conf. Proc. **34**, 340.
Burilla, C.T., W.R. Bekebrede, M. Kestigian and A.B. Smith, 1978, J. Appl. Phys. **49**, 1750.
Busch, G., M. Campana and H.C. Siegmann, 1969, Solid State Commun. **117**, 775.
Busch, G., J. Schoenes and P. Wachter, 1970, Solid State Commun. **8**, 1841.
Busch, G., J. Schoenes and P. Wachter, 1971, Czech. J. Phys. **B21**, 570.
Buschow, K.H.J., 1976, Solid State Commun. **19**, 421.
Buschow, K.H.J., 1977a, J. Less Common Met. **51**, 173.
Buschow, K.H.J., 1977b, Physica **86–88B**, 79.
Buschow, K.H.J. and A.G. Dirks, 1980, J. Phys. D, Appl. Phys. **13**, 251.
Buschow, K.H.J. and A.M. Van Diepen, 1976, Solid State Commun. **19**, 79.
Bzhalava, T.L., T.B. Zukova, I.A. Smirnov, S.G. Schul'man and N.A. Yakovleva, 1974, Sov. Phys. Solid State **16**, 2428.
Bzhalava, T.L., S.G. Schul'man, T.T. Dedegkayev, T.B. Zhukova and I.A. Smirnov, 1975, Phys. Letters **55A**, 161.
Campana, M. and H.C. Siegmann, 1973, Phys. Kodens. Mater. **15**, 274.
Campana, M., K. Sattler and H.C. Siegmann, 1974, AIP Proc. Conf. **18**, 1388.
Campana, M. and G. Crecelius, 1975, Appl. Phys. **8**, 241.
Cargill III, G.S., 1974, AIP Conf. Proc. **18**, 634.
Cargill III, G.S., 1975a, Solid State Physics, Vol. 30, eds. H. Ehrenreich, F. Seitz and D. Turnbull (Academic Press, New York) p. 227.
Cargill III, G.S., 1975b, AIP Conf. Proc. **24**, 138.
Cargill III, G.S., 1978a, Rapidly Quenched Metals III, Vol. 2B, ed. B. Cantor (The Metals Society, London) p. 364.
Cargill III, G.S., 1978b, Thin Film Phenomena—Interfaces and Interactions, eds. J.E. Baglin and J.M. Poate (The Electrochemical Society, Princeton) p. 221.
Cargill III, G.S. and T. Mizoguchi, 1978, J. Appl. Phys. **49**, 1753.
Caro, P.E., G. Schiffmacher, C. Boulesteix, C. Loier and R. Portier, 1974, Defects and Transport in Oxides, eds. M.S. Seltzer and R.I. Jafee (Plenum Press New York) p. 519.
Chander, R., R. Kumar and B.B. Sharma, 1973, Phys. Stat. Sol. a **17**, K157.
Chappert, J., 1979, J. Physique **40**, Suppl. C-2, 107.
Chappert, J., M. Bogé, B. Boucher and B. Barbara, 1980, J. Physique **41**, Suppl. C-8, 634.
Charles, S.W., J. Popplewell and P.A. Bates, 1971, Rare Earths and Actinides, Conference Digest of Durham (Institute of Physics, London–Bristol) p. 113.
Charles, S.W., J. Popplewell and P.A. Bates, 1973, J. Phys. F, Metal Phys. **3**, 664.
Chaudari, P. and D.C. Cronemeyer, 1976, AIP Conf. Proc. **29**, 113.
Chaudari, P. and S. R. Herd, 1976, IBM J. Res. Dev. **20**, 102.
Chaudari, P., J.J. Cuomo and R.J. Gambino, 1973a, Appl. Phys. Lett. **22**, 337.
Chaudari, P., J.J. Cuomo and R.J. Gambino, 1973b, IBM J. Res. Dev. **17**, 66.
Chaudari, P., J.J. Cuomo, R.J. Gambino, S. Kirkpatrick and L.J. Tao, 1975, AIP Conf. Proc. **24**, 562.
Chaudari, P., J.J. Cuomo, R.J. Gambino and E.A. Giess, 1977, Physics of Thin Films, No. 9, eds. G. Hass, M.H. Francombe and R.W. Hoffmann (Acad. Press, New York) p. 263.
Chen, C.N. and S. Zeitman, 1965, J. Appl. Phys. **36**, 669.
Chen, C.T., W.L. Wilson Jr. and G.E. Roberts, 1978, J. Appl. Phys. **49**, 1756.
Chen, T., D. Gheng and G.B. Gharlan, 1980, IEEE Trans. Mag. MAG **16**, 1194.
Chenevas Paule, A., P. Haen, F. Lapierre, R. Tournier and L. Vieux-Rochas, 1977,

Valence Instability and Related Narrow Band Phenomena, ed. R.D. Parks (Plenum Press, New York) p. 513.
Chernobrovkin, D.I., I.A. Korzh and M.N. Piganov, 1976, Inst. Exp. Techn. **19**, 1137.
Chernobrovkin, D.I., V.V. Volkoza, M.N. Piganov and E.V. Kostryukov, 1979, Inorg. Mater. **15**, 133.
Christner, G.L., B. Bradford, L.E. Toth, R. Cantor, E.D. Dahlberg, A.M. Goldman and C.Y. Huang, 1979, J. Appl. Phys. **50**, 5820.
Chung, S.W., D. Hafner and H. Hoffmann, 1979, IEEE Trans. Mag. MAG **15**, 1343.
Coey, J.M.D., 1978, J. Appl. Phys. **49**, 1646.
Coey, J.M.D. and J. Chappert, 1976, Phys. Rev. Letters **36**, 1061.
Coey, J.M.D. and S. Von Molnar, 1978, J. Physique Letters **39**, L327.
Coey, J.M.D., S. Von Molnar and R.J. Gambino, 1977, Solid State Commun. **24**, 167.
Colliex, C., 1980, private communication.
Covault, M.L., S.R. Doctor and C.S. Comstock, 1976, AIP Conf. Proc. **34**, 337.
Craven, R.A., G.A. Thomas and R.D. Parks, 1971, Phys. Rev. **B4**, 2185.
Cronemeyer, D.C., 1974, AIP Conf. Proc. **18**, 85.
Cuomo, J.J. and R.J. Gambino, 1975, J. Vac. Sci. Technol. **12**, 79.
Cuomo, J.J. and R.J. Gambino, 1977, J. Vac. Sci. Technol. **14**, 152.
Cuomo, J.J., P. Chaudari and R.J. Gambino, 1974, J. Electron. Mater. **3**, 517.
Damba, L., 1974, Sb. Fiz. Magnit. Plenok **6**, 115.
Delfs, R.J., B.J. Beaudry and D.K. Finnemore, 1975, Phys. Rev. **B11**, 4212.
De Luca, J.C., R.J. Gambino and A.P. Malozemoff, 1978, IEEE Trans. Mag. MAG **14**, 500.
Demchenko, A.I., I.M. Romanov, S.V. Sukhvalo and L.T. Romanova, 1978, Sov. Tech. Phys. Letters **4**, 139.
Dick, G.J. and F. Reif, 1969, Phys. Rev. **181**, 774.
Dirks, A.G. and J.R.M. Gijsbers, 1979a, Thin Solid Films **58**, 333.
Dirks, A.G. and J.R.M. Gijsbers, 1979b, J. Phys. D, Appl. Phys. **12**, 149.
Dirks, A.G. and H.J. Leamy, 1978a, J. Appl. Phys. **49**,1735.
Dirks, A.G. and H.J. Leamy, 1978b, IEEE Trans. Mag. MAG **14**, 835.
Dirks, A.G., J.W.M. Biesterbos and K.H.J. Buschow, 1977, Physica **86–88B**, 761.
Dodds, S.A. and J. Sanny, 1978, Phys. Rev. **B18**, 39.
Domyshev, V.A., V.A. Yegorov, V.A. Buravikhin, L.M. Sidorenko and N.I. Luzgin, 1974, Phys. Met. Metall. **38**(1), 102.
Donoho, P.L., L.V. Benninfield, P.K. Wunsch, M.B. Mac Lane and H.A. Blackstead, 1973, AIP Conf. Proc. **10**, 769.
Dumas, J. and C. Schlenker, 1974, Phys. Stat. Sol. a **22**, 89.
Egorov, V.A., V.A. Buravikhin, A.A. Nedelko, A.I. Injutkin and L.I. Kleshinchii, 1974, Fiz. Tverd. Tela p. 5 (in Russian).
Eschenfelder, A.H., 1980a, Ferromagnetic Materials, Vol. 2, ed. E.P. Wohlfarth (North-Holland, Amsterdam) Ch. 6, p. 345.
Eschenfelder, A.H., 1980b, Springer Series in Solid State Sciences 14 (Springer Verlag, Berlin, New York) ch. 6-4.
Esho, S., 1976, Suppl. Jpn J. Appl. Phys. **15**, 93.
Esho, S., 1979, J. Appl. Phys. **50**, 1006.
Esho, S. and S. Fujiwara, 1976, AIP Conf. Proc. **34**, 331.
Feierabend, S., U. Kuchko and R. Niedermayer, 1976, Phys. Stat. Sol. a **34**, K135.
Ferré, J., M. Billardon, J. Badoz, R. Suryanarayanan and C. Paparoditis, 1971, J. Physique **32**, Suppl. C-1, 930.
Ferré, J., B. Briat, C. Paparoditis, S. Pokrzywnicki and R. Suryanarayanan, 1972, Solid State Commun. **11**, 1173.
Fert, A. and R. Asomoza, 1979, J. Appl. Phys. **50**, 1886.
Fert, A., R. Asomoza, I.A. Campbell and H. Jouve, 1977, C.R. Acad. Sci. (Paris) **B285**, 113.
Fitzgerald, A.G. and T.G. May, 1974, J. Mater. Sci. **9**, 456.
Forester, D.W., C. Vittoria, J. Schelleng and P. Lubitz, 1978, J. Appl. Phys. **49**, 1966.
Frait, Z., I. Nagy and T. Tarnoczi, 1976, Phys. Letters **55A**, 429.
Freiser, M.J., 1979, IBM J. Res. Dev. **13**, 330.
Freiderich, A., B. Boucher and A. Fert, 1979, Solid State Commun. **30**, 443.
Frish, M.A. and W. Reuter, 1979, J. Vac. Sci. Technol. **16**, 1020.
Funakoshi, N., 1975, Jpn J. Appl. Phys. **14**, 565.
Gambino, R.J. and J.J. Cuomo, 1978, J. Vac. Sci. Technol. **15**, 296.
Gambino, R.J., J.F. Ziegler and J.J. Cuomo, 1974a, Appl. Phys. Lett. **24**, 99.
Gambino, R.J., P. Chaudari and J.J. Cuomo, 1974b, AIP Conf. Proc. **18**, 578.
Gandra, F.G., C.A. Pelá, G.E. Barberis, D. Davidov and C. Rettori, 1980a, Phys. Rev. **B22**, 4161.
Gandra, F.G., C.A. Pelá, G.E. Barberis, D. Davidov and C. Rettori, 1980b, J. Magn. Magn. Mater. **15–18**, 1112.
Gangulee, A. and R.J. Kobliska, 1978a, J. Appl. Phys. **49**, 4169.
Gangulee, A. and R.J. Kobliska, 1978b, J. Appl. Phys. **49**, 4896.
Gangulee, A. and R.C. Taylor, 1978, J. Appl. Phys. **49**, 1762.
Gasgnier, M., 1980, Phys. Stat. Sol. a **57**, 11.
Gasgnier, M., 1981, 15th Rare Earth Research Conf., Rolla, USA, and J. Less-Common Metals, submitted.
Gasgnier, M., 1982, J. Less-Common Metals, **83**, L17.
Gasgnier, M. and P. Caro, 1977, French Patent 77-08517.
Gasgnier, M. and C. Colliex, 1978, 21e Coll. Métallurgie "Alliages et Matériaux Amorphes" (INSTN Saclay, France) p. 491.
Gasgnier, M. and J.P. Senateur, 1980, J. Physique **41**, 1127.
Gasgnier, M., G. Schiffmacher and P. Caro, 1976, J. Less Common Met. **50**, 177.

Gasgnier, M., G. Schiffmacher and P. Caro, 1978, Intern. Phys. Conf. Ser. no. 41, eds P.J. Dobson, J.B. Pendry and C.J. Humphreys (Institute of Physics, Bristol–London) Ch. 3, p. 182.
Gasgnier, M., R. Asomoza, C. Colliex, C. Mory and P. Trebbia, 1979, J. Physique **40**, Suppl. C-5, 253.
Ghosh, A.K. and D.H. Douglas, 1977, Solid State Commun. **23**, 223.
Gill, H.S. and J.H. Judy, 1979, J. Appl. Phys. **50**, 1648.
Gill, H.S., M. Chen and J.H. Judy, 1978, J. Appl. Phys. **49**, 1741.
Glurdzhidze, L.N., A.V. Gigineishvili, T.L. Bzhalava, Z.V. Dzhabua, T.A. Pagava, V.V. Snadze and V.S. Oskotskii, 1978, Sov. Phys. Solid State **20**, 1573.
Goncharova, E.V., V.S. Oskotskii, T.L. Bzhalava, M.V. Romanova and I.A. Smirnov, 1976, Sov. Phys. Solid State **18**, 1201.
Grachev, A.I., A.A. Kukharskii, V.V. Kaminskii, S.V. Pogarev, I.A. Smirnov and S.G. Shul'man 1976, Sov. Tech. Phys. Letters **7**, 246.
Graczyk, J.F., 1976, AIP Conf. Proc. **34**, 343.
Graczyk, J.F., 1978, J. Appl. Phys. **49**, 1738.
Gron, T. and T. Stobiecki, 1979, 9th Intern. Coll. Magnetic Films and Surfaces (Univ. Lodz) p. 104.
Grundy, P.J., 1977, Contemp. Phys. **18**, 47.
Grundy, P.J., 1980, J. Magn. Magn. Mater. **21**, 1.
Grundy, P.J., A. Ali and S.S. Nandra, 1977, Physica **86–88B**, 758.
Güntherodt, G., 1974, Phys. Cond. Matter **18**, 37.
Güntherodt, G. and N.V. Shevchik, 1976, AIP Conf. Proc. **29**, 174.
Güntherodt, G., J. Schoenes and P. Wachter, 1970, J. Appl. Phys. **41**, 1083.
Hackfort, H. and W. Zinn, 1979, J. Magn. Magn. Mater. **13**, 205.
Hafner, D. and H. Hoffmann, 1979, Phys. Stat. Sol. a **52**, 549.
Hafner, D. and F.B. Humphrey, 1977, Appl. Phys. Lett. **30**, 303.
Hafner, D., H. Hoffmann and F. Stobiecki, 1980, J. Magn. Magn. Mater. **20**, 221.
Hansen, P. and M. Urner-Wille, 1979, J. Appl. Phys. **50**, 7471.
Hardt, R.W., 1966, AFML-TR-66-212 (Microfilm).
Hart, S.C., P. Wigen and A.P. Malozemoff, 1979, J. Appl. Phys. **50**, 1620.
Hasegawa, R., 1974, J. Appl. Phys. **45**, 3109.
Hasegawa, R., 1975, J. Appl. Phys. **46**, 5263.
Hasegawa, R. and R.C. Taylor, 1975, J. Appl. Phys. **46**, 3606.
Hasegawa, R., R.J. Gambino, J.J. Cuomo and J.F. Ziegler, 1974, J. Appl. Phys. **45**, 4036.
Hasegawa, R., B.E. Argyle and L.J. Tao, 1975a, AIP Conf. Proc. **24**, 110.
Hasegawa, R., R.J. Gambino and R. Ruf, 1975b, Appl. Phys. Lett. **27**, 512.
Hauser, J.J., 1975, Phys. Rev. **B12**, 5160.
Hauser, J.J., H.C. Theuerer and N.R. Werthamer, 1966, Phys. Rev. **142**, 118.
Heiman, N. and N. Kazama, 1978, J. Appl. Phys. **49**, 1686.
Heiman, N. and N. Kazama, 1979, Phys. Rev. **B19**, 1623.
Heiman, N. and K. Lee, 1974, Phys. Rev. Letters **33**, 778.
Heiman, N. and K. Lee, 1975, Phys. Letters **55A**, 297.
Heiman, N. and K. Lee, 1976, AIP Conf. Proc. **34**, 319.
Heiman, N., K. Lee and R.I. Potter, 1975a, AIP Conf. Proc. **29**, 130.
Heiman, N., A. Onton, D.F. Kyser, K. Lee and C.R. Guarnieri, 1975b, AIP Conf. Proc. **24**, 573.
Heiman, N., K. Lee, R.I. Potter and S. Kirkpatrick, 1976, J. Appl. Phys. **47**, 2634.
Heiman, N., N. Kazama, D.F. Kyser and V.J. Minkiewicz, 1978, J. Appl. Phys. **49**, 366.
Heiman, N., N. Kazama and K. Lee, 1979, J. Appl. Phys. **50**, 4891.
Heitmann, H., I. Sander, M. Urner-Wille and K. Witter, 1980, J. Magn. Magn. Mater. **20**, 233.
Herd, S.R., 1976, Phys. Stat. Sol. a **38**, 305.
Herd, S.R., 1977, Phys. Stat. Sol. a **44**, 363.
Herd, S.R., 1978, J. Appl. Phys. **49**, 1744.
Herd, S.R., 1979, J. Appl. Phys. **50**, 1645.
Herd, S.R. and P. Chaudhari, 1973, Phys. Stat. Sol. a **18**, 603.
Hirano, M., T. Katayama, Y. Koizumi, M. Kanakami and T. Tsushima, 1977, J. Phys. Soc. Jpn **42**, 347.
Hischii, T., S. Matsushita and Y. Sakuraï, 1977, Jpn J. Appl. Phys. **16**, 1467.
Hoffmann, H. and R. Winkler, 1979a, J. Magn. Magn. Mater. **13**, 89.
Hoffmann, H. and R. Winkler, 1979b, 9th Intern. Coll. Magnetic Films and Surfaces (Univ. Lodz) p. 125.
Hoffmann, H., A.J. Owen and F. Schröpf, 1979, Phys. Stat. Sol. a **52**, 161.
Holtzberg, F. and J.B. Torrance, 1972, AIP Conf. Proc. **5**, 860.
Imamura, N. and T. Kobayashi, 1975, J. Phys. Soc. Jpn **39**, 829.
Imamura, N. and Y. Mimura, 1976, J. Phys. Soc. Jpn **41**, 1067.
Imamura, N., Y. Mimura and T. Kobayashi, 1975, Appl. Phys. Lett. **27**, 634.
Imamura, N., Y. Mimura and T. Kobayashi, 1976a, IEEE Trans. Mag. MAG **12**, 55.
Imamura, N., Y. Mimura and T. Kobayashi, 1976b, Jpn J. Appl. Phys. **15**, 715.
Imamura, N., Y. Mimura and T. Kobayashi, 1977, J. Appl. Phys. **48**, 2634.
Ivanchenko, L.A., G.V. Lashkarev, Yu B. Paderno, S.V. Drodzdova, V.A. Obolonchik, E.I. Yarembash and V.F. Gol'nik, 1971, Ukr. Phys. J. **16**, 624.
Jain, H. and E.C. Subbarao, 1975, Appl. Phys. Lett. **26**, 655.
Jamet, J.P. and A.P. Malozemoff, 1978, Phys. Rev. **B18**, 75.
Jouve, H., J.P. Rebouillat and R. Meyer, 1976, AIP Conf. Proc. **29**, 97.
Kaminskii, V.V., A.I. Shelykh, T.T. Dedegkaev, T.B. Zhukova, S.G. Schul'man and I.A.

Smirnov, 1975, Sov. Phys. Solid State **17**, 1015.
Katayama, T., Y. Koizumi, K. Hasegawa, S. Teraji, M. Hirano, K. Kawanishi and T. Tsushima, 1976, Bull, Electrotechn. Lab. **40**, 988.
Katayama, T., M. Hirano, Y. Koizumi, K. Kawanishi and T. Tsushima, 1977a, IEEE Trans. Mag. MAG **13**, 1603.
Katayama, T., Y. Koizumi, M. Hirano and T. Tsushima, 1977b, J. Phys. Soc. Jpn **42**, 1057.
Katayama, T., K. Hasegawa, K. Kawanishi and T. Tsushima, 1978, J. Appl. Phys. **49**, 1759.
Katayama, T., Y. Nishihara, Y. Yamaguchi, S. Ogawa and T. Tsushima, 1979, J. Physique **40**, Suppl. C-2, 135.
Kehaiov, T.D., N.G. Zurabishvili, E.R. Kutelia, T.L. Bzalava, L.N. Glurdzhidze and V.V. Sanadze, 1979, Bull. Acad. Sci. Georgian SSR **96**, 569.
Kemeneva, G.A., V.N. Shelkovnikov, N.A. Manakov, A.G. Semensov, V.V. Tyn and V.N. Utsin, 1976, Russian Patent 1903-76.
Kirenskii, L.V., A.A. Nedelko, V.A. Buravikhin and I.M. Puzei, 1965, Bull. Acad. Sci. USSR, Phys. Ser. **29**, 691.
Knappe, B., H.R. Müller and B. Springmann, 1978, Phys. Stat. Sol. a **47**, 523.
Kobayashi, K., Y. Togami and T. Teranishi, 1980, Jpn J. Appl. Phys. **19**, L581.
Kobliska, R.J. and A. Gangulee, 1975, AIP Conf. Proc. **24**, 567.
Kobliska, R.J., R. Ruf and J.J. Cuomo, 1975, AIP Conf. Proc. **24**, 570.
Kobliska, R.J., A. Gangulee, D.E. Coxe and H. Bajouk, 1977, IEEE Trans. Mag. MAG **13**, 1767.
Köhne, J., G. Mair, N. Rasula, B. Saftic and W. Zinn, 1980, J. Physique **41**, Suppl. C-5, 127.
Konishi, H., S. Kuriki and G. Matsumoto, 1980, Jpn J. Appl. Phys. **19**, 1009.
Korn, D., 1965, Z. Phys. **187**, 463.
Korotkov, N.A., A.A. Zaytsev and E.M. Lazarev, 1978, Russian Metall. **4**, 186.
Kosicik, R., P. Duda, W. Keilig and R. Mattheis, 1978, Phys. Stat. Sol. a **49**, K67.
Krishnan, R., G. Suran, J. Sztern, H. Jouve and R. Meyer, 1978a, J. Appl. Phys. **49**, 1683.
Krishnan, R., G. Suran, J. Sztern, H. Jouve and R. Meyer, 1978b, J. Appl. Phys. **49**, 4592.
Kryder, M.H., K.Y. Ahn, G.S. Almasi, G.E. Keefe and J.V. Powers, 1974, IEEE Trans. Mag. MAG **10**, 825.
Kryder, M.H., K.Y. Ahn and J.V. Powers, 1975, IEEE Trans. Mag. MAG **11**, 1145.
Kryder, M.H., C.H. Bajorek and R.J. Kobliska, 1976a, IEEE Trans. Mag. MAG **12**, 346.
Kryder, M.H., L.J. Tao and C.H. Wilts, 1976b, IEEE Trans. Mag. MAG **12**, 701.
Kryder, M.H., L.J. Tao and C.M. Wilts, 1977, IEEE Trans. Mag. MAG **13**, 1626.
Kukharskii, A.A., S.G. Schul'man and I.A. Smirnov, 1977, Sov. Phys. Solid State **19**, 862.
Kumar, K. and D. Das, 1978, Thin Solid Films **54**, 263.
Kumar, K., D. Das and E. Wettsten, 1978, J. Appl. Phys. **49**, 2052.
Larsen, J.W. and B.R. Livesay, 1978, J. Appl. Phys. **49**, 1506.
Larsen, J.W. and B.R. Livesay, 1979a, J. Appl. Phys. **50**, 7687.
Larsen, J.W. and B.R. Livesay, 1979b, Bull. Amer. Phys. Soc. **24**, 643.
Larsen, J.W. and B.R. Livesay, 1979c, ORO-5246-3 Microfilms (US DOE).
Lashkarev, G.V. and L.A. Ivanchenko, 1972, J. Non-Cryst. Solids **8–10**, 670.
Lashkarev, G.V., L.A. Ivanchenko and Yu. B. Paderno, 1972, Phys. Stat. Sol. b **49**, K61.
Lazorenko, V.I., V.M. Vereshchak, B.M. Rud' and V.N. Paderno, 1978, Inorg. Mater. **14**, 834.
Leamy, H.J. and A.G. Dirks, 1977, J. Phys. D, Appl. Phys. **10**, L95.
Leamy, H.J. and A.G. Dirks, 1978, J. Appl. Phys. **49**, 3430.
Leamy, H.J. and A.G. Dirks, 1979, J. Appl. Phys. **50**, 2871.
Le Dang, K., P. Veillet, R. Krishnan and G. Suran, 1980, J. Magn. Magn. Mater. **15–18**, 1399.
Lee, K. and N. Heiman, 1975a, AIP Conf. Proc. **24**, 108.
Lee, K. and N. Heiman, 1975b, J. Vac. Sci. Technol. **12**, 121.
Levin, E.M., 1979, Ukr. Fiz. Zh. **24**, 1386.
Loier, C., P. Caro, R. Portier and M. Fayard, 1974, Mater. Res. Bull. **9**, 1553.
Lubitz, P., J. Schelleng and C. Vittoria, 1976a, Solid State Commun. **18**, 965.
Lubitz, P., J. Schelleng and C. Vittoria, 1976b, AIP Conf. Proc. **29**, 178.
Lutes, O.S., J.O. Holmen, R.L. Kooyer and O.S. Aadland, 1977, IEEE Trans. Mag. MAG **13**, 1615.
Luzgin, N.I., 1975, Industr. Lab. **41**, 1062.
Luzgin, N.I. and V.A. Domyshev, 1975, Sov. Phys. J. **18**, 1374.
Luzgin, N.I. and V.A. Domyshev, 1977, Sov. Phys. J. **20**, 1350.
Maksymowicz, L., A. Kobadziejczik, H. Jankowski and J. Wenda, 1977, Thin Solid Films **44**, L23.
Maksymowicz, L., H. Jankowski and J. Wenda, 1979, 9th Intern. Coll. Magnetic Films and Surfaces (Univ. Lodz) p. 102.
Malozemoff, A.P. and S.C. Hart, 1980, Phys. Rev. **B21**, 29.
Malozemoff, A.P. and J.P. Jamet, 1977, Phys. Rev. Letters **39**, 1293.
Malozemoff, A.P., J.P. Jamet and R.J. Gambino, 1977, IEEE Trans. Mag. MAG **13**, 1609.
Manning, J.S. and C.V. Briscoe, 1978, Phys. Rev. **B18**, 1177.
Maple, T.G. and R.A. Buchanan, 1973, J. Vac. Sci. Technol. **10**, 616.
Matsushita, S., K. Sunago and Y. Sakuraï, 1975a, IEEE Trans. Mag. MAG **11**, 1109.
Matsushita, S., K. Sunago and Y. Sakuraï, 1975b, Jpn J. Appl. Phys. **14**, 1851.

Matsushita, S., K. Sunago and Y. Sakuraï, 1976, Jpn J. Appl. Phys. **15**, 713.
Matsushita, S., Y. Yamada, K. Sunago and Y. Sakuraï, 1977, IEEE Trans. Mag. MAG **13**, 1382.
Matsushita, S., H. Tsujimoto, T. Miyama and Y. Sakuraï, 1978, IEEE Trans. Mag. MAG **14**, 719.
Mayr, F. Metawe, P. Grünberg and W. Zinn, 1979, J. Magn. Magn. Mater. **13**, 177.
McGuire, T.R. and R.J. Gambino, 1978, IEEE Trans. Mag. MAG **14**, 838.
McGuire, T.R. and R.J. Gambino, 1979, J. Appl. Phys. **50**, 7653.
McGuire, T.R. and R.J. Gambino, 1980, J. Magn. Magn. Mater. **15–18**, 1401.
McGuire, T.R. and R.C. Taylor, 1979, J. Appl. Phys. **50**, 1605.
McGuire, T.R., R.C. Taylor and R.J. Gambino, 1976, AIP Conf. Proc. **34**, 346.
McGuire, T.R., R.J. Gambino and R.C. Taylor, 1977a, IEEE Trans. Mag. MAG **13**, 1598.
McGuire, T.R., R.J. Gambino and R.C. Taylor, 1977b, J. Appl. Phys. **48**, 2965.
McGuire, T.R., T. Mizoguchi, R.J. Gambino and S. Kirkpatrick, 1978, J. Appl. Phys. **49**, 1689.
McLane, L.B., P.L. Donoho and W.L. Wimbush, 1975, AIP Conf. Proc. **24**, 653.
Melvane, L.B., 1974, AIP Conf. Proc. **24**, 653.
Meyer, R., H. Jouve and J.P. Rebouillat, 1975, IEEE Trans. Mag. MAG **11**, 1335.
Mimura, Y. and N. Imamura, 1976a, Appl. Phys. Letters **28**, 746.
Mimura, Y. and N. Imamura, 1976b, Jpn J. Appl. Phys. **15**, 937.
Mimura, Y., N. Imamura and T. Kobayashi, 1976a, J. Appl. Phys. **47**, 368.
Mimura, Y., N. Imamura and Y. Kushiro, 1976b, J. Appl. Phys. **47**, 3371.
Mimura, Y., N. Imamura and T. Kobayashi, 1976c, Jpn J. Appl. Phys. **15**, 181.
Mimura, Y., N. Imamura and T. Kobayashi, 1976d, Jpn J. Appl. Phys. **15**, 933.
Mimura, Y., N. Imamura and T. Kobayashi, 1976e, IEEE Trans. Mag. MAG **12**, 779.
Mimura, Y., N. Imamura, T. Kobayashi, A. Okada and Y. Kushiro, 1978a, J. Appl. Phys. **49**, 1208.
Mimura, Y., N. Imamura and T. Kobayashi, 1978b, Jpn. J. Appl. Phys. **17**, 2007.
Mimura, Y., N. Imamura and T. Kobayashi, 1978c, Jpn J. Appl. Phys. **17**, 1365.
Minkiewicz, V.J., P.A. Albert, R.I. Potter and C.R. Guarnieri, 1976, AIP Conf. Proc. **29**, 107.
Mitami, T., M. Ishibashi and T. Koda, 1975, J. Phys. Soc. Jpn **38**, 731.
Miyama, T., S. Matsushita, H. Tsujimoto and Y. Sakuraï, 1978, IEEE Trans. Mag. MAG **14**, 728.
Miyama, T., S. Matsushita and Y. Sakuraï, 1980, IEEE Trans. Mag. MAG **16**, 1212.
Mizoguchi, T. and G.S. Cargill III, 1979, J. Appl. Phys. **50**, 3570.
Mizoguchi, T., R.J. Gambino, W.M. Hammer and J.J. Cuomo, 1977a, IEEE Trans. Mag. MAG **13**, 1618.
Mizoguchi, T., T.R. McGuire, R.J. Gambino and S. Kirkpatrick, 1977b, Physica **86–88B**, 783.
Mizoguchi, T., T.R. McGuire, S. Kirkpatrick and R.J. Gambino, 1977c, Phys. Rev. Letters **38**, 89.
Mrstik, B.J. and D.M. Ginsberg, 1973, Phys. Rev. **B7**, 4844.
Müller, H.R., 1978, Phys. Stat. Sol. a **49**, K63.
Müller, H.R. and R. Perthel, 1978, Phys. Stat. Sol. b **87**, 203.
Müller, H.R., B. Knappe, R. Kosicik, P. Rosemann, D. Schmidt and A. Funke, 1976, Phys. Stat. Sol. a **36**, 617.
Müller, H.R., E. Jäger and M. Bitterlich, 1977, Phys. Stat. Sol. b **80**, K85.
Müller, H.R., W. Keilig, R. Kosicik, P. Rosemann and Z. Frait, 1978, Phys. Stat. Sol. a **50**, 537.
Nagy, I., G. Peto and T. Tarnoczi, 1976a, Thin Solid Films **34**, 229.
Nagy, I., T. Tarnoczi and Z. Frait, 1976b, Magn. Letters **1**, 7.
Nagy, I., T. Tarnoczi and Z. Frait, 1977, Physica **86–88B**, 764.
Nandra, S.S. and P.J. Grundy, 1976, J. Phys. D, Appl. Phys. **9**, L167.
Nandra, S.S. and P.J. Grundy, 1977a, Phys. Stat. Sol. a **41**, 65.
Nandra, S.S. and P.J. Grundy, 1977b, J. Phys. F, Metal Phys. **7**, 207.
Nedelko, A.A., 1965, Bull. Acad. Sci. USSR, Phys. Ser. **29**, 686.
Nedelko, A.A. and V.A. Buravikhin, 1966, Sov. Phys. J. **9**, 92.
Netherlands Patent, 1977, No. 77-13503.
Nishihara, Y., T. Katayama, Y. Yamaguchi, S. Ogawa and T. Tsushima, 1978, Jpn J. Appl. Phys. **17**, 1083.
Nishihara, Y., T. Katayama, Y. Yamaguchi, S. Ogawa and T. Tsushima, 1979, Jpn J. Appl. Phys. **18**, 1281.
Nowak, J. and W. Scharff, 1979, J. Phys. D, Appl. Phys. **12**, L139.
Ogawa, A., T. Katayama, M. Hirano and T. Tsushima, 1975, AIP Conf. Proc. **24**, 575.
Ogawa, A., T. Katayama, M. Hirano and T. Tsushima, 1976, Suppl. Jpn J. Appl. Phys. **15**, 87.
Ohashi, K., H. Takagi, S. Tsunashima and S. Uchiyama, 1979, J. Appl. Phys. **50**, 1611.
Ohashi, K., H. Tsush, S. Tsunashima and S. Uchiyama, 1980, Jpn J. Appl. Phys. **19**, 1333.
Ohkoshi, M., R. Ohkata, K. Inoue, S. Honda and T. Kusada, 1980, Jpn J. Appl. Phys. **19**, 1807.
Okamoto, K., T. Shirakawa, S. Matsushita and Y. Sakurai, 1974, IEEE Trans. Mag. MAG **10**, 7999.
Okamoto, K., T. Shirakawa, S Matsushita and Y. Sakuraï, 1975, AIP Conf. Proc. **24**, 113.
Onishi, K., H. Tonomura and Y. Sakuraï, 1979, J. Appl. Phys. **50**, 7624.
Onton, A. and K. Lee, 1976, AIP Conf. Proc. **34**, 328.
Onton, A., N. Heiman, J.C. Suits and W. Parrish, 1976, IBM J. Res. Dev. **20**, 409.

Orehotsky, J. and K. Schröder, 1972, J. Appl. Phys. **43**, 2413.
Osipov, K.A., V.G. Krasov, I.I. Orlov and A.D. Kromov, 1976, Inorg. Mater. **12**, 108.
Oskotskii, V.S., 1977, Sov. Phys. Solid State **19**, 1065.
Ousset, J.C., J.P. Ulmet, R. Asomoza, J.B. Biéri, S. Askenazy and A. Fert, 1980, J. Physique **41**, Suppl. C-8, 470.
Palatnik, L.S., G.V. Lashkarev, V.K. Sorokin, V.E. Marincheva and L.P. Zozulya, 1971, Inorg. Mater. **9**, 37.
Palatnik, L.S., V.E. Marincheva and M.N. Naboka, 1975, Inorg. Mater. **11**, 540.
Paparoditis, C. and R. Suryanarayanan, 1972, J. Crystal Growth **13/14**, 389.
Paparoditis, C., R. Garrigas and J.C. Gillou, 1975, C. R. Acad. Sci. (Paris) **B281**, 535.
Pelá, C.A., G.E. Barberis, J.F. Suassuna and C. Rettori, 1980, Phys. Rev. **B21**, 34.
Pelá, C.A., J.F. Suassuna, G.E. Barberis and C. Rettori, 1981, Phys. Rev. **B23**, 3149.
Perthel, R., W. Keilig, R. Kosicik, U. Röpke and C. G. D'Ambly, 1977, Phys. Stat. Sol. a **40**, K135.
Petrov, M.P., A.I. Grachev, A.A. Kukharskii, I.A. Smirnov and S.G. Schul'man, 1977, Opt. Commun. **22**, 293.
Pfisterer, H., E. Fuchs and P. Tischer, 1969, Z. Angew. Phys. **27**, 179.
Pogarev, S.V., S.G. Schul'man, T.L. Bzhalava and I.A. Smirnov, 1976, Sov. Phys. Solid State, **18**, 140.
Pohl, S.W. and F. Holtzberg, 1975, J. Appl. Opt. **14**, 1060.
Pohl, S.W., R. Jaggi, K. Gisler and H. Weibel, 1975, Solid State Commun. **17**, 705.
Popplewell, J. and S.W. Charles, 1977, Inst. Phys. Conf. Ser. **37**, 238.
Popplewell, J. and S.W. Charles, 1978, J. Magn. Magn. Mater. **7**, 195.
Popplewell, J., S.W. Charles and D.D. Jenkins, 1975, J. Phys. F, Metal Phys. **5**, L137.
Popplewell, J., D.D. Jenkins and S.W. Charles, 1978, J. Non-Cryst. Solids **27**, 319.
Potter, R.I., V.J. Minkiewicz, K. Lee and P.A. Albert, 1976, AIP Conf. Proc. **29**, 76.
Prasad, S., R. Krishnan, G. Suran and J. Sztern, 1979, J. Appl. Phys. **50**, 1623.
Prinz, G.A., R.J. Wagner, C. Vittoria and J. Schelleng, 1977, Physica **89B**, 277.
Prinz, G.A., J.J. Krebs, D.W. Forester and W.G. Maisch, 1979, 9th Intern. Coll. Magnetic Films and Surfaces (Univ. Lodz) p. 134.
Prinz, G.A., J.J. Krebs, D.W. Forester and W.G. Maisch, 1980, J. Magn. Magn. Mater. **15–18**, 779.
Przylucki, J., M. Mazanek, M. Wasielewski and M. Pietron, 1979, Surf. Technol. **8**, 491.
Przyslupski, P., R. Horyn and B. Gren, 1979, Solid State Commun. **32**, 1341.
Ratajczak, H. and I. Goscianska, 1979, 9th Intern. Coll. Magnetic Films and Surfaces (Univ. Lodz) p. 112.
Ratajczak, H. and I. Goscianska, 1980, Phys. Stat. Sol. a **62**, 163.
Ratajczak, H. and I. Labedzka, 1977, Phys. Stat. Sol. a **44**, K103.
Ratajczak, H., F. Stobiecki, T. Stobiecki, R. Gontarz and L. Giersig, 1977, Acta Phys. Pol. **A52**, 767.
Ratajczak, H., I. Goscianska and A. Szlaferek, 1979, 9th Intern. Coll. Magnetic Films and Surfaces (Univ. Lodz) p. 115.
Reichelt, K. and J. Viehweg, 1973, J. Appl. Phys. **44**, 4242.
Roberts, G.E., W.L. Wilson Jr. and H.C. Bourne Jr., 1977, IEEE Trans. Mag. MAG **13**, 1535.
Robinson, A.L., 1977, Science **196**, 966.
Rowell, J.M., R.C. Dynes and P.H. Schmidt, 1979, Solid State Commun. **30**, 191.
Sattikulov, M., V.V. Lemamov, I.A. Smirnov and S.G. Schul'man, 1978, Sov. Phys. Tech. Phys. Letters **4**, 509.
Savitskii, E.M., Yu. V. Efimov, V.N. Sumarokov and A.I. Pozin, 1974, Strukt. Svoistva Sverkhprovod. Mater., ed. E.M. Saviskii (Nauka, Moscow) p. 108.
Savitskii, E.M., Yu. V. Efimov and V.N. Sumarokov, 1975, Fiz. Khim. Obrab. Mater. **3**, 77.
Savitskii, E.M., Yu. V. Efimov and V.N. Sumarokov, 1977, Metallofiz. **68**, 47.
Schewe, H. and A. Harpaintner, 1978, J. Magn. Magn. Mater. **9**, 9.
Schewe, H. and H. Hoffmann, 1977a, J. Magn. Magn. Mater. **6**, 11.
Schewe, H. and H. Hoffmann, 1977b, Physica **89B**, 59.
Schienben, K., G. Mair and K. Reichelt, 1978, Thin Solid Films **52**, L5.
Schiffmacher, G., M. Gasgnier and P. Caro, 1978, The Rare Earths in Modern Science and Technology, eds. G.J. McCarthy and J.J. Rhyne (Plenum Press, New York) p. 223.
Schneider, J., 1975, IBM J. Res. Dev. **19**, 587.
Schneider, J. and A. Brunsch, 1978, J. Appl. Phys. **49**, 1747.
Schoenes, J., 1975, Z. Physik **B20**, 345.
Schoenes, J. and P. Wachter, 1977, Physica **86–88B**, 125.
Schul'man, S.G., T.L. Bzhalava, T.B. Zhukova, T.T. Dedegkaev and I.A. Smirnov, 1975, Sov. Phys. Solid State **17**, 1984.
Schwidtal, K., 1960, Z. Phys. **158**, 563.
Schwidtal, K., 1962, Z. Phys. **169**, 564.
Sella, C., J.C. Martin, Y. Charreire and J. Loriers, 1979, Le Vide—Couches Minces, Suppl. **196**, 201.
Shelkovnikov, V.N., P.A. Andreev, N.A. Manokov and A.N. Belousov, 1976, Sov. Phys. J. **19**, 785.
Shinoda, T., S. Tsunashima, S. Uchiyama and T. Fujii, 1979, J. Appl. Phys. **50**, 7645.
Shirakawa, T., K.O. Okamoto, K. Onishi, S. Matsushita and Y. Sakurai, 1974, IEEE Trans. Mag. MAG **10**, 795.
Shirakawa, T., Y. Nakajima, K. Okamoto, S. Matsushita and Y. Sakurai, 1976, AIP Conf. Proc. **34**, 349.
Sichel, E.K. and R.E. Miller, 1976, Thin Solid Films **37**, L19.

Singh, A.K. and O.N. Srivastava, 1977, Z. Metallkunde **68**, 768.
Singh, A.K. and O.N. Srivastava, 1979, Jpn J. Appl. Phys. **18**, 1603.
Singh, A.K. and O.N. Srivastava, 1980, Z. Metallkunde **71**, 57.
Singh, A.K., B.M.S. Bist and O.N. Srivastava, 1976, Thin Solid Films **35**, L11.
Smirnov, I.A., R. Suryanarayanan and S.G. Schul'man, 1976, Phys. Stat. Sol. b **73**, K137 and b **75**, K153.
Stobiecki, T. and H. Hoffmann, 1980, J. Magn. Magn. Mater. **15–18**, 1127.
Stobiecki, F., H. Hoffmann and W. Pamler, 1980, IEEE Trans. Mag. MAG **16**, 1206.
Stobiecki, T., H. Jankowski and J. Wenda, 1978, Thin Solid Films **51**, 197.
Stoffel, A.M., 1968, J. Appl. Phys. **39**, 563.
Stoffel, A. and K. Strnat, 1965, Proc. INTERMAG Conf., Washington, DC, Paper 2.5.
Suassuna, J.F., G.E. Barberis, C. Rettori and C.A. Pela, 1977, Solid State Commun. **22**, 347.
Suits, J.C. and B.E. Argyle, 1965, J. Appl. Phys. **36**, 1251.
Sunago, K., S. Matsushita and S. Sakuraï, 1976, IEEE Trans. Mag. MAG **12**, 776.
Suran, G., R. Krishnan, H. Jouve and R. Meyer, 1977, IEEE Trans. Mag. MAG **13**, 1532.
Suran, G., R. Krishnan, J. Sztern, H. Jouve and R. Meyer, 1978, J. Magn. Magn. Mater. **7**, 178.
Suran, G., S. Prasad, H. Jouve and R. Meyer, 1979, J. Appl. Phys. **50**, 1617.
Suran, G., R. Krishnan, S. Prasad, H. Jouve and R. Meyer, 1980, IEEE Trans. Mag. MAG **16**, 1342.
Suryanarayanan, R., 1977, Valence Instability and Related Narrow Band Phenomena, ed. R.D. Parks (Plenum Press. New York) p. 541.
Suryanarayanan, R., 1978, Phys. Stat. Sol. b **85**, 9.
Suryanarayanan, R. and G. Brun, 1976, Thin Solid Films **35**, 263.
Suranarayanan, R. and C. Paparoditis, 1970, C. R. Congr. Intern. Coucher Minces, Cannes, p. 637.
Suryanarayanan, R., C. Paparoditis, J. Ferré and B. Briat, 1970, Solid State Commun, **8**, 1853.
Suryanarayanan, R., C. Paparoditis, J. Ferré and B. Briat, 1972, J. Appl. Phys. **43**, 4105.
Suryanarayanan, R., J. Ferré and B. Briat, 1974, Phys. Rev. **B9**, 554.
Suryanarayanan, R., G. Güntherodt, J.L. Freeonfand and F. Holtzberg, 1975, Phys. Rev. **B12**, 4215.
Suryanarayanan, R., I.A. Smirnov, G. Brun and S.G. Schul'man, 1977, J. Physique **37**, Suppl. C-4, 271.
Sylvester, J.G., A. Ambrosio, H.A. Blackstead and A.E. Miller, 1978, J. Appl. Phys. **49**, 1564.
Tagaki, H., S. Tsunashima, S. Uchiyama and T. Fujii, 1979, Jpn J. Appl. Phys. **18**, 399.
Tagirov, R.I. and A.A. Glazer, 1978, Phys. Met. Metall. **46**(1), 58.
Tao, L.J., S. Kirkpatrick, R.J. Gambino and J.J. Cuomo, 1973, Solid State Commun. **13**, 1491.
Tao, L.J., R.J. Gambino, S. Kirkpatrick, J.J. Cuomo and H. Lilienthal, 1974, AIP Conf. Proc. **18**, 641.
Tarnoczi, T., I. Nagy, G. Mezey, T. Nagy, E. Kotai and G. Peto, 1976, C.R. 2nd Intern. Coll. on Sputtering and Applications, Nice, p. 141.
Tarnoczi, T., I. Nagy and A. Kovacs, 1977, Physica **86–88B**, 1333.
Taylor, R.C., 1974, J. Vac. Sci. Technol. **11**, 1148.
Taylor, R.C., 1976a, J. Appl. Phys. **47**, 1164.
Taylor, R.C., 1976b, AIP Conf. Proc. **29**, 190.
Taylor, R.C., 1980, IEEE Trans. Mag. MAG **16**, 902.
Taylor, R.C. and A. Gangulee, 1976, J. Appl. Phys. **47**, 4666.
Taylor, R.C. and A. Gangulee, 1977, J. Appl. Phys. **48**, 358.
Taylor, R.C., T.R. McGuire, J.M.D. Coey and A. Gangulee, 1978, J. Appl. Phys. **49**, 2885.
Terao, N., 1973a, C. R. Acad. Sci. (Paris) **C276**, 5.
Terao, N., 1973b, C. R. Acad. Sci. (Paris) **C276**, 125.
Terzieff, P. and K. Lee, 1979, J. Appl. Phys. **50**, 3565.
Theuerer, H.C., E.A. Nesbitt and D.D. Bacon, 1969, J. Appl. Phys. **40**, 2994.
Tibbetts, G.G. and W.F. Egelhorff Jr., 1980, J. Vac. Sci. Technol. **17**, 458.
Tischer, P., 1971, Z. Angew. Phys. **32**, 89.
Tischer, P., 1973, IEEE Trans. Mag. MAG **9**, 9.
Tissier, B., R. Buder and J.M.D. Coey, 1980, J. Magn. Magn. Mater. **15–18**, 1393.
Togami, Y., 1978, Appl. Phys. Lett. **32**, 673.
Togami, Y., 1979a, Oyo Buturi **48**, 273.
Togami, Y., 1979b, Jpn J. Appl. Phys. Suppl. **18**–1, 231.
Togami, Y., K. Kobayashi and I. Yanagida, 1980, Jpn J. Appl. Phys. **19**, 1663.
Tsujimoto, H., D.F. Shen, S. Matsushita and Y. Sakurai, 1980, IEEE Trans. Mag. MAG **16**, 1209.
Tsunashima, S., K. Imamura, T. Fujii, S. Vehiyama and M. Masuda, 1977, Jpn J. Appl. Phys. **16**, 1051.
Tsunashima, S., H. Tagaki, K. Kamegaki, T. Fujii and S. Uchimaya, 1978, IEEE Trans. Mag. MAG **14**, 844.
Tu, K.N., K.Y. Ahn and J.C. Suits, 1972, IEEE Trans. Mag. MAG **8**, 651.
Twarowski, K. and H.K. Lachovicz, 1979a, J. Appl. Phys. **50**, 7722.
Twarowski, K. and H.K. Lachowicz, 1979b, Phys. Stat. Sol. a **53**, 599.
Twarowski, K. and H.K. Lachowicz, 1979c, 9th Intern. Coll. Magnetic Films and Surfaces (Univ. Lodz) p. 96.
Twarowski, K., H.K. Lachowicz, W. Kaz-

inieczuk and M. Pekala, 1979, Thin Solid Films **62**, 49.
Urner-Wille, M., 1980, J. Magn. Magn. Mater. **16**, 1339.
Urner-Wille, M. and P. Hansen, 1979, 9th Intern. Coll. Magnetic Films and Surfaces (Univ. Lodz) p. 93.
Urner-Wille, M. and K. Witter, 1979, J. Magn. Magn. Mater. **13**, 77.
Urner-Wille, M., T.S. Tevelde and P.G. Van Engen, 1978, Phys. Stat. Sol. a **50**, K29.
Urner-Wille, M., P. Hansen and K. Witter, 1980, IEEE Trans. Mag. MAG **16**, 1188.
Vasilkovskii, A.A., E.T. Sharnopolskaya, N. Yu. Shitsevalova and S.V. Shchegolkov, 1977, Inorg. Mater. **13**, 595.
Venturini, E.L. and P.M. Richards, 1976, J. Appl. Phys. **47**, 1632.
Venturini, E.L., P.M. Richards, J.A. Borders and E.P. Fernisse, 1976, AIP Conf. Proc. **29**, 119.
Visnovsky, S., B. Knappe, V. Prosser and H.R. Müller, 1976, Phys. Stat. Sol. a **38**, K53.
Vittoria, C., P. Lubitz and J. Schelleng, 1976, AIP Conf. Proc. **29**, 196.
Vittoria, C., P. Lubitz and V. Ritz, 1978, J. Appl. Phys. **49**, 4908.
Volkonskaya, T.I. and I.A. Smirnov, 1975, Sov. Phys. Solid State **17**, 751.
Voskobojnik, D.I., A.A. Nedelko and V.N. Shelkovnikov, 1967, Sb. Fiz. Magnit. Plenok **1**, 1137.
Wachter, P. and J. Wollschleger, 1972, J. Phys. Chem. Sol. **33**, 939.
Wagner, C.N.J., N. Heiman, T.C. Huang, A. Onton and W. Parrish, 1976, AIP Conf. Proc. **29**, 188.
Wandelt, K., C.R. Brundle, E. Kay, A. Cenish and H.C. Siegmann, 1977, Proc. 7th Intern. Vacuum Congr. and 3rd Intern. Conf. Solid Surfaces, Vienna, p. 2153.
Wang, Y.J., F.H. Li, Zh. Q. Wang and J.J. Gao, 1979, J. Physique **40**, Suppl C-5, 239.
Wieder, H., 1973, AIP Conf. Proc. **18**, 1128.
Winters, H.F., D.L. Raimondi and D.E. Horne, 1969, J. Appl. Phys. **40**, 2996.
Wong C.C. and C. Wood, 1971, Phys. Letters **34A**, 125.
Woolf, M.A. and F. Reif, 1965, Phys. Rev. **137**, A557.
Yamaguchi, M., K.Y. Hashimoto, H. Kogo and M. Naoe, 1980, IEEE Trans. Mag. MAG **16**, 916.
Yamanaka, S., M. Naoe and K. Ishii, 1977, Jpn J. Appl. Phys. **16**, 843.
Yegorov, V.A., L.M. Sidorenko and V.A. Domyshev, 1977, Phys. Met. Metall. **4**, 187.
Yim, W.R., E.J. Stofko and R.T. Smith, 1972, J. Appl. Phys. **43**, 524.
Zaytsev, A.A., D.V. Ignatov, N.A. Korotkov and E.M. Lazarev, 1975, Russian Metall. **3**, 186.
Zdanowics, W., T. Uliasz, J. Jurusik and J. Sznajder, 1978, J. Mater. Sci. **13**, 1588.
Zhang, C., R. Lia and G. Feng, 1980, IEEE Trans. Mag. MAG **16**, 1215.
Zwingman, R., W.L. Wilson Jr. and H.C. Bourne Jr., 1976, AIP Conf. Proc. **34**, 334.

Additional references

These papers, conference proceedings and microfilms, are not discussed in the text because they were received too late for inclusion.

1. *R–Fe systems*

a) *GdFe*

Blackstead, H.A., J.G. Sylvester, A. Ambrosio, S.C. Hart and A.E. Miller, 1978, The Rare Earths in Modern Science and Technology, ed. G.J. McCarthy (Plenum Press, New York) p. 447.
Bochkarev, V.V., A.E. Hafner, E.C. Chizhik and T.I. Kodinstseva, 1976, Sb. Fiz. Magnit. Plenok **9**, 3.
Buravikhin, V.A., V.F. Bochkarev, O.P. Budanov and T.M. Martynova, 1976, Sb. Fiz. Magnit. Plenok **9**, 47.
Buravikhin, V.A., V.I. Kryzkyov and V.N. Shelkovnikov, 1976, Sb. Fiz. Magnit. Plenok **9**, 79.

b) *TbFe*

Beloussov, A.N., I.N. Kondratiev, N.A. Manakov and V.N. Shelkovnikov, 1977, Sb. Fiz. Magnit. Plenok **10**, 96.

2. *R–Co systems*

a) $SmCo_5$

Beloussov, A.N., N.A. Manakov, V.N. Shelkovnikov and V.V. Tolmachev, 1976, Sb. Fiz. Magnit. Plenok **9**, 214.
Beloussov, A.N., L.M. Sidorenko, N.A. Manakov and V.A. Egorov, 1977, Sb. Fiz. Magnit. Plenok **10**, 213.
Egorov, V.A., L.M. Sidorenko and V.B. Apkhanov, 1977, Sb. Fiz. Magnit. Plenok **10**, 189.
Manakov, N.A., A.N. Beloussov, V.N. Shelkovnikov and V.V. Tolmachev, 1976, Sb. Fiz. Magnit. Plenok **9**, 6.

b) *GdCo*

Bochkarev, V.B., E.S. Chizhik, E.S. Gafner, A.E. Baryshev and S.N. Svistunov, 1976, Sb. Fiz. Magnit. Plenok **9**, 56.
Domyshev, V.A. and N.I. Luzgin, 1976, Sb. Fiz. Magnit. Plenok **9**, 140.
Gill, H.S., UMI Order 79/12005.
Hamzaoui, S., 1980, Thesis, Paris.
Karpovich, V.I., V.V. Makarov and B.I. Lukin, 1980, Sov. Phys. Solid State **22**, 1375.
Krasnikova, G.N., A.A. Kazhaev, T.M. Martynova, V.F. Bochkarev and V.G. Baryshev, 1976, Sb. Fiz. Magnit. Plenok **9**, 99.
Rusov, G.I., S.P. Zherikhov, V.F. Bochkarev and G.F. Torba, 1980, Phys. Met. Metall. **49**, 1262.
Zherikov, S.P., V.F. Bochkarev, G.I. Rusov and G.F. Torba, 1976, Sb. Fiz. Magnit. Plenok **9**, 63.

3. *R–Ni* (*R* = *Sm*, *Gd*)
Shelkovnikov, V.N., V.V. Tyr, G.A. Kamenev and N.A. Manakov, 1976, Sb. Fiz. Magnit. Plenok **9**, 30.

4. *General* (*congresses*)
2nd Intern. Conf. Magnetic Bubbles, 1976, Eindhoven, The Netherlands.
Proc. Conf. Physics of Magnetism, 1978, Poznan, Poland.

Handbook on the Physics and Chemistry of Rare Earths, edited by K.A. Gschneidner, Jr. and L. Eyring

Chapter 42

TRANSPORT PROPERTIES (ELECTRICAL RESISTIVITY, THERMOELECTRIC POWER AND THERMAL CONDUCTIVITY) OF RARE EARTH INTERMETALLIC COMPOUNDS

E. GRATZ
Institut für Experimentalphysik, Technische Universität, Vienna, Austria

M.J. ZUCKERMANN
Physics Dept., McGill University, Montreal, PQ, Canada

Contents

Symbols

$a_{11}(g)$	= partial structure factor
e	= electronic charge
$\boldsymbol{E}$	= electric field vector
E_i	= energy of the crystal field level i
g	= Landé g-factor
H	= magnetic field
$\tilde{H}$	= Hamiltonian in the molecular field model
H_c	= molecular field for the conduction electrons
$\tilde{H}_{ex}$	= exchange interaction Hamiltonian in the RKKY theory
H_0	= molecular field for the localized spin
$\tilde{H}_{sf}$	= s–f exchange interaction Hamiltonian
i	= initial crystal field level
i'	= final crystal field level
I	= effective interaction energy between the electrons
J	= total angular momentum quantum number
$\mathcal{J}$	= direct exchange integral
$\mathcal{J}_{ex}$	= exchange constant in the RKKY theory
$\boldsymbol{k}$	= conduction electron wave vector
k_B	= Boltzmann's constant
$\boldsymbol{k}_F$	= Fermi wave vector
l	= mean free path of conduction electrons

L = orbital momentum quantum number for the R-atoms
L_0 = Lorentz number
m_s = magnetic spin quantum number of the conduction electrons
m^* = effective electronic mass
M_0 = spontaneous magnetization
$\langle n_\sigma \rangle$ = average occupation numbers for itinerant electrons of spin σ
N = number of (magnetic) ions per unit volume
$N(\epsilon_F)$ = density of states at the Fermi energy
$\boldsymbol{q}$ = wave vector
$\boldsymbol{r}_i$ = coordinate vector of conduction electrons i.
R = chemical symbol for rare earth
R = resistance
$\boldsymbol{R}_j$ = coordinate vector of R-atoms j
S = spin quantum number for the R-atoms
S_e = electron diffusion thermopower
S_e^m = diffusion thermopower of a magnetic RI compound
S_e^{nm} = diffusion thermopower of a non-magnetic RI compound
S_g = phonon drag thermopower
S_m = contribution to the thermopower due to magnon drag
S_{mag} = thermopower due to magnetic scattering processes
S_0 = diffusion thermopower due to impurity scattering
S_{ph} = diffusion thermopower due to electron–phonon scattering
S_{spd} = diffusion thermopower due to spin disorder scattering
$S(T)$ = total thermopower
T_c = Curie point
T_D = temperature corresponding to the anisotropy energy
T_F = Fermi temperature
T_K = Kondo temperature
T_N = Neél point
T_{ord} = magnetic ordering temperature (Curie point or Neél point)
T_S = magnetic order to order transition temperature
$\boldsymbol{v}$ = conduction electron velocity
$v_{ab} = V_a - V_b$ = difference in the Coulomb interaction of the conduction electrons with the component a and b of a binary system
W = total thermal resistivity
W_e = electronic component of the thermal resistivity
W_0 = residual thermal resistivity
W_{ph} = lattice component of the thermal resistivity
x = concentration
Γ = spin–spin correlation function
Δ_b = band gap between spin-up and spin-down conduction electrons (Stoner gap)
ΔE = energy difference between crystal field states
Δ_s = gap in the spin waves spectrum
ϵ_F = Fermi energy
$\epsilon(\boldsymbol{k})$ = conduction band energy
θ = paramagnetic Curie temperature
θ_D = Debye temperature
λ = total thermal conductivity
λ_e = electronic component of the thermal conductivity
λ_ℓ = lattice component of the thermal conductivity
μ = chemical potential
μ_B = Bohr magneton
μ_ℓ = parameter describing the local magnetic order
ρ_c = critical resistivity
$\rho_{mag}(T)$ = electrical resistivity due to magnetic scattering processes
ρ_M = proportional to ρ_{spd} of eq. (23)
ρ_n = normal resistivity (i.e. $\rho_{ph} + \rho_{mag}$)
ρ_0 = residual resistivity
$\rho_{ph}(T)$ = lattice electrical resistivity due to electron–phonon interaction
ρ_{spd} = spin-disorder resistivity
$\rho(T)$ = total electrical resistivity
σ = itinerant electron spin
$\sigma(\epsilon)$ = electrical conductivity from the electron energy surface ϵ = const.
$\langle \sigma_z \rangle$ = average polarization of the conduction band
$\chi_0(q, \omega)$ = dynamic susceptibility
$\chi^{+-}(q, \omega$ = transverse component of the dynamic susceptibility
ω = frequency
$\omega(q)$ = spin waves spectrum

1. Introduction

Rare earth intermetallic (RI) compounds have been the subject of many recent experimental investigations because of the nature and variety of their physical properties (Buschow, 1977, 1979; Kirchmayr and Poldy, 1979). In this review article we concentrate on one aspect of such investigations, namely the transport properties of these interesting compounds. We describe in particular experimental data for the resistivity, thermopower and the thermal conductivity.

The term rare earth and the abbreviation R in this article refer to the lanthanide elements from La (atomic number 57) to Lu (atomic number 71) plus the element yttrium Y. Of these elements La, Lu, and Y have no magnetic moment. The element Ce can exist as either Ce^{3+} or Ce^{4+} in RI compounds – the former possessing a magnetic moment and the latter being non-magnetic. This is similar for Yb^{3+} and Yb^{2+} (Gschneidner, 1969; Havinga et al., 1973). Compounds containing these elements are therefore of interest from the point of view of valence fluctuations and Kondo lattices (Doniach, 1977; Lacroix and Cyrot, 1979). Alloys and pseudobinary compounds containing low concentrations of Ce(Yb) often exhibit a Kondo effect (Maple et al., 1978). The remainder of the rare earth elements except for Eu^{2+} are found in a 3+ valence state and all have magnetic moments with both an orbital quantum number L and a spin quantum number S. The only R element for which $S \neq 0$ and $L = 0$ is Gd^{3+} which is therefore not sensitive to the effect of crystal fields.

The magnetic R-elements exhibit a variety of magnetic behaviour in the solid state both as pure metals and as metallic alloys. For example, Gd is ferromagnetic with a Curie temperature (T_c) of 293 K, whereas Eu is an antiferromagnet with a Neél temperature (T_N) of 90 K (McEwen, 1978).

The other pure R-metals show diverse magnetic behaviour including low-temperature ferromagnetism followed by antiferromagnetism at higher temperatures and also canted magnetic structures. One would therefore expect RI compounds to show a similar variety of magnetic behaviour.

Rare earth elements form intermetallic compounds with non-transition metals or transition metals. Such RI compounds exist in a variety of crystalline structures which were described in detail by Taylor (1971) and Wallace (1973). The review articles of Buschow (1977a, 1979) and Iandelli and Palenzona (1979) contain more recent information about the crystalline structure of new RI compounds. We refer the reader to these articles for details. More recently it has been found that amorphous alloys can be prepared from R-atoms and both non-transition and transition metals at the same concentration of elements found in RI compounds (Cochrane et al., 1979). These alloys therefore serve as useful systems for comparison purposes.

The above-mentioned review articles dealing with RI compounds have considered the magnetic nature of these compounds. There has as yet been no detailed description of the transport properties. This is the purpose of this article. The transport properties will be classified according to the magnetic nature of the compounds.

Section 2 contains a detailed description of the transport properties of

non-magnetic RI compounds. The section begins with a theoretical overview for the transport properties of non-magnetic metals such as the Bloch–Grüneisen theory for electrical resistivity, the semiclassical theory for the diffusion thermopower of the conduction electrons and the Wilson formula for the thermal conductivity. The section continues with a description of the resistivity of R–non-transition metal compounds such as YAl_2, LaNi, and Ce(Ag, In). Data for the thermopower and the thermal conductivity of some of these systems are then presented. We exclude the enhanced paramagnetic compound YCo_2 since it serves as a basis for the magnetic RCo_2 compounds and is therefore described in section 4.

Section 3 deals with the transport properties of those RI compounds which have a magnetic R component and a second component which is non-magnetic. The long-range magnetic order in such compounds is due to indirect spin exchange interactions between the localized magnetic moments on the R-atoms. These indirect interactions act via the conduction electrons. The section begins with a theoretical introduction which describes the nature of the exchange interactions and their effect on the transport properties in both the magnetically ordered and the paramagnetic regimes. A subsection is devoted to critical phenomena. The section continues with a description of the experimental data for the transport properties of RI compounds containing Al, Ni, Cu, Rh, Ag, Cd, In, Sb, and Au. Each experimental subsection contains an analysis of the data and a comparison with existing theories when possible.

Section 4 concentrates on the transport properties of those RI compounds which have a magnetic rare earth component and at least one second magnetic 3d transition metal component. The compounds may also contain a third magnetic or non-magnetic component. The theoretical introduction contains a resumé of the current theories of itinerant electron ferro- and paramagnetism for magnetic 3d metals and alloys and a description of their application to transport properties. The section continues with a detailed description of experimental data for the resistivity and thermopower of RI compounds containing Mn, Fe, Co, and Ni as a second magnetic component. The third component of the pseudobinaries may either be a magnetic 3d component or a non-magnetic component such as Al. A comparison with theory is given when possible.

The fifth section contains a brief summary of recent theoretical and experimental research for R-amorphous alloys. This section is included in order to give an overview and is not intended to cover all aspects of this field. This section is followed by a conclusion to the entire article.

We wish to emphasize that this review article is primarily intended as a survey of experimental data for the transport properties of RI compounds. The theory is summarized for the benefit of the reader and is therefore not complete.

One topic has not been included in this article. Many authors have made a thorough study of dilute pseudobinary alloys containing low concentrations of magnetic rare earth atoms. We feel that these investigations, many of which are related to the Kondo effect, belong properly to the field of dilute magnetic alloys and they are therefore reported there. An excellent review of this topic has been

published by Steglich (1977) and several other articles exist in this field (see e.g. Sütsch and Umlauf, 1981; Franz et al., 1980).

2. Transport properties of non-magnetic rare earth intermetallic compounds

2.1. *Theoretical introduction*

In this section we discuss the standard theoretical results for the temperature dependence of transport phenomena in simple metals. The experimental results for non-magnetic rare earth intermetallic compounds (RI) will be summarized in the light of these results in section 2.2. The enhanced paramagnetic RI compound YCo_2 will be considered in section 4 for the reasons given in the Introduction.

2.1.1. *Electrical resistivity*

We begin by assuming that the resistivity of non-magnetic RI compounds obeys Matthiessen's rule. This rule states that the temperature dependence of the resistivity is given by

$$\rho(T) = \rho_0 + \rho_{ph}(T), \tag{1}$$

where ρ_0 is the residual (defect) resistivity and $\rho_{ph}(T)$ is the lattice resistivity due to the electron–phonon interaction. The effect of the electron–electron interaction is neglected since RI compounds are usually not of sufficiently high purity (Ziman, 1960; Volkenshtein, 1973). In the compounds consisting of non-magnetic rare earth with noble metals, ρ_0 was frequently found to be in the range of a few $\mu\Omega$ cm (see section 2.2). It should be pointed out that in most of the cases it is extremely difficult to obtain reliable values for ρ_0 because of the brittleness of the RI compounds, especially if the system crystallizes in the $MgCu_2$ structure (e.g. RAl_2) or in the $CeCu_2$ structure (e.g. RCu_2). The scattering of electrons by vacancies, dislocations, impurities, etc. is assumed to be elastic. As the temperature rises ρ_0 remains constant, but ρ_{ph} increases rapidly because of electron scattering by the quantized lattice vibrations (phonons). It can be assumed that the influence of d-electrons on the physical properties of non-magnetic RI compounds with noble metals is negligible. The electrons responsible for the charge transport, belonging to s–p conduction bands, are scattered by the electron–phonon and electron–impurity interaction into vacant energy states within these bands. The general result for $\rho_{ph}(T)$ in this case is given by the Bloch–Grüneisen law (Ziman, 1972)

$$\rho_{ph}(T) = 4R\left(\frac{T}{\theta_D}\right)^5 \int_0^{\theta_D/T} \frac{x^5\,dx}{(1-e^{-x})(e^x-1)}. \tag{2}$$

The constant R includes the electron–phonon coupling constant, the atomic masses of the different types of atoms and a characteristic temperature θ_D (Debye temperature) for the phonons. Using the limits of integration indicated,

the standard integral reduces to an expression proportional to $(\theta_D/T)^4$ at high temperatures and to a constant equal to 124.4 at low temperatures. ρ_{ph} is therefore proportional to T^5 at low temperatures and proportional to T at high temperatures. The derivation of eq. (2) is based on four assumptions:

(i) The electrical field $\boldsymbol{E}$ and the current density are described by semiclassical theory. This implies that the $\boldsymbol{E}$ field "accelerates" electrons according to $\boldsymbol{k} = -e\boldsymbol{E}/\hbar$ and the current density is caused by the resulting excess of conduction-band electrons with a velocity $\boldsymbol{v} = -(1/\hbar)\nabla_k \epsilon(k)$.

(ii) The scattering events are separated spatially by a sufficient number of wavelengths so that an electron "recovers" from a previous collision before experiencing the next one. For free electrons the criterion is $|\boldsymbol{k}_F| l \gg 1$ ($\boldsymbol{k}_F$ is the Fermi wave vector, l is the mean free path).

(iii) The effective mass approximation is applicable.

(iv) The phonons are in thermal equilibrium and can be described by the Debye model.

Resistivity data for non-magnetic RI compounds are discussed in conjunction with eq. (2) in section 2.2.

2.1.2. *Thermopower*

The thermopower for a simple metal can be written as follows:

$$S = S_e + S_g, \tag{3}$$

where S_e and S_g are the thermopowers due to electron diffusion and phonon drag, respectively. The standard expression for the thermopower S_e due to electron diffusion is given in the relaxation time approximation by (Ziman, 1960)

$$S_e(T) = -\frac{\pi^2 k_B^2 T}{3|e|}\left[\frac{1}{\sigma(\epsilon)}\frac{\partial\sigma(\epsilon)}{\partial\epsilon}\right]_{\epsilon=\epsilon_F}. \tag{4}$$

$\sigma(\epsilon)$ is the contribution to the electrical conductivity from the electron energy surface $\epsilon(k)$ = constant. At high temperatures the total thermopower is usually a linear function of temperature for many metals as predicted by the theory of the electron-diffusion thermopower, i.e. eq. (4). It is also in agreement with the phonon-drag theory which predicts that the phonon-drag contribution should be negligible at high temperatures due to the dominance of the phonon–phonon interaction over the electron–phonon interaction at these temperatures (Bailyn, 1960). At lower temperatures the deviation of the total thermopower from linearity is usually ascribed to the phonon-drag term S_g. However, Guénault (1971) was able to show that S_g is quenched at low temperatures by strong scattering between phonons and impurities. This is in agreement with the experimental data for metals such as Ag containing small amounts of Hg (Craig and Crisp, 1978), Ag–As (Song and Crisp, 1978) and Cu–Ga alloys (Crisp, 1978). However, in some metals, the introduction of impurities results in an increase in the magnitude of the thermopower at low temperature. In particular this was found in the case of dilute aluminium (Huebener, 1968) and indium alloys (Duddenhoeffer and Bourassa, 1977).

By taking into account second-order effects in the electron–phonon interaction, Nielsen and Taylor (1974) have suggested that the low-temperature deviation from linearity of the thermopower may be partially explained in terms of the diffusion component itself. The Nielsen–Taylor effect is sometimes referred to as "phony phonon drag".

2.1.3. *Thermal conductivity*

The thermal conductivity λ of metals has two components, an electronic component λ_e and a lattice component λ_ℓ for which the phonons are the heat carriers. The electronic component λ_e can be written as follows in terms of the thermal resistivity W of the electron system

$$\lambda_e = 1/W_e. \tag{5}$$

W_e is in general given by

$$W_e = W_0 + W_{ph}, \tag{6}$$

where W_0 is the thermal resistivity due to scattering of electrons by imperfection and W_{ph} is due to electron–phonon scattering: eq. (6) assumes the validity of Matthiessen's rule. W_0 is related to the residual resistivity ρ_0 by the Wiedemann–Franz law

$$W_0 = A/T. \tag{7}$$

$A = \rho_0/L_0$ and L_0 is given by

$$L_0 = \frac{\pi^2}{3}\left(\frac{k_B}{e}\right)^2 = 2.44 \times 10^{-8}\ \mathrm{W\,\Omega\,K^{-1}}.$$

Eq. (7) is only true if the relaxation times for W_0 and ρ_0 are equal. The following expression of W_{ph} was obtained by Wilson (Ziman, 1960) for all temperatures using the variational principle and assuming a constant relaxation time

$$W_{ph}(T) = \frac{4A}{L_0 T}\left(\frac{T}{\theta_D}\right)^5\left[\left\{1 + \frac{3}{4\pi^2}\left(\frac{2}{N}\right)^{2/3}\left(\frac{\theta_D}{T}\right)^2\right\} J_5\left(\frac{\theta_D}{T}\right) - \frac{1}{2\pi^2} J_7\left(\frac{\theta_D}{T}\right)\right], \tag{8a}$$

$$J_n\left(\frac{\theta_D}{T}\right) = \int_0^{\theta_D/T} \frac{x_n\, e^x\, dx}{e^x - 1}. \tag{8b}$$

θ_D is the Debye temperature and N is the number of ions per unit volume. At low temperatures eq. (8a) becomes

$$W_{ph}(T) \cong BT^2 \qquad (T \ll \theta_D). \tag{9}$$

Eqs. (5)–(9) then give the following expression for λ_e at low temperatures:

$$\lambda_e = \frac{T}{A + BT^3}. \tag{10}$$

In the limit where $W_{ph} \ll W_0$, eq. (10) shows that λ_e is given by

$$\lambda_e \cong \frac{T}{A} = \frac{L_0}{\rho_0} T. \tag{11}$$

We now assume that the electron and the lattice contribution to λ are additive, giving the following result for the total thermal conductivity:

$$\lambda = \lambda_e + \lambda_\ell. \tag{12}$$

Then from eqs. (11) and (12)

$$\lambda_\ell \simeq \lambda - L_0 T/\rho_0 \qquad (W_{ph} \ll W_0). \tag{13}$$

This expression is used in section 2.2.3 to obtain values for λ_ℓ from the experimental results for λ at very low temperatures.

Another ansatz used in the literature (Włosewicz et al., 1979) assumes that the Wiedemann–Franz law holds for the total electrical resistivity

$$\lambda_e = \frac{L_0 T}{\rho_0 + \rho_{ph}(T)}, \tag{14}$$

where ρ_{ph} is the resistivity due to electron–phonon scattering given by eq. (2). Then λ_ℓ is given from eqs. (12) and (14) by

$$\lambda_\ell = \lambda - \frac{L_0 T}{\rho_0 + \rho_{ph}(T)}. \tag{15}$$

Eq. (15) is also used in section 2.2.3 to analyse the experimental data.

2.1.4. *Mechanisms for saturation of the resistivity at high temperatures*

It is well known that the high-temperature resistivity of several intermetallic compounds and alloys saturates at high temperatures. The best-known example of a non-magnetic compound in which such saturation effects occur is Nb_3Sn (Woodard and Cody, 1964). These phenomena have also been observed for enhanced paramagnetic compounds and alloys, such as YCo_2 and $CeRu_2$, and itinerant ferromagnetic metals well above the Curie temperature (see sections 4 and 2.2.1.1 below). The saturation phenomenon has been theoretically investigated in a rigorous and complete way by Allen (1980). Allen shows that the Boltzmann equation for transport phenomena is only valid under the conditions given in section 2.1.1. It is important to note that the theoretical results presented in sections 2.1.1–2.1.3 are all derived from the Boltzmann equation. Allen notes how sophisticated and successful the Boltzmann equation is in spite of these limitations.

Allen has analysed the following eight mechanisms for the saturation effect. The first three lie within the formalism of the Boltzmann equation and the remaining do not.

(a) Anharmonicity: This word is used to convey the idea that the phonon frequencies ω are temperature dependent. Normal anharmonic behaviour causes $\langle\omega\rangle^2$ to decrease with increasing temperature and therefore causes an increase in

$\rho(T)$ above linearity. However, $\langle\omega\rangle^2$ is known to increase abnormally for A15 compounds. Bader and Fradin (1976) have estimated that at least one third of the deviation from linearity associated with saturation can be explained by anharmonicity.

(b) Fermi smearing: This is due to the fact that the derivative of the Fermi function with respect to kinetic energy is not a delta function at non-zero temperatures. This clearly affects the resistivity significantly but Allen points out that this mechanism probably does not lead to a systematic tendency to saturation.

(c) Alteration of the band structure with temperature: Allen regards this as a small effect which is less significant than (a).

(d) Anderson localization: The Anderson criterion for localization of electrons is connected with the degree of disorder of the system. Allen remarks that it has been shown that the electrical conductivity vanishes at zero temperature when the degree of disorder is close to a critical value. He, however, indicates that there is no hint of an excess conductivity before localization occurs and that the situation is unclear at finite temperatures.

(e) Debye–Waller factors: Allen regards the effect of Debye–Waller factors on the resistivity as requiring more theoretical investigations. One objection is that the Debye–Waller factor should have the same effect on both weak and strong scattering metals and secondly, that multiphonon effects and Debye–Waller effects enter in the same order of perturbation theory in the resistivity. The degree of cancellation of the two effects is not yet known.

(f) Phonon drag: Allen discounts phonon drag as a saturation mechanism since it is only expected to be important for pure metals with weak phonon anharmonicity at low temperatures.

(g) Phonon ineffectiveness: Morton et al. (1978) and Cote and Meisel (1978) have both proposed that phonons of wave vector q become ineffective scatterers when $q\ell < 1$. Allen feels this mechanism is dubious and, if at all true, should be related to phonon drag.

(h) Non-classical conduction channels: Allen states that the generalized Boltzmann equation due to Chakraborty and himself (1978, 1979) can be used to solve the effect of temperature-dependent electron bands on the resistivity. He also points out that non-classical terms related to interband dipole transition and interband electron currents must be included. He further notes that the theory is complicated and that conclusions are difficult to make at this point. However, he feels that this is the most likely mechanism for explaining the saturation tendency.

We have given a summary of Allen's excellent review article. We refer the reader to the original papers for further details. Allen clearly points out that it is important to include interband effects in the formalism. This also follows from experiments since saturation effects in the resistivity at high temperatures seem to occur in metallic compounds and alloys with unfilled d or f bands. Allen and Chakraborty's theory may therefore lead to the understanding of saturation effects if s–d(f) scattering and electron–phonon scattering effects are treated on

the same footing. Clearly Matthiessen's rule will no longer hold in this case, particularly if the electrons are strongly scattered by the phonons.

Another scattering mechanism which may lead to saturation of the resistivity in enhanced paramagnetic materials is the scattering of electrons by spin fluctuations. This point is discussed further in section 4.

Allen (1980) points out that the maximum resistivity for d-band compounds and alloys is of the order of 150 $\mu\Omega$ cm. He suggests that this value is reasonable from a theoretical point of view since it is related to the lower limit of the mean free path, i.e. the interatomic distance. However, certain alloys, such as $Y_6(Fe, Mn)_{23}$ and $Y(Fe, Co)_2$ have resistivities which saturate above 220 $\mu\Omega$ cm (see section 4 for details). This may well be due to resonance scattering effects for the d-electrons in disordered pseudobinaries (Harris et al., 1978).

2.2. *Experimental results and discussion*

2.2.1. *Electrical resistivity data*

2.2.1.1. RAl_2 (R = *Y, La, Yb, Lu*), CeT_2 (T = *Co, Ru, Ir*)

All the compounds under consideration crystallize in the cubic $MgCu_2$ structure. The R–Al compounds are typical examples of compounds with negligible d-electron effect on resistivity. Eq. (2) should then be applicable. A nearly linear temperature dependence was indeed found by Van Daal and Buschow (1970) in the high-temperature region for non-magnetic RAl_2 compounds (fig. 1).

Fig. 2 exhibits the temperature dependence of the resistivity for some Ce–transition metal compounds (Van Daal and Buschow, 1970). In all these compounds Ce is in its tetravalent state. These compounds are therefore all non-magnetic but the susceptibility is about one order of magnitude higher than in the RAl_2 compounds (Buschow, 1977, 1979). As mentioned in section 2.1.4 the influence of d-electrons in the enhanced paramagnetic compounds gives rise to

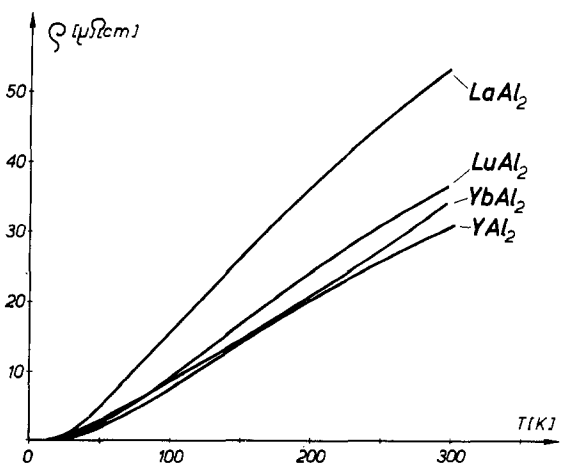

Fig. 1. ρ vs. T curves of some non-magnetic RAl_2 compounds (Van Daal and Buschow, 1970).

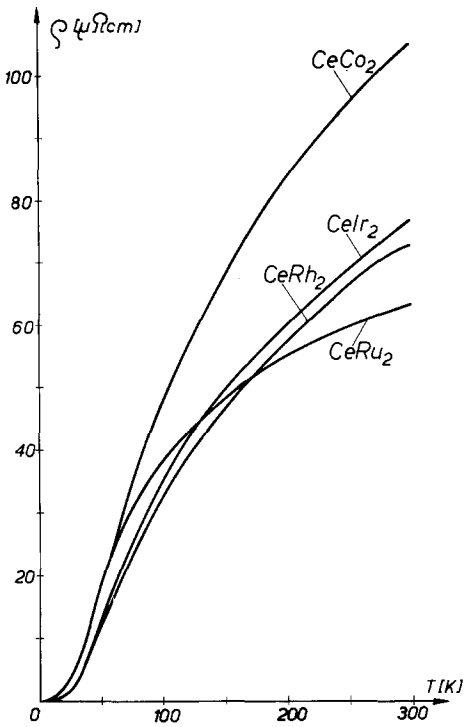

Fig. 2. ρ vs. T curves of some CeT_2 compounds (T = Co, Ru, Rh, Ir) (Van Daal and Buschow, 1970).

pronounced curvature in the ρ vs. T curve as shown in fig. 2. The residual resistivity ρ_0 is subtracted in both fig. 1 and fig. 2.

2.2.1.2. *Fit of the Bloch–Grüneisen law to experimental data*

The ρ vs. T curves of the non-magnetic R-compounds YAl_2, $LuAl_2$, YCu_2, $LuCu_2$, and LaNi measured by Nowotny and Gratz (1981) are shown in fig. 3. The authors fitted eq. (2) to the experimental data and the results are given in table 1. Although this fit is within an error of about 1% the calculated Debye temperatures θ_D are considerably smaller than those obtained from specific heat measurements (e.g. $\theta_D = 473$ K for YAl_2 and 384 K for $LuAl_2$). The discrepancy can be understood in terms of the theory proposed by Kelly and McDonald (1952). These authors state that the Debye temperature θ_D obtained from specific heat comes from low-temperature contributions, whereas θ_D obtained from resistivity measurements represents an average over all temperatures.

2.2.1.3. *$La(Ag_{1-x}In_x)$, $Ce(Ag_{1-x}In_x)$*

The presence of the 5d electrons at the Fermi level is important not only for magnetic coupling but also for the stability of the crystal structure (Ihrig and Methfessel, 1976a, b). La(Ag, In) and Ce(Ag, In) crystallize in the CsCl structure and undergo a martensitic transition to a tetragonal phase at low temperatures. This cubic to tetragonal transition is ascribed to the Jahn–Teller effect. The effect of such a transition on the resistivity in the La(Ag, In) pseudobinary system is shown in fig. 4 (Balster, 1972). The corresponding measurements in the

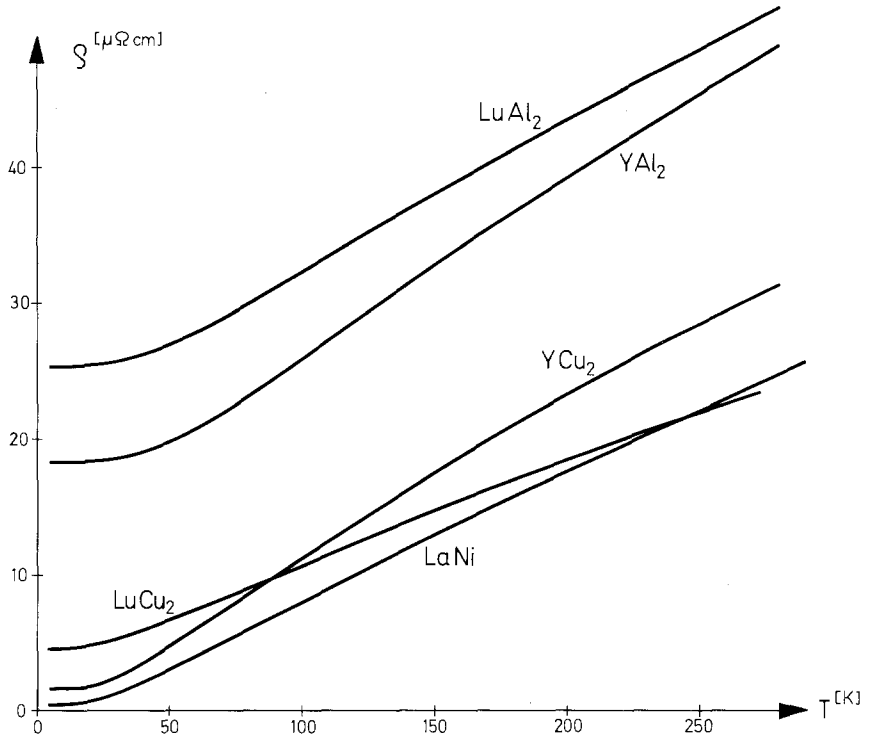

Fig. 3. ρ vs. T curves of YAl_2, $LuAl_2$, YCu_2, $LuCu_2$, and LaNi (Nowotny and Gratz, 1981).

Ce(Ag, In) system are given in fig. 5 (Ihrig, 1973). The hysteresis observable in the ρ vs. T curve is due to this structural transition. Fig. 6 gives a survey of the transition temperatures of such systems (Ihrig and Methfessel, 1976a). The transition temperature was obtained from the midpoint of the hysteresis loops. The anomalies in the resistivity behaviour can therefore be understood by a dramatic change of the phonon spectrum at this transition.

TABLE 1
The Debye temperatures θ_D and mean square deviations obtained by a fit procedure of the Bloch–Grüneisen law (eq. (2)) to the experimental data.

Compound	Crystal structure	θ_D (K)	Mean square deviation (%)
YAl_2	$MgCu_2$ structure	289	0.25
$LuAl_2$		269	0.19
YCu_2	$CeCu_2$ structure	169	1.17
$LuCu_2$		177	0.90
LaNi	CrB structure	166	1.28

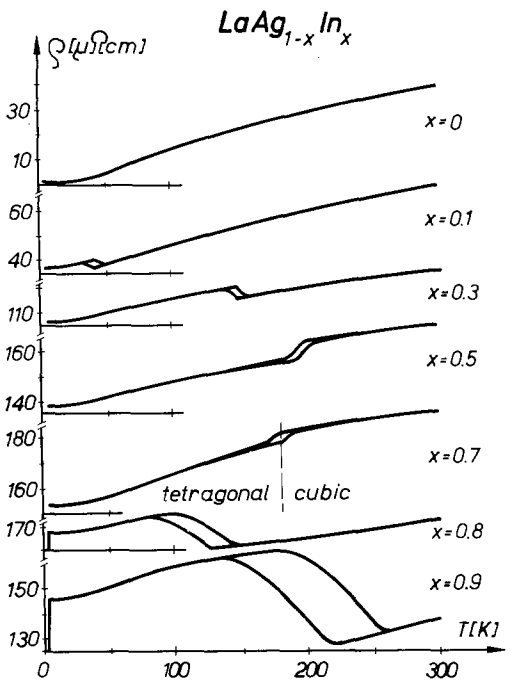

Fig. 4. ρ vs. T curves of the $La(Ag_{1-x}In_x)$ pseudobinary system (Balster, 1972).

2.2.1.4. $YbAl_3$, $YbAl_2$

The resistivity for these compounds is shown in fig. 7. Havinga et al. (1973) analysed both the resistivity data and the thermodynamic data of these compounds in terms of a two-band system.

The lower level is a narrow resonance (virtual bound) state which represents non-magnetic Yb^{2+} ions. The upper state represents the magnetic Yb^{3+} ion with a total angular momentum of $J = 7/2$. The model was fitted to the susceptibility of $YbAl_3$ and the value of 270 K was found for the energy difference ΔE between the two levels. The value of the paramagnetic Curie temperature for the upper level was given by $\theta = 220$ K. Havinga et al. (1973) then derived the following expression for the resistivity using the two-level model

$$\rho(T) = b(1-c)[1-\exp(-aT^2/b)] + c\rho_{spd}, \tag{16}$$

where c is the concentration of the Yb ions in the 3+ state and is given by

$$c = 8\exp(-\Delta E/k_B T)/[1+8\exp(-\Delta E/k_B T)]. \tag{17}$$

a and b are parameters related to the virtual bound state. ρ_{spd} is, as usual, the spin-disorder resistivity.

Eq. (16) was fitted to the resistivity of $YbAl_3$ after the lattice contribution had been subtracted. The results of the fits are shown in fig. 7. The authors remark that the value of ΔE obtained by fitting the resistivity is given by $\Delta E = 290$ K and is in good agreement with that obtained from the susceptibility fit. However,

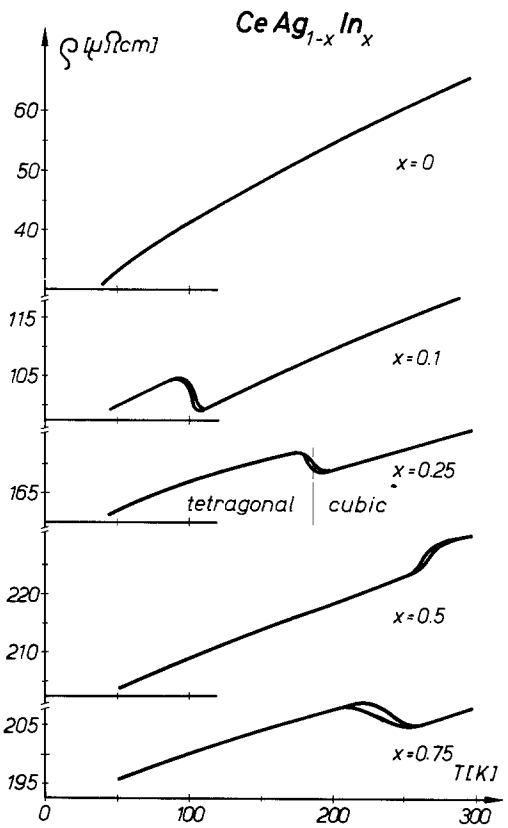

Fig. 5. ρ vs. T curves of the $Ce(Ag_{1-x}In_x)$ pseudobinary system (Ihrig, 1973).

the values of ρ_{spd} and θ obtained from the fit are at least one order of magnitude larger than one would expect. This indicated to the authors that the two-level model was somewhat too simple for Yb systems.

The authors also fit the resistivity data of $YbAl_2$ using the same method (see fig. 7). In this case the value of ΔE obtained from the resistivity was found to be 1770 K which was again in good agreement with the value of 1800 K obtained from susceptibility. However, the values of ρ_{spd} and θ found from the fit to the resistivity and suceptibility data were again too high.

The authors concluded by stating that the T^2 term in the resistivity may well be fitted, that such a behaviour can be ascribed to the spin fluctuations (see section 4).

2.2.2. *Thermopower data*

2.2.2.1. RAl_2 (R = Y, La, Lu), RCu_2 (R = Y, Lu)

The temperature dependence of thermopower for several non-magnetic RI compounds is shown in fig. 8 ($LaAl_2$), fig. 9 (YAl_2, $LuAl_2$), and fig. 10 (YCu_2, $LuCu_2$).

Most of the S vs. T curves are characterized by a nearly linear temperature

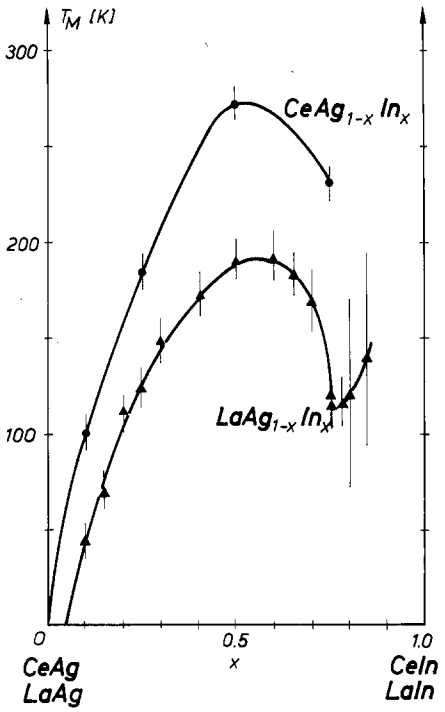

Fig. 6. Concentration dependence of the transition temperatures, T_M, in La(Ag, In) and Ce(Ag, In) (Ihrig and Methfessel, 1976a).

dependence above 150 K. This is in agreement with eq. (4) assuming that $\partial \ln \sigma / \partial \epsilon$ at the Fermi energy hardly changes with the temperature. In the low-temperature range pronounced minima are observed in some of these compounds (YAl_2, YCu_2). As discussed in section 2.1.2 there are two possible explanations for such anomalies. One possibility is that these minima are caused by phonon drag. The other mechanism is the Nielsen–Taylor effect of section 2.1.2.

Although the structure of the YAl_2, $LaAl_2$, and $LuAl_2$ compounds is the same and the rare earth ions are all in the 3+ state, the shape of the S vs. T curves is considerably different for different compounds. The significant difference be-

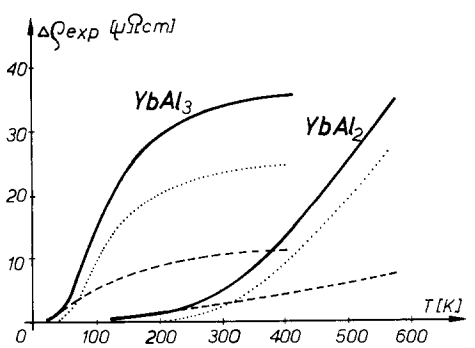

Fig. 7. Resistivity data of $YbAl_3$ and $YbAl_2$. The solid lines give the experimentally obtained $\Delta\rho_{exp}$ vs. T curves corrected for residual and electron–phonon scattering contributions. The dotted lines show the estimated contributions due to spin-disorder scattering by the Yb^{3+} magnetic moments described by the second term of eq. (16). The dashed lines show the estimated contribution connected with scattering processes on Yb^{2+} virtual bound states which is described by the first term of eq. (16) (Havinga et al., 1973).

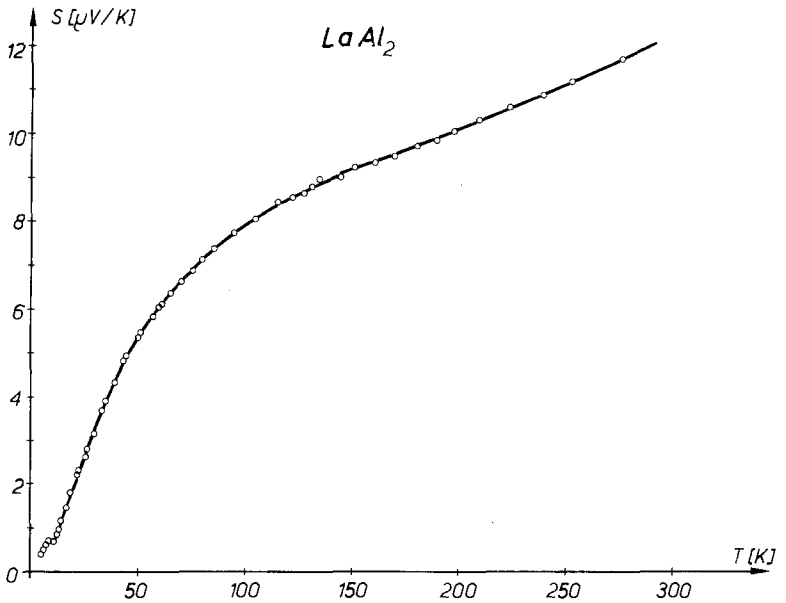

Fig. 8. S vs. T curve of $LaAl_2$ (Mikovits, 1981).

tween $LaAl_2$ as compared to YAl_2 and $LuAl_2$ is also evident in the electronic specific heat constant as shown by Hungsberg and Gschneidner (1972). We feel that the differences must therefore be due to differences in the electronic band structure and/or the electron–phonon coupling between the different compounds.

2.2.2.2. *$YbAl_2$, $YbAl_3$*

The ambivalent character of the Yb ions in the compounds $YbAl_2$ and $YbAl_3$ was discussed in terms of a two-band model for the electronic state of the Yb ion in these compounds (Havinga et al., 1973) (see also section 2.2.1.4). Van Daal

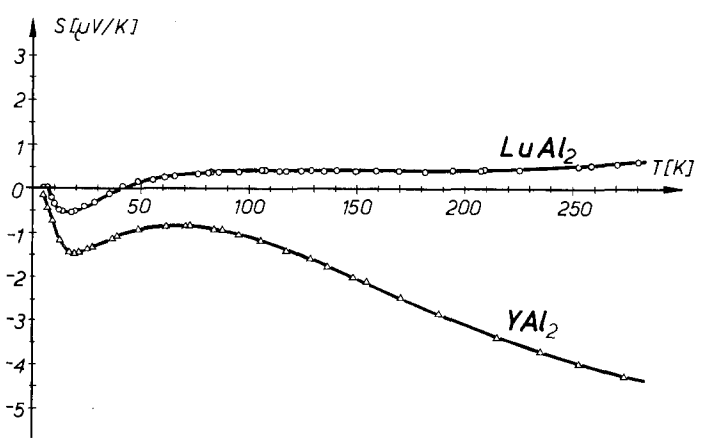

Fig. 9. S vs. T curve of YAl_2 and $LuAl_2$ (Mikovits, 1981).

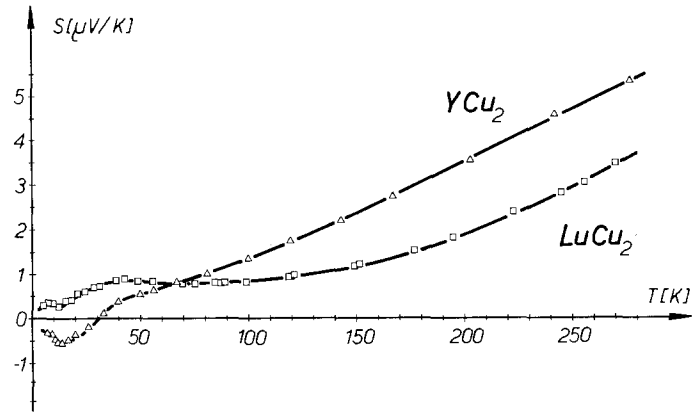

Fig. 10. S vs. T curve of YCu_2 and $LuCu_2$ (Mikovits, 1981).

et al. (1974) investigated the influence of such a behaviour on the temperature dependence of thermopower. The analysis of the data was done on the basis of the Nordheim–Gorter rule which states that the total thermopower is the weighted sum of the partial contribution (see section 2.1.2). For the estimation of the normal diffusion thermopower effect Van Daal et al. (1974) used the thermopower data of the isostructural $LuAl_2$ and $LuAl_3$ compounds. For the resistivity data it was found that at about 70 K already half of $\rho(T)$ is due to spin-disorder scattering whereas in the results for $S(T)$ no clear evidence for the increasing importance of spin-disorder scattering at high temperatures could be found. In this connection it should be pointed out that the thermopower curve for $LuAl_2$ obtained by Van Daal et al. (1974) does not agree with the thermopower data obtained by Mikovits (1981) (see section 2.2.2.1). A possible reason for this discrepancy could be the purity of the $LuAl_2$ samples. It is generally known that Lu compounds are difficult to prepare in the pure phase.

2.2.3. *Thermal conductivity data*

2.2.3.1. *YAl_2, $LuAl_2$*

Figs. 11 and 12 show the temperature dependence of the thermal conductivity, λ, for YAl_2 and $LuAl_2$ from 4.2 K to room temperature (Bauer, 1981). Both compounds are non-magnetic and crystallize in the cubic $MgCu_2$ structure. The shape of the λ vs. T curves is considerably different from those of a pure metal such as Al (Rosenberg, 1955). For pure and well-annealed Al samples, an extremely pronounced peak in the low-temperature range near 0.1 θ_D is observable. Further, the magnitude of thermal conductivity at room temperature is normally found to be about 10 times larger than the values measured in the above RI compounds. As discussed in section 2.1.3 the thermal conductivity of a metal consists of two contributions, namely an electronic part λ_e and a lattice part λ_ℓ. λ_ℓ is usually assumed to give a small contribution to the total conductivity for pure metals (Ziman, 1960).

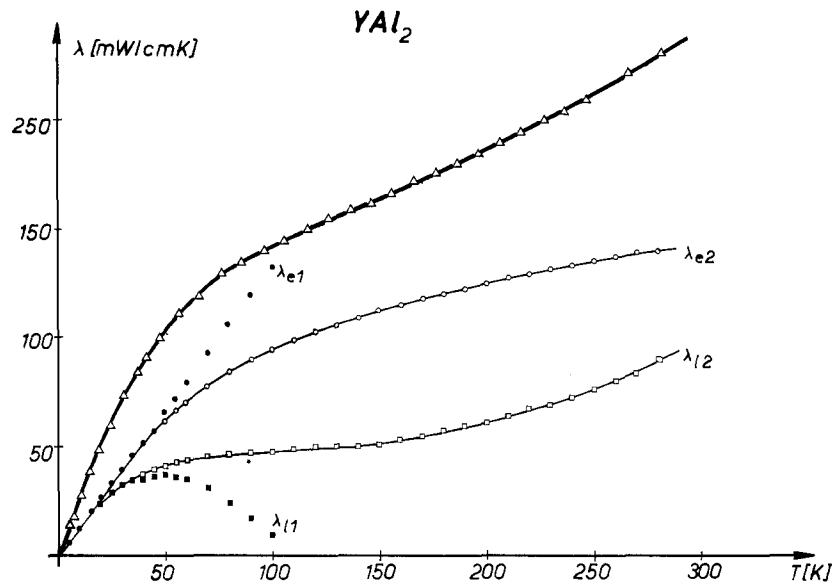

Fig. 11. λ vs. T curve of YAl_2 (for the meaning of λ_{e1}, $\lambda_{\ell 1}$, λ_{e2}, and $\lambda_{\ell 2}$ see the text) (Bauer, 1981).

One of the problems in interpreting the thermal conductivity is to find a way of decomposing λ into λ_e and λ_ℓ. Two methods which can be used for this analysis have been described in section 2.1.3. The results for YAl_2 and $LuAl_2$ are shown in figs. 11 and 12, respectively. It can be seen that use can only be made of eq. (13) up to about 40 K (see λ_{e1} in figs. 11 and 12) since the total resistivity ρ

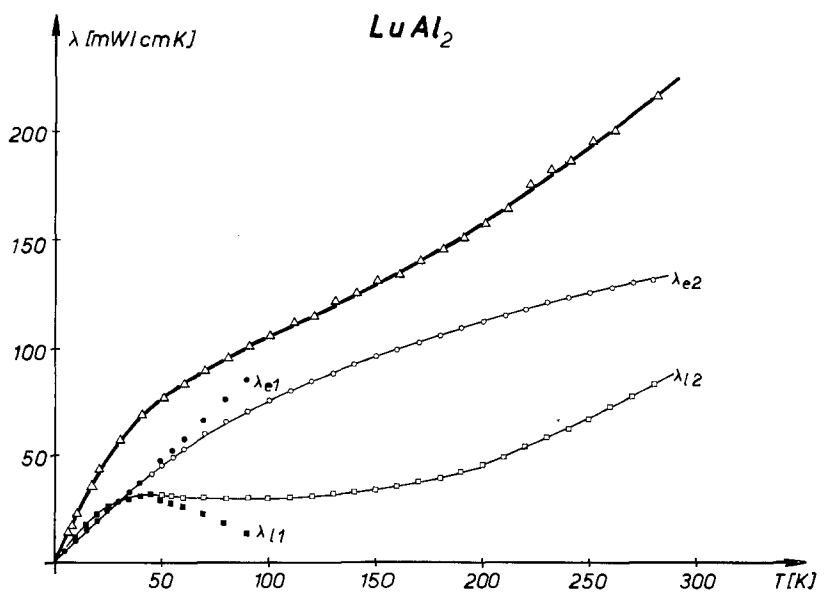

Fig. 12. λ vs. T curve of $LuAl_2$ (for the meaning of λ_{e1}, $\lambda_{\ell 1}$, λ_{e2}, and $\lambda_{\ell 2}$ see the text) (Bauer, 1981).

can no longer be described by the residual resistivity ρ_0 alone. Also eq. (13) is meaningless when $\lambda < L_0 T/\rho_0$. This implies that it is reasonable to use the second method contained in eq. (15). The resulting curves for the temperature dependence of the electronic part λ_{e2} and the lattice part $\lambda_{\ell 2}$ obtained by the second method are also shown in figs. 11 and 12 for both compounds. The $\lambda_{e2}(T)$ curves should now obey eq. (8a). This equation gives a reasonable fit to $\lambda_{e2}(T)$ for both compounds and the value of the Debye temperature obtained from the fitting procedure is close to that obtained using the Bloch–Grüneisen law for the resistivity.

3. Transport properties of rare earth–non-transition-metal compounds exhibiting long-range magnetic order

3.1. *Theoretical introduction*

The purpose of section 3.1 is to give a detailed description of the transport properties of those RI compounds whose magnetic properties are due to the localized magnetic moments of the rare earth component only. The collective magnetic properties of such compounds are based on the polarization of the conduction band by the rare earth moments. The resultant exchange interaction is known as the Rudermann–Kittel–Kasuya–Yosida (RKKY) interaction between sp- and f-electrons. Since the magnetic properties of these systems have a strong influence on the transport properties it is appropriate to begin the theoretical discussion with a description of the magnetic moments of free rare earth ions. This section continues with a description of the RKKY interaction and with theoretical predictions for the magnetic effect on the electrical resistivity in several temperature regions.

The influence of magnetic order on the thermopower and thermal conductivity is not as well understood theoretically as is the resistivity. Theoretical models have been presented in a small number of publications only and they are in reasonably good agreement with experimental data. A short description of some of these calculations will be given in section 3.1.4 below.

3.1.1. *Rare earth magnetic moments*

The free ions of the lanthanides are usually trivalent both in their atomic state and in the solid state. However, exceptions are often found for the elements Ce, Eu, and Yb in the solid state, since these elements tend to have either empty, half-full or full 4f shells.

The electronic structure of rare earth atoms can be described in terms of a core of filled shells equivalent to a xenon atom plus the following configuration

$$4f^n 5d^{0-1} 6s^2 \qquad (n = 1, 2, \ldots, 14).$$

This configuration can be described as follows:

(i) a 4f shell which is gradually filled and may give rise to a magnetic moment,

(ii) ($5s^25p^6$) shells which are completely filled and screen the 4f shell,
(iii) ($5d^{0-1}6s^2$) valence shells which form conduction bands in the solid state.

As noted by Liu (1961) a partially filled 4f shell has a magnetic moment of $g\mu_B J$. μ_B is the Bohr magneton and J is the total angular moment. From the Russell–Saunders coupling scheme $J = L + S$ or $|L - S|$ depending upon whether the 4f shell is more than or less than half filled. The Landé g-factor, g, is given by

$$g = 1 + \frac{J(J+1) - L(L+1) + S(S+1)}{2J(J+1)}. \tag{18}$$

A description of the exchange interaction between two rare earth magnetic moments is given in section 3.1.2.

3.1.2. *Exchange interaction*

Liu (1961) noted that the wave functions of the 4f electrons on different rare earth (R) atoms in the solid state do not usually overlap. This is because the radius of the 4f shell is almost 0.35 Å and the wave functions are therefore zero on the Wigner–Seitz sphere. There can therefore be no direct exchange, and exchange interactions between different R-magnetic moments must be mediated by the conduction electrons. Liu points out that there are two possible interaction types. In the first type the 4f magnetic moment on the R-atom polarizes the sp conduction bands of the compound via a direct s–f exchange interaction given by

$$\tilde{H}_{sf} = -2(g-1)\sum_{ij} \mathcal{J}(\boldsymbol{r}_i - \boldsymbol{R}_j)\boldsymbol{s}_i \cdot \boldsymbol{J}_j, \tag{19}$$

where $\boldsymbol{s}_i$ and $\boldsymbol{r}_i$ are the spins and spatial coordinates of the conduction electrons, respectively and $\boldsymbol{J}_j$ and $\boldsymbol{R}_j$ are those of the R-atoms, respectively. $\mathcal{J}$ is the exchange integral for this interaction and has been calculated by several authors (Liu, 1961; Kondo, 1962). Eq. (19) is important for the analysis of transport properties.

The polarization of the conduction band due to the Hamiltonian of eq. (19) oscillates spatially with a long-range damping factor. The polarized conduction electrons can now scatter magnetically with another R atom. The resultant exchange interaction is known as the RKKY interaction and accounts for most of the magnetic properties of RI compounds.

The Hamiltonian for the RKKY interaction is given by

$$\tilde{H}_{ex} = -2(g-1)^2 \sum_{ij} \mathcal{J}_{ex}(\boldsymbol{R}_{ij})\boldsymbol{J}_i \cdot \boldsymbol{J}_j, \tag{20}$$

where the indirect exchange $\mathcal{J}_{ex}(\boldsymbol{R})$ is now given by

$$\mathcal{J}_{ex}(\boldsymbol{R}) = \frac{m|\mathcal{J}|^2}{4\pi^3|\boldsymbol{R}|^4}[2k_F\boldsymbol{R}\cos(2k_F\boldsymbol{R}) - \sin(2k_F\boldsymbol{R})]. \tag{21}$$

$\boldsymbol{k}_F$ is the Fermi wave vector and $\mathcal{J}$ is the direct exchange interaction between sp- and f-electrons of eq. (19). It is important to note that $\mathcal{J}_{ex}(\boldsymbol{R})$ of eq. (21) is an

isotropic function of $\boldsymbol{R}$ since it was derived in the free electron approximation. However, the position of the nodes and peaks of $\mathcal{J}_{ex}(\boldsymbol{R})$ will be shifted when crystal structure effects are included in the calculation.

As described by Liu (1961) the nature of the exchange interaction changes when the energy required to promote an electron from the conduction band into the 4f band is small. In this case the admixture interaction between conduction and 4f electrons must be taken into account. This interaction leads to an effective attractive sp–f exchange interaction of the Schrieffer–Wolff kind though the form of the Hamiltonian is still given by eq. (19). Such admixture interactions are applicable to Ce and Yb alloys (see Coqblin and Blandin, 1968) and lead to a Kondo effect.

3.1.3. *Influence of localized magnetism on resistivity*

In section 2.1.1 it was assumed that the temperature dependence of the non-magnetic RI compounds is determined by the residual resistivity ρ_0 and the lattice resistivity ρ_{ph} due to electron–phonon interaction. In RI compounds showing magnetic order, an additional contribution to the resistivity must be taken into consideration. This contribution, ρ_{mag}, describes scattering processes of conduction electrons due to disorder in the arrangement of the magnetic moments.

Assuming the validity of Matthiessen's rule it follows that the total temperature dependence of the resistivity in these compounds is given by

$$\rho(T) = \rho_0 + \rho_{ph}(T) + \rho_{mag}(T). \tag{22}$$

In fig. 13 the temperature dependence of the electrical resistivity of RI compounds without d-electron contribution is shown schematically. For the case of resistivity the contribution $\rho_{mag}(T)$ will now be the subject of discussion. $\rho_{mag}(T)$

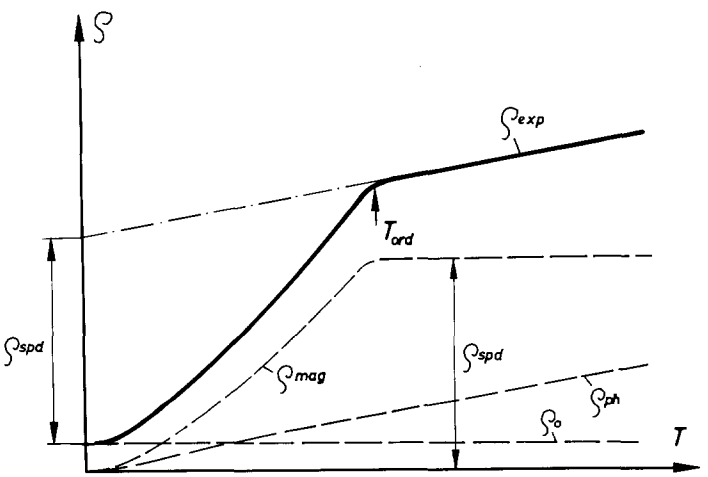

Fig. 13. Schematic temperature dependence of the electrical resistivity of magnetic RI compounds with negligible d-electron contribution.

is characterized by the following traits:

(i) a temperature independent behaviour for $T > T_{ord}$,

(ii) a pronounced kink at $T = T_{ord}$,

(iii) a strong decrease for $T < T_{ord}$ with decreasing temperature.

T_{ord} is the transition temperature for magnetic ordering. A short discussion of the theoretical models describing such a behaviour will now be given.

3.1.3.1. *Paramagnetic regime* ($T > T_{ord}$)

Several authors (Kasuya, 1956; de Gennes and Friedel, 1958; Dekker, 1965) were able to solve the conduction electron scattering problem in the paramagnetic regime ($T > T_{ord}$) by using the Hamiltonian of eq. (19). The magnitude $\rho_{mag}(T > T_{ord}) \equiv \rho_{spd}$ is then given by

$$\rho_{spd} = \frac{3\pi N m^*}{2\hbar e^2 \epsilon_F} |\mathcal{J}|^2 (g-1)^2 J(J+1). \tag{23}$$

Eq. (23) was derived by solving the Boltzmann equation in the relaxation time approximation. The conduction electrons were considered to be free particles with an effective mass m^*. The transition probability was obtained in the first Born approximation. Furthermore, it was assumed that in the paramagnetic region the local magnetic moments are completely decoupled with each moment having $(2J+1)$ possible orientational states in a given direction z (neglecting the influence of the crystal field). For the other symbols used in eq. (23) see Dekker (1965). Eq. (23) shows that ρ_{spd} is proportional to the de Gennes factor $(g-1)^2 \times J(J+1)$. ρ_{spd} provides a large additive contribution to the total resistivity as shown in fig. 13. We assume that the linear increase of the total $\rho(T)$ curve is caused by electron–phonon scattering (in accordance to the Bloch–Grüneisen law of eq. (2). An extrapolation procedure from high temperature to absolute zero then gives the magnitude of ρ_{spd}.

Eq. (23) can be written as

$$\rho_{spd}(x) = \frac{3\pi N m^*}{2\hbar e^2 \epsilon_F} \{x|\mathcal{J}_a|^2 (g_a-1)^2 J_a(J_a+1) + (1-x)|\mathcal{J}_b|^2 (g_b-1)^2 J_b(J_b+1) - x(1-x)[\mathcal{J}_a(g_a-1)J_a - \mathcal{J}_b(g_b-1)J_b]^2\}, \tag{24}$$

for a compound consisting of two different magnetic R elements where $\mathcal{J}_a$ and $\mathcal{J}_b$ are the (sp)–f direct exchange integrals for the alloy components and g_a, g_b are the respective Landé g-factors. The expression in eq. (24) is derived under the assumption that the domains of ferromagnetically aligned spins have dimensions which are small compared to the conduction electron mean free path. When the system contains only one magnetic rare earth component as in (Gd_xY_{1-x}), eq. (24) reduces to

$$\rho_{spd}(x) = \frac{3\pi N m^*}{2\hbar e^2 \epsilon_F} (g-1)^2 |\mathcal{J}|^2 Jx(1+Jx). \tag{25}$$

Dekker (1965) proposed the following expression for $\rho_0(x)$

$$\rho_0(x) = \frac{3\pi N m^*}{2\hbar e^2 \epsilon_F} x(1-x)[v_{ab}^2 + |\mathcal{J}|^2 (g-1)^2 J^2] \tag{26}$$

for the case where the mean free path of the conduction electrons is much greater than the size of the magnetic domains for a system with a single magnetic component. $v_{ab} = V_a - V_b$ is the difference in the Coulomb interaction of the conduction electrons with the two components of the binary system.

3.1.3.2. *Influence of crystal field on spin-disorder resistivity*

The expression for the spin-disorder resistivity has the following form in the presence of a crystal field:

$$\rho_{spd}(T) = \frac{3\pi N m^*}{\hbar e^2 \epsilon_F} |\mathcal{J}|^2 (g-1)^2 \sum_{\substack{m_s m_s' \\ i i'}} |\langle m_s' i' | \mathbf{s} \cdot \mathbf{J} | m_s i \rangle|^2 p_i f_{ii'}. \tag{27}$$

m_s and m_s' represent the spins of the conduction electrons in the initial and final states, i and i' are the initial and final crystal field levels of the rare earth ion, p_i is the Boltzmann probability that the rare earth ion is in a crystal field level with energy E_i and is given by

$$p_i = \frac{\exp(-E_i/k_B T)}{\sum_j \exp(-E_j/k_B T)}, \tag{28}$$

E_i depends on the extent of the crystal field splitting and $f_{ii'}$ is given by

$$f_{ii'} = \frac{2}{1 + \exp[(E_{i'} - E_i)/k_B T]}. \tag{29}$$

Rao and Wallace (1970) applied eq. (27) to experimental data for $CeAl_2$ in order to explain the unusually broad "knee" in the ρ vs. T curve at about 70 K. They ascribed this behaviour to the influence of the crystal field on ρ_{spd} given by eq. (27). One of the important consequences of the influence of crystal fields on resistivity in the paramagnetic state is that ρ_{spd} now becomes temperature dependent.

3.1.3.3. *Kondo effect and Kondo lattices*

The occurrence of minima in the temperature dependence of the electrical resistivity of metallic systems has been known for a long time in the metallic systems consisting of elements such as Cu, Ag or Au as solvents with very small amounts ($\leq$0.1 at%) of magnetic impurities such as Cr, Mn, Fe as solutes (Van den Berg, 1964). The theoretical explanation of this effect is due to Kondo (1964). Kondo showed that the spin-disorder resistivity is not a constant (as given by eq. (23)) but increases with decreasing temperature under certain circumstances. This result follows from third-order perturbation theory using the Hamiltonian given by eq. (19). In Kondo's model it is shown that the conduction electrons can be scattered from an initial state to a final state via intermediate states. The efficiency of this additional "channel" is large in the low-temperature range and gives rise to the observed increase of the spin-disorder resistivity for $\mathcal{J} < 0$ (see below). The appearance of a minimum in the ρ vs. T curve follows from the combined effect of the increased spin-disorder resistivity and the decreasing lattice scattering resistivity on cooling the sample. The expression for

the Kondo resistivity is then given by

$$\rho_{\text{Kondo}}(T) = \rho_{\text{spd}}[1 + \alpha N(\epsilon_F)\mathcal{J} \ln(T/T_F)]. \tag{30}$$

where α depends on the nature of the local moment, T_F is the temperature corresponding to the Fermi energy, $\mathcal{J}$ is the direct exchange integral of eq. (19) and $N(\epsilon_F)$ is the density of states at the Fermi energy.

Summing up it can be said that the Kondo anomaly should be observable if:

(a) localized magnetic moments exist in a metallic matrix,

(b) these local moments are decoupled and spin-flips can take place,

(c) the sign of $\mathcal{J}$ is negative due to sp(d)–f admixture interactions.

Some of the Kondo systems investigated in this section are not in fact dilute magnetic alloys. Instead they are "Kondo lattices" in which the magnetic moments lie on a sublattice of the RI compound (e.g. $CeAl_2$). The R-atom in all these compounds is Ce for which the d–f admixture interaction mentioned in section 3.1.2 is dominant. Such RI compounds are therefore Kondo systems in which eq. (30) for the resistivity holds. However, for temperatures $T < T_K$ the magnetic moment is usually not totally compensated in a Kondo lattice since now there are too few conduction electrons to achieve full compensation on every magnetic lattice site.

Another feature of the Kondo lattice is that the same d–f admixture interaction which gives rise to the Kondo behaviour also generates an RKKY interaction between magnetic moments on different sites. The competition between the Kondo compensation and the magnetic ordering due to the RKKY interaction then determines the magnetic properties of the system. For example, $CeAl_2$ exhibits a Kondo-like minimum in the resistivity above the Neél temperature T_N. Below T_N the compound is an antiferromagnet. In contrast, $CeAl_3$ is non-magnetic because its f- and d-band are too broad to support magnetic moments.

3.1.3.4. *Critical phenomena at $T \sim T_c$ or T_N*

As was discussed in section 3.1.3 the resistivity curves for the RI compounds in question show pronounced kinks at T_{ord}. This is a critical phenomenon which is due to the influence of magnetism on electrical resistivity as shown schematically in fig. 13. It is therefore useful at this point to review the theory of critical phenomena in magnetically ordered systems. In particular, the Curie point T_c of a ferromagnet and the Neél point T_N of an antiferromagnet are examples of critical points which are analogous to critical points of liquid–vapour systems. Order–disorder phase transitions involving long-range order parameters occur at these magnetic critical points. For the ferromagnetic case the order parameter is the spontaneous magnetization M_0. At $T = 0$ the ferromagnetic spin systems of a pure crystal are completely ordered but with increasing temperature, M_0 decreases continuously. The breakdown of long-range magnetic order is initially slow, because when most of the spins are well aligned, a large amount of energy is required to reverse a spin in the presence of the exchange field. However, as the temperature increases, a breakdown of long-range order occurs more rapidly until the long-range order vanishes at the Curie point. Nevertheless, critical spin fluctuations still maintain a limited order among the spins in small regions of the

lattice which contain comparatively few spins well above T_c or T_N. When the temperature is sufficiently high ($T \gg T_c$ or T_N) complete disorder can be assumed. However, close to the critical point the amplitude of spin fluctuations is small, but the fluctuating domains are quite extended in space. The total net spontaneous magnetization is always zero above T_c.

Many physical properties are influenced by critical fluctuations. These include both equilibrium properties such as the specific heat and the magnetic susceptibility and non-equilibrium phenomena such as the transport properties. Here we distinguish between two classes of magnetic materials. One is the class which can be described in terms of localized spins represented by the rare earth compounds. The other class comprises the weak ferromagnetic materials whose magnetic properties can satisfactorily be explained using the band model. Our experiments on RI compounds show that an anomaly in the resistivity occurs only for the first class of magnetic materials for which the magnetic moments are localized. In rare earth compounds containing Al, Ni, Cu, Ag, Au, etc. the kink in the ρ vs. T curve in the vicinity of T_c or T_N is found to be extremely sharp, whereas practically no anomaly could be found at T_c for weak ferromagnetic substances like $ZrZn_2$ (Ogawa, 1976). De Gennes and Friedel (1958) examined the effect of short-range order spin fluctuations on the resistivity of ferromagnetic metals with localized spins interacting via the exchange Hamiltonian of eq. (19). The calculation was carried out in the first Born approximation using the Ornstein–Zernicke method for evaluating the static spin–spin correlation function needed to derive $\rho_{mag}(T)$. They found that $\rho_{mag}(T)$ close to T_c is given by

$$\rho_{max}(T) = \rho(T_c) - b \left|\frac{T - T_c}{T_c}\right| \ln\left|\frac{T - T_c}{T_c}\right|^{-1} \tag{31}$$

with $b > 0$.

Fisher and Langer (1968) improved the analysis by introducing a modified correlation function which gave a theoretical expression for the divergence in $d\rho_{mag}/dT$ similar to that found for the specific heat in the temperature range just above T_c. Richard and Geldart (1973) extended this model and showed that the result of Fisher and Langer also holds for temperatures below T_c. In antiferromagnetic materials $d\rho_{mag}/dT$ at T_N is influenced by the existence of superzones (Elliott and Wedgwood, 1963). The anomalous behaviour of transport properties at the magnetic critical points have been studied in detail by Ausloos et al. (1980) and applied to TbZn. Zoric et al. (1973) show that the product of the thermopower S and the resistivity ρ can be written as follows in the critical regime:

$$\rho S_e/T = A\rho_n + B\rho_c + C\Gamma(2k_F T). \tag{32}$$

S_e is the electron diffusion thermopower, ρ_n is the normal resistivity and ρ_c is the critical resistivity given by

$$\rho_c \propto k_F^{-4} \int_0^{2k_F} \Gamma(k, T) k^3 \, dk. \tag{33}$$

$\Gamma(k, T)$ is the spin–spin correlation function, k_F is the Fermi momentum, T is the temperature, and A, B, C are constants. If ρ_n is assumed to be linear in T, the derivation of eq. (32) can be written

$$d(\rho S_e/T)/dT = A' + B'\, d\rho_c/dT + C'\, d\Gamma/dT. \tag{34}$$

Zoric et al. (1973) then use eq. (34) in conjunction with "mental differentiation" of the curve of $\Gamma(k, T)$ vs. T of Fisher and Langer (1968) (see inset to fig. 54) to suggest the following qualitative differences between $d\rho/dT$ and $d(\rho S_e/T)/dT$ in the critical region:

(i) The anomaly in $d\rho/dT$ should be more articulated than that in $d(\rho S_e/T)/dT$.

(ii) The minimum in $d\rho/dT$ should be closer to T_c than $d(\rho/T)/dT$.

These results were used by Zoric et al. (1973) to analyse the critical behaviour of S_e for $GdNi_2$. This is discussed in section 3.2.2.4.

3.1.3.5. *Intermediate temperature range* ($0.2T_{ord} \leqslant T \leqslant T_{ord}$)

ρ_{mag} is usually temperature dependent in this temperature range. Below T_c the localized spins begin to order so that the conduction electrons scattering sharply decrease causing the pronounced kink at the ordering temperature. As was first demonstrated by Kasuya (1956) one can use the molecular field approximation instead of the s–f exchange interaction given in eq. (19) in the temperature regime $T \leqslant T_c$ or T_N. This model neglects correlations between the spins and only the interaction of a spin with the average exchange field produced by the neighbouring spins is taken into account. The scattering of the conduction electrons by a particular local moment at R_j is now due to the difference between $\boldsymbol{S}$ and $\langle \boldsymbol{S} \rangle_T$ where $\langle \boldsymbol{S} \rangle_T$ is the average ionic spin. The Hamiltonian for the molecular field model is then given by

$$\tilde{H} = -\mathcal{J}s \cdot (\boldsymbol{S} - \langle \boldsymbol{S} \rangle_T). \tag{35}$$

The magnetic contribution ρ_{mag} to the resistivity can now be calculated using $\tilde{H}$ of eq. (35) and the result is given by

$$\rho_{mag}(T) = \rho_{spd}\left[1 - \frac{\langle \boldsymbol{S} \rangle_T^2}{S(S+1)}\right], \tag{36}$$

where ρ_{spd} is the spin-disorder resistivity (see above). A knowledge of $\langle \boldsymbol{S} \rangle_T$ as a function of temperature enables us to obtain the temperature dependence of ρ_{mag} for $T \leqslant T_c$ or T_N.

3.1.3.6. *Low-temperature regime* ($T \ll T_c$ *or* T_N)

In the lowest temperature regime the magnetic properties of the RI compounds discussed in this section can be described satisfactorily using the spin wave model. The low-energy collective excitations of a system of coupled 4f moments are known as spin waves. Therefore at low temperatures the conduction electrons can be scattered both by phonons and by spin waves. In most of the magnetic materials electron spin wave scattering gives a large contribution to the total resistivity. In particular, several authors (Kasuya, 1959; Mannari, 1959; Volkenshtein et al., 1973) derived a T^2 dependence for the spin wave contribution to the total resistivity in ferromagnetic materials. Such calculations

require a knowledge of the spin wave spectrum $\omega(q)$ at small q. A T^2 dependence of the spin waves resistivity for ferromagnets was obtained by assuming that $\omega(q) \propto q^2$ for ferromagnetic materials. However, the temperature dependence of the resistivity of ferromagnets is modified when a gap Δ_s in the spin wave spectrum occurs due to magnetic anisotropy (Mackintosh, 1963)

$$\rho(T) = AT^2 \exp(-\Delta_s/k_B T). \tag{37}$$

Δ_s represents the minimum energy required to excite a spin wave in the anisotropy field. The assumption of $\omega(q) \propto q$ for the spin waves in antiferromagnetic materials gives a T^4 temperature dependence in resistivity. The T^4 law, however, is questionable for two reasons: (i) more sophisticated calculations for the resistivity of antiferromagnetic materials at low temperature give (Yamada and Takada, 1974)

$$\rho(T) = \begin{cases} AT^5 & \text{for } T_N \gg T \gg T_D \\ BT \exp(-\sqrt{TT_D}/T) & \text{for } T_N, T_D \gg T, \end{cases} \tag{38}$$

where T_N is the Neél temperature and T_D is the temperature corresponding to the anisotropy energy of the spin system. (ii) There appears to be as yet no experimental verification of any of the calculated temperature dependences in the case of antiferromagnetic order.

3.1.4. *Influence of localized magnetic moments on thermopower*

For systems containing localized magnetic moments, the thermopower has not been theoretically investigated in such detail as the resistivity. An expression for the thermopower of ferromagnetic materials with localized moments has been obtained by Kasuya (1959) in both the molecular field approximation and the spin wave approximation. In the former case, Kasuya used a molecular field approximation to obtain the energy spectrum of the conduction electrons and the localized magnetic moments. In addition he assumed that the spin-flip transition probabilities for scattering of electrons by local moments dominate the non-spin-flip transition probabilities.

He then obtained the following result for the thermopower

$$S(T) = S_e + S_{mag}, \tag{39}$$

where S_e is given by eq. (4) and S_{mag}, the anomalous magnetic thermopower in the molecular field approximation, reads

$$S_{mag} = \frac{2H_c k_B}{\epsilon_F e} \left\{ \frac{1 - \exp(-H_0/k_B T)}{1 + \exp(-H_0/k_B T)} \right\}. \tag{40}$$

ϵ_F is the Fermi energy, H_0 is the molecular field for the localized spin and H_c is the molecular field for the conduction electrons. H_0 is given by

$$H_0 = 2(g-1)\mathcal{J}\langle\sigma\rangle_z, \tag{41}$$

where $\mathcal{J}$ is the direct exchange integral of the (sp)–f interaction of eq. (19) and $\langle\sigma\rangle_z$ is the average polarization of the conduction band. The expression for the

anomalous magnetic thermopower in the spin wave approximation is quite complicated and will not be reproduced here. These results will be used to discuss the thermopower data for RAl_2 compounds.

3.1.4.1. *Magnon drag*

Magnon drag is analogous to phonon drag and was first analysed theoretically by Bailyn (1962). The magnons therefore create an additional thermopower by driving the electrons along their thermal gradient. Bailyn showed that the expression for the thermopower S_m due to magnon drag is similar in form to the phonon drag thermopower S_g. This implies that S_m and S_g are difficult to distinguish. However, at low temperatures S_m is proportional to the contribution of the specific heat due to magnons and therefore varies as $T^{3/2}$. Thus S_m and S_g could be distinguished if their magnitude were comparable. This does not seem to be the case. An analysis of the specific heat of Ni and Fe at 50 K leads to the conclusion that S_m is 200 times smaller than S_g for these metals. An increase in the size of the magnetic moment will result in an increase of S_m. For example, Bhandari and Verma (1969) have argued that S_m is 5% of S_g for pure Gd, though Umklapp processes were neglected in their theory.

Not all authors agree that magnon drag is always negligible. For example, Blatt et al. (1967) ascribed the pronounced peak at 200 K in the thermopower of Fe to magnon drag. Further Trego and Mackintosh (1968) give evidence that magnon drag effects occur in the thermopower of antiferromagnetic chromium. For more details see Blatt et al. (1976).

Experimental data presented in section 3.1.4 for the thermopower of magnetic RI compounds also suggest that magnon drag effects may indeed influence the thermopower quite strongly. For example, a pronounced peak is found in $GdAl_2$ at 80 K whereas no such anomaly occurs in the thermopower of the isostructural YAl_2. This is discussed further below.

3.1.4.2. *Kondo effect*

It is well known that dilute magnetic alloys which have a Kondo minimum in the resistivity, also exhibit a giant thermopower anomaly. This anomaly was first treated theoretically by Kondo (1965) and later by Suhl and Wong (1967), Fischer (1967) and Maki (1969).

Kondo's treatment omitted several important interaction terms but the latter authors were able to show that the thermopower depends in an interconnected manner on exchange coupling, potential scattering, and the range of the interaction (see Blatt et al., 1976). No theoretical work has as yet been done for Kondo lattices. However, the thermopower of $CeAl_2$ which is a Kondo lattice does in fact show a giant thermopower anomaly similar to that found in dilute Kondo alloys.

3.1.4.3. *Contribution of spin-disorder scattering to the thermopower in* $T > T_{ord}$

Gratz (1981) was able to obtain the contribution of spin-disorder scattering to the thermopower by using the Nordheim–Gorter rule in the following manner. The thermopower of the following RI compounds was compared: YAl_2 and $GdAl_2$ ($MgCu_2$ structure), YCu_2 and $GdCu_2$ ($CeCu_2$ structure), and LaNi and GdNi (orthorhombic CrB structure). The above selection of RI compounds

allows for the comparison of the thermopower of a non-magnetic compound and that of a magnetic compound with the same crystal structure. Gd was chosen as the magnetic component of the compound because it is in an s-state ion, and the effect of magnetic anisotropy on the thermopower is therefore avoided.

The Nordheim–Gorter rule is given for non-magnetic RI compounds by

$$S_e^{nm} = \frac{\rho_0}{\rho} S_0 + \frac{\rho_{ph}}{\rho} S_{ph} \tag{42}$$

and for magnetic RI compounds by

$$S_e^{m} = \frac{\rho_0}{\rho} S_0 + \frac{\rho_{ph}}{\rho} S_{ph} + \frac{\rho_{spd}}{\rho} S_{spd}. \tag{43}$$

S_e^{nm} and S_e^{m} denote the diffusion thermopower of a non-magnetic RI compound and a magnetic RI compound, respectively. S_0, S_{ph}, and S_{spd} are the contributions to the thermopower due to impurity scattering, phonon scattering, and spin-disorder scattering, respectively. ρ, ρ_0, ρ_{ph}, and ρ_{spd} represent the total resistivity, and residual resistivity, the phonon resistivity, and the spin-disorder resistivity, respectively.

The first two terms in eq. (43) are replaced by S_e^{nm} of eq. (42). This is equivalent now to the assumption that to the first approximation the impurity and the phonon contribution of corresponding magnetic and non-magnetic compounds are equal. These considerations lead to the following expression for the spin-disorder contribution for the thermopower of GdX (X = Al_2, Cu_2, Ni)

$$S_{spd} = [S_e^{m}(T) - S_e^{nm}(T)] \frac{\rho}{\rho_{spd}}, \tag{44}$$

ρ is the total resistivity of GdX and ρ_{spd} is the spin-disorder contribution to the resistivity of the corresponding magnetic compound. Gratz (1981) analysed the data for the above-mentioned compounds GdX using eq. (44). The results are given in fig. 14 which shows that S_{spd} has a linear temperature dependence well

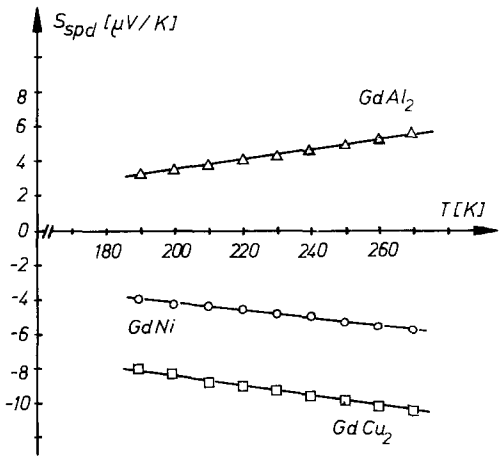

Fig. 14. Temperature dependence of S_{spd} for $GdAl_2$, $GdCu_2$, and GdNi (Gratz, 1981).

above T_c for each compound and that the magnitude of the gradient is the same for all compounds within the experimental error. However, the signs of the gradients are different. This is probably due to differences in the band structures.

The analysis of the thermopower of other magnetic R-compounds (RAl_2, RCu_2) using eqs. (42)–(44) shows that S_{spd} is a linear function of the temperature and the slope behaves in a systematic manner as a function of the rare earth. Another analysis which uses the method of Foiles (1980, 1981) is in progress. The results will be published elsewhere.

3.2. *Experimental results and discussion*

3.2.1. *Electrical resistivity data*

3.2.1.1. *RAl_2 (R = Y, La, Pr, Nd, Sm, Gd, Tb, Dy, Ho, Er, Tm)*

The temperature dependence of the resistivity of the heavy RAl_2 compounds (R = Gd, Tb, Dy, Ho, Er, Tm) is shown in fig. 15. Note the similarity of the ρ vs. T curves to the behaviour predicted by fig. 13. The dependence of ρ_{spd} on the de Gennes factor $(g-1)^2J(J+1)$ for the heavy RAl_2 compounds is shown in fig. 16. The numerical values for ρ_{spd} obtained by Van Daal and Buschow (1969a) and those quoted in Gratz et al. (1981a) are presented in this figure. The agreement with the theoretical model discussed in section 3.1.3 and given by eq. (23) is seen to be satisfactory. The ρ vs. T curves of some of the light RAl_2 compounds (R = La, Pr, Nd, Sm) are shown in fig. 17.

3.2.1.2. *RCu_2 (R = Pr, Nd, Sm, Gd, Tb, Dy, Ho, Er, Tm)*

The temperature dependence of the electrical resistivity of most of the RCu_2 compounds is shown in fig. 18 ($PrCu_2$, $NdCu_2$, $SmCu_2$), fig. 19 ($GdCu_2$, $TbCu_2$, $DyCu_2$), fig. 20 ($HoCu_2$, $LuCu_2$), and fig. 21 ($ErCu_2$, $TmCu_2$) (Sassik and Gratz,

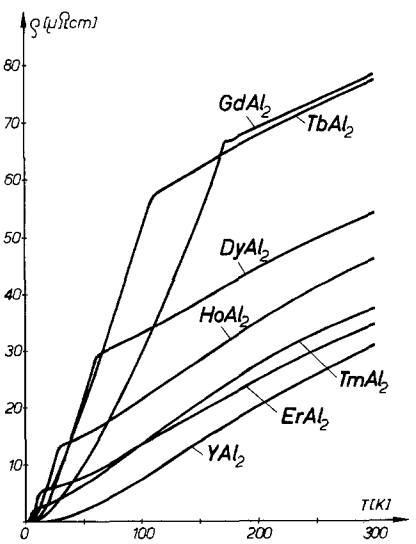

Fig. 15. ρ vs. T curves of heavy RAl_2 compounds (Van Daal and Buschow, 1969a).

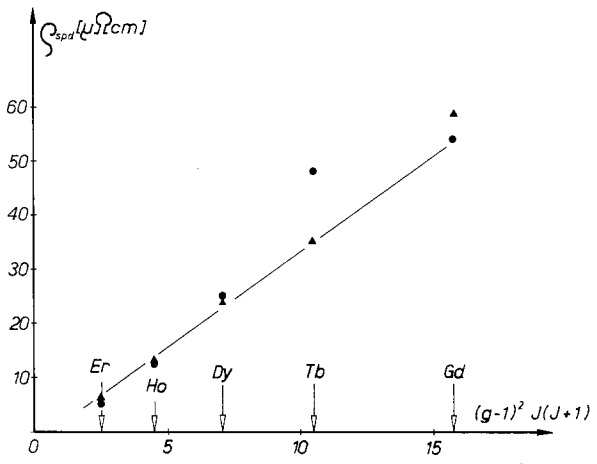

Fig. 16. The dependence of ρ_{spd} on the de Gennes factor $(g-1)^2 \times J(J+1)$ of some heavy RAl_2 compounds. (● Van Daal et al., 1969a; ▲ Gratz et al., 1981a).

1981). The RCu_2 compounds crystallize in the orthorhombic $CeCu_2$ structure except for $LaCu_2$ which crystallizes in the hexagonal AlB_2 structure.

The RCu_2 compounds are all antiferromagnets except for YCu_2, $LaCu_2$, $CeCu_2$, $SmCu_2$, and $LuCu_2$ where no magnetic order could be found. An anomaly in susceptibility and specific heat measurements of $PrCu_2$ was found at 54 mK by Andres et al. (1972) which was interpreted as due to the onset of antiferromagnetism at this temperature. The Neél temperatures of the heavy RCu_2 compounds were first measured by Sherwood et al. (1964) and later by Hashi-

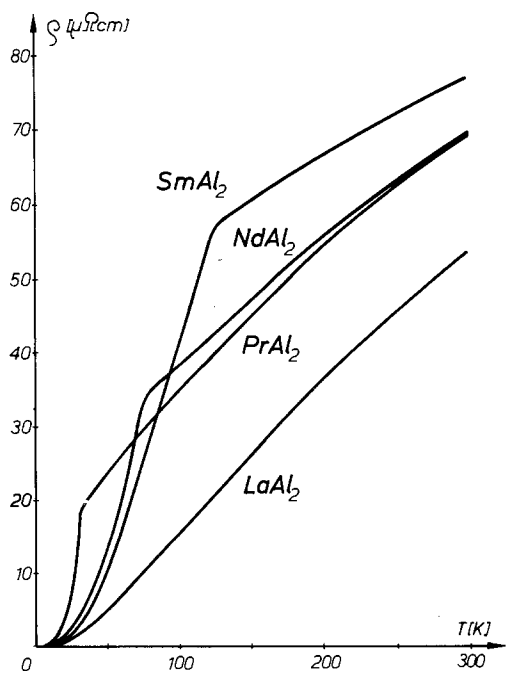

Fig. 17. ρ vs. T curves of some light RAl_2 compounds (Van Daal and Buschow, 1969a).

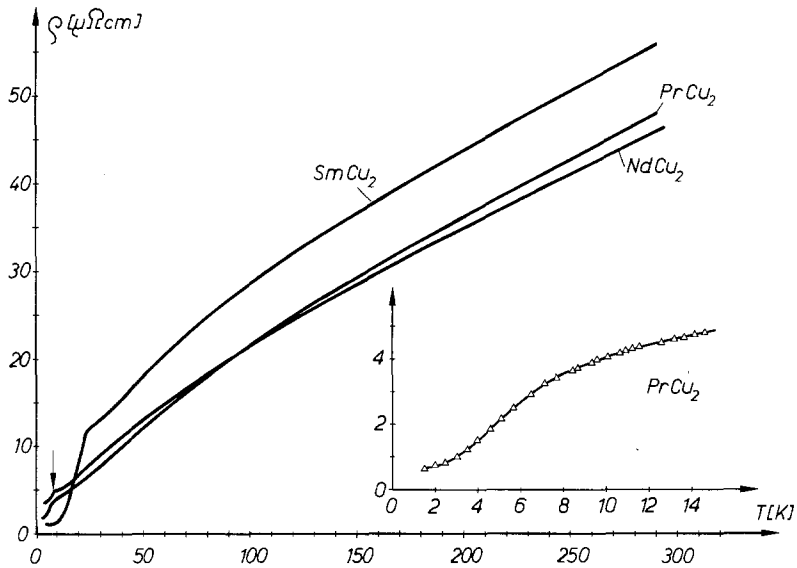

Fig. 18. ρ vs. T curves of $PrCu_2$, $NdCu_2$, and $SmCu_2$. The inset shows the resistivity behaviour in the vicinity of the Jahn–Teller transition temperature in $PrCu_2$ (Sassik and Gratz, 1981).

moto et al. (1979a, b). Sassik and Gratz (1981) obtained the Neél temperatures of these compounds from initial susceptibility measurements using samples which were then used for transport measurements. Their results were in agreement with the previous investigations cited. The highest value of T_N in the RCu_2 series was found for $TbCu_2$ ($T_N = 53$ K) whereas that found in most other series is for

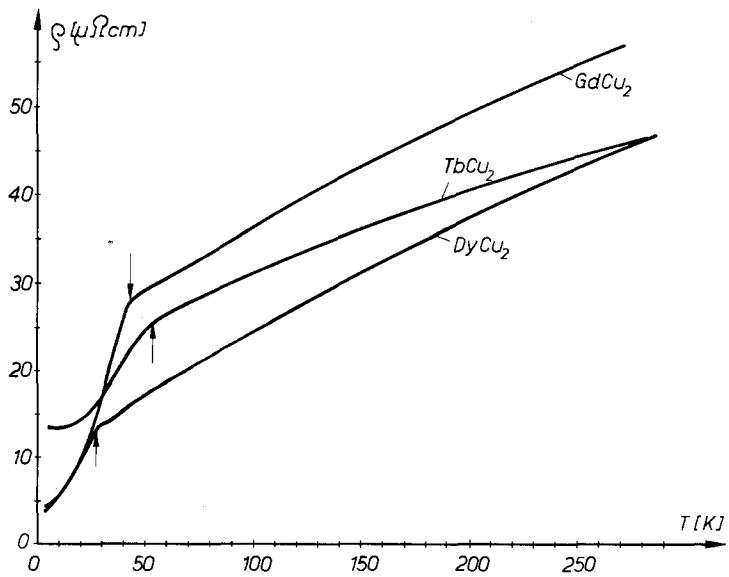

Fig. 19. ρ vs. T curves of $GdCu_2$, $TbCu_2$, and $DyCu_2$ (Sassik and Gratz, 1981).

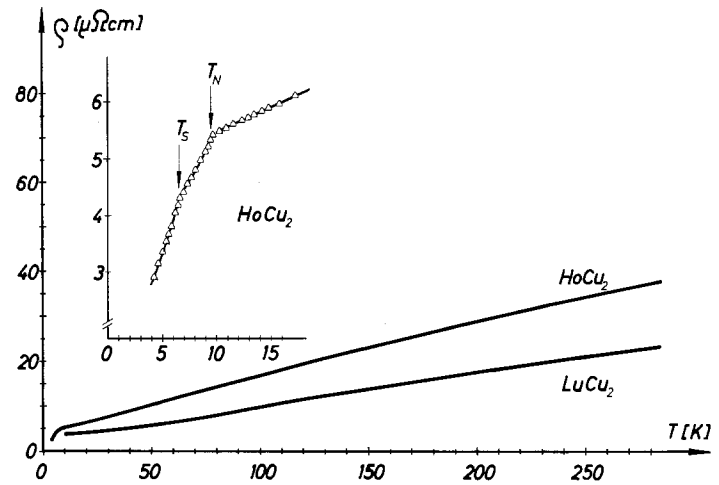

Fig. 20. ρ vs. T curves of $HoCu_2$ and $LuCu_2$. The inset shows the resistivity behaviour in the vicinity of the order-to-order transition, T_S, and the Neél temperature, T_N, of $HoCu_2$ (Gratz et al., 1982a).

Gd compounds. A kink occurs in the ρ vs. T curves of the magnetically ordered compounds. Kinks are also observed in the ρ vs. T curve of the compounds $PrCu_2$ and $SmCu_2$ at 8 K and 25 K, respectively. The data for $PrCu_2$ are analysed below, while no explanation has been offered for the kink in the resistivity of $SmCu_2$.

Wun and Phillips (1974) conclude from specific heat measurements that the two low-lying singlet states of the Pr^{3+} ion are further split due to the Jahn–Teller effect below 7 K. Andres et al. (1976) found that the susceptibility of

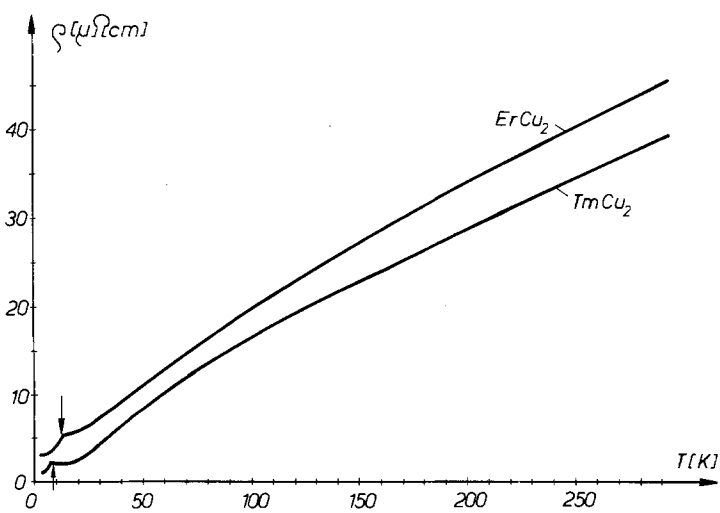

Fig. 21. ρ vs. T curves of $ErCu_2$ and $TmCu_2$ (Sassik and Gratz, 1981).

$PrCu_2$ shows hardly any anomaly while a marked anomaly is observable in the resistivity. The resistivity measurements on a $PrCu_2$ single crystal performed by Andres et al. (1976) show strong anisotropic behaviour for the *a*, *b*, and *c* direction of this orthorhombic structure. Because of the temperature-independent nature of this anisotropic behaviour Andres et al. (1976) conclude that the anisotropy in the resistivity is due to the anisotropy of the Fermi surface and not due to anisotropy in the scattering cross section between conduction electrons and f-electrons.

The inset in fig. 18 shows the ρ vs. T curve of polycrystalline $PrCu_2$ obtained by Sassik and Gratz (1981) in the vicinity of the Jahn–Teller transition temperature. Fig. 18 also shows the ρ vs. T behaviour of $NdCu_2$. The arrow indicates the magnetic ordering temperature.

The kinks in the resistivity curves of $GdCu_2$, $TbCu_2$, and $DyCu_2$ all correspond with the Neél temperature. Magnetic measurements showed that a change of the magnetic structure below T_N occurs in $HoCu_2$ (Gratz et al. 1982a), which also has an effect on the $\rho(T)$ behaviour. The ρ vs. T curves of $HoCu_2$ together with those of the non-magnetic $LuCu_2$ are given in fig. 20. The inset in this figure shows the ρ vs. T curve of $HoCu_2$ in the vicinity of the Neél temperature T_N and the order to order transition temperature T_s (6.5 K). Evidence of a change in the magnetic structure was also found in the resistivity data of the pseudobinary $Tb(CuNi)_2$ system and of some RAg_2 and RAu_2 compounds (see sections 3.2.1.5–3.2.1.7). Fig. 21 gives the ρ vs. T curves of $ErCu_2$ and $TmCu_2$ which behave as expected.

3.2.1.3. *$PrAl_3$*

$PrAl_3$ is considered to be a classical example for the effect of crystal field on local R-moments in the paramagnetic state. The results obtained for this compound from heat capacity, susceptibility, and spin-disorder resistivity provide a unique description of such effects on physical properties (Wallace et al., 1977). Non-magnetic $PrAl_3$ crystallizes in the hexagonal Ni_3Sn structure. A comparison of the experimental results and the corresponding calculations for the susceptibility, the specific heat, and the resistivity of $PrAl_3$ is shown in figs. 22, 23, and 24, respectively. The same crystal field parameter has been used for all calculations. Fig. 22 also includes the corresponding energy level scheme. $\rho_{spd}(T)$ and $\rho_{spd}(T = \infty)$ were calculated using eqs. (27) and (23), respectively.

3.2.1.4. *$Gd(Al_{1-x}Cu_x)_2$; $0 \leq x \leq 0.3$*

The pseudobinary compounds $Gd(Al_{1-x}Cu_x)_2$ are used to study the effect of the variation of the conduction electron concentration on the ordering temperature and the resistivity (Sakurai et al., 1977). The ρ vs. T curves of several samples of this cubic pseudobinary system are given in fig. 25. The concentration dependence of ρ_{spd} and of the Curie temperature are shown in fig. 26. $\rho_{spd}(x)$ and $T_c(x)$ vary in a similar manner with increasing Cu concentration. The change in these two quantities can be explained by the variation of the exchange integral $\mathcal{J}$ with conduction electron concentration (Sakurai et al., 1977).

3.2.1.5. *$R(Ni_xCu_{1-x})_2$, (R = Tb, Gd): $0 \leq x \leq 0.4$*

The concentration dependence of ρ_{spd} in $R(Ni_xCu_{1-x})_2$ (R = Tb, Gd) ($0 \leq x \leq$

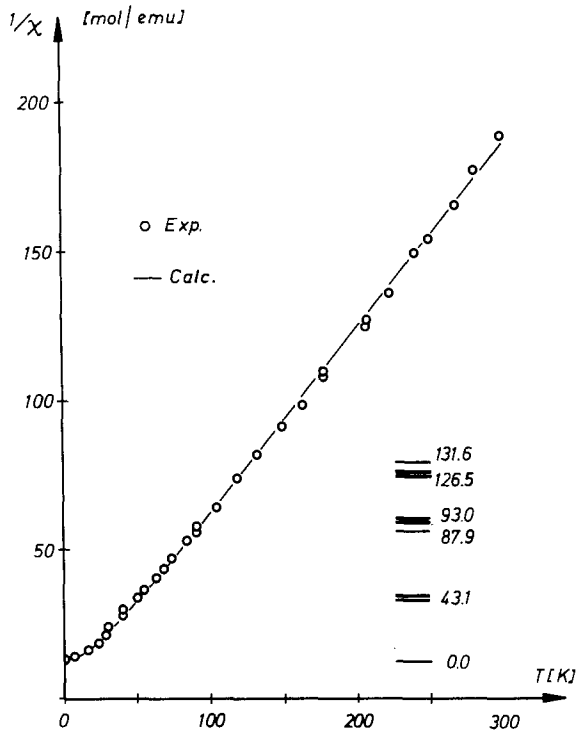

Fig. 22. Experimental and calculated inverse susceptibility of $PrAl_3$ as a function of temperature (Wallace et al., 1977).

0.4) has been investigated by Gratz and Poldy (1977) and Poldy and Gratz (1978). In both of these orthorhombic pseudobinaries (having $CeCu_2$ structure), a transition from an antiferromagnetic to a ferromagnetic ordered state was found which depends on the Ni concentration. The critical concentration is about 13% Ni in the Gd system and 8% Ni in the Tb system. The temperature dependence

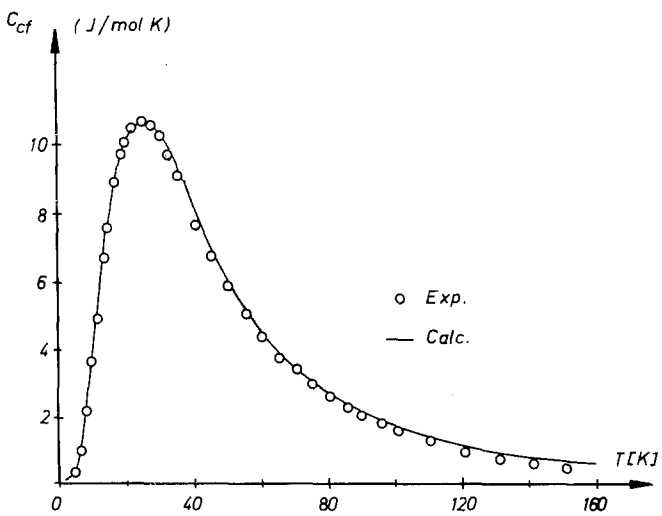

Fig. 23. Experimental and calculated crystal field heat capacity of $PrAl_3$ as a function of temperature (Wallace et al., 1977).

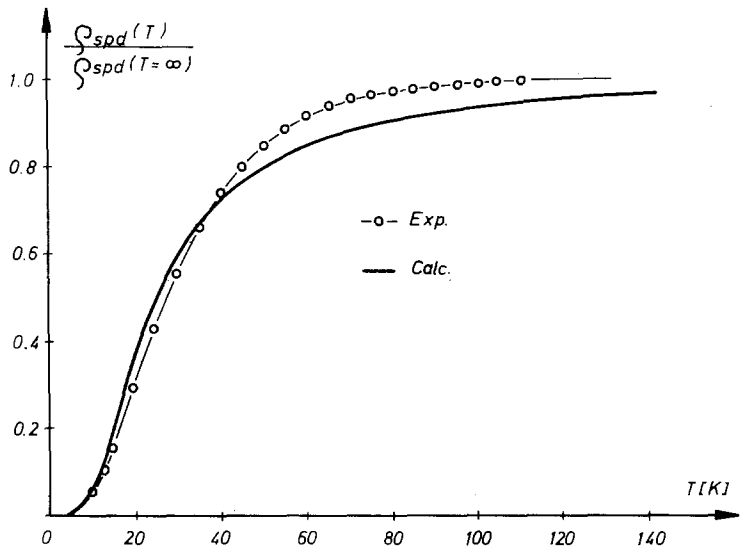

Fig. 24. Comparison of experimental and calculated ρ_{spd} data in a reduced representation ($\rho_{spd}(T)$ is given by eq. (27), $\rho_{spd}(T = \infty)$ is given by eq. (23) (Wallace et al., 1977).

of resistivity in the $Tb(Ni, Cu)_2$ system is given in fig. 27. The corresponding concentration dependence of ρ_{spd} for both pseudobinaries is shown in fig. 28. In both cases jumps related to the change of the magnetic structure in ρ_{spd} were found at the critical concentration. It follows that these anomalies can be explained by the influence of superzone boundaries on the resistivity (Gratz and Poldy, 1977). Superzone boundaries exist if the static arrangement of localized

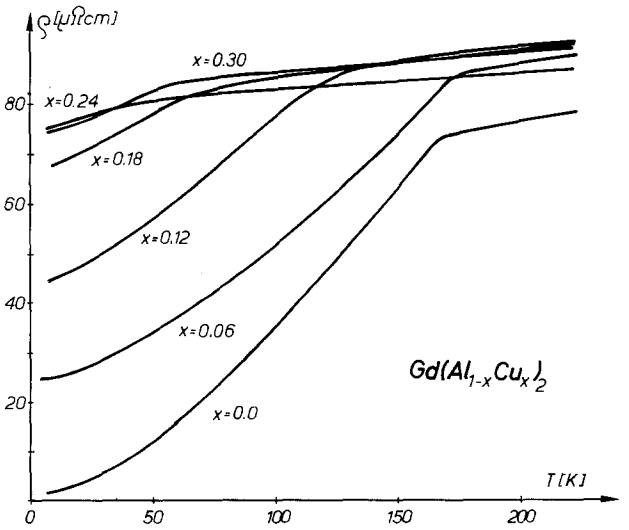

Fig. 25. ρ vs. T curves of several concentrations of the $Gd(Al_{1-x}Cu_x)_2$ pseudobinary system (Sakurai et al., 1977).

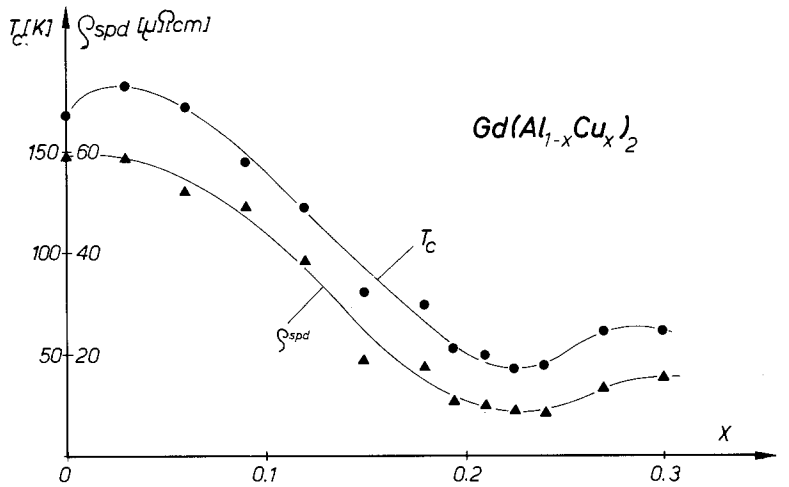

Fig. 26. ρ_{spd} and T_c as a function of the Cu concentration in $Gd(Al_{1-x}Cu_x)_2$ (Sakurai et al., 1977).

moments is not collinear (e.g. for an antiferromagnetic or spin spiral structure). The non-collinearity gives rise to an exchange field which acts on the conduction electrons with a lower symmetry than that of the lattice (Elliott and Wedgwood, 1963). The superzone effect makes the use of ρ_{spd} in eq. (23) for the calculation of the parameters $|\mathcal{J}|$ and m^* meaningless. This is the reason for the step obtained in the (Gd, Y) binary system as will be seen in section 3.2.1.13.

No sharp kink at T_N is observable in the resistivity of the antiferromagnetically ordered samples of the $Tb(Ni, Cu)_2$ system. Instead a pronounced increase in the ρ vs. T curves at about 30 K was found and is shown in fig. 27. Magnetic

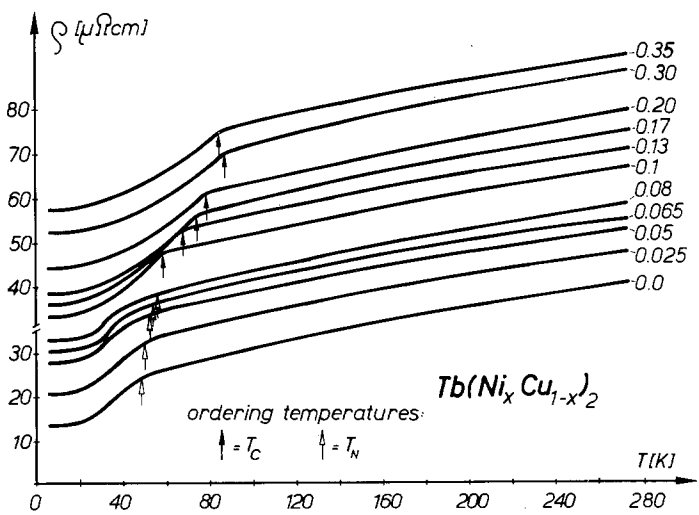

Fig. 27. ρ vs. T curves of several concentrations of the $Tb(Ni_xCu_{1-x})_2$ pseudobinary system (Poldy and Gratz, 1978).

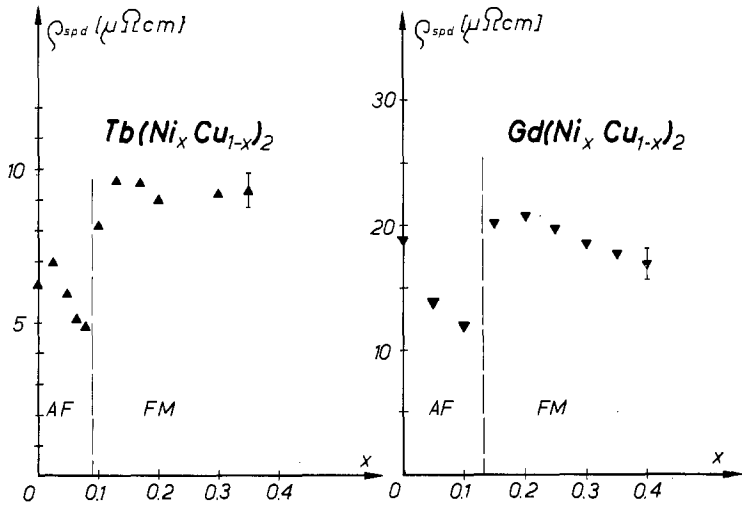

Fig. 28. Concentration dependence of ρ_{spd} in $R(Ni_xCu_{1-x})_2$ (R = Gd, Tb) pseudobinaries (AF = antiferromagnetism, FM = ferromagnetism) (Gratz and Poldy, 1977).

measurements (Poldy and Gratz, 1978) show that a change of the magnetic structure appears above 30 K and the ordering temperatures in the samples with $x = 0.05$, 0.065, and 0.08 in the $Tb(Ni_xCu_{1-x})_2$ system are indicated in fig. 27 by arrows. This kind of transition between ordered phases is typical of most of the heavy RA_2 compounds (A = Cu, Ag, Au) as will be shown for the RAg_2 and RAu_2 system (see sections 3.2.1.6 and 3.2.1.7).

3.2.1.6. *RAg_2 (R = Gd, Tb, Dy, Ho, Er)*

The heavy RAg_2 compounds crystallize in the $MoSi_2$ structure. Magnetic measurements give Neél temperatures in the range of 5 K for $ErAg_2$ and 25 K for $GdAg_2$ (Miura et al., 1974). The temperature dependence of the resistivity of these compounds according to Ohashi et al. (1975) is shown in fig. 29. In some of the compounds (R = Dy, Ho, Er) an abrupt increase in resistivity with increasing temperature was observed below the ordering temperature T_N. However no such anomalies in the resistivity or the magnetic properties were observed for $GdAg_2$ and $TbAg_2$. The sharp increases (as marked by the arrows in fig. 29) indicate transitions between ordered phases similar to those found in RAu_2 compounds (see section 3.2.1.7). $|\mathcal{J}|$ was found to be about 0.08 eV from the experimental data for ρ_{spd} and eq. (23). This value is considerably smaller than the value for $|\mathcal{J}|$ obtained from magnetic investigations (Miura et al., 1974; Ohashi et al., 1975). This is because eq. (23) is not applicable to antiferromagnetic systems (Gratz and Poldy, 1977).

3.2.1.7. *RAu_2 (R = Gd, Tb, Dy, Ho, Er)*

The RAu_2 compounds crystallize in the $MoSi_2$ structure. Neutron diffraction experiments (Atoji, 1969) have shown that most of these compounds exhibit a layered antiferromagnetic spin structure below $T_N(\beta)$ and a linear-transverse wave spin structure between $T_N(\beta)$ and $T_N(\alpha)$. The temperature dependence of

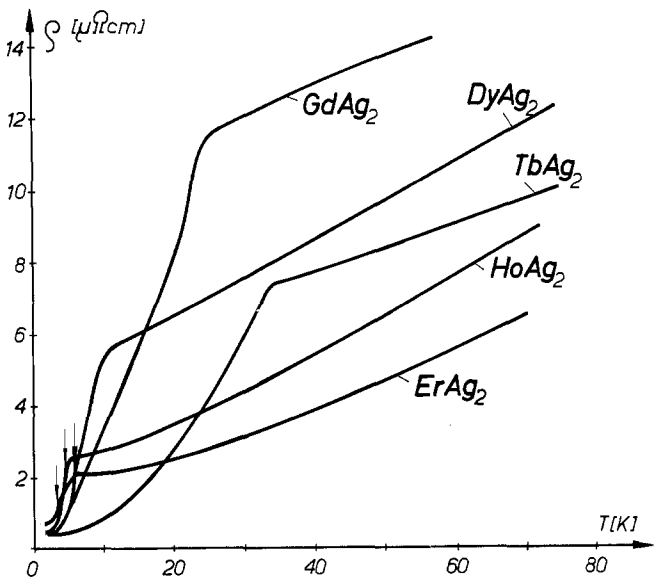

Fig. 29. ρ vs. T curves of some RAg_2 compounds (R = Gd, Tb, Dy, Ho and Er). The arrows indicate and order-to-order transitions in $ErAg_2$, $HoAg_2$, and $DyAg_2$ (Ohashi et al., 1975).

the resistivity of these compounds is shown in fig. 30 (Kaneko et al., 1974). The jump in the ρ vs. T curves for $TbAu_2$, $DyAu_2$, and $HoAu_2$ is due to the magnetic transition between ordered phases discussed above. In contrast to the RAl_2 compounds ρ_{spd} is not proportional to the de Gennes factor for the RAu_2 systems. The experimentally determined ρ_{spd} values were used to calculate the exchange integral $|\mathcal{J}|$ (Kaneko et al., 1974) as in the RAg_2 system (see section 3.2.1.6).

3.2.1.8. *RA (R = Gd, Tb, Dy, Ho, Er, Tm; A = Cu, Ag, Au)*

The electrical resistivity of a number of CsCl structure type binary systems is shown in fig. 31 (RCu), fig. 32 (RAg), and fig. 33 (RAu) (R = Gd,

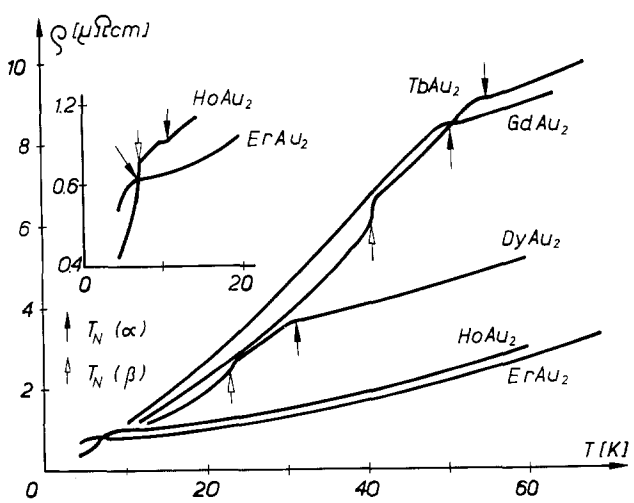

Fig. 30. ρ vs. T curves of some RAu_2 compounds (R = Gd, Tb, Dy, Ho, and Er) (Kaneko et al., 1974).

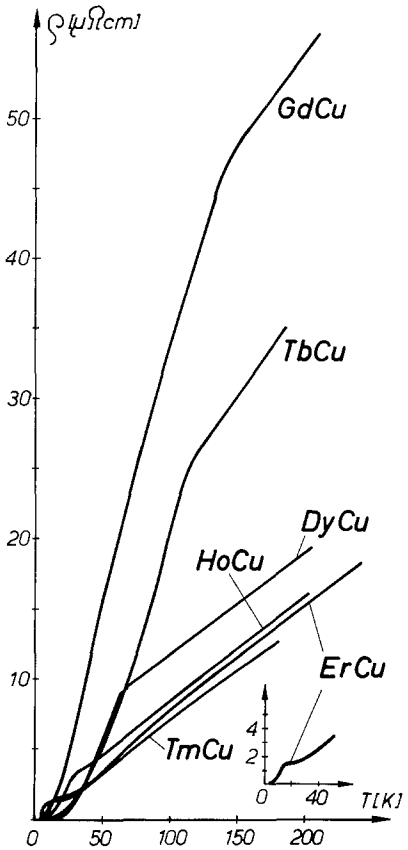

Fig. 31. ρ vs. T curves of some magnetic RCu compounds (Chao Chang-Chih, 1966).

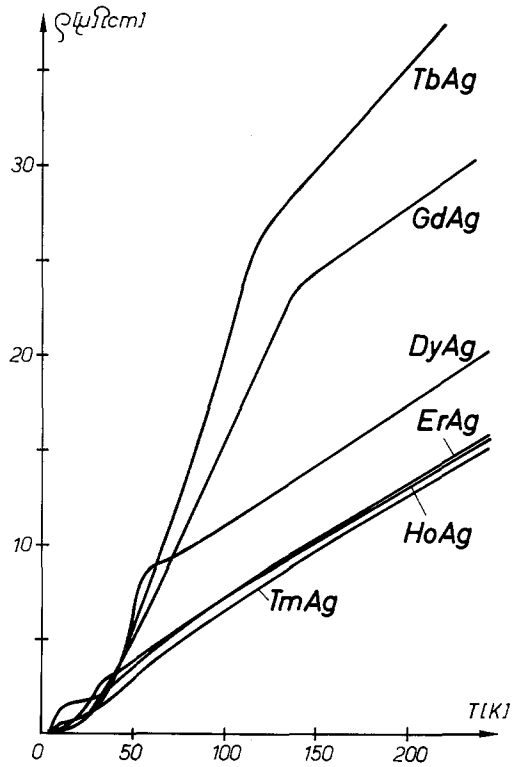

Fig. 32. ρ vs. T curves of some magnetic RAg compounds (Chao Chang-Chih, 1966).

Tb, Dy, Ho, Er, Tm) (Chao Chang-Chih, 1966). The residual resistivity was subtracted out in all the cases. The shape of the ρ vs. T curves is in agreement with those one expects for materials possessing local moments only, as represented by the schematic diagram of fig. 13. It should, however, be pointed out that in the case of low magnetic ordering temperatures (<20 K) the ρ vs. T curves are not linear just above the transition temperature (see e.g. the inset of fig. 31). This is due to the fact that the phonon contribution ρ_{ph} is not a linear function of temperature in this temperature range. The experimental data were also used to obtain ρ_{spd} by the extrapolation method (Chao Chang-Chih, 1966). This method is not applicable to systems with low ordering temperatures and resulted in a negative sign of the ρ_{spd} values. It is preferable to subtract the resistivity value of the isostructural non-magnetic Y-compound assuming that the phonon contribution ρ_{ph} for the magnetic and the non-magnetic compound is the same (Pierre, 1969). Use of this method excludes the effect of the superzone boundary in the analysis in ρ_{spd}. The spin-disorder resistivity ρ_{spd} is not proportional to the de Gennes factor for these compounds (Chao Chang-Chih, 1966).

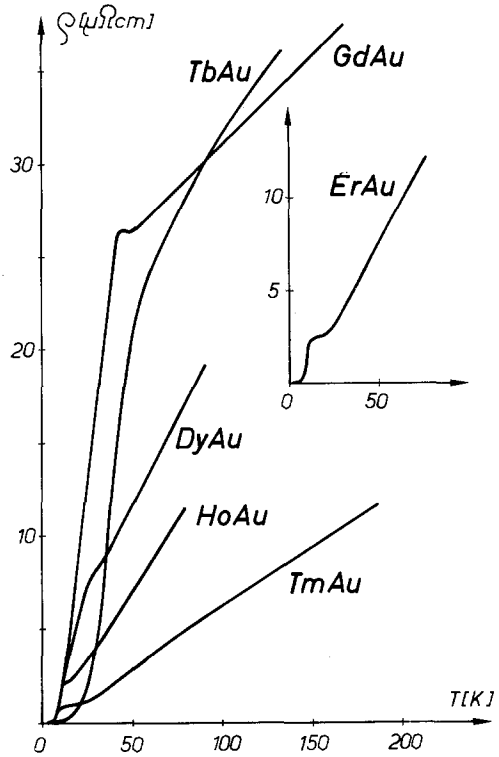

Fig. 33. ρ vs. T curves of some magnetic RAu compounds (Chao Chang-Chih, 1966).

3.2.1.9. *RCd* (R = *Sm, La*)

These compounds crystallize in the CsCl structure. Fig. 34 shows the temperature dependence of resistance, $R(T)$, of the magnetic compound SmCd (T_c = 194 K) and the non-magnetic compound LaCd which is superconducting below 3 K (Stewart et al., 1974). The shape of the R vs. T curve of SmCd is typical of a material possessing localized magnetic moments. Magnetization data for SmCd at 77 K exhibit extremely small magnetic moments for the Sm ions ($0.05\mu_B$ per Sm) (Stewart et al., 1974). One possible explanation is that the small bulk magnetization is due to the magnetic order being non-collinear (e.g. conical spiral) which does not allow the Sm moments to become parallel until a large external magnetic field is applied. The influence of the crystal field which would reduce the magnetic moment of the Sm atoms in the ordered state was also discussed by Stewart et al. (1974). The shape of the resistance curve (pronounced kink at T_c and large values of ρ_{spd}) implies a much larger magnetic moment on the Sm atoms. No anomaly was reported by Stewart et al. (1974) apart from the jump in the resistance curve of LaCd at about 3 K indicating the onset of superconductivity. In another investigation (Ihrig, 1973) a small jump in the resistivity curve was measured at 70 K; it can be explained in terms of a structural transition which occurs in LaCd at this temperature (Ihrig et al., 1973). The influence on such structural transitions on resistivity is described in section 2.2.1.3 for the La(Ag, In) and Ce(Ag, In) compounds.

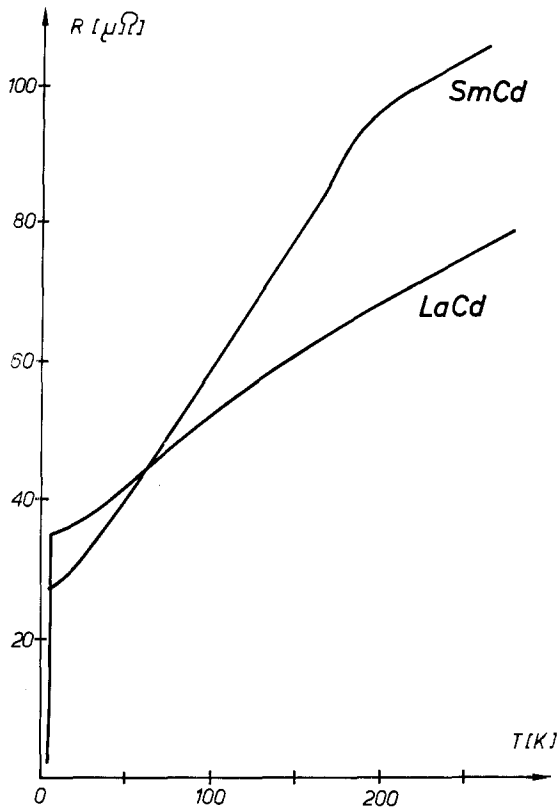

Fig. 34. Temperature dependence of electrical resistance, $R(T)$, of SmCd and LaCd. The discontinuity in the $R(T)$ curve of LaCd indicates the superconducting transition (Stewart et al., 1974).

3.2.1.10. RA_2 (R = *Gd, Dy*; A = *Al, Ni, Co, Rh, Pt*)

The critical phenomena at T_c were investigated for six ferromagnetic R-cubic Laves phase compounds ($GdAl_2$, $DyAl_2$, $GdNi_2$, $GdCo_2$, $GdRh_2$, and $GdPt_2$) by Kawatra et al. (1970). All samples are characterized by pronounced anomalies in the $d\rho/dT$ vs. T dependence in the vicinity of the Curie temperature T_c. Both the electrical resistivity and the computed values of $d\rho/dT$ vs. T for $GdNi_2$, $GdRh_2$, and $GdPt_2$ are shown from 4.2 K to room temperature in fig. 35. All three $d\rho/dT$ vs. T curves show a broad maximum at high temperature well above T_c and a minimum as T is decreased. This is followed by a sharp rise towards a well-defined maximum. The temperature corresponding to the maximum for each system is associated with the magnetic ordering temperature. The magnetic behaviour in these systems is explained in terms of s–f exchange fluctuations in the short-range order which contribute significantly to the conduction electron scattering close to T_c. According to the interpretation given by Kawatra et al. (1970) the shape of the $d\rho/dT$ curve can be explained using the spin-correlation function derived by Kim (1964) and de Gennes and Friedel (1958). The application of this correlation function leads to a cusp in the ρ vs. T curve and an infinite discontinuity in $d\rho/dT$ vs. T, with positive values for $d\rho/dT$ for $T < T_c$ and negative values for $T > T_c$. Fig. 36 shows the ρ vs. T curves and the

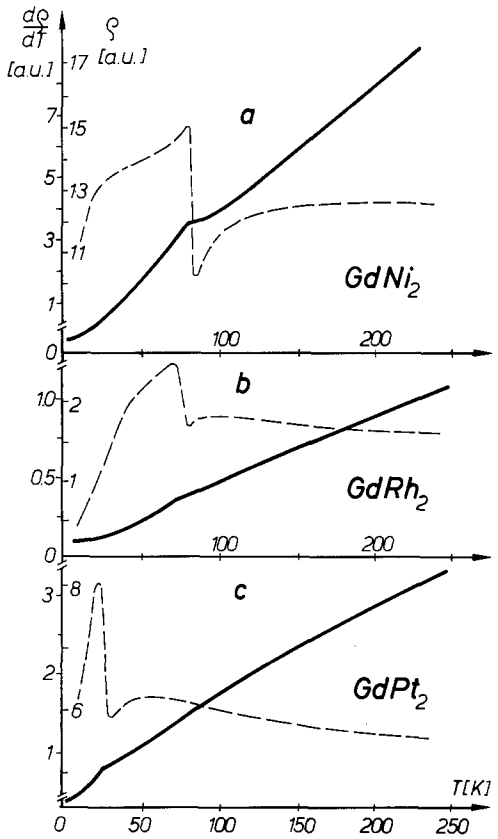

Fig. 35. ρ vs. T curves and the temperature dependence of $d\rho/dT$ of (a) $GdNi_2$, (b) $GdRh_2$, and (c) $GdPt_2$ (----- $d\rho/dT$, ——— $\rho(T)$) (Kawatra et al., 1970).

computed values of $d\rho/dT$ for $GdCo_2$, $GdAl_2$, and $DyAl_2$ near the Curie temperature (Kawatra et al., 1970). As one goes from $DyAl_2$ to $GdAl_2$ and then to $GdCo_2$ one can see a more pronounced peak in $d\rho/dT$. This behaviour was related to the linear temperature dependence of the phonon contribution which can be expected at higher temperatures (Kawatra et al., 1970). The weak maximum in $DyAl_2$ gives a limit to the accuracy of determining T_c from resistivity data. Controversially, $GdAl_2$ shows a sharp and well-defined maximum in $d\rho/dT$ at about 160 K which is associated with the Curie temperature. The behaviour of $GdCo_2$ is to a certain extent comparable to the behaviour of pure Ni (Craig et al., 1967). As will be discussed in section 4.1, the R–Co coupling plays a significant role in the magnetic properties in these compounds. The moments on the Co atom sites which are aligned antiparallel to the R-moments are not so well localized as they are on the Gd atom sites. The effect of 3d electrons on the resistivity of this compound is probably the reason for the similarity of $d\rho/dT$ to that of Ni.

3.2.1.11. *GdSb*

The temperature dependence of the resistance, $R(T)$, and its temperature coefficient dR/dT in the vicinity of the Neél temperature $T_N = 22.8$ K of the

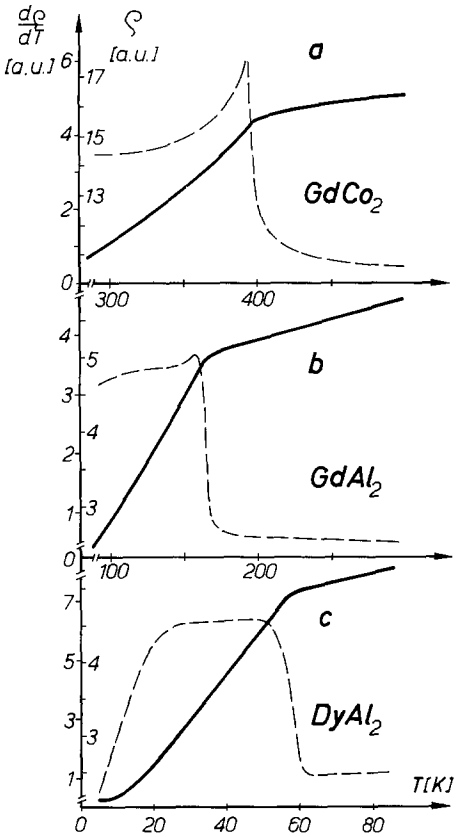

Fig. 36. ρ vs. T curves and the temperature dependence of $d\rho/dT$ of (a) $GdCo_2$, (b) $GdAl_2$, and (c) $DyAl_2$ (---- $d\rho/dT$, ——— $\rho(T)$) (Kawatra et al., 1970).

antiferromagnetic GdSb compound is shown by fig. 37 (Taub and Williamson, 1973). GdSb crystallizes in the rocksalt structure. In this compound it could be demonstrated that the magnitude of the sharp decrease in dR/dT above T_N is of the same order as that observed in the ferromagnetic nickel (Craig et al., 1967). This can be shown by using the second derivative d^2R/dT^2 (Taub and Williamson, 1973).

3.2.1.12. $(La_xGd_{1-x})Ni$: $0 \leq x \leq 1.0$

The effect of diluting magnetic R-components in RI compounds was studied in the orthorhombic (CrB structure) $(La_xGd_{1-x})Ni$ pseudobinary (Gratz et al., 1981c). Fig. 38 gives a survey of the ρ vs. T curves in this system. The arrows indicate the Curie temperatures T_c as obtained by initial susceptibility measurements. Both ρ_{spd} and T_c decrease with increasing La concentration and $\rho_{spd}(x)$ is given in fig. 39. A determination of ρ_{spd} from experimental data in the high La concentration region was not possible using the extrapolation procedure shown schematically in fig. 13. Fig. 39 also shows the concentration dependence of the residual resistivity ρ_0. $\rho_0(x)$ deviates significantly from the parabolic shape predicted by Nordheim's rule. The asymmetric shape of the $\rho_0(x)$ curve of fig. 39

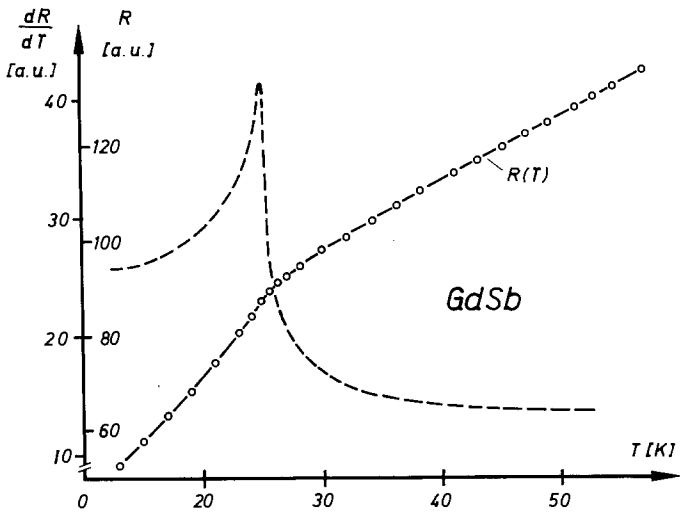

Fig. 37. The resistance vs. temperature (R vs. T) and the temperature dependence of dR/dT of the antiferromagnetic GdSb compound (Taub and Williamson, 1973).

indicates that additional spin-disorder scattering from domain walls contributes to the residual resistivity for increasing Gd concentration below $x = 0.6$.

The temperature dependence of the resistivity in the range 4.2 K to about 20 K for the two boundary compounds GdNi and LaNi is presented on a double logarithmic scale in fig. 40. LaNi is representative of a non-magnetic RI compound. The experimentally observed T^5 dependence (given by the slope of the straight line in fig. 40) is in good agreement with the temperature dependence predicted by the Bloch–Grüneisen law (eq. (2)). The ferromagnetic GdNi compound shows a T^2 dependence as expected from the spin wave contribution to the resistivity. The resistivity results obtained for the antiferromagnetic TbCu compound are also presented in this diagram for the purpose of comparison. The TbCu measurement shows a rather large deviation from the T^5 behaviour predicted by eq. (38).

3.2.1.13. Gd_xY_{1-x}: $0.2 \leq x \leq 1.0$

Although the (Gd, Y) binary system does not belong to the family of RI compounds, we have included it since this system is an ideal candidate for demonstrating the influence of superzone boundary on spin-disorder scattering. Popplewell et al. (1967) used eq. (25) to calculate the exchange integral $|\mathcal{J}|$ for the Gd_xY_{1-x} binary system from experimental data for ρ_{spd}. It was assumed that ϵ_F and m^*, the Fermi energy and the effective mass of the conduction electrons, respectively, are unchanged in the whole binary system. An estimate of $|\mathcal{J}|$ was also given by Arnold and Popplewell (1973), who took into account the variation of m^* using the formula for the paramagnetic Curie temperature in the molecular field model. Fig. 41 shows the concentration dependence of $|\mathcal{J}|$ in the Gd–Y system. The pronounced step at $x = 0.6$ is caused by the transition from

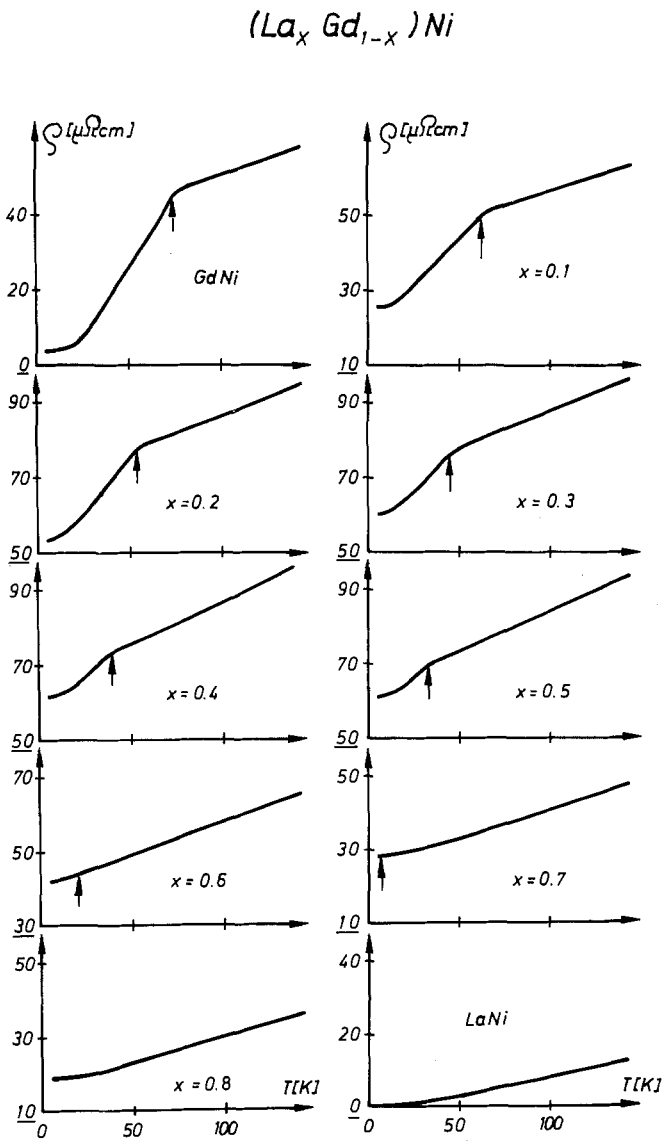

Fig. 38. ρ vs. T curves of the $(La_xGd_{1-x})Ni$ pseudobinary system (Gratz et al., 1981c).

ferromagnetism ($x > 0.6$ to antiferromagnetism ($x < 0.6$). The concentration dependence of ρ_{spd} is clearly shown by Ito (1973). In his careful investigation using single crystals, Ito has shown that ρ_{spd} exhibits anomalous behaviour only for the c-direction. This can be explained by the influence of superzone boundaries on the magnetic contribution to the resistivity below the ordering temperature (Elliott and Wedgwood, 1963; Poldy and Gratz, 1978).

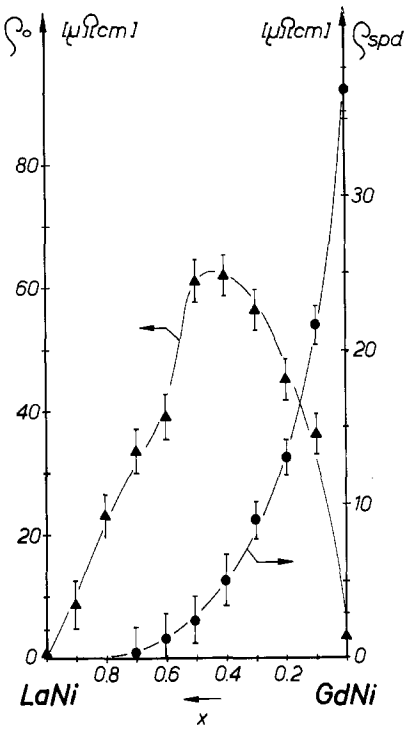

Fig. 39. ρ and ρ_{spd} vs. concentration in the $(La_xGd_{1-x})Ni$ pseudobinary system (Gratz et al., 1981c).

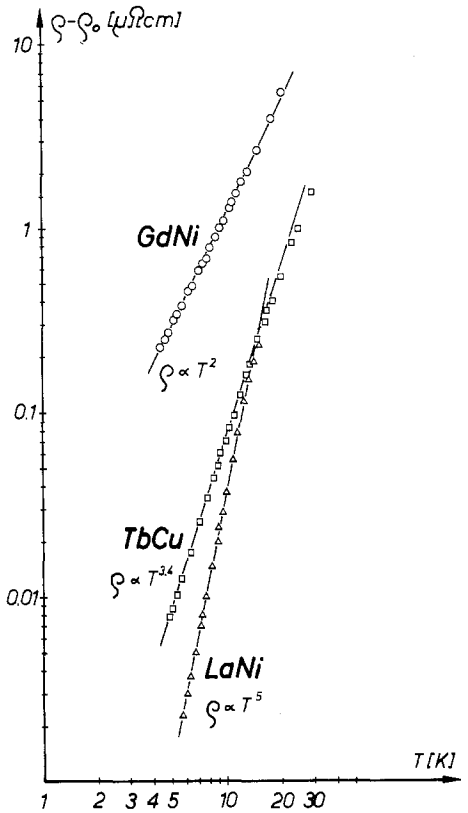

Fig. 40. The electrical resistivity behaviour at low temperatures of the ferromagnetic GdNi, the antiferromagnetic TbCu and the non-magnetic LaNi.

3.2.1.14. *$CeAl_2$, $CeAl_3$, Ce_3Al_{11}, and $CeIn_3$*

Fig. 42 shows the temperature dependence of the resistivity of $CeAl_2$, $CeAl_3$, Ce_3Al_{11}, and $CeIn_3$ (Buschow, 1979). In each case a minimum in the corresponding ρ vs. T curve is observable. The shape of the resistivity curve of $CeAl_2$ deviates drastically from that of the other RAl_2 compounds as shown in figs. 15–17 even although $CeAl_2$ crystallizes in the same $MgCu_2$ structure. The ρ vs. T curve of $CeAl_2$ is characterized by

(i) A well-defined curvature at about 70 K which was attributed to the influence of the crystal field on the spin-disorder resistivity (see section 3.1.3.2).

(ii) A Kondo-like minimum in the vicinity of 15 K which was interpreted in terms of Kondo effect by Van Daal and Buschow (1969b) and Maple (1969).

(iii) A sharp kink at about 5 K indicating the onset of antiferromagnetism ($T_N = 4.5$ K) (Walker et al., 1973).

Cornut and Coqblin (1972) derived an expression for the resistivity taking into account the influence of both the crystal field and the Kondo effect. A fit of this

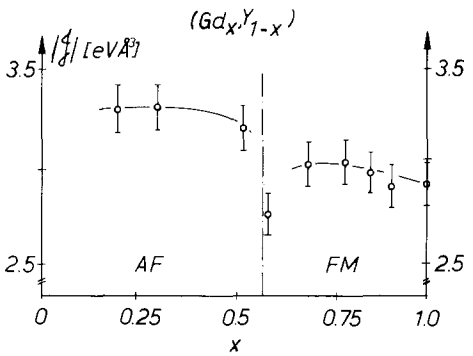

Fig. 41. The variation of $|\mathcal{J}|$ (exchange integral) with compositions for the Gd_xY_{1-x} binary system (AF = antiferromagnetism, FM = ferromagnetism) (Arnold and Popplewell, 1973).

expression to the resistivity data of $CeAl_2$ gives good agreement from 10 K to 300 K (Nicolas-Francillon et al., 1972). There is, however, no agreement below about 10 K. This is due to the presence of a RKKY interaction between residual magnetic moments via s–f admixture interactions which gives rise to an antiferromagnetic state. This can be seen in the resistivity below 10 K.

The resistivity of the non-magnetic $CeAl_3$ compound (Ni_3Sn structure) has a broad minimum at room temperature and a distinct maximum near 35 K. It has proved impossible to explain the behaviour of the resistivity of $CeAl_3$ in terms of a crystal field influence by including thermal repopulation of the three doublet levels of the Ce ions. A model has been proposed in which the resistivity anomalies are explained either by Kondo exchange scattering of the conduction electrons (Maranzana, 1970; Coqblin et al., 1976), or by considering conduction electron scattering against virtual bound states situated at the Fermi level with a width narrower than the crystal field splitting (Andres et al., 1975).

Magnetic data for Ce_3Al_{11} show the onset of ferromagnetism at about 6 K, followed by a further magnetic transition near 3 K. Both transitions can clearly

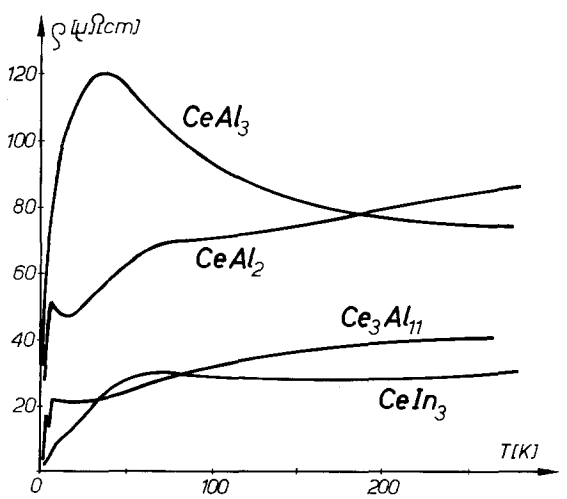

Fig. 42. ρ vs. T curves of $CeAl_2$, $CeAl_3$, Ce_3Al_{11}, and $CeIn_3$ (Buschow, 1979).

be seen in the ρ vs. T curve. Ce_3Al_{11} crystallizes in the orthorhombic La_3Al_{11} structure (Elenbaas et al., 1980). The resistivity minimum at about 20 K is again attributed to the Kondo effect.

Another example of Kondo-like behaviour in the presence of magnetic ordering effects has been found in the resistivity of the cubic $CeIn_3$ compound. The sharp change in the temperature dependence of the resistivity of $CeIn_3$ at 9 K is due to magnetic ordering (Elenbaas et al., 1980). A comparison of the crystal field parameter $A_4\langle r\rangle^4$ and $A_6\langle r\rangle^6$ indicates an increase of the energy separation between the 4f level and the conduction band in going from $CeIn_3$ to $NdIn_3$ (Lethuillier and Chaussy, 1976). A small separation between the 4f level and the Fermi level can explain the observation of the resistivity minimum in this compound (Buschow, 1979).

At this point it should be mentioned that many more pseudobinary RI compounds are known to exhibit a Kondo-like behaviour ((LaCe)Al_2, (LaCe)Al_3), (LaCe)$_3$Al, (LaCe)$_3$In, (LaCe)In_3, (YCe)Al_2, (LaPr)Sn_3, (La, Sm)Sn_3, (AgAu)Yb, etc.). Of the thirteen lanthanide ions with partially filled 4f shells, Kondo-like behaviour has been observed in RI compounds with Ce, Pr, Sm, Eu, Tm, and Yb (Van Daal and Buschow, 1969a, b; Buschow and Van Daal, 1970; Rao et al., 1971; Bakanowski and Mihalisin, 1977).

3.2.2. *Thermopower data*

3.2.2.1. *RAl_2 (R = Pr, Nd, Sm, Gd, Tb, Dy, Ho, Er, and Tm)*

The thermopower S as a function of temperature for RAl_2 compounds is shown in figs. 43–45 (Mikovits, 1981). The shape of the S vs. T curves for these

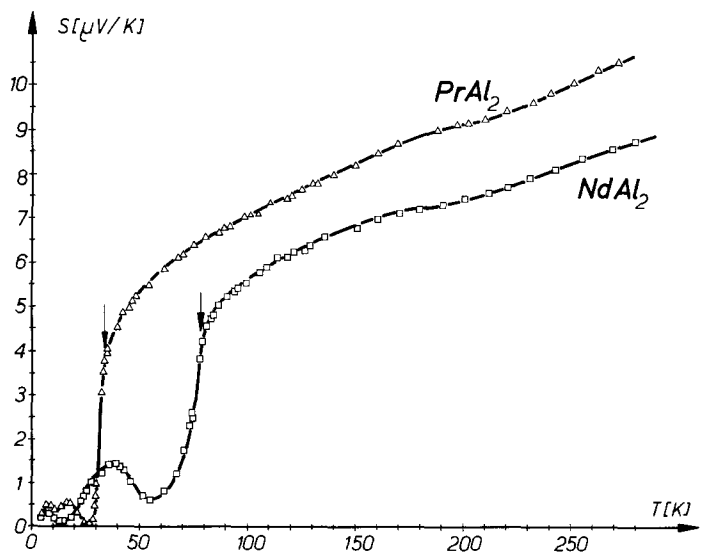

Fig. 43. S vs. T curves of $PrAl_2$ and $NdAl_2$ (Mikovits, 1981).

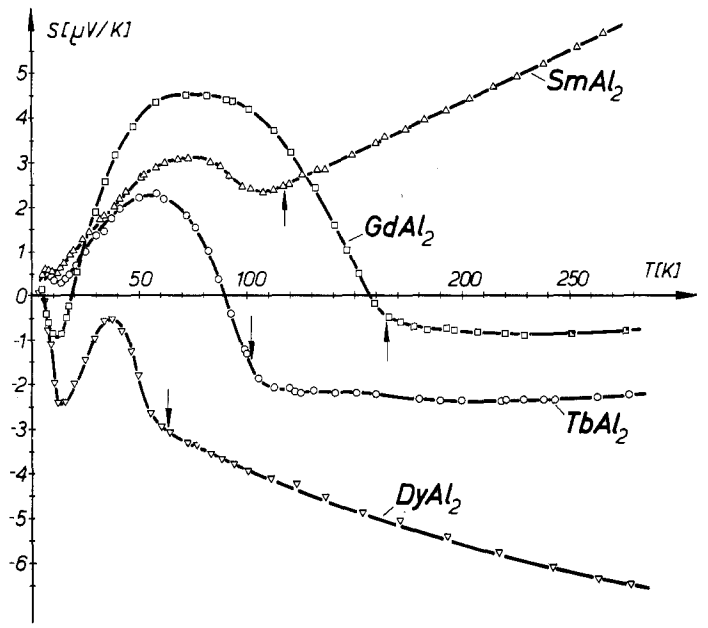

Fig. 44. S vs. T curves of $SmAl_2$, $GdAl_2$, $TbAl_2$, and $DyAl_2$ (Mikovits, 1981).

compounds implies that they should be divided into the following three groups:
(i) $PrAl_2$, $NdAl_2$

$PrAl_2$ and $NdAl_2$ are ferromagnetic at low temperatures, their Curie temperature being 33 K and 73 K, respectively. Fig. 43 shows that the thermopower of both compounds jumps almost discontinuously at the Curie temperature. The

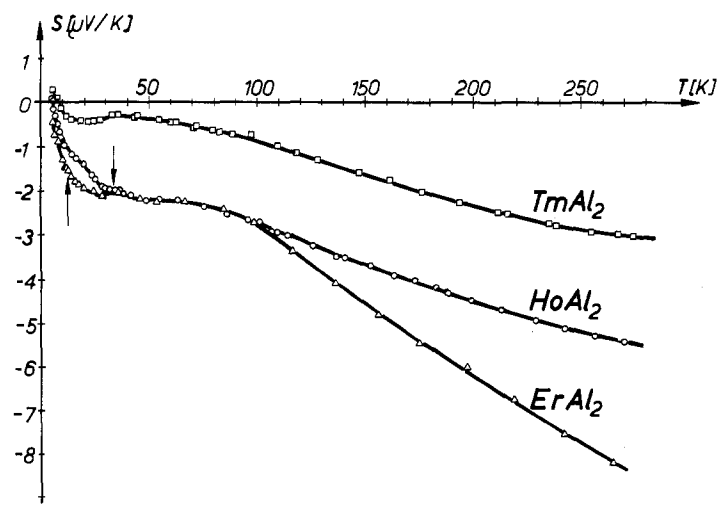

Fig. 45. S vs. T curves of $HoAl_2$, $ErAl_2$, and $TmAl_2$ (Mikovits, 1981).

thermopower below the Curie temperature exhibits a small bump which may be due to electron magnon scattering effects. The thermopower is almost linear above T_c and has a slight dip at about 200 K. This dip is not a magnetic effect since it also occurs for the non-magnetic $LaAl_2$ compound. The almost discontinuous increase in the thermopower may well be due to the change in magnetic scattering of electrons across the Curie point. Purwins et al. (1976) showed that the magnetic scattering of neutrons at zero frequency from $PrAl_2$ changes by a factor of nearly three as the temperature rises from 32.6 K to 37 K. We feel that this is the case for the magnetic scattering of electrons in both materials. Anomalies are also seen in the resistivity and the thermal conductivity of both compounds.

(ii) $SmAl_2$, $GdAl_2$, $TbAl_2$, and $DyAl_2$

All four order ferromagnetically at low enough temperatures. Fig. 44 shows that there is no longer a sharp jump in the thermopower obtained for the light RI compounds in this case. Instead, the following behaviour occurs:

(a) A kink at the ordering temperature.

(b) An extremely pronounced non-linear behaviour is found for all three compounds below the ordering temperatures.

(c) The temperature dependence of the thermopower in the paramagnetic regime is smooth and nearly linear with temperature.

(d) The slope of the thermopower above T_c changes from positive to negative in going from Sm to Dy.

(iii) $HoAl_2$, $ErAl_2$, and $TmAl_2$

These three compounds are again ferromagnetically ordered at low temperatures. However, no anomalous behaviour is seen in the thermopower of these three compounds below T_c. There is also no observable kink at the Curie temperature. The temperature coefficient at high temperatures continues to decrease up to the Er compound and increases in going from Er to Tm (see fig. 45).

Fig. 46 shows the magnitude of the room temperature thermopower S_{273} across the lanthanide series. The figure shows that S_{273} has a nearly linear behaviour and goes from a positive value of 12 μV/K for $LaAl_2$ to a minimum at $ErAl_2$ (-8 μV/K) and then it rises again for the remainder of the series. S_{273} is nearly zero for $GdAl_2$. This systematic behaviour is difficult to understand. One possibility is that it reflects in some way the electronic band structure of the RAl_2 series, since it does not correlate with magnetic properties such as the total quantum number.

3.2.2.2. *RCu_2 (R = Pr, Nd, Sm, Gd, Tb, Dy, Ho, Er, and Tm)*

The temperature dependence of the thermopower S of RCu_2 compounds is shown in figs. 47–49 (Mikovits, 1981). As mentioned above the light RCu_2 compounds are paramagnetic and the rest are antiferromagnetic (see section 3.2.1.2).

The curves of the thermopower have been divided into three groups, in the same way as for RAl_2. However, it can be seen that thermopower curves of RCu_2 exhibit no anomalies except for slight structure at low temperatures. The S vs. T curves increase monotonically at high temperatures.

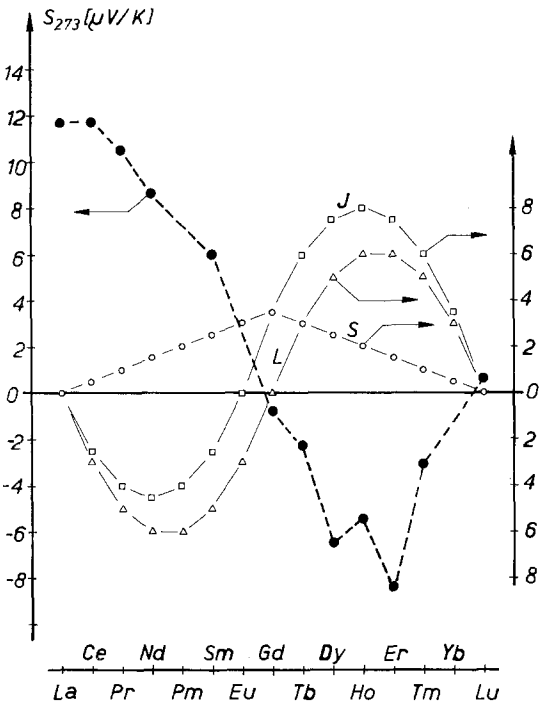

Fig. 46. The thermopower at $T = 273$ K (S_{273}) vs. the lanthanide atomic number for the RAl_2 series together with the spin quantum numbers (S), orbital quantum numbers (L), and total quantum numbers (J).

Fig. 50 shows the room thermopower S_{273} for RCu_2 compounds across the lanthanide series. It can be seen that the behaviour of S_{273} for RCu_2 compounds is completely different to that for RAl_2 compounds which is shown in fig. 46. Indeed, the curvature of S_{273} with R atomic number has a similar shape to that of the quantum number J and L of the 4f multiplet of the R ions. This implies a magnetic correlation, though no theoretical explanation is extant. (The way to plot J and L in figs. 46 and 50 is the same as in fig. 14.1 in Kirchmayr and Poldy (1979).)

3.2.2.3. $Gd(Al_{1-x}Cu_x)_2$: $0 \leq x \leq 0.3$

The thermopower of the RI-compounds $Gd(Al_{1-x}Cu_x)_2$ was measured at temperatures between about 20 K and 250 K by Yamamoto et al. (1979) (see fig. 51).

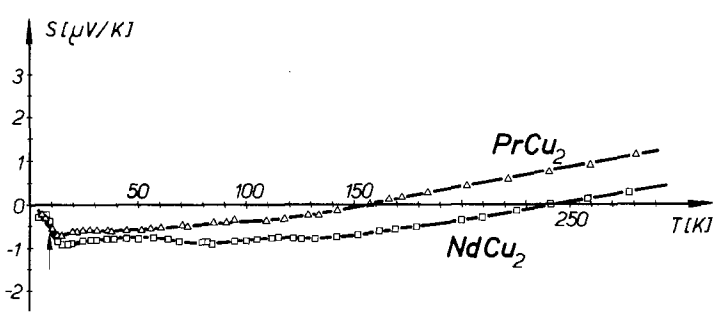

Fig. 47. S vs. T curves of $PrCu_2$ and $NdCu_2$ (Mikovits, 1981).

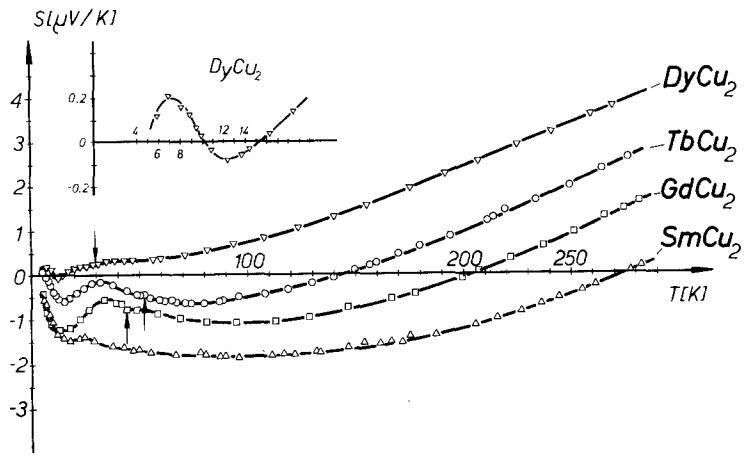

Fig. 48. S vs. T curves of $SmCu_2$, $GdCu_2$, $TbCu_2$, and $DyCu_2$ (Mikovits, 1981).

All samples crystallize in the cubic $MgCu_2$ structure. The concentration dependence of T_c is given in fig. 26. The shape of the S vs. T curve for $GdAl_2$ is in good agreement with that given in fig. 44. The substitution of Al by Cu causes a drastic change of the S vs. T curve. The behaviour for each concentration of the thermopower is linear with temperature above the Curie temperature. The non-linear behaviour in RAl_2 compounds below T_c vanishes at a concentration of 12% Cu even though the number of local moments (Gd atoms) is not changed on substitution of Cu. One can therefore conclude that the density of conduction electrons which varies with Al concentration plays an important role.

The slope of the S vs. T behaviour above T_c is shown in fig. 52 as a function of the Cu concentration x. Using eqs. (39) and (40) Yamamoto et al. (1979) have estimated $|\mathcal{J}|/\epsilon_F$. They found that the value and the sign change with concentration assuming that ϵ_F remains constant. This is a rather surprising assumption since the Fermi energy is bound to change with concentration in this case.

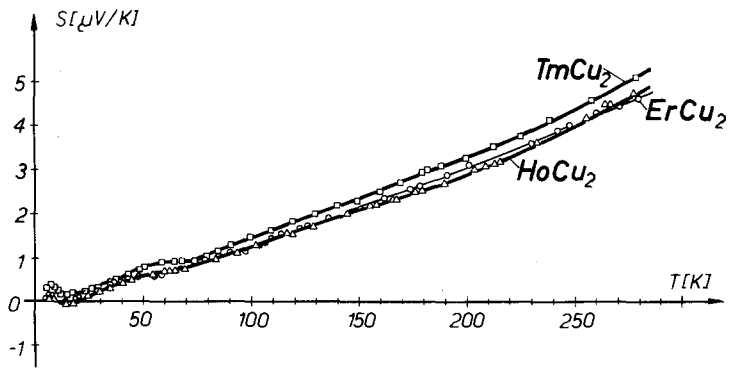

Fig. 49. S vs. T curves of $HoCu_2$, $ErCu_2$, and $TmCu_2$ (Mikovits, 1981).

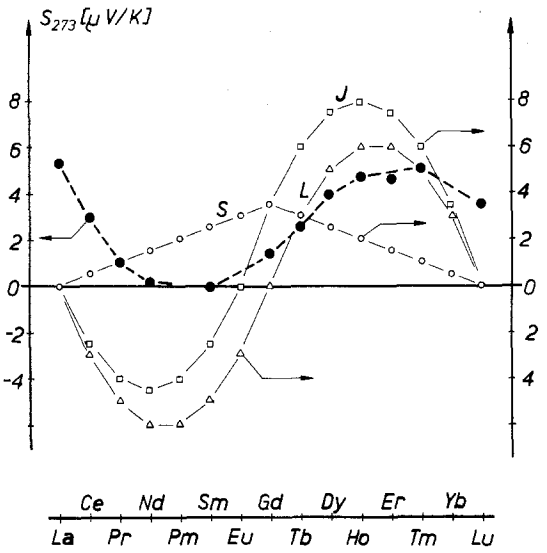

Fig. 50. The thermopower at $T = 273$ K (S_{273}) vs. the lanthanide atomic number for the RCu_2 series together with the spin quantum numbers (S), orbital quantum numbers (L), and total quantum numbers (J).

3.2.2.4. $GdNi_2$

This compound is ferromagnetic ($T_c = 74$ K, cubic $MgCu_2$ structure) and exhibits a kink in the resistivity (see section 3.2.1.10) and the absolute thermopower (fig. 53) near the Curie temperature T_c. Zorić et al. (1973) have shown that these are correlated discontinuities in the temperature dependence of the thermopower and the resistivity at T_c in $GdNi_2$. This is shown in fig. 54. These anomalies have been described theoretically by Zorić et al. (1973) and the agreement between the results shown in fig. 54 and the theoretical conclusion described in section 3.1.3.4 is good.

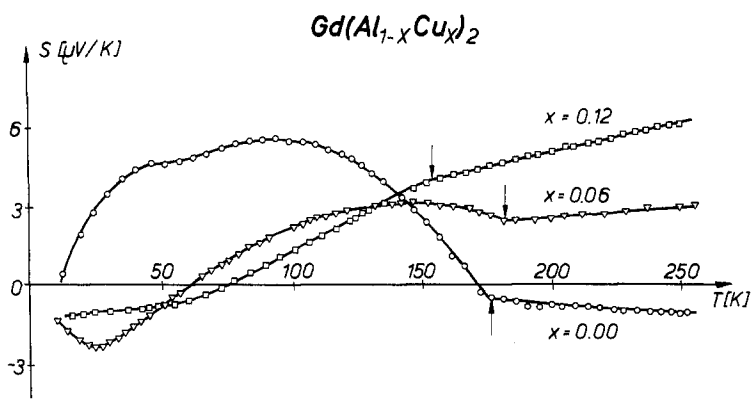

Fig. 51. S vs. T curves for some concentrations ($x = 0.0$, 0.06, and 0.12) for the $Gd(Al_{1-x}Cu_x)_2$ pseudobinary system. The arrows indicate the Curie temperature (Yamamoto et al., 1979).

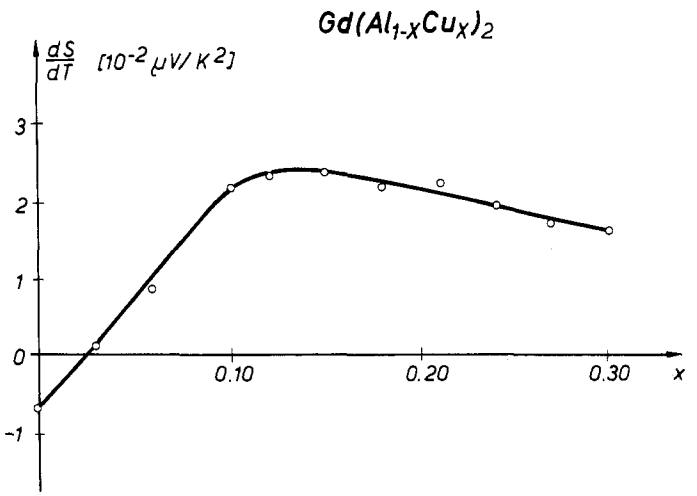

Fig. 52. The slope of the S vs. T behaviour (dS/dT) of $Gd(Al, Cu)_2$ above the Curie temperature as a function of the Cu concentration x (Yamamoto et al., 1979).

3.2.3. *Thermal conductivity data*

3.2.3.1. RAl_2 (R = *Pr, Nd, Sm, Gd, Tb, Dy, Ho, Er, Tm*)

The temperature dependence of the thermal conductivity, λ, of RAl_2 compounds is shown in figs. 55–58 (Bauer, 1981). The slope of the λ vs. T curves for these compounds implies that they can be divided into the following three groups.

(i) $PrAl_2$, $NdAl_2$

As was already discussed in connection with the thermopower data, both of these ferromagnetic compounds show anomalous behaviour in the thermopower

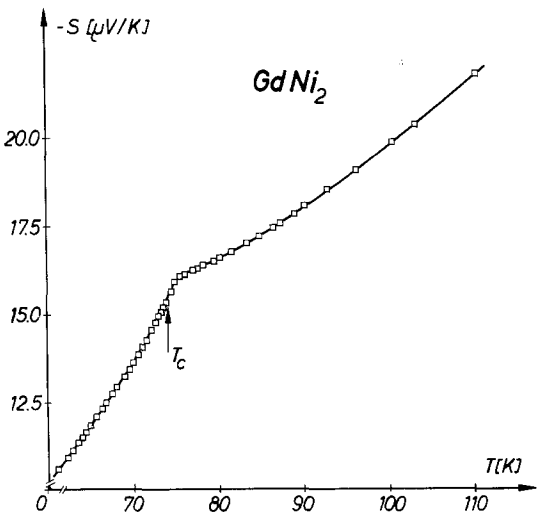

Fig. 53. S vs. T curve of $GdNi_2$ in the vicinity of the Curie temperature (T_c = 74 K) (Zorić et al., 1972).

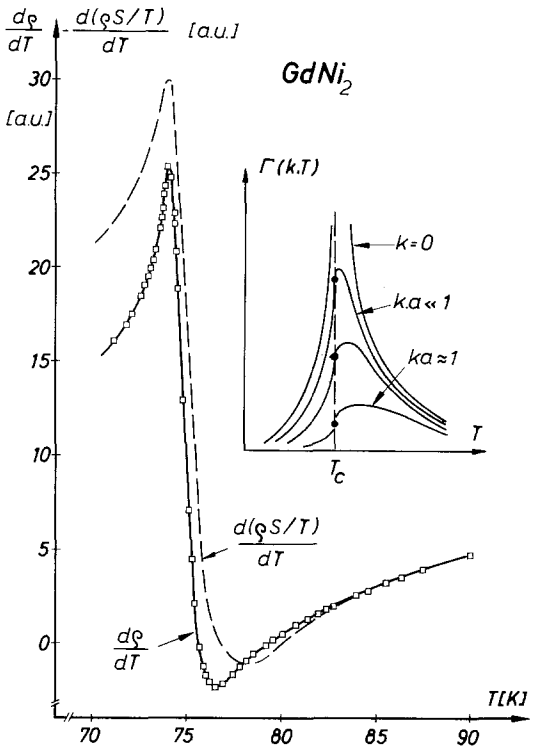

Fig. 54. $d\rho/dT$ and $d(\rho S/T)/dT$ for the $GdNi_2$ compound in the vicinity of the Curie temperature (Zorić et al., 1972). The inset shows the temperature dependence of the spin–spin correlation function $\Gamma(k, T)$ in the vicinity of T_c (after Fisher and Langer, 1968).

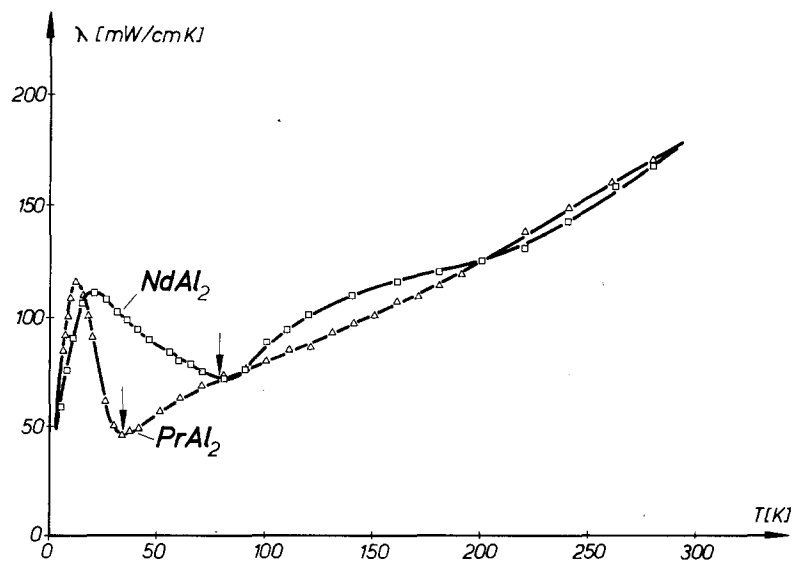

Fig. 55. λ vs. T curves of $PrAl_2$ and $NdAl_2$ (Bauer, 1981).

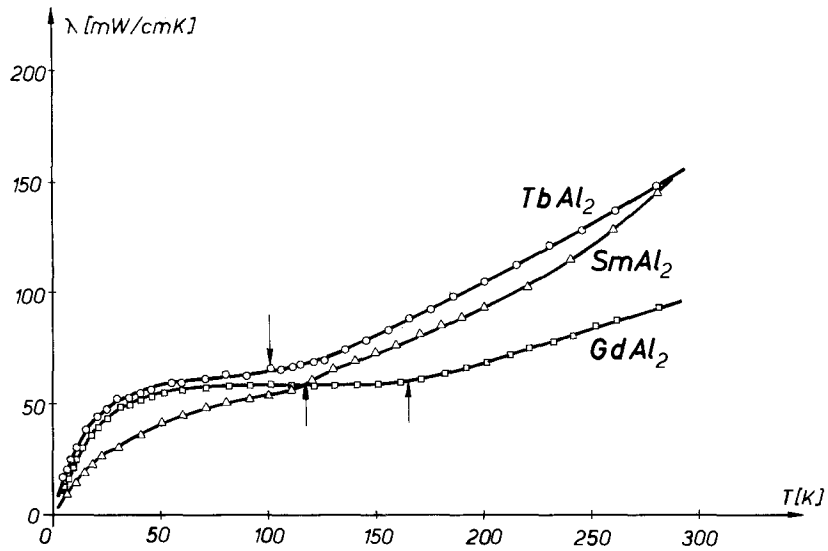

Fig. 56. λ vs. T curves of $SmAl_2$, $GdAl_2$, and $TbAl_2$ (Bauer, 1981).

and resistivity below T_c. Also extremely pronounced bumps were measured in the temperature dependence of thermal conductivity below the ferromagnetic ordering temperature (see fig. 55). The disappearance of these bumps at T_c (T_c is indicated by arrows in fig. 55) implies that the anomalous behaviour should be of magnetic origin. In section 3.2.2.1 it was pointed out that the magnetic scattering of neutrons from $PrAl_2$ below and above T_c is extremely different. This also seems to support the assumption of the magnetic origin of these bumps below T_c

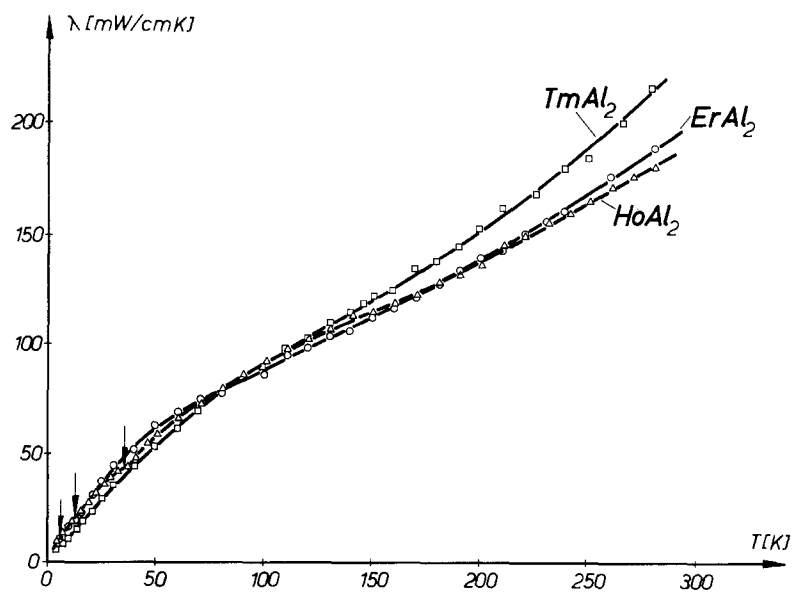

Fig. 57. λ vs. T curves of $HoAl_2$, $ErAl_2$, and $TmAl_2$ (Bauer, 1981).

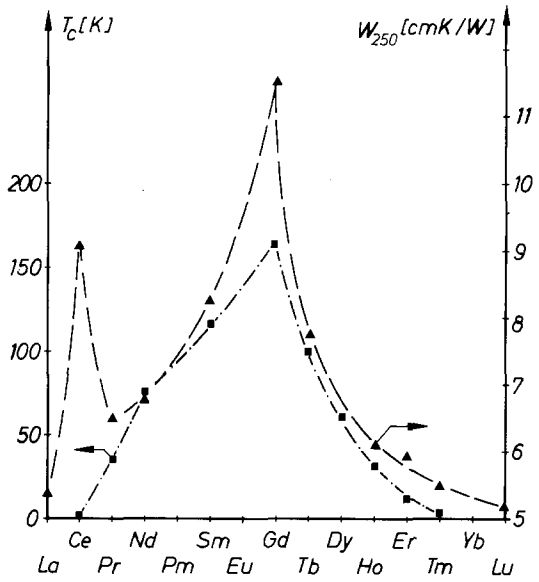

Fig. 58. The thermal resistivity at T = 250 K (W_{250}) together with the Curie temperatures for the RAl_2 series as a function of the lanthanide atomic number (Sassik, 1981).

in $PrAl_2$ and $NdAl_2$. Such a strong influence of magnetism on thermal conductivity is not detectable in the other RAl_2 compounds.

(ii) $SmAl_2$, $GdAl_2$, $TbAl_2$

These compounds all order ferromagnetically. The ordering temperatures are indicated by arrows in the λ vs. T curves of fig. 56. In contrast to what was observed for the Pr and Nd compound, the behaviour of $\lambda(T)$ is not anomalous at T_c.

(iii) $HoAl_2$, $ErAl_2$, $TmAl_2$

The λ vs. T curves of the heavy RAl_2 compounds are all shown in fig. 57. Again the arrows indicate the Curie temperature as found by initial susceptibility measurements. It is interesting to note that the λ vs. T curves of these compounds are nearly linear with temperature in the whole temperature range. Such a behaviour is different from what is found for pure metals such as Al.

At present there is no detailed understanding of the temperature dependence of the thermal conductivity of these RAl_2 compounds. However, we believe that the systematic investigation of the temperature dependence of λ across the rare earths of this section can give us an indication of the effect of local magnetic moments on the thermal conductivity. This is analogous to the situation for the thermopower.

A first step in this direction was made by Sassik (1981) who plotted the magnitude of the thermal resistivity W at 250 K (W_{250}) across the rare earths and compared the result to the variation of the ordering temperatures in this RAl_2 system. This is shown in fig. 58. As can be seen in this figure, the magnitude of the thermal resistivity at 250 K and the magnitude of T_c behave similarly except for $CeAl_2$ which shows an unexpected high W_{250} value which does not fit to the T_c behaviour. We therefore feel that there exists an important contribution to the thermal resistivity from s–f scattering of the conduction electrons.

4. Transport properties of rare earth–transition metal compounds exhibiting itinerant magnetism

4.1. *Theoretical introduction*

It was shown in section 3 that the transport properties of magnetic R–non-transition metal compounds can be understood in terms of a direct exchange interaction between conduction electrons and R localized moments. This interaction leads to an indirect RKKY interaction between the localized moments which describes the magnetic properties of these compounds.

A more complex magnetic behaviour is expected for RI compounds in which the second component is a 3d transition metal such as Mn, Fe, or Co. The magnetic behaviour of the transition metal component is now based on the magnetic polarization of the electronic d-bands. Consequently, in this section we summarize the theory of itinerant or band magnetism and its application to transport properties. We begin with the Stoner–Wohlfarth model and include a summary of recent works.

4.1.1. *Theories for itinerant magnetism*

The first theoretical description of itinerant ferro- and paramagnetism in transition metals is due to Stoner and Wohlfarth (Wohlfarth, 1976). These authors use Fermi statistics to describe the conduction electrons in the d-band. They consider the case of a single conduction band in which the electrons interact via an intraatomic Coulomb interaction. This model is formally equivalent to the Hubbard model for correlations between electrons in a single conduction band.

Stoner and Wohlfarth were able to derive a self-consistent equation for the spontaneous magnetization M_0 in the molecular field approximation (MFA) using the model described above. M_0 is then written in terms of the average occupation numbers $\langle n_\sigma \rangle$ for electrons of spin σ:

$$M_0 = \mu_B\{\langle n_\uparrow \rangle - \langle n_\downarrow \rangle\}. \tag{45}$$

The self-consistent equations for $\langle n_\sigma \rangle$ are given in the MFA by

$$\langle n_\sigma \rangle = \int_0^\infty d\epsilon\, N(\epsilon) f(x_\sigma), \tag{46}$$

$$x_\sigma = (\epsilon + I\langle n_{-\sigma} \rangle - \sigma\mu_B H) \qquad \sigma = \pm 1,$$

where I is an effective interaction energy between the electrons, $N(\epsilon)$ is the density of states of conduction electrons of energy ϵ, μ_B is the Bohr magneton, H is the external magnetic field and $f(x)$ is the Fermi function given by

$$f(x) = [\exp(x - \mu)/k_B T + 1]^{-1}, \tag{47}$$

μ is a chemical potential.

From eqs. (45) and (46) it can be seen that the paramagnetic state is equivalent to taking $\langle n_\uparrow \rangle = \langle n_\downarrow \rangle$. A ferromagnetic state occurs when $\langle n_\uparrow \rangle \neq \langle n_\downarrow \rangle$, i.e. when $M_0 \neq 0$. The criterion for the occurrence of ferromagnetism is obtained by expanding eq. (46) in powers of M_0 and is given by

$$1 \leqslant IN(\epsilon_F). \tag{48}$$

$N(\epsilon_F)$ is the density of state at the Fermi surface and ϵ_F is the Fermi energy. Eq. (48) is known as the Stoner criterion. Eq. (48) divides the range of values of $IN(\epsilon_F)$ into two regimes:

(i) Paramagnetic regime: $IN(\epsilon_F) < 1$. In that case the kinetic energies of spin-up and spin-down electrons are equal and the static magnetic susceptibility χ is given at zero temperature by

$$\chi = 2\mu_B^2 N(\epsilon_F)/[1 - IN(\epsilon_F)]. \tag{49}$$

$1 - IN(\epsilon_F)$ is known as the Stoner enhancement factor.

(ii) Ferromagnetic regime: $IN(\epsilon_F) > 1$. In that case the spontaneous magnetization M_0 is non-zero. Eq. (46) shows that the kinetic energy of spin-up and spin-down conduction electrons are separated by a band gap Δ_b. In the absence of an external magnetic field Δ_b is given by

$$\Delta_b = IM_0/\mu_B \tag{50}$$

and is known as the Stoner gap. Numerical methods are required to obtain values of M_0 and Δ_b in general but analytical expressions exist for the Curie temperature predicted by the Stoner–Wohlfarth theory (T_c^{SW}) and for the susceptibility in the case of very weak ferromagnets. In particular T_c^{SW} is given by

$$T_c^{SW} \cong A(\alpha - 1)^{1/2} \qquad (\alpha = IN(\epsilon_F)), \tag{51}$$

where A depends on the band structure.

It should be noticed that the spontaneous magnetization M_0 vanishes for temperatures $T > T_c^{SW}$ and therefore no magnetic moment, localized or otherwise is present in this temperature range.

In the case of weak ferromagnets ($1 \leqslant IN(\epsilon_F)$) Wohlfarth has shown that the Stoner model predicts a magnetic susceptibility for $T > T_c^{SW}$ which is non-Curie like and has the following form:

$$\chi \propto \frac{1}{T^2 - (T_c^{SW})^2}. \tag{52}$$

One problem with the Stoner–Wohlfarth theory is that most systems to which it has been applied exhibit a Curie–Weiss law for $T > T_c$. The Stoner–Wohlfarth theory is a molecular field theory and therefore includes neither spin correlations nor dynamics, nor is the detailed band structure taken into account explicitly. Several authors have recently turned their attention to this problem. Moriya and Takashashi (1978) used a renormalized theory of spin fluctuations (described in section 4.1.2) to obtain a Curie–Weiss law for χ above T_c for weak ferromagnets. They also showed that the critical indices are different, for example

$T_c \propto (\alpha - 1)^{3/4}$ from their theory. Also the ratio $n(T)$ of the mean square of the local moment at T to that at $T = 0$ remains finite at T_c whereas it vanishes for the Stoner–Wohlfarth theory, i.e.

$$\begin{aligned} n(T_c) &= 3/5 \qquad \text{Moriya–Takahashi,} \\ n(T) &= 1 - (T/T_c)^2 \qquad \text{Stoner–Wohlfarth.} \end{aligned} \tag{53}$$

Liu (1976) used a quasispin model in conjunction with the coherent potential approximation to examine the properties of itinerant ferromagnets at high temperatures. He showed that local moments persist above T_c in the absence of long-range order. Capellmann (1979) and Korenmann and Prange (1979a, b) use equivalent descriptions of itinerant ferromagnetism which allow for local exchange splitting without long-range magnetic order. They find that

(i) The Curie temperature $T_c \ll T_c^{SW}$, (the characteristic temperature of Stoner–Wohlfarth theory is given by eq. (51)).

(ii) Local magnetic moments persist above T_c and vanish at T_c^{SW}.

Usami and Moriya (1980) and Moriya and Takahashi (1978b) applied an extension of the theory of Moriya and Takahashi (1978a) to narrow band ferromagnetism.

The most recent theory is that of Hasegawa (1980b). Hasegawa has been able to develop a single-site spin fluctuation theory by generalizing a local saddle-point theory proposed by himself (Hasegawa, 1980a). The theory was developed by combining the functional integral method with the alloy analogy (coherent potential approximation) and applying it to the Hubbard model. The author obtains a value for the Curie temperature of strong itinerant ferromagnetism within much less than T_c^{SW} and predicts the existence of localized moments above T_c. The theory gives good semiquantitative agreement with experiment. However, Hasegawa stresses that the explanation of the quantitative difference between the magnetization curves of Fe and Ni requires the inclusion of dynamical spin fluctuations in the formalism.

These recent theories have not been reviewed in detail (with the exception of Moriya's theory of section 4.1.2) since they have not yet been applied to transport properties. We do, however, suggest that such an application should be made. The effect of spin fluctuations and spin waves on the transport properties of itinerant systems is discussed separately in section 4.1.2.

4.1.2. *Spin dynamic of itinerant magnetic systems and their effect on transport properties*

We begin by describing the spin fluctuations for the paramagnetic regime ($T > T_c$ or $1 > IN(\epsilon_F)$) in the random phase approximation (RPA) and related approximations. In the RPA spin fluctuations are described by the dynamic susceptibility

$$\chi(q, \omega) = \frac{\chi_0(q, \omega)}{1 - I\chi_0(q, \omega)}, \tag{54}$$

where $\chi_0(q, \omega)$ is the dynamic susceptibility of the conduction band, q is the

wave vector and ω is the frequency. $\chi(q, \omega)$ of eq. (54) has poles for small q which represent critical damped excitations, i.e. whose "dispersion relation" is given by

$$\omega_q \propto i(1-\alpha)^{1/2}q, \qquad \alpha = IN(\epsilon_F). \tag{55}$$

Eq. (55) indicates that the spin fluctuations are linear in q. Doniach (1967) showed that for small q, $\chi(q, \omega)$ can be written

$$\chi(q, \omega) \propto \frac{\omega}{\omega^2 + \omega_q^2}, \tag{56}$$

i.e. $\chi(q, \omega)$ has a maximum at $\omega = \omega_q$. When $1 - \alpha \geq 0$, the maximum becomes a sharp low-lying peak for low enough q. Rice (1967) showed that, from his point of view, low-lying spin fluctuations could be considered as particles which obey Bose–Einstein statistics. These particles were called paramagnons and were used to describe the scattering of electrons by spin fluctuations. $\chi(q, \omega)$ of eq. (54) reduces to χ of eq. (49) in the limit of $q \to 0$ and $\omega \to 0$. The transverse component of the dynamic susceptibility has the same form as $\chi(q, \omega)$ in eq. (54) for ferromagnetic metals ($\alpha > 1$) except that $\chi_0(q, \omega)$ must be replaced by $\chi^{-+}(q, \omega)$ which now includes the splitting Δ_b of the conduction band. The poles of $\chi^{-+}(q, \omega)$ at small q now describe undamped spin waves which can be shown to have a quadratic dispersion relation. The longitudinal component of the dynamic susceptibility is more complicated due to the existence of a gap Δ_b between the two-particle (Stoner) excitations and the spin waves. Δ_b is given by eq. (50) at zero frequency. A continuum of two-particle excitations exists for $\omega > 0$. The spin waves spectrum merges with the two-particle continuum at a critical value of q and becomes progressively damped. The two-particle continuum is a feature of magnetic metals and does not exist for magnetic insulators (Murata and Doniach, 1972).

Moriya and Kawabata (1973) made significant improvements to the RPA theory of spin excitations above by renormalizing the dynamic susceptibility. Their theory is known as the self-consistent renormalization (SCR) theory. In the SCR theory $\chi^{-+}(q, \omega)$ is given by

$$\chi^{-+}_{MI}(q, \omega) = \frac{\chi^{-+}_{M0}(q, \omega)}{1 - I\chi^{-+}_{M0}(q, \omega) + \lambda_{MI}(q, \omega)}. \tag{57}$$

x^{-+}_{M0} now depends on the spontaneous magnetization M_0 and $\lambda_{MI}(q, \omega)$ is a renormalization function which must be determined self-consistently.

The main purpose of the SCR theory is to show that the spin fluctuations strongly affect the equilibrium properties of weak ferromagnets, in contrast to the RPA treatment (see section 4.1.1). The function $\lambda_{MI}(q, \omega)$ is taken to be independent of q and ω in the long-wavelength approximation, i.e.

$$\lambda_{MI}(q, \omega) \to \lambda_{MI}(0, 0) = \lambda_{MI}. \tag{58}$$

Also if the dependence of λ_{MI} on I is assumed to be sufficiently weak, Moriya showed that the contribution of spin fluctuations to the free energy can be

written

$$\Delta F = k_B T \sum_{qn} \{\ln[1 - I\chi^{-+}_{M0}(q, i\omega_n) + \lambda_{MI}] + I\chi^{-+}_{M0}(q, i\omega_n)\} \tag{59}$$

$$\omega_n = 2\pi n k_B T, \qquad n = 0, \pm 1, \pm 2, \ldots .$$

Moriya then gives the following general relationship:

$$\frac{\partial F_0(M, T)}{\partial M} - 2IM + \frac{\partial \Delta F(M, I)}{\partial M} = 2H, \tag{60}$$

$$\frac{H}{M} = \frac{1}{\chi_{MI}(0, 0)} = \frac{1 + \lambda_{MI}}{\chi^{-+}_{MI}(0, 0)} - I. \tag{61}$$

$\chi_{MI}(0, 0)$ is the static susceptibility. Eqs. (59) to (61) form a set of self-consistent equations from which λ_{MI} can be calculated if $\chi^{-+}_{M0}(q, \omega)$ is known. However, this function depends on the band structure and is usually unavailable in analytic form. Moriya (1979) points out that for weak ferromagnets an expansion of $\chi^{-+}_{M0}(q, \omega)$ to second order in (ω/q) and q is sufficient.

The resulting analysis in the long-wavelength limit shows that the temperature dependence of λ is dominant and gives rise to the following results for weak ferromagnets:

(i) The Curie temperature T_c is given by

$$T_c \propto (\alpha - 1)^{3/4}.$$

This is in contrast to the Stoner–Wohlfarth (SW) theory which gives

$$T_c^{SW} \propto (\alpha - 1)^{1/2} \qquad \text{(see also section 4.1.1).}$$

(ii) The static spin susceptibility χ_0 obeys a Curie–Weiss law for $T_F \gg T \gtrsim T_c$ whereas the SW theory gives the result of eq. (52).

(iii) The magnetization near T_c is given by $M \propto (T_c^{4/3} - T^{4/3})^{1/2}$ whereas the SW theory gives the usual MF result, i.e. $M \propto (T_c^2 - T^2)^{1/2}$. Ueda and Moriya (1975) state that these results are in good agreement with the physical properties of weakly ferromagnetic metals $ZrZn_2$ and Sc_3In.

The SCR theory was then used to analyse the temperature dependence of the resistivity $\rho(T)$ for weak ferromagnets. At low temperature $\rho(T)$ can be written as follows

$$\rho(T) = \rho_0 + AT^2. \tag{62}$$

The coefficient A can be calculated using the ansatz that the (sp)-conduction electrons are responsible for carrying the electric current, whereas the d-electrons contribute mainly to the spin fluctuations (see Schindler and Rice, 1967; Kaiser and Doniach, 1970). Schindler and Rice have shown that A can be written as follows for enhanced paramagnets:

$$A \propto (1 - \alpha)^{-1/2}. \tag{63}$$

This result has been confirmed by Ueda and Moriya (1975) using the SCR theory

for both enhanced paramagnetic and weakly ferromagnetic metals far enough from T_c. They show that this temperature dependence is replaced by the following behaviour of $\rho(T)$ with T in the neighbourhood of T_c

$$\rho(T) \propto T^{5/3} \tag{64}$$

which is in agreement with Mathon's earlier result (Mathon, 1968). This was confirmed by fits to resistivity data for $ZrZn_2$.

The analogous results for nearly and weakly antiferromagnetic metals are (Ueda, 1977)

$$\begin{aligned} &\rho(T) = \rho_0 + AT^2, \qquad T \ll T_N \\ &A \propto |\alpha - 1|^{-1/2}, \\ &\rho(T) \propto T^{3/2}, \qquad T \sim T_N. \end{aligned} \tag{65}$$

Moriya notes that the resistivity $\rho(T)$ as calculated using the SCR theory goes smoothly through T_c. No explicit reason is given, however.

The thermal resistivity W at low temperature is given by

$$W \propto AT. \tag{66}$$

SCR theory shows that for weak ferromagnets

$$A \propto (1-\alpha)^{3/2}. \tag{67}$$

The above description of the SCR theory and its application to weak ferromagnetic materials is taken from the review article by Moriya (1979). The reader is referred to the original articles by Ueda and Moriya (1975) for details.

The collective excitation spectrum of strong itinerant ferromagnets is dominated by the Stoner gap Δ_b given by eq. (50) rather than the transverse spin fluctuations. As mentioned above the poles of $\chi^{-+}(q, \omega)$ are undamped spin waves with energies $\omega_q \ll \Delta_b$ in the long-wavelength limit.

The quadratic dispersion relation of the spin waves should therefore give rise to the usual resistivity for local moment ferromagnetism at low temperature, i.e.

$$\rho(T) = \rho_0 + AT^2, \tag{68}$$

where A is proportional to Δ_b.

The analogous result for antiferromagnets at low temperatures is

$$\rho(T) = \rho_0 + AT^4. \tag{69}$$

The critical region for strong itinerant ferromagnets has not yet been analysed. This may be possible using Liu's theory (Liu, 1976) but it remains a difficult problem.

4.2. *Experimental results and discussion*

4.2.1. *Resistivity data*

4.2.1.1. YCo_2, $Y(Co_{1-x}Fe)_2$: $0.05 \leq x \leq 0.15$, $Y(Ir_{1-x}Fe_x)_2$: $x = 0.2, 0.3$

Although the compound YCo_2 does not exhibit long-range magnetic order, it is included in this section because it forms the basis for the magnetic RCo_2

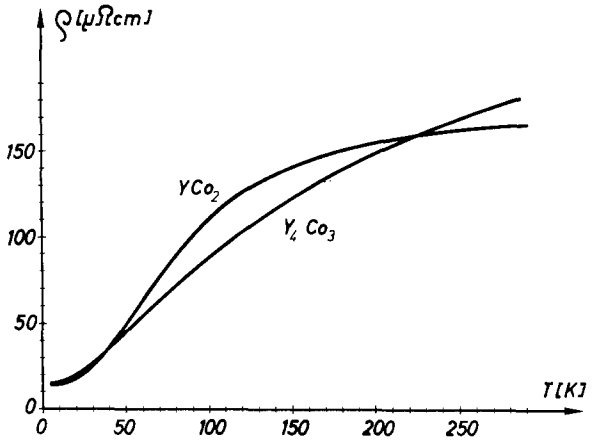

Fig. 59. ρ vs. T curves of YCo_2 and Y_4Co_3 (Gratz et al., 1980a).

compounds. The curve of ρ vs. T for YCo_2 obtained by Gratz et al. (1980a) is shown in fig. 59. This shows that a pronounced curvature in the ρ vs. T curve is seen near 100 K above which the resistivity tends to saturate. This curvature is not observed in the resistivity of Y–non-transition metal compounds such as YAl_2 and YCu_2 (see section 2.2.1.2). The resistivity of YCo_2 was shown to follow a T^2 law below 20 K by Ikeda (1977a) (see fig. 60), in contrast to the low-

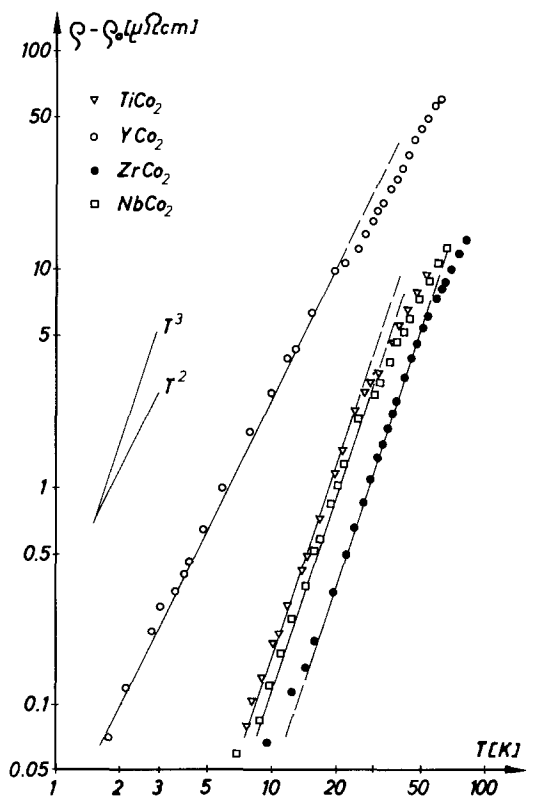

Fig. 60. $\log(\rho - \rho_0)$ vs. $\log T$ plots of $TiCo_2$, YCo_2, $ZrCo_2$, and $NbCo_2$ (Ikeda, 1977a).

temperature behaviour of $TiCo_2$ and $NbCo_2$ which is proportional to T^3 below 30 K. Ikeda (1977a) interpreted both the T^2 law at low temperatures and the high-temperature saturation of ρ for YCo_2 in terms of the theory of spin fluctuations due to Ueda and Moriya (1975) described in section 4.1.2. He concluded that YCo_2 is an enhanced paramagnet and that the resistivity is dominated by electron–paramagnon scattering. The T^3 behaviour of the resistivity of the other ACo_2 compounds is also shown in fig. 60 and was interpreted in terms of s–d scattering by phonons. In a later article Ikeda (1977b) examines the resistivity of $Y(Co_{1-x}Fe_x)_2$. He shows that the electron-spin fluctuation scattering is suppressed as the Fe concentration is increased as shown in figs. 61 and 62. He interprets this behaviour in terms of the polarization of Co atoms by neighbouring Fe atoms. Magnetic clusters then form and the Co atoms in the cluster can no longer contribute to electron–paramagnon scattering.

Van Dongen et al. (1980) measured the resistivity of $Y(Co_{1-x}Fe_x)_2$ for Fe concentrations in the range $0.02 \leq x \leq 0.15$. The residual resistivity increases to 250 $\mu\Omega$ cm at $x = 0.1$ and then decreases to about 100 $\mu\Omega$ cm at $x = 0.15$ (see fig. 63). This decrease is associated with the onset of magnetic order. The resistivity data are consistent with the occurrence of spin glass freezing for $x < 0.12$ and with long-range ferromagnetic order for $x > 0.12$. Small "kneelike" anomalies were seen in resistivity at the ordering temperatures as marked by the arrows in fig. 63. This implies a degree of localization of the magnetic moments on the Fe sites.

Van Dongen et al. (1980) suggest that the magnetic moments do not form on the Fe sites in $Hf(Co_{1-x}Fe_x)_2$ below $x = 0.2$ since no spin-glass freezing occurs. An ordered magnetic state appears in this system for $x > 0.2$. Van Dongen et al. (1980) state that although in $Y(Ir_{1-x}Fe_x)_2$ for $x \leq 0.4$ a non-zero hyperfine field is detected, no evidence is found for magnetic order from the susceptibility and magnetization measurements. They argue that the large contribution to the resistivity with a negative temperature coefficient in $Y(Ir_{1-x}Fe_x)_2$ for $x < 0.4$ (see

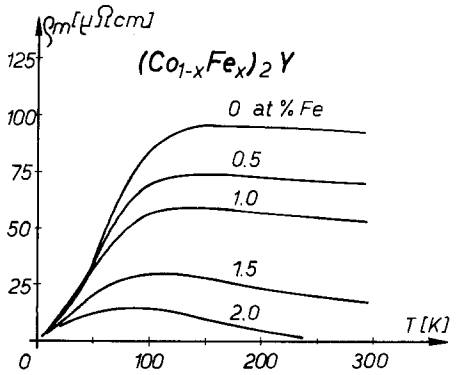

Fig. 61. The temperature variation of the resistivity due to magnetic scattering (ρ_m) in $Y(Co_{1-x}Fe_x)_2$ (Ikeda, 1977b).

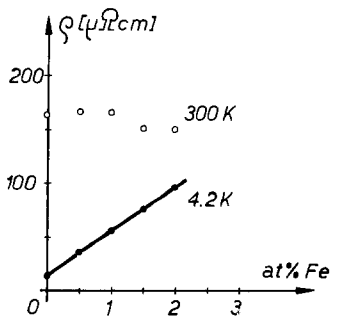

Fig. 62. The concentration dependence of the electrical resistivity of $Y(Co_{1-x}Fe_x)_2$ at 4.2 K and 300 K (Ikeda, 1977b).

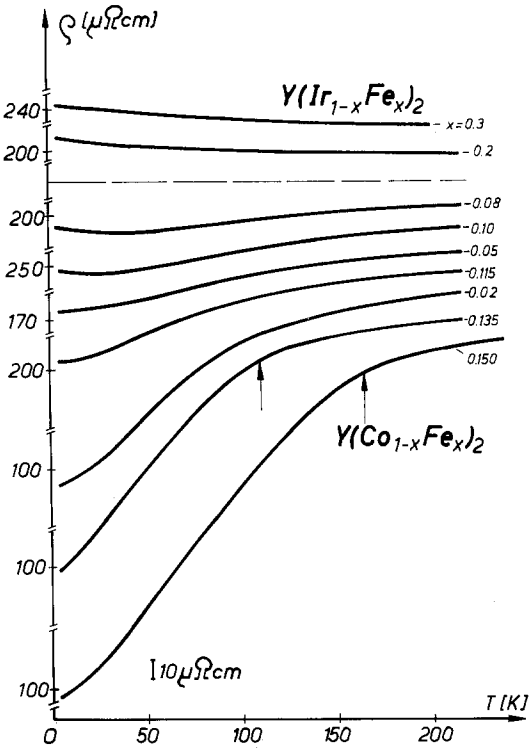

Fig. 63. ρ vs. T curves of $Y(Co_{1-x}Fe_x)_2$ and $Y(Ir_{1-x}Fe_x)_2$ for different x. The arrows indicate the magnetic ordering temperature (Van Dongen et al., 1980).

fig. 63) is probably related to a short-range magnetic ordering mechanism. The Mössbauer measurements indicate a polarization of the Co atoms in $Y(Co_{1-x}Fe_x)_2$ for $x > x_c$, whereas in $Y(Ir_{1-x}Fe_x)_2$ no polarization is found on the Ir atoms. This means that more *short*-range magnetic ordering is expected for the latter system.

4.2.1.2. RCo_2 (R = *Tb, Dy, Ho, Er*), $(Ho_xY_{1-x})Co_2$: $0 \leq x \leq 1.0$

In a large number of investigations concerning the RCo_2 compounds, it was shown that in $DyCo_2$, $HoCo_2$, and $ErCo_2$ the magnetic transition is a first-order phase transition in contrast to the other RCo_2 compounds where it is second order. In the case of a first-order transition most of the physical parameters such as lattice constants (Lee and Pourarian, 1976), magnetization (Lemaire, 1966), specific heat (Voiron et al., 1974), and electrical resistivity (Gratz et al., 1980b) change abruptly at the transition temperature. Fig. 64 shows the temperature dependence of the resistivity of the RCo_2 compounds in question. The discontinuities observed in the ρ vs. T curve of the Er, Ho, Dy compounds represent the influence of this first-order transition on resistivity. Note that e.g. in $ErCo_2$ at 32 K the magnitude of the electrical resistivity increases by about 600% on heating up the sample by a few tenths of a degree. Precise measurements of the resistivity in the vicinity of T_c for $ErCo_2$ show a hysteresis in temperature of about 0.8 K. The magnitude of this jump in the ρ vs. T curve

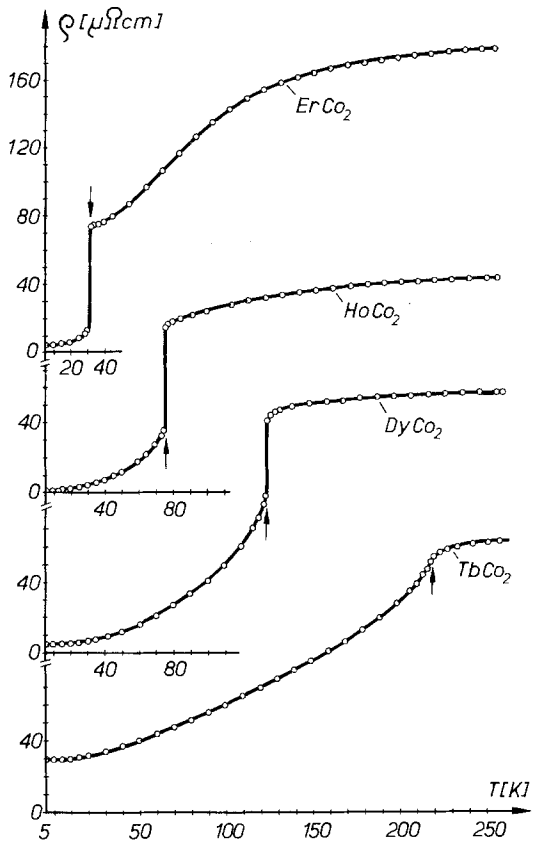

Fig. 64. Electrical resistivity as a function of temperature for: $ErCo_2$; $HoCo_2$; $DyCo_2$; $TbCo_2$. Arrows indicate T_c (Gratz et al., 1980b).

decreases with increasing ordering temperature ($ErCo_2$: $T_c = 32$ K, $HoCo_2$: $T_c = 78$ K, $DyCo_2$: $T_c = 135$ K). This is due to the increasing effect of temperature (Gratz et al., 1980b). The discontinuities at T_c are related to the sudden appearance of a high degree of order in rare earth moments immediately below T_c (in contrast to a second-order transition where the alignment in the moments increases continuously below T_c). Coupled with the ordering of the R-moments is a splitting of the Co 3d band and the appearance of an induced 3d moment of about $1\mu_B$ which enhances the ordering process. The extremely slow increase of the ρ vs. T curve in the high-temperature range experimentally found in all the RCo_2 compounds (YCo_2 included) is assumed to be due to the s–d scattering processes of conduction electrons into available d-states (Gratz et al., 1980b; Steiner et al., 1977).

The magnetic properties of RCo_2 compounds have been analysed by Bloch et al. (1975) in the following way. The localized magnetic moments on the R sites were assumed to polarize the 3d band of the Co component and then to interact via this polarization. The polarization of the d-band is described by the Landau theory, the important parameter being the coefficient B of the term in the order

parameter to the fourth power. B is shown to change from negative to positive as a function of temperature at 200 K. The behaviour of B determines whether the phase transition is of first or of second order at the Curie point. Unfortunately, the calculation of B using the Stoner–Wohlfarth theory relies upon the existence of a minimum in the density of states function at the Fermi energy. Recent band structure calculations show that this is not the case (Cyrot and Lavagna, 1979; Nowotny, 1980). There is also experimental evidence that the minimum does not exist (Gignoux et al., 1978). However, the idea of a negative value for B below 200 K is sound and it would therefore be of interest to calculate the resistivity using the analysis of Bloch et al. (1975). The ρ vs. T curves are presented in fig. 65 for several concentrations of the (Ho, Y)Co_2 pseudobinary system (Steiner et al., 1977). It appears that the discontinuity found in $HoCo_2$ at the Curie temperature exists for $0.7 \leq x \leq 1.0$. The cause of the minimum in the resistivity curves in the intermediate concentration range is unknown. A reorientation of the easy axis of magnetization at 14 K was found from magnetic measurements in $HoCo_2$. The small discontinuity observable for alloys in the concentration range $0.7 \leq x \leq 1.0$ around 14 K (shown in the inset in fig. 65) is connected with this reorientation. In this connection it should be

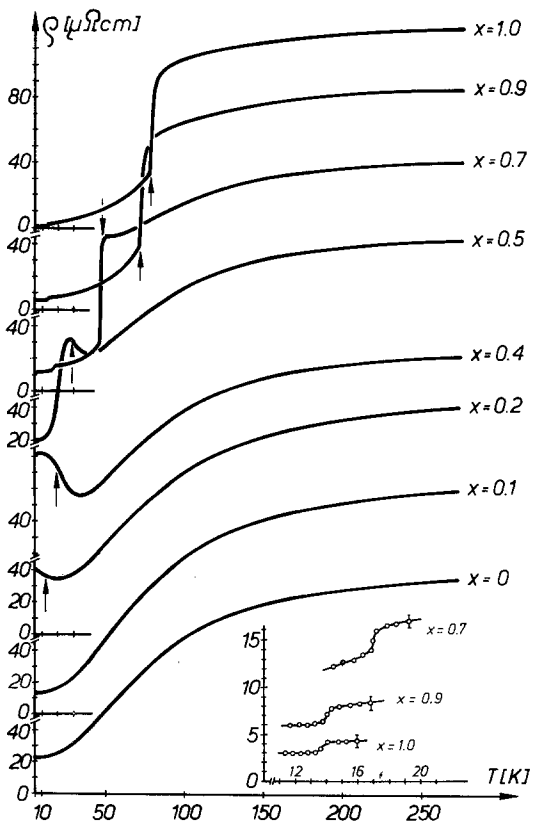

Fig. 65. ρ vs. T curves of some concentrations of the $(Ho_xY_{1-x})Co_2$ pseudobinary system. The magnetic ordering temperature T_c is given by the arrows. The inset shows the effect of the reorientation of the easy axis of magnetization on an expanded scale (Steiner et al., 1978).

pointed out that Sousa et al. (1980) have studied the influence of the spin reorientation in TbZn in detail.

4.2.1.3. Y_4Co_3

The compound YCo_2 is an enhanced paramagnet (see section 4.2.1.1). If the Co content of such compounds is sufficiently increased they become magnetically ordered. This is the case for the concentration range from YCo_3 to Y_2Co_{17}. On this basis it was expected that Y_4Co_3 would be a paramagnet and somewhat less enhanced than YCo_2. However, Y_4Co_3 exhibited long-range magnetic order below 6 K. In addition to the magnetic state, a superconducting state was found below 2 K by a.c. susceptibility measurements and confirmed by resistivity, specific heat, and magnetization measurements. The coexistence of magnetism and superconductivity below 2 K is clearly seen in the magnetization curve of fig. 66 (Gratz et al., 1981d). Y_4Co_3 crystallizes in the hexagonal Ho_4Co_3 structure. An important feature of this structure is that the Co atoms lie on three crystallographic non-equivalent sites. Susceptibility and NMR measurements show that only some of the Co atoms are magnetic (Figiel et al., 1980). The relation of the magnetic structure to the coexistence of superconductivity and magnetism has been described in Kolodziejczyk et al. (1980), Šebek et al. (1981), Cheng et al. (1982), and Gratz et al. (1981b).

The resistivity of Y_4Co_3 is given in fig. 59 which shows that there is some curvature at higher temperature. No kink is seen at 6 K at which long-range

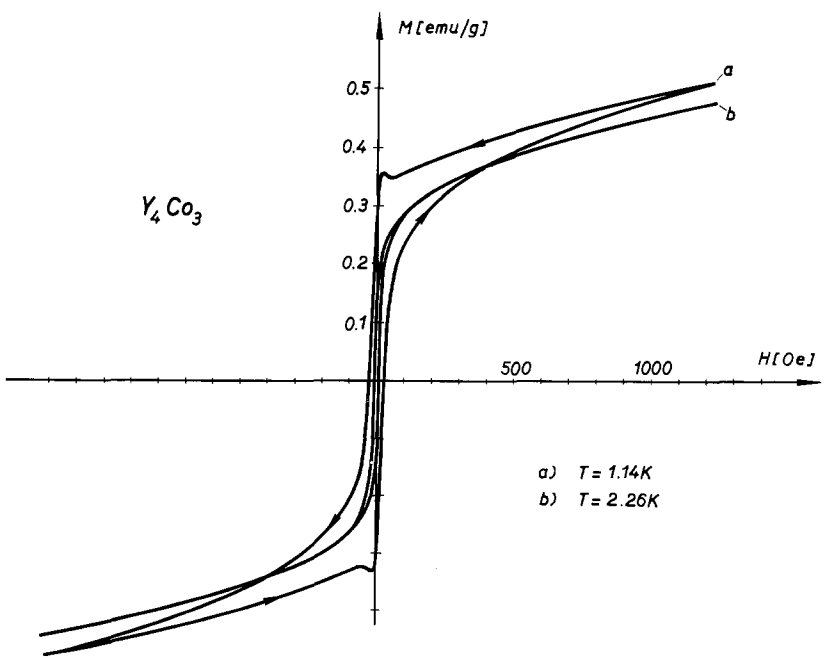

Fig. 66. The field dependence of the magnetization of Y_4Co_3 in the neighbourhood of the superconducting transition temperature (Gratz et al., 1981b).

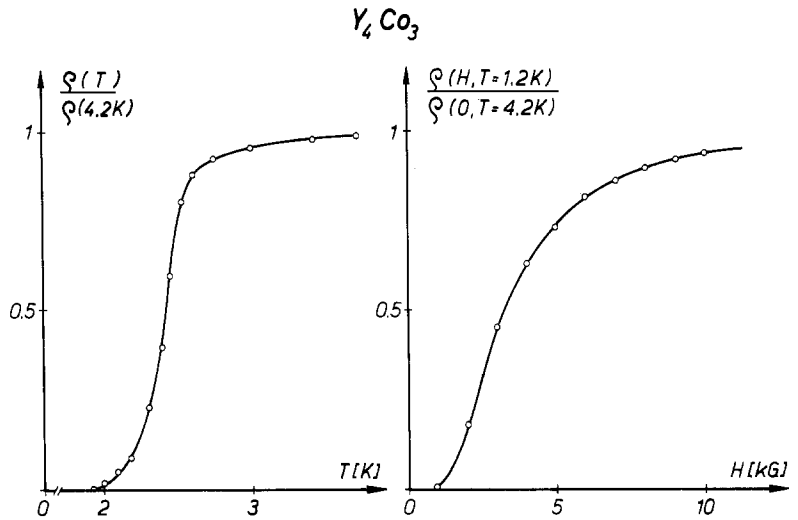

Fig. 67. (Left) The resistivity as a function of temperature of Y_4Co_3 in $1.5\,K \leq T \leq 3.5\,K$. $\rho_{4.2}$ is the resistivity at 4.2 K. (Right) The resistivity as a function of applied transverse magnetic field at 1.2 K (Cheng et al., 1982).

magnetic order sets in. However, the resistivity decreases to zero with decreasing temperature below 2 K indicating a broad superconducting transition (fig. 67). Fig. 67 also shows the magnetic field dependence of the resistivity at 1.2 K (Cheng et al., 1982). These data give a superconducting critical field of the order of 10 kOe.

4.2.1.4. $(Gd_xY_{1-x})_4Co_3$: $0 \leq x \leq 1.0$

The ρ vs. T curves for various concentrations of the pseudobinary $(Gd, Y)_4Co_3$ system are shown in fig. 68 (Gratz and Wohlfarth, 1980). This system exhibits a solid solution in the hexagonal Ho_4Co_3 structure and was selected to investigate the effect of dilution of the magnetic Gd by non-magnetic Y. The Y ions can be considered as "blanks" with respect to magnetism. Gd was chosen because of its S-state to avoid the influence of the crystal field on the results. It was found that the ordering temperature is nearly a linear function of the Gd concentration. The arrows in fig. 68 give the Curie temperature, T_c, as found by initial susceptibility measurements. Berthet-Colominas et al. (1968) investigated Gd_4Co_3 and have found an average moment of about $0.6\mu_B$ per Co atom induced by the Gd moments. Gratz et al. (1980d) showed that the induced Co moment disappeared in the $(Gd, Y)_4Co_3$ system at a concentration of $x < 0.75$. Fig. 69 shows the concentration dependence of the Co moment, $\Delta\mu$, per formula unit and the effective moment, μ_{eff}, per Gd atom. A constant Co moment of about $0.3\mu_B$ per formula unit was found at higher Y concentrations. This is due to the presence of localized moments on some of the cobalt sites as in pure Y_4Co_3. Fig. 68 shows that there are two important magnetic contributions to the resistivity. One contribution is due to the spin-disorder scattering on the Gd sites and leads to a kink in the resistivity at the Curie temperature, T_c. The other contribution is

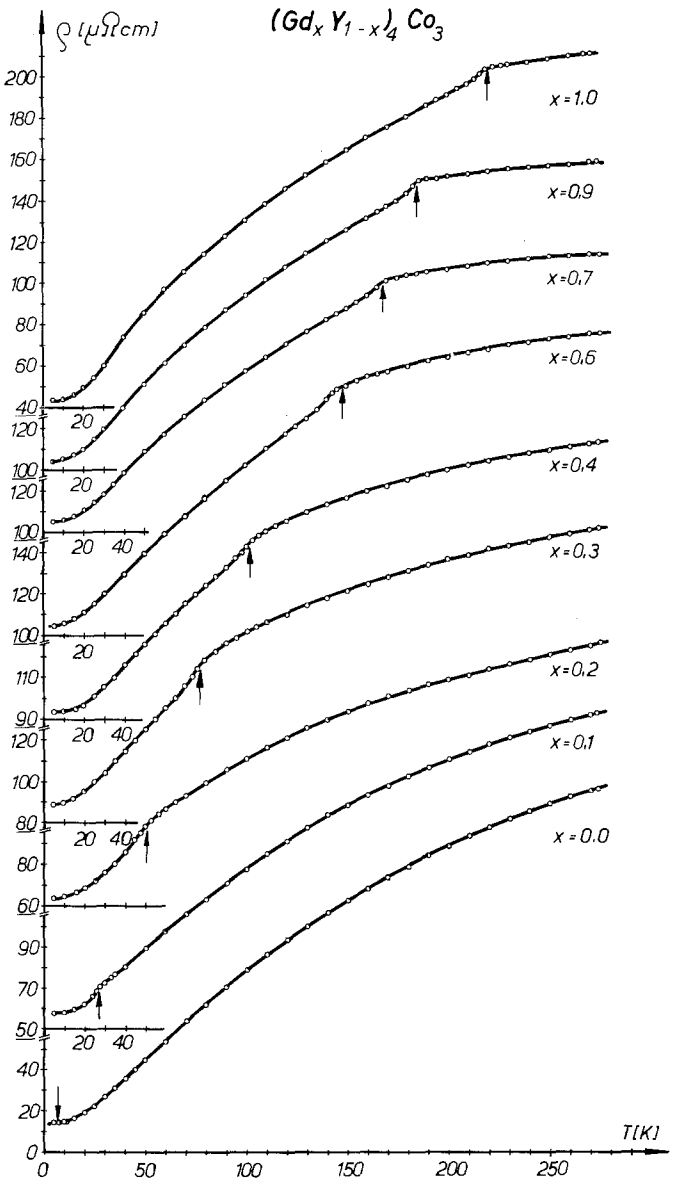

Fig. 68. ρ vs. T curves for various concentrations of the pseudobinary $(Gd_xY_{1-x})_4Co_3$ system. The ordering temperatures are indicated by arrows (Gratz and Wohlfarth, 1980).

due to the Co 3d bands and gives rise to pronounced negative curvature in the resistivity curves (Gratz et al., 1980d).

4.2.1.5. $Gd_4(Co_{1-x}Ni_x)_3$: $0 \leq x \leq 0.2$

The effect of the substitution of Co by Ni on the resistivity of Gd_4Co_3 is shown in fig. 70 (Gratz et al., 1982b). The solid solubility limit is reached at 20%

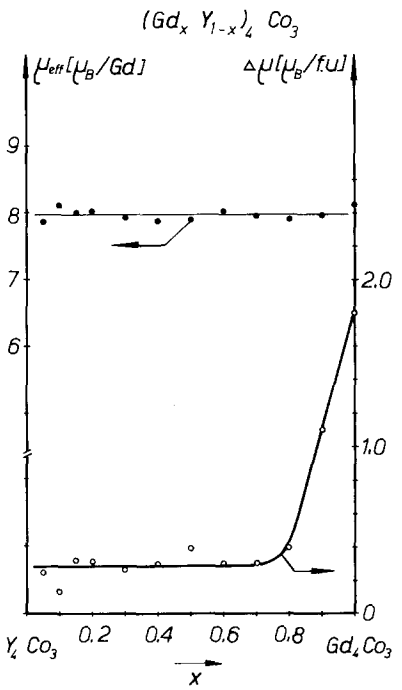

Fig. 69. The effective magnetic moment μ_{eff} per Gd atom and the Co moment $\Delta\mu$ per formula unit as a function of concentration (Gratz et al., 1980d).

Ni concentration. In contrast to the previously described $(Gd, Y)_4Co_3$ system where the ordering temperatures are proportional to the Gd content, the $Gd_4(Co, Ni)_3$ system shows hardly any change of T_c with Ni content. Although the replacement of Co by Ni is expected to raise the Fermi level, the 3d band appears not to become totally filled as indicated by the remaining convexity of the ρ vs. T curves. This observation is supported by magnetic investigations (Gratz et al., 1982b). One interesting feature is that the kink in the temperature dependence of the resistivity disappears with increasing Ni concentration even though the pseudobinary system remains ferromagnetic.

The Ho_4Co_3 structure of the system becomes unstable for Ni concentrations greater than 0.2. This can be interpreted in terms of a rule due to Wilson which states that an alloy becomes unstable as either a partially empty d-band becomes filled or as a completely filled d-band begins to empty.

4.2.1.6. $Gd(Co_xNi_{1-x})$: $0 \leq x \leq 0.3$

These pseudobinary compounds crystallize in the CrB structure. Pure GdNi is a ferromagnet with a Curie temperature $T_c = 72$ K. The d-band of GdNi is full and there is no magnetic moment due to the Ni component. The d-band empties progressively as Co is substituted for Ni until the concentration of Co reaches a value $x = 0.25$. The Curie temperature therefore increases with x since the d-band is now polarizable. This can be seen clearly in the resistivity as shown in fig. 71 (Gratz et al., 1980c). The pseudobinary system becomes unstable when $x > 0.25$. This instability can be detected by the occurrence of a discontinuity in the residual resistivity as a function of the Co concentration (fig. 72).

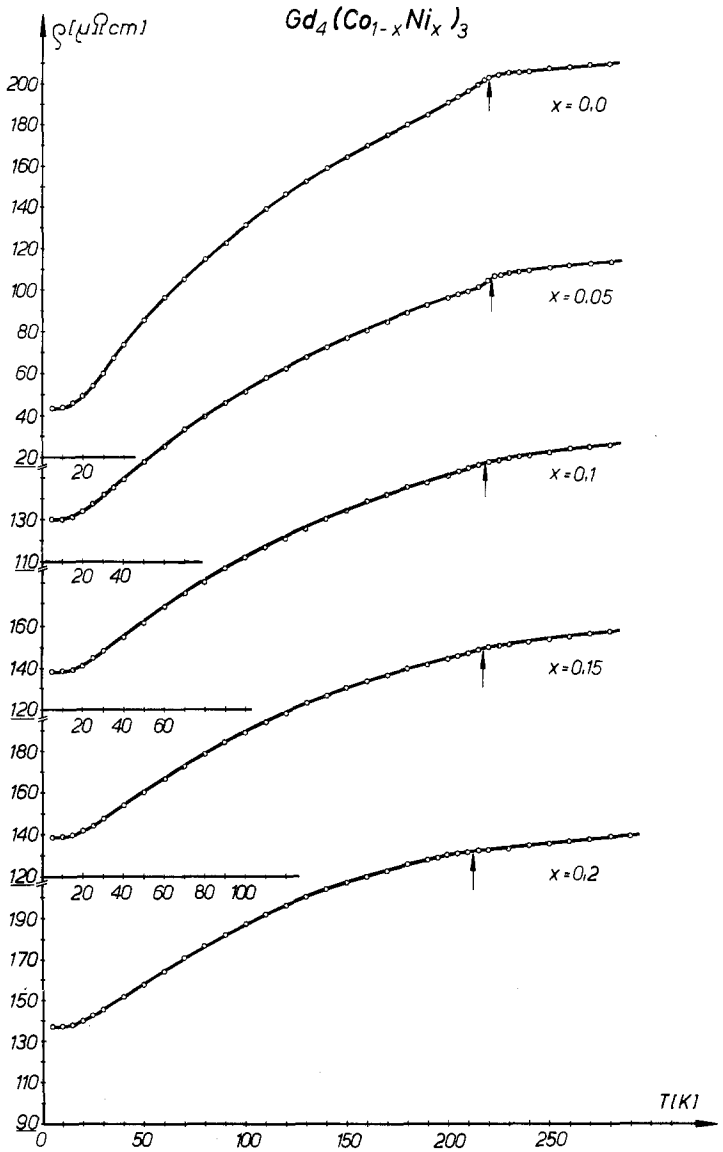

Fig. 70. ρ vs. T curves of various concentrations of the pseudobinary $Gd_4(Co_{1-x}Ni_x)_3$ system. The ordering temperatures are indicated by arrows (Gratz et al., 1982b).

4.2.1.7. $Y(Ni_{1-x}Co_x)_3$: $0 \leq x \leq 0.5$

The compounds YNi_2 and YNi_5 are both non-magnetic, whereas YNi_3 and Y_2Ni_7 exhibit ferromagnetic order. Hilscher et al. (1980) and Poldy and Taylor (1972) showed that the substitution of Ni by Co in YNi_3 decreases both the Curie temperature and the magnetization for $0 < x < 0.2$. The pseudobinary compounds are paramagnetic in the concentration range $0.2 \leq x \leq 0.30$. The magnetic order

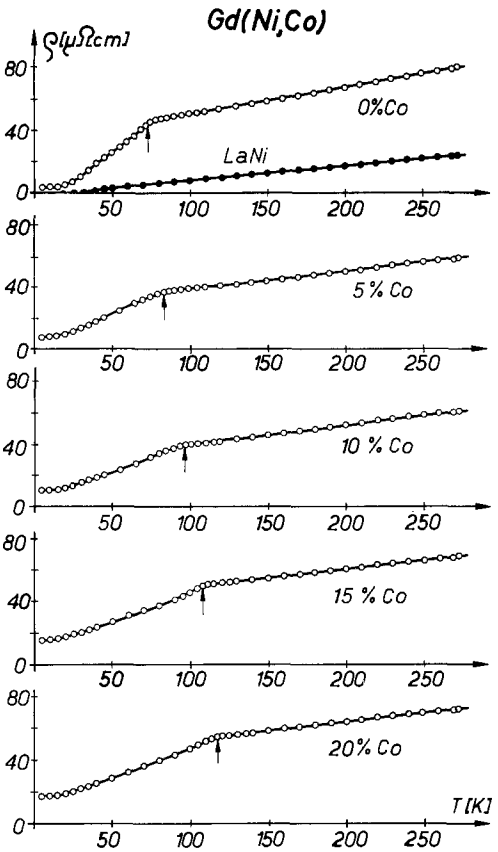

Fig. 71. ρ vs. T curves of various concentrations of the pseudobinary $Gd(Co_xNi_{1-x})$ system. The ordering temperatures are indicated by arrows (Gratz et al., 1980c).

reappears at higher Co concentration when $x > 0.30$. The concentration dependence of the Curie temperature is shown in fig. 73. Gignoux et al. (1980) also measured the resistivity as a function of temperature for YNi_3 and found a T^2 dependence for $T < 20$ K. This in agreement with the theory of weak itinerant ferromagnets (see eq. (65)).

Fig. 74 shows the ρ vs. T curves for the $Y(Ni, Co)_3$ pseudobinary system at several Co concentrations.

The effect of the substitution of Ni by Co is characterized by

(i) a dramatic increase of the residual resistivity (from a few $\mu\Omega$ cm at $x = 0$ to 200 $\mu\Omega$ cm for $x = 0.5$),

(ii) a small "kneelike" anomaly occurs at T_c in the resistivity at low Co concentrations.

The curvature in the ρ vs. T curves found for $T > 100$ K was analysed in terms of the s–d scattering mechanism proposed by Mott (Jones, 1956). Hilscher et al. (1980) were able to estimate the density of states of the d-electrons, $N_d(\epsilon_F)$, at the Fermi level for these compounds. They used a result due to Jones (1956) which expresses the temperature dependence of the resistivity in terms of $N_d(\epsilon_F)$

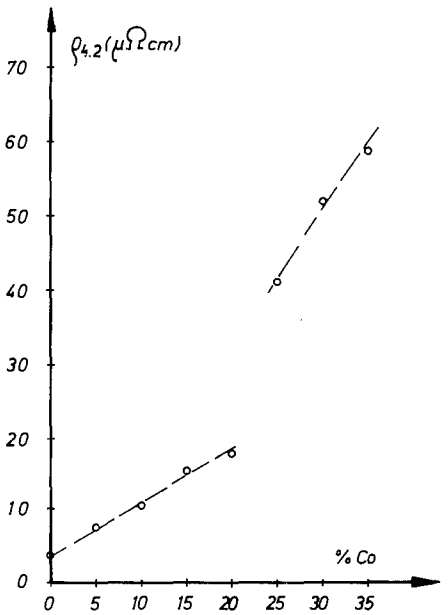

Fig. 72. $\rho_{4.2}$ vs. Co concentration for the $Gd(Co_xNi_{1-x})$ series (Gratz et al., 1980c).

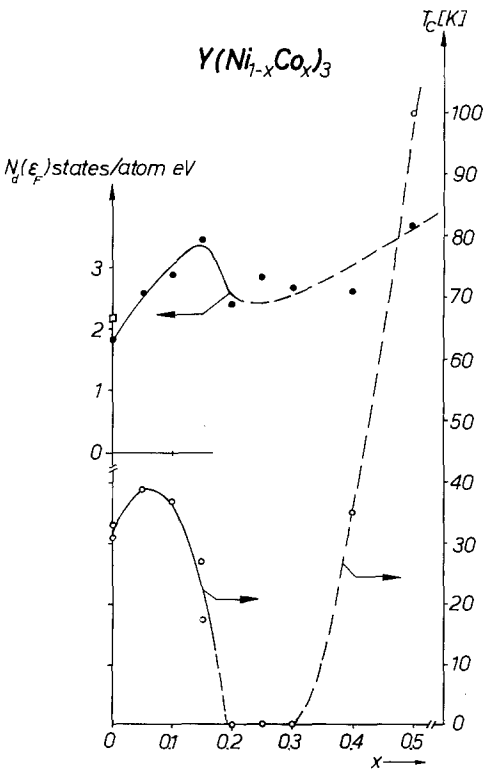

Fig. 73. The Curie temperatures (T_c) and the density of states of the d-electrons at the Fermi level ($N_d(\epsilon_F)$) for the $Y(Ni_{1-x}Co_x)_3$ system (Hilscher et al., 1980) (□ indicates $N_d(\epsilon_F)$ obtained by Gignoux et al., 1980).

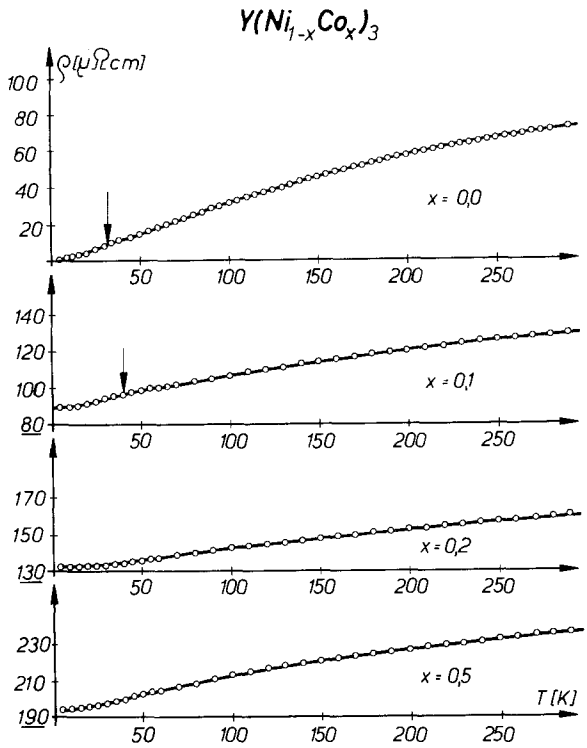

Fig. 74. ρ vs. T curves for various concentrations of the pseudobinary $Y(Ni_{1-x}Co_x)_3$ system. The ordering temperatures are indicated by arrows (Hilscher et al., 1980).

and its derivative with respect to energy in conjunction with the slope of the magnetization in the Arrott plots. The curve of $N_d(\epsilon_F)$ vs. Co concentration obtained in this manner is shown in fig. 73.

4.2.1.8. $R(Al_{0.9}T_{0.1})_2$ (R = *Y, Gd, Dy, Er*; T = *Fe, Co*)

Fig. 75 shows the influence of a 10% substitution of Al by transition metals on the resistivity of RAl_2 (R = Gd, Dy, Er) (Gratz et al., 1981a). Two features are apparent:

(i) a dramatic increase of the residual resistivity ρ_0 and

(ii) a pronounced decrease of ρ_{spd} in the substituted samples was found.

These effects are not observed when the magnetic R-atoms are replaced by Y (as in $(Dy_{0.9}Y_{0.1})Al_2$ of fig. 75) or Cu is substituted for Al (Sakurai et al., 1977). The results are summarized in table 2. The ratio r of table 2 is given by

$$r = \rho_{spd}[R(Al_{0.9}T_{0.1})_2]/\rho_{spd}(RAl_2). \tag{70}$$

Features (i) and (ii) are related to the presence of local structural and magnetic distortion (Gratz et al., 1981a). X-ray investigations of the $R(Al_{0.9}T_{0.1})_2$ (T = Co, Fe) show considerable broadening of the X-ray reflections. Furthermore, it has been found that the magnetization of the pseudobinary compounds with Fe or Co is extremely hard to saturate.

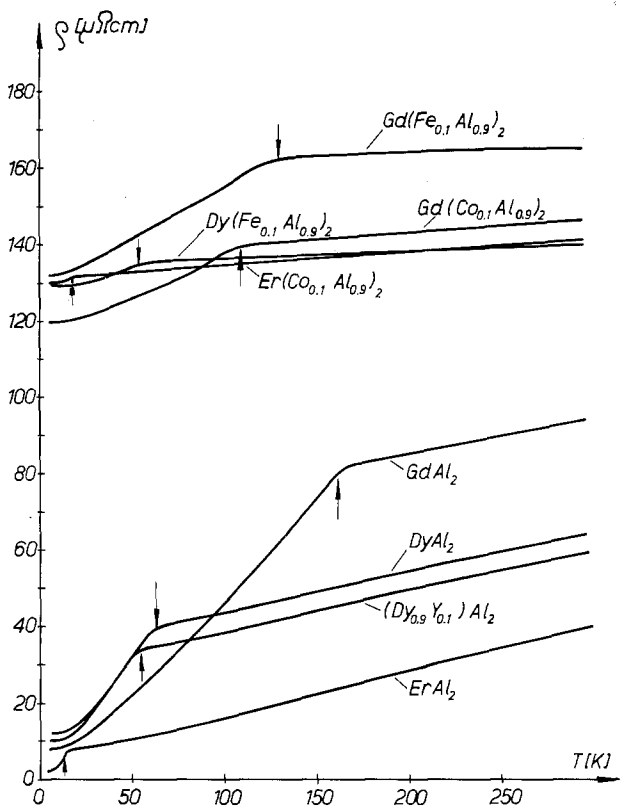

Fig. 75. The effect of a 10% substitution of Al by Fe or Co (and Dy by Y) on the ρ vs. T curves in RAl_2 compounds (R = Gd, Dy, Er). The ordering temperatures are indicated by arrows (Gratz et al., 1981a).

TABLE 2
Electrical resistivity features of materials based on $GdAl_2$, $DyAl_2$, and $ErAl_2$. The ratio r is given by eq. (70).

Compound	ρ_0 [$\mu\Omega$ cm]	ρ_{spd} [$\mu\Omega$ cm]	r
$GdAl_2$	8	59	(1)
$Gd(Al_{0.9}Fe_{0.1})_2$	132	31	0.53
$Gd(Al_{0.9}Co_{0.1})_2$	120	20	0.34
$Gd(Al_{0.9}Cu_{0.1})_2$	42	46	0.78
$DyAl_2$	10	24	(1)
$Dy(Al_{0.9}Fe_{0.1})_2$	129	5.3	0.22
$(Dy_{0.9}Y_{0.1})Al_2$	12	17	0.71
$ErAl_2$	1.5	5	(1)
$Er(Al_{0.9}Co_{0.1})_2$	130	1	0.2

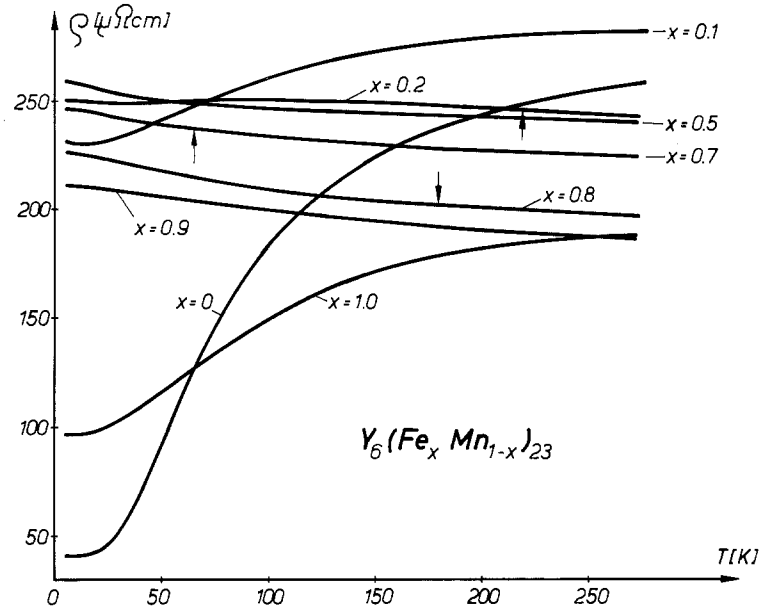

Fig. 76. ρ vs. T curves for various concentrations of the pseudobinary $Y_6(Fe_xMn_{1-x})_{23}$ system (Gratz and Kirchmayr, 1976).

4.2.1.9. $R_6(Fe_xMn_{1-x})_{23}$ ($R = Y, Er$): $0 \leq x \leq 1.0$

Unusually interesting magnetic behaviour was found in the R-transition metal compounds with the Th_6Mn_{23} structure. The temperature dependence of the resistivity of two $R_6(Fe, Mn)_{23}$ pseudobinary series is shown in fig. 76 ($Y_6(Fe, Mn)_{23}$) and fig. 77 ($Er_6(Fe, Mn)_{23}$) (Gratz and Kirchmayr, 1976). The substitution of only a small fraction of Fe or Mn in the compounds R_6Fe_{23} or R_6Mn_{23} causes an extremely strong increase of the residual resistivity ρ_0. The concentration dependence of ρ_0 for both systems are given in fig. 78. In the middle concentration range the ρ vs. T curves are dominated by a negative temperature coefficient of resistivity irrespective of whether the R-atom carries a local moment (Er compounds) or not (Y compounds). This behaviour is related to the complex crystallographic structure of these compounds (Gratz and Kirchmayr, 1976). In this case Mooij's rule may well apply. Mooij (1973) proposed that if the mean free path of the conduction electrons is reduced to the size of the atomic distances, the ρ vs. T curves become temperature independent. We note that no anomalies were found at the Curie temperature in these highly resistive crystalline systems. (The Curie temperatures are given by arrows in figs. 76 and 77.)

4.2.2. *Thermopower data*

4.2.2.1. YCo_2, Y_4Co_3

Many of the physical properties of YCo_2 are determined by the 3d electrons of the Co component. For example, the magnitude of the thermopower of YCo_2 is

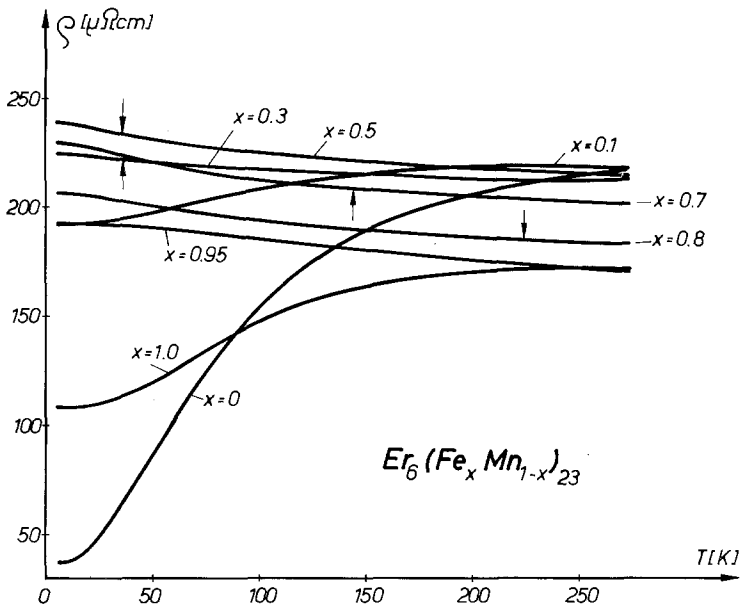

Fig. 77. ρ vs. T curves for various concentrations of the pseudobinary $Er_6(Fe_xMn_{1-x})_{23}$ system (Gratz and Kirchmayr, 1976).

three times larger than that of the isostructural compound YAl_2. Furthermore, the thermopower saturates above 200 K. This was not observed for YAl_2. We feel that this saturation of the thermopower may be characteristic of metal in which the d-electrons play a dominant role in the transport properties. In fact, Muir and Zuckermann (1975) used an s–d scattering mechanism for the conduc-

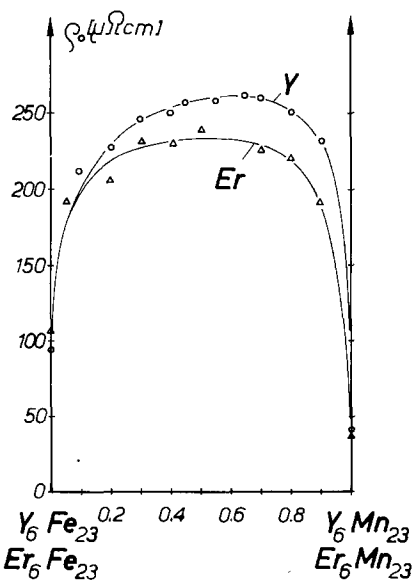

Fig. 78. Concentration dependence of ρ_0 in $Y_6(Fe, Mn)_{23}$ and $Er_6(Fe, Mn)_{23}$ (Gratz and Kirchmayr, 1976).

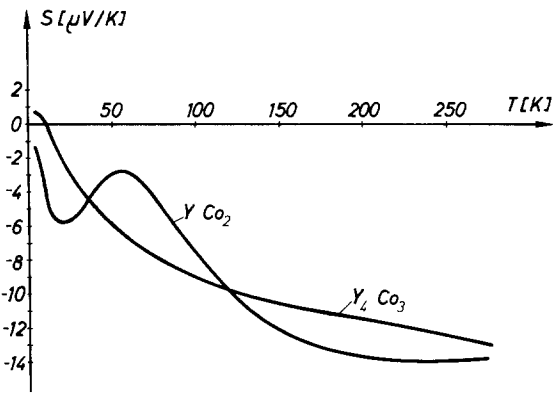

Fig. 79. S vs. T curves of YCo_2 and Y_4Co_3 (Gratz et al., 1980a).

tion electrons to show that the diffusion thermopower is a sensitive function of the density of state of the d-electrons and its derivatives at the Fermi level.

The T^2 dependence of the low-temperature resistivity of YCo_2 was analysed in terms of spin fluctuations in section 4.2.1.1 alone. It is possible that the minimum in the thermopower of YCo_2 at 20 K may also be due to spin fluctuations though no analysis is as yet extant. The absolute thermopower of YCo_2 and Y_4Co_3 is negative from 10 K to room temperature as seen in fig. 79 (Gratz et al., 1980a). The magnitude of the thermopower of Y_4Co_3 at high temperatures is about 10 μV/K which is comparable to the thermopower of YCo_2 in the same temperature range.

4.2.2.2. *RCo_2 (R = Tb, Dy, Ho, Er)*

Gratz et al. (1980b) studied the effect of a first-order magnetic phase transition on the thermopower of RCo_2 compounds. The results are shown in fig. 80. The first-order phase transition causes a discontinuity in the thermopower. The magnitude of the discontinuity increases with decreasing T_c, i.e. as the lanthanide atoms change from Tb to Er. This is consistent with the resistivity data of section 4.2.1.1 and the thermal expansion of Lee and Pourarian (1976).

The curvature in the thermopower found for RCo_2 compounds above T_c is the same for all the compounds and has the same character as the thermopower of YCo_2 above 70 K (see section 4.2.2.1). The magnitude of S found in this temperature range is about 12–15 μV/K. Gratz et al. (1980b) postulated that the curvature is caused by an s–d scattering mechanism which cannot occur in compounds with a low density of d-states at the Fermi level. The similarity of the S vs. T curves in the paramagnetic temperature range implies that the contribution of the localized moments above T_c is practically temperature independent for these compounds. Note the similarity of the S vs. T curve of YCo_2 to that of $ErCo_2$ above T_c.

4.2.2.3. *$Gd(Co_xNi_{1-x})$: $0 \leq x \leq 0.3$*

The thermopower of these compounds was measured by Gratz et al. (1980c) and is shown in fig. 81. Fig. 81 shows that the thermopower depends in a complex manner on the temperature below T_c. There is clear evidence for the

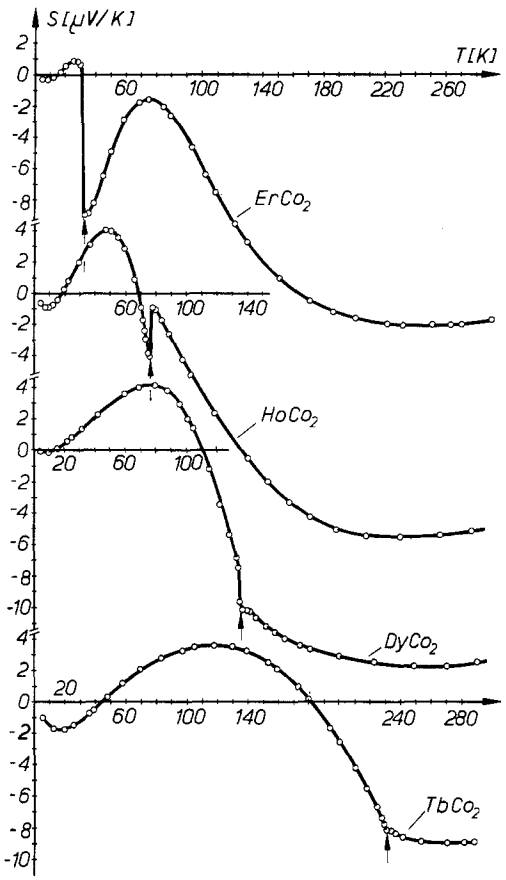

Fig. 80. Thermopower as a function of temperature for: $ErCo_2$, $HoCo_2$, $DyCo_2$, $TbCo_2$. Arrows indicate T_c (Gratz et al., 1980b).

influence of magnetic order on the thermopower. This can be seen from a comparison between the thermopower of the non-magnetic isostructural compound LaNi and that of Gd(Co, Ni) compounds (fig. 81). The behaviour of the S vs. T curve below T_c shows a systematic variation with increasing Co concentration. The maximum found in the S vs. T curves near 25 K may be due to either the influence of the magnons on thermopower or the influence of the splitting of the conduction band due to magnetic order or both. The thermopower was found to be a linear function of temperature in the paramagnetic regime. The gradient of the linear portion of the thermopower was analysed by Gratz et al. (1980c) using eq. (4) for different Co concentrations and the results are shown in fig. 82. These results show that dS/dT decreases linearly with increasing Co concentration.

4.2.2.4. $(Gd_xY_{1-x})_4Co_3$: $0 \leq x \leq 1.0$

The temperature dependence of the thermopower of $(Gd, Y)_4Co_3$ compounds is given in fig. 83 for several Gd concentrations. Gratz et al. (1980d) have shown that the Curie temperature of these compounds varies almost linearly with Gd

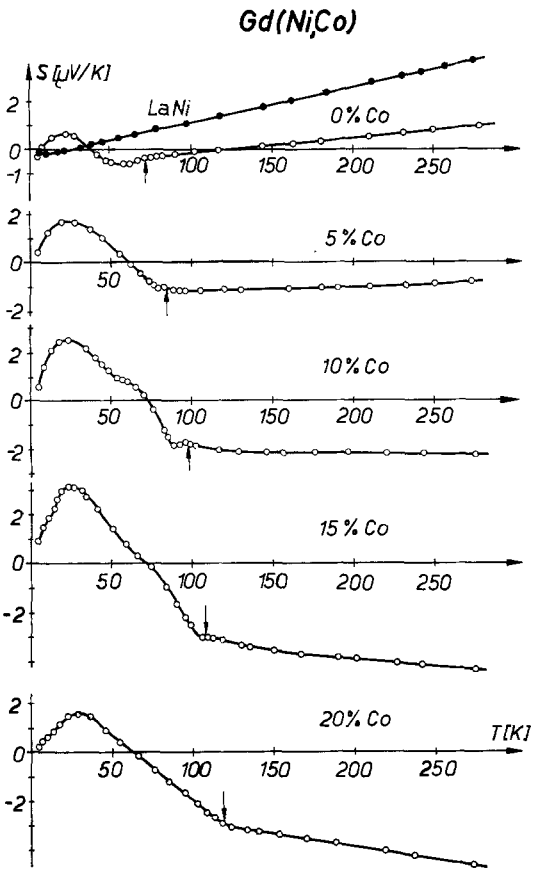

Fig. 81. S vs. T curves of various concentrations of the pseudobinary $Gd(Co_xNi_{1-x})$ system. The ordering temperatures are indicated by arrows (Gratz et al., 1980c).

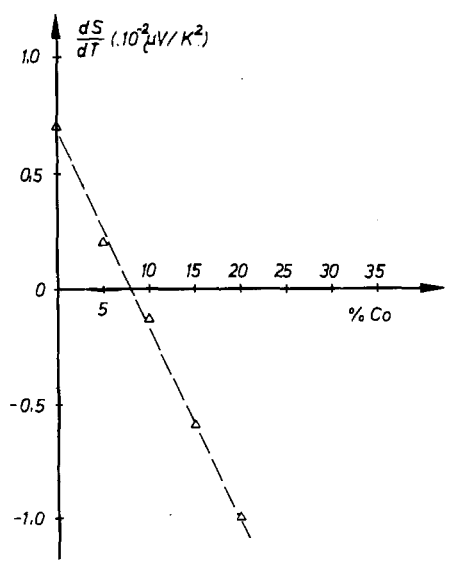

Fig. 82. The slope of $S(T)$ in the paramagnetic temperature range (dS/dT) as a function of the Co concentration for the $Gd(Co_xNi_{1-x})$ system (Gratz et al., 1980c).

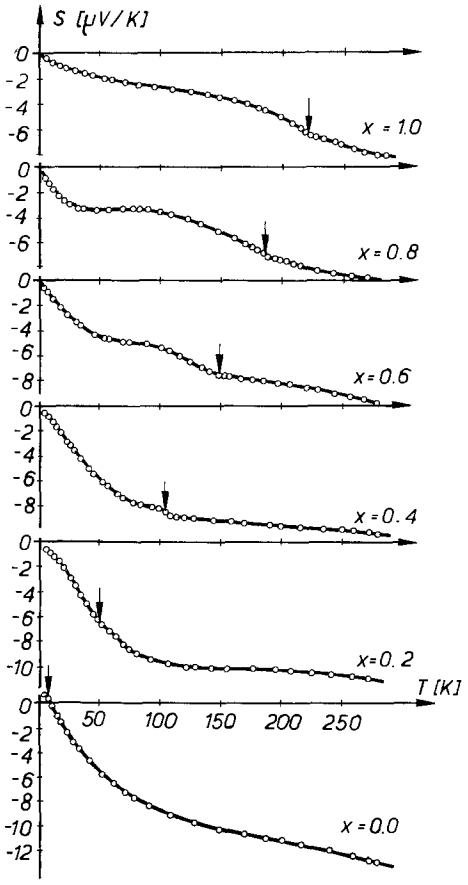

Fig. 83. S vs. T curves of various concentrations of the pseudobinary $(Gd_xY_{1-x})_4Co_3$ system. The ordering temperatures are indicated by arrows (Gratz et al., 1980d).

concentration. Fig. 83 shows that a kink appears in the thermopower at the Curie temperature for high Gd concentrations. It can also be seen from fig. 83 that the thermopower is negative for all temperatures above 10 K.

4.2.2.5. $Gd_4(Co_{1-x}Ni_x)_3$: $0 \leq x \leq 0.2$

The thermopower of some $Gd_4(Co, Ni)_3$ pseudobinary compounds is given in fig. 84 (Gratz et al., 1982b). Note that the substitution of only 5% for Co causes a pronounced change in the S vs. T curve. This could possibly imply that a variation of the conduction electron concentration has considerably more effect on the thermopower than the substitution of the isoelectronic Gd by Y ions (see section 4.2.2.4). Fig. 84 shows that the kink disappears with increasing Ni concentration. This is also seen in the behaviour of the resistivity of these compounds (see section 4.2.1.5).

4.2.2.6. $Y(Ni_{1-x}Co_x)_3$: $0 \leq x \leq 0.5$

The variation of the thermopower of these compounds with Co concentration is given in fig. 85 (Hilscher et al., 1980). We see that the thermopower is negative for the whole temperature range and for all Co concentrations. It is interesting to

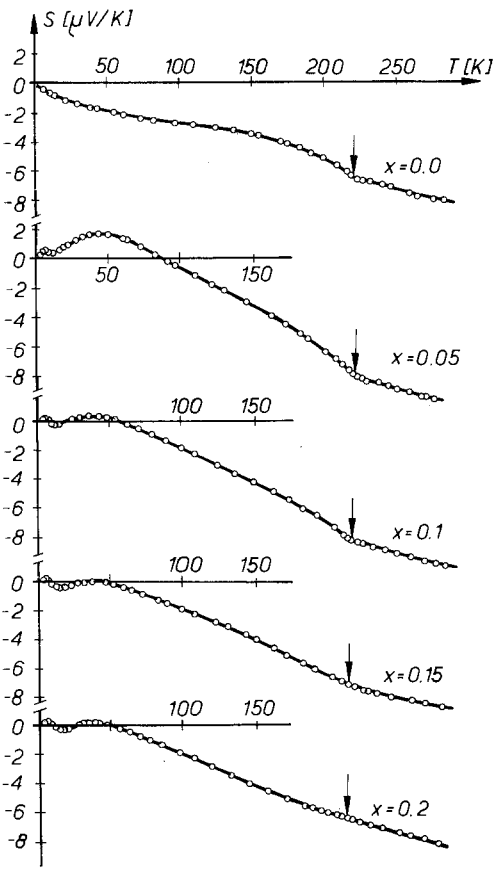

Fig. 84. S vs. T curves of various concentrations of the pseudobinary $Gd_4(Co_{1-x}Ni_x)_3$ system. The ordering temperatures are indicated by arrows (Gratz et al., 1982b).

note that the sign of the thermopower is generally found to be negative for those compounds in which d-electrons contribute to the transport properties. However, a negative thermopower is not exclusive to d-electron metals and has also been found in metals with no d-electron contribution.

5. Electrical resistivity of amorphous rare earth alloys

5.1. *Theoretical introduction*

Amorphous rare earth alloys exhibit the same variety of magnetic effects as is found for RI compounds. In addition their resistivity often manifests a behaviour which is typical of amorphous metals such as resistivity minima and negative temperature coefficients of resistivity. It is important to note that the unifying feature of all amorphous metals is the real space structure which can be described in terms of a random close packing model of hard spheres (Cargill, 1975). The magnetic feature thus depends on the type and concentration of the

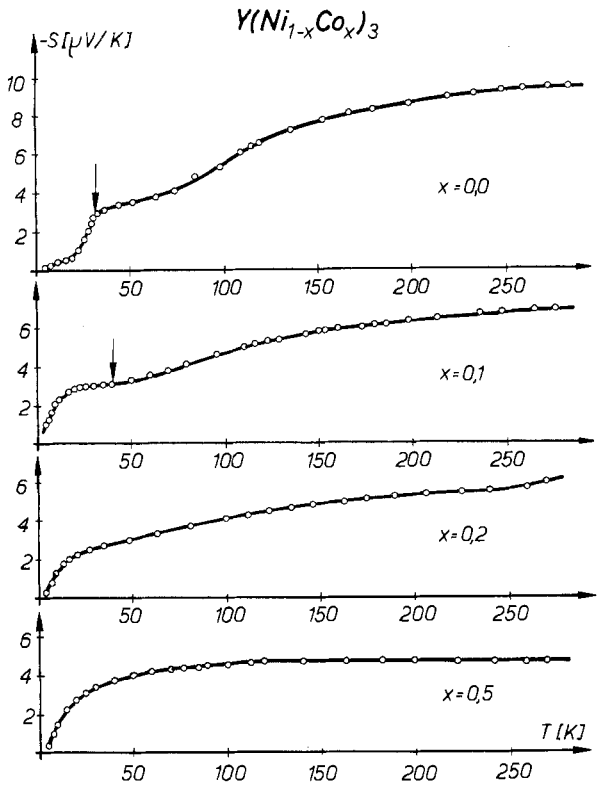

Fig. 85. S vs. T curves of various concentrations of the pseudobinary $Y(Ni_{1-x}Co_x)_3$ system. The ordering temperatures are indicated by arrows (Hilscher et al., 1980).

magnetic components. Alloys of 3d transition metals (Fe, Co, Ni) with metalloids (B, S, Si, P) tend to be soft ferromagnets. Most R-amorphous alloys have at least another metallic component, either Al, a noble metal or a transition metal and hence may exhibit a more complicated magnetic behaviour. Under some conditions such alloys may therefore be hard magnetic materials. We begin by summarizing the theory of the resistivity of amorphous metals and continue with a description of the resistivity data for R-amorphous alloys. (For more information see chapter 41 by Gasgnier.)

The temperature dependence of the resistivity of amorphous non-magnetic metals has been studied by many authors. The most popular theory is still Ziman's theory for the resistivity of liquid metals and several authors have extended this theory to include a dynamic structure factor. Cote and Meisel (1979) used an isotropic Debye spectrum for the phonons to calculate the dynamic structure factor. They obtained a quadratic dependence of the resistivity on temperature at low temperatures. Froböse and Jäckle (1977) used both a Debye model and a model of uncorrelated Einstein oscillators in conjunction with a dynamic structure factor to analyse the resistivity. They found that the second model leads to a satisfactory fit for the temperature dependence of the resistivity of CuSn alloys for $T \geq 10$ K. Ohkawa and Yosida (1977) predict a T^4

term in the resistivity of non-magnetic amorphous metals at low temperatures from anharmonicity effects. The existence of negative temperature coefficients of resistivity can be understood in terms of both the Ziman theory and theories of disorder such as the coherent potential approximation (CPA). The "logarithmic" minimum which occurs in the resistivity of a great number of alloys most of which are magnetic, has been explained in terms of both the scattering of electrons by a two-level tunneling system (Cochrane et al., 1975) and the Kondo effect (Nagel, 1978). The reader is referred to the original articles for details.

There are several theories for the resistivity of amorphous ferromagnetic alloys. Richter et al. (1979) obtain expressions for the spin-disorder resistivity using a structurally disordered Heisenberg model. They found a $T^{3/2}$ law for the resistivity at low temperatures ($T \ll T_c$). Silver and McGill (1974) and Continentino and Rivier (1978) investigated the resistivity minima of amorphous ferromagnetic alloys in terms of dynamic spin excitation spectra. In particular, Continentino and Rivier predict both a logarithmic term and a resistivity minimum for amorphous ferromagnets from an analysis of the inelastic scattering of conduction electrons by diffuse modes associated with the longitudinal compound of the magnetization. We have not made an exhaustive survey of the subject but we hope that we have informed the reader of some of the more important aspects of the transport properties of amorphous metals. (For more information see chapter 41 by Gasgnier.)

Very little theory exists for amorphous alloys containing rare earth metals. It is of interest to note that since nearly all R-amorphous alloys are composed of at least two metallic components, they are analogous to RI compounds. Asomoza et al. (1979) found that $DyNi_3$, $HoNi_3$, and $ErNi_3$ exhibit a minimum in the ρ vs. T curve which is sensitive to a magnetic field and which is clearly associated with the magnetic ordering. They analysed this in terms of the quasi-elastic approximation used by de Gennes and Friedel (1958) for the spin-disorder scattering of lanthanide metals. They obtain the following modified expression for the resistivity due to the exchange interaction

$$\rho_{\text{mag}} = [J/(J+1)]\rho_{\text{M}}[C_1 + C_1^2(a_{11}(2k_{\text{F}}) - 1)\mu_\ell^2]. \tag{71}$$

ρ_{M} is proportional to ρ_{spd} of eq. (23), $a_{11}(2k_{\text{F}})$ is the partial structure factor at $2k_{\text{F}}$, μ_ℓ is a parameter characteristic of the local magnetic order and C_1 is the concentration of magnetic ions. Eq. (71) describes the contribution from magnetic ordering to ρ_{mag} which is positive or negative according to whether $a_{11} > 1$ or $a_{11} < 1$. The application of this expression to R-amorphous alloys will be discussed in section 5.2.5.

One theory which has been successfully applied to the magnetic properties of R-compound alloys containing non-S-state R-ions is the theory of random magnetic anisotropy (RMA) of Harris et al. (1973). This has been used to calculate the magnetoresistivity of amorphous alloys exhibiting RMA. Bhattacharjee and Coqblin (1979) first obtained the static spin–spin correlation function of the RMA model by using a self-consistent two-spin cluster approximation. The quasi-elastic approximation of de Gennes and Friedel is then

used to obtain values for the magnetoresistivity from the two-spin correlation functions for both ferromagnetic and antiferromagnetic materials.

5.2. *Resistivity of amorphous alloys containing rare earth components*

A common feature of R-amorphous alloys and transition metal–metalloid alloys is that they show similar transport properties such as high resistivities with weak temperature dependence and often at low temperature a logarithmic variation with temperature (Kästner et al., 1980). The magnetic R-alloys often show additional transport behaviour. We will now discuss this in detail for several R-amorphous alloys.

5.2.1. $Gd_{1-x}B_x$ (B = *C, Ni, Cu, Ga*)

Buschow and Beekmans (1978) have shown that these alloys are all ferromagnets (except for the GdC compound) whose magnetic properties do not seem to be described by a RKKY type coupling. The magnetization saturates in a field of 18 kOe and the magnetization per Gd atom corresponds to the value of $g\mu_B J$ for Gd^{3+}. The magnetic susceptibility follows a Curie–Weiss behaviour whose intercept is close to 0 K. For all magnetic alloys T_c is of the order of 110 to 160 K as given by the arrows in fig. 86.

The resistivity of Gd_8C_2, Gd_7Ni_3, Gd_7Cu_3, and Gd_8Ga_2 is shown in fig. 86. It can be seen that there are no important magnetic contributions to the resistivity. The spin-disorder resistivity does not disappear below T_c and kinks or "knee-like" singularities are absent at T_c. Fig. 86, however, shows that the temperature

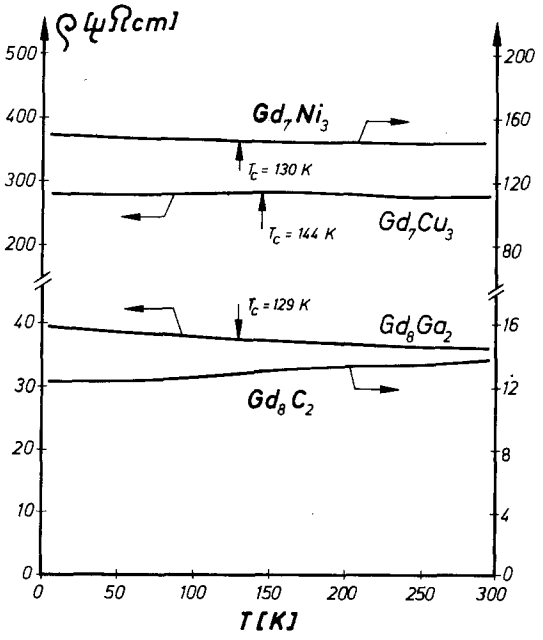

Fig. 86. ρ vs. T curves of amorphous RI alloys (Gd_8C_2, Gd_7Ni_3, Gd_7Cu_3, and Gd_8Ga_2) (Buschow and Beekmans, 1978).

coefficients of resistivity are weakly negative for all temperatures in the case of Gd_7Ni_3 and Gd_8Ga_2.

Buschow and Beekmans (1978) conclude that the behaviour of these alloys is very different from their RI compound analogues and that the RKKY coupling is of little importance because of the large nearest neighbour separation. They deem it more likely that the Gd moments couple via a direct 5d–5d interaction.

5.2.2. $Ni_{1-x}Y_x$ ($x = 0.044$, 0.07); Fe_5Y, Fe_2Y

Cochrane and Strom-Olsen (1978) report resistivity and magneto-resistivity measurements on several samples of amorphous NiY and FeY over the temperature range from 1.1 K to 350 K and in magnetic fields up to 50 kOe. Although both systems are amorphous their transport and magnetic behaviour is in strong contrast. NiY is extremely soft magnetic exhibiting characteristics of a weak itinerant ferromagnet. Its resistivity exhibits a minimum near 10 K with a log T region at lower temperatures and a relatively large positive $d\rho/dT$ at higher temperatures (see fig. 87). The onset of magnetic order is seen in the transport data as a step in $d\rho/dT$ around T_c. On the other hand, FeY is hard magnetically and has a resistivity characterized by a negative $d\rho/dT$ at all temperatures (see fig. 88). The magnetoresistivity is positive and no effect is observed at the magnetic ordering temperature.

5.2.3. $(R_{0.65}Fe_{0.35})_{0.9}B_{0.1}$ ($R = Gd$, Er); $(Er_{1-x}X_x)_yB_{1-y}$ ($X = Al$, Ga, Au, Ni, Co) $y = 0.8$ *or* 0.9, $x = 0.2$, 0.25, 0.32, 0.35

Hadjipanayis et al. (1980) measured the magnetization, the magnetic susceptibility, and the resistivity of amorphous alloys of the above-mentioned type.

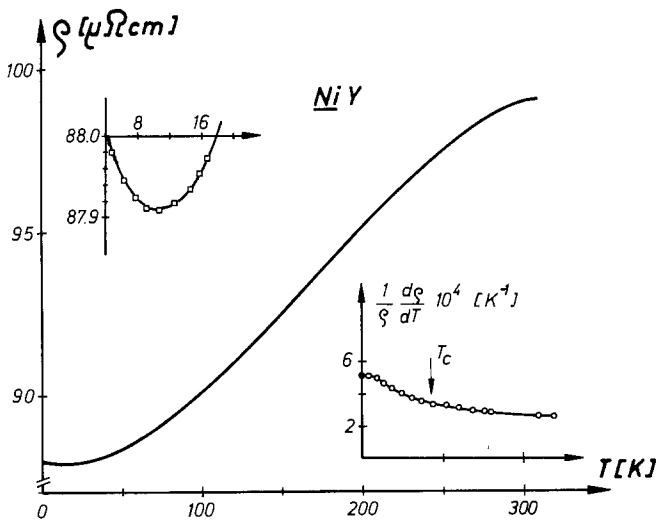

Fig. 87. The ρ vs. T curve of amorphous $Ni_{0.93}Y_{0.07}$. The inset on the left shows the low-temperature region on expanded scales. The inset on the right shows the relative slope of $\rho(T)$ in the neighbourhood of T_c (Cochrane and Strom-Olsen, 1978).

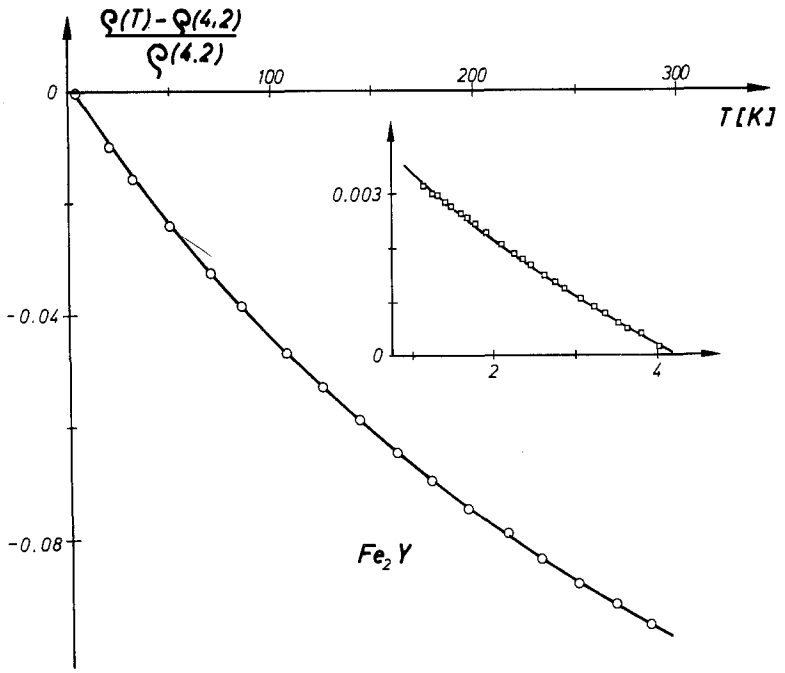

Fig. 88. The normalized electrical resistivity of amorphous Fe_2Y as a function of temperature with the low-temperature region in the inset (Cochrane and Strom-Olsen, 1978).

They showed that the magnetization of $(Er_{0.65}Fe_{0.35})_{0.9}B_{0.1}$ does not saturate below 80 kOe whereas that of $(Gd_{0.65}Fe_{0.35})_{0.9}B_{0.1}$ saturates above 40 kOe. They conclude that the Er alloys exhibit RMA (see section 5.1) and should therefore be a good candidate for spin glass behaviour. Then they study several Er-based amorphous alloys. The magnetic susceptibility is shown in fig. 89 for all except the Fe and Co alloys. A broad maximum can be seen in $\chi(T)$ for all samples at low temperatures. They deduce from the behaviour of $\chi(T)$, from the existence of field cooling effects, and from the behaviour of the resistivity that these Er-based alloys are spin glasses.

The resistivity of all the Er-based alloys is shown in fig. 90. It can be seen that the alloys containing Al, Ga, and Au all have positive temperature coefficients of resistivity at high temperatures whereas the alloys containing transition metals have negative temperature coefficients. Hadjipanayis et al. (1980) interpret this behaviour in terms of the Ziman theory of liquid metals.

The liquid helium temperature coefficient of resistivity also changes from positive to negative in going from $(Er_{0.8}Al_{0.2})_{0.8}B_{0.2}$ to $(Er_{0.65}Fe_{0.35})_{0.9}B_{0.1}$ as can be seen in fig. 90. This is interpreted in terms of the structure factor a_{11} of eq. (71) which is due to magnetic ions. Fig. 90 further shows that anomalies are observable in ρ at 80 K for the Er alloys containing Ga and Au. The authors deduce from the shape of the hysteresis loop of the Au alloys that these

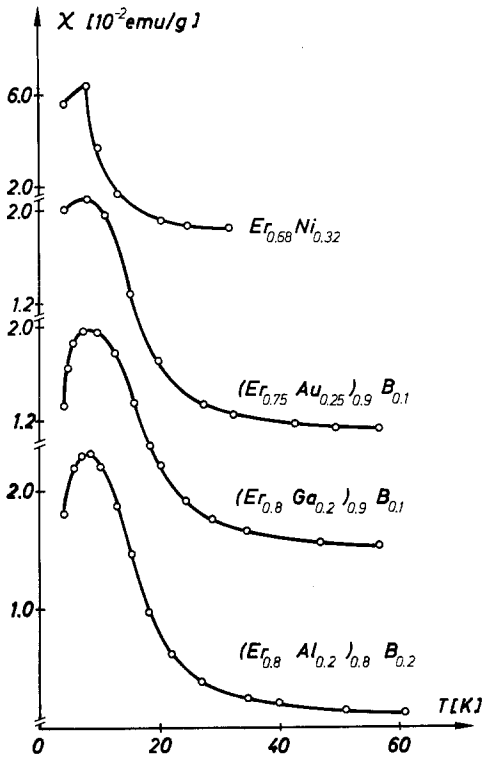

Fig. 89. The magnetic susceptibility for erbium-rich metallic glasses ($H = 700$ Oe) (Hadjipanayis et al., 1980).

anomalies may be due to local antiferromagnetic spin correlations and suggest that the Er alloys are on the borderline of magnetic order. Further experiments would therefore be of interest to examine this point.

5.2.4. R_xAg_{1-x}, $R_xLu_{0.5-x}Ag_{0.5}$ (R = *lanthanide*)

Figs. 91 and 92 show the temperature and field dependence of the normalized resistivity for $Gd_{0.5}Ag_{0.5}$ and $Dy_{0.35}Lu_{0.15}Ag_{0.5}$ amorphous alloys, respectively. (To remove the anisotropic contribution to the magnetoresistance from quadrupole scattering, $\bar{\rho}$ is plotted as a function of temperature, $\bar{\rho}$ is given by eq. (72) in section 5.2.5.) The samples were made using a sputtering technique (Ousset et al., 1980). An upturn in the resistivity below the magnetic ordering temperature was observed for both alloys. The ordering temperatures are indicated by arrows in figs. 91 and 92. Similar behaviour was reported for amorphous $Dy_{0.5}Ag_{0.5}$ and $Er_{0.5}Ag_{0.5}$ alloys (Ousset et al., 1980). As can be seen from figs. 91 and 92 the magnetoresistance is negative for these two alloys. Both the upturn in the $\bar{\rho}/\rho(4.2)$ vs. T curves and the negative magnetoresistance were accounted for by coherent exchange scattering with a dominant contribution from antiferromagnetic pairs having a negative interference factor (see Ousset et al. (1980) and eq. (71)). A structural mechanism for the upturn in the resistivity was ruled out because of a pronounced dependence on the external magnetic field.

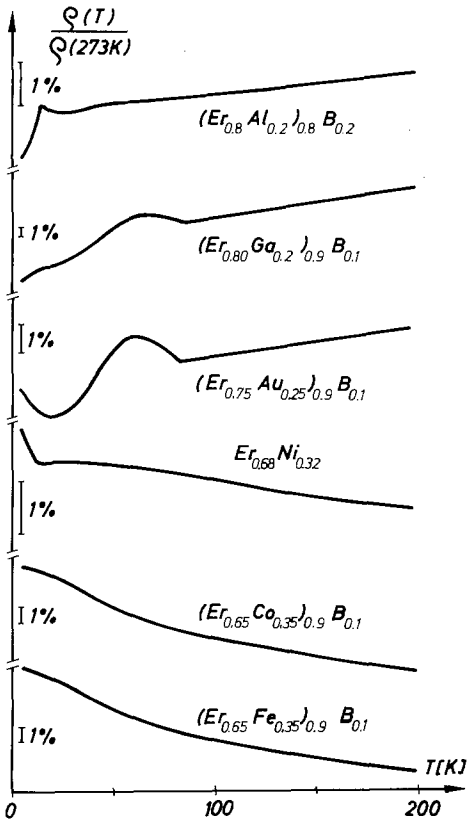

Fig. 90. The normalized electrical resistivity for erbium-rich metallic glasses (Hadjipanayis et al., 1980).

5.2.5. *RNi_3 (R = Y, Gd, Ho, Er)*

Asomoza et al. (1979) studied the magnetic and transport properties of several amorphous RNi_3 (R = Y, Gd, Ho, Er) alloys prepared by sputtering. They found that YNi_3 is non-magnetic and that the other RNi_3 amorphous alloys order magnetically at low temperatures (between 2 K and 50 K). It was shown that the R-moments order asperomagnetically (ferromagnetically in the case of $GdNi_3$). In most of the alloys under consideration Ni carries no magnetic moment. Above the ordering temperature the magnetic susceptibilities obey a Curie–Weiss law. Fig. 93 shows the normalized resistivity as a function of temperature. The value of the residual resistivity was found to be of the order of 150 to 300 $\mu\Omega$ cm. The resistivity measurements exhibit minima in the resistivity curves which behave differently for different amorphous alloys. The minima in the Y and Gd compound show practically no magnetic field dependence whereas those found in the Dy, Ho, and Er alloys are quite sensitive to magnetic fields.

The field dependence of the resistivity minimum in $HoNi_3$ is given in fig. 94. The resistivity in the applied field was taken to be the average resistivity $\bar{\rho}(H, T)$ given by

$$\bar{\rho}(H, T) = \tfrac{1}{3}\rho_{\parallel}(T, H) + \tfrac{2}{3}\rho_{\perp}(T, H), \tag{72}$$

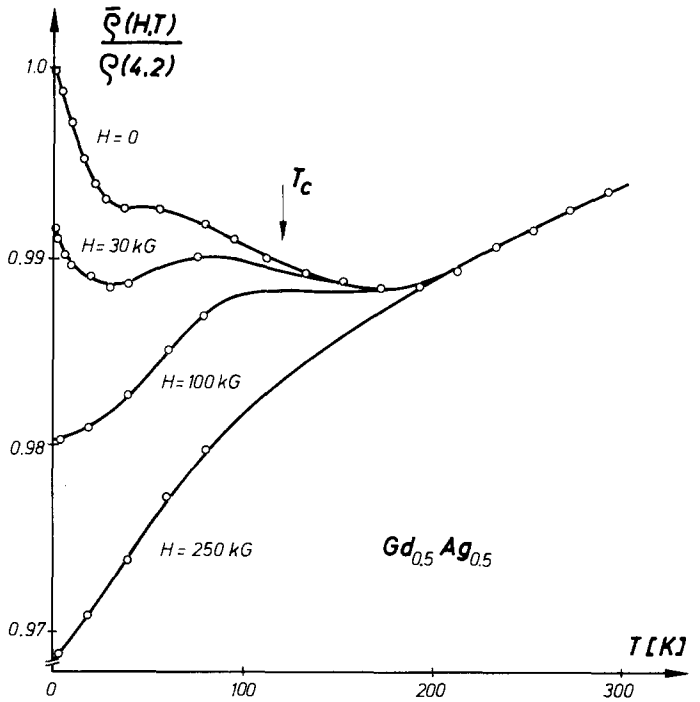

Fig. 91. The normalized electrical resistivity as a function of temperature at different magnetic fields of amorphous $Gd_{0.5}Ag_{0.5}$. The arrow indicates the magnetic ordering temperature (Ousset et al., 1980).

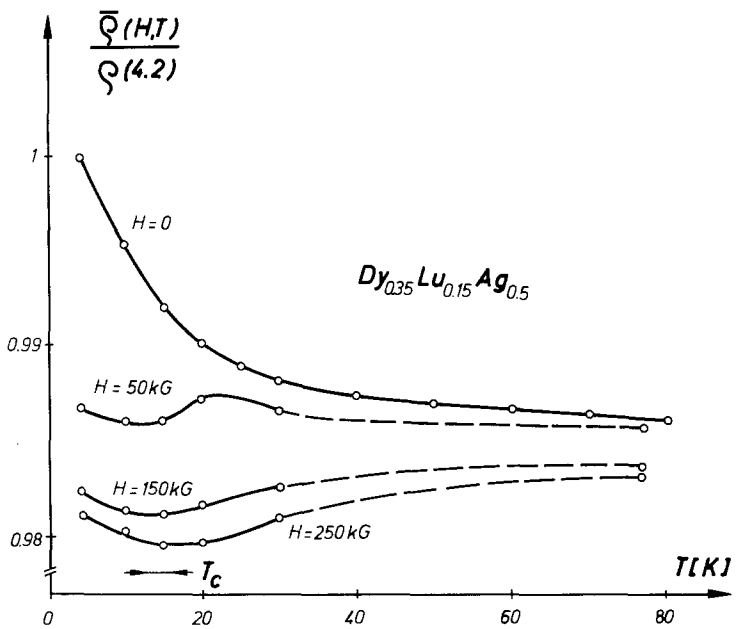

Fig. 92. The normalized electrical resistivity as a function of temperature at different magnetic fields of amorphous $Dy_{0.35}Lu_{0.15}Ag_{0.5}$. The arrows indicate the region where the magnetic order appears (Ousset et al., 1980).

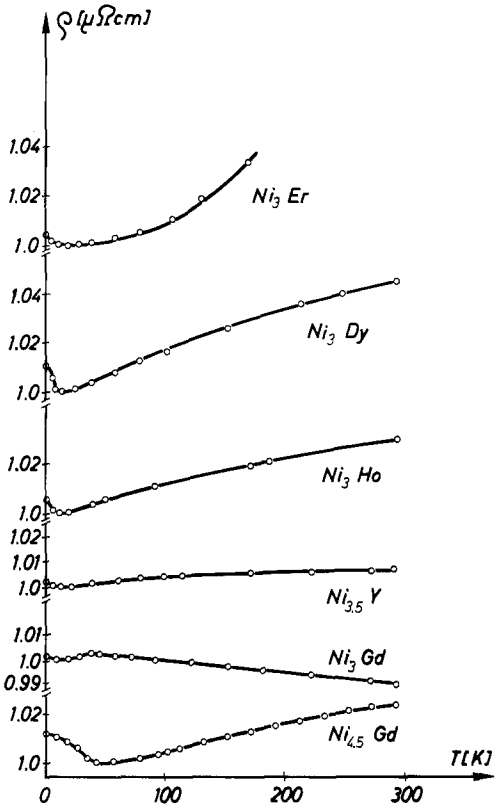

Fig. 93. The normalized electrical resistivity as a function of temperature of various amorphous Ni_3R alloys (R = Y, Gd, Dy, Ho, Er) (Asomoza et al., 1979).

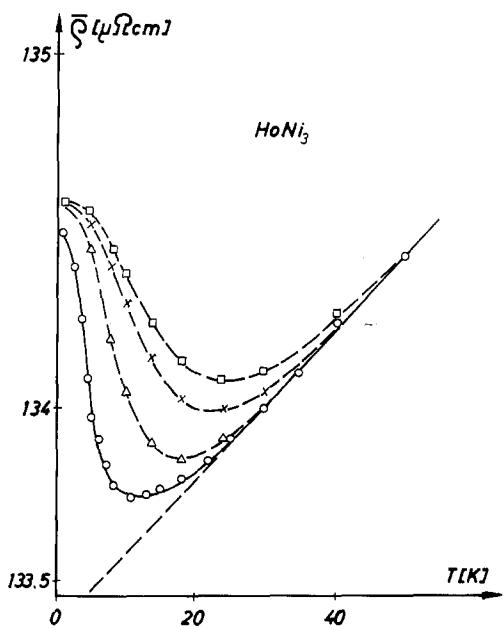

Fig. 94. The electrical resistivity of amorphous $HoNi_3$ as a function of temperature in several magnetic fields ($\bar{\rho}(H, T)$ is given by eq. (72), ∘, $H = 0$ kG; △, $H = 8$ kG; × $H = 20$ kG; □, $H = 30$ kG) (Asomoza et al., 1979).

where $\rho_{\parallel}$ and $\rho_{\perp}$ are the resistivities measured in longitudinal and transverse fields, respectively. It can be seen from fig. 94 that the minimum of $HoNi_3$ becomes less deep as the external magnetic field is increased.

The experimental results for $DyNi_3$, $HoNi_3$, and $ErNi_3$ are in good agreement with the behaviour predicted by eq. (71) provided that $a_{11} > 1$. The positive contribution from magnetic ordering to ρ appears somewhat above T_c. This can be explained by the dependence of the resistivity on the parameter μ_ℓ of eq. (71) which describes the short-range local order. The reader is referenced to the original articles for details.

6. Conclusion

In this article we have attempted to give a systematic description of the existing data for the transport properties of RI compounds. We have been able to distinguish four main trends:

(i) The non-magnetic compounds, for which the d-bands are fully occupied have transport properties which are dominated by electron–phonon scattering at high temperatures. YAl_2 is a typical example.

(ii) When the d-bands of the non-magnetic RI-compounds are no longer full and the conduction electrons have a partial d-character, the resistivity no longer obeys the Bloch–Grüneisen law and tends to saturate at higher temperatures. Some of these compounds, such as YCo_2 are enhanced paramagnets and their low-temperature resistivity is dominated by electron–paramagnon scattering. The saturation of the resistivity is, however, not well understood and we have therefore given a summary of Allen's analysis which describes possible non-magnetic mechanisms for saturation in section 2. A magnetic mechanism for saturation based on spin fluctuations in the d-band, is described in section 4. This interesting problem requires further detailed theoretical analysis and the authors feel that the saturation of resistivity can never be entirely due to magnetic effects alone. There are as yet insufficient data for the thermopower and thermal conductivity of these compounds. However, we are able to distinguish some trends.

(iii) When the R-component of the RI compounds sustains a localized magnetic moment, but the other components are non-magnetic in the sense of (i), the behaviour of the resistivity with temperature is correctly described by fig. 13. These compounds are all magnetically ordered at low temperatures and an anomaly always occurs at the ordering temperature in all the transport properties. The large magnitude of the R-magnetic moments appears to dominate the transport properties which therefore reflect the magnetic behaviour of these RI compounds. We thus feel that the experimental data are well described by the theory of section 3.1 in this case. The resistivity in the paramagnetic regime is usually described for these compounds by a constant resistivity due to spin-disorder scattering on which the usual linear contribution from electron–phonon scattering is superimposed.

The contribution from magnetic scattering to the total thermopower well above the magnetic ordering temperature appears to be linear in temperature in these compounds. Data for the thermal conductivity exist to our knowledge for RAl_2 compounds only. These data show the effect of magnetic scattering in a manner similar to that of the other transport properties.

(iv) The transport properties become much more complex when the R-component has a localized moment and when there is also a magnetic 3d transition metal component present. In this case a kink is observed in the transport properties at the ordering temperature together with a tendency of the resistivity and the thermopower to saturate in the paramagnetic regime. This is similar to the case of enhanced paramagnetic compounds (see (ii) above).

Some of the pseudobinary compounds in this group have transport properties which give evidence of high substitutional disorder. For example, the residual resistivity of $R_6(Fe, Mn)_{23}$ compounds is 250 $\mu\Omega$ cm and the ρ vs. T curves show a negative temperature coefficient of resistivity at some concentrations.

We have also described some of the existing data for the transport properties of amorphous rare earth alloys. We feel that these are parallel systems to the crystalline RI compounds since they can be made in the same concentration. Also a greater range of concentrations is available in RI amorphous alloys because they all have similar real space structure and are therefore not subject to the metallurgical constraints of crystalline RI compounds. These alloys should prove useful in helping to establish the variety of scattering mechanisms for electrons in RI intermetallic systems.

The study of the transport properties of RI compounds gives useful information on the physical properties of these compounds. We hope therefore that this article will stimulate further theoretical and experimental investigations in this field.

Acknowledgement

We particularly wish to thank Prof. Hans Kirchmayr for having made available the resources of the Institute of Experimental Physics of the Technical University of Vienna and for helpful discussions. One of us (E.G.) wishes to thank the "Österreichische Forschungsgemeinschaft" for a travel grant to Montreal and McGill University for its hospitality during a one-month leave of absence. The second author (M.Z.) is very grateful to the NSERC of Canada for a travel grant to Vienna and to the Technical University of Vienna for its hospitality during a one-month visit.

We both wish to thank Bernard Muir, John Strom-Olsen, Richard Harries of the McGill University, and Charles Foiles of the Michigan State University for useful and interesting discussions. One of us (E.G.) acknowledges with extreme gratitude the co-operation of Herbert Sassik, Ernst Bauer and Wolfgang Mikovits.

The authors are very grateful to Ernst Bauer, Sonja Romanyszyn, and Albert Zuser for their help during the preparation of the manuscript.

References

Allen, P.B., 1980, Theory of Resistivity Saturation, in: Suhl H. and M.B. Maple, eds., Superconductivity in d- and f-Band Metals (Academic Press, New York) p. 291.

Andres, K., E. Bucher, J.P. Maita and A.S. Cooper, 1972, Phys. Rev. Lett. **28**, 1652.

Andres, K., J.E. Graebner and H.R. Ott, 1975, Phys. Rev. Lett. **35**, 1779.

Andres, K., P.S. Wang, Y.H. Wang, B. Lüthi and H.R. Ott, 1976, Jahn–Teller Transition in $PrCu_2$, in: AIP Conference Proceedings 34, p. 222.

Arnold, P.G. and J. Popplewell, 1973, J. Phys. **F3**, 1985.

Asomoza, R., I.A. Campbell, A. Fert, A. Liénard and J.P. Rebouillat, 1979, J. Phys. **F9**, 349.

Atoji, M., 1969, J. Chem. Phys. **51**, 3877.

Ausloss, H., J.B. Sousa, M.M. Amado, R.F. Pinto, J.M. Moreira, M.E. Bragal and M.F. Pinheiro, 1980, On Various Anomalies in the Temperature Derivative of Transport Properties in Rare Earth Metallic Compounds, in: Gregory, J., J. McCarthy, J. James, J. Rhyne and H. Silber, eds., The Rare Earths in Modern Science and Technology (Plenum, New York) p. 273.

Bader, S. and F.Y. Fradin, 1976, in: Douglass, D.H., ed., Superconductivity in d- and f-Band Metals (Plenum, New York) p. 567.

Bailyn, M., 1960, Phil. Mag. **5**, 1059.

Bailyn, M., 1962, Phys. Rev. **126**, 2040.

Bakanowski, S., J.E. Crow and T. Mihalisin, 1977, Sol. State Comm. **22**, 241.

Balster, H., 1972, Diplomarbeit (undergraduate thesis), Ruhr-University Bochum (unpublished).

Bauer, E., 1981, Diplomarbeit (undergraduate thesis), Technical University Vienna, Austria (to be published).

Berthet-Colominas, C., J. Laforest, R. Lemair, R. Pauthenet and J. Schweizer, 1968, Cobalt **39**, 97.

Bhandari, C.M. and G.S. Verma, 1969, Nuovo Cimento **B60**, 249.

Bhattacharjee, A.K. and B. Coqblin, 1979, J. de Phys. **C5**, 225.

Blatt, F.J., D.J. Flood, W. Rowe, P.A. Schroeder and J.E. Cox, 1967, Phys. Rev. Lett. **18**, 395.

Blatt, F.J., P.A. Schroeder, C. Foiles and D. Greig, 1976, Thermoelectric Power of Metals (Plenum, New York) p. 170.

Bloch, D., D.M. Edwards, M. Shimizu and J. Voiron, 1975, J. Phys. **F5**, 1217.

Buschow, K.H.J., 1977, Rep. Prog. Phys. **40**, 1179.

Buschow, K.H.J., 1979, Rep. Prog. Phys. **42**, 1373.

Buschow, K.H.J. and N.M. Beekmans, 1979, Magnetic and Electrical Properties of Amorphous Alloys of Gd and C, Al, Ga, Ni, Cu, Rh, or Pd, in: Cantor, B., ed., Proc. Third Int. Conf. on Rapidly Quenched Metals, Brighton, England.

Buschow, K.H.J. and J.H. van Daal, 1970, Sol. State Comm. **8**, 363.

Capellmann, H., 1979, Z. Phys. **B34**, 29.

Cargill, G.S., 1975, Solid State Physics **5**, 227.

Chakraborty, B. and P.B. Allen, 1978, Phys. Rev. **B18**, 5225.

Chakraborty, B. and P.B. Allen, 1979, Phys. Rev. Lett. **42**, 736.

Chao Chang-Chih, 1966, J. Appl. Phys. **37**, 2081.

Cheng, W., G. Creuzet, P. Garoche, I.A. Campbell and E. Gratz, 1982, J. Phys. **12**, 475.

Cochrane, R.W., R. Harris and M.J. Zuckermann, 1978, Physics Reports **48**, 1.

Cochrane, R.W., R. Harris, J.O. Strom-Olsen and M.J. Zuckermann, 1975, Phys. Rev. Lett. **35**, 676.

Cochrane, R.W., R. Harris and M.J. Zuckermann, 1978, Physics Reports **48**, 1.

Continentino, M.A. and N. Rivier, 1977, J. Phys. **8**, 1187.

Coqblin, B. and A. Blandin, 1968, Advan. Phys. **17**, 281.

Coqblin, B., A.K. Bhattacharjee, B. Cornut, F. Gonzales-Jimenez, J.R. Iglesias-Sicardi and R. Jullien, 1976, J. Mag. Mag. Mat. **3**, 67.

Cornut, B. and B. Coqblin, 1972, Phys. Rev. **B5**, 4541.

Cote, P.J. and L.V. Meisel, 1978, Phys. Rev. Lett. **40**, 1586.

Cote, P.J. and L.V. Meisel, 1979, Amorphous Metals: Unique Test Material for Electron Transport Theory, in: B. Cantor, ed., Proc. Third Int. Conf. on Rapidly Quenched Metals Brighton, England, p. 62.

Craig, R. and R.S. Crisp, 1978, Electron Transport in Ag–Hg Alloys, in: First Int. Conf. on Thermoelectric Properties of Metallic Conductors, Michigan, 1977, pp. 51–56.

Craig, P.P., W.I. Goldberg, T.A. Kitchens and J.I. Budnick, 1967, Phys. Rev. Lett. **19**, 1334.

Crisp, R.S., 1978, The Diffusion Thermopower on the Two-band Model Separation of Diffusion and Phonon Drag Components in Noble Metal Alloy Systems, in: Proc. First Int. Conf. on Thermoelectric Properties of Metallic Conductors, Michigan, 1977, pp. 65–70.

Cyrot, M. and M. Lavagna, 1979, J. Physique **40**, 763.

de Gennes, P.G. and J. Friedel, 1958, J. Phys. Chem. Solids **4**, 71.

Dekker, A.J., 1965, J. Appl. Phys. **36**, 906.

Doniach, S., 1967, Proc. Phys. Soc. (London) **91**, 86.

Doniach, S., 1977, Physica **91B**, 231.

Duddenhoeffer, A.D. and R.R. Bourassa, 1977, Phys. Rev. **B15**, 3592.

Elenbaas, R.A., C.J. Schinkel and C.J.M. van Deudekom, 1980, J. Mag. Mag. Mat. **15–18**, 979.

Elliott, R.J. and F.A. Wedgwood, 1963, Proc. Phys. Soc. **81**, 846.

Figiel, H., E. Gratz and Cz. Kapusta, 1980, J. Mag. Mag. Mat. **23**, 123.

Fischer, K., 1967, Phys. Rev. **158**, 613.
Fisher, M.E. and J.S. Langer, 1968, Phys. Rev. Lett. **20**, 665.
Foiles, C.L. 1980, Phase Transitions **1**, 351.
Foiles, C.L. 1981, J. Appl. Phys. **52**, 2217.
Franz, W., F. Steglich, W. Zell, D. Wohlleben and F. Pobell, 1980, Phys. Rev. Lett. **45**, 64.
Froböse, K. and J. Jäckle, 1977, J. Phys. **F7**, 2331.
Gignoux, D., F. Givord, R. Lemaire and N. Nguyen Van Tinh, 1978, Influence on Nonmagnetic Impurities on the Ordering Temperature of the Rare Earth Compounds RCo_2, in: Corner, W.D. and B.K. Tanner, eds., Conference Series Nr. 37, (The Institute of Physics, Bristol and London) ch. 9, p. 300.
Gignoux, D., R. Lemaire, P. Mohlo and F. Tasset, 1980, J. Mag. Mag. Mat. **15–18**, 903.
Gratz, E., 1981, J. Mag. Mag. Mat. **24**, 1.
Gratz, E. and H.R. Kirchmayr, 1976, J. Mag. Mag. Mat. **2**, 187.
Gratz, E. and C. Poldy, 1977, Phys. Stat. Sol. (b) **82**, 159.
Gratz, E. and E.P. Wohlfarth, 1980, J. Mag. Mag. Mat. **15–18**, 903.
Gratz, E., H.R. Kirchmayr, V. Sechovsky and E.P. Wohlfarth, 1980a, J. Mag. Mag. Mat. **21**, 191.
Gratz, E., H. Sassik and H. Nowotny, 1980b, J. Phys. **F11**, 429.
Gratz, E., G. Hilscher, H.R. Kirchmayr and H. Sassik, 1980c, Transport and Magnetic Properties of the $Gd(Co_xNi_{1-x})$ Series, in: McCarthy, G.J., J.J. Rhyne, and H.B. Silber, eds., The Rare Earth in Modern Science and Technology, vol. 2 (Plenum, New York) p. 327.
Gratz, E., V. Sechovsky, E.P. Wohlfarth and H.R. Kirchmayr, 1980d, J. Phys. **F10**, 2819.
Gratz, E., R. Grössinger, H. Österreicher and F.T. Parker, 1981a, Phys. Rev. **B23**, 2542.
Gratz, E., J. Strom-Olsen and M.J. Zuckermann, 1981b, Sol. State Comm. **40**, 833.
Gratz, E., G. Hilscher, V. Sechovsky and H. Sassik, 1981c, (to be published).
Gratz, E., V. Sechovsky, V. Sima, Z. Smetana and J. Strom-Olsen, 1982a, Phys. Stat. Sol. (b) **111**, 1.
Gratz, E., G. Hilscher, H.R. Kirchmayr and H. Sassik, 1982b, Transport and Magnetic Properties of the $Gd_4(Co_{1-x}Ni_x)_3$ in: McCarthy, G.J., H.B. Silber and J.J. Rhyne, eds., The Rare Earth in Modern Science and Technology, vol. 3 (Plenum, New York) p. 167.
Gschneidner, K.A., Jr., 1969, J. Less Common Metals **29**, 293.
Guénault, A.M., 1971, J. Phys. **F1**, 373.
Hadjipanayis, G., G.S. Cornelison and D.J. Sellmyer, 1980, J. de Physique **41**, C8-512.
Haringa, E.F., K.H.J. Buschow and H.J. van Daal, 1973, Sol. Stat. Comm. **13**, 621.
Harris, R., M. Plischke and M.J. Zuckermann, 1973, Phys. Rev. Lett. **31**, 160.
Harris, R., M. Shalmon and M.J. Zuckermann, 1978, Phys. Rev. **B18**, 5906.
Hasegawa, H., 1980a, J. Phys. Soc. Japan **49**, 178.
Hasegawa, H., 1980b, J. Phys. Soc. Japan **49**, 963.
Hashimoto, Y., H. Fujii, H. Fujiwara and T. Okamoto, 1979a, J. Phys. Soc. Japan **47**, 67.
Hashimoto, Y., H. Fujii, H. Fujiwara and T. Okamoto, 1979b, J. Phys. Soc. Japan **47**, 73.
Hilscher, G., E. Gratz, H. Sassik, and H.R. Kirchmayr, 1980, Magnetic and transport properties of $Y(Ni_{1-x}Co_x)_3$, in: Rhodes, P., ed., Physics of Transition Metals, 1980, (Conference Series Nr. 55, The Institute of Physics, Bristol and London) p. 291.
Huebener, R.P., 1968, Phys. Rev. **171**, 634.
Hungsberg, R.E. and K.A. Gschneidner, Jr. 1972, J. Phys. Chem. Solids **33**, 401.
Iandelli, A. and A. Palenzona, 1979, Crystal Chemistry of intermetallic compounds, in: Gschneidner, Jr., K.A. and L. Eyring, eds., Handbook on the Physics and Chemistry of Rare Earths, Vol. 2 (North-Holland, Amsterdam) ch. 1, pp. 1–54.
Ihrig, H., 1973, thesis, Ruhr University, Bochum (unpublished).
Ikeda, K., 1977a, J. Phys. Soc. Japan **42**, 1541.
Ikeda, K., 1977b, J. Less Comm. Met. **52**, 101.
Ihrig, H. and S. Methfessel, 1976a, Z. Phys. **B24**, 381.
Ihrig, H. and S. Methfessel, 1976b, Z. Phys. **B24**, 385.
Ihrig, H., D.T. Vigren, J. Kübler and S. Methfessel, 1973, Phys. Rev. **B8**, 4525.
Ito, T., 1973, J. Sci. Hiroshima Univ. Ser. A **37**, 107.
Jones, H., 1956, Theory of Electrical and Thermal Conductivity in Metals, in: Flügge, S., ed., Handbuch der Physik, Vol. XIX (Springer Verlag, Berlin, Göttingen, Heidelberg) p. 266.
Kaiser, A.B. and S. Doniach, 1970, Intern. J. Mag. **1**, 11.
Kaneko, T., S. Miura, M. Ohashi and H. Yamauchi, 1974, The Magnetic Susceptibility and the Electrical Resistivity of the Compounds RAu_2 and RAg_2 (R = Gd, Tb, Dy, Ho, and Er), in: Proc. Int. Conf. Magn. Moscow, p. 370.
Kästner, J., H.J. Schink and E.F. Wassermann, 1980, Sol. State Comm. **33**, 527.
Kasuya, T., 1956, Prog. Theor. Phys. (Kyoto) **16**, 45.
Kasuya, T., 1959, Prog. Theor. Phys. (Kyoto) **22**, 227.
Kawatra, M.P., J.A. Mydosh and J.I. Budnick, 1970, Phys. Rev. **B2**, 665.
Kelly, F.M., 1953, Can. J. Phys. **31**, 81.
Kelly, F.M. and D.K.C. McDonald, 1952, Can. J. Phys. **31**, 147.
Kim, D.J., 1964, Prog. Theor. Phys. **31**, 921.
Kirchmayr, H.R. and C.A. Poldy, 1979, Magnetic Properties of Intermetallic Compounds, in: Gschneidner, Jr., K.A. and L. Eyring, eds., Handbook on the Physics and Chemistry of Rare Earths, Vol. 2 (North-Holland, Amsterdam) ch. 14, pp. 55–230.
Kolodziejczyk, A., B.V.B. Sarkissian and B.R. Coles, 1980, J. Phys. **F10**, L333.
Kondo, J., 1962, Prog. Theor. Phys. **27**, 772.
Kondo, J., 1965, Prog. Theor. Phys. **34**, 372.

Kondo, J., 1964, Prog. Theor. Phys. (Kyoto) **32**, 37.
Korenmann, V. and R.E. Prange, 1979, Phys. Rev. **B19**, 4691.
Lacroix, C. and M. Cyrot, 1979, Phys. Rev. **B20**, 1969.
Lee, E.W. and F. Pourarian, 1976, Phys. Stat. Sol. (a) **34**, 383.
Lemaire, R., Cobalt **33**, 201.
Lethuillier, P. and J. Chaussy, 1976, J. de Physique **37**, 123.
Liu, S.H., 1961, Phys. Rev. **121**, 451.
Liu, S.H., 1976, Phys. Rev. **B13**, 3962.
McEwen, K.A., 1978, Magnetic and Transport Properties of the Rare Earths, in: Gschneidner, Jr., K.A. and L. Eyring, eds., Handbook on the Physics and Chemistry of Rare Earths, Vol. 1, (North-Holland, Amsterdam) ch. 6, pp. 411–488.
Mackintosh, A.R., 1963, Phys. Lett. **4**, 140.
Maki, K., 1969, Prog. Theor. Phys. (Kyoto) **22**, 335.
Maple, M.B., 1969, Thesis, University of California, San Diego, USA.
Maple, M.B., L.E. Delong and B.C. Sales, 1978, Kondo effect: Alloys and Compounds, in: Gschneidner, Jr., K.A. and L. Eyring, eds., Handbook on the Physics and Chemistry of Rare Earths, Vol. 1 (North-Holland, Amsterdam) ch. 11, pp. 797–846.
Maranzana, F.E., 1970, Phys. Rev. Lett. **25**, 239.
Mathon, J., 1968, Proc. Roy. Soc. **A306**, 355.
Mikovits, W., 1981, Diplomarbeit (undergraduate thesis), Technical University Vienna, Austria (to be published).
Miura, S., T. Kaneko, M. Ohashi and H. Yamauchi, 1974, J. Phys. Soc. Japan **37**, 1464.
Mooij, J.H., 1973, phys. stat. sol. (a) **17**, 521.
Moriya, T., 1979, J. Mag. Mag. Mat. **14**, 1.
Moriya, T. and A. Kawabata, 1973, J. Phys. Soc. Japan **34**, 639.
Moriya, T. and Y. Takahashi, 1978a, J. Phys. Soc. Japan **45**, 397.
Moriya, T. and Y. Takahashi, 1978b, J. de Physique **39**, C6-1466.
Morton, N., B.W. James and G.H. Wostenholm, 1978, Cryogenics **18**, 131.
Muir, W.B. and M.J. Zuckermann, 1975, Can. J. Phys. **53**, 1777.
Murata, K.K. and S. Doniach, 1972, Phys. Rev. Lett. **29**, 285.
Nagel, S.R., 1978, Phys. Rev. Lett. **41**, 990.
Nicolas-Francillon, M., A. Percheron, J.C. Achard, O. Gorochov, B. Cornut, D. Jerome and B. Coqblin, 1972, Sol. Stat. Comm. **11**, 845.
Nielsen, P.E. and P.L. Taylor, 1974, Phys. Rev. **B10**, 4061.
Nowotny, H., 1980, private communication.
Ogawa, S., 1976, J. Phys. Soc. Japan **40**, 1007.
Ohashi, M., T. Kaneko and S. Miura, 1975, J. Phys. Soc. Japan **38**, 588.
Ohkawa, F.J. and K. Yosida, 1977, J. Phys. Soc. Japan **43**, 1545.
Ousset, J.C., J.P. Ulmet, R. Asomoza, J.B. Bieri, S. Askenazy and A. Fert, 1980, J. de Phys. **41**, C8-470.
Pierre, J., 1969, Sol. Stat. Comm. **7**, 165.
Poldy, C.A. and E. Gratz, 1978, J. Mag. Mag. Mat. **8**, 223.
Poldy, C.A. and K.N.R. Taylor, 1972, J. Phys. **F2**, L 105.
Popplewell, J., P.G. Arnold and P.M. Davies, 1967, Proc. Phys. Soc. **92**, 177.
Purwins, M.G., W.J.L. Buyers, T.M. Holden and E.C. Svensson, 1976, AIP Conf. Proc. **29**, 259.
Rao, V.U.S. and W.E. Wallace, 1970, Phys. Rev. **B2**, 4613.
Rao, V.U.S., R.D. Hutchens and J.E. Greedan, 1971, J. Phys. Chem. **32**, 2755.
Rice, M.J., 1967, Phys. Rev. **159**, 153.
Richard, T.G. and D.J.W. Geldart, 1973, Phys. Rev. Lett. **30**, 290.
Richter, R., M. Wolf and F. Goedsche, 1979, Phys. Stat. Sol. (b) **95**, 473.
Rosenberg, H.M., 1955, Phil. Trans. Roy. Soc. **A247**, 441.
Sakurai, J., T. Ishimasa and Y. Komura, 1977, J. Phys. Soc. Japan **43**, 5.
Sassik, H., thesis 1981, Technical University Vienna, Austria.
Sassik, H. and E. Gratz, 1981, to be published.
Schindler, A.I. and M.J. Rice, 1967, Phys. Rev. **164**, 759.
Šebek, J., J. Stehno, V. Sechovsky and E. Gratz, 1981, Sol. State Comm. **40**, 457.
Sherwood, R.C., H.J. Williams and J.H. Wernik, 1964, J. Appl. Phys. **35**, 1049.
Silver, R.N. and T.C. McGill, 1974, Phys. Rev. **B9**, 272.
Song, S.J. and R.S. Crisp, 1978, Thermopower in Alloys of Ag with Zn, Ga, Ge, and As at low temperatures, in: Proc. First Int. Conf. on Thermoelectric Properties of Metallic Conductors (Michigan, 1977) pp. 57–64.
Sousa, J.B., M.M. Amada, R.P. Pinto, J.M. Moreira, M.E. Braga, M. Ausloos, J.P. Leburton, J.C. van Hay, P. Clippe, J.P. Vigneron and P. Morin, 1980, J. Phys. **F10**, 933.
Steglich, F., 1977, Magnetic Moments of Rare Earth Ions in a Metallic Environment, in: Treusch, J., ed., Festkörperprobleme (Advances in Solid State Physics) Vol. XVII (Vieweg, Braunschweig) p. 319.
Steiner, W., E. Gratz, H. Ortbauer and H.W. Carnen, 1978, J. Phys. **F8**, 1525.
Stewart, A.M., G. Costa and G. Olcese, 1974, Austr. J. Phys. **27**, 383.
Suhl, H. and D. Wong, 1967, Physics **3**, 17.
Sütsch, P. and E. Umlauf, 1981, J. Low Temp. Phys. **42**, 11.
Taub, H. and S.J. Williamson, 1973, Sol. State Comm. **13**, 1021.
Taylor, K.N.R., 1971, Adv. Phys. **20**, 551.
Trego, A.L. and A.R. Mackintosh, 1968, Phys. Rev. **166**, 465.
Ueda, K., 1977, J. Phys. Soc. Japan **43**, 1497.
Ueda, K. and T. Moriya, 1975, J. Phys. Soc. Japan **39**, 605.
Usami, K. and T. Moriya, 1980, J. Mag. Mag. Mat. **20**, 171.
Van Daal, H.J. and K.H.J. Buschow, 1969a, Sol. Stat. Comm. **7**, 217.

Van Daal, H.J. and K.H.J. Buschow, 1969b, Phys. Rev. Lett. **23**, 408.
Van Daal, H.J. and K.H.J. Buschow, 1970, Phys. Stat. Sol. (a) **3**, 853.
Van Daal, H.J., P.B. van Aken and K.H.J. Buschow, 1974, Phys. Lett. **49A**, 246.
Van den Berg, G.J., 1964, Prog. Low. Temp. Phys. **4**, 194.
Van Dongen, J.C.M., G.J. Nieuwenhuys, J.A. Mydosh, A.H. van der Kraan and K.H.J. Buschow, 1980, Magnetic Properties and Electrical Resistivity of Transition Metal Laves Phase Compounds: $Y(Co_{1-x}Fe_x)_2$, $Y(Ir_{1-x}Fe_x)_2$, and $Hf(Co_{1-x}Fe_x)_2$, in: Rhodes, P., ed., Physics of Transition Metals, 1980 (Conference Series Nr. 55. The Institute of Physics, Bristol and London) p. 275.
Voiron, J., A. Berton and J. Chaussy, 1974, Phys. Lett. **50A**, 17.
Volkenshtein, N.V., V.P. Dyakina and V.E. Startsew, 1973, Phys. Stat. Sol. (b) **57**, 9.
Walker, E., H.G. Purwins, M. Landolt and F. Hullinger, 1973, J. Less Comm. Met. **33**, 203.
Wallace, W.E., 1973, Rare Earth Intermetallics (Academic Press, New York).
Wallace, W.E., S.G. Sankar and V.U.S. Rao, 1977, Crystal Field Effects in Rare Earth Intermetallic Compounds, in: Dunitz, J.D., P. Hemmerich, J.A. Ibers, C.K. Jørgensen, J.B. Neilands, D. Reinen and R.J.P. Williams, eds., Structure and Bonding, Vol. 33 (Springer Verlag, New York) pp. 1–52.
Włosewicz, D., K. Bartkowski and J. Rafalowicz, 1979, Acta Physica Polonica **A56**, 787.
Wohlfarth, E.P., 1976, Band magnetism and application, in: Foner, S., ed., Magnetism (Gordon and Breach, New York) ch. 2, p. 59.
Woodward, D.W. and G.D. Cody, 1964, Phys. Rev. **136**, A166.
Wun, M. and N.E. Phillips, 1974, Phys. Lett. **50A**, 195.
Yamada, H. and S. Takada, 1974, Progr. Theor. Phys. **52**, 1077.
Yamamoto, T., J. Sakurai and Y. Komura, 1979, J. de Physique, **C5**, 120.
Ziman, J.M., 1960, Electrons and Phonons, 4th ed. (Clarendon Press, Oxford) p. 412.
Zorić, I., G.A. Thomas and R.D. Parks, 1973, Phys. Rev. Lett. **30**, 22.

Handbook on the Physics and Chemistry of Rare Earths, edited by K.A. Gschneidner, Jr. and L. Eyring

Chapter 43

ADSORPTION AND CATALYSIS ON RARE EARTH SURFACES

Falko P. NETZER and Erminald BERTEL
Institut für Physikalische Chemie, Universität Innsbruck, A-6020 Innsbruck, Austria

Contents

Symbols

AES = Auger electron spectroscopy
A_0 = preexponential factor
BIS = Bremsstrahlung isochromat spectroscopy
b_{H_2,O_2} = Langmuir adsorption coefficient
DOS = density of states
E_i = initial state energy
E_f = final state energy
E_F = Fermi energy
$E_{B,X,Y,Z}$ = electron binding energy
E_{kin} = kinetic energy of photoelectron
E_{XYZ} = kinetic energy of Auger electron
E_p = energy of primary electron
E_a = activation energy
ΔE = electron loss energy
ELS = electron energy loss spectroscopy
ESCA = electron spectroscopy for chemical analysis
e = electron charge
fcc = face centered cubic
h = Planck's constant
ΔH_f = heat of formation
ΔH_s = heat of sublimation
ΔH_v = heat of vaporization
IR = infrared
k = rate constant
L = Langmuir (1 L corresponds to an exposure of 1 s at 10^{-6} torr)
LEED = low energy electron diffraction
m = free electron mass
N = particle concentration
n = free electron density
$O_{\square}^{2-}$ = lattice oxygen ion

P_T	= total pressure	ϵ_o	= dielectric constant of the vacuum
$P_{H_2,O_2,\ldots}$	= partial pressure	μ	= chemical potential
PSD	= photon stimulated desorption	μ	= magnetic moment
R	= molar gas constant	ν	= photon frequency
r	= reaction rate	ϕ	= work function
U_{eff}	= effective Coulomb interaction energy between two holes	$\Delta\phi$	= work function change
		χ	= electrostatic potential energy
UHV	= ultra high vacuum	χ	= magnetic susceptibility
UPS	= ultraviolet photoelectron spectroscopy	ω_p, ω_s	= electron plasma frequency
		$\square_s$	= surface anion vacancy
XPS	= X-ray photoelectron spectroscopy		

1. Introduction

Surface chemistry and surface physics, commonly referred to as surface science, are among the most rapidly growing areas of modern physical sciences. The fast development during the last decade or so has been greatly stimulated by the importance of heterogeneous catalysis in many industrial processes, which has stimulated interest in basic research in this area. On the other hand, considerable progress in the understanding of surface phenomena has been made possible by the commercial availability of modern ultra-high vacuum techniques. Applying these techniques it became feasible to obtain surfaces clean on a microscopic scale and to investigate processes on structurally well-defined surfaces without undue interference from background contaminants. The application of spectroscopic techniques, which have been useful to study gas-phase and liquid-phase phenomena, to the solid state and its interfaces and the additional development of specific surface-sensitive techniques have contributed to reaching the present level of understanding, where it can be hoped that surface processes may be understood on a microscopic scale.

In this chapter we review surface chemistry on rare earth related materials, that is, published information on the interaction of gases on and with rare earth surfaces will be evaluated. The present treatment is therefore confined to phenomena occurring on the gas–solid interface. Conventional studies of catalytic processes on rare earth surfaces have been known for quite a number of years, but it is only recently that studies on well-defined rare earth surfaces involving modern methods of surface science have been initiated. This field, however, is rapidly expanding. It therefore seems timely to examine surface reactions on rare earth materials in the light of the present knowledge of surface science in order to establish the present state of the art and to provide a basis for future research in this area.

A catalytic reaction on a solid surface involving gaseous reactants can be divided schematically into the following sequence of processes: (1) adsorption of at least one reactant at the surface of the catalyst, (2) formation of a reaction complex at the surface which then yields the reaction product, and (3) release of the product into the gas phase. In a strictly classical sense the catalyst surface

should remain unchanged after the catalytic reaction. If the reactants or the solid surface are very reactive, the initial adsorption step may lead to irreversible changes of the catalyst surface. This may be termed as reactive chemisorption. Reactive chemisorption can be followed by surface compound formation, and finally a bulk compound may be formed. Depending on the reactivity of the system it may or may not be possible to isolate the different reaction steps. In any case, if the reactivity of one of the reactants towards the catalyst surface is high so that compound formation occurs, the catalytic reaction between gaseous reactants will be largely suppressed at the extent of the reaction with the catalyst surface. As at least one class of rare earth materials, namely the metals, is very reactive towards most common reactants, we approach the description of gas–rare earth surface interactions in this article by dividing it into *reactions on* and *reactions with* rare earth surfaces. Whereas investigation of reactions *on* rare earth surfaces is aimed at understanding catalytic processes at these surfaces, study of reactions *with* rare earth surfaces focusses on the initial stages of compound formation in a gas–solid reaction, e.g. in metal to oxide or metal to hydride transitions. The latter area has attracted increasing scientific interest recently, mainly because of the possible application of rare earth materials in hydrogen storage devices.

Both areas of rare earth surface chemistry are connected by the adsorption process, which is the initial step in both types of surface reactions. Despite the obvious importance of the adsorption process in all kinds of surface reactions, relatively few detailed studies of gas adsorption have been performed on rare earth materials. This may be partly due to the high reactivity of the systems under consideration, which require careful control of experimental conditions. Experimental equipment to fulfill these requirements is commercially available now. Similar progress in the understanding of adsorption phenomena, as has been achieved for the d transition metals and their compounds in recent years, can therefore be expected for rare earth materials in the near future.

The division of surface reactions, which we introduce in this chapter, into catalytic reactions and reactions leading to compound formation can be kept more or less rigorously in the following sections depending on the materials to be considered. For example, the reactivity of rare earth metals precludes their use as catalysts in most catalytic reactions, and the aspects of surface compound formation will be emphasized. On the other hand, rare earth oxides have been shown to be good catalysts in many reactions, and the description of catalytic reactions will be the major matter of concern in the discussion. In several instances, however, both aspects of surface chemistry are difficult to separate. The division outlined above should therefore be regarded as a general guideline of presentation rather than as a matter of principle.

In discussing reactive interactions of gases *with* rare earth materials we will concentrate mainly on processes at the surface and in near-surface regions of the solid, whereas subsequent processes leading to the formation of bulk compound such as transport processes and bulk phase transformations will not be considered. The term surface compound is thereby somewhat ill-defined; according to our understanding it should refer to a compound phase, which extends only a

few layers perpendicular to the surface into the solid, while the main body of bulk material still retains its unreacted identity. Various aspects of reactive chemisorption and surface compound formation during the reaction of gases such as oxygen, hydrogen, water and carbon oxides with rare earth metals and intermetallic compounds are discussed in sections 3 and 6 of this chapter, respectively.

The most important catalyst systems involving rare earth elements are the oxides and intermetallics. Catalytic properties of rare earth oxides are described in section 4 and those of intermetallic compounds in section 6. Reports on surface reactivities of other binary rare earth compounds are only sparse, and this is mentioned in section 5. A very interesting class of catalyst systems comprises the mixed oxides of the perovskite structure type. As catalysis on these oxides is mainly determined by the d transition metal component and the rare earth cations can be regarded essentially as spectator cations from the catalytic viewpoint, these materials have not been included in this chapter. Instead, we refer the interested reader to a review by Voorhoeve (1977). Catalytic properties of rare earth containing zeolites are, in our opinion, more adequately treated in the general context of zeolite catalysis (see e.g. Rabo, 1976; Katzer, 1977; Haynes, 1978) and have therefore been omitted here.

In order to provide information on some experimental aspects important for the discussion of surface reactions in subsequent sections, we continue this chapter with a brief account of experimental techniques and surface preparation and pretreatment conditions in section 2.

2. Experimental aspects

2.1. *Determination of catalytic activity*

The term *catalytic activity* is commonly used to specify the reactivity of a catalyst system in a catalytic reaction under given reaction conditions, and it should therefore in principle contain information on yields or rates of formation of the desired reaction products. Despite the obvious importance of this term in comparing different catalyst systems or various reaction conditions, catalytic activity is by no means uniquely defined in the literature, and in many cases investigators seem to use as the catalysts' activity that quantity which is most easily obtained from their particular experimental arrangement. This diversity of physical or chemical parameters used to specify the reactivity of catalysts then makes it difficult to compare, even qualitatively, results obtained in different laboratories. The desired finding of trends along a series of related catalyst systems, e.g. rare earth derived materials, therefore often has to be confined to reports where comparative studies have been performed by the same research group. For example, while a number of authors use the yield of reaction products to determine the catalytic activity, others use the percentage of unreacted reactants, reaction rates at some stage of the reaction, specific rate constants derived from rate equations or parameters indirectly related to one of

the foregoing quantities. Normalization of these quantities to unit weight, unit volume or unit surface area of the catalyst samples introduces a further source of diversity. A very useful measure of catalytic activity is the so-called turnover number, defined as the number of molecules produced or reacted per active surface atom per second. It has to be acknowledged, however, that the determination of the number of active surface sites is not trivial, because in general the catalyst surfaces under consideration here are structurally not well defined. Adsorption of CO has been used to determine the number of active surface atoms in some cases (see e.g. Atkinson and Nicks, 1977; Luengo et al., 1977; Elattar et al., 1979), but this method is certainly not applicable for all systems. We will therefore report catalytic activities in this review, without commitment to any value judgement, as they are given by the various authors, but will specify their meaning where necessary.

For catalytic reactions where more than one reaction path can be pursued, the *selectivity* of the catalyst system towards a particular reaction product is an important parameter. The selectivity is usually defined as the ratio of the yield of the considered reaction product to the total reaction yield, but yield ratios of two competing reaction products have also been employed.

As implicitly evident from the beginning of this section a variety of experimental methods has been adopted to study activities of rare earth related materials in catalytic reactions, but most of them can be essentially reduced to two types of measuring process: determination of (1) the composition of the gas phase during or after reaction and of (2) changes of some physical property of the solid catalyst system proportional to the reaction rate. Reactions have been carried out in static, circulatory static, flow, or pulsed flow reactor systems and compositions of the gas phase have been monitored using, e.g., gas chromatography, mass spectrometry or IR spectroscopy. Mass (microgravimetry), temperature of the catalyst and its environment (microcalorimetry and differential thermal analysis) and electrical conductivity are among the physical parameters whose changes have been followed during catalytic reactions. Whereas the former methods give more direct information on reaction yields and related kinetic parameters, the latter rely on some model of the reactant–catalyst interaction, but then are able to provide additional information. In-situ combination of gas-phase product determination with measurement of solid-state catalyst properties would clearly be most profitable, but has been performed up to date only in isolated cases (e.g. Breysse et al., 1972, 1973; Pountney et al., 1979). As a detailed description of the variety of apparatuses and experimental procedures used by the different authors is beyond the scope of the present review, we refer the interested reader for further information to the original publications cited in the following discussion sections.

2.2. *Modern methods in surface science*

It is well established in modern surface science that any reaction involving a solid surface depends critically on the chemical state of the surface, that is on surface cleanliness. There are numerous mechanisms by which contaminants can

affect a surface reaction: the blocking of adsorption sites can change the kinetics, direct or substrate mediated adsorbate–contaminant interaction can influence not only the energetics of a reaction but also the reaction path itself. In some cases contaminants are able to change the substrate surface structure (e.g. by adsorbate induced reconstruction) even if their surface concentration is very low. Therefore, if detailed understanding of a surface reaction is required, it has to be investigated under well-defined conditions; that means in particular the reaction should start on a clean surface and undesired species should adsorb (or segregate) on the surface only to a negligible extent during the investigation time period.

The above conditions are only met under ultra-high vacuum (UHV) environment. Even if the partial pressure of a contaminant gas is as low as 10^{-8} torr, a monolayer coverage may be built up within a few hundred seconds. Of course the uptake rate depends on both the reactivity of the sample surface and the composition of the residual gas atmosphere. Rare earth metals are highly reactive towards hydrogen, oxygen, water, carbon monoxide and carbon dioxide, gases which are the main constituents of the residual atmosphere in any vacuum system. Thus, if a rare earth metal surface has to be kept clean for a time long enough to carry out measurements, the base pressure should be below 5×10^{-10} torr. It is only recently that such stringent requirements have been sufficiently fulfilled in basic catalytic research, and many of the earlier data have therefore been somewhat misleading for this reason (see e.g. Gasgnier (1980) and the question of the so-called rare earth suboxides).

Having established the need of UHV conditions for detailed study of surface reactions we now proceed to a short survey of modern methods used to study surface phenomena today. A typical UHV system as used for multi-technique surface investigations in the authors' laboratory is shown in fig. 1. Out of a large

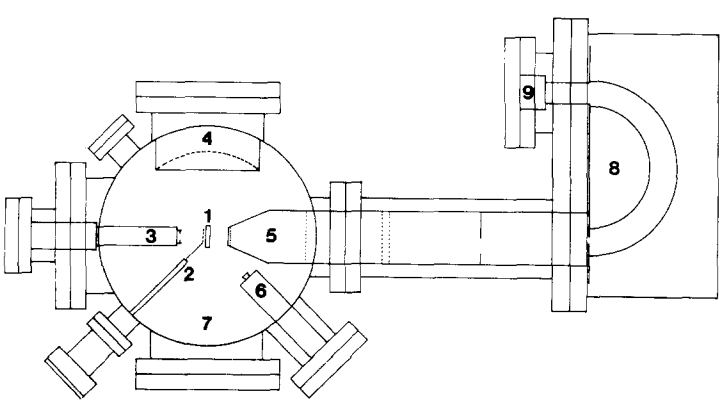

Fig. 1. Schematic cross section of a typical UHV system for multi-technique surface studies as employed in the authors' laboratory: (1) sample, (2) vibrating Kelvin probe, (3) quadrupole mass spectrometer, (4) LEED screen, (5) electron energy analyzer (electron lens system), (6) electron gun, (7) viewport, (8) concentric hemispherical analyzer, (9) electron detection system (electron multiplier). The system is also equipped with an ion sputter gun, a specimen manipulator and various gas inlet and pumping facilities.

variety of experimental techniques we will mention only a small selection, in particular those which will be most relevant in the discussion of results in the following sections. We only present some basic information here, but as the review literature on modern techniques in surface science is ample, we refer the reader for further details to key reviews and to the references cited therein.

2.2.1. *Electron spectroscopic methods*

Recent developments of electron energy analyzers capable of high energy as well as high angular resolution have rendered electron spectroscopy one of the most powerful tools for surface studies. The energy distribution of electrons, which have been interacting with a surface or are created by a process at the surface, contains a wealth of chemical information as we will discuss below. From the angular distribution of emitted electrons conclusions can be drawn referring to band structure as well as to the geometry of adsorbates. To the authors' knowledge, however, no angle resolved electron spectroscopic studies have as yet been carried out on rare earth materials, and we shall be concerned in the following mainly with electron energy distribution and the chemical information contained therein.

Photoelectron spectroscopy: UPS, XPS (ESCA)

In photoelectron spectroscopy a photon incident on a surface is absorbed and its energy is transferred to an electron, which is excited from a bound state into the continuum. The energy distribution of these photoemitted electrons is measured.

The experimental equipment consists of a photon source and an electron energy analyzer combined with an electron detecting system (usually a secondary electron multiplier or a channeltron). Conventional photon sources are rare gas discharge lamps in ultraviolet photoelectron spectroscopy (UPS) or X-ray anodes in X-ray photoelectron spectroscopy (XPS or ESCA). Photon energies from gas discharge lamps are typically between 10 and 40 eV, the most commonly used energies being that of He I (21.2 eV) and He II (40.8 eV) radiation. In XPS the most common target materials are Al and Mg yielding photons of 1486.6 eV and 1253.6 eV energy, respectively. Recently, synchrotron radiation has attracted considerable interest in photoelectron spectroscopy, because high intensities of photons with energies continuously tunable from far infrared up to several keV can be obtained (Kunz, 1979).

The photon linewidth is only of the order of some meV in the case of UPS making a resolution of about 0.3 eV in UPS valence band spectra easily obtainable. The full width at half maximum (FWHM) of the Al and Mg Kα lines, however, is about 1 eV and does not allow details in line shape or band structure to be resolved. To improve the resolution a crystal monochromator may be used, but the resulting intensity loss causes severe experimental problems. In fig. 2 a comparison is made between an Er valence band spectrum taken with ordinary Mg Kα radiation by Netzer et al. (1981a) and the same spectrum recorded using monochromatized Al Kα radiation (FWHM < 0.3 eV) by Baer and Busch (1974). Both spectra show the 5d 6s emission between E_F and 4 eV binding energy. The

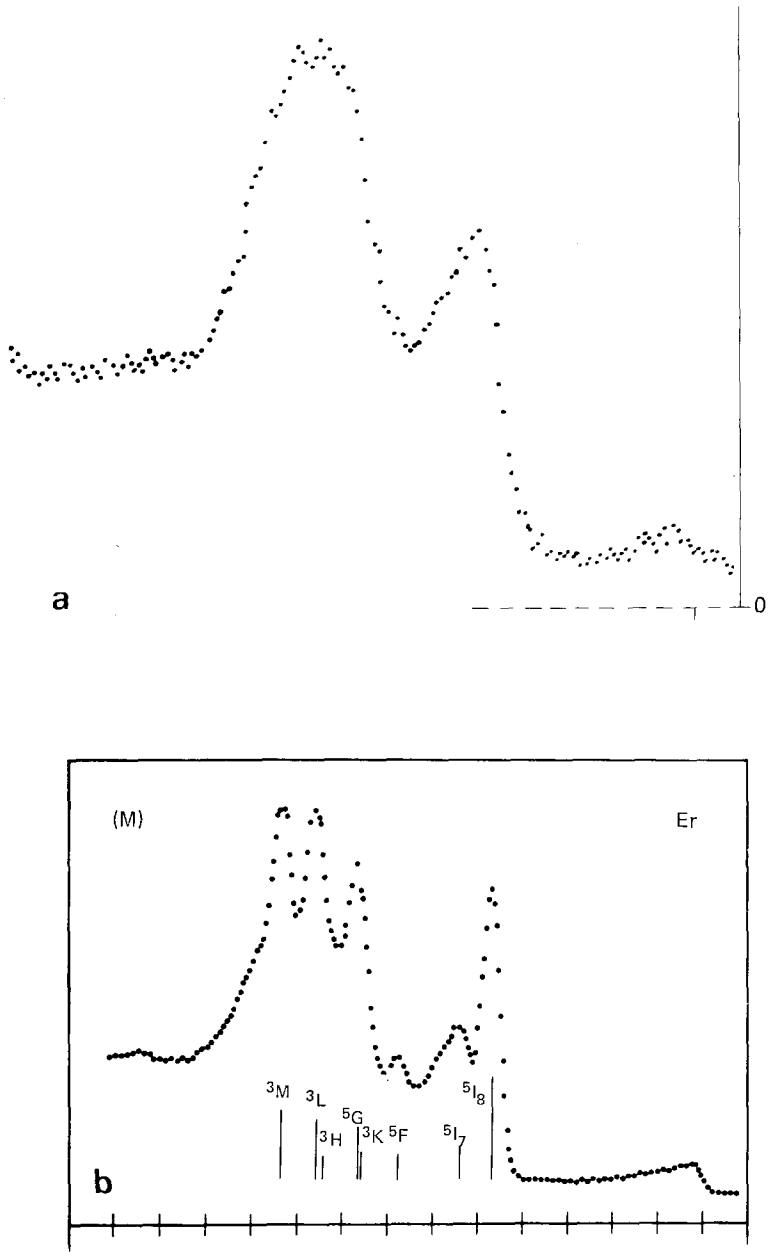

Fig. 2. Photoelectron spectra of the valence region of clean Er metal excited with (a) Mg Kα (Netzer et al., 1981a) and (b) monochromatized Al Kα (Baer and Busch, 1974) radiation.

comparatively high intensity between 4 eV and 11 eV below the Fermi level is due to 4f emission. The 4f multiplet is only resolved in the lower spectrum, which was excited with monochromatized radiation.

The process of photoemission will now be considered briefly. If an electron is ejected from an excited atom after photon absorption, the kinetic energy of the electron is determined by the following equation:

$$h\nu + E_i = E_{kin} + E_f, \tag{1}$$

where E_i is the initial state energy (neutral atom), E_f is the final state energy (ion), E_{kin} is the kinetic energy of the photoelectron and $h\nu$ is the photon energy. The binding energy of the electron E_B is measured as the difference between the photon energy (energy input) and the kinetic energy of the outcoming electron:

$$E_B = h\nu - E_{kin} = E_f - E_i. \tag{2}$$

According to eq. (2), the binding energy is also a measure of the difference between the total energy of the one-hole final state and the initial state energy. The final state energy is modified by spin–orbit coupling and by coupling with the non-zero spin of an unfilled shell (the latter gives rise to the so-called exchange splitting). Additionally, both the magnitude of the multiplet splitting and the relative intensities are influenced by electron correlation effects (Cox, 1981). The intensity of transitions from bound to continuum states depends also on the density of states (DOS) in both the initial and the final state of the electron. At higher kinetic energies of the photoelectron the final state DOS shows little structure, and the photoelectron spectra mainly reflect the initial state DOS, but resonant transitions may be observed into continuum states at kinetic energies below 20 eV (e.g. Allen et al., 1980; Johansson et al., 1980). The transition intensity depends critically on the dipole matrix element of the initial and final state. As a consequence $f \rightarrow g$ continuum transitions are largely suppressed at low photon energies (i.e. in UPS) due to the centrifugal barrier, whereas at high photon energies (XPS) the f levels have much larger photoionization cross sections than the s or p levels. This is illustrated in fig. 3, where the Er valence region is probed with different photon energies (Netzer et al., 1981a). The XPS valence spectrum (Mg Kα) is dominated by 4f emission, while 4f emission is barely visible at He I photon energies. Calculation of relative transition intensities is possible by using the method of fractional parentage (Cox, 1975). Finally, it has to be mentioned that electron correlation effects can result in shake-up satellites at higher binding energies.

As an example for the effects outlined above, XPS spectra of 4f and 4d levels in Yb metal and oxide are shown in fig. 4 (Padalia et al., 1977). Yb undergoes a valence change upon oxidation from Yb^{2+} in the metal to Yb^{3+} in the oxide (see section 3.1). Accordingly, the simple spin–orbit doublets in the clean metal are broadened upon oxidation because the valence change gives rise to multiplet splitting. This is best seen in the 4d spectra, where multiplet structure is observed in the oxide. Furthermore, the peaks are shifted to higher binding energy due to the increased ionic charge.

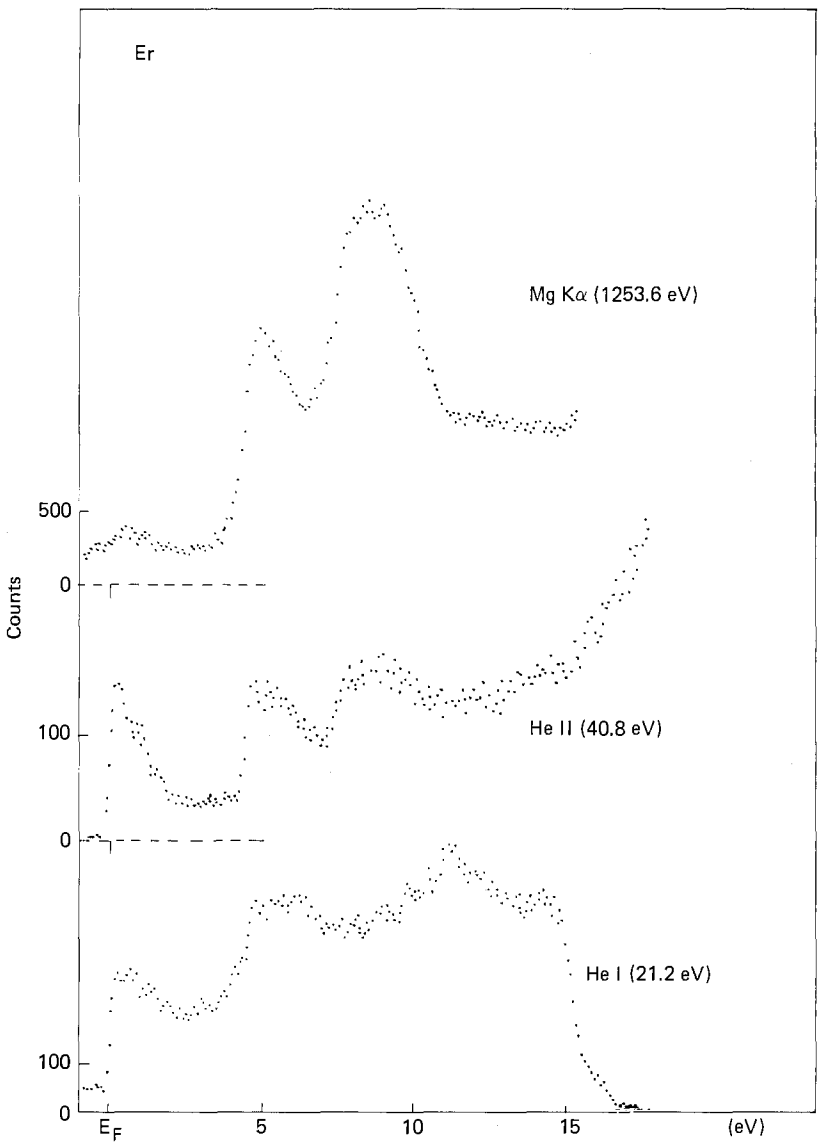

Fig. 3. Photoelectron spectra of the valence region of clean Er metal excited with Mg Kα, He II and He I radiation (Netzer et al., 1981a).

In summary, photoemission spectroscopy provides a useful means for measuring the binding energy of core and valence electrons. Thereby the chemical composition of a sample surface can be determined (Electron Spectroscopy for Chemical Analysis: ESCA. A recent review on ESCA has been published by Seah (1980).) Furthermore, the valence band DOS can be probed and the valence state of surface atoms can be examined. Atoms in different

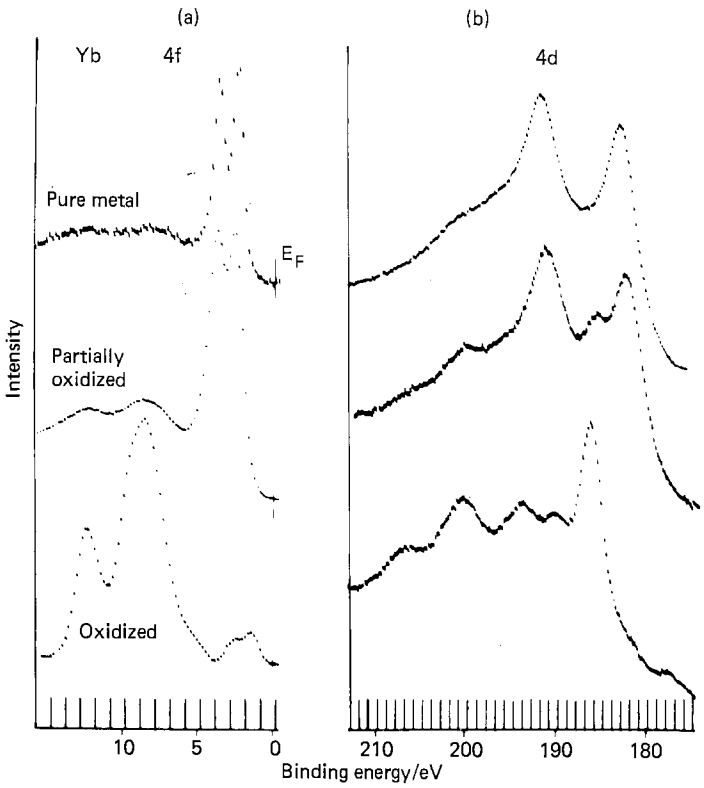

Fig. 4. Measured 4f (a) and 4d (b) spectra for pure, partially oxidized and fully oxidized ytterbium metal (Padalia et al., 1977).

chemical environments can be distinguished because of different correlation effects, and surface states may be detected. Metal to semiconductor transitions – as they occur in rare earth oxidation – can be monitored directly by observing the depletion of the metal conduction band as well as by the general increase of core level binding energies. For further information about technique and applications of photoelectron spectroscopy we refer to the ample literature on this subject (e.g. Brundle and Baker, 1978; Cardona and Ley, 1978). An extensive treatment of techniques and applications of synchrotron radiation in photoelectron spectroscopy has been presented by Kunz (1979).

Last, but not least, we have to consider the following question: To what extent does the process of photoemission influence the surface phenomena under investigation? The most important processes to be considered in this context are the creation of defect centers in semiconductors and insulators and photon stimulated desorption (PSD). As pointed out above the photoemission process ends up in a one-hole final state. This highly excited state may decay in a number of different ways, which sometimes involve repulsive interaction between the excited particle and the surface. In this case desorption of both neutral species

and ions will occur, the cross section of neutral desorption being much larger than for ion desorption. An overview of radiation-induced surface damage in photoelectron spectroscopy is given by Copperthwaite (1980).

Auger electron spectroscopy (AES)

In Auger electron spectroscopy an atom is ionized by X-ray, electron or ion bombardment. This ionic state has a certain probability to decay in a radiationless transition whereby an additional electron is emitted (the so-called Auger electron). Thus the atom is finally left in a double ionized state. The energy distribution of the Auger electrons is recorded.

The apparatus required for AES studies comprises a radiation or particle beam source and an electron energy analyzer. For X-ray excited Auger spectra the same sources as in XPS may be used, whereas excitation by electrons is performed by means of electron guns designed for kinetic energies typically between 100 eV and 5 keV. Ion excitation is rarely used in surface studies because of the extensive radiation damage caused by heavy particles.

The initial state of the nonradiative (Auger) decay process is the one-hole state with an energy E_i. Adopting the energy of the originally undisturbed atom as zero reference E_i becomes the binding energy E_X of the removed electron. The final state is a two-hole state with energy E_f. The holes correspond to the removal of two electrons with binding energies E_Y and E_Z, respectively (electron Y may be thought to have jumped from a higher level into hole X thereby releasing energy, which is absorbed by electron Z to escape into the continuum). The two holes may be regarded as two positive charges subject to a Coulomb interaction U_{eff}, the strength of which depends on the localization of the final state holes and on exchange and correlation effects similar to those operating in photoemission. The kinetic energy of an Auger electron, E_{XYZ}, may be described by the following formula:

$$E_{XYZ} = E_f - E_i = E_X - (E_Y + E_Z) - U_{eff}, \tag{3}$$

U_{eff} is typically in the range of several eV.

For the intensity distribution in Auger spectra similar considerations apply in principle as in photoelectron spectroscopy. The transition probability depends critically upon the wave function overlap of the occupied levels with the initial state hole. This is why interatomic Auger transitions are comparatively rarely observed, because the intraatomic transitions are generally more rapid (Matthew and Komninos, 1975). Exceptions have been reported, for instance in maximal valency ionic compounds (see Knotek and Feibelman, 1979, and references cited therein). In heavy elements and for high energy transitions the Auger yield is limited by the competing mechanism of fluorescence decay, where the initial hole state energy is converted into a photon rather than an Auger electron.

An additional process deserves attention in the interpretation of Auger spectra, especially if rare earth metals and compounds are considered. The high 4f density of states above the Fermi level in these materials gives rise to resonant transitions $4d \rightarrow 4f$ (Zimkina et al., 1967; Sugar, 1972), which can decay by autoionization processes. The electrons ejected in such direct recombination

processes contribute to the secondary electron yield in the region of Auger transitions originating from 4d initial state holes and complicate the interpretation of Auger spectra of rare earths in that energy range (Netzer et al., 1981b).

In analyzing Auger spectra it has to be kept in mind that surface and bulk contributions vary in their relative intensities, depending on the energy of the Auger transition one is looking at. The electron escape depth shows a minimum of about 5 Å for 100 eV electrons, whereas at 1000 eV it is about 20 Å (Ertl and Küppers, 1974). At very low kinetic energies the mean free path greatly depends on the material. In semiconductors and insulators it may become fairly large for low energy electrons. As many elements show characteristic Auger transitions in the energy range 50–500 eV, where the electron escape depth is small, Auger spectroscopy is one of the most sensitive methods for chemical analysis of the outermost layers of a solid. Of course, these considerations on electron escape depth also apply to photoelectron spectroscopy.

Finally, the problem of beam damage effects occurring in Auger spectroscopy has to be considered (Pantano and Madey, 1981). An electron beam impinging on a surface may affect the surface properties by a number of different processes such as excitation with subsequent dissociation or desorption of some surface species (electron stimulated desorption), defect production within the bulk, undue heating of the surface, chemical reactions and charging in non-conductors. In principle, there is much less beam damage caused if the Auger spectra are excited by X-rays. However, long counting times have often to be allowed for, as photons with energies high above thresholds have low ionization cross sections. If electron excitation is used, possible beam effects have to be taken into account and spectra of sensitive surface species have to be interpreted with due caution.

Comprehensive reviews on high-resolution Auger spectroscopy of solids, surfaces and adsorbed molecules have been compiled recently by Fuggle (1981) and by Netzer (1981).

Electron energy loss spectroscopy (ELS)

In electron energy loss spectroscopy an electron incident on a surface is inelastically scattered and the distribution of electrons $n(\Delta E)$ having transferred an energy ΔE to the target is measured. Both vibrational and electronic transitions can be excited, but this section will be confined to ELS in the range of electronic excitations.

The experimental arrangement is the same as for electron excited Auger spectroscopy, consisting of an electron gun and an electron energy analyzer. In principle, there are two different ways of performing ELS on solids. In transmission energy loss spectroscopy electrons with high primary energies (E_p of the order of several 10 keV) impinge on a thin target and electrons having penetrated the target are analyzed with respect to their energy loss ΔE. Another possibility is the energy analysis of back reflected electrons. In contrast to transmission experiments, this requires an additional elastic scattering process for the electrons to be deflected into the analyzer. The elastic scattering event should not affect the principal features of loss processes outlined below, but the con-

tribution of inelastic surface processes relative to that of bulk loss processes is enhanced in reflection electron loss spectroscopy. In addition, the surface sensitivity can be varied in the reflection mode by varying the primary energy of the incident electron beam within a wide range.

The following discussion of theoretical aspects shall be restricted to fast collisions, i.e. to cases where the incident electron acts only as a momentum perturbation on the target system, which in turn responds as an isolated system. The momentum transfer is small in such a process and dipole selection rules apply for single electron excitations.

The electronic excitations caused by electron energy loss processes can be divided into two main classes: collective electronic excitations and single electron excitation. The collective excitations may be regarded as plasma oscillations of a free or nearly free electron gas embedded in a homogeneously distributed positive charge. An extensive treatment of collective excitation losses is given by Lucas and Sunjic (1972). In a classical treatment the electron plasma frequency ω_p is given by

$$\omega_p^2 = ne^2/m\epsilon_0, \tag{4}$$

where n is the free electron density, e the electron charge, m the free electron mass and ϵ_0 the dielectric constant of the vacuum.

Plasma oscillations have to be considered as elementary quantized excitations, characterized by energy and momentum. This has two important consequences: Firstly, the interaction of the valence electrons with an incident electron may result not only in the excitation of one plasmon but also generate its harmonics, the double, triple, etc. plasmon (a double plasmon loss peak is seen, for instance, in fig. 8 at 28–30 eV, the single volume plasmon being located at 13.5–15 eV). Secondly, the plasmon having a momentum component normal to the surface, i.e. the volume plasmon is distinguished from the surface plasmon with a momentum parallel to the surface. The surface plasmon frequency ω_s is related to the volume plasmon frequency by

$$\omega_s = \omega_p/\sqrt{2}. \tag{5}$$

It has to be kept in mind, however, that the plasma frequency ω_p as given in eq. (4) is modified due to limited validity of the nearly free electron model. Interference of plasmon excitation with interband and intraband transitions may shift the plasma frequency in a complicated way, as discussed by Raether (1965).

The probability for single electron excitations depends on the kinematics of the incident electron and the transition probability (Celotta and Huebner, 1979). Within the approximation of fast collisions this transition probability is described by the dipole matrix element of the initial and final state of the target. Summing up over all possible excitations with $\Delta E < E_p$ the energy distribution of fast inelastically scattered electrons is obtained.

Summarizing thus, an electron energy loss spectrum may be characterized as follows: If a monochromatic electron beam of primary energy E_p is incident on a

solid target, the transmitted or reflected electron energy distribution will show considerable structure in the energy region below the primary energy. This structure is due to electrons having lost energy by excitation of quantized collective excitations (plasmons) and by single electron excitations. Peaks corresponding to single electron excitations result from initial to final state transitions of the solid which are characterized by a high probability (i.e. large overlapping of initial and final state wave functions and high final state DOS). Consequently, information on the valence electron density may be obtained from both the plasmon frequency and the intensity of valence band transitions. Single electron excitation losses contain convoluted information on the initial and final state electronic properties, but using XPS and UPS results it is possible to extract information on final state DOS. Due to the characteristic features of ELS, this technique proved to be a valuable tool for monitoring resonant transitions (e.g. $4d \rightarrow 4f$ transitions in rare earths, Trebbia and Colliex, 1973; Bertel et al., 1981a). In addition to the dipole selection rule other selection rules may be developed from symmetry considerations (Celotta and Huebner, 1979 and references cited therein). Furthermore, in adsorption studies it may be possible to derive information about the geometry of adsorbate–substrate complexes from ELS (Netzer et al., 1980). Finally, it has to be mentioned that slow inelastic collisions may result in a breakdown of the dipole selection rule. Despite considerable complexity these processes have attracted increasing interest because excitations may be observed which are not accessible by optical spectroscopy (Ludeke and Koma, 1975).

Bremsstrahlung isochromat spectroscopy (BIS)

Recent work of Lang and Baer (1979) has focussed interest onto still another kind of electron spectroscopy, which somehow may be considered as the inverse of X-ray photoelectron spectroscopy: Bremsstrahlung isochromat spectroscopy (BIS). In BIS a beam of monoenergetic electrons is accelerated onto the sample surface. Besides elastic and inelastic scattering another process may happen, though less frequently: the direct radiative deceleration of an incoming electron into an empty state above the Fermi level. The radiation emitted in such a process (Bremsstrahlung) is detected using an X-ray monochromator followed by an X-ray photon detector.

The transition probability of electrons with initial state kinetic energy of the order of 1 keV into a final state just above the Fermi level is proportional to the final state DOS. Thus the DOS of unoccupied states above the Fermi level can be directly recorded by firing electrons with varying primary energy onto the target, whilst the X-ray photon intensity originating from the radiative deceleration processes is measured at a fixed energy $h\nu$.

Using this technique Lang et al. (1981) have mapped the valence band density of states in rare earth metals. Due to long counting times necessary to acquire a BIS spectrum extensive beam damage effects are expected to occur. This confines the application of BIS at present to clean metal surfaces. Nevertheless, the exact determination of the density of unoccupied states yields very valuable information for reaction studies as pointed out, for instance, in section 3.1.3.

2.2.2. *Low energy electron diffraction (LEED)*

Despite the fact that only a little work has been done concerning low energy electron diffraction on rare earth surfaces it seems worthwhile to mention this technique in the present context. First studies using LEED to characterize rare earth metal and oxide single crystal surfaces have been published by Felton et al. (1979), Onsgaard (1981) and Tougaard and Ignatiev (1980). Such studies are expected to be of increasing importance in the near future.

In low energy electron diffraction slow electrons elastically backscattered from a single crystal surface are investigated. Due to the periodic arrangement of surface atoms backscattered waves will interfere to produce a set of discrete diffracted beams displaying the symmetry of the surface unit cell. The high inelastic scattering cross sections of low energy electrons with solid matter and the resulting small elastic mean free path of electrons confines the observation of elastically backscattered electrons to scattering events within the surface region. While the symmetry of the diffraction pattern mirrors the symmetry of the surface unit mesh in reciprocal space, analysis of the intensities of LEED reflexes as a function of electron energy can yield the position of atoms within the surface unit cell. LEED may therefore be regarded as a method of surface crystallography. In the case of ordered adsorbate layers the symmetry of the adsorbate unit cell may be obtained from additional diffraction reflexes appearing in LEED, and the position of adsorbed particles with respect to the substrate surface may be derived from LEED intensity analysis. The review literature on LEED is ample, and various aspects have been treated by Estrup and McRae (1971), Pendry (1974) or Van Hove and Tong (1979). An introduction is given by Ertl and Küppers (1974).

2.2.3. *Work function measurements*

The work function may be defined (somewhat loosely) as the energy barrier preventing an electron from escaping out of a solid into the vacuum to a point close to the surface. It is a quantity of great technical interest and has therefore been the subject of numerous studies in recent decades (Rivière, 1969). The recent development of advanced experimental methods has stimulated great interest in work function measurements as an instrument for observing surface processes. Accuracies in measuring work function changes up to 0.1 meV have been obtained with modern versions of the Kelvin vibrating capacitor method (e.g. Engelhardt et al., 1977; Besocke and Berger, 1976). Other methods, such as the photoelectric method (capable of measuring absolute values) and the diode method have also been brought to a highly sophisticated level, but in contrast to the Kelvin method, they have the disadvantage of disturbing the surface under investigation by incident photons or electrons.

The work function as defined above can be considered to consist of two parts: First, a step in electrostatic potential energy χ due to a surface dipole charge density. This may have various reasons such as the "spilling out" of electrons at the surface or charge transfer to and from adsorbate particles. The second contribution to the work function is the change in energy caused by the

interaction of the electron with the bulk phase of the material under consideration (which in turn consists of various contributions such as electrostatic interaction with the ion cores and kinetic energy at the Fermi level). This purely bulk dependent contribution to the energy change in removing an electron into the vacuum is denoted as the chemical potential μ. Thus the work function ϕ may be written as

$$\phi = -(\mu + e\chi). \tag{6}$$

A more detailed definition and a lengthy account of theoretical aspects is given by Hölzl and Schulte (1979).

If metal/adsorbate systems are considered where the bulk properties are not changed during surface reactions, the work function changes are directly connected with the surface dipole layer. Hence, increase or decrease of work function is a measure of how much charge is transferred from the metal to the adsorbate and vice versa. Changes in slope of the work function versus exposure curve may indicate changes of the sticking coefficient and/or the occupation of different adsorption sites. Furthermore, depolarization effects in densely packed adsorbate layers have been reported (e.g. Bertel and Netzer, 1980a).

In very reactive systems the bulk properties are sometimes influenced following adsorption or absorption of a reactant. This happens, for instance, in the rare earth/oxygen system. In this case the work function changes are not only due to changes in surface charge distribution but also to changes in the chemical potential μ (i.e. changes in the position of the Fermi level relative to the vacuum level). A discussion of the work function in such systems is given by Morrison (1977).

As already pointed out, there is no disturbance of the surface under investigation caused by the Kelvin method. Nevertheless there may be important sources of error. Firstly, the work function of the reference electrode may not be constant during an experiment (for example, on account of gas adsorption). Secondly, electrical stray fields of surrounding parts of the apparatus may render the measured work function change dependent on the position of the sample with respect to the reference electrode. Therefore, careful control experiments are important for correct interpretation of work function measurements. Finally it has to be mentioned that there may be substantial differences between equilibrium values of work function changes measured after the reaction, when the reactants have been pumped away, and so-called dynamical work function measurements, where the changes are monitored during the reaction in the presence of the reacting gases.

For compilations of work function data (including rare earths) the reader is referred to Eastman (1970), Michaelson (1977), Rivière (1969) and Hölzl and Schulte (1979), the latter two being review articles which include discussion of methods and theory.

2.2.4. *Thermal desorption*

While the techniques discussed in the preceding paragraphs may be applied to both clean and adsorbate covered surfaces, thermal desorption spectroscopy is

an adsorbate-specific method. In thermal desorption an adsorbate covered surface is heated with a defined heating rate, and particles desorbing into the gas phase are detected.

If thermal desorption experiments are carried out on typical catalyst materials, the sample surface is usually large. Consequently, large quantities of gas will desorb, which are easily detectable by the change in partial or even total pressure. Due to the heterogeneity of those surfaces, however, analysis of thermal desorption spectra in terms of distinct adsorption states is difficult to perform. To assess the finer details of the energetics of an adsorbate system, single crystal surfaces have to be used in desorption experiments. This requires UHV environment and provisions for well-defined heating rates, sample temperature control and mass spectrometer detection of desorbing particles.

The desorption from a solid surface can be described by the following rate equation:

$$-\mathrm{d}N/\mathrm{d}t = kN^x \exp(-E/RT), \tag{7}$$

where N is the particle concentration on the sample surface, x the order of the desorption reaction, k a rate constant (sometimes called the frequency factor or entropy factor) and E the activation energy for desorption. In special cases these kinetic parameters may be obtained from a simple analysis of the mass spectrometer signal versus temperature plot (Redhead, 1962). In general, however, k and E are coverage (and temperature) dependent and analysis requires a large set of desorption experiments with different initial coverage and/or different heating rates. Even small statistical errors impose severe limitations on the accuracy of the results finally obtained. For details about methods of data analysis see e.g. Falconer and Madix (1977).

Thermal desorption experiments yield information about the chemical nature of desorbing species as well as the kinetics of the desorption process itself. If the mass spectrometer signal can be calibrated, the absolute adsorbate coverage can be determined by thermal desorption. The coverage dependence of the desorption energy permits conclusions regarding both the adsorbate–substrate bonding and the adsorbate–adsorbate interaction. The coverage dependence of the rate constant may be related to a first approximation to the entropy change of the system during desorption and some insight into the character of particle motion and adsorbate–substrate coupling may be obtained. For reviews on thermal desorption phenomena we refer to Menzel (1975) and Yates (1981).

2.3. *Catalyst synthesis and pretreatment*

As the history of a catalyst sample is of prime importance for its subsequent activity in catalytic reactions, this subsection is devoted to a brief description of common methods of catalyst preparation and pretreatment. The preparation and pretreatment procedure determines the surface area accessible in the catalytic reaction, the distribution of active surface sites and also the chemical nature of the surface actually involved in the catalytic process. It has to be noted, however, that the detailed microscopic characterization of rare earth derived

catalyst surfaces in terms of atomic structure and chemical composition is still in its infancy, and that the effects of various pretreatment or activation recipes are often not well defined on a microscopic scale. We consider here synthesis and pretreatment procedures for the two main classes of catalyst systems to be discussed later in this chapter, namely catalytic rare earth oxides and rare earths containing intermetallic compounds. According to the division of this article, which we outlined in the introduction, the preparation of clean rare earth metal surfaces is treated in a separate subsection 2.4.

2.3.1. *Rare earth oxides*

Structural, physical and chemical properties of bulk rare earth oxides can be found in Chapter 27, Volume 3 of this series and have been compiled with a view towards catalysis in a recent review by Rosynek (1977). An important parameter for the catalytic behavior of rare earth oxides is their basicity. The basicities of rare earth oxides resemble those of the alkaline-earth oxides, and scale directly with the respective cation radii. Thus, La_2O_3 shows the strongest basicity and Sc_2O_3 the weakest, with sesquioxide basicities decreasing smoothly along the lanthanide series going from La to Lu. This periodic trend allows one to study the influence of subtle variations in basicity on catalytic behavior in a class of related materials with similar electronic and geometrical structure.

High-purity rare earth oxides are commercially available from several suppliers and can in principle be used directly in catalytic studies after pretreatment at 700–800°C in vacuum or inert gas to remove water and surface carbonates. Due to the high temperature preparation procedures these samples have usually very low surface areas. It is therefore advantageous to prepare the oxides in higher surface area forms by thermal decomposition of rare earth hydroxides (Tosun and Rase, 1972; Minachev, 1973; Rosynek and Magnuson, 1977a; Bernal and Trillo, 1980), carbonates (Sazonov et al., 1966a, 1972; Sokolovskii et al., 1968b), oxalates (Ashmead et al., 1964; Winter, 1969a; Selwood, 1970; Artamonov and Sazonov, 1971; Takasu et al., 1977), nitrates (Arias and Selwood, 1974; Matsuda et al., 1975), chlorides (Matsuda et al., 1975) or other thermally unstable rare earth compounds (Guenin, 1973; Breysse et al., 1972, 1973) in vacuum or in oxidizing atmospheres. Because of their relatively low dehydration temperatures rare earth hydroxides seem to be particularly well suited to yield high surface area oxides. Rare earth hydroxides, however, if prepared in the conventional way by precipitation with aqueous ammonia from solutions of the corresponding nitrates, chlorides or sulfates occlude large amounts of these anions (Musorin et al., 1974), which cannot be easily removed and which can affect the catalytic properties of the resulting oxides. Rosynek and Magnuson (1977a) have therefore proposed to prepare high surface area La_2O_3 by hydrating La_2O_3 with gas-phase H_2O to form $La(OH)_3$ and subsequent dehydration, and were able to show drastic increases of surface area by careful rehydration/dehydration cycles. The interaction of gas-phase H_2O with La_2O_3 is not confined to the near-surface region, but H_2O molecules can penetrate into the bulk lattice along channels between "complex $(LaO)_n^{n+}$ cations" and oxygen

planes (Bacquet et al., 1976) thus forming bulk $La(OH)_3$. Although the elegant method described by Rosynek and Magnuson (1977a) can generate reproducibly high surface area La_2O_3 catalysts, this method may not be applicable for all rare earth oxides due to the lack of complete gas-phase hydrolysis of the heavier members of the series (Touret and Queyroux, 1972).

Rare earth oxides supported on other oxide materials (Al_2O_3, SiO_2, MgO) or mixed rare earth oxides have been prepared by several authors (Minachev and Khodakov, 1966; Selwood, 1966; Antoshin et al., 1971; Hattori et al., 1976) by impregnation of the carrier oxide with rare earth nitrates or by coprecipitation from mixed solutions of nitrates followed by calcination in air.

Evaporated thin films of rare earth oxides have, to our knowledge, not yet been used in catalytic investigations. We feel that rare earth oxides in thin film form should be particularly useful in catalytic studies because they can be easily generated under controlled preparation conditions, and because their structure and surface chemical composition can be readily monitored by modern surface science techniques. We hope therefore that work in this area will be stimulated in the near future. Preparation and characterization of rare earth oxide thin films have been compiled recently in a comprehensive review by Gasgnier (1980).

In-situ activation of rare earth oxide catalysts is usually done by temperature treatment (400–700°C) in vacuum or inert gas atmosphere for several hours or in oxidizing atmospheres followed by evacuation. Activation in hydrogen at elevated temperatures has also been reported to be effective in increasing the catalytic activity in cases where hydrogen is involved in the catalytic reaction (Read and Conrad, 1972; Baron and Selwood, 1973; Read et al., 1974; Read and Crandlemire, 1975; Read and Perkins, 1976a,b). The effects of initial pretreatment and in-situ activation temperatures on catalytic activities have been investigated (e.g. Sazonov and Logvinenko, 1962; Ashmead et al., 1964; Sazonov et al., 1966c, 1972; Tosun and Rase, 1972; Eley et al. 1974; Khodakov et al., 1975b; Read and Perkins, 1976a,b; Rosynek and Fox, 1977), and changes in catalytic activities due to the chemical composition of the gas phase during activation steps have been used to speculate on the nature of catalytically active surface sites (e.g. Tosun and Rase, 1972; Read et al., 1974; Read and Perkins, 1976a,b). Different oxygen stoichiometries in CeO_2 have been noted by Guenin (1973) and Breysse et al. (1972, 1973) after activation procedures in air and in hydrogen, and the two samples exhibited different adsorption and catalytic properties.

Despite the pronounced effects of pretreatment and activation on the catalysts' activities relatively few detailed studies have been performed to reveal the changes in surface structure and surface chemistry introduced by these procedures. Tosun and Rase (1972) have investigated a Nd_2O_3 catalyst prepared from $Nd(OH)_3$ after various pretreatment conditions by infrared spectroscopy, X-ray diffraction, differential thermal analysis and using the dehydration of ethanol as a test reaction. They suggested that dehydroxylation of the hydroxide to the sesquioxide proceeds via an oxyhydroxide NdOOH, and that the different concentration of surface hydroxyl groups after various activation conditions

might be responsible for the observed variation in the catalytic activity. More recently, Rosynek and Magnuson (1977a) have studied surface parameters and thermal dehydration behavior of the $La(OH)_3/La_2O_3$ system by a number of techniques in order to establish a suitable way to prepare catalytically active La_2O_3. As most of the rare earth hydroxides are expected to show similar thermal behavior, we reproduce in fig. 5 a thermogram of $La(OH)_3$ as recorded by Rosynek and Magnuson (1977a). Following an initial small weight loss at 100–200°C (a–b) due to removal of adsorbed water and water of crystallization, the first step of $La(OH)_3$ decomposition is observed in the temperature range 250–350°C resulting in the formation of the oxyhydroxide intermediate, LaOOH; this is represented by the prominent peak in the derivative curve in fig. 5. Subsequent dehydration of the oxyhydroxide to La_2O_3 occurs at 350 to 420°C

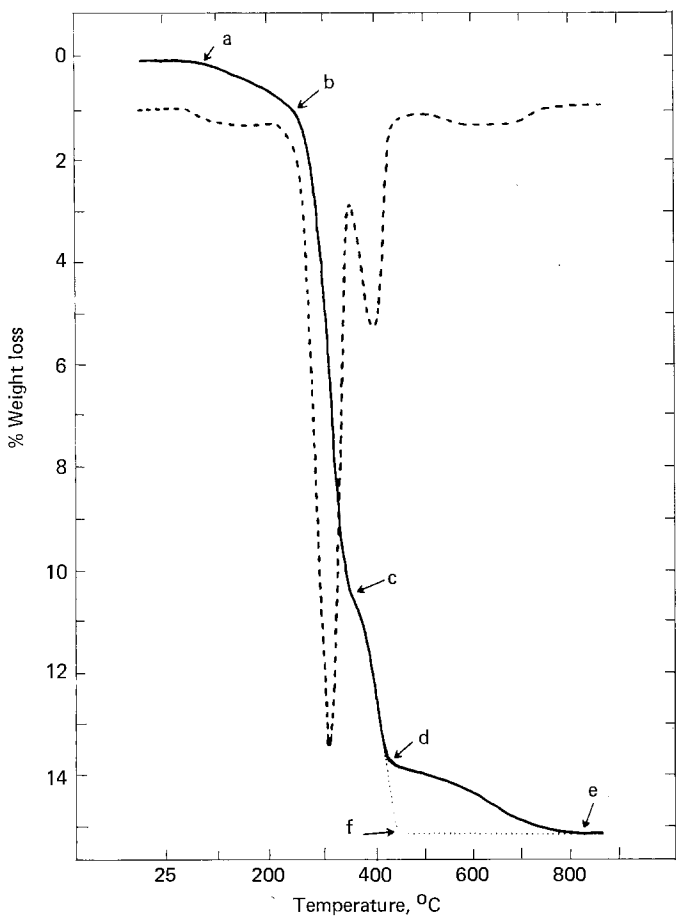

Fig. 5. Thermogram of prepared $La(OH)_3$ obtained at 2°C/min in vacuo. (—): Integral weight loss curve. (---): Time/temperature derivative. (···): Pathway followed by rehydrated La_2O_3 sample during second stage of dehydration (Rosynek and Magnuson, 1977a).

(c–d). The final broad weight loss in the temperature range 450 to 800°C (d–e) has been attributed to the decomposition of a surface layer of unidentate carbonate species (Rosynek and Magnuson, 1977b), which was formed by the interaction of the hydroxide with atmospheric CO_2 during preparation and handling. When the La_2O_3 was rehydrated by CO_2-free gaseous water at 25°C and the programmed decomposition repeated, the dotted curve in the thermogram (fig. 5) indicates the absence of surface carbonate species. These results indicate that the maximum catalytic activity of La_2O_3 in the isomerization of 1-butene reported by Khodakov et al. (1975b) after pretreatment of the catalyst at 700°C is therefore partly due to the removal of surface carbonate species, as pointed out explicitly in the work of Rosynek and Fox (1977) (see section 4.2.5).

The examples given above clearly demonstrate the need for detailed surface characterization in order to establish the most effective pretreatment and activation conditions.

2.3.2. *Intermetallic compounds*

Intermetallic compounds of rare earth metals with d transition metals constitute a fascinating new class of catalyst materials with very interesting catalytic and solid state chemical properties. An outstanding feature of these catalysts is their decomposition under most reaction conditions, in that the rare earth component forms a stable compound with one of the reactants or its surface dissociation products leaving precipitates of the clean transition metal as the active agents at the surface. This decomposition of the intermetallic compound has already been suggested in the first report on a catalytic investigation by Takeshita et al. (1976), and has meanwhile been substantiated (Coon et al., 1978; Siegmann et al., 1978; Von Waldkirch and Zürcher, 1978; Elattar et al., 1979; Schlapbach et al., 1979a, 1980). Siegmann et al. (1978) were first to point out a self-restoring mechanism of the catalytic activity in $LaNi_5$ due to surface segregation, which may provide the basis for a new class of catalysts with improved lifetime and resistance to contaminants (Schlapbach et al., 1978, 1979b). The surface processes induced by the interaction with reactive gases will be further discussed in section 6. An aspect worth noting in the present context is that the catalyst pretreatment conditions are less important for these materials, as the samples are extensively transformed during the course of the reaction, so that pretreatment effects are rapidly obliterated.

Compositions and structure types of rare earth containing intermetallics have been collected in Chapter 13, Volume 2 of this series. Intermetallic compounds are usually prepared by standard metallurgical techniques involving induction or arc-melting in a cooled crucible under Ar atmosphere. Single crystals have also been prepared and used in surface studies (Von Waldkirch and Zürcher, 1978; Schlapbach et al., 1979a; Landolt et al., 1979). Most catalytic investigations have been performed on so-called "activated" samples. Activation consists of exposing the samples to hydrogen at pressures of several atmospheres at elevated and low temperatures. This converts the massive samples to the hydride phase and the concomitant lattice expansion results in disintegration of the samples into

TABLE 1
Surface areas (m^2/g) before and after methanation reaction (Wallace, 1978).

	Initial	Final		Initial	Final
$LaNi_5$	–	0.7	$ThNi_5$	–	18
$CeNi_5$	0.03	28.3	UNi_5	–	30
$GdNi_5$	0.03	28.36	$ZrNi_5$	–	28
$TbNi_5$	0.03	28.03	Ni/Al_2O_3	39.7	36.6
$HoNi_5$	0.01	28.26	$CeCo_5$	0.06	5.4
$YbNi_5$	0.02	28.70			

larger surface area powders. Several authors have taken advantage of the results mentioned in the foregoing paragraph, and have activated their mechanically crushed samples by pretreating them in the reaction gas mixture before measuring catalytic data. This activation not only affects the chemical state of the catalyst surface, but also results in a dramatic increase of surface area. For example, Wallace (1978) has reported drastic increases of surface areas after methanation reaction on a number of intermetallic compounds, while the surface area of a conventional Ni/Al_2O_3 catalyst remained virtually unchanged. The data of Wallace (1978) are shown in table 1, and illustrate this interesting behavior of intermetallic catalysts.

Hydrides of intermetallic compounds have been used as catalysts in hydrogenation reactions (Soga et al., 1977a, 1979b; Oesterreicher and Spada, 1980). The hydrides were prepared by exposing the samples to hydrogen at high pressures (20–100 atm) and the hydrogen content was determined from the hydrogen pressure drop during the up-take process.

Very recently, Imamura and Wallace (1981) have used the decomposition tendency of rare earth and transition d metal intermetallics under oxygen atmosphere to prepare highly reactive supported catalysts. X-ray diffraction showed that they consist of mixtures of transition metal and rare earth oxide, the transition metal particle sizes ranging from 90 to 350 Å. These catalysts exhibited superior catalytic activity compared to oxide-supported catalysts prepared by the conventional impregnation method for the hydrogenation of ethylene. Although further studies are necessary to elucidate the detailed structure of these catalysts, it appears that the oxidation process of rare earth intermetallics provides a novel means of producing active supported catalysts.

2.4. *Clean metal surfaces*

As already pointed out, the preparation of clean metal surfaces is an indispensable prerequisite for the study of surface reactions. The term "clean", however, needs further definition. As it is commonly used in surface science, it means that the concentration of any contaminants on a "clean" surface is below or near the limits of detectability in Auger spectroscopy. Of course, this

definition depends somewhat on the electron spectroscopy apparatus used, but in any case a surface with a contaminant concentration below 0.01 monolayers will only yield marginal contaminant signals in Auger spectroscopy and will not deviate significantly from the behavior of an ideal clean surface.

Surface contamination has two main sources: firstly, reaction of the surface with the residual gases in the UHV chamber, and secondly, the segregation of impurities from the bulk phase. It has to be pointed out that even samples which are of high purity in a chemical sense may have their surfaces severely contaminated due to both uptake and segregation. The high reactivity of rare earth metals makes it quite difficult to achieve the desired cleanliness, and it is therefore worthwhile to comment on the procedures applied in modern surface science to obtain contamination-free surfaces.

2.4.1. *Evaporated thin films*

The most common technique to obtain clean rare earth metal surfaces is the deposition of thin films by evaporation of highly purified rare earth samples in an ultrahigh vacuum system onto a suitable substrate. The high reactivity and thermal stability of the rare earth metals and oxides demand both careful design of the evaporation source and an elaborate procedure.

The evaporation sources commonly used are tungsten coils or tungsten crucibles (tungsten crucibles for free and equilibrium evaporation have been developed by Kaldis and Peteler, (1980)). Tantalum as crucible material seems to be less suited because of its reactivity towards sesquioxides (Foex and Traverse, 1966). Evaporation can be performed either by resistance heating or by electron bombardment (Gasgnier, 1980). In the latter case gas outbursts may cause a discharge in the electron accelerating electric field thereby making it difficult to keep the evaporation process under control. To avoid undesired rare earth deposits in the UHV chamber the evaporation source has to be shielded by a system of apertures making allowance for a well collimated beam. Pressure conditions during evaporation are positively influenced by such a shield due to the gettering action of the rare earth deposits inside the covering. Using such an arrangement we were able to obtain thin films by rapid evaporation without raising the pressure above 5×10^{-10} torr.

The substrate materials used for film deposition are not very critical unless heating experiments are performed on the deposited film. Of course, thorough cleaning of the substrate is essential to avoid contamination. Several support materials have been reported in the literature, such as glass slides, fused silica, copper, stainless steel and molybdenum sheets. If substrate heating is desired, molybdenum seems to be best suited because direct resistance heating is easy and segregation of impurities upon heating is negligible.

The evaporation procedure is by no means trivial. Even if high purity samples are used, which have been handled only under inert atmosphere, contamination by oxygen and hydrogen will be an inevitable problem. The hydrogen content of the starting material can be sufficiently reduced by outgassing at elevated temperature in UHV, but this procedure may take hours or even days depending

on the sample size and hydrogen content. The removal of the oxygen content then remains as the most difficult step.

According to Ames et al. (1967) the vaporization of rare earth sesquioxides can be represented by the equation

$$R_2O_3(s) \rightarrow x\,RO(g) + (2-x)R(g) + (3-x)O(g). \quad (8)$$

The value of x is nearly 2 for all rare earth sesquioxides with the exception of Tm_2O_3 ($x = 1.1$) and Yb_2O_3 ($x = 0.04$). x is also observed to be almost constant in the temperature range of interest. In table 2 heats of sublimation of rare earth

TABLE 2
Vaporization characteristics of rare earth metals and rare earth sesquioxides.

Rare earth	ΔH_s [a]	$-\Delta H_{f\,R_2O_3}$ [a]	$-\Delta H_{f\,RO}$ [a]	ΔH_v [a]	Temp. [b]
Sc	379	1899	66	2014	1243
Y	424	1898	48	2049	1458
La	431	1787	131	1772	1566
Ce	468	(1796)	(104)	(1843)	1554
Pr	374	(1810)	(150)	(1765)	1333
Nd	320	1793	154	1732	1175
Sm	203	1808	144	1767	642
Eu	176	1637	137	1610	515
Gd	402	1802	74	1901	1408
Tb	395	(1865)	(95)	(1930)	1354
Dy	298	1854	84	1933	988
Ho	292	1871	100	1918	1036
Er	316	1889	72	1992	1113
Tm	249	1877	87	1950	748
Yb	153	1807	−30		400
Lu	428	1872	23	2073	1483

[a] Values in brackets for 298 K, others for 0 K (kJ mol^{-1}).

[b] Temperature (°C) needed to obtain a vapor pressure of $p_v = 0.101$ Pa.

ΔH_s = heat of sublimation of rare earth metals at 0 K (Ames et al., 1967).

$\Delta H_{f\,R_2O_3}$ = heat of formation at 0 K of solid rare earth sesquioxides (Ames et al., 1967) with the exception of values in brackets which are given for 298 K (Eyring, 1979).

$\Delta H_{f\,RO}$ = heat of formation at 0 K of gaseous rare earth monoxides (Ames et al., 1967) with the exception of values in brackets which are given for 298 K. These values are estimated from the data given by Ames et al. (1967).

ΔH_v = heat of vaporization at 0 K for the reaction $R_2O_3(s) \rightarrow 2\,RO(g) + O(g)$ with the exception of values in brackets which are calculated for 298 K.

The vapor pressure data are taken from Beaudry and Gschneidner (1978).

metals, heats of formation of sesquioxides and monoxides and heats of vaporization for the reaction $R_2O_3(s) \rightarrow 2RO(g) + O(g)$ are listed together with some values of the vapor pressure of rare earth metals. From this data an exceptional behavior of Yb may be expected, although it is not possible to obtain quantitative results for the nonequilibrium process of free evaporation. Nguyen and Saint-Simon (1972) performed a systematic study by mass spectrometry of rare earth oxide decomposition and, using a semiempirical approach, they derived a quantitative expression for the ratio $i(MO^+)/i(M^+)$ as a function of atomic number and temperature. This, together with table 2 and eq. (8) allows us to make the following conclusions: Outgassing of a partially oxidized sample at temperatures well below the melting point is possible, but in most cases only by evaporating gaseous monoxides, i.e. under substantial loss of the rare earth material. The evaporation process itself for producing a clean film should be rapid for two reasons: firstly, to minimize reactions with the remanent atmosphere, and secondly, to prevent contamination by impurities segregating from the bulk during evaporation. This procedure, however, does not work for Yb. Atkinson et al. (1976) have noticed that Yb refused to outgas in contrast to other rare earth metals. In a series of evaporation experiments performed in our laboratory we have also observed that it was impossible to produce a clean deposit in this way. Instead of outgassing the relative oxygen content in the Yb sample increased. This peculiar behavior may be better understood, if not only thermodynamical data but also the structure of partly oxidized Yb is taken into account. In contrast to the other rare earth metals the oxidation of Yb proceeds probably via island formation (see section 3.1). The island structure of the oxide overlayer permits the metal underneath to penetrate easily to the surface. Thus, the metal remains available at the surface of an incompletely oxidized sample. If the sample is heated, the clean metal exhibits a high vapour pressure and instead of outgassing, the sample becomes depleted of clean metal. Yb needs therefore just the reverse treatment as compared to the other rare earth metals: rapid short heating to high temperatures removes both metal and oxide from the surface. Subsequent evaporation at comparatively low temperatures ($700\ K < T < 900\ K$) yields good results provided the base pressure in the UHV chamber is sufficiently low to prevent contamination from the background atmosphere. Further experimental observations concerning evaporation of larger rare earth metal quantities from tungsten crucibles have been reported by Gasgnier (1980).

2.4.2. *Cleaning procedures for foils and single crystals*

In spite of the lengthy cleaning procedures involved, a growing number of rare earth metal surface studies is done on foils and even on single crystals. The mechanically polished foils or spark cut crystals are first of all degreased in an ultrasonic bath using ethanol or acetone. Afterwards they are mounted on a sample holder, but provision has to be made for sample heating.

Onsgaard et al. (1980a) used an indirectly heated stainless steel holder with a tantalum back-up ring in order to prevent alloying. Koel et al. (1980) spotwelded their Ce foil along the edges to a tantalum foil. To prevent oxidation this was

done under ethanol. The Ta foil was then attached to a button heater; the Ce foil was polished with fine grain sand paper wetted with acetone and immediately placed in vacuum. In our own investigations on foils we used electron bombardment heating (Bertel et al., 1981). The rare earth foils were spotwelded to two thin Ta wires, which in turn were spotwelded to the main manipulator rods. Electrons from a tungsten filament were fired onto the back side of the foil using an acceleration voltage of about 800 eV. Current limitation is necessary in order to prevent discharge and foil melting due to gas outbursts which may happen to occur during the first heating cycles.

The further steps of surface cleaning generally consist of a number of noble gas sputtering cycles with subsequent annealing at elevated temperatures. A rather detailed report about the cleaning procedure of a Sc single crystal has been given by Onsgaard et al. (1979). They used Ar^+ ions with 500 eV energy for sputtering and annealing temperatures up to 840°C. Praline et al. (1980) obtained a clean surface on a Ce foil after bombardment with 5 keV Ar^+ ions at a current density of 150 $\mu A\,cm^{-2}$ whilst the sample was held at a temperature of about 330°C. Bertel et al. (1981) used 1 keV Ar^+ ions and subsequent annealing at ~900°C to clean their Er foil, while Kr^+ ion bombardment at 1 keV, 20 $\mu A\,cm^{-2}$ and annealing temperatures between 400 and 900°C have been reported by Tougaard et al. (1980) for a Sc single crystal.

The main impurities reportedly observed on bulk samples are C, N, O, S, Cl and in one case Zr (Chamberlain and Baun, 1975). Carbon proves to be one of the most persistent contaminants, but we have observed that it could be removed by oxidizing the surface with water vapor and subsequent heating. The oxide is reduced by sputtering and annealing as described above.

Finally, it should be mentioned that Alvarado et al. (1980) used a carbide steel brush to prepare a clean Yb surface, which has the advantage of being a time saving technique.

3. Adsorption on and reactions with rare earth metal surfaces

As long as fifty years ago the rare earth oxides were recognized to be catalytically active (Cremer, 1929). Since then a considerable amount of research has been devoted to studying catalysis on rare earth compounds, which is reviewed in the other sections of this article. Comparatively few studies, however, have been done on clean rare earth metal surfaces due to their high reactivity, which makes UHV conditions and lengthy cleaning procedures necessary preconditions for obtaining reliable results. The main body of these investigations centers around oxidation, hydration and hydrogenation of rare earth metals. Besides that, occasional studies of the interaction with other gases such as carbon monoxide, carbon dioxide and nitrogen have been carried out. In the following subsections the main results in the recent literature are discussed and some additional information is given from our own work on rare earth metal surface reactions.

3.1. *Rare earth metal surface oxidation by oxygen*

In a recent review Gasgnier (1980) has discussed the problem of the existence of Ln-monoxides in the bulk phase. He showed conclusively that the experimental results invoked to indicate the formation of solid state Ln-monoxides can either be attributed to bulk dihydrides or to partial substitution of nitrogen instead of oxygen in the sesquioxides (Felmlee and Eyring, 1968; Work and Eick, 1972). Thus, with the exception of EuO, the existence of solid Ln-monoxides has been denied. The question, however, arises: what happens during the initial stages of rare earth metal oxidation, when kinetic effects dominate the behavior of the rare earth–oxygen system?

3.1.1. *Cerium: A case study*

The rare earth–oxygen system studied most extensively is probably the cerium–oxygen system. Helms and Spicer (1972) have published a comparative UPS study of the oxidation process in strontium and cerium, where they followed the growth of UPS peaks in the valence band region during initial oxidation (exposure $\leqslant 500$ L O_2) of Sr and Ce. In cerium the oxygen derived valence band features are quite broad from the beginning and show little change in shape during oxidation. The oxygen uptake follows logarithmic kinetics (Lawless, 1974). Helms and Spicer (1972) therefore concluded that a semiprotective layer of Ce_2O_3 is formed immediately resulting in a diffusion controlled oxidation process (CeO_2 as another possible surface species is believed to form a porous nonprotective overlayer). A pronounced decrease in work function (about -1.0 eV) during the initial stages of Ce oxidation was thought to be due to the low electron affinity of the oxide. This conclusion was corroborated by the contrasting behavior of strontium, where an initially much sharper O-derived UPS peak and a different growth curve indicated the initial solution of O^{-2} ions into the Sr matrix with formation of SrO only after further exposure. A somewhat peculiar result is the large drop in work function of Ce which is unexpected in view of the behavior of heavy rare earth–oxygen systems as we shall see below. Such a large decrease of the work function, however, is commonly observed, if OH groups are formed at the surface due to the interaction with water from the residual atmosphere. If hydration occurs, it may well influence the kinetics of oxidation.

Platau et al. (1977) have studied the oxidation of evaporated Ce films using XPS. They found two O 1s peaks at 529.9 and 532.6 eV which they assigned to oxygen in Ce_2O_3 and to physisorbed oxygen, respectively. In accordance with Helms and Spicer (1972) these authors assumed the build-up of a protective oxide layer, but a thickness of only 7 Å was estimated after 100 L exposure. Shifts in absolute binding energy of O 1s were attributed to sample charging, work function changes and relaxation effects.

In 1978, the same authors (Platau and Karlsson, 1978) performed a thorough XPS and UPS study of the valence band emission of Ce. Using the different energy dependence of photoemission cross sections of the 4f level and the sd

band states Platau and Karlsson (1978) were able to localize the 4f electron in metallic cerium at 1.9 ± 0.2 eV below the Fermi level. Oxidation up to 3000 L O_2 resulted in a suppression of the sd band emission, but the 4f level remained nearly unaffected unless exposures were made at high temperature (1000 L O_2 at 600°C). In this case the 4f emission was heavily attenuated. The complete vanishing of conduction band features indicated a thickness of the protective layer larger than the electron escape depth of about 20 Å, in contrast to the earlier results. From the behavior of the 4f emission Platau and Karlsson (1978) concluded that the sesquioxide only is formed at room temperature, whereas at elevated temperature appreciable amounts of Ce^{4+} species lead to a decrease in 4f intensity. Residual 4f emission has been interpreted as due to oxide phases of intermediate stoichiometry or to a porous CeO_2 overlayer.

In addition to these results Platau and Karlsson (1980) observed a decaying phase of CeO_2 even at room temperature immediately after exposure to oxygen. Identification of different chemical species was accomplished by using the rather specific satellite structure of the Ce 3d doublet in XPS.

In an ESCA study of the passivation of metals by Barr (1978a,b) true passivation has not been detected on Y, La and Ce, i.e. a horizontal stage in their oxide thickness vs. time curve. Consistent with the results of Platau and Karlsson (1978) he observed in Ce oxidation the appearance of Ce^{4+} species. Using photoelectron lines of different kinetic energy Barr (1978a) argued that the CeO_2 species were not mixed with the Ce_2O_3 but formed specific layers on top of the sesquioxide.

Praline et al. (1980) have recently investigated the oxidation of Ce foils at 300 K and 120 K under UHV conditions. In accordance with Helms and Spicer (1972) they found that the uptake curve followed a logarithmic relationship. An oxygen 1s peak initially observed at 530.3 eV binding energy was assigned to Ce_2O_3. At exposures between 20 and 30 L the peak position changed to 529.8 eV. Upon further oxidation to saturation an additional shift of 0.2 eV to lower binding energy was observed. This has been explained by the formation and the subsequent increase in relative contribution of CeO_2 species. It has to be mentioned that this could also explain the O 2p shift observable in the valence band spectra of Helms and Spicer (1972) and the O 1s binding energy shift observed by Platau et al. (1977), which they attributed to relaxation and charging effects. An O 1s peak appearing at 532.7 eV was attributed by Praline et al. (1980) to adsorbed OH groups or hydroxyl containing oxide formed by interaction with residual water. This contradicts the assumption of physisorbed oxygen made by Platau et al. (1977). A thorough analysis of the Ce 3d spectra confirmed the conclusion of initial Ce_2O_3 formation with subsequent appearance of CeO_2 in a thin passivating layer (about 24 Å thick at 20 L O_2 and probably substantially thicker after higher exposures). At 120 K the formation of CeO_2 was slightly enhanced, but the relative instability of this species, already observed by Platau and Karlsson (1980), was confirmed by the loss of Ce^{4+} spectral features upon heating to room temperature.

Additional information has been obtained from inspection of the valence band

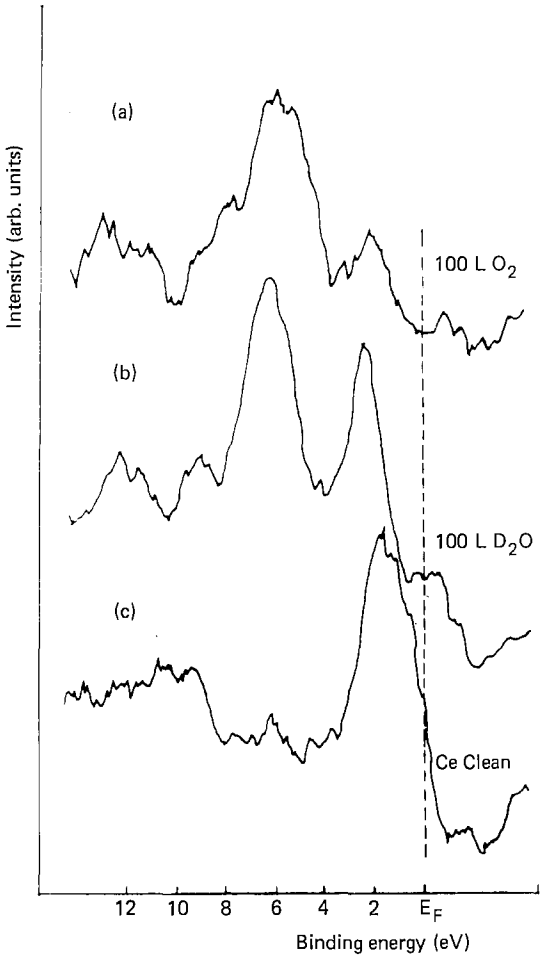

Fig. 6. Mg Kα photoelectron spectra of (a) cerium exposed to 100 L O_2, (b) cerium exposed to 100 L D_2O and (c) the valence region of clean cerium (Praline et al., 1980).

XPS. As shown in fig. 6 (Praline et al., 1980) the spectrum of clean Ce is characterized by the combined contribution of the sd conduction band and the 4f level. Oxidation with 100 L O_2 reduces the conduction band emission almost completely, whereas the 4f emission is attenuated due to Ce^{4+} formation, but a contribution of Ce_2O_3 is still indicated. In contrast, the oxidation by interaction with water vapor reduces the metallic emission only, leaving the 4f intensity unchanged. This is in accordance with the observation that only Ce_2O_3 is formed upon exposure to water vapor (Koel et al., 1980).

In conclusion, there seems to be evidence that exposure of Ce to oxygen results in the immediate formation of Ce_2O_3. At higher exposures a more or less passivating layer is formed with CeO_2 being present. It is not yet quite clear whether there is a mixed layer or whether the CeO_2 is built up in a specific layer on top of the sesquioxide. The protective properties of the oxide layer seem to be pressure dependent.

3.1.2. *The heavier rare earth metals*

One of the earliest studies of rare earth metal oxidation in UHV has been carried out by Loescher (1971). He measured the oxide thickness on evaporated Er films as well as on polycrystalline bulk samples as a function of time at various pressures and temperatures. The oxide film thickness was determined by ellipsometry. Although he started the oxidation process on already heavily contaminated surfaces (initial surface oxide thickness up to 7 Å) the results are of interest here, because at room temperature he found a logarithmic oxide growth as was observed with cerium, whereas at higher temperatures a power law $d = At^{\alpha}$ applied, d being the oxide layer thickness, t the time of exposure, A and α empirical parameters with $0.2 < \alpha < 0.5$. The saturation thickness after exposure to air at 625 torr and room temperature varied between 60 and 120 Å and was only about 2 to 3 times larger than after exposure at 5×10^{-7} to 5×10^{-6} torr. The measured values of the absorption index were much larger than expected for stoichiometric Er_2O_3, and therefore formation of a substoichiometric oxide was assumed. It remains doubtful, however, whether this conclusion is stringent, or whether contamination could equally well account for the high absorption index.

Färber and Braun (1974) have used Auger electron spectroscopy to monitor changes in electronic structure upon oxidation of Sm, Gd and Tb. After an initial linear stage in oxygen uptake they found a logarithmic growth, but this was deduced from the observed O Auger peak-to-peak heights without any corrections for the electron escape probability.

Considerable new insight into the oxidation mechanism has been provided by the work of Padalia et al. (1976). These authors investigated the reaction of oxygen and water with rare earth metal films of terbium to lutetium using X-ray photoelectron spectroscopy. As in the case of cerium two O 1s peaks were observed, one at about 531 eV binding energy and another at 533 eV, the latter being weaker and of varying intensity in different experiments. Again, by comparison with water interaction and some other experimental findings the peak at 533 eV was unequivocally assigned to OH groups originating from water contamination and not attributed to chemisorbed or physisorbed oxygen.

Concerning the assignment of the main O 1s peak at about 531 eV Padalia et al. (1976) have argued as follows: In ytterbium, the formation of the oxide is accompanied by a valence change which is easily recognized in the metal core level XPS spectra (as mentioned in section 2.2.2). This valence change is already well defined at the very initial stages of oxidation, when the O 1s peak at 530.8 eV starts to develop. This peak can therefore be assigned to sesquioxide oxygen. By analogy, the O 1s peaks appearing at roughly the same energy in the other rare earth metals have been attributed to sesquioxide formation, too. If these oxides, however, were produced by evaporation in oxygen atmosphere (10^{-4} torr), the corresponding O 1s peaks were invariably observed at somewhat higher binding energy. Padalia et al. (1976) explained this difference by different charging effects in bulk oxide as compared to surface oxidized films.

The oxidation kinetics was observed to be pressure independent and to follow

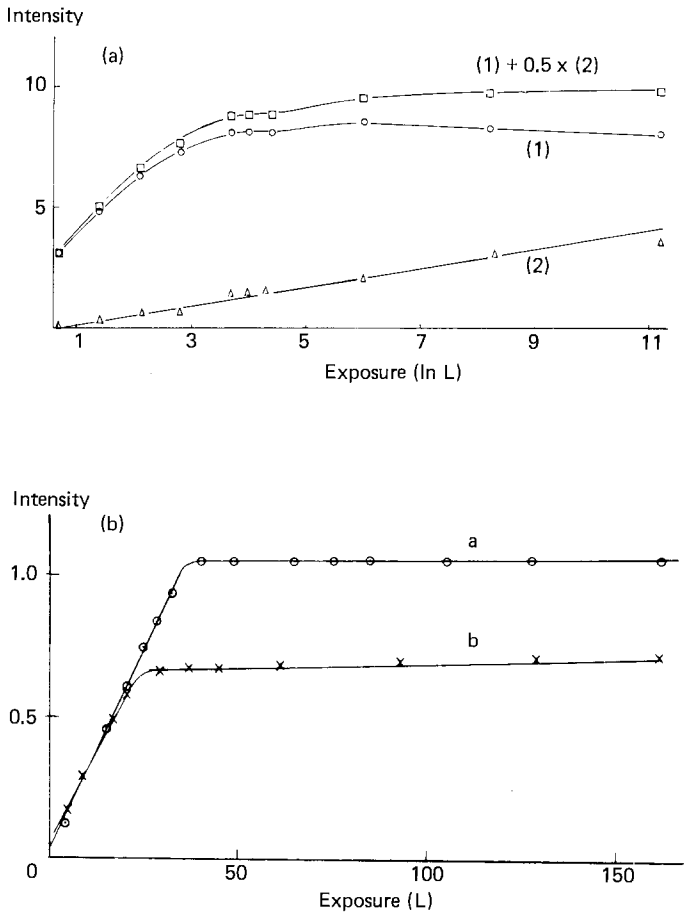

Fig. 7. (a) Variation in intensity of O 1s peaks (1:531.1 eV and 2:533.2 eV) with exposure to O_2 for erbium. (b) Variation in intensity of the O 1s peak at 530.8 eV with exposure to (a) O_2 and (b) H_2O for ytterbium. The curves are not corrected for escape depth (Padalia et al., 1976).

a logarithmic relationship. Yb, however, showed a markedly different behavior, namely a linear oxygen uptake curve. This is illustrated in fig. 7, where oxygen 1s peak intensities as a function of O_2 and H_2O exposure are compared for Er and Yb (Padalia et al., 1976).

In order to account for these results Padalia et al. (1976) have proposed the following model of oxidation: In Yb the oxide was assumed to be nucleated in islands and the linear kinetics was attributed to island growth. In the case of the other heavy rare earth metals the oxide was assumed to form a continuous film at the surface, which grows steadily deeper into the bulk thus accounting for the logarithmic relationship between exposure and O 1s peak intensity. After an exposure of about 40 L O_2 the oxide film was thought to form a protective layer which slows down the further oxidation as can be recognized in fig. 7.

This interpretation in terms of immediate sesquioxide formation is consistent with both the currently accepted model of oxidation of Ce and the comments of Gasgnier (1980) concerning the question of solid rare earth suboxides. It is in disagreement, however, with the earlier observations of Loescher (1971). A word of caution should be added. A difference in the O 1s peak position of bulk oxide and surface oxidized samples has been observed, which was attributed to charging effects. Yb seems to be the only rare earth metal where the O 1s binding energy in bulk and surface oxide is the same within experimental error limits. In a later study by Gimzewski et al. (1979) concerning the oxidation of scandium similar small differences in O 1s binding energy between bulk and surface oxide constituted an argument for O^{-2} dissolution instead of immediate oxide nucleation. It appears, therefore, that oxygen dissolution instead of immediate oxide phase formation at the initial stages of oxygen interaction cannot be completely excluded on the basis of XPS results.

A detailed investigation of the changes in the Er valence band region upon interaction with oxygen, water and hydrogen has been carried out by Netzer et al. (1981a) using X-ray and ultraviolet photoelectron spectroscopy. The O 1s peak was found at a constant position of 531.6 eV already after exposures of only 0.5 L O_2 in close agreement with Padalia et al. (1976). The oxygen 2p emission appeared after a dosage of 0.1 L O_2 at 6 eV. Further exposure caused broadening and splitting into two features at 5.6 and 7 eV, respectively, the shift being complete after an oxygen dose of only 2 L. These results suggest that oxidation starts with chemisorbed oxygen characterized by the narrow 6 eV photoemission peak (a similar feature in Sr was attributed to dissolved O^{-2} by Helms and Spicer (1972)). But already after 2 L O_2 exposure photoemission from oxygen 2p derived valence bands seems to dominate indicating oxide formation.

Systematic electron energy loss experiments with emphasis made towards the rare earths' oxidation process have been performed by Bertel et al. (1981) on the Er/O system. Fig. 8 shows electron loss spectra of Er as a function of oxygen exposure (a) and corresponding difference spectra "oxygen exposed minus clean" (b) (Bertel et al., 1981). In agreement with the UPS results (Netzer et al., 1981a) depletion of the metallic conduction band can be inferred. The bulk plasmon peak, having an energy of 13.5 eV in the clean metal, shifts to 15 eV upon oxidation (and, correspondingly, the double plasmon from 28 to 30.5 eV). An additional loss peak is observed at 9 eV upon oxidation which is attributed to an excitation from the valence band of the oxide (mainly O 2p character) to the conduction band. The 3.5 eV loss vanishes upon oxidation and can be associated with excitations originating in the metal conduction band.

All the changes in electron loss spectra reported above progress steadily with increasing O_2 exposure and are completed after 30 L O_2 dosage. Slight differences in the spectra excited with 1000 eV and 210 eV primary electrons indicate that the changes are caused by steady penetration of an oxidized layer throughout the probing depth. The results are consistent with both the immediate nucleation of stoichiometric sesquioxide with subsequent oxide growth and the gradual dissolution of oxygen into the bulk. The only difference expected for the

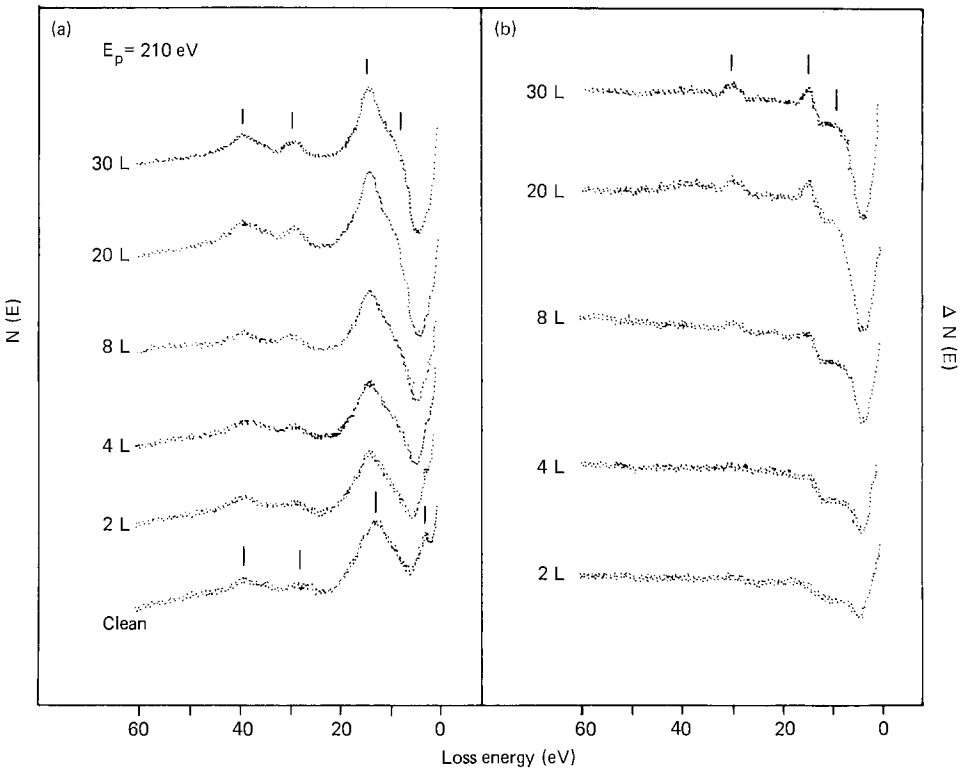

Fig. 8. (a) Electron energy loss spectra of Er as a function of O_2 exposure in $N(E)$ form. (b) Corresponding difference spectra (Er + O_2) minus (clean Er) (Bertel et al., 1981).

two possibilities would be the behavior of the plasmon peak. In the case of oxide nucleation there should be two distinct peaks at the respective positions of the clean metal and the oxide, which gradually exchange their intensity as is clearly observed in the Yb ELS spectra (fig. 9, Bertel et al., 1982). Note the two plasmon peaks at 9.5 and 15 eV in the spectra after 2 L and 5 L O_2 exposures in fig. 9. Dissolution of oxygen, on the other hand, should result in a steady shift of only one plasmon peak. However, due to the broadness of the plasmon peak and the small separation of the respective energy values in Er, it is difficult to decide which one of the two mechanisms is actually working (cf. fig. 8). The situation is much more favourable in Yb, where the valence change occurring upon oxidation causes large separation of the plasmon energies of metal and oxide.

In a study of the Auger and autoionization spectra of clean and oxidized samarium and erbium by Netzer et al. (1981b) the oxygen KLL peak position was also monitored as a function of coverage. It was found to vary continuously in energy from 516.5 eV (small traces of oxygen only) to 512.5 eV in Er (Bertel and Netzer, 1980b) and to 514 eV in Sm at about 20 L O_2. This seems to favor the oxygen dissolution model for low exposures on Er and Sm.

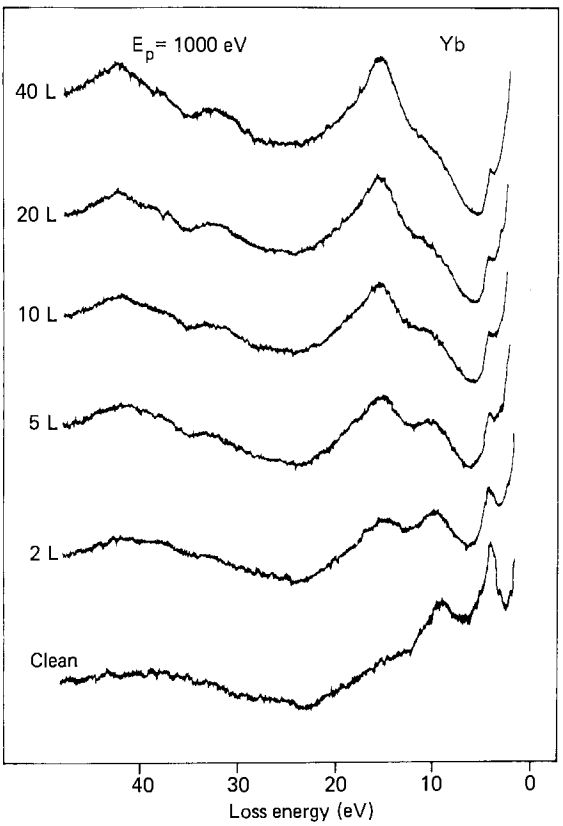

Fig. 9. Electron energy loss spectra of Yb as a function of O_2 exposure in $N(E)$ form (Bertel et al., 1982).

Support for this mechanism is provided by work function measurements (Strasser et al., 1982). In fig. 10 $\Delta\phi$ curves are presented for Er and Yb, which show the work function changes measured dynamically during oxygen, water and hydrogen exposures at various constant pressures. For the Er/O system the main features are an initial decrease followed by a minimum and a subsequent increase which does not reach saturation up to very high exposures. The measurements have been made by means of a vibrating Kelvin probe using tin oxide as the reference surface. The results at low exposures are in good agreement with the work function measurements of Müller (1977), who used a gold reference probe. In contrast to the measurements presented in fig. 10, Müller (1977) observed a decrease in work function at very high exposures. This decrease at high exposures, however, may be due to reaction with residual water resulting in a surface dipole layer of OH groups (see below). The work function curves $\Delta\phi$ vs. exposure are strongly dependent on the oxygen pressure in contrast to the oxygen uptake curves obtained by Padalia et al. (1976) from XPS measurements.

An initial decrease of the work function is commonly attributed to immediate incorporation of oxygen beneath the surface thus building up an inverse surface

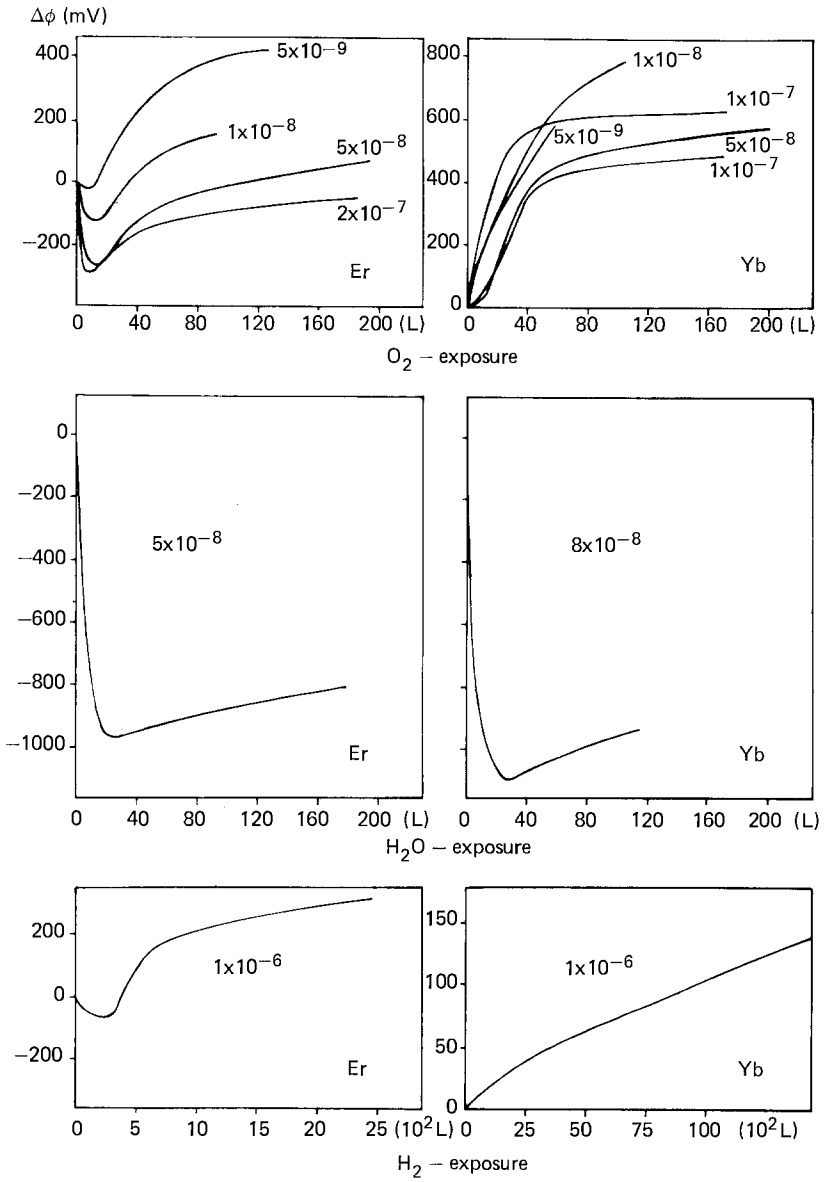

Fig. 10. Work function changes during exposure of a clean Er metal film (left) and a clean Yb metal film (right) to oxygen, water and hydrogen, respectively (Strasser et al., 1982).

dipole layer. The subsequent increase in work function to values higher than the clean metal can be explained by the formation of the oxide phase with concomitant changes of the chemical potential and the Fermi level position. The oxygen pressure dependence of the work function curves can be rationalized by assuming different concentrations of subsurface oxygen, which is consistent

with an initial oxygen dissolution mechanism (Strasser et al., 1982). Alternatively, a pressure dependent surface oxide structure would also explain these results.

As already mentioned a very contrasting behavior is found in the oxidation of Yb. Padalia et al. (1976) have pointed out the different oxygen uptake kinetics and have concluded that oxide island growth as opposed to a continuous overlayer formation, as in the case of the other heavy rare earths, takes place. This is supported by the ELS work performed in our laboratory (cf. figs. 8 and 9). Furthermore, the O KLL Auger peak position has been found to be shifted from about 514 eV in nearly clean Yb to 513 eV in fully oxidized Yb indicating only minor changes in the oxygen chemical state (Bertel et al., 1982). The work function changes presented in fig. 10 show a markedly different behavior as compared to Er. There is no systematic variation with pressure, hence the observed differences are more likely to be due to different film structure and perhaps different initial oxygen contamination. The absence of the initial decrease and the pressure independence of the overall curve shape is just what is expected for immediate oxide island nucleation, and the conclusions of Padalia et al. (1976) on Yb oxidation are therefore fully supported by our own results.

3.1.3. *Scandium, yttrium and lutetium*

Recently, the interaction of scandium with oxygen and water has been studied by Gimzewski et al. (1979) using XPS. If Sc was exposed to oxygen at successive low dosages the O 1s binding energy shifted from initially 530.0 to 530.3 eV, whereas after one large single exposure and also in the bulk oxide the O 1s binding energy was observed to be 530.8 eV. Adsorption of oxygen at low pressures caused a broadening of the Sc 2p emission and the oxide overlayer thickness calculated from the metal signal attenuation differed significantly from the thickness obtained by evaluating the O 1s signal increase.

From these results the authors concluded that stepwise small oxygen exposures result in O^{2-} dissolution into the bulk, whereas high exposures for a short time (i.e. at high pressure) cause a high oxygen concentration near the surface allowing nucleation of the oxide.

This behavior of scandium exposed to oxygen is quite similar to that of the heavy rare earths. Remarkable similarities in the behavior of Sc, Y and Lu with that of the heavy trivalent rare earths are also reported by Onsgaard (1981). The ELS spectra of both metallic and oxidized Sc, Y and Lu closely resemble that of Er (Bertel et al., 1981). A comparison between changes in the Auger spectra as a function of oxygen exposure and ion scattering measurements corroborates the conclusion that the adsorbed oxygen diffuses immediately into the bulk. A LEED study of the oxidized Y(0001) surface indicated the oxygen occupies sites in a hexagonal pattern between the first and second atomic layer of yttrium (Onsgaard, 1981).

Due to the similarities in oxidation behavior revealed by XPS, AES and ELS it seems to be justified to extend the conclusions of Gimzewski et al. (1979)

concerning the initial stages of scandium oxidation to all trivalent rare earths. Thus, oxidation of trivalent rare earths probably starts with oxygen dissolution. The depth profile of oxygen concentration at a given oxygen dosage and consequently the oxygen exposure needed for oxide nucleation is then strongly pressure dependent. The formation of a protective oxide layer seems to occur only at partial oxygen pressures higher than 10^{-7} torr. In ytterbium, however, the oxide phase is immediately nucleated irrespective of oxygen pressure.

3.1.4. *Changes in electronic structure upon oxidation*

The uptake of oxygen by rare earth metals causes rapid depletion of the 5d6s conduction band electrons. The loss of conduction band electrons is accompanied by a strong increase in emission from the O 2p levels in UPS (Helms and Spicer, 1972). In Ce as well as in Er the O 2p emission already splits into two components at low exposures indicating the onset of O 2p overlap and the resulting formation of a new band (Platau and Karlsson, 1978; Netzer et al., 1981a). The transfer of electrons from the metallic conduction band to the O 2p valence band is also well demonstrated in the electron loss spectra of Er and Yb (Bertel et al., 1981, 1982). ELS studies of Onsgaard et al. (1980a) on Sc single crystals have shown similar results. The conduction band depletion causes a rapid increase in electrical resistivity as has been reported by Singh and Curzon (1977) on rare earth thin films.

A further consequence of oxygen uptake is the plasmon shift as observed in ELS investigations. In the clean rare earth metals the bulk plasmons are observed at somewhat higher energy than expected from the nearly free electron model (Bakulin et al., 1971; Brousseau et al., 1974; Dufour et al., 1976; Colliex et al., 1976; Onsgaard et al., 1980a,b; Bertel et al., 1981, 1982). The reason for this is not quite clear as 4f contribution seems to be weak. Upon oxidation the plasmon peak position changes by about 2 eV from 13 eV in the metal to 15 eV in the oxide. Assuming 18 "quasi-free" electrons per R_2O_3 unit the calculated plasmon energies are of the order of 21 eV. The large discrepancy between measured and calculated plasmon energies is probably due to the failure of the free electron approximation. It is interesting to note in this context the exceptional behavior of Eu (Nigavekar and Matthew, 1980) and Yb (Brousseau et al., 1974; Bertel et al., 1982). Both divalent metals have bulk plasmon peaks at ~9.5 eV. In Yb_2O_3 the bulk plasmon is observed at an energy of 15 eV as in the other rare earth sesquioxides. In EuO, however, the bulk plasmon is located at ~14 eV, which is higher than expected if compared to the trivalent oxides. This may indicate that the valence electrons in the divalent oxide behave in a rather more free-electron-like way.

The 4f levels of rare earth metals remain in general unaffected by oxidation due to their largely atomic-like nature. The map of the 4f and valence band density of states, however, presented by Lang et al. (1981), shows 4f levels in critical proximity to the Fermi level for Ce (1.9 eV below E_F), Eu (1.5 eV below E_F), Yb (1.3 eV below E_F), Sm (0.5 eV above E_F) and Tm (1.1 eV above E_F). Thus, due to changes in the chemical environment, the external pressure or by

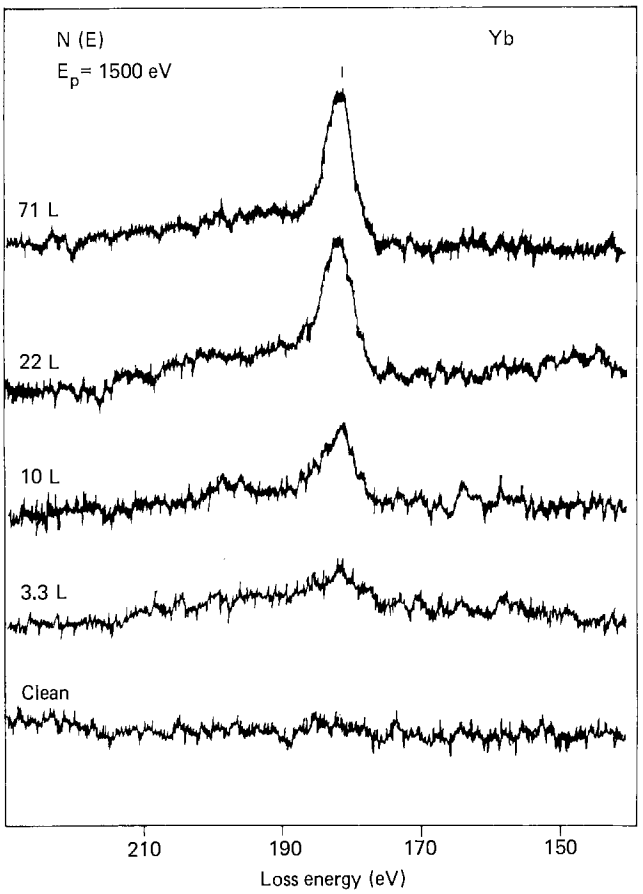

Fig. 11. Electron energy loss spectra of Yb as a function of O_2 exposure in $N(E)$ form. The loss process at 181 eV is due to a 4d→4f resonant excitation in the ytterbium oxide (Bertel et al., 1982).

surface relaxation the 4f levels may be shifted to E_F in these elements allowing transitions between the valence band and the 4f states. Hence a valence change or interconfiguration fluctuation may happen. Upon oxidation such a valence change is observed in Ce from 3+ to 4+ (cf. fig. 6) (Platau and Karlsson, 1978; Praline et al., 1980) and in Yb from 2+ to 3+. The valence change in Yb is reflected in the "turning-on" of the 4d→4f resonance as observed by Johansson et al. (1980). This resonance can also be observed in ELS, and in fig. 11 the appearance and growth of the "giant" 4d→4f resonance as a function of oxygen exposure is demonstrated (Bertel et al., 1982). Eu is known to form different stable oxide phases. Hyperstoichiometric sesquioxides with considerable O excess are observed for Pr and Tb, where the 4f to Fermi energy distance is as large as 3.3 and 2.2 eV, respectively (Eyring, 1979).

Changes in the XPS core level spectra are partly discussed in section 2.2.2. For more detailed information the reader is referred to the literature cited therein.

3.2. *Rare earth metal surface interaction with water vapor*

Dexpert-Ghys et al. (1975) have published an X-ray diffraction and electron microscopy study of the reaction of rare earth metal thin films with water vapor. The results appeared to be quite exciting: whereas neodymium slowly converted to the hexagonal $Nd(OH)_3$ under exposure to air at room temperature, as judged from the X-ray diffraction pattern, dysprosium did not show diffraction lines indicative of oxidation under these conditions. At a temperature of 413 K and a partial pressure of water of about 10 torr, however, the metallic diffraction pattern converted into the pattern characteristic of DyH_2. Only at higher temperature (453 K) the sesquioxide was observed in X-ray diffraction. Electron micrographs seemed to support these results. The authors therefore concluded that the following reaction takes place:

$$Dy + H_2O \rightarrow DyH_2 + \tfrac{1}{2}O_2. \tag{9}$$

Such a reaction could be used for water splitting and therefore would be of enormous technical importance. Some doubt, however, arises from thermodynamic considerations because the free energy change is positive for this reaction (+71 kJ). Surface energy contributions or photochemical mechanisms were therefore invoked as possible sources to improve the energy balance (Smith et al., 1980).

In order to investigate the influence of water contamination on the hydrogen storage in rare earth materials and to verify the results of Dexpert-Ghys et al. (1975), Holloway and Swartz (1977) have studied the interaction of Er and ErD_2 with water vapor at various temperatures. They found that Er reacted with water vapor (partial pressure ~20 torr) only above a critical temperature of 573 K. The reaction products observed by X-ray diffraction were both oxide and hydride. The absence of any reaction at lower temperature was attributed to surface oxygen which, according to Auger spectroscopy, was removed at the critical temperature (presumably due to migration into the bulk). Due to the different experimental conditions the results of Dexpert-Ghys et al. (1975) could be neither verified nor invalidated in this study. However, in an X-ray diffraction study of water vapor interaction with thin films of Gd and particles of Y, Dy and Er Oesterreicher et al. (1979) confirmed the observations of Dexpert-Ghys et al. (1975). They noticed virtually complete dihydride formation after exposure of Gd thin films to water vapor for 180 min at 423 K. Exposure of Y, Dy and Er particles to water at various temperatures resulted either in partial oxide and hydride formation or in no reaction at all.

The question of hydride formation by interaction with water vapor has been addressed recently by Smith et al. (1980). Extending the investigations to powders of Pr, Gd, Dy and Er and applying Auger spectroscopy in addition to X-ray diffraction they were able to exclude the possibility of water dissociation into hydrogen and gaseous oxygen. Experiments with ^{18}O-enriched water showed conclusively that no gaseous oxygen was formed during the reaction. Moreover, Auger spectroscopy showed large amounts of oxygen in Dy films

after interaction with water vapor at 413 K. The results of Dexpert-Ghys et al. (1975), however, were confirmed in that no oxide lines were observable in the X-ray diffraction pattern, but only those of DyH_2. Thus, the oxide formed may be considered as an amorphous oxide or oxygen dissolved in Dy or DyH_2. The oxygen concentration estimated from O KLL Auger peak heights exceeded that of Dy_2O_3; this may be due to the presence of $Dy(OH)_3$.

After reaction with water vapor under similar conditions Pr and Gd showed the characteristic diffraction patterns of both the hydroxide and the dihydride in agreement with the results of Dexpert-Ghys et al. on neodymium. Consistent with the observations of Holloway and Swartz (1977) Er showed no signs of reaction according to X-ray diffraction after water exposure at 413 K.

In contrast to the X-ray diffraction studies oxide formation upon exposure of rare earth metals to water vapor was already clearly evidenced in 1976 by XPS, when Padalia et al. (1976) made their fundamental study on the oxidation of the heavier rare earth metals Tb to Lu. Two oxygen 1s peaks were observed after water exposure at room temperature, which were attributed to oxide oxygen and surface OH groups, respectively. The intensity ratio of the two peaks was explained by the authors by assuming the formation of oxide islands, which grow laterally and are covered by a hydroxide overlayer. The growth curve upon H_2O exposure, however, is very similar in shape to the oxidation curve obtained with oxygen exposure. The regions in between the islands showed metallic emission in XPS, but taking into account the X-ray diffraction results, they are likely to be a hydride phase. Padalia et al. claimed that there are no signs of $R(OH)_3$ formation in the bulk (i.e. no characteristic O 1s signal differing from the oxide oxygen signal was observed).

Sorption of water on clean films at low temperature produced two additional O 1s peaks at higher binding energy, which have been assigned to condensed water and chemisorbed water, respectively. Both peaks could be removed by heating or converted into the peaks which were observed after room temperature exposure.

Ytterbium, again, showed a significantly different behavior. The intensity ratio of the signals from oxide oxygen and surface OH groups was the same as in the other heavy rare earths indicating the same depth of the oxide islands but the uptake kinetics following water exposure was linear (see fig. 7). This difference was tentatively attributed by Padalia et al. (1976) to the lack of hydride formation in the reaction of Yb with water.

An XPS investigation of the scandium–water interaction by Gimzewski et al. (1979) revealed interesting differences to the behavior of the heavier rare earths. The OH signal was observable only after about 50 L water exposure and the hydroxide to oxide ratio reached its maximum of 0.5 only after a water dosage of 10^3 L. In contrast, the heavier rare earths already exhibited this ratio after about 50 L exposure. The oxide depth on Sc after 10^3 L H_2O was estimated to be 6 Å. Further differences were found at low temperature, where hydroxide oxygen signals were first observed and at higher exposures the signals of chemisorbed and condensed water (ice), but no signs of oxidation, could be detected.

Additional evidence for the absence of low temperature oxidation of scandium under water exposure was provided by considering the Sc $2p_{3/2}$:$2p_{1/2}$ metal peak intensity ratio, which changes upon oxidation and may be used therefore as an indicator of oxidation. Accordingly, oxidation of Sc by water seems to be much slower and less extensive than that of the lanthanides Tb to Lu.

The interaction of deuterium water vapor with cerium has been studied in XPS recently by Koel et al. (1980). A very similar behavior as compared to the heavy rare earths was found, in that a nonlinear uptake was obtained after exposures of about 80 L. Calculations of overlayer thickness using the Ce 3d metal peaks indicated, however, that the ratio corresponds to more than one monolayer of OD. Another argument for the formation of a bulk hydroxide or oxy-hydroxide was derived from the different splitting of the peaks associated with each component of the 3d spin–orbit doublet in the metal. This splitting was 3.7 eV upon oxidation by O_2 and 4 eV upon exposure to water, indicating a different chemical species.

The formation of a hydride has been denied by Koel et al. (1980) (after 50 L exposure no measurable metallic contribution could be seen). In contrast to Ce oxidation by oxygen no signs of Ce^{4+} species were detectable even after prolonged exposure to water vapor. This can be recognized from the valence band spectra shown in fig. 6, where the 4f emission is not attenuated by water exposure.

Er, which seemed to be unreactive to water vapor at room temperature as judged from X-ray diffraction results, has been studied recently by UPS (Netzer et al., 1981a). Probably due to the preparation of much cleaner metallic surfaces, the reactivity towards H_2O proved to be high. The changes in the valence band region were very similar to those observed during oxidation by oxygen. The metallic conduction band was found to be depleted and O 2p derived bands were slightly shifted to higher binding energy as compared to the oxide spectrum. This shift has been attributed to contributions from OH groups, where the O 2p levels are at slightly higher binding energy than in adsorbed oxygen. A peak at 11.8 eV has been ascribed to emission from O–H σ bonding orbitals. Netzer et al. (1981a) have suggested that H_2O is initially dissociated at the surface into oxygen and hydrogen. The atomic oxygen then penetrates into the bulk and a bulk oxide phase is gradually formed. The observed OH spectral features have been associated with surface OH species on top of the oxide phase. The eventual formation of hydride which may happen in view of the results of Holloway and Swartz (1977) is, however, not expected to be observable in UPS, because it is overshadowed by the oxidation effects (see section 3.3).

Dynamic work function measurements showed a high reactivity of metallic rare earth film surfaces towards water vapor (Strasser et al. 1982). The initial fast work function decrease (fig. 10) indicates the rapid build-up of a surface dipole layer with the positive charge pointing away from the surface. This can be explained by a surface layer of OH groups. In contrast to the XPS results of Padalia et al. (1976) the work function curves show a similar behavior for Er and Yb.

Summarizing the results of rare earth metal interaction with water vapor, it can be concluded that the reactivity of the lanthanides is generally high. Sc seems to behave somewhat differently, with a much lower reactivity. Water is adsorbed dissociatively at room temperature in all cases and extensive oxidation seems to occur. The uptake kinetics suggest island growth of the oxidized phases, but a different mechanism as compared to the other rare earths seems to be indicated for Yb. While surface OH group formation is well established, the composition of the bulk phases following H_2O interaction is less clear. Pure oxide phases, hydroxide and oxyhydroxide phases together with dihydride phases have been discussed.

3.3. *Rare earth metal surface interaction with hydrogen*

The rare earth–hydrogen system has been the subject of several theoretical and experimental studies. In recent years the understanding of the hydrogen–metal interaction in the rare earth dihydrides has been greatly improved by the ground breaking work of Switendick (1970, 1971), who determined the electronic band structure of various hydrides using the augmented plane wave (APW) model. He demonstrated that the rigid band model is not applicable and thereby proved the controversy about the protonic or anionic nature of hydrogen in the metal lattice to be obsolete. The combined experimental and theoretical efforts of Weaver, Peterman and coworkers (Weaver et al., 1978, 1979a,b; Peterman et al. 1979a,b, 1980; Peterman and Harmon, 1979; Weaver and Peterson, 1979, 1980) have refined the picture and led to an excellent agreement between theory and experiment. The methods used by Weaver and coworkers were optical absorptivity and thermoreflectivity measurements as well as photoelectron spectroscopy. Unfortunately, it is very difficult to detect hydrogen by electron spectroscopic methods. Therefore, there are comparatively few UHV studies concerning the initial stages of hydrogen uptake. There are several investigations of hydrogen uptake using volumetric methods and conventional high vacuum conditions. It is highly probable, however, that under those circumstances rare earth metal surfaces are heavily contaminated and the uptake behavior is likely to deviate from that expected for hydrogen interaction with clean metal surfaces.

Based on a short discussion of the electronic structure of the rare earth dihydrides, we shall compare theoretical predictions with some experimental results concerning the initial stages of hydrogen uptake.

3.3.1. *The rare earth dihydrides*

The dihydrides of the trivalent rare earths exhibit the same fluorite type crystal structure at room temperature: a face-centered cubic metal sub-lattice with hydrogen atoms situated in the tetrahedral sites. Existence ranges and phase diagrams are given by Libowitz and Maeland (1979). The divalent dihydrides EuH_2 and YbH_2 have an orthorhombic crystal structure (Curzon and Singh, 1975a,b). The electronic structure of the dihydrides may be visualized in

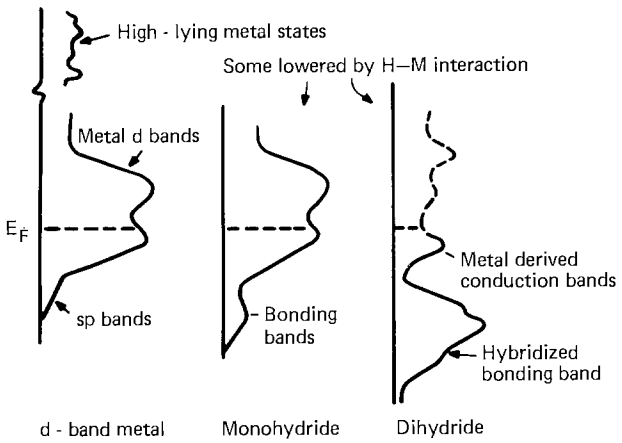

Fig. 12. Schematic representation of the DOS of a d-band metal (left), a monohydride (center) and a dihydride (right) (Weaver and Peterson, 1980).

the following way: For typical d band metals free of hydrogen the DOS is sketched in the left-hand panel of fig. 12 (Weaver and Peterson, 1980). It starts with sp band states at the bottom of the conduction band, but the d bands provide the main contribution to the DOS. They are partially occupied and have a full width of about 10 eV. Calculations of the band structure for an fcc metal lattice (without hydrogen) show only minor differences in the DOS as compared to an hcp metal lattice (which is the room temperature structure of most rare earth metals) (Switendick, 1978).

If the tetrahedral sites are occupied by hydrogen and the corresponding potential is included in the band structure calculations, the DOS is considerably changed. The sp bands already occupied in the metal combine with the hydrogen bonding states and are lowered in energy by about 4 eV. Empty metal states well above the Fermi level become mixed with the antibonding combination of Bloch sums of hydrogen orbitals and are pulled down in energy by as much as 10 eV. Antibonding metal hydrogen combinations contribute to the DOS above the original metal d band states. As a net result one new band (two states) is added below the Fermi energy. Metal states with s-like character on the hydrogen sites are lowered in energy and the DOS near the Fermi level is made up by rather pure d-like bands. A typical DOS for a rare earth dihydride is shown in the right-hand panel of fig. 12. The bonding bands are located 3–10 eV below the Fermi energy and the d-derived conduction band DOS near the Fermi level is lower than in the metal. Calculations of the DOS for CeH_2 (Fujimori et al., 1980) indicated that the low-lying bonding bands are separated from the d states by a small energy gap. A comparison of measured (Weaver and Peterson, 1979) and calculated (Peterman et al., 1979a) density of states in YH_2 is made in figs. 13 and 14 respectively. Apart from the double peak structure in the low-lying binding states which could not be resolved in the experimental spectra and a slight difference in peak positions the agreement is quite satisfying. Still better agreement is obtained in the theoretical treatment, if some hydrogen is allowed to occupy octahedral sites.

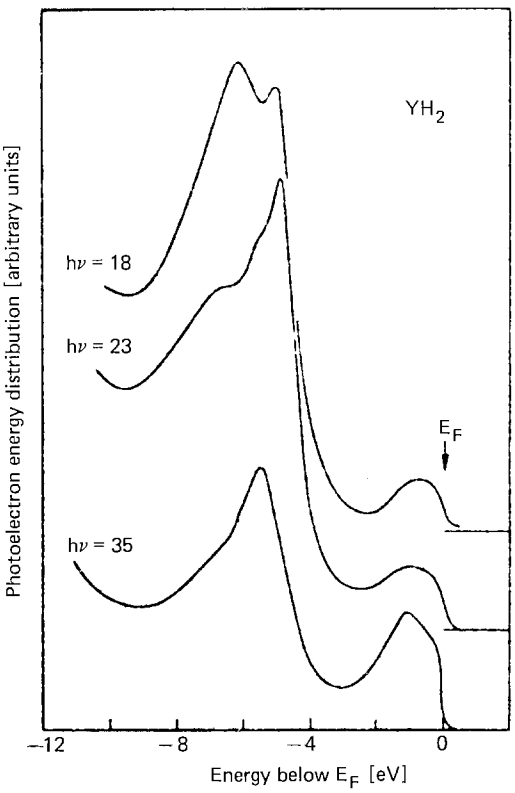

Fig. 13. Photoelectron energy distributions for YH_2 for low photon energies. The bonding band is revealed by the emission form 3 to 10 eV below E_f; the narrow band at E_f is the metal derived conduction band (Weaver and Peterson, 1979).

An analysis of the charge distribution for YH_2 (Switendick, 1970) showed a similar charge to be associated with the hydrogen in the tetrahedral sites as inside the same sized sphere for the hydrogen atom. In contrast Fujimori et al. (1980) calculated considerable charge transfer from metal to hydrogen for CeH_2.

Conductivity measurements proved the dihydrides of the trivalent rare earths to be metallic conductors, the conductivity of hydrogen deficient dihydrides exceeding considerably that of the clean metals (Libowitz, 1972; Libowitz and Maeland, 1979). The sudden increase in resistivity, which is observed if the H/M ratio approaches a value of 2, is thought to be caused by the increasing occupancy of octahedral sites. The high conductivity of the dihydrides as compared to the rare earth metals could be due to the lower density of d states with high effective mass at the Fermi energy (Viallard and Daou, 1973) and the reduced s–d scattering.

Finally, it should be mentioned that in the divalent dihydrides EuH_2 and YbH_2 there are only four electrons per formula unit in the conduction band. These four electrons can be accommodated in the low-lying metal–hydrogen bonding states which are separated by a small energy gap from the d band states. Therefore these dihydrides are expected to show semiconducting rather than metallic behavior (Gupta, 1978; Libowitz, 1972). Singh and Curzon (1977) have verified

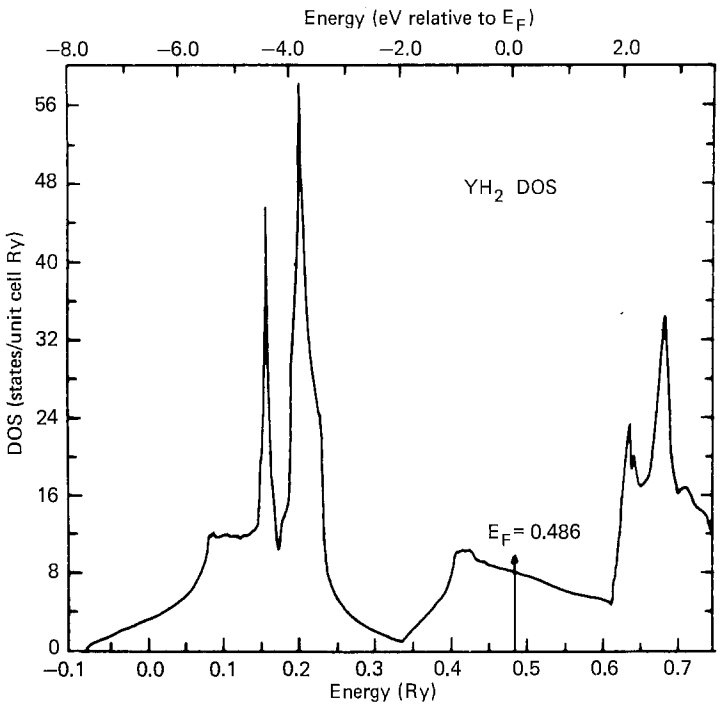

Fig. 14. Calculated electronic density of states for the self-consistent energy bands of YH_2 (Peterman et al., 1979a).

this assumption by resistivity measurements on rare earth thin films exposed to H_2.

3.3.2. *The initial stages of rare earth metal hydrogenation: theory*

As evident from the foregoing discussion, the energetically favorable situation of having an additional bonding band well below the Fermi level is only met in the rare earth dihydrides. There are two possible approaches to calculate the electronic structure of mono- and submonohydrides. Switendick (1971) has used band structure calculations and found considerable lowering of metal states which can interact with the hydrogen 1s orbital in the (sub)monohydride. On the other hand, there are no new bands formed below the Fermi level and the electrons added by the hydrogen fill metal d states. This situation is exemplified in the central panel of fig. 12. However, the resultant increase in energy due to the filling of d states, $\Delta E = \Delta n\ (\mathrm{d}E/\mathrm{d}n)$, is too large in the case of the rare earths to allow the monohydrides to be formed. Instead two phases are formed, the metal and the (slightly substoichiometric) dihydride (Libowitz and Maeland, 1979).

The electronic structure of hydrogen solutions can also be calculated considering the interstitial hydrogen as a Coulomb perturbation in the metal crystal

potential (Friedel, 1972). The proton is then partly screened by valence electrons. The charge density at the hydrogen site is similar to that of a free H atom. The incomplete screening causes a small lattice expansion due to interaction with neighboring ions. This is in agreement with experimental results obtained by Bonnet (1976). The interaction with adjacent interstitial H atoms will always be weak and consequently the solid solution of H should be nearly regular. This approach, however, does not yield correct solution energies up to now.

3.3.3. *The initial stages of rare earth metal hydrogenation: experiments*

Gayer and coworkers (Gayer and Bos, 1964; Gayer and Melotik, 1968; Gayer and Grunwald, 1969) have investigated the hydrogen uptake behavior of cerium and neodymium. They observed a sigmoidal curve shape in a composition (H/Ce, H/Nd) versus time curve, but the initial induction and the subsequent autoacceleration period were probably due to a surface oxide layer, which hindered hydrogen penetration into the bulk. Nucleation of the hydride presumably resulted in increasing exposure of the metal surface to hydrogen and consequent acceleration of the uptake. Hence the kinetics seemed to be governed mainly by contamination effects.

One of the first investigations involving exposure of clean rare earth metal surfaces to hydrogen was carried out by Singh et al. (1976). They measured the change in resistivity of an evaporated Er film during exposure to hydrogen. The results are shown in fig. 15 (lower curve). An initial increase in resistivity is followed by a large decrease to values well below the clean metal resistivity, which in turn is superseded by a large increase at high H_2 exposures. The small inset (lower left) is the proposed correlation of the points marked on the curve with the phase diagram (α: hydrogen solution, $\alpha+\beta$: hydrogen solution and dihydride phase coexisting, β: dihydride with slight variations in stoichiometry, γ: trihydride). The initial increase in resistivity is what is expected for a hydrogen solution, where the additional electron is filled into metallic d-like states above the Fermi level in the model of Switendick (1971), or where the interstitial hydrogen causes perturbation of the crystal potential according to the treatment of Friedel (1972). The reduction in resistivity after dihydride formation reflects the decrease in d band DOS at the Fermi level as predicted by theory. The final increase is due to random occupation of octahedral sites and subsequent trihydride formation, which is accompanied by a metal to semiconductor transition (Libowitz, 1972; Switendick, 1980; Libowitz and Maeland, 1979). This behavior of Er is closely paralleled by the behavior of yttrium (Curzon and Singh, 1978) and other rare earth metal films exposed to hydrogen (Singh and Curzon, 1977). The upper part of fig. 15 is a display of the change of work function of an Er film during exposure to hydrogen as measured by Müller and Surplice (1977). The interpretation of the $\Delta\phi$ curve is less straightforward, because contributions of both the change in surface charge and the difference in the Fermi level position of metal and dihydride have to be considered. The initial decrease in work function (in different experiments always between -50 and

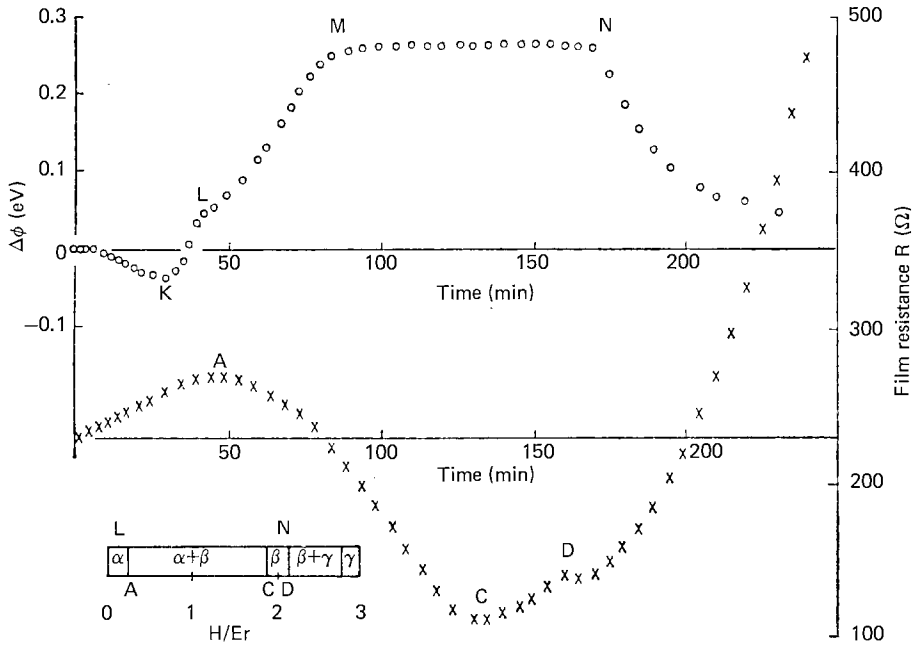

Fig. 15. Resistance $R(\times)$ and change of work function $\Delta\phi(\bigcirc)$ observed simultaneously for the same film with a constant rate of flow of H_2. Inset: Schematic representation of the H/Er phase diagram at 295 K (Müller and Surplice, 1977).

-100 meV) was associated by Müller and Surplice with adsorption of $H^{-\delta}$ ($\delta < 1$) species into adsorption sites below the plane of the surface atoms. The subsequent work function increase up to point L in fig. 15 was explained by the occupation of adsorption sites on top of the surface layer. At point L the dihydride is nucleated (as can be inferred from the resistivity curve) and the further rise of the work function can be attributed not only to surface dipole barrier effects, but also to changes in the Fermi energy. A plateau is reached when the surface consists entirely of the dihydride phase. Further work function changes occur only upon trihydride formation.

It is worthwhile to compare these results, which were obtained by H_2 exposure at about 10^{-4} torr, with the work function changes measured dynamically by Strasser et al. (1982) during exposure of Er to H_2 at a pressure of 10^{-6} torr (see fig. 10). The initial work function decrease is confirmed, and its magnitude seems to be pressure independent. Strasser et al. (1982), however, were not able to observe a discontinuity in the slope of the $\Delta\phi$ curve which could be related to point L in fig. 15. It may be possible that, due to the lower pressure, hydrogen diffusion into the bulk keeps the surface concentration quite low and the dihydride is nucleated only when the critical concentration is reached throughout the bulk at much higher exposures.

At this point it is interesting to digress shortly to mention the work of

Feibelman and Hamann (1980) concerning hydrogen adsorption on Sc(0001) and Ti(0001). These authors have calculated the surface density of states and band structure and have concluded that a Sc(0001)–H(1 × 1) or Ti(0001)–H(1 × 1) configuration would be most favorable for energetical reasons. With the hydrogen atoms in three-fold sites outside the metal surface layer a surface DOS has been obtained, which resembles closely the bulk DOS of the dihydrides. The charge associated with the hydrogen atoms in this case has been calculated to be about 1.3 electrons. For such a surface configuration the work function should be appreciably higher than for the clean metal surface. This model seems to be in contrast to the interpretation of Müller and Surplice (1977) of initial hydrogen incorporation beneath the surface layer.

Singh et al. (1976) have derived from their resistivity measurements on Er the solubility limit of hydrogen in the α phase as a function of temperature. The value of $H/M \approx 0.25$ at room temperature decreased with decreasing temperature to about 0.15 at 130 K. At 77 K the dihydride formation seemed to be kinetically restricted.

McQuillan (1976) has measured pressure–composition–temperature relationships for hydrogen with Gd, Tb, Dy and Lu. He found solubility limits of about $H/M = 0.4$ to 0.5, but a deviation from the ideal solution behavior was observed for concentrations as low as $H/M = 0.05$. The exothermic heat of solution increased until the dihydride was formed. The exothermic heats of solution of H_2 are in the range between -125 and -165 kJ mole^{-1}, whereas the heat of formation of the nonstoichiometric dihydrides from the primary hydrogen solutions in the metal are about -200 kJ mole^{-1} of H_2. Additional enthalpy and free energy data for hydrogen solution and hydride formation are given by Libowitz and Maeland (1979), Bouten and Miedema (1980) and Korst and Warf (1966). Bonnet (1976) obtained solubility limits for hydrogen in Er, Tm and Lu of $H/M = 0.31$, 0.32 and 0.39, respectively.

The results presented so far suggest a similar behavior of trivalent rare earths towards hydrogen. A remarkable exception has been reported by Atkinson et al. (1976). They measured the kinetics of adsorption and absorption of hydrogen and deuterium on evaporated films of Sc, Ce, Pr, Nd, Sm, Gd, Dy, Ho and Er. The initial sticking probabilities were found to be typically above 0.1 at 300 K and somewhat higher at 77 K. Samarium, however, showed values of only 2×10^{-3} at both temperatures. The authors suggested that hydrogen is adsorbed on Sm only on a few active adsorption sites. It is interesting to note, however, that Sm has been found recently to be divalent at the surface (Allen et al., 1980 and references cited therein). Yb is also divalent in the metallic state and seems to parallel this behavior. In fig. 10 the change of work function of Yb and Er exposed to hydrogen at 10^{-6} torr are compared (Strasser et al., 1982). There are not only differences in curve shape – the initial work function decrease is absent for Yb – but also the uptake velocity seems to be much lower for Yb (note different scales).

As already pointed out, it is very difficult to extract information about the initial stages of rare earth hydrogenation from electron spectroscopy. Netzer et

al. (1981a) have measured the UPS spectra of clean Er and Er exposed to 50 L H_2 at room temperature. A slight attenuation of conduction band states near E_F has been observed and a moderate emission enhancement was noticed in the 3–9 eV region below the Fermi level. These results may be explained by beginning dihydride nucleation. The structure 3–9 eV below the Fermi level could be due to the formation of bonding bands, which causes in turn a lowering of the DOS at the Fermi energy. Electron energy loss experiments (Bertel et al. 1981) on an Er film evaporated in 10^{-6} torr H_2 can be interpreted in a similar way. A reduction of the low energy metal loss indicated a depletion of states just below E_F, whereas a new loss observed at about 9 eV can be attributed to excitation from the bonding bands. The plasmon loss was shifted from 13.5 eV to only 14.5 eV, in contrast to a plasmon energy of 16.8 eV found by Colliex et al. (1976) for ErH_2. Therefore, the system was probably still in the early stages of hydride formation.

To summarize briefly, hydrogen has a high sticking probability on rare earth metal surfaces with the exception of Sm, Yb and probably Eu. It seems to be incorporated below the surface layer and forms a solution in the α phase. During this stage the conduction band DOS is not much influenced but the resistivity as well as the exothermic heat of solution increases. The solubility limit at room temperature is about $H/M = 0.3$. At higher concentrations the dihydride phase is nucleated. The f electrons do not seem to be influenced by the hydriding process. Evidently much more work has to be done to elucidate the adsorption process itself, the dissociation mechanism and the rate limiting steps during the various stages of uptake. Comprehensive information about hydrogen in metals has been presented by Mueller et al. (1968) and Alefeld and Völkl (1978). Special emphasis to rare earth hydrides has been given by Libowitz and Maeland (1979) and by Gasgnier (1980).

3.4. *Rare earth metal surface interaction with other gases*

3.4.1. *Nitrogen*

Onsgaard et al. (1980a) have investigated the interaction of Sc(100) with nitrogen by AES and ELS. As evidenced by AES nitrogen reacted with the clean metal surface but the sticking coefficient was at least one order of magnitude smaller than that of oxygen. The first and second bulk plasmon losses showed a slight shift to lower energy. A new loss at 6.2 eV was assigned to excitation of N 2p electrons into unoccupied 3d conduction band states in accordance with DOS calculations of Neckel et al. (1976). The Sc 3p to conduction band transitions remained unaffected by N adsorption. According to the band structure calculations of Neckel et al. (1976) ScN is a borderline case between metallic and semiconducting behavior because the valence band (N 2p and Sc 3d) and the conduction band (mainly Sc 3d) have, if any, only very little overlap.

3.4.2. *Carbon monoxide*

Carbon monoxide is isoelectronic with N_2 and behaves in various aspects in a quite similar way. Onsgaard (1981) has reported a high reactivity of CO with Sc,

Y and Lu (0001) surfaces with a sticking coefficient similar to that of oxygen. Surplice and Brearley (1978) have measured the work function change on an Er film exposed to CO. For small doses the work function was lowered by about 45–60 meV, whereas further exposure led to an increase and saturation at about 700 meV above the clean metal value. These results could be confirmed qualitatively by Strasser et al. (1982). In dynamic work function measurements a small but reproducible initial decrease of 5–10 meV was followed by an increase to +800–1000 meV after 250 L exposure (where still no saturation was observed). The slope seemed to be slightly pressure dependent. A slow decay of the work function after stopping CO admission indicated redistribution processes (Surplice and Brearley, 1978). Work function changes in the Yb/CO system (Strasser et al., 1982) showed similar trends. The initial decrease of −80 meV was more pronounced.

Auger and electron loss spectra of Er and Yb films exposed to CO (Bertel et al., 1980b) revealed changes similar to those observed after oxygen exposure. The carbon KVV Auger line shapes were different from those usually observed for molecular CO adsorption (Netzer, 1981), and dissociative adsorption of CO seems to be indicated.

Darnell (1978) has reported the formation of a carbon–oxygen compound R_2CO with rare earths Ce, Sm, Eu, Gd, Tm and Yb by heating the metals in a quartz tube with a stoichiometric amount of CO to 800°C. The crystal structure of these compounds was observed to be similar to the NaCl structure of the corresponding nitrides (the nitrogen in the metal nitrides being replaced alternately by carbon and oxygen). Only traces of the sesquioxide phase were detected by X-ray diffraction.

3.4.3. *Carbon dioxide*

Preliminary experiments on CO_2 interaction with Er and Yb have been performed in our laboratory. The reaction of CO_2 with Er and Yb films has been followed by work function measurements (Strasser et al., 1982) and using AES and ELS (Bertel and Netzer, 1980b). The work function curve obtained after exposing Er to CO_2 showed a small initial decrease as in the case of CO, but the subsequent uprise was much steeper resulting in saturation at about +1.4 eV after dosage of ~60 L CO_2. In contrast, the Yb/CO_2 work function curve showed no initial decrease. No qualitative difference was detected in AES or ELS between surface species formed on Er or Yb after CO or CO_2 interaction.

4. Adsorption and catalysis on binary rare earth oxides

4.1. *Adsorption studies on rare earth oxides*

Hitherto, basic principles of the adsorption of simple gases on rare earth oxides have been investigated only to a limited extent, despite the fact that rare earth oxides are the most commonly used materials in rare earth catalytic science. The substrates, on which gas adsorption studies have been performed,

were usually in the form of rare earth oxide powders, and very few data are available on surfaces with well-defined structure and composition. The surface structure of a rare earth oxide single crystal surface, EuO(100), has been investigated by Felton et al. (1979) under UHV conditions using LEED, and surface disorder was reported for the UHV cleaved surfaces. It has been suggested that trivalent Eu might be present at the surface of this divalent compound, and that the corresponding change in anion coordination might drive the surface to disorder. The electronic structure of rare earth oxides has been investigated by photoelectron spectroscopy. Orchard and Thornton (1977) have used XPS to study the valence region on powdered oxide samples, while Padalia et al. (1977) have reported XPS valence spectra and core level spectra on oxidized films and powdered substrates. Padalia et al. (1977) noted differences in core level binding energies between surface-oxidized samples and bulk oxides, and emphasized the importance of surface effects (see section 3). No adsorption experiments on oxide surfaces, however, have been performed in the studies cited above.

The adsorption studies to be discussed below have been carried out in general in the torr pressure range and on substrates which are also used in catalytic investigations. The experimental conditions were therefore close to those employed in actual catalysis, which is certainly an advantage for comparison purposes. Exemplifying results will be presented in the following for several gases relevant in the catalysis on rare earth oxides.

The adsorption of hydrogen on oxides of La, Nd, Sm, Dy and Er has been studied by Minachev et al. (1972) in the temperature range −78° to 800°C. Two forms of adsorbed hydrogen have been distinguished, a weakly bound form, which completely desorbed at −20°C, and a strongly bound form with desorption at around 200°C. On La_2O_3 only weakly bound hydrogen was reported, and this weakly bound hydrogen was inferred to be responsible for the low-temperature hydrogenation of ethylene on this oxide. Kreisberg et al. (1973) have observed physical adsorption of hydrogen below −100°C, a low-temperature chemisorption state in the temperature range −100°C to 200°C and dissociative high-temperature chemisorption from 200–800°C on Ho_2O_3. At temperatures above 500°C hydrogen was shown to react with oxygen ions of the lattice thus forming oxygen vacancies, if the samples were not prereduced in hydrogen at 800°C. In the temperature range 300–600°C the formation of surface hydroxyl structures has been suggested. The adsorption of H_2O and CO_2 at room temperature prevented subsequent low-temperature chemisorption of hydrogen, indicating the poisoning of the surface by hydroxyl or carbonate species (Kreisberg et al., 1973). Similar types of hydrogen adsorption have also been observed on Y_2O_3 and on La_2O_3 by Loginov et al. (1972). The adsorption of hydrogen on Nd_2O_3, Dy_2O_3, Sm_2O_3 and Gd_2O_3 has been measured by Read (1972). Besides physisorption at low-temperature two chemisorption states have been inferred for Nd and Gd oxide.

A rather detailed study of the adsorption of hydrogen on Sc_2O_3 has been performed by Gonzales Tejuca et al. (1979) and by Garcia Fierro and Pajares

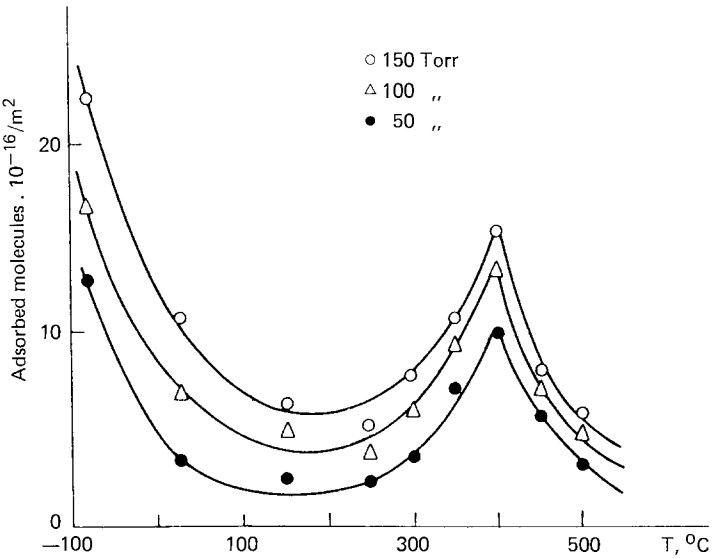

Fig. 16. Adsorption isobars for the system H_2/Sc_2O_3 (Gonzales Tejuca et al., 1979).

(1980). Adsorption isobars for the system H_2/Sc_2O_3 are shown in fig. 16 (Gonzales Tejuca et al., 1979). A low-temperature and a high-temperature adsorption regime can be recognized, with low coverage isosteric adsorption heats of $-6.27\,kJ\,mol^{-1}$ and $-121\,kJ\,mol^{-1}$, respectively. The adsorption heat calculated in the temperature region 450–500°C decreased exponentially with coverage from -121 to $-88\,kJ\,mol^{-1}$, consistent with Freundlich's model of adsorption on a heterogeneous adsorbent surface. Infrared (IR) spectra taken after adsorption at 400°C (maximum coverage for chemisorption in the isobars, fig. 16) showed four bands in the OH stretching region between 3697 and $3640\,cm^{-1}$, which were interpreted in terms of hydroxyl groups in different crystallographic environments. The two adsorption regimes of H_2 on Sc_2O_3 were associated with physical adsorption at low temperature and activated dissociative chemisorption at higher temperatures. The kinetics of hydrogen adsorption on scandia has been analyzed by Garcia Fierro and Pajares (1980), and the data could be fitted by an Elovich-type equation (Aharoni and Tompkins, 1970). The hydroxylation state of the surface prior to adsorption has a decisive influence on the initial adsorption rate and on the amounts of H_2 adsorbed at equilibrium. This is shown in fig. 17, where the adsorbed amounts at equilibrium are plotted as a function of outgassing temperature for H_2 and also for CO_2 adsorption on Sc_2O_3 (Garcia Fierro and Pajares, 1980). The outgassing temperature is proportional to the hydroxylation state of the surface, and both systems show a marked decrease of the adsorbed amount for outgassing temperatures lower than 470 K, where OH coverage has been estimated to be greater than $2\,OH/nm^2$.

It appears that a low-temperature physisorbed state and an activated chemisorbed state at higher temperatures can be inferred from these studies for

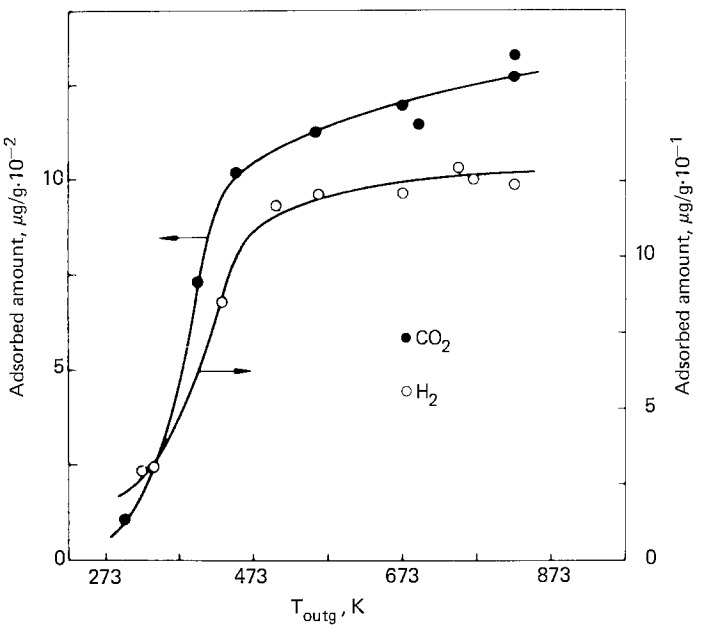

Fig. 17. Adsorbed amount at equilibrium vs. outgassing temperature: (○) H_2 at 429 K and 4×10^3 Pa; (●) CO_2 at 296 K and 4×10^3 Pa (Garcia Fierro and Pajares, 1980).

hydrogen adsorption on rare earth oxides, but that the situation is less clear for adsorption at room temperature. We note, however, an interesting coincidence in figs. 16 and 17. The adsorbed amount of hydrogen drops sharply for outgassing temperatures of the oxide below 200°C (fig. 17), and it is in this temperature range that the so-called activated chemisorbed state in fig. 16 begins to populate. It is therefore tempting to speculate on the possibility of OH group formation at room temperature, which might occur involving hydrogen impurities during set-up of the lower adsorption temperatures, and which may then limit the amount of hydrogen uptake at these temperatures.

Netzer et al. (1981a) have investigated the reaction of H_2 with an oxidized Er surface at room temperature under UHV conditions using UPS. HeII UPS spectra of Er exposed to 100 L O_2 and subsequently to 100 L H_2 are shown in fig. 18. The oxidized Er spectrum (fig. 18, dashed curve) is characterized by a broad emission peak in the region 4–9 eV, which has been ascribed to emission from O 2p derived valence band states, and by a weaker shake-up satellite around 11.2 eV. Upon H_2 exposure a new peak appears at 11.8 eV, which is due to emission form OH σ bonds, and a shift of the O 2p bands towards higher binding energy is observed (fig. 18, solid curve). Both effects demonstrate the formation of surface OH species. Decisive evidence of surface hydroxyl group formation at room temperature has also been obtained by Strasser et al. (1982) in a study of the reaction of hydrogen with oxidized rare earth films by work function measurements. Dissociative chemisorption of hydrogen on rare earth oxides at

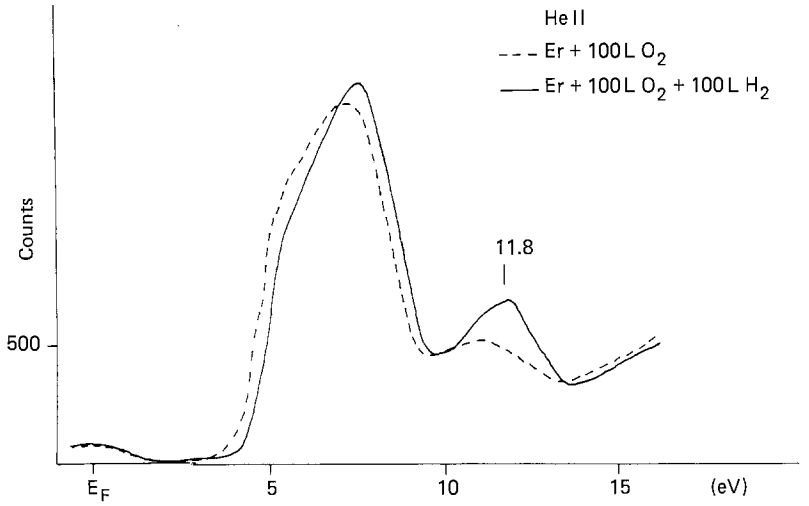

Fig. 18. He II spectrum of a heavily oxidized Er surface (Er + 100 L O_2) compared to a spectrum recorded after exposing that surface to 100 L H_2 (Er + 100 L O_2 + 100 L H_2) (Netzer et al., 1981a).

room temperature can therefore be inferred. The results concerning the "activated" higher temperature chemisorption of hydrogen have therefore to be regarded with some caution in view of the blocking effect of OH groups possibly formed at lower temperatures.

The adsorption of CO_2 on rare earth oxides is illustrated by the results of Rosynek and Magnuson (1977b) on La_2O_3. Based on IR spectroscopy, Rosynek and Magnuson (1977b) proposed the formation of a unidentate surface carbonate species at room temperature, according to the reaction sequence

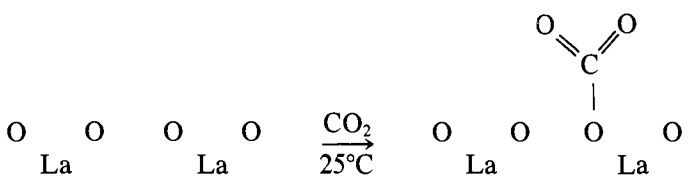

(10)

Quantitative adsorption measurements indicated a surface coverage of approximately one CO_2 molecule/surface O^{2-} ion (based on the geometry of a (111) face of hexagonal La_2O_3). Evacuation at 275°C decreased the adsorbed CO_2 amount and a surface rearrangement has been suggested, leading to bidentate carbonate species:

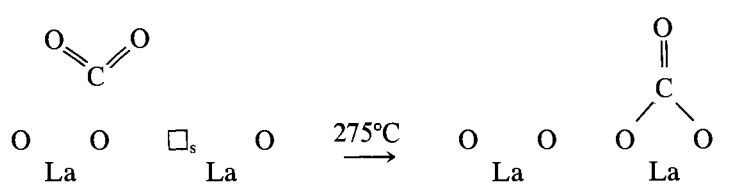

(11)

Formation of such bidentate carbonate structure requires the existence and accessibility of appropriate anion vacancies on the oxide surface. Spectral evidence for unidentate carbonate species disappeared at 300°C, and was followed by complete removal of the bidentate structures at $\geq$350°C (Rosynek and Magnuson, 1977b). Similar IR results as those discussed above have been reported by Filippova et al. (1973) for CO_2 adsorption on Nd_2O_3 and also by Pajares et al. (1976) on Sc_2O_3. Pajares et al. (1978) have described the kinetics of CO_2 adsorption on Sc_2O_3 by a modified Langmuir equation, and have emphasized the influence of surface hydroxylation on the kinetics of CO_2 adsorption. The influence of surface hydroxyl species on the adsorbed CO_2 amount is shown in fig. 17.

Monodentate and bidentate surface carbonate species have been discussed by Guenin (1973) and Breysse et al. (1973) for CO_2 adsorption on CeO_2. This group of authors reported higher thermal stability for monodentate species than for bidentate species, and a dependence of adsorbate coverage on pretreatment conditions of the CeO_2 samples. Accordingly, a partially reduced sample with slight oxygen deficiency showed increased CO_2 uptake with predominantly monodentate species.

Filippova et al. (1973) have investigated the adsorption of CO on Nd_2O_3 by IR spectroscopy. Little evidence for CO interaction was found at adsorption temperatures below 100°C, but IR bands appearing in the temperature range 100–200°C were associated with the formation of carboxylate species, while monodentate carbonate complexes were invoked to interpret the spectra after CO adsorption above 200°C. On CeO_2, the surface species formed after CO adsorption were strongly dependent on pretreatment conditions (Guenin, 1973; Breysse et al., 1973). After oxidizing pretreatment conditions, IR spectra have been observed after CO adsorption at 250°C, which are consistent with carbonate species. A reduction of the surface by CO and the formation of CO_2-like species and anion vacancies has therefore been proposed. On oxygen deficient CeO_2 no surface reduction was detected and IR spectra of carboxylate complexes were observed. The carboxylate species could be converted into carbonate species upon exposure to gaseous oxygen (Guenin, 1973). Pajares et al. (1976) have found only reversible CO adsorption on scandia at room temperature, but have detected surface carbonates after adsorption at 200°C. In experiments performed in our laboratory the absence of irreversible CO adsorption at room temperature on oxidized Er films has been confirmed by Auger spectroscopy (Bertel and Netzer, 1980b). It can therefore be concluded that CO chemisorption on rare earth oxides is initiated at elevated temperatures only, and that rearrangement of the oxide surface is involved at temperatures >200°C.

Investigations of the interaction of oxygen with rare earth oxides have been mostly concerned with the exchange reaction of lattice oxygen with gas-phase oxygen. This will be discussed in section 4.2.1. Some data of oxygen adsorption on Nd_2O_3 and Dy_2O_3 have been reported by Read (1972). Adsorption measurements of oxygen on Sc_2O_3 in the temperature interval $-196°$ to 500°C have been performed by Pajares et al. (1976). Adsorption energies of $-13.8\,kJ\,mol^{-1}$ and

$-142\,kJ\,mol^{-1}$ have been calculated from adsorption isobars for adsorption at low temperature ($-78°$ to $-196°C$) and between 300° and 350°C, respectively. Above 350°C incorporation of oxygen into the scandium oxide was inferred by Pajares et al. (1976). Reversible adsorption of oxygen, probably in molecular form, has been noted by Bertel and Netzer (1980c) on Er oxide at room temperature.

The pronounced influence of surface hydroxyl groups on adsorption properties and catalytic activity has already been emphasized in this section and in section 2.3.1. Surface hydroxyl species on rare earth oxides can be formed by interaction of hydrogen (see above) or by dissociative chemisorption of water. The dissociative chemisorption of water has been pointed out by Filippova et al. (1973) on Nd_2O_3, by Rosynek and Magnuson (1977a) on La_2O_3 (here, conversion to bulk $La(OH)_3$ also takes place), and by Strasser et al. (1982) on oxidized Sm, Er and Yb. Dissociative chemisorption of water on rare earth oxides at room temperature or above therefore seems well established.

Brief reports on the adsorption of other molecules on rare earth oxides have appeared in the literature, e.g. NH_3 on La_2O_3 and Nd_2O_3 (Khodakov et al., 1975a) or ethane on several rare earth oxides (Minachev et al., 1972). No detailed characterization of adsorption properties or of the nature of the adsorption complex has been made in these studies.

4.2. *Catalysis on rare earth oxides*

A great variety of catalytic reactions has been investigated on rare earth oxides, and many studies have attempted to establish correlations between the catalytic activity and the varying physicochemical properties of the rare earth cations along the rare earth series. For example, the continuous filling of the 4f shell in going from La to Lu and concomitant trends in catalytic activity have prompted speculations on the participation of 4f electrons in catalytic processes. In our opinion, no decisive evidence for the *direct* involvement of 4f electrons in surface reactions has been presented up to date, and this is also not to be expected on theoretical grounds. The 4f states, albeit at low binding energy, are highly localized, atomic-like states in the solid environment due to the centrifugal barrier potential (Ziman, 1972), and they are therefore insensitive to the chemical environment. They can be regarded as core-like states rather than as valence states. Some exceptions may exist in certain cases, where the 4f occupancy and therewith the valency can change during the course of a chemical reaction, e.g. in Ce, Sm, Eu or Yb. In these cases a transfer of electrons from 4f states to valence states of 5d, 6s or O 2p (in oxides) character occurs rather than a direct participation of 4f electrons in the chemical bonding. Different valency of rare earth atoms at surfaces of several rare earth materials as compared to the corresponding bulk phase has been recognized recently (Rowe et al., 1976; Wertheim and Crecelius, 1978; Campagna et al., 1979), and this has to be taken into account in discussing surface reactions. On the other hand, more indirect influence of 4f occupancy on catalytic reactivity via magnetic moments, cation

radii, etc., has to be acknowledged. Emphasis will therefore be placed in the following on those studies, where a large enough number of the oxides was investigated for a given reaction to enable behavior trends, if any, to be identified.

Catalytic investigations on rare earth oxides of mostly Russian workers have been reviewed up to about 1973 by Minachev (1973), and catalytic properties of rare earth oxides in many reactions have been compiled more recently by Rosynek (1977). To evaluate catalysis on rare earth oxides in this chapter we will present selected examples of important catalytic results in some detail at the expense of a more exhaustive listing. Reactions are classified into several groups for ease of presentation following closely the reaction categories employed by Rosynek (1977).

4.2.1. *Exchange-type reactions*

Ortho–para hydrogen conversion

The rare earth oxides with their paramagnetic cations provide an excellent test case for the para–ortho hydrogen conversion reaction, for which theoretical considerations predict a catalytic activity proportional to the square of the magnetic moment for a physical, paramagnetic conversion mechanism (Wigner, 1933). The concept of a physical mechanism is that of a hydrogen molecule approaching a paramagnetic ion and interacting with the electronic spin so as to decouple the proton spins, thus allowing recoupling in the equilibrium ratio appropriate to the corresponding temperature. Several possible mechanisms have been developed from the original theory of paramagnetic conversion proposed by Wigner (1933), e.g., the translation mechanism, put forward by Harrison and McDowell (1953), or the vibrational mechanism, originally proposed by Sandler (1954) and extended by Ashmead et al. (1963). Alternatively, a chemical conversion mechanism has to be considered, which involves the presence of adsorbed hydrogen atoms at the surface. A distinction between the physical and the chemical conversion mechanism is usually made by comparing o–p H_2 conversion rates with H_2–D_2 exchange rates, and in the absence of H_2–D_2 equilibration the physical mechanism is thought to be operative.

Ashmead et al. (1963, 1964) have measured parahydrogen conversion and H_2–D_2 equilibration on several rare earth oxides in the temperature range 77 to 657 K. It has been established that at temperatures <400 K, where the equilibration reaction is absent, the conversion proceeds by a paramagnetic mechanism, and good correlation of conversion rates with magnetic moments was obtained. This is shown in fig. 19, where the experimental absolute rates, k_m, are plotted against the square of the magnetic moment for two different low-temperature regimes (Ashmead et al., 1964). Ashmead et al. (1963, 1964) found the best agreement between experimental and calculated conversion rates by applying the vibrational mechanism of Sandler (1954), in which vibrations perpendicular to the surface of a hydrogen molecule adsorbed at an active center can lead to conversion. This is in agreement with the findings of Rossington and

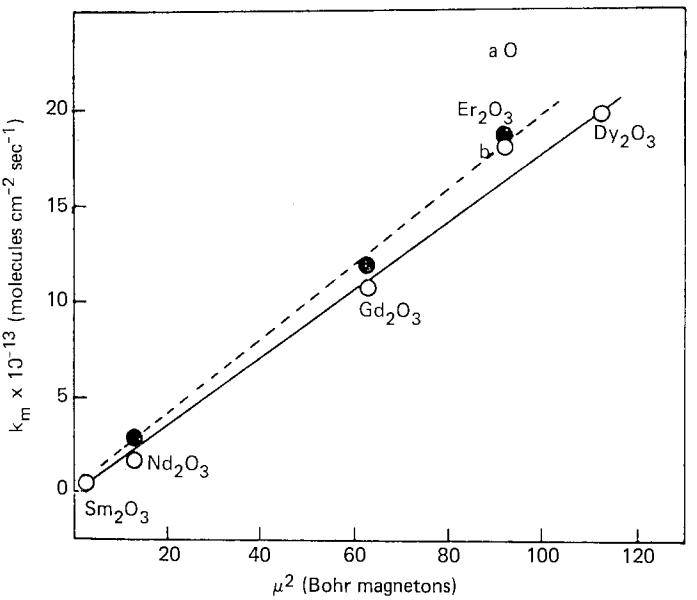

Fig. 19. Plots of k_m at 4 mm pressure against μ^2; O: 90 K; ●: the maximum rate at intermediate temperatures (140–400 K) (Ashmead et al., 1964).

Capozzi (1974), who also pointed out that the active sites constitute only a small fraction of the total available surface.

At temperatures >400 K both the conversion and H_2–D_2 equilibration reaction proceeded with comparable rates, and the same chemical mechanism has therefore been inferred (Ashmead et al., 1963, 1964).

Selwood (1970) has investigated parahydrogen conversion at room temperature over most rare earth oxides. He also found that the conversion rates are proportional to the square of the magnetic moment of the paramagnetic species in the absence of an extrinsic magnetic field. With the catalyst in an extrinsic magnetic field of 18 kOe, large increases in conversion rates were observed, which could not be correlated with the number of f electrons. The explanation for the extrinsic magnetic field effect in terms of changes of electron-spin relaxation times (Leffler, 1965) by the applied field has been refuted by Selwood (1970), but local field gradients at the surface of paramagnetics have been discussed as a possible reason. Effects of a weak magnetic field of a few oersteds on para-hydrogen conversion rates over self-supported rare earth oxides and rare earth oxides supported on diamagnetic La_2O_3 have been reported by Selwood (1971), where a decrease in conversion rates was detected in some cases. The changes observed when oxides were shifted from paramagnetic supports (their own bulk phase) to a diamagnetic support seem to be consistent with an explanation in terms of surface field gradients established in an external field. The increase of parahydrogen conversion on Nd_2O_3 induced by a magnetic field has been correlated with surface dehydration by Eley et al. (1972). A

possible influence of the extent of surface dehydration on the surface electrostatic field has been suggested.

Eley et al. (1974) have studied the parahydrogen conversion on Nd_2O_3 and Dy_2O_3 as a function of the catalysts' outgassing temperature. While the earlier conclusions about the conversion mechanisms could be confirmed in this work, increased activity was found with increasing outgassing temperature. This has been ascribed to additional exposure of trivalent rare earth ions in positions of high adsorption potential by the progressive elimination of hydroxyl groups as molecular water.

The activation of diamagnetic Y_2O_3 and Lu_2O_3 for parahydrogen conversion by the magnetic mechanism using high-temperature hydrogen treatment has been demonstrated by Baron and Selwood (1973) and by Arias and Selwood (1974). The catalytic activity is apparently due to the presence of paramagnetic Y^{2+} and Lu^{2+} ions at the surface, which are generated during high-temperature hydrogen treatment. An interesting increase in catalytic activity has been observed on Yb_2O_3 following high-temperature hydrogen treatment (Arias and Selwood, 1974). If normal reduction of Yb^{3+} to Yb^{2+} is assumed to occur, the resulting Yb^{2+} ions should be in a $4f^{14}\,5d^0$ configuration with zero magnetic moment, and a decrease in catalytic activity should be observed. Arias and Selwood (1974) have therefore suggested that the electronic configuration of surface-active Yb^{2+} is probably $4f^{13}\,5d^1$ and not $4f^{14}\,5d^0$.

Oxygen exchange

Knowledge of the interaction of oxygen with oxide surfaces is of prime importance to understand the catalysis of oxidation reactions on these surfaces. Much information concerning adsorption properties and the mobility of oxygen ions in the solid can be gained by studying the oxide-catalyzed isotopic exchange reaction of gas phase oxygen molecules. Both types of exchange reactions, the homomolecular reaction $^{16}O_2 + {}^{18}O_2 \rightarrow 2\,{}^{16}O\,{}^{18}O$ and the direct exchange of gaseous $^{18}O_2$ with lattice oxygen, have been investigated extensively on rare earth oxides. Despite numerous efforts in this field, the agreement between results of different research groups is far from good, and the elementary steps involved in the exchange reactions have only vaguely been commented on. In principle, isotopic exchange of oxygen in the system gas–oxide can proceed by three types of exchange (Sazonov et al., 1971):

(1) Exchange between adsorbed oxygen of the gas phase without participation of the oxide oxygen;

(2) Exchange of one adsorbed oxygen atom by one oxide oxygen atom;

(3) Exchange of two atoms of adsorbed oxygen by two oxide oxygen atoms.

While the direct exchange of gaseous oxygen with lattice oxygen must obviously involve types 2 and/or 3, the homomolecular exchange can proceed by any one or by a combination of all types of exchange.

Both exchange reactions occur to varying extents on all the rare earth oxides in the temperature range 200° to 500°C, indicating a relatively high oxygen mobility in these materials. At reaction temperatures >200°C, a close similarity of the apparent activation energies was consistently found for both exchange

reactions on a given oxide, and a common reaction mechanism has been proposed involving participation of oxygen from the oxide (e.g. Minachev et al., 1964, for Nd_2O_3 and Er_2O_3; Sazonov et al., 1966b, for CeO_2; Sazonov et al., 1966a, for Gd_2O_3; Antoshin et al., 1967a, for CeO_2; Antoshin et al., 1968, for all rare earth oxides; Sokolovskii et al., 1968a, for La_2O_3; Sokolovskii et al., 1968b, for Sm_2O_3). The reaction mechanism at elevated temperatures has been designated as "adsorption–desorption mechanism", which means essentially that the common rate-determining step is assumed to be the dissociative adsorption or the associative desorption of oxygen molecules (Sazonov et al., 1966a,b; Sokolovskii et al., 1968a,b; Winter, 1969a). The participation of two lattice oxygen ions in the homomolecular exchange process (type 3 exchange) has been suggested by Antoshin et al. (1967a) for CeO_2 and by Sokolovskii et al. (1968a) for La_2O_3. Sazonov et al. (1966b) have noted the influence of diffusion of oxygen in the lattice of the oxide to determine exchange rates above 440°C on CeO_2.

At temperatures below 200°C the homomolecular exchange reaction has been shown to follow a different reaction mechanism, as indicated by different activation energies compared to reaction at higher temperatures. Sazonov et al. (1966a) have investigated the isotopic exchange reaction on Gd_2O_3 in the temperature range −78° to 500°C, and suggested exchange between adsorbed oxygen molecules (type 1 exchange) at lower temperatures. Similar results have been obtained on La_2O_3 and on Sm_2O_3 for the homomolecular exchange at low temperature (Sokolovskii et al., 1968a,b).

A pronounced influence of pretreatment conditions on isotopic exchange rates and apparent activation energies has been reported in several investigations (Sazonov et al., 1966a,b, 1972; Antoshin et al., 1967a, 1968; Sokolovskii et al., 1968a,b). Samples which have been preconditioned in vacuum at 700°C showed considerably higher activities for isotopic exchange at all temperatures compared to those equilibrated in oxygen prior to reaction. This effect has been attributed by Sokolovskii et al. (1968a) to the creation of anion vacancies by the vacuum ageing process. The number of anion vacancies at the surface of rare earth oxides seems to maximize after vacuum treatment at around 700°C, as indicated by the minimum in the work function at this temperature (Sazonov and Lyadno, 1966).

Activation energies and exchange rates vary widely for the various rare earth oxides (Antoshin et al., 1967a, 1968; Winter, 1969a; Sazonov et al., 1972). Relative activities of rare earth oxides in isotopic exchange with molecular oxygen at 370°C are shown in fig. 20, where comparison is made with the relative activities in hydrogen oxidation (Minachev, 1973). As isotopic exchange at this temperature seems to involve the participation of lattice oxygen, the data in fig. 20 should also be representative of relative oxygen mobilities. Highest activities are observed for Pr and Tb oxides, which are known to exist as highly nonstoichiometric compounds of the form Pr_6O_{11} and Tb_4O_7. In the structure of these oxides the metal cations are present both as Ln^{4+} and Ln^{3+}, and the oxygen part of the structural lattice is characterized by a large number of oxygen vacancies. High oxygen mobility can therefore be expected, and it appears that

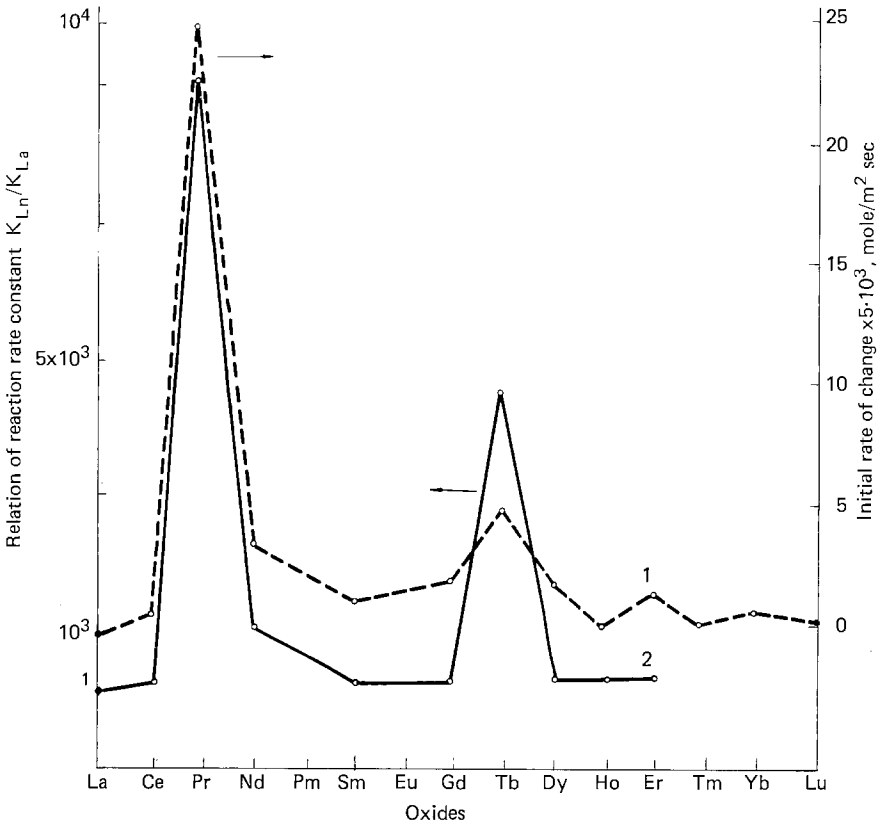

Fig. 20. Initial rate of isotopic exchange of the oxygen of oxides with molecular oxygen at 370°C (1), and their relative activity in hydrogen oxidation at 340°C (2). The activity of lanthanum oxide is taken to be unity (Minachev, 1973).

this high mobility is well reflected in the catalytic activity. The close correspondence of the isotopic oxygen exchange activity with the catalytic activity in the hydrogen oxidation reaction suggests that in the latter reaction, too, oxygen ion mobility plays an important role in the catalytic process (Minachev, 1973).

The situation is less clear, however, if trends of the apparent activation energy for oxygen exchange across the rare earth series are examined. Sazonov et al. (1972) have attempted to correlate activation energies of homomolecular oxygen exchange at 300–400°C with effective magnetic moments of the respective rare earth cations, but Winter (1969a) found no dependence of kinetic parameters on electronic properties. Winter (1969a) has reported a strong compensation effect between the preexponential factor A_0 and the activation energy, E, in the rate expression, i.e. log A_0 and E vary in sympathy across the rare earth series. As for other metal oxides Winter (1969a) found a correlation between the size of the unit cell and the activation energy for oxygen exchange on rare earth oxides (fig.

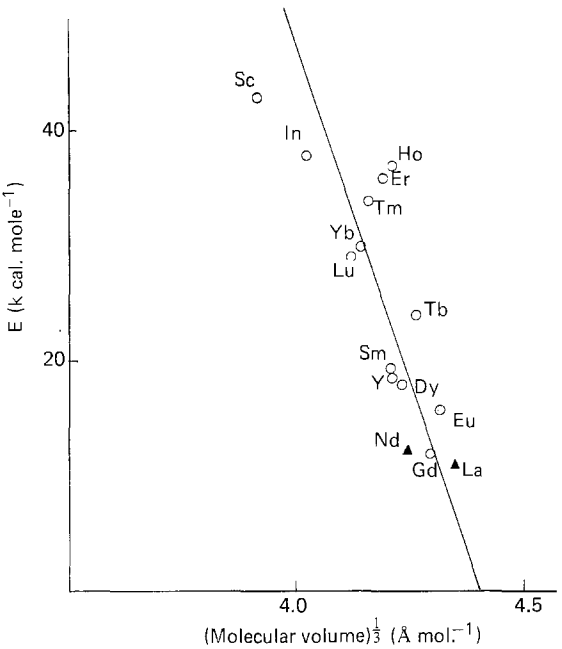

Fig. 21. Activation energy for isotopic oxygen exchange versus crystal parameter of rare earth oxides (Winter, 1969a).

21). The activation energies decrease in a roughly linear manner with increase in crystal parameters such as metal–oxygen or oxygen–oxygen distances. Closer inspection of fig. 21, however, reveals that the relationship between E and the lattice parameter in the form of (molecular volume)$^{1/3}$ is not as striking as it first appears: the activation energies of Ho_2O_3 and Y_2O_3 differ by a factor of two at almost identical crystal size (Winter, 1969a). It appears, therefore, that the significance of such correlations has to be regarded with due caution in view of the large experimental uncertainties of the kinetic parameters, their strong dependence on catalyst pretreatment and the discrepancies between data of different authors.

4.2.2. *Oxidation reactions*

Catalysis of oxidation reactions on oxide surfaces has been described in terms of oxidation–reduction cycles of the catalyst surface (e.g. Boreskov, 1964), but the presence of reactants and products at the surface may complicate this simple picture. The significance of oxygen ion mobility in oxidation reactions has already become apparent in the preceding subsection. The nonstoichiometric oxides of Pr and Tb show high catalytic activities in oxidation reactions, comparable to the activities of MnO_2 or Co_3O_4, which are good oxidation catalysts. On the other hand, the mobility of oxygen in the least active rare earth oxides (La_2O_3, Lu_2O_3, Tm_2O_3) is still at the level of such oxides as iron oxide or nickel oxide, which are also used in oxidation catalysis (Antoshin et al., 1967a). However, the activity pattern suggested on the basis of oxygen mobilities is not

followed in all oxidation reactions catalyzed by rare earth oxides. This implies that effects other than oxygen mobility may also be of importance in determining oxidation activities. Three different reaction types shall be considered here, and the following subsections summarize reported catalytic behavior for the hydrogen–oxygen reaction, the oxidation of carbon monoxide and the oxidation of hydrocarbons.

Hydrogen–oxygen reaction

The oxidation of hydrogen over rare earth oxides has been studied by Bakumenko (1965) and by Antoshin et al. (1967b) at temperatures >300°C for both stoichiometric and nonstoichiometric mixtures of hydrogen and oxygen. Both investigations showed a distinct variation of catalytic activity across the lanthanide series, and Antoshin et al. (1967b) established a striking correlation between the activities of hydrogen oxidation and isotopic oxygen exchange. The data are compared in fig. 20, where catalytic activities for hydrogen oxidation are expressed by the velocity constants of the first-order rate equation at 340°C (curve 2 in fig. 20). Similar activation energies for oxygen exchange and hydrogen oxidation were found by Antoshin et al. (1967b), and the reaction of oxygen with the rare earth oxide surface was suggested to be the rate-limiting step. The high catalytic activities of Pr and Tb oxides have already been discussed in section 4.2.1 in terms of the high oxygen ion mobility in these oxides.

In order to clarify the role of oxide oxygen in this reaction, Antoshin et al. (1971) have investigated the H_2–D_2 exchange and the $^{16}O_2$–$^{18}O_2$ exchange reaction during hydrogen oxidation conditions on a Ce-doped La_2O_3 catalyst (ratio La/Ce = 99). They found that the oxygen exchange reaction was inhibited during hydrogen oxidation, whereas the H_2–D_2 exchange rate was fast and equal to the rate of oxidation under all experimental conditions. These results led to a reformulation of the reaction mechanism for hydrogen oxidation. It was concluded that the rate-limiting step is the interaction between hydrogen in molecular form and adsorbed oxygen, and that surface oxygen of the catalyst does not play an important role in the reaction of hydrogen oxidation (Antoshin et al., 1971). The implications of these results on the hydrogen oxidation mechanism on other rare earth oxides have not been examined, but the mutual influence of reactants to alter their individual adsorption properties has to be acknowledged.

Read and coworkers have investigated the hydrogen–oxygen reaction on a number of rare earth sesquioxides using stoichiometric and nonstoichiometric gas mixtures (Read and Conrad, 1972; Read et al., 1974, 1978, 1979a,b; Read and Crandlemire, 1975; Read and Perkins, 1976a,b). A similar kinetic expression was found to describe the data on all oxides, in the form

$$-\frac{dP_T}{dt} = \frac{k b_{H_2}^2 P_{H_2}^2 b_{O_2} P_{O_2}}{(1 + b_{H_2} P_{H_2} + b_{O_2} P_{O_2})^3} \tag{12}$$

which has been derived assuming Langmuir adsorption kinetics. k designates a proportionality constant, b_{H_2} and b_{O_2} are the Langmuir adsorption coefficients for H_2 and O_2, respectively, P_T is the total pressure of hydrogen plus oxygen, and

P_{H_2} and P_{O_2} are the partial pressure for H_2 and O_2, respectively. Competitive adsorption of molecular hydrogen and oxygen has been suggested as the most likely reaction mechanism, and the interaction between adsorbed H_2O_2 and H_2 species was inferred as the rate-determining step from the kinetic data. The adsorbed H_2O_2 species was thought to consist of two adjacent OH groups. Pretreatment of the catalysts in H_2 or O_2 has been reported by Read and coworkers to influence the reaction rates; the details of these effects, however, have not been revealed on a microscopic scale.

It seems, therefore, that the water formation reaction on the less active rare earth oxides takes place by interaction between adsorbed species, but clarification of the nature of the reacting species must await additional, preferably spectroscopic, evidence.

Oxidation of carbon monoxide

The rate of oxidation of CO on rare earth oxides seems to follow the general trend established for the mobility of lattice oxygen, but the reaction product CO_2 adsorbs immediately at the catalyst surface forming stable carbonate-like complexes. The overall CO_2 production rate is therefore determined by the rate of release of CO_2 from the oxide surface. Sazonov et al. (1971) have reported that the rate of CO oxidation increased with increasing mobility of oxygen, while the rate of CO_2 desorption fell as a result of the ease of formation of carbonate-like complexes with surface oxygen. The strong interaction of the reaction product with the catalyst surface thus provides a self-inhibiting mechanism of the catalytic reaction at temperatures <250°C. Artamonov and Sazonov (1971) have proposed that CO from the gas phase reacts with adsorbed oxygen and subsequently forms two kinds of carbonate complexes involving adsorbed oxygen and lattice oxygen. The following reaction scheme has been suggested:

$$\begin{array}{l} O_{ads} + CO_g \rightarrow CO_{2,ads} \\ \qquad\qquad\quad \downarrow \\ \qquad\qquad\quad CO_{2,g} \end{array} \begin{array}{l} \nearrow +O_{Sb} \rightleftharpoons CO_{3,Sb} \\ \searrow +O_{ads} \rightleftharpoons CO_{3,ads} \end{array} \qquad (13)$$

O_{Sb} and O_{ads} denote lattice and adsorbed oxygen, respectively, and $CO_{3,Sb}$ and $CO_{3,ads}$ are the respective carbonate complexes involving these oxygen species. $CO_{3,Sb}$ was assumed to be the most stable surface compound. The surface concentrations of $CO_{3,Sb}$, $CO_{3,ads}$ and $CO_{2,ads}$ at 350°C in the case of a stoichiometric mixture of initial pressure 1 torr have been estimated to be 2.9×10^{14}, 1.5×10^{13} and 8.0×10^{12} molecules cm^{-2}, respectively (Artamonov and Sazonov, 1971). According to this scheme the overall reaction for CO_2 production involves adsorbed oxygen and CO from the gas phase.

A detailed study of the oxidation of CO on CeO_2 has been performed by Guenin (1973) and Breysse et al. (1972, 1973) using microgravimetry, electrical conductivity measurements, IR spectroscopy and kinetic investigations. These authors obtained evidence that the catalytic reaction consists of successive oxidation and reduction cycles of the surface, and the following sequence has

been proposed:

$$CO_g + (*) \rightleftharpoons CO_{ads} \tag{14}$$

$$CO_{ads} + O^{2-}_{\square} \rightleftharpoons CO_{2,ads} + \square^{2-}_{s} \tag{15}$$

$$CO_{2,ads} \rightleftharpoons CO_{2,g} + (*) \tag{16}$$

$$O_{2,g} + 2\square^{2-}_{s} \rightleftharpoons 2O^{2-}_{\square} \tag{17}$$

$O^{2-}_{\square}$ and $\square^{2-}_{s}$ represent lattice oxygen ions and surface anion vacancies, respectively, and (*) designates a free adsorption site. The CO_2 produced can remain adsorbed at the surface or be readsorbed later as a stable carbonate at the active surface, thus effecting the self-poisoning that is invariably observed. The direct participation of lattice oxygen in the oxidation reaction has been substantiated in this study by in-situ electrical conductivity measurements.

A rather interesting effect should be mentioned in this context, which has been reported recently by Aras et al. (1977) and Breysse et al. (1978) upon CO oxidation on rare earth doped ThO_2. Aras et al. (1977) have observed so-called "cataluminescence", i.e. chemiluminescence specific to catalysis, on ThO_2 doped with Pr and Tb during a CO oxidation reaction. The rare earth component can be regarded as an electronic probe, and lines characteristic of optical transitions from excited Tb^{3+} and Pr^{3+} ion states were recognized. As both Tb and Pr can be expected to exist as tetravalent ions in the ThO_2 host lattice, it has been suggested that a transition from Ln^{4+} to Ln^{3+} ions via an excited Ln^{3+} state occurs during catalysis, according to the reaction

$$Ln^{4+} + O^{2-} + CO_g \text{—} Ln^{3+} + \square^{2-}_{s} + e^- + CO_{2,g} \tag{18}$$

Breysse et al. (1978) have investigated CO oxidation-induced cataluminescence on Eu-doped ThO_2, and luminescence arising from transitions of an excited Eu^{3+} state has been observed. As an intermediate Eu^{2+} state has been invoked to account for these transitions, Breysse et al. (1978) attempted to explain the presence of Eu^{2+} in ThO_2 by a series of elementary steps during the catalytic reaction. The cataluminescence phenomenon involving rare earth activators seems to be restricted to those rare earth elements, which can easily undergo valence changes. No luminescence characteristic of the activators was found for ThO_2 activated with Er or Gd (Breysse et al., 1978). The effect of cataluminescence offers a direct means of substantiating the existence of electronic transfer between adsorbates and adsorbent during a catalytic reaction. For the catalytic oxidation of CO this suggests a mechanism with the participation of oxide oxygen in the reaction process.

Oxidation of hydrocarbons

Rare earth oxides catalyze the oxidation of hydrocarbons in the temperature range 300–500°C, and both saturated and unsaturated hydrocarbons undergo almost complete oxidation to CO_2 and water in the presence of gaseous oxygen. In this respect rare earth oxides resemble the so-called "outer" transition metal oxides such as Cr_2O_3 or MnO_2, but they show considerably lower activity than

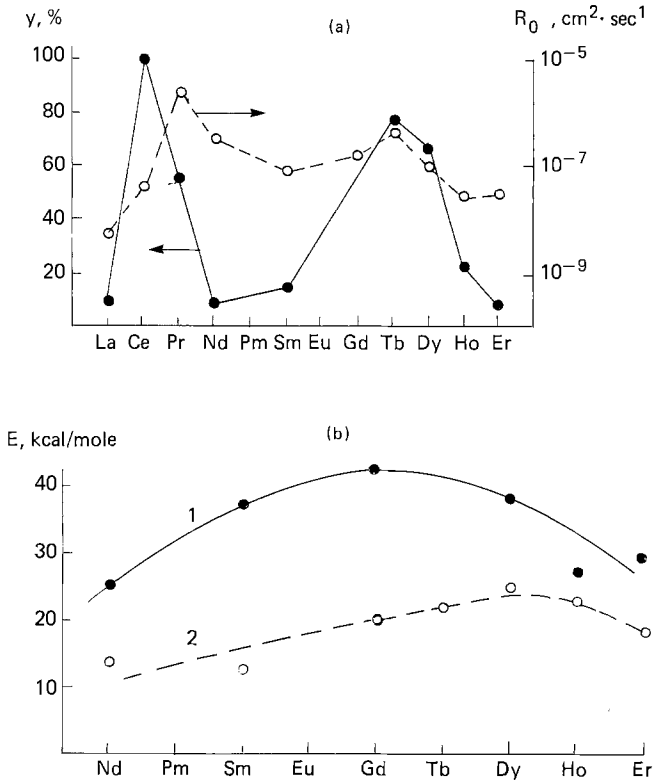

Fig. 22. (a) Yield of CO_2, y, and initial rate of isotopic exchange of oxygen, R_0, plotted versus atomic number of rare earth. (b) Activation energies of complete oxidation of propylene (1) and isotopic exchange (2), plotted versus atomic number of rare earth (Minachev et al., 1967).

the latter. Some connection between catalytic activity and oxygen mobility again seems to be indicated, but the correlation is not perfect and important exceptions do exist. This has been shown by the work of Minachev et al. (1967), who have made a comparative study of the oxidation of propylene over most rare earth oxides. Their principal findings are summarized in fig. 22 (Minachev et al., 1967). In fig. 22a the yield of CO_2 production at 360°C is compared with the initial rate of isotopic oxygen exchange. While a reasonable correlation between activities of both reactions is recognized for the heavier rare earth oxides, an important exception is noted with CeO_2, which has the highest activity in hydrocarbon oxidation but a comparatively low exchange acrivity. The exceptional behavior of CeO_2 will be further discussed below. Minachev et al. (1967) also compared apparent activation energies of propylene oxidation and oxygen exchange for several rare earth oxides. From the similar trend (fig. 22b) it was concluded that the catalytic activity with respect to complete oxidation of propylene is determined by the energy of the bond between oxygen and the oxide surface. Minachev et al. (1967) have observed a small amount of acrolein

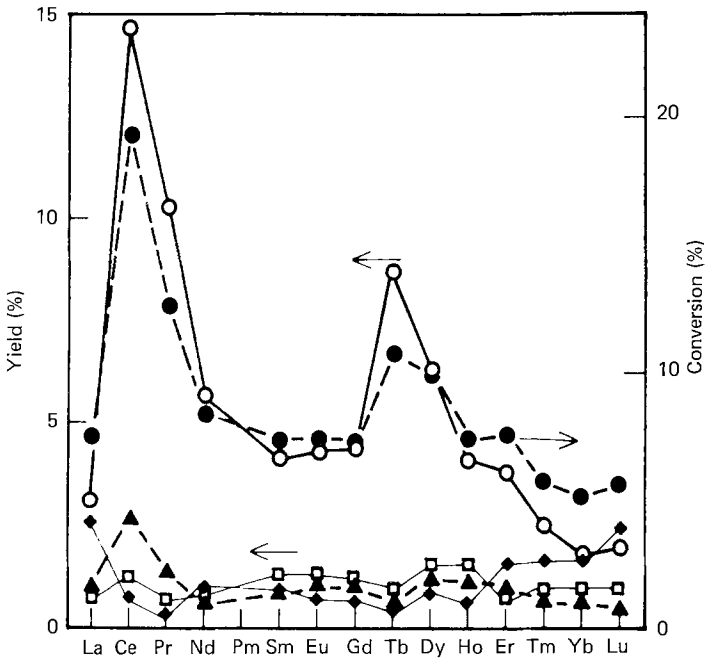

Fig. 23. Oxidation of butane at 450°C (conversion and yield). ●: butane, ○: CO_2, ▲: C_2–C_3, □: CO, ◆ butenes (Hattori et al., 1976).

in the reaction product, and they emphasized a possible influence of the reaction product CO_2 on reaction rates by the blocking of reactive sites.

Further light on the mechanism of hydrocarbon oxidation on rare earth oxides has been shed by Hattori et al. (1976), who investigated the oxidation of n-butane. Their results for reaction at 450°C are shown in fig. 23, where a similar activity pattern as for propylene oxidation is recognized with two maxima at Ce and Tb. The high activity of CeO_2 suggested an important role of Ln^{4+} ions in the catalytic process. Hattori et al. (1976) have therefore compared the activity pattern of butane oxidation with the fourth ionization potentials of the lanthanide metals, which may be taken as a measure of the stability of the tetravalent ions relative to the trivalent ions. A strong inverse correlation between the fourth ionization potentials and catalytic activities was obtained. The correlation between the CO_2 yields at 450°C and the fourth ionization potentials is demonstrated in fig. 24 (Hattori et al., 1976). This correlation has been rationalized by assuming that the rate-determining step of the catalytic reaction is the oxidation of the trivalent ion to the tetravalent ion. The dependence of the fourth ionization potential on the atomic number has been discussed by Hattori et al. (1976) in terms of the Coulomb attraction energy between the positive charge of the closed Xe shell and the 4f electrons and the 4f intrashell electron interaction. An interesting connection between 4f shell occupancy and catalytic behavior has therefore been established.

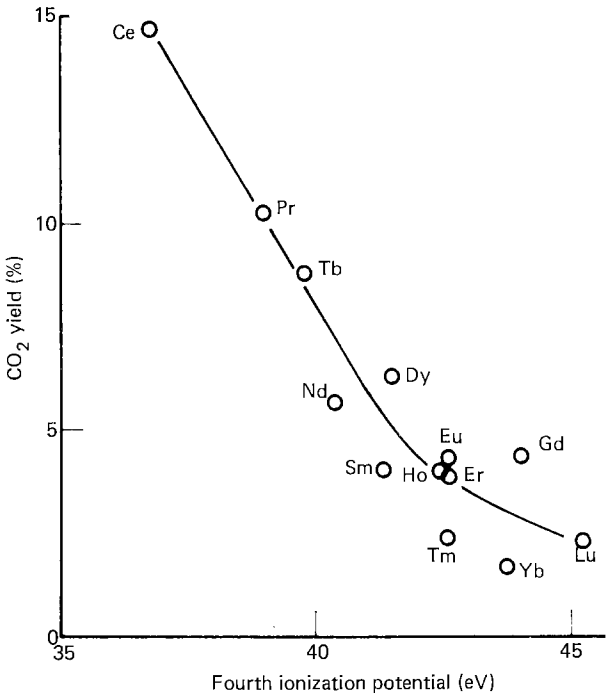

Fig. 24. Correlation between CO_2 yield at 450°C and the fourth ionization potential of the rare earth ion (Hattori et al., 1976).

4.2.3. *Conversion of nitrogen oxides*

In this subsection the decomposition of N_2O and NO to N_2 and O_2 and the oxidation of NO to NO_2 will be considered. All three reactions are catalyzed to various extents on rare earth oxides above 350°C, and they follow a common activity pattern, which is that of the isotopic exchange reaction of oxygen. As the molecular desorption of oxygen occurs in both decomposition reactions, it is suggested that the associative desorption of oxygen plays a major role in the rate-limiting processes.

Winter (1969b) has studied the decomposition of N_2O on rare earth sesquioxides, and has found that the decomposition could be represented by a common rate equation, viz.,

$$-\frac{dP_{N_2O}}{dt} = k\frac{P_{N_2O}}{P_{O_2}^{1/2}}. \tag{19}$$

The preexponential factor A_0 and the activation energy E derived from the rate constants showed a strong compensation effect and a good correlation with the corresponding parameter of the oxygen exchange reaction. This correlation is exemplified in fig. 25, where the rates of N_2O decomposition are plotted against the rates of oxygen exchange (Winter, 1969b). As in the case of oxygen exchange correlation between the kinetic parameters A_0 and E and lattice parameters of the oxide was found, but no correlation was observed between catalytic activity and magnetic properties of the Ln^{3+} ions. Winter (1969b) has

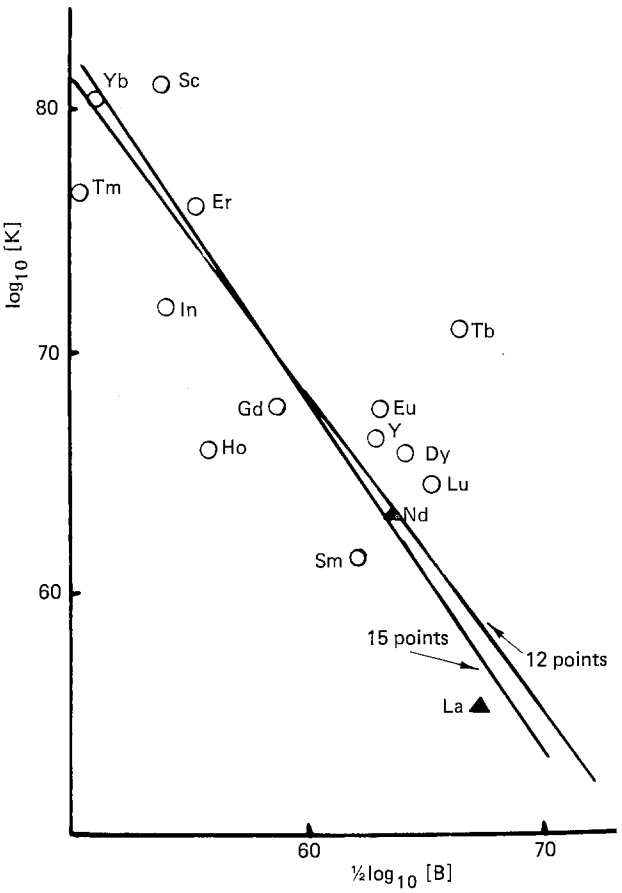

Fig. 25. Correlation between the rate of O_2 exchange and the rate of N_2O decomposition at 450°C (Winter, 1969b).

suggested that the decomposition occurs by chemisorption of N_2O molecules onto single anion vacancies at the oxide surface. These vacancies are assumed to contain trapped electrons (surface F centers) or else the adsorbed molecule acquires one by surface migration:

$$(e^-/\square_s^-) + N_2O_g \rightleftharpoons (N_2O^-/\square_s^-) \tag{20}$$

or

$$(O^{2-}/\square_s^-) + (N_2O/\square_s^-) \rightleftharpoons (O^-/\square_s^-) + (N_2O^-/\square_s^-), \tag{21}$$

where $\square_s^-$ represents an anion vacancy. Then follows the decomposition of the charged adsorption complex

$$(N_2O^-/\square_s^-) \rightleftharpoons N_{2,g} + (O^-/\square_s^-). \tag{22}$$

The O^- can migrate across the surface by charge-exchange until two singly-charged oxygen species "collide", and desorption can occur

$$2(O^-/\square_s^-) \rightleftharpoons O_{2,g} + (e^-/\square_s^-)(e^-/\square_s^-), \tag{23}$$

thus leaving a surface R_2-center, i.e. two adjacent, charged anion vacancies. The last step is identical to the desorption step occurring during oxygen exchange, and was assumed to be the rate-determining step here also (Winter, 1969b). It has been suggested that the R_2-centers are relatively stable, but that they could be destroyed by chemisorption of oxygen, i.e. the reversal of eq. (23), or also by migration of neighboring O^{2-} ions. Chemisorption of N_2O on R_2-centers has been considered as unlikely, but an inhibitory effect of gaseous oxygen was anticipated. However, N_2O decomposition on a number of oxides was found to be unaffected by the presence of oxygen (Winter, 1974a). It has therefore been concluded that the catalytic decomposition is restricted to special small areas of the surface, where R_2-centers formed by the desorption of oxygen from decomposing N_2O are rapidly coverted to F-centers by surface migration.

Read (1973) has essentially confirmed the mechanism proposed by Winter (1969b) in a study of N_2O decomposition on Nd_2O_3, Dy_2O_3 and Er_2O_3, but assumed the surface decomposition of adsorbed N_2O to be the rate-determining step, with O_2 desorption also an important rate-controlling factor, particularly at high oxygen pressure.

The decomposition of NO on rare earth oxides was found to be first order with respect to NO pressure under conditions where the O_2 formed was continuously removed from the system as NO_2 by a reaction with the remaining NO on the colder parts of the apparatus (Winter, 1971). The parameters and rate of NO decomposition at a given temperature were observed to depend closely upon those of the O_2-desorption step. Due to the requirement of two NO molecules necessary to yield the primary reaction product N_2, decomposition of NO molecules adsorbed on an R_2-center has been proposed followed by desorption of O_2 thus reforming the R_2-center (Winter, 1971). This leads to the following reaction sequence:

$$(e^-/\square_s^-)_1(e^-/\square_s^-)_2 + 2NO_g \rightleftharpoons (NO^-/\square_s^-)_1(NO^-/\square_s^-)_2, \tag{24}$$

$$(NO^-/\square_s^-)_1(NO^-/\square_s^-)_2 \rightleftharpoons N_{2,g} + (O^-/\square_s^-)_1(O^-/\square_s^-)_2, \tag{25}$$

$$(O^-/\square_s^-)_1(O^-/\square_s^-)_2 \rightleftharpoons O_{2,g} + (e^-/\square_s^-)_1(e^-/\square_s^-)_2, \tag{26}$$

where the subscripts denote particular adjacent surface sites. Unlike the case of N_2O decomposition gas-phase O_2 has a retarding effect on NO decomposition due to the competition of O_2 and NO for the same surface centers (Winter, 1974b).

The catalytic oxidation of NO to NO_2 has been investigated by Matsuda et al. (1975) and Takasu et al. (1977) on both supported (SiC) and unsupported rare earth oxides at 300 to 450°C. Catalytic activities showed the familiar variation along the lanthanide series. The results of Takasu et al. (1977) are reproduced in fig. 26, where the specific activity, R_s, signifies the rate of formation of NO_2 at a steady state on a unit surface area per minute. The similarity of the data in fig. 26 with those of fig. 20 for isotopic exchange of oxygen clearly indicates that the rate-determining processes of both reactions are closely related.

Finally, the reaction of N_2O with CO to yield N_2 and CO_2 should be men-

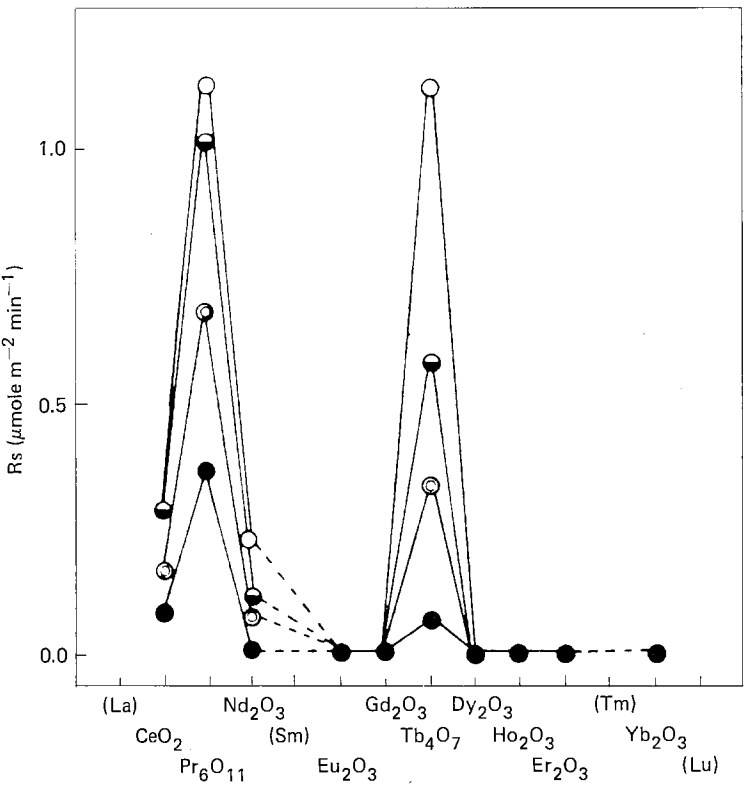

Fig. 26. Specific activities of the rare earth oxides in the oxidation of nitrogen oxide. Reaction temperatures: ●: 300°C, ⊙: 350°C, ◒: 400°C, ○: 450°C (Takasu et al., 1977).

tioned; the kinetics has been examined by Krupay and Ross (1978) on Sc_2O_3. The surface mechanism has been interpreted by a reaction scheme involving each reactant as an adsorbed species and a cyclic transition state.

4.2.4. *Hydrogenation of olefins*

Comparative studies of olefin hydrogenations on rare earth oxides have been performed only to a limited extent, and most studies have been largely confined to the reactions of ethylene (Khodakov et al., 1971; Nakhshunov et al., 1972; Minachev, 1973; Minachev et al., 1977) and propylene (Topchieva and Ibragimova, 1967, 1968; Ibragimova and Topchieva, 1969). The catalytic hydrogenation of ethylene will serve as an example here to illustrate this type of catalytic reaction.

The hydrogenation of ethylene on rare earth sesquioxides occurs at temperatures as low as −120°C, and the most active members of the series, La_2O_3, Pr_2O_3 and Nd_2O_3, show catalytic activities comparable to that of Cr_2O_3, which is one of the most highly active oxide catalysts for hydrogenating ethylene (Khodakov et al., 1971). In contrast to the oxides with sesquioxide stoichiometry

the nonstoichiometric oxides of Pr and Tb, and CeO_2 exhibit low activities or no activity at all. Minachev et al. (1977) have therefore suggested that the coordination number of the cation might play an important role, in that increasing coordination number would decrease the catalytic activity. Minachev et al. (1977) have investigated the effects of catalyst pretreatment on hydrogenation activities, and the highest activity for a given oxide was obtained when the surface was freed of hydroxyl groups. Activities in ethylene hydrogenation at −78°C of Sc, Y and the lanthanide oxides pretreated at temperatures, which produced their highest activities, are shown in fig. 27 (Minachev et al., 1977). The decrease in hydrogenation activity in the series of oxides from La to Lu was

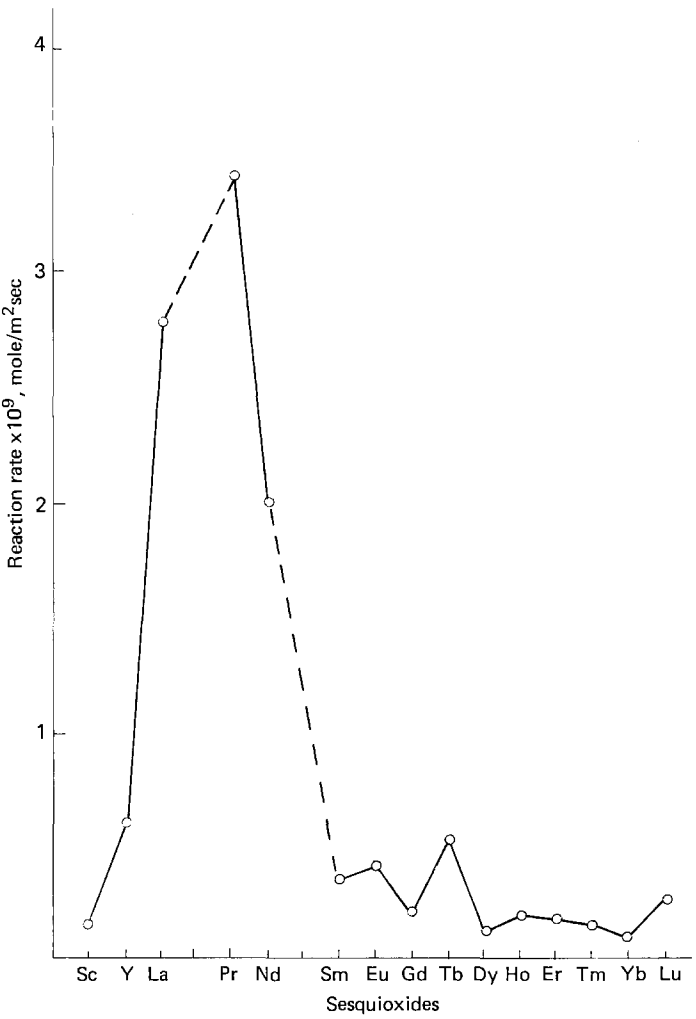

Fig. 27. Activity of rare earth sesquioxides in ethylene hydrogenation at −78°C after catalyst pretreatment at temperatures, which produced their highest activities (Minachev et al., 1977).

correlated with the decrease in their basicity, and the changes observed in the series Sc, Y and La also scale with their increasing basicity. Minachev et al. (1977) have therefore suggested that the "activation" of hydrogen at the surface, i.e. some sort of dissociation, is likely to be the rate-determining step in the hydrogenation reaction. The role of the oxide's basicity may be understood in terms of the polarization of an adsorbed hydrogen molecule by a cation–anion pair, and a reaction complex of the form

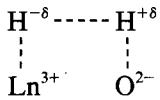

has been proposed for the "activation" step.

In order to reveal the mechanism of ethylene hydrogenation, reactions under various experimental conditions involving deuterated species have been performed by Minachev et al. (1977). The following reaction scheme has been formulated:

$$\begin{array}{lll} H_{2,g} & & C_2H_{4,g} \\ \uparrow\downarrow & & \uparrow\downarrow \\ H_{2,ads}(2H)_{ads} & + C_2H_{4,ads} \rightarrow & C_2H_{5,ads} \rightarrow C_2H_{6,g}. \end{array} \tag{27}$$

Accordingly, the hydrogenation of ethylene on rare earth oxide surfaces should involve associatively adsorbed ethylene and should proceed via a semihydrogenated complex.

4.2.5. *Olefin isomerizations*

Isomerization reactions can be regarded as highly diagnostic in testing concepts of the reaction mechanism and of the nature of active surface sites, because sometimes very specific structural requirements of active surface sites seem to be necessary to rationalize the observed product distributions. Migrations of double bonds in cyclic olefins and higher normal olefins have been reported to occur on rare earth oxides (e.g. Minachev et al., 1961; Minachev and Loginov, 1963; Sosnina and Meshcheryakova, 1969), but only n-butene double bond isomerization has been studied extensively by several groups of investigators.

Khodakov et al. (1975b) have investigated the isomerization of 1-butene on La_2O_3, Nd_2O_3 and Dy_2O_3 in the temperature range $-30°$ to 20°C, and found activities decreasing in the order $La_2O_3 > Nd_2O_3 > Dy_2O_3$ in accordance with the decreasing basicity of these oxides. High selectivity towards cis-2-butene and a corresponding high cis-2-butene/trans-2-butene ratio were observed at the initial stages of the reaction, which decreased as the reaction proceeded. Accordingly, Khodakov et al. (1975b) have proposed a reaction sequence

$$\text{1-butene} \rightarrow \text{cis-2-butene} \rightarrow \text{trans-2-butene} \tag{28}$$

which implies that trans-2-butene is formed from cis-2-butene by a secondary reaction. The influence of catalyst pretreatment on catalytic activity has been

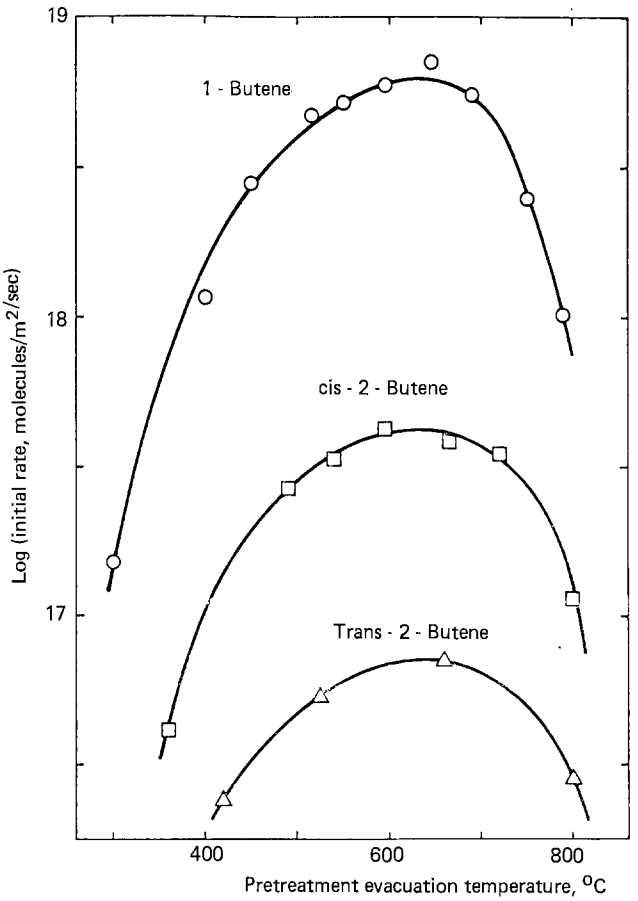

Fig. 28. Effect of catalyst pretreatment temperature on initial rates of conversion of n-butene reactants over La_2O_3 at 0°C (Rosynek et al., 1981).

investigated by Khodakov et al. (1975b) and maximum activity was observed for pretreatment in vacuum at 700°C.

Rosynek and Fox (1977) have reported a similar dependence of isomerization activity on catalyst pretreatment in their detailed study of n-butene isomerization on La_2O_3. They attributed the rising activity up to pretreatment temperatures of about 650°C to the elimination of surface hydroxyl and carbonate species. The effects of catalyst pretreatment on initial rates of conversion of n-butene reactants over La_2O_3 is illustrated in fig. 28, where conversion rates of all n-butene isomers are given according to the most recent work of Rosynek et al. (1981). The decline in specific activity for pretreatment temperatures beyond 650°C has been associated with a decrease in the concentration of surface defect structures, which are thought to form active sites together with adjacent surface O^{2-} ions. In the temperature range 0° to 50°C the isomerization reaction on La_2O_3 was found to be zero order in 1-butene with very high initial turnover numbers, but a cumulative self-poisoning of the catalyst has been reported, probably due to some strongly held, unreactive form of n-butene (Rosynek and Fox, 1977;

Rosynek et al., 1981). Rosynek and Fox (1977) have also observed high initial cis-2-butene/trans-2-butene ratios, but contrary to the results of Khodakov et al. (1975b) the preponderance of the cis-2-butene product over La_2O_3 remained uniformly large until high (>80%) 1-butene conversions were attained. This suggested that the rates of reaction of cis- and trans-2-butene are much slower than that of 1-butene, and that direct interconversion of the two 2-butenes occurs very slowly or not at all. Furthermore, the observed decrease in initial cis/trans product ratio with increasing reaction temperature implied that the apparent activation energy of the pathway by which trans-2-butene is formed from 1-butene exceeds that involved in cis-2-butene formation. Rosynek and Fox (1977) have therefore represented the overall reaction by the scheme

$$\text{cis-2-butene} \leftarrows \text{1-butene} \rightleftharpoons \text{trans-2-butene}. \tag{29}$$

In order to resolve the controversy between the results of Khodakov et al. (1975b) and those of Rosynek and Fox (1977), Goldwasser and Hall (1980) reinvestigated the isomerization of 1-butene on La_2O_3, using the catalysts employed by Khodakov et al. (1975b) and Rosynek and Fox (1977). The results of Goldwasser and Hall (1980) essentially confirmed the findings of Rosynek and Fox (1977).

Very recently, Goldwasser and Hall (1981) have compared the isomerization of n-butenes on ZnO and La_2O_3. They found on La_2O_3 that the initial selectivity of cis-2-butene towards formation of trans-2-butene increased with temperature from nearly zero at 30°C to noticeable amounts at 42.5°C. On the other hand, the inverse reaction, trans- to cis-2-butene already occurred at 30°C and was about 10 times faster than the conversion of trans-2-butene to 1-butene. The results of Goldwasser and Hall (1981) for reactions performed at 30°C are summarized in table 3. In analogy to the mechanism of n-butene isomerization on basic oxides (Dent and Kokes, 1969; Chang et al., 1973), where an allylic carbanion intermediate state at the surface is postulated, Goldwasser and Hall (1981) proposed

TABLE 3
Initial rates and activation energies for n-butene isomerization on La_2O_3 (T = 30°C) (Goldwasser and Hall, 1981).

Step	Initial rate (molec/sec $\times$ cm^2 $\times$ 10^{-10})	Activation energy (kJ/mol)
trans → 1-butene	3.5	76.1
trans → *cis*	36.3	54.3
cis → 1-butene	2500.0	33.4
cis → *trans*	*trans* was not produced initially	83.6
1-butene → *trans*	2300.0	37.6
1-butene → *cis*	21 000.0	16.7

the following π-allyl scheme for La_2O_3:

$$\begin{array}{ccc} & \text{1-butene} & \\ \swarrow & & \searrow \\ \text{syn-}\pi\text{-allyl} & \rightleftharpoons & \text{anti-}\pi\text{-allyl} \\ \downarrow\uparrow & & \downarrow\uparrow \\ \text{trans-2-butene} & & \text{cis-2-butene} \end{array} \qquad (30)$$

This mechanism therefore involves interconversion between trans- and cis-2-butene in accordance with their experimental results. The activation energy for the anti- to syn-π-allyl conversion is about 50 kJ mol^{-1} higher than that for the conversion of cis-2-butene to 1-butene. The forbidding activation energy for cis → trans-2-butene conversion therefore effectively eliminates the direct anti- to syn-π-allyl transformation at lower temperatures.

The question of the interconversion of cis- and trans-2-butene, however, seems still not to be completely resolved. Rosynek et al. (1981) found no evidence for direct cis⇌trans interconversion on La_2O_3 up to 50°C, and they concluded that surface sites that permit the necessary anti-π-allyl⇌syn-π-allyl rotation may be absent on La_2O_3. Tracer studies employing deuterated species indicated that initial proton abstraction is the rate-determining step for each interconversion, and that the hydrogen transfer process involved in double bond migration occurs via an intramolecular mechanism. This has also been substantiated by Goldwasser and Hall (1981). The reason for the discrepancy between the observations of Rosynek et al. (1981) and Goldwasser and Hall (1981) concerning cis⇌trans interconversion seems to be unclear at present, in particular since similar catalyst pretreatment conditions have been used in both studies. The general reaction mechanism for n-butene isomerization on rare earth oxides, however, seems to be similar to that postulated for other basic oxide surfaces.

4.2.6. *Dehydration of alcohols*

One of the first studies of rare earth oxide catalysis has been performed by Cremer (1929) on the dehydration of ethanol. In this pioneering work it was shown that the activation energy increased in the series Sc–Y–La, while almost constant activation energy was found along the lanthanide series from Ce to Dy. As the activity of the catalysts increased with increasing activation energy, a correlation between the preexponential factor and the activation energy in the rate equation, the compensation effect, has been formulated (Cremer, 1929).

Both unimolecular dehydration of alcohols to olefins and dehydrogenation to CO and aldehydes have been reported in the literature (Tolstopyatova et al., 1961; Tosun and Rase, 1972; Ganichenko, 1967; Minachev, 1973), but permanent dehydration activity was observed only at reaction temperatures higher than 300°C due to the contamination of the oxide surfaces with product water molecules.

Tosun and Rase (1972) have investigated the dehydration of ethanol on Nd_2O_3 as a function of catalyst pretreatment, and concluded that surface hydroxyl

groups are a major source of activity. Alternatively, oxygen bridges formed by dehydroxylation of the surface have been proposed to act as highly active centers (Tosun and Rase, 1972). The role of surface hydroxyl groups as active centers, however, has been questioned by Rosynek (1977), because they are expected to be absent after catalyst calcination at >400°C.

In order to gain insight into the dehydration mechanism of butanols, Thomke (1977) has studied the dehydration of deuterated butan-2-ols over UO_2, ThO_2 and CeO_2 in the temperature range 250–500°C. Various elimination mechanisms have been discussed by Thomke (1977), and a proton-abstraction mechanism involving a carbanion in the β position (E1cB) was proposed on CeO_2 below 400°C, while an α-carbonium ion mechanism (E1) was suggested to occur at temperatures above 400°C.

The selectivities of rare earth oxide catalysts for dehydration of 2-propanol and butanols have been examined recently by Bernal and Trillo (1980) as a function of reaction temperature. No definite variations of selectivity have been observed along the lanthanide series, but the highest percentage of 1-butene was found on Ho_2O_3 and Lu_2O_3 and the lowest on La_2O_3. This is opposite to what was expected on the basis of the respective basicities of these oxides. Bernal and Trillo (1980) have noted that the reaction temperature influences product distributions, and that care has to be exerted in establishing trends of a series of related catalysts because of these temperature effects.

4.2.7. *Concluding remarks*

We have attempted in this section to illustrate catalysis on rare earth oxides by discussing selected examples of various catalytic reaction types. Not all the reactions which have been investigated on rare earth oxides up to date have been mentioned, but the major reaction types have been considered. An exhaustive bibliography of this field may be found in the review of Rosynek (1977). Emphasis has been placed on more recent data where available, and mechanistic concepts have been discussed in some detail. Of course, some of these concepts are still highly speculative, but they may stimulate further research. A number of trends along the rare earth series for several reaction types have been established, although critical evaluation is indicated in some instances. Numerical data have been included in this section only in isolated cases, as their dependence on apparatus and experimental conditions often seems to preclude general comparisons. For example, the significance of apparent activation energies of reaction and overall rate constants is difficult to evaluate, if the reaction mechanism is not well established.

5. Catalysis on other binary, non-metallic rare earth compounds

Solid state physical and chemical properties of binary rare earth compounds involving non-metallic elements have attracted considerable scientific interest in recent years (see volumes 3 and 4 of this series). Some of the compounds exhibit

very interesting electronic configurations, and photoelectron spectroscopy on these compounds has been reviewed by Campagna et al. (1979). In contrast, investigation of surface reactivities of binary, non-metallic rare earth compounds other than oxides has been almost completely neglected, and only very few isolated studies have been reported in the literature.

One group of investigators (Konenko et al., 1970, 1971) has used the high-temperature o–p-H_2 conversion as a catalytic test reaction to compare catalytic activities of the rare earth metals, Y, Sc, Nd with those of their hydrides, carbides and oxides. The compounds have been chosen to modify the electron donor properties of the metal cations, which were thought to be of importance in determining the hydrogen dissociation capabilities of the respective metal cations. The high-temperature o–p-H_2 conversion reaction proceeds via a chemical mechanism involving the recombination of H atoms at the surface (cf. section 4.2.1). A decreasing activity was found for the series metal > hydride > carbide > oxide, and this was attributed to an increase in the acceptor capacity of the non-metal atoms according to H < C < O. The activation energies for a given metal-compound series remained approximately constant, and the variation in catalytic activity was attributed to variations of the preexponential factor of the rate equation. Konenko et al. (1975) have extended these investigations of the high-temperature o–p-H_2 conversion over most lanthanide metals and their hydrides, and the metals showed consistently higher activities than the hydrides. An attempt was made by Konenko et al. (1975) to correlate the trend of the catalytic activity along the lanthanide series with the stabilization energies of the respective rare earth cations, but as pointed out in section 4 some scepticism seems also to be indicated here.

Stimulated by the excellent catalytic behavior of rare earth oxides in the hydrogenation of ethylene Khodakov et al. (1972) have investigated Nd and Ce hydrides as catalysts for this reaction. The hydrides showed lower activities than the corresponding oxides, and the participation of hydride hydrogen in the hydrogenation reaction has been suggested. While the stoichiometric LnH_2 was found to be almost inactive, the presence of superstoichiometric hydrogen, i.e. lattice hydrogen in excess of the dihydride stoichiometry, has been associated with the catalytic activity observed under some experimental conditions. La fluorides and Nd and Ce silicates have been tested as catalysts for ethylene hydrogenation (Khodakov et al., 1975c), but were found to show no or very low activity.

The hydrogen–oxygen reaction on neodymium sulfide has been studied by Read et al. (1970). The reaction was zero order in total pressure of hydrogen plus oxygen, and the deactivation of the catalyst during the course of the reaction was attributed to the blocking of the surface by irreversibly adsorbed products, presumably water. The isotopic exchange reaction of nitrogen with rare earth nitrides has recently attracted some interest due to the practical importance of molecular nitrogen activation, and Kharitonov et al. (1980) have reported some data on LaN and CeN. While CeN seems to exhibit a high catalytic activity in the nitrogen exchange reaction at 673 K, the isotope exchange on LaN could be

initiated only at higher temperatures (873 K). The reason for this differing behavior has not as yet been revealed.

A more thorough evaluation of surface chemistry on binary, non-metallic rare earth compounds, excluding the oxides, is not possible at present because of the lack of available data. We note, however, that investigation of surface reactivities on some of these compounds, in particular those showing intermediate valence phenomena (Campagna et al., 1976), should provide an exciting new field of activity in the surface chemistry of rare earth materials.

6. Surface chemistry on rare earth intermetallic compounds

Surface chemistry on intermetallic compound surfaces containing rare earth metals has been greatly stimulated by the discovery that these materials can absorb large quantities of hydrogen (Van Vucht et al., 1970). As some intermetallics containing large amounts of hydrogen can readily release this hydrogen again, they are being considered in efforts to exploit hydrogen as a fuel. Many rare earth intermetallics were therefore studied from a hydrogen storage point of view (Van Mal et al., 1976). Since the dissolved hydrogen exists in the atomic state and occupies interstitial positions in the parent compound (Van Vucht et al., 1970; Kuijpers and Loopstra, 1971), increased attention has been paid recently to the surfaces of these materials, where dissociation of hydrogen molecules must obviously take place prior to incorporation into the lattice. The influence of impurities in the hydrogen gas on the decrease in the hydrogen absorption capability after a number of absorption–desorption cycles has also been recognized (Gualtieri et al., 1976). This prompted investigations of the interaction of other gases with these surfaces as the blocking of active surface sites by strongly adsorbed species, a well-known phenomenon in catalytic science, seemed to be one likely reason for decreasing reactivity towards hydride formation. Considerable progress has been made in understanding physicochemical aspects of hydride formation, and information is now available for a large number of intermetallic compound systems (Van Mal et al., 1976; Goudy et al., 1978; Oesterreicher, 1980; Craig et al., 1981). In this review, however, we will consider only those studies where surface-related aspects of hydride formation have been addressed.

The capability of rare earth containing intermetallic compounds to dissociate molecular hydrogen into adsorbed atoms led Takeshita et al. (1976) to investigate these materials as catalysts in hydrogenation reactions. High catalytic activity was indeed found for ammonia synthesis (Takeshita et al., 1976) and in the methanation reaction (Coon et al., 1976). As already pointed out in section 2.3.2, the catalysts undergo dramatic changes in structure and chemistry during the catalytic reactions due to the interaction of reactants or impurities with the catalyst surfaces. The two aspects of surface chemistry on rare earth materials, namely reactions on and reactions with rare earth surfaces, are therefore intimately connected in the catalysis of rare earth intermetallics. For presen-

tation purposes, however, section 6.1 will be mainly concerned with phenomena related to reactions of gases with intermetallic compound surfaces, whereas in section 6.2 the catalytic viewpoint will be more strongly emphasized.

6.1. *Reactions with rare earth intermetallic compounds*

As many studies of gas–solid surface reactions involving rare earth intermetallics are in some sense or other related to hydride formation, the interaction with hydrogen shall be of central interest in this section. The interaction of hydrogen with the intermetallic compounds under consideration can be represented schematically by the following sequence of processes:

(1) $H_2(g) \rightarrow H_2$ (ads),
(2) H_2 (ads) $\rightarrow 2$ H (ads),
(3) H diffusion into the bulk,
(4) hydride phase formation.

While steps (1) and (2) symbolize the usual dissociative chemisorption and step (4) the phase transformation from the pure intermetallic to the hydride, step (3) may involve diffusion processes actually more complex than simple bulk diffusion. Inversion of the above sequence leads to associative desorption of hydrogen. In order to assess the kinetics and also the mechanism of hydrogen absorption/desorption, the slowest step, i.e. the rate-determining process, has to be recognized. Raichlen and Doremus (1971) have measured the kinetics of hydriding of $SmCo_5$ and concluded that the rate of release of hydrogen is related to the rate of transformation of the hydride to the unhydrided compound. Boser (1976) has determined the sorption rates of hydrogen in activated $LaNi_5$ as a function of temperature. He suggested on the basis of the similarity of the activation energy of sorption with the formation energy of $LaNi_5$ hydride that the phase transition is the rate-controlling process. Tanaka et al. (1977) have performed absorption measurements on a massive, unactivated $LaNi_5$ sample, where they inferred bulk diffusion as the rate-limiting step. Little attention has been devoted in these studies to processes at or near the surface region of the absorbing materials, but Gualtieri et al. (1976) pointed out the importance of the absorber surface and its catalytic properties for hydrogen dissociation in the absorption process.

The first detailed surface study of an intermetallic compound under the influence of hydrogen and oxygen has been performed by Siegmann et al. (1978) for $LaNi_5$. XPS has been used to analyze the composition and chemical state of the $LaNi_5$ surface, and measurements of the magnetic susceptibility were carried out to trace magnetic precipitations. The magnetic susceptibility as a function of the number of hydrogenation cycles as shown in fig. 29 according to Siegmann et al. (1978) increases with the number of cycles suggesting that hydrogenation produces magnetic Ni or Ni-rich precipitations at the surface. The chemical state of the $LaNi_5$ surface after various treatments was revealed by XPS, and La $3d_{5/2}$, O 1s and Ni $2p_{1/2}$ spectra are shown in fig. 30. Curves I are for the $LaNi_5$ samples

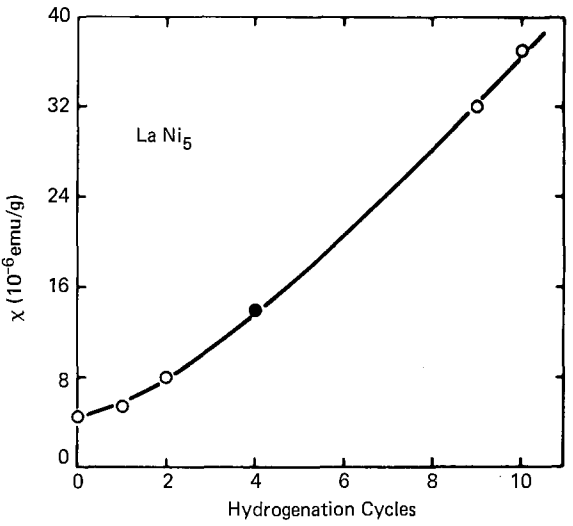

Fig. 29. The magnetic susceptibility χ at $T = 20°C$ and $H = 4$ kOe as a function of the number of hydrogenation cycles (Siegmann et al., 1978).

as inserted into the vacuum chamber, and curves II–IV were recorded after the indicated treatments. In comparing the spectra with standard core level spectra of La metal, La_2O_3 and $La(OH)_3$, Siegmann et al. (1978) were able to specify the chemical identity of the respective surfaces. Accordingly, all the La seen at the surface of the inserted $LaNi_5$ is oxidized, and in the form of $La(OH)_3$, while the

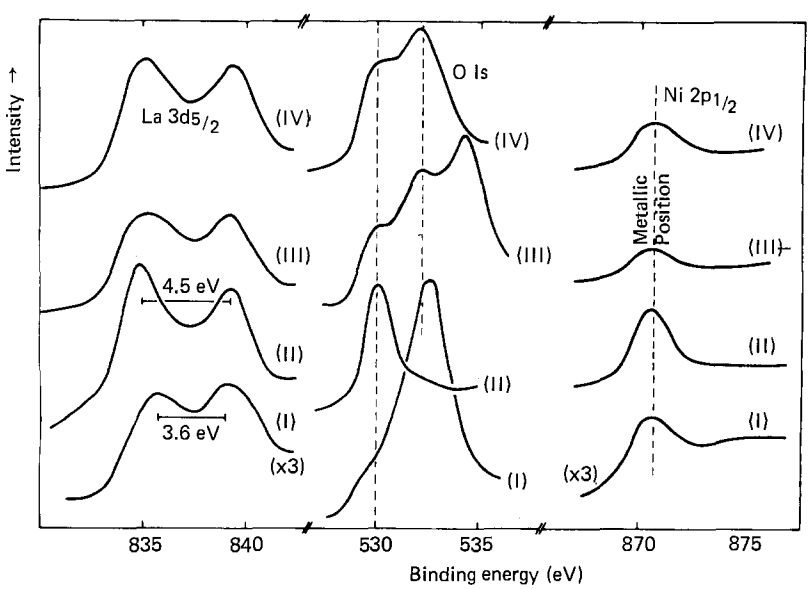

Fig. 30. La $3d_{5/2}$, O 1s, and Ni $2p_{1/2}$ spectra of $LaNi_5$: Curve I, as inserted; II, ion bombarded and annealed; III, exposed to H_2 at >1 torr at −20°C; and IV warmed to 0°C (Siegmann et al., 1978).

Ni seems to be predominantly metallic. After Ar^+ ion bombardment followed by annealing to 650°C, $La(OH)_3$ converts to La_2O_3 and presumably also some metallic La is formed, while the Ni remains in the metallic form. Exposing the annealed sample to hydrogen at −20°C results in the appearance of three O 1s lines indicating adsorbed H_2O (binding energy 536 eV), hydroxide and oxide at the surface (curves III). The shape of the Ni $2p_{1/2}$ spectrum remains unchanged, representing metallic Ni. Finally, on warming to 0°C (curve IV) the H_2O desorbs and dissociates leaving a La oxide–hydroxide mixture at the surface. From these results Siegmann et al. (1978) concluded that La was always dominantly non-metallic and in abundance compared to the bulk concentration, while the Ni was always dominantly metallic. La seems to diffuse to the surface of $LaNi_5$ in the presence of O_2 or H_2O, and its affinity towards these gases keeps the Ni precipitates essentially metallic, and they are then able to split H_2 molecules. Siegmann et al. (1978) therefore proposed that this surface segregation provides an excellent self-restoring mechanism of the active surface in $LaNi_5$. It is worth noting in this context that the XPS data discussed above are consistent with an XPS study of Wandelt et al. (1977) on a Gd/Fe alloy. There it was found that the surface consisted essentially of metallic Fe and oxidized Gd.

The surface segregation in $LaNi_5$ was further investigated by Von Waldkirch and Zürcher (1978) and by Schlapbach et al. (1979a) using Auger spectroscopy in combination with Ar^+ ion bombardment to obtain AES depth profiles. The surface segregation seems to be driven by O_2 or H_2O, but not by the presence of H_2. Von Waldkirch and Zürcher (1978) proposed the chemical exchange reaction

$$(\text{La–Ni}) + \text{O} \rightarrow (\text{La} + \text{O}) + \text{Ni} \tag{31}$$

to be responsible for the La surface segregation. A schematic model of the surface layer of $LaNi_5$ based on AES measurements on a $LaNi_5$ single crystal sample, is shown in fig. 31 according to Schlapbach et al. (1980).

On a freshly cleaved sample the surface composition is the same as the bulk composition (fig. 31A). Because the surface energy of La is lower than that of Ni the surface becomes somewhat La enriched in thermodynamic equilibrium (fig. 31B). This segregation is enhanced by reaction with oxygen, and a La-oxide layer covers a Ni-rich layer (fig. 31C). The concentration profile of the decomposed surface layer is depicted schematically in fig. 31D.

The surface layer containing the segregated La and Ni precipitates probably does not store hydrogen, and the thickness of the decomposed layer increases with the number of hydrogenation cycles as indicated by magnetization measurements (Schlapbach et al., 1979a; Schlapbach, 1980). The storage capacity of the intermetallic is therefore limited and decreases with the number of hydrogenation cycles (Schlapbach et al., 1980). In addition to the decomposition at the surface another degradation effect upon cycling has to be acknowledged: the disproportionation of $LaNi_5$ into LaH_3 and Ni (Cohen et al., 1980). The latter degradation effect, however, has been reported to be reversible by treatment in vacuum at around 200°C (Schlapbach, 1980). Similarly, the degradation of the hydrogen-absorbing capacity of $EuRh_2$ has been ascribed to the formation of a

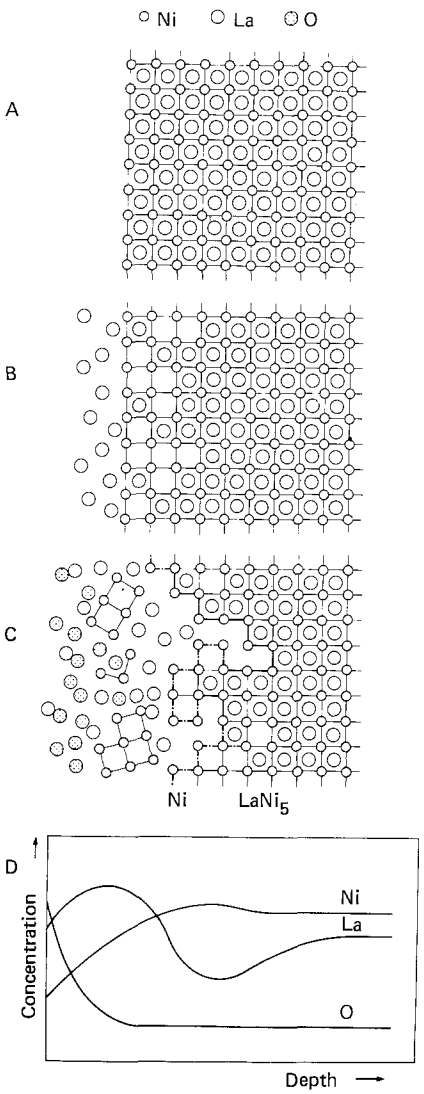

Fig. 31. Surface segregation and decomposition of $LaNi_5$ (Schlapbach et al., 1980).

relatively stable EuH_2 phase (Cohen et al., 1978). Annealing to 350°C in vacuum also restores the initial hydrogen absorption capacity in this case.

The effects of hydrogen and oxygen adsorption on an $ErFe_2$ surface have been studied by Landolt et al. (1979) using spin polarized photoemission. These authors suggested that no hydrogen or oxygen induced surface segregation occurs at room temperature in $ErFe_2$. However, examination of this system by XPS (Schlapbach et al., 1980) showed that surface segregation does occur in $ErFe_2$ much in the same way as in $LaNi_5$. Exposing a UHV cleaved, clean $ErFe_2$ surface to 10 L O_2 increased the Er:Fe ratio from 0.5 to 1, and the Er became completely oxidized, while the Fe remained essentially metallic. Higher

exposures to O_2 or H_2 had no further influence on the Er:Fe ratio, but about 10% of the Fe atoms were oxidized (Schlapbach et al., 1980). Surface segregation and decomposition under the influence of oxygen and possibly also of other reactive gases seem to be therefore universal phenomena in rare earth intermetallic compounds.

The influence of SO_2, a well-known poison for Ni catalysts, on the surface segregation of $LaNi_5$ has been investigated by Schlapbach and Brundle (1979, 1981). The effects were dramatic: Exposures as low as 10 L SO_2 were sufficient to oxidize the La on a freshly prepared surface and to prevent further reaction upon subsequent exposures to high oxygen doses. SO_2 seems to "seal off" the surface for surface segregation by blocking reactive surface sites for oxygen interaction. This blocking has been attributed to the formation of La sulfide and La sulfate overlayers (Schlapbach and Brundle, 1981). The effects of SO_2 on hydrogen absorption/desorption on several rare earth intermetallics have been recognized previously by Gualtieri et al. (1976). They noted that SO_2 treatment prevented hydrogen absorption or desorption from the hydrided samples for $HoCo_3$, $PrCo_3$ and $LaNi_5$, but not in the case of $ErCo_3$ and $ErFe_2$. On $ErCo_3$ and $ErFe_2$ hydrogen uptake after SO_2 treatment was observed after an induction period. The delayed hydrogen uptake by the latter compounds was tentatively explained by some slow SO_2 desorption.

Sandrock and Goodell (1980) have recently addressed the issue of surface poisoning of metal hydrides by impurities in the hydrogen used. The alloys investigated were $LaNi_5$, FeTi and $Fe_{0.85}Mn_{0.15}Ti$ and the gaseous impurities were O_2, H_2O and CO. Marked differences in the degree of poisoning and ease of reactivation were noted from alloy to alloy and from impurity to impurity. Concentrating here on $LaNi_5$, the effects of cycling with H_2 containing impurities are expressed as the loss of hydrogen transfer capacity (in terms of the atomic hydrogen-to-metal ratio H/M) in fig. 32 (Sandrock and Goodell, 1980). After an initial loss of capacity in O_2^- or H_2O-containing H_2, $LaNi_5$ almost completely recovers and then exhibits substantial immunity. This is consistent with the self-restoring mechanism of active surface as discussed above. With CO all hydrogen capacity is soon lost and it can only be recovered by reactivation, e.g. by about 20 cycles in pure hydrogen. Sandrock and Goodell (1980) suggested that CO forms a simple chemisorbed overlayer thus rendering inactive Ni atom sites at which catalytic dissociation of hydrogen occurs. It has to be mentioned that CO adsorption on the oxidized rare earth component does not easily occur, but that CO seems to adsorb dissociatively on rare earth metals followed by the formation of surface oxide and carbon deposits at the surface (Bertel and Netzer, 1980b).

The interaction of nitrogen with $LaCo_5$ has been investigated by Soga et al. (1979a) at elevated temperatures (300–500°C) in the pressure range of several hundred torr to a few atmospheres. The formation of bulk nitride, presumably in the form of La nitride, together with some molecularly adsorbed N_2 at the surface was inferred by Soga et al. (1979a). The absence of in-situ surface analytical techniques, however, prevents more detailed conclusions to be drawn.

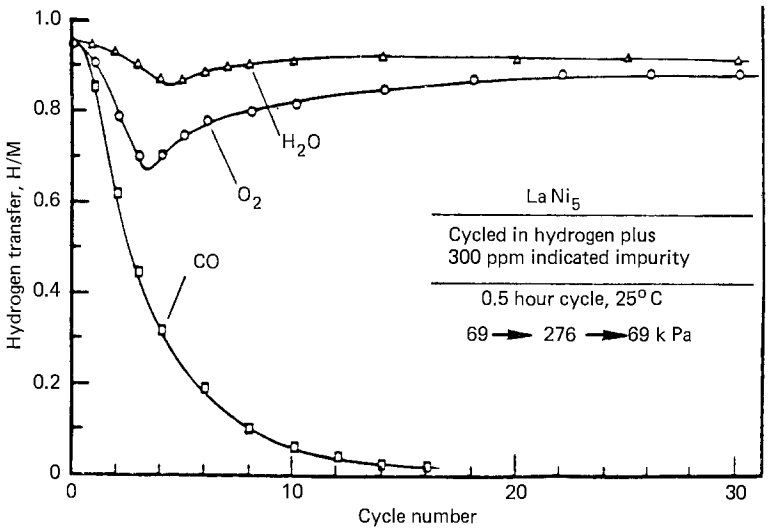

Fig. 32. The cycling response of $LaNi_5$ in H_2 containing 300 ppm H_2O (△), O_2 (○) or CO (□) impurity. 0.5 h cycle at 25°C, pressure course 69→276→69 kPa (Sandrock and Goodell, 1980).

Returning now to the mechanism of hydrogen absorption or release, Wallace et al. (1979) have combined the recent information on surface structure and composition with kinetic data and data on the catalytic hydrogenation of ethylene (Soga et al., 1977a) to propose a detailed model for the $H_2/LaNi_5$ system. The following experimental observations had to be accommodated:

(1) The desorption process is second order with respect to the hydrogen concentration in the solid (Boser, 1976; Goudy et al., 1978), while initial absorption is proportional to the hydrogen pressure (Boser, 1976).

(2) Hydrogen extraction from the hydride by hydrogenation of ethylene over $LaNi_5H_{2.4}$ is first order with respect to the hydrogen concentration (Soga et al., 1977a).

(3) Gaseous hydrogen inhibits the hydrogenation reaction of ethylene; there exists therefore a blocking effect (Soga et al., 1977a).

(4) Hydrogenation of ethylene over $LaNi_5$ is much slower than over $LaNi_5H_{2.4}$ (Soga et al., 1977a).

(5) H_2–D_2 exchange is very rapid on $LaNi_5$ hydrides (Soga et al., 1977b).

(6) The surface region of $LaNi_5$ under these reaction conditions consists of oxidized La (La_2O_3 or $La(OH)_3$) and metallic Ni precipitates (Siegmann et al., 1978).

Wallace et al. (1979) proposed that adsorption and dissociation of hydrogen on Ni, diffusion of atomic hydrogen through the interfacial region between oxidized La and metallic Ni to reach $LaNi_5$, and the following bulk processes in $LaNi_5$ are fast processes, but that dissociation or recombination at the top of the interfacial region between La_2O_3 and Ni are rate-determining processes for H_2 absorption/desorption. In particular, the blocking at the top of the interfacial region by

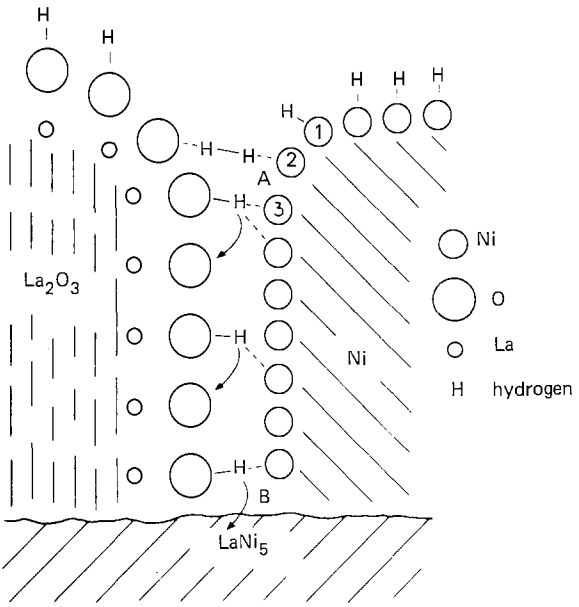

Fig. 33. Schematic representation of the interface region in $LaNi_5$. One of the possibilities for the blocking effect of molecular hydrogen is indicated. The configuration shown for H_2 could result if H_2 attempted to chemisorb on Ni atom 2 when Ni atom 1 and 3 are already bounded to atomic hydrogen. Alternatively, failure to interact with Ni atom 3 could be due to its inaccessibility because of geometrical constraints (Wallace et al., 1979).

molecular species has been considered as crucial. This is illustrated in fig. 33, where the interfacial region is schematically depicted (Wallace et al., 1979). The region between A and B shows a channel of the interfacial region and the diffusion of H atoms by hopping between OH and Ni is indicated. A blocking H_2 molecule, which cannot dissociate because of occupied neighboring sites, is shown on Ni atom 2 at the top of the interfacial region (fig. 33). In the case of C_2H_4 hydrogenation on hydrided $LaNi_5$, the H_2 molecule on Ni atom 2 may be thought of as being replaced by a C_2H_4 molecule, which can easily react with atomic hydrogen diffusing along the interfacial channel. As the reaction of C_2H_4 at the top of the interfacial region can be considered as fast, migration of hydrogen atoms through the interface has been assumed to be the rate-limiting process for the hydrogenation of ethylene on hydrided $LaNi_5$.

Wallace et al. (1979) suggested that the mechanism outlined above for $LaNi_5$ might be of rather general validity, and indeed, it seems to explain results on a number of intermetallic compounds (Goudy et al., 1978). However, a word of caution has to be added. The RFe_2H_n systems (R = Gd, Tb, Ho, Er, Tm) show first order desorption kinetics irrespective of the method of hydrogen extraction (decrease of ambient pressure or reaction with C_2H_4) (Imamura and Wallace, 1980a). The blocking influence of gaseous H_2 in the hydrogenation of C_2H_4 (Soga et al., 1977a), a key feature in the discussion of Wallace et al. (1979), has been confirmed recently by Soga et al. (1979b) for $LaNi_5H_{2.4}$, but not for $CeCo_5$, $PrCo_5$, $SmCo_5$ and $LaCo_5$ hydrides, where partly the opposite effect was observed (see section 6.2.2). While Imamura and Wallace (1980a) suggested that the different composition of the intergranular region of RFe compounds – in addition

to rare earth oxides and metallic Fe oxidized Fe is also found (Schlapbach et al., 1980; Wallace et al., 1980) – might be at the root of the different behavior of RFe_2 compounds, rationalization of the observation of Soga et al. (1979b) must await further investigations.

6.2. *Catalysis on rare earth intermetallics*

Having already backed up discussions in the preceding subsection with catalytic results, we may now proceed with a more close inspection of catalytic processes on rare earth intermetallics. Consistent with the central role of hydrogen in rare earth intermetallic surface chemistry, hydrogenation reactions have been predominantly investigated on these materials.

6.2.1. *Ammonia synthesis and methanation reactions*

In the pioneering work of Takeshita et al. (1976) and Coon et al. (1976) rare earth intermetallics have been tested as catalysts in ammonia synthesis and CO methanation reactions, respectively. Takeshita et al. (1976) investigated thirty-six intermetallics involving rare earths in combination with Fe, Co or Ru for the formation of NH_3 from the elements. Several of these showed specific activities exceeding that of a standard high activity synthetic Fe ammonia catalyst. In table 4 specific activities of the sixteen most active materials are listed together with apparent activation energies (Takeshita et al., 1976). A comparison is also made in table 4 with data of a standard synthetic ammonia catalyst, designated as 416. On a weight basis, 416 was the most active catalyst, because of its large surface area. However, when expressed as specific activity (table 4), several of the rare earth intermetallics are substantially superior. The catalysts were examined by X-ray diffraction before and after reaction and decomposition of the intermetallics into rare earth nitride and finely divided transition metal has

TABLE 4
Rank ordering for NH_3 synthesis (at 450°C) (Takeshita et al., 1976).

	Yield[a)]	E_a		Yield[a)]	E_a
$CeCo_3$	17.4	36.4	$PrCo_3$	3.3	–
$CeRu_2$	13.5	43.1	$ErFe_3$	3.3[b)]	51.4
Ce_2Co_7	9	–	$CeFe_2$	2.3	55.2
Ce_2Fe_{17}	6.7[b)]	33.4	416	1.8	85.7
$PrCo_5$	6	–	$TbFe_3$	1.7[b)]	–
$CeCo_5$	5.5	38.9	$PrCo_2$	1.3	–
$CeCo_2$	4.3	24.2	$ThFe_3$	0.9	44.3
$Ce_{24}Co_{11}$	4.3[b)]	39.3	$DyFe_3$, $HoFe_3$	0.5[b)]	–

[a)]Yield in NH_3 (ml)/m^2 of cat. min.; E_a in kJ/mol.

[b)]Surface areas of these systems were not measured. Calculations were made assuming their areas per gram were the average of the intermetallics studied.

TABLE 5
Relative activity (R.A.) at 450°C of several RCo_3 systems as synthetic ammonia catalysts (Wallace et al., 1977).

	$CeCo_3$	$NdCo_3$	$GdCo_3$	$TbCo_3$
R.A.	1.00	0.85	0.47	0.09

been observed. Takeshita et al. (1976) therefore proposed that the active catalytic agent is the finely divided transition metal. The variation of the apparent activation energy suggests that the rare earth constituent also has some effect. This has been clearly demonstrated in comparing activities on RCo_3 (R = Ce, Nd, Gd, Tb) compounds as shown in table 5 (Wallace et al., 1977). The nature of the influence of the rare earth component, however, has still not been revealed.

Coon et al. (1976) have shown that a number of compounds of various stoichiometries between rare earth and transition metals are active catalysts for the reaction of CO and H_2 to form CH_4. Typical results for $LaNi_5$ are presented in fig. 34 (Coon et al., 1976). The reaction begins at ~200°C and reaches saturation at ~380°C. It was found that hydrocarbon synthesis begins at some

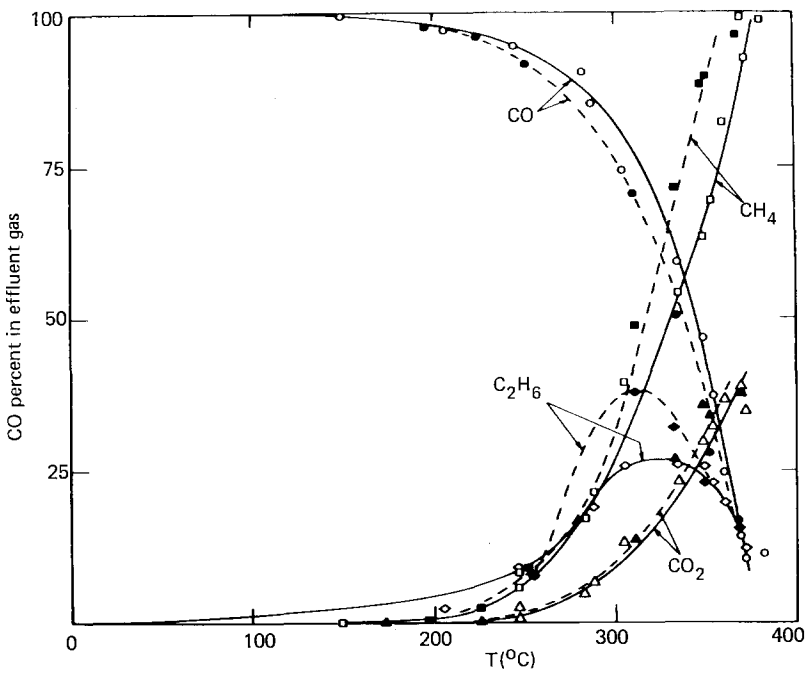

Fig. 34. Conversion of CO over $LaNi_5$ in a $CO + 3\,H_2$ gas mixture. Relative amounts of CH_4, CO_2 and C_2H_6 (×32), as deduced from the GC peak areas are also given. The solid line and open circles are results obtained in the sequence involving rising temperatures; filled circles and dashed lines give corresponding results for decreasing temperature. At the highest temperature studied (381°C) 95% of the CO is converted into CH_4 (83%), CO_2 (17%), C_2H_6 (trace) and C_2H_4 (trace) (Coon et al., 1976).

minimum temperature T_{min} with a systematic variation being observed for this temperature in the sequence T_{min} (RNi_5) < T_{min} ($CeCo_5$) < T_{min} ($ErFe_2$ or $ErFe_3$). Coon et al. (1976) noted that the catalytic effectiveness of $LaNi_5$ increased with time at a given temperature, as illustrated in fig. 34 by the data for reaction sequences involving rising temperature and subsequently decreasing temperature. This effect of variation of catalytic activity with time has been confirmed in the systematic study of Coon et al. (1978), where the methanation reaction was investigated for the catalyst series RNi_5 (R = La, Ce, Gd, Tb, Ho, Yb), $CeCo_5$, $ErFe_2$, $ErFe_3$ and Er_2Fe_{17}. The best catalyst in the RNi_5 series was found to be $TbNi_5$ in terms of specific activity, and $CeNi_5$ in terms of maximum percent conversion (88%) into CH_4. The properties of $CeNi_5$ were very similar to a commercial Ni catalyst. The increasing activity of RNi_5 compounds with reaction time has been rationalized by Coon et al. (1978) in terms of the progressive decomposition of the intermetallic compound into rare earth oxide and transition metal during the course of the reaction. This decomposition has already been discussed in section 6.1. The essentially constant activity of the RNi_5 catalysts after the induction period over a long time period then emphasizes the dynamical aspects of the self-restoring mechanism of the active surface, which have been pointed out by Schlapbach et al. (1980).

A pronounced decrease of the catalytic activity with reaction time, however, has been found for Fe containing intermetallics by Elattar et al. (1978, 1979). This may be due to the formation of heavy carbon deposits at the surface of the metallic Fe modules of the decomposed intermetallics. Some carbon deposition during methanation reaction also occurs on Ni containing intermetallics, as shown by the Auger spectra of $TbNi_5$ (fig. 35) taken after methanation reaction (Wallace, 1978). The lineshape of the carbon Auger signal in the spectrum taken before sputtering (fig. 35, top curve) indicates the presence of graphitic carbon at the surface (Netzer, 1981), while the lineshape change of the carbon spectrum after sputtering together with the intensity increase of the Ni transitions suggest a smaller amount of carbon dissolved in the intermetallic. It has been shown by Kelley and Goodman (1981) that graphitic carbon inhibits the methanation reaction on Ni surfaces, whereas carbidic carbon is actually involved in the reaction path. We would therefore also expect some decrease in catalytic activity for Ni containing compounds, but the formation of graphitic carbon at the surface does depend on the reaction conditions (Kelley and Goodman, 1981).

Atkinson and Nicks (1977) have measured turnover numbers for the methanation reaction on mischmetal–Ni_x catalysts (mischmetal consists of a mixture of La, Ce, Pr and Nd). The active surface was determined by CO chemisorption. Atkinson and Nicks (1977) found that the system with $x = 5$ was the most effective catalyst with a turnover number about 10 times as large as on a Ni/Al_2O_3 catalyst. Luengo et al. (1977) have compared the catalytic activities of $CeAl_2$, $CeCo_2$ and $CeNi_2$ with pure Co and Ni for the methanation reaction of CO and CO_2. In their decomposed states, $CeCo_2$ and $CeNi_2$ had activities comparable to those of pure Co and Ni, but they were generally more selective than pure Co and Ni towards the formation of hydrocarbons higher than

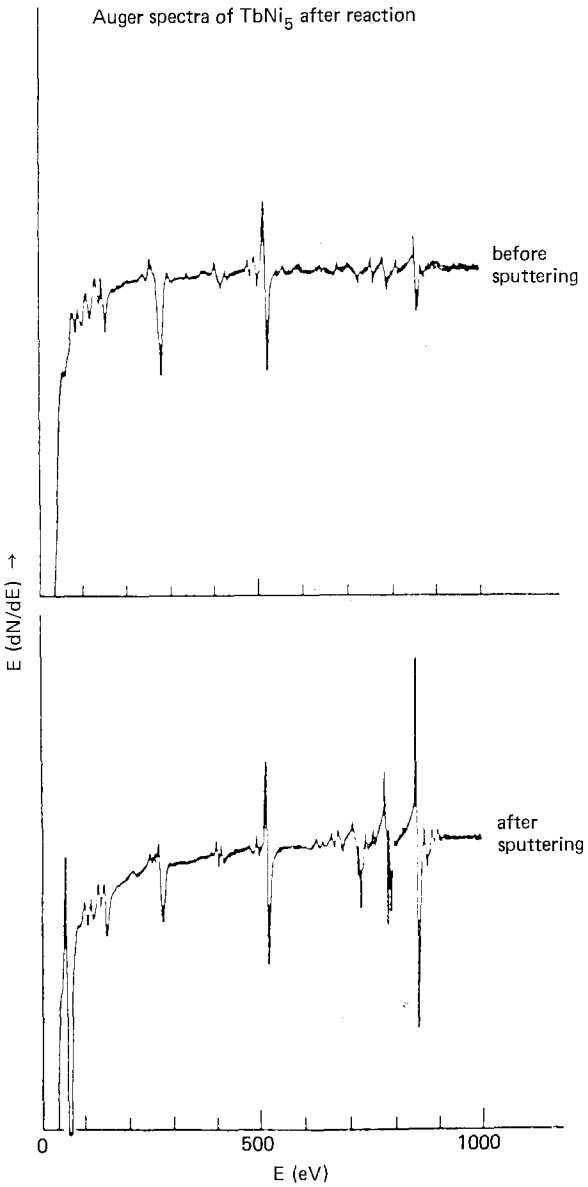

Fig. 35. The Auger spectrum of $TbNi_5$ after use as a methanation catalyst. The Ni signal at ~830 V is weak before sputtering; it intensifies with sputtering. The carbon signal at ~270 V behaves in an opposite way (Wallace, 1978).

methane. $CeAl_2$ did not decompose under reaction conditions and exhibited only moderate activity for methanation in comparison to the other catalysts, but was more stable with respect to sintering. The activities for CO_2 methanation were smaller than for CO methanation for all catalysts investigated (Luengo et al., 1977).

Considerable lower activities as compared to Fe, Co and Ni containing intermetallics have been reported for RMn_2 compounds in the methanation of

CO and CO_2 (Elattar et al., 1978). These compounds decomposed into rare earth oxides and manganese oxides under reaction conditions. The low activities of RMn_2, however, are not too surprising in view of the poor activity observed for pure Mn powder (Elattar et al., 1978).

Finally, the recent work of Elattar and Wallace (1980) should be mentioned, where CO methanation on catalysts with varying R:Ni and R:Co ratios has been investigated. While the $LaNi_x$ and $ThNi_x$ systems both showed maximum activity for $x = 2$, a very different behavior was noted for $LaCo_x$, $HoCo_x$ and $ThCo_x$ systems. As shown in fig. 36, a U-shaped curve was found for $ThCo_x$ with Th_7Co_3 exhibiting the highest activity, but $HoCo_x$ showed decreasing activity and $LaCo_x$ increasing activity with increasing Co content. The reason for this differing behavior is not yet clear.

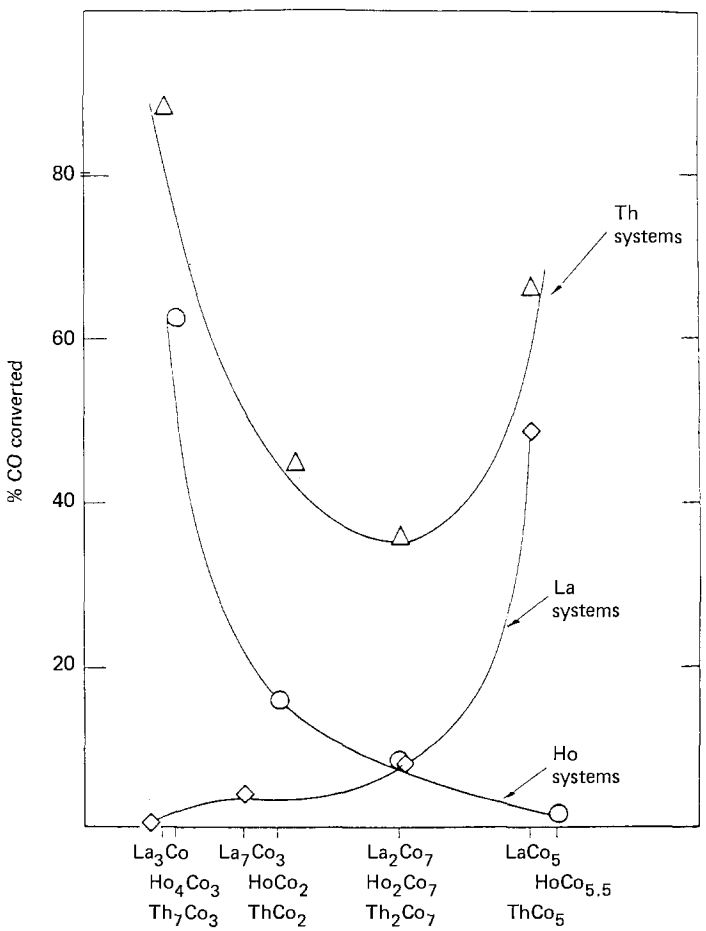

Fig. 36. Conversion of CO and H_2 to CH_4 over La–Co, Ho–Co and Th–Co systems (Elattar and Wallace, 1980).

Summarizing briefly the results on ammonia synthesis and methanation catalysis, it can be concluded that a number of rare earth intermetallics show catalytic activities exceedingly higher than those of conventional ammonia or methanation catalysts. The intermetallic compounds decompose under reaction conditions and form catalytically active transition metal particles embedded in a matrix of rare earth oxide (nitride); they can be regarded therefore as a "new class of supported catalysts". Some of these catalysts seem to be considerably more resistive towards surface poisoning than conventional supported catalysts (Wallace et al., 1977; Schlapbach et al., 1979b). The catalytic activities scale approximately with those of the respective transition metal components. The influence of the rare earth component on catalytic activity has been demonstrated, but no clear trends have as yet emerged. Although a large number of intermetallic compounds of varying composition and stoichiometry has been investigated up to date and the gross features of their catalytic behavior have been fairly well established, further work is needed to elucidate finer details of their catalytic action. For example, the influence of the stoichiometry and chemical composition of the original intermetallic on the structure of the resulting "activated" catalyst seems to be worth further investigation to understand the different activities of related intermetallics.

6.2.2. *Hydrogenation of ethylene*

The hydrogenation of ethylene over $LaNi_5$ and its hydrides $LaNi_5H_n$ (n = 0.62–2.4) has been investigated by Soga et al. (1977a) in the temperature range −60 to −84°C. Some of the results of this study have been discussed briefly in section 6.1 in conjunction with the mechanism of hydrogen absorption/desorption proposed by Wallace et al. (1979). Soga et al. (1977a) observed that the rate of formation of ethane over $LaNi_5$ hydrides was about two orders of magnitude greater than over $LaNi_5$. The rate of formation of ethane, r_t, was independent of ethylene pressure over $LaNi_5H_{2.4}$, and may be expressed by the equation

$$r_t = k_1 C_t, \tag{32}$$

where k_1 denotes a rate constant (g^{-1} of $LaNi_5$ min^{-1}), and C_t is the hydrogen concentration of the hydride at time t. Eq. (32) was found to be valid for hydrides of varying stoichiometry n, but the rate constants k_1 decreased with decreasing n of the initial hydride. The rate constants k_1 also decreased with increasing hydrogen pressure in the gas phase, thus indicating a blocking effect of molecular hydrogen.

On the other hand, the slower hydrogenation reaction over $LaNi_5$ could be described by

$$r_0 = k_2 P_{H_2}^{1} P_E^{0}, \tag{33}$$

where r_0 is the initial rate of hydrogenation, k_2 is the rate constant, and P_{H_2} and P_E the initial pressures of hydrogen and ethylene, respectively. Eq. (33), of course, leads to

$$r_t = k_2 P_{H_2,t} \tag{34}$$

which describes the time course of the hydrogenation in analogy to eq. (32). As already mentioned, k_1 was observed to be far greater than k_2.

As hydrogenation of ethylene over $LaNi_5H_n$ takes place using the hydride hydrogen, Soga et al. (1977a) suggested that the migration process of absorbed hydrogen from the bulk to the catalyst surface is the rate-determining process in this reaction. This process has been specified in more detail in the model of Wallace et al. (1979) (see section 6.1). For the hydrogenation of ethylene over $LaNi_5$, which involves H_2 from the gas phase, Soga et al. (1977a) proposed adsorption of ethylene and hydrogen on two separate parts of the surface with interaction at the borderline. Following an older model of hydrogenation of ethylene on Ni catalysts with weak molecular hydrogen adsorption and strong ethylene adsorption (Bond, 1962), the experimental rate expression of eq. (33) can be derived. This model, however, does not hold in the light of recent evidence on hydrogen and ethylene chemisorption on transition metal surfaces (Demuth, 1977, 1979; Demuth et al., 1978; Benninghoven et al., 1980).

Extending their investigations on ethylene hydrogenation, Soga et al. (1979b) have studied $PrCo_5$, $LaCo_5$, $CeCo_5$ and $SmCo_5$ and their respective hydrides as catalysts in this reaction. In general, very similar results as for $LaNi_5$ were obtained for the other intermetallics, but a different behavior was noted on the influence of hydrogen pressure on reaction rates over hydrides. This is shown in fig. 37, where initial hydrogenation rates are plotted as a function of hydrogen pressure (Soga et al., 1979b). With increasing hydrogen pressure the hydrogenation rate was markedly diminished in the case of $LaNi_5H_{2.4}$, but hardly affected in the cases of $CeCo_5H_{1.7}$ and $SmCo_5H_{1.2}$, and even accelerated to some extent for $PrCo_5H_{2.4}$ and $LaCo_5H_{1.9}$. The reason for such a different effect of hydrogen pressure over various alloy hydrides is not clear at present. Further investigation of this effect would be highly desirable in view of the possible implication of these observations on the mechanism of ethylene hydrogenation.

An interesting experimental approach has been adopted recently by Soga et al. (1980) in a study of the hydrogenation of ethylene on a compact $LaNi_5$ plate. The two reactants, hydrogen and ethylene, were kept separated on the two sides of the plate, and a reaction was observed to occur, caused by hydrogen which came out from the plate after passing through the plate from the opposite side. The results led to the conclusion that the rate-determining step of the hydrogen transfer through the plate is the migration of atomic hydrogen from the bulk of the plate to its surface.

Finally, Imamura and Wallace (1980c) prepared active catalysts for ethylene hydrogenation by treating intermetallics ($LaNi_5$, $CeNi_5$, $PrNi_5$, $ThNi_5$ and $ThCo_5$) with oxygen at 350°C. This treatment, of course, decomposes the intermetallic compounds into transition metal and rare earth or Th oxide. Accordingly, it has been observed that there was a progressive increase in the quantity of the transition metal phase and the oxide phase as the extent of oxidation increased. The kinetics of ethylene hydrogenation over these catalysts was the same as observed by Soga et al. (1977a, 1979b), i.e. first order with respect to hydrogen and zero order in ethylene. Imamura and Wallace (1980c) compared the first order

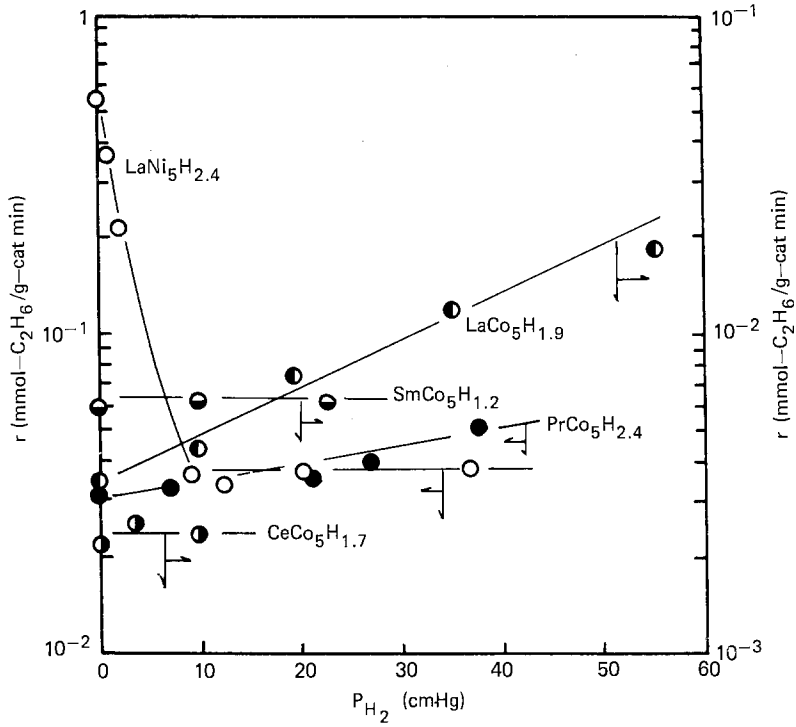

Fig. 37. Dependence of the initial hydrogenation rates, r, on the pressure of hydrogen. Hydrogenation reactions were conducted at −78°C over 0.4 g of each alloy (Soga et al., 1979b).

rate constants obtained on the decomposed intermetallics with those on several oxide-supported Ni catalysts, which were prepared by the conventional impregnation method (Ni/La_2O_3, Ni/CeO_2, Ni/Pr_2O_3 etc.). The activities of the decomposed intermetallics were clearly superior to those of the corresponding Ni catalysts prepared by the wet chemical method. These results indicate that the increased activity of the catalysts derived from intermetallics must be due to a geometrical structure effect, and they emphasize the need for detailed structure information of these materials.

6.2.3. *Other catalytic reactions*

Oesterreicher et al. (1980) and Oesterreicher and Spada (1980) have recently reported the formation of H_2O by catalytic reaction of metal hydrides with ambient oxygen. Several hydrides of rare earth intermetallics were found to be active for this reaction at room temperature, e.g. hydrides of $YbNi_2$, $DyRu_2$, $CeNi_3$, $LaNi_5$, $LaNi_4Mn$, while others were not ($ErFe_2$, $ErFe_3$). A number of rehydriding and water forming cycles could be performed on the active intermetallics, and Oesterreicher et al. (1980) concluded from X-ray diffraction measurements that no decomposition of the intermetallics had occurred under reaction conditions. In view of the experimental evidence presented in this section, however, the surface region of the respective intermetallics was most

probably decomposed into transition metal and rare earth oxide (or hydroxide). This surface decomposition, of course, cannot be detected by X-ray diffraction. It appears, therefore, that transition metal particles are most likely to be the active agents in these reactions, too. Concerning the Ni containing compounds it is interesting to note that water formation at room temperature does not occur by reaction of coadsorbed oxygen and hydrogen on clean Ni surfaces (Netzer and Madey, 1981). The rare earth component must have a decisive influence on the reaction in the present case.

As oxidation of rare earth intermetallics with oxygen proved to be successful in preparing active hydrogenation catalysts (Imamura and Wallace, 1980c), these authors investigated intermetallic compounds oxidized with bromine in the n-pentane isomerization (Imamura and Wallace, 1980b). Intermetallic compounds of rare earth metals (La, Ce, Pr, Sm and Th) and aluminum were chosen to be oxidized with bromine, because Lewis acids combined with halogen containing promoters are known to be active catalysts for isomerization reactions (Pines and Hoffman, 1964). The oxidation with bromine and the subsequent isomerization reaction were performed in the liquid phase with methylene chloride as solvent. All catalysts showed activity for n-pentane isomerization with a high selectivity for isopentane. The chemical identity of the active catalysts has to be revealed in further investigations, but a compound different from a simple mixture of $AlBr_3$ and rare earth bromides has been suggested.

In closing this section, mention should be made of the work of Pountney et al. (1979), where an attempt was made to correlate catalytic behavior with electronic structure, lattice structure and surface composition. The two pseudobinary systems $CeRh_{3-x}Pd_x$ and $ZrRh_{3-x}Pd_x$ ($0 \leq x \leq 3$) were chosen as catalysts in the hydrogenation of 1-octyne, since a systematic variation in electron concentration may be obtained. Lattice parameter and magnetic susceptibility measurements on the two sets of powdered alloys indicated significant differences at $x > 2.4$, which were interpreted in terms of differences in the rate of filling of the d-type conduction band with increasing Pd content. As differences in the catalytic behavior between the two systems were observed in the same composition range, these have been related to the change in density of d-states as the Rh is replaced by Pd. Surface analysis has been performed by Auger spectroscopy, and pronounced deviations from the bulk composition at the surface were noted, in particular in the case of the Ce alloys. Although complete unfolding of the strongly overlapping electronic and geometrical effects on catalytic activity could not be achieved by Pountney et al. (1979), this work shows the direction for future studies to reveal the influence of physical and chemical parameters in catalytic processes.

7. Synopsis and outlook for future developments

We have attempted in this chapter to highlight various aspects of surface chemistry on rare earth materials. Due to the very different reactivities of

various rare earth surfaces towards common gaseous reactants we have divided surface reactions into two categories: (1) reactive interactions of gases with rare earth surfaces leading eventually to compound formation, and (2) reactions between gaseous reaction partners on rare earth surfaces, i.e. catalytic reactions. The high reactivity of rare earth metals limits their usefulness as catalysts in most catalytic reactions, but interesting insights into the initial stages of compound formation have been obtained from studies of the reactions of several gases with these surfaces. We have discussed changes in electronic structure during metal-to-compound transitions, and have assessed kinetic data of surface compound formation. These results may be of importance for many practical applications of rare earth metals, as the metals are most likely to be covered by a compound layer under usual practical conditions.

Rare earth oxide surfaces are rather stable under common catalytic reaction conditions and they have been shown to exhibit high catalytic activities in a variety of catalytic reactions. The rare earth oxides provide an interesting class of catalytic materials with similar geometrical structure and cation valency, but continuously varying properties such as ion radii or magnetic moments. This is associated with the filling of the 4f shell in going from La to Lu. We have compiled reported catalytic data for a number of reaction types, and have attempted to evaluate critically the connection of trends in catalytic activity with the variation of physical parameters along the rare earth series.

In the surface chemistry of rare earth containing intermetallic compounds aspects of both reactions on and reactions with rare earth surfaces are intimately related. These surfaces decompose under the influence of many gaseous reactants, but the resulting surfaces show high activities in the catalysis of hydrogenation reactions. As hydrides of rare earth intermetallics may be of technical importance as hydrogen storage devices, surface processes and kinetics of hydride formation have been discussed here in some detail. The interesting catalytic properties of these materials have been described, and their possible application as a new class of catalysts has been emphasized.

For future developments, many questions are left to be answered. The application of modern techniques of surface science has begun only recently, and progress in understanding surface phenomena on rare earth materials can be expected in the near future. For example, one of the most urgent problems in catalysis, the characterization of the catalyst surface, can now be tackled using surface analysis techniques such as XPS and AES, and information on the chemical state of the surface can be obtained. The influence of catalyst pretreatment procedures on catalytic activities can then be recognized and the most appropriate conditions be established. More detailed data on adsorption properties on surfaces relevant in catalysis are clearly needed and should be obtained under well-defined conditions. The preparation of catalyst surfaces under contamination-free conditions, in the case of oxides, for instance, by oxidation of UHV evaporated rare earth metal films, and in-situ characterization of these surfaces is now possible and should be encouraged. Also, the investigation of catalytic reactions by techniques able to yield information on a

microscopic scale should contribute to solving questions concerning reaction mechanisms. In the case of rare earth oxides, the correlation between trends of catalytic activity and varying physicochemical parameters of the rare earth cations, which has been claimed to exist for several reactions, can only be substantiated by more reliable results. In general, the developments made in catalytic science on d transition metal materials in recent years should be reflected in rare earth catalysis, and no overoptimism seems necessary to predict similar progress for surface reactions on rare earth materials.

Concerning reactions with rare earth metals the changes in electronic structure during metal-to-compound transitions are now being studied extensively in several laboratories using combinations of surface-sensitive techniques. Data are now available for polycrystalline substrates, and most likely future developments might involve studies on single crystal surfaces. Although surface cleaning is a serious problem, it should be possible to obtain reasonably clean single crystal surfaces for the more reactive metals. The surface structure information, which can be obtained on single crystal surfaces, is necessary to specify proposed models for various gas–rare earth metal interactions, and studies are likely to be prompted in these directions.

Rare earth intermetallics show many fascinating surface features, so that continuing scientific interest seems to be guaranteed. In particular, the surface structure of catalysts derived from intermetallic compounds should be investigated in detail to understand their catalytic behavior. Chemical analysis with high spacial resolution, as can be obtained in scanning Auger microscopes (SAM), may be suited to achieve this goal. Surface studies of gas interaction with intermetallic compounds are likely to be further stimulated by a growing interest in technical applications of these materials.

Acknowledgements

We would like to thank many colleagues working in this field for sending us reprints of their work and, in particular, W.K. Hall, J. Onsgaard, M.P. Rosynek, L. Schlapbach, H.C. Siegmann and W.E. Wallace for providing preprints prior to publication. F.P.N. acknowledges the excellent hospitality of T.E. Madey and C.J. Powell, Surface Science Division, National Bureau of Standards, Washington D.C. and the Max-Kade-Foundation, New York, for financial support during his stay at NBS. E.B. wishes to thank H.L. Gruber, E. Bechtold and R. Kramer, Institut für Physikalische Chemie, Universität Innsbruck, for many enlightening discussions as well as M. Gasgnier for some suggestions and critical remarks. We are grateful to G. Strasser, H.P. Martinz and H. Leonhard, University of Innsbruck, for help in preparing this manuscript, and to Ms. Monika Hassl for typing the manuscript. This work was supported in part by the Jubiläumsfonds of the Austrian Nationalbank.

References

Aharoni, C. and F.C. Tompkins, 1970, Advan. Catal. **21**, 1.

Alefeld, G. and J. Völkl, eds., 1978, Hydrogen in Metals, Vols. 1 and 2 (Springer, Berlin).

Allen, J.W., J.I. Johansson, I. Lindau and S.B. Hagström, 1980, Phys. Rev. B **21**, 1335.

Alvarado, S.F., M. Campagna and W. Gudat, 1980, J. Electr. Spectr. Rel. Phen. **18**, 43.

Ames, L.L., P.N. Walsh and D. White, 1967, J. Phys. Chem. **71**, 2707.

Antoshin, G.V., K.M. Minachev and R.V. Dmitriev, 1967a, Russ J. Phys. Chem. **41**, 1587.

Antoshin, G.V., K.M. Minachev and R.V. Dmitriev, 1967b, Izv. Akad. Nauk SSSR, Ser. Khim. **8**, 1864.

Antoshin, G.V., K.M. Minachev and R.V. Dmitriev, 1968, Kinet. Katal. **9**, 816.

Antoshin, G.V., K.M. Minachev and M.E. Lokhuary, 1971, J. Catal. **22**, 1.

Aras, V.M., M. Breysse, B. Claudel, L. Faure and M. Guenin, 1977, J. Chem. Soc. Faraday Trans. I, **73**, 1039.

Arias, J.A. and P.W. Selwood, 1974, J. Catal. **33**, 284.

Artamonov, E.V. and L.A. Sazonov, 1971, Kinet. Katal. **12**, 961.

Ashmead, D.R., D.D. Eley and R. Rudham, 1963, Trans. Faraday Soc. **59**, 207.

Ashmead, D.R., D.D. Eley and R. Rudham, 1964, J. Catal. **3**, 280.

Atkinson G., S. Coldrick, J.P. Murphy and N. Taylor, 1976, J. Less-Common Met. **49**, 439.

Atkinson, G.B. and L.J. Nicks, 1977, J. Catal. **46**, 417.

Bacquet, G., C. Bouysset and C. Escribe, 1976, J. Solid State Chem. **18**, 247.

Baer, Y. and G. Busch, 1974, J. Electr. Spectr. Rel. Phen. **5**, 611.

Bakulin, E.A., L.A. Balabanova, E.V. Stepin and V.V. Shcherbinina, 1971, Sov. Phys.–Solid State **13**, 189.

Bakumenko, T.T., 1965, Kinet. Katal. **6**, 74.

Baron, K. and P.W. Selwood, 1973, J. Catal. **28**, 422.

Barr, T.L., 1978a, J. Phys. Chem. **82**, 1801.

Barr, T.L., 1978b, ESCA Examination of Rare Earth and Near Rare Earth Species, in: Quantitative Surface Analysis of Materials, ASTM STP 643, ed. N.S. McIntyre (ASTM, Philadelphia).

Beaudry, B.J. and K.A. Gschneidner, Jr., 1978, Preparation and Basic Properties of the Rare Earth Metals, in: Handbook on the Physics and Chemistry of Rare Earths, Vol. 1, eds. K.A. Gschneidner, Jr. and L. Eyring (North-Holland, Amsterdam) ch. 2.

Benninghoven, A., P. Beckmann, D. Greifendorf and M. Schlemmer, 1980, Appl. Surf. Sci. **6**, 288.

Bernal, S. and J.M. Trillo, 1980, J. Catal. **66**, 184.

Bertel, E. and F.P. Netzer, 1980a, Surf. Sci. **97**, 409.

Bertel, E. and F.P. Netzer, 1980b, unpublished results.

Bertel, E. and F.P. Netzer, 1980c, Proc. 4th Int. Conf. Solid Surfaces, Cannes, 1980, Vol. 1, eds. D.A. Degras and M. Costa (Soc. Franc. du Vide, Paris) p. 462.

Bertel, E., F.P. Netzer and J.A.D. Matthew, 1981, Surf. Sci. **103**, 1.

Bertel, E., G. Strasser, F.P. Netzer and J.A.D. Matthew, 1982, Surface Sci. **118**, 387.

Besocke, K. and S. Berger, 1976, Rev. Sci. Instr. **47**, 840.

Bond, G.C., 1962, Catalysis by Metals (Academic Press, London).

Bonnet, J.E., 1976, J. Less-Common Met. **49**, 451.

Boreskov, G.K., 1964, Advan. Catal. Relat. Subj. **15**, 285.

Boser, O., 1976, J. Less-Common Met. **46**, 91.

Bouten, P.C.P. and A.R. Miedema, 1980, J. Less-Common Metals **71**, 147.

Breysse, M., M. Guenin, B. Claudel, H. Latreille and J. Veron, 1972, J. Catal. **27**, 275.

Breysse, M., M. Guenin, B. Claudel and J. Veron, 1973, J. Catal. **28**, 54.

Breysse, M., B. Claudel, L. Faure and M. Guenin, 1978, Chemiluminescence induced by Catalysis, in: The Rare Earths in Modern Science and Technology, eds. G.J. McCarthy and J.J. Rhyne (Plenum, New York) p. 99.

Brousseau, B., F. Frandon, C. Colliex, P. Trebbia and M. Gasgnier, 1974, Energy Loss Spectra and Optical Constants of Rare Earth Metals, Hydrides and Oxides between 5 and 200 eV, in: Vacuum UV Radiation Physics, eds. E. Koch, R. Haensel and C. Kunz (Pergamon-Vieweg, Braunschweig) p. 622.

Brundle, C.R. and A.D. Baker eds., 1978, Electron Spectroscopy: Theory, Techniques and Applications, Vol. 2 (Academic Press, London).

Campagna, M., G.K. Wertheim and E. Bucher, 1976, Spectroscopy of Homogeneous Mixed Valence Rare Earth Compounds, in: Structure and Bonding, Vol. 30 (Springer, Berlin) p. 99.

Campagna, M., G.K. Wertheim and Y. Baer, 1979, Unfilled Inner Shells: Rare Earths and their Compounds, in: Photoemission in Solids II, eds. L. Ley and M. Cardona (Springer, Berlin) ch. 4.

Cardona, M. and L. Ley eds., 1978, Photoemission in Solids, Vols. 1 and 2 (Springer, Berlin).

Celotta, R.J. and R.H. Huebner, 1979, Electron Impact Spectroscopy, in: Electron Spectroscopy: Theory, Techniques and Applications, Vol. 3, ed. C.R. Brundle and A.D. Baker (Academic Press, London).

Chamberlain, M.B. and W.L. Baun, 1975, J. Vac. Sci. Technol. **12**, 1047.

Chang, D.C., W.C. Conner and R.J. Kokes, 1973, J. Phys. Chem. **77**, 1957.

Cohen, R.L., K.W. West and K.H.J. Buschow, 1978, Solid State Commun. **25**, 293.

Cohen, R.L., K.W. West and J.H. Wernick, 1980, J. Less-Common Met. **73**, 273.

Colliex, C., M. Gasgnier and P. Trebbia, 1976, J. Physique **37**, 397.
Coon, V.T., T. Takeshita, W.E. Wallace and R.S. Craig, 1976, J. Phys. Chem. **80**, 1878.
Coon, V.T., W.E. Wallace and R.S. Craig, 1978, Methanation by Rare Earth Intermetallic Catalysts, in: The Rare Earth in Modern Science and Technology, eds. G.J. McCarthy and J.J. Rhyne (Plenum, New York) p. 93.
Copperthwaite, R.G., 1980, Surf. Interface Anal. **2**, 17.
Cox, P.A., 1975, Fractional Parentage Methods for Ionization of Open Shells of d and f Electrons, in: Structure and Bonding, Vol. 24 (Springer, Berlin) p. 59.
Cox, P.A., 1981, J. Electr. Spectr. Rel. Phen. **22**, 77.
Craig, R.S., W.E. Wallace and H.K. Smith, 1981, Hydrogenation of Intermetallic Compounds, in: The Science and Technology of Rare Earth Materials, eds. W.E. Wallace and E.C. Subbarao (Academic Press, New York), to be published.
Cremer, E., 1929, Z. Phys. Chem. A **144**, 231.
Curzon, A.E. and O. Singh, 1975a, J. Less-Common Met. **39**, 227.
Curzon, A.E. and O. Singh, 1975b, J. Phys. D.: Appl. Phys. **8**, 1703.
Curzon, A.E. and O. Singh, 1978, J. Phys. F: Metal Phys. **8**, 1619.
Darnell, A.J., 1978, The Rare Earth Carboxides, in: The Rare Earth in Modern Science and Technology, eds. G.J. McCarthy and J.J. Rhyne (Plenum, New York) p. 297.
Demuth, J.E., 1977, Surf. Sci. **65**, 369.
Demuth, J.E., 1979, Surf. Sci. **80**, 367.
Demuth, J.E., H. Ibach and S. Lehwald, 1978, Phys. Rev. Lett. **40**, 1044.
Dent, A.L. and R.J. Kokes, 1969, J. Phys. Chem. **73**, 3781.
Dexpert-Ghys, J., C. Loier, Ch.H. La Blanchetais and P.E. Caro, 1975, J. Less-Common Met. **41**, 105.
Dufour, G., R.C. Karnatak, J.-M. Mariot and C. Bonelle, 1976, Chem. Phys. Lett. **42**, 433.
Eastman, D.E., 1970, Phys. Rev. B **2**, 1.
Elattar, A. and W.E. Wallace, 1980, Catalysis Using Rare Earth Intermetallics, in: The Rare Earths in Modern Science and Technology, Vol. 2, eds. G.J. McCarthy, J.J. Rhyne and H.B. Silber (Plenum, New York) p. 533.
Elattar, A., W.E. Wallace and R.S. Craig, 1978, Intermetallic Compounds as Catalysts for Hydrogenation of Carbon Oxides, in: The Rare Earths in Modern Science and Technology, eds. G.J. McCarthy and J.J. Rhyne (Plenum, New York) p. 87.
Elattar, A., W.E. Wallace and R.S. Craig, 1979, Hydrocarbon Synthesis using Catalysts Formed by Intermetallic Compound Decomposition, in: Advan. Chem. Ser. **178**, eds. E.L. Kugler and F.W. Steffgen (Am. Chem. Soc., Washington D.C.) p. 7.
Eley, D.D., H. Forrest, D.R. Pearce and R. Rudham, 1972, J.C.S. Chem. Commun. 1176.
Eley, D.D., H. Forrest and R. Rudham, 1974, J. Catal. **34**, 35.
Engelhardt, H.A., P. Feulner, H. Pfnür and D. Menzel, 1977, J. Phys. E: Sci. Instr. **10**, 1133.
Ertl, G. and J. Küppers, 1974, Low Energy Electrons and Surface Chemistry (Verlag Chemie, Weinheim).
Estrup, P.J. and E.G. McRae, 1971, Surf. Sci. **25**, 1.
Eyring, L., 1979, The Binary Rare Earth Oxides, in: Handbook on the Physics and Chemistry of Rare Earths, Vol. 3, eds. K.A. Gschneidner, Jr. and L. Eyring (North-Holland, Amsterdam) ch. 27.
Falconer, J.L. and R.J. Madix, 1977, J. Catal. **48**, 262.
Färber, W. and P. Braun, 1974, Surf. Sci. **41**, 195.
Feibelman, P.J. and D.R. Hamann, 1980, Solid State Commun. **34**, 215.
Felmlee, T.L. and L. Eyring, 1968, Inorg. Chem. **7**, 660.
Felton, R.C., M. Prutton, J.A.D. Matthew and W. Zinn, 1979, Surf. Sci. **79**, 117.
Filippova, A.A., A.A. Davydov and Y.M. Shchekochikhin, 1973, Kinet. Katal. **14**, 1333.
Foex, M. and J.P. Traverse, 1966, Bull. Soc. Franc. Miner. Crist. **89**, 184.
Friedel, J., 1972, Ber. Bunsen-Ges. **8**, 828.
Fuggle, J.C., 1981, High Resolution Auger Spectroscopy of Solids and Surfaces in: Electron Spectroscopy: Theory, Techniques and Applications, Vol. 4, eds. C.R. Brundle and A.D. Baker (Academic Press, London).
Fujimori, A., F. Minami and N. Tsuda, 1980, Phys. Rev. B **22**, 3573.
Ganichenko, L.G., 1967, Kinet. Katal. **8**, 924.
Garcia Fierro, J.L. and J.A. Pajares, 1980, J. Catal. **66**, 222.
Gasgnier, M., 1980, Phys. Stat. Sol.(a) **57**, 11.
Gayer, K.H. and W.G. Bos, 1964, J. Phys. Chem. **68**, 2569.
Gayer, K.H. and J.J. Grunwald, 1969, Z. Anorg. Allgem. Chemie **368**, 327.
Gayer, K.H. and D.J. Melotik, 1968, Z. Anorg. Allgem. Chemie **363**, 105.
Gimzewski, J.K., S. Affrossman, M. Gibson, L.M. Watson and D.J. Fabian, 1979, Surf. Sci. **80**, 298.
Goldwasser, J. and W.K. Hall, 1980, J. Catal. **63**, 520.
Goldwasser, J. and W.K. Hall, 1981, J. Catalysis **71**, 53.
Gonzales Tejuca, L., C. Jandula Cordoba and J.L. Garcia Fierro, 1979, Z. Phys. Chem. NF **118**, 99.
Goudy, A., W.E. Wallace, R.S. Craig and T. Takeshita, 1978, Thermodynamics and Kinetics of Hydrogen Absorption in Rare Earth–Cobalt and Rare Earth–Iron Compounds, in: Advan. Chem. Ser. **167**, ed. R. Bau (Am. Chem. Soc. Washington D.C.) p. 312.
Gualtieri, D.M., K.S.V.L. Narasimham and T. Takeshita, 1976, J. Appl. Phys. **47**, 3432.
Guenin, M., 1973, Ann. Chim. **8**, 147.
Gupta, M., 1978, Solid State Commun. **27**, 1355.

Harrison, L.G. and C.A. McDowell, 1953, Proc. Roy. Soc., Ser. A **220**, 77.
Hattori, T., J. Inoko and Y. Murakami, 1976, J. Catal. **42**, 60.
Haynes, H.W., Jr., 1978, Catal. Rev.-Sci. Eng. **17**, 273.
Helms, C.R. and W.E. Spicer, 1972, Appl. Phys. Lett. **21**, 237.
Holloway, D.M. and W.E. Swartz, Jr., 1977, Appl. Spectrosc. **31**, 167.
Hölzl, J. and F.K. Schulte, 1979, Work Function of Metals, in: Solid Surface Physics, ed. G. Höhler (Springer, Berlin).
Ibragimova, F.M. and K.V. Topchieva, 1969, Vestn. Mosk. Univ. Khim. **24**, 14.
Imamura, H. and W.E. Wallace, 1980a, Kinetics of Desorption of Hydrogen from RFe_2H_n Systems, in: The Rare Earths in Modern Science and Technology, Vol. 2, eds. G.J. McCarthy, J.J. Rhyne and H.B. Silber (Plenum, New York) p. 571.
Imamura, H. and W.E. Wallace, 1980b, J. Catal. **64**, 238.
Imamura, H. and W.E. Wallace, 1980c, J. Phys. Chem., **84**, 3145.
Johansson, L.I., J.W. Allen, I. Lindau, M.H. Hecht and S.B. Hagström, 1980, Phys. Rev. B **21**, 1408.
Kaldis, E. and W. Peteler, 1980, Proc. Int. Conf. Thermal Analysis, Bayreuth, 1980 (Birkhaeuser, Basel) p. 67.
Katzer, J.R., 1977, Molecular Sieves II, ACS Symposium Series **40** (Am. Chem. Soc., Washington D.C.).
Kelley, R.D. and D.W. Goodman, 1981, The Methanation Reaction, in: Chemical Physics of Solid Surfaces and Heterogeneous Catalysis, Vol. 4, eds. D.A. King and P.D. Woodruff (Elsevier, Amsterdam) to be published.
Kharitonov, A.S., G.I. Panov, G.K. Boreskov and E.M. Moroz, 1980, React. Kin. Catal. Lett. **15**, 263.
Khodakov, Y.S., V.S. Nakhshunov and K.M. Minachev, 1971, Kinet. Katal. **12**, 535.
Khodakov, Y.S., S.N. Torbin and K.M. Minachev, 1972, Izv. Akad. Nauk SSSR, Ser. Khim. **5**, 1048.
Khodakov, Y.S., V.V. Lobachev and K.M. Minachev, 1975a, Izv. Akad. Nauk SSSR, Ser. Khim. **10**, 2167.
Khodakov, Y.S., V.K. Nesterov and K.M. Minachev, 1975b, Izv. Akad. Nauk SSSR, Ser. Khim. **9**, 2012.
Khodakov, Y.S., P.A. Makarov, E.B. Panasenko, V.A. Masloboev and K.M. Minachev, 1975c, Izv. Akad. Nauk SSSR, Ser. Khim. **9**, 2015.
Knotek, M.L. and P.J. Feibelman, 1979, Surf. Sci. **90**, 78.
Koel, B.E., G. Praline, H.-I. Lee, J.M. White and R.L. Hance, 1980, J. Electr. Spectr. Rel. Phen. **21**, 31.
Konenko, I.R., A. Nazhm, A.A. Tolstopyatova, G.N. Makarenko and G.V. Samsonov, 1970, Izv. Akad. Nauk SSSR, Ser. Khim. **12**, 2710.
Konenko, I.R., A. Nazhm, A.A. Tolstopyatova, G.V. Samsonov and G.N. Makarenko, 1971, Ivz. Akad. Nauk SSSR, Ser. Khim. **1**, 100.
Konenko, I.R., R.K. Gaifutdinova, L.S. Gorshkova, G.V. Samsonov, A.A. Tolstopyatova and N.I. Moreva, 1975, Kinet. Katal. **16**, 431.
Korst W.L. and J.C. Warf, 1966, Inorg. Chem. **5**, 1719.
Kreisberg, V.A., K.V. Topchieva and A.Y. Loginov, 1973, Kinet. Katal. **14**, 1065.
Krupay, B.W. and R.A. Ross, 1978, Can. J. Chem. **56**, 2447.
Kuijpers, F.A. and B.D. Loopstra, 1971, J. Phys. Suppl. **32**, C1-667.
Kunz. C., ed., 1979, Synchrotron Radiation: Techniques and Applications (Springer, Berlin).
Landolt, M., F. Meier, P. Zürcher, H. Oestereicher, W. Ensslen, J. Hoenigschmid and E. Bucher, 1979, Solid State Commun. **32**, 1009.
Lang, J.K. and Y. Baer, 1979, Rev. Sci. Instr. **50**, 221.
Lang, J.K., Y. Baer and P.A. Cox, 1981, J. Phys. F: Metal Phys. **11**, 121.
Lawless, K.R., 1974, Rep. Prog. Phys. **37**, 231.
Leffler, A.J., 1965, J. Chem. Phys. **43**, 4410.
Libowitz, G.G., 1972, Ber. Bunsen-Ges. **8**, 837.
Libowitz, G.G. and A.J. Maeland, 1979, Hydrides, in: Handbook on the Physics and Chemistry of Rare Earths, Vol. 3, eds. K.A. Gschneidner, Jr. and L. Eyring (North-Holland, Amsterdam) ch. 26.
Loescher, D.H., 1971, Proc. 9th RE Res. Conf., ed. P.E. Field (NTIS, Springfield, Va.) p. 397.
Loginov, A.Y., V.A. Kreisberg and K.V. Topchieva, 1972, Vestn. Univ., Khim. **13**, 389.
Lucas, A.A. and M. Sunjić, 1972, Fast Electron Spectroscopy of Collective Excitations in Solids, in: Progress in Surface Science, Vol. 2, ed. S.G. Davison (Pergamon, Oxford).
Ludeke, R. and A. Koma, 1975, Phys. Rev. Lett. **34**, 817.
Luengo, C.A., A.L. Cabrera, H.B. McKay and M.B. Maple, 1977, J. Catal. **47**, 1.
Matsuda, Y., S. Nishibe and Y. Takasu, 1975, React. Kin. Catal. Lett. **2**, 207.
Matthew, J.A.D. and Y. Komninos, 1975, Surf. Sci. **53**, 716.
McQuillan, A.D., 1976, J. Less-Common Met. **49**, 431.
Menzel, D., 1975, Desorption Phenomena, in: Interactions on Metal Surfaces, ed. R. Gomer (Springer, Berlin) ch. 4.
Michaelson, H.B., 1977, J. Appl. Phys. **48**, 4729.
Minachev, K.M., 1973, The Catalytic Activity of Rare Earth Oxides, in: Catalysis, ed. J.W. Hightower (North-Holland, Amsterdam) p. 219.
Minachev, K.M. and Y.S. Khodakov, 1966, Izv. Akad. Nauk SSSR, Ser. Khim. **9**, 789.
Minachev, K.M., M.A. Markov and G.A. Loginov, 1961, Neftekhymia **1**, 356.

Minachev, K.M. and G.A. Loginov, 1963, Neftekhymia **3**, 181.
Minachev, K.M., G.V. Antoshin and E.A. Nasedkin, 1964, Izv. Akad. Nauk SSSR, Ser. Khim. **9**, 1715.
Minachev, K.M., D.A. Kondratev and G.V. Antoshin, 1967, Kinet. Katal. **8**, 131.
Minachev, K.M., Y.S. Khodakov and V.S. Nakhshunov, 1972, Izv. Akad. Nauk SSSR, Ser. Khim. **8**, 1892.
Minachev, K.M., Y.S. Khodakov and V.S. Nakhshunov, 1977, J. Catal. **49**, 207.
Morrison, S.R., 1977, The Chemical Physics of Surfaces (Plenum, New York).
Mueller, P., J.P. Blackledge and G.G. Libowitz, eds., 1968, Metal Hydrides (Academic Press, New York).
Müller, J., 1977, Surf. Sci. **69**, 708.
Müller, J. and N.A. Surplice, 1977, J. Phys. D: Appl. Phys. **10**, 213.
Musorin, V.A., V.V. Sakharov and L.M. Zaitsev, 1974, Russ. J. Inorg. Chem. **19**, 804.
Nakhshunov, V.S., Y.S. Khodakov, R.V. Dmitriev and K.M. Minachev, 1972, Izv. Akad. Nauk SSSR, Ser. Khim **6**, 1451.
Neckel, A., P. Rastl, R. Eibler, P. Weinberger and K. Schwarz, 1976, J. Phys. C: Solid State Phys. **9**, 579.
Netzer, F.P., 1981, Appl. Surf. Sci. **7**, 289.
Netzer, F.P. and T.E. Madey, 1981, unpublished results.
Netzer, F.P., E. Bertel and J.A.D. Matthew, 1980, Surf. Sci. **92**, 43.
Netzer, F.P., R.A. Wille and M. Grunze, 1981a, Surf. Sci. **102**, 75.
Netzer, F.P., Bertel E. and J.A.D. Matthew, 1981b, J. Phys. C: Solid State Phys. **14**, 1891.
Nguyen, L. and M. de Saint-Simon, 1972, Int. J. Mass Spectrom. Ion Phys. **9**, 299.
Nigavekar, A. and J.A.D. Matthew, 1980, Surf. Sci. **95**, 207.
Oesterreicher, H., 1980, Appl. Phys. **24**, 1.
Oesterreicher, H. and F. Spada, 1980, Mat. Res. Bull. **15**, 477.
Oesterreicher, H., H. Bittner and K. Shuler, 1979, J. Sol. State Chem. **29**, 191.
Oesterreicher, H., K. Ensslen and E. Bucher, 1980, Appl. Phys. **22**, 303.
Onsgaard, J., 1981, Proc. Symposium on Physics of Solid Surfaces, Czechoslovakia, 1980, to be published.
Onsgaard, J., S. Tougaard and P. Morgen, 1979, Appl. Surf. Sci. **3**, 113.
Onsgaard, J., S. Tougaard, P. Morgen and F. Ryborg, 1980a, J. Electr. Spectr. Rel. Phen. **18**, 29.
Onsgaard, J., S. Tougaard, P. Morgen and F. Ryborg, 1980b, Proc. 4th Int. Conf. Solid Surfaces, Cannes 1980, Vol. 2, eds. D.A. Degras and M. Costa (Soc. Franc. du Vide, Paris) p. 1361.
Orchard, A.F. and G. Thornton, 1977, J. Electr. Spectr. Rel. Phen. **10**, 1.
Padalia, B.D., J.K. Gimzewski, S. Affrossman, W.C. Lang, L.M. Watson and D.J. Fabian, 1976, Surf. Sci. **61**, 468.
Padalia, B.D., W.C. Lang, P.R. Norris, L.M. Watson and D.J. Fabian, 1977, Proc. Roy. Soc. Lond. A **354**, 269.
Pajares, J.A., J.E. Gonzales de Prado, J.L. Garcia Fierro, L. Gonzales Tejuca and S. Weller, 1976, J. Catal. **44**, 421.
Pajares, J.A., J.L. Garcia Fierro and S. Weller, 1978, J. Catal. **52**, 521.
Pantano, C.G. and T.E. Madey, 1981, Appl. Surf. Sci. **7**, 115.
Pendry, J.B., 1974, Low Energy Electron Diffraction (Academic Press, London).
Peterman, D.J. and B.N. Harmon, 1979, Phys. Rev. B **20**, 5313.
Peterman, D.J., B.N. Harmon, J. Marchiando and J.H. Weaver, 1979a, Phys. Rev. B **19**, 4867.
Peterman, D.J., B.N. Harmon, D.L. Johnson and J. Marchiando, 1979b, Z. Phys. Chem. NF **116**, 47.
Peterman, D.J., D.T. Peterson and J.H. Weaver, 1980, J. Less-Common Met. **74**, 167.
Pines, H. and N.E. Hoffman, 1964, in: Friedel-Crafts and Related Reactions, Vol. 2, ed. G.A. Olah (Wiley-Interscience, New York) p. 1211.
Platau A. and S.-E. Karlsson, 1978, Phys. Rev. B **18**, 3820.
Platau, A. and S.-E. Karlsson, 1980, Oxidation of Cerium Studied by Photoelectron Spectroscopy, in: The Rare Earths in Modern Science and Technology, eds. G.J. McCarthy and J.J. Rhyne (Plenum, New York) p. 487.
Platau, A., L.I. Johansson, A.L. Hagström, S.-E. Karlsson and S.B.M. Hagström, 1977, Surf. Sci. **63**, 153.
Pountney, J.M., I.R. Harris, J.M. Winterbottom and J.F. Smith, 1979, Surface Technol. **8**, 145.
Praline, G., B.E. Koel, R.L. Hance, H.-L. Lee and J.M. White, 1980, J. Electr. Spectr. Rel. Phen. **21**, 17.
Rabo, J.A., 1976, Zeolite Chemistry and Catalysis, ACS Monograph 171 (Am. Chem. Soc., Washington D.C.).
Raether, H., 1965, Solid State Excitations by Electrons, in: Springer Tracts in Modern Physics, Vol. 38, ed. G. Höhler (Springer, Berlin).
Raichlen, J.S. and R.H. Doremus, 1971, J. Appl. Phys. **42**, 3166.
Read, J.F., W.H. Bouma and S.E. Robertson, 1970, J. Catal. **19**, 1.
Read, J.F., 1972, Can. J. Chem. **50**, 490.
Read, J.F., 1973, J. Catal. **28**, 428.
Read, J.F. and R.E. Conrad, 1972, J. Phys. Chem. **76**, 2199.
Read, J.F. and A.L. Crandlemire, 1975, J. Catal. **38**, 54.
Read, J.F. and E.W. Perkins, 1976a, J. Catal. **42**, 443.
Read, J.F. and E.W. Perkins, 1976b, J. Catal. **42**, 455.
Read, J.F., L.G. Dunfield, R.M. Shreve and E.A. Spinney, 1974, J. Catal. **33**, 335.
Read, J.F., Y.T. Chan and R.E. Conrad, 1978, J. Catal. **55**, 166.
Read, J.F., A.R. Maxwell, V.C. Storey and G.A. Wallace, 1979a, J. Catal. **59**, 176.

Read, J.F., S.J. Amirault and Y.T. Chan, 1979b, J. Catal. **59**, 188.
Redhead, P.A., 1962, Vakuum **12**, 203.
Rivière, J.C., 1969, Work Function: Measurements and Results, in: Solid State Surf. Sci., Vol. 1, ed. M. Green (Dekker, New York) ch. 4.
Rossington, D.R. and V.F. Capozzi, 1974, J. Am. Ceram. Soc. **57**, 474.
Rosynek, M.P., 1977, Catal. Rev.-Sci. Eng. **16**, 111.
Rosynek, M.P. and J.S. Fox, 1977, J. Catal. **49**, 285.
Rosynek, M.P. and D.T. Magnuson, 1977a, J. Catal. **46**, 402.
Rosynek, M.P. and D.T. Magnuson, 1977b, J. Catal. **48**, 417.
Rosynek, M.P., J.S. Fox and J.L. Jensen, 1981, J. Catal., **71**, 64.
Rowe, J.E., M. Campagna, S.B. Christman and E. Bucher, 1976, Phys. Rev. Lett. **36**, 148.
Sandler, Y.L., 1954, Can. J. Chem. **32**, 249.
Sandrock, G.D. and P.D. Goodell, 1980, J. Less-Common Met. **73**, 161.
Sazonov, L.A. and M.G. Logvinenko, 1962, Kinet. Katal. **3**, 761.
Sazonov, L.A. and V.A. Lyadno, 1966, Kinet. Katal. **7**, 1094.
Sazonov, L.A., V.D. Sokolovskii and G.K. Boreskov, 1966a, Kinet. Katal. **7**, 284.
Sazonov, L.A., V.D. Sokolovskii and G.K. Boreskov, 1966b, Kinet. Katal. **7**, 521.
Sazonov, L.A., M.G. Logvinenko and L.M. Plyasova, 1966c, Kinet. Katal. **7**, 795.
Sazonov, L.A., E.V. Artamonov and G.N. Mitrofanova, 1971, Kinet. Katal. **12**, 378.
Sazonov, L.A., G.N. Mitrofanova, L.V. Preobrazhenskaya and Z.V. Moskvina, 1972, Kinet. Katal. **13**, 789.
Schlapbach, L., 1980, J. Phys. F: Metal Phys. **10**, 2477.
Schlapbach, L. and C.R. Brundle, 1979, Helvet. Phys. Acta **52**, 352.
Schlapbach, L. and C.R. Brundle, 1981, J. Physique, **42**, 1025.
Schlapbach, L., A. Seiler and F. Stucki, 1978, Swiss Patent 8088/78-8.
Schlapbach, L., A. Seiler, H.C. Siegmann, T. von Waldkirch and P. Zürcher, 1979a, Int. J. Hydrogen Energy **4**, 21.
Schlapbach, L., A. Seiler and F. Stucki, 1979b, Mat. Res. Bull. **14**, 785.
Schlapbach, L., A. Seiler, F. Stucki and H.C. Siegmann, 1980, J. Less-Common Met. **73**, 145.
Seah, M.P., 1980, Surf. Interface Anal. **2**, 222.
Selwood, P.W., 1966, J. Am. Chem. Soc. **88**, 2676.
Selwood, P.W., 1970, J. Catal. **19**, 353.
Selwood, P.W., 1971, J. Catal. **22**, 123.
Siegmann, H.C., L. Schlapbach and C.R. Brundle, 1978, Phys. Rev. Lett. **40**, 972.
Singh, B., N.A. Surplice and J. Müller, 1976, J. Phys. D: Appl. Phys. **9**, 2087.
Singh, O. and A.E. Curzon, 1977, Thin Solid Films **44**, 233.
Smith, H.K., A.G. Moldovan, R.S. Craig, W.E. Wallace and S.G. Gankar, 1980, J. Sol. State Chem. **32**, 239.
Soga, K., H. Imamura and S. Ikeda, 1977a, J. Phys. Chem. **81**, 1762.
Soga, K., H. Imamura and S. Ikeda, 1977b, Nippon Kagaku Kaishi **9**, 1304.
Soga, K., M. Sato, T. Sano and S. Ikeda, 1979a, J. Less-Common Met. **68**, 59.
Soga, K., H. Imamura and S. Ikeda, 1979b, J. Catal. **56**, 119.
Soga, K., T. Otsuka, M. Sato, T. Sano and S. Ikeda, 1980, J. Less-Common Met. **71**, 259.
Sokolovskii, V.D., L.A. Sazonov, G.K. Boreskov and Z.V. Moskvina, 1968a, Kinet. Katal. **9**, 130.
Sokolovskii, V.D., L.A. Sazonov, G.K. Boreskov and Z.V. Moskvina, 1968b, Kinet. Katal. **9**, 784.
Sosnina, I.E. and T.V. Meshcheryakova, 1969, Vestn. Mosk. Univ. Khim. **24**, 27.
Strasser, G., E. Bertel and F.P. Netzer, 1982, J. Catalysis, to be published.
Sugar, J., 1972, Phys. Rev. B **5**, 1785.
Surplice, N.A. and W. Brearley, 1978, Surf. Sci. **72**, 84.
Switendick, A.C., 1970, Solid State Commun. **8**, 1463.
Switendick, A.C., 1971, Int. J. Quantum Chem. **5**, 459.
Switendick, A.C., 1978, Topics Appl. Phys. **28**, 101.
Switendick, A.C., 1980, J. Less-Common Met. **74**, 199.
Takasu, Y., S. Nishibe and Y. Matsuda, 1977, J. Catal. **49**, 236.
Takeshita, T., W.E. Wallace and R.S. Craig, 1976, J. Catal. **44**, 236.
Tanaka, S., J.D. Clewley and T.B. Flanagan, 1977, J. Phys. Chem. **81**, 1684.
Thomke, K., 1977, Proc. Int. Congr. Catal. 6th, London 1977 (Chemistry Society, London) p. 303.
Tolstopyatova, A.A., I.R. Kinenko and A.A. Balandin, 1961, Kinet. Katal. **2**, 135.
Topchieva, K.V. and F.M. Ibragimova, 1967, Russ. J. Phys. Chem. **41**, 812.
Topchieva, K.V. and F.M. Ibragimova, 1968, Vestn. Mosk. Univ. Khim. **23**, 26.
Tosun, G. and H.F. Rase, 1972, Ind. Eng. Chem. Prod. Res. Develop. **11**, 249.
Tougaard, S., A. Ignatiev and D.L. Adams, 1980, Proc. 4th Int. Conf. Solid Surfaces, Cannes, 1980, Vol. 1, eds. D.A. Degras and M. Costa (Soc. Franc. du Vide, Paris) p. 667.
Touret, D. and F. Queyroux, 1972, Rev. Chim. Miner. **9**, 883.
Trebbia, P. and C. Colliex, 1973, Phys. Stat. Sol.(b) **58**, 523.
Van Hove, M.A. and S.Y. Tong, 1979, Surface Crystallography by LEED. Theory, Computation and Structural Results (Springer, Berlin).
Van Mal, H.H., K.H.J. Buschow and A.R. Miedema, 1976, J. Less-Common Met. **49**, 473.
Van Vucht, J.H.N., F.A. Kuijpers and

H.C.A.M. Bruning, 1970, Philips Res. Repts. **25**, 133.
Viallard, R. and J.N. Daou, 1973, Conf. Int. Hydrogéne Met., 1972, **1**, 123.
Von Waldkirch, T. and P. Zürcher, 1978, Appl. Phys. Lett. **33**, 689.
Voorhoeve, R.J.H., 1977, Perovskite-Related Oxides as Oxidation–Reduction Catalysts, in: Advanced Materials in Catalysis, eds. J.J. Burton and R.L. Garten (Academic Press, New York) ch. 5.
Wallace, W.E., 1978, Rare Earth and Actinide Intermetallics as Hydrogenation Catalysts, in: Hydrides for Energy Storage, eds. A.F. Andresen and A.J. Maeland (Pergamon, Oxford) p. 501.
Wallace, W.E., A. Elattar, T. Takeshita, V. Coon, C.A. Bechman and R.S. Craig, 1977, Rare Earth and Actinide Intermetallics as Catalysts, in: Proc. 2nd Int. Conf. Electronic Structure of Actinides, Wroclaw (Poland) 1977, p. 93.
Wallace, W.E., R.F. Karlicek Jr. and H. Imamura, 1979, J. Phys. Chem. **83**, 1708.
Wallace, W.E., R.F. Karlicek Jr. and H. Imamura, 1980, The Kinetics of Hydrogen Absorption by Rare Earth Intermetallics, in: The Rare Earths in Modern Science and Technology, Vol. 2, eds. G.J. McCarthy, J.J. Rhyne and H.B. Silber (Plenum, New York) p. 583.
Wandelt, K., C.R. Brundle, E. Kay, A. Poenisch and H.C. Siegmann, 1977, Proc. 7th Int. Vac. Congr. and 3rd Int. Conf. Solid Surfaces, Vienna 1977, eds. K. Dobrozemsky et al., p. 1171.
Weaver, J.H. and D.T. Peterson, 1979, Z. Phys. Chem. NF **116**, 57.
Weaver, J.H. and D.T. Peterson, 1980, J. Less-Common Met. **74**, 207.
Weaver, J.H., R. Rosei and D.T. Peterson, 1978, Solid State Commun. **25**, 201.
Weaver, J.H., R. Rosei and D.T. Peterson, 1979a, Phys. Rev. B **19**, 4855.
Weaver, J.H., D.T. Peterson and R.L. Benbow, 1979b, Phys. Rev. B **20**, 5301.
Wertheim, G.K. and G. Crecelius, 1978, Phys. Rev. Lett. **40**, 813.
Wigner, E., 1933, Z. Phys. Chem., Abt. B **23**, 28.
Winter, E.R.S., 1969a, J. Chem. Soc. A, 1832.
Winter, E.R.S., 1969b, J. Catal. **15**, 144.
Winter, E.R.S., 1971, J. Catal. **22**, 158.
Winter, E.R.S., 1974a, J. Catal. **34**, 431.
Winter, E.R.S., 1974b, J. Catal. **34**, 440.
Work, D.E. and H.A. Eick, 1972, J. Less-Common Met. **26**, 413.
Yates, J.T., Jr., 1981, Thermal Desorption of Adsorbed Species, in: Methods of Experimental Physics, ed. R.L. Park (Academic Press, New York) to be published.
Ziman, J.M., 1972, Principles of the Theory of Solids (Cambridge University Press) ch. 3.
Zimkina, J.M., V.A. Formichev, S.A. Gribovskii and T.I. Zhukova, 1967, Sov. Phys.–Solid State **9**, 1128.

Handbook on the Physics and Chemistry of Rare Earths, edited by K.A. Gschneidner, Jr. and L. Eyring

Chapter 44

DEFECTS AND PHASE TRANSFORMATION NEAR ROOM TEMPERATURE IN RARE EARTH SESQUIOXIDES

C. BOULESTEIX
Laboratoire de Microscopie Electronique Appliquée, E.R.A. No. 545,
Université Aix-Marseille III, Centre Saint-Jérôme,
Rue H. Poincaré, 13397 Marseille Cedex 13, France

Contents

Symbols

A = hexagonal, A-type sesquioxide
B = monoclinic, B-type sesquioxide
C = cubic, C-type sesquioxide
LCT = lattice conserving twins, or merohedral twins
NLCT = nearly lattice conserving twins, or pseudo-merohedral twins
NSLCT = nearly superlattice conserving twins, or reticular pseudo-merohedral twins
SLCT = superlattice conserving twins, or reticular merohedral twins
USP = unsplit plane
USR = unsplit row
ZAP = zone axis pattern
K_i, η_i = twinning elements
$\boldsymbol{d}$ = sh = shear displacement
s = shear vector
h = thickness of the twin layer, step height
θ = rotation angle
D = distance between two steps

ϕ = angle between the coherent and incoherent interface
n_{01} = number of orientation domains
g_0 = order of the point group of symmetry g_1
S_i = structures indicated by subscript

1. Introduction

Rare earth sesquioxides (R_2O_3) exhibit three different structures at room temperatures: A hexagonal, B monoclinic and C cubic (Pauling and Shappel, 1930; Koehler and Wollan, 1953; Cromer, 1957). The phase diagram showing the stability of the different structures versus temperature and atomic number is given in fig. 1. The knowledge of the high temperature phases is due to Foëx and Traverse (1966). For La_2O_3, Pr_2O_3 and Nd_2O_3 the usual structure at room temperature is hexagonal (A), but C can also occur. For Sm_2O_3, Gd_2O_3, ... the usual structure at room temperature is cubic (C), but the monoclinic (B) high temperature phase can easily be obtained for Sm_2O_3 and Gd_2O_3 at room temperature (Boulesteix et al., 1970a; Portier et al., 1973). B has also been obtained by quenching of Tb_2O_3, Dy_2O_3 and Ho_2O_3 inside an electron microscope (Boulesteix et al., 1971a). It has also been shown by Boulesteix et al. (1971a,b,c) that heated A type Nd_2O_3 and Pr_2O_3 can give the B type by quenching inside an electron microscope. In this case B is unstable and appears in an epitaxial growth on A; B type Nd_2O_3 had been observed earlier (first by Shafer and Roy (1959) by high pressure hydrothermal techniques), while the existence of the B type for

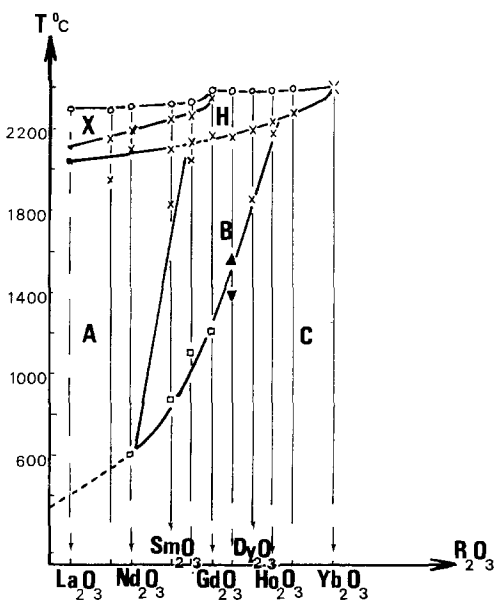

Fig. 1. Structure of R_2O_3 related to the atomic number and to the temperature, at room pressure. Three structures can be stable at $T <$ 800°C: A hexagonal, B monoclinic, C cubic; B-Nd_2O_3 could have a slight domain of stability. X and H are high temperature phases.

La_2O_3 and Pr_2O_3 (Willer and Daire, 1969; Kern and Perakis, 1970) has been strongly criticized by Gasgnier (1977, 1980).

Caro (1968) has described the R_2O_3 structure referring to the linkage of OLn_4 tetrahedra. The C structure (space group Ia3) can be described as a three dimensional framework of OR_4 tetrahedra linked by four edges among six. This structure derives from the fluorite structure (CaF_2) by eliminating one quarter of the oxygen atoms (located on the fluorine atom positions). The A structure (space group $P\bar{3}m$) can be described by slabs of OR_4 tetrahedra linked by three of their edges and forming a complex group cation $(RO)_n^{n+}$ separated by ionic oxygens O^{2-}, so that the structure appears like a pile-up of sheets. The B structure (space group C2/m) is very similar to A, but the tetrahedra are distorted. The trigonal symmetry is lost and a small displacement occurs between each $(RO)_n^{n+}$ slab. The description of the R_2O_3 structures given by Caro (1968) is very useful for the understanding of the twinning phenomena in these structures as well as for an understanding of the observed cooperative transformation between A and B. Moreover A and B types exhibit a very strong anisotropy for surface energy in good agreement with the given description of these structures as a pile-up of sheets.

The samples (thin crystals) are prepared by oxidation of metal thin films inside an electron microscope by pulse heating using the electron beam (Boulesteix et al., 1970b,c, 1971d; Gasgnier et al., 1971d, 1974; Caro et al., 1974). A general study of oxidation mechanism for thin metal films can be found in Gasgnier's thesis (1977) or in a critical review article (Gasgnier, 1980).

We shall now describe some crystallographic properties of the very similar A and B layer structures. We have especially studied twinning phenomena, antiphase domains and phase transformations and the B phase, and the A, B cooperative transformation. Then we shall describe twins and stacking faults of C. The results have been obtained by electron microscopy which is a powerful way of studying these phenomena.

2. The hexagonal (A) and monoclinic (B) structures

These two structures are very similar; each of them can be described (Caro, 1968) as slabs of ionic complex cations $(RO)_n^{n+}$ separated by ionic oxygens O^{2-} (fig. 2a,b). Each complex cation itself can be described by a slab of OR_4 tetrahedra sharing three of their edges (fig. 3). The R atoms are located at the corners of the tetrahedra and each corner is shared by four tetrahedra. The oxygen atoms are located inside the tetrahedra, so that there are the same number of R and O atoms inside the complex cation. One third of the oxygen atoms are ionic and located between the slabs of ionic complex cations.

The A structure has a hexagonal symmetry (with a S_6 axis only), while the B structure is monoclinic. In A the slabs of complex cations are parallel to the basal plane: (00 . 1), while they are parallel to the $(20\bar{1})$ plane in B (figs. 2 and 4). The B structure can be described as a deformation of A both in the basal plane

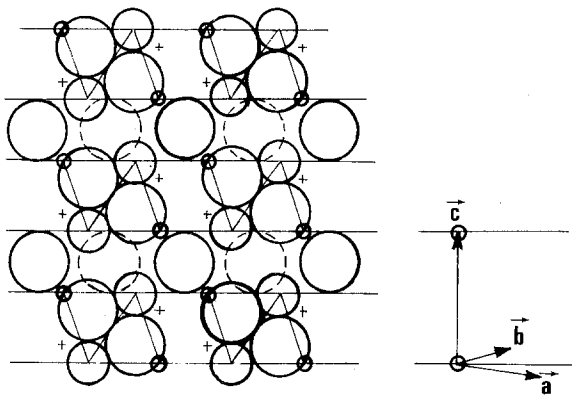

Fig. 2. (a) Hexagonal A-R_2O_3 structure with the plane of the paper parallel to the (11 . 0). The unit cell is indicated. O atoms are the larger ones. The small circles indicate R atoms above and under the plane of the paper. The projection of the OR_4 tetrahedra is indicated on the drawing.

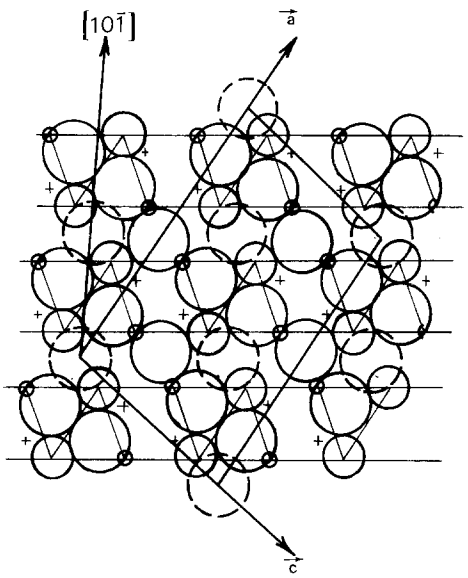

Fig. 2. (b) Monoclinic B-R_2O_3 structure with the plane of the paper parallel to the (010). The unit cell is indicated. O atoms are the larger ones. The small circles indicate R atoms above and under the plane of the paper. The projection of the OR_4 tetrahedra is indicated on the drawing.

(as shown in figs. 2 and 5), and by tilting the C axis in the symmetry plane of the B structure (010) by about 3°. This C axis of A becomes [10$\bar{1}$] in B where it has no special symmetry properties (fig. 2b).

We shall see that this description of B explains most of its special properties (except for the existence of antiphase domains and extra spots in the electron diffraction pattern that can be deduced also by comparison to the A structure, but taking into account some more sophisticated details). We shall first study the common properties of the A and B phases: the orientation of thin crystals and the existence of steps at the surface of these crystals. Then we shall study the special properties of B and finally the A, B phase transformation that we have shown to be cooperative.

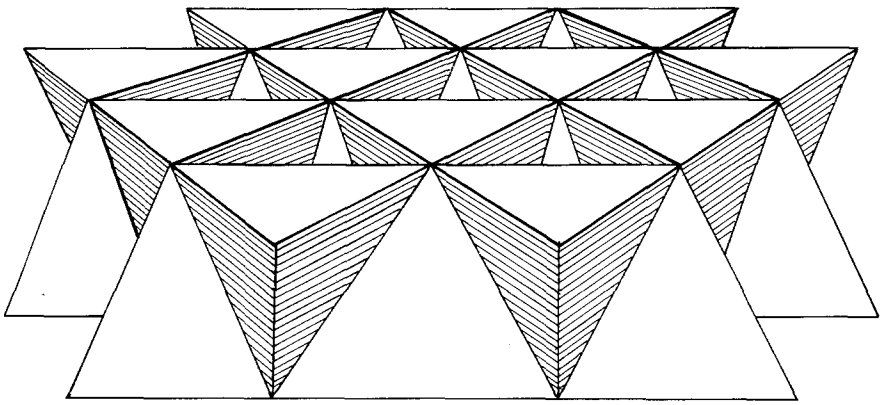

Fig. 3. Linkage of OR_4 tetrahedra in the A structure. The same linkage occurs in B but slightly deformed.

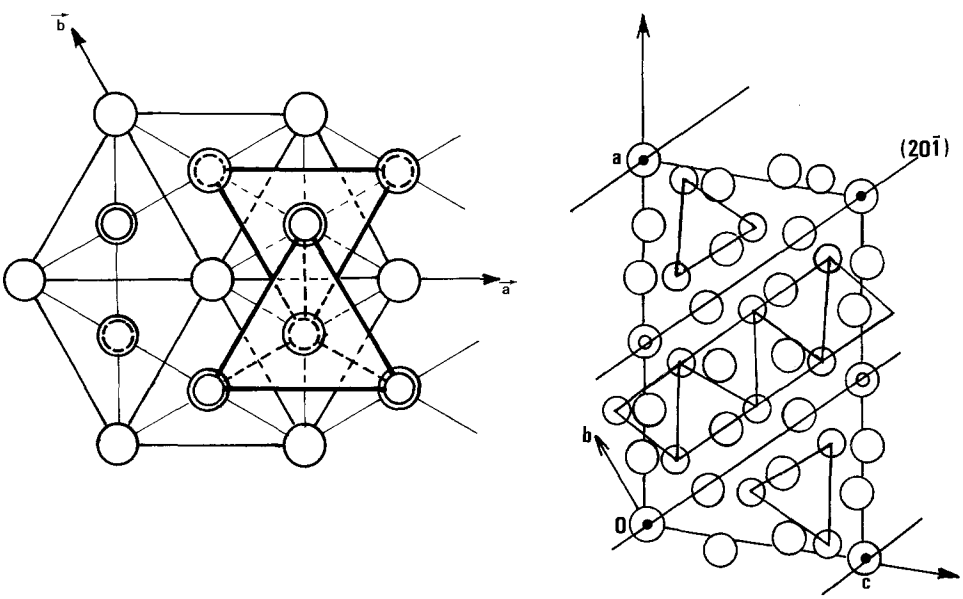

Fig. 4. (a) A structure with the plane of the paper parallel to (00 . 1); O atoms are the larger ones. The linkage of OR_4 tetrahedra has been indicated. Dotted R atoms are hidden by O atoms. (b) B structure with the plane of the paper parallel to (010). O atoms are the larger ones. The linkage of tetrahedra is parallel to the (20$\bar{1}$) plane. Centers of symmetry are located at 0,0,0: filled circles, and at 1/2,1/2,0: open circles.

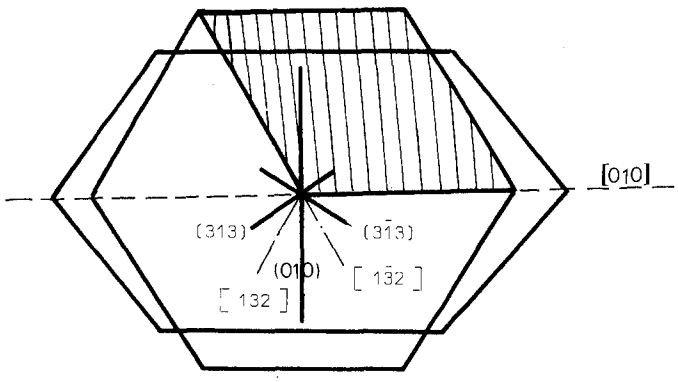

Fig. 5. B structure as a deformation of A; plane of the paper is (20$\bar{1}$) for B, (00 . 1) for A. The three symmetry planes of A{11 . 0}, are related to the (313), (3$\bar{1}$3) and (010) planes of B. The last one is the symmetry plane of B. The three symmetry axes of A, ⟨100⟩, are related to the [132], [1$\bar{3}$2] and [010] axes of B. The last one is the symmetry axis of B. The three-fold axis of A, [001], is related to the [10$\bar{1}$] axis of B; it is located inside the (010) plane, about 3° off the normal to the (20$\bar{1}$) plane.

2.1. *Properties of thin crystals of A and B structures*

The oxidation of rare earth thin films gives large thin crystals of sesquioxides (except for Ce and Eu for which one can obtain CeO_2 and EuO and for Pr and Tb which can give nonstoichiometric oxides). The diameter of these crystals is several μm, their thickness is about 500 Å. The surfaces are parallel to (00 . 1) for A crystals and to (20$\bar{1}$) for B crystals. Some other orientations can be observed, but only for thick crystals (more than 1000 Å). This orientation cannot be related to the metal thin film made up of micro-crystals without any special orientation. This result shows that the surface energy is much lower when the surface is parallel to the (00 . 1) and (20$\bar{1}$) planes than for any other orientation. They are parallel, in each case, to the $(RO)_n^{n+}$ slabs, so that the observed orientation for the thin crystals reinforces the hypothesis of Caro (1968) concerning the existence of these slabs.

If the thin crystals exhibit some holes they are hexagonal (A) or pseudo-hexagonal (B), the sides of the hexagons being parallel to the edges of the OR_4 tetrahedra (fig. 6) (Boulesteix et al., 1971d).

Defects parallel to the surface are observed very often. These defects have been identified as steps by gold evaporation in a direction 30° off the surface (Portier et al., 1973). Some of these steps show, after annealing, crystallographic directions (fig. 7a,b) parallel to the edges of the OR_4 tetrahedra. Pyramids looking like "ziggourats" (pyramids with steps) have also been observed but only in B crystals. This has been explained by the transformation of spherical C crystals in B, the free surfaces being faces of the OR_4 tetrahedra and the edges being, once more, parallel to the edges of these tetrahedra. Small steps ($\approx$ 10 Å) are

quite common on these samples; they look like dislocations (parallel to the surface) with which they could be confused. Nevertheless, the distinction is possible because the image is not modified by tilting as in the case of dislocations, while it is by defocusing; moreover the image of the defect disappears when it is perfectly focused. This shows that the contrast is due to a phase effect, and from this it can be concluded that the defects are surface steps. These steps are visible down to a height probably smaller than 10 Å. This height (if not too large and if the crystal is thin) can be evaluated by looking at the contrast under special conditions (Boulesteix et al., 1978a). If the crystal is very thick the inelastic scattering lowers the contrast and the steps get less visible. Nevertheless, for very thick crystals (15000 Å) such steps can be observed easily using multi-beam illuminating conditions (Pardo, 1977).

2.2. *Twinning of the B structure (B treated as a deformation of A)*

The space group for the A structure is (Koehler, 1953)

$$D_{3d}^3 \text{ or } P\bar{3}m: \quad \left(A_3, \frac{3A_2}{3M}, C\right),$$

while it is

$$C_{2h}^3 \text{ or } C\frac{2}{m}: \quad \left(\frac{A_2}{M}, C\right)$$

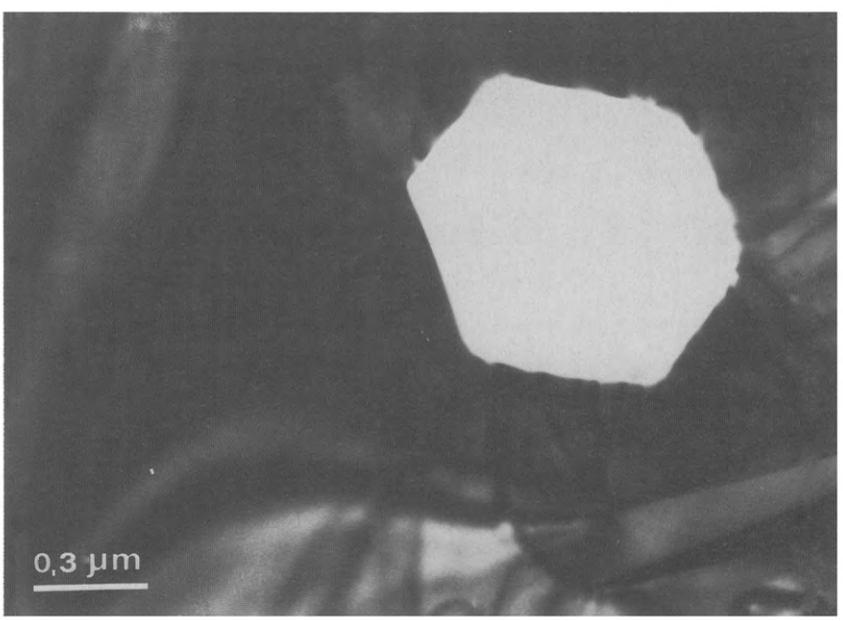

Fig. 6. Thin crystal of B-Sm_2O_3 exhibiting a hole with sides parallel to the edges of the OR_4 tetrahedra.

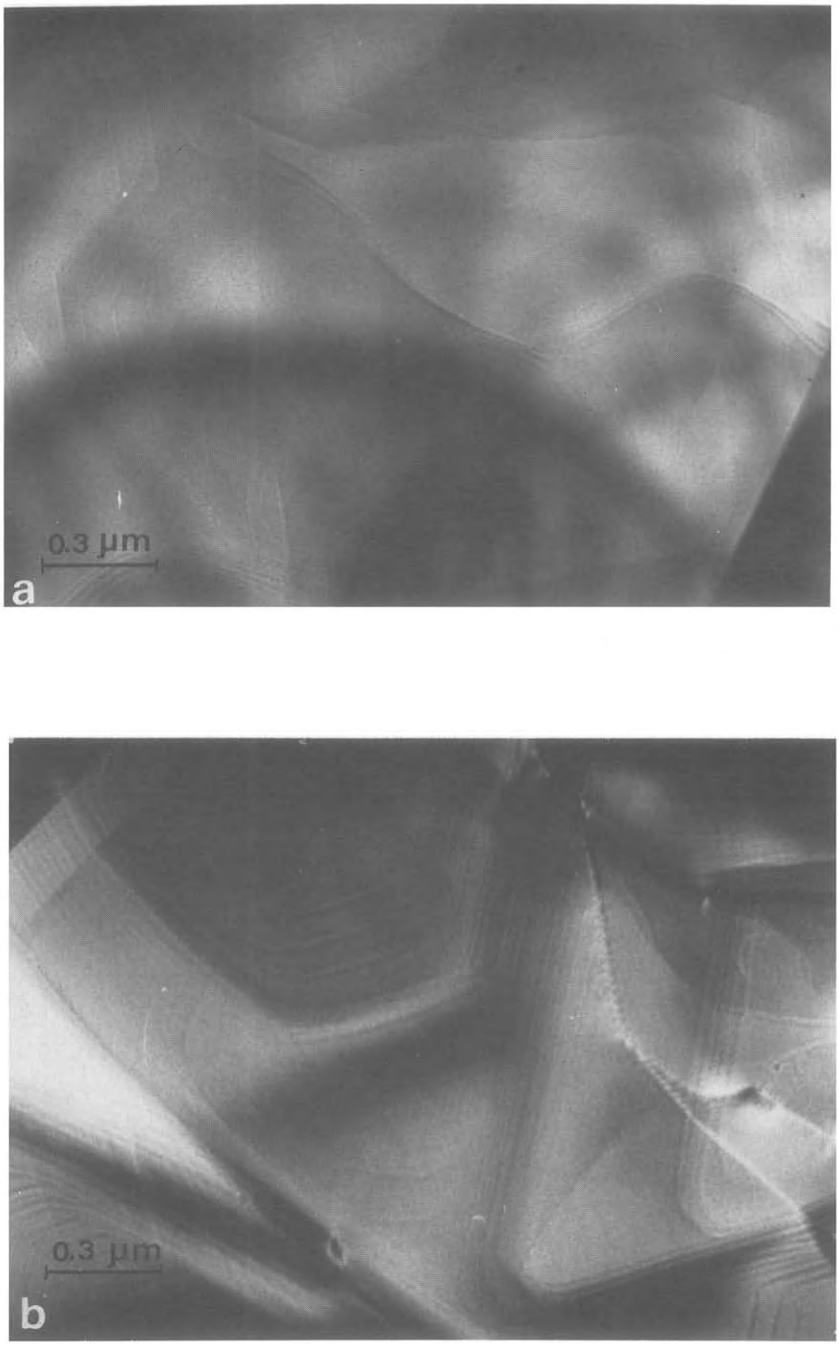

Fig. 7. (a) Surface steps of B-Sm_2O_3 visible out of focus. (b) Surface steps of B-Sm_2O_3 after annealing.

for the B structure (Cromer, 1957). Both structures have a center of symmetry located at the origin (or, for B, located at 1/2, 1/2, 0, which is equivalent to 0, 0, 0, B being base centered). Since B is a slight deformation of A (Caro, 1968), two symmetry planes, two symmetry axes and the A_3 rotation axis become pseudo-symmetry elements (fig. 5). It is quite usual that symmetry through a pseudo-symmetry element (plane or axis) gives rise to a twin, said to be a pseudo-merohedral twin or a nearly lattice conserving twin: NLCT (appendix). This happens for B-R_2O_3 (Boulesteix et al., 1972) where the two pseudo-symmetry planes give rise to two type I twins, and where the two pseudo-symmetry axes give rise to two type II twins; type I and type II twins are reciprocal twins. These twins being pseudo-merohedral twins (or NLCT), the twinning occurs with a shear displacement and the shape of a crystal is different before and after twinning (fig. 8). In this case, twinning can occur by stressing the crystal (mechanical twins). This is the case for the two kinds of twins of the B structure.

We shall study the following topics: twinning elements, mechanical twin formation, twin junction and twin intersection, twin by crystal growth and grain boundaries, the real structure of B, and A, B phase transformation and the domains of B by phase transformation.

2.2.1. *Twinning elements*

The three {11 . 0} planes of the A structure, which are symmetry elements, are related in B to the (010) plane which is a symmetry element and to the two pseudo-symmetry elements (313) and ($3\bar{1}3$) which are equivalent. (313) and ($3\bar{1}3$) are the twinning planes K_1 (appendix) of type I twins in B (fig. 5).

The three [100] axes of A, which are symmetry elements, are related in B to the [010] axis which is a symmetry element and to the two pseudo-symmetry elements [132] and [$1\bar{3}2$] which are equivalent. [132] and [$1\bar{3}2$] are the twinning axes η_1 (appendix) of type II twins in B (fig. 5).

This description of these four kinds of twins of B, related to A, gives immediately the position of the twin elements in B: the symmetry elements of A containing the center of symmetry, it is the same for the twinning elements of B. So that the twinning planes {313} and the twinning axes ⟨132⟩ contain the origin 0, 0, 0 or the equivalent node 1/2, 1/2, 0 (fig. 4a). Then the twin planes {313} related to the {11 . 0} planes of A contain the R atoms, while the twin axes ⟨132⟩ do not

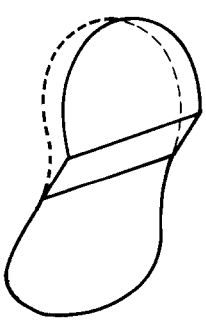

Fig. 8. Shear deformation of B crystals by twinning. Dotted line indicates the formal location of the crystal.

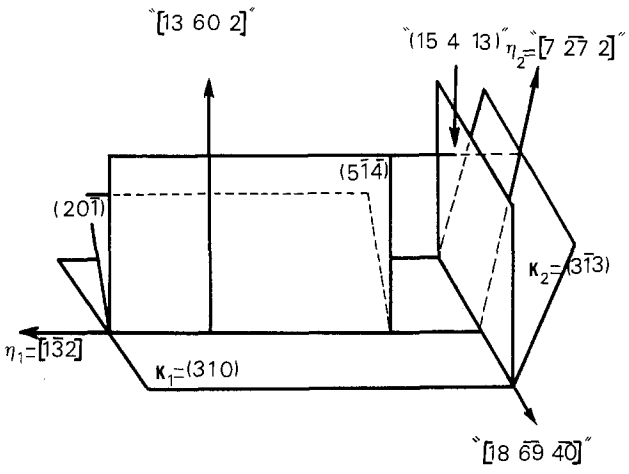

Fig. 9. Relative position of the twinning elements of a [1$\bar{3}$2] twin; planes and axes normal to the twinning elements have been indicated. Symbol " " indicates that the element is not rational. The twinning elements of the (3$\bar{1}$3) twin, which is the reciprocal of [1$\bar{3}$2], are obtained by inverting K_1 and K_2 and η_1 and η_2.

contain the R atoms. They contain the ionic O atoms and relate one $(RO)_n^{n+}$ slab with another. All the twinning elements of type I and type II twins: K_1, K_2, η_1, η_2 (appendix), have been determined (Boulesteix et al., 1972). They are given in table 1. The notation " " is used when the element is irrational, i.e., is not a reticular element. For type I twins K_1 and η_2 are rational, for type II twins η_1 and K_2 are rational. The relative position of the most important planes and axes for this twinning is given in fig. 9. Let us notice that K_1 for a (313) twin becomes K_2 for a [1$\bar{3}$2] twin and η_1 for a [1$\bar{3}$2] becomes η_2 for a (313) twin; (313) and [1$\bar{3}$2] twins are reciprocal as are the (3$\bar{1}$3) and [132] twins. In each case the shear displacement is parallel to η_1 and occurs for planes parallel to the interface of the two twinned crystals. The shear modulus being s, the shear displacement for a reticular distance d is ds. The surface energy between the twinned crystals is minimum when the twin boundary is parallel to the K_1 plane both for a type I twin and for a type II twin. Then the boundary is said to be coherent. In our case the boundary is coherent when it is parallel to the {313} plane for the same type I twin and when it is parallel to the "{310}" plane for a ⟨132⟩ twin. This is specially important in the case of a type I twin where the coherent boundary is a reticular plane. The observed twins in B appear as twin layers whose surfaces are

TABLE 1
Twinning elements of {313} and ⟨132⟩ twins.

Twin	K_1	η_1	K_2	η_2
Type I	(313)	"[7 2$\bar{7}$ 1]"	"(3$\bar{1}$0)"	[132]
	(3$\bar{1}$3)	"[7 27 2]"	"(310)"	[1$\bar{3}$2]
Type II	"(3$\bar{1}$0)"	[132]	(313)	"[7 2$\bar{7}$ 2]"
	"(310)"	[1$\bar{3}$2]	(3$\bar{1}$3)	"[7 27 2]"
Shear plane	{51$\bar{4}$}		$s = 0.186$	

coherent, or nearly coherent, and we have only two interfaces, each of them being coherent or nearly coherent. So the twin layer passes through the whole crystal and the two coherent interfaces end on the grain boundaries. These observations were made on thin crystals inside an electron microscope; it is not obvious that the results would be the same for bulk crystals.

The three {10 . 0} planes of A are related in B to (202) and to (111) and ($1\bar{1}1$) which are equivalent. The ratio d_{202}/d_{111} can represent the deformation relating B to A. Table 2 gives the calculated and experimental values of d_{202}/d_{111} for the different B oxides and the calculated value of θ and s, where θ is the angle between (202) and (111) and s is the shear modulus.

It has been shown also (Boulesteix et al., 1972) that only one third of the nodes of the reciprocal lattice have homologues in twinned crystals both for a type I twin and for a type II twin, which makes these twins indeed reticular pseudo-merohedral twins (or nearly superlattice conserving twins: NSLCT) with multiplicity 3 (appendix). This is shown in fig. 10 for the ($13\bar{2}$)* reciprocal plane and for a type I twin. This cannot be explained by the description of B as a mere deformation of A but we shall explain this property later on: it is related to the existence of antiphase domains.

In the identification of the twin elements it is difficult to distinguish between type I and type II twins because for special orientations the same diffraction pattern, taken on the boundary between the twinned crystals, can be obtained for both types, fig. 11. In the first paper concerning twins in the B structure the ⟨132⟩ twin (type II) was confused with a {111} twin (type I) (Boulesteix et al., 1970c). The error was corrected when the identification was made by tilting the crystal (Boulesteix et al., 1972). In the case of a type I twin the reciprocal lattice of both twinned crystals shows an unsplit row (USR), fig. 12, while in the case of a type II twin the reciprocal lattice of both twinned crystals shows an unsplit plane (USP), fig. 13 (Boulesteix et al., 1976). The identification of the USR or of the USP by tilting the crystal inside the electron microscope is a powerful method for the determination of the type of the twin and of the twinning elements. Another way to identify the type of the twin is to examine the image when the electron beam is parallel to a crystallographic axis near the interface of

TABLE 2
Variation of the reticular distances and of the shear modulus of twins of R_2O_3 with the atomic number of R.

R	a (Å)	b (Å)	c (Å)	d_{202} (Å)	d_{111} (Å)	θ_{calc}	d_{020}/d_{111} calc.	d_{020}/d_{111} exp.	d_{111}/d_{020} calc.	d_{111}/d_{020} exp.	s
Pr	14.36	3.72	8.97	3.48	3.28	61.9°	1.06_2	1.06_0	1.76	1.73	0.16_9
Nd	14.30	3.69	8.93	3.47	3.26	61.99°	1.06_5	1.06_3	1.76	1.78	0.17_6
Sm	14.18	3.63	8.84	3.44	3.21	62.16°	1.07_1	1.07_3	1.77	1.79	0.18_6
Gd	14.06	3.565	8.76	3.42	3.16	62.36°	1.07_8	1.08_1	1.77	1.81	0.20_1
Dy	13.97	3.52	8.66	3.37	3.12	62.44°	1.08_1	1.08_3	1.77	1.82	0.21_2
Ho	13.90	3.49	8.59	3.35	3.10	62.45°	1.08_1	1.08_1	1.77	1.82	0.21_5

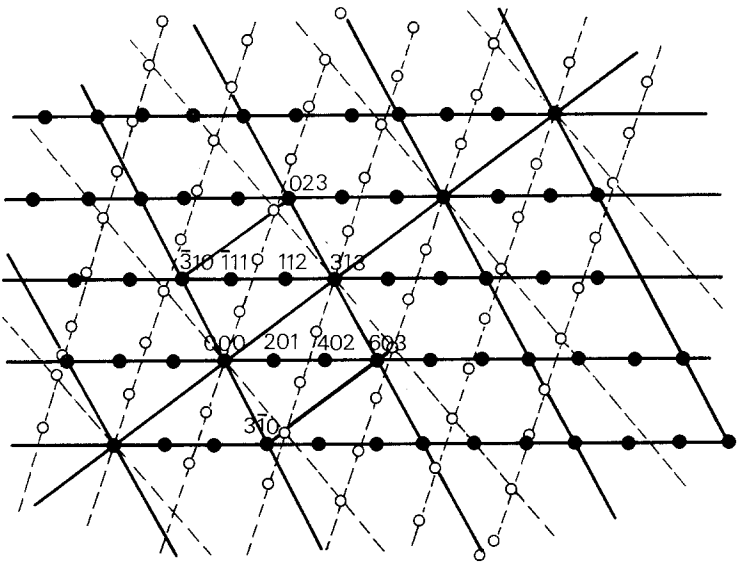

Fig. 10. Relative position of the two different $(13\bar{2})^*$ reciprocal planes for (313) twinned crystals of B. Filled circles are relative to one crystal, open circles to the other. The indexing is given for one crystal only (for the filled circles). Only one node in three has a homologue in the twinning operation: 313, $3\bar{1}0$, 023, 603, ... have homologues, but 201, 402, $\bar{1}11$, 112, ... have not.

the twinned crystals. In this region the image appears with a characteristic aspect, called "zone axis pattern" (ZAP), related to the symmetry of the axis. For a type II twin the direction of any crystallographic axis is slightly tilted on each side of the twin (out of the twinning axis itself) so that the electron beam cannot be parallel to a crystallographic axis on both sides of the twin boundary. For a type I twin the direction of any crystallographic axis is the same on both sides of the twin boundary if this axis is parallel to the twin plane. This is the case for the $[10\bar{1}]$ axis which is parallel to both (313) and $(3\bar{1}3)$ twinning planes, so that by tilting the $[10\bar{1}]$ zone axis pattern will pass through the interface of {313} twins and vanish at the interface of ⟨132⟩ twins. This really occurs (fig. 14a,b,c) and confirms the determination of the twinning elements.

Recently Yangui (1981) has shown the existence of {111} twin and of ⟨192⟩ twin. (111) and $[1\bar{9}2]$ are reciprocal twins as well as $(1\bar{1}1)$ and [192]. These twins had not been seen previously because the diffraction pattern can be easily confused with the diffraction pattern of the other well-known twins except in a systematic study. They have been suspected by observation of both the diffraction pattern and the image (the way of crossing twin boundaries for the Z.A.P. was not in agreement with the diffraction pattern for the well-known twins). Like the other ones they can be mechanical twins and are indeed quite common. Table 3 gives their twinning elements: K_1, K_2, η_1, η_2. Such twins cannot be related, as are the well-known {313} and ⟨132⟩ twins, to symmetry elements of the A structure. Nevertheless both can be related to a possible {10 . 0} twin of the A structure. This twin would be a rational twin, i.e., all the twinning elements K_1,

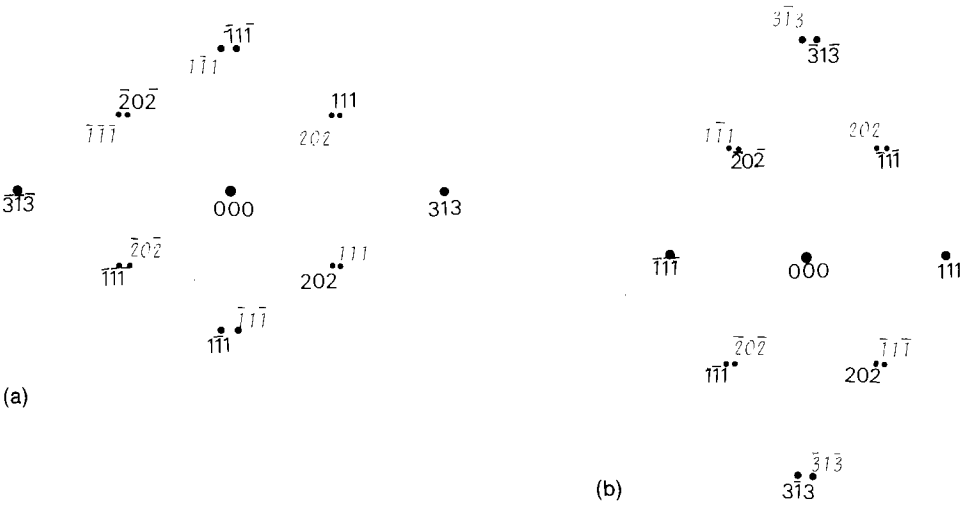

Fig. 11. (a) Indexing of the diffraction pattern of twinned crystals, when the electron beam is parallel to the [10$\bar{1}$] axis. The same indexing is obtained for a (313) twin and for a [1$\bar{9}$2] twin. A second plane of the reciprocal lattice is necessary to distinguish between the two kinds of twins. The indexing of the spots of each crystal is indicated by different characters. (b) Indexing of diffraction pattern of twinned crystals, when the electron beam is parallel to the [10$\bar{1}$] axis. The same indexing is obtained for a (111) twin and for a [1$\bar{3}$2] twin.

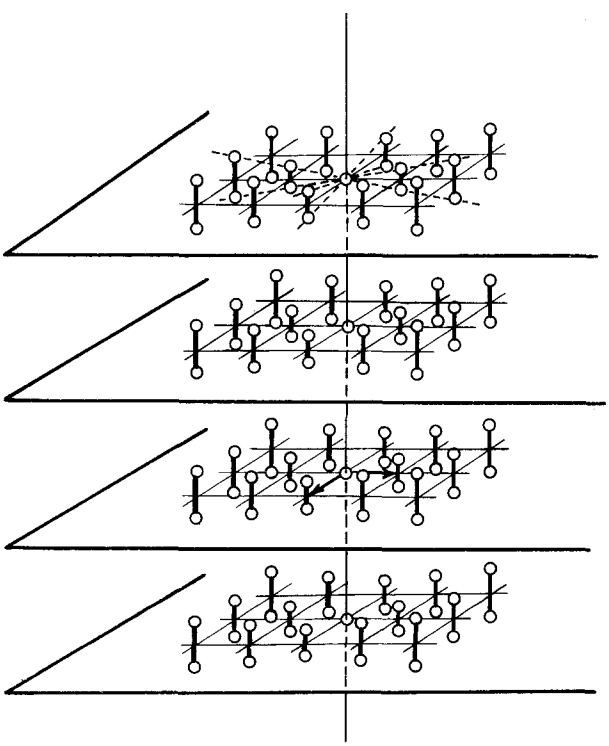

Fig. 12. Reciprocal space drawing for a type I twin. An unsplit row occurs.

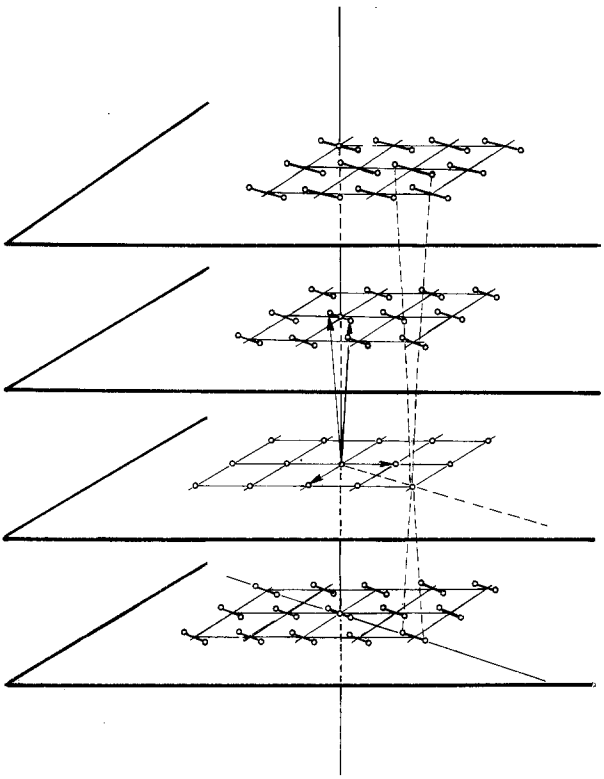

Fig. 13. Reciprocal space drawing for a type II twin. An unsplit plane ocurs.

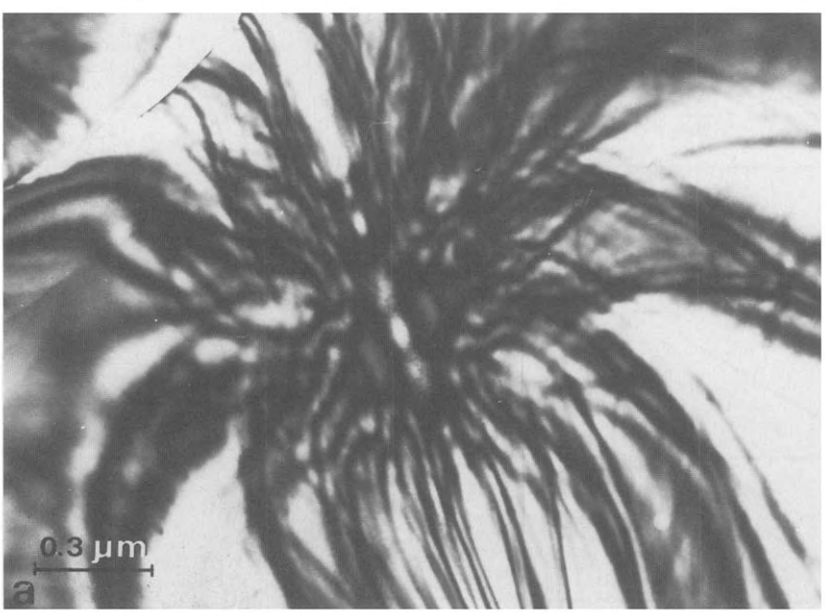

Fig. 14a.

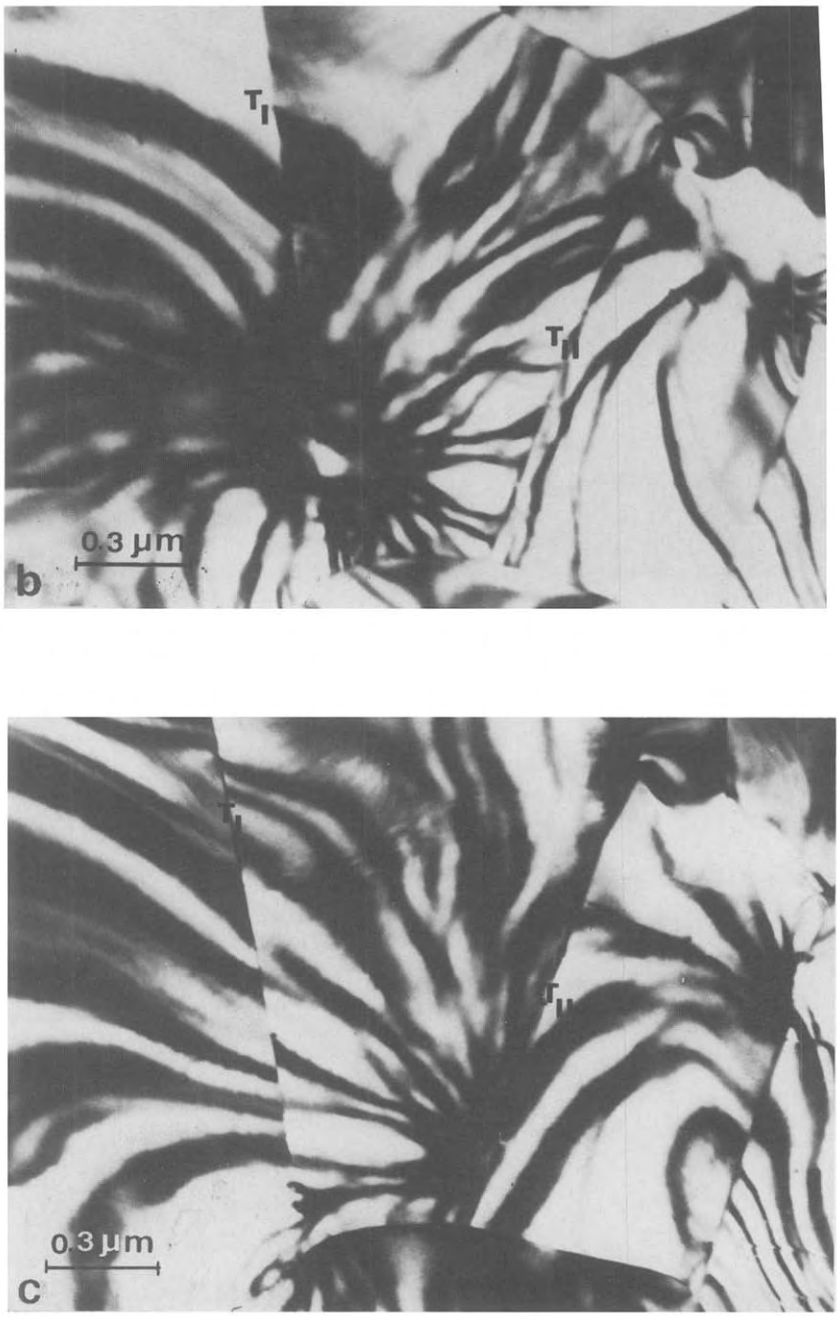

Fig. 14. (a) General view of the [10$\bar{1}$] zone axis pattern of B-Sm_2O_3. (b) Continuity of the [10$\bar{1}$] zone axis pattern through a (313) twin boundary (T_I). (c) Discontinuity of the [10$\bar{1}$] zone axis pattern through a [1$\bar{3}$2] twin boundary (T_{II}).

Fig. 15. (a) Mechanical twin (T) at the tip of a fracture in a B-Sm_2O_3 crystal.

Fig. 15. (b) Displacement of the twin with the fracture.

TABLE 3
Twinning elements of {111} and ⟨192⟩ twins.

Twin	K_1	η_1	K_2	η_2
Type I	(111)	"[1$\bar{2}$1]"	"(12 $\bar{2}$ 3)"	[192]
	(1$\bar{1}$1)	"[121]"	"(12 2 3)"	[1$\bar{9}$2]
Type II	"(12 $\bar{2}$ 3)"	[192]	(111)	"[1$\bar{2}$1]"
	"(12 2 3)"	[1$\bar{9}$2]	(1$\bar{1}$1)	"[121]"
Shear plane "(30$\bar{2}$)"			$s = 0.177$	

K_2, η_1, η_2 are rational (appendix) so that it can be treated at once as a type I or a type II twin with [210] for the twin axis. The existence of a possible twin for A has been indicated previously (Müller-Buschbaum and Von Schnering, 1965). But the authors gave a space group for A that seems to be unlikely so that the existence of a twin for A is still to be confirmed.

2.2.2. *Mechanical twin formation*

{313} and ⟨132⟩ twins of B can appear during the A to B phase transformation, but they appear much more generally in the B phase, by stressing the crystal (mechanical twins). In this case, they have some common features that we shall describe now. As for {111} and ⟨192⟩ twins they could probably have the same origin but are not as well known.

The observation, inside an electron microscope, of the mechanical twinning of B shows that this twinning occurs when crystals are strained so as to relax the stress. For instance, a mechanical twin can appear at the tip of a fracture inside a crystal (fig. 15). Except for this situation it always appears at the boundary of a crystal when, for example, a mechanical twin has just occurred at the neighbouring crystal. In this case a wedge microtwin starts from the grain boundary and passes through the crystal, giving rise to a twin layer (fig. 16a,b), and this for a type I as well as for a type II twin.

The shear displacement is $\boldsymbol{d} = s\boldsymbol{h}$, where s is the shear vector and $\boldsymbol{h}$ the thickness of the twin layer (i.e., the distance between two coherent boundaries of the twin) for either a type I or a type II twin, so that the shear displacement is always merely proportional to the thickness h of the twin layer (fig. 16). The formation of twin layers beginning by the formation of wedge microtwins that pass through the crystal, the study of such wedge microtwins is of special interest in understanding the mechanism of the mechanical twinning. Two studies have been done using the high-resolution electron microscope technique: the first one by lattice imaging (Schiffmacher et al., 1976) (electron beam parallel to a reticular plane) and the second one by atomic row imaging (Yangui et al., 1980, 1982) (electron beam parallel to an atomic row). Near the tip of a wedge

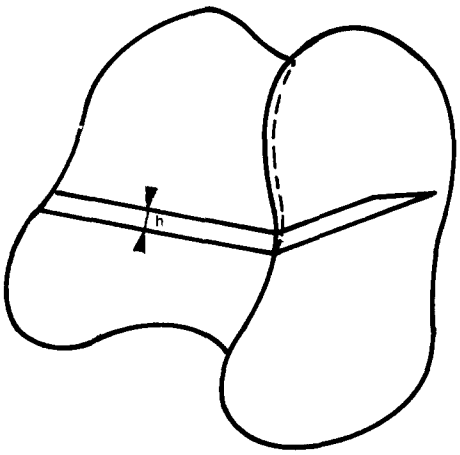

Fig. 16. (a) Mechanical twins start from grain boundaries in polycrystalline samples. They can go through grain boundaries so that the shear deformation is nearly the same on each side of the grain boundary.

Fig. 16. (b) Isolated wedge microtwin (T) in a B-Sm_2O_3 crystal.

microtwin at least one of the twin boundaries is slightly incoherent (if not, the two surfaces would be parallel). The first work revealed that the incoherent boundaries of wedge microtwins appear like a succession of coherent regions separated by steps with always the same height. The existence of such steps had been suggested previously by Hasson (1982) in the case of {111} twins of fcc metals but it seems unlikely that it had been observed earlier.

In the second study, the electron beam was parallel to the $[10\bar{1}]$ axis (i.e., the pseudo c axis of the B structure) allowing the imaging of atomic rows parallel to the axis, which is nearly perpendicular to the $(20\bar{1})$ plane (plane of the sheets of the complex cation and surface of the thin crystal). The high-resolution image was made without tilting the electron beam, and using the transmitted electron beam and 12 diffracted beams (fig. 17a,b): 202, 111, $1\bar{1}1$, $\bar{2}0\bar{2}$, $\bar{1}\bar{1}\bar{1}$, $\bar{1}1\bar{1}$, 313, $3\bar{1}3$, 020, $\bar{3}\bar{1}\bar{3}$, $\bar{3}1\bar{3}$ and $0\bar{2}0$. This technique does not allow a type II twin to be studied. In this case any crystallographic axis, except the twinning axis itself, is tilted on one side of a twin (as seen in 2.2.1), so that the two $[10\bar{1}]$ axes on each side of the twin boundary cannot be parallel to the electron beam at the same time. In contrast, this technique can be used in the case of a type I twin for any axis parallel to the twinning plane. This occurs for the $[10\bar{1}]$ axis which is parallel to the two twinning planes of the structure: (313) and $(3\bar{1}3)$, and so has the same direction for both twinned crystals. The incoherent boundaries have been studied when the angle between the boundary and the twinning plane is near 10°. The incoherent boundary looks then like a succession of coherent boundaries separated by steps of incoherent regions. The height of the steps can be 40 Å (rarely observed) or more generally 20 Å. The method of visualisation of atomic rows used here, with electron beam parallel to the $[10\bar{1}]$ axis, allows the component of the Burgers vector in the $(20\bar{1})$ plane to be determined on each step, by the usual method of the Burgers circuit. In the case of 20 Å steps two different values of this component can be found while for all the 40 Å high steps this component is unique. So, three kinds of steps can be distinguished, labelled A,B,C (fig. 18), each of which is isolated on figs. 19–21.

A step (fig. 19) has $[0\bar{1}0]$ for the component of the Burgers vector in the $(20\bar{1})$ plane, determined as shown on fig. 19, nearly 30° off the twinning plane and nearly parallel to the local incoherent boundary (fig. 22a). The height of the step of about 20 Å fits with 11 ± 1 reticular distances {313}.

B step (fig. 20) has $\frac{1}{6}[1\bar{3}2]$ for the component of the Burgers vector in the (201) plane, determined under the same conditions as for A and as shown on fig. 20, nearly 30° off the twinning plane and nearly 60° off the incoherent step region (fig. 22b). The height of the step is the same as in A.

C step (fig. 21) has $\frac{1}{6}[1\bar{9}2]$ for the component of the Burgers vector in the $(20\bar{1})$ plane, parallel to the twinning plane (fig. 22c). The height of the step which is about 40 Å fits with 22 ± 2 reticular distances {313}.

These steps deform the crystal in the same way as dislocations. A and B are the most important because they are much more usual and because they appear at the incoherent region of wedge microtwins. Fig. 23 shows a wedge microtwin. All the steps are of the same height and of the same type (A); each of them acts

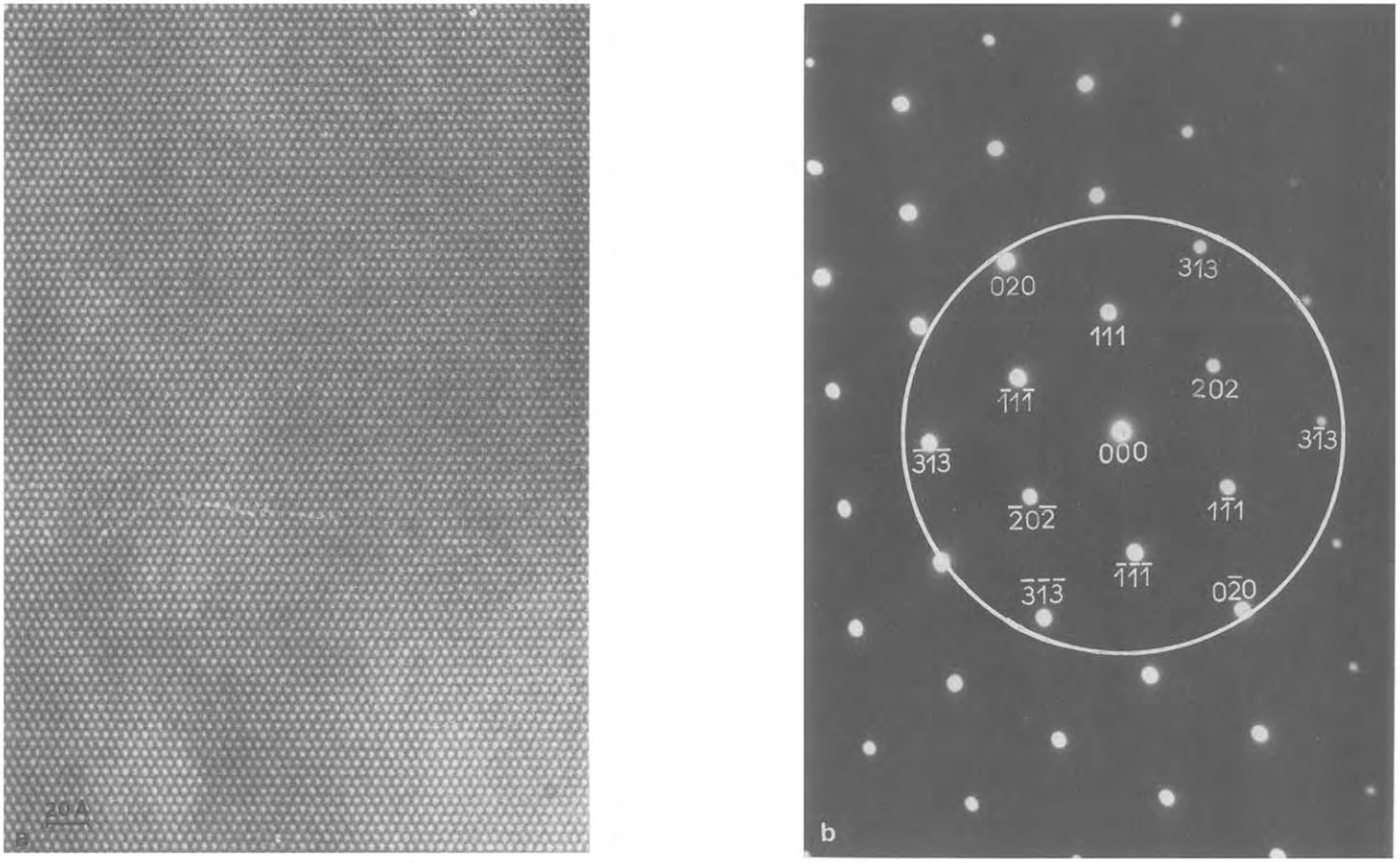

Fig. 17. (a) High resolution image of a perfect B-Sm_2O_3 crystal, when the electron beam is parallel to the [10$\bar{1}$] axis. (b) Diffraction of (a). The high resolution image is obtained without tilting the electron beam inside the electron microscope, using the transmitted electron beam and 12 diffracted electron beams (inside the white circle).

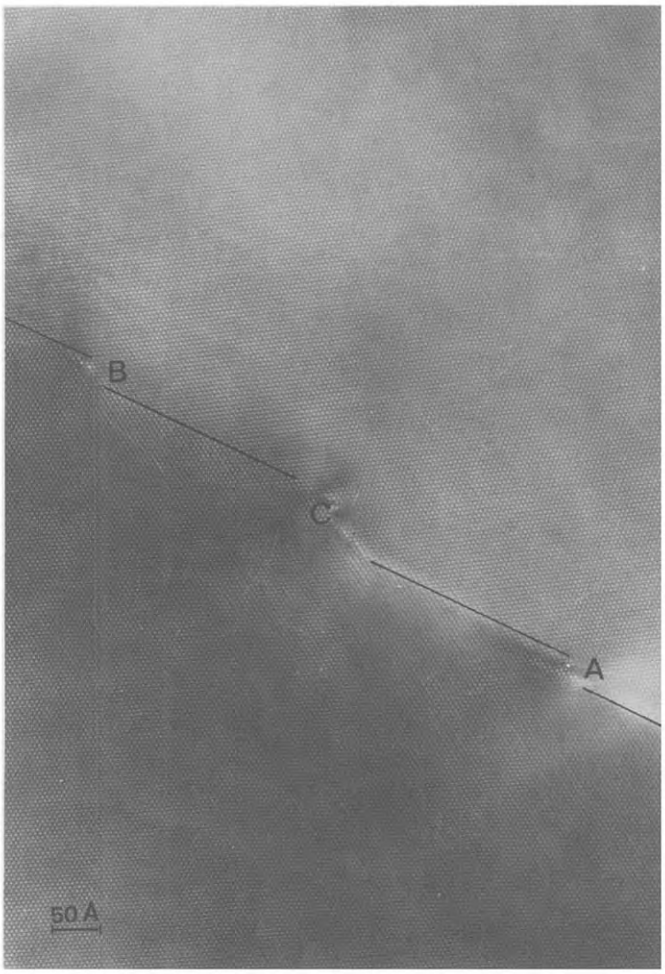

Fig. 18. High resolution image of a (313) twin when the electron beam is parallel to the [10$\bar{1}$] axis. The three kinds of steps are visible at the interface. (Photo: B. Yangui.)

at once as an edge dislocation and as a screw dislocation, but probably for the latter with an alternate Burgers vector, so that the pile-up of steps at the incoherent interface acts as a pure edge dislocation wall (disclination) which tilts the crystal near the tip of the wedge microtwin (fig. 24). Each step introduces one supplementary (313) plane causing a rotation angle of $\theta = d_{313}/D$, where d_{313} is the reticular distance of the {313} plane and D is the distance between two steps; ϕ is the angle of the incoherent interface with the {313} coherent interface ($\phi = h/D$, where h is the step height). The height of each step h is 11 d_{313}: $\phi = 11\ d_{313}/D$ and $\theta = \phi/11$. For $\phi = 12°$ this gives $\theta = 1.1°$. In this case (fig. 23) the measured value of θ is between 1° and 1.5° in good agreement with the value calculated from the value of ϕ.

A very high stress occurs near the tip of the wedge microtwin due to the existence of the shear displacement only in that part of the crystal where there is

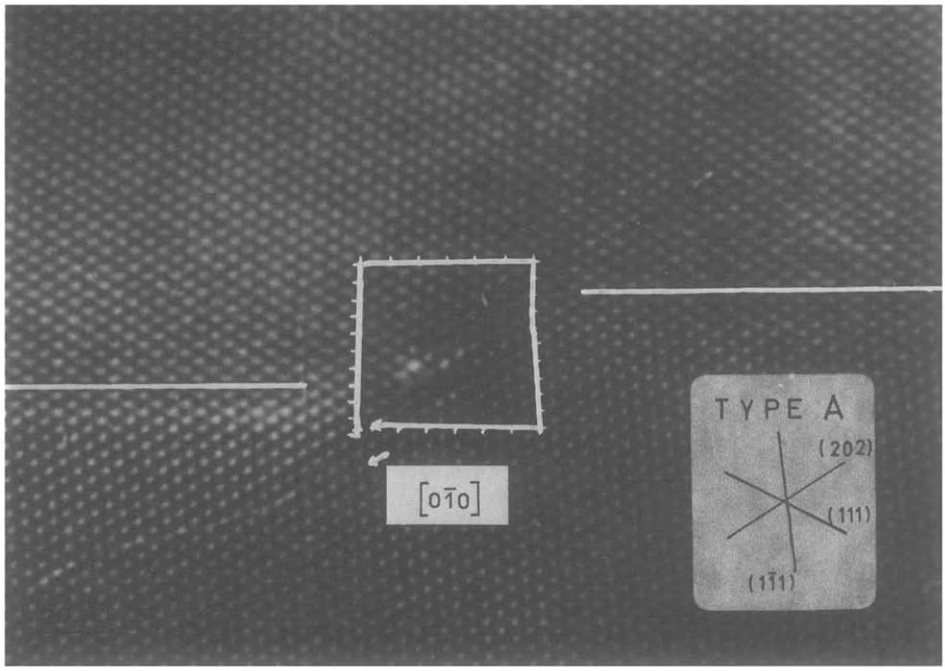

Fig. 19. High resolution image of a type A step on a (313) twin, with Burgers circuit and vector, and plane directions of one crystal. (Photo: B. Yangui.)

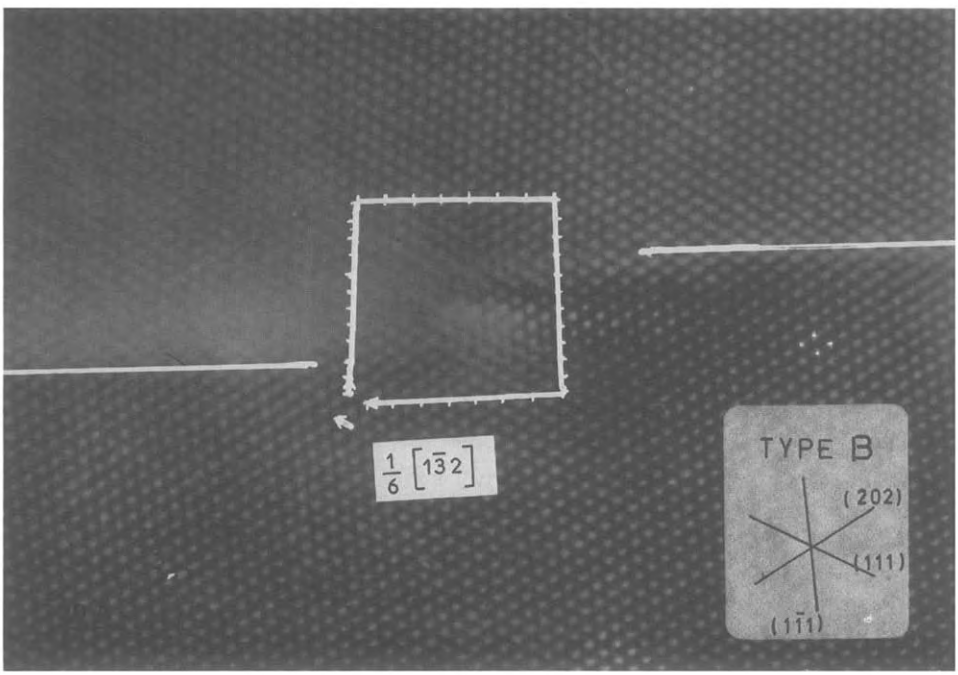

Fig. 20. High resolution image of a type B step on a (313) twin, with Burgers circuit and vector, and plane directions of one crystal. (Photo: B. Yangui.)

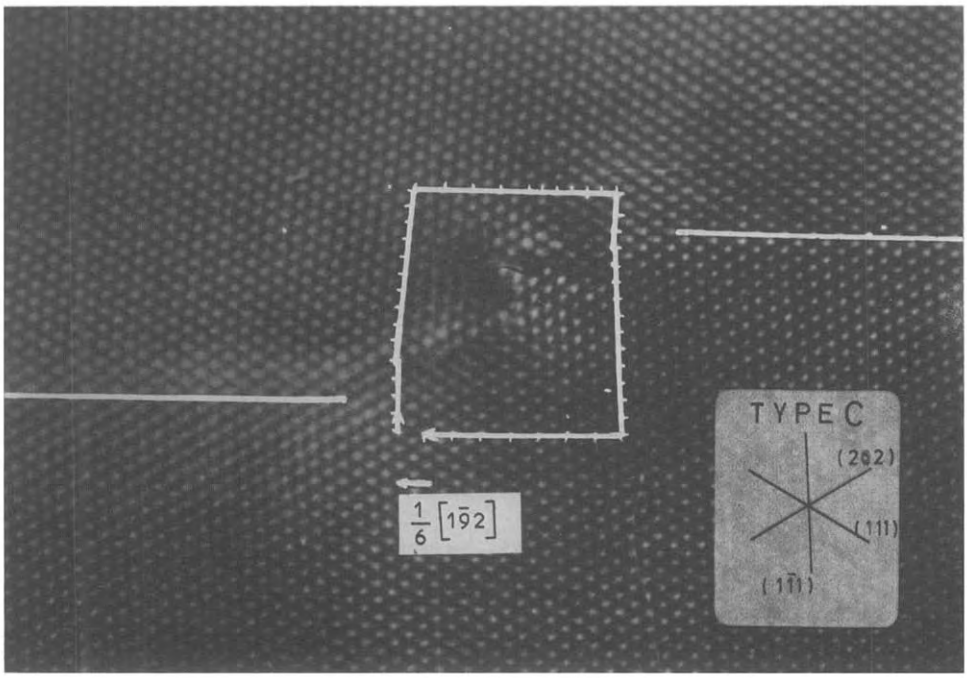

Fig. 21. High resolution image of a type C step on a (313) twin, with Burgers circuit and vector, and plane directions of one crystal. (Photo: B. Yangui.)

a microtwin. In the case of fig. 24 the shear displacement occurs such that the region near the tip of the wedge microtwin is in compression and the small rotation due to the incoherent boundary relaxes the stress.

It is important to notice that the A or B steps occurring at the incoherent boundaries of wedge microtwins deform the crystal as dislocations do, but that the phenomenon is slightly more sophisticated. At each A or B step one has supplementary planes (fig. 22) parallel to (313), the habit planes, and to (1$\bar{1}$1). These supplementary planes, which are nearly perpendicular to each other play very different roles. The plane parallel to the habit plane deforms the crystal over a long range, while the other one does not; it is only related with the existence of the step. The same situation occurs for a C step where it can be more easily understood. For a C step the atoms are in perfect twin position on each side of the step (fig. 22d) without any deformation of the crystal (except for a slight screw deformation). Nevertheless there are two supplementary planes parallel to (1$\bar{1}$1) which are associated with the step. In the case of an A or B step, half the height of a C step, the atoms cannot be in perfect twin position simultaneously on each side of the step (fig. 22e). Experiments show the existence of a supplementary plane parallel to (313), which allows a perfect twin on each side of the step; it is this plane which deforms the crystal over a long range. It is the position of this supplementary plane relative to the step which distinguishes steps A and B. The same result could be obtained with planes

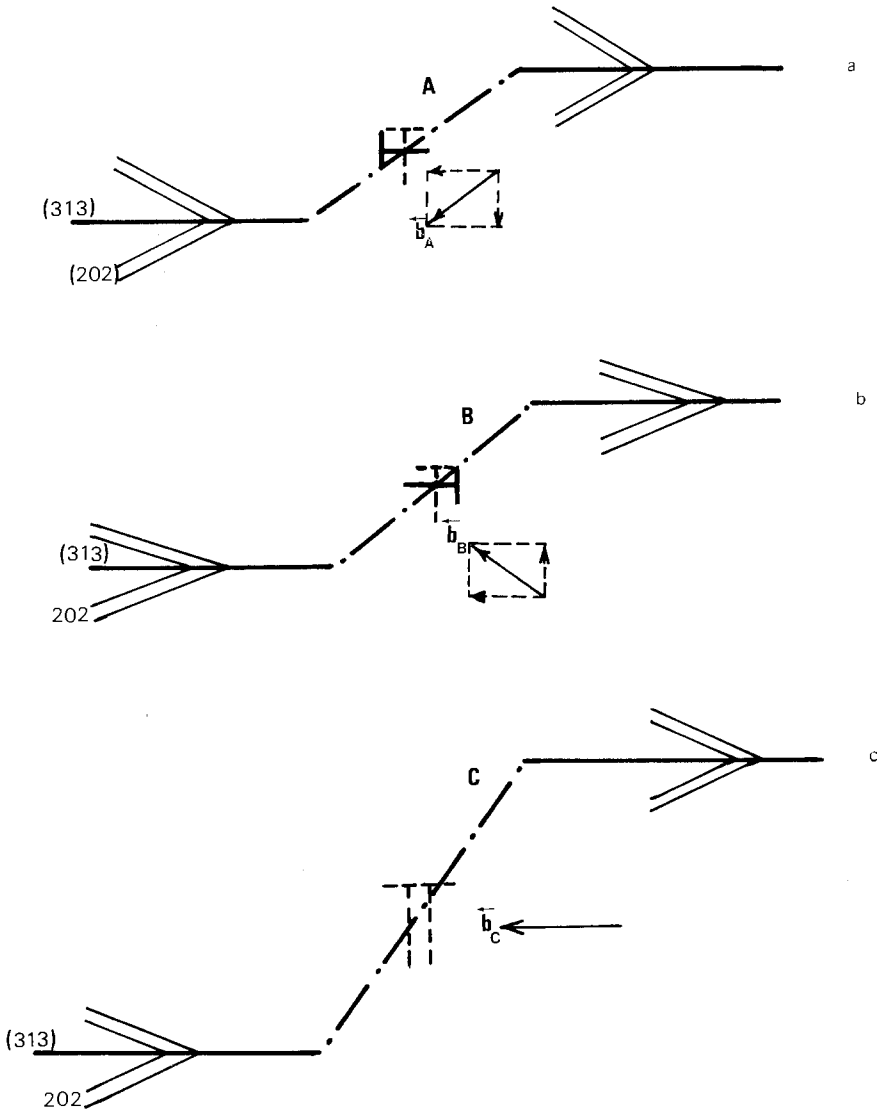

Fig. 22. (a) A step for a (313) twin. A $(1\bar{1}1)$ and a (313) supplementary plane occur at the same time; the latter deforms the crystal over a long range, the first does not. (b) B step for a (313) twin. The same phenomenon occurs as for A, but with a different position of the (313) supplementary plane. (c) C step for a (313) twin. Two $(1\bar{1}1)$ supplementary planes occur at the same time . They do not deform the crystal over a long range. (d) Representation of the atoms in a plane parallel to $(20\bar{1})$ on each side of a C step. It occurs without any deformation of the lattice in $(20\bar{1})$. Open and filled circles represent R atoms in two successive planes. (e) Representation of the atoms on each side of a step half the height of a C step. Introducing or suppressing a (313) atomic plane permits having an epitaxial continuity on each side of the step, giving an A or B step. In a small region the atomic rows are indicated as they appear on the electron microscope images.

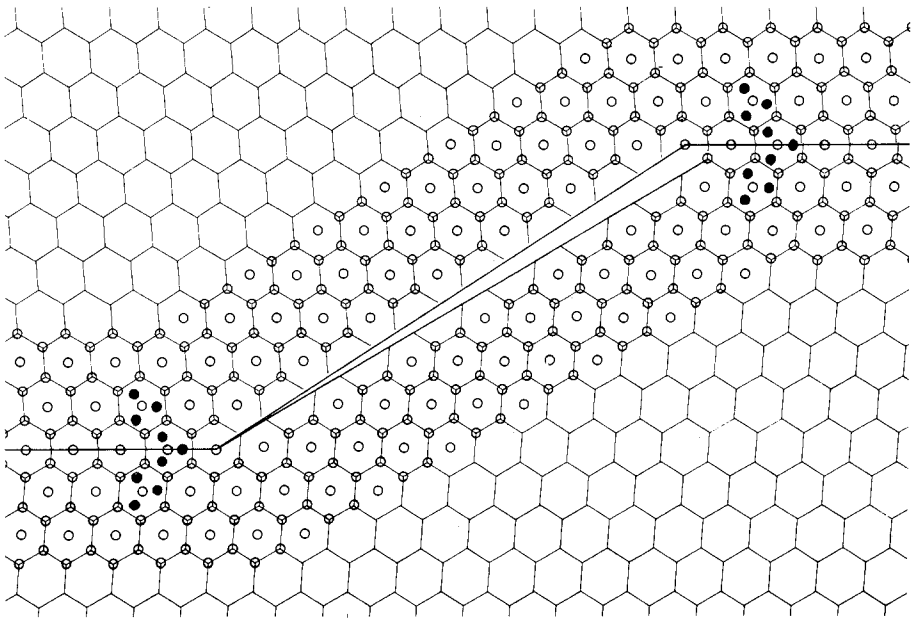

d

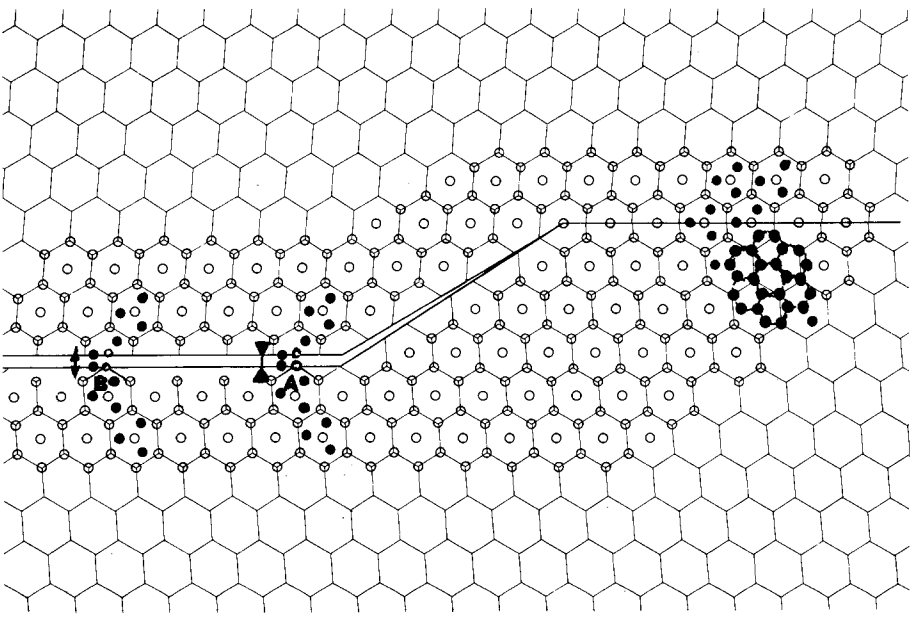

e

Fig. 22. (d), (e).

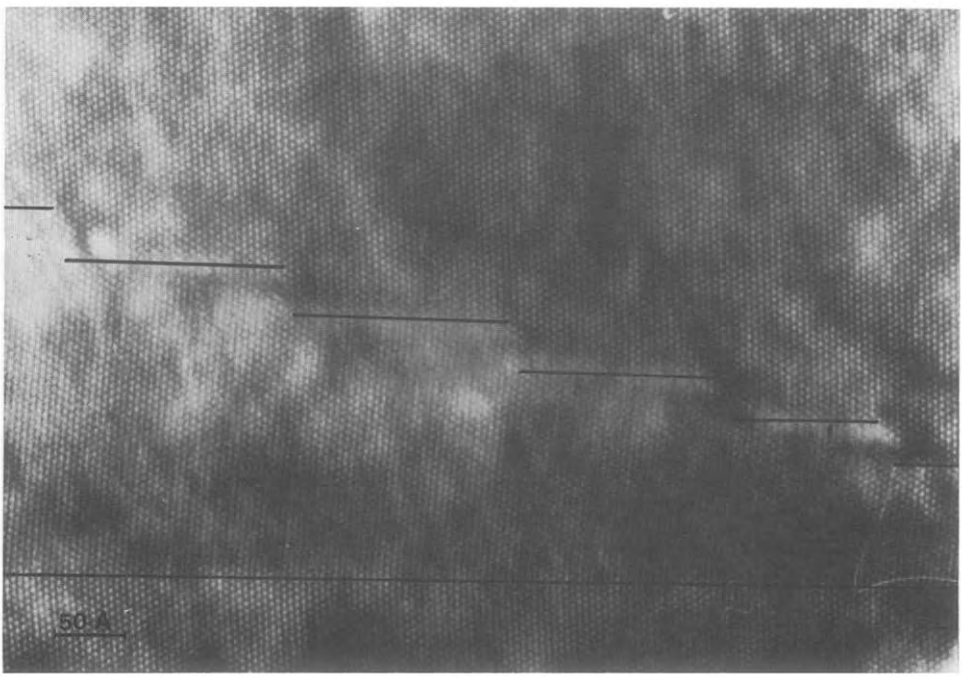

Fig. 23. High resolution image of an isolated wedge microtwin exhibiting steps at the incoherent twin boundary. (Photo: B. Yangui.)

parallel to $(1\bar{1}1)$ but this has not been seen in any experiment. All these steps could relax the stress near an incoherent twin boundary (specially near the top of an isolated wedge microtwin). It would appear by incorporation or emission of a dislocation at the incoherent interface (Cahn, 1954). The final state corresponds to a stabilization that can be observed after annealing (Friedel, 1964).

Mechanical twin formation has been studied by high-resolution methods for type I twins; for type II twins the same kind of study is not possible, as seen previously. Since the study is made by electron microscopy, the observed phenomena occur in thin crystals with a special orientation (the plane of the complex cation $(20\bar{1})$ parallel to the crystal surface). In such conditions the growth mechanism of twins that have been observed could be related to the fact that we are dealing with thin crystals. The phenomenon is probably more general, but only a study by the Lang X-ray method, imaging bulk crystals, could confirm that these mechanisms are always operative. Obviously this method could not give any information concerning small details, for example steps on incoherent boundaries, because of its poor resolution; but it would be important to know if the twinning always starts at grain boundaries and if the interfaces are always planes parallel to the coherent twin interface.

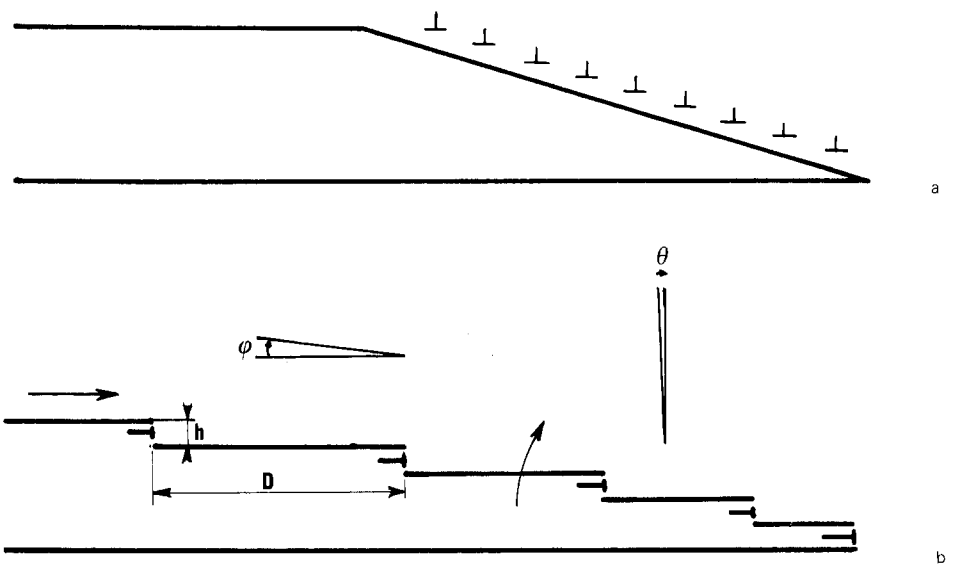

Fig. 24. (a) Classical model of incoherent twin boundary: the interface is regular and the deformation due to a distribution of microdislocations is equivalent to a unique superdislocation located near the tip of the wedge microtwin. (b) Step model of an incoherent twin boundary, as seen by electron microscopy. Near the coherent boundary of the microtwin the crystal is deformed by shearing, while a slight rotation θ occurs in the incoherent region due to the edge dislocation wall. If ϕ is the angle between the coherent and the incoherent boundaries $\sin \phi = h/D$, hence $\theta = \frac{1}{11} h/D = \phi/11$.

2.3. *Twin junction and twin intersection*

We deal with a twin junction if a twin layer is extended by another twin layer with different twinning elements. We deal with a twin intersection if a twin layer goes through a preexisting twin layer.

2.3.1. *Twin junction*

It has been shown (Boulesteix and Loier, 1973) that twin layers can join each other when they are related by a small rotation of an angle less than 10° or by a twin and a small rotation, for instance (313) and [1$\bar{3}$2] or (3$\bar{1}$3) and [132] twin layers (fig. 25). These twins, which are not of the same type, are not reciprocal twins. In this case the twin layers are related by a rotation of 5° about an axis which is nearly the [10$\bar{1}$] axis. A subgrain (fig. 25), or more generally a repeated microtwinning (fig. 26a,b) occurs at the boundary. It allows the rotation between the two twin layers. The repeated microtwinning is made of wedge microtwins (fig. 27). Using the classical theory of incoherent twin boundaries, Bassinski and Christian (1954) explain the role that is played by the microtwinning. Each wedge microtwin is equivalent to a super dislocation located near the tip of the wedge microtwin, and the repeated microtwinning acts as an edge dislocation wall, giving a rotation of the crystal. If h is the thickness of each microtwin, h'

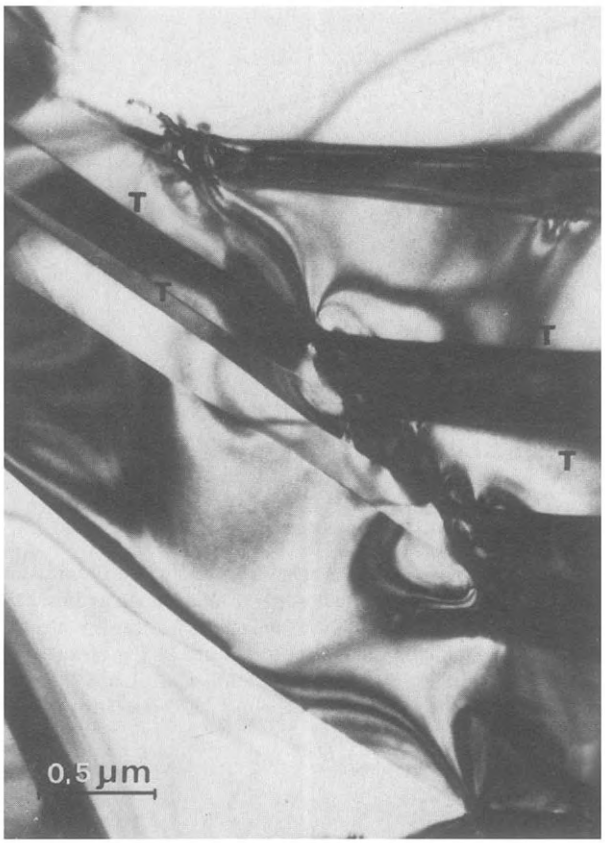

Fig. 25. Twin layer junction without microtwinning; twin layers are due to (313) and [1$\bar{3}$2] twins (T).

the distance between two microtwins, and s the shear modulus, a rotation occurs, as shown in fig. 28 between c and C regions, over an angle $\theta = sh/(h + h')$ about an axis which is parallel to the dislocation wall and perpendicular to the Burgers vector of the dislocations. In our case, the calculation gives for θ a value which is in good agreement both with the value of the rotation angle necessary to join the two twin layers and with the value which is directly measured by electron diffraction (fig. 26b). This microtwinning is quite usual and very stable. It replaces a dislocation wall, but it probably needs less energy than the dislocation wall creating the same rotation.

The calculation of Bassinski and Christian is founded on the classical model of incoherent twin boundaries. In this classical model the incoherent boundary is treated as a regular interface, quite different from the boundary that we have observed by a high resolution technique for the B structure. This classical model for the interface is a succession of microsteps of one habit plane (K_1), while in the model that we have described earlier the incoherent boundary is made of coherent regions separated by steps (fig. 24a,b). The measured value of the rotation angle related with repeated microtwinning is in good agreement with the

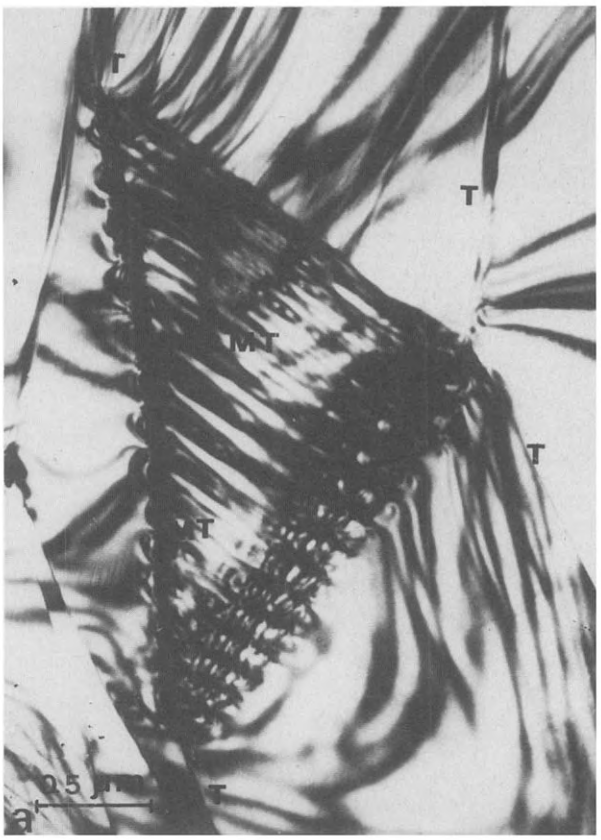

Fig. 26. (a) Twin layer junction with repeated type II microtwins (MT); twin layers are due to (313) and [1$\bar{3}$2] twins (T).

classical theory (Bassinski and Christian, 1954; Boulesteix and Loier, 1973; Vicens et al., 1978) and cannot be explained by the step model. The high resolution study of repeated microtwins was then necessary to understand what could happen. It can be seen, fig. 29, that in this case there is no step at the interface and that we deal with a continuous incoherent boundary, or more exactly with a succession of microsteps of one K_1 plane (to be published). Each microstep is associated with a microdislocation whose Burgers vector is $\boldsymbol{b} = d_k \boldsymbol{s}$, where d_k is the recticular distance of the K_1 plane and $\boldsymbol{s}$ the shear vector. In our case, for a {313} twin the microdislocations (like the deformations associated with steps) have both screw and edge character: $\boldsymbol{s}$ has a component perpendicular to [10$\bar{1}$] and a component parallel to [10$\bar{1}$]. The whole incoherent boundary acts like a pile-up of microdislocations (fig. 24a) which is equivalent to a unique superdislocation. The repeated microtwins act then like a dislocation wall (fig. 28), but with both an edge and a screw character. The edge character of each super dislocation produces the rotation between the C and c regions, about the [10$\bar{1}$] axis and the calculated value of the rotation angle is in good agreement with experimental values. The screw part of the dislocation twists

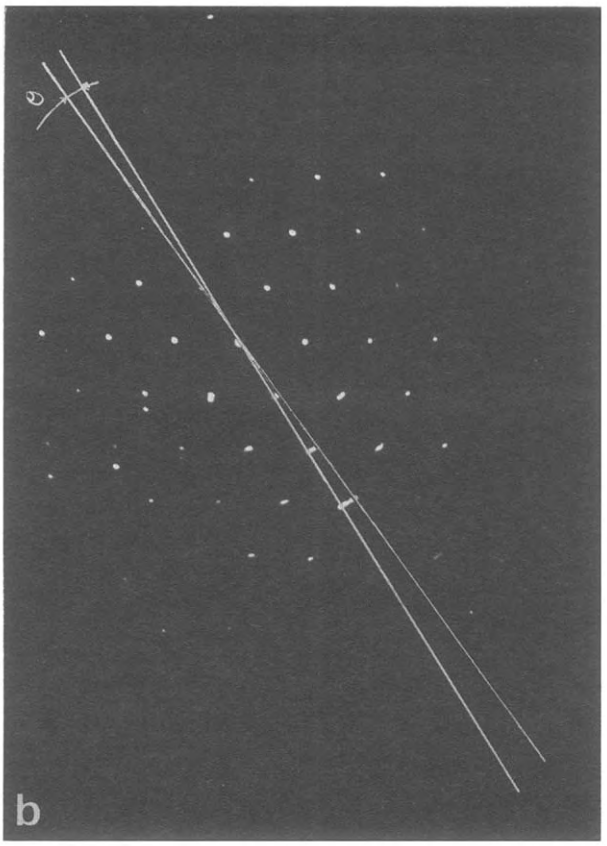

Fig. 26. (b) Diffraction of (a) showing the existence of a crystal rotation of an angle θ due to the microtwinning.

the crystal, changing the direction of the $[10\bar{1}]$ axis. This explains the generally poor aspect of the high-resolution image obtained in this case for (313) wedge microtwins. One has a good image only if the diffraction conditions are identical over the whole micrograph. In the case of type II wedge microtwins, the study would be easier because s is nearly perpendicular to the $[10\bar{1}]$ axis so that the microdislocations have only an edge character. Unfortunately, as seen previously, we cannot use our high-resolution technique in this case.

The different kinds of incoherent twin boundaries that have been observed can be related to the very different roles they play: isolated wedge microtwins are equivalent to disclinations. They are probably stabilized by the A or B steps visible on the images, while repeated wedge microtwins which do not present any step are equivalent to superdislocations. They allow the junction between different regions and are very stable. The incoherent boundaries are as different as the role that the microtwins play.

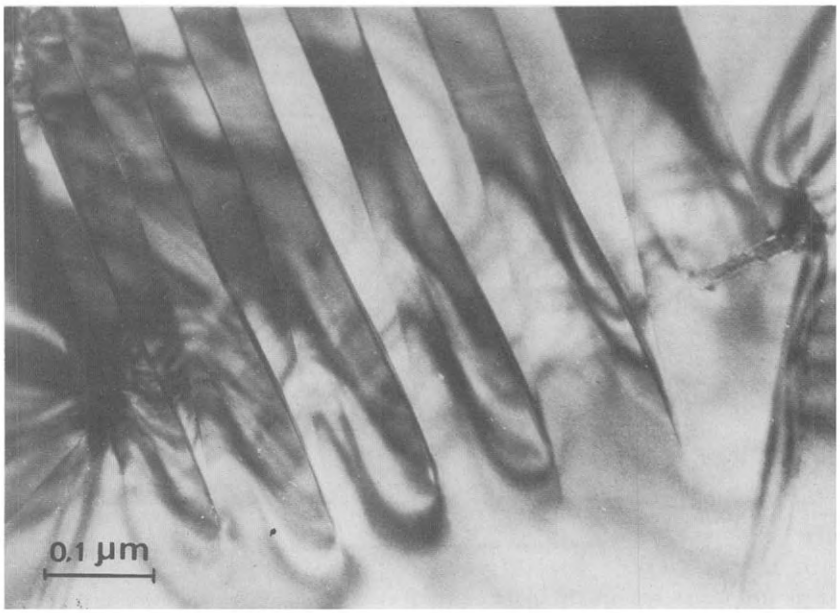

Fig. 27. High magnification of repeated type I microtwins near the tip region.

2.3.2. *Twin intersection*

The mechanical twins of the B structure appear by stressing the crystals: shear, tension or extension. The first case is related to the simplest phenomenon where only one kind of twin layer is generated. In the other cases, generally two kinds of twin layers are generated at once, which makes the phenomenon rather complex.

The situation where two successive shears of different directions are applied to the crystal giving rise to different twin layers is easier to study. We shall now look for what happens in this especially important case because it gives information on the twin intersection and hence on the possibility of twinning for a previously twinned crystal and finally on the plasticity of crystals related to their history. Each crystal can be twinned in eight different ways related to the eight different twins (313), (3$\bar{1}$3), [132], [1$\bar{3}$2], (111), (1$\bar{1}$1), [192], [1$\bar{9}$2] with respectively "[7 2$\bar{7}$ 2]", "[7 27 2]", [132], [1$\bar{3}$2] "[1$\bar{2}$1]", "[121]", [192], [1$\bar{9}$2] for shear directions. The new twin layers appear as wedge microtwins starting from the grain boundaries and going through the crystal. The wedge microtwins can be stopped by the preexisting twin layers but in some cases they go through this twin layer. For the B structure this has been usually observed,

1) when the two twins are not of the same type;
2) when they are not reciprocal twins.

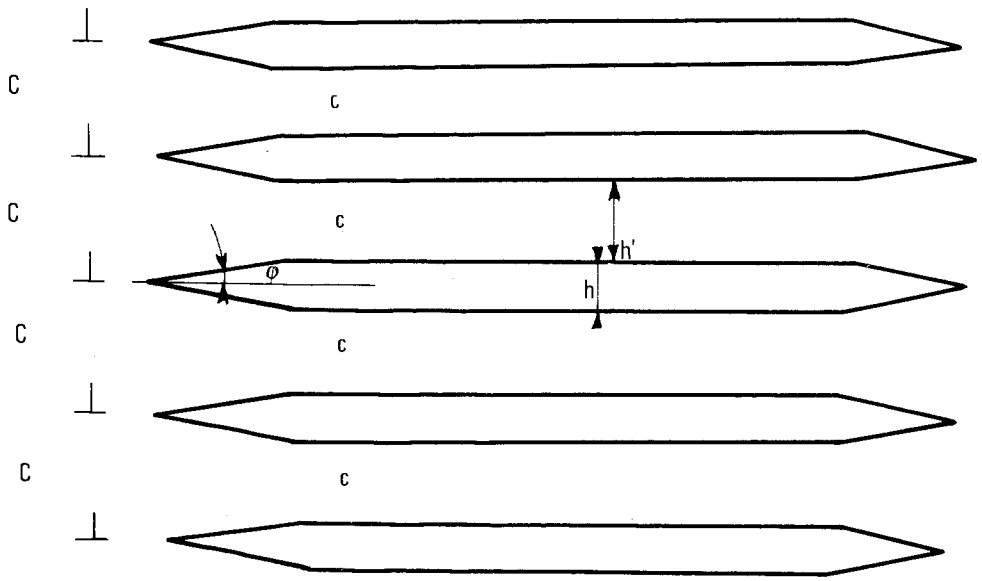

Fig. 28. Repeated wedge microtwins. In the classical model each wedge microtwin is equivalent to a superdislocation, so that the repeated wedge microtwins act as a dislocation wall of edge dislocations, creating a rotation between C and c regions.

For example, it occurs for $[1\bar{3}2]$ and (313) twins or for [132] and $(3\bar{1}3)$ twins, but not for [132] and (313) or $[1\bar{3}2]$ and $(3\bar{1}3)$ which are reciprocal twins or for (313) and $(3\bar{1}3)$ and [132] and $[1\bar{3}2]$ which are of the same type.

The general conditions for twin intersections have been given by Cahn (1953). These conditions are (fig. 30):

1) the traces of C and of D in the K_1 plane of B must be parallel to each other;
2) the direction and magnitude of shear must be identical in C and D.

This is generally satisfied when the shear vector is parallel to the habit plane K_1 of the preexisting twin, occurring when C and D are in twinned position. It can also occur, but much more rarely, in the special conditions indicated by the author.

In our case neither the first nor the second condition are satisfied. The first condition can perhaps be left unsatisfied assuming, for example, the existence of some incoherent boundary. For the second, if it is not satisfied, at least the displacement must be the same on each side of the preexisting twin. If not, it would create a fracture inside the crystal. We shall see now how it can be realized. It occurs in such a sophisticated way that the observed phenomenon was first differentiated from a twin intersection (Boulesteix and Loier, 1973). However, this phenomenon fits exactly the definition of a twin intersection, i.e., "the situation where one twin passes right through another, rather than tapering to a point and starting afresh on the other side" (Cahn, 1953), and so must be really treated as a twin intersection.

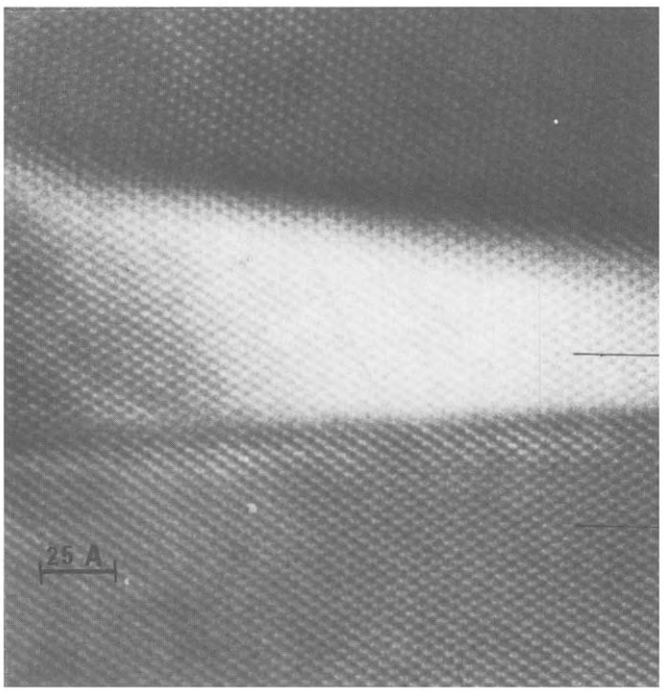

Fig. 29. High resolution image of a wedge microtwin of repeated microtwins. The (313) plane direction is indicated by a dark line. (Photo: B. Yangui.)

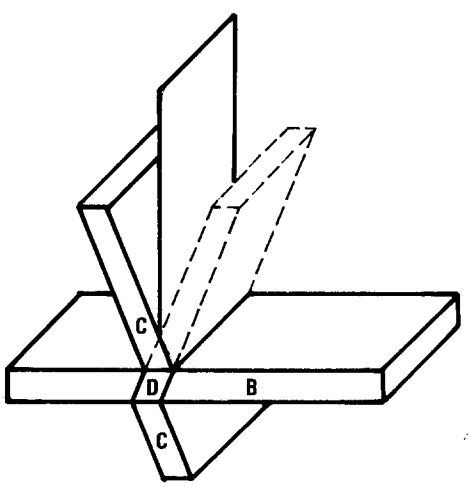

Fig. 30. General conditions given by Cahn for twin intersection. They are generally satisfied when B and D and C and D are in twin position at the same time.

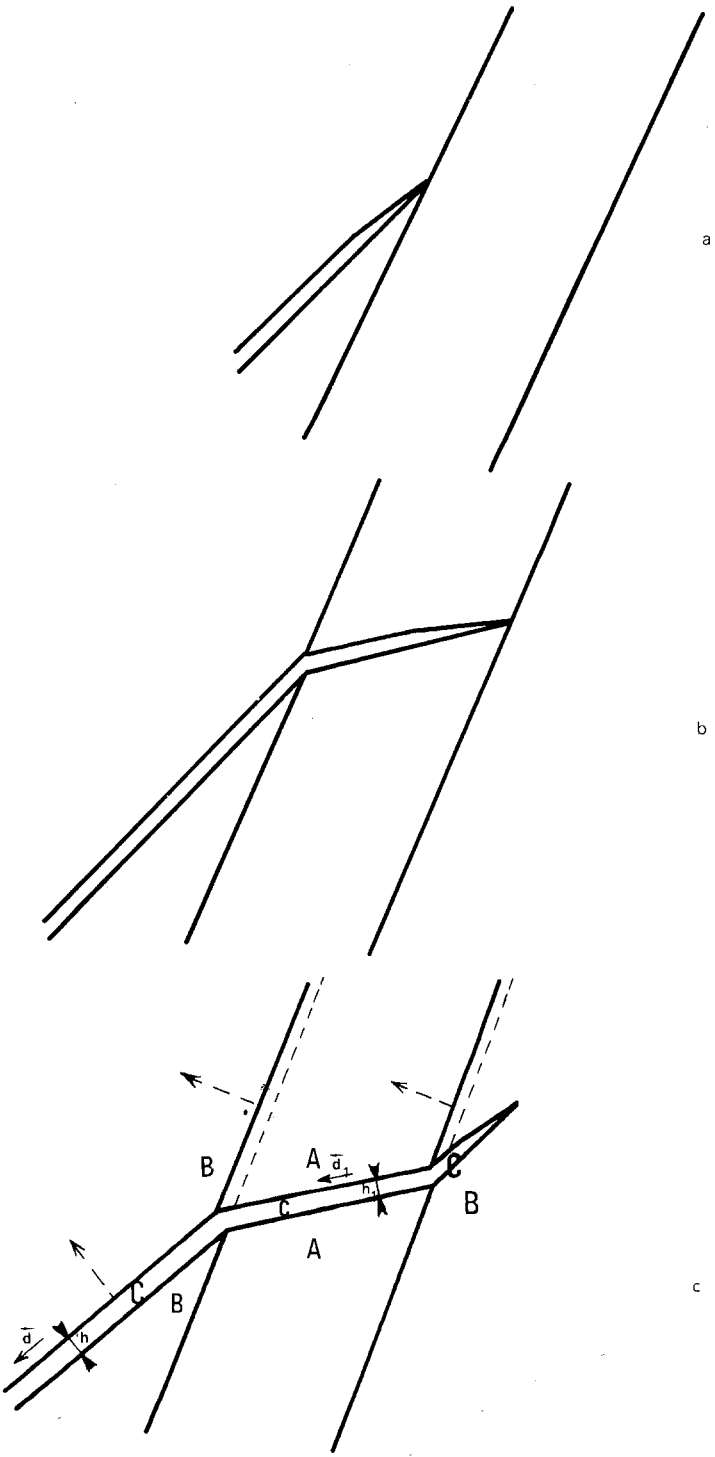

Fig. 31.

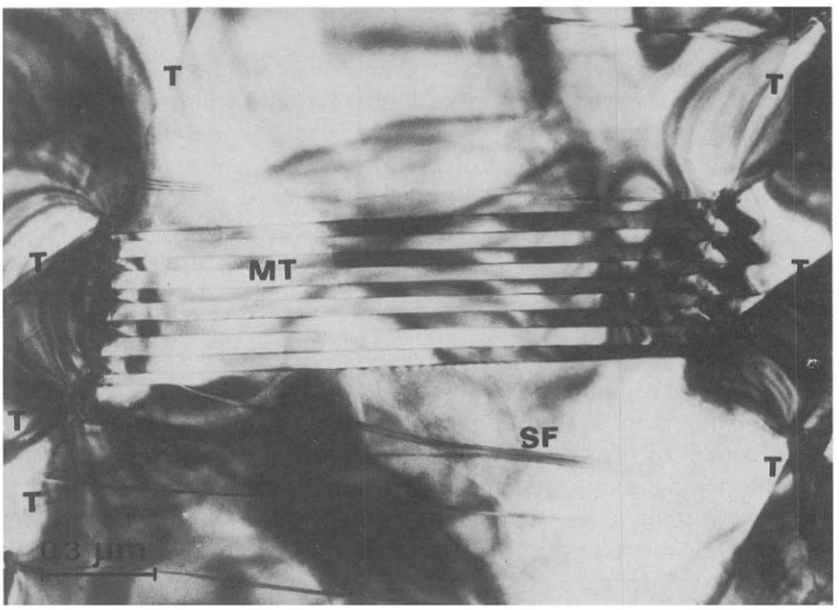

Fig. 32. Twin (T) intersection exhibiting type I microtwins (MT). The displacement of the preexisting twin boundary is clearly visible on each side of the twin intersection. Stacking faults (SF) are also visible.

Let us consider what happens when a [132] wedge microtwin encounters a (313) twin layer (fig. 31a). The angle between the traces of the twins in the $(20\bar{1})$ plane is about 30°. The wedge microtwin goes through the twin layer where it becomes a (313) wedge microtwin (with twin indices related to the preexisting twin layer) (fig. 31b) and then gives once more a [132] wedge microtwin in the first crystal (fig. 31c). This occurs with a displacement, in the direction perpendicular to the K_1 plane of the boundaries of the preexisting twin layer, on one side of the new twin, of about three times the displacement of this boundary due to the shear of the new twin. The shear displacement due to the new twin, on each side of the preexisting twin layer is $\boldsymbol{d} = s\boldsymbol{h}$ and $\boldsymbol{d}_1 = s_1\boldsymbol{h}_1$, where s and s_1 are the shear vectors and $\boldsymbol{h}$ and $\boldsymbol{h}_1$ the thickness of the new twin, respectively outside and inside the preexisting twin layer. The direction and the magnitude of these shear displacements are different, so that the second condition of Cahn for twin intersection is certainly not satisfied. When the new twin gets larger a microtwinning occurs in the region of the intersection (fig. 32). The wedge

Fig. 31. (a) Junction of a [132] wedge microtwin and of a (313) twin layer. (b) The wedge microtwin goes through the twin layer where it becomes a (313) wedge microtwin. (c) A new [132] wedge microtwin starts from the boundary of the preexisting twin layer. A displacement of the boundaries of the preexisting twin layer occurs. The shear displacements outside of the preexisting twin layer, $\boldsymbol{d}$, and inside, $\boldsymbol{d}_1$, are different. A more sophisticated phenomenon is necessary for the growth of the new twin layer.

microtwins which occur are of the same type as the intersecting twin inside the preexisting twin layer.

The shear displacement in the first crystal $\boldsymbol{d} = s\boldsymbol{h}$ can be treated as the sum of two vectors $\boldsymbol{d}'$ and $\boldsymbol{d}''$ chosen such that $\boldsymbol{d} = \boldsymbol{d}' + \boldsymbol{d}''$ and where $\boldsymbol{d}''$ is parallel to the interface of the preexisting twin layer and where $\boldsymbol{d}'$ is parallel to the new twin (inside the twin layer). The shear displacement due to the new twin (inside the twin layer) is $\boldsymbol{d}_1 = s_1\boldsymbol{h}_1$ parallel to $\boldsymbol{d}'$ but larger than $\boldsymbol{d}'$. The microtwinning that appears in that region reduces the value of the shear displacement so that $\boldsymbol{d}_1 = \boldsymbol{d}'$ by changing the value of $\boldsymbol{h}_1$. As for the component $\boldsymbol{d}''$ of the shear displacement it appears thanks to a displacement of the boundary of the preexisting layer creating a shear displacement $d_2 = d''$, as shown in fig. 33a. Both phenomena allow the shear displacement to be the same on each side of the boundary of the preexisting twin layer, though the shear vector is not the same inside and outside of the preexisting twin layer. Let us notice that we have not taken into account here a component of the shear displacement for $\boldsymbol{d}_1$ and $\boldsymbol{d}_2$ along the $[10\bar{1}]$ vector. These components are opposite so that we really have $\boldsymbol{d} = \boldsymbol{d}_1 + \boldsymbol{d}_2$.

The microtwinning does something further which is just as important. It allows the epitaxial continuity between the different regions to be satisfied. The two twin layers inside and outside the preexisting twin are related by a rotation of 5° about the $[10\bar{1}]$ axis so that the regions labelled C and c on fig. 33b are related by a rotation of 5° about the $[10\bar{1}]$ axis. This rotation is obtained by the microtwining under the same conditions as seen previously in the case of twin

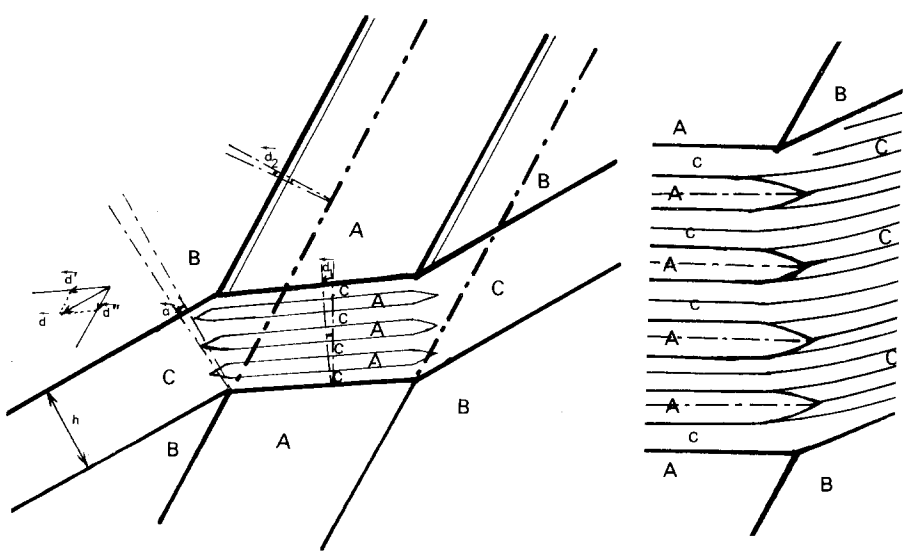

Fig. 33. (a) Repeated microtwining reduces the value of the shear displacement inside the preexisting twin layer $\boldsymbol{d}_1$ until $\boldsymbol{d}_1 = \boldsymbol{d}'$, while the displacement of the boundaries of the preexisting twin layer creates a shear displacement $\boldsymbol{d}_2 = \boldsymbol{d}''$, where $\boldsymbol{d}'$ and $\boldsymbol{d}''$ are the components of $\boldsymbol{d}$ parallel to $\boldsymbol{d}_1$ and $\boldsymbol{d}_2$. (b) The rotation of the reticular planes, due to the repeated microtwinning, allows an epitaxial continuity between C and c regions.

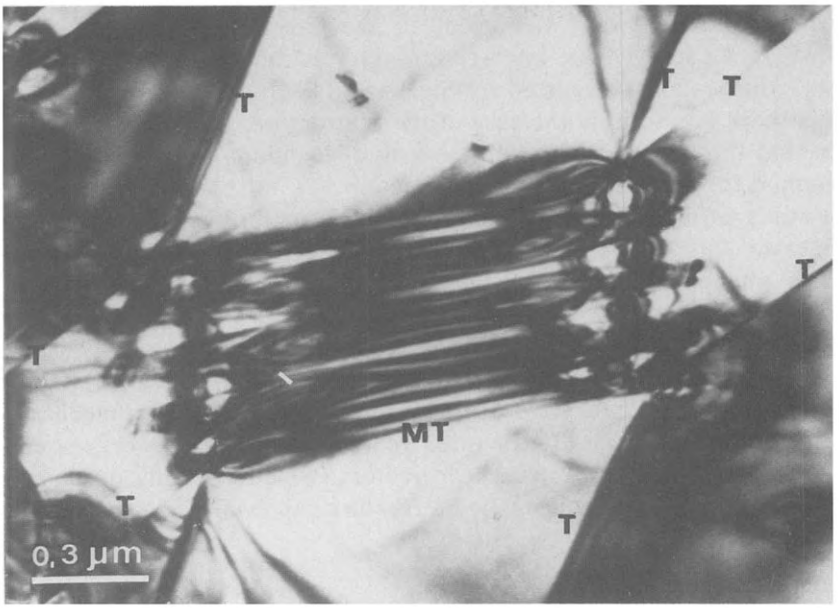

Fig. 34. Twin (T) intersection exhibiting type II microtwins (MT). The displacement of the preexisting twin boundary is clearly visible on each side of the twin intersection.

junction, i.e. because of the incoherent region of the microtwins with $\theta = sh/(h + h')$ (fig. 28). Notice that the microtwinning which here is due to type I can be obtained as well with type II (fig. 34), in relation to the nature of the intersecting twin inside the preexisting twin layer. Because of this microtwinning, an epitaxial continuity occurs everywhere. We can consider that an epitaxial continuity is a condition for twin intersection. This condition is more general than the first condition of Cahn, and we suggest replacing the first condition of Cahn by this one.

So we suggest, for twin intersection, the two following conditions:

1) an epitaxial continuity must be assured everywhere;

2) the displacement must be the same on each side of the preexisting twin.

These two conditions must be satisfied during the formation and the growth of the intersecting twins by any available mechanism, but no condition is "a priori" necessary and it is not necessary, for instance, to have the same shear vector inside and outside of the preexisting twin.

Reed-Hill (1964) had shown previously that the two conditions of Cahn were not necessary to obtain a twin intersection. He had shown that slip mechanisms could allow the displacement to be the same on each side of the preexisting twin layer even if the shear vector was not the same. The mechanism in this case is quite different from the one that we observed in the B structure. Reed-Hill took into account the fact (which is obvious) that the displacement must be the same on each side of the preexisting twin layer but did not suggest any condition for epitaxial continuity.

A quite different way was used, in the case of α iron, by Levasseur (1969, 1971) to study twin intersection, in relation to the properties of the emissary dislocations suggested by Sleeswyk (1962). This kind of investigation could perhaps be useful in the case of the B structure. Moreover, Levasseur has shown that the real existence of emissary dislocations is not necessary to use this method for the study of twin intersection.

The study of mechanical twinning of the B structure by electron microscopy shows that:

1) this phenomenon is no longer reversible as soon as twin intersection occurs;

2) when two kinds of twins occur together, another twinning is generally not possible; so it seems very unlikely that one can obtain a perfect crystal in which any kind of defects would have been swept away by a twinning mechanism.

On the contrary, for the B structure, we obtain crystals of a very poor quality after two twinnings of different shear vectors (which can only occur in special conditions). If a new shear is applied a fracture can even occur instead of a new kind of twinning.

2.4. *Twins by crystal growth and grain boundaries*

The four kinds of twins we deal with, in the B structure, can occur by two ways other than stressing the crystal (which gives mechanical twins). These two ways are crystal growth and phase transformation. The latter will be studied later with the A, B cooperative phase transformation. The first occurs when B crystals grow from C microcrystals. Generally a large single crystal grows but some small crystals of B can be generated near the boundary. They can be absorbed by the bigger one, or on the contrary stop the growth of the large crystal. Rarely do they remain inside the large crystal. If the small crystal is in a nearly twinned position it can give rise to a twinned domain of the large crystal (fig. 35). The twinning elements are the same as for mechanical twins, but the twin boundaries are different. Here, most of them are incoherent which makes these twins very different from mechanical twins. It can be suspected that a great deal of impurities can be located at these kinds of incoherent boundaries. The same phenomenon probably occurs at grain boundaries. A micro-analysis would be necessary to study the influence of impurities on the phenomena related to the growth of these large crystals. A mere observation by electron microscopy shows that this growth is always stopped after some time, probably in relation with tie impurities. Moreover, an internal grain boundary can occur during crystal growth, nearly parallel to the direction of growth. The orientation of the crystal is the same on each side of this grain boundary. Its formation could be due to a supersaturation of impurities.

2.5. *The real structure of B*

Three phenomena at least: planar defects, reticular character of the twins, and extra spots in electron diffraction in B, cannot be explained if B is treated as a

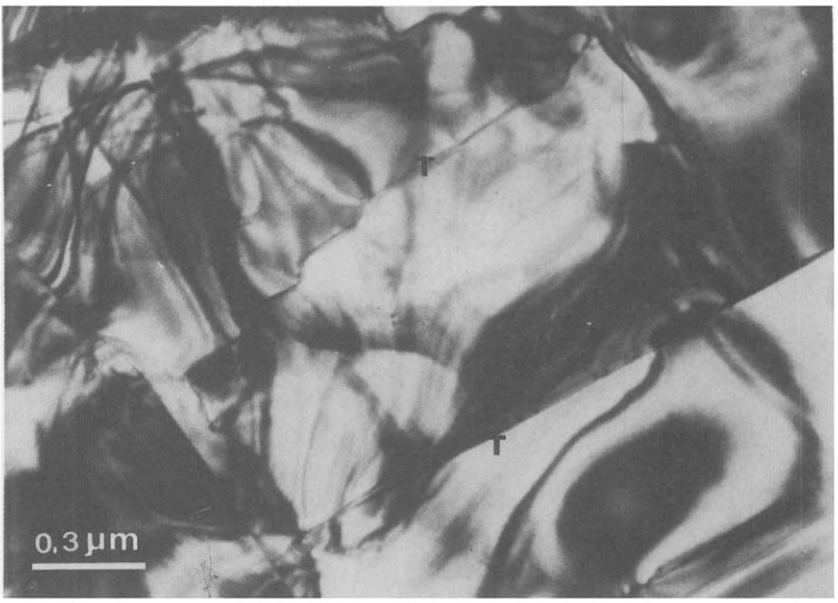

Fig. 35. Twin (T) by crystal growth exhibiting a characteristic feature.

mere deformation of A. The Bravais lattice is primitive for A, base centred for B. The space group of B is C2/m. ***b*** axis and (010) plane are symmetry elements. The center of symmetry is located at the origin and at 1/2, 1/2, 0 which are equivalent positions. Fig. 4b gives the position of the center of symmetry and of the R and O atoms in a plane parallel to (010). The volume of the B unit cell is six times that of the A unit cell, but three times only for a unit cell of a primitive lattice of B. As a consequence, the density of the reciprocal lattice is three times that for A. This means that if B is a deformation of A, we need three unit cells of A to generate one unit cell of B. Fig. 36 gives the relative position of the monoclinic B unit cell, a unit cell of the B primitive lattice and the A unit cell. The three A unit cells which are necessary to generate one B unit cell are deformed in a very similar way, which allows one to treat this deformation in a unique way for explaining most of the properties of B. This has been done until now. Indeed slight differences occur in the deformation of A unit cells to generate B, mainly for the O atoms, but we shall consider the R atoms, which are the most important for electron diffraction as well as for X-ray diffraction. The most important difference between the R atoms is their neighbourhood of O atoms. Each B unit cell (monoclinic base centred) contains six R atoms. They are related to each other by point symmetry, about one of the symmetry centers: 0, 0, 0 or 1/2, 1/2, 0 so that we can have three kinds of R atoms, labelled 1, 2, 3 as shown fig. 37a in a plane parallel to $(20\bar{1})$. Environments of these three kinds of R atoms can be found in a refinement of the B structure by Yakel (1979). We shall see now some consequences of the existence of these three kinds of R atoms in the B structure.

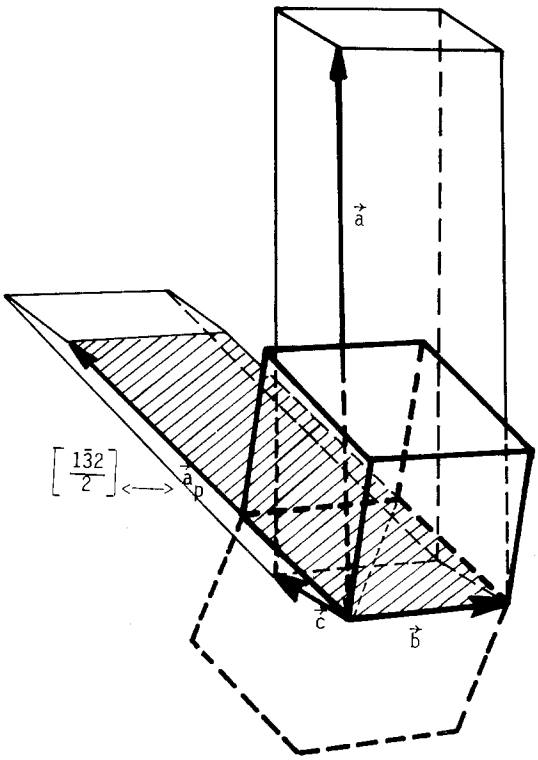

Fig. 36. Relative position of the hexagonal A of the monoclinic B unit cell (a, b, c), and of a primitive unit cell for B (a_p, b, c).

2.5.1. *Planar defects*

The very small differences between the three kinds of R atoms make possible the existence of faults in their stacking. For example, an R_1 atom can give an R_2 atom or an R_3 atom, giving three kinds of translation domains, and two kinds of translation boundaries inside one crystal. These boundaries (fig. 38) can be treated as stacking faults with respect to their origins or as antiphase boundaries. The two smallest glide vectors from one domain to another are $\frac{1}{6}[132]$, which is equivalent to $\frac{1}{6}[1\bar{3}2]$, and $-\frac{1}{6}[132]$, which is equivalent at once to $-\frac{1}{6}[1\bar{3}2]$ and to $\frac{1}{3}[132]$. Fig. 37a gives the three domains and the two kinds of boundaries that can exist in each crystal. Fig. 37b gives the indices of these boundaries in each crystal. Notice that each boundary has two different indices in the two different domains on each side of the boundary. We shall see later that these domains are generally due to a phase transformation. Dislocations can occur with Burgers vector $\frac{1}{2}[132]$. They are dissociated into three partials $\frac{1}{6}[132]$. These partials are separated by the two kinds of planar defects we deal with. They can then be treated as mere stacking faults.

When a stacking fault ends on a twin boundary, a step of one K_1 plane allows the same twinning phenomenon on each side of the stacking fault. Therefore it is possible for a stacking fault to end on a twin boundary (fig. 39) without any

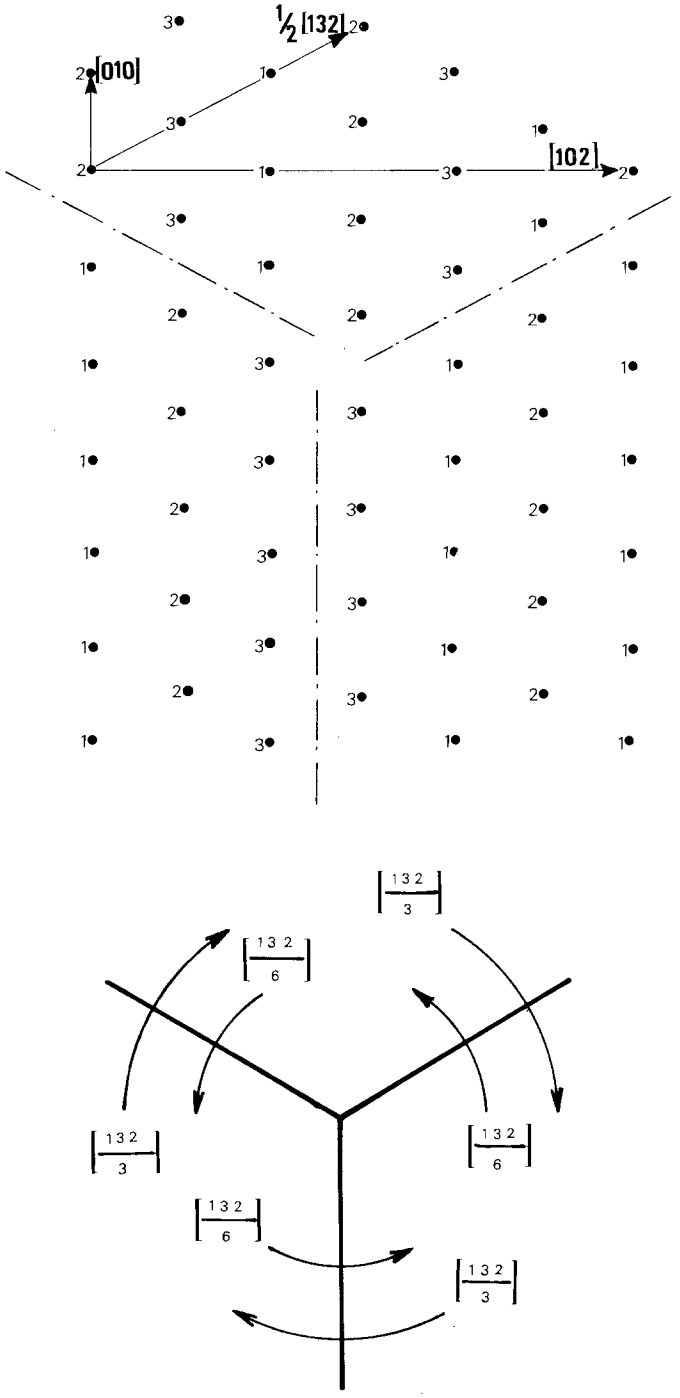

Fig. 37. (a) Translation domains in the B structure, in a plane parallel to $(20\bar{1})$; 1, 2, 3 are the different kinds of R atoms. Juxtaposition of two R atoms of the same kind is possible. Three translation domains and two anti-phase boundaries can occur in each crystal. (b) The two kinds of anti-phase boundaries; they can be indexed $\frac{1}{6}[132]$ and $\frac{1}{3}[132]$ which is equivalent to $-\frac{1}{6}[132]$. The same boundary between two regions is indexed in a different way in each region.

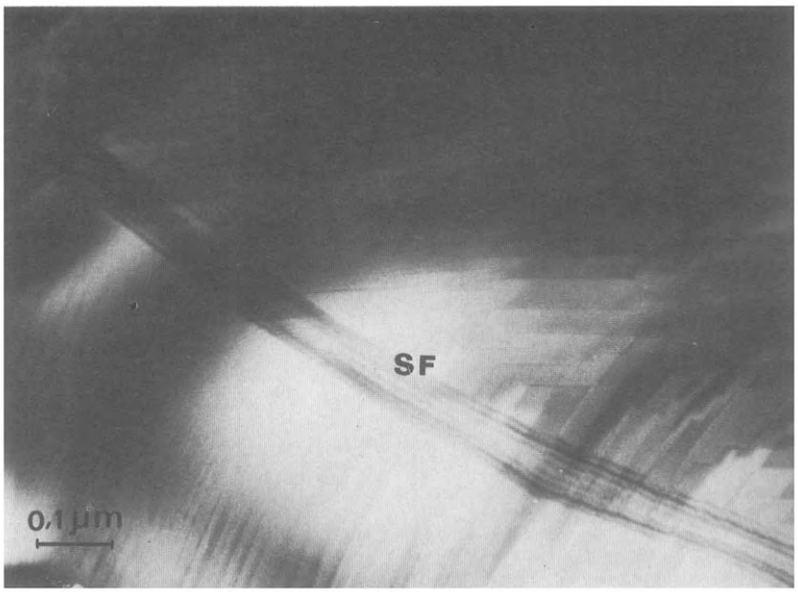

Fig. 38. Stacking fault (SF) of a B-SM_2O_3 crystal ending on a twin (T). Surface steps are visible on the crystal.

modification of the twinning phenomenon on either side of the stacking fault. This is commonly observed (fig. 32). In the case of steps on twin boundaries of types A, B or C the situation of the twinning phenomenon would be the same if each step contains $3n$ (where n is an integer) K_1 planes. The precision of the determination of the height of the steps is not sufficient to assert that it really occurs.

2.5.2. *Reticular character of the twins*

It has been shown previously that B twins have a reticular character for both type I and type II twins. This means that not all the nodes of the reciprocal lattice have homologues in the twin operation (one over three for all the twins of B). This is due to the fact that the unit cell of the primitive lattice of B is three times the unit cell of the lattice of A, so that the reciprocal lattice of B is three times as dense. All B twins are related to the structure of A, so that only the nodes related to A have an homologue in the twin operation. For instance nodes 111, 202, 020, 313, 310, ... of the reciprocal lattice that can be related to nodes of A have homologues in each of the twin operation, while nodes $\bar{1}11$, 112, 201, 402, ... that are not related to nodes of A have no homologues in a twin operation, as shown on fig. 10. So the reticular character of the B twins, nearly superlattice conserving twins (NSLCT), can be related to the complete description of the relationship existing between the A and B structures.

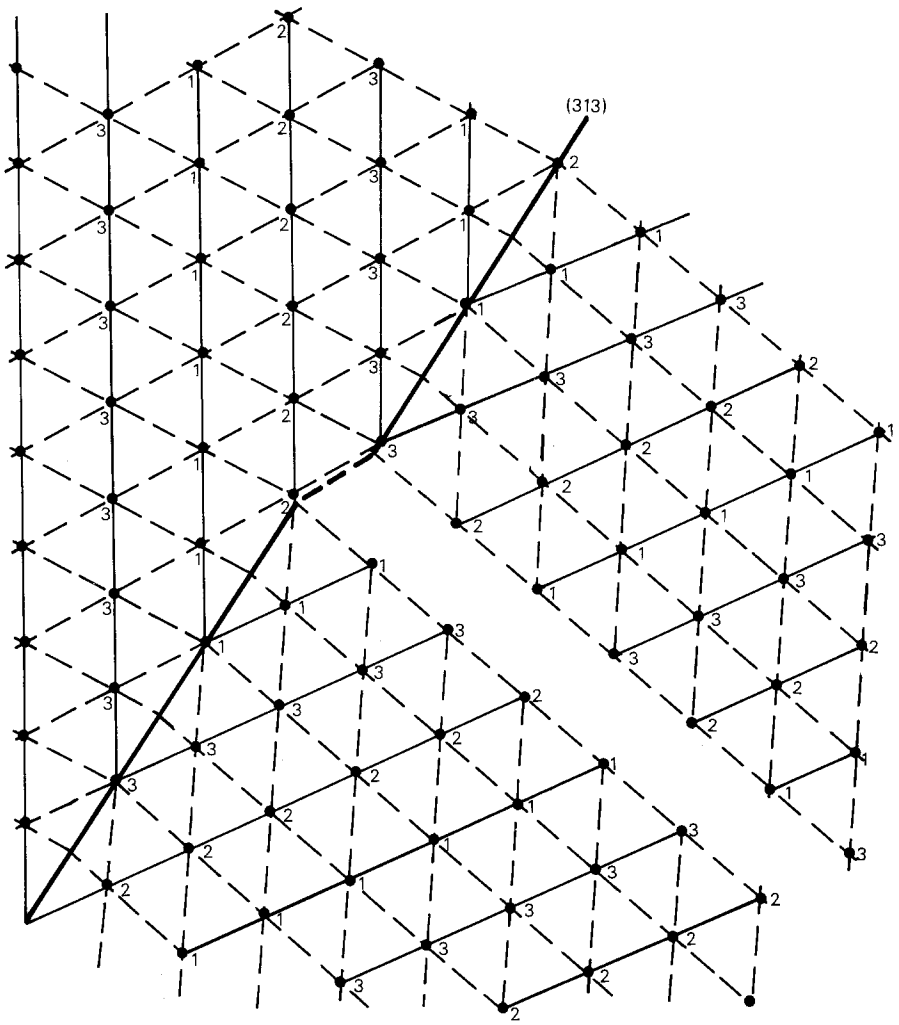

Fig. 39. Anti-phase boundary ending on a (313) twin, with plane of paper parallel to $(20\bar{1})$. The twinning is the same on each side of the anti-phase boundary if a step of one reticular plane occurs on the twin.

2.5.3. *Extra spots in electron diffraction*

It has been noticed (Boulesteix et al., 1970c) that the $(10\bar{1})^*$ plane of the reciprocal lattice shows extra spots in the $[101]^*$ direction and in directions parallel to this. These extra spots appear at one third the distance between two successivé nodes of the reciprocal lattice in the $[101]^*$ direction (fig. 40a). They do not appear near the origin of the reciprocal lattice. The $(10\bar{1})^*$ plane of the reciprocal lattice is obtained by electron diffraction when the electron beam is parallel to the $[10\bar{1}]$ axis. The Ewald sphere is then tangent to the $(10\bar{1})^*$ plane as shown on fig. 41. An electron diffraction is obtained for all the nodes of the reciprocal lattice neighbouring the Ewald sphere, i.e. all the nodes of the $(10\bar{1})^*$

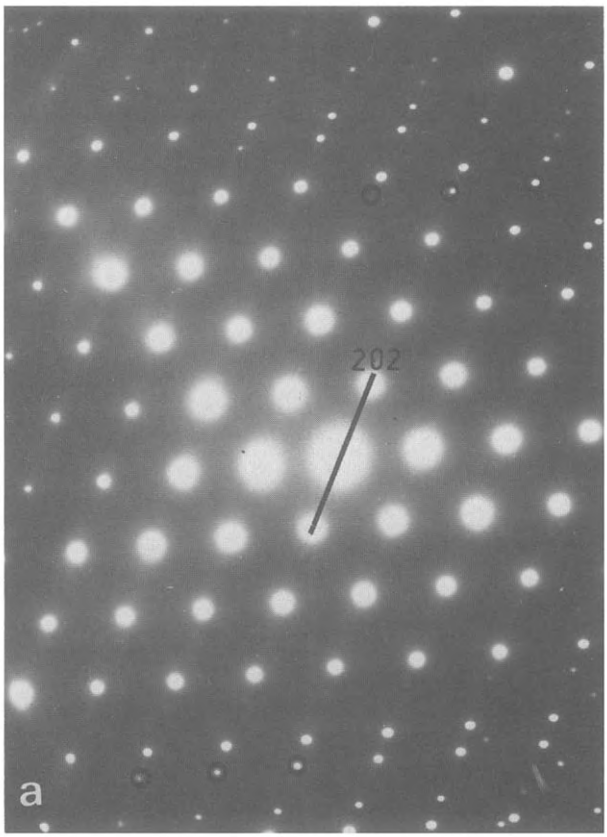

Fig. 40. (a) Diffraction of a B-Sm_2O_3 crystal when the electron beam is parallel to the $[10\bar{1}]$ axis. Extra spots are visible in the direction of 202 spots; they are indicated on the micrograph by black circles. Notice the lack of symmetry of their position in the direction of 202 spots.

plane, but also all the nodes of the upper Laue zones near the Ewald sphere. The extra spots are due to the nodes of the first and second upper Laue zones near the Ewald sphere that are projected in the $(10\bar{1})^*$ plane at one third the distance between two successive nodes in the $[101]^*$ direction. Notice that the $[10\bar{1}]$ axis has no special symmetry, so that the twofold symmetry of the diffraction pattern obtained with the zero layer only (because of Friedel's rule) disappears with the extra spots (fig. 40a).

A variation of the high voltage values gives a variation of the curvature of the Ewald sphere and so of the relative positions of this sphere and the reciprocal lattice nodes (fig. 41). This variation has shown that these nodes have a contribution to the electron microscope image when the electron beam is parallel to the $[10\bar{1}]$ axis. This contribution appears as dark lines that move with a slight variation of the high voltage value (visible for a variation of 2 keV). The contribution of the upper Laue zones to the image exposes the real symmetry of the crystal about the axis parallel to the electron beam (fig. 40b). The $[10\bar{1}]$ axis has no special symmetry as can be seen on the image which has no center of symmetry (related to a symmetry about the $[10\bar{1}]$ axis). There is a symmetry about

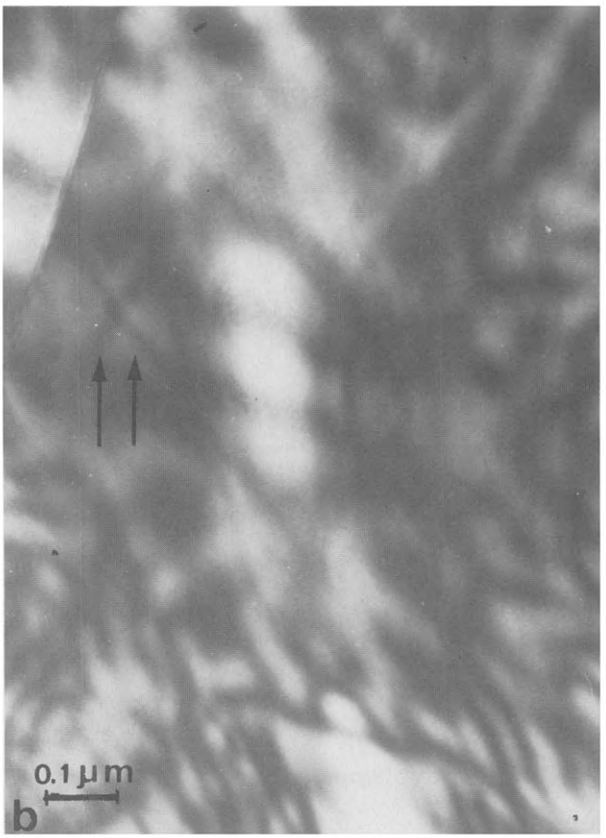

Fig. 40. (b) High magnification image of the [10$\bar{1}$] zone axis pattern related to the diffraction in (a). The lack of symmetry about an axis normal to the image is due to the influence of the image of the nodes of the upper Laue zones. Arrows indicate the position of the bend contours due to these nodes.

a direction related to the symmetry about the (010) plane. Except for the contribution of the upper Laue zones this would not be the case: Friedel's rule makes the nodes h, k, l and $\bar{h}$, $\bar{k}$, $\bar{l}$ play the same role, so that any crystallographic axis appears to be a symmetry axis and each image has at least a center of symmetry if only the zero Laue zone is taken into account. A calculation has been made to identify the nodes of the upper Laue zones responsible for the contribution to the image that can be seen at 100 kV (Boulesteix et al., 1982).

2.6. *The A, B phase transformation and the domains of B resulting from phase transformation*

The symmetry of the high temperature phase A is higher than the symmetry of the low temperature phase B. The A, B phase transformation occurs by temperature variation inside the same crystal. The new structure appears in epitaxial growth on the first one and the displacement of the atoms is very small, so that the transformation is a cooperative phase transformation (diffusionless

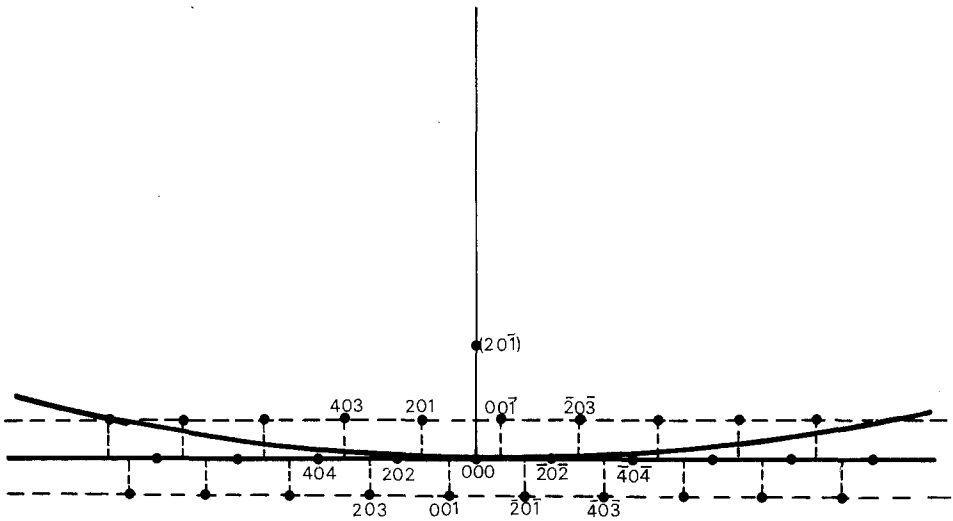

Fig. 41. Intersection of the Ewald sphere with the reciprocal lattice of B, when the Ewald sphere is tangent to the (10$\bar{1}$)* plane. This situation occurs for the electron beam parallel to the [10$\bar{1}$] axis. The [20$\bar{1}$]* direction is slightly different from the direction of the radius of the Ewald sphere. Nodes of the upper Laue zones give extra spots in the [202]* direction, but not near the origin of the reciprocal lattice. The asymmetry of the upper Laue zones is generally visible in electron diffraction.

phase transformation). The loss of symmetry from A to B has been described earlier in section 2.2, but not the transformation itself. We shall see now how this phase transformation occurs and what kind of phenomena are related to it.

2.6.1. *The A, B phase transformation*

The A, B phase transformation has been studied by electron microscopy in the case of Pr_2O_3 and Nd_2O_3 (Boulesteix et al., 1971a,b,c), Sm_2O_3 and Gd_2O_3 (Boulesteix et al., 1970a, 1971a; Portier et al., 1973). A is stable at high temperature and C is stable at room temperature for the two first oxides; for the others, B is stable in a temperature domain higher than room temperature. The B structure can also be obtained for Tb_2O_3, Dy_2O_3 and Ho_2O_3 by a rapid quench inside the electron microscope but in this case it has not been possible to study the A, B transformation.

For Pr_2O_3 and Nd_2O_3, the formation of B occurs by quenching inside the electron microscope, the high temperature being obtained by heating the sample with the electron beam itself (taking off the apertures of the condenser lenses). B appears then like layers in epitaxy on A. The B layers are unstable and disappear after a few minutes. The epitaxy occurs such that a (313) B plane is parallel to a (11 . 0) A plane and the (20$\bar{1}$) B plane is nearly parallel to the (00 . 1) A plane. However, another epitaxial growth, slightly different from this, can also occur with the (424) B plane parallel to (3$\bar{1}$. 0) A plane and the (0$\bar{1}$) B plane nearly parallel to (00 . 1) A plane. The B layers appear on grain boundaries and go through the A crystal. They can pass through grain boundaries but with a

disorientation due to the difference of orientation of the two neighbouring crystals of A. Using thin crystals with surfaces parallel to the (00 . 1), the different (11 . 0) planes are always separated by angles less than 30°, so that the disorientation of the B layers through a grain boundary is also less than 30°. This phenomenon is quite similar to the mechanical twinning of B where twin layers can go through grain boundaries. We suppose then that in the case of Pr_2O_3 and Nd_2O_3 the B layers are induced by the stress related to the quenching and not by the quenching itself; the formation of B then allowing a relaxation of the stress.

For Sm_2O_3 the B structure is obtained by cooling down the A phase. Quenching is not necessary, though the stable phase at room temperature is C. As for A it has not been obtained at room temperature, even by strong quenching. This can be related to the cooperative character of the A to B phase transformation. The transformation in this case must be observed at high temperature. The formation of B can be seen by slowly cooling down an A crystal. A triangular shaped region of B appears in epitaxial growth on A, fig. 42. This triangle starts from a grain boundary and finishes inside the A crystal. The angle at the summit is about 60°. Inside the triangle B is twinned, showing one or sometimes two twins. These twins play a very important role: they allow an epitaxy of B on A on each side of the triangle (fig. 43). These twins, caused by phase transformation, are the same as the mechanical twins of B but their origin is quite different. It is generally not possible to distinguish, when the phase transformation is over, if the observed twins of B are mechanical or phase transformation twins.

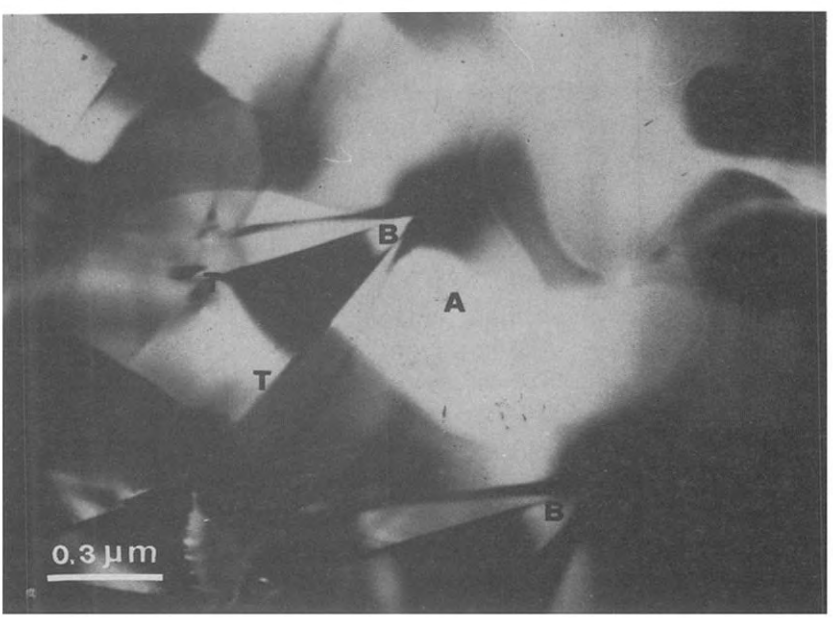

Fig. 42. High temperature hexagonal (A) structure of a Sm_2O_3 crystal, with domains of monoclinic (B) structure exhibiting twins (T).

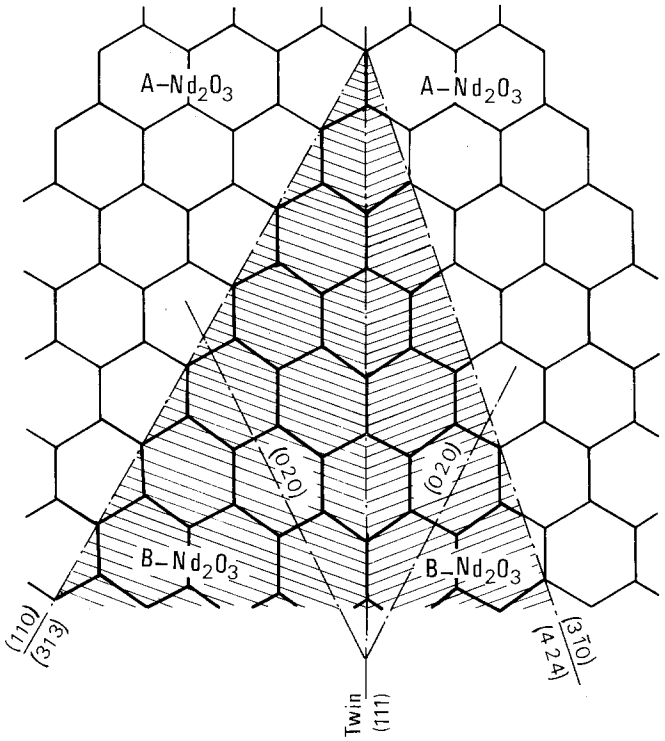

Fig. 43. Crystal seed of B in epitaxial growth on A. The twinning of the B seed allows a good epitaxial continuity on each boundary.

The same phenomenon has been observed in the case of Nd_2O_3 but not for Pr_2O_3, so that the existence of a very narrow domain of stability for B could be possible for Nd_2O_3. This is very unlikely for Pr_2O_3. Fig. 1 gives the domains of stability of structures of R_2O_3 crystals as a function of atomic number and temperature. Nd_2O_3 would be the first oxide for which B could have a stability domain.

2.6.2. *Domains of B by phase transformation*

In the A to B phase transformation two kinds of domains can occur: translation and orientation. The existence of translation domains is due to the higher volume of the unit cell of the primitive lattice of B related to the volume of the unit cell of the primitive lattice of A (three times higher). It is well known that the number of translation domains equals the ratio of the volumes of the unit cells of the primitive lattices. In our case, it gives three translation domains. As seen previously this can be related to the fact that an R atom of A can give one of three kinds of R atoms of B: 1, 2, 3 in the transformation. The value of the translation vector has been given previously.

The existence of orientation domains is due to the fact that the symmetry of B is not as high as the symmetry of A. Following the classical theory for

order–disorder transformations (Amelinckx, 1977) the number of orientation domains n_{01} is equal to the ratio of the order of the point group of symmetry g_0 of the high temperature structure over the order of the point group of symmetry g_1 of the low temperature structure: n_{01} = order of g_0/order of g_1. This result cannot be used in our case since we must use a more general formulation. A general determination of the number of orientation and translation domains by phase transformation has been given recently for any kind of domain (Gracias and Portier, 1979). Following this determination, if the phase transformation is induced by temperature variation, the number of orientation domains is equal to the ratio n_{01} of the order of g_0 the point group of symmetry (that can be used here because we do not take into account the translation domains) of the high temperature structure (S_0) over the order of the intersection, $g_0 \cap g_1$, of g_0 and of g_1 (g_1 is the point group of symmetry of the low temperature structure S_1):

$$n_{01} = \frac{\text{order of } g_0}{\text{order of } g_0 \cap g_1}.$$

If the symmetry elements of S_1 are parallel to their homologues of S_0: $g_0 \cap g_1 = g_1$ and

$$n_{01} = \frac{\text{order of } g_0}{\text{order of } g_1},$$

which is the classical result for order–disorder transformations when the symmetry elements of S_1 are parallel to their homologues of S_0 (fig. 44a).

When a deformation of the lattice (and of the unit cell) occurs by phase transformation as seen for a two dimensional unit cell (fig. 44b) the low temperature phase generally grows in epitaxy on the high temperature phase and the symmetry elements of S_0 and S_1 are generally not parallel. Then if the two structures are centrosymmetric $g_0 \cap g_1 = i$ (where i is the inversion), and

$$n_{01} = \frac{\text{order of } g_0}{\text{order of } i} = \frac{\text{order of } g_0}{2}.$$

In the case of our two dimensional model the classical theory would give:

$$n_{01} = \frac{\text{order of } g_0}{\text{order of } g_1} = \frac{8}{4} = 2,$$

which is right when the symmetry elements of S_0 and S_1 are parallel, i.e. when $g_0 \cap g_1 = g_1$. The transformation occurs then with domains of the low temperature structure oriented as shown on fig. 44a. It is more likely that it occurs as shown on fig. 44b because the conservation of the volume (here the surface) of the unit cell occurs with the conservation of the length of the diagonals so that the best epitaxy occurs when they are superimposed. In this case the symmetry elements of s and S_1 are not parallel and n_{01} (order of g_0)/2 = 8/2 = 4 and then four orientation domains occur.

In the case of the B structure of R_2O_3, the epitaxy of B on A always occurs such that the symmetry elements of B are not parallel to their homologues of A,

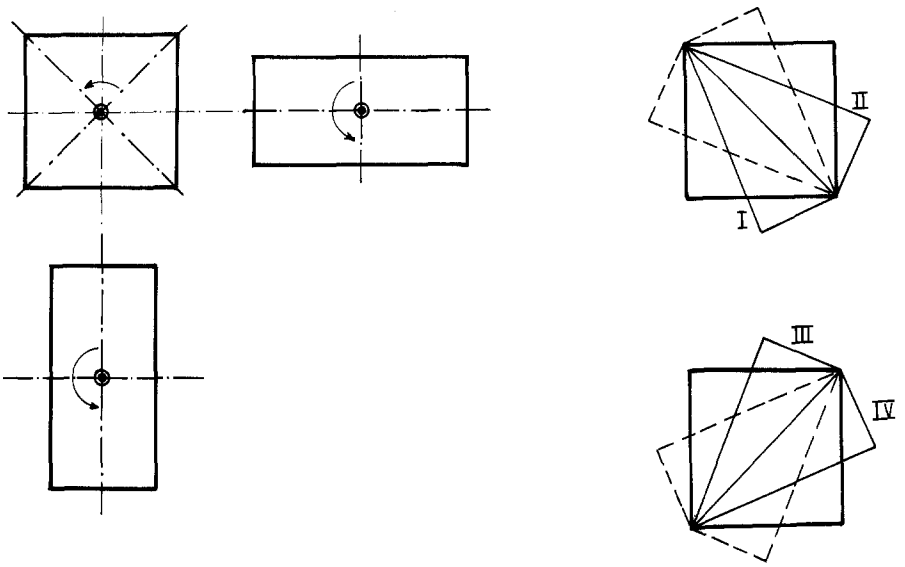

Fig. 44. (a) Classical representation of a group, subgroup phase transformation. The number of domains is n_{01} = order of g_0/order of $g_1 = \frac{8}{4} = 2$, where g_0 is the point group of the square lattice and g_1 the point group of the rectangular lattice. (b) The same transformation occurring with epitaxial growth of the rectangular lattice on the square one. Generally the surfaces of the unit cells are the same so that the length of the diagonals are also the same (up to first order terms). In the epitaxy the diagonals of the two unit cells are then generally parallel. The symmetry elements of the two structures are no longer parallel so that the inversion is the only common element of symmetry. The number of domains is then n_{01} = order of g_0/order of $i = \frac{8}{2} = 4$. The four domains are visible on the drawing. I and II as well as III and IV are in twin position; I and IV as well as II and III are related by a rotation of $\pi/2$ about an axis normal to the plane of the lattice which is a symmetry operation of the square lattice.

so that the number of orientation domains in n_{01} = (order of g_0)/2 = 12/2 = 6, while it would have been n_{01} = order of g_0/order of g_1 = 12/4 = 3 if the symmetry elements of B had been parallel to the symmetry elements of A. This means that for any kind of epitaxy of B on A, six equivalent domains can occur.

We have seen that two different kinds of epitaxy can occur:

1) (424) B plane parallel to $(3\bar{1}\,.\,0)$ A plane and $(20\bar{1})$ B plane nearly parallel to (00 . 1) A plane. In this case, the domains of B have neither their symmetry elements nor their twinning elements parallel to the symmetry elements of A. Six domains occur which are only related by symmetry operations about symmetry elements of A, but which are not related by symmetry operations of B (fig. 45). If they join together, their junction will not be easy because they are not in a twinned position. Notice that domains n_a and n_b of B (fig. 45) are identical: they are related by inversion in a centrosymmetric structure.

2) (313) B plane parallel to (11 . 0) A plane and $(20\bar{1})$ B plane nearly parallel to (00 . 1) A_1 plane. In this case, the domains of B have a twinning element parallel to a symmetry element of A. The six domains are related one by one by a twin about a {313} plane: 1 with 2, 3 with 4, 5 with 6 as shown fig. 46.

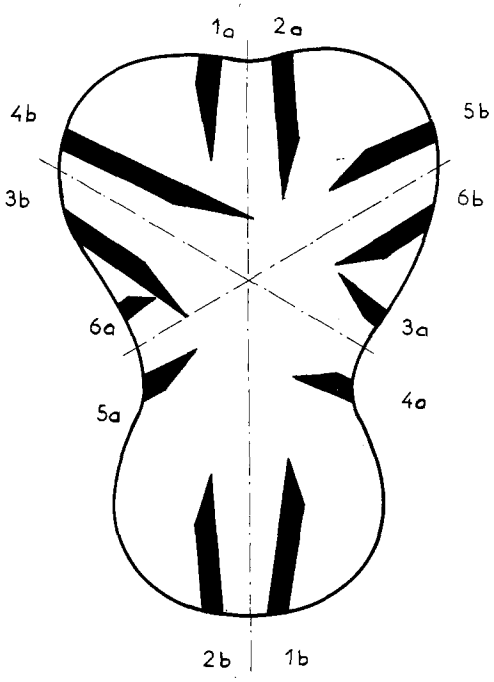

Fig. 45. Equivalent domains of B in epitaxial growth on A, in the most general case. Domains 1 and 2, 1 and 3, 1 and 4, 1 and 5, 1 and 6, ... are related by symmetry operations of A but not by twinning operations of B. Domains *n*a and *n*b are identical because they are related by the inversion for a centro-symmetrical structure. This situation occurs, for example, when the (424) plane of B is parallel to the (00 . 1) plane of A.

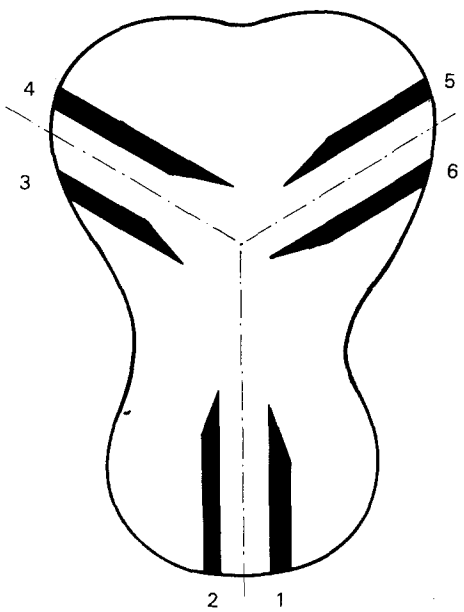

Fig. 46. Equivalent domains of B in epitaxial growth on A, when a twinning element of B is parallel to a symmetry element of A. The number of different domains is always 6 but the domains 1 and 2, 3 and 4, 5 and 6 are related by a twinning operation of B. This situation occurs when the (313) plane of B is parallel to the (11 . 0) plane of A.

The growth of B on A occurs with the formation of a region of B showing a twin, as seen previously. This twin is a (111) twin, and both twinned regions are at once in epitaxy on A with (313) parallel to (11 . 0) for one region and (424) parallel to ($3\bar{1}$. 0) for the second region. Each of these two kinds of epitaxy has six equivalent orientation domains so that twelve domains of B can occur, as shown on fig. 47. Domains I and I′ are in twinned position, domains I and II are also in twinned position (like 1 and 2 in fig. 46); but generally domains are not related by a twin operation. For instance, I′ and II′ are related only by a symmetry operation about a symmetry element of A (like 1a and 2a fig. 45); I and III or V are only related by a rotation of $2\pi/3$ about the C axis of A. The encounter of these different domains can produce very different situations depending on whether they are in a twinned position or not. In the first case a mere twin occurs, in the second the junction can be obtained in some cases by a twin plus a rotation produced (if less than 10°) by microtwinning, but a {111} twin or a ⟨192⟩ twin can also occur so that the encounter of domains is generally very complex. Such a situation has been described in section 2.3.1 (fig. 26a,b).

A very interesting situation occurs when I, III, and V meet as shown on fig. 48a and fig. 49, giving rise to a star pattern. This star pattern is characteristic of orientation domains; it has also been seen for the same kind of transformation in other materials (Manolikas and Amelinckx, 1980a,b,c). New regions of B occur which are only related to regions of B but not of A (fig. 48b). A new region V″ occurs between I and III which is at once in twinned position with each of them, in the same way I″ occurs between III and V and III″ between V and I. These new domains I″, III″ and V″ are related by a rotation of $2\pi/3$ and new twins occur when they encounter, giving new domains and so on.

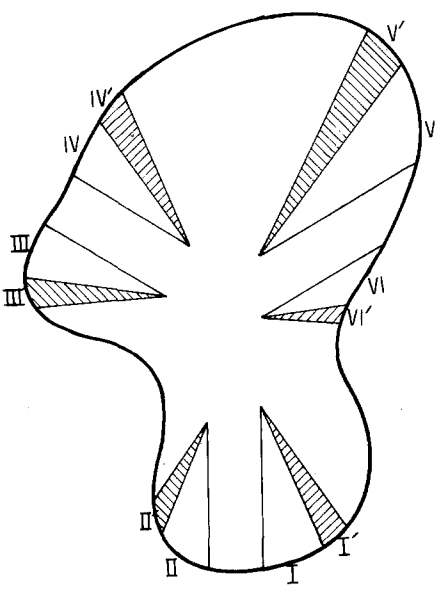

Fig. 47. The real situation occurring in the formation of B crystal seeds on A. Each seed is made of two twinned crystals: I and I′ for example. I and II are in twin position; I and III or V are related by a symmetry operation of A, but not by a twin of B.

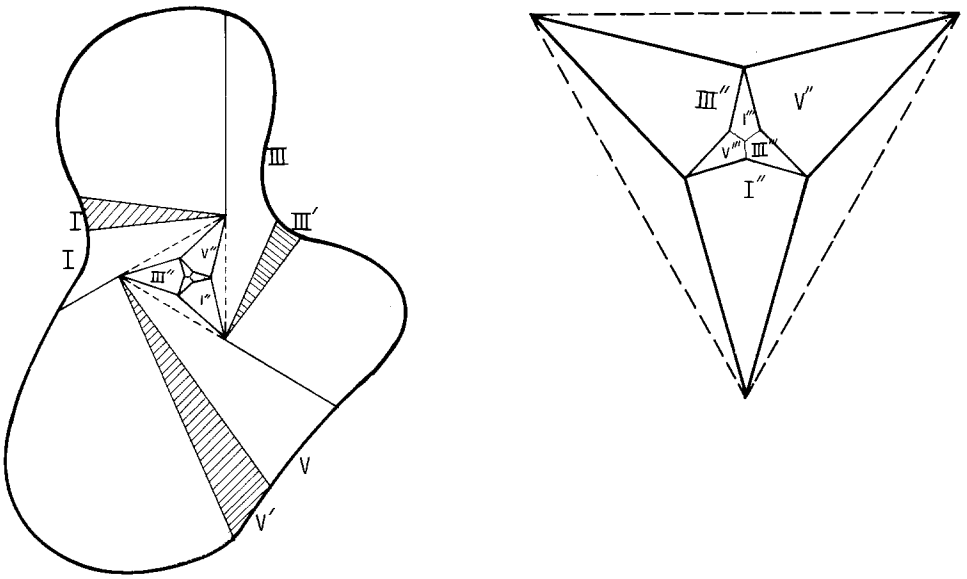

Fig. 48. (a) Junction of three different crystals of B in epitaxial growth on A, related to each other by a rotation of $2\pi/3$ about the [001] axis of A; I′ and III, III′ and V, V′ and I are in quite perfect twin position, but not I and III, I and V or III and V. In the region where these three domains meet, new domains I″, III″, V″ can occur. They are in twin position with their neighbouring crystals: with III and V for I″, V and I for III″, I and III for V″. When they meet, since they are not related by twin position, new domains occur, and so on. This situation gives rise to a star feature which is characteristic of this kind of phase transformations. (b) When I″, III″, V″ meet, three new domains I‴, III‴, V‴ occur, and so on. Finally, domains are separated by irregular grain boundaries.

It is very likely that for reasons of epitaxy the same kind of phenomena that occur in the A to B phase transformation can occur as soon as any phase transformation occurs with deformation of the unit cell. Then

1) the number of orientatation domains is, for centrosymmetrical structures: n_{01} = (order of g_0)/2 orientation domains and not n_{01} = order of g_0/order of g_1;

2) the orientation domains can be, or not, in a twinned position; it is not right to say that the orientation domains are always in twinned position;

3) special features such as star patterns can occur when domains which are not in a twinned position meet.

As for the translation domains of B, they occur because the unit cell of the primitive lattice of B is three times larger than for A, so that each R atom of A can give an R_1 or R_2 or R_3 atom of B, as seen previously. This gives three translation domains, separated by planar defects of translation vectors $\frac{1}{6}$[132] and $-\frac{1}{6}$[132] which are in this case antiphase boundaries. Each kind of epitaxy of B on A gives $6 \times 3 = 18$ equivalent domains. When we deal with B regions made of two twinned regions the number of domains is doubled. We can see that the study of the transformation domains is rather complicated for the B structure. It is probably

Fig. 49. Star feature of domains formed by phase transformation in B-Sm_2O_3 occurring when three domains related by a rotation of $2\pi/3$ meet.

a quite general phenomenon as soon as the unit cell is deformed in the transformation. The case of an order–disorder transformation with conservation of a common lattice, which is well known, is much simpler.

3. The cubic (C) structure

3.1. *Space group of the C structure*

The space group of the C structure of rare earth sesquioxides had been first identified at T^5 ($I2_13$) by Zachariasen (1927). But the most recent work of Pauling and Shappell (1930) has shown that it was T_h^7 (Ia3) with two kinds of R atoms (in

24 d and 8 b sites) and one kind of O atoms (in 48 e sites). This situation was confirmed by several authors (Fert, 1962; Paton and Maslen, 1965; Zachariasen, 1965; Geller et al., 1967), but an NBS circular (1956) has given the wrong space group after a very likely confusion between allowed and forbidden reticular distances in T_h^7 of different Miller indices but of the same reticular distance (Boulesteix et al., 1974). Moreover, Mürr (1967) also suggested T^5 for the space group of the C structure, because forbidden spots in T_h^7 occurred by electron diffraction (figs. 50a,b, 51). But it has been shown:

1) that these forbidden spots disappear in a {100}* reticular plane of the reciprocal lattice, and then are not nodes of the reciprocal lattice; these forbidden spots appear for any other orientation by multibeam diffraction (Boulesteix et al., 1974);

2) that the observed intensity of the forbidden spots, when they occurred, was in good agreement with calculated values (Pardo and Zogheib, 1974).

It seems that the space group T_h^7 is now accepted for the C structure, as well as the position of the O and R atoms related to it. This structure can be described as a fluorite type structure with one quarter of the anions missing. The O atoms are located inside an OR_4 tetrahedron with R atoms located at the four

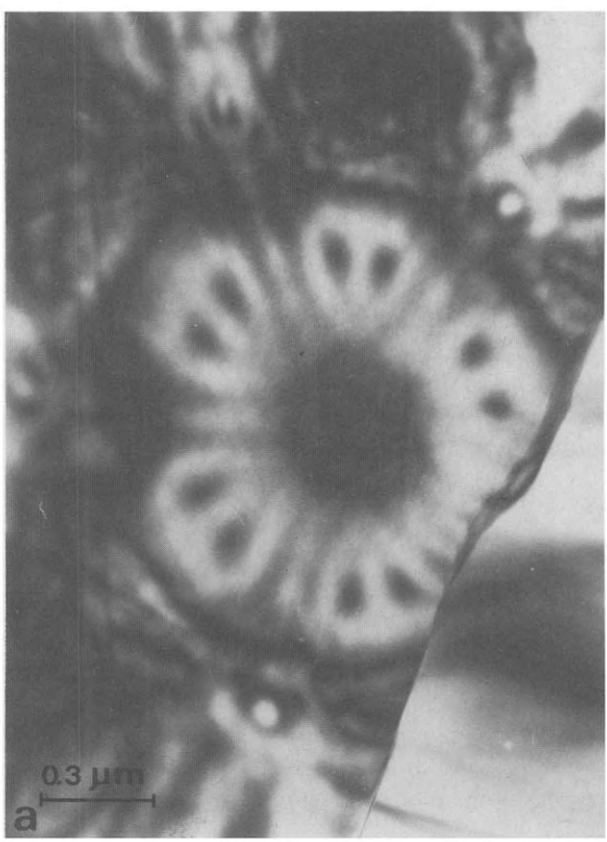

Fig. 50. (a) ⟨111⟩ zone axis pattern of a C-Dy_2O_3 crystal, 800 Å thick. Out of the fine structure, located near the center of the zone axis pattern, the symmetry is a six-fold symmetry for a perfectly sphere-shaped crystal.

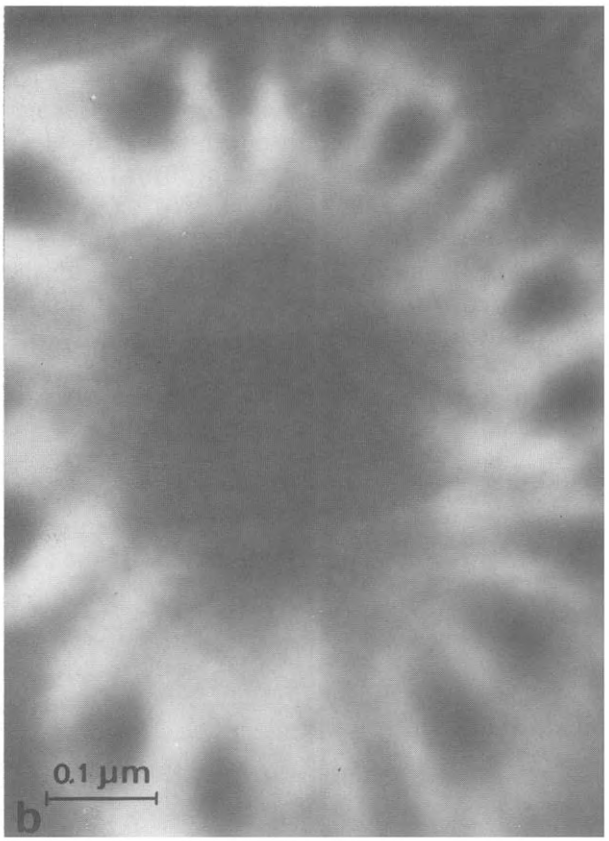

Fig. 50. (b) High magnification of the fine structure visible on a ⟨111⟩ zone axis pattern of a C-Dy_2O_3 crystal. The fine structure exhibits a three-fold symmetry like the crystal itself, about a ⟨111⟩ axis.

corners. Each R atom is common to six tetrahedra giving the general formula R_2O_3 (Caro, 1968). A slight deformation of the tetrahedra and of the position of the missing atoms occur for their different locations inside the unit cell. The structure could be obtained from a fluorite structure by taking off one anion in four. This operation could be done in different ways giving rise to both translation and orientation domains giving twins.

3.2. *Twinning of the C structure*

The fluorite structure and the C type have a common cubic lattice which is a superlattice of the fluorite structure, and which is the lattice for the C structure, so that the symmetry elements of C are also symmetry elements of the fluorite structure. This is the situation of the well-known order–disorder transformation with a common lattice. In this case the number of orientation domains is n_{01} = order of g_0/order of $g_1 = 48/24 = 2$, a relationship which can be deduced from the more general one n_{01} = order of g_0/order of $g_0 \cap g_1$ because in this case $g_0 \cap g_1 = g_1$, where g_0 and g_1 are the point groups of symmetry, respectively, of

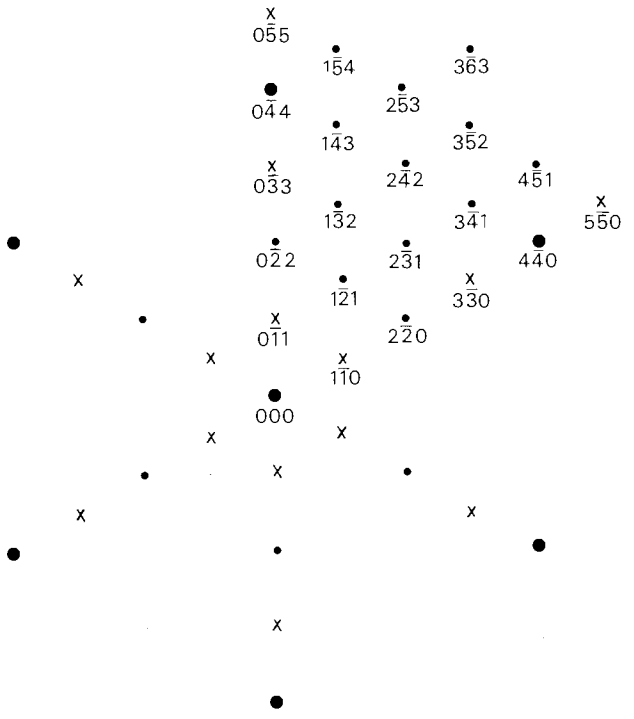

Fig. 51. Indexing of spots of the diffraction pattern of the (111)* plane of the reciprocal lattice of the C structure. Black spots are related to nodes of the reciprocal lattice, crosses are related to forbidden spots which appear by dynamical diffraction.

the fluorite and of the C structure. So, only one kind of twin can occur (but with different possible translations) if we suppose that the most probable defects are related to the location of the vacancies of the O atoms. This twin has been observed (fig. 52) and studied in the case of Sm_2O_3 (Nihoul-Boutang and Boulesteix, 1976). The two twinned crystals are related by symmetry about any {110} plane or about any ⟨110⟩ axis or even by a rotation of $2\pi/6$ about any ⟨111⟩ axis. But this operation does not give the relative position of the two twinned crystals which is defined only in orientation but not in translation. (Indeed different twins can occur in the same crystal, related by a translation operation and joining through a stacking fault.) To know the relative position of the two twinned regions exactly, the twinning operation must be defined about one of the possible twinning elements and, furthermore, we must know the position of the twinning element inside the unit cell. This has been determined in the case of Yb_2O_3 (Fayard et al., 1978) by using many beam diffraction contrast. This allows the knowledge of both the orientation and the relative position in translation of the two twinned crystals. They have shown that the twin occurs so that the R atoms are nearly unchanged in the twin operation and that 16 of the 48 O atoms of the unit cell are also invariant, which is the situation when a maximum number of atomic sites are unchanged by twinning. A general description of the method used can be found in a paper by Gratias et al. (1977).

The twin of the C structure is a merohedral twin or lattice conserving twin

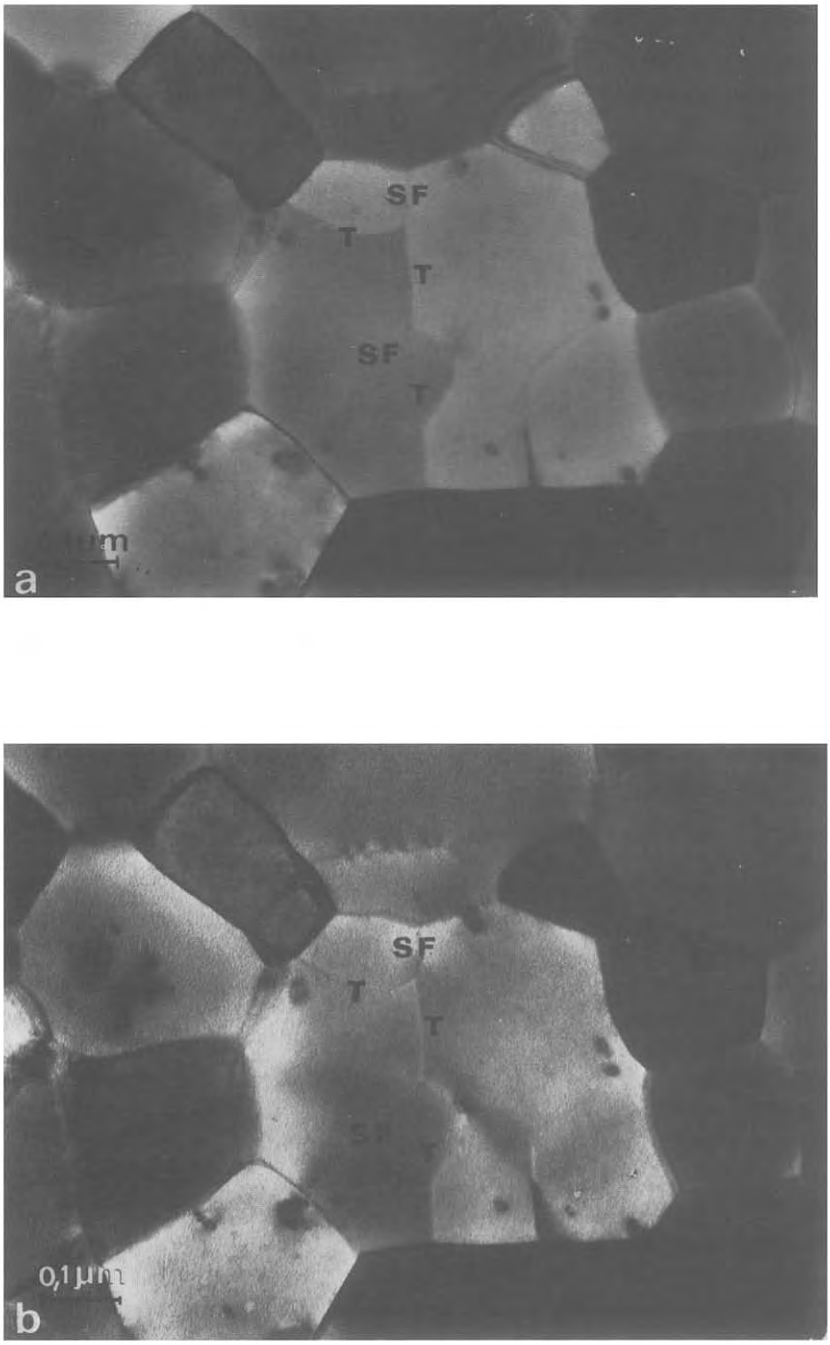

Fig. 52. (a) Small crystals of C-Sm_2O_3 exhibiting twin (T) and stacking faults (SF). Twins are clearly visible. (b) Same crystals as in (a) with stacking faults and twins visible at the same time.

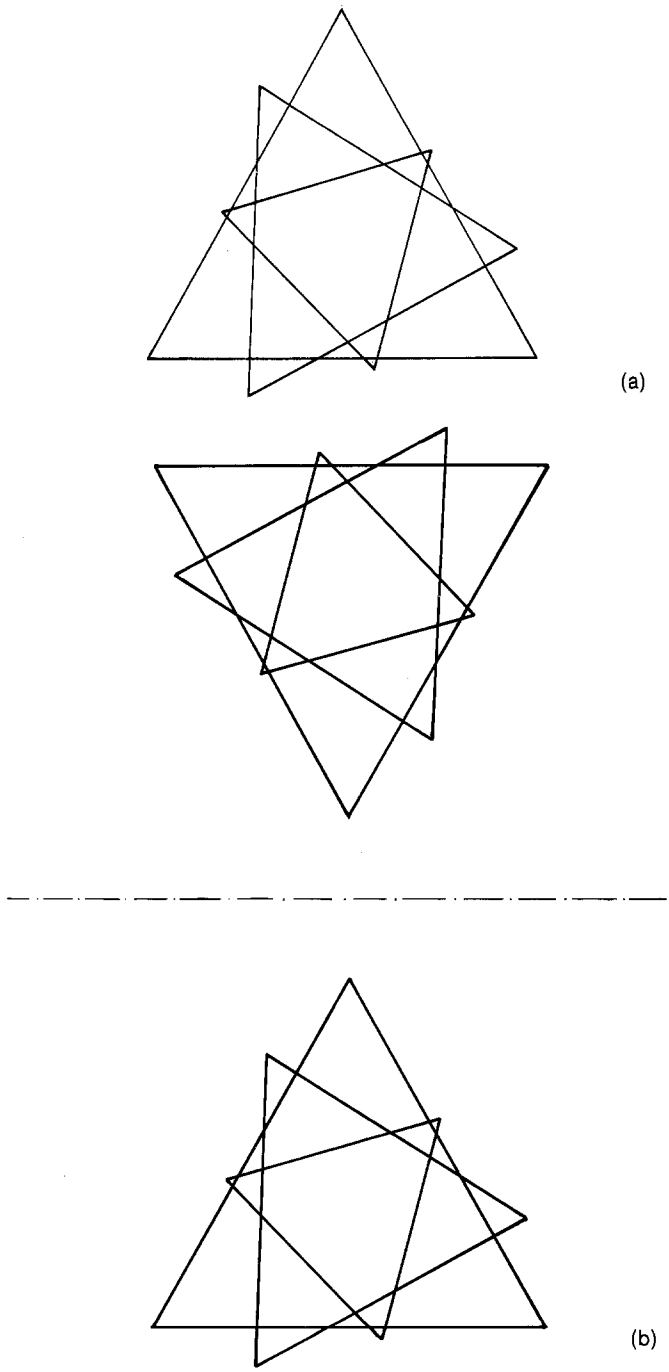

Fig. 53. (a) General feature of the fine structure near a ⟨111⟩ zone axis pattern. This fine structure is due to the influence of the upper Laue zones, the image has only a three-fold symmetry. (b) Relation between two fine structures occurring on each side of a twin of C.

LCT (appendix), i.e., all the nodes of the reciprocal lattice are common to the two twinned crystals, but with different structure coefficients for some of them. Generally these coefficients are the same when we deal with a node with a large structure coefficient, but they can be very different for the nodes having a small structure coefficient. These nodes are responsible for the existence of a slight difference in the background intensity of the image on each side of the twin boundary. This difference is always weak, so that merohedral twins can be easily confused with stacking faults. The use of the fine structure of a zone axis pattern (ZAP) can be very useful to distinguish them.

Near a ⟨111⟩ ZAP of C a fine structure of the image occurs (Boulesteix et al., 1978b). This fine structure appears like interwoven equilateral triangles (fig. 53a), giving to the image (fig. 50b) a three-fold symmetry which is the real symmetry of the [111] axis, so that the fine structure is related to the influence on the image of the nodes of the upper Laue zones. If not, the symmetry of the image would be a six-fold symmetry (fig. 50a) due to the three-fold symmetry of the axis and to the two-fold symmetry of the zero layer (due to Friedel's rule). The high voltage value has a strong influence on the fine structure which changes more quickly than the whole image. This is to be related to the origin of the fine structure. The nodes of the upper Laue zones which give the fine structure, change with the high voltage value, as does the intersection of the Ewald sphere with the plane including these nodes (fig. 54). In the twin of the C structure the two twinned crystals are related by a symmetry operation that can be a rotation of $\pi/3$ about the [111] axis, so that the fine structure is different on each side of the twin boundary (Boulesteix et al., 1979). The two fine structures are related by a rotation of $\pi/3$ about an axis perpendicular to the plane of the image (fig. 53b). This property can be used to identify twins of the C structure. One must orient the crystal so that a ⟨111⟩ ZAP is located on the defect. The fine structure is different on each side if it is a merohedral twin (fig. 55); it is the same if the defect is a stacking fault.

Twins of C being merohedral twins cannot be mechanical twins. They are not

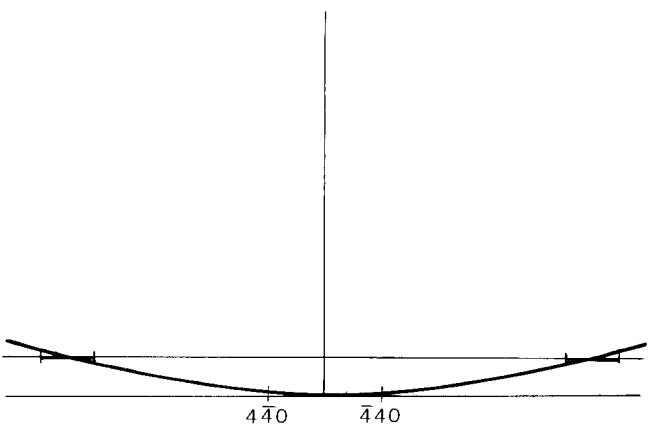

Fig. 54. A small variation of the high voltage value modifies the intersection of the Ewald sphere with the plane of the upper Laue zone, so that the fine structure (due to the nodes of the upper Laue zones) is strongly modified by variations of the high voltage value.

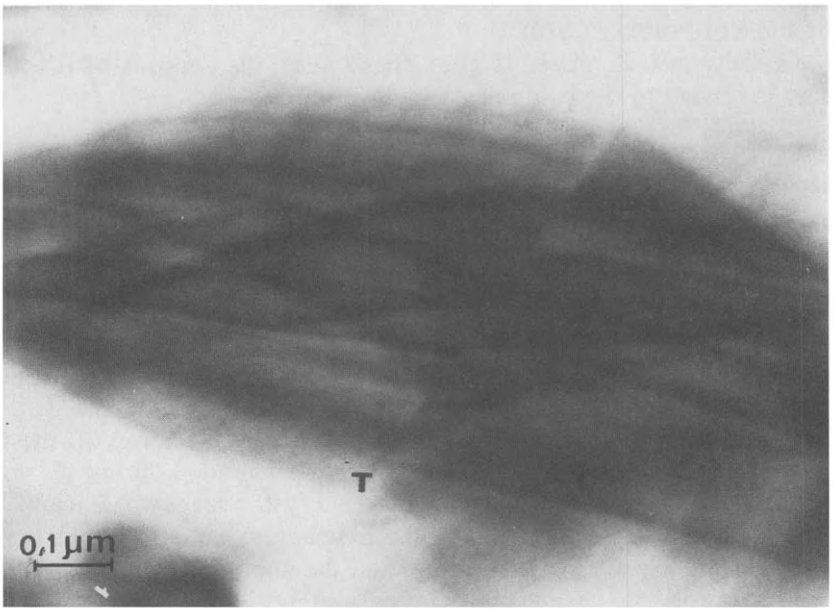

Fig. 55. High magnification image of a twin (T) of a C-Dy_2O_3 crystal visible by using the fine structure of a ⟨111⟩ zone axis pattern.

phase transformation twins. They could be due to a recrystallisation phenonenon, but is seems much more likely that they occur in the crystal seed itself. Then the twin grows with the crystal itself.

3.3. *Stacking faults and dislocations*

Theoretical calculations of stacking fault energy has been performed in the case of Y_2O_3 (C type structure) by Boisson and Gaboriaud (1977). A low value of the stacking fault energy is obtained (80 mJ/m^2) in a {100} plane corresponding to a shear $\frac{1}{2}\langle 110\rangle$ (with (001) for the plane of the defect). This shear vector is a vector of the lattice of the fluorite structure; it changes the lattice of R atoms very little but does change the lattice of missing O atoms (Y_2O_3 or R_2O_3 being treated as derived from a CaF_2 structure).

Dislocations have been studied in the case of Y_2O_3 by Gaboriaud and Boisson (1980). In low temperature and high stress experiments dislocations with Burgers vector ⟨110⟩ occur. In high temperature and low stress experiments dislocations with Burgers vector ⟨100⟩ occur. Both are dissociated according to the weak value of the energy of the stacking fault $\frac{1}{2}\langle 110\rangle$ (100).

Motion of dislocations in C leads to an important plasticity of C even at low temperature. Notice that if at low temperature and high stress, the plasticity can be analysed in terms of glide dissociation of the dislocations, it is analysed at

high temperature and low stress in terms of climb dissociation of the dislocations (Gaboriaud and Boisson, 1980).

The plasticity of C is related to glide phenomena, the opposite of B where the plasticity is related to the twinning phenomena.

4. Conclusion

We have tried to show here that most properties of defects and cooperative phase transformation can be related to the properties of structures. Defects of the rare earth sesquioxides have been studied in detail for the B and C structures but they are presently unknown for the A structure where the experimental studies are more difficult. Twins and stacking faults of B can be explained and even predicted due to the relationship existing between the A and B structures. The A, B cooperative phase transformation occurs because of the strong similarity of these two structures. Their relative orientation during the epitaxial growth of B on A and the twinning of the crystal seeds of B can also be explained in the same way. Defects of the C structure can also be related to the similarity existing between this structure and the fluorite structure.

A special effort has been made to enlarge our knowledge of the rather complex twinning phenomenon in the B structure. Type I as well as type II twins occur at the same time. Moreover, their origin can be either mechanical twins or twins by phase transformation. High resolution studies have been made on incoherent boundaries of wedge microtwins to try to explain some of their properties. This study has shown that the results could be different depending on the role the wedge microtwin plays inside the crystal.

The most important lack in the knowledge of defects occurs for the A structure. It seems very likely that this structure could present twins and stacking faults. Their study is now necessary to have a general view of most of the phenomena dealing with defects in the rare earth sesquioxides.

Acknowledgements

I would like to thank Dr. Yangui of the University of Tunis for all the high-resolution electron micrographs.

I would like to thank Mrs. Billia, who had to do a rather stressing double typing, and Mr. De Nantes, who made most of the drawings, for their very kind help.

I would also like to thank my colleague Pr. Minary for some very helpful comments.

Appendix. Twins and twinning elements

Twinning is a symmetry operation about a plane or an axis which is not a symmetry element. Twins occur when this operation leaves unchanged or nearly

unchanged the crystal lattice and the reciprocal lattice or a superlattice. Using these properties, Friedel (1926) has classified twins in four different kinds: 1) Twins which leave the lattice unchanged: lattice conserving twins: LCT (or merohedral twins)*. This can occur if the lattice has a symmetry higher than that of the crystal. The twinning element is then a symmetry element of the lattice but not of the crystal. For this kind of twin, only the unit cell is modified by a twinning operation. The position of the nodes of the reciprocal lattice is unchanged in the twinning operation, but the indexing and the structure factor can be different. These twins always appear in electron microscopy with a very weak difference in the background intensity on either side of the defect, so that they can easily be confused with stacking faults. Their boundaries are generally irregular. This kind of twin has been studied only recently by electron microscopy. Twins of the C structure are of this kind.

2) Twins which leave a superlattice unchanged: superlattice conserving twins: SLCT (or reticular merohedral twins)*. This can occur if the superlattice has some symmetry elements that are not symmetry elements of the lattice. The twinning element is then a symmetry element of the superlattice which is not a symmetry element of the lattice. For this kind of twin, only some nodes of the lattice and of the reciprocal lattice are unchanged, so that they appear in electron microscopy with a strong difference in the background intensity on each side of the defect. The ratio of the nodes common to the two twinned crystals over the total number of nodes is called multiplicity of the twin (each number is infinite but not the ratio which is an integer). Their boundaries are generally regular. They are very common. The {111} twins of fcc metals are of this kind. Here, the superlattice is hexagonal and has a symmetry element (about the (111) plane or about the [111] axis) which does not exist in the cubic lattice. The symmetry operation about the (111) plane or the [111] axis leaves the superlattice unchanged but changes the lattice.

3) Twins that leave the lattice nearly unchanged: nearly lattice conserving twins: NLCT (or pseudo-merohedral twins)*. The symmetry element is then a pseudo-symmetry element of the crystal (or at least of the lattice). Homologous nodes are then related by a symmetry operation about this pseudo-symmetry element. Homologous nodes of the reciprocal lattice have the same indexing and then the same structure factor (at least if the element is a pseudo-symmetry element of the crystal, which is the most usual case), but they are not located at the same position so that they give, in electron microscopy, a strong difference in the background intensity on each side of the defect. The boundaries are generally regular.

4) Twins that leave a superlattice nearly unchanged: nearly superlattice conserving twins: NSLCT (or reticular pseudo-merohedral twins)*. The pseudo-

*Merohedral twin, reticular merohedral twin, pseudo-merohedral twin, and reticular pseudo-merohedral twin have been obtained by a simple translation of Friedel's expressions "macle par mériédrie", "macle par mériédrie réticulaire", "macle par pseudo-mériédrie" and "macle par pseudo-mériédrie réticulaire"; lattice conserving twin (LCT), superlattice conserving twin (SLCT), nearly lattice conserving (NLCT) and nearly superlattice conserving twin (NSLCT) could be a better translation.

symmetry element is a pseudo-symmetry element of the superlattice. Only the nodes of the superlattice have homologues. The multiplicity of these twins is the ratio of the number of nodes having homologues to the total number of nodes. There is a strong difference in the background intensity on each side of the defect. The boundaries are generally regular. Twins of B are of this kind with a multiplicity of 3.

The twinning element can be either a twinning plane or a twinning axis. If we only want to take into account reticular axes or reticular planes we must distinguish between these two cases (even if the crystal is centro-symmetric). Twins are said to be type I twins if the symmetry element is a reticular plane; they are said to be type II twins if the symmetry element is a reticular axis. They are said to be rational or compound twins when they can be described either by a twinning operation about a plane or about an axis, as in the case of the twin of fcc metals. Compound twins occur generally in high symmetry crystals. In the case of Uranium, compound, type I and type II twins, occur at the same time.

Twins occur by different mechanisms, generally by crystal growth or recrystallisation for merohedral or reticular merohedral twins, by mechanical twinning or by phase transformation for pseudo-merohedral twins and in some cases for reticular merohedral twins.

Mechanical twins are of special interest. They can be either type I or type II twins or even compound twins. They can appear by shear deformation of the

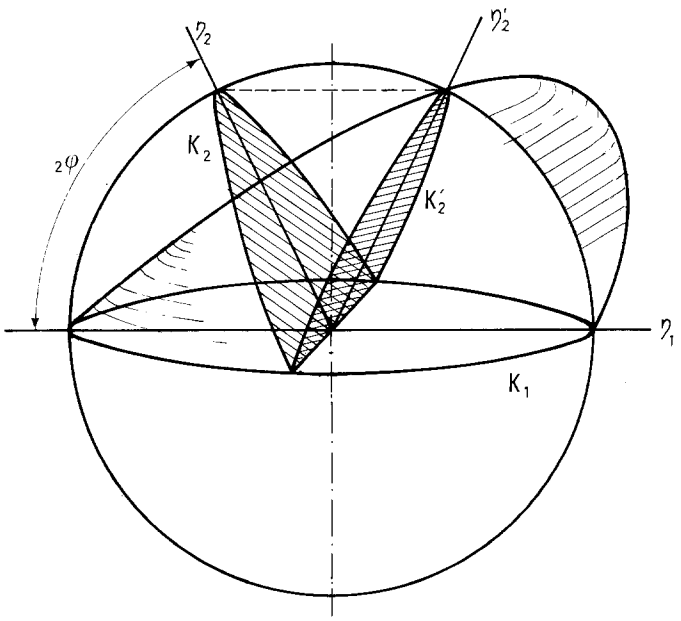

Fig. 56. Relationship of a spherical crystal and of a twinned ellipsoidal crystal. K_1 is the habit plane, η_1 is the shear direction, K_2 is the second undeformed plane, η_2 is located at the intersection of the shear plane and of K_2. The shear modulus is $s = 2 \cot 2\phi$.

crystal. The shear direction is called η_1 and the boundary between twinned crystals K_1 is parallel to η_1. η_1 is also the twinning axis for a type II twin and K_1 is also the twinning plane for a type I twin; K_1 is generally said to be the "habit plane". In each case a sphere (fig. 56) is transformed by twinning in an ellipsoid, where only two planes are undeformed: K_1 (the habit plane), which is only translated by twinning in the direction of η_1, and K_2, whose direction is only changed by twinning; K_2 is called the second undistorted plane. The plane perpendicular to K_1 and containing η_1 is the "plane of shear". It intersects K_2 in a direction η_2. K_1 and η_2, or K_2 and η_1 are sufficient to determine twinning completely. In the most general case K_1, η_1, K_2, η_2 are not rational at the same time. For type I twins K_1 and η_2 are rational and for type II twins η_1 and K_2 are rational. For compound twins all four indices are rational. If 2ϕ is the smaller dihedral angle between K_1 and K_2 the magnitude of the shear is given by $s = 2\cot 2\phi$ (fig. 56). When two kinds of twins A and B have at the same time: $K_{1A} \equiv K_{2B}$, $\eta_{1A} \equiv \eta_{2B}$, $K_{2A} \equiv K_{1B}$ and $\eta_{2A} \equiv \eta_{1B}$, they are said to be reciprocal twins. In this case two elements, K_{1A} and η_{2A}, or η_{1A} and K_{2A}, are rational at the same time.

References

Amelinckx, S., 1977, J. Microsc. Spectrosc. Electron. **2**, 345.

Bassinski, Z.S. and J.W. Christian, 1954, Acta Met. **2**, 101.

Boisson, M. and R.J. Gaboriaud, 1977, J. Physique **38**, L177.

Boulesteix, C. and Ch. Loier, 1973, Phys. Stat. Sol. a **18**, 553.

Boulesteix, C., L. Valiergue, M. Gasgnier and Ch. Henry La Blanchetais, 1970a Thin Solid Films **8**, 51.

Boulesteix, C., P.E. Caro, M. Gasgnier and Ch. Henry La Blanchetais, 1970b Acta Cryst. **B26**, 1043.

Boulesteix, C., B. Pardo, L. Valiergne, P.E. Caro, M. Gasgnier and Ch. Henry La Blanchetais, 1970c, Phys. Letters **A32**, 5, 361.

Boulesteix, C., P.E. Caro, M. Gasgnier and Ch. Henry La Blanchetais, 1971a, in: Etudes des transformations cristallines à haute températures au-dessus de 2000 K Coll. Intern. CNRS no. 205, p. 361.

Boulesteix, C., P.E. Caro, M. Gasgnier, Ch. Henry La Blanchetais and G. Schiffmacher, 1979b, Acta Cryst. **A27**, 552.

Boulesteix, C., P.E. Caro, M. Gasgnier, Ch. Henry La Blanchetais and G. Schiffmacher, 1971c, Phys. Letters **34A**, 437.

Boulesteix, C., B. Pardo, P.E. Caro, M. Gasgnier and Ch. Henry La Blanchetais, 1971d Acta Cryst. **B27**, 216.

Boulesteix, C., P.E. Caro, Ch. Loier and R. Portier, 1972, Phys. Stat. Sol. a **11**, 771.

Boulesteix, C., P.E. Caro, M. Gasgnier, Ch. Henry La Blanchetais, B. Pardo and G. Schiffmacher, 1974, Phys. Stat. Sol. a **23**, 597.

Boulesteix, C., J. Van Landuyt and S. Amelinckx, 1976, Phys. Stat. So. a **33**, 595.

Boulesteix, C., C. Colliex, C. Mory, D. Renard and B. Yangui, 1978a, J. Microsc. Spectrosc. Electron. **3**, 185.

Boulesteix, C., G. Nihoul-Boutang and B. Yangui, 1978b, Phys. Stat. Sol. a **45**, 639.

Boulesteix, C., G. Nihoul-Boutang, C. Césari and B. Yangui, 1979, J. Microsc. Spectrosc. Electron. **4**, 213

Cahn, R.W., 1953, Acta Met. **1**, 49.

Cahn, R.W., 1954, J. Inst. Met. **79**, 129.

Caro P.E., 1968, J. Less Common Met. **16**, 367.

Caro, P.E., G. Schiffmacher, C. Boulesteix, Ch. Loier and R. Portier, 1974, in: Defects and transport in oxides, eds. M.S. Seltzer and R.I. Jaffer (Plenum Press, New York).

Cromer, D.T., 1957, J. Phys. Chem. **61**, 753.

Fayard, D. Gratias, R. Portier and M. Guymont, 1978, Inst. Phys. Conf. Ser. **41**, 391.

Fert, A., 1962, Bull. Soc. Franç. Miner. Crist. **85**, 267.

Foëx, M. and J.P. Traverse, 1966, Bull. Soc. Franç. Miner. Crist. **89**, 184.

Friedel, G., 1926, Leçon de cristallographie (Berger-Levrault, Paris).

Friedel, J., 1964, Dislocations (Pergamon Press, Oxford) p. 178.

Gaboriaud, R.J. and M. Boisson, 1980, J. Physique **41**, C-6, 171.

Gasgnier, M., 1977, Thesis Orsay (France).

Gasgnier, M., 1980, Phys. Stat. Sol. a **57**, 11.

Gasgnier, M., J. Ghys, G. Schiffmacher, Ch. Henry La Blanchetais, P.E. Caro, C. Boulesteix, Ch. Loier and B. Pardo, 1974, J. Less Common Met. **34**, 131.

Geller, S., P. Romo and J.P. Remeika, 1967, Z. Krist. **124**, 136.

Gratias, D., M. Guymont, R. Portier and M. Fayard, 1977, Phil. Mag. **35**, 5, 1199.

Gratias, D. and R. Portier, 1979, in: Proceedings of ICOMAT, Cambridge.
Hasson, G., 1972, Thesis Paris (France).
Kern, F. and N. Perakis, 1970, C.R. Acad. Sci. (Paris) **B270**, 1593.
Koehler, W.C. and E.O. Wollan, 1953, Acta Cryst. **6**, 741.
Levasseur, J., 1969, Met. Sci. Eng. **4**, 343.
Levasseur, J., 1971, Thesis Paris (France).
Loier, Ch., 1973, Thesis Orsay (France).
Manolikas, C. and S. Amelinckx, 1980a, Phys. Stat. Sol. a **60**, 607.
Manolikas, C. and S. Amelinckx, 1980b, Phys. Stat. Sol. a **61**, 179.
Manolikas, C. and S. Amelinckx, 1980c, in: Electron microscopy 1980, Seventh European Congress of Electron Microscopy Foundation, Leiden, Vol. I, p. 396.
Müller-Buschbaum, M.K. and M.G. Von Schnering, 1965, Z. Anorg. Allgem. Chemie **340**, 232.
Mürr, L.E., 1967, Phys. Stat. Sol. **24**, 135.
NBS Circular, 1956, no. 539, Vol. 8, p. 25.
Nihoul, G. and C. Boulesteix, 1976, Phys. Stat. Sol. a **34**, 331.
Pardo, B., 1977, Thesis Orsay (France).
Pardo B., and H. Zogheib, 1974, Phys. Stat. Sol. a **24**, 91.
Paton, M.G. and E.N. Maslen, 1965, Acta Cryst. **19**, 307.
Pauling, L. and L.D. Shappel, 1930, Z. Krist. **7**, 128.
Portier, R., M. Fayard, C. Boulesteix and P.E. Caro, 1973, Mater. Res. Bull. **8**, 693.
Reed-Hill, R.E., 1964, Trans. AIME **230**, 809.
Schiffmacher, G., P.E. Caro and C. Boulesteix, 1976, Phys. Stat. Sol. a **33**, K9.
Shafer, M.W. and R. Roy, 1959, J. Amer. Ceram. Soc. **42**, 563.
Sleeswyk, A.W., 1962, Acta Met. **10**, 705.
Vicens, J., P. Delavignette and A. Deschanvres, 1978, J. Microsc. Spectrosc. Electron. **1**, 15.
Willer, B. and M. Daire, 1969, Bull. Soc. Franç. Miner. Crist. **92**, 33.
Yakel, H.L., 1979, Acta Cryst. **B35**, 564.
Yangui, B., 1981, Thesis Tunis (Tunisia).
Yangui, B., C. Boulesteix, A. Bourret, G. Nihoul and G. Schiffmacher, 1980, in: Electron Microscopy 1980, Seventh European Congress of Electron Microscopy Foundation, Leiden, Vol. I, p. 372.
Yangui, B., C. Boulesteix, A. Bourret, G. Nihoul and G. Schiffmacher, 1982, Phil. Mag. (A)**45**, 443.
Zachariasen, W., 1927, Norsk. Geol. Tidsok **9**, 310.
Zachariasen, W., 1965, Z. Krist. **80**, 187.

General references

Cahn, R.W., 1953, Acta Met. **1**, 49.
Reed-Hill, R.E., J.P. Hirth and H.E. Rogers, 1963, Deformation twinning (Gordon and Breach, New York).
Friedel, J., 1964, Dislocations (Pergamon Press, Oxford).
Nabarro, F.R., ed., 1979, Dislocations in solids (North-Holland, Amsterdam).
Friedel, G., 1926, Leçons de Cristallographie (Berger-Levrault, Paris); republished 1965 (Blanchard, Paris).
Hirth, J.P. and J. Lothe, 1968, Theory of dislocations (McGraw-Hill, New York).
Hall, E.O., 1954, Twinning and diffusionless transformations in metals (Butterworths, London).

Handbook on the Physics and Chemistry of Rare Earths, edited by K.A. Gschneidner, Jr. and L. Eyring

Chapter 45

RARE EARTH FLUORIDES

Ortwin GREIS
Department of Chemistry University of Petroleum and Minerals, P.O. Box 144, Dhahran, Saudi Arabia

John M. HASCHKE
Rockwell International, Rocky Flats Plant, P.O. Box 464, Golden, Colorado 80401, USA

Contents

Symbols

A = alkali or alkaline earth metal
C_p° = standard state heat capacity ($J\,K^{-1}\,mol^{-1}$)
D_T° = dissociation (atomization) energy of gaseous molecule ($kJ\,mol^{-1}$)
ΔG_{xT}° = standard state free energy change for process x at temperature T ($kJ\,mol^{-1}$)
ΔH_{xT}° = standard state enthalpy change for process x at temperature T ($kJ\,mol^{-1}$)
K_{eq} = equilibrium constant
k = Boltzmann constant = 1.38054×10^{-6} erg K^{-1}
M = molarity in mol ℓ^{-1}
m = molality in mol kg^{-1}
R′ = second rare earth
R^* = gas constant = $8.3143\,J\,K^{-1}\,mol^{-1}$
S_T° = standard state entropy at temperature T ($J\,K^{-1}\,mol^{-1}$)

ΔS°_{xT} = standard state entropy change for process x at temperature T ($J\,K^{-1}\,mol^{-1}$)
T_x = temperature of process x in K
x = process subscript for state variables
$x = b$ normal boiling process
$x = f$ formation process from standard state elements
$x = m$ normal melting process
$x = t$ solid–solid phase transition
$x = v$ vaporization or sublimation process
( ) in tables, all estimated numerical values are enclosed in parenthesis

1. Introduction

The anhydrous fluorides are by far the most important halides of the rare earth elements. This results mainly from their chemical and thermal stability in comparison to the other halides and, therefore, to their advantageous application in research and industry. The chemistry of the rare earth fluorides has been reviewed by Batsanova (1971), in the Gmelin Handbook (1976), and partially together with the other rare earth halides by Haschke (1979) in chapter 32 of this Handbook. With respect to the importance of the fluorides, it seems to be appropriate to devote a separate chapter to this class of compounds, especially because many new and exciting results have been found more recently which are not covered in the above reviews. This review deals mainly with preparation, phase relationships, structural chemistry, and thermodynamic properties of RF_3, RF_2, $RF_{2+\delta}$, RF_4, and mixed fluorides of the systems AF–RF_3 and AF_2–RF_3, A(I) being alkali and A(II) alkaline earth elements. Special regard is paid to aspects which are omitted from or inadequately covered in the Gmelin Handbook (1976) and by Haschke (1979).

2. Binary rare earth fluorides

2.1. *Trifluorides*

Within the rare earth fluorides, most attention has been paid to the anhydrous trifluorides which represent in many ways the key to this field of rare earth chemistry. Considerable interest grew in the early fifties when Daane and Spedding (1953) and Spedding and Daane (1956) prepared large amounts of pure rare earth metals by calciothermal reduction of the corresponding trifluorides. Further applications are only suggested by a few keywords: carriers for the separation of transuranic elements from hydrous acids and spent nuclear fuels, fluxes for electroslag melting of metals, fluorine anion selective electrodes, fast anionic conductors, additives for glasses, optical filter and thin film technologies, chemiluminescence, electroluminescence, thermoluminescence, laser and up-conversion materials, discharge lamps etc. Many of the above applications are due to properties of the rare earth cations; fluorides, however, are chosen because of their chemical stability in contrast to the other halides. Very recently, two reviews appeared on industrial applications of rare earths (Greinacher, 1981; Greinacher and Reinhardt, 1982).

The large number of publications on the preparation of rare earth trifluorides have been reviewed by Carlson and Schmidt (1961), and more recently in the Gmelin Handbook (1976) and by Haschke (1979). Most of the reported methods, however, are of little value as far as ease of technique and purity of the anhydrous trifluorides are concerned. With respect to the latter point, only the oxides can be recommended as suitable starting materials. Their conversion to trifluorides is possible in principle in two ways employing either a dry or a wet method (Zalkin and Templeton, 1953). Greis (1976), however, has shown that anhydrous trifluorides without detectable amounts of oxide fluorides or enclosed bubbles of unreacted oxides can be obtained in an optimal way by combining both methods. In the first step, the oxides are dissolved in HCl or HCl/HNO_3 and hydrated trifluorides are precipitated with fluoric acid (wet method). The dehydration is then carried out by means of either the so-called ammonium fluoride technique at 200–400°C (see e.g. Carlson and Schmidt, 1961) or under a stream of HF or HF/N_2 at temperatures up to about 700°C (dry method). The advantageous employment of vitreous carbon tubes and boats should be mentioned because they are inert against HF and RF_3 up to about 1000°C. Further details are described by Greis and Petzel (1974), Greis (1976), and in the Brauer Handbook (1975).

The rare earth trifluorides are stable in air and moisture at room temperature, but not at higher temperatures where oxide fluorides and finally oxides are formed at about 1000°C. They melt congruently between 1140 and 1550°C and are dimorphic except for LaF_3–PmF_3, TbF_3–HoF_3 and ScF_3. So far, four different structure types are known among the rare earth trifluorides: the LaF_3 or tysonite structure ($P\bar{3}c1$–$P6_3/mmc$), the β-YF_3 structure (Pnma), the hexagonal/trigonal α-YF_3 structure (related to α-UO_3 or α-$UO_{3-\delta}$), and the ReO_3 structure (Pm3m). Additional structural details are given and discussed below. The first systematic investigations of the dimorphism of the rare earth trifluorides were carried out by Thoma and Brunton (1966). Their results, however, were open to discussion for many years mainly with respect to the transformation temperatures and the existence of high-temperature modifications. De Kozak et al. (1973) clarified the uncertainties in the case of GdF_3. They found that small amounts of oxide fluoride or oxide lowered the α–β phase transformation significantly from 1075 to 900°C and increased the melting point from 1250 to 1325°C. A similar influence of oxygen in the form of OH^- in the case of GdF_3, DyF_3, and HoF_3 has been noticed by Pastor and Robinson (1974). Spedding and Henderson (1971) and Spedding et al. (1974) re-investigated the high-temperature data on rare earth trifluorides containing less than 20 ppm oxygen by weight. In contrast to the work by Thoma and Brunton (1966), they found rather different transition temperatures and in the case of TbF_3, DyF_3, and HoF_3 even no phase transition. Later, Sobolev et al. (1976a,b,c) confirmed these findings. In contrast, de Kozak et al. (1980) reported that DyF_3 is dimorphic, but gave no data on the purity of their DyF_3. It is now obvious that Thoma and Brunton (1966) studied trifluorides which were contaminated with intolerable amounts of oxygen. The most reliable transformation temperatures and melting

TABLE 1
Stability ranges and lattice parameters of the different modifications of the rare earth trifluorides.

RF_3	Temp. (°C)	Symm.	a (Å)	b (Å)	c (Å)
LaF_3	up to 1493[a]	$P\bar{3}c1$[c]	7.1862		7.3499
CeF_3	up to 1432[b]	$P\bar{3}c1$[c]	7.1294		7.2831
PrF_3	up to 1399[a]	$P\bar{3}c1$[c]	7.0785		7.2367
NdF_3	up to 1377[a]	$P\bar{3}c1$[c]	7.0299		7.1959
PmF_3	up to (1338)	$P\bar{3}c1$[d]	6.97		7.19
α-SmF_3	490–1300[b]	$P\bar{3}c1$[c]	6.9536		7.1183
β-SmF_3	up to 490[b]	Pnma[c]	6.6715	7.0584	4.4028
α-EuF_3	647–(1262)[b]	$P\bar{3}c1$[c]	6.9193		7.0895
β-EuF_3	up to 647[b]	Pnma[c]	6.6193	7.0175	4.3958
α-GdF_3	1075–1232[b]	$P\bar{3}c1$[c]	(6.883)		(7.057)
β-GdF_3	up to 1075[b]	Pnma[c]	6.5684	6.9818	4.3915
TbF_3	up to 1177[b]	Pnma[c]	6.5079	6.9455	4.3869
DyF_3	up to 1157[b]	Pnma[c]	6.4506	6.9073	4.3859
HoF_3	up to 1143[a]	Pnma[c]	6.4038	6.8734	4.3777
α-YF_3	1077–1155[a]	hex.[e,f]	4.12		4.23
β-YF_3	up to 1077[a]	Pnma[c]	6.3654	6.8566	4.3916
α-ErF_3	1117–1146[b]	hex.[e,f]	4.02		4.14
β-ErF_3	up to 1117[b]	Pnma[c]	6.3489	6.8417	4.3824
α-TmF_3	1053–1158[b]	hex.[e,f]	4.05		4.17
β-TmF_3	up to 1053[b]	Pnma[c]	6.2779	6.8133	4.4095
α-YbF_3	986–1162[b]	hex.[e,f]	4.03		4.16
β-YbF_3	up to 986[b]	Pnma[c]	6.2165	6.7855	4.4314
α-LuF_3	957–1184	hex.[e,f]	4.02		4.15
β-LuF_3	up to 957[a]	Pnma[c]	6.1504	6.7617	4.4679
ScF_3	up to 1552[b]	Pm3m[b]	4.0137		

[a]Spedding and Henderson (1971). [b]Spedding et al. (1974). [c]Greis and Petzel (1974). [d]Weigel and Scherer (1967). [e]Thoma and Brunton (1966). [f]Sobolev and Fedorov (1973).

points are compiled in table 1 and graphically compared with the data by Thoma and Brunton (1966) in fig. 1. As in most of the subsequent tables, data were chosen from the literature only if the purity of the samples has been proved by chemical and/or physical analyses. Comparison of data is enhanced if several or all rare earth fluorides have been investigated in the same study. Estimated values are given in parentheses.

The lattice parameters of all rare earth trifluoride modifications are also listed in table 1. They represent room-temperature data except for the α-forms of ErF_3–LuF_3 and YF_3. Because these high-temperature phases cannot be quenched, one relies on high-temperature diffraction data which are only reported by Thoma and Brunton (1966). Their data, however, have been re-indexed by Sobolev and Fedorov (1973) on the basis of a smaller unit cell, ($a_{TB} = \sqrt{3}a_{SF}$, $c_{TB} = 2c_{SF}$, $Z_{TB} = 6Z_{SF}$), the lattice parameters of which are listed in table 1. Sobolev and Fedorov (1973) found also that this so-called α-YF_3 type is

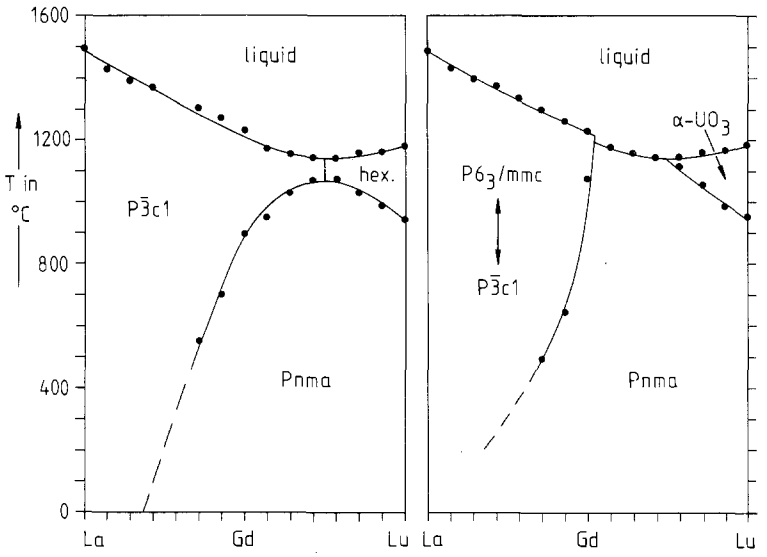

Fig. 1. Dimorphism of the rare earth trifluorides: (left) after Thoma and Brunton (1966) from samples containing significant amounts of oxide fluorides; (right) from pure trifluorides after the data of table 1.

isostructural with α-UO_3 in spite of the fact that the latter structure is still questionable as far as chemical composition (α-$UO_{3-\delta}$?), symmetry (hexagonal/trigonal, distorted orthohexagonal, superstructure?), and atomic parameters are concerned. Nevertheless, the α-YF_3 type appears to be closely related to α-UO_3 or α-$UO_{3-\delta}$, but more structural (high-temperature) data are needed. On the other hand, the α-YF_3 type modifications are easily detectable by thermal analyses due to the surprisingly high enthalpies of the α–β transformation (Spedding and Henderson, 1971; Spedding et al., 1974). The same authors also found high entropy changes in comparison to the transformations between the β–YF_3 and LaF_3-type structures. High entropy changes, however, indicate premelting of a sublattice (O'Keeffe and Hyde, 1976; O'Keeffe, 1977), and, indeed, high anionic conductivity has been observed with α-YF_3 and α-LuF_3 (O'Keeffe, 1973). Within the rare earth trifluorides, this α-UO_3-related high-temperature phase appears half-way between HoF_3 and ErF_3 as shown in a phase study of the HoF_3–ErF_3 system by Sobolev et al. (1976c). As far as its crystal chemistry is concerned, YF_3, which also has the α-UO_3-related high-temperature form, fits in the series of rare earth trifluorides just before ErF_3.

In contrast to this high-temperature modification, the structure of the orthorhombic low-temperature form is well established. Full structural analyses have been carried out on β-YF_3 (Zalkin and Templeton, 1953; Cheetham and Norman, 1974) and on β-SmF_3, HoF_3, and β-YbF_3 (Bukvetskii and Garashina, 1977). An anomalous change occurs in the lattice parameters. This is especially true for c, which decreases from SmF_3 to ErF_3 and increases between ErF_3 and LuF_3 (Greis and Petzel, 1974). Sobolev et al. (1973) came to similar conclusions after interpreting the data of Zalkin and Templeton (1953). Garashina et al. (1980)

pointed out that this behavior correlates with a simultaneous decrease of the R^{3+} coordination number from 9 to 8 corresponding to a change of the coordination polyhedron from a tricapped to a bicapped trigonal prism. There is, however, another possible interpretation. The effective coordination number for R^{3+} is 8 in all cases because the ninth anion has a significantly longer distance. This can also be seen from an analysis of the ionic radii (Greis and Petzel, 1974; Shannon, 1976). The change at ErF_3 is more likely the result of a change from a bicapped trigonal prism (SmF_3–ErF_3) to a slightly distorted square antiprism (TmF_3–LuF_3). The latter, however, is the coordination polyhedron found in many mixed rare earth fluorides (see below) and also in BiF_3 which is isotypic to β-YF_3 (Greis and Martinez-Ripoll, 1977). These two polyhedra are very closely related, and the square antiprism may be regarded as a special case of the bicapped trigonal prism (Wells, 1975). The crystal chemistry of β-YF_3 (and LaF_3) type structures based on trigonal prisms has been described earlier and in a much more elaborate way by O'Keeffe and Hyde (1975, 1977) than by Garashina and Vishnyakov (1977) and Garashina et al. (1980).

The LaF_3 or tysonite structure has been the topic of many structural investigations, and there is no doubt that well annealed rare earth trifluorides of high purity have the $P\bar{3}c1$ structure as established by Mansmann (1964, 1965), Zalkin et al. (1966), and Cheetham et al. (1976). The coordination polyhedron of the R^{3+} cations is a somewhat distorted tricapped trigonal prism with two more anions at a significantly larger distance (coordination number 9 + 2). The effective coordination number, however, is 9, as shown on the basis of effective ionic radii (Greis and Petzel, 1974; Shannon, 1976). In many structural studies, however, the tysonite structure is described with a smaller unit cell ($Z = 2$ in comparison to $Z = 6$) and the space group $P6_3/mmc$ (e.g. Schlyter, 1952; for further papers see Gmelin Handbook, 1976) which is a supergroup of $P\bar{3}c1$ (Haschke, 1976, 1979). On reading all these papers it is difficult to believe that the so-called Schlyter structure is just the result of erroneous structure interpretations or chemical impurities, e.g. $La(O, F)_{3-\delta}$. Greis and Bevan (1978) demonstrated in an electron diffraction study of high-purity LaF_3 that actually both structure types exist within the same sample. Because of the poor quality of the reproductions in the original paper, the electron diffraction patterns are shown again in fig. 2. It is now obvious that at low temperatures the highly ordered superstructure with $Z = 6$ dominates, but at elevated temperatures the anion disordered basis structure with $Z = 2$ becomes more and more important. This behavior correlates well with the unusually high anionic mobility of LaF_3 or, more generally speaking, of materials with the tysonite structure (Nagel and O'Keeffe, 1973; Morozov et al., 1979; see also the reviews by Portier, 1976; Réau and Portier, 1978).

The structure of the fourth RF_3 modification appears under normal pressure only in the case of ScF_3. It is cubic (e.g. Spedding et al., 1974) or slightly rhombohedrally distorted (e.g. Nowacki, 1939) if oxygen contaminations cannot be excluded unambiguously. In both cases, however, the structure is ReO_3-type or ReO_3-related with R in an octahedral environment (effective coordination number 6).

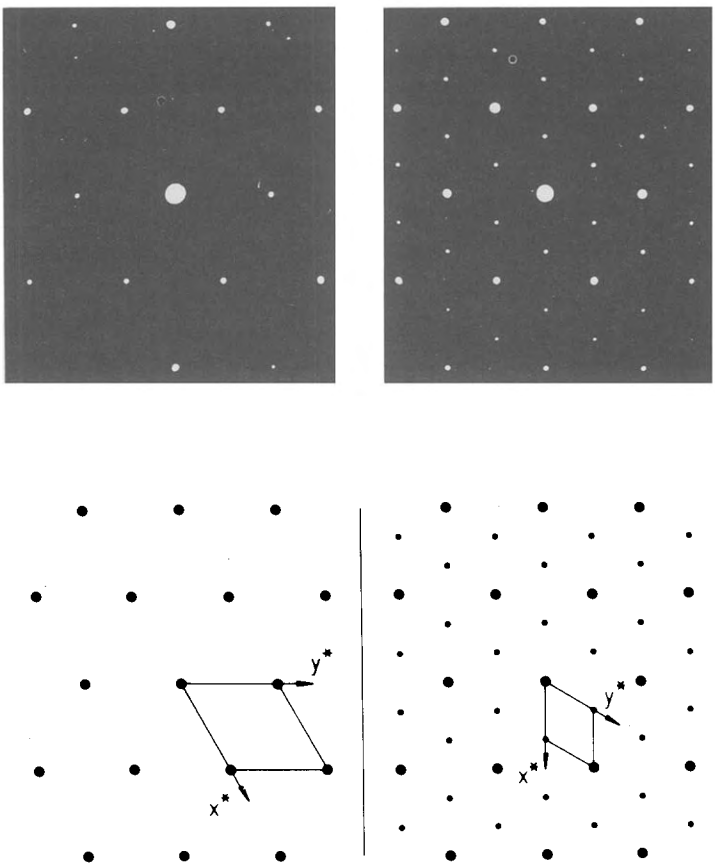

Fig. 2. Electron diffraction photographs of the [001] zones of the sublattice (left) and the superlattice (right) of LaF_3 (Greis and Bevan, 1978).

The crystal chemistry of RF_3 under pressures up to about 100 kbar has also been reported, e.g. DyF_3 (Vezzoli, 1970), ScF_3 (Bendeliani, 1974), YF_3 (Atabaeva and Bendeliani, 1979), and LaF_3 (Atabaeva and Bendeliani, 1980). Further pressure studies on the systems RF_3–ROF or RF_3–$R(OH)_3$ were published by Atabaeva, Bendeliani, and Poryvkin in 1974–1979, but are not referenced here in detail. The consequences for the crystal chemistry of pure rare earth trifluorides, however, are open to question in most cases. This is mainly because the influence of oxygen impurities on the observed phase transformations to tysonite or fluorite-related pressure modifications is still not clear. More work is needed with special emphasis on pure trifluorides, though the experimental difficulties are hard to overcome. Some phase diagrams of mixed RF_3–$R'F_3$ systems have also been studied, mainly to obtain more information on the stabilities of the different RF_3 modifications (Sobolev et al., 1976c, 1977a, 1978, 1980). The results are in agreement with what one would expect from the crystal chemistry of the

simple rare earth trifluorides. Formation of intermediate ordered phases has not been found by thermal analyses, at least not at temperatures above 900°C.

2.2. *Difluorides*

It is well-known that some rare earth elements, especially Eu and Yb, also show the tendency to form compounds in their divalent oxidation state. This behavior correlates well with the greater stability of half or fully filled f-shells. From data presented in the thermodynamic section below, it is evident that all rare earth difluorides are stable in comparison to their elements, but not with regard to the disproportionation, $3RF_2 \rightarrow R + 2RF_3$. Greis (1976) calculated the disproportionation enthalpies of all hypothetical rare earth difluorides using measured and estimated standard enthalpies of formation. The results are shown in fig. 3 where three sections can be distinguished. In the case of Eu, Yb, and Sm, these values are positive, and the formation of stable difluorides can be expected (section III). In contrast, elements like La, Ce, Gd, Tb, Y, and Lu show very negative values and, therefore, difluorides are very unlikely to be formed (section I). There are, however, a few elements in section II which have negative disproportionation enthalpies, but their values are so close to zero that under special circumstances metastable difluorides can be expected. They may not be available in pure form, but in mixed fluorides with lattices stabilizing the divalent state, e.g. fluorite or fluorite-related host structures.

All experimental results on the preparation of reduced fluorides agree with these predictions. Only EuF_2, YbF_2, and SmF_2 are known (e.g. Petzel and Greis,

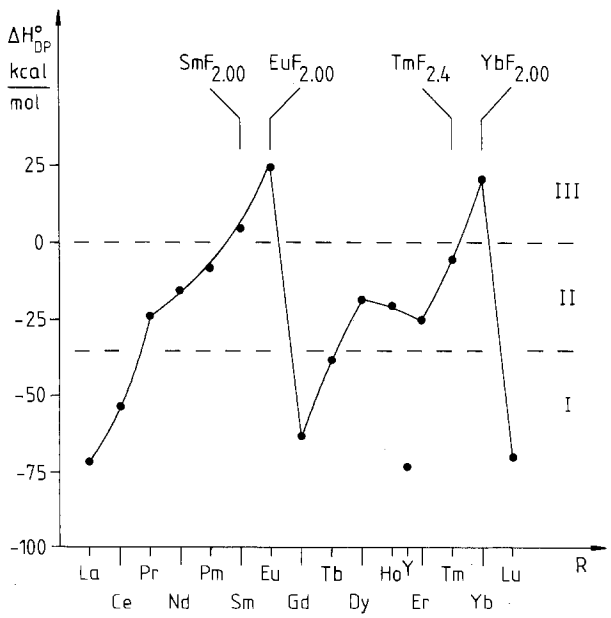

Fig. 3. Standard disproportionation enthalpies ΔH°_{DP} of the rare earth difluorides (Greis, 1976).

1972, 1973; Greis, 1976). These phases crystallize with the fluorite structure and show significant nonstoichiometry with an anion/cation ratio greater than two. The crystal chemistry of these solid solutions can be described in a first approximation by the so-called Goldschmidt–Zintl model (Goldschmidt, 1926; Zintl and Udgård, 1939), in which, like in yttrofluorites, the divalent cations are statistically replaced by the trivalent cations with the charge compensating fluorine anions in interstitial lattice sites. The formulae of these nonstoichiometric fluorides have, therefore, to be written as $(R^{II}, R^{III})F_{2+\delta}$ or, in short, as $RF_{2+\delta}$. Their temperature-dependent phase widths can be very extended up to about $RF_{2.4}$ (see below). Anion-deficient nonstoichiometry, as observed among the fluorite-related rare earth dioxides $RO_{2-\delta}$, can be excluded unambiguously at room temperature (Petzel and Greis, 1972, 1973; Greis, 1976, 1977b, 1978a,b). Samples of the composition $RF_{2-\delta}$ are reported in the literature (see Gmelin Handbook, 1976), but proved to be diphasic mixtures of amorphous metal and $RF_{2.00}$ (Greis, 1976). In contrast, Dworkin and Bredig (1971) indicated the possibility of such solid solutions containing not more than five mol % rare earth metal at 1250–1400°C in the case of the Sm–SmF_2 and Yb–YbF_2 systems.

Of all the different preparation methods reported in the literature, only two are recommended as suitable for preparing rare earth difluorides of high purity. The reduction of anhydrous EuF_3 with highly purified hydrogen at 1000°C yields $EuF_{2.00}$, which is yellowish white and stable in air and at room temperature (Greis, 1970; Petzel and Greis, 1972; Tanguy et al., 1972). In the other cases of interest, $YbF_{2.30-2.40}$ and $SmF_{2.40-2.45}$ form, but no reduction of TmF_3 occurs (Greis, 1976). It has been indicated, however, that the corresponding rare earth metals are more suitable reduction agents, especially for SmF_3 and YbF_3 (Catalano et al., 1969; Bedford and Catalano, 1970; Stezowski and Eick, 1969, 1970). Nearly complete reduction is possible by annealing of appropriate mixtures of R and RF_3 in sealed tantalum or molybdenum capsules at 1600–1800°C. This method, however, has one great disadvantage because the well-known impurities of rare earth metals (e.g. Busch et al., 1971) show up in the final products. To overcome these difficulties, the so-called double cell technique has been developed where only the vapor of the corresponding rare earth metal is employed (Petzel and Greis, 1973; Greis, 1976; see also the Brauer Handbook, 1975, and the Gmelin Handbook, 1976). In fig. 4 two models of the double cell are shown which are constructed of molybdenum or tantalum to avoid reactions with the rare earth elements. The cells consist of two chambers, A for the metal and B for the trifluoride. They are separated by the aperture C, so that no mixing of the adducts/products can occur. The reactions are carried out at 940–1000°C for $SmF_{2.00}$, at 920–980°C for $EuF_{2.00}$, and at 650–750°C for $YbF_{2.00}$ under high vacuum. At these comparatively low temperatures, the metals vaporize slowly and reduce the trifluorides. Excess metal disappears in model I through the Knudsen effusion orifice E (vapor pressure controlled reaction) or in model II through the loose connection between the two half-cells. Experience has shown that very pure difluorides, $RF_{2.000\pm0.005}$, can be prepared for R = Sm, Eu, and Yb, while the reduction is incomplete for TmF_3. In the latter case only $TmF_{2.4} \approx$

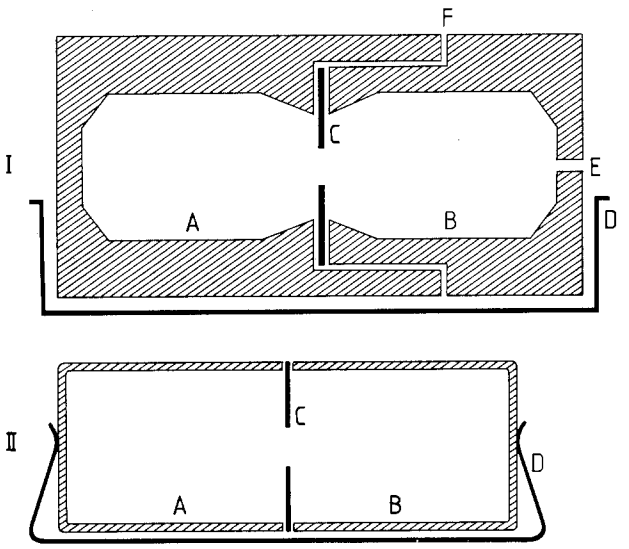

Fig. 4. Double cells for the preparation of rare earth difluorides (Greis, 1976): A, chamber for the metal; B, chamber for the trifluoride; C, aperture; D, molybdenum boat; E, Knudsen effusion orifice; F, plug-in connection.

$Tm_{13}F_{32-\delta}$ can be achieved (Greis and Petzel, 1977). This mixed-valence compound is discussed in more detail in section 2.3.

Kirshenbaum and Cahill (1960) used graphite to reduce molten samarium trifluoride, and more recently, Adachi et al. (1976) described a method of preparing EuF_2 by reducing EuF_3 with silicon at 1000°C. The contradictory analytical results, however, indicate that the reproducible preparation of pure EuF_2 is very difficult to achieve, and the advantages of this technique are difficult to understand. Of greater interest is the shock compression of R/RF_3-mixtures at $\geqq$200 kbar and $\geqq$1000°C (Batsanov et al., 1976; Egorov et al., 1979). Analytical examination of the reaction products showed that reduced fluorides of the composition $RF_{2.3-2.5}$ for R = La, Ce, Pr, Nd, Er had been prepared. Their structures are fluorite-related, but a plot of $V' = V/Z$ in fig. 5 demonstrates that the unit cells are significantly smaller than expected for the solid solutions $RF_{2.0-2.4}$ ($c\alpha$) of the extended series of barides, AF_2 and RF_2 (Gschneidner, 1969; Greis, 1976). This relates most likely to contamination of calcium or calcium difluoride in the rare earth metals, but oxygen contamination also cannot be excluded unambiguously, leading to cubic solid solutions within the systems $ROF–RF_2$. Nevertheless, shock compression seems to be a first step for increasing the number of reduced rare earth fluorides beyond those of Sm, Eu, Tm, and Yb.

The lattice parameters of the rare earth difluorides (fluorite structure, Fm3m, $Z = 4$) are listed in table 2 for the composition $RF_{2.00}$. The analytical function $a = mx + t$ describes the relationships between the lattice parameter a and the chemical composition within the solid solutions RF_x for $2.0 \leqq x \leqq 2.2$. This function is also a valid approximation for compositions with $2.2 < x \leqq 2.4$ if the samples are quenched from 1200–1400°C. Attention, however, is called to partial ordering which can be seen in the X-ray diffraction patterns as broadening and

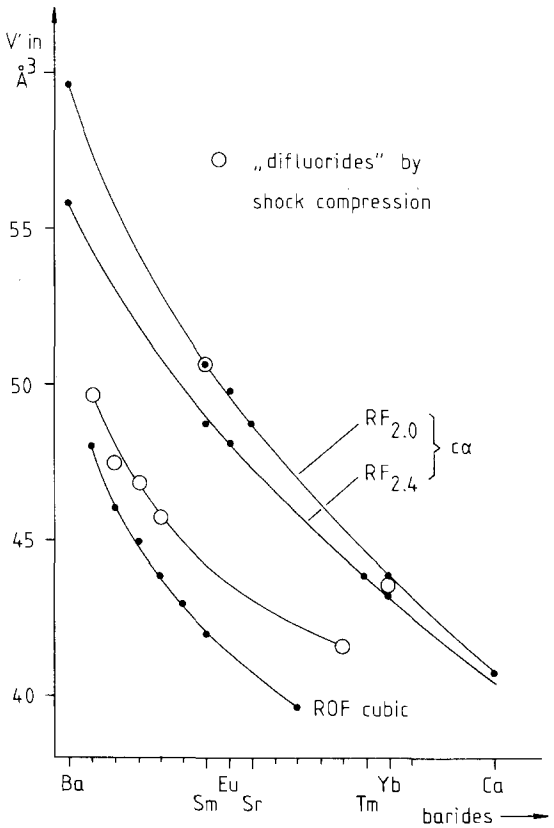

Fig. 5. Reduced volumes $V' = V/Z$ of fluorite-related rare earth difluorides and oxide fluorides (see text).

finally splitting of the parent structure reflections. Europium difluoride converts at 400°C and 114 kbar to a $PbCl_2$-type phase with $a = 6.324$ Å, $b = 3.803$ Å, $c = 7.435$ Å, Pnma, $Z = 4$ (Seifert, 1968).

The colors of the difluorides are also listed in table 2. Within the solid solutions no significant color change is observed in $EuF_{2+\delta}$. In contrast, samarium difluoride changes gradually from violet and purple to burgundy ($\rightarrow SmF_{2.4}$). Ytterbium difluoride is stable in air at least at room temperature, but

TABLE 2

Rare earth difluorides: color, lattice parameter, and function of lattice parameter versus chemical composition for the solid solutions $(R^{II}, R^{III})F_{2+\delta}$ (after Greis, 1976).

$RF_{2.00}$	Color	a (Å)	$a = mx + t$ for RF_x
$SmF_{2.00}$	black, in thin films dark-blue	5.8710	$a = -0.1794x + 6.2298$
$EuF_{2.00}$	yellowish white	5.8423	$a = -0.2020x + 6.2443$
$YbF_{2.00}$	grey-olive	5.5993	$a = -0.0768x + 5.7529$

samarium difluoride decomposes within a few days with the above color changes. Finally, $TmF_{2.4}$ has an intensive dark-brown color which brightens rapidly due to decomposition in air ($\rightarrow TmF_3/TmOF$).

2.3. *Ordered R(II,III)-fluorides*

The most significant progress in the chemistry of binary rare earth fluorides occurred in the field of mixed-valence compounds during the last few years (see also Greis, 1980a). The first systematic phase investigations on RF_2–RF_3 systems with R = Sm, Eu, Yb indicated the existence of intermediate phases with fluorite-related superstructures (Catalano et al., 1969; Bedford and Catalano, 1970; Stezowski and Eick, 1969, 1970; Tanguy et al., 1972). The number of these phases, their compositions, and their formulae, however, could not be established because of shortcomings in the analytical and X-ray characterizations. Problems were especially acute as far as the indexing of powder diffraction patterns is concerned. The latter difficulties have been overcome by the development of a systematic procedure for indexing powder patterns of superstructure phases (Greis, 1976, 1977a). This method has been applied for the first time and with great success to the case of intermediate phases of the systems YbF_2–YbF_3 (Greis, 1977b), SmF_2–SmF_3 (Greis, 1978a), EuF_2–EuF_3 (Greis, 1978b), and "TmF_2"–TmF_3 (Greis and Petzel, 1977). In total, thirteen new binary rare earth fluorides with mixed valency could be determined (see table 3 and fig. 6). Their formulae belong to four different types and are rather complicated mainly due to the fact that the superstructure unit cells are quite extended, and the relations between the lattice parameters of the super-, basis-, and parent-structure cells are irrational in most cases (e.g. $\sqrt{5}$, $\sqrt{7}$, $\sqrt{13}$ etc.). Nevertheless, these formulae fit the homologous series law R_nF_{2n+5} with $n = 13$ (rhβ), $n = 14$ (rhα), and $n = 15$ (t), while cβ with $n = 13 + 14$ represents obviously a mixed member of rhα and rhβ. The phase designations refer to crystal symmetry (c = cubic, t = tetragonal, and rh = rhombohedral) and to different chemical compositions ($\alpha, \beta, \ldots$) or modes of tessellation (Greis, 1980b, 1981a), respectively. The lattice parameters of the different superstructure phases are listed in table 4. In the case of rhomohedral unit cells, only the hexagonal settings are

TABLE 3
Phase designations and formulae of binary rare earth fluorides with mixed valency (Greis, 1976).

t $R_2^{II}R^{III}F_7$	rhα $R_9^{II}R_5^{III}F_{33}$	cβ $R_{17}^{II}R_{10}^{III}F_{64}$	rhβ $R_{7+\delta}^{II}R_{6-\delta}^{III}F_{32-\delta}$
Sm_3F_7	$Sm_{14}F_{33}$	$Sm_{27}F_{64}$	$Sm_{13}F_{32-\delta}$
Eu_3F_7	$Eu_{14}F_{33}$	$Eu_{27}F_{64}$	$Eu_{13}F_{32-\delta}$
			$Tm_{13}F_{32-\delta}$
Yb_3F_7	$Yb_{14}F_{33}$	$Yb_{27}F_{64}$	$Yb_{13}F_{32-\delta}$

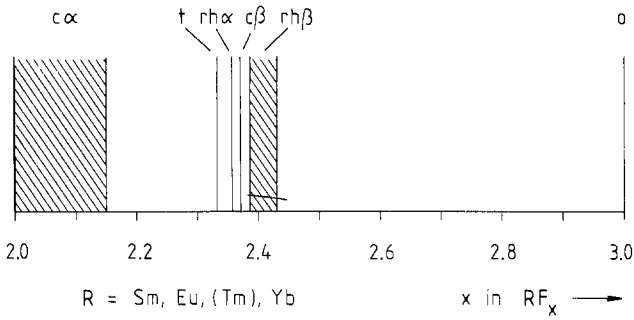

Fig. 6. Phase relationships in RF_2–RF_3 systems (Greis, 1976).

listed, but more data for the corresponding basis and parent cells are given in the original publications.

The new R(II, III)-fluorides represent long-range order phases, where ordering takes place in both the cationic and anionic sublattices of the fluorite parent structure. They are related to the corresponding high-temperature solid solutions with cubic symmetry (cα) by a continuous break-down of long-range order. The membership to a common homologous series indicates that all these superstructure phases may have a common structural principle. It has been pointed out by Greis (1976, 1977b) that $Yb^{II}_{8-\delta}Yb^{III}_{5+\delta}F_{31+\delta} = Yb^{II}_{7+\delta}Yb^{III}_{6-\delta}F_{32-\delta}$, or more generally rhβ, is isostructural to $Na_7Zr_6F_{31}$ (Burns et al., 1968a,b). The central unit of this structure type is a F_{13} cuboctahedron and six surrounding ZrF_8 or $R^{III}F_8$ square

TABLE 4
Crystallographic data of binary rare earth fluorides with mixed valency (Greis, 1976).

Formula	Exp. comp. x in RF_x	a (Å)	c (Å)	$V' = V/Z$ (Å^3)	ρ_{calc} (g/cm^3)
Sm_3F_7	2.33(1)	9.1806	17.488	49.131	6.581
Eu_3F_7	2.333(5)	9.1363	17.394	48.398	6.734
Yb_3F_7	2.333(5)	8.7870	16.760	43.136	8.367
$Sm_{14}F_{33}$	2.35(1)	10.851	20.200	49.037	6.609
$Eu_{14}F_{33}$	2.357(5)	10.794	20.127	48.352	6.756
$Yb_{14}F_{33}$	2.357(5)	10.367	19.489	43.191	8.374
$Sm_{27}F_{64}$	2.37(1)	17.423		48.974	6.625
$Eu_{27}F_{64}$	2.370(5)	17.342		48.293	6.773
$Yb_{27}F_{64}$	2.370(5)	16.712		43.218	8.378
$Sm_{13}F_{32-\delta}$	2.41(1)	14.736	10.100	48.703	6.688
$Eu_{13}F_{32-\delta}$	2.410(5)	14.686	10.043	48.100	6.826
$Tm_{13}F_{32-\delta}$	2.42(1)	14.242	9.7067	43.721	8.162
$Yb_{13}F_{32-\delta}$	2.410(5)	14.187	9.6710	43.224	8.406

The space groups and the formula contents Z for $RF_{2+\delta}$ are: I4/m and $Z = 30$ (t); $R\bar{3}$ and $Z_{hex} = 42$ (rhα); Pa3 and $Z = 108$ (cβ); $R\bar{3}$ and $Z_{hex} = 39$ (rhβ).

antiprisms sharing common squares. The resulting isolated cluster has the formula Zr_6F_{37} or $R_5^{III}F_{37}$ which is obviously a very stable short-range order defect cluster in fluorite structures (see section 3.6). If this cluster occurred in rhβ, the formula would be $R_7^{II}R_6^{III}F_{32} = RF_{2.462}$, which is not achieved. The experimentally observed RF_x phases are solid solutions with $2.38 \leqq x \leqq 2.42$. This indicates that in the case of II, III-compounds a compromise takes place between the idealized cation framework (7:6-compounds $RF_{2.462}$, six interstitial anions corresponding to R_nF_{2n+6}) and the idealized anion framework (8:5-compounds $RF_{2.385}$, five interstitial anions corresponding to R_nF_{2n+5}). Further structural details are discussed below together with the corresponding and isotypic superstructure phases of the systems CaF_2–RF_3 and BaF_2–RF_3 (see sections 3.2, 3.4, and 3.6).

The intermediate R(II, III)-fluorides can be prepared by several methods: (a) annealing of RF_2/RF_3 mixtures in sealed platinum tubes at temperatures below 800°C, (b) partial reduction of RF_3 with the corresponding metal vapor or hydrogen, and (c) thermal decomposition of RF_3. The important aspect for all these methods is that after equilibration a careful annealing procedure at lower temperatures must be applied to achieve optimal long-range order. Otherwise, the superstructures will not be well pronounced, and the cubic high-temperature solid solutions will be dominant. Results show that step-wise cooling from 800°C to room temperature over two weeks yields well-developed superstructure phases. For more experimental details see the original publications (Greis, 1977b, 1978a,b; Greis and Petzel, 1977). The colors of the intermediate phases are identical with the corresponding solid solutions $RF_{2+\delta}$ (cα). In comparison to $SmF_{2.00}$ and $YbF_{2.00}$, a significant increase of stability is observed for the R(II, III)-phases. This refers to their durability in moist air at room temperature and also at elevated temperatures under inert gas atmosphere or under high-vacuum (see also the thermodynamic section below). It is our belief that in the future one can expect a successful preparation of a few more intermediate R(II, III)-fluorides, most likely in the case of Pm, Nd, Dy, Ho, and Er.

2.4. *Tetrafluorides*

A few rare earth elements form compounds in their tetravalent state, especially Ce and Tb. This behavior again correlates with the stability of half and fully filled f-shells similar to the case of the difluorides. Up to now, only three tetrafluorides are known, CeF_4, TbF_4, and PrF_4, which are listed in order of decreasing stability.

Cerium and terbium tetrafluoride can be prepared by the action of fluorine, xenon difluoride, and chlorine trifluoride on CeO_2 or CeF_3, and Tb_4O_7 or TbF_3, respectively. These reactions are carried out at temperatures of 300–400°C in nickel or monel containers with exclusion of moisture and oxygen. For further details see the Gmelin Handbook (1976) and the literature cited therein. The preparation of

PrF_4 is much more difficult and was obtained in early studies only be extracting sodium fluoride with anhydrous fluoric acid from complex compounds like Na_2PrF_6 (Soriano et al., 1966; Asprey et al., 1967). The products, however, were not free of impurities in most cases. The major breakthrough came from Spitsyn et al. (1974) who prepared pure PrF_4 by solid state reaction of krypton difluoride with Pr_6O_{11} or PrO_2 at room temperature!

Kiselev et al. (1975b) studied the thermal decomposition of PrF_4 and compared the data with their earlier study on CeF_4 and TbF_4 (Kiselev et al., 1975a). It has been shown that the maximum of the decomposition is at 90°C for PrF_4, at 180°C for TbF_4, and at 400°C for CeF_4. In all cases the products are the corresponding trifluorides. These data are qualitatively in agreement with the work by Batsanova et al. (1973). At room temperature, all tetrafluorides are more or less sensitive to moist air.

The rare earth tetrafluorides are isostructural with ZrF_4, HfF_4, ThF_4, and UF_4 and crystallize with monoclinic symmetry (space group C2/c and $Z = 12$). This structure type is characterized by square antiprismatic coordination of the tetravalent metals. The lattice parameters are listed in table 5. A recent interesting publication (Batsanov et al., 1980), which describes the shock compression of UF_4 and CeF_4, supplements an earlier paper on ThF_4 (Batsanov et al., 1979). A transformation occurs to a tysonite-related phase in all these experiments. In the case of CeF_4, the yield was about 30%. One can conclude that probably CeF_3 or an oxide-fluoride $Ce(O, F)_{3\pm\delta}$ has been partially formed by comparing observed lattice parameters ($a = 7.10$ Å and $c = 7.27$ Å) with those of CeF_3 in table 1. Thermal analysis, however, shows that the initial form of CeF_4 is formed again with a small exothermic effect at 320°C without any mass change! These results are indeed remarkable and have been interpreted by the formation of a defect structure of the tysonite type with 25% vacancies which correlates to the formula $Ce_{0.75}\square_{0.25}F_3$. One can expect an extraordinary ionic conductivity since the normal tysonite structure without these defects is already an excellent ionic conductor (see section 2.1). Until now, no intermediate phases have been found in the RF_3–RF_4 systems, but they can be expected with respect to RF_3–MF_4 systems, where such phases have been revealed (see section 5).

TABLE 5
Lattice parameters of rare earth tetrafluorides (C2/c, $Z = 12$).

RF_4	Color	a (Å)	b (Å)	c (Å)	β (°)
CeF_4[a]	white	12.587	10.473	8.041	126.15
PrF_4[b]	cream	12.27	10.19	7.96	126.5
TbF_4[c]	white	12.11	10.15	7.92	126.1

[a]Kiselev et al. (1975). [b]Spitsyn et al. (1974). [c]Templeton and Dauben (1954).

3. Mixed fluorides of the systems AF_2–RF_3

3.1. *Survey*

The most important of these systems are undoubtedly CaF_2–RF_3, SrF_2–RF_3, and BaF_2–RF_3 because of the interesting crystal chemistry of intermediate phases and their applications, e.g. optical processing of information, up-conversion effect, thin film condensers, electroslag melting, calciothermal reduction methods, etc. Much attention has been given recently to fast anionic conduction of fluorite-related solid solutions such as (Ca, Y)$F_{2+\delta}$ (Réau et al., 1976, 1977, 1980; Réau and Portier, 1978; Lucat et al., 1979) and (Ca, La)$F_{2+\delta}$ (Svantner et al., 1979) as well as of tysonite-related solid solutions (Ca, Y)$F_{2.73}$, (Sr, La)$F_{2.95}$, (Ca, Er)$F_{2.71}$ (Nagel and O'Keeffe, 1973), (Sr, Y)$F_{2.71}$, and (Sr, Y, Lu)$F_{2.71}$ (Buznik et al., 1979).

The high-temperature phase relationships of many AF_2–RF_3 systems have been studied extensively, mainly by Sobolev, Fedorov, and co-workers in the last decade. Their data on thermal analyses are rather reliable, but, unfortunately, not their crystallographic interpretations, which are insufficient or wrong in most cases. The latter refers especially to X-ray single crystal and powder diffraction data of fluorite- and tysonite-related superstructure phases and is based on shortcomings in both the diffraction methods and indexing. This gap has been overcome recently by Greis and co-workers, who were able to solve the superstructure geometries (Greis, 1977a) by X-ray Guinier techniques and electron diffraction from single crystals. Furthermore, the formulae of these interesting phases could be established with this knowledge. In some cases, the atomic structures could also be revealed. However, additional high-quality work is needed in this dramatically expanding field of solid state chemistry.

3.2. *The systems CaF_2–RF_3*

Since the discovery of the mineral yttrofluorite, $20CaF_2 \cdot 3YF_3$, by Vogt (1911, 1914) and the establishment of its crystal chemistry by Goldschmidt (1926) and by Zintl and Udgård (1939), much attention has been paid to the CaF_2–YF_3 system and the yttrofluorite-related CaF_2–RF_3 systems. The literature on the high-temperature phase relationships has been reviewed by Sobolev and Fedorov (1978) and by Fedorov and Sobolev (1979a). About 75 references are included in each of these reviews, and, therefore, most of the earlier publications on this subject will not be cited here. The phase diagrams of 14 CaF_2–RF_3 systems are reported; they are based on thermal analyses in the temperature range 700–1500°C and on X-ray powder diffraction data of quenched samples. Estimated diagrams were given in the case of CaF_2–PmF_3 and CaF_2–EuF_3. The high-temperature phase studies on the systems CaF_2–LaF_3 (Svantner et al., 1979), CaF_2–GdF_3 (Fedorov et al., 1975), and CaF_2–YF_3 (Seiranian et al., 1974) may be taken as representative. Naturally, thermal analyses reveal primarily solidus–liquidus curves, high-temperature solid solutions, and rapid phase tran-

sitions in the solid state, but the presence of ordered phases will often not be detected. In addition, the recorded transformation temperatures for the latter phases do not represent true equilibrium and are, therefore, questionable. In these cases, annealing over a long time is necessary and is achieved by lowering the temperature gradually. Such studies carried out recently by Greis and co-workers represent a significant addition to the above phase diagrams because numerous superstructure phases have been established (e.g. Greis, 1980a). Furthermore, tveitite, an ordered yttrofluorite mineral, has been found (Bergstøl et al., 1977). Thus far, it has not been prepared in the laboratory (Greis, 1978c). All the available data on CaF_2–RF_3 systems have been critically compared with each other and are summarized in the following section.

If a generalization is possible at all, three types of phase diagrams can be distinguished (see fig. 7). Type I occurs in the systems CaF_2–LaF_3 to CaF_2–GdF_3 and is characterized by the cubic fluorite-related solid solution, cα, and the hexagonal tysonite-related solid solution, TYS. The cα phase has a width up to $0 < \delta \leqq 0.5$ for $(Ca, R)F_{2+\delta}$, which decreases at lower temperatures. The boundary between cα and the solid diphasic field is probably in all cases not linear, but S-shaped as in the system CaF_2–LaF_3 (Svantner et al., 1979), or in $UO_{2+\delta}$ (compare e.g. Bevan, 1973). In contrast, the shape of the broad TYS phases is not as uniform as for cα (see for further details Sobolev and Fedorov, 1978), but what is important is the fact that in no case the phase width exceeds $0 < \delta \leqq 0.3$ for $(Ca, R)F_{3-\delta}$. Type II is characteristic of the systems CaF_2–TbF_3 to CaF_2–HoF_3. The cα phase has a well-pronounced maximum in the fusion curve within

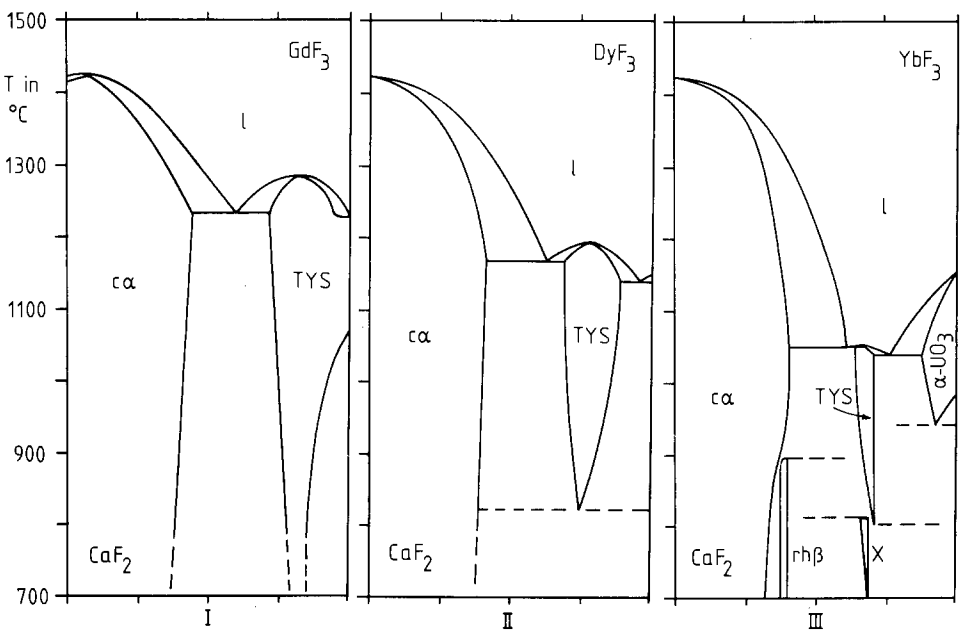

Fig. 7. Representative CaF_2–RF_3 phase diagrams after Sobolev and Fedorov (1978).

the solid solution. Such behavior is only observed in the case of heterovalent isomorphous substitution with a change of the number of ions in the unit cell (Fedorov and Sobolev, 1979b). In contrast to I, the tysonite-related solid solution TYS no longer includes the trifluoride. This correlates well to the fact that TbF_3 to HoF_3 are only monomorphous (see section 2.1 and table 1). The lower limit of the phase widths, however, is again at about $(Ca, R)F_{2.70}$, but it is at this composition where long-range order is evidenced by the formation of the so-called X-phase which has the formula $Ca_3R_7F_{27}$ (Bevan and Greis, 1978). TYS and X are not stable at room temperature. As far as these two phases are concerned, a similar behavior is found in type III for the systems CaF_2–YF_3 and CaF_2–ErF_3 to CaF_2–LuF_3. Furthermore, the expected α-$UO_{3-\delta}$-related high-temperature solid solution is observed at the trifluoride-rich side of the phase diagram which, as in the case of the pure trifluorides, cannot be quenched. The fluorite-related solid solution cα is now somewhat narrower than in I and II, and several superstructure phases are observed at lower temperatures. Their crystallization, however, is more or less continuous from the corresponding solid solutions and correlates with a continuous increase of long-range order (see below). The different phases will be discussed in more detail.

The cubic fluorite-related solid solutions cα (Fm3m) are characterized by linearly increasing unit cell volumes (Vegard's rule) with increasing defect concentrations. The rule applies also with a few restrictions on the lattice parameter a (e.g. Gettmann and Greis, 1978; Lechtenböhmer and Greis, 1978). In contrast, Sobolev and Fedorov (1978) state that most cases deviate from Vegard's rule at $(Ca, R)F_{2.30-2.45}$. As pointed out by Gettmann and Greis (1978), such findings refer to an erroneous or insufficient X-ray powder analysis. Samples quenched from the melting points show linearity over the full region $(Ca, R)F_{2.00-2.45}$. In contrast, samples annealed at somewhat lower temperatures show a significant degree of ordering, which is reflected in most cases in closer packing and smaller values for the unit cell volumes. The reduced formula volumes $V' = V/Z$ are already those of the corresponding low-temperature superstructure phases (see e.g. the system CaF_2–YF_3 by Gettmann and Greis, 1978). Therefore, the functions $a = a_0 + k_1x + k_2x^2$ given by Sobolev and Fedorov (1978) are not valid for the description of $(Ca, R)F_{2+\delta}$ with $0 < \delta \leqq 0.45$ and should be replaced by linear functions (see Greis and Kieser, 1981). At present, five different fluorite-related superstructure types are known in the CaF_2–RF_3 systems: $Ca_9R_5F_{33}$ (rhα), $Ca_{8-\delta}R_{5+\delta}F_{31+\delta} = Ca_{7+\delta}R_{6-\delta}F_{32-\delta}$ (rhβ), $Ca_{14-\delta}R_{5+\delta}F_{43+\delta} = Ca_{13+\delta}R_{6-\delta}F_{44-\delta}$ (rhγ), $Ca_{17}R_{10}F_{64}$ (cβ), and Ca_2RF_7 (t). The appearance of these phases has been studied systematically only in the case of Ca_2RF_7 (t) by Greis and Kieser (1981). Knowledge of the other phases derives from systematic phase studies on the systems CaF_2–YbF_3 (Lechtenböhmer and Greis, 1978), CaF_2–YF_3 (Gettmann and Greis, 1978), and of rhγ from studies on the mineral tveitite (Bergstøl et al., 1977; Greis, 1978c; Bevan et al., 1980, 1981). It is true that rhβ has been identified earlier (Fedorov et al., 1974) as stated by Sobolev and Fedorov (1978). However, the crystallographic characterization of their A-phases $Ca_8R_5F_{31}$ (R = Y, Ho–Lu) proved to be erroneous despite the use of X-ray

TABLE 6
Lattice parameters of fluorite-related superstructure phases of the systems CaF_2–RF_3.

Formula	phase[a]	a (Å)	c (Å)	$V' = V/Z$ (Å^3)[b]
Ca_2DyF_7[d]	t[c]	3.907	5.578	42.57
Ca_2HoF_7[d]	t[c]	3.899	5.562	42.28
Ca_2YF_7[d]	t	8.7109	16.661	42.141
Ca_2ErF_7[d]	t	8.6998	16.660	42.032
Ca_2TmF_7[d]	t	8.6833	16.596	41.711
Ca_2YbF_7[d]	t	8.6732	16.557	41.516
Ca_2LuF_7[d]	t	8.6599	16.520	41.297
$Ca_9Y_5F_{33}$[e]	rhα	10.255	19.486	42.254
$Ca_9Yb_5F_{33}$[f]	rhα	10.204	19.385	41.615
$Ca_{7+\delta}Y_{6-\delta}F_{32-\delta}$[e]	rhβ	14.156	9.5794	42.628
$Ca_{7+\delta}Yb_{6-\delta}F_{32-\delta}$[f]	rhβ	14.066	9.5333	41.885
$Ca_{13+\delta}Y_{6-\delta}F_{44-\delta}$[g]	rhγ	16.962	9.6664	42.255
$Ca_{17}Yb_{10}F_{64}$[f]	cβ	16.520		41.744

[a]Space groups: I4/m (t), $R\bar{3}$ (rhα, rhγ), Pa3 (cβ). [b]Z for the formula unit (Ca, R)$F_{2+\delta}$: 30 (t), 42 (rhα), 39 (rhβ), 57 (rhγ), 108 (cβ). [c]Basis structure only. [d]Greis and Kieser (1981). [e]Gettmann and Greis (1978). [f]Lechtenböhmer and Greis (1978). [g]Greis (1978c).

single crystal methods. The crystallographic data of all presently known fluorite-related superstructure phases are summarized in table 6; more information on their structure is given in section 3.6.

Phase widths and lattice parameters of the tysonite-related solid solution TYS have been studied in great detail by Fedorov and Sobolev (1975) and by Sobolev et al. (1976d). The variation of the lattice parameters agrees with Vegard's rule. The lattice parameters given in these studies, however, are based on the superstructure cell with $Z = 6$ even when the appropriate superstructure reflections have not been observed (compare also section 2.1). It seems that as a result of the work by Mansmann (1965) and Zalkin et al. (1966) this cell is generally preferred, but no experimental evidence exists in the case of anion-deficient tysonite-related solid solutions. The results of Bevan and Greis (1978), who used electron diffraction data from single crystals of (Ca, R)$F_{3-\delta}$ with R = Gd, Tb, Dy, Yb, Tm, Lu and $0.2 \leqq \delta \leqq 0.3$, show only a unit cell with $Z = 2$. Furthermore, the so-called D-phase "CaR_2F_8" (Sobolev and Fedorov, 1978) or X-phase (Ca, R)$F_{2.7}$ (Greis, 1976) has been clarified. For further details see the original paper by Bevan and Greis (1978). Crystallographic data for the tysonite-related superstructure phases at the $Ca_3R_7F_{27}$ formula are given in table 7. Some minor uncertainties exist about the thermal behavior reported by Seiranian et al. (1974) and Bevan and Greis (1978) on one hand and Sobolev and Fedorov (1978)

TABLE 7
Lattice parameters of the tysonite-related superstructure phases $Ca_3R_7F_{27}$ after Bevan and Greis (1978).

Formula[a]	a (Å)	b (Å)	c (Å)	β(°)	V' (Å^3)
$Ca_3Tb_7F_{27}$	19.970	6.790	8.050	119.93	47.299
$Ca_3Dy_7F_{27}$	19.890	6.763	8.003	119.80	46.709
$Ca_3Ho_7F_{27}$	19.810	6.741	7.970	119.70	46.225
$Ca_3Y_7F_{27}$	19.803	6.716	7.971	119.80	45.997
$Ca_3Er_7F_{27}$	19.792	6.702	7.952	119.43	45.798
$Ca_3Tm_7F_{27}$	19.735	6.678	7.928	119.70	45.379
$Ca_3Yb_7F_{27}$	19.689	6.656	7.915	119.75	45.026

[a]Space groups Cc or C2/c; Z for the formula unit (Ca, R)$F_{2.70}$ is 20; relations to the tysonite parent-structure, see the original paper.

on the other. Determination of the actual atomic structure of the tysonite-related phase remains to be completed.

At present, minimal information is available on the α-$UO_{3-\delta}$-related solid solutions (see Sobolev and Fedorov, 1978). This is a consequence of difficulties in quenching these phases. According to unpublished results (Greis, 1981b), the true situation is much more complicated in the RF_3-rich regions of the CaF_2–RF_3 phase diagrams than shown in fig. 7. More work is needed to establish more details on the phase relationships at intermediate or low temperatures.

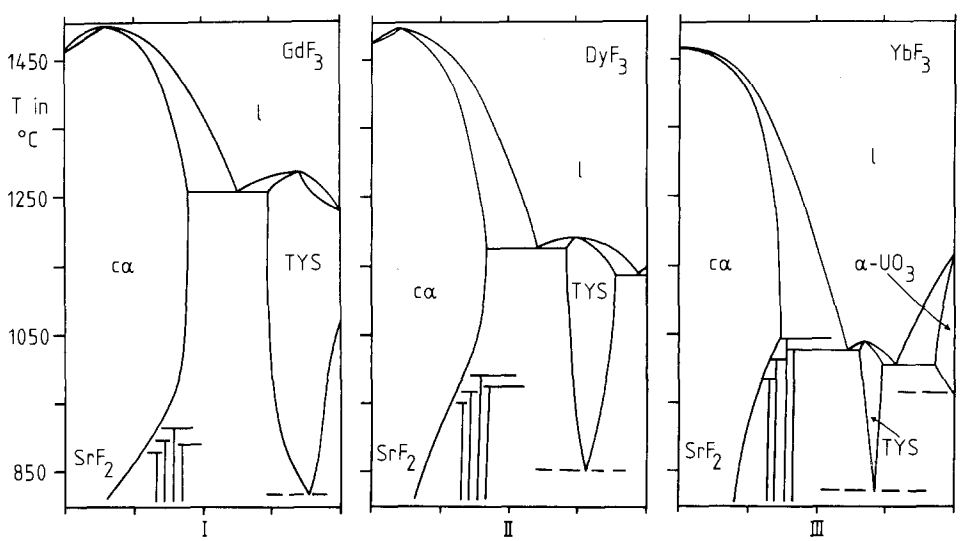

Fig. 8. Representative SrF_2–RF_3 phase diagrams after Seiranian et al. (1975).

3.3. *The systems SrF_2–RF_3*

Sobolev et al. (1979) recently reviewed the X-ray characteristics of intermediate phases of the systems SrF_2–RF_3 as well as their phase diagrams (Sobolev and Seiranian, 1981). The high-temperature phase relationships were given initially in the form of phase diagrams (Seiranian et al., 1975; Sobolev and Seiranian, 1975). Most of the earlier publications, therefore, are not cited here. A few representative phase studies follow: SrF_2–LaF_3 (Holcombe, 1980), SrF_2–EuF_3 (Greis, 1978b), SrF_2–HoF_3 (Seiranian et al., 1972), and SrF_2–YF_3 (Nafziger et al., 1973).

As in the case of the CaF_2–RF_3 systems, three different types of phase diagrams can be distinguished (see fig. 8). Type I represents the systems SrF_2–LaF_3 to SrF_2–GdF_3. There exists a cubic fluorite-related solid solution cα with a strongly pronounced maximum within the solidus–liquidus curve. At low temperatures, fluorite-related superstructure phases occur, at least in SrF_2–EuF_3 (Greis, 1978b) and SrF_2–GdF_3 (Seiranian et al., 1975). The SrF_2–EuF_3 system has been studied for comparison with the system EuF_2–EuF_3 (Tanguy et al., 1972; Greis, 1976, 1978b). The fluorite-related superstructure phases are isotypic to those in RF_2–RF_3 with R = Sm, Eu, and Yb. The lattice parameters of t, rhα, cβ and rhβ are listed in table 8. At high RF_3 contents, tysonite-related solid solutions, TYS, are observed. The TYS phases undergo transitions to orthorhombic YF_3-related solid solutions in the case of SrF_2–EuF_3 (Greis, 1978b) and SrF_2–GdF_3 (Greis and Petzel, 1974). The type II diagram is typical for SrF_2–TbF_3 to SrF_2–HoF_3 and is similar to type I except that the tysonite-related solid

TABLE 8
Lattice parameters of fluorite-related superstructure phases of the systems SrF_2–RF_3.

Formula	phase[a]	a (Å)	c (Å)	$V' = V/Z$ (Å^3)[b]
Sr_2EuF_7[c]	t	9.1034	17.320	47.845
Sr_2HoF_7[d]	t	9.023	17.22	46.73
Sr_2YbF_7[e]	t	8.9819	17.144	46.102
$Sr_9Eu_5F_{33}$[c]	rhα	10.759	20.059	47.879
$Sr_9Ho_5F_{33}$[d]	rhα	10.67	19.87	46.65
$Sr_4Yb_3F_{17}$[e]	rhα'	10.629	19.568	45.589
$Sr_{17}Eu_{10}F_{64}$[c]	cβ	17.296		47.905
$Sr_{17}Ho_{10}F_{64}$[d]	cβ	17.13		46.54
$Sr_{17}Yb_{10}F_{64}$[e]	cβ	17.035		45.768
$Sr_{7+\delta}Eu_{6-\delta}F_{32-\delta}$[c]	rhβ	14.668	10.007	47.809
$Sr_{7+\delta}Ho_{6-\delta}F_{32-\delta}$[d]	rhβ	14.58	9.854	46.52

[a]Space groups: I4/m (t), R$\bar{3}$ (rhα, rhα', rhβ), Pa3 (cβ). [b]Z for the formula unit (Sr, R)$F_{2+\delta}$: 30 (t), 42 (rhα, rhα'), 39 (rhβ), and 108 (cβ). [c]Greis (1978b). [d]Greis (unpublished) after Sobolev et al. [e]Greis (unpublished data on the system SrF_2–YbF_3, 1981).

solution is now separated from the RF_3 composition. In type III, observed for SrF_2–YF_3 and SrF_2–ErF_3 to SrF_2–LuF_3, the TYS region narrows to a composition near $(Sr, R)F_{2.70}$, and the expected α-$UO_{3-\delta}$-related solid solution is found in the RF_3-rich region. This diagram is analogous to some of the CaF_2–RF_3 systems. Ordering in the cα solid solution, however, occurs as high as 950–1050°C and can be detected easily by thermal analyses. First results on the low-temperature phase relationships of the system SrF_2–YbF_3 (Greis, 1981b) show that the nature of the observed superstructure phases differs from that in the case of SrF_2–EuF_3 (Greis, 1978b). X-ray powder and electron diffraction from single crystals show t and cβ, but not rhα and rhβ. Instead, rhα' is observed; it has the same unit cell as rhα, but a different formula, $Sr_4Yb_3F_{17}$. Obviously both border-line cases exist in the systems SrF_2–RF_3 for the rhα-geometry, $Sr_9Eu_5F_{33} \leftrightarrow Sr_8Yb_6F_{34}$; the first has a fully ordered anion sublattice and the second has a fully ordered cation sublattice (cf. sections 2.3 and 3.6). The lattice parameters of the $(Sr, Yb)F_{2+\delta}$ phases are also given in table 8. Sobolev et al. (1979) correctly indexed the basis structure reflections of their fluorite-related superstructure phases in the systems SrF_2–GdF_3 to SrF_2–LuF_3; however, it seems that the $a_S = 4a_F$ assignment for cβ is in error and should be $a_S = 3a_F$. For the phases of the system SrF_2–HoF_3, the powder diffraction patterns are reported. In spite of their poor quality, one can assume from a comparison with the Guinier patterns of the $(Sr, Eu)F_{2+\delta}$ and $(Sr, Yb)F_{2+\delta}$ superstructure phases that t, rhα, cβ, and rhβ are present. Reindexing and recalculations of the reported data give the superstructure parameters listed for R = Ho in table 8 (Greis, 1981b). It is very likely that in SrF_2–RF_3 systems of type I and type II, analogous fluorite-related superstructures occur, while in type III the situation is much more complicated. Single crystal electron diffraction data (Greis, 1981b) show that at least six different superstructures occur in $(Sr, Yb)F_{2.3-2.7}$, but the data evaluations are not complete.

3.4. *The systems BaF_2–RF_3*

Numerous systematic phase investigations exist on these systems. The phase diagram of BaF_2–YF_3 by Tkachenko et al. (1977) can be taken as representative (see fig. 9). Recently, Sobolev et al. (1977b) reviewed the phase diagrams of all BaF_2–RF_3 systems and included their earlier data on the tysonite-related solutions (Sobolev and Tkachenko, 1975; Sobolev et al., 1976d). In contrast to the CaF_2–RF_3 and SrF_2–RF_3 systems, it is more difficult to find three simplified types of diagrams because the appearance of intermediate phases is not as uniform. On the other hand, recent studies gave different results in many respects (Kieser and Greis, 1980a,b; Greis and Kieser, 1979, 1980; Greis et al., 1981). Therefore, the presently known phase diagrams are not very reliable and should be improved.

At least six different intermediate phases are reported. The fluorite-related solid solution $(Ba, R)F_{2+\delta}$ (cα) occurs in all systems and becomes significantly narrower at lower temperatures, $(Ba, R)F_{2.0-2.4} \rightarrow (Ba, R)F_{2.0-2.2}$. Two fluorite-related superstructure phases are observed: Ba_2RF_7 (t') for R = Y, Dy–Lu and

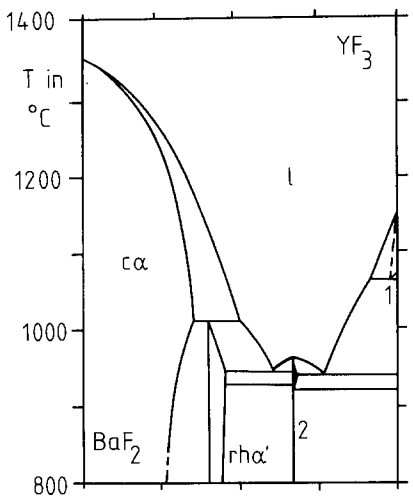

Fig. 9. BaF_2–YF_3 phase diagram after Tkachenko et al. (1977): 1, α-UO_3-related solid solution (Ba, Y)$F_{3-\delta}$; 2, BaY_2F_8 and its high-temperature modification.

$Ba_4R_3F_{17}$ (rhα') for R = Y, Ce–Lu. The first compound is stable only at high temperatures and shows many different modes of ordering. This can be regarded as a partial order on the way to the fully ordered t-phases like in the systems CaF_2–RF_3 and SrF_2–RF_3 (Greis and Kieser, 1979; Kieser and Greis, 1980a). The second type of phases has been studied earlier by Tkachenko et al. (1973) by X-ray single crystal methods. Their results on the superstructure geometry, however, proved to be wrong as shown with high-resolution Guinier techniques and electron diffraction from single crystals (Greis and Kieser, 1980; Kieser and Greis, 1980b). Crystal data are not reported for the α-$UO_{3-\delta}$-related solid solutions, which cannot be quenched. They are detected by thermal analyses only and may occur for R = Er–Lu and Y. The tysonite-related solid solution TYS is found for R = La–Dy and is described mainly by the large cell with $Z = 6$. The electron diffraction studies by Greis (1981b) show that only the cell with $Z = 2$ is correct, because no superstructure reflections can be observed. The best characterized phases are those with the formula BaR_2F_8 for R = Dy–Lu and Y. The low-temperature forms have monoclinic symmetry. The structure has been solved by Izotova and Aleksandrov (1970) for $BaTm_2F_8$. The coordination number of R^{3+} is 8 as in many other rare earth fluorides, but now the rather rare dodecahedron is observed. These polyhedra share edges and form rings of six members. As a result of their superposition over common vertices, channels occurring along the c-axis contain the 12-coordinate barium cations (compare also Tkachenko et al., 1973). Accurate lattice parameters are reported for all isostructural BaR_2F_8 modifications as well as for the two orthorhombic high-temperature modifications of $BaYb_2F_8$ and $BaLu_2F_8$ (Greis et al., 1981). The geometric relations between these two modifications are described by $a_0 \approx 2b_m$, $b_0 \approx 2c_m$, $c_0 \approx a_m$, and $Z_0 = 4Z_m$. In table 9 the lattice parameters of several selected intermediate phases of the systems BaF_2–RF_3 are listed. For further data, however, the original papers should be consulted.

TABLE 9
Lattice parameters of selected phases of the systems BaF_2–RF_3.

Formula	Phase[a]	a (Å)	b (Å)	c (Å)	β(°)	$V' = V/Z$ (Å^3)[b]
Ba_2DyF_7[c]	t'	4.2271		17.983		53.554
⋮						
Ba_2YF_7[c]	t'	4.2161		17.997		53.318
⋮						
Ba_2LuF_7[c]	t'	4.1966		17.951		52.692
$Ba_4Ce_3F_{17}$[d]	rhα'	11.332		20.901		55.347
⋮						
$Ba_4Gd_3F_{17}$[d]	rhα'	11.155		20.523		52.656
⋮						
$Ba_4Y_3F_{17}$[d]	rhα'	11.066		20.366		51.423
⋮						
$Ba_4Lu_3F_{17}$[d]	rhα'	10.995		20.251		50.481
$BaDy_2F_8$[e]	m	7.0185	10.563	4.2825	99.79	52.121
⋮						
BaY_2F_8[e]	m	6.9781	10.510	4.2603	99.68	51.332
⋮						
$BaLu_2F_8$[e]	m	6.8897	10.400	4.2185	99.27	49.717
$BaYb_2F_8$[e]	o	21.908	8.120	6.928		51.349
$BaLu_2F_8$[e]	o	21.895	8.0892	6.9043		50.953

[a]Space groups: I4/m (t), $R\bar{3}$ (rhα'), C2/m (m), and Pmmn (o). [b]Z for the formula unit (Ca, R)F_x: 6 (t'), 42 (rhα'), 6 (m), and 24 (o). [c]Kieser and Greis (1980a). [d]Kieser and Greis (1980b). [e]Greis et al. (1981).

Two points should be mentioned. First, ordering of chemical defects takes place even at very high temperatures (~1000°C) and can be explained by the significant difference in the radii of the cations. This implies once more, that cation order is the dominant aspect in all these AF_2–RF_3 systems, while anion order is less important. Secondly, the utility of single crystal electron diffraction data has been demonstrated in many ways. This was not evident initially because fluorides were thought to be unstable in the electron beam and difficult to investigate in the electron microscope (heating up, poor vacuum etc.). These difficulties, however, can be overcome using lower beam intensities and modern microscopes equipped with ion getter pumps. If one considers that crystals with diameters of $\leq$100 Å can be studied by single crystal methods, it becomes obvious that this technique has advantages in all cases where the growth of single crystals suitable for X-ray analyses is difficult to achieve. Electron microscopy and diffraction techniques are discussed more fully by Greis (1980b).

3.5. *Other AF_2–RF_3 systems*

The early literature includes a few reports on MgF_2–RF_3 systems such as MgF_2–LaF_3 (Nafziger and Riazance, 1972) and MgF_2–YF_3 (Nafziger et al., 1973). Very recently, however, 14 MgF_2–RF_3 systems have been studied by Olkhovaya et al. (1979), and for the two systems MgF_2–PmF_3 and MgF_2–EuF_3 hypothetical phase diagrams have been presented by these authors. In contrast to the systems AF_2–RF_3 with A = Ca, Sr, Ba, the only observed intermediate phases are the α-$UO_{3-\delta}$-related solid solutions $(Mg, R)F_{3-\delta}$ for R = Y, Er–Lu and the tysonite-related solid solution $(Mg, Gd)F_{3-\delta}$. These solid solutions are significantly less extended than in the case of A = Ca, Sr, Ba. The maximum phase width is observed in $(Mg, Lu)F_{2.85-3.00}$.

As expected from the crystal chemistry of rare earth trifluorides (see section 2.1), rather different phase relationships are observed in the systems MgF_2–ScF_3 (Komissarova and Pokrovsky, 1963), CaF_2–ScF_3, SrF_2–ScF_3 (Maklachkov and Ippolitov, 1970), and BaF_2–ScF_3 (Ippolitov and Maklachkov, 1970). The latter systems have, therefore, not been included in the above sections. At high temperatures, solid solutions are observed of ScF_3 in AF_2 and AF_2 in ScF_3 with structures which are based on the corresponding parent structures. These solid solutions are not as extended as in the case of the above AF_2–RF_3 systems (see sections 3.2–3.4). Intermediate compounds are not found in MgF_2–ScF_3 or CaF_2–ScF_3, but occur in SrF_2–ScF_3 and BaF_2–ScF_3. In the two latter cases a phase observed at the composition $(A^{II}, Sc)F_{2.39}$ is monoclinic with the space group $P2_1/c$ and reportedly isotypic to "$SrFeF_5$" (Ravez et al., 1967). The lattice parameters in Å are given as $a = 14.61$, $b = 7.28$, $c = 7.08$, $\beta = 95.13°$ for $(Sr, Sc)F_{2.39}$ and $a = 15.14$, $b = 7.27$, $c = 7.00$, and $\beta = 102.50°$ for $(Ba, Sc)F_{2.39}$ (Ippolitov and Maklachkov, 1970). A phase study on the system CaF_2–ScF_3 up to 100 kbar pressure shows beside the known phases the presence of a tysonite-related solid solution $(Ca, Sc)F_{2.85-2.90}$ (Bendeliani and Orlov, 1976).

There are no systematic phase investigations on BeF_2–RF_3 systems like those of the other AF_2–RF_3 systems. Some information is available, however, for ternary systems, e.g. KF–BeF_2–YF_3 by Borzenkova et al. (1970). These studies are mainly carried out with respect to the formation of glasses. A general conclusion which can be drawn is that BeF_2–RF_3 systems are of simple eutectic character and no intermediate phases have been observed. In connection with laser studies, some information is available on fluorite-related solid solutions $(Cd, R)F_{2+\delta}$, but systematic phase studies on CdF_2–RF_3 systems are absent.

3.6. *A structural essay on anion-excess, fluorite-related structures*

One of the most eye-catching structural features in RF_2–RF_3 (see section 2.3) and AF_2–RF_3 (see sections 3.2–3.4) systems are the fluorite-related solid solutions cα and the related superstructure phases t, rhα/rhα', rhβ, rhγ, and cβ. This structural essay is devoted to their common structural chemistry, but both speculative models and experimental facts are included. The main emphasis is to

draw a picture of what is known and to provide a directive basis for further studies on this subject.

Early neutron diffraction studies on the structure of anion-excess, fluorite-related solid solutions have been carried out by Willis (1963, 1964a,b, 1965) on $UO_{2+\delta}$. It has been found that the incorporation of the interstitial anions does not take place at the octahedral site as in the Goldschmidt–Zintl model (see section 2.3). This is in agreement with what one would expect from a geometrical point of view, because this site is too small for such an incorporation (see e.g. Greis, 1976). In contrast, short-range order reorganization occurs in the anion sublattice. Three "particles" to be considered are: interstitial anions with displacements as large as 1 Å away from the ideal octahedral sites, anions of the parent structure also shifted away from their original sites up to 1 Å, and vacancies created by these relaxed anions. In summary, no point defects are observed, but short-range-order clusters, known as Willis clusters and having notations such as 2:1:2 and 2:2:2 etc., occur. Further details are given in the original publication or in the review by Bevan (1973). The yttrofluorites have been studied by Cheetham et al. (1970, 1971) and Steele et al. (1972) also using neutron diffraction. Other methods, such as transport studies, EPR, and ENDOR (Hayes, 1974) provide direct and indirect structural information. More recently, Catlow (1980) reviewed the structural chemistry of highly disordered alkaline earth fluorides doped with rare earth trifluorides. It is now evident that rather extended "short-range-order" clusters are important as far as high defect concentrations are concerned, e.g. "4:3:2" at $(Ca, Y)F_{2.10-2.30}$ (Cheetham et al., 1971). All these structural clusters and models, however, are mainly focused on the anions, and cations play only a very minor role. This, in our opinion, is incomplete because from all we know today, cation order plays the dominant role in yttrofluorites and related structures. This may be valid for both high and low temperatures. In the first case, fast anionic conduction (section 3.1) is well documented at temperatures far below those which are indicated as the beginning of ordering in $c\alpha$ by thermal analyses (see mainly the work by Sobolev, Fedorov, and co-workers quoted in sections 3.2–3.4). The second case, ordering at low temperatures, will now be discussed in more detail.

The geometric relations between the lattice parameters of the observed superstructure phases t, t', $rh\alpha/rh\alpha'$, $rh\beta$, $rh\gamma$, $c\beta$, and the fluorite parent structures are listed in table 10. Rhombohedral phases are presented in hexagonal settings. The intermediate basis structures are also considered. They are the smallest possible cells required to index all strong basis structure reflections derived from the parent structure F by symmetry reduction (splitting). Z refers to the formula unit $MF_{2+\delta}$.

From these relations, from the fundamental principle of anion-excess fluorite-related structures (see section 2.2), and from the chemical compositions, it is possible to establish the chemical formulae of the different superstructures as shown in table 11 for AF_2–RF_3 systems. In the case of RF_2–RF_3, A must be replaced by R^{II}. All observed phases belong to one or two homologous series, M_nF_{2n+5} and M_nF_{2n+6}. The mineral tveitite ($rh\gamma$) and the phase $rh\beta$ can be

TABLE 10
Geometric relations between the lattice parameters of the fluorite parent structure F, of the basis structures B, and the superstructures S.

Cell	a (c, t, rh)		c (t, rh)		Z_S
cα	a_F				4
cβ	$=3a_F$				108
t_B	$=0.5\sqrt{2}a_F$		$=a_F$		2
t'	$=a_B$	$=0.5\sqrt{2}a_F$	$=3c_B$	$=3a_F$	6
t	$=\sqrt{5}a_B$	$=0.5\sqrt{10}a_F$	$=3c_B$	$=3a_F$	30
rh_B	$=0.5\sqrt{2}a_F$		$=\sqrt{3}a_F$		3
rhα, rhα'	$=\sqrt{7}a_B$	$=0.5\sqrt{14}a_F$	$=2c_B$	$=2\sqrt{3}a_F$	42
rhβ	$=\sqrt{13}a_B$	$=0.5\sqrt{26}a_F$	$=c_B$	$=\sqrt{3}a_F$	39
rhγ	$=\sqrt{19}a_B$	$=0.5\sqrt{38}a_F$	$=c_B$	$=\sqrt{3}a_F$	57

represented by both formulae (Greis, 1978c; Lechtenböhmer and Greis, 1978). Especially in the latter case, extended solid solutions have been observed between both border-lines. The phase t is always observed close to $MF_{2.33}$ showing in a few cases a narrow phase width like Eu_3F_7 (Greis, 1978b). It belongs, therefore, to the M_nF_{2n+5} series. In contrast, the phase T can be regarded as a M_nF_{2n+6} member because it has been observed by Sobolev et al. (1977b) at about $(Ba, R)F_{2.41}$ for R = Sm–Tb, but the crystal data are not yet available (therefore the ?). The phase rhα belongs to M_nF_{2n+5}, while rhα' is a M_nF_{2n+6} member and shows an extended phase width in the direction of rhα. The phase cβ can be regarded as a combination of rhα and rhβ. The actual atomic structures are known so far only for the rh phases. Greis (1976, 1977b) pointed out that rhβ is isostructural with $Na_7Zr_6F_{31}$ (Burns et al., 1968a,b), which was the first structure with M_6F_{37} clusters (one F_{13} cuboctahedron and six surrounding MF_8 square antiprisms). A similar structural principle has been postulated for tveitite on the basis of the superstructure geometry and the chemical composition (Greis, 1978c): rhγ = rhβ + 6CaF_2 corresponding to a diluted arrangement of the same clusters as in rhβ. Bevan et al. (1980, 1981) confirmed this by an X-ray structure analysis from a single crystal. Greis (1980b) also postulated a

TABLE 11
Superstructure phases of the systems RF_2–RF_3 and AF_2–RF_3.

		Homologous series	
Phase	n	M_nF_{2n+5}	M_nF_{2n+6}
rhγ	19	$Ca_{14-\delta}Y_{5+\delta}F_{43+\delta}$ =	$Ca_{13+\delta}Y_{6-\delta}F_{44-\delta}$
t, T(?)	15	$Ca_{10}Yb_5F_{35}$	$Ba_{9+\delta}Gd_{6-\delta}F_{36}$ (?)
rhα, rhα'	14	$Ca_9Yb_5F_{33}$	$Ba_{8+\delta}Yb_{6-\delta}F_{34-\delta}$
cβ = rhα + rhβ	13 + 14	$Ca_{17}Yb_{10}F_{64}$	
rhβ	13	$Ca_{8-\delta}Yb_{5+\delta}F_{31+\delta}$ =	$Ca_{7+\delta}Yb_{6-\delta}F_{32-\delta}$

similar principle for rhα/rhα' where the R_6F_{37} clusters would be packed so densely that doubling of the c-axis must occur for rhombohedral structures. The structure solved by Löchner (1980) for an analogous phase, $Nd_8^{II}Nd_6^{III}Cl_{28+4}O$, corresponds exactly to the model for rhα' as far as the cations are concerned. The anion problem (see section 2.3 and below) has been solved by postulating that one oxygen replaces the central anion in the cuboctahedron as in one of the models for tveitite (Bevan et al., 1980, 1981). This may be true in the case of the very reactive rare earth chlorides and, to a lesser degree, in the case of the mineral tveitite, but is inconsistent with synthetic behavior of the fluorides. Even if one accepts such relatively large amounts of oxygen, observed facts such as the phase widths between the border-line cases and the appearance of both rhα and rhα' cannot be explained. It is much more likely that nature in reality finds a compromise between the fully cation-ordered M_nF_{2n+6} structures with one further interstitial anion statistically distributed over the remaining "octahedral" parent structure sites and the fully anion-ordered M_nF_{2n+5} structures with a statistical distribution of one divalent and five trivalent cations in the six square antiprisms. As expected, large cations such as Ba^{2+} and Sr^{2+} favor more the M_nF_{2n+6} structures (T, rhα'), small cations such as R^{2+} and Ca^{2+} favor the M_nF_{2n+5} structures (rhα, rhβ, t, cβ etc.). For further details see Greis (1980b).

In figs. 11–13, the different rhombohedral superstructures are shown in projection along the c-axes. First, the constituent elements of these structures are demonstrated in fig. 10: an AF_8 cube of the parent structure, one half-icosahedron (rhα and rhα', for $c = 2c_B$) $\triangleq$ with a (full) icosahedron (rhβ, rhγ etc., $c = c_B$), both residing above and below the F_{13} cuboctahedra, and the R_6F_{37} clusters with three further AF_{10} polyhedra which are formed by the combination of AF_8 cubes with the R_6F_{37} clusters. The resulting unit would have the composition $A_6R_6F_{37+24}$ if isolated as in fig. 10. The most densely packed structure, rhα, is shown in fig. 11 with four $A_6R_6F_{37+24}$ units at the corners of the hexagonal unit and with one half-icosahedron. Clustering is already less dense in

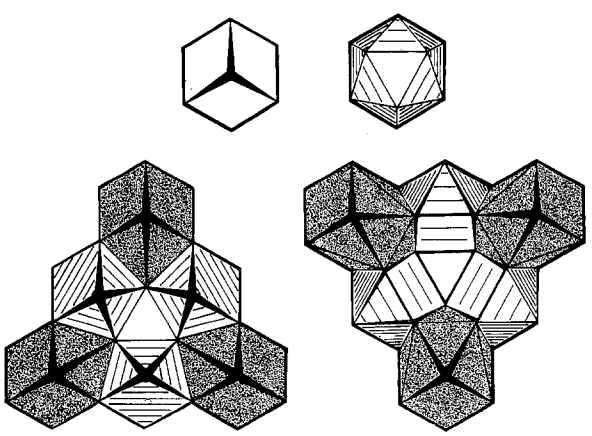

Fig. 10. Constituent structural elements of rhombohedral fluorite-related superstructures with anion excess (AF_8 cube, icosahedron, and $A_6R_6F_{37+24}$ clusters, seen from the outside and from the interior).

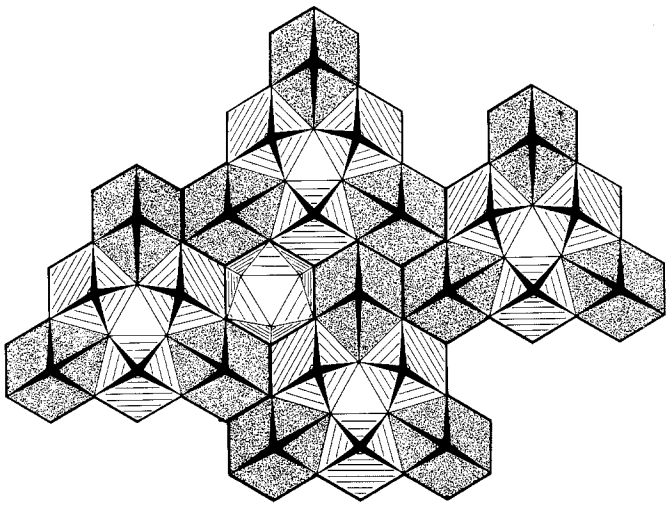

Fig. 11. Arrangement of the structural elements in the unit cell of rhα/rhα' in projection [001].

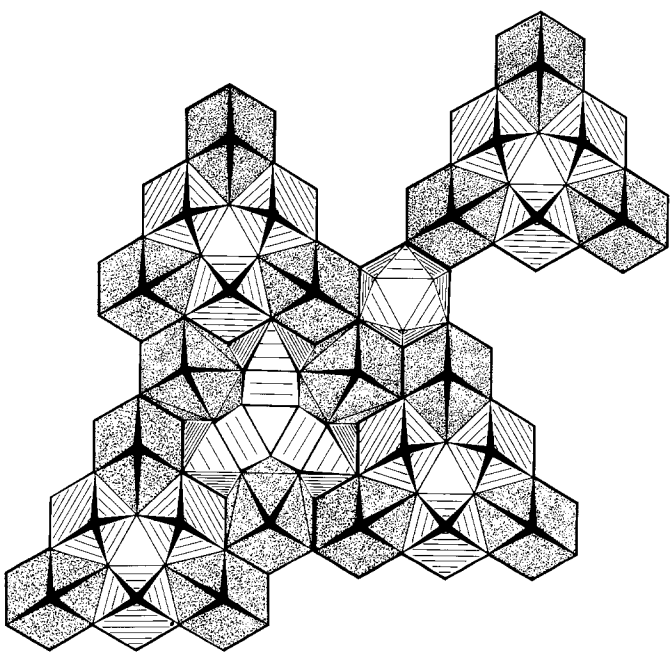

Fig. 12. Arrangement of the structural elements in the unit cell of rhβ in projection [001].

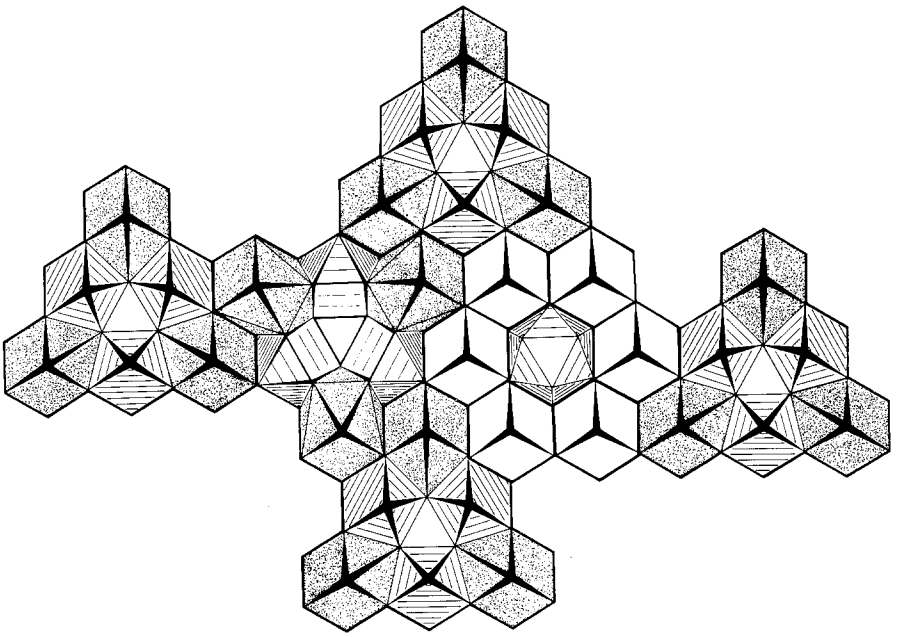

Fig. 13. Arrangement of the structural elements in the unit cell of rhγ in projection [001].

rhβ (fig. 12), but now one further cluster (seen from the interior) has a place in $\frac{2}{3}$, $\frac{1}{3}$, $\frac{1}{3}(c = c_B)$. In $x = \frac{1}{3}$ and $y = \frac{1}{3}$ the icosahedron is shown which separates two clusters along the threefold axis. Finally, rhγ in fig. 13 is characterized by an analogous arrangement as in rhβ, but diluted by six MF_8 cubes of the parent structure. Extending these principles of tessallation (Greis, 1981a) one obtains, for example the hypothetical phase rhδ with $n = 25$ for M_nF_{2n+5} or M_nF_{2n+6} (see fig. 14). For more information on the structural principles of these rh phases see Greis (1977b, 1978c, 1980a,b, 1981a) and Bevan et al. (1979, 1980, 1981). For the t phase, only models exist so far, but it is very likely that the actual structure is based on analogous principles (Bevan et al., 1979). No information is available on c_β and T.

With respect to experimental aspects, it follows that equilibrium will be more and more difficult to achieve, the more diluted the clusters occur in their parent structures. In the case of tveitite, this equilibrium is not obtainable in the laboratory but occurs in nature. Therefore, for further superstructure phases one should not only search in phase studies on synthetic AF_2–RF_3 systems, but also in minerals of the yttrofluorite class (and tysonites for their corresponding superstructure phases).

One further structural aspect concerning the cα solid solutions should also be discussed. Electron diffraction on (Ca, Y)$F_{2+\delta}$ and (Ca, Yb)$F_{2+\delta}$ samples with RF_3 concentrations as low as 5 mol% show the superstructure phases t and rhβ along with the fluorite parent structure (Greis, 1980b). In other words, microdomains

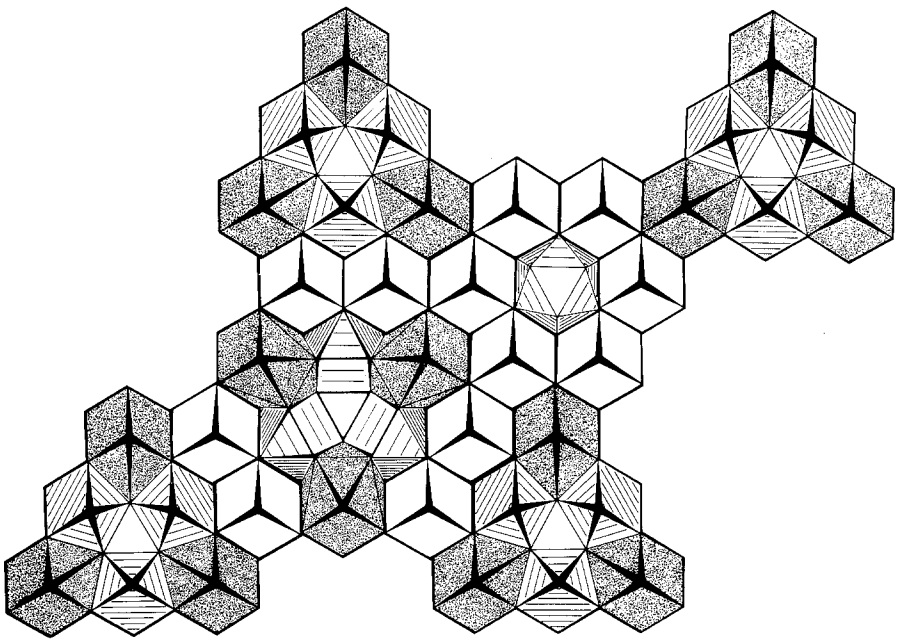

Fig. 14. Structural model of the hypothetical superstructure $A_{19+\delta}R_{6-\delta}F_{56-\delta}$ (rhδ, $Z = 75$, $a = 5a_B$, $c = c_B$).

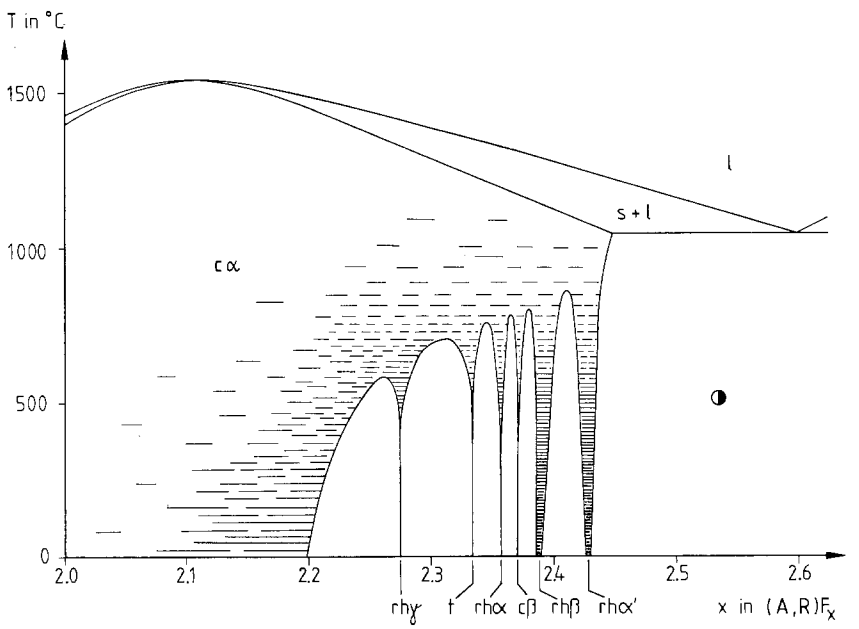

Fig. 15. Tentative phase diagram for the fluorite-related cα solid solutions $(A,R)F_{2+\delta}$ and their corresponding superstructure phases of the AF_2–RF_3 systems (after Greis, 1980b).

of the ordered phases already exist within $c\alpha$, but are too small to be revealed by X-ray diffraction techniques. Their size and concentration, however, increase gradually in the direction of $(Ca, R)F_{2.33}$ or $(Ca, R)F_{2.41}$, where they are also observed by X-ray methods. The predisintegration phenomenon has also been found by scanning electron microscopy in CaF_2:EuF_2, CaF_2:MnF_2, CaF_2:EuF_2:GdF_3, and CaF_2:EuF_2:MnF_2 at low concentration of the dopants in the CaF_2 host lattice (Orlov et al., 1980). From all these observations, one can construct the $c\alpha$ section of the AF_2–RF_3 phase diagrams in a new way (see fig. 15). The continuous crystallization of superstructure phases from the solid solution is influenced by concentration and temperature.

4. Mixed fluorides of the systems AF–RF_3

4.1. *Survey*

The most complete phase studies have been carried out on LiF–RF_3 and NaF–RF_3 systems in 1960–1970. This interest was mainly based on their importance in Molten-Salt Reactor Programs (e.g. Thoma and co-workers at Oak Ridge National Laboratory, USA; Keller and Schmutz of the Society of Nuclear Research in Karlsruhe, West Germany). Furthermore, some of the intermediate phases are suitable as host lattices for lasers, e.g. $A(R:R')F_4$, and up-conversion materials, e.g. $A(R:R':R'')F_4$. Magnetic properties of ARF_4 phases have also been studied and are reviewed in the Gmelin Handbook (1976). A few $NaRF_4$ phases show fluorescence after irradiation with cathodic rays.

In contrast to LiF–RF_3 and NaF–RF_3, the systems AF–RF_3 with R = K, Rb, and Cs were investigated only sporadically in the 1960's mainly because their hygroscopic nature limits their applications. This behavior naturally causes many difficulties in the preparation and characterization of intermediate phases. Nevertheless, many of these troublesome phase studies have been carried out mainly by French and Russian workers in the last ten years. It turned out that these systems are much more complicated than LiF–RF_3 and NaF–RF_3 as far as number and polymorphism of intermediate phases are concerned.

A few publications have appeared on phase relationships and/or intermediate phases of AgF–RF_3, TlF–RF_3, and NH_4F–RF_3 systems. On the basis of ionic radii (Shannon, 1976), Ag^+ fits into the alkaline cations between Na^+ and K^+, while Tl^+ and NH_4^+ have similar sizes as Rb^+. Therefore, phases with analogous formulae and structures can be expected.

Information on the more recent literature of systematic phase studies of the title systems is compiled in table 12. In the following sections, attention is mainly focused upon intermediate phases and their properties. All presently known types of compounds are listed in table 13. Known phases also include fluorite-related solid solutions $(Na, R)F_{2\pm\delta}$ and $(K, R)F_{2+\delta}$. In the first case, ordered phases with the postulated formulae $Na_5R_9F_{32}$ are reported. The appearance of ARF_4 phases for the alkali metals is very controversial.

TABLE 12
Literature on AF–RF_3 phase diagrams.

LiF–RF_3	R = La–Nd, Sm–Lu, Y	reviewed in the Gmelin Handbook (1976) and by Thoma (1973)
NaF–RF_3	R = La–Nd, Sm–Lu, Y	
KF–RF_3	R = La, Ce, Nd, Gd, Tb, Dy, Er, Yb, Y	
RbF–RF_3	R = Sm, Gd, Ho, Er, Yb, Y	
CsF–RF_3	R = Sm, Gd, Ho	
NaF–YF_3		Fedorov et al. (1979)
KF–EuF_3		Arbus et al. (1977)
KF–GdF_3		De Kozak and Samouël (1977)
KF–DyF_3		De Kozak and Almai (1978)
KF–RF_3 (Tb–Lu, Y)		Ardashnikova et al. (1980)
RbF–LaF_3		Filatova et al. (1980)
RbF–NdF_3		Nafikova et al. (1976a)
RbF–EuF_3		Arbus et al. (1978)
RbF–GdF_3		De Kozak and Samouël (1977)
RbF–DyF_3		De Kozak et al. (1979)
CsF–NdF_3		Nafikova et al. (1976b)
CsF–EuF_3		Arbus et al. (1978)
CsF–DyF_3		De Kozak et al. (1979)
TlF–GdF_3		De Kozak and Samouël (1977)
TlF–YbF_3		Védrine et al. (1973)
TlF–YF_3		Chassaing and Bizot (1973)
TlF–ScF_3		Chassaing (1972)

The $A_xR_yF_z$ phases can be prepared in an optimal manner by direct synthesis from corresponding mixtures AF/RF_3 in closed systems (Pt or Au ampoules). Preparations in open systems, even under inert gases, have to be avoided for two reasons. First, the formation of oxide fluorides cannot be excluded rigorously, and second, preferable vaporization of AF leads to almost uncontrollable changes in the compositions, so that troublesome chemical analyses of the reaction products must be made in all cases. The appropriate reaction temperatures can be taken from phase diagrams of the investigated systems or

TABLE 13
Types of intermediate phases in AF–RF_3 systems.

anion / cation	6:(3 + 1) 1.5	5:(2 + 1) 1.667	4:(1 + 1) 2.0	7:(1 + 2) 2.333	10:(1 + 3) 2.5
LiF			$LiRF_4$		
NaF			$NaRF_4$		
AgF	Ag_3RF_6		$AgRF_4$		
KF	K_3RF_6	K_2RF_5	KRF_4	KR_2F_7	KR_3F_{10}
NH_4F	$(NH_4)_3RF_6$				$NH_4R_3F_{10}$
RbF	Rb_3RF_6	Rb_2RF_5	$RbRF_4$	RbR_2F_7	RbR_3F_{10}
TlF	Tl_3RF_6			TlR_2F_7	TlR_3F_{10}
CsF	Cs_3RF_6		$CsRF_4$	CsR_2F_7	CsR_3F_{10}

related systems, if data are not reported. Many phases show polymorphism. The thermal stabilities of the different forms are given together with the lattice parameters in subsequent tables or figures.

4.2. *A_3RF_6 and A_2RF_5 phases*

Phases with an anion/cation ratio of 1.5 are mainly found in the case of A = K, Rb, and Cs, while those with an anion/cation ratio of 1.667 exist only for A = K and Rb. The crystal chemistry of all these A_3RF_6 and A_2RF_5 phases has been reviewed very recently by Greis (1982) and, therefore, only an overview will be given here.

The most striking feature of the A_3RF_6 compounds is their polymorphism and occurrence in at least nine different, but closely related structure types (see table 14). The close resemblance of all observed structure types is nicely demonstrated in a family tree of their space groups (see fig. 16). All structures are derived mainly by tilting and rotation of the RF_6 octahedra of the α-$(NH_4)_3FeF_6$ parent structure (Fm3m, $Z = 4$, a_p) in which these octahedra form a face-centered cubic lattice as Ca in CaF_2 or Bi in $BiLi_3$. The NH_4^+ cations occupy all the tetrahedral (t) and octahedral (o) interstices similar to $CaF(t)_2\square(o)$ or $BiLi(t)_2Li(o)$. Almost all high-temperature modifications crystallize with cubic symmetry, while tetragonal and monoclinic forms are stable at lower or room temperatures. K_2NaRF_6, Rb_2NaRF_6, Rb_2KRF_6, Cs_2NaRF_6, Cs_2KRF_6, and Cs_2RbRF_6 have all the cubic elpasolite structure. These phases are of great interest for studies of the magnetic behavior of R^{3+} cations in octahedral coordination (e.g. Urland, 1979; Urland et al., 1980). The structure with the lowest symmetry is the monoclinic Na_3AlF_6 cryolite structure. An extensive

TABLE 14
Structure types of A_3RF_6 and $A_2A'RF_6$ phases at high (HT) and low temperatures (LT).

Structure type	Space group	Z	Lattice parameters	Occurrence
α-$(NH_4)_3FeF_6$[a]	Fm3m	4	$a = 9.12 = a_{parent}$	K, Rb, Cs/Sm–Lu, Y(HT)
K_3FeF_6[b]	Fm3m	4	$a = 8.58 < a_p$	K, Rb, Cs/La–Nd (HT)
K_2NaAlF_6[c]	Fm3m	4	$a = 8.12 = a_p$	elpasolite
K_3CeF_6[d]	Pa3 (?)	4	$a = 9.07 < a_p$	K, Rb, Cs/La–Nd (HT)
K_3TlF_6[b]	Fd3	32	$a = 17.86 = 2a_p$	K_3ScF_6, Rb_3YF_6 (LT)
Rb_3TlF_6[b]	I4/mmm	2	$a = 6.51 < 0.5\sqrt{2}a_p$	Rb/Nd–Tb (LT)
			$c = 9.34 = a_p$	Cs/Pr–Lu, Y (LT)
β-Rb_3ErF_6[e]	$I4_1/amd$	16	$a = 13.29 < \sqrt{2}a_p$	Rb/Dy–Lu, Y (LT)
			$c = 18.39 = 2a_p$	
β-$(NH_4)_3ScF_6$[b]	P4/mnc	2	$a = 6.49 = 0.5\sqrt{2}a_p$	$(NH_4)_3ScF_6$ (LT)
			$c = 9.45 = a_p$	
Na_3AlF_6[f]	$P2_1/n$	2	$a = 5.46 < 0.5\sqrt{2}a_p$	K/Eu–Lu, Y (LT)
			$b = 5.61 > 0.5\sqrt{2}a_p$	
			$c = 7.80 = a_p$, $\beta = 90.18°$	

[a]Pauling (1924). [b]Bode and Voss (1957). [c]Morss (1974). [d]Besse and Capestan (1968). [e]Aléonard et al. (1975). [f]Náray-Szabó and Sasváry (1938).

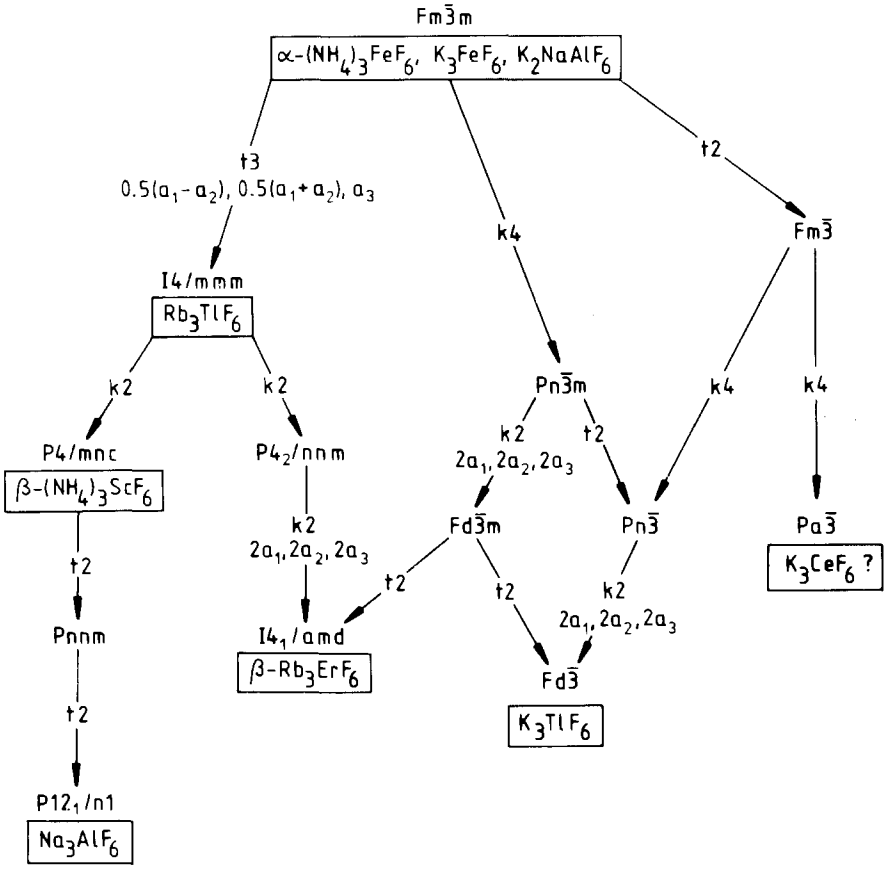

Fig. 16. Family tree of the A_3RF_6 and $A_2A'RF_6$ structures derived from the parent structure with Fm3m and a_1, a_2, a_3 (after Greis, 1982).

compilation of the thermal stabilities and lattice parameters of the A_3RF_6 phases is included in the review by Greis (1982).

All A_2RF_5 phases are monomorphous and isotypic to K_2SmF_5 which forms an orthorhombic phase with space group $Pna2_1$, or possibly with space group Pnam (Bochkova et al., 1973). This structure is built up by RF_7 polyhedra which share two edges along the c-axis thus forming $(RF_5)_\infty$ strings with the A cations between. Perpendicular to the b-axis, the cations are arranged in $(ARA)_\infty$ stripes with a somewhat distorted hexagonal symmetry (see fig. 17). A critical data evaluation by Pistorius (1975) and Greis (1980b) showed that several so-called low-temperature modifications of A_3RF_6 phase and "$K_3Tb_2F_9$" were in fact A_2RF_5 phases. Furthermore, the interpretation of several unindexed powder diffraction patterns of samples with compositions of $(A,R)F_{1.5}$ to $(A,R)F_{1.8}$ revealed additional A_2RF_5 phases (Greis, 1982). The lattice parameters of several selected phases are listed in table 15. For further details see the review by Greis (1982).

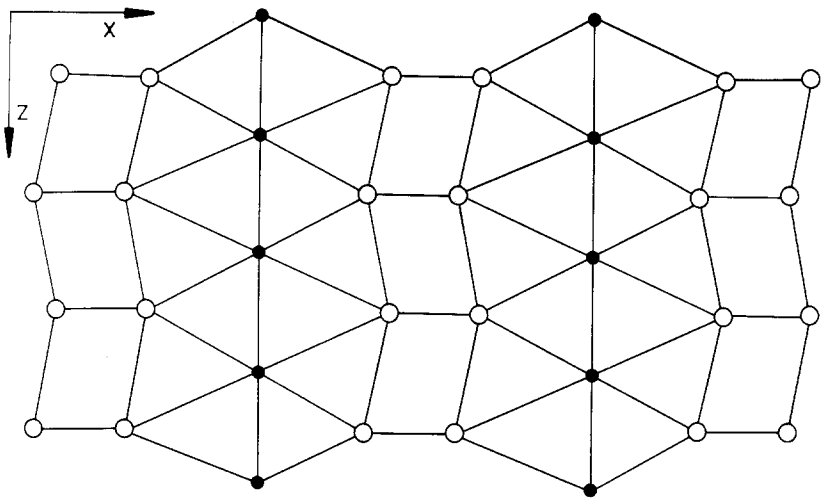

Fig. 17. Arrangement of Sm^{3+} (●) and K^+ (○) in the K_2SmF_5 structure (Bochkova et al., 1973; after Greis, 1982).

TABLE 15
Thermal stabilities and lattice parameters of selected K_2RF_5 and Rb_2RF_5 phases with the K_2SmF_5 ($Pna2_1$, $Z = 4$) structure (after a data compilation by Greis, 1982).

A_2RF_5	T (°C)	a (Å)	b (Å)	c (Å)
K_2NdF_5	590–690	(10.9)	(6.7)	(7.6)
K_2SmF_5	(< 500)	10.80	6.62	7.51
⋮				
K_2YF_5	(< 500)	10.80	6.597	7.313
⋮				
K_2LuF_5	(< 500)	10.72	6.562	7.253
Rb_2LaF_5	440–590	11.40	6.985	7.821
⋮				
Rb_2YbF_5	< 180	11.320	6.843	7.361

4.3. *ARF_4 and "$Na_5R_9F_{32}$" phases*

Phases of the composition ARF_4 are reported for A = Li, Na, Ag, K, Rb, and Cs. From a structural view-point, they can all be considered as metal difluorides with a disordered or partially/fully ordered cation sublattice. Disordered phases can be expected mainly if A^+ and R^{3+} have similar radii and in fact, cubic fluorite-related (Na, R)F_2 phases are observed at high temperatures as well as a few (K, R)F_2 phases. In most cases, they are part of solid solutions (A, R)$F_{2\pm\delta}$, which are structurally related to yttrofluorites as far as the anion-excess phases

are concerned (see section 3.2). The cation sites of the fluorite parent structure are statistically occupied by A^+ and R^{3+}, while charge compensation is obtained by interstitial anions. Some of the nonstoichiometric $(Na, R)F_2$ phases are also reported to show anion/cation ratios <2, and the formula $(Na, R)F_{2-\delta}$ seems to be more correct than $(Na, R, \square)F_2$ with respect to the crystal chemistry of fluorites. This is unusual for fluorides, but not oxides. Ranges of phase widths and regions of thermal stabilities (Thoma et al., 1966) as well as lattice parameters (Schmutz, 1966; Thoma, 1973) are compiled in table 16 for the sodium phases. Analogous data are also listed for the potassium phases. The lattice parameters of $(K, R)F_{2.33}$ are taken from Schmutz (1966), those of $(K, La)F_2$ and $(K, Ce)F_2$ are from Zachariasen (1948) and those of $(K, Sm)F_2$ and $(K, Eu)F_2$ are unpublished data from Hoppe and Odenthal (Gmelin Handbook, 1976). Analogous $(Rb, R)F_2$ phases with R = Sm–Lu and Y are reported by Hebecker and Lösch (1975) and Lösch and Hebecker (1976), who obtained them after annealing of the corresponding low-temperature phases at 550–660°C. This work, however, is open to discussion (see below). $(Cs, R)F_2$ phases are not reported.

At lower temperatures, ordering takes place in the cationic sublattice. We begin with a discussion of the $LiRF_4$ phases, which are the only intermediate

TABLE 16
Thermal stabilities, composition ranges, and variation of lattice parameters of fluorite-related solid solutions $(A, R)F_{2\pm\delta}$ with Fm3m and $Z = 4$ (references are cited in the text).

$(A, R)F_{2\pm\delta}$	T (°C)	x in $(A, R)F_x$	a (Å)
$(Na, Pr)F_{2+\delta}$	806–1025	2.11–2.29	5.695–5.702
$(Na, Nd)F_{2+\delta}$	785–1056	2.10–2.29	5.670–5.678
$(Na, Sm)F_{2+\delta}$	765–1060	2.07–2.29	5.605–5.628
$(Na, Eu)F_{2+\delta}$	796–1091	2.05–2.29	5.575–5.605
$(Na, Gd)F_{2+\delta}$	751–1080	2.03–2.29	5.552–5.583
$(Na, Tb)F_{2+\delta}$	734–1031	2.00–2.29	5.525–5.563
$(Na, Dy)F_{2\pm\delta}$	700–1020	1.97–2.29	5.508–5.545
$(Na, Ho)F_{2\pm\delta}$	~700–1010	1.94–2.29	5.480–5.526
$(Na, Y)F_{2\pm\delta}$	~680–975	2.00–2.29	5.447–5.530
$(Na, Er)F_{2\pm\delta}$	~680–975	1.90–2.29	5.443–5.515
$(Na, Tm)F_{2\pm\delta}$	~650–940	1.87–2.29	5.435–5.497
$(Na, Yb)F_{2\pm\delta}$	~550–928	1.83–2.29	5.420–5.478
$(Na, Lu)F_{2\pm\delta}$	~550–930	1.78–2.29	5.411–5.461
$(K, La)F_{2+\delta}$	750–1100	2.00–2.33	5.944–5.934
$(K, Ce)F_{2+\delta}$	700–1100	2.00–2.33	5.906–5.906?
$(K, Pr)F_{2+\delta}$	~1000	–2.33	–5.880
$(K, Nd)F_{2+\delta}$	730–1100	2.20–2.33	–5.846
$(K, Sm)F_{2+\delta}$		2.00–2.33	5.802–5.820
$(K, Eu)F_{2+\delta}$	710–1000	2.00–2.33	5.794–5.801
$(K, Gd)F_{2+\delta}$	~950	2.33	5.783

TABLE 17
Thermal stabilities of $LiRF_4$ phases with scheelite structure ($I4_1/a$, $Z = 4$) (references are cited in the text).

$LiRF_4$	T (°C)	a (Å)	c (Å)	$LiRF_4$	T (°C)	a (Å)	c (Å)
$LiEuF_4$	<710	5.228	11.03	$LiYF_4$	<819	5.175	10.74
$LiGdF_4$	<755	5.219	10.97	$LiErF_4$	<840	5.162	10.70
$LiTbF_4$	<790	5.200	10.89	$LiTmF_4$	<835	5.145	10.64
$LiDyF_4$	<820	5.188	10.83	$LiYbF_4$	<850	5.1335	10.588
$LiHoF_4$	<798	5.175	10.75	$LiLuF_4$	<825	5.124	10.54

compounds in $LiF–RF_3$ systems. Structural analyses on single crystals of $LiYF_4$ (Thoma et al., 1961), $LiYbF_4$ (Thoma et al., 1970), and $LiTbF_4$ (Als-Nielsen et al., 1975) show that all these phases crystallize in the tetragonal scheelite structure ($I4_1/a$). X-ray powder diffraction studies prove the remaining $LiRF_4$ phases to be isostructural. The lattice parameters compiled in table 17 were selected as the most reliable in the literature. They were taken from Keller and Schmutz (1965) and Schmutz (1966) and in the case of $LiYbF_4$ from Thoma et al. (1970), and are accompanied by the decomposition points (R = Eu–Er and Y) and the melting points (R = Tm–Lu). There is some evidence that $LiScF_4$ also exists, but no crystal data are reported (Babaeva and Bukhalova, 1966a,b; Sidorov et al., 1974).

Hexagonal $NaRF_4$ phases exist for R = La–Lu and Y. Then show no significant phase widths and are stable below 600–800°C (Thoma et al., 1966; see table 18). Their crystal structures have been solved by Burns (1965). In the case of $NaRF_4$ with R = La–Nd and Eu–Er he found the space group $P\bar{6}$, but $P6_3/m$ for R = Sm, Y, and Tm, and $NaDyF_4$ showed both. A full structure analysis has been carried out for $NaNdF_4$ (Burns, 1965). In contrast to the cubic high-temperature phases, partial ordering occurs in the cation sublattice. The order is greater in $P\bar{6}$ than in $P6_3/m$. Gagarinite phases with the general formula $NaCaRF_6$ and space group $P\bar{3}$ (or also $P6_3/m$?) are related to the latter form, but are not identical (Stepanov and Severov, 1961; Sobolev et al., 1963; Burns, 1965). The lattice parameters of all known $NaRF_4$ phases are listed in table 18; the data were taken from Keller and Schmutz (1964) and Schmutz (1966). A comparison between the formula volumes V'_o of the ordered hexagonal phases ($Z = 3$ for $(Na, R)F_2$) and V'_d of the corresponding disordered cubic phases (see also table 16) shows that ordering causes a very significant decrease in volume. Consequently, the region of thermal stability of the hexagonal phases increase remarkably under pressure, e.g. $NaHoF_4$ (Roy and Roy, 1964; see also Seifert, 1968). Several $AgRF_4$ phases with R = Nd–Ho are also found to be isostructural with $NaNdF_4$, though the space group is reported as $P6_322$ (Lösch and Hebecker, 1977). The thermal stabilities and lattice parameters are given in table 18.

The KRF_4 phases of the lighter rare earth elements La–Gd crystallize as the $RbRF_4$ phases with R = La–Sm in the orthorhombic $KCeF_4$ structure (table 19). It appears that the cationic sublattice of the latter structure type (Brunton, 1969; Saf'yanov et al., 1973) is arranged in a similar way as in $NaNdF_4$ as far as

TABLE 18
Thermal stabilities and lattice parameters of $NaRF_4$ and $AgRF_4$ phases with the $NaNdF_4$ structure ($P\bar{6}$ and/or $P6_3/m$, $Z = 3$ for MF_2) (references are cited in the text).

$NaRF_4$	T (°C)	a (Å)	c (Å)	V'_0 (Å^3)	V'_d (Å^3)
$NaLaF_4$	<810	6.176	3.827	42.139	–
$NaCeF_4$	<810	6.148	3.781	41.256	–
$NaPrF_4$	<800	6.111	3.745	40.376	46.177
$NaNdF_4$	<850	6.099	3.714	39.881	45.571
$NaSmF_4$	<834	6.064	3.658	38.830	44.022
$NaEuF_4$	<825	6.042	3.633	38.286	43.319
$NaGdF_4$	<835	6.025	3.611	37.840	42.785
$NaTbF_4$	<789	6.010	3.585	37.381	42.164
$NaDyF_4$	<770	5.991	3.559	36.875	41.776
$NaHoF_4$	<745	5.975	3.538	36.462	41.142
$NaYF_4$	<691	5.969	3.525	36.255	40.403
$NaErF_4$	<710	5.962	3.518	36.098	40.314
$NaTmF_4$	<640	5.959	3.493	35.806	40.136
$NaYbF_4$	<590	5.947	3.473	35.458	39.805
$NaLuF_4$	<600	5.928	3.459	35.089	39.607
$AgNdF_4$	<500	6.341	3.643	Lösch and Hebecker (1977)	
$AgSmF_4$	<500	6.280	3.618		
$AgEuF_4$	<500	6.246	3.631		
$AgGdF_4$	<500	6.239	3.601		
$AgTbF_4$	<500	6.212	3.588		
$AgDyF_4$	<500	6.176	3.584		
$AgHoF_4$	<500	6.146	3.581		

TABLE 19
Thermal stabilities and lattice parameters of KRF_4 and $RbRF_4$ phases with the $KCeF_4$ structure (Pnma, $Z = 4$).

ARF_4	T (°C)	a (Å)	b (Å)	c (Å)	Ref.
$KLaF_4$	(<750)	(6.32)	(3.83)	(15.7)	estimated
$KCeF_4$	<755	6.289	3.804	15.596	Brunton (1969)
$KPrF_4$	(<750)	(6.24)	(3.78)	(15.5)	estimated
$KNdF_4$	<750	6.202	3.749	15.43	Zakharova et al. (1974)
$KSmF_4$	<700	6.24	3.73	15.57	Saf'yanov et al. (1973)
$KEuF_4$	<658	6.185	3.680	15.47	Arbus et al. (1977)
$KGdF_4$	<625	6.153	3.654	15.428	De Kozak and Samouël (1977)
$RbLaF_4$	<740	6.455	3.856	16.23	Filatova et al. (1980)
$RbCeF_4$	<650	6.479	3.832	16.33	Védrine et al. (1974)
$RbPrF_4$	<536	6.418	3.793	16.22	Arbus et al. (1978)
$RbNdF_4$	<585	6.340	3.755	16.03	Nafikova et al. (1976a)
$RbSmF_4$	<522	(6.3)	(3.7)	(16.0)	Védrine et al. (1975)

TABLE 20
Thermal stabilities and lattice parameters of ARF_4 phases with the $KErF_4$ ($P3_112$, $Z = 18$) structure.

ARF_4	T (°C)	a (Å)	c (Å)	Ref.
$KTbF_4$	<730	14.158	10.166	Ardashnikova et al. (1980)
$KDyF_4$	<790	14.143	10.151	De Kozak and Almai (1978)
$KHoF_4$	<750	14.108	10.140	Ardashnikova et al. (1980)
KYF_4	<760	14.083	10.117	Ardashnikova et al. (1980)
$KErF_4$	<800	14.082	10.122	Aléonard et al. (1973, 1978a)
$KtmF_4$	<770	14.031	10.115	Ardashnikova et al. (1980)
$KYbF_4$	<755	13.977	10.081	Labeau et al. (1974a,b)
$KLuF_4$	<815	13.912	10.032	Ardashnikova et al. (1980)
$AgYF_4$	~600	13.63	9.764	Lösch and Hebecker (1977)
$AgErF_4$	~600	13.62	9.746	Lösch and Hebecker (1977)
$AgTmF_4$	~600	13.57	9.735	Lösch and Hebecker (1977)
$AgYbF_4$	~600	13.52	9.677	Lösch and Hebecker (1977)
$AgLuF_4$	~600	13.46	9.633	Lösch and Hebecker (1977)
$NaScF_4$	<600	12.97	9.27	Thoma and Karraker (1966)

double-layers with hexagonal symmetry are concerned. The KRF_4 phases of the heavier rare earth elements Tb–Lu and Y crystallize in the trigonal $KErF_4$ structure as well as some $AgRF_4$ phases and $NaScF_4$ (see table 20). The $KErF_4$ structure has been solved by Aléonard et al. (1973, 1978a). The superstructure with $Z = 18$, however, is not always observed, but a smaller subcell with $a = a_S/\sqrt{3}$, $c = c_S$, and $Z = 6$ is found (e.g. Ardashnikova et al., 1980). This may be a consequence of poor X-ray resolution or of differences in preparation techniques. Here one would expect the smaller cell in quenched samples with a smaller degree of cation order, while the superstructure cell with $Z = 18$ represents the higher order and should be favored after long-time annealing. In table 20 the lattice parameters for the latter structure only are given. The cationic arrangement in the superstructure (and of course also in the substructure) can be described again with hexagonal nets, but in contrast to the structures above, we now have a three-level structure (Aléonard et al., 1978a).

Lösch and Hebecker (1976) and Hebecker and Lösch (1975) reported thirty-one $RbRF_4$ (R = Y, Sm–Lu) and $CsRF_4$ (R = Y, Ce–Lu) compounds as well as a few $TlRF_4$ compounds with R = Y, Ho–Lu. All these phases were prepared at 400–600°C and are obviously stable at room temperature. They are all isotypic with $TlTmF_4$ ($P6_3$, $P6_3/m$, or $P6_322$, $a = 15.48$ Å, $c = 11.92$ Å, $Z = 24$). In contrast, several careful phase investigations on the following systems in question did not reveal ARF_4 compounds at all: RbF–DyF_3 and CsF–DyF_3 (De Kozak et al., 1979), RbF–EuF_3 and $CsEuF_3$ (Arbus et al., 1978), RbF–GdF_3 and CsF–GdF_3 (De Kozak and Samouël, 1977; De Kozak et al., 1973), RbF–HoF_3 (Reshetnikova et al., 1976), RbF–ErF_3 (Aléonard et al., 1975), RbF–YF_3 (Chassaing, 1975), CsF–HoF_3 (Shaimuradov et al., 1975), CsF–SmF_3 (Védrine et al., 1975), RbF–YbF_3 (Védrine et al., 1973), and see also the Gmelin Handbook (1976) for the older

literature. Arbus et al. (1978) pointed out that the "ARF_4" phases reported by Lösch and Hebecker (1976) were in fact the corresponding AR_2F_7 phases. This would also explain the findings by Lösch and Hebecker (1976) that the X-ray patterns of almost all their "ARF_4" phases showed reflections of the corresponding A_3RF_6 phases. It seems that indeed diphasic samples of AR_2F_7 and A_3RF_6 were studied.

In summary, the stability regions of the well-documented ARF_4 structure types ($LiYF_4$, $NaNdF_4$, $KCeF_4$, and $KErF_4$) are shown in fig. 18. As a compromise, the radii were taken for alkali ions in coordination number six and for the rare earth cations in coordination number eight. The following are additional ARF_4 phases which are not covered by this scheme: $LiScF_4$ (<438°C, no crystal data; Babaeva and Bukhalova, 1966a,b), NH_4ScF_4 (<440°C, tetragonal, $a = 4.06$ Å, $c = 6.67$ Å; Hajek, 1965), $CsScF_4$ (<500°C, tetragonal, $a = 3.989$ Å, $c = 6.799$ Å, $TlAlF_4$-type; Hebecker and Lösch, 1975), $AgScF_4$ (<600°C, monoclinic, $a = 11.78$ Å, $b = 6.100$ Å, $c = 5.898$ Å, $\beta = 91.6$°; Lösch and Hebecker, 1979), and $TlGdF_4$ (<540°C, cubic fluorite superstructure, $a = 11.795$ Å; De Kozak and Samouël, 1977). The existence and/or the crystal data are still open to question or unknown for $RbSmF_4$, $RbScF_4$, $CsLaF_4$, $CsCeF_4$, and $CsNdF_4$.

With respect to the fluorite-related high-temperature solid solution $(Na, R)F_{2+\delta}$, ($c\alpha$), ordering occurs not only at the composition $MF_{2.0}$, but also at $MF_{2.286}$. Below about 400°C, fluorite-related superstructure phases $5NaF{\cdot}9RF_3 = Na_5R_9F_{32}$ with R = Dy–Lu and Y have been observed (Steinfink and Brunton, unpublished, 1964, as quoted by Thoma et al., 1966). X-ray data from a single crystal of $Na_5Lu_9F_{32}$ gave the following results: Cmmm, $a_S = a_F$, $b_S = 5\sqrt{2}a_F$, $c_S = \sqrt{2}a_F$, and $V_S = 10V_F = 40V'$. In the light of present knowledge about anion-excess fluorite-related superstructures, there are two aspects open to discussion. With the above setting, a C-centered lattice is questionable and the chemical formula is not in agreement with $Z = 40$ for $MF_{2+\delta}$. In table 21 the lattice parameters of

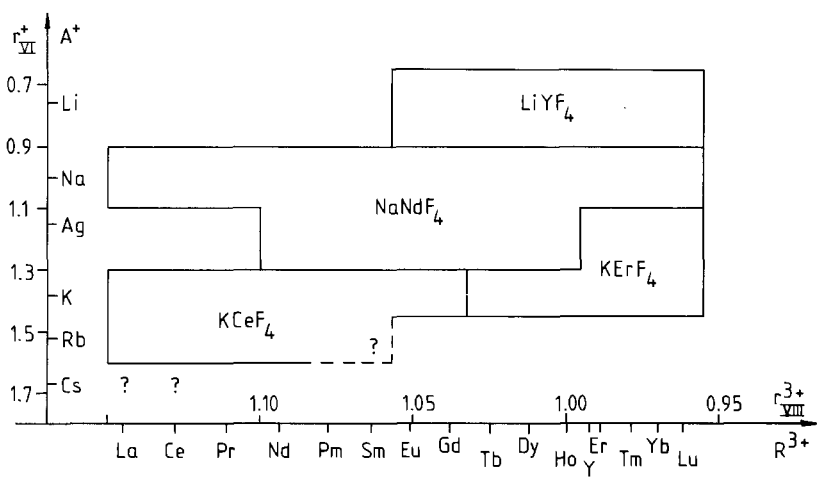

Fig. 18. Stability regions of ordered ARF_4 structure types.

TABLE 21
Thermal stabilities and lattice parameters of the so-called $Na_5R_9F_{32}$ phases (Cmmm, $Z = 40$ for $MF_{2+\delta}$) (references are cited in the text).

"$Na_5R_9F_{32}$"	T (°C)	a (Å)	b (Å)	c (Å)	V'_o (Å^3)	V'_d (Å^3)
"$Na_5Dy_9F_{32}$"	~700	5.547	39.23	7.845	42.679	42.623
"$Na_5Ho_9F_{32}$"	633–767	5.525	39.07	7.814	42.169	42.186
"$Na_5Y_9F_{32}$"	537–710	5.520	39.04	7.805	42.039	42.278
"$Na_5Er_9F_{32}$"	530–682	5.514	38.99	7.798	41.912	41.935
"$Na_5Tm_9F_{32}$"	475–710	5.493	38.84	7.768	41.432	41.526
"$Na_5Yb_9F_{32}$"	450–750	5.480	38.75	7.750	41.143	41.097
"$Na_5Lu_9F_{32}$"	<778	5.463	38.63	7.725	40.756	40.715

all known "$Na_5R_9F_{32}$" phases are listed with their ranges of thermal stability (Thoma et al., 1966). In addition, the reduced formula volumes V' are compared for the ordered and disordered phases of composition $(Na, R)F_{2.286}$ (see also table 16). The good agreement indicates that at least the lattice geometry could be correct, but more work is obviously needed to clarify formula and structure.

4.4. *AR_2F_7 phases*

Phases with the composition $AF{\cdot}2RF_3$ exist for (Na), K, Rb, Tl, and Cs. Sodium has been set in brackets due to the uncertainties about the "$Na_5R_9F_{32}$" phases and their corresponding high-temperature solid solutions cα (see section 4.3). Yttrofluorite-related $(K, R)F_{2.33}$ phases (Fm3m, $Z = 4$) are reported for R = La–Gd (see table 16), for $RbLa_2F_7$ with $a = 6.000$ Å by Filatova et al. (1980), and for $RbCe_2F_7$ with $a = 5.984$ Å by Védrine et al. (1974). A small tetragonal distortion of this cubic parent structure has been observed for $RbCe_2F_7$ below 470°C by Védrine et al. (1974) and for $RbNd_2F_7$ by Nafikova et al. (1976a). All other AR_2F_7 phases crystallize in one or two of the four well-documented structure types: KHo_2F_7; Cm, (Le Fur et al., 1982), KEr_2F_7; $Pna2_1$, (Aléonard et al., 1980), KYb_2F_7; P2, (Le Fur et al., 1980), and $RbEr_2F_7$; $P6_3$, $P6_3/m$, $P6_322$, (Aléonard et al., 1975, 1981). The appearance of the different structure types among the KR_2F_7 phases is shown in fig. 19. Lattice parameters are given in table 22. The AR_2F_7 phases with A = Rb, Tl, Cs crystallize predominantly with the $RbEr_2F_7$ structure at high temperatures, but with the KEr_2F_7 structure at low temperatures. More data, however, are needed to get a better understanding of the polymorphism of AR_2F_7 phases. The most reliable lattice parameters for a few selected phases are listed in tables 23 and 24. A comparison of the crystal data of the "ARF_4" phases as reported by Lösch and Hebecker (1976) with those of the hexagonal AR_2F_7 phases in table 24 shows a remarkable agreement with respect to both space groups and lattice parameters. Therefore, the number of hexagonal AR_2F_7 phases may actually be much larger than shown in table 24. The hexagonal structure type obviously undergoes a symmetry reduction to the orthorhomic low-temperature form with $a_{hex} = 2c_{ortho}$ and $c_{hex} =$

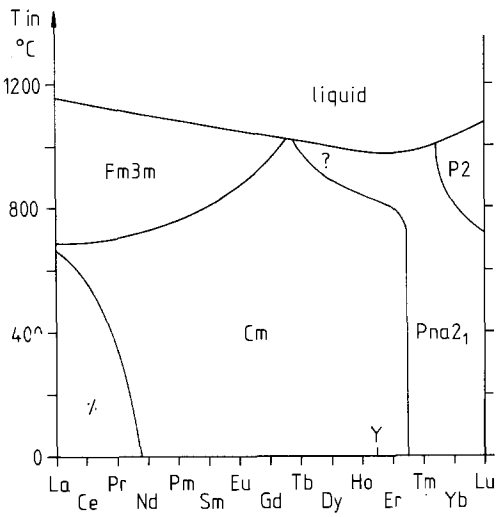

Fig. 19. Approximate stability regions of KR_2F_7 structure types.

a_{ortho}. A close structural relation between these types is found in the four-layer sequence of hexagonally arranged cations in the direction of z_{hex}; similar layers occur in the direction of x_{ortho} of the KEr_2F_7 ($Pna2_1$) structure.

The actual atomic arrangements are known for KHo_2F_7 (Le Fur et al., 1982), KEr_2F_7 (Aléonard et al., 1980), and KYb_2F_7 (Le Fur et al., 1980). The first structure type is a fluorite-related superstructure with the cation sequence –ABC–. Ordering of cations takes place in A and B with the ratio 1K:3Ho, but 1K:1Ho in C. The coordination number of Ho^{3+} is eight in all cases; one quarter

TABLE 22

Lattice parameters of KR_2F_7 phases with the (I) KHo_2F_7 structure (Cm, $Z = 8$, Le Fur et al., 1981), (II) KEr_2F_7 structure ($Pna2_1$, $Z = 8$, Aléonard et al., 1980), and (III) KYb_2F_7 structure (P2, $Z = 8$, Le Fur et al., 1980).

KR_2F_7	Type	a (Å)	b (Å)	c (Å)	β (°)	Ref.
KGd_2F_7	I	14.414	8.123	12.142	125.65	De Kozak and Samouël (1977)
KTb_2F_7	I	14.432	8.062	12.091	125.63	Le Fur et al. (1982)
KDy_2F_7	I	14.430	8.071	12.077	125.53	De Kozak and Almai (1978)
KHo_2F_7	I	14.287	8.004	11.950	125.33	Le Fur et al. (1982)
KY_2F_7	I	14.265	7.990	11.930	125.16	Le Fur et al. (1982)
KEr_2F_7	I	14.275	7.991	11.923	125.15	Aléonard et al. (1973)
KY_2F_7	II	11.820	13.337	7.821		Aléonard et al. (1980)
KEr_2F_7	II	11.770	13.295	7.789		Aléonard et al. (1973)
KTm_2F_7	II	11.761	13.273	7.763		Aléonard et al. (1980)
KYb_2F_7	II	11.715	13.241	7.735		Labeau et al. (1974b)
KLu_2F_7	II	11.686	13.165	7.689		Aléonard et al. (1980)
KYb_2F_7	III	6.528	4.217	6.435	115.94	Le Fur et al. (1980)
KLu_2F_7	III	6.501	4.202	6.420	115.99	Le Fur et al. (1980)

TABLE 23
Thermal stabilities and lattice parameters of selected RbR_2F_7, TlR_2F_7, and CsR_2F_7 phases with the KEr_2F_7 structure ($Pna2_1$, $Z = 8$, Aléonard et al., 1980).

AR_2F_7	T (°C)	a (Å)	b (Å)	c (Å)	Ref.
$RbSm_2F_7$	~700	12.26	13.75	7.995	Védrine et al. (1975)
$RbGd_2F_7$	<724	12.225	13.857	7.906	after De Kozak and Samouël (1977)
$RbDy_2F_7$	<706	12.060	13.643	7.804	after De Kozak et al. (1979)
$RbYb_2F_7$	<654	11.98	13.37	7.760	Védrine et al. (1973)
$TlYb_2F_7$	~600	12.02	13.42	7.796	Védrine et al. (1973)
$CsNd_2F_7$	<693	12.58	14.058	8.148	Nafikova et al. (1976b)
$CsSm_2F_7$	< 640	12.54	13.97	8.15	Védrine et al. (1975)
$CsGd_2F_7$	<1104?	12.483	13.880	8.030	after De Kozak and Samouël (1977)
$CsHo_2F_7$	<855	(12.4)	(13.8)	(8.0)	Shaimuradov et al. (1975)

TABLE 24
Thermal stabilities and lattice parameters of selected RbR_2F_7, TlR_2F_7, and CsR_2F_7 phases with the $RbEr_2F_7$ structure ($P6_3$, $P6_3/m$, $P6_322$; $Z = 16$; Aléonard et al., 1975).

AR_2F_7	T (°C)	a (Å)	c (Å)	Ref.
$RbEu_2F_7$	718–1022 (?)	15.80	12.17	Arbus et al. (1978)
$RbGd_2F_7$	724–1060	15.86	12.23	De Kozak and Samouël (1977)
$RbDy_2F_7$	706–1081	15.67	12.06	De Kozak et al. (1979)
RbY_2F_7	682–1110	15.521	11.978	Chassaing (1975)
$RbEr_2F_7$	< 1106	15.586	11.968	Aléonard et al. (1975)
TlY_2F_7	360–925	15.96	11.99	Chassaing (1975)
$CsNd_2F_7$	693–1045	16.050	14.212 (?)	Nafikova et al. (1976b)
$CsEu_2F_7$	< 1117	16.04	12.48	Arbus et al. (1978)
$CsGd_2F_7$	1104–1160	16.06	12.48	De Kozak and Samouël (1977)
$CsDy_2F_7$	< 1170	15.874	12.378	De Kozak et al. (1979)

of the polyhedra are cubes and the others square antiprisms. The coordination number of potassium is 10 (a cube with one vertex substituted by a triangle) and 14 (less regular polyhedra). The clustering of the polyhedra is described by Ho_3F_{18} (3 square antiprisms); two of them form Ho_8F_{42} blocks together with two HoF_8 cubes. However, other descriptions of the structure are possible.

The two other structure types are not fluorite-related. KEr_2F_7 (Aléonard et al., 1980) has the cation sequence –ABAC– of hexagonally arranged layers: A (2K:1Er), B and C with smaller meshes (1□:3Er). The coordination number of Er^{3+} is again eight; one quarter of the polyhedra are dodecahedra and the others square antiprisms. The coordination of potassium is irregular, (5 + 4) and (9 + 2). Two square antiprisms and one dodecahedron share faces thus forming Er_3F_{17} groups. They are linked together in a network with large tunnels where the potassium cations are located. The KYb_2F_7 structure is characterized by cation nets with internal order (1K:2Yb) and with the sequence –AA– in the direction

of the y-axis. The coordination number of ytterbium is seven (pentagonal bipyramid), while the coordination number of potassium is 10 (bicapped rhombohedron). Edge-sharing bipyramids form Yb_3F_{17} groups which are linked with other groups by common vertices forming a network with channels for the potassium cations which are squeezed out of the hexagonal planes A and reside half way between them. The structure is very similar to KIn_2F_7 (Champarnaud-Mesjard and Frit, 1977) and closely related to α-U_3O_8, Nb_3O_7F, and Ta_3O_7F.

4.5. *AR_3F_{10} phases*

AR_3F_{10} phases are reported for A = K, NH_4, Rb, Tl, and Cs. The available information on their thermal stabilities, however, is incomplete or contradictory. A general description of the phases is not yet possible. It seems, however, that most of the observed phases can be prepared by solid-state reactions at 900–1000°C. At present, five different structure types are known: KY_3F_{10}, KYb_3F_{10}, KEr_3F_{10}, KTm_3F_{10}, and $CsYb_3F_{10}$. The actual atomic structure are well established except for the KTm_3F_{10} type. The lattice parameters of many AR_3F_{10} phases with the three most common structure types are listed in tables 25–27.

The KY_3F_{10} structure has been solved by Pierce and Hong (1974) and has been confirmed later for KTb_3F_{10} by Podberezskaya et al. (1976b) and for $RbEu_3F_{10}$ by Arbus et al. (1980). The relationship to fluorite has been discussed by Aléonard et al. (1978a) and Borisov and Podberezskaya (1979). The fluorite-related KY_3F_{10} structure type is characterized by hexagonal nets of cations with an ordered arrangement of 1K:3Y. The sequence of these layers along $[111]_F$ is –ABCABC– like that in rhα (see section 3.6). The coordination number of the yttrium cations is eight (square antiprism), while potassium is surrounded by (12 + 4) fluorines in a somewhat irregular polyhedron. Six of the YF_8 square antiprisms share edges to form a Y_6F_{32} cluster with an empty central F_8 cube. These clusters show an

TABLE 25
Lattice parameters of AR_3F_{10} phases with the KY_3F_{10} structure (Fm3m, $Z = 8$).

AR_3F_{10}	a (Å)	Ref.
KTb_3F_{10}	11.611	Podberezskaya et al. (1976b)
KDy_3F_{10}	11.635	Védrine et al. (1975)
KHo_3F_{10}	11.626	Védrine et al. (1975)
KY_3F_{10}	11.536	Pierce and Hong (1974)
KEr_3F_{10}	11.517	Aléonard et al. (1978)
KTm_3F_{10}	11.448	Védrine et al. (1975)
KYb_3F_{10}	11.432	Védrine et al. (1975)
KLu_3F_{10}	11.392	Védrine et al. (1975)
$RbSm_3F_{10}$	11.954	Védrine et al. (1975)
$RbEu_3F_{10}$	11.844	Arbus et al. (1980)
$RbGd_3F_{10}$	11.828	Védrine et al. (1975)
$RbTb_3F_{10}$	11.787	Védrine et al. (1975)

TABLE 26
Lattice parameters of AR_3F_{10} phases with the KYb_3F_{10} structure ($P6_3mc$, $Z = 4$).

AR_3F_{10}	a (Å)	c (Å)	Ref.
KYb_3F_{10}	8.067	13.203	Aléonard et al. (1976)
KLu_3F_{10}	8.050	13.201	Ardashnikova et al. (1980)
$RbDy_3F_{10}$	8.283	13.514	De Kozak et al. (1979)
RbY_3F_{10}	8.200	13.392	Chassaing (1975)
$RbEr_3F_{10}$	8.251	13.463	Aléonard et al. (1975)
$NH_4Er_3F_{10}$	8.10	13.34	Podberezskaya et al. (1976a)
TlY_3F_{10}	8.208	13.392	Chassaing (1975)

TABLE 27
Lattice parameters of AR_3F_{10} phases with the $CsYb_3F_{10}$ structure (Pc, $Z = 2$); Aléonard et al., 1982).

AR_3F_{10}	a (Å)	b (Å)	c (Å)	β (°)
$RbTm_3F_{10}$	4.2538	6.6436	16.134	90.0
$RbYb_3F_{10}$	4.2409	6.6179	16.088	90.0
$RbLu_3F_{10}$	4.2226	6.5990	16.032	90.0
$CsTm_3F_{10}$	4.303	6.758	16.265	90.0
$CsYb_3F_{10}$	4.2893	6.7437	16.196	90.0
$CsLu_3F_{10}$	4.2721	6.7230	16.178	90.0

octahedral arrangement of the cations; three of them belong to one of two succeeding hexagonal nets. The cubic close-packing of the clusters is rhombohedral along $[111]_F$ and, therefore, a double-fluorite structure is derived with the sequence –ABCABC– = $-\alpha\beta\gamma-$ (cf. Aléonard et al., 1978a). The situation is very similar as in rhα, but the types of clusters are different (R_6F_{32} for KY_6F_{10} and R_6F_{37} for rhα).

The KYb_3F_{10} structure has been solved by Aléonard et al. (1976), whose data are in agreement with those of Podberezskaya et al. (1976a) for the isotypic $NH_4Er_3F_{10}$ phase. This structure type is characterized again by hexagonal nets of cations (1K:3Yb) as in the case of KY_3F_{10} (see above). The sequence along z_{hex}, however, is now –ABAC– as in KEr_2F_7 (see section 4.4). The coordination number of Yb is eight (square antiprism) and 15/16 for potassium (irregular polyhedra). Six square antiprisms form a R_6F_{32} cluster as in KY_3F_{10}, but their three-dimensional arrangement leads to a network with the cation layer sequence of –ABAC– = $-\alpha\beta-$.

The KEr_3F_{10} structure can be regarded as fluorite-related with respect to the basic cation sequence of –ABC–, which is observed as a subunit (Aléonard et al., 1978b). As in the preceding structure types, six RF_8 square antiprisms form R_6F_{32} clusters. The three-dimensional arrangement, however, leads to a very complicated cation sequence perpendicular to (001):

$$-\underbrace{ACABCAB}\underbrace{ACBCABCAC}\underbrace{BABCABCB}- = -\alpha\beta\gamma-.$$

So far, only one example of this type has been observed. The lattice parameters are: $a = 14.088$ Å, $b = 8.1378$ Å, $c = 28.280$ Å, $\beta = 109.45°$ (Cm, $Z = 16$) (Aléonard et al., 1978b). Another structure type has been found in the case of KTm_3F_{10}, which is also the only representative. The atomic structure is not yet known, but the monoclinic parameters are $a = 20.90$ Å, $b = 8.20$ Å, $c = 20.90$ Å, and $\beta = 109.50°$, and $Z = 18$ (Aléonard et al., 1978a).

Very recently, Aléonard et al. (1982) solved the structure of $CsYb_3F_{10}$, which is very similar to the KYb_2F_7 structure (see section 4.4) and can be regarded as a superstructure of the latter. The ytterbium cations are again seven-coordinated, and the pentagonal bipyramids form a network of hexagonal cation layers with the sequence –AA– in the direction of the x-axis. The cesium cations are similar to the potassium ions in KYb_2F_7 because they also reside halfway between the ytterbium layers*.

5. Miscellaneous mixed fluorides

Several other mixed fluorides containing RF_2, RF_3, or RF_4 are known, but are not covered in the preceding sections. Many of these phases are mentioned below under the heading of the corresponding systems.

AF–RF₂: Pseudocubic perovskite-related $CsEuF_3$ with $a = 4.77$ Å is the only reported intermediate compound (Shafer, 1965).

AF₂–RF₂: Very recently, orthorhombic $SmMgF_4$ ($a = 3.915$ Å, $b = 14.440$ Å, $c = 5.661$ Å) and $EuMgF_4$ ($a = 3.933$ Å, $b = 14.43$ Å, $c = 5.608$ Å) have been described. They are structurally related to $BaMF_4$ (M = Mg, Mn–Zn, $A2_1am$), but have the different space group Amam (Banks et al., 1980).

RF₂–R′F₃: Two systems that have been studied are EuF_2–GdF_3 (Greis and Petzel, 1974; Banks and Nemiroff, 1974; Greis, 1976) and EuF_2–YF_3 (Banks and Nemiroff, 1974). Three intermediate solid solutions have been observed: cubic fluorite-related cα for $2.0 \leqq F/M \leqq 2.4$, hexagonal tysonite-related TYS for $2.7 \leqq F/M \leqq 2.9$, and surprisingly extended orthorhombic solid solutions with the YF_3 structure for $2.9 \leqq F/M \leqq 3.0$. The phase widths are significantly dependent on the annealing conditions and, therefore, on the temperature. At lower temperatures, fluorite-related superstructure phases occur in $(Eu, Gd)F_{2.3-2.4}$ similar to those in the system EuF_2–EuF_3 (Greis, 1976). Analogous behavior can be expected for the other RF_2–$R'F_3$ systems.

RF₂–MF₃: Two intermediate phases have been found in the system EuF_2–AlF_3 (Ravez and Dumors, 1969). A cubic fluorite-related solid solution, cα, exists for $(Eu, Al)F_{2.00-2.44}$ with $a = 5.836$ Å to $a = 5.787$ Å; $EuAlF_5$ is tetragonal ($SrAlF_5$-type, I4, $a = 14.12$ Å, $c = 7.185$ Å).

RF₂–MF₄: Colorless $EuZrF_6$ has been described by Laval et al. (1974) and

**Addendum*: At the same time, Arbus et al. (1982) described the structure of the high-temperature form of $RbLu_3F_{10}$. These authors found a different unit cell with $a = 16.013(4)$ Å, $b = 13.182(2)$ Å, $c = 8.435(3)$ Å, $Z = 8$, $V = 1780.5(1.1)$ Å^3, and the space group Acam. A comparison between the drawings of the $CsYb_3F_{10}$ structure (fig. 1 of Aléonard et al., 1982) and of the $RbLu_3F_{10}$ structure (fig. 1 of Arbus et al., 1982) shows that both structures are obviously identical.

Mehlhorn and Hoppe (1976). This compound crystallizes with orthorhombic symmetry ($a = 7.5$ Å, $b = 10.9$ Å, $c = 5.3$ Å, $Z = 4$) and in space group Cmma. It is isostructural to $RbPaF_6$ (Burns et al., 1968b), $PbZrF_6$ (Laval et al., 1974), and $BaZrF_6$ (Mehlhorn and Hoppe, 1976). $EuSiF_6$ has been found to be isostructural with $BaSiF_6$ (Latourrette et al., 1977). The tysonite-related phase $EuThF_6$ is also reported (Keller, 1967). The crystal chemistry of $M^{II}M^{IV}F_6$ compounds has been reviewed by Reinen and Steffens (1978).

RF_3–MF_4: The systems RF_3–ZrF_4 (Poulain et al., 1972), RF_3–HfF_4 (Korenev et al., 1980), and RF_3–UF_4 (Denes et al., 1973) have been studied extensively in the last decade. Three types of intermediate phases have been observed, RMF_7, RM_2F_{11}, and RM_3F_{15}. The $RZrF_7$ and $RHfF_7$ compounds exist for all rare earth elements and are isostructural with $SmZrF_7$ ($P2_1$, $a = 6.154$ Å, $b = 5.739$ Å, $c = 8.299$ Å, $\beta = 102.89°$, $Z = 2$) (Poulain et al., 1973). The ReO_3-related superstructure contains ZrF_6 octahedra and SmF_8 polyhedra in an ordered arrangement which can be considered as a 1:1 intergrowth of the ReO_3 and SnF_4 structure types. The $RZrF_7$ phases with R = Er–Lu also show a cubic high-temperature modification, which has a more or less cation-ordered $ReO_{3+\delta}$ structure with Fm3m or Pm3m symmetry (Poulain et al., 1975). In contrast, RUF_7 phases exist only for R = Y, Tm–Lu and crystallize with a different monoclinic structure (e.g. $YbUF_7$: $a = 8.18$ Å, $b = 8.25$ Å, $c = 11.20$ Å, $b = 92.70°$). The RUF_{11} phases with R = Dy–Er are reported to have lattice parameters similar to those of $YbUF_7$. The crystal data for RHf_2F_{11} with R = La–Nd have not been indexed. The formulas of $(Sm, Zr)F_{3.66\text{-}3.85}$, RZr_3F_{15} with R = Y, Sm–Lu, and RHf_3F_{15} with R = Pr, Y, Sm–Lu are open to question. Nevertheless, their crystal data indicate that these phases are isotypic to UZr_2F_{11} ($a = 5.308$ Å, $b = 6.319$ Å, $c = 8.250$ Å, $\beta = 105.8°$, $Z = 1$) (Thoma et al., 1974). Many of the above phases are nonstoichiometric at higher temperatures.

AF–RF_4: These systems have been investigated extensively to study the tetravalent oxidation state of rare earth elements in fluorides. The major con-

TABLE 28
Intermediate phases in AF–RF_4 systems.

F/M	Formula	Ce	Tb	Pr
3.57	AR_6F_{25}	Rb, Cs	Rb, Cs	
3.4	AR_4F_{17}	Li		
3.0	AR_2F_9	K	K, Rb	
2.8	$A_2R_3F_{14}$	Rb, Cs		Rb
2.5	ARF_5	Li, K–Cs, NH_4	K–Cs	Na, Rb, Cs
2.38	$A_7R_6F_{31}$	Na, K, NH_4	Na, K	Na, K
2.2	$A_3R_2F_{11}$	Na	Cs	
2.13	$A_5R_3F_{17}$	K	Na, Rb	Na
2.0	A_2RF_6	Na–Cs, NH_4	Li, K–Cs	Na–Cs
1.86	$A_5R_2F_{13}$	K	Na	
1.75	A_3RF_7	Na–Cs, NH_4	Na–Cs	Na–Cs
1.6	A_4RF_8	Li, NH_4	Li	

tributions come from the research groups of Asprey et al., Hoppe et al., and Cousseins et al. Their work through 1976 is completely reviewed in the Gmelin Handbook (1976). The systems LiF–TbF_4 and AF–PrF_4 have been studied more recently by Avignant and Cousseins (1978). In addition, Hoppe (1979) has reported the preparation of Cs_2RbNdF_7 and Cs_2RbDyF_7 by high-pressure fluorination. Both phases are isostructural with $(NH_4)_3ZrF_7$. Data for all presently known (I, IV)-phases are compiled in table 28. Further details on preparation and structural properties are given in the Gmelin Handbook (1976) and in the original publications cited therein.

6. Thermodynamic properties

6.1. *Survey*

As one might expect from early estimates of the enthalpies of formation of the halides (Brewer et al., 1950), the rare earth fluorides are among the most stable of all compounds. Their potential as refractory materials is diminished only by their volatilities and melting points. The availability of accurate data for the rare earth fluorides has been limited in part by the experimental difficulties associated with fluorine chemistry. However, significant advances have been made in the thermochemistry of the fluorides. The areas of greatest impact are the reliable determination of the enthalpies of formation and entropies of solid trifluorides and the evaluation of thermal functions of the gaseous trifluorides. These data are the requisite information for completing numerous thermochemical cycles and generating a reliable and consistent set of thermodynamic data for the condensed and gaseous rare earth fluorides.

In light of the situation, an effort has been made to evaluate critically the available data and wherever possible to present selected values for the fluorides. Since the thermochemical literature of the rare earth fluoride prior to 1976 has been thoroughly reviewed in the Gmelin Handbook (1976), only recent reports and those selected from the earlier literature are cited here. In order to obtain an internally consistent set of values, all thermochemical cycles involving the rare earth elements and fluorine have been reevaluated using single sources of reference data. The compilation by Hultgren et al. (1973) has been used for the rare earth elements, and the JANAF Tables (Stull and Prophet, 1971) have been used for fluorine and other metal fluorides. As in other sections of this review, data for Sc and Y are included with those of La–Lu.

6.2. *Condensed trifluorides*

The condensed (solid or liquid) trifluorides occupy a strategic position in the thermochemistry of the rare earth fluorides. Their uniqueness arises because of the numerous equilibria of the trifluorides with tetrafluorides and reduced fluorides.

The availability of experimental heat capacity data for the trifluorides permits the calculation of thermal functions of the solid and liquid trifluorides and estimation of S°_{298} values across the series. Recent low-temperature heat capacity measurements for LaF_3 (Lyon et al., 1978), PrF_3 (Lyon et al., 1979a), and NdF_3 (Lyon et al., 1979b) and the earlier measurements for CeF_3 (Westrum and Beale, 1961) have been combined with the high-temperature heat capacity measurements (Spedding and Henderson, 1971; Spedding et al., 1974) to generate thermal functions for $RF_3(s, \ell)$. The functions evaluated for the trifluorides of La, Pr and Nd by Lyons and coworkers have been selected for those solids. Functions for the liquid trifluorides of these elements and for the remaining trifluorides have been taken from the reports of Spedding and coworkers. The C°_p and $(H^\circ_T - H^\circ_{298})$ data are readily available in the original publications and in part are reviewed in the Gmelin Handbook (1976). The heat capacities of the liquids have been assumed constant over the entire liquid ranges. However, as noted by Hong and Kleppa (1979), the C°_p of 338 J K^{-1} mol^{-1} for $LaF_3(\ell)$ is more than twice that of $LaF_3(s)$ at the melting point and twice that of the neighboring liquid trifluorides. Since this value significantly alters the S°_T and ΔG°_{fT} results for LaF_3 at $T >$ 2000 K, a constant value of 169 J K^{-1} mol^{-1} has been adopted for C°_p of $LaF_3(\ell)$. Magnetic properties of the trifluorides are reviewed in the Gmelin Handbook (1976). Data for several trifluorides in the 4–300 K range show obedience to the Curie–Weiss law. Curie constants and temperatures and magnetic moments are reported. Ferromagnetic transitions are observed for TbF_3 and DyF_3 at 2.5 and 3.9 K, respectively; magnetic ordering of GdF_3 occurs at 1.2 K.

The S°_{298} results obtained from the low-temperature heat capacity measurements are presented with estimated values in table 29. The experimental data are particularly useful in that they provide a basis for reliably estimating the entropies of the remaining trifluorides using a method of Latimer (1951). Since the lattice contribution of a fluoride with trivalent cations is rather uncertain, a revised value has been derived using the method described by Haschke (1979). The procedure involves subtracting the lattice and magnetic, $R^*\ln(2J + 1)$, contributions recommended by Westrum (1967) from the measured entropies of LaF_3, CeF_3, PrF_3, and NdF_3 at 298 K. The average lattice contribution obtained for F by this procedure is (13.6 ± 0.5) J K^{-1} mol^{-1}. This value has been combined with the lattice and magnetic contributions for the trivalent cations to generate S°_{298} values for the remaining trifluorides.

The temperatures and thermodynamics for phase transitions and melting of the solid trifluorides (Spedding and Henderson, 1971; Spedding et al., 1974) are presented in table 30. The ReO_3-related ScF_3 phase and the tysonite-type trifluorides of La–Nd melt without transition, whereas the remaining orthorhombic YF_3-type phases undergo single transitions prior to melting. The differences in the magnitude of ΔH°_t for Sm–Ho and for Er–Lu plus Y are consistent with X-ray data showing that tysonite and α-UO_3-related structures are formed by these groups of fluorides. The tysonite and YF_3-type structures are related by a displacive transition (Haschke, 1976) and the ΔH°_t values are small. The fact that the α-UO_3 and YF_3 structures are markedly different is

TABLE 29
Standard enthalpies of formation and entropies of RF_3(s).

RF_3	$-\Delta H^\circ_{f298}$	S°_{298}	RF_3	$-\Delta H^\circ_{f298}$	ΔS°_{298}
ScF_3[a]	1629 ± 42	(87.4)	GdF_3[c,ℓ]	1700 ± 4	(117.2)
YF_3[b]	1719 ± 4	(97.1)	TbF_3[m]	1708 ± 5	(120.5)
LaF_3[c,d,e]	1701 ± 4	107.0 0.1	DyF_3[c]	1693 ± 2	(121.3)
CeF_3[d,e,fg]	1703 ± 15	115.2 ± 0.8	HoF_3[c,n,o]	1698 ± 4	(121.3)
PrF_3[c,d]	1691 ± 3	120.8 ± 0.1	ErF_3[c]	1694 ± 2	(120.1)
NdF_3[c,d]	1681 ± 3	120.8 ± 0.1	TmF_3	(1695 ± 10)	(118.0)
SmF_3[e,h,i]	1669 ± 4	(120.8)	YbF_3	(1630 ± 20)	(113.4)
EuF_3[j,k]	1571 ± 20	(115.1)	LuF_3[m]	1701 ± 5	(95.8)

References for S°_{298} are cited in the text.

[a]Wagman et al. (1971). [b]Rudzitis et al. (1965). [c]Johnson et al. (1980). [d]Afanas'ev et al. (1975). [e]Kondrat'ev et al. (1967). [f]Wilcox (1962). [g]King and Christensen (1959). [h]Kim et al. (1977). [i]Khanaev et al. (1976). [ℓ]Kim et al. (1978). [m]Kholokhonova and Rezukhina (1976). [n]Kim et al. (1979a). [o]Zmbov and Margrave (1966a); data of E. Rudzitis and E. Van Dentner.

TABLE 30
Thermodynamics of phase transitions of RF_3.

	Structural transition		Melting		Vaporization/boiling		
RF_3(s)	T_t(K)	ΔH°_t[a]	T_m(K)	ΔH°_m[a]	ΔH°_{v298}	T_b(K)	ΔH°_b
ScF_3	–	–	1825 ± 2	62.8	369 ± 2	2152	273
YF_3	1350	32.6	1425 ± 2	28.0	408 ± 3	2908	229
LaF_3	–	–	1777 ± 4	50.2	439 ± 4	2632	261
CeF_3	–	–	1705 ± 4	58.6	435 ± 5	2434	302
PrF_3	–	–	1672 ± 5	57.3	431 ± 1	2495	302
NdF_3	–	–	1646 ± 2	54.8	439 ± 8	2556	268
SmF_3	763	2.1	1577 ± 5	52.3	435 ± 8	2670[b]	272[b]
EuF_3	920	6.7	1549 ± 3	(48.1)	438 ± 13	2955[b]	245[b]
GdF_3	1348	5.9	1502 ± 2	52.3	449 ± 1	2700	302
TbF_3	1225[c]	(0.8)[c]	1445 ± 4	58.6	442 ± 1	2819	266
DyF_3	1305[c]	(0.4)[c]	1426 ± 4	58.6	441 ± 7	2866	256
HoF_3	1343[c]	0.0[c]	1415 ± 2	56.5	448 ± 4	2528	303
ErF_3	1390	29.7	1414 ± 5	27.6	442 ± 3	2805	274
TmF_3	1326	30.1	1431 ± 2	28.9	434 ± 1	2567	329
YbF_3	1259	24.9	1431 ± 4	29.7	441 ± 1	2700[b]	304[b]
LuF_3	1230	25.1	1455 ± 2	30.1	437 ± 15	2582	291

[a]Values in parenthesis are estimated; the uncertainties in ΔH°_{tr} and ΔH°_m are ±0.4 kJ mol^{-1} except for ScF_3 which has an uncertainty of ±2 kJ mol^{-1} in ΔH°_m. [b]Hypothetical boiling point. [c]The existence of a solid–solid transition for these trifluorides is questionable (see section 2.1 and fig. 1).

reflected in the larger values of ΔH_t° for Er–Lu and Y. The melting points listed in table 30 are averages of values selected from references cited in the Gmelin Handbook (1976). Although the values for TmF_3 are generally in agreement, such is not the case for ΔH_t°. Calorimetric data for the LiF–SmF_3 system (Holm and Grønvold, 1972) yield a ΔH_m° for SmF_3 (37 ± 3 kJ mol^{-1}) which is only 70% of that reported by Spedding et al. (1974). Recent calorimetric results for ΔH_m° of YF_3, LaF_3, and YbF_3 (Hong and Keppa, 1979) are in close agreement with those of Spedding and coworkers, and their enthalpies of transition have been adopted for evaluation of thermal functions. A particularly interesting feature of the transition and melting behavior of the rare earth trifluorides is the fact that $(\Delta H_t^\circ + \Delta H_m^\circ)$ is remarkably constant at a value of (57 ± 3) kJ mol^{-1}.

Enthalpies for the vaporization (sublimation) reactions of the trifluorides at 298 K, normal boiling points and enthalpies of vaporization at T_b are also presented in table 30. These values have been determined using thermodynamic values derived for the condensed and gaseous trifluorides (see below and section 6.3). The boiling point is defined as the temperature at which $\Delta G_f^\circ(RF_3, \ell)$ equals $\Delta G_f^\circ(RF_3, g)$. The gas phase is assumed to consist only of monomeric vapor (see section 4.6). The ΔH_{v298}° values are derived from equilibrium vapor pressure data using the third-law method (see section 6.3), and $\Delta H_b^\circ = [S^\circ(RF_3, g, T_b) - S^\circ(RF_3, \ell, T_b)]T_b$. As noted in table 30, the vaporization reactions for SmF_3, EuF_3 and YbF_3 are hypothetical because they simultaneously vaporize to form $SmF_3(g)$ and decompose to form reduced fluorides and fluorine (see section 6.5). The data presented for these fluorides in table 30 are for the hypothetical congruent reactions to form only gaseous RF_3.

Examination of the vaporization behavior of the trifluorides is also instructive. The T_b value of (2421 ± 120)K for CeF_3 (Lim and Searcy, 1966) and that of (2580 ± 30)K for TmF_3 (Biefeld and Eick, 1976) are in excellent agreement with those derived here. The average boiling point, excluding the low value of ScF_3, is (2672 ± 160)K. Several boiling points, such as those of YF_3 and EuF_3, are higher than those of neighboring trifluorides, but ΔH_{v298}° and ΔH_b° values are all remarkably constant. The average ΔH_{v298}°, excluding the value for ScF_3, is (437 ± 9) kJ mol^{-1}; that for ΔH_b° is (280 ± 26) kJ mol^{-1}. This consistency is similar to that observed for ΔH_m°. In comparing the boiling points, it must be remembered that high-temperature free energy values are particularly sensitive to heat capacity (i.e. to entropy). The average C_p° for liquid TbF_3, DyF_3 and ErF_3 is (149 ± 9) J K^{-1} mol^{-1}, while that for liquid HoF_3 and TmF_3 is (97 ± 1) J K^{-1} mol^{-1}. Those fluorides with high C_p° values also have high boiling points.

Additional insight into the properties of the molten trifluorides is provided by the entropy of vaporization at the boiling point. The average ΔS_v° for the trifluorides is (104 ± 15) J K^{-1} mol^{-1}. This value, which is somewhat higher than the 88 J K^{-1} mol^{-1} value of Trouton's rule and identical to that observed for vaporization of NH_3, suggests the presence of substantial intermolecular forces in the liquid phase.

Free energy functions, $(G_T^\circ - H_{298}^\circ)/T$, have been derived for the condensed trifluorides using the heat capacity data cited above, the $S_{298}^\circ(RF_3, s)$ values from

table 29 and the values for ΔH_t° and ΔH_m° given in table 30. The results are presented in table 31 as polynomial functions of T for the range 298–2500 K. For calculating these functions at temperatures beyond the experimental heat capacity ranges (Spedding and Henderson, 1971; Spedding et al., 1974), the C_p° values of the liquids were assumed constant.

The most significant advancement in the thermochemistry of the trifluorides has been the measurement of reliable enthalpies of formation. The non-availability of these data has in large measure precluded completion of critical cycles and tabulation of thermodynamic properties for the trifluorides. This situation has been altered by recent fluorine-bomb calorimetric measurements (Kim et al., 1977, 1978, 1979a,b; Johnson et al., 1980), calorimetric measurements of the dissolution of the trifluorides in aqueous HCl–H_3BO_3 solutions (Afanas'ev et al., 1975; Khanaev et al., 1976; Storozhenko et al., 1976a) and calorimetric measurements of enthalpies of precipitation (Kondrat'ev et al., 1967). Selected ΔH_{f298}° values from these and additional reports are presented in table 29. In each case, the tabulated value is the average obtained from the cited references and the uncertainty is the standard error in the average. Selection of the enthalpy data has been guided in large measure by the results of the fluorine-bomb measurements. Several ΔH_f° results not reviewed in the Gmelin Handbook (1976) or included in table 29 are those of Khanaev et al. (1975). Storozkenko et al. (1976b), Kotov et al. (1977) and Khanaev et al. (1977). The recommended enthalpies of formation are generally in excellent agreement with the values estimated by Kim and Johnson (1981) via a Born–Haber method. A particularly interesting feature of the enthalpies of formation is the fact that except for EuF_3 and YbF_3, the ΔH_{f298}° values are remarkably constant across the rare earth series.

The selection of enthalpies of formation for EuF_3, TmF_3 and YbF_3 merit special comment. Experimental ΔH_{f298}° values for EuF_3 range from -1584 to $-1795\ kJ\ mol^{-1}$ (Gmelin Handbook, 1976), whereas a value of (-1609 ± 15) has been obtained by Kim and Johnson (1981) from lattice energy calculations. The selected ΔH_{f298}° (EuF_3, s) of $(-1571 \pm 20)\ kJ\ mol^{-1}$ lies outside the limits of the Born–Haber calculation, but is based on two calorimetric measurements and is consistent with a value of $-1553\ kJ\ mol^{-1}$ which has been derived from the enthalpy of formation of $EuF_3 \cdot 0.5H_2O$ (see section 6.7). Available data for TmF_3 (Gmelin Handbook, 1976) are inconsistent with the trend established by the neighboring RF_3 phases, and a value of $-1695\ kJ\ mol^{-1}$ has been estimated using the trend in the solid-state emf results for DyF_3, HoF_3, ErF_3, and TmF_3 (Rezukhina and Sisoeva, 1979). Since the results of fluorine-bomb measurements for YbF_3 (Kim et al., 1978) are inconsistent with both established chemical trends of the rare earths and calculated values, the average ΔH_{f298}° value estimated by Kim and Johnson (1981) has been adopted.

Free energies of formation of the condensed trifluorides at high temperatures have been calculated using reference data for the elements, free energy functions for the trifluorides (see table 31) and the enthalpies of formation of the solid trifluorides at 298 K (see table 29). Values for ΔG_f° (RF_3, s) at selected temperatures and at the normal boiling point are presented in table 32. With the

TABLE 31
Free energy functions for RF_3(s, ℓ) in the range $298 < T < 2500$ K:
$(G^\circ_T - H^\circ_{298})/T = A + B \times 10^{-2}T + C \times 10^{-5}T^2 + D \times 10^{-8}T^3 + E \times 10^{-11}T^4 + F \times 10^{-14}T^5 + G \times 10^{-18}T^6$.

RF_3(s, ℓ)	A	B	C	D	E	F	G	Std. error
ScF_3	−100.6	14.42	−44.45	42.50	−20.14	4.64	− 4.09	0.3
YF_3	−125.2	27.10	−82.98	95.65	−56.86	16.77	−19.38	0.5
LaF_3	−124.1	17.62	−53.29	53.04	−26.57	6.55	− 6.30	0.3
CeF_3	−135.4	20.29	−61.50	63.81	−33.63	8.77	− 8.97	0.3
PrF_3	−145.0	22.54	−66.20	68.29	−35.91	9.38	− 9.64	0.3
NdF_3	−145.3	23.20	−68.37	71.73	−38.33	10.15	−10.56	0.3
SmF_3	−145.3	27.00	−78.87	84.81	−46.91	12.92	−14.00	0.3
EuF_3	−135.0	20.35	−62.45	66.12	−36.65	10.22	−11.26	0.3
GdF_3	−147.8	28.28	−84.09	94.61	−54.67	15.68	−17.64	0.3
TbF_3	−151.4	28.59	−85.26	96.37	−56.20	16.28	−18.50	0.4
DyF_3	−151.9	28.60	−85.94	97.97	−57.57	16.78	−19.17	0.4
HoF_3	−149.6	26.68	−80.57	91.86	−54.11	15.87	−18.26	0.5
ErF_3	−148.9	27.51	−83.51	95.95	−56.72	16.65	−19.15	0.5
TmF_3	−143.0	24.77	−76.77	87.92	−52.22	15.46	−17.97	0.5
YbF_3	−135.1	22.48	−70.97	81.08	−48.12	14.25	−16.57	0.4
LuF_3	−114.4	19.55	−61.99	69.94	−41.20	12.14	−14.06	0.4

TABLE 32
Free energies of formation of the RF_3(s, ℓ) and RF_3(g) at selected temperatures.

	$-\Delta G^\circ_{fT}$ of RF_3(s, ℓ) (kJ mol^{-1})					$-\Delta G^\circ_{fT}$ of RF_3(g) (kJ mol^{-1})					
T(K)	298	500	1000	1500	2000	298	500	1000	1500	2000	$-\Delta G^\circ_{fT_b}$
ScF_3	1554	1504	1386	1271	1160	1245	1234	1206	1176	1142	1129
YF_3	1644	1594	1487	1373	1287	1296	1285	1258	1228	1195	1136
LaF_3	1625	1575	1456	1341	1239	1250	1242	1221	1197	1169	1132
CeF_3	1626	1575	1455	1338	1236	1257	1249	1230	1206	1180	1157
PrF_3	1615	1564	1446	1330	1228	1248	1240	1219	1194	1166	1136
NdF_3	1605	1555	1437	1321	1222	1232	1225	1206	1184	1156	1123
SmF_3	1592	1542	1423	1308	1211	1222	1215	1195	1169	1139	1047[a]
EuF_3	1491	1438	1316	1205	1107	1114	1103	1078	1049	1008	880[a]
GdF_3	1624	1574	1454	1341	1248	1240	1233	1213	1191	1164	1122
TbF_3	1631	1581	1462	1352	1264	1255	1247	1227	1206	1179	1128
DyF_3	1615	1564	1446	1337	1250	1240	1232	1212	1191	1164	1111
HoF_3	1621	1570	1449	1337	1239	1239	1231	1212	1191	1165	1133
ErF_3	1617	1566	1448	1340	1252	1240	1233	1213	1191	1165	1115
TmF_3	(1617)	(1566)	(1446)	(1338)	(1246)	(1249)	(1241)	(1220)	(1198)	(1172)	(1109)
YbF_3	(1555)	(1506)	(1390)	(1279)	(1147)	(1180)	(1173)	(1056)	(1031)	(1063)	(969)[a]
LuF_3	1623	1572	1450	1340	1247	1252	1244	1223	1201	1177	1169

[a]Hypothetical boiling point.

exception of EuF_3 and YbF_3, the free energies of formation of the condensed trifluorides are also remarkably similar at all temperatures.

An independent check on the free energy of formation data in table 32 is obtained from the results of high temperature emf measurements using solid-electrolyte cells of the type R, $RF_3|CaF_2|M, MF_x$. In many cases, the metal M is another rare earth. The ΔG°_{f1000} results of Skelton and Patterson (1973) for several fluorides are consistently more negative than those in table 32 by 15–35 kJ mol^{-1}. Values of ΔG°_{f800} obtained for ScF_3, YF_3, LaF_3, and PrF_3 by Rezukhina et al. (1974) are 15–25 kJ mol^{-1} more negative than those derived from calorimetric data. The ΔG°_{f900} values reported by Rezukhina and Sisoeva (1979) for the trifluorides of Dy–Tm are also more negative than those in table 32, but agree within experimental uncertainty. The consistent difference in the results suggests the presence of a systematic effect which might be introduced by data for reference electrode potentials. The ΔG°_{fT} values obtained by correcting

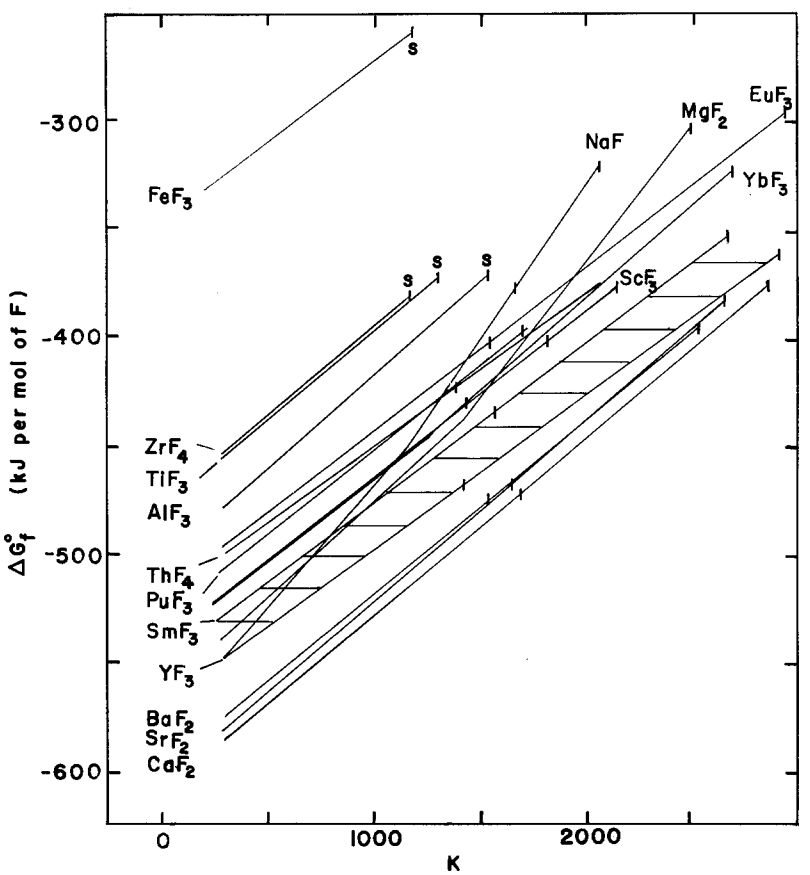

Fig. 20. Comparison of the free energies of formation of the rare earth fluorides with those of other metal fluorides. (Data for ThF_4 and PuF_3 are from Oetting, 1981; values for the remaining fluorides are from Stull and Prophet, 1971).

calorimetric data with derived thermal functions and those measured by high-temperature emf methods are actually in excellent agreement. The maximum difference between the values is less than 3% of ΔG°_{T}.

The free energies of formation of the rare earth trifluorides are compared with those of other binary fluorides in fig. 20. The free energy values are normalized per mole of fluorine to provide a direct comparison of relative stability. Melting and boiling points are indicated by vertical marks; normal sublimation points are marked with an "s". Except for ScF_3, EuF_3, and YbF_3, the free energies all lie within the cross-hatched band bounded by SmF_3 and YF_3. The similarities between the thermodynamic properties of the rare earth trifluorides and the fluorides of the alkali and alkaline earth trifluorides are immediately evident. These fluorides have normal melting points near 1600 K, substantial liquid ranges and normal boiling points. Their behavior is markedly different from that of other metal fluorides, e.g. AlF_3 and FeF_3, which have substantially lower stabilities and sublime at relatively low temperatures without melting. The data for ThF_4 and PuF_3 (Oetting, 1981) show that the actinide fluorides also have normal melting points, but are less stable than the rare earth trifluorides. The unique capability of Ca, Sr and Ba for producing the rare earth metals by metallothermic reduction is clearly demonstrated by fig. 20.

6.3. *Gaseous fluorides*

Important developments in the thermochemistry of the gaseous trifluorides closely parallel those of the condensed phases. A particularly significant advancement has been made in the calculation of thermal functions for all the monoatomic trifluoride gases (Meyers and Graves, 1977a). A critical consideration, the molecular geometry of $RF_3(g)$, is addressed in an earlier review (Haschke, 1979) and by Meyers and Graves. Results from diverse experimental data yield conflicting conclusions; data supporting both the pyramidal (C_{3v}) and planar (D_{3h}) geometries are observed. The evaluation by Meyers and Graves (1977a) shows that the inversion barrier for pyramidal $RF_3(g)$ is equal to or less than kT for $T \geqq 300$ K. The entropy difference resulting from use of symmetry number 6 for D_{3h} or 3 for C_{3v} is negligible, and the planar geometry has been adopted. This decision is consistent with results of the recent ab initio calculations by Yates and Pitzer (1979), who concluded that $ScF_3(g)$ is planar. The thermal functions derived by Krasnov and Danoliva (1969) for ScF_3 and YF_3 are consistent with the values of Meyers and Graves and have been adopted for these fluorides. The molecular constants employed by both sets of authors are present in the original reports. Measured vibrational frequencies, amplitudes, force constants as well as bond lengths and angles are reviewed in the Gmelin Handbook (1976).

Since $(H^{\circ}_{T} - H^{\circ}_{298})$ values (Meyers and Graves, 1977a; Krasnov and Danoliva, 1969) are only reported for a limited set of temperatures, the enthalpy increments reported by Meyers and Graves for the 298–2000 K range have been fit to a polynomial function of temperature. Interpolated results for ScF_3 and YF_3

TABLE 33
Enthalpy functions for $RF_3(g)$ in the range $298 < T < 2000$ K:
$(H^\circ_T - H^\circ_{298}) = A \times 10^4 + BT + C \times 10^{-3}T^2 + D \times 10^{-7}T^3 + E \times 10^5 T^{-1}$.

$RF_3(g)$	A	B	C	D	E	Std. error
ScF_3	−2.559	74.02	4.127	− 6.183	9.444	65
YF_3	−2.648	77.15	2.705	− 3.996	9.671	58
LaF_3	−2.656	80.13	1.941	− 4.366	7.467	24
CeF_3	−2.480	74.00	9.595	−22.50	5.797	42
PrF_3	−2.452	73.35	9.571	−17.12	5.500	16
NdF_3	−2.496	73.80	10.09	−20.40	6.299	39
PmF_3	−2.700	78.21	7.622	−15.63	9.080	42
SmF_3	−3.124	86.86	3.773	− 9.522	15.00	28
EuF_3	−4.296	113.4	−13.14	25.15	30.58	250
GdF_3	−2.668	79.66	2.122	− 4.530	8.198	25
TbF_3	−2.438	72.45	10.23	−20.63	5.751	17
DyF_3	−2.614	78.24	2.891	− 0.429	7.633	20
HoF_3	−2.671	79.71	1.587	− 0.136	8.360	19
ErF_3	−2.696	80.17	1.320	− 0.860	8.774	27
TmF_3	−2.688	79.91	1.426	− 0.446	8.734	25
YbF_3	−2.671	79.27	2.262	− 4.534	8.622	26
LuF_3	−2.669	79.06	2.488	− 5.334	8.678	21

have also been fit. The combined set of functions is presented in table 33. The similarities in the C°_p functions of the gaseous trifluorides are demonstrated by the consistency of the refined constants. Only the data for $EuF_3(g)$ show anomalous behavior. The C°_p (EuF_3, g) curve derived from the $(H^\circ_T - H^\circ_{298})$ equation shows a pronounced peak in the 600–800 K range. This feature, which is attributed to an electronic contribution from low-lying Eu levels, increases the uncertainty in the least-squares refinement and in some instances might dictate reference to the original values given as supplementary material in the report of Meyers and Graves (1977a).

Standard entropies and free energy functions for LaF_3–LuF_3 are reported by Meyers and Graves (1977a) and those for ScF_3 and YF_3 are given by Krasnov and Danoliva (1969). These functions, which have also been fit to temperature-dependent equations, are presented in table 34. The S°_{298} values are given in table 35 with data for other gaseous fluorides. The consistency of these entropy values with those listed for the solid trifluorides (see table 29) is indicated by the fact that the S°_{298} (RF_3, g):S°_{298} (RF_3, s) ratio is constant at (2.92 ± 0.16).

The enthalpies of formation of the gaseous trifluorides at 298 K are also given in table 35. These values have been calculated from the ΔH°_{f298} data for the solid trifluorides (see table 29) and the enthalpies of vaporization (sublimation) of the trifluorides at 298 K (see table 30). The ΔH°_{v298} values have been obtained from the results of a large number of equilibrium vapor pressure measurements. These data are reviewed by Meyers and Graves (1977b) and in the Gmelin Handbook (1976). The enthalpies of vaporization at 298 K have also been

TABLE 34
Free energy functions for $RF_3(g)$ in the range $298 < T < 2500$ K:
$(G^\circ_T - H^\circ_{298})/T = A + B \times 10^{-2}T + C \times 10^{-5}T^2 + D \times 10^{-8}T^3 + E \times 10^{-11}T^4 + F \times 10^{-14}T^5 + G \times 10^{-18}T^6$.

$RF_3(g)$	A	B	C	D	E	F	G	Std. error
ScF_3	−298.4	12.55	−38.79	39.54	−20.77	5.54	−5.92	0.2
YF_3	−309.5	12.90	−39.89	40.74	−21.42	5.72	−6.11	0.2
LaF_3	−334.1	13.37	−41.70	42.79	−22.52	6.03	−6.45	0.1
CeF_3	−349.4	13.40	−41.63	42.50	−22.35	5.97	−6.38	0.1
PrF_3	−351.4	13.32	−41.39	42.22	−22.20	5.93	−6.34	0.2
NdF_3	−353.2	13.42	−41.60	42.38	−22.27	5.94	−6.35	0.2
SmF_3	−348.9	14.46	−44.09	44.78	−23.46	6.24	−6.66	0.2
EuF_3	−344.1	16.02	−48.25	48.94	−25.57	6.79	−7.22	0.2
GdF_3	−347.5	13.28	−41.34	42.36	−22.32	5.96	−6.38	0.2
TbF_3	−352.0	13.25	−41.09	41.89	−22.02	5.88	−6.29	0.2
DyF_3	−353.2	13.20	−41.09	42.06	−22.16	5.92	−6.33	0.2
HoF_3	−354.4	13.23	−41.16	42.17	−22.21	5.93	−6.35	0.2
ErF_3	−352.3	13.25	−41.20	42.19	−22.22	5.93	−6.35	0.2
TmF_3	−350.0	13.23	−41.14	42.13	−22.19	5.93	−6.34	0.2
YbF_3	−345.7	13.22	−41.09	42.00	−22.16	5.92	−6.33	0.2
LuF_3	−327.5	13.20	−41.02	41.98	−22.10	5.90	−6.31	0.2

calculated by Meyers and Graves from the pressure data and thermal functions for the gaseous and condensed trifluorides. Their evaluation shows that the so-called third-law method for calculating ΔH°_{v298} from measured pressure and free energy functions is more reliable than the second-law (Clausius–Clapeyron) method.

The ΔH°_{v298} values in table 30 have been derived using the third-law procedure. The free energy functions for $RF_3(g)$ are from Meyers and Graves (1977b) and those for $RF_3(s)$ are from table 31. Vapor pressure results for ScF_3 (Suvorov and Novikov, 1968; Petzel, 1973), for YF_3 (Kent et al., 1966; Suvorov and Novikov, 1968), for SmF_3 (Biefeld and Eick, 1979), for TmF_3 (Biefeld and Eick, 1976) and for YbF_3 (Biefeld and Eick, 1975; Petzel and Greis, 1976) have been combined with the vapor pressure data compiled by Meyers and Graves (1977b). Absolute pressure data are not available for EuF_3 vaporization and the reported enthalpy at 298 K has been obtained by second-law analysis of the mass spectrometric results reported by Zmbov and Margrave (1968). As noted in the previous section, the ΔH°_{v298} values are remarkably constant across the rare earth series and the resulting ΔH°_{f298} values closely parallel those of the solids. The congruent vaporization reactions for SmF_3, EuF_3 and YbF_3 are hypothetical because these fluorides simultaneously vaporize and decompose to form reduced fluorides and fluorine (see section 6.5). This behavior, however, does not alter the ΔH°_{v298} and H°_{f298} results for these fluorides.

Free energies of formation of the gaseous trifluorides at selected temperatures are presented with those of the solids and liquids in table 32. These data have

TABLE 35
Thermodynamic data for $RF_3(g)$, $RF_2(g)$ and RF(g).

		$RF_3(g)$			$RF_2(g)$			RF(g)		
			$D^\circ_{298}(R+3F)$			$D^\circ_{298}(R+2F)$			$D^\circ_{298}(R+F)$	
R	S°_{298}	$-\Delta H^\circ_{f298}$	Exp.	Calc.	$-\Delta H^\circ_{f298}$	Exp.	Calc.	$-\Delta H^\circ_{f298}$	Exp.	Calc.
Sc	286.6	1260 ± 42	1869 ± 45	1837	642	1174	1240			645
Y	297.4	1311 ± 5	1966 ± 7	1916			1270			645
La	321.8	1261 ± 6	1923 ± 8	1912			1240			630
Ce	337.0	1268 ± 16	1921 ± 18	1937			1235			630
Pr	339.1	1260 ± 3	1864 ± 5	1858			1160			565
Nd	340.7	1242 ± 9	1800 ± 11	1854	656 ± 8	1137 ± 9	1110	97 ± 8	502 ± 9	515
Sm	335.1	1234 ± 9	1671 ± 11	1690			1015	255 ± 21	539 ± 21	435
Eu	328.3	1130 ± 24	1537 ± 26	1548			920	283 ± 17	535 ± 18	340
Gd	335.2	1251 ± 4	1879 ± 6	1862	685 ± 25	1236 ± 25	1215	130 ± 7	604 ± 18	615
Tb	339.7	1255 ± 5	1885 ± 7	1874			1235			660
Dy	341.0	1251 ± 4	1772 ± 6	1791	694 ± 17	1138 ± 18	1145	172 ± 17	539 ± 18	585
Ho	342.2	1250 ± 6	1781 ± 8	1795	702 ± 13	1157 ± 14	1155	172 ± 12	550 ± 13	595
Er	340.0	1251 ± 4	1799 ± 6	1812	708 ± 21	1178 ± 22	1170	182 ± 16	576 ± 17	610
Tm	337.7	(1261 ± 10)	(1724 ± 12)	1757			(1095)			(530)
Yb	333.4	(1189 ± 25)	(1571 ± 25)	1636			(945)			(375)
Lu	315.3	1264 ± 16	1922 ± 18	1941			1295			725

been calculated using reference values for the elements, $\Delta H_f^\circ(RF_3, g)$ data from table 35, and free energy functions from table 34. The $\Delta G_{fT}^\circ(RF_3, g)$ values are therefore directly traceable to the enthalpies of formation of the condensed trifluorides (see table 29).

Enthalpies of dissociation (atomization) of the gaseous RF_3 molecules to form the gaseous elements at 298 K are presented in table 35. In this table, these D_{298}° values, which have been obtained from the ΔH_{f298}° results and reference data for the elements, are compared with those calculated by Meyers (1976) using a "polarized ion" model. Values for D_{298}° calculated by Meyers using a "hard sphere" model are consistently lower than the experimental values by 250–375 kJ mol^{-1}. A strong argument can be made for the presence of substantial covalent bonding in the gaseous trifluoride molecules (Meyers, 1975). The calculated D_{298}° data for ScF_3 and YF_3 are those derived by Hildebrand (1979) using an electrostatic model which included ionicity corrections.

Thermodynamic data are also compiled for gaseous rare earth difluorides and monofluoride molecules in table 35. These species are observed in high-temperature mass spectrometric studies of the vapor in equilibrium with R–RF_3 and R′–RF_3 melts. The original literature is thoroughly reviewed in the Gmelin Handbook (1976). Evaluation of the ΔH_{f298}° results for $RF_2(g)$ and RF(g) is based on gas-phase equilibrium measurements (Zmbov and Margrave, 1966a,b, 1967). Key studies of their work are those with R–RF_3 systems having the following equilibrium reactions: (a) $2RF_3(g) + R(g) \rightleftarrows 3RF_2(g)$ and (b) $RF_3(g) + 2R(g) \rightleftarrows 3RF(g)$. Enthalpy changes, which were derived from the temperature dependence of the equilibrium constants for the reactions and reduced to 298 K by the authors, have been combined with ΔH_{f298}° for $RF_3(g)$ and R(g) to obtain values for the fluorides of Nd and Ho. The remaining ΔH_{f298}° results for $RF_2(g)$ and RF(g) are based on simple and complex isomolecular exchange reactions of the type $R'(g) + RF_2(g) \rightleftarrows R'F_2(g)$. The results obtained for RF_2 molecules are consistent with those derived from the enthalpies of formation and vaporization of SmF_2, EuF_2 and YbF_2 (see section 6.5); the ΔH_{f298}° values for these gaseous fluorides by this method are (-721 ± 50), (-736 ± 15) and (-692 ± 50) kJ mol^{-1}, respectively.

The calculated values for D_{298}° of RF_2 and RF in table 35 have been obtained from the bond dissociation energies derived and estimated by Zmbov and Margrave (1968). Values for $RF_2(g)$ were calculated using data for the dissociation of $RF_3(g)$ to form $RF_2(g)$ and F(g); values for RF(g) were then obtained using the dissociation enthalpy for the formation of RF(g) and F(g) from $RF_2(g)$. Except for SmF and EuF, the experimental and calculated values are in good agreement. The periodicity of the rare earth series is evident in the D_{298}° values for $RF_3(g)$, $RF_2(g)$ and RF(g) (see table 35), but is not observed in the estimated D_0° values reported by Hildenbrand (1979). The estimated energies decrease steadily from 619 kJ mol^{-1} for LaF to 510 kJ mol^{-1} for YbF. Other properties of $RF_2(g)$ and RF(g), e.g. spectroscopic data and molecular constants, are reviewed in the Gmelin Handbook (1976). Additional spectroscopic data for $YF^+(g)$ and YF(g) (Shenyavskaya and Ryabov, 1976) and LuF(g) (Effantin et al., 1976) have

also been reported. Properties of matrix-isolated ScF_2 have been investigated by ESR methods (Knighton, 1979). A value of 33.4 J K^{-1} mol^{-1} is reported for C_p°(LaF, g) at 298 K (Schumm et al., 1973). Entropies and thermal functions of the difluoride and monofluoride gases are given by Krasnov and Danoliva (1969) and similar data are reported for SmF_2(g) (Biefeld and Eick, 1979), EuF_2(g) (Petzel and Greis, 1972) and YbF_2(g) (Biefeld and Eick, 1975).

The presence of gaseous dimer, R_2F_6, in the equilibrium vapor of several RF_3 systems has been detected by mass spectrometric methods. In the initial work, Skinner and Searcy (1971) concluded that La_2F_6 constitutes about 1% of the vapor phase at 1577 K. Pressure data from subsequent studies of the La and Ce systems by Roberts and Searcy (1972) and the Sc system by Sonin et al. (1973) suggest that the dimer is approximately 1% of the vapor at the boiling points of the trifluorides. The situation is confused by the fact that the log P vs. T^{-1} equation reported for La_2F_6 in the initial study is identical to that given by Mar and Searcy (1967) for LaF_3(g). The later studies demonstrate that the boiling points of the trifluorides (see table 30) are not significantly altered by the presence of dimer.

Thermodynamic data for the gaseous R_2F_6 dimers of Sc, La and Ce have been derived from the vapor pressure data of Roberts and Searcy (1972) and Sonin et al. (1973). The results presented in table 36 were obtained from the second-law enthalpies and entropies of vaporization reported for La_2F_6 and Ce_2F_6 and derived from the pressure data presented for Sc_2F_6. The high-temperature values for ΔH° and ΔS° of the vaporization reaction were reduced to 298 K using estimated thermal functions for R_2F_6(g) and those reported for the condensed trifluoride (see section 6.2). The enthalpy and entropy functions of the dimers were obtained from estimated heat capacities based on the observation of Skinner and Searcy (1971) that C_p° of metal halide dimers are greater than twice those of the monomers by a constant amount. The C_p° equations were derived from data in table 33 as follows: $C_p^\circ(R_2F_6, g) = 2C_p^\circ(RF_3, g) + 15.5$ J K^{-1} mol^{-1}. The $S^\circ(R_2F_6, g)$, $\Delta H_{f\,298}^\circ(R_2F_6, g)$ and $\Delta G_{f\,298}^\circ(R_2F_6, g)$ values in table 36 were calculated from the vaporization results and data for the solid trifluoride (see section 6.2). As with other gaseous rare earth fluorides, the enthalpies of formation of the dimers are rather constant. The free energy changes for the dimerization reactions $2RF_3(g) \rightarrow R_2F_6(g)$ of Sc, La and Ce at 298 K are −273, −334 and

TABLE 36
Thermodynamic data for R_2F_6(g).

	$2RF_3(s) \rightarrow R_2F_6(g)$		$R_2F_6(g)$		
R	$\Delta H_{298}^?$	$\Delta S_{298}^?$	$S_{298}^?$	$-\Delta H_{298}^?$	$-\Delta G_{298}^?$
Sc	508 ± 10	255 ± 10	430 ± 15	2750 ± 45	2676 ± 45
La	603 ± 9	238 ± 8	452 ± 9	2799 ± 10	2719 ± 10
Ce	607 ± 9	239 ± 8	469 ± 8	2799 ± 20	2717 ± 20

$-324\ kJ\ mol^{-1}$, respectively. These values, which show the presence of intermolecular attraction between the monomeric fluorides, are consistent with the somewhat high values for the entropies of vaporization of the trifluorides at their boiling points.

6.4. *Tetrafluorides*

The absence of reliable thermodynamic data for the tetrafluorides has contributed to difficulties in defining the chemistry of the rare earth elements. The fact that only Ce, Pr, and Tb form stable $RF_4(s)$ phases has been established (see section 2.4); however, the thermochemistry of these fluorides has remained uncertain. Insight is provided by the work of Johansson (1978), who has correlated data for lanthanide and actinide oxides and halides and derived energy differences between the trivalent and tetravalent metal ions. The results, which have been used to estimate enthalpies of disproportionation of RF_4 phases, agree with preparative observations and the stability order $PrF_4 < TbF_4 < CeF_4$. However, the results also indicate that tetravalent Nd and Dy have sufficient stability to occur in mixed metal systems like those described by Hoppe (1981).

Results of recent studies of the tetrafluorides disagree with earlier observations. Asker and Wylie (1964) conducted effusion experiments showing that CeF_4 vaporizes congruently at low temperatures and begins to decompose to reduced compositions and fluorine at temperatures above 850 K. The TG, DTA and X-ray diffraction results of Kiselev et al. (1975a) show that in air or nitrogen atmospheres, the RF_4 phases decompose in single-step stoichiometric processes at relatively low temperatures to form solid trifluoride and fluorine (see section 2.4). These results are obviously inconsistent and cannot be easily reconciled by the fact that the effusion measurements and thermal studies represent equilibrium versus nonequilibrium conditions.

Several questions concerning the stabilities and chemical behavior of the RF_4 phases are resolved by an additional study (Kiselev et al., 1976). The vapor pressures of $F_2(g)$ in equilibrium with $RF_3(s)$ and $RF_4(s)$ have been measured manometrically over the limited temperature ranges shown in table 37. The

TABLE 37
Thermodynamic data for $RF_4(s)$.

	$RF_4(s) \rightleftharpoons RF_3(s) + F_2(g)$					$RF_4(s)$		
		Second law		Third law				
RF_4	T (Exp.)	ΔH°_T	ΔS°_T	ΔH°_{298}	ΔS°_{298}	$-\Delta H^\circ_{f298}$	S°_{298}	$-\Delta G^\circ_{f298}$
CeF_4	537–560	152 ± 4	246 ± 6	106 ± 1	(150)	1809 ± 16	(141)	1709 ± 19
PrF_4	303–379	51 ± 4	115 ± 6	66 ± 5	(161)	1758 ± 10	(142)	1656 ± 13
TbF_4	390–415	80 ± 4	157 ± 6	78 ± 1	(159)	1786 ± 7	(144)	1685 ± 10

second-law enthalpy and entropy changes for the incongruent vaporization reactions are also given. These results verify the stability order, but the large variations in ΔS°_T demonstrate that the experimental ranges are too short for reliable determination of ΔH°_T and ΔS°_T by the second-law method. The reactions and experimental temperature ranges of the tetrafluorides are similar, and a relatively constant ΔS° value of approximately 155 J K^{-1} mol^{-1} is expected for all three systems.

In an effort to obtain reliable thermodynamic data for the tetrafluorides, the vapor pressure data reported by Kiselev et al. (1976) have been reevaluated using the third-law method. Estimated $S^\circ_{298}(RF_4, s)$ values obtained by the method of Latimer (1951) are presented in table 37. Heat capacity equations for the solid tetrafluorides were estimated from those of $RF_3(s)$ using a modified Kopp's rule method (Haschke and Eick, 1970) as follows: $C^\circ_p(RF_4, s) = C^\circ_p(RF_3, s) + 3(R^*)$. Free energy functions generated from these data were used to obtain the third-law values in table 37. The third-law ΔS°_{298} results agree with the anticipated values. Although the ΔH°_{298} results for CeF_4 and PrF_4 differ from the second-law results by 30%, the agreement achieved by the two methods demonstrates that the equilibrium reactions are correctly formulated. The $\Delta H^\circ_{f\,298}(RF_4, s)$ and $\Delta G^\circ_{f\,298}(RF_4, s)$ results have been derived from the third-law data.

The free energies of formation of CeF_4, PrF_4 and TbF_4 at elevated temperatures have been calculated using the $\Delta H^\circ_{f\,298}$ data in table 37. Free energy functions for the tetrafluorides were estimated as outlined above. However, since the calculations for CeF_4 extend beyond the 1106 K melting point reported by Asker and Wyle (1964), an estimated enthalpy of fusion of 42 kJ mol^{-1} has been included. The C°_p of $CeF_4(\ell)$ has been assumed constant at 130 J K^{-1} mol^{-1}. The temperature dependences of the free energies of formation are described by linear functions of the form $\Delta G^\circ_{fT}(RF_4, s, \ell) = A + BT$. For $CeF_4(s)$ and $298 < T < 1106$ K, $A = -1800$ and $B = 0.3125$; for $CeF_4(\ell)$ and $1106 < T < 1700$ K, $A = -1764$ and $B = 0.2750$; for $PrF_4(s)$ and $298 < T < 900$ K, $A = -1751$ and $B = 0.3193$ and for $TbF_4(s)$ and $298 < T < 1000$, $A = -1777$ and $B = 0.3146$. The temperatures for decomposition of $RF_4(s, \ell)$ into $RF_3(s)$ and $F_2(g, 1\ atm)$ are defined by the points at which $\Delta G^\circ_f(RF_4) = G^\circ_f(RF_3)$. The respective temperatures for CeF_4, PrF_4 and TbF_4 are (1675 ± 50), (850 ± 50) and (1025 ± 50)K. These results are quite consistent with the preparative chemistry and decomposition behavior of the tetrafluorides; however, neither the reported exothermic decomposition of TbF_4 (Kiselev et al., 1975a) nor its complete decomposition via an autocatalytic process (Kiselev et al., 1976) can be explained by the thermodynamic results.

6.5. *Difluorides and ordered R(II, III)-fluorides*

Since the preparative chemistry and phase equilibria of the reduced fluorides have only recently been characterized, their thermochemistry is in large measure undefined. Although the most thoroughly studied area has been their high-

temperature vaporization behavior, calorimetric results have also been reported. Results of the thermodynamic correlations by Johannson (1978) indicate that the difluorides of Sm, Eu and Yb should be stable. The somewhat surprising aspect of rare earth fluoride chemistry is the stability of the R(II, III)-fluorides.

Vaporization studies provide insight into the phase equilibria and relative stabilities of the various fluorides in Sm–F, Eu–F and Yb–F systems. As noted in section 6.2, the trifluorides of these elements vaporize in part by incongruent processes which produce reduced fluorides and fluorine (Biefeld and Eick, 1975, 1979; Petzel and Greis, 1972, 1976). For SmF_3 and YbF_3 vaporization, the reduced fluoride products have compositions near that of the cβ phase; compositions of $RF_{2.40}$ and $RF_{2.375}$ are reported. The overall vaporization process reported for YbF_3 by Biefeld and Eick (1975) shows that 95% of the product is YbF_3(g) and 5% is $YbF_{2.40}$(s) plus F(g). For EuF_3, the reduced fluoride product is EuF_2(s, ℓ) which vaporizes congruently as EuF_2(g) (Petzel and Greis, 1972). The vaporization reactions of SmF_2(s, ℓ) and YbF_2(s, ℓ) are also incongruent and produce the same cβ phases as the trifluorides. The $RF_{2.375}$ phases of Sm and Yb vaporize congruently to form a mixture of RF_2(g) and RF_3(g).

Thermodynamic data for the condensed difluorides are presented in table 38. The enthalpies and entropies of vaporization reported for SmF_2 and YbF_2 have been derived by Biefeld and Eick (1975, 1979) for the hypothetical congruent reactions. The S°_{298} values of RF_2(s) are those reported in the vaporization studies. The enthalpy of formation of SmF_2(s) has been measured calorimetrically by Khanaev et al. (1975). The calorimetric value for EuF_2 is from data for $EuF_2 \cdot 0.76H_2O$ (Storozhenko et al., 1976a); the results for the hydrate were corrected for the presence of water as described in section 6.7. A

TABLE 38
Thermodynamic data for difluorides and intermediate fluorides.

	$RF_2(s) \rightarrow RF_2(g)$		RF_2(s)				
	ΔH°_{298}	ΔS°_{298}	S°_{298}	$-\Delta H^\circ_{f298}$[b]			$-\Delta G^\circ_{f298}$
Phase				A	B	C	
SmF_2[a]	413 ± 48	171 ± 28	133 ± 36	966 ± 5	1046 ± 65	(1134)	(1087)
EuF_2	417 ± 13	205 ± 10	(113)	1177 ± 2	1134 ± 65	(1153)	(1102)
TmF_2	–	–	–	–	–	(1052)	(1003)
YbF_2[a]	460 ± 50	192 ± 23	98 ± 29	–	1142 ± 65	(1152)	(1076)

	$RF_{2.375}(s) \rightarrow 0.625\ RF_2(g) + 0.375\ RF_3(g)$		$RF_{2.375}$(s)		
	ΔH°_{298}	ΔS°_{298}	S°_{298}	$-\Delta H^\circ_{f298}$	$-\Delta G^\circ_{f298}$
$SmF_{2.375}$	428 ± 15	193 ± 12	125 ± 20	1341 ± 53	1286 ± 54
$YbF_{2.375}$	461 ± 11	212 ± 9	100 ± 14	1339 ± 55	1279 ± 56

[a]Hypothetical vaporization reaction. [b]A: calorimetric, B: calculated, C: Born–Haber.

$\Delta H^\circ_{f298}(EuF_2, s)$ value of (-1188 ± 71) kJ mol^{-1} has been derived from vaporization data (Petzel and Greis, 1972). The calculated values of $\Delta H^\circ_{f298}(RF_2, s)$ in table 38 were obtained from $D^\circ_{298}(RF_2, g)$ (see table 35) and ΔH°_{298} of vaporization of the difluorides. Since these experimental enthalpies of formation are not in good agreement, the values derived by Born–Haber methods (Petzel and Greis, 1979) are preferred and have been used in calculating the free energies of formation of the difluorides. The average $\Delta S^\circ_{f298}(RF_2, s)$ value for Sm, Eu and Yb is (-165 ± 6) J K^{-1} mol^{-1}; $\Delta G^\circ_{f298}(TmF_2, s)$ has been estimated using this entropy value. Available data (Gmelin Handbook, 1976) show that the known difluorides melt in the 1680–1690 K range.

Thermodynamic properties of the cβ R(II, III)-fluorides of Sm and Yb are also presented in table 38. For the congruent vaporization reaction, the $RF_{2.375}$ composition determined by Petzel and Greis (1976) has been combined with the thermodynamic values reported by Biefeld and Eick (1975, 1979). Enthalpies and free energies of formation of the $RF_{2.375}$ phases were derived from the vaporization results and data for the gaseous difluorides and trifluorides (see section 6.3).

Estimated functions, which describe the dependence of ΔG°_f of $EuF_2(s, \ell)$, $SmF_{2.375}(s, \ell)$ and $YbF_{2.375}(s, \ell)$ on temperature, indicate that the corresponding RF_3 phases do not spontaneously disproportionate into the reduced fluorides and F_2(1 atm) at temperatures up to the boiling points of the trifluorides. The results show that the ΔG°_f values for the trifluorides are more negative than those of the lower fluorides by 50–150 kJ mol^{-1} at T_b. However, partial disproportionation of SmF_3, EuF_3 and YbF_3 is observed under dynamic conditions, e.g. effusion studies, in which the low equilibrium fluorine pressure is maintained only by continual decomposition of RF_3. At all temperatures, congruent vaporization to RF_3(g) is the dominant process. When the free energies of formation of EuF_2, $SmF_{2.375}$ and $YbF_{2.375}$ are normalized per mole of F, the values lie in or near the cross-hatched bond of stability shown for the trifluorides in fig. 20.

6.6. *Mixed fluorides*

As one might expect from the complex phase relationships of the mixed fluoride systems (see sections 3 and 4), thermochemical studies of the condensed phases are difficult and limited in number. However, the enthalpies of mixing and the interaction parameters of the AF–RF_3 systems with A = Li, Na and K and R = Y, La and Yb have been determined by Hong and Kleppa (1979). The results show relatively simple behavior for Li and complex behavior for K. The existence of cryolite-type ions YF_6^{3-} and YbF_6^{3-} is indicated. The Curie temperature of $LiTbF_4$, 2.85 K, has been determined by Holmes et al. (1974) from low-temperature heat capacity results. The high-temperature heat capacity of the $0.35SmF_3 + 0.65LiF$ system has been measured by Holm and Grønvold (1972).

The equilibrium vapor of the mixed fluorides has been most extensively studied, but the work is limited primarily to alkali metal systems. A series of reports by Sidorov and coworkers is reviewed by Sidorov and Shol'ts (1972). Mass spectrometric data for equilibrium species of the LiF–ScF_3, NaF–ScF_3,

TABLE 39
Thermodynamic data for gaseous ARF_4 molecules.

	$ARF_4(g) \rightarrow AF(g) + RF_3(g)$			$ARF_4(g)$
ARF_4	T	ΔH°_T	ΔS°_T	$-\Delta H^\circ_{f\,298}$
$LiScF_4$	1145	308 ± 16	137 ± 5	1894 ± 21
$NaScF_4$	1219	322 ± 20	138 ± 5	1856 ± 25
$NaYF_4$	1321	332 ± 26	142 ± 5	1915 ± 29
$NaLaF_4$	1267	309 ± 21	142 ± 5	1849 ± 25

$NaF–YF_3$ and $NaF–LaF_3$ systems and similar data for the $KF–ScF_3$ system (Alikhanyan et al., 1974) show the presence of $(AF)_n(g)$ molecules with $n = 1$, 2 and 3, $RF_3(g)$ and $ARF_4(g)$. The average second- and third-law enthalpy and entropy values for dissociation of $ARF_4(g)$ are presented in table 39. Enthalpies of formation have been derived from these results after correction to 298 K assuming a ΔC°_p correction of 14 J K^{-1} mol^{-1} for the equilibrium reaction. A more recent study of the $NaF–ScF_3$ system (Tsirlina et al., 1976) indicates that the vapor is more complex than reported in the earlier work. Observed mixed fluoride ions include $NaScF_3^+$, $Na_2ScF_4^+$, $Na_3ScF_5^+$ and $Na_4ScF_6^+$. Thermal functions are calculated for several species and the enthalpies of formation of the gaseous ions are derived.

Studies of other mixed fluoride systems are limited to those of $AlF_3–YF_3$ (Kaplenkov and Kulifeev, 1979) and of $CoF_2–CeF_3$ (Buryleva et al., 1977). Examination of fig. 20 shows that unless large deviations from ideality are observed, the free energies of formation of mixed fluorides in the $AF_2–RF_3$ (A = Ca, Sr, Ba) system are expected to lie in a rather narrow gap between the values for the binary phases.

6.7. *Hydrated fluorides*

Hydrated rare earth trifluorides, $RF_3 \cdot nH_2O$, having compositions with $n = 0.5$ are described in the recent survey by Haschke (1979) and in the Gmelin Handbook (1976), but their thermodynamic properties have not been critically evaluated. An important question is whether these tysonite-type phases are true hydrated fluorides or simply anhydrous fluorides with adsorbed or occluded water. Insight into the problem is provided by the results of calorimetric studies (Kondrat'ev et al., 1967; Storozhenko et al., 1975, 1976b; Afanas'ev et al., 1975). Measured enthalpies of formation of several trifluoride hydrates and values derived for the enthalpies of hydration of the anhydrous trifluorides are presented in table 40.

The calorimetric results demonstrate that the hydrates are not thermodynamically stable relative to the anhydrous trifluorides and water. In all cases except for Dy, the hydration reactions are endothermic (Storozhenko et al. 1975; Afanas'ev et al., 1975). Since the entropies of hydration are most certainly

TABLE 40
Thermodynamic data for hydrated rare earth trifluorides, $RF_3 \cdot nH_2O$.

R	n	$RF_3 \cdot nH_2O(s)$ $-\Delta H^\circ_{f298}$	$RF_3(s) + nH_2O(\ell)$ $\rightarrow RF_3 \cdot nH_2O(s)$ ΔH°_{298}	$-\Delta H^\circ_{f298}(RF_3, s) +$ $-N\Delta H^\circ_{f298}(H_2O, \ell)$
La	0.5	1845	3.0 ± 0.3	1844 ± 4
Ce	0.5	1833	1.5 ± 0.3	1846 ± 15
Pr	0.5	1838	2.3 ± 0.3	1834 ± 3
Nd	0.5	1830	4.8 ± 0.3	1824 ± 3
Sm	0.5	1825	4.1 ± 0.3	1812 ± 4
Eu	0.5	1731,1707	3.9 ± 0.3	1714 ± 20
Tb	–	–	3.8 ± 0.3	1843 ± 5
Dy	1.0	–	−0.3 ± 0.3	1835 ± 2

negative, the hydration reactions cannot be spontaneous. The enthalpies of formation of the hydrates presented in table 40 are in agreement with enthalpies of hydration that are near zero. This is demonstrated by comparing the reported $\Delta H^\circ_{f298}(RF_3 \cdot nH_2O, s)$ values with the sum of $\Delta H^\circ_{f298}(RF_3, s)$ and $n\Delta H^\circ_f(H_2O, \ell)$ in table 40.

Thermodynamic results are also reported for $EuF_2 \cdot 0.76H_2O$ by Storozhenko et al. (1976a). The calorimetric $\Delta H^\circ_{f298}(EuF_2, s)$ in table 38 has been calculated under the assumption that ΔH°_{f298} for the hydrated phase also equals the sum of $\Delta H^\circ_{f298}(EuF_2, s)$ and $0.76H^\circ_{f298}(H_2O, \ell)$.

6.8. *Solutions*

The rare earth trifluorides are only slightly soluble in water and are extensively used as fluoride-selective electrodes (Butler, 1969). Their solubilities in aqueous HCl containing H_3BO_3 are complete and permit measurement of heats of solution (Khanaev et al., 1976). The solubilities of NdF_3 and YF_3 in concentrated solutions of HCl, HNO_3 and HF have been investigated by Baryshnikov and Gol'shtein (1972). Potentiometric titration data for solutions at various ionic strengths yield a $\log K_{eq} = -17.95$ at 298 K for $LaF_3(s) \rightleftarrows La^{3+}(aq) + 3F^-(aq)$ (Pan et al., 1974). However, the enthalpy of formation of $LaF_3(s)$ derived from this result is 107 kJ mol^{-1} less negative than the average calorimetric value in table 29.

The formation of fluoride complexes in aqueous NaCl solutions at various ionic strengths has been studied by potentiometric methods (Bilal et al., 1979; Bilal and Becker, 1979). Monofluoro and difluoro complexes are observed, but evidence is not found for higher fluoride complexes. The stability constants, β_1, for the monofluoro complexes of La and Nd are $4.8 \pm 0.4 \times 10^2\ M^{-1}$, while those for Tb, Er and Lu are in the range $1.2\text{–}1.8 \times 10^3\ M^{-1}$. The β_1 values vary with ionic strength. Stability constants, β_2, for the difluoro complexes all increase monotonically across the rare earth series from 1.3×10^5 to $3.1 \times 10^5\ M^{-2}$. The

observed differences in solubilities of the fluorides are applicable to the geological segregation of the rare earths in fluoride milieus. The free energies of formation of RF^{2+}(aq, 1 m std state) for La, Gd and several heavy rare earths are in the range -901 to -979 kJ mol^{-1} (Schumn et al., 1973).

Several nonaqueous solvent systems have also been investigated. Solubilities of the trifluoride in nitrosyl fluoride solutions are reported (Galkin et al., 1978), and the solubilities of a variety of fluorides, including several rare earth trifluorides, in UF_6 have been measured and the results correlated with their crystal lattice energies (Nikolaev and Sodikova, 1975).

Acknowledgement

The authors are very much indebted to Mrs. Karin Greis, Dr. D. Eppelsheimer, and Mr. Rainer Matthes (Heidelberg), to Dr. S. Aléonard (Grenoble), to Dr. A. de Kozak (Paris), to Dr. B.P. Sobolev and Dr. P.P. Fedorov (Moscow) for their assistance. The contributions of Julie Lanterman, G.E. Bixby and Dr. F.L. Oetting are appreciated. Support of the US Department of Energy, Contract DE-AC04-76DP03533, in manuscript preparation is gratefully acknowledged.

References

Adachi, G., T. Nishihata, K. Uchiyama and J. Shiokawa, 1976, Chem. Lett. 189.

Afanas'ev, Yu. A., E.I. Khanaev and M.G. Kotov, 1975, Radiokhimiya **17**, 203; Soviet Radiochem. **17**, 206.

Aléonard S., M. Labeau, Y. LeFur and M.F. Gorius, 1973, Mater. Res. Bull. **8**, 605.

Aléonard, S., O. Gonzales, M.F. Gorius and M.T. Roux, 1975, Mater. Res. Bull. **10**, 1185.

Aléonard, S., J.C. Guitel, Y. LeFur and M.T. Roux, 1976, Acta Crystallogr. **B32**, 3227.

Aléonard, S., Y. LeFur, L. Pontonnier, M.F. Gorius and M.T. Roux, 1978a, Ann. Chim. Sci. **3**, 417.

Aléonard, S., J.C. Guitel and M.T. Roux, 1978b, J. Solid State Chem. **24**, 331.

Aléonard, S., Y. LeFur, M.F. Gorius and M.T. Roux, 1980, J. Solid State Chem. **34**, 79.

Aléonard, S., M.T. Roux and B. Lambert, 1982, J. Solid State Chem. **42**, 80.

Alikhanyan, A.S., V.B. Shol'ts and L.N. Sidorov, 1974, Zh. Fiz. Khim. **48**, 765.

Als-Nielsen, J., L.M. Holmes, F.K. Larsen and H.J. Guggenheim, 1975, Phys Rev. **B12**, 191.

Arbus, A., B. Picaud, M.T. Fournier and J.C. Cousseins, 1977, C.R. Acad. Sci. Paris, Ser. **C284**, 129.

Arbus, A., B. Picaud, M.T. Fournier, A. Verdrine and J.C. Cousseins, 1978, Mater. Res. Bull. **13**, 33.

Arbus, A., M.T. Fournier, B. Picaud, G. Boulon and A. Vedrine, 1980, J. Solid State Chem. **31**, 11.

Arbus A., M.T. Fournier, J.C. Cousseins, A. Védrine, and R. Chevalier, 1982, Acta Crystallogr. **B38**, 75.

Ardashnikova, E.I., M.P. Borzenkova and A.V. Novoselova, 1980, Zh. Neorg. Khim. **25**, 1501; Russ. J. Inorg. Chem. **25**, 833.

Asker, W.J. and A.W. Wylie, 1964, Aust. J. Chem. **18**, 959.

Asprey, L.B., J.S. Coleman and M.J. Reisfeld, 1967, Adv. Chem. Ser. **71**, 122.

Atabaeva, E.Y. and N.A. Bendeliani, 1979, Izv. Akad. Nauk SSSR, Neorg. Mater. **15**, 1888; Inorg. Mater. **15**, 1487.

Atabaeva, E.Y. and N.A. Bendeliani, 1980, Geokhimiya **1980**, 136.

Avignant, D. and J.C. Cousseins, 1978, Rev. Chim. Miner. **15**, 360.

Babaeva, E.P. and G.A. Bukhalova, 1966a, Zh. Neorg. Khim. **11**, 648; Russ. J. Inorg. Chem. **11**, 351.

Babaeva, E.P. and G.A. Bukhalova, 1966b, Zh. Neorg. Khim. **11**, 1559; Russ. J. Inorg. Chem. **11**, 1044.

Banks, E. and M. Nemiroff, 1974, Mater. Res. Bull. **9**, 965.

Banks, E., S. Nakajima and M. Shone, 1980, J. Electrochem. Soc. **127**, 2234.

Baryshnikov, N.V. and T.V. Gol'shtein, 1972, Nauchn. Tr. Gos. Nauchno-Issled. Proektn, Inst. Redkomet. Prom-sti. **45**, 56; Chem. Abstr. 85:131 323 k.

Batsanov, S.S., V.A. Egorov and Yu. B. Khvostov, 1976, Dokl. Akad. Nauk SSSR **227**, 860.

Batsanov, S.S., Y.M. Kiselev and L.I. Kpaneva, 1979, Zh. Neorg. Khim. **24**, 2827; Russ. J. Inorg. Chem. **24**, 1573.

Batsanov, S.S., Y.M. Kiselev and L.I.

Kpaneva, 1980, Zh. Neorg. Khim. **25**, 1978; Russ. Chem. Rev. **40**, 465.
Batsanova, L.R., 1971, Usp. Khim. **40**, 945; Russ. Chem. Rev. **40**465.
Batsanova, L.R., Y.V. Zakhar'ev and A.A. Opalovskii, 1973, Zh. Neorg. Khim. **18**, 905; Russ. J. Inorg. Chem. **18**, 476.
Bedford, R.G. and E. Catalano, 1970, A Study of the Systems SmF_2–SmF_3, EuF_2–EuF_3 and YbF_2–YbF_3 and their Equilibria with Corresponding Ln–Pt Systems, in: Proc. Eight Rare Earth Research Conf., Reno, Nevada, vol. 1, pp. 388–399.
Bendeliani, N.A., 1974, Dokl. Akad, Nauk SSSR **219**, 851.
Bendeliani, N.A. and M.R. Orlov, 1976, Dokl. Akad. Nauk SSSR **229**, 1098.
Bergstøl, S., B.B. Jensen and H. Neumann, 1977, Lithos **10**, 81.
Besse, J.P. and M. Capestan, 1968, Bull. Soc. Chim. Fr. **1968**, 2717.
Bevan, D.J.M., 1973, Non-stoichiometric Compounds: an Introductory Essay in: Bailar, J.C., Jr., H.J. Emele'us, R. Nyholm and A.F. Trotman-Dickenson, eds., Comprehensive Inorganic Chemistry, vol. **4** (Pergamon Press, Oxford pp. 453–540.
Bevan, D.J.M. and O. Greis, 1978, Rev. Chim. Miner. **15**, 346.
Bevan, D.J.M., J. Strähle and O. Greis, 1979, Structural Principles in Fluorite-related Anion-excess Super-lattice Phases: The Crystal Structure of Tveitite, an Ordered Ytrrofluorite Mineral, and the Synthetic Compound Ca_2YbF_7, in: Proc. of the Fifty European Crystallographic Meeting, Copenhagen, Denmark.
Bevan, D.J.M., O. Greis and J. Strähle, 1980, Acta Crystallogr. **A36**, 889.
Bevan, D.J.M., O. Greis and J. Strähle, 1981, Acta Crystallogr. **A37**, 266.
Biefeld, R.M. and H.A. Eick, 1975, J. Chem. Phys. **63**, 1190.
Biefeld, R.M. and H.A. Eick, 1976, J. Less-Common Metals **45**, 117.
Biefeld, R.M. and H.A. Eick, 1979, J. Chem. Thermod. **11**, 639.
Bilal, B.A. and P. Becker, 1979, J. Inorg. Nucl. Chem. **41**, 1607.
Bilal, B.A., F. Herrmann and W. Fleischer, 1979, J. Inorg. Nucl. Chem. **41**, 347.
Bochkova, R.I., Y.N. Saf'yanov, E.A. Kuz'min and N.V. Belov, 1973, Dokl. Akad. Nauk SSSR **211**, 357.
Bode, H. and E. Voss, 1957, Z. Anorg. Allg. Chem. **290**, 1.
Borisov, S.V. and N.V. Podberezskaya, 1979, Zh. Strukt. Khim. **20**, 659; J. Struct. Chem. **20**, 559.
Borzenkova, M.P., V.N. Galina and A.V. Novoselova, 1970, Izv. Akad. Nauk SSSR, Neorg. Mater. **6**, 25.
Brauer, G., 1975, Handbuch der Präparativen Anorganischen Chemie, vol. **1**, 3rd ed. (Enke Verlag, Stuttgart).
Brewer, L., L.A. Bromley, P.W. Gilles and N.L. Lofgren, 1950, Thermodynamic Properties of the Halides: in, Quill, L.L., ed., Chemistry and Metallurgy of Miscellaneous Materials: Thermodynamics, (McGraw-Hill, New York) ch. 6.
Brunton, G., 1969, Acta Crystallogr. **B25**, 600.
Bukvetskii, B.V. and L.S. Garashina, 1977, Koord. Khim. **3**, 1024.
Burns, J., 1965, Inorg. Chem. **4**, 881.
Burns, J.H., R.D. Ellison and H.A. Levy, 1968a, Acta Crystallogr. **B24**, 230.
Burns, J.H., H.A. Levy and O.L. Keller, Jr., 1968b, Acta Crystallogr. **B24**, 1675.
Buryleva, E.B., V. Ya. Gershuina and V.L. Mironov, 1977, Deposited Doc., VINITI 1360-77; Chem. Abstr. 90:62 007z.
Busch, G., E. Kaldis, J. Muheim and R. Bischof, 1971, J. Less-Common Metals **24**, 453.
Butler, J.N., 1969, Nat. Bur. Stds. (US) Spec. Publ. 304 143.
Buznik, V.M., Yu. N. Moskvich, V.V. Sokolivich, A.E. Livshits, K.B. Seiranyan and B.P. Sobolev, 1979, Zh. Strukt. Khim. **20**, 622.
Carlson, O.N. and F.A. Schmidt, 1961, Preparation of the Rare Earth Fluorides, in: Spedding, F.H. and A.H. Daane, eds., The Rare Earths (Wiley, New York) pp. 77–88.
Catalano, E., R.G. Bedford, V.G. Silveira and H.H. Wickman, 1969, J. Phys. Chem. Solids **30**, 1613.
Catlow, C.R.A., 1980, Rev. Inorg. Chem. **2**, 1.
Champarnaud-Mesjard, J.C. and B. Frit, 1977, Acta Crystallogr. **B33**, 3722.
Chassaing, J., 1972, Rev. Chim. Miner. **9**, 265.
Chassaing, J., 1975, J. Inorg. Nucl. Chem. **37**, 1555.
Chassaing, J. and D. Bizot, 1973, C.R. Acad. Sci., Ser. C **276**, 679.
Cheetham, A.K. and N. Norman, 1974, Acta Chem. Scand. **A28**, 55.
Cheetham, A.K., B.E.F. Fender, D. Steele, R.I. Taylor and B.T.M. Willis, 1970, Solid State Commun. **8**, 171.
Cheetham, A.K., B.E.F. Fender and M.J. Cooper, 1971, J. Phys. **C4**, 3107.
Cheetham, A.K., B.E.F. Fender, H. Fuess and A.F. Wright, 1976, Acta Crystallogr. **B32**, 94.
Daane, A.H. and F.H. Spedding, 1953, J. Electrochem. Soc. **100**, 442.
De Kozak, A. and M. Almai, 1978, Rev. Chim. Miner. **15**, 139.
De Kozak, A. and M. Samouël, 1977, Rev. Chim. Miner. **14**, 93.
De Kozak, A., M. Samouël and A. Chretien, 1973, Rev. Chim. Miner. **10**, 259.
De Kozak, A., Almai and M. Samouël, 1979, Rev. Chim. Miner. **16**, 441.
De Kozak, A., M. Samouël and A. Erb, 1980, Rev. Chim. Miner. **17**, 440.
Denes, G., G. Fonteneau and J. Lucas, 1973, C.R. Acad. Sci., Paris, Ser C **276**, 1553.
Dworkin, A.S. and M.A. Bredig, 1971, J. Phys. Chem. **73**, 2340.
Effantin, C., G. Wannous, J. D'Incan and C. Athenour, 1976, Can. J. Phys. **54**, 279.
Egorov, V.A., I.N. Temnitskii, A.I. Martynov and S.S. Batsanov, 1979, Zh. Neorg. Khim. **24**, 3373; Russ. J. Inorg. Chem. **24**, 1881.

Fedorov, P.P. and B.P. Sobolev, 1975, Kristallografiya **20**, 949.
Fedorov, P.P. and B.P. Sobolev, 1979a, J. Less-Common Metals **63**, 31.
Fedorov, P.P. and B.P. Sobolev, 1979b, Zh. Neorg. Khim. **24**, 1038; Russ. J. Inorg. Chem. **24**, 574.
Fedorov, P.P., O.E. Izotova, V.B. Aleksandrov and B.P. Sobolev, 1974, J. Solid State Chem. **9**, 368.
Fedorov, P.P., Yu.G. Sizganov, B.P. Sobolev and M. Shvanner, 1975, J. Thermal Anal. **8**, 239.
Fedorov, P.P., B.P. Sobolev and S.F. Belov, 1979, Izv. Akad, Nauk SSSR, Neorgan. Mater. **15**, 816; Inorg. Mater. **15**, 640.
Filatova, T.G., B.S. Zakharov, L.P. Reshetnikova and A.V. Novoselova, 1980, Zh. Neorg. Khim. **25**, 1427; Russ. J. Inorg. Chem. **25**, 793.
Galkin, N.P., Yu.D. Shishkov and V.I. Khomyakov, 1978, Radiokhimiya **20**, 136.
Garashina, L.S. and Yu.S. Vishnyakov, 1977, Krystallografiya **22**, 547; Sov. Phys. Crystallogr. **22**, 313.
Garashina, L.S., B.P. Sobolev, V.B. Aleksandrov and Yu.S. Vishnyakov, 1980, Krystallografiya **25**, 294; Sov. Phys. Crystallogr. **25**, 171.
Gettmann, W. and O. Greis, 1978, J. Solid State Chem. **26**, 255.
Gmelin, 1976, Handbuch der Anorganischen Chemie, Selten-erdelemente, Teil C3 (Springer-Verlag, Berlin).
Goldschmidt, V.M., 1926, Skrifter Norske Videnskops Akad. Oslo, I: Mat.-Naturw. Kl. **2**, 88.
Greinacher, E., 1981, Industrial Applications of Rare Earth Elements, ed. by K.A. Gschneidner, Jr., ACS Symposium Series 164, (ACS, Washington, D.C.) pp. 3–17.
Greinacher, E. and K. Reinhardt, 1982, Seltene Erden, in Chemische Technologie, 4. Aufl., Band 2 (Carl Hanser Verlag, München-Wien) pp. 678–707.
Greis, O., 1970, Verdampfungstudie am System Europium-Flour, Diplom Thesis, University of Freiburg i. Br., West Germany.
Greis, O., 1976, Präparative, röntgenographische und thermochemische untersuchungen an Selten-Erd-Fluoriden unter besonderer Berucksichtigung der Elemente Samarium, Europium, Thulium und Ytterbium, Inaugural-Dissertation Thesis, University of Freiburg, i. Br., West Germany.
Greis, O., 1977a, Monatsh. Chem. **108**, 205.
Greis, O., 1977b, Z. Anorg. Allg. Chem. **430**, 175.
Greis, O., 1978a, J. Solid State Chem. **24**, 277.
Greis, O. 1978b, Z. Anorg. Allg. Chem. **441**, 39.
Greis, O., 1978c, Rev. Chim. Miner. **15**, 481.
Greis, O., 1980a, New Anion-excess Fluorite-related Superstructure Phases in LnF_2–LnF_3, CaF_2–LnF_3 and related systems, in: McCarthy, G.J., J.J. Rhyne and H.B. Silder, eds., The Rare Earths in Modern Science and Technology, vol. **2** (Plenum Press, New York) pp. 167–172.
Greis, O., 1980b, Ein Beitrag zur Kristallchemie schneller Ionenliter: Einkristall. Elektronen-Diffraction an Yttrofluoriten, Tysoniten und Naturium-Beta-Alumina, Habilitation Thesis, University of Heidelberg, West Germany.
Greis, O., 1981a, Z. Kristallogr. **154**, 47.
Greis, O., 1981b, unpublished results, University of Heidelberg, West Germany.
Greis, O., 1982, Rev. Inorg. Chem. **4**, August.
Greis, O. and D.J.M. Bevan, 1978, J. Solid State Chem. **24**, 113.
Greis, O. and M. Kieser, 1979, Rev. Chim. Miner. **16**, 520.
Greis, O. and M. Kieser, 1980, J. Less-Common Metals **75**, 119.
Greis, O. and M. Kieser, 1981, Z. Anorg. Allg. Chem. **479**, 165.
Greis, O. and M. Martinez-Ripoll, 1977, Z. Anorg. Allg. Chem. **477**, 133.
Greis, O. and T. Petzel, 1974, Z. Anorg. Allg. Chem. **403**, 1.
Greis, O. and T. Petzel, 1977, Z. Anorg. Allg. Chem. **434**, 89.
Greis, O., P. Stede and M. Kieser, 1981, Z. Anorg. Allg. Chem. **477**, 133.
Gschneidner, K.A., 1969, J. Less-Common Metals, **17**, 13.
Hajek, B., 1965, Z. Chem. (Leipzig) **5**, 341.
Haschke, J.M., 1976, J. Solid State Chem. **18**, 205.
Haschke, J.M., 1979, Halides, in: Gschneidner, K.A. and L. Eyring, eds., Handbook on the Physics and Chemistry of Rare Earths, vol. **4** (North-Holland, Amsterdam) ch. 32.
Haschke, J.M. and H.A. Eick, 1970, Inorg. Chem. **9**, 851.
Hayes, W., 1974, Crystals with the Fluorite Structure – Electronic, Vibrational and Defect Properties (Clarendon Press, Oxford).
Hebecker, C. and R. Lösch, 1975, Naturwissenschaften **62**, 37.
Hildenbrand, D.L., 1979, J. Electrochem. Soc. **126**, 1396.
Holcombe, C.E., 1980, J. Amer. Ceram. Soc. **63**, 112.
Holm, J.L. and F. Grønvold, 1972, Acta Chem. Scand. **26**, 1733.
Holmes, L.M., F. Hulliger, H.J. Guggenheim and J.P. Maita, 1974, Phys. Lett. A 50, 163.
Hong, K.C. and O.J. Kleppa, 1979, J. Phys. Chem. **83**, 2589.
Hoppe, R., 1979, J. Solid State Chem. **27**, 99.
Hoppe, R., 1981, New Fluorides with Ce(IV), Pr(IV), Nd(IV) and Dy(IV), in: McCarthy, G.J., J.J. Rhyne and H.E. Silver, eds., Abstracts of the Fifteenth Rare Earth Research Conference (University of Missouri-Rolla) abstr. E-5.
Hultgren, R., P.D. Desai, D.T. Hawkins, M. Gleiser, K.K. Kelley and D.D. Wagman, 1973, Selected Values of the Thermodynamic Properties of the Elements (American Society for Metals).
Ippolitov, E.G. and A.G. Maklachkov, 1970, Izv. Akad. Nauk SSSR, Neorg. Mater. **6**, 1422.
Izotova, O.E. and V.B. Aleksandrov, 1970, Dokl. Akad. Nauk SSSR **192**, 1037.

Johansson, B., 1978, J. Phys. Chem. Solids **39**, 467.
Johnson, G.K., R.G. Pennell, K-Y Kim and W.N. Hubbard, 1980, J. Chem. Thermodyn. **12**, 125.
Kaplenkov, V.N. and V.K. Kulifeev, 1979, Nauch Tr. Mosk. Int. Stali i Splavov; Chem. Abstr. 91:163 829v.
Keller, C., 1967, J. Inorg. Nucl. Chem. **29**, 2930.
Keller, C. and H. Schmutz, 1964, Z. Naturforsch. **19b**, 1080.
Keller, C. and H. Schmutz, 1965, J. Inorg. Nucl. Chem. **27**, 900.
Kent, R.A., K.F. Zmbov, A.S. Kana'an, G. Besenbruch, J.D. McDonald and J.L. Margrave, 1966, J. Inorg. Nucl. Chem. **28**, 1419.
Khanaev, E.I., Yu.A. Afanas'ev and T.P. Storozhenko, 1975, Zh. Fiz. Khim. **49**, 2454; Russ. J. Phys. Chem. **49**, 1443.
Khanaev, E.I., Yu.A. Afanas'ev and Yu.N. Solov'eva, 1976, Zh. Fiz. Khim. **50**, 2166.
Khanaev, E.I., M.G. Kotov and Yu.A. Afanas'ev, 1977, Radiokhimiya **19**, 265.
Kholokhonova, L.I. and T.N. Rezukhina, 1976, Zu. Fiz. Khim. **50**, 767; Chem. Abstr. **85**: 10 945f.
Kieser, M. and O. Greis, 1980a, J. Less-Common Metals **71**, 63.
Kieser, M. and O. Greis, 1980b, Z. Anorg. Allg. Chem. **469**, 164.
Kim, K.-Y. and C.E. Johnson, 1981, J. Chem. Thermodyn. **13**, 13.
Kim, Y.-C., J. Oishi and S.-H. Kang, 1977, J. Chem. Thermodyn. **9**, 973.
Kim, Y.-C., J. Oishi and S.-H. Kang, 1978, J. Chem. Thermodyn. **10**, 975.
Kim, Y.-C., M. Misumi, H. Yano and J. Oishi, 1979a, J. Chem. Thermodyn. **11**, 657.
Kim, Y.-C., M. Misumi, H. Yano and J. Oishi, 1979b, J. Chem. Thermodyn. **11**, 429.
King, E.G. and A.U. Cristensen, 1959, U.S. Bur. Mines Rept. Invest. No. 5510.
Kirshenbaum, A.D. and J.A. Cahill, 1960, J. Inorg. Nucl. Chem. **14**, 148.
Kiselev, Yu.M., L.I. Martynenko and V.I. Spitsyn, 1975a, Zh. Neorg. Khim. **20**, 1788; Russ. J. Inorg. Chem. **20**, 998.
Kiselev, Yu.M., L.I. Martynenko, V.G. Sevostyanov and V.I. Spitsyn, 1975b, Dokl. Akad. Nauk SSSR **222**, 356.
Kiselev, Yu.M., V.G. Sevast'yanov and V.I. Spitsyn, 1976, Akad. Nauk SSSR, Ser. Khim. **5**, 959.
Knighton, L.B. Jr., 1979, J. Chem. Phys. **71**, 1578.
Komissarova, L.N. and B.I. Pokrovsky, 1963, Dokl. Akad. Nauk SSSR **149**, 599.
Kondrat'ev, Yu.V., R.B. Dobrotin and A.V. Surorov, A.M. German, 1967, Vestn. Leningrad Univ. 22, Fiz. Chem. No. 4, 128; Chem. Abstr. 69:39 259r.
Korenev, Yu.M., P.I. Antipov and A.V. Novoselova, 1980, Zh. Neorg. Khim. **25**, 1255; Russ. J. Inorg. Chem. **25**, 698.
Kotov, M.G., E.I. Khanaev and Yu.A. Afanas'ev, 1977, Radiokhymiya **19**, 376.
Krasnov, K.S. and T.G. Danilova, 1969, Teplofiz, Vys. Temp. 7, 1213; High Temp. 7, 1131.
Labeau, M., Y. LeFur and S. Aléonard, 1974a, J. Solid State Chem. **10**, 282.
Labeau, M., S. Aléonard, A. Vedrine, R. Boutounet and J.C. Cousseins, 1974b, Mater. Res. Bull. **9**, 615.
Latimer, W.M., 1951, J. Am. Chem. Soc., **73**, 1480.
Latourrette, B., C. Fouassier, B. Tanguy and P. Hagenmuller, 1977, Z. Anorg. Allg. Chem. **431**, 31.
Laval, J.P., D. Mercurio-Lavaud and B. Gaudreau, 1974, Rev. Chim. Mineral. **11**, 742.
Lechtenböhmer, C. and O. Greis, 1978, J. Less-Common Metals **61**, 177.
LeFur, Y., S. Aléonard, M.F. Gorius and M.T. Roux, 1980, J. Solid State Chem. **35**, 29.
LeFur, Y., S. Aléonard, M.F. Gorius and M.T. Roux, 1982, Acta Crystallogr. **B38**, 1431.
Lim, M. and A.W. Searcy, 1966, J. Phys. Chem., **70**, 1762.
Löchner, U., 1980, Neue Hologenide des Neodyms und ihre Kristallstrukturen, Dissertation Thesis, University of Karlsruhe, West Germany.
Lösch, R. and C. Hebecker, 1976, Rev. Chim. Miner. **13**, 207.
Lösch, R. and C. Hebecker, 1977, Z. Naturforsch. **B32**, 1093.
Lösch, R. and C. Hebecker, 1979, Z. Naturforsch. **B34**, 1765.
Lucat, C., A. Rhandour, J.M. Re'au, J. Portier and P. Hagenmuller, 1979, J. Solid State Chem. **29**, 373.
Lyon, W.G., D.W. Osborne, H.E. Flotow, F. Grandjean, W.N. Hubbard and G.K. Hohnson, 1978, J. Chem. Phys. **69**, 167.
Lyon, W.G., D.W. Osborne and H.E. Flotow, 1979a, J. Chem. Phys. **70**, 675.
Lyon, W.G., D.W. Osborne and H.E. Flotow, 1979b, J. Chem. Phys. **71**, 4123.
Maklachkov, A.G. and E.G. Ippolitov, 1970, Izv. Akad. Nauk SSSR, Neorg. Mater. **6**, 1713.
Mansmann, M., 1964, Z. Anorg. Allg. Chem. **331**, 98.
Mansmann, M., 1965, Z. Kristallogr. **122**, 375.
Mar, R.W. and A.W. Searcy, 1967, J. Phys. Chem. **71**, 888.
Mehlhorn, B. and R. Hoppe, 1976, Z. Anorg. Allg. Chem. **425**, 180.
Meyers, C.E., 1975, Inorg. Chem. **14**, 199.
Meyers, C.E., 1976, Inorg. Nucl. Chem. Letters **12**, 575.
Meyers, C.E. and D.T. Graves, 1977a, J. Chem. Eng. Data **22**, 436.
Meyers, C.E. and D.T. Graves, 1977b, J. Chem. Eng. Data **22**, 440.
Morozov, V.I., L.N. Tretyankova, P.P. Federov and B.P. Sobolev, 1979, Izv. Akad. Nauk SSSR, Neorgan. Mater. **15**, 2238; Inorg. Mater. **15**, 1761.
Morss, L.R., 1974, J. Inorg. Nucl. Chem. **36**, 3876.
Nafikova, S. Kh., L.P. Reshetnikova and A.V. Novoselova, 1976a, Zh. Neorg. Khim. **21**, 2521; Russ J. Inorg Chem. **21**, 1386.
Nafikova, S. Kh., L.P. Reshetnikova and A.N. Novolelova, 1976b, Vestn. Mosk. Univ. Khim. **17**, 123.

Nafziger, R.H. and N. Riazance, 1972, J. Am. Ceram. Soc. **55**, 130.
Nafziger, R.H., R.L. Lincoln and N. Riazance, 1973, J. Inorg. Nucl. Chem. **35**, 421.
Nagel, L.E. and M. O'Keeffe, 1973, Highly Conducting Fluorides Related to Fluorite and Tysonite, in: Van Gool, W., ed., Proc. NATO Advanced Study Institute on Fast Ion Transport, Solids, Solid State Batteries Devices (North-Holland, Amsterdam) pp. 165–172.
Na'ray-Szab'o, S.V. and K. Sasva'ry, 1938, Z. Kristallogr. Mineralog. Petrogr. **A99**, 27.
Nikolaev, N.S. and A. Sodikova, 1975, (USSR) At. Energ. 39 338; Chem. Abstr. 84:36 512s.
Nowacki, W., 1939, Z. Kristallogr. **101**, 273.
Oetting, F.L., 1981, Rockwell International, Rocky Flats Plant, Golden, Colorado, personal communication.
O'Keeffe, M., 1973, Science **180**, 1276.
O'Keeffe, M., 1977, Comments Solid State Phys. **7**, 163.
O'Keeffe, M., and B.G. Hyde, 1975, J. Solid State Chem. **13**, 172.
O'Keeffe, M. and B.G. Hyde, 1976, Phil. Mag. **33**, 219.
O'Keeffe, M. and B.G. Hyde, 1977, Acta Crystallogr. **B33**, 3802.
Olkhovaya, L.A., P.P. Fedorov, D.D. Ikrami and B.P. Sobolev, 1979, J. Therm. Anal. **15**, 355.
Orlov, Y.N., V.E. Bozhevol'nov, L.N. Ivanov, V.I. Sulev, S.K. Obyden, G.V. Saparin, G.V. Spivak and V.V. Karelin, 1980, J. Cryst. Growth **49**, 109.
Pan, K., S.-C. Hsin and M.-L. Lee, 1974, J. Chin. Chem. Soc. (Taipei) **21**, 1; Chem. Abstr. 81:55 075f.
Pastor, R.C. and M. Robinson, 1974, Mater. Res. Bull. **9**, 569.
Pauling, L., 1924, J. Amer. Chem. Soc. **46**, 2738.
Petzel, T., 1973, Z. Anorg. Allg. Chem. **395**, 1.
Petzel, T. and O. Greis, 1972, Z. Anorg. Allg. Chem. **388**, 137.
Petzel, T. and O. Greis, 1973, Z. Anorg. Allg. Chem. **396**, 95.
Petzel, T. and O. Greis, 1976, J. Less-Common Metals **16**, 197.
Petzel, T. and O. Greis, 1979, Rev. Chim. Mineral. **16**, 411.
Pierce, J.W. and H.Y.-P. Hong, 1974, Structural Studies in the System Potassium Fluoride–Yttrium Fluroide, in: Kevane, C.J. and T. Moeller, Proc. Tenth Rare Earth Research Conf., Carefree, AZ, (NTIS, Springfield, VA) 527–37.
Pistorius, C.W.F.T., 1975, Mater. Res. Bull. **10**, 1079.
Podberezskaya, N.V., I.A. Baidina, S.V. Borisov and N.V. Belov, 1976a, Zh. Strukt. Khim. **17**, 147.
Podberezskaya, N.V., O.G. Potapova, S.V. Borisov and Y.V. Gatilov, 1976b, Zh. Strukt. Khim. **17**, 948.
Portier, J., 1976, Angew. Chem. **88**, 524.
Poulain, M., M. Poulain and J. Lucas, 1972, Mater. Res. Bull. **7**, 319.
Poulain, M., M. Poulain and J. Lucas, 1973, J. Solid State Chem. **8**, 132.
Poulain, M., M. Poulain and J. Lucas, 1975, Rev. Chim. Mineral. **12**, 9.
Ravez, J. and D. Dumora, 1969, C.R. Acad. Sci. Paris, Ser. C **269** 331.
Ravez, J., J. Viollet, R. DePape and P. Hagenmuller, 1967, Bull. Soc. Chim. Fr. **4**, 1325.
Réau, J.M. and J. Portier, 1978, Fluorine Ion Conductors, in: Hagenmuller, P. and W. van Gool, eds., Solid Electrolytes (Academic Press, New York) pp. 313–333.
Réau, J.M., C. Lucat, G. Campet, J. Portier and A. Hammou, 1976, J. Solid State Chem. **17**, 123.
Réau, J.M., C. Lucat, G. Campet, J. Claverie and J. Portier, 1977, Electrochim. Acta **22**, 761.
Réau, J.M., G. Villeneuve, J. Portier, P. Hagenmuller, C. Lucat and J.L. Soubeyroux, 1980, Rev. Chim. Miner. **17**, 342.
Reinen, D. and F. Steffens, 1978, Z. Anorg. Allg. Chem. **441**, 63.
Reshetnikova, L.P., I.B. Shaimuradov and A.V. Novoselova, 1976, Izv. Akad. Nauk SSSR, Neorg. Mater. **12**, 638; Inorg. Mater. **12**, 550.
Rezukhina, T.N. and T.F. Sisoeva, 1979, J. Chem. Thermodyn. **11**, 1095.
Rezukhina, T.N., T.F. Sisoeva, L.E. Holokhonova and E.G. Ippolitov, 1974, J. Chem. Thermodyn. **6**, 883.
Roberts, J.A. and A.W. Searcy, 1972, High Temp. Sci. **4**, 411.
Roy, D.M. and R. Roy, 1964, J. Electrochem. Soc. **111**, 421.
Rudzitis, E., H.M. Feder and W.N. Hubbard, 1965, J. Chem. Phys. **69**, 2305.
Saf'yanov, Y.N., R.I. Bochkova, E.A. Kuz'min and N.V. Belov, 1973, Dokl. Akad. Nauk SSSR **212**, 96.
Schlyter, K., 1952, Ark. Kemi **5**, 73.
Schmutz, H., 1966, US At. Energy Comm. Rept. KFK-431, 73 pp.
Schumm, R.H., D.D. Wagman, S. Bailey, W.H. Evans and V.B. Parker, 1973, Nat. Bur. Stds. (US) Tech. Note, 270–7.
Seifert, K.F., 1968, Fortschr. Miner. **45**, 214.
Seiranian, K.B., R.O. Sharchatunian, L.S. Garashina and B.P. Sobolev, 1972, The Solubility of LnF_3 in SrF_2 and Crystal Growth of $Sr_{1-x}Ln_xF_{2-x}$ Single Crystals, Abstracts of Fourth Conference on Crystallography, Erevan, SSSR (Akad. Nauk SSSR) pp. 127–129.
Seiranian, K.P., P.P. Fedorov, L.S. Garashina, G.V. Molev, V.V. Karelin and B.P. Sobolev, 1974, J. Cryst. Growth **26**, 61.
Seiranian, K.B., L.S. Garashina, K.S. Gavrichev and B.P. Sobolev, 1975, Phase Diagrams of the SrF_2–$(Y, Ln)F_3$ Systems and New Phases with Fluorite-derived Structures, Abstracts of Fourth Conference on the Chemistry of Inorganic Fluorides, Dushanbe, SSSR (Akad. Nauk SSSR) p. 21.
Shafer, M.W., 1965, J. Appl. Phys. **36**, 1145.
Shaimuradov, I.B., L.P. Reshetnikova and

A.V. Novoselova, 1975, Zh. Neorg. Khim. **20**, 1077; Russ. J. Inorg. Chem. **20**, 604.
Shannon, R.D., 1976, Acta Crystallogr. **A32**, 751.
Shenyavskaya, E.A. and B.S. Ryabov, 1976, J. Mol. Spectrosc. **63**, 23.
Sidorov, L.N. and V.B. Shol'ts, 1972, Int. J. Mass. Spectrom. Ion Phys. **8**, 437.
Sidorov, L.N., A.S. Alikhanyan, V.B. Shol'ts and L.V. Novikova, 1974, Zh. Fiz. Khim. **48**, 766; Russ. J. Phys. Chem. **48**, 444.
Skelton, W.H. and J.W. Patterson, 1973, J. Less-Common Metals **31**, 47.
Skinner, H.B. and A.W. Searcy, 1971, J. Phys. Chem. **75**, 108.
Sobolev, B.P. and P.P. Fedorov, 1973, Krystallografiya **18**, 624.
Sobolev, B.P. and P.P. Fedorov, 1978, J. Less-Common Metals **60**, 33.
Sobolev, B.P. and K.B. Seiranian, 1975, Kristallografiya **20**, 763.
Sobolev, B.P. and N.L. Tkachenko, 1975, Kristallografiya **20**, 1204.
Sobolev, B.P., D.A. Mineer and V.P. Pashutin, 1963, Dokl. Akad. Nauk SSSR, **150**, 791.
Sobolev, B.P., L.S. Garashina, P.P. Fedorov, N.L. Tkachenko and K.B. Seiranian, 1973, Krystallografiya **18**, 751; Sov. Phys. Crystallogr. **18**, 473.
Sobolev, B.P., P.P. Fedorov, D.B. Shteynberg, B.V. Sinitsyn and G.S. Shakhkalamian, 1976a, J. Solid State Chem. **17**, 191.
Sobolev, B.P., P.P. Fedorov, K.B. Seiranian and N.L. Tkachenko, 1976b, J. Solid State Chem. **17**, 201.
Sobolev, B.P., I.D. Ratnikova, P.P. Fedorov, B.V. Sinitsyn and G.S. Shakhkalamian, 1976c, Mat. Res. Bull. **11**, 999.
Sobolev, B.P., V.B. Aleksandrov, P.P. Fedorov, K.B. Seiranian and N.L. Tkachenko, 1976d, Kristallografiya **21**, 96; Sov. Phys. Crystallogr. **21**, 49.
Sobolev, B.P., V.S. Sidorov, P.P. Fedorov and D.D. Ikrami, 1977a, Krystallografiya **22**, 1009; Sov. Phys. Crystallogr. **22**, 574.
Sobolev, B.P., N.L. Tkachenko, V.S. Sidorov, P.P. Fedorov and D.D. Ikrami, 1977b, Thermal Stabilization of Fluorite and Rhombic Yttrium Fluoride Systems. Abstracts of the Fifth Conference on Crystallography, Tiflis, SSSR, vol. **2** (Akad. Nauk SSSR) pp. 25–26.
Sobolev, B.P., P.P. Fedorov, D.D. Ikrami, A.K. Galkin and V.S. Sidorov, 1978, Phase Diagrams of some LnF_3–$Ln'F_3$ systems, in: Abstracts, EUCHEM Conference on the Chemistry of the Rare Earths, Helsinki, Finland, pp. 134.
Sobolev, B.P., K.B. Seiranian, L.S. Garashina and P.P. Fedorov, 1979, J. Solid State Chem. **28**, 51.
Sobolev, B.P., P.P. Fedorov, A.K. Galkin, V.S. Sidorov and D.D. Ikrami, 1980, Akad. Nauk SSSR, Rost Kristallov **13**, 198.
Sobolev, B.P. and K.B. Seiranian, 1981, J. Solid State Chem. **39**, 337.
Sonin, V.I., O.G. Polyachenok and E.G. Ippolitov, 1973, Zh. Neorg. Khim. **18**, 2918; Russ. J. Inorg. Chem. **18**, 1552.
Soriano, J., M. Givon and J. Shamir, 1966, Inorg. Nucl. Chem. Letters **2**, 13.
Spedding, F.H. and A.H. Daane, 1956, Progr. Nuclear Energy **4**, 413.
Spedding, F.H. and D.C. Henderson, 1971, J. Chem. Phys. **54**, 2476.
Spedding, F.H., B.J. Beaudry, D.C. Henderson and J. Moorman, 1974, J. Chem. Phys. **60**, 1578.
Spitsyn, V.I., Yu.M. Kiselev, L.I. Martynenko, V.N. Prusakov and V.B. Sokolov, 1974, Dokl. Adad. Nauk SSSR **219**, 621.
Steele, D., P.E. Childs and B.E.F. Fender, 1972, J. Phys. **C5**, 2677.
Stepanov, A.V. and E.A. Severov, 1961, Dokl. Akad. Nauk SSSR **141**, 954.
Stezowski, J.J. and H.A. Eick, 1969, The Preparation of a Nonstoichiometric Samarium Fluoride Phase, in: Proc. Seventh Rare Earth Research Conference, vol. **2** (National Technical Information Service, Springfield, VA) pp. 741–750.
Stezowski, J.J. and H.A. Eick, 1970, Inorg. Chem. **9**, 1102.
Storozhenko, T.P., E.I. Khanaev and Yu.A. Afanas'ev, 1975, Zh. Fiz. Khim. **49**, 2117; Russ. J. Phys. Chem. **49**, 1241.
Storozhenko, T.P., E.I. Khanaev and Yu.A. Afanas'ev, 1976a, Z. Fiz. Khim. **50**, 2165; Russ. J. Phys. Chem. **50**, 1304.
Storozhenko, T.P., E.I. Khanaev and Yu.A. Afanas'ev, 1976b, Zh. Fiz. Khim. **50**, 1060.
Stull, D.R. and H. Prophet, 1971, JANAF Thermochemical Tables, NSRDS-NBS37, (US National Bureau of Standards, Washington).
Suvorov, A.L. and Al.L. Novikov, 1968, Vestn. Leningrad. Univ., Fiz. Khim. **23**, 83; Chem. Abstr. 69, 13 117 t.
Svantner, M., E. Mariani, P.P. Fedorov and B.P. Sobolev, 1979, Krist. Tech. 14, 365.
Tanguy, B., J. Portier, M. Vlasse and M. Pouchard, 1972, Bull. Soc. Chim. Fr. **3**, 946.
Templeton, D.H. and C.H. Dauben, 1954, J. Amer. Chem. Soc. **76**, 5237.
Thoma, R.E., 1973, Rev. Chim. Miner. **10**, 363.
Thoma R.E. and G.D. Brunton, 1966, Inorg. Chem. **5**, 1937.
Thoma, R.E. and R.H. Karraker, 1966, Inorg. Chem. **5**, 1933.
Thoma, R.E., C.F. Weaver, H.A. Friedman, H. Insley, L.A. Harris and H.A. Yakel, Jr., 1961, J. Phys. Chem. **65**, 1096.
Thoma, R.E., H. Insley and G.M. Hebert, 1966, Inorg. Chem. **5**, 1222.
Thoma, R.E., G.D. Brunton, R.A. Renneman and T.K. Keenan, 1970, Inorg. Chem. **9**, 1096.
Thoma, R.E., G.D. Brunton and M. Insley, 1974, J. Inorg. Nucl. Chem. **36**, 1515.
Tkachenko, N.L., L.S. Garashina, O.E. Izotova, V.B. Aleksandrov and B.P. Sobolev, 1973, J. Solid State Chem. **8**, 213.
Tkachenko, N.L., M. Svantner and B.P. Sobolev, 1977, Izv. Akad. Nauk SSSR, Neorg. Mater. **13**, 847.

Tsirlina, E.A., A.V. Gusarov and L.N. Gorokhov, 1976, Teplofiz. Vys. Temp. **14**, 1187.
Urland, W., 1979, Ber. Bunsenges. Phys. Chem. **83**, 1042.
Urland, W., K. Feldner and R. Hoppe, 1980, Z. Anorg. Allg. Chem. **465**, 7.
Védrine, A., R. Boutonnet and J.-C. Cousseins, 1973, C.R. Acad. Sci. Paris, Ser. C **277**, 1129.
Védrine, A., A. Delaigue and J.-C. Cousseins, 1974, Rev. Chim. Miner. **11**, 217.
Védrine, A., R. Boutonnet, R. Sabatier and J.-C. Cousseins, 1975, Bull. Soc. Chim. Fr. 445.
Vezzoli, G.C., 1970, Mater. Res. Bull. **5**, 213.
Vogt, T., 1911, Zentralbl. f. Mineral. u. Geol. **15**, 373.
Vogt, T., 1914, Neues Jahrb. Mineral. **9**, 15.
Wagman, D.D., W.H. Evans, V.B. Parker, J. Holow, S.M. Bailey, R.H. Schumm and K.L. Churney, 1971, Natl. Bur. Std. (US) Tech Note 207-5 (U.S. Bureau of Standards, Washington).
Weigel, F. and V. Scherer, 1967, Radiochim. Acta **7**, 40.
Wells, A.F., 1975, Structural Inorganic Chemistry, 4th ed. (Clarendon Press, Oxford).
Westrum, E.F., Jr., 1967, Adv. Chem. Ser. **71**, 25.
Westrum, E.F., Jr., and A.F. Beale, Jr., 1961, J. Phys. Chem. **65**, 353.
Wilcox, D.E., 1962, USAEC Rept. UCRL-10397; Nat. Sci. Abstr. 16:31 568.
Willis, B.T.M., 1963, Nature **197**, 755.
Willis, B.T.M., 1964a, J. Phys. (Paris) **25**, 431.
Willis, B.T.M., 1964b, Proc. Brit. Ceram. Soc. **1**, 9.
Willis, B.T.M., 1965, Thermodynamic Properties of Uranium Dioxide and Related Phases, in: Technical Reports Series No. 39 (International Atomic Energy Agency, Vienna) ch. II.
Yates, J.H. and R.M. Pitzer, 1979, J. Chem. Phys. **70**, 4049.
Zachariasen, W.H., 1948, J. Amer. Chem. Soc. **70**, 2147.
Zakharova, B.S., L.P. Reshetnikova and A.V. Novoselova, 1974, Dokl. Akad. Nauk SSSR **216**, 1302.
Zalkin, A. and D.H. Templeton, 1953, J. Amer. Chem. Soc. **75**, 2453.
Zalkin, A., D.H. Templeton and T.E. Hopkins, 1966, Inorg. Chem. **5**, 1466.
Zintl, E. and A. Udgård, 1939, Z. Anorg. Allg. Chem. **240**, 150.
Zmbov, K.F. and J.L. Margrave, 1966a, J. Phys. Chem. **70**, 3379.
Zmbov, K.F. and J.L. Margrave, 1966b, J. Chem. Phys. **45**, 3167.
Zmbov, K.F. and J.L. Margrave, 1967, J. Inorg. Nucl. Chem. **29**, 59.
Zmbov, K.F. and J.L. Margrave, 1968, Adv. Chem. Ser. 72 267.

Handbook on the Physics and Chemistry of Rare Earths, edited by K.A. Gschneidner, Jr. and L. Eyring

Chapter 46

SPECTROSCOPIC PROPERTIES OF TRIPLY IONIZED LANTHANIDES IN TRANSPARENT HOST CRYSTALS

Clyde A. MORRISON and Richard P. LEAVITT
Harry Diamond Laboratories, Applied Physics Branch 13 200, 2800 Powder Mill Road, Adelphi, Maryland 20 783, USA

Contents

Symbols

a, b, c = lattice constants (in Å)
A_{km} = crystal-field components (spherical tensor notation)
$A_k^m\langle r^k\rangle$ = crystal-field parameters (operator equivalent notation)
$A_k(R_j)$ = parameters in superposition model
$\boldsymbol{B}$ = magnetic field vector
B_{km} = crystal-field parameters (spherical tensor notation)

$\bar{B}_{km}$ = crystal-field parameters (unit tensor notation)
C_{km} = spherical tensor
$\boldsymbol{E}$ = electric field vector
e = magnitude of electron charge
E^i = Racah's electrostatic parameters
F^k = Slater's electrostatic parameters
g_e = electron g-factor (equal to 2.00233)
g_{ij} = components of g-tensor of a Stark level
$g_{km}(j)$ = geometrical parameters in superposition model
H_1 = electrostatic (Coulomb) Hamiltonian
H_2 = spin–orbit Hamiltonian
H_{CI} = configuration-interaction Hamiltonian (two-body)
H'_{CI} = configuration-interaction Hamiltonian (three-body)
H_{ESO} = electrostatically correlated spin–orbit Hamiltonian
H_R = relativistic interaction Hamiltonian (spin–spin plus spin–other-orbit)
H_{CEF} = crystal-field Hamiltonian
$\boldsymbol{J}$ = total angular momentum
$\boldsymbol{L}$ = orbital angular momentum
M^k = Marvin integrals (parameters in H_R)
$n(\lambda)$ = index of refraction
n_a, n_b, n_c = indices of refraction for $\boldsymbol{E}$ along a, b, or c
n_o, n_e = ordinary and extraordinary indices of refraction
O_k^m = operator equivalents
P^i = parameters in H_{ESO}
p_j = dipole moment of jth lattice point
$Q_{km}(j)$ = multipole moment of jth lattice point
$R_j(\theta)$ = rotation operator about j axis by θ ($j = x, y, z$)
$R_{nl}(r)$ = radial wave function
$\langle r^k \rangle$ = expectation value of r^k
$\boldsymbol{S}$ = spin angular momentum
$S^e_{J'J}$ = line strength for electric dipole transitions
$S^m_{J'J}$ = line strength for magnetic dipole transitions
T = temperature in K
T^i = parameters in H'_{CI}
$U(r)$ = central potential
U_{km} = unit irreducible tensor
$V^{(11)}_{m\mu}$ = unit irreducible double tensor
V_k^m = polynomials in operator equivalent method
x, y, z = positions of unit cell constituents (fractions of lattice constants) (in tables)
Y_{lm} = spherical harmonics
Z_j = charge of jth lattice point (in units of e)
α, β, γ = parameters in H_{CI} (in text)
α, β, γ = lattice angles (in tables)
$\alpha_J, \beta_J, \gamma_J$ = operator equivalent factors
α_j = polarizability of jth lattice point
λ = wavelength
μ = crystal quantum number
σ_k = shielding factor for crystal field
τ = radial scaling parameter
ζ = spin–orbit parameter
Ω_t = Judd–Ofelt intensity parameters

1. Introduction

1.1. *Purpose of chapter*

This chapter presents a compendium of experimental data on impurity-ion spectra of lanthanide ions in crystals. In particular, we tabulate crystallographic data, refractive index data, crystal-field parameters, intensity parameters, and experimental energy levels derived from optical absorption and fluorescence spectra for 26 host crystals. By host crystals we mean materials in which the triply ionized lanthanide ions can enter specific sites by chemical substitution and do not change the symmetry of the sites or appreciably distort the lattice near the sites. Thus, the lanthanide ions act as almost ideal probes, extracting information concerning the chemical environment of the sites without perturbing them significantly. Our definition is sufficiently broad to include R^{3+}:$CaWO_4$, in which the substitution takes place for Ca^{2+} and charge compensation is necessary to minimize lattice distortion, and R^{3+}:Y_2O_3, in which there are two distinct Y^{3+} sites, one with C_2 symmetry and one with C_{3i} symmetry. Cases such as CaF_2, however, where interstitial doping occurs, are excluded. Thus, we include most, but not all, situations in which the standard methods of crystal-field analysis apply.

In a review of this type, certain compromises must be made so that the end product is reasonably sized. Our main emphasis in the tables is on the experimental energy levels as derived from optical data. Our criterion for whether or not a certain host material is included in our tabulation can be stated roughly as follows: if *substantial* optical data and energy levels are available for at least three lanthanides in a particular material, then that material is included. The key word in the above criterion is *substantial*; this criterion, of course, is somewhat subjective, and in some cases we have had to decide whether or not to include marginal cases essentially according to our own personal tastes. Most cases that are questionable were omitted. The exception to this rule is the host YCl_3, which we included (because of the interest in its spectroscopic properties) in spite of the fact that we were able to find data on only two rare-earth ions. We realize that we have not included all the possible hosts that would satisfy our criteria; specifically, the rare-earth double nitrates, phosphates, and vanadates would have been informative additions to our selection. Unfortunately, we did not have the time to cover these interesting hosts adequately. Even so, this selection process left us with 26 host materials. We apologize to those readers who have anticipated our including their favorite host materials, only to find them omitted from this review. We can only say that, perhaps in some future review after more data have been analyzed, we will return to this subject.

It is perhaps more informative to define the scope of this article by stating what it is not, rather than what it is. We approach the subject from a theoretical background; therefore we touch only lightly on the various experimental techniques. This is somewhat unfortunate, as recent advances, particularly in the laser field, allow refined measurements that go beyond what is considered to be

traditional lanthanide ion spectroscopy. Techniques involving tunable dye lasers to selectively excite lanthanide ion levels, double resonance methods, magnetic circular dichroism, and other techniques too numerous to mention here have slowly crept into a field that previously was the domain of the classical absorption and fluorescence spectroscopists. At the present time, the original literature is the best place to read about these advances. Our interest is in the interpretation of the data, not in how it was obtained, although these subjects are somewhat intermingled.

Although technological considerations have had a great deal of influence on the direction of research in lanthanide-ion spectroscopy, they have not motivated us in our determination of what host materials to cover. Nevertheless most of our host materials have had considerable technological impact in the past and will continue to do so in the future, particularly as solid-state laser materials. We will keep our discussions of technological applications of individual host materials to a minimum, and interested readers can consult the literature.

We do not attempt to give a full review of crystal-field theory, although we do include a substantial discussion that is perhaps somewhat lengthy. We believe that this is warranted from the point of view of the unique role that crystal-field theory has in the interpretation of lanthanide spectra. Numerous questions in this field still remain unanswered, and many of the major contributors over the years are still quite active, indicating that this area of research is mature but by no means exhausted. It is hoped that, by providing an extensive compendium of experimental data on lanthanide-ion spectroscopy, we will provide a further incentive for theoretical advances.

Following a brief historical introduction in section 1.2, we begin our discussion with a section that covers several areas relating to the interpretation of the experimental data. Splittings of the free-ion lanthanide ions are so extensive that, in general, specialized "tools" are needed to unravel the optical data. For sites of high symmetry, the appropriate tool is group theory in the form of selection rules for electric and magnetic dipole transitions and group-theoretical classifications of the crystal-field split energy levels. For sites of low symmetry, group theory plays a reduced role and other considerations must enter in order to obtain a correct and consistent interpretation of lanthanide ion spectra. Measurements of excited state g-factors by the Zeeman effect can also play a subsidiary role in interpreting spectra and assigning energy levels.

Section 3 is a theoretical discussion that covers the free-ion Hamiltonian, crystal-field theory, and intensities. We discuss the effect of interelectronic Coulomb interactions and the spin–orbit interaction in determining the structure of the free-ion levels. Several additional interactions that are weaker than the above shift the free-ion levels by a few hundred wavenumbers and are necessary to give good agreement between calculated free-ion levels and experiment. These include spin-independent configuration interaction by the Coulomb interaction, spin-dependent configuration interaction by the spin–orbit interaction, and relativistic interactions that couple orbital and spin angular momenta of different electrons.

In our discussion of crystal-field theory, group theory again plays a central role. The point group of the lanthanide-ion site determines the number of nonvanishing crystal-field parameters. We consider the crystal-field interaction in the modern sense (mixing the free-ion levels as well as splitting them), although the operator-equivalent method is discussed to some degree. Theoretical models are discussed briefly, as they can provide a good theoretical picture of the ion–crystal host interactions, although these models are not accurate from a quantitative point of view. In spite of the fact that two-electron crystal-field effects have been shown to yield significant departures in isolated instances from the simple single-electron crystal-field model, we stick throughout our tabulation to the one-electron model. A short discussion of two-electron effects is included at the end of the crystal-field section. Finally, we give a short discussion of the Judd–Ofelt theory of forced electric dipole transitions and the intensity parameters, Ω_t.

The tables themselves are given in a somewhat condensed format, and the purpose of section 4 is to allow the reader to interpret the material in the tables properly. The tables cover a wide variety of host materials ranging from $LaCl_3$ and $R(C_2H_5SO_4)_3 \cdot 9H_2O$, which were among the first to be spectroscopically investigated, through R_2O_3, which has interesting magnetic properties at low temperature, to the garnets, scheelites, and zircons, which have applications as solid-state laser materials. The tables cover crystallographic data, index of refraction, crystal-field parameters, intensity parameters, and energy levels derived from optical spectra for each lanthanide ion in each host crystal. Related data that can be extracted from spectroscopic measurements, such as Zeeman splittings and group-theoretical assignments of energy levels, are not covered in the tables; the references to the literature should be sufficiently detailed that the reader can obtain this information from the literature. A summary of the material presented in the tables in this chapter is given in table 1.

The referencing system that we have used here is somewhat different from that used in other chapters in this series. Each subsection in section 5, which covers the various host materials, is a self-contained unit covering crystallographic data, refractive index, crystal fields, intensities, and spectra for a particular crystal and contains its own set of numbered references; this system should facilitate retrieval of information on a particular material. The remainder of the text (sections 1 through 4 and the introductions to each subsection in section 5) conforms to the system used in the rest of this series; that is, references are grouped alphabetically at the end of the chapter and cited in the text by authors and year. In addition to referencing articles in the open literature, we have also cited a number of unpublished reports. These reports are available from the U.S. National Technical Information Service (NTIS), Springfield, Virginia; they are cited in an abbreviated form giving the "NTIS number" and may be ordered from NTIS.

1.2. *Historical outline*

The impurity-ion spectra of triply ionized lanthanides in transparent materials consist of a series of sharp lines that more closely resemble free-ion, atomic, or

TABLE 1
Summary of data presented in the tables

Sect. (host)	Symm.[a]	X-ray[b]	$n(\lambda)$[c]	Ce[d]	Pr	Nd	Pm	Sm	Eu	Gd	Tb	Dy	Ho	Er	Tm	Yb
5.1 ($LaCl_3$)	C_{3h}	X	*	BE	BE	BE	BΩE	BE	BE	BE	BE	BE	BE	BE	BE	
5.2 (LaF_3)	C_2[e]	X[e]	X	E	BΩE	BΩE	Ω	BΩE	BΩE	BΩE	Ω	BΩE	BΩE	BΩE	BΩE	
5.3 ($LaBr_3$)	C_{3h}	X	X		BE	BΩE				BE	E			BE		
5.4 (YCl_3)	C_2	X												BE	E	
5.5 (YF_3)	C_s	X	*			E				E	E	E		BE		E
5.6 (RF_3)	C_2, C_s[f]	X[f]	X	E	E	BE[g]			BE		E[h]	E	BE	E		
5.7 ($RCl_3 \cdot 6H_2O$)	C_2	X				E		E	E	E	E	E	BE	BE	BE	E
5.8 ($Y(OH)_3$)	C_{3h}	X	*							BE	BE		BE	BE		
5.9 ($R(OH)_3$)	C_{3h}	X			BE				BE	BE	BE	BE		BE		
5.10 (Y_2O_3)	C_2, C_i	X	*	E	Ω	BΩE		BE	BΩE			BE		BΩE	BΩE	E
5.11 (R_2O_3)	C_{3v}, C_s, C_2, C_{3i}[i]	X[i]	X			BE[i]			E[k]			E		B[l]E		
5.12 (Y_2O_2S)	C_{3v}	*						BE	BΩE		BE	BE	BE	BE		
5.13 ($LiNbO_3$)	C_3	X	X			E							E	E	E	
5.14 ($YAlO_3$)	C_s	X	X	E	E	BΩE			ΩE		BΩE	BE	BΩE	BΩE	BΩE	E

5.15 (YVO_4)	D_{2d}	X	X			BΩE	E		BE	E			E	BE	BE	
5.16 (YPO_4)	D_{2d}	X		E		BE			BE		E		BE	BE	BE	
5.17 ($CaWO_4$)	S_4	X	X		BE	BE				E	BE	BE	BE	BE	BE	BE
5.18 ($PbMoO_4$)	S_4	X	X		BE	BE							BE			
5.19 ($LiYF_4$)	S_4	X	X		BE	BE					E	BE	BE	BE	BE	BE
5.20 ($Y_3Al_5O_{12}$)	D_2	X	*		E	BΩE		BE	BE	E	BE	BE	ΩE	BΩE	ΩE	E
5.21 ($Y_3Ga_5O_{12}$)	D_2	X	X	BE	E	BE		BE	BE		E	BE	BE	BE	E	BE
5.22 ($R_3Al_5O_{12}$)	D_2	X	X								BE	BE	E	BE	E	E
5.23 ($R_3Ga_5O_{12}$)	D_2	X	X			E		BE	BE		E	BE	E	BE	BE	E
5.24 (KY_3F_{10})	C_{4v}	X	X		BE	BE			BΩE							
5.25 (Cs_2NaRCl_6)	O_h	*		BE	BE	BE		BE	BE		BE	BE	BE	BE	BE	BE
5.26 (RES)[m]	C_{3h}	X	*	B	BE	BE		BE	BΩE	BE	BE	BE	BE	BE	BΩE	BE

[a]Point-group symmetry of the rare earth substitutional site. [b]X-ray or neutron-diffraction data. X indicates that the refinement of the crystal structure is given in the tables; * indicates that the refinement is for a different crystal with the same structure. [c]X indicates *n* is given in the tables; * indicates *n* is given in the introduction to the subsection. [d]For each ion in each host material, B indicates crystal-field parameters, Ω indicates intensity parameters, and E indicates energy levels. [e]C_2 is the commonly accepted symmetry; we have, however, provided data on two alternate structures. [f]Two different structures, X-ray data presented for both. [g]Energy levels are presented for Nd:CeF_3 and Nd:NdF_3. [h]Energy levels are presented for Tb:GdF_3, Tb:TbF_3, and Tb:DyF_3. [i]Three different structures, X-ray data presented for all three. [j]Energy levels are presented for Nd:La_2O_3, Nd:Nd_2O_3, and Nd:Gd_2O_3. [k]Energy levels for Eu:Gd_2O_3. [l]B_{km} for Er_2O_3, C_{3i} sites. [m]Rare-earth ethyl sulfates, $R(C_2H_5SO_4)_3 \cdot 9H_2O$.

molecular spectra than other solid-state impurity ion spectra, which generally have a broad band structure. These features of lanthanide spectra were noted by Becquerel (1906, 1908). Unfortunately, technological difficulties in separating the rare earths obviated the possibility of studying spectra from carefully prepared laboratory samples and restricted the experiments to natural minerals. Thus, progress in the experimental arena was slow, at least up until the advent of quantum mechanics.

The invention of crystal-field theory by Bethe (1929) and the application of group theory to impurity-ion spectroscopy by Bethe (1930) and Kramers (1930) paved the way for a more complete understanding of the spectra. Van Vleck (1937) gave a qualitative explanation of how $f \rightarrow f$ transitions can occur by admixing of opposite-parity configurations by the crystal field or by lattice vibrations. At the same time, experimental advances allowed the observation of spectra in carefully prepared laboratory samples (Freed and Spedding, 1929a, b, 1931; Spedding, 1931, 1933; Spedding and Nutting, 1931).

In the late forties and early fifties the discovery of paramagnetic resonance techniques provided a further impetus to the study of impurity ions in solids. An excellent review of paramagnetic resonance results and a discussion of the theory is given by Abragam and Bleaney (1970). Theoretically, the techniques of angular-momentum algebra and irreducible tensors began to be applied (Stevens, 1952; Elliot and Stevens, 1953; Judd, 1955) to lanthanide-ion spectra. This period saw the development of the operator-equivalent method; extensive tabulations of quantities associated with irreducible tensor analysis (Rotenberg et al., 1959; Nielson and Koster, 1963) allowed the incorporation of Racah's techniques (Racah, 1942a, b, 1943, 1949) into the analysis. The electrostatic point-charge model (Hutchings and Ray, 1963) provided a theoretical basis for describing the ion–host interactions. This model was investigated at Harry Diamond Laboratories (Karayianis and Morrison, 1973, 1975; Leavitt et al., 1975) and later work included point dipoles in a self-consistent manner (Morrison, 1976). Much of the above work is summarized in the books by Judd (1963) and Wybourne (1965). Experimental advances were made by Dieke and co-workers at Johns Hopkins University; this group made detailed systematic studies of lanthanide-ion spectra in a variety of host crystals and solutions and identified many of the free-ion levels in the spectra for the first time. Much of this material is covered in Dieke's book (1968), which also fills in many of the gaps in this historical sketch.

The superposition model (Newman, 1970) provided a framework for understanding crystal-field effects without the necessity of considering specific mechanisms such as electrostatic interactions. In the late sixties and the seventies, the possibility of technological applications in the laser field spurred experimental and theoretical research to the point that today we have been able to identify at least two hundred host crystals that have been studied, with greater than four hundred ion–host combinations whose spectra have been reported in the literature. This review is an attempt to systematize some of this material.

2. Interpretation of experimental data

2.1. *Absorption and fluorescence spectra*

Lanthanide impurity-ion spectra consist of a series of sharp lines that appear in groups of closely spaced sublevels that correspond to transitions between crystal-field split free-ion levels. The simplest absorption spectra occur at very low temperatures (~4 K), at which only the lowest Stark level is populated, in general. As the temperature is raised, transitions originating from thermally accessible excited levels are possible, thus complicating the spectrum. In fluorescence spectra, transitions arise at low temperature only from the lowest lying sublevel of the excited free-ion level. At higher temperatures, other transitions become possible.

This situation is best illustrated by an example. Fig. 1 gives a partial energy level diagram for Nd^{3+}:$LaCl_3$ (Dieke, 1968), which shows the splitting of the $^4F_{3/2}$, $^4I_{11/2}$, and $^4I_{9/2}$ levels (all in cm^{-1}) by the crystal field. The $^4I_{13/2}$ and $^4I_{15/2}$ levels, which are situated between the $^4F_{3/2}$ and $^4I_{11/2}$ levels, are not shown. The crystal quantum numbers, μ, are also shown; these will be explained in section 2.2. The features illustrated in the figure are common to most lanthanide impurity-ion spectra, i.e. sharp levels in well-separated groups.

In the absence of selection rules, one would expect transitions at 4 K from the ground level to all upper levels. In fact, the $^4I_{9/2} \rightarrow {}^4I_{11/2}$ transitions are in most cases not observable because of infrared absorption by the lattice vibrations, so all that would be observed (of the levels depicted in the figure) would be the $^4I_{9/2} \rightarrow {}^4F_{3/2}$ transitions, which are used to establish the positions of the $^4F_{3/2}$

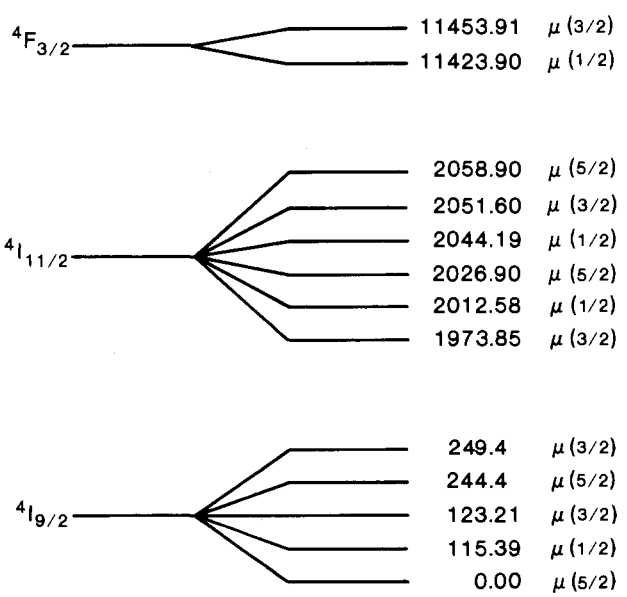

Fig. 1. Energy level scheme for Nd^{3+}:$LaCl_3$, showing the Stark levels of the $^4I_{9/2}$, $^4I_{11/2}$, and $^4F_{3/2}$ terms. The crystal quantum numbers are also shown.

energy levels. At higher temperatures (say 77 K, liquid-nitrogen temperature) one would observe not only transitions from the ground state but also transitions from low-lying excited states; the temperature dependence of the intensity is determined by the Boltzmann factor for the ith level

$$\rho_i = \eta_i \exp(-E_i/k_B T) \Big/ \sum_j \eta_j \exp(-E_j/k_B T), \tag{1}$$

where η_i is the degeneracy of the ith level and E_i is its energy. In our example, $\rho_i \sim 0.1$ at 77 K for the 115.39 and 123.21 cm^{-1} levels; thus transitions originating from these levels should be weak but observable. Thus, the positions of the low-lying excited levels in the ground ($^4I_{9/2}$) manifold can be established from the 77 K absorption spectrum.

The fluorescence spectrum can be used to define the positions of these levels more accurately and to establish the positions of the remaining $^4I_{9/2}$ and $^4I_{11/2}$ levels. At 4 K, transitions emanate primarily from the lower $^4F_{3/2}$ level at 11 423.90 cm^{-1}. Provided all transitions are allowed, all the $^4I_{9/2}$ and $^4I_{11/2}$ levels can be determined. In the case of Nd^{3+}:$LaCl_3$, this is not the case and measurements at 77 K are necessary.

Because the widths of the spectral lines increase markedly with temperature, one should attempt to extract as much information as possible from low-temperature measurements. Often, the spectrum is not as clear-cut as that in fig. 1, as there may be an excited level at $\sim 10\ cm^{-1}$ that complicates the 4 K spectrum. Also, the positions of the free-ion levels $^{2S+1}L_J$ may be such that the corresponding crystal-field split levels overlap, prohibiting a definitive assignment of individual crystal-field sublevels to particular free-ion levels.

2.2. *Symmetry*

2.2.1. *Group-theoretical classification of states*

In general, the crystal-field interaction can split a free-ion level with total angular momentum J into $2J + 1$ distinct sublevels if J is an integer and $(J + \frac{1}{2})$ sublevels if J is a half-odd integer. In the latter case, the levels remain doubly degenerate because of Kramers' theorem (Kramers, 1930). This degree of splitting is not usually observed, however, because of the constraints imposed by group theory.

The crystal-field Hamiltonian, regardless of its form, must be invariant under all operations of the point group of the lanthanide-ion site, which is the set of all rotations, reflections, and inversions about the lanthanide ion that leave the surrounding lattice invariant. There are 32 point groups possible in an infinite crystal lattice (Koster et al., 1963). As required by group theory, the eigenstates of the crystal-field Hamiltonian must transform according to irreducible representations of the appropriate point groups. In some cases these are non-degenerate, but in other cases they can be doubly, triply, or even quadruply degenerate (the latter being the case for the double octahedral groups). Kramers' theorem imposes additional degeneracies that do not arise strictly from point-

group symmetry; rather, they are consequences of time-reversal invariance.

Group-theoretical labels for the eigenstates may be written in several forms, the most common usage being A or B for singlets, E for doublets, and T for triplets (Hamermesh, 1962) in which subscripts, primes, etc. are used in addition to the letters to distinguish different irreducible representations. Another notation due to Bethe (1929) is Γ_j, where j runs over the various representations of the group (Koster et al., 1963).

Another alternative is to use the crystal quantum number scheme of Hellwege (1949), which has a more direct connection with the crystal-field Hamiltonian. This Hamiltonian contains parameters B_{km}, where the allowed values of k and m are determined by the point-group symmetry. Each point group is characterized by an integer parameter q such that allowed values of m are given by

$$m = 0 \,(\mathrm{mod}\, q), \tag{2}$$

so that allowed values of m in the crystal-field Hamiltonian are integral multiples of q. Then the crystal-field Hamiltonian couples the states $|JM\rangle$ in such a manner that a given eigenfunction contains only those states whose M values differ by integral multiples of q. The crystal quantum number of a representation, μ, is then defined as the smallest possible (in absolute value) M value that is contained in the representation. Thus, if the number of electrons is even, the crystal quantum numbers are

$$\mu = 0, \pm 1, \ldots, q/2 \qquad q \text{ even}, \tag{3a}$$

$$\mu = 0, \pm 1, \ldots, \pm(q-1)/2, \qquad q \text{ odd}, \tag{3b}$$

and if the number of electrons is odd, we have

$$\mu = \pm\tfrac{1}{2}, \pm\tfrac{3}{2}, \ldots, \pm(q-1)/2, \qquad q \text{ even}, \tag{4a}$$

$$\mu = \pm\tfrac{1}{2}, \pm\tfrac{3}{2}, \ldots, q/2, \qquad q \text{ odd}. \tag{4b}$$

That is, for any q-group, the representations $\mu = 0$ and $\mu = q/2$ are nondegenerate and all others are doubly degenerate. This notation clearly does not cover the case of cubic groups, in which triplets and quartets occur. Also, if the group contains rotations perpendicular to the z-axis or reflections through planes containing the z-axis, a superscript (+) or (−) is necessary to uniquely specify the one-dimensional representations. Allowed values of q are $q = 1, 2, 3, 4$, or 6.

Application of this formalism to the previously considered example of Nd^{3+}:$LaCl_3$ is straightforward. The lanthanide-ion site symmetry is C_{3h}; therefore, we have $q = 6$ and, from eqs. (3a) and (4a), the relevant crystal quantum numbers are $\mu = 0, \pm 1, \pm 2$, and 3 for an even number of electrons and $\mu = \pm 1/2$, $\pm 3/2$, and $\pm 5/2$ for an odd number of electrons. All representations are two-dimensional except for $\mu(0)$ and $\mu(3)$, which are singlets. The manner in which a $(2J + 1)$-dimensional irreducible representation of the rotation group (eigenstate of the total angular momentum) breaks up into representations of a particular point group is well known, and can be looked up for any of the 32 point groups (Koster et al., 1963). Thus, the levels in fig. 1 split under the

influence of a C_{3h} crystal field into the levels shown, and the number of levels of each type is determined only by the point group and not by the details of the crystal-field interaction.

2.2.2. *Selection rules*

One of the most important aspects of group theory as applied to impurity-ion spectra is that it imposes severe restrictions on the types of transitions that can take place. In uniaxial crystals where the crystal c-axis coincides with the quantization axis of the lanthanide ion, polarized absorption and fluorescence spectra can be of great value in identifying the energy levels and determining which transitions are electric dipole and which are magnetic dipole. The latter can easily be done by comparing axial spectra (propagation vector, $\boldsymbol{k}$, of the light parallel to the c-axis, $\boldsymbol{E}$ and $\boldsymbol{B}$ perpendicular to the c-axis) with pi (π) spectra ($\boldsymbol{E} \parallel c$, $\boldsymbol{B} \perp c$, $\boldsymbol{k} \perp c$) and sigma (σ) spectra ($\boldsymbol{E} \perp c$, $\boldsymbol{B} \parallel c$, $\boldsymbol{k} \perp c$). If the spectra are of electric-dipole origin, then the axial and sigma spectra are similar, whereas if the spectra are of magnetic-dipole origin, then axial and pi spectra are similar. Most observed lanthanide-ion spectra arise from induced electric-dipole $f \rightarrow f$ transitions (Judd, 1962; Ofelt, 1962).

Once the electric or magnetic dipole nature of the transitions is known, selection rules are determined from group theory. The components of the electric and magnetic field vectors transform according to definite representations of the point group (often different ones, as $\boldsymbol{E}$ is a polar vector and $\boldsymbol{B}$ is an axial vector). A particular transition is allowed (forbidden) if the irreducible representation of the final state is (is not) contained in the Kronecker product of the initial state representation and the representation of the appropriate component of $\boldsymbol{E}$ or $\boldsymbol{B}$ (Tinkham, 1964).

To illustrate these ideas, let us return to our example of Nd^{3+}:$LaCl_3$. The z-component of $\boldsymbol{E}$ transforms as $\mu(3)$, and x- and y-components transform as $\mu(\pm 2)$. For magnetic-dipole transitions, B_z transforms as $\mu(0)$, and B_x and B_y transform as $\mu(\pm 1)$. Thus, for Kramers ions, the selection rules shown in tables 2 and 3 apply to electric and magnetic dipole transitions, respectively. The $^4I \rightarrow {}^4F$ transitions are predominantly electric dipole for Nd^{3+}:$LaCl_3$, since the magnetic-dipole selection rules $\Delta L = 0$ and $|\Delta J| \leq 1$ are violated. Thus, for the 4 K absorption spectrum, the transition $^4I_{9/2}$ ($\mu = 5/2$) $\rightarrow {}^4F_{3/2}$ ($\mu = 3/2$) occurs in σ only, whereas $^4I_{9/2}$ ($\mu = 5/2$) $\rightarrow {}^4F_{3/2}$ ($\mu = 1/2$) occurs in both σ and π. If the

TABLE 2
Electric-dipole selection rules for Kramers ions in C_{3h} symmetry.

μ	$\pm 1/2$	$\pm 3/2$	$\pm 5/2$
$\pm 1/2$	–	σ	$\sigma\pi$
$\pm 3/2$	σ	π	σ
$\pm 5/2$	$\sigma\pi$	σ	–

TABLE 3
Magnetic-dipole selection rules for Kramers ions in C_{3h} symmetry.

μ	$\pm 1/2$	$\pm 3/2$	$\pm 5/2$
$\pm 1/2$	$\sigma\pi$	π	–
$\pm 3/2$	π	σ	π
$\pm 5/2$	–	π	$\sigma\pi$

ground level were $\mu(3/2)$, one σ line and one π line would appear; if the ground level were $\mu(1/2)$, only one σ line and no π lines would appear. Thus, the 4 K absorption spectra can be used to identify not only the crystal quantum numbers of the $^4F_{3/2}$ levels but also the crystal quantum number of the ground level. Polarization data for fluorescence and higher temperature absorption can then be used to assign crystal quantum numbers to the remaining levels, as illustrated in fig. 1.

The preceding type of analysis applies to all uniaxial crystals in which the lanthanide ion has threefold or higher symmetry. The selection rules imply that some transitions that would otherwise be expected are missing altogether and that others appear only in one polarization. In other types of crystals, such detailed information cannot be extracted. For example, in cubic crystals such as $Y_3Al_5O_{12}$, there are sites of D_2 symmetry whose orientations differ, so that quantization axes of these sites do not correspond to a unique axis of the crystal. As a result, polarized spectra do not aid in unraveling the energy level diagram; nevertheless, selection rules still operate, and certain transitions are allowed, while others are forbidden.

For sites of low symmetry such as C_2, C_s, or C_1, all $f \rightarrow f$ transitions are allowed, and group-theoretical considerations play a reduced role in the analysis. We shall consider these types of spectra in more detail later on.

2.3. *Zeeman effect*

The Zeeman effect can be used as an auxiliary tool for unraveling lanthanide-ion spectra. Degenerate crystal-field levels are split in a magnetic field and the magnitude of the splitting can be compared with results of a crystal-field calculation to aid in assigning energy levels. The partial g-sum rule (Karayianis, 1972) can be used in conjunction with experimentally determined g-factors to assign levels whose crystal quantum numbers are uncertain. The rule states roughly that the sum of g-factors over levels belonging to a particular irreducible representation of a particular $^{2S+1}L_J$ state is approximately independent of the host crystal; deviations from this rule are a measure of the degree of J-mixing by the crystal field. Partial g-sums have been calculated by Karayianis (1972).

The Hamiltonian representing the interaction of a lanthanide ion with a magnetic field $\boldsymbol{B}$ is given by

$$H_M = \frac{e\hbar}{2mc}(\boldsymbol{L} + g_e\boldsymbol{S}) \cdot \boldsymbol{B}, \tag{5}$$

where $\boldsymbol{L}$ and $\boldsymbol{S}$ are the total orbital and spin angular-momentum operators and $g_e = 2.00233$ is the electron g-factor. This operator is diagonalized within the doublet, triplet, or quartet level to determine the splitting in the magnetic field. For doublets, the splitting can be characterized by a g-tensor defined by (Dieke, 1968)

$$\epsilon^2 = \left(\frac{e\hbar}{mc}\right)^2 \sum_{ij} g_{ij}B_iB_j, \tag{6}$$

where the sum is over Cartesian indices (note that g_{ij} is twice the μ_{ij} defined by Dieke), and ϵ is the splitting of the doublet. In particular, for uniaxial crystals, $g_{xx} = g_{yy} = g_\perp$, $g_{zz} = g_\parallel$, and all other components vanish, by symmetry. In this particular case, the partial g-sum rule applies to the $g_\parallel$ values.

2.4. *Sites of low point-group symmetry*

Because of the technological importance of R^{3+} ions as active elements in solid-state lasers, optical spectra of lanthanides in sites of low symmetry have been studied extensively. For these sites, the constraints imposed by group theory are weak, and selection rules are often nonexistent (such is the case with Kramers ions in C_2 symmetry, for example). Thus, it becomes difficult to unravel the optical spectrum unambiguously. Even if this has been done, it is not straightforward to fit the data with a crystal-field Hamiltonian. The parameter space is large (14 crystal-field parameters in C_2 symmetry) and several minima may exist that are indistinguishable from one another insofar as the quality of the fit is concerned.

These difficulties may be alleviated by imposing theoretical constraints. First of all, a theoretical model of the crystal-field interaction can be compared with crystal-field parameters that correspond to the various minima, and the "best" set selected on the basis of agreement with the model. The simple point charge model extended by means of the three-parameter theory (Leavitt et al., 1975) is a step in this direction. Additional guidance at a more phenomenological level can be provided by the superposition model (Bradbury and Newton, 1967). Theoretical models can also be used to provide a set of starting parameters in the search for the correct minimum.

Even if a theoretical model is not available or is inaccurate, progress can be made in this problem. Normal expectations (as bolstered by theoretical calculations and analysis of spectra on ions in high symmetry sites) are that the variation of crystal-field parameters along the periodic table is smooth. Particularly, previous experience indicates that the two-fold parameters B_{2m} are nearly independent of Z, the atomic number of the lanthanide, whereas the B_{4m} and B_{6m} decrease monotonically in magnitude with Z. Reliable starting values for the B_{km} can therefore be obtained if values for other lanthanides in the same host crystal are known. If this is not the case, it is often preferable to analyze spectra for more than one lanthanide simultaneously rather than to attempt the analysis of a single spectrum. These approaches were combined in a recent analysis of R^{3+}:LaF_3, in which starting values of B_{km} were obtained from the point-charge model and final B_{km} were selected as those that gave a smooth variation from one lanthanide to another (Morrison and Leavitt, 1979). In this way a consistent set of B_{km} were obtained for the entire lanthanide series.

It is clear that further work is necessary in the development of a reliable general method of deriving good first approximations to crystal-field parameters for lanthanides in the low-symmetry sites.

3. Theoretical considerations

3.1. *Free-ion Hamiltonian*

Except in the simplest (4f) configuration, Russell–Saunders coupling does not hold rigorously in the $4f^q$ configurations of triply ionized lanthanide ions. Therefore, in performing crystal-field calculations, one must take into account the mixing of different LS terms by the spin–orbit interaction and other spin-dependent interactions. Any crystal-field calculation reported in the literature should therefore be accompanied by a description of the "free-ion" calculation used to generate matrix elements of the crystal-field Hamiltonian. The books of Condon and Shortley (1959), Judd (1963), and Wybourne (1965), as well as Chapter 1, Volume 1 (Goldschmidt, 1978) of this series, give thorough descriptions of the contributions to the free-ion Hamiltonian for lanthanides; we merely summarize the results here and refer the interested reader to the above cited works for details.

3.1.1. *Coulomb and spin–orbit interactions*

In the lowest approximation (Slater, 1929), the potential seen by an electron on a lanthanide ion is treated as spherically symmetric ("central field approximation"); in this approximation, the Hamiltonian is

$$H_0 = \sum_{i=1}^{q} \left[-\frac{\hbar^2}{2m} \nabla_i^2 + U(r_i) \right], \tag{7}$$

where the sum is over all electrons in the $4f^q$ configuration (contributions involving electrons in closed shells are neglected). As is well known (Condon and Shortley, 1959) the eigenfunctions of eq. (7) are Slater determinants with elements of the form

$$\psi_{nlm_l m_s}(\boldsymbol{r}) = \frac{1}{r} R_{nl}(r) Y_{lm_l}(\theta, \phi) \chi_{m_s}, \tag{8}$$

where n is the principal quantum number, l is the orbital angular-momentum quantum number, m_l is its z-component, m_s is the z-component of the spin, $R_{nl}(r)$ is the radial wave function (with $n-l-1$ nodes), Y_{lm_l} is a spherical harmonic, and χ_{m_s} is a two-component spinor (with $m_s = \pm 1/2$). For 4f electrons, $n = 4$ and $l = 3$.

In the central-field approximation, the entire $4f^q$ configuration is degenerate, with degeneracy $\binom{4l+2}{q}$, where $\binom{a}{b}$ is a binomial coefficient. The degeneracy is partially lifted by the interelectronic Coulomb interaction, which is given by

$$H_1 = \frac{e^2}{2} \sum_{i \neq j=1}^{q} \frac{1}{|\boldsymbol{r}_i - \boldsymbol{r}_j|}. \tag{9}$$

The eigenfunctions of the combined Hamiltonian, $H_0 + H_1$, can be obtained by degenerate perturbation theory by assuming that $H_1 \ll H_0$; they are linear combinations of Slater determinants that are also eigenfunctions of the total orbital

and spin angular-momentum operators, $\boldsymbol{L}^2$ and $\boldsymbol{S}^2$, with eigenvalues $L(L+1)$ and $S(S+1)$. For many-electron ions, group-theoretical methods are used to classify terms in the $4f^q$ configuration that have the same values for L and S (Racah, 1942a, b, 1943, 1949).

Eq. (9) is usually expanded in terms of spherical tensors defined by (Judd, 1963)

$$C_{km}(\hat{r}) = \left[\frac{4\pi}{2k+1}\right]^{1/2} Y_{km}(\theta, \phi), \tag{10}$$

to obtain the following form for H_1, which is valid between $4f^q$ states

$$H_1 = \tfrac{1}{2} \sum_{\substack{k=0 \\ k \text{ even}}}^{6} F^k \sum_{\substack{i \neq j \\ m}} C^{\dagger}_{km}(\hat{r}_i) C_{km}(\hat{r}_j), \tag{11}$$

where the Slater integrals, F^k, are given by

$$F^k = 2e^2 \int_0^{\infty} \mathrm{d}r\, R^2_{4f}(r) \int_r^{\infty} \mathrm{d}r'\, R^2_{4f}(r') \frac{r^k}{r'^{k+1}}. \tag{12}$$

It is useful to introduce the following linear combinations of the F^k (Racah, 1942b):

$$\begin{aligned} E^0 &= F^0 - 2F^2/25 - F^4/33 - 50F^6/1287, \\ E^1 &= 14F^2/405 + 7F^4/297 + 350F^6/11\,583, \\ E^2 &= F^2/2025 - F^4/3267 + 175F^6/1\,656\,369, \\ E^3 &= F^2/135 + 2F^4/1089 - 175F^6/42\,471. \end{aligned} \tag{13}$$

The Coulomb interaction can be written in terms of the E's as follows

$$H_1 = \sum_{i=0}^{3} E^i e_i, \tag{14}$$

where the e_i are operators that transform according to definite irreducible representations of the Lie groups G_2 and R_7. Thus, the E's are useful for computing matrix elements of H_1 between many-electron states that are classified according to Racah's scheme. The only off-diagonal matrix elements that occur are between states of the same L and S; this requires at most the diagonalization of a 10×10 matrix (for the ^{2}F and ^{2}G states in the $4f^7$ configuration of Gd^{3+}). Matrix elements of the e_i operators are tabulated for all states of the $4f^q$ configurations (Nielson and Koster, 1963).

The spin–orbit coupling in lanthanides is large enough so that, in general, deviations from Russell–Saunders coupling (that is, L and S good quantum numbers) are appreciable. Methods have been devised (Karayianis, 1970) to treat these deviations within a single LS term in a perturbative manner. It is preferable, however, to diagonalize the Coulomb and spin–orbit interactions simultaneously and thereby determine the so-called "intermediate coupling" eigenfunctions.

The spin–orbit interaction is given by (Condon and Shortley, 1959)

$$H_2 = \frac{\hbar^2}{2m^2c^2} \sum_{i=1}^{q} \frac{1}{r_i} \frac{dU(r_i)}{dr_i} \mathbf{s}_i \cdot \mathbf{l}_i, \tag{15}$$

where s_i and l_i are the spin and orbital angular-momentum operators. This interaction may be written in a form appropriate for matrix elements between $4f^q$ states as follows:

$$H_2 = \zeta \sum_{i=1}^{q} \mathbf{s}_i \cdot \mathbf{l}_i, \tag{16}$$

where the spin–orbit parameter, ζ, is given by

$$\zeta = \frac{\hbar^2}{2m^2c^2} \int_0^\infty R_{4f}^2(r) \cdot \frac{1}{r} \frac{dU(r)}{dr} dr. \tag{17}$$

Defining the unit double tensor (Racah, 1942b)

$$V_{m\mu}^{(11)} = \sum_{i=1}^{q} v_{m\mu}^{(11)}(i), \tag{18}$$

where the single-electron reduced matrix element is given by

$$(sl\|v^{(11)}\|sl) = \sqrt{s(s+1)(2s+1)}, \tag{19}$$

we may write the spin–orbit interaction as

$$H_2 = \zeta \sqrt{l(l+1)(2l+1)} \sum_{\mu} (-1)^{\mu} V_{\mu,-\mu}^{(11)} \tag{20}$$

which (for 4f electrons) is

$$H_2 = 2\zeta\sqrt{21} \sum_{\mu} (-1)^{\mu} V_{\mu,-\mu}^{(11)} \tag{21}$$

and matrix elements between states of total angular momentum J can be written as

$$\langle \alpha' L'S'J'M'|H_2|\alpha LSJM\rangle = -2\zeta\sqrt{21} W(S1J'L'; S'L) \times (\alpha' L'S'\|V^{(11)}\|\alpha LS)\delta_{JJ'}\delta_{MM'}, \tag{22}$$

where α represents the set of quantum numbers necessary to distinguish states of the same L and S, and where $W(abcd; ef)$ is a Racah coefficient (Rose, 1957). The reduced matrix element on the right-hand side of eq. (22) is tabulated for states of $4f^q$ configurations (Nielson and Koster, 1963).

3.1.2. *Configuration interaction and spin-dependent interactions*

Section 3.1.1 provides a basic framework for computing free-ion energies and eigenfunctions. When the simple Coulomb and spin–orbit interactions are used, however, discrepancies of the order of a few hundred wave numbers remain between calculated and experimental energy levels. A more complete free-ion Hamiltonian includes the following additional interactions:

(a) *Spin-independent configuration interaction*, which arises from coupling of configurations by the Coulomb interaction, eq. (9). This interaction includes

three-electron terms in addition to two-electron terms. The two-electron terms can be written as follows (Wybourne, 1965; Rajnak and Wybourne, 1963)

$$H_{\mathrm{CI}} = \alpha L(L+1) + \beta G(\mathrm{G}_2) + \gamma G(\mathrm{R}_7), \tag{23}$$

where $G(\mathrm{G}_2)$ and $G(\mathrm{R}_7)$ are the Casimir operators for the Lie groups G_2 and R_7. The three-electron terms can be written as (Judd, 1966)

$$H'_{\mathrm{CI}} = \sum_i T^i t_i, \tag{24}$$

where the sum runs over $i = 2, 3, 4, 6, 7$, and 8, and where the t_i are operators that transform according to definite irreducible representations of G_2 and R_7. A group-theoretical treatment of the configuration interaction problem has been given by Judd (1969).

(b) *Electrostatically correlated spin–orbit interaction*, which arises from coupling of configurations by the Coulomb interaction, eq. (9), and the spin–orbit interaction, eq. (15). This interaction can be written as (Judd et al., 1968)

$$H_{\mathrm{ESO}} = \sum_k P^k p_k, \tag{25}$$

where the p_k are spin-dependent two-electron operators, and where the sum runs over $k = 2$, 4, and 6.

(c) *Relativistic interactions*, which arise from the couplings of orbital and spin angular moments on different electrons (Breit, 1930). These interactions include the orbit–orbit interaction, the spin–spin interaction, and the spin–other-orbit interaction. The orbit–orbit interaction is usually ignored since it can be written in the form of eq. (23), and therefore its effect can be absorbed into the parameters α, β, and γ. Similarly, there is a contact term in the spin–spin interaction (Malli and Saxena, 1969) whose effects can be absorbed by the E^i in eq. (14). The remaining part of the spin–spin interaction transforms like a tensor of the second rank in orbital space and in spin space; the spin–other-orbit interaction is a first-rank tensor in both spaces (Judd, 1963). Both interactions may be parametrized in the form

$$H_{\mathrm{R}} = \sum_k M^k m_k, \tag{26}$$

where the Marvin integrals, M^k, are (Marvin, 1947)

$$M^k = \left(\frac{e\hbar}{2mc}\right)^2 \int_0^\infty \mathrm{d}r\, R_{4\mathrm{f}}^2(r) \int_r^\infty \mathrm{d}r'\, R_{4\mathrm{f}}^2(r') \frac{r^k}{r'^{k+3}}, \tag{27}$$

and where k has the values 0, 2, and 4.

Thus all the important interactions in the free-ion Hamiltonian can be represented by 19 parameters: the three E^i, ζ, α, β, γ, six T^i, three P^k, and three M^k. Numerous studies (Rajnak, 1965; Crosswhite et al., 1968, 1976, 1977; Carnall et al., 1976; Goldschmidt et al., 1968) have been performed to determine the

sensitivity of the $4f^q$ levels to the various interactions. A rough approximation to the energy levels, as well as adequate eigenfunctions, can be obtained with just the Coulomb and spin–orbit interactions. The interactions described in this subsection have been given in their relative order of importance; that is, in general,

$$H_{CI} > H'_{CI} > H_{ESO} \sim H_R. \tag{28}$$

Of course, the three-electron interaction H'_{CI} does not contribute at all in f^2 configurations.

Our interest in the free-ion Hamiltonian in this chapter is in its parametrization; that is, the 19 parameters (or some subset of them) are usually varied along with the appropriate set of crystal-field parameters (to be described later) in a least-squares fitting of the total Hamiltonian to experimental energy levels in order to obtain information about the host crystal. As explained earlier, a remarkable feature of lanthanide spectra in solids is that their gross features (e.g., positions of free-ion levels) are relatively insensitive to the nature of the host material. This feature can be exploited by using free-ion parameters obtained by fitting either another host crystal or the true free-ion spectrum to calculate matrix elements of the crystal field for the host material of interest, thus obviating the variation of free-ion parameters in the fit. In any event, an understanding of the free-ion Hamiltonian is useful in interpreting crystal-field calculations.

3.2. *Crystal-field interaction*

The crystal-field interaction in lanthanide-ion spectra in solids is weak in the sense that perturbations that shift the positions of the free-ion levels are small (compared to corresponding shifts in transition-metal spectra) and the effects of coupling different free-ion levels by the crystal field are small. The weakness of the lanthanide crystal-field interaction is a consequence of the shielding of the $4f^q$ configuration by the outer $5s^2$ and $5p^6$ atomic shells and is reflected in the historical sequence of theoretical advances in lanthanide crystal-field theory.

The electrostatic interaction between an electron at r situated on a lanthanide ion at the origin and the surrounding crystal lattice can be written as (Hüfner, 1978)

$$H_{CEF} = -e \int d\tau' \frac{\rho(r')}{|r - r'|}, \tag{29}$$

where $\rho(r')$ is the external charge distribution and where the integral is over the entire lattice. If $\rho(r')$ is completely external to the lanthanide ion, then $|r'| > |r|$ always, and we may expand the denominator of eq. (29) as follows

$$|r - r'|^{-1} = \sum_{k=0}^{\infty} \sum_{m=-k}^{k} \frac{r^k}{r'^{k+1}} C^{\dagger}_{km}(\hat{r}') C_{km}(\hat{r}), \tag{30}$$

and substitute this expansion into eq. (29) to obtain

$$H_{\mathrm{CEF}} = \sum_{km} A_{km}^{\dagger} \sum_{i} r_i^k C_{km}(\hat{r}_i), \tag{31}$$

where we have summed over all the electrons in the $4f^q$ configuration and where (Abragam and Bleaney, 1970)

$$A_{km} = -e \int \mathrm{d}\tau' \frac{\rho(r') C_{km}(\hat{r}')}{r'^{k+1}}. \tag{32}$$

Matrix elements of eq. (31) between $4f^q$ states can be represented by the parametrized form

$$H_{\mathrm{CEF}} = \sum_{km} B_{km}^{\dagger} \sum_{i} C_{km}(\hat{r}_i), \tag{33}$$

where the B_{km} are *crystal-field parameters*, given in the electrostatic model by

$$B_{km} = A_{km} \langle r^k \rangle, \tag{34}$$

where

$$\langle r^k \rangle = \int_0^{\infty} \mathrm{d}r\, R_{4f}^2(r)\, r^k. \tag{35}$$

The A_{km} are called *crystal-field components*. The parametrized crystal-field Hamiltonian is valid for a wide range of single electron–lattice interactions; the decoupling represented by eq. (34), however, breaks down when nonelectrostatic effects such as overlap of neighboring ions (ligands), exchange, and covalency are included. In interpreting experimental data, the B_{km} are usually treated as variable parameters in a least-squares fit.

3.2.1. *Operator equivalents*

Historically, the first extensive developments in crystal-field theory made use of the fact that the crystal-field coupling in lanthanide ions is small. In the *operator-equivalent method* (Stevens, 1952; Elliot and Stevens, 1953), the coupling of different free-ion levels by the crystal-field interaction is ignored and the crystal-field splitting of each $^{2S+1}L_J$ level is treated separately. Traditionally, in this method, the crystal-field Hamiltonian is written as

$$H_{\mathrm{CEF}} = \sum_{km} A_k^m \sum_{i} V_k^m(\mathbf{r}_i), \tag{36}$$

where the A_k^m are crystal-field components (related to those in eq. (31) by constant factors, to be discussed later), and the $V_k^m(\mathbf{r}_i)$ are polynomials in the x, y, and z coordinates of the ith electron. These polynomials are tabulated for $2 \leq k \leq 6$ and $|m| \leq k$ (Hüfner, 1978).

In the operator-equivalent method, one is concerned with matrix elements of eq. (36) within a given free-ion state denoted by $^{2S+1}L_J$. The V_k^m polynomials may be replaced as follows

$$\sum_i V_2^m(r_i) \rightarrow \alpha_J \langle r^2 \rangle O_2^m,$$

$$\sum_i V_4^m(r_i) \rightarrow \beta_J \langle r^4 \rangle O_4^m, \tag{37}$$

$$\sum_i V_6^m(r_i) \rightarrow \gamma_J \langle r^6 \rangle O_6^m,$$

where α_J, β_J, and γ_J are the *operator-equivalent factors* and where the O_k^m are *operator equivalents* formed from the V_k^m by replacing x, y, and z by J_x, J_y, and J_z, and symmetrizing the result, so that the O_k^m are Hermitean. These have been tabulated (Abragam and Bleaney, 1970). The operator-equivalent factors depend on the nature of the free-ion state $^{2S+1}L_J$ and have been extensively tabulated for low-lying levels of the $4f^q$ configuration (Stevens, 1952; Elliot and Stevens, 1953; Judd, 1955). In general, an intermediate-coupling calculation, as described earlier, is necessary to give accurate values of the α_J, β_J, and γ_J (Judd, 1955; Dieke, 1968). These do not depend strongly on the host crystal, and so this calculation need only be performed once for each lanthanide. Matrix elements of the O_k^m, on the other hand, depend only on the angular structure of the states; these also have been tabulated (Dieke, 1968; Abragam and Bleaney, 1970).

Crystal-field calculations based on the operator-equivalent method are performed by diagonalizing small matrices containing matrix elements of H_{CEF} within a given $^{2S+1}L_J$ state. The dimensions of these matrices are at most $(2J+1)\times(2J+1)$; often they are smaller because of the point-group symmetry of the lanthanide-ion site (more about this later). Matrices representing the crystal-field interaction are diagonalized simultaneously for several $^{2S+1}L_J$ states for which data on experimental energy levels exist, and the crystal-field parameters $A_k^m\langle r^k \rangle$ are determined in a least-squares fit to the data. This is a relatively straightforward procedure; often, if the crystal symmetry is high, analytic expressions for crystal-field splittings of low-J levels can be inverted to obtain the $A_k^m\langle r^k \rangle$ without recourse to a least-squares fit (Morrison and Farrar, 1964; Lea et al., 1962).

Unfortunately, the operator-equivalent method does not take into account the mixing of different free-ion levels by the crystal-field interaction (J-mixing). Consequently, the use of the method in crystals with strong fields (such as the garnets) can lead to considerable error. Nevertheless, it is quite useful for obtaining estimates of the crystal-field parameters from experimental measurements on an isolated level such as the $^4F_{3/2}$ of neodymium. In particular, the method works adequately in the Hund ground states of most of the lanthanide ions; hence, its popularity in computations relating to electron paramagnetic resonance (Abragam and Bleaney, 1970; see also Chapter 18, Volume 2 [Barnes, 1979] of this series), magnetic susceptibility, and Schottky contributions to the heat capacity, all of which involve only the crystal-field splitting of the ground state. As far as the fitting of energy levels derived from optical spectra is concerned, the method has had varying degrees of success. It is totally useless in cases such as Dy^{3+}, in which the ^6F and ^6H levels are so thoroughly mixed that

the concept of an isolated free-ion level has little meaning. For these reasons, the operator-equivalent method has been largely supplanted by methods in which J-mixing is included in fitting optical spectra.

3.2.2. *Different forms for* H_{CEF}

The crystal-field Hamiltonian that describes the interaction of a lanthanide ion with the host crystal lattice has been chosen in a number of different forms. Two of these have already been described; one, eq. (33), in terms of the irreducible spherical tensors C_{km} and the second, eq. (36), in terms of the V_k^m polynomials. A third notation, less common than the first two, is (Morrison et al., 1970)

$$H_{CEF} = \sum_{km} \bar{B}^{\dagger}_{km} U_{km}, \tag{38}$$

where the U_{km} are unit irreducible tensors introduced by Racah (1942b) defined by

$$U_{km} = \sum_{i} u_{km}(i), \tag{39}$$

and where the single-particle tensors $u_{km}(i)$ have unit reduced matrix elements between one-electron states (Nielson and Koster, 1963)

$$(l\|u_k\|l) = 1. \tag{40}$$

The notation of the operator-equivalent method has persisted although the method itself has largely been discarded. Thus, many of the reported results of fitting experimental data are given in the form $A_k^m\langle r^k\rangle$. These are related to the B_{km} of eq. (33) by simple coefficients. A simple relation also exists between the $\bar{B}_{km}$ of eq. (38) and the B_{km}:

$$B_{km} = [\sqrt{2l+1}\langle l(0)k(0)\,|\,l(0)\rangle]^{-1}\bar{B}_{km}, \tag{41}$$

TABLE 4
Conversion factors for crystal-field Hamiltonians.

k	m	$B_{km}/A_k^m\langle r^k\rangle$	$B_{km}/\bar{B}_{km}$
2	0	2	−0.73193
2	2	0.81650	−0.73193
4	0	8	0.88641
4	2	1.26491	0.88641
4	3	−0.33806	0.88641
4	4	0.95618	0.88641
6	0	16	−0.78285
6	2	1.56144	−0.78285
6	3	−0.78072	−0.78285
6	4	1.42539	−0.78285
6	6	1.05272	−0.78285

where the quantity in brackets is a Clebsch–Gordan coefficient (Rotenberg et al., 1959) and where $l = 3$ for f-electrons. We shall use the B_{km} throughout our discussion; whenever we report crystal-field parameters obtained in the literature, we will have converted them to B_{km}. The appropriate conversion factors for both $A_k^m\langle r^k\rangle$ and $\bar{B}_{km}$ are given in table 4.

3.2.3. *Symmetry*

Symmetry considerations have a profound effect on the interpretation of lanthanide spectra. We have already mentioned the effect of symmetry on selection rules for electric and magnetic dipole transitions and on the classification of crystal-field split energy levels. In this section, we consider the effect of symmetry on the crystal-field Hamiltonian itself.

The crystal-field Hamiltonian, H_{CEF}, must be invariant under all operations belonging to the point-symmetry group of the lanthanide-ion site. This symmetry is usually determined by X-ray and neutron-diffraction studies of the host crystal, which yield the space group of the entire crystal, the lattice constants, and the positions of all the constituents of the crystal within a unit cell. If X-ray or neutron-diffraction experiments have not been performed, the symmetry of the lanthanide-ion sites can be determined (although not with the same level of confidence) by electron paramagnetic resonance studies or by the optical spectrum itself. This symmetry must be known or assumed before the crystal-field calculation is initiated.

Invariance under the point-group operations requires that the crystal-field Hamiltonian contain only operators that transform as the identity representation of the point group. These operators are easy to determine in general, since, for all the point groups except the cubic groups (T, T_d, T_h, O, and O_h), all group operators may be constructed from the following operators (Leavitt, 1980):

(a) n-fold rotation about z, $R_z(2\pi/n)$;
(b) coordinate inversion, I;
(c) 2-fold rotation about x, $R_x(\pi)$.

It may be easily shown that the C_{km} transform as follows under these operations:

$$R_z(2\pi/n)C_{km} = \exp(-2\pi\, im/n)C_{km}, \tag{42a}$$

$$IC_{km} = (-1)^k C_{km}, \tag{42b}$$

$$R_x(\pi)C_{km} = (-1)^k C_{k,-m}. \tag{42c}$$

Further, since H_{CEF}, when acting between $4f^q$ states, connects two states of the same parity, odd-parity terms in H_{CEF} drop out and, from eq. (42b), k must be even. In addition, C_{km} is an irreducible tensor that connects single electron states with $l = 3$; therefore, by the triangular inequalities, we must have $0 \leq k \leq 6$. These considerations are sufficient to determine which B_{km} are nonvanishing for all point groups except the cubic groups. For the cubic groups, operations besides those in eqs. (42) are required; for these groups, the only nonvanishing B_{km} are B_{40}, B_{44}, B_{60}, and B_{64}, which are constrained by (Morrison et al., 1980a)

$$B_{44} = \frac{5}{\sqrt{70}} B_{40}, \qquad B_{64} = -\sqrt{\frac{7}{2}} B_{60}, \tag{43}$$

and are all real. The B_{km} are real in any symmetry group that contains a rotation about the y-axis by π or a reflection through the x–z plane; otherwise they are complex. In the latter case, one of the B_{km} ($m \neq 0$) can be made real by a rotation about the z-axis. The B_{km} for $m < 0$ are related to those for $m > 0$ by

$$B_{k,-m} = (-1)^m B_{km}^{\dagger}, \tag{44}$$

which follows from the hermiticity of H_{CEF} and from the properties of the C_{km}.

Table 5 lists, for each of the thirty-two point groups, the B_{km} that are nonzero. An example is given for each group (where available) of a crystal in which the lanthanide ion has the stated symmetry. The point groups are listed in sets, each of which has the same nonvanishing B_{km}. Thus, groups within a set are indistinguishable insofar as the symmetry properties of H_{CEF} are concerned. To distinguish groups within a set, the odd-parity part of the crystal-field interaction (which we have ignored in this discussion) must be examined. Equivalently, the point groups within a set can be distinguished by their different electric-dipole selection rules.

TABLE 5
Independent nonvanishing B_{km} for the 32 point groups

Group	Nonvanishing B_{km}	Example	Group	Nonvanishing B_{km}	Example
C_1 C_i	all B_{km} (B_{21} réal)	NdP_5O_{14}[a]	C_3 $S_6(C_{3i})$	$B_{20}, B_{40}, ReB_{43}, B_{60}, B_{63}, B_{66}$	$LiNbO_3$
C_2 $C_s(C_{1h})$ C_{2h}	$B_{20}, ReB_{22}, B_{40}, B_{42}, B_{44}, B_{60}, B_{62}, B_{64}, B_{66}$	LaF_3	D_3 C_{3v} D_{3d}	$B_{20}, B_{40}, ReB_{43}, B_{60}, ReB_{63}, ReB_{66}$	Y_2O_2S
D_2 C_{2v} D_{2h}	$B_{20}, ReB_{22}, B_{40}, ReB_{42}, ReB_{44}, B_{60}, ReB_{62}, ReB_{64}, ReB_{66}$	$Y_3Al_5O_{12}$	C_6 C_{3h} C_{6h} D_6 C_{6v} D_{3h} D_{6h}	$B_{20}, B_{40}, B_{60}, ReB_{66}$	$LaCl_3$
C_4 S_4 C_{4h}	$B_{20}, B_{40}, ReB_{44}, B_{60}, B_{64}$	$CaWO_4$			
D_4 C_{4v} D_{2d} D_{4h}	$B_{20}, B_{40}, ReB_{44}, B_{60}, ReB_{64}$	YVO_4	T T_d T_h O O_h	$B_{40}, ReB_{44}, B_{60}, ReB_{64}$[b]	Cs_2NaRCl_6

[a] Not considered here. [b] See eq. (43).

3.2.4. *Theoretical models*

An electrostatic model of crystal-field interactions can be developed in which the crystal-field components A_{km} defined by eq. (32) are expanded in a multipolar series (Hutchings and Ray, 1963). It is assumed that the lattice consists of a series of points, one for each ion in a lattice, that have multipolar moments associated with them that are defined by

$$Q_{km}(j) = \int \mathrm{d}^3 r\, \rho_j(r) r^k C_{km}(\hat{r}), \tag{45}$$

where $\rho_j(r)$ is the charge density of the jth ion and r is measured relative to the jth lattice point. In writing eq. (45), it is assumed that contributions to $\rho(r)$ can be identified as to which ions they arise from; the simplest way to ensure this is to require that there be no overlap between any pairs of ions in the lattice. Although this is never strictly true in practice, the multipolar expansion is still a useful parametrization of the crystal-field interaction.

The two-center expansion (Carlson and Rushbrooke, 1950) can be substituted into eq. (32) to obtain

$$A_{km} = -e \sum_{k'm'} (-1)^{k'} \binom{2k+2k'}{2k}^{1/2} \langle k(0)k'(0) \,|\, k+k'(0)\rangle \times \langle k(m)k'(m') \,|\, k+k'(m+m')\rangle \sum_j \frac{Q^{\dagger}_{k'm'}(j) C_{k+k',m+m'}(\hat{R}_j)}{R_j^{k+k'+1}}, \tag{46}$$

where $\binom{a}{b}$ is a binomial coefficient. The leading term in eq. (46), with $k' = m' = 0$, gives the point-charge contribution to the crystal field (with $Q_{00}(j) = eZ_j$) as follows

$$A^{pc}_{km} = -e^2 \sum_j \frac{Z_j C_{km}(\hat{R}_j)}{R_j^{k+1}}, \tag{47}$$

where the sum runs over all ions in the lattice.

The point-charge model has been used extensively in attempts to reconcile B_{km} obtained by fitting spectra with theoretical calculations. In its crudest form (Hutchings and Ray, 1963; Burns, 1965; Karayianis and Morrison, 1973; Faucher and Caro, 1977), valence charges (e.g., $Z_j = +3$ for R^{3+}, $Z_j = -2$ for O^{2-}) are used in eq. (47) and Hartree–Fock radial wave functions (Freeman and Watson, 1962) are used to evaluate $\langle r^k \rangle$ in eq. (34). When this model is used, the following general observations can be made:

(a) The calculated parameters B_{2m} are at least an order of magnitude too large;

(b) The calculated B_{4m} are the correct order of magnitude;

(c) The calculated B_{6m} are an order of magnitude too small.

Soon after the advent of the point-charge model, it was recognized that shielding of the crystalline field by the outer $5s^2$ and $5p^6$ shells of the lanthanide ion played an important role. This shielding results in eq. (34) being replaced by

$$B_{km} = A_{km} \langle r^k \rangle (1 - \sigma_k), \tag{48}$$

where the σ_k are ion-dependent, host-independent quantities: $\sigma_2 \sim 0.8$, $\sigma_4 \sim \sigma_6 \sim 0.1$. These have been calculated by numerous authors for several lanthanides (Burns, 1962; Sternheimer et al., 1968; Sengupta and Artman, 1970; Erdös and Kang, 1972).

The introduction of the shielding factors into the model largely rectified discrepancies in the B_{2m}. The largest discrepancy at this point remained in the B_{6m} (see (c) above); this fact led many authors to conclude that nonelectrostatic contributions account for the greatest part of the B_{6m} parameters. We believe that this conclusion is in error; in general, the electrostatic point-charge model can account for the observed magnitudes of the B_{6m} in most host crystals if it is recognized that Hartree–Fock radial wave functions do not give an adequate approximation to the true radial charge distribution. It is well known, for example, that Hartree–Fock calculations of the Slater parameters, F^k (see section 3.2.3), give values that are ~25% too large when compared with F^k deduced from spectra; this is generally believed to be due to the effects of configuration interaction. The same effects can be expected to modify the crystal-field interaction. We have parametrized these effects by scaling the Hartree–Fock wave functions, so that $r \rightarrow r/\tau$ everywhere, where τ is a scaling parameter (Leavitt et al., 1975). This scaling modifies the Hartree–Fock Slater integrals and radial matrix elements as follows (Karayianis and Morrison, 1975).

$$F^k = \tau F^k_{\mathrm{HF}}, \tag{49}$$

$$\langle r^k \rangle = \tau^{-k} \langle r^k \rangle_{\mathrm{HF}}. \tag{50}$$

Values of $\tau \sim 0.75$ have been found that simultaneously reconcile calculated F^k and calculated $\langle r^k \rangle$ with corresponding quantities determined by experiment.

The effects of covalency require that effective charges be used in eq. (47) that are, in general, different from the valence charges (they are usually smaller in magnitude) (Leavitt et al., 1975). These charges are treated as parameters to be varied in a fit of the model to experimentally determined B_{km}. The scaling parameter τ is assumed to be independent of the host crystal; it has been determined once and for all by considering lanthanide spectra in $CaWO_4$ (Leavitt et al., 1975; Morrison et al., 1977a). This procedure has been used with some success in a number of studies of lanthanides in various host crystals (Morrison et al., 1976, 1980; Karayianis et al., 1976; Morrison and Leavitt, 1979).

The point-charge model can be improved by considering the effects of higher multipole moments in eq. (46). Dipole and quadrupole contributions (terms with $k' = 1$ and 2 in eq. (46)) have been evaluated for $PrCl_3$ (Hutchings and Ray, 1963). It is possible to include the dipole contributions to the crystal field in a self-consistent manner (Morrison, 1976); in that treatment, point charge and dipole contributions to the electric field at various lattice sites are evaluated, and the dipole moments at these sites

$$\boldsymbol{p}_j = \alpha_j \boldsymbol{E}_j \tag{51}$$

are calculated, where $\boldsymbol{E}_j$ contains point-charge and dipole contributions and α_j is

the polarizability of the jth site. As the dipole contribution to $\boldsymbol{E}_j$ depends on all the $\boldsymbol{p}_j$, a set of simultaneous equations must be solved to obtain the dipole moments at all the sites. These may then be used to evaluate the dipole contributions to the crystal-field components via eq. (46). (The mth component of $\boldsymbol{p}_j$ is equal to $Q_{1,m}(j)$.)

The earliest calculations of the dipole and quadrupole contributions to the crystal field used free-ion values for the dipole polarizability, α_j, and for the quadrupole polarizability (Hutchings and Ray, 1963). It is generally recognized today, however, that the polarizability of an ion in a solid is generally much less than the corresponding value for the free ion (Chakrabarti et al., 1976; Bogomolova et al., 1977). How much less, however, is not clear. For this reason, therefore, computations of dipole and quadrupole contributions to the crystal field should be regarded as imprecise, even if they are performed with reduced polarizability values.

Calculations of nonelectrostatic contributions to the crystal field have been performed for several host crystals, including overlap, exchange, and charge-penetration contributions, none of which are accounted for by the simple electrostatic model given by eq. (32). The most extensively studied of these is the $PrCl_3$ lattice, for which 10 different contributions to the crystal-field have been isolated (Newman, 1971). In that study, good agreement was obtained between theory and experiment. However, in view of the neglect of configuration interaction (i.e., Hartree–Fock values of $\langle r^k \rangle$ were used) and the known incorrectness of the quoted value of the point-charge contribution to B_{20} (Gruber et al., 1981), these results should be regarded with suspicion.

In an attempt to parametrize the crystal-field interaction, Bradbury and Newman (1967) introduced the *superposition model*. In this model, it is assumed that the A_{4m} and A_{6m} are dominated by ligand (nearest-neighbor) contributions, which may be written as follows

$$A_{km} = \sum_j g_{km}(j)\bar{A}_k(R_j), \tag{52}$$

where j runs over the ligand ions and where g_{km} is a geometrical factor that depends only on the orientations of the ligands and not on their distances from the lanthanide ion. Thus, the g_{km} are calculated a priori and the $\bar{A}_k(R_j)$ are treated as parameters. Often the $\bar{A}_k(R_j)$ are parametrized further by means of a power-law dependence on R_j. There are thus two parameters for each k, or four in all. In cases of low point-group symmetry, this model reduces considerably the number of free parameters.

3.2.5. *Two-electron crystal-field effects*

Comparison of the single-electron crystal-field calculations performed by diagonalizing eq. (33) together with a free-ion Hamiltonian and experimental data has demonstrated conclusively that, in the great majority of cases, the single-electron model is adequate to account for observed crystal-field splittings of lanthanides in solids. There are, however, some irritating exceptions. Some

earlier studies based on the operator-equivalent method showed that different sets of crystal-field parameters were required to describe splittings of different $^{2S+1}L_J$ levels of the same lanthanide ion in the same host crystal. While much of the discrepancy can be attributed to the neglect of J-mixing in these studies, a few difficulties remain even after J-mixing is included. For example, it is notoriously difficult to obtain a fit to crystal-field splittings of the $4f^2$ configuration in Pr^{3+}; if this is attempted, large errors remain in the description of the $^1D_2$ level (and, to some extent, the $^1G_4$ level). This problem has been reviewed by Judd (1979) and Newman (1977b).

The theoretical origin of these difficulties is not hard to understand. The role of configuration interaction as a source of two-electron crystal-field effects was pointed out in 1964 (Rajnak and Wybourne, 1964). The parametrization of two-electron crystal-field interactions in terms of general two-electron operators was discussed (Bishton and Newman, 1970). Other mechanisms involving polarization of the ligands by transient electrostatic fields of the electrons associated with the lanthanide ion (Judd, 1976; Morrison, 1980) lead to two-electron operators of the same form as that given by Bishton and Newman.

A phenomenological method of handling the major contribution to the two-electron crystal-field interaction has been given (Judd, 1977; Newman, 1970); in this method, the C_{km} operators in eq. (33) are replaced by

$$C_{km}(\hat{r}_i)[1 + c_k(\boldsymbol{S} \cdot \boldsymbol{s}_i)], \tag{53}$$

where $\boldsymbol{S}$ is the total spin operator and $\boldsymbol{s}_i$ is the spin operator for the ith electron. Judd points out that, in order that the strong attractive exchange interaction between electrons of parallel spin lead to a contracted radial wave function, the coefficients c_k should be negative for all k. In addition, if configuration interaction makes up the major contribution to two-electron effects, the c_k should depend only on the lanthanide ion and not on the host crystal. They have been calculated for Gd^{3+} by Newman (1977a). Thus, they can be determined for each lanthanide by fitting data for one host crystal with extensively reported energy levels and fixed at the resultant values in analyses of other host materials. Judd has generalized this formalism (Judd, 1980) to account for charge transfer by introducing additional parameters multiplying $C_{km}(\hat{r}_i)$. In any event, only a few new parameters are introduced into the analysis, and the marked improvement that appears possible as a consequence seems well worth the effort of computing reduced matrix elements of the unit double tensors $V^{(1k)}$, which are necessary in the analysis of eq. (53). This useful modification of the crystal-field Hamiltonian does not appear to have taken hold as of yet; all the results of crystal-field analyses of experimental data that we report here are based on a one-electron crystal-field Hamiltonian.

3.3. *Intensities*

Transitions between states of the $4f^q$ configuration of lanthanide ions in crystals are known to originate predominantly through mixing of opposite-parity

states by odd-parity components of the crystal field. In the Judd–Ofelt theory of forced electric-dipole transitions (Judd, 1962; Ofelt, 1962), this concept is quantified by the use of perturbation theory and by the assumption that excited electronic configurations are degenerate. In this theory, the α-component of the effective electric dipole operator is given by (Leavitt and Morrison, 1980)

$$\mu_\alpha = -2e\sqrt{\frac{7}{3}}\sum_{k,t}(2t+1)N_k(t)(A^{(k)}U^{(t)})^{(1)}_\alpha, \tag{54}$$

where

$$N_k(t) = \sum_l \sqrt{2l+1}\,W(k133;tl)R_k(l)\langle l(0)1(0)\,|\,3(0)\rangle\langle 3(0)k(0)\,|\,l(0)\rangle, \tag{55}$$

where the sum runs over $l = 2$ and 4, $W(abcd;ef)$ is a Racah coefficient (Rose, 1957), and the $R_k(l)$ are given by

$$R_k(l) = \sum_n \langle 4f|r^k|nl\rangle\langle nl|r|4f\rangle/\Delta E_{nl}, \tag{56}$$

where the $\langle n'l'|r^k|nl\rangle$ are radial matrix elements of r^k between the states nl and $n'l'$ and ΔE_{nl} is the difference in energy between the configurations $4f^{q-1}nl$ (or $3d^94f^{q+1}$) and the ground configuration $4f^q$. In eq. (54), the quantity $(A^{(k)}U^{(t)})^{(1)}_\alpha$ represents the coupling of the irreducible tensors $A^{(k)}$ and $U^{(t)}$ by a Clebsch–Gordan coefficient to form a tensor of rank 1 and projection α. $A^{(k)}$ is a tensor whose components A_{km} are the crystal-field components given by eq. (32), and $U^{(t)}$ is a unit irreducible tensor. The sums in eq. (54) run over the values $k = 1$, 3, 5, and 7 and $t = 2$, 4, and 6.

The A_{km} can be calculated from a model such as the modified point-charge model presented in section 3.2.4, the $R_k(l)$ can be calculated as well, and matrix elements of μ_α can be computed between crystal-field split sublevels for a particular lanthanide ion in a particular host crystal a priori, without fitting experimental intensity measurements (Esterowitz et al., 1979a; Leavitt and Morrison, 1980). However, this method is not prevalent in the literature; rather, usually the theory is expressed in terms of a few adjustable parameters and a fit is made to intensity data. To this end, we consider the *line strength*, defined by (Condon and Shortley, 1959)

$$S^e_{J'J} = \sum_{i\ni J,\, f\ni J'} |\langle f|\boldsymbol{\mu}|i\rangle|^2, \tag{57}$$

where the sum is over all sublevels belonging to the levels J' and J. The line strength is a measure of the strength of induced electric-dipole transitions from level J to level J' and is easily related to measurable quantities such as absorption coefficients and Einstein A and B coefficients (Krupke, 1966; see also Chapter 24, Volume 3 [Carnall, 1979] and Chapter 35, Volume 4 [Weber, 1979a] of this series).

In the Judd–Ofelt theory, the line strength can be written as (Axe, 1963)

$$S^e_{J'J} = e^2\sum_t \Omega_t(\tau'J'\|U^{(t)}\|\tau J)^2, \tag{58}$$

where the Judd–Ofelt intensity parameters Ω_t are given by

$$\Omega_t = 28(2t+1)\sum_{km}\frac{|A_{km}|^2}{2k+1}N_k(t)^2, \tag{59}$$

and where $N_k(t)$ is given by eq. (55).

Thus, if we are concerned only with the line strength for transitions between J-levels (as opposed to crystal-field split sublevels), the intensities are characterized by three parameters Ω_2, Ω_4, and Ω_6. Selection rules imposed by the reduced matrix elements of $U^{(t)}$ in eq. (58) are

$$\Delta L \leq 6, \qquad \Delta S = 0, \qquad \Delta J \leq 6. \tag{60}$$

The first two of these hold strictly only in the limit of Russell–Saunders coupling; the third is true whenever J-mixing by the crystal field is negligible. In fact, eq. (58) also holds only in the limit of no J-mixing. The form given in eq. (58) has been used extensively in analyzing experimental intensity data (see, for example, Reisfeld and Jørgensen, 1977); we will report values for the Ω_t whenever they are available.

Magnetic-dipole transitions also are allowed between states of the $4f^q$ configuration. The magnetic-dipole operator is

$$\boldsymbol{M} = \frac{-e\hbar}{2mc}(\boldsymbol{L} + g_e\boldsymbol{S}), \tag{61}$$

where g_e is the electron g-factor, equal to 2.00233. The line strength can be written as

$$S^m_{J'J} = \sum_{i\ni J, f\ni J'}|\langle f|\boldsymbol{M}|i\rangle|^2, \tag{62}$$

which becomes using eq. (61),

$$S^m_{J'J} = \left(\frac{e\hbar}{2mc}\right)^2(\tau'J'\|\boldsymbol{L} + g_e\boldsymbol{S}\|\tau J)^2. \tag{63}$$

The reduced matrix element in eq. (63) depends only on the free-ion Hamiltonian and not on the crystal field, and therefore the study of magnetic dipole transitions gives little information on the crystal interactions. Nevertheless, in making accurate comparisons of calculated intensities to experimental data, the magnetic-dipole transitions should be accounted for. Interference between electric and magnetic dipole intensities has been considered for ions in a Zeeman field (Van Siclen, 1981). Other mechanisms such as electric-quadrupole interactions and phonon coupling also lead to f→f transitions, but these mechanisms are generally weaker than those considered here and will not be discussed further. Peacock (1975) has given an extensive review of the various mechanisms contributing to lanthanide-ion intensities.

4. Explanation of tables

The following section presents crystallographic data, crystal-field parameters, intensity parameters, and experimental energy levels for lanthanides in 26 host materials. Because of space limitations, the data are presented in a highly condensed format, which requires some interpretation. This section is devoted to explaining these tables. Each subsection on an individual host material will contain introductory paragraphs that discuss selected features such as the growth of the material, index of refraction as a function of wavelength, physical properties, optical measurements not given in the tables, and some technological applications, with the appropriate references, where available.

4.1. *Crystallographic data*

Crystallographic data are invaluable in the interpretation of experimental optical spectra, both in identifying the symmetry of the lanthanide ion site and in providing input data to a superposition analysis (Newman, 1970) or to an ab initio crystal-field calculation. Crystallographic data are presented in a short table for each host that lists the following information:

(a) The crystal class (i.e., triclinic, monoclinic, orthorhombic, tetragonal, trigonal, hexagonal, or cubic);

(b) The full space-group symbol and the identifying number in the International Tables (Henry and Lonsdale, 1969) (from #1 to #230, one for each possible space group);

(c) The number of chemical formula units per unit cell, Z;

(d) The setting, if there is more than one for that space group in the International Tables;

(e) The position (site type in the International Tables), site symmetry (in the Schoenflies notation), and general x, y, z coordinates (expressed as fractions of the lattice constants) for that site type, for each constituent of the host crystal;

(f) The lattice constants a, b, and c (in Å) and angles α, β, and γ (in degrees and decimal parts);

(g) x, y, and z coordinates for each constituent, where necessary. If a site has coordinates 0, 1/2, 1/2, these will be designated under (e), and no entry for that site will be made under (g). On the other hand, if a site has coordinates 0.2602, 0.0275, 1/2, these will be designated as x, y, 1/2 under (e), and the specific values $x = 0.2602$, $y = 0.0275$ will be listed under (g). A discussion of the International Tables is given by Burns (1977).

4.2. *Index of refraction*

We have attempted to include in the tables a listing of the index of refraction data covering the visible and near-infrared. In cases where little data exists, we have included these data in the introductory paragraphs rather than in the tables. In some cases, we have not been able to find any index of refraction data.

4.3. *Crystal-field parameters*

Crystal-field parameters that were obtained by fitting the optical spectra for various lanthanides in the host crystal are reported. In cases where more than one such analysis appears in the literature for a given lanthanide, we report all sets of B_{km} that are appreciably different. In all cases, we have converted reported crystal-field parameters to the Wybourne notation (eq. (33)) by means of the conversion factors listed in table 4. In addition, if the B_{km} are complex, we have rotated the coordinate system such that the first B_{km} in table 5 with $m > 0$ is real.

In general, the variation of the reported B_{km} across the lanthanide series should be smooth, although this is not always the case. The reader should exercise caution in interpreting the values quoted in the tables of crystal-field parameters, for the following reasons:

(a) Neglect of J-mixing can substantially affect the B_{km}. Most recent analyses include the effects of J-mixing; however, earlier results may neglect J-mixing.

(b) The free-ion Hamiltonian and resultant free-ion wavefunctions used to calculate reduced matrix elements of the crystal-field interaction may not be accurate. The most favorable situation in fitting experimental data is the diagonalization of a many-parameter free-ion Hamiltonian, together with the crystal-field Hamiltonian, in a basis that spans the entire $4f^q$ configuration (Crosswhite et al., 1976). Unfortunately, this method is extremely time-consuming, as the matrices involved are large, and a large quantity of experimental data is required to ensure its success. Therefore, methods have been developed to truncate the basis to include only the first several low-lying levels and to either neglect the remaining levels or to treat them by second-order perturbation theory (Hüfner, 1978). One particular method (Morrison et al., 1977b; Morrison and Leavitt, 1979) is to treat the free-ion levels as adjustable parameters to be varied along with crystal-field parameters in fitting the data. These methods unavoidably bias the crystal-field parameters because of the effect of neglecting upper levels. These effects can be made small, however, by ensuring that the neglected levels are far removed from those that are considered.

(c) In some instances, the theoretical model may not be adequate, and two-electron effects may affect the quoted one-electron parameters. As mentioned in section 3, attempts to fit the data by a one-electron Hamiltonian in cases where two-electron effects are significant will lead to a term dependence of the B_{km}.

(d) In all fitting methods, the problem of multiple minima arises, particularly when fitting spectra in host materials where the lanthanide ion is in a site of low symmetry (see section 2). The question of which minimum to select in these cases is not entirely clear; in any event, the minimum found by fitting is not necessarily the global minimum.

(e) Many of the crystal-field analyses in the literature report errors in the crystal-field parameters. In a least-squares fit, the rms deviation can be expanded in a Taylor series in the B_{km} about the minimum value, and the variance–

covariance matrix can be calculated. This matrix provides a great deal of information not only about the errors in the B_{km} but also about how the various B_{km} are correlated. This valuable technique should be incorporated as a standard feature in future crystal-field analyses of experimental data. Unfortunately, this is not the case today, and error estimates that accompany crystal-field analyses today include not only the variance–covariance method but also other methods that range from educated guesses to error estimates based on individual variations of the B_{km} that produce a stated increase in the rms deviation.

We have mentioned just a few of the problems that may occur in comparing results of two different crystal-field analyses. These should be sufficient to make the reader aware of the difficulties that can arise; we strongly advise the reader to consult the original references if he is to make use of crystal-field parameters in the tables.

4.4. *Intensity parameters*

Judd–Ofelt parameters are listed in the tables for each lanthanide in each host when they are available in the literature. In most cases, they are determined by fitting absorption intensities. As is the case with crystal-field parameters, we simply list the Ω_t, and we do not attempt to give any details on the manner in which the parameters were derived and their accuracy. In each host, we refer the interested reader to the published literature for further details.

4.5. *Experimental energy levels*

Experimental energy levels obtained from absorption and fluorescence measurements are reported for each lanthanide, where available, for all 26 host crystals. We present the data in a condensed format in order to conserve space. Each table (one for each lanthanide in each host crystal) presents the ion–host combination and a list of energy levels for each $^{2S+1}L_J$ state. In cases where crystal-field splittings for two or more states overlap, we present these together and make no attempt to identify which crystal-field split levels belong to which free-ion states. For each state, we list energy levels such that the last three digits to the left of the decimal point (plus whatever is to the right of the decimal point) are tabulated for each level, and the remaining digits ("prefix") are listed to the left for all digits. An asterisk to the right of an entry indicates that, for that entry and all following entries the prefix should be increased by unity. As an example, for $Pr:Y_3Al_5O_{12}$ (section 5.20), we have the following:

State	Prefix	Energy (cm^{-1})
$^1G_4$	9	718 781 829 121* 275

which gives the energy levels of the $^1G_4$ state 9718, 9781, 9829, 10 121, and 10 275. Also listed in each table is the temperature (in K) at which the data were obtained.

Much of the information that is available in the literature is not tabulated here. This includes the following:

(a) Point-group irreducible representations or crystal quantum numbers, which can be obtained from polarized spectra by using selection rules (see section 2). These should be obtained from the original references in which the spectra are reported, as they are invaluable in performing crystal-field calculations.

(b) Zeeman splitting measurements, which aid in assigning experimental levels.

(c) Information concerning the accuracy of the measurements. Most of the data reported here are accurate to $\sim 1\,\mathrm{cm}^{-1}$. Some instances exist where the accuracy is much better than this, however; we will report the data in these cases to one or two decimal places, and the reader can consult the individual cases for details.

(d) Crystal-field calculations, which can help tremendously in assigning and interpreting optical spectra, especially in cases of low symmetry.

It is hoped that this section has given the reader a clear description of the not-too-obvious aspects of the tables and an indication of the difficulty involved in the interpretation of optical spectra of impurity ions. These tables should not be an end unto themselves but should serve as starting points. Readers interested in particular host materials should by all means consult the original references on these materials.

5. Presentation of experimental data

5.1. $LaCl_3$

The optical spectra of R^{3+} in lanthanum trichloride ($LaCl_3$) are probably the most completely studied of those belonging to any host material. Dieke (1968) gives an excellent review of the experimental data and results of its analysis as of 1968; the results since 1969 have been summarized by Crosswhite (1977). The energy levels of the entire R^{3+} series resulting from the experimental and theoretical analysis of the spectra of these ions in $LaCl_3$ have been presented by Dieke and coworkers at Johns Hopkins University in the form of a chart. These charts (Dieke and Crosswhite, 1963), "Dieke Charts", have been invaluable in the analysis of the spectra of rare-earth ions in new host materials and have been practically a necessity in the technological application of rare-earth ions to lasers. The hygroscopic nature (Spedding and Daane, 1961) of $LaCl_3$ has hindered the application of this material to practical devices such as lasers or quantum counters.

The indices of refraction of $LaCl_3$ have been measured by LaFrance (1970) and are given by the Sellmeier equation

$$n^2(\lambda) = 1 + C\lambda^2/(\lambda^2 - B),$$

where for the ordinary ray $C = 2.235$ and $B = 0.01734$ $(\mu m)^2$, and for the extraordinary ray $C = 2.469$ and $B = 0.017674$ $(\mu m)^2$, and where λ is in μm.

5.1.1 Crystallographic data for $LaCl_3$

Hexagonal $P6_3/m$, #176, Z = 2

Ion	Pos.	Symm.	x	y	z
La	2(c)	C_{3h}	1/3	2/3	1/4
Cl	6(h)	C_s	x	y	1/4

X-ray data

		Cl		
a	c	x	y	Ref.
7.4779	4.3745	0.38741	0.30155	1

5.1.2 Crystal-field parameters for R:$LaCl_3$ (cm^{-1})

R	B_{20}	B_{40}	B_{60}	B_{66}	Ref.
Ce	129	-326	-997	403	2
Pr	95	-325	-634	449	3
Pr	107	-342	-677	466	4
Nd	195	-309	-711	466	5
Nd	163	-336	-713	462	4
Pm	143	-395	-666	448	4
Sm	162	-182	-710	448	6
Sm	186	-270	-623	470	4
Eu	178	-300	-820	521	7
Eu	189	-287	-801	525	4
Gd	195	-340	-480	305	8
Gd	216	-272	-688	474	4
Tb	184	-320	-480	305	9
Tb	185	-291	-457	302	4

Crystal-field parameters for R:$LaCl_3$ (cm^{-1}) (continued)

R	B_{20}	B_{40}	B_{60}	B_{66}	Ref.
Dy	183	-312	-371	271	6
Dy	193	-328	-470	287	4
Ho	227	-271	-445	291	10
Ho	216	-282	-444	297	11
Ho	216	-284	-448	294	4
Er	188	-298	-425	279	12
Er	216	-271	-411	272	4
Tm	227	-241	-424	256	13

5.1.3 Intensity parameters for R:$LaCl_3$ (10^{-20} cm^2)

R	Ω_2	Ω_4	Ω_6	Ref.
Pm	0.97	1.63	1.66	14

5.1.4 Energy levels for R:$LaCl_3$

Ce:$LaCl_3$

Term	Prefix	Energy (cm^{-1})				T	Ref.
$^2F_{5/2}$	-	0	37.5	110.0		90	2
$^2F_{7/2}$	2	166.0	208.6	282.6	399.5	90	2

Pr:$LaCl_3$

Term	Prefix	Energy (cm^{-1})						T	Ref.
$^3H_4$	-	0	33.1	96.4	130.2	137.0		4.2	15
$^3H_5$	2	137.2	169.8	188.5	202.2	222.6		4.2	15
$^3H_6$	4	230.4	295.3	423.1	431.0			4.2	15
$^3F_2$	4	922.6	950.4					4.2	15
$^3F_3$	6	279	303.5	308.5	352.1	367.2		4.2	15
$^3F_4$	6	700.6	751.5	772.1	782	785.7	804.3	4.2	15
$^1G_4$	9	733.5	762.9	772.2	806.6	927		4.2	15

$Pr:LaCl_3$ (continued)

Term	Prefix	Energy (cm^{-1})						T	Ref.
$^1D_2$	16	630.5	730.9	780.5				4.2	15
$^3P_0$	20	474.8						4.2	15
$^3P_1$	21	066.4	096.2					4.2	15
$^1I_6$	21	298.9	301.1	395.6	411.4			4.2	15
$^3P_2$	22	207.0	226.0	246.7				4.2	15
$^1S_0$	48	800						4.2	16

$Nd:LaCl_3$

Term	Prefix	Energy (cm^{-1})						T	Ref.
$^4I_{9/2}$	-	0	115.39	123.21	244.40	249.35		4.2	17,18
$^4I_{11/2}$	1	973.85	012.58*	026.90	044.19	051.60	058.90	4.2	17,18
$^4I_{13/2}$	3	931.84	974.88	998.89	012.92*	031.86	042.08	4.2	17,18
	3	083						4.2	17,18
$^4I_{15/2}$	5	869.3	942.4	992.2	079.5*	154.2		4.2	17,18
$^4F_{3/2}$	11	423.90	453.91					4.2	17,18
$^4F_{5/2}$, $^2H_{9/2}$	12	458.37	480.65	487.67	536.14	557.73	643.52	4.2	17,18
	12	662.91						4.2	17,18
$^4F_{7/2}$, $^4S_{3/2}$	13	396.05	400.02	474.53	488.08	527.22	529.37	4.2	17,18
	13	531.23	533.33					4.2	17,18
$^4F_{9/2}$	14	705.73	710.70	715.30	721.87	759.25		4.2	17,18
$^2H_{11/2}$	15	907.08	923.91	948.12	953	960.77		4.2	17,18
$^4G_{5/2}$, $^2G_{7/2}$	17	095.12	165.17	228.75	297.44			4.2	17,18
$^4G_{7/2}$	18	993.59	012.88*	042.24	078.02			4.2	17,18
$^2G_{9/2}$	19	430.93	434.75	454.60	458.72	546.65	556.10	4.2	17,18
	19	653.67						4.2	17,18
$^4G_{9/2}$,$^2D_{3/2}$,$^4G_{11/2}$	21	029.08	042.33	161.71	187.72	369.56	393.35	4.2	17,18
	21	407.90						4.2	17,18
$^4G_{11/2}$, $^2K_{15/2}$	21	465.95	527.55	554.38	572.64	651.16		4.2	17,18
$^2P_{1/2}$, $^2D_{5/2}$	23	214.93	759.73	778.42				4.2	17,18
$^2P_{3/2}$	26	134.85						4.2	17,18
$^4D_{3/2}$, $^4D_{1/2}$	27	972.88	975.68	514.52*				4.2	17,18
$^2I_{11/2}$	29	218.34	314.53	320.19	327.76			4.2	17,18
$^2L_{15/2}$, $^2I_{13/2}$	30	042.85	110.82	165	252	289.90	603	4.2	17,18

Nd:$LaCl_3$ (continued)

Term	Prefix	Energy (cm^{-1})					T	Ref.
$^2L_{17/2}$	31	608.9	628.9				4.2	18
$^2H_{9/2}$	32	683	754.8	785.5			4.2	18
$^2H_{11/2}$, $^2D_{5/2}$	33	387	043.3*	048.8	127.9	235.3	4.2	18
$^2F_{5/2}$, $^2F_{7/2}$	38	219	267	637*	664		4.2	18

Pm:$LaCl_3$

Term	Prefix	Energy (cm^{-1})						T	Ref.
$^5I_4$	-	0	66.6	84.5	100.1	127.0	240.0	298	19
$^5I_5$	1	537	550	583	598	620	620	298	19
$^5I_6$	3	170	211	238				298	19
$^5I_7$	4	893	897	905	918	933		298	19
$^5I_8$	6	525	543	580	621	722	752	298	19
$^5F_1$	12	333.8	349.9					4.2	19,20
$^5F_2$	12	757.4	770.6	811.0				4.2	19,20
$^5F_3$	13	584.2	588.6	606.8	650.6			4.2	19,20
$^5S_2$	14	200.0						4.2	19,20
$^5F_4$	14	529.9	578.3	582.2	609.9			4.2	19,20
$^5F_5$	15	868.2	888.0	894.8	908.8	912.8		4.2	19,20
$^3K_6$	16	883.0	887.6	893.8	903.1	920.6	926.9	4.2	19,20
$^5G_2$	17	446.3	512.6	537.5				4.2	19,20
$^3H_4$	17	829.8						4.2	19,20
$^3K_7$, $^5G_3$	17	923.0	029.0*	098.7	143.5	168.3	170.5	4.2	19,20
	17	197.1	254.0	280.7	287.8	302.7		4.2	19,20
$^3K_8$	19	725.3	730.7	792.4	807.3	822.8		4.2	19,20
$^5G_5$	19	972.5	018.3*	037.9	061.4			4.2	19,20
$^5G_4$	20	116.4	150.0	172.4	192.7	208.3		4.2	19,20
$^3G_3$	21	660.4	674.0	680.0				4.2	19,20
$^5G_5$	22	106.9	127.9	140.5	149.3			4.2	19,20
$^5G_6$	22	396.0						4.2	19,20
$^3D_2$	22	936.5	983.0					4.2	19,20

$Pm:LaCl_3$ (continued)

Term	Prefix	Energy (cm^{-1})						T	Ref.
$^3L_7$	23	592.8	602.5	657.3				4.2	19,20
$(^3P, ^3D)_1$	24	018.0						4.2	19,20
$^3H_6$	24	401.5	446.0	525.0				4.2	19,20
$^3G_4, ^5G_4$	24	602.0	617.5	631.0	643.0			4.2	19,20
$^3L_8$	24	730.2	760.3	792.4	798.2			4.2	19,20
$^3D_3, ^3P_0$	25	584.2	612.7	656.6				4.2	19,20
$^3M_8, ^3P_2$	25	974.7	272.3*	307.6				4.2	19,20
$^3F_4, ^3G_5$	27	027.9	113.6	146.6				4.2	19,20
$^3P_2, ^3I_5$	28	632.8						77	19
$^3F_3, ^3M_9, ^5D_0$	29	209.2	599.0					77	19
$^5D_1, ^3I_7, ^1L_8$	30	034.0						77	19
$^5D_2, ^1L_8, ^5D_3$	30	862.0	660.5*					77	19

$Sm:LaCl_3$

Term	Prefix	Energy (cm^{-1})						T	Ref.
$^6H_{5/2}$	-	0	40.7	66.1				77	21,6
$^6H_{7/2}$	0	992.8	051.2*	104.7	172.6			4.2	21,6
$^6H_{9/2}$	2	211.7	230.2	308.0	324.5	376.9		4.2	21,6
$^6H_{11/2}$	3	522.7	571.1	599.6	614.0	646.0	697.9	4.2	21,6
$^6H_{13/2}$	4	957.38	968.06	988.0	997.35	023.1*	034.0	4.2	6
$^6H_{15/2}, ^6F_{1/2}$	5	767.0	280.3*	331.5	725.6			4.2	21
$^6F_{3/2}$	6	737.6	738.1					4.2	21
$^6F_{5/2}$	7	046.80	051.9					4.2	21,6
$^6F_{7/2}$	7	871.07	900.94	931.26	937.06			4.2	6
$^6F_{9/2}$	9	047.60	052.76	088.46	114.20			4.2	21,6
$^6F_{11/2}$	10	449.25	468.15	478.83	480.17			4.2	6
$^4G_{5/2}$	17	849.55	870.85					4.2	21
$^4F_{3/2}$	18	857.21						4.2	21
$^4G_{7/2}$	20	003.27	014.01					4.2	21
$^4I_{9/2}$	20	454.35	518.02	565.13	707.90	752.21		4.2	21

$Sm:LaCl_3$ (continued)

Term	Prefix	Energy (cm^{-1})						T	Ref.
$^4I_{11/2}$, $^4I_{13/2}$	20	976.68	519.77*	545.50	594.14			4.2	21
$^4F_{5/2}$,$^4G_{9/2}$,$^6P_{5/2}$	22	115.69	134.73	137.00	515.88	518.06	528.73*	4.2	21
	22	774.34	803.34					4.2	21
$^6P_{3/2}$, $^4L_{13/2}$	24	519.92	520.30	530.73	533.04	534.95	550.69	4.2	21
	24	553.43	563.93	566.64	569.53			4.2	21
$^4F_{9/2}$, $^4K_{11/2}$	24	824.95	836.07	051.41*	072.54	086.22	520.01	4.2	21
	24	522.72	547.73	566.14	678.85			4.2	21
$^4K_{11/2}$	26	300.11	328.78	350.29	352.36	502.19	627.97	4.2	21
	26	674.38	797.30	835.03				4.2	21
?	27	284.64	314.65	356.50	402.00	419.35	096.96*	4.2	21
	27	113.94	188.22	607.06				4.2	21
?	28	621.58	739.08	765.78	785.78	806.27	887.62	4.2	21
	28	050.85*						4.2	21

$Eu:LaCl_3$

Term	Prefix	Energy (cm^{-1})						T	Ref.
$^7F_0$	-	0						4	7
$^7F_1$	-	355.05	405.27					4	7
$^7F_2$	1	022.54	027.52	084.33				4	7
$^7F_3$	1	846.77	862.41	880.36	900.61	919.70		4	7
$^7F_4$	2	751.48	833.30	866.87	867.38	903.14	041.15*	4	7
$^7F_5$	3	801.98	838.74	844.31	918.05	957.10	992.70	4	7
	3	010.01*						4	7
$^7F_6$	4	907.35	930.05	949.63	967.42			4	7
$^5D_0$	17	267.35						4	7
$^5D_1$	19	025.61	034.37					4	7
$^5D_2$	21	494.18	504.70	513.42				4	7
$^5D_3$	24	373.85	388.12	408.55				4	7
$^5D_4$	27	610.97	628.01	630.72	661.32			4	7
$^5L_9$	27	891.40	901.56	912.87	914.71	972.28	976.60	4	7
$^5L_{10}$	28	372.34	376.64					4	7
$^5H_3$, $^5H_7$	31	272.47	295.87	385.27	400.29	400.85		4	7
$^5H_4$	31	448.64	472.92	490.09	506.19			4	7

$Gd:LaCl_3$

Term	Prefix	Energy (cm^{-1})						T	Ref.
$^8S_{7/2}$	-	0						1.5	22,8
$^6P_{7/2}$	32	101.86	119.23	130.87	133.64			1.5	22
	32	100.35	117.97	129.81	132.62			1.7	8
$^6P_{5/2}$	32	702.63	723.28	726.93				1.5	22
	32	702.42	723.15	726.84				1.7	8
$^6P_{3/2}$	33	281.20	295.96					1.5	22
	33	(282.39)	295.65					1.7	8
$^6I_{7/2}$	35	842.44	847.47	853.36	853.46			1.5	22
	35	842.93	847.97	853.80	853.80			1.7	8
$^6I_{9/2}$	36	184.80	191.52	192.58	196.84	208.76		1.5	22
	36	185.30	191.92	193.13	197.30	205.23		1.7	8
$^6I_{17/2}$	36	239.50	239.50	241.78	247.20	247.20	248.38	1.5	22
	36	239.50	240.27	242.19	246.23	247.11	248.92	1.7	8
	36	248.38	251.88	251.88				1.5	22
	36	248.92	251.53	252.43				1.7	8
$^6I_{11/2}$	36	460.84	465.56	467.78	474.42	474.92	483.08	1.5	22
	36	461.31	465.82	468.24	475.24	475.24	483.48	1.7	8
$^6I_{15/2}$	36	578.82	582.15	582.15	586.23	586.23	590.88	1.5	22
	36	579.23	582.59	583.70	586.46	586.99	591.48	1.7	8
	36	596.79	599.95					1.5	22
	36	597.24	600.31					1.7	8
$^6I_{13/2}$	36	613.55	616.31	620.68	622.93	624.95	631.33	1.5	22
	36	614.15	616.80	621.01	623.14	625.57	631.71	1.7	8
	36	636.14						1.5	22
	36	636.51						1.7	8
$^6D_{9/2}$	39	534.85	543.60	556.75	563.90	577.70		1.5	22
	39	535.83	544.63	557.65	564.84	578.54		1.7	8
$^6D_{1/2}$	40	491.25						1.5	22
$^6D_{7/2}$	40	579.70	583.85	589.75	593.10			1.5	22
	40	580.81	584.70	590.23	593.68			1.7	8
$^6D_{3/2}$	40	729.7	761.1					1.5	22
$^6D_{5/2}$	40	882.9	893.4	(926.0)				1.5	22

$Tb:LaCl_3$

Term	Prefix	Energy (cm^{-1})						T	Ref.
$^7F_6$	-	0	56.83	90.56	97.22	99.31	104.64	4	9
	-	112.80	117.99					4	9
$^7F_5$	2	043.26	080.34	096.76	112.81	151.53	167.79	4	9
	2	200.44						4	9
$^7F_4$	3	266.42	354.21	362.84	373.27	397.63	437.69	4	9
$^7F_3$	4	325.97	346.65	348.06	363.97	379.20		4	9
$^7F_2$	4	973.92	036.10*	037.55				4	9
$^7F_1$	5	440.14	487.78					4	9
$^7F_0$	5	700.93						4	9
$^5D_4$	20	462.60	468.61	472.29	490.21	495.75	496.06	4	9
$^5D_3$, $^5D_{10}$	26	267.30	269.10	270.33	271.69	280.51	373.67	4	9
	26	393.48	397.26	398.33	402.14	423.20	456.61	4	9
	26	480.66	881.23	972.68	008.71*	044.40	051.46	4	9
	26	057.95	770.85	777.41	782.22	785.16	787.76	4	9
	26	805.68	809.53	814.40	822.32			4	9
$^5D_2$	28	147.91	357.36	426.67	437.67	468.21		4	9
?	29	184.43	194.06	236.06	245.63	426.50	436.46	4	9
?	29	481.79	492.96	555.18				2	9
?	31	347.08	362.12	366.46				2	9
?	32	857.36	869.43	881.58	885.86	930.72	971.69	2	9
?	33	721.22	787.71					2	9
?	34	814.86	816.09	818.35	820.29	824.93	844.72	2	9
	34	869.68						2	9
?	35	005.10	012.42	081.83	082.83	088.83	089.40	2	9
	35	098.87	106.40	107.47	269.34			2	9

$Dy:LaCl_3$

Term	Prefix	Energy (cm^{-1})						T	Ref.
$^6H_{15/2}$	-	0	9.82	9.97	15.65	40.75	80.48	4.2	23
	-	121.65	140.51					4.2	23
$^6H_{13/2}$	3	457.03	490.30	493.13	522.31	546.62	551.93	4.2	23
	3	556.60						4.2	23
$^6H_{11/2}$	5	793.28	801.42	842.54	850.29	860.69	864.68	4.2	23
$^6H_{9/2}$, $^6F_{11/2}$	7	592.16	593.59	598.01	612.9	660.33	669.52	4.2	23
	7	675.08	698.97	746.5				4.2	23

Dy:$LaCl_3$ (continued)

Term	Prefix	Energy (cm^{-1})						T	Ref.
$^6H_{7/2}$, $^6F_{9/2}$	8	937.16	944.40	952.14	975.06	981.14	999.32	4.2	23
	8	011.78*	091.57					4.2	23
$^6H_{5/2}$, $^6F_{7/2}$	10	124.48	151.57	913.36	917.16	922.23	949.45	4.2	23
$^6F_{5/2}$	12	315.60	317.87	336.08				4.2	23
$^6F_{3/2}$	13	114.47	116.84					4.2	23
$^4F_{9/2}$	20	963.31	066.91*	097.18				4.2	23,24
$^4I_{15/2}$	21	954.07	174.42	175.47	193.12	207.49	226.41	4.2	23,24
	21	247.30						4.2	23,24
$^4G_{11/2}$	23	215.12	302.76	337.65	352.22	367.68	375.02	4.2	23,24
	23	379.79						4.2	23,24
?	24	938.52	938.85	944.62				?	24
?	25	571.32	604.68	616.11	621.91	622.68	635.87	?	24
	25	653.04	686.16	701.21	702.63	709.79		?	24
?	26	089.14	098.72	100.58	104.99	116.05	163.35	?	24
	26	196.28							
?	27	260.25	289.71	291.43	827.10	326.17*		4.2	23
?	29	467.81	481.59	489.88	866.96	583.30*	996.51	4.2	23
?	31	462.30	978.10*	992.81				4.2	23
?	33	262.40	443.90	781.50	600.17*			4.2	23
?	35	744.48	279.36*					4.2	23

Ho:$LaCl_3$

Term	Prefix	Energy (cm^{-1})						T	Ref.
$^5I_8$	-	0	12.51	43.80	66.42	89.92	104.12	4.2	25
	-	118.40	154.21	155.41	203.69	212.78		4.2	25
$^5I_7$	5	119.50	120.39	131.78	149.80	154.38	157.92	4.2	25
	5	174.13	175.47	176.08	176.59			4.2	25
$^5I_6$	8	636.98	637.21	638.46	638.77	649.46	653.56	4.2	25
	8	666.64	685.60	692.95				4.2	25
$^5I_5$	11	199.80	204.75	207.84	208.70	224.56	240.05	4.2	25
	11	249.15						4.2	25
$^5I_4$	13	185.87	262.69	272.75	274.81	307.45		4.2	25

Ho:$LaCl_3$ (continued)

Term	Prefix	Energy (cm^{-1})						T	Ref.
$^5F_5$	15	458.94	466.11	466.80	479.14	482.48	485.17	4.2	25
	15	517.68						4.2	25
$^5S_2$	18	429.88	432.11					4.2	25
$^5F_4$	18	514.47	525.52	539.49	558.64	565.93	591.33	4.2	25
$^5F_3$	20	590.34	603.26	633.01	640.25			4.2	25
$^5F_2$	21	073.54	074.50					4.2	25
$^3K_8$	21	288.46	294.29	318.80	319.64	340	352.50	4.2	25,11
	21	366.33	376.61	381.09	409.83	411.45		4.2	25,11
$^5G_6$	22	064.37	070.94	079.20	085.70	104.11	112.02	4.2	25,11
	22	131.77	148.79	157				4.2	25,11
$^5F_1$	22	299.00						4.2	25,11
$^5G_5$	23	917.88	917.90	926.05	934.44	938.93	950.63	4.2	25,11
	23	968.41						4.2	25,11
$^5G_4$	25	774.75	815.83	816.59	828.89	873.76		4.2	25,11
$^3K_7$	26	110.80	116.35	133.27	140.01	146.46	161.37	4.2	25,11
$^5G_5$, $^3H_6$	27	608.68	627.21	630.13	632.57	635.23	693.12	4.2	25,11
	27	716.42						4.2	25,11
$^5F_2$	28	260.21	270.04					4.2	25,11
$^5G_3$	28	782.04	787.75					4.2	25,11
$^3L_9$	28	811.68	820.94	849.53	900.59	908.46	913.39	4.2	11
	28	925.07	932.35	939.31	948.73	953.10		4.2	11
$^3F_4$	29	896.75	914.33	936.24	942.78	950.06		4.2	11
$^3K_6$, $^5G_2$	30	009.83	038.77	048.17	052.37	746.81		4.2	11
$^3D_3$, $^3P_1$	33	055.74	063.64	291.61	782.49			4.2	11
$^3M_{10}$	33	830.32	830.56	832.95	836.13	999.27	005.39*	4.2	11
	33	010.73						4.2	11
$^3L_8$	34	103.20	125.93	222.48	229.60			4.2	11
$^5G_4$	34	704.36	705.06	723.65	725.97	736.68	741.18	4.2	11
$^3G_3$	35	122.02	212.88	896.49	906.14	932.99	934.56	4.2	11
	35	965.10	023.51*					4.2	11
$^1L_8$, $^3F_2$, $^3H_5$	36	265.00	288.31	308.38	700.63	705.85	709.76	4.2	11
	36	726.42						4.2	11
$^1K_7$, $^3I_7$	37	932.43	965.90	2821.49*	290.84	311.38	321.08	4.2	11
	37	326.97	334.06					4.2	11

$Er:LaCl_3$

Term	Prefix	Energy (cm^{-1})						T	Ref.
$^4I_{15/2}$	-	0	37.91	64.27	96.52	113.70	141.61	2	26,27
	-	181.04	229.31					2	26,27
$^4I_{13/2}$	6	549.51	565.62	574.11	587.61	590.59	615.85	2	26
	6	643.99						2	26
$^4I_{11/2}$	10	207.46	209.17	210.53	222.04	226.71	240.59	2	26,27
$^4I_{9/2}$	12	392.70	397.92	468.2	491.51	547.70		2	26,27
$^4F_{9/2}$	15	251.92	269.06	276.56	303.86	316.67		2	26,27
$^4S_{3/2}$	18	386.63	410.80					2	26,27
$^2H_{11/2}$	19	135.08	140.36	161.13	178.34			2	26
$^4F_{7/2}$	20	481.07	501.23	552.17				2	26
$^4F_{5/2}$	22	168.66	174.56	183.76				2	26
$^4F_{3/2}$	22	503.88	530.88					2	26
$^2H_{9/2}$	24	502.93	511.71	522.60	569.70	602.69		2	26
$^4G_{11/2}$	26	331.12	354.65	357.34	367.08	385.90	408.46	2	26,27
$^2G_{9/2}$	27	346.14	361.34	367.36	370.15			2	26,27
$^2K_{15/2}$, $^2G_{7/2}$	27	601.32	623.95	990.74	994.47			2	26,27
$^2P_{3/2}$	31	474.24	511.68					2	27
$^2K_{13/2}$, $^4G_{7/2}$	32	899.64	920.90	033.49*	962.78	966.73		2	27
$^2D_{5/2}$	34	754.79	771.02					2	27
$^4G_{9/2}$	36	423.78						2	27
$^2I_{11/2}$, $^4D_{9/2}$	38	940.90	944.54	954.54	963.66	080.42*		2	27
$^2I_{13/2}$	40	830.24	846.19	849	853.13	974.99		2	27
$^2D_{3/2}$, $^4D_{3/2}$	40	993.03	224.92*	231.37				2	27

$Tm:LaCl_3$

Term	Prefix	Energy (cm^{-1})					T	Ref.
$^3H_6$	-	0	29	92	121	127	77	13
$^3H_4$	12	600	632	647	702		4.2	13
$^3F_3$	14	408	453	463	472		4.2	13
$^3F_2$	15	049	079				4.2	13
$^1G_4$	21	038	069	109	151	235	4.2	13
$^1D_2$	27	661	723	730			4.2	13
$^3P_1$	36	196	263				4.2	13
$^3P_2$	37	876	921				4.2	13

References for 5.1. $LaCl_3$

1. Morosin, B., 1968, J. Chem. Phys. **49**, 3007.
2. Hellwege, K.H., E. Orlich and G. Schaack, 1965, Phys. Kondens. Materie **4**, 196.
3. Margolis, J.S., 1961, J. Chem. Phys. **35**, 1367.
4. Crosswhite, H.M., 1977, Spectroscopie des Elements de Transition et des Elements Lourds dans les Solids, C.N.R.S. Colloquium No. 225, Paris, p. 65.
5. Eisenstein, J. C., 1963, J. Chem. Phys. **39**, 2134.
6. Axe, J.D. and G.H. Dieke, 1962, J. Chem. Phys. **37**, 2364.
7. DeShazer, L.G. and G.H. Dieke, 1963, J. Chem. Phys. **38**, 2190.
8. Piksis, A.H., G.H. Dieke and H.M. Crosswhite, 1967, J. Chem. Phys. **47**, 5083.
9. Thomas, K.S., S. Singh and G.H. Dieke, 1963, J. Chem. Phys. **38**, 2180.
10. Rajnak, K. and W.F. Krupke, 1967, J. Chem. Phys. **46**, 3532.
11. Crosswhite, H.M., H. Crosswhite, N. Edelstein and K. Rajnak, 1977, J. Chem. Phys. **67**, 3002.
12. Eisenstein, J.C., 1963, J. Chem. Phys. **39**, 2128.
13. Gruber, J.B., R.P. Leavitt and C.A. Morrison, 1981, J. Chem. Phys. **74**, 2705.
14. Wagner, F., D. Mehaffy and W.T. Carnall, 1975, unpublished results.
15. Sarup, R. and M.H. Crozier, 1965, J. Chem. Phys. **42**, 371.
16. Makovsky, J., W. Low and S. Yatsiv, 1962, Phys. Lett. **2**, 186.
17. Carlson, E.H. and G.H. Dieke, 1961, J. Chem. Phys. **34**, 1602.
18. Crosswhite, H.M., H. Crosswhite, F.W. Kaseta and R. Sarup, 1976, J. Chem. Phys. **64**, 1981.
19. Carnall, W.T., H. Crosswhite, H.M. Crosswhite and J.G. Conway, 1976, J. Chem. Phys. **64**, 3582.
20. Baer, W., J.G. Conway and S.P. Davis, 1973, J. Chem. Phys. **59**, 2294.
21. Magno, M.S. and G.H. Dieke, 1962, J. Chem. Phys. **37**, 2354.
22. Schweisow, R.L. and H.M. Crosswhite, 1969, J. Opt. Soc. Am. **59**, 592.
23. Crosswhite, H.M. and G.H. Dieke, 1961, J. Chem. Phys. **35**, 1535.
24. Dieke, G.H., 1968, Spectra and Energy Levels of Rare Earth Ions in Crystals (Interscience, New York), p. 269 ff.
25. Dieke, G.H. and B. Pandey, 1964, J. Chem. Phys. **41**, 1952.
26. Dieke, G.H. and S. Singh, 1961, J. Chem. Phys. **35**, 555.
27. Varsanyi, F. and G.H. Dieke, 1962, J. Chem. Phys. **36**, 2951.

5.2. LaF_3

Lanthanum fluoride (LaF_3) has traditionally been important in the study of rare-earth impurity-ion spectra. There has been considerable controversy over the crystal structure of LaF_3; the generally accepted structure is $P\bar{3}c1$ (Cheetham et al., 1976; Zalkin et al., 1966), although several other structures have been reported (see, for example, De Rango et al., 1966). We have presented the three most frequently reported structures in our crystallographic tables. Studies other than X-ray or neutron-diffraction experiments have contributed to the controversy and its resolution (Hudson, 1976; Afanasiev et al., 1972). LaF_3 has been the subject of several fundamental investigations including measurements of extremely narrow linewidths in optical transitions (Macfarlane et al., 1979; Yen et al., 1964) and hyperfine splittings (Erickson, 1977). Fundamental crystal-field studies of rare-earth ions in LaF_3 have been performed assuming D_{3h} symmetry (Carnall et al., 1978) as well as the true C_2 symmetry (Morrison and Leavitt, 1979). The optical spectrum of LaF_3:Pr has been analyzed along with neutron scattering results in PrF_3 using a C_2 crystal-field Hamiltonian (Hennig et al., 1974). A priori line-to-line intensity calculations have been performed for all the rare earths in LaF_3 by means of the Judd–Ofelt theory (Leavitt and Morrison, 1980). In addition, several R^{3+}:LaF_3 lasers have been built including Ce:LaF_3, the shortest wavelength rare-earth doped solid-state laser known (Ehrlich et al., 1980), Pr:LaF_3 (Solomon and Mueller, 1963), and Er:LaF_3 (Krupke and Gruber, 1964).

5.2.1 Crystallographic data for LaF_3

Trigonal $P\bar{3}c1$, #165, Z = 6

Ion	Pos.	Symm.	x	y	z
La	6(f)	C_2	x	0	1/4
F_1	12(g)	C_1	x	y	z
F_2	4(d)	C_3	1/3	2/3	z
F_3	2(a)	D_3	0	0	1/4

X-ray data

		La	F_1			F_2	
a	c	x	x	y	z	z	Ref.
7.185	7.3511	0.6609	0.3667	0.0540	0.0824	0.1855	1
7.185	7.351	0.6587	0.3758	0.0623	0.0813	0.1825	2
7.185	7.351	0.6599	0.362	0.050	0.081	0.187	3

Crystallographic data for LaF_3 (continued)

Hexagonal $P6_3/mcm$, #193, Z = 6

Ion	Pos.	Symm.	x	y	z
La	6(g)	C_{2v}	x	0	1/4
F_1	2(a)	D_{3h}	0	0	1/4
F_2	4(c)	C_{3h}	1/3	2/3	1/4
F_3	12(k)	C_s	x	0	z

X-ray data

		La	F_3		
a	c	x	x	z	Ref.
7.185	7.351	-	0.29	0.56	4

Hexagonal $P6_3cm$, #185, Z = 6

Ion	Pos	Symm.	x	y	z
La	6(c)	C_s	x	0	1/4
F_1	2(a)	C_{3v}	0	0	z
F_2	4(b)	C_3	1/3	2/3	z
F_3	6(c)	C_s	x	0	z
F_4	6(c)	C_s	x	0	z

X-ray data

		La	F_1	F_2	F_3		F_4		
a	c	x	z	z	x	z	x	z	Ref.
7.16	7.36	0.671	0.310	0.210	0.276	0.067	0.372	0.404	5
7.186	7.352	-	-	-	-	-	-	-	6

5.2.2 Index of refraction for LaF_3

Thin film; Ref. 7		Ref. 8		
λ(μm)	n(λ)	λ(Å)	n_e	n_o
2.0	1.57	2536.5	1.64866	1.65587
1.2	1.575	3131.5	1.61803	--
0.8	1.58	3663.3	1.61803	--
0.6	1.585	4046.5	1.61184	1.61797
0.45	1.60	4358.3	1.60950	1.61664
0.40	1.61	5460.7	1.60223	1.60597
0.30	1.625			
0.27	1.65			

$n = n' + C/(\lambda - \lambda')$ (λ in μm) (Ref. 9)

	n'	C(μm)	λ'(μm)
n_e	1.583	0.00778	0.1346
n_o	1.574	0.01531	0.0686

5.2.3 Crystal field parameters for R:LaF_3 (cm^{-1})

R	B_{20}	B_{22}	B_{40}	RB_{42}	IB_{42}	RB_{44}	IB_{44}	Ref.
Pr	-120	-98	644	375	123	483	343	10
Nd	-216	-36	700	341	123	397	314	10
Nd	116	-145	216	211	-519	276	-803	11
Sm	-133	-91	803	379	84	151	187	10
Eu	-232	-63	521	227	153	250	458	10
Gd	-203	-128	716	267	2	419	546	10
Dy	-227	-46	460	341	167	541	240	10
Ho	-205	-78	460	260	150	372	242	10
Er	-228	-119	545	301	108	358	219	10
Er	30	-174	-128	16	207	691	-137	11
Tm	-135	-39	523	178	-16	204	343	10

Crystal field parameters for R:LaF_3 (cm^{-1}) (continued)

R	B_{60}	RB_{62}	IB_{62}	RB_{64}	IB_{64}	RB_{66}	IB_{66}	Ref.
Pr	503	-1000	78	-131	-509	-381	-608	10
Nd	490	-928	-23	-131	-449	-427	-653	10
Nd	208	-569	728	-413	51	250	828	11
Sm	454	-749	-109	-101	-533	-330	-493	10
Eu	415	-790	120	-79	-355	-347	-400	10
Gd	593	-942	-35	-236	-325	-502	-613	10
Dy	223	-617	-46	-72	-279	-298	-505	10
Ho	297	-601	-7	-52	-260	-294	-436	10
Er	275	-520	-73	56	-305	-307	-368	10
Er	176	-549	-25	14	239	-497	-75	11
Tm	244	-525	-56	84	-453	-256	-294	10

5.2.4 Intensity Parameters for R:LaF_3 (10^{-20} cm^2)

R	Ω_2	Ω_4	Ω_6	Ref.
Pr	0.11	1.77	4.78	12
Nd	0.35	2.57	2.50	12
Pm	0.5	1.9	2.2	13
Sm	1.0	0.5	1.5	13
Eu	1.19	1.16	0.39	14
Gd	1.1	1.2	0.5	13
Tb	1.1	1.4	0.9	13
Dy	1.1	1.4	0.9	13
Ho	1.16	1.38	0.88	9
Er	1.07	0.28	0.63	15
Tm	0.52	0.59	0.22	13

5.2.5 Energy levels for R:LaF_3

Ce:LaF_3

Term	Prefix	Energy (cm^{-1})				T	Ref.
$^2F_{5/2}$	-	0	151			4.2	16
$^2F_{7/2}$	2	160	240	635	845	4.2	16

Pr:LaF_3

Term	Prefix	Energy (cm^{-1})						T	Ref.
$^3H_4$	-	0	57	76	136	195	204	4.2	17
	-	0	59	136	195	322	508	77	18
	-	0	58.6	72.0	137.1	195.7	203.9	77	19
	-	0	57	77	141	195	203	77	20
	-	295	508					4.2	17
	-	323.0	508.2					77	19
	-	299	338	506				77	20
$^3H_5$	2	179.2	299.0	304.6	309.5	356.5	434.1	77	19
	2	179	235	274	305	352	412	4.2	20
	2	428	457	469	561			4.2	20
$^3H_6$	4	223	268	305	388	440	504	4.2	17
	4	222.2	266.8	301.1	384.5	439.6	504.5	77	19
	4	222	267	305	388	506	528	4.2	20
	4	529	558	581	591	673	785	4.2	17
	4	526.1	552.4	578.4	590.9	668.5	773.8	77	19
	4	558	585	672	779			4.2	20
$^3F_2$	5	137	182	201	275	280		4.2	17
	5	135.5	181.0	199.6	274.9	280.3		77	19
	5	137	183	201	277			4.2	20
$^3F_3$	6	453	495	499	587	602	622	4.2	17
	6	452	490	498	589	603	621	4.2	20
	6	722						4.2	17
	6	722						4.2	20
$^3F_4$	6	927	946	980	998	029*	035	4.2	17
	6	928	944	980	031*	105	163	4.2	20
	6	093	104	165				4.2	17
$^1G_4$	9	716	751	876	912	005*	042	4.2	17
	9	749.1	872.6	906.6	039.9*	048.5	159.3	4.2	18
	9	703	746	869	908	995	035*	4.2	20
	9	048	163	499				4.2	17
	9	042	153	501				4.2	20
$^1D_2$	16	873	893	083*	183	204		4.2	17
	16	872.4	895.2	186.5*	206.4			4.2	18
	16	796	820	842	875	898		4.2	20

Pr:LaF_3 (continued)

Term	Prefix	Energy (cm^{-1})						T	Ref.
$^3P_0$	20	927						4.2	17
	20	925.2						4.2	18
	20	923.8						4.2	20
$^3P_1$, $^1I_6$	21	458	475	479	484	487	498	4.2	17
	21	469.8	520.2	565.2				4.2	18
	21	469	474	476	483	486	504	4.2	20
	21	516	522	529	536	554	567	4.2	17
	21	515	518	524	534	547	563	4.2	20
	21	580						4.2	17
	21	579	605					4.2	20
$^3P_2$	22	691	714	734	772	819		4.2	17
	22	691.5	715.2	734.3	819.4			4.2	18
	22	700	728	744	778	822		4.2	20
$^1S_0$	46	986						4.2	17

Nd:LaF_3

Term	Prefix	Energy (cm^{-1})						T	Ref.
$^4I_{9/2}$	-	0	45	136	296	500		4.2	13
$^4I_{11/2}$	1	978	037*	068	091	187	223	4.2	13,21
	1	984	042*	073	095	190	225	77	22
$^4I_{13/2}$	3	918	978	038*	076	118	208	4.2	13
	3	919	979	039*	078	120	213	4.2	21
	3	921	982	039*	078	121	206	77	22
	3	278						4.2	13
	3	278						4.2	21
	3	279						77	22
$^4I_{15/2}$	5	816	874	986	141*	167	323	4.2	13
	5	815	877	988				4.2	21
	5	816	878	990	140*	171	316	77	22
	5	454	556					4.2	13
	5	447	552					77	22
$^4F_{3/2}$	11	592	634					4.2	13,21
	11	591.6	633.6					4.2	23
$^2H_{9/2}$, $^4F_{5/2}$	12	596	614	622	676	694	754	4.2	13,21
	12	595.6	612.9	620.7	674.6	692.6	755.3	4.2	23
	12	843	902					4.2	13,21
$^4F_{7/2}$, $^4S_{3/2}$	13	514	590	671	676	711	715	4.2	13,21
	13	514.8	590.8	670.9	676.7	710.1	714.2	4.2	23
$^4F_{9/2}$	14	834	861	892	926	959		4.2	13
	14	835	860	891	927	958		4.2	21
	14	834.7	861.8	890.6	959.4			4.2	23

Nd:LaF_3 (continued)

Term	Prefix	Energy (cm^{-1})						T	Ref.
$^2H_{11/2}$	15	997	033*	046	060	100	165	4.2	13
	15	998	033*	045	059	103		4.2	21
	15	998.1	046.4*					4.2	23
$^4G_{5/2}$, $^2G_{7/2}$	17	306	316	363	510	520	571	4.2	13
	17	304	315	364	512	520	570	4.2	21
	17	304.6	316.0	362.9	509.2	520.3	603.2	4.2	23
	17	605						4.2	13
	17	601						4.2	21
$^4G_{7/2}$	19	147	235	252	324			4.2	13,21
	19	152	237	251	325			77	22
	19	147.4	236.2	252.1	325.4			4.2	23
$^4G_{9/2}$, $^2K_{13/2}$	19	567	615	651	686	704	741	4.2	13
	19	568	617	651	685	702	739	4.2	21
	19	569	613	651	680	705	740	77	22
	19	568.2	650.9	686.2	704.0	739.4		4.2	23
	19	799	835	960				4.2	13
	19	801	839					4.2	21
	19	832						77	22
$^2G_{9/2}$	21	155	176	198	232	252		4.2	13
	21	158	176	201	234	254	302	4.2	21
	21	156	176	203	232	252	343	77	22
	21	356						77	22
$^2D_{3/2}$	21	338	353					4.2	13
	21	339	351					4.2	21
$^4G_{11/2}$, $^2K_{15/2}$	21	633	718	846	992			4.2	13
$^2P_{1/2}$	23	473						4.2	13
	23	468						4.2	21
	23	470						77	22
$^2D_{5/2}$	23	991	080*					4.2	13,21
$^2P_{3/2}$	26	378	426					4.2	13
	26	364	404					77	22
$^4D_{3/2}$	28	341	374					4.2	13
	28	340	371					77	22
$^4D_{5/2}$, $^2I_{11/2}$	28	525	676	962	463*	489	568	4.2	13
	28	525	544	823	929	970	404*	77	22
	28	644	773					4.2	13
	28	551						77	22
$^2L_{15/2}$, $^4D_{7/2}$	30	275	576	631	682	719	807	4.2	13
$^2I_{13/2}$	30	893	933	994	030*	068		4.2	13
$^2L_{17/2}$	31	781	859					4.2	13
$^2H_{9/2}$, $^2D_{3/2}$	33	030	107	181	228	255	619	4.2	13
	33	649						4.2	13
$^2H_{11/2}$, $^2D_{5/2}$	34	292	380	419	521	678	706	4.2	13

Nd:LaF_3 (continued)

Term	Prefix	Energy (cm^{-1})				T	Ref.
$^2F_{5/2}$	38	690	735	841		4.2	13
$^2F_{7/2}$	40	103	155	288		4.2	13
$^2G_{9/2}$	47	894	937	999	043*	4.2	13
$^2G_{7/2}$	48	839	908	977	088*	4.2	13

Sm:LaF_3

Term	Prefix	Energy (cm^{-1})						T	Ref.
$^6H_{5/2}$	-	0	48	115				4.2	13,24
	-	0	44.50	159.39				?	25
$^6H_{7/2}$	1	000	044	185	280			4.2	13
	1	000.4	044.1	185.4	280			4.2	24
	1	003.41	046.97	100.58	187.01			?	25
$^6H_{9/2}$	2	210	245	343	409	473		4.2	13
	2	209.7	244.6	342.5	409.4	473		4.2	24
	2	213.03	247.68	344.56	504.62	593.77		?	25
$^6H_{11/2}$	3	520	568	651	676	727	791	4.2	13
	3	517	567	647	670	726	791	4.2	24
$^6H_{13/2}$	4	972	983	007*	046	056	123	4.2	13
	4	975	046*	117	156			4.2	24
	4	969.5	005.2*	044.1				?	25
	4	160						4.2	13
$^6H_{15/2}$, $^6F_{1/2}$, $^6F_{3/2}$	6	309	342	406	450	461	567	4.2	13
	6	352	417	609				4.2	24
	6	404.1						?	25
	6	567	691	707				4.2	13
$^6F_{5/2}$	7	176	184	223				4.2	13
	7	174	184	225				4.2	24
	7	173.8	180.2					?	25
$^6F_{7/2}$	7	992	041*	060	092			4.2	13
	7	993	042*	059	092			4.2	24
	7	987.7	034.4*	054.7	086.5			?	25
$^6F_{9/2}$	9	170	178	228	252	268		4.2	13
	9	170	180	231	254	270		4.2	24
	9	162.9	173.6	222.1	247.2	262.8		?	25
$^6F_{11/2}$	10	561	584	593	603	613	644	4.2	13
	10	559	581	590	602			4.2	24
$^4G_{5/2}$, $^4F_{3/2}$	17	858	949	045*	924	942		4.2	13
	17	858.40	949.42	046.81*	924.24	942.04		?	25
$^4G_{7/2}$	20	037	093	112	164			4.2	13
	20	037.36	093.45	111.89				?	25

Sm:LaF_3 (continued)

Term	Prefix	Energy (cm^{-1})						T	Ref.
$^4I_{9/2}$	20	416	473	499	526			4.2	13
	20	417.43	471.01	497.69	523.65			?	25
$^4I_{13/2}$	21	663	674	706	736			4.2	13
	21	476.60	520.42	637.04	674.53	709.71		?	25
$^4F_{5/2}$, $^4M_{17/2}$	22	164	207	240				4.2	13
	22	164.47	207.41	240.65	501.34	532.05		?	25
$^4M_{19/2}$	24	034	119	153				4.2	13
	24	034.38	119.941	153.57				?	25
$^4L_{13/2}$	24	608	629	631	644	678	682	4.2	13
	24	607.85	628.63	631.00	643.93	678.62	683.23	?	25
	24	710						4.2	13
	24	709.92						?	25
$^4G_{7/2}$, $^6P_{3/2}$	24	911	993	007*	064	081		4.2	13
	24	911.18	959.04	993.02	007.26*	019.86		?	25
$^4K_{11/2}$	25	166	182	204	216	248	282	4.2	13
$^4L_{15/2}$	25	614.92	666.72	681.25	767.66	787.92	798.11	?	25
$(^4K,^4L)_{17/2}$,	26	495.48	699.27	709.47	712.01	758.39	776.34	?	25
$^4D_{1/2}$, $^6P_{7/2}$	26	791.13	796.54	810.94	822.14	857.65		?	25
$^4F_{9/2}$	27	363	417	432	448	508		4.2	13
	27	419.29	434.06	448.56				?	25
$^4D_{3/2}$, $^6P_{5/2}$	27	648	658	691	734	758		4.2	13
	27	648.64	658.99	691.74	734.79	758.78		?	25
$(^6P,^4H)_{7/2}$	28	248	262	343	409			4.2	13
	28	247.98	262.08	410.70				?	25
$^4K_{15/2}$	28	715	726	753	778	790	810	4.2	13
	28	732.35						?	25
$^4H_{9/2}$, $^6P_{7/2}$	28	938	981	037*	055	086	094	4.2	13
	28	938.08	980.98	036.29*	052.48	083.31	092.02	?	25
	28	111.15						?	25
$^4G_{7/2}$, $^4G_{9/2}$	30	027	125	141	219	235	286	4.2	13
	30	028.12	120.76	136.01				?	25
	30	329						4.2	13
$^2L_{15/2}$, $^4G_{11/2}$	31	420	442	473	627	716	761	4.2	13
	31	435.58	465.04	489.16	511.92	533.98	538.14	?	25
	31	627.05						?	25
$^4P_{5/2}$	32	808	829	861				4.2	13
$^2F_{5/2}$, $^2K_{13/2}$	33	608	681	765				4.2	13
$^4I_{11/2}$	35	890	905	954	996	007*	055	4.2	13

Sm:LaF_3 (continued)

Term	Prefix	Energy (cm^{-1})						T	Ref.
$^4F_{5/2}$, $^4F_{3/2}$	36	567	651	755				4.2	13
$^2H_{9/2}$	37	623	634	634	657	679		4.2	13
$^2P_{3/2}$	38	467	492					4.2	13
$^2G_{9/2}$	42	066	124	135	176	227		4.2	13
$^4G_{5/2}$	42	378	462	486				4.2	13
$^4G_{7/2}$	42	616	658	711				4.2	13
$^4H_{9/2}$, $^4H_{11/2}$	42	959	990	040*	074	258	324	4.2	13
$^2G_{9/2}$	44	597	122*	366				4.2	13
$^2H_{11/2}$, $^4H_{13/2}$	46	284	402	603	336*	374		4.2	13

Eu:LaF_3

Term	Prefix	Energy (cm^{-1})						T	Ref.
$^7F_0$	-	0						77	26
$^7F_1$	-	313	375	415				77	26
$^7F_2$	-	964	997	098*				77	26
$^7F_3$	1	843	867	884	889	908	996	77	26
$^7F_4$	2	614	788	847	852	873	894	77	26
	2	926	047*	068				77	26
$^7F_5$	3	764	090*					77	26
$^5D_0$	17	293						77	26
$^5D_1$	19	043.4	056.0	062.8				77	26
$^5D_2$	21	507.4	512.3	532.0	541	565		77	26

$Gd:LaF_3$

Term	Prefix	Energy (cm^{-1})						T	Ref.
$^8S_{7/2}$	-	0						4.2	13,27
$^6P_{7/2}$	32	177.11	185.62	199.61	228.57			1.5	13,28
	32	176	185	199	226			77	27
$^6P_{5/2}$	32	771.75	791.96	809.29				1.5	13,28
	32	771	791	808				77	27
$^6P_{3/2}$	33	352.00	370.00					77	13,27
$^6I_{7/2}$	35	923.00	945.24	969.03	996.14			1.5	13,28
	35	923	945	968	996			77	27
$^6I_{9/2}$	36	275.25	286.08	306.24	314.26	333.45		1.5	13,28
	36	274	285	305	313	332		77	27
$^6I_{17/2}$	36	340.81	343.03	347.18	351.69	354.80	364.51	1.5	13,28
	36	340	342	346	351	354	363	77	27
	36	371.71	377.86	384.90				1.5	13,28
	36	370	377	384				77	27
$^6I_{11/2}$	36	551.43	563.33	573.18	586.14	594.86	613.04	1.5	13,28
	36	549	561	571	584	592	611	77	27
$^6I_{15/2}$, $^6I_{13/2}$	36	661.81	670.99	679.93	690.17	700.50	703.65	1.5	13,28
	36	659	668	677	687	698	701	77	27
	36	713.00	715.52	720.08	724.82	734.46	738.99	1.5	13,28
	36	710	712	717	722	731	736	77	27
	36	752.81	763.02	772.50				1.5	13,28
	36	749	760	769				77	27
$^6D_{9/2}$	39	667.00	686.00	719.00	742.00	758.00		77	13,27
$^6D_{7/2}$	40	734.00	740.00	744.00	751.00			77	13,27
$^6G_{7/2}$	49	170.00	221.00	240.00	298.00			77	13,27
$^6G_{11/2}$	49	533	560	604	638	651	680	77	27
	49	740	824	889				77	27

$Dy:LaF_3$

Term	Prefix	Energy (cm^{-1})						T	Ref.
$^6H_{15/2}$	-	0	17	69	124	184	208	4.2	13,29
	-	307						4.2	13,29
$^6H_{13/2}$	3	502	522	576	618	630	645	4.2	13,29
	3	695						4.2	13,29
$^6H_{11/2}$	5	882	908	924	944	975	020*	4.2	13
	5	332	909	925	945	977	024*	4.2	29
$^6H_{9/2}$, $^6F_{11/2}$	7	633	665	728	758	801	814	4.2	13
	7	633	665	727	758	803	813	4.2	29

Dy:LaF_3 (continued)

Term	Prefix	Energy (cm^{-1})						T	Ref.
	7	838	842	933	998	077*		4.2	13
	7	842	887	933	019*	075		4.2	29
$^6F_{9/2}$, $^6H_{7/2}$	8	992	074*	087	144	181	235	4.2	13
	8	990	071	085	141	179	235	4.2	29
	8	282	343	435				4.2	13
	8	279	343	438				4.2	29
$^6H_{5/2}$	10	222	285	345				4.2	13
	10	222	284	344				4.2	29
$^6F_{7/2}$	11	037	109	140	153			4.2	13
	11	044	116	159	206			4.2	29
$^6F_{5/2}$	12	456	504	520				4.2	13,29
$^6F_{3/2}$	13	271	285					4.2	13,29
$^4F_{9/2}$	21	057	142	159	205	395		4.2	13
	21	059	141	159	175	218		4.2	29
$^4I_{15/2}$	22	022	132	175	189	213	292	4.2	13
	22	020	126	169	190	214	290	4.2	29
	22	342	379					4.2	13
	22	342	380					4.2	29
$^4G_{11/2}$	23	468	497	513	537	551		4.2	13
	23	468	501	513	534	550		4.2	29
$^4M_{21/2}$	24	990	008*	073	098	195	303	4.2	13
$^4I_{13/2}$, $^4K_{17/2}$	25	661	691	740	748	778	824	4.2	13
	25	849	867	903	918	940		4.2	13
$^4I_{17/2}$	25	953	990					4.2	13
$^4M_{19/2}$	26	260	358	429	448	509	571	4.2	13
	26	583						4.2	13
$(^4P,^6P)_{3/2}$	27	482	536					4.2	13
$^6P_{5/2}$	27	581	624	665				4.2	13
$^4I_{11/2}$	27	919	988	036*	074			4.2	13
$^4M_{15/2}$, $^6P_{7/2}$	28	347	381	536	577	613	636	4.2	13
	28	658	674	715	734			4.2	13
$^4F_{5/2}$, $^4I_{9/2}$	29	535	638	667	684	752	787	4.2	13
	29	855						4.2	13
$^4G_{9/2}$, $^4K_{17/2}$	29	890	982	075*	141	243	302	4.2	13
$^6P_{3/2}$	30	887	924					4.2	13
$^4K_{15/2}$, $^4L_{19/2}$	31	055	134	169	194	211	225	4.2	13
	31	259	282	294	328	379	452	4.2	13
$^4G_{7/2}$	31	580	660	716				4.2	13

Dy:LaF_3 (continued)

Term	Prefix	Energy (cm^{-1})						T	Ref.
$^4K_{13/2}$	33	146	202	218	236	256		4.2	13
$^4H_{13/2}$	33	527	527	527	527	623	558	4.2	13
$^4F_{3/2}$	33	666	652					4.2	13
$^4D_{7/2}$	34	029	040	052	080			4.2	13
$^4L_{17/2}$, $^4H_{9/2}$	34	247	250	298	313	366	393	4.2	13
	34	418	426	466	477	525		4.2	13
$(^4G,^4H)_{11/2}$	34	854	873	904	914	935	973	4.2	13
$^4K_{11/2}$, $^4G_{7/2}$	35	940	966	994	006*	055	055	4.2	13
	35	080						4.2	13
$^4L_{15/2}$, $^4L_{13/2}$	36	494	512	536	634	668	653	4.2	13
	36	686						4.2	13
$^4G_{9/2}$	36	752	780					4.2	13
$^2L_{15/2}$	37	944	978					4.2	13
$^4P_{5/2}$	38	937	996	090*				4.2	13
$^4P_{3/2}$	39	152	176					4.2	13

Ho:LaF_3

Term	Prefix	Energy (cm^{-1})						T	Ref.
$^5I_8$	-	0	4.5	42.1	50.1	68.7	122.0	1.5	30
	-	145.2	201.2	215.1	226.8	260.6	306.7	1.5	30
	-	321.6	348.7	387.1	397.5	409.4		1.5	30
$^5I_7$	5	191.7	246.4	252.1	261.0	272.3	279.4	1.5	30
	5	286.9	295.3	305.0	314.4	389.4	460.6	1.5	30
	5	503.9	586.4	641.9				1.5	30
$^5I_6$	8	726.2	732.8	752.5	765.8	737.0	782.7	1.5	30
	8	787.1	812.0	833.8				1.5	30
$^5I_5$	11	304	306	308	311	321	332	1.5	30
	11	363	386					1.5	30
$^5I_4$	13	286	362	380				1.5	30
$^5F_5$	15	589	591	593	601	602	608	1.5	30
	15	613	614	625	641	708	730	1.5	30
$^5S_2$	18	590	600	603	620			1.5	30
$^5F_4$	18	677	688	701	709	720	737	1.5	30
	18	753	776	814				1.5	30
$^5F_3$	20	744	754	796	799	826	832	1.5	30
	20	866						1.5	30

Ho:LaF_3 (continued)

Term	Prefix	Energy (cm^{-1})						T	Ref.
$^5F_2$	21	238	249	265	275	286		1.5	30
$^3K_8$	21	411	419	423	432	440	451	1.5	30
	21	461	481	495	514	527	532	1.5	30
	21	550	566	579				1.5	30
?	22	254	257	263	267	271	276	1.5	30
	22	279	283					1.5	30
$^5G_6$	22	328	346	359	361	374	389	1.5	30
	22	392	407	424	438			1.5	30
$^5G_5$	24	102	103	112	116	125	130	1.5	30
	24	146	170	182	196	247		1.5	30
$^5G_4$	25	985	008*	037	054	084	096	1.5	30
	25	132	143	161				1.5	30
$^3K_7$	26	255	266	277	288	293	298	1.5	30
	26	312	320	328				1.5	30
$^3H_6$, $^3H_5$	27	749	758	804	825	839	854	1.5	30
	27	869	879	932	945	997	092*	1.5	30
$^5G_3$, $^3L_9$	28	931	011*	020	032	035	039	1.5	30
	28	068	120	161	187	292		1.5	30
$^3K_6$, $^3F_4$	30	058	078	101	116	157	186	1.5	30
	30	197	213	234	330			1.5	30
$^3D_2$	31	002						1.5	30
$^3L_8$, $^3M_{10}$	34	022	061	116	205			1.5	30
$^5D_4$	34	994	003*	023	049			1.5	30
$^3F_3$	35	335	489					1.5	30
$^3H_4$, $^3F_2$	36	058	070	086	100	111	123	1.5	30
	36	244						1.5	30
$^3G_5$	36	852	869	894	001*	034		1.5	30
$^3I_7$	38	570	599					1.5	30

$Er:LaF_3$

Term	Prefix	Energy (cm^{-1})						T	Ref.
$^4I_{15/2}$	-	0	51	121	200	219	314	4.2	13
	-	0	51.2	121.2	199.7	219.4	313.8	4.2	31
	-	400	443					4.2	13
	-	400.3	442.9					4.2	31
$^4I_{13/2}$	6	604	630	670	700	723	754	4.2	13,32
	6	604.5	628.9	670.9	700.9	722.7	742.7	4.2	31
	6	823						4.2	13,32
	6	824.7						4.2	31
$^4I_{11/2}$	10	301	311	330	344	358	395	4.2	13,32
	10	301.7	311.8	331.7	345.9	360.5	398.3	4.2	31
$^4I_{9/2}$	12	419	518	615	701	730		4.2	13,32
	12	419.7	519.4	594.7	620.7	692.0		4.2	31
$^4F_{9/2}$	15	391	432	443	474	527		4.2	13
	15	390.8	433.1	444.3	475.4	528.0		4.2	31
	15	395	436	448	479	530		4.2	32
$^4S_{3/2}$	18	557	588					4.2	13
	18	557.0	586.7					4.2	31
	18	561	589					4.2	32
$^2H_{11/2}$	19	266	307	314	359	359	418	4.2	13
	19	265.1	304.9	312.0	358.7	358.7	417.4	4.2	31
	19	268	308	315	362	368	419	4.2	32
$^4F_{7/2}$	20	656	703	734	786			4.2	13
	20	652.8	700.3	731.2	758.5			4.2	31
	20	655	703	736	789			4.2	32
$^4F_{5/2}$	22	370	374	407				4.2	13
	22	366.6	371.6	403.2				4.2	31
	22	371	376	409				4.2	32
$^4F_{3/2}$	22	684	751					4.2	13
	22	683.3	742.6					4.2	31
	22	689	756					4.2	32
$^2H_{9/2}$	24	602	680	754	840	862		4.2	13
	24	600.6	680.1	752.2	836.5	857.5		4.2	31
	24	611	689	763	848	871		4.2	32
$^4G_{11/2}$	26	530	558	583	647	647	709	4.2	13
	26	502.2	525.4	553.6	581.8	650.6	709.0	4.2	31
	26	540	628	640	655	681		4.2	32
$^4G_{9/2}$	27	606	620	631	646	671		4.2	13
	27	602.7	615.7	627.1	640.9	667.6		4.2	31
	27	616	628	640	655	681		4.2	32
$^2K_{15/2}$	27	813	820	830	904	935	127*	4.2	13
	27	828.3						4.2	31
	27	(822)	829	839	885	910	944	4.2	32

Er:LaF_3 (continued)

Term	Prefix	Energy (cm^{-1})						T	Ref.
	27	076*	136					4.2	32
$^4G_{7/2}$	28	243	257	265				4.2	13
	28	241.0	253.1	338.1	368.3			4.2	31
	28	252	267	275	352			4.2	32
$^2P_{3/2}$	31	688	746					4.2	13
	31	690.2	749.0					4.2	31
	31	701	758					4.2	32
$^2K_{13/2}$, $^4G_{5/2}$	33	108	119	167	201	201		4.2	13
	33	110.3	120.2	191.9				4.2	31
	33	115	122	128	198	214	358	4.2	32
$^4G_{7/2}$	34	157	196	221	280			4.2	13
	34	155.5	194.5	223.9	279.4			4.2	31
	34	170	206	237	294			4.2	32
$^2D_{5/2}$	35	026	052	085				4.2	13
	35	031.7	054.3	084.8				4.2	31
	35	041	054	100				4.2	32
$^2H_{9/2}$	36	522	555	624	721	805		4.2	13
	36	520.2	553.6	624.6	710.6	805.3		4.2	31
	36	519	552	620	712	801		4.2	32
$^4D_{5/2}$	38	804	841	834				4.2	13
	38	803.6	836.6					4.2	31
	38	828	857	866				4.2	32
$^4D_{7/2}$	39	454	535	606	634			4.2	13
	39	459.2	526.3	545.1	598.3			4.2	31
	39	459	501	551	617			4.2	32
$^2I_{11/2}$	41	238	297	315	382	497		4.2	13
	41	204	252	303	323	388		4.2	32
$^4D_{3/2}$	42	495	526	088*	126			4.2	13
	42	506	535					4.2	32
$^2I_{13/2}$	43	687	746	746	760	834	915	4.2	13
	43	692	712	770	787	836	865	4.2	32
	43	941						4.2	32
$^2D_{5/2}$	49	223	272	357				4.2	13
	49	253	304	381				4.2	32

Tm:LaF_3

Term	Prefix	Energy (cm^{-1})						T	Ref.
$^3H_6$	-	0	67	118				4.2	33
$^3F_4$	5	706	814	826	859	866	918	4.2	33
	5	921	958					4.2	33
$^3H_5$	8	248	258	285	296	305	318	4.2	33
	8	332	338	366	400	550		4.2	33
$^3H_4$	12	561	570	616	700	727	737	4.2	33
	12	799	825	868				4.2	33
$^3F_3$	14	508	539	554	569	588	596	4.2	33
$^3F_2$	15	113	138	169	207	240		4.2	33
$^1G_4$	21	037	196	309	349	366	380	4.2	33
	21	478	519	532				4.2	33
$^1D_2$	28	021	034	057	088	106		4.2	33
$^1I_6$	34	675	696	769	827	896	960	4.2	33
	34	107*	160					4.2	33
$^3P_0$	35	604						4.2	33
$^3P_1$	36	531	587					4.2	33
$^3P_2$	38	250	291	320	336	414	451	4.2	33

References for 5.2. LaF_3

1. Cheetham, A.K., B.E.F. Fender, H. Fuess and A.F. Wright, 1976, Acta Cryst. **B32**, 94.
2. Mansmann, M., 1965, Z. Kristallogr. **122**, 375.
3. Zalkin, A., D.H. Templeton and T.E. Hopkins, 1966, Inorg. Chem. **5**, 1466.
4. Afanasiev, M.L., S.P. Habuda and A.G. Lundin, 1972, Acta Cryst. **B28**, 2903.
5. De Rango, C., G. Tsoucaris and C. Zelwer, 1966, C.R. Acad. Sci. Paris Ser. **C263**, 64.
6. Sobolev, B.P., V.B. Aleksandrov, P.P. Federov, K.B. Seranyan and N.L. Tkachenko, 1976, Sov. Phys. Crystallogr. **21**, 49.
7. Haas, G., J.B. Ramsey and R. Thun, 1959, J. Opt. Soc. Am. **49**, 116.
8. Wirich, M.P., 1966, Appl. Opt. **5**, 1966.
9. Weber, M.J., B.H. Matsinger, V.L. Donlan and G.T. Surratt, 1972, J. Chem. Phys. **57**, 562.
10. Morrison, C.A. and R.P. Leavitt, 1979, J. Chem. Phys. **71**, 2366. An extensive bibliography of experimental data for LaF_3 is given in this paper.
11. Stedman, G.E. and D.J. Newman, 1971, J. Phys. Chem. Solids **32**, 109.
12. Krupke, W.F., 1966, Phys. Rev. **145**, 325.
13. Carnall, W.T., H. Crosswhite, and H.M. Crosswhite, 1978, Argonne Natl. Lab. Report ANL-78-XX-95.
14. Weber, M.J., 1967, in: Crosswhite, H.M. and H.W. Moos, Eds., Optical Properties of Ions in Crystals (Interscience, New York), p. 467.
15. Weber, M.J., 1967, Phys. Rev. **157**, 262.
16. Buchanan, R.A., H.E. Rast and H.H. Caspers, 1966, J. Chem. Phys. **44**, 4063.
17. Carnall, W.T., P.R. Fields and R. Sarup, 1969, J. Chem. Phys. **51**, 2587.
18. Wong, E.Y., O.M. Stafsudd and D.R. Johnston, 1963, J. Chem. Phys. **39**, 786.
19. Yen, W.M., W.C. Scott and A.L. Schawlow, 1964, Phys. Rev. **A136**, 271.
20. Caspers, H.H., H.E. Rast and R.A. Buchanan, 1965, J. Chem. Phys. **43**, 2124.

21. Caspers, H.H., H.E. Rast and R.A. Buchanan, 1965, J. Chem. Phys. **42**, 3214.
22. Kumar, U.V., H. Jagannath, D.R. Rao and P. Venkateswarlu, 1976, Indian J. Phys. **50**, 90.
23. Wong, E.Y., O.M. Stafsudd and D.R. Johnston, 1963, Phys. Rev. **131**, 990.
24. Rast, H.E., J.L. Fry and H.H. Caspers, 1967, J. Chem. Phys. **46**, 1460.
25. Dieke, G.H., 1968, Spectra and Energy Levels of Rare Earth Ions in Crystals (Wiley, New York), p. 238.
26. Kumar, U.V., D.R. Rao and P. Venkateswarlu, 1977, J. Chem. Phys. **66**, 2019.
27. Carnall, W.T., P.R. Fields and R. Sarup, 1971, J. Chem. Phys. **54**, 1476.
28. Schwiesow, R.L. and H.M. Crosswhite, 1969, J. Opt. Soc. Am. **59**, 602.
29. Fry, J.L., H.H. Caspers, H.E. Rast and S.A. Miller, 1968, J. Chem. Phys. **48**, 2342.
30. Caspers, H.H., H.E. Rast and J.L. Fry, 1970, J. Chem. Phys. **53**, 3208.
31. Krupke, W.F. and J.B. Gruber, 1964, J. Chem. Phys. **41**, 1225.
32. Carnall, W.T., P.R. Fields and R. Sarup, 1972, J. Chem. Phys. **57**, 43.
33. Carnall, W.T., P.R. Fields, J. Morrison and R. Sarup, 1970, J. Chem. Phys. **52**, 4054.

5.3. *$LaBr_3$*

Rare-earth ion spectra in $LaBr_3$ are of interest in the study of anion dependence by comparison with the spectra in the more thoroughly studied host $LaCl_3$. The site symmetry (C_{3h}) is the same in both $LaCl_3$ and $LaBr_3$. Laser emission has been observed for Pr:$LaBr_3$ at 4 different wavelengths (German et al., 1975). Detailed comparisons of the multiplet energies for Pr^{3+} in $LaBr_3$ with the corresponding energies for similar hosts and the free ion have been made by Wensky and Moulton (1970). The hyperfine spectrum of Pr^{3+} in $LaBr_3$ has been investigated using laser spectroscopic techniques (Delsart et al., 1977). Recently the spectrum of the 5f analog of Pm^{3+}, Np^{3+}, has been thoroughly investigated by Carnall et al. (1980). Anomalies in the optical absorption spectrum of $NdBr_3$ were observed by Prinz and first explained by him in terms of an Ising interaction of the Nd^{3+} ions (Prinz, 1966).

5.3.1 Crystallographic data for $LaBr_3$

Hexagonal $P6_3/m$, #176, Z = 2

Ion	Pos.	Symm.	x	y	z
La	2(d)	C_{3h}	2/3	1/3	1/4
Br	6(h)	C_s	x	y	1/4

X-ray data

		Br		
a	c	x	y	Ref.
7.697	4.510	0.375	0.292	1

5.3.2 Index of refraction for $LaBr_3$ (Ref. 2)

λ = 0.6328 μm

$LaBr_3$	n_o = 1.945
$LaBr_3$ + 1.61% Pr	n_o = 1.937
$LaBr_3$ + 12.35% Pr	n_o = 1.986

5.3.3 Crystal-field parameters for R:$LaBr_3$ (cm^{-1})

R	B_{20}	B_{40}	B_{60}	B_{66}	Ref.
Pr	108	-356	-567	409	4
Nd	200.3	-305.2	-706.3	476.4	5
Gd	256	-288	-688	600	6
Er	234	-317	-307	223	7

5.3.4 Intensity parameters for R:$LaBr_3$ (10^{-20} cm^2)

R	Ω_2	Ω_4	Ω_6	Ref.
Nd	180	9	9	3 ($NdBr_3$)

5.3.5 Energy levels for R:$LaBr_3$

Pr:$LaBr_3$

Term	Prefix	Energy (cm^{-1})					T	Ref.
$^3H_4$	-	0	18.0	86.0	156.5		77	4
	-	0	15.76	86.0	156.5		4.2	7,8
	-	0	90	130	170		93	9
$^3H_5$	2	137.6	164.9	185.7			77	4
	2	159.99	182.95	185.7			4.2	7,8
	2	149	160	170	244	277	93	9
$^3H_6$	4	214	226	250.5	274	298.2	77	4
	4	245.90	290.94				4.2	7,8

Pr:$LaBr_3$ (continued)

Term	Prefix	Energy (cm^{-1})					T	Ref.
$^3F_2$	4	919.2					77	4
	4	912.89					4.2	7,8
$^3F_3$	6	253.4	281.1	284.1	312.5	329.0	77	4
	6	253.4	276.32	279.12	308.66	323.67	4.2	7,8
$^3F_4$	6	688	734.6	750.4	763	779.1	77	4
	6	682.07	727.12	743.06	758.18	771.60	4.2	7,8
$^1G_4$	10	732.0	745.5	783.1			77	4
$^1D_2$	16	571.9	671.8	718.1			77	4
	16	570.50	671.8	718.1			4.2	7,8
$^3P_0$	20	377.9					77	4
	20	372.24					4.2	7,8
$^3P_1$	20	966.82	995.32				4.2	7
	20	970.8	997.3				77	4
$^1I_6$	21	235.9	339.5	352.4			77	4
$^3P_2$	22	110.60	127.80	147.30			4.2	7
	22	114.7	129.0	153.0			77	4

Nd:$LaBr_3$

Term	Prefix	Energy (cm^{-1})				T	Ref.
$^4I_{9/2}$	-	0	113.1	117.1	245.9	77	10
$^4F_{3/2}$	11	365.1	397.3			77	10
$^4F_{5/2}$	12	397.8	423.5	430.0		77	10
	12	398.29	423.02			?	8
$^2H_{9/2}$	12	530.4				77	10
$^4F_{7/2}$	13	339.6	406.7	421.8		77	10
$^4S_{3/2}$	13	473.7	479.0			77	10
$^4F_{9/2}$	14	651.7	660.2	668.2	707.7	77	10
$^2H_{11/2}$	15	873.2	918.2	924.9		77	10
$^4G_{5/2}$	16	990.7	058.4*			77	10
$^2G_{7/2}$	17	169.4	222.4			77	10
$^4G_{7/2}$	18	915.7	955.3			77	10
	18	915.72	953.41			?	8
$^2G_{9/2}$	19	344.8	361.7			77	10
$^2K_{15/2}$	19	490.4	502.2	505.6	598.2	77	10

Nd:$LaBr_3$ (continued)

Term	Prefix	Energy (cm^{-1})						T	Ref.
$^4G_{9/2}$	20	983.2						77	10
$^2D_{3/2}$	21	096.1	126.8					77	10
$^4G_{11/2}$	21	265.7	291.5	296.5	352.0			77	10
$^2P_{1/2}$	23	139.0						77	10
$^2D_{5/2}$	23	687.8	703.0					77	10
$^2P_{3/2}$	26	058.6						77	10
$^4D_{3/2}$	27	822.5						77	10
	27	823.70						?	8

Gd:$LaBr_3$

Term	Prefix	Energy (cm^{-1})						T	Ref.
$^8S_{7/2}$	-	0						1.5	6
$^6P_{7/2}$	32	074.69	093.60	106.98	112.16			1.5	6
$^6P_{5/2}$	32	674.15	699.10	703.13				1.5	6
$^6P_{3/2}$	33	255.83	271.37					1.5	6
$^6I_{7/2}$	35	817.60	823.06	828.27	830.18			1.5	6
$^6I_{9/2}$	36	156.41	163.11	164.76	168.82	177.07		1.5	6
$^6I_{17/2}$	36	189.97	190.82	193.10	199.82	202.53	203.44	1.5	6
	36	204.25	205.11	208.73				1.5	6
$^6I_{11/2}$	36	428.77	433.06	435.82	435.82	442.33	452.43	1.5	6
$^6I_{15/2}$	36	538.03	538.03	540.86	540.86	544.88	550.17	1.5	6
	36	555.94	599.56					1.5	6
$^6I_{13/2}$	36	577.75	580.43	585.33	585.52	588.01	596.01	1.5	6
	36	600.34						1.5	6
$^6D_{9/2}$	39	481.93	490.49	510.15	518.55	533.27		1.5	6
$^6D_{1/2}$	40	426.52						1.5	6
$^6D_{7/2}$	40	505.54	514.53	518.64	526.67			1.5	6
$^6D_{3/2}$	40	661.6	696.2					1.5	6
$^6D_{5/2}$	40	758.7	776.3	823.6				1.5	6

Tb:$LaBr_3$

Term	Prefix	Energy (cm^{-1})						T	Ref.
$^7F_6$	-	0	50.3	94.8	100.5			77	11
$^7F_5$	2	045.3	079.8	100.6	115.9	147.4	169.7	77	11
	2	209.9						77	11
$^7F_4$	3	276.1	346.6	363.0	373.4	400.8	425.8	77	11
$^7F_3$	4	329.0	349.0	358.4	379.2			77	11
$^7F_2$	4	965.8	035.8*	037.4				77	11
$^7F_1$	5	436.6	491.6					77	11
$^7F_0$	5	696.5						77	11
$^5D_4$	20	448.0	453.6	460.5	475.2	490.0		77	11
$^5D_3$	26	252.8	258.6	259.8	266.9			77	11

Er:$LaBr_3$

Term	Prefix	Energy (cm^{-1})						T	Ref.
$^4I_{15/2}$	-	0	28.96	60.20	67.61	94.40	117.35	4.2	7
	-	154.80	189.95					4.2	7
$^4I_{13/2}$	6	531.98	538.80	543.35	565.37	566.65	590.96	4.2	7
	6	613.00						4.2	7
$^4I_{11/2}$	10	178.09	181.50	194.90	200.90	210.20		4.2	7
$^4I_{9/2}$	12	375.40	376.09	436.36	448.83	503.46		4.2	7
$^4F_{9/2}$	15	200.27	226.03	235.39	360.13	273.47		4.2	7
$^4S_{3/2}$	18	335.91	364.07					4.2	7
$^2H_{11/2}$	19	040.98	071.00	082.40	099.99	119.60		4.2	7
$^4F_{7/2}$	20	417.43	447.74					4.2	7
$^4F_{5/2}$	22	101.05	110.00	121.63				4.2	7
$^4F_{3/2}$	22	440.34	472.30					4.2	7
$^2H_{9/2}$	24	436.20	444.44	497.23	523.32			4.2	7
$^4G_{11/2}$	26	214.34	229.31	255.87	300.19	306.31	309.12	4.2	7
$^2G_{9/2}$	27	233.38	245.37	251.52	255.40	256.71		4.2	7
$^2P_{3/2}$	31	368.23	379.36					4.2	7
$^2K_{13/2}$	32	737.00						4.2	7
$^4G_{7/2}$	33	778.50						4.2	7

References for 5.3. $LaBr_3$

1. Zachariasen, W.H., 1948, Acta Cryst. **1**, 265.
2. Chivian, J.S., B.R. King and J.R. Trimmier, 1975, J. Opt. Soc. Am. **65**, 357.
3. Gruen, D.M., C.W. DeKock and R.L. McBeth, 1967, Adv. Chem. Ser. **71**, 102.
4. Wong, E.Y. and I. Richman, 1962, J. Chem. Phys. **36**, 1889.
5. Nutter, P., M. Weber and M. Harrison, 1965, Raytheon Report, AFML-TR-65-57, NTIS # 461 737.
6. Schwiesow, R.L. and H.M. Crosswhite, 1969, J. Opt. Soc. Am. **59**, 592.
7. Kiess, N.H. and G.H. Dieke, 1966, J. Chem. Phys. **45**, 2729.
8. Dieke, G.H., 1968, Spectra and Energy Levels of Rare Earth Ions in Crystals (Interscience, New York), pp. 196, 202.
9. Chivian, J.S., N.J. Krasutsky and W.E. Case, 1979, J. Opt. Soc. Am. **69**, 1622.
10. Richman, I. and E.Y. Wong, 1962, J. Chem. Phys. **37**, 2270.
11. Joshi, B.D., B.M. Patel, A.G. Page, T.R. Bangia and R.N. Saxena, 1973, J. Lumin. **6**, 125.

5.4. YCl_3

The compound yttrium trichloride, YCl_3, is extremely deliquescent and perhaps because of this it has enjoyed very few technical applications. The monoclinic structure is typified by $AlCl_3$, whose detailed X-ray data was first reported by Katelaar et al. (1947). The rare earth trichlorides were found to have the same structure for R = Dy, Ho, Er, Tm, Yb, and Lu (Templeton and Carter, 1954). Unfortunately, the spectra of R^{3+} ions in RCl_3 have not been reported, except for a few inferences given by Thomas et al. (1963), Dieke and Singh (1961), and Dieke (1968). Electron paramagnetic resonance of Nd^{3+} in YCl_3 has been reported by Hutchison and Kim (1979), and the lack of optical data on the R:YCl_3 system is emphasized by these workers. The coordination of rare earth trichlorides in aqueous solutions has been extensively studied by Habenschuss and Spedding (1979), where they determined (among other factors) the R^{3+}–Cl^- distance.

The lifetimes of R^{3+} in YCl_3 have been studied (Gandrud and Moos, 1968) by the infrared quantum counter and infrared fluorescence techniques for R = Ho, Er and Tm. The differential magnetic susceptibility of $HoCl_3$ and Ho:YCl_3 has been reported by Hellwege et al. (1968). The electron spin resonance of the excited state $^4S_{3/2}$ of Er:YCl_3 has been detected by Furrer et al. (1971).

5.4.1 Crystallographic data for YCl_3

Monoclinic C2/m #12, Z = 4

Ion	Pos.	Symm.	x	y	z
Y	4(g)	C_2	0	y	0
Cl_1	4(i)	C_s	x	0	z
Cl_2	8(j)	C_1	x	y	z

Crystallographic data for YCl_3 (continued)

X-ray data

				Y	Cl_1		Cl_2			
a	b	c	β	y	x	z	x	y	z	Ref.
6.92	11.94	6.44	111.0°	0.166	0.211	0.247	0.229	0.179	0.760	1

5.4.2 Crystal-field parameters for R:YCl_3 (cm^{-1})

R	B_{40}	B_{60}	Ref.	
Er	1400	166	2	(Cubic approx.)
Er	1536	138	3	(Cubic approx.)
Er	1312	211	3	(Cubic approx.)

5.4.3 Energy levels for R:YCl_3

Er:YCl_3

Term	Pre-fix	Energy (cm^{-1})						T	Ref.
$^4I_{15/2}$	-	0	22.26	24.15	60.83	66.24	256.55	4.2	2
	-	289.26	291.53					4.2	2
$^4I_{13/2}$	6	504.17	525.50	527.40	538.20	681.64	685.13	4.2	2
	6	690.29						4.2	2
$^4I_{11/2}$	10	174.38	181.22	182.38	205.85	218.99	238.83	4.2	2
$^4I_{9/2}$	12	341.80	391.74	500.49	521.05	522.93		4.2	2
$^4F_{9/2}$	15	166.44	168.43	248.99	254.47	269.80		4.2	2
$^4S_{3/2}$	18	274.47	295.31					4.2	2
$^2H_{11/2}$	19	018.30	019.32	023.17	061.14	145.69	185.01	4.2	2
$^4F_{7/2}$	20	390.11	448.97	458.71				4.2	2
$^4F_{5/2}$	22	069.61	079.93	105.03				4.2	2
$^4F_{3/2}$	22	447.12	469.53					4.2	2
$^2H_{9/2}$	24	416.22	468.21	470.46	529.39	548.01		4.2	2
$^4G_{11/2}$	26	122.17	125.82	127.85	209.31	371.80	426.53	4.2	2

$Er:YCl_3$ (continued)

Term	Prefix	Energy (cm^{-1})					T	Ref.
$^2G_{9/2}$	27	207.49	245.15	254.67	287.08	357.27	4.2	2
$^2K_{15/2}$	27	537.92	625.31				4.2	2
$^2G_{7/2}$	27	793.39	798.54				4.2	2
$^2P_{3/2}$	31	372.61					4.2	2

$Tm:YCl_3$

Term	Prefix	Energy (cm^{-1})						T	Ref.
$^3H_6$	-	0	16.25	150.99	180.09	350.61	396.88	?	4
$^3H_4$	5	545.86	587.39	588.82	826.46	830.77	850.13	?	4
	5	867.07	880.15	910.57				?	4
$^3H_5$	8	229.52	302.31	316.50	340.11	455.62	518.19	?	4
$^3F_4$	12	517.74	518.67	533.04	534.66	617.70	624.21	?	4
	12	732.33	734.89	736.93				?	4
$^3F_3$	14	423.37	433.58	447.66	448.85	460.95	464.94	?	4
	14	466.56						?	4
$^3F_2$	14	975.76	978.66	980.98	158.66*	160.20		?	4
$^1G_4$	20	881.94	885.90	900.40	903.35	905.58	369.27*	?	4
	20	372.62	373.99	442.24				?	4
$^1D_2$	27	641.90	682.43	687.10	737.57	756.36		?	4
$^1I_6$	34	116.80	172.53	350.98	393.18			?	4
$^3P_0$	35	496.20						?	4
$^3P_1$	35	872.70						?	4
$^3P_2$	37	484.20	489.76	685.00	717.94			?	4

References for 5.4. YCl_3

1. Templeton, D.H. and G.F. Carter, 1954, J. Phys. Chem. **58**, 940.
2. Rakestraw, J.W. and G.H. Dieke, 1965, J. Chem. Phys. **42**, 873.
3. Vishwamittar and S.P. Puri, 1974, J. Phys. C**7**, 2077.
4. Dieke, G.H., 1968, Spectra and Energy Levels of Rare Earth Ions in Crystals (Interscience, New York), pp. 310 ff.

5.5. YF_3

Much of the interest in yttrium fluoride stems from its applicability as an up-converter of infrared into visible radiation. In these applications, YF_3 is doped with two or more rare-earth ions, and conversion takes place by means of multistep energy transfer processes between them. Several processes of this type have been studied experimentally in YF_3, including Yb→Tb transfer (Ostermayer and Van Uitert, 1970), Yb→Ho transfer (Ovsyankin and Feofilov, 1971; Ettinger and Niemczyk, 1978), Yb→Er transfer (Monemar and Titze, 1971; Kuroda et al., 1972; Ettinger and Niemczyk, 1978), and Yb→Tm transfer (Ostermayer et al., 1971). Theoretical studies of Ho→Ho energy transfer in YF_3 have also been performed (Pouradier and Auzel, 1978). In addition to the above, Pr:YF_3 has been found to be an efficient down-converter of ultraviolet into visible radiation, the quantum yield being greater than unity for cascade fluorescence (Piper et al., 1974). Several other luminescence mechanisms in Pr:YF_3 have also been studied (Sommerdijk et al., 1974).

The crystal structure of YF_3 at room temperature is Pnma, with Y^{3+} ions in sites of C_s symmetry (Wyckoff, 1964). A higher temperature hexagonal form has also been observed (Sobolev and Fedorov, 1973). The index of refraction is 1.550 at the sodium D line doublet ($\lambda = 0.589\ \mu m$) and the dielectric constant is 10.0 at $f = 760$ kHz (Dulepov et al., 1976). The polarized infrared spectrum of YF_3 has been obtained and the lattice vibrations have been analyzed and assigned to symmetry species (Rast et al., 1969). Electron-beam and ultraviolet excitation of rare-earth doped YF_3 has determined the energy separation of the configurations $4f^{n-1}5d$ and $4f^n$ for several rare earths (Yang and DeLuca, 1976).

5.5.1 Crystallographic data for YF_3

Orthorhombic Pnma, #62, Z = 4

Ion	Pos.	Symm.	x	y	z
Y	4(c)	C_s	x	1/4	z
F_1	4(c)	C_s	x	1/4	z
F_2	8(d)	C_1	x	y	z

Crystallographic data for YF_3 (continued)

X-ray data

a	b	c	Ref.
6.353	6.850	4.393	1
6.3537	6.8545	4.3953	2

Y		F_1		F_2			
x	z	x	z	x	y	z	Ref.
0.367	0.058	0.528	0.601	0.165	0.060	0.363	1
0.3673	0.0591	0.5227	0.5910	0.1652	0.0643	0.3755	2

5.5.2 Crystal-field parameters for R:YF_3 (cm^{-1})

R	B_{20}	B_{22}	B_{40}	RB_{42}	IB_{42}	RB_{44}	IB_{44}	Ref.
Er	318	407	150	328	-198	-429	209	3

R	B_{60}	RB_{62}	IB_{62}	RB_{64}	IB_{64}	RB_{66}	IB_{66}	Ref.
Er	312	-311	156	-218	278	-53	313	3

5.5.3 Energy levels for R:YF_3

Nd:YF_3

Term	Prefix	Energy (cm^{-1})						T	Ref.
$^4I_{9/2}$	-	0	113	306	358	454		?	4
$^4I_{11/2}$	2	010	070	111	138	204	233	?	4
$^4I_{13/2}$	3	965	035*	069	111	171	210	?	4
	3	259						?	4
$^4I_{15/2}$	6	771	796	815	835	870	882	?	4
$^4F_{3/2}$	11	627	663					?	4

$Gd:YF_3$

Term	Prefix	Energy (cm^{-1})						T	Ref.
$^8S_{7/2}$	-	0						77	5
$^6P_{7/2}$	32	091.4	127.5	165.7	222.7			77	5
$^6P_{5/2}$	32	700.0	739.7	794.4				77	5
$^6I_{7/2}$	35	851.3	883.4	906.6	929.9			77	5

$Tb:YF_3$

Term	Prefix	Energy (cm^{-1})						T	Ref.
$^7F_6$	-	0	115	152	171	181	257	77	6
	-	384	445					77	6
$^7F_5$	2	130	169	199	202	217	247	77	6
	2	282	320	354				77	6
$^5D_4$	20	598	608	619	656	667	717	77	6

$Dy:YF_3$

Term	Prefix	Energy (cm^{-1})						T	Ref.
$^6H_{15/2}$	-	0	37	59	111	150	211	?	4
	-	276	502					?	4
$^6H_{13/2}$	3	491	546	568	586	658	762	?	4
	3	830						?	4
$^6H_{11/2}$	5	838	862	904	951	034*	087	?	4
$^4F_{9/2}$	21	049	155	188	267	297		?	4

$Er:YF_3$

Term	Prefix	Energy (cm^{-1})						T	Ref.
$^4I_{15/2}$	-	0	90	131	175	194	248	?	4
	-	0	76	173	230	255	294	4.2	7
	-	276	502					?	4
	-	341	423					4.2	7
$^4I_{13/2}$	6	584	607	666	687	718	735	?	4
	6	545	766					4.2	7
	6	801						?	4

Er:YF_3 (continued)

Term	Prefix	Energy (cm^{-1})						T	Ref.
$^4I_{11/2}$	10	257	281	317	335	346	369	4.2	7
$^4F_{9/2}$	15	339	389	397	475	490		4.2	7
$^4S_{3/2}$	18	494	575					4.2	7
$^2H_{11/2}$	19	234	270	284	314	328	361	?	4
$^4F_{7/2}$	20	596	652	686	771			?	4
$^4F_{5/2}$	22	312	325	355				?	4

Yb:YF_3

Term	Prefix	Energy (cm^{-1})			T	Ref.
$^2F_{7/2}$	-	0	116		?	4
$^2F_{5/2}$	10	230	367	587	4.2	7

References for 5.5. YF_3

1. Zalkin, A. and D.H. Templeton, 1953, J. Am. Chem. Soc. **75**, 2453.
2. Cheetham, A.K. and N. Norman, 1974, Acta Chem. Scand. **A28**, 55.
3. Morrison, C.A., D.E. Wortman and R.P. Leavitt, unpublished results.
4. Davydova, M.P., B.N. Kazakov and A.L. Stolov, 1978, Sov. Phys. Solid State **20**, 1378.
5. Orlov, M.S. and A.L. Stolov, 1975, Opt. Spectrosc. **39**, 640.
6. Bumagina, L.A., B.N. Kazakov, B.Z. Malkin and A.L. Stolov, 1977, Sov. Phys. Solid State **19**, 624.
7. Kuroda, H., S. Shionoya and T. Kushida, 1972, J. Phys. Soc. Japan **33**, 125.

5.6. RF_3

Rare-earth fluorides exist in two structures at room temperature. For $La \leq R \leq Pm$, the appropriate structure is that of tysonite (LaF_3), which is generally agreed upon as $P\bar{3}cl$, although some controversy still exists (see section 5.2: LaF_3 for a discussion of some of the alternative structures). For $Sm \leq R \leq Lu$, the fluorides are orthorhombic with space group Pnma at room temperature; a hexagonal phase exists at elevated temperatures (Sobolev and Fedorov, 1973). Structural properties (Garashina and Vishnyakov, 1977) and growth methods (Garton and Walker, 1978) have been discussed.

Infrared spectra (Wesley and DeKock, 1971) and Raman spectra (Bauman and Porto, 1967; Lesiecki et al., 1972) have been measured, the latter providing additional support for the $P\bar{3}cl$ space group of the light rare-earth fluorides. Crystal-field splittings have been obtained by optical spectroscopy, infrared and

Raman spectroscopy (see tables), and also inelastic neutron scattering (Feldman et al., 1971, 1975). Magnetic ordering in TbF_3 has been investigated by means of neutron diffraction (Piotrowski, 1980) and nuclear magnetic resonance (NMR) (Al'tshuler et al., 1972). NMR studies of other rare-earth fluorides have also been performed (Reuveni and McGarvey, 1978; Hansen et al., 1978). Laser action has been observed in several rare earth fluorides including $Nd:CeF_3$ (O'Connor and Hargreaves, 1964), PrF_3 (Hegarty and Yen, 1980), and HoF_3 (Devor et al., 1971).

5.6.1 Crystallographic data for RF_3

Tysonite structure:

Trigonal $P\bar{3}c1$, #165, Z = 6

Ion	Pos.	Symm.	x	y	z
R	6(f)	C_2	x	0	1/4
F_1	12(g)	C_1	x	y	z
F_2	4(d)	C_3	1/3	2/3	z
F_3	2(a)	D_3	0	0	1/4

X-ray data

R	a	c	Ref.
Ce	7.114	7.273	1
Ce	7.131	7.286	2
Pr	7.061	7.218	1
Nd	7.021	7.196	1
Pm	6.970	7.188	1

	R	F_1			F_2	
R	x	x	y	z	z	Ref.
Ce	0.6607	0.3659	0.0540	0.0824	0.1871	2

Crystallographic data for RF_3(continued)

Yttrium fluoride structure:

Orthorhombic Pnma, #62, Z = 4

Ion	Pos.	Symm.	x	y	z
R	4(c)	C_s	x	1/4	z
F_1	4(c)	C_s	x	1/4	z
F_2	8(d)	C_1	x	y	z

X-ray data

R	a	b	c	Ref.
Sm	6.669	7.059	4.405	3
Eu	6.622	7.019	4.396	3
Eu	6.620	7.020	4.395	4
Gd	6.570	6.984	4.393	3
Tb	6.513	6.949	4.384	3
Tb	6.515	6.950	4.385	4
Dy	6.460	6.906	4.376	3
Dy	6.465	6.900	4.375	4
Ho	6.404	6.875	4.379	3
Er	6.354	6.846	4.380	3
Tm	6.283	6.811	4.408	3
Tm	6.285	6.815	4.405	4
Yb	6.216	6.786	4.434	3

	R		F_1		F_2			
R	x	z	x	z	x	y	z	Ref.
Tb	0.368	0.061	0.522	0.584	0.165	0.066	0.384	5
Ho	0.367 •	0.059	0.525	0.584	0.166	0.066	0.377	5

5.6.2 Index of refraction for RF_3 (Ref. 1)

Tysonite structure

R	n_o	n_e
Ce	1.613	1.607
Pr	1.618	1.614
Nd	1.628	1.621

Yttrium fluoride structure

R	n_a	n_c
Sm	1.577	1.608
Eu	1.570	1.600
Gd	1.570	1.600
Tb	1.570	1.600
Dy	1.570	1.600
Ho	1.566	1.598
Er	1.566	1.598
Tm	1.564	1.598
Yb	1.558	1.594
Lu	1.554	1.588

5.6.3 Crystal-field parameters for $R:RF_3(cm^{-1})$

Tysonite structure

R	B_{20}	B_{22}	B_{40}	RB_{42}	IB_{42}	RB_{44}	IB_{44}	Ref.
Nd	-322	-36	414	456	0	541	0	6

R	B_{60}	RB_{62}	IB_{62}	RB_{64}	IB_{64}	RB_{66}	IB_{66}	Ref.
Nd	685	-1028	0	-524	0	-758	0	6

Yttrium fluoride structure

R	B_{20}	B_{22}	B_{40}	RB_{42}	IB_{42}	RB_{44}	IB_{44}	Ref.
Eu	407	371	-150	39	113	-202	123	7
Ho	78.5	337.9	17.9	10.5	106.5	-108.5	260.8	8

R	B_{60}	RB_{62}	IB_{62}	RB_{64}	IB_{64}	RB_{66}	IB_{66}	Ref.
Eu	161	-487	-63	52	-303	-236	240	7
Ho	224.6	-568.6	79.6	-4.7	75.6	-374.6	-159.3	8

5.6.4 Energy levels for R':RF_3

Ce:CeF_3

Term	Prefix	Energy (cm^{-1})						T	Ref.
$^2F_{5/2}$	-	0	148					4.2	9
$^2F_{7/2}$	2	158	238	638	848			4.2	9

Pr:PrF_3

Term	Prefix	Energy (cm^{-1})						T	Ref.
$^3H_4$	-	0	68	98	248	460	539	4.2	10
	-	0	65	68.5	77	91		4.2	11
$^3H_5$	2	194	(288)					4.2	10

Nd:CeF_3

Term	Prefix	Energy (cm^{-1})						T	Ref.
$^4I_{9/2}$	-	0	45	144	303	510		77	12
$^4I_{11/2}$	1	986	043*	077	101	199	237	77	12
$^4F_{3/2}$	11	598	643					77	12
$^2P_{1/2}$	23	480						77	12

Nd:NdF_3

Term	Prefix	Energy (cm^{-1})						T	Ref.
$^4I_{9/2}$	-	0	38	142	331	522		4.2	6
	-	0	45					4.2	11
$^4I_{13/2}$	3	929	982	052*	090	131	210	4.2	6
	3	305						4.2	6
$^4I_{15/2}$	5	808	882	996	157*	181	344	4.2	6
	5	500	590					4.2	6
$^4F_{3/2}$	11	600	646					4.2	6
$^4F_{5/2}$, $^2H_{9/2}$	12	600	614	658	684	703	770	4.2	6
	12	860	923					4.2	6
$^4F_{7/2}$, $^4S_{3/2}$	13	521	604	671	691	738	738	4.2	6

Nd:NdF_3 (continued)

Term	Pre-fix	Energy (cm^{-1})						T	Ref.
$^4F_{9/2}$	14	846	870	912	941	972		4.2	6
$^2H_{11/2}$	16	003	041	057	067	111	179	4.2	6
$^4G_{5/2}$	17	313	319	376				4.2	6
$^2G_{7/2}$	17	525	535	590	621			4.2	6
$^4G_{7/2}$	19	150	238	260	342			4.2	6
$^2K_{13/2}$, $^4G_{9/2}$	19	585	612	658	689	712	751	4.2	6
	19	806	849	897	980			4.2	6
$^2G_{9/2}$	21	160	177	200	236			4.2	6
$^2D_{3/2}$, $^2K_{15/2}$,	21	259	340	354	687	725	777	4.2	6
	21	786	815	853	901	944	964	4.2	6
$^4G_{11/2}$	21	993	007*					4.2	6
$^2P_{1/2}$	23	471						4.2	6
$^2D_{5/2}$	23	952	004*	056				4.2	6
$^2P_{3/2}$	26	350	406					4.2	6
$^4D_{3/2}$	28	313	361					4.2	6
$^4D_{5/2}$	28	498	522	653				4.2	6
$^4D_{1/2}$	28	952						4.2	6
$^2I_{11/2}$	29	429	455	553	603	753		4.2	6
$^2L_{15/2}$, $^4D_{7/2}$	30	221	248	312	403	432	525	4.2	6
	30	544	572	637	665	769		4.2	6
$^2I_{13/2}$	30	845	941	998	027*	133		4.2	6
$^2L_{17/2}$	31	736	847					4.2	6
$^2H_{9/2}$	32	992	058*	146	200	234		4.2	6
$^2D_{3/2}$	33	568	602					4.2	6

Eu:EuF_3

Term	Prefix	Energy (cm^{-1})						T	Ref.
$^7F_0$	-	0						4.2	13
$^7F_1$	-	258	420	454				4.2	13
$^7F_2$	-	997	013*	045	098	144		4.2	13
$^7F_3$	1	865	881	898	917	959	990	4.2	13
	1	995						4.2	13
$^7F_4$	2	775	810	819	851	862	904	4.2	13
	2	923	964	996				4.2	13
$^7F_5$	3	779	807	864	916	928	983	4.2	13
	3	007*	018	037	065			4.2	13
$^7F_6$	4	827	897	019*	084	122	136	4.2	13
	4	229						4.2	13
$^5D_0$	17	290						4.2	13
$^5D_1$	19	026	057	067				4.2	13
$^5D_2$	21	512	516	536	546			4.2	13

Tb:GdF_3

Term	Prefix	Energy (cm^{-1})						T	Ref.
$^7F_6$	-	0	82	98	136	144	152	77	14
	-	221	340	423				77	14
$^7F_5$	2	111	145	176	187	196	225	77	14
	2	265	295	340				77	14
$^5D_4$	20	581	592	594	602	639	651	77	14
	20	695						77	14

Tb:TbF_3

Term	Prefix	Energy (cm^{-1})						T	Ref.
$^7F_6$	-	0	42	43	60	125	140	4.2	15
	-	0	110	112	162	174	185	77	14
	-	169	209	212	217	232	319	4.2	15
	-	250	365	439				77	14
	-	353	488					4.2	15
$^7F_5$	2	139	176	197	201	208	216	4.2	15
	2	134	171	192	202	213	246	77	14
	2	219	250	287	321	357		4.2	15
	2	281	317	352	454	484		77	14

Tb:TbF_3 (continued)

Term	Prefix	Energy (cm^{-1})						T	Ref.
$^7F_4$	3	366	452	470	539	597	633	4.2	15
	3	667						4.2	15
$^7F_3$	4	455	468	520	559	572	578	4.2	15
	4	598						4.2	15
$^7F_2$	5	109	194	239	253	289		4.2	15
$^7F_1$	5	606	656	801				4.2	15
$^7F_0$	5	945						4.2	15
$^5D_4$	20	603	615	630	(643)	666	676	4.2	15
	20	607	609	617	619	633	669	77	14
	20	721						4.2	15
	20	679	727					77	14

Tb:DyF_3

Term	Prefix	Energy (cm^{-1})						T	Ref.
$^7F_6$	-	0	101	146	152	160	229	77	14
	-	348	417					77	14
$^7F_5$	2	112	148	179	183	197	226	77	14
	2	268	299	334				77	14
$^5D_4$	20	581	591	592	602	639	649	77	14
	20	691						77	14

Dy:DyF_3

Term	Prefix	Energy (cm^{-1})		T	Ref.
$^6H_{15/2}$	-	0	15.5	4.2	11

Ho:HoF_3

Term	Prefix	Energy (cm^{-1})						T	Ref.
$^5I_8$	-	0	7.3	18.7	32.5	54.1	76.7	77	16
	-	0	5.9	38.0				2	17
	-	0	54.6					4.2	11
	-	103.5	125.3	149.4	204.2	211.1		77	16
$^5I_6$	8	607.1	621.8	646.6	670.0	680.0	703.5	77	16
	8	716.0	745.7	761.7	771.6	787.6	822.1	77	16
	8	858.6						77	16
$^5I_5$	11	170.3	176.7	201.7	245.2	254.9	277.5	77	16
	11	298.8	311.6	334.9	353.6	406.8		77	16
$^3K_8$	21	419.84	423.16	431.98	454.53	457.85	460.49	2	17
	21	466.13	467.23	475.52	484.13	486.17	492.57	2	17
	21	520.06	522.50	542.96	554.48	557.79		2	17
$^5G_4$	25	939.43	987.77	011.31*	024.67	041.75	056.99	2	17
	25	059.93	111.20	120.53				2	17

Er:ErF_3

Term	Prefix	Energy (cm^{-1})		T	Ref.
$^4I_{15/2}$	-	0	52	4.2	11

References for 5.6. RF_3

1. Hellwege, K.H., Ed., 1973, Landolt-Bornstein, Numerical Data and Functional Relationships in Science and Technology, New Series, Group III, Vol. 7a (Springer-Verlag, New York).
2. Cheetham, A.K., B.E.F. Fender, H. Fuess and A.F. Wright, 1976, Acta Cryst. **B32**, 94.
3. Zalkin, A. and D.H. Templeton, 1953, J. Am. Chem. Soc. **75**, 2453.
4. Jones, D.A. and W.A. Shand, 1968, J. Crystal Growth **2**, 361.
5. Piotrowski, M., H. Ptasiewicz-Bak and A. Muraskik, 1979, Phys. Stat. Sol. (a) **55**, K163.
6. Caro, P., J. Derouet, L. Beaury, G. Teste de Sagey, J.P. Chaminade, J. Aride and M. Pouchard, 1981, J. Chem. Phys. **74**, 2698.
7. Wortman, D.E., C.A. Morrison and R.P. Leavitt (unpublished results).
8. Sharma, K.K., F.H. Spedding and D.R. Blinde, 1981, Phys. Rev. **B24**, 82.
9. Buchanan, R.A., H.E. Rast and H.H. Caspers, 1966, J. Chem. Phys. **44**, 4063.
10. Koningstein, J.A. and P. Grunberg, 1971, Can J. Chem. **45**, 2336.
11. Hadni, A. and P. Strimer, 1972, Phys. Rev. **B5**, 4609.
12. Dmitruk, M.V., A.A. Kaminskii and I.A. Shcherbakov, 1968, Sov. Phys. JETP **27**, 900.
13. Caspers, H.H., H.E. Rast and J.L. Fry, 1967, J. Chem. Phys. **47**, 4505.
14. Bumagina, L.A., B.N. Kazakov, B.Z. Malkin and A.L. Stolov, 1977, Sov. Phys. Solid State **19**, 624.
15. Krupka, D.C. and H.J. Guggenheim, 1969, J. Chem. Phys. **51**, 4006.
16. Sharipov, Kh.T., Yu.P. Agureev, K.I. Petrov and N.V. Porotnikov, 1975, in: Spektroskopiya Kristallov (Nauka, Moscow), p. 287.
17. Blinde, D.R., 1974, M.S. Thesis, Iowa State University.

5.7. $RCl_3 \cdot 6H_2O$

The early work on rare-earth trichloride hexahydrates, $RCl_3 \cdot 6H_2O$, was done by Spedding and his co-workers (Freed and Spedding, 1929a, b, 1931; Spedding, 1931, 1933; Spedding and Nutting, 1931; Spedding et al., 1940). In this early series of papers, Spedding outlined the motive for his subsequent work and his intention to pursue the analysis of the optical spectra of rare-earth ions in solids. Much of this material makes good reading today, some fifty years later. The analysis of the $YbCl_3 \cdot 6H_2O$ spectrum has been reported by Eisenstein (1961) assuming predominantly axial symmetry; he also suggests the possibility of the material being ferroelectric or antiferroelectric. The analysis of optical spectra of $GdCl_3 \cdot 6H_2O$ has been performed by Jones and Judd (1970); they show that, with the crystal field assumed predominately axial, they get good agreement with the experimental Zeeman splittings of the crystal field levels of Gd^{3+}. Pressure dependence of Stark splittings in $NdCl_3 \cdot 6H_2O$ has been studied (Voloshin et al., 1976). From specific heat measurements, Lagendijk et al. (1970) reported the possibility of a phase transition in $ErCl_3 \cdot 6H_2O$ at 0.356 K. Later Felsteiner (1970) showed that ferromagnetic rather than antiferromagnetic ordering was favorable in this compound if the interaction between rare-earth ions was assumed to be dipolar. Zeeman-effect measurements have been reported by Dieke and Heroux (1956) on $NdCl_3 \cdot 6H_2O$, and similar measurements have been reported on $SmCl_3 \cdot 6H_2O$ by Friedrich et al. (1960) and on $TmCl_3 \cdot 6H_2O$ by Gruber et al. (1970). A very thorough study of the electron paramagnetic resonance of Gd^{3+} in $RCl_3 \cdot 6H_2O$ for R = Nd, Sm, Eu, Tb, Dy, Ho, Er, Tm, Y, and Yb has been given by Misra and Mikolajczak (1979). These workers report the spin-Hamiltonian values for all of the compounds above and compare their result with a point-charge lattice-sum evaluation.

Linewidths and lineshifts of $EuCl_3 \cdot 6H_2O$ have been reported by Hill and Hüfner (1970) and by Sovers et al. (1976), with the rather surprising result that the shifts are toward shorter wavelength at higher temperature. Usually such shifts are in the opposite direction such as, for example, in the ruby R lines (Imbusch et al., 1964). The hypersensitive transitions of $NdCl_3 \cdot 6H_2O$ have been investigated by Karraker (1968) and the interference between the electric and magnetic dipole absorption of $EuCl_3 \cdot 6H_2O$ has been reported by Nordmann (1970). In the latter work, the interference is observed by measuring the oscillator strengths of two absorption lines with polarized radiation. The infrared spectra of $RCl_3 \cdot 6H_2O$ for R equal to all the rare earths and yttrium have been reported by Kharzeeva and Serehrennikov (1973).

An interesting experiment on multiphonon depopulation of excited states for R = Tb or Eu in $RCl_3 \cdot 6H_2O$ has been reported by Heber (1967). Selecting states of Eu^{3+} or Tb^{3+} that were depopulated by multiphonon excitation of the H_2O molecules, Heber compared the fluorescence lifetimes to those obtained when H_2O is replaced by D_2O. The results were striking. In all cases considered the lifetimes in the deuterium compounds were much longer.

5.7.1 Crystallographic data for $RCl_3 \cdot 6H_2O$

Monoclinic P2/n, #13, Z = 2

Ion	Pos.	Symm.	x	y	z
R	2(e)	C_2	1/4	y	1/4
Cl_1	2(f)	C_2	3/4	y	1/4
Cl_2	4(g)	C_1	x	y	z
O_1	4(g)	C_1	x	y	z
O_2	4(g)	C_1	x	y	z
O_3	4(g)	C_1	x	y	z
H_1	4(g)	C_1	x	y	z
H_2	4(g)	C_1	x	y	z
H_3	4(g)	C_1	x	y	z
H_4	4(g)	C_1	x	y	z
H_5	4(g)	C_1	x	y	z
H_6	4(g)	C_1	x	y	z

X-ray data

R	a	b	c	β	Ref.
Nd	9.761	6.579	8.033	93.75	1
Sm	9.67	6.55	7.96	93.67	2
Eu	9.67	6.52	7.99	94.60	3
Eu	9.68	6.53	7.96	93.67	2
Gd	9.64	6.53	7.93	93.67	2
Gd	9.651	6.525	7.923	93.65	4
Tb	9.63	6.51	7.89	93.67	2
Dy	9.61	6.49	7.87	93.67	2
Ho	9.58	6.47	7.84	93.67	2
Er	9.582	6.447	7.834	93.70	1
Er	9.57	6.47	7.84	93.67	2
Tm	9.55	6.45	7.82	93.67	2

Crystallographic data for $RCl_3 \cdot 6H_2O$ (continued)

	R	Cl_1	Cl_2			O_1			
R	y	y	x	y	z	x	y	z	Ref.
Eu	0.1512	0.373	0.057	0.840	0.259	0.281	0.040	0.552	3,5
Gd	0.1521	0.3769	0.0587	0.8370	0.2601	0.2813	0.0471	0.5432	3
Dy	0.15391	0.3749	0.05999	0.83865	0.26015	0.2823	0.0519	0.5419	5
Ho	0.15483	0.25000	0.06023	0.83972	0.26009	0.2815	0.0515	0.5401	5

	O_2			O_3			H_1			
R	x	y	z	x	y	z	x	y	z	Ref.
Eu	0.152	0.427	0.088	0.440	0.297	0.110	-	-	-	3,5
Gd	0.1423	0.4254	0.0888	0.4406	0.2988	0.1058	0.272	0.920	0.605	3
Dy	0.1460	0.4254	0.0890	0.4382	0.2999	0.1063	-	-	-	5
Ho	0.1456	0.4235	0.0896	0.4363	0.3002	0.1064	-	-	-	5

	H_2			H_3			H_4			
R	x	y	z	x	y	z	x	y	z	Ref.
Gd	0.364	0.082	0.608	0.174	0.484	0.987	0.117	0.548	0.140	3

	H_5			H_6			
R	x	y	z	x	y	z	Ref.
Gd	0.534	0.322	0.149	0.476	0.258	0.002	3

5.7.2 Crystal-field parameters for $R:RCl_3 \cdot 6H_2O$ (cm^{-1})

R	B_{20}	B_{22}	B_{40}	IB_{42}	IB_{42}	RB_{44}	IB_{44}	Ref.
Ho	108	392	-63	-338	-37	-301	79	6
Er	116	306	-88	-396	13	-295	220	7
Tm	76	423	-80	-342	-28	-298	140	8

Crystal-field parameters for $R:RCl_3 \cdot 6H_2O$ (cm^{-1}) (continued)

R	B_{60}	RB_{62}	IB_{62}	RB_{64}	IB_{64}	RB_{66}	IB_{66}	Ref.
Ho	-4.5	-102	-77	-52	248	-262	198	6
Er	-9.8	-157	13	-6	266	-237	25	7
Tm	-5.7	-93	-79	-34	198	-199	218	8

5.7.3 Energy levels for $R:RCl_3 \cdot 6H_2O$

$NdCl_3 \cdot 6H_2O$

Term	Prefix	Energy (cm^{-1})						T	Ref.
$^4I_{9/2}$	-	0						4.2	9,10
$^4F_{3/2}$	11	457.38	531.44					4.2	9
$^4F_{5/2}$, $^2H_{9/2}$	12	475.47	508.61	539.64	571.30	617.74	673.69	4.2	9
	12	705.20	739.07					4.2	9
$^4F_{7/2}$, $^2S_{3/2}$	13	408.71	484.42	524.33	567.25	578.44	586.28	4.2	9
$^4F_{9/2}$	14	687.29	732.05	768.77	806.75	862.36		4.2	9
	14	688.0	732.6	770.2	807.4	862.0		80	10
$^2H_{11/2}$	15	885.06	921.27	936.65	019.67*	050.17		4.2	9
	15	885.3	921.7	935.9	020.4*	048.5		80	10
$^4G_{5/2}$, $^2G_{7/2}$	17	129.29	158.04	228.91	330.14	451.15	470.22	4.2	9
$^4G_{7/2}$	19	000.87	033.17	095.67	143.98			4.2	9
	19	001.8	034.7	096.2	144.8			80	10
$^2G_{9/2}$	19	514.77	524.60	539.46	570.96	581.41		4.2	9
	19	515.2	522.8	540.3	574.0	582.0		80	10
$^4G_{9/2}$	20	657.61	668.64					4.2	9
$^2D_{3/2}$, $^4G_{11/2}$	21	008.66	036.32	076.68	128.19			4.2	9
$^2D_{5/2}$, $^2P_{1/2}$	23	283.42	757.77					4.2	9
	23	284.5						80	10
$^2P_{3/2}$	26	159.73						4.2	9
$^4D_{3/2}$	28	009.87	075.26					4.2	9
$^4D_{5/2}$	28	282.79	312.34	337.82				4.2	9
$^2I_{11/2}$, $^4D_{1/2}$	28	366.84	402.11	419.16				4.2	9

$SmCl_3 \cdot 6H_2O$

Term	Prefix	Energy (cm^{-1})						T	Ref.
$^6H_{5/2}$	-	0	145	315				4.2	11
$^4G_{7/2}$	20	023.90	041.45					4.2	11
$^2P_{3/2}$, $^4L_{13/2}$	24	540.2	568.1	585.8	617.0	634.5	652.6	4.2	11
	24	654	(659)					4.2	11

$EuCl_3 \cdot 6H_2O$

Term	Prefix	Energy (cm^{-1})					T	Ref.
$^7F_0$	-	0					58	12
$^7F_1$	-	304.65	395.83	423.29			58	12
$^5D_0$	17	259.58					58	12
$^5D_1$	19	003.02	025.19	027.80			58	12
$^5D_2$	21	455.68	477.67	479.88	514.64	522.42	58	12

$GdCl_3 \cdot 6H_2O$

Term	Prefix	Energy (cm^{-1})					T	Ref.
$^8S_{7/2}$	0						1.7	13-16
$^6P_{7/2}$	32	065	091	121	145		4	13
	32	059.6	091.7	123.3	147.6		1.8	14
	32	065.60	090.95	121.49	144.86		1.7	15
	32	067.2	087.9	116.7	139.5		300	16
$^6P_{5/2}$	32	658	698	739			4	13
	32	660.4	699.9	740.9			1.8	14
	32	658.67	698.57	739.19			1.7	15
	32	658.0	695.7	733.6			300	16
$^6P_{3/2}$	33	256	288				4	13
	33	254.9	290.3				1.8	14
$^6I_{7/2}$	35	792	826	844	873		4	13
	35	791.2	825.5	844.5	873.3		1.8	14
	35	790.27	823.94	844.03	872.95		1.7	15
	35	786.4	818.3	836.0	866.0		300	16
$^6I_{9/2}$	36	136	164	180	195	203	4	13
	36	136.9	164.5	182.4	196.3	204.3	1.8	14
	36	134.0	159.3	175.4	189.2	200.2	300	16

$GdCl_3 \cdot 6H_2O$ (continued)

Term	Prefix	Energy (cm^{-1})						T	Ref.
$^6I_{17/2}$	36	217	219	229	235	241	246	4	13
	36	220.3	230.4	235.9	242.0	247.5	253.6	1.8	14
	36	212.5	225.1	229.2	235.3	239.9	245.5	300	16
	36	252	261					4	13
	36	262.6						1.8	14
	36	253.1						300	16
$^6I_{11/2}$	36	410	438	452	457	483	499	4	13
	36	413.0	439.7	455.8	485.0	500.1		1.8	14
	36	408.3	433.0	448.0	452.7	477.6	492.8	300	16
$^6I_{15/2}$, $^6I_{13/2}$	36	533	548	557	565	577	590	4	13
	36	530.4	546.0	553.9	556.3	563.3	571.7	300	16
	36	603	615	626	646	657		4	13
	36	583.4	587.8	595.2	599.6	608.0	617.8	300	16
	36	621.9	640.4	649.5				300	16
$^6D_{9/2}$	39	507	525	565	593	627		4	13
	39	504.4	524.6	564.8	591.4	623.4		1.8	14
	39	499.4	518.9	557.1	582.6	618.6		300	16
$^6D_{1/2}$	40	478						4	13
	40	467.7						1.8	14
	40	470.3						300	16
$^6D_{7/2}$	40	579	582	593	598			4	13
	40	565.7	583.7					1.8	14
	40	570.8	582.0					300	16
$^6D_{3/2}$	40	725	776					4	13
	40	729.2	779.6					1.8	14
	40	717.4	764.2					300	16
$^6D_{5/2}$	40	859	885	943				4	13
	40	862.0	895.6	946.5				1.8	14
	40	848.6	881.0	931.7				300	16
$^6G_{7/2}$	48	939	999	100*	153			77	13
$^6G_{9/2}$, $^6G_{11/2}$	49	301	335	405	457	484	530	77	13
	49	572	614	698	708			77	13

$TbCl_3 \cdot 6H_2O$

Term	Prefix	Energy (cm^{-1})						T	Ref.
$^7F_6$	-	0	35.1	50.4	77.2	(83.8)	159.1	2.2	17
	-	168.6	(179.5)	(190.9)	233.0	300.4	(345.9)	2.2	17
	-	359.4						2.2	17
$^7F_5$	2	105.7	125.8	137.8	179.4	197.7	205.1	2.2	17
	2	230.2	242.9	246.3	414.0	431.0		2.2	17

$TbCl_3 \cdot 6H_2O$ (continued)

Term	Prefix	Energy (cm^{-1})						T	Ref.
$^7F_4$	3	345.3	350.6	354.0	403.0	406.8	433.9	2.2	17
	3	471.3	482.5	524.1				2.2	17
$^7F_3$	4	375.9	458.1	468.4	495.5	500.8	505.9	2.2	17
	4	510.7						2.2	17
$^7F_2$	5	038.9	108.7	241.2	245.8	285.6		2.2	17
$^7F_1$	5	537.5	544.1	600.4				2.2	17
$^7F_0$	5	847.0						2.2	17
$^5D_4$	20	538.9	544.3	549.3	555.1	562.1	576.7	2.2	17
	20	580.8	641.6	643.3				2.2	17
$^5D_3$, $^5L_{10}$	26	335.1	338.4	355.7	368.2	378.6	401.5	2.2	17
	26	420.7						2.2	17
$^5G_5$, $^5G_6$	26	951.2	965.4	008.6*	013.6	069.6	072.8	2.2	17
	26	117.1	146.1	150.4	191.8			2.2	17
$^5L_9$	27	821.7	826.9	838.5	843.7	850.0	875.5	2.2	17
	27	880.6	888.2	891.7*	898.7	904.2	906.1	2.2	17
	27	994.8	006.6*					2.2	17
$^5D_2$, $^5G_4$, $^5L_8$	28	224.0	227.1	258.9	288.8	347.5	352.6	2.2	17
	28	373.9	401.8	413.8	437.1	444.3	465.1	2.2	17
	28	469.9	473.4	478.5	484.8	491.4	507.0	2.2	17
	28	587.9	603.1	655.1				2.2	17
$^5G_2$, $^5L_7$, $^5L_6$	29	048.1	051.9	060.4	119.4	130.1	224.5	2.2	17
	29	226.3	247.0	249.2	270.2	328.7	350.1	2.2	17
	29	364.7	488.3	490.0	731.4			2.2	17

$DyCl_3 \cdot 6H_2O$

Term	Prefix	Energy (cm^{-1})						T	Ref.
$^6H_{15/2}$	-	0	34.1	(62.5)	77.5	93.3	113.3	4.2	18
	-	155.2	495.6					4.2	18
$^6H_{13/2}$	3	491.7	503.3	546.0	562.1	590.0	551.0	4.2	18
	3	(776)						4.2	18
$^6H_{11/2}$	5	811.0	840.8	858.2	918.2			4.2	18
$^6H_{9/2}$, $^6F_{11/2}$	7	607.0	610.8	658.1	675.5	746.9		4.2	18
$^6H_{7/2}$	8	958.51	992.49					4.2	19
$^6F_{9/2}$	9	101.80	117.65					4.2	19
$^6H_{5/2}$	10	131.99	182.62					4.2	19
$^6F_{7/2}$	10	970.41	987.83	045.27	067.74			4.2	19

$DyCl_3 \cdot 6H_2O$ (continued)

Term	Prefix	Energy (cm^{-1})						T	Ref.
$^6F_{5/2}$	12	372.07	396.36	452.49	472.99	538.44		4.2	19
	12	372.1	396.4	452.5				4.2	18
$^6F_{3/2}$	13	199.94	207.10					4.2	19
$^4F_{9/2}$	20	958.80	037.35*	091.55	097.89	180.73	183.90	4.2	19
	20	283.49	294.58					4.2	19
$^4I_{15/2}$	22	032.1	046.4	083.4	110.5	117.6	122.1	4.2	18
	22	161.7	221.4	260	297.7			4.2	18
$^4G_{11/2}$	23	351.0	406.0	444.4	475.5	500.7	547.2	4.2	18

$HoCl_3 \cdot 6H_2O$

Term	Prefix	Energy (cm^{-1})						T	Ref.
$^5I_8$	-	0	8.69	17.68	30.63	69.57	130.0	4.2	22
$^5I_6$	8	658.52	662.70	672.97	677.25	682.86	686.85	2.2	20
	8	690.79	704.52	709.77				2.2	20
$^5I_5$	11	224.83	226.90	237.37	251.89	252.68	253.50	2.2	20
	11	224.80	226.78	237.28	246.42	251.81	252.62	4.2	22
	11	256.06	264.20	340.2				2.2	20
	11	253.39	256.10	264.21	334.60	340.20		4.2	22
$^5I_4$	13	180.9	193.9	203.1	277.6	296.1	304.6	2.2	20
	13	347.6	397.4	427.9				2.2	20
$^5F_5$	15	426.07	457.56	458.73	490.64	490.95	540.36	2.2	20
	15	457.66	458.89	490.73	490.92			14	21
	15	457.92	459.11	490.90	491.14	540.79	547.4	4.2	22
	15	553.7	632	639.3	649	653		2.2	20
	15	554.4	575.51	593.3	597.5	620.0		4.2	22
$^5S_2$, $^5F_4$	18	462.45	469.03	470.58	486.64	491.09	530.1	2.2	20
	18	462.59	469.22	470.82	486.52	491.20	530.36	14	21
	18	462.29	469.12	470.82	486.50	491.18	530.26	4.2	22
	18	535.79	595.2	603.42	621.2	632.5	651	2.2	20
	18	535.93	595.41	603.56	621.18	631.51	651.06	14	21
	18	536.13	595.02	603.60	621.06	629.49	651.56	4.2	22
	18	673						2.2	20
	18	656.18	672.71					14	21
	18	656.36	676.69					4.2	22
$^5F_3$	20	599.68	608.61	629.48	689.2	696.2	707.7	2.2	20
	20	599.88	608.78	629.64	690.07	696.43	708.18	14	21
	20	599.76	608.63	629.47	690.06	696.30	707.21	4.2	22
	20	711.2						2.2	20
	20	711.26						14	21
	20	708.27						4.2	22

$HoCl_3 \cdot 6H_2O$ (continued)

Term	Prefix	Energy (cm^{-1})						T	Ref.
$^5F_2$	21	091.6	102.3	154.3	161.9	163.9		2.2	20
	21	091.55	102.53	163.41				14	21
	21	091.37	101.61	102.68	146.02	163.43		4.2	22
$^3K_8$	21	353.44	363.09	371.78	390.78	392.58	404.3	2.2	20
	21	353.22	353.91	363.38	372.08	372.68	391.04	14	21
	21	352.42	353.01	362.78	371.22	372.27	390.15	4.2	22
	21	407.50	412.14	417.56	440.53	442.17	443.4	2.2	20
	21	392.80	404.63	407.69	412.44	417.85	440.86	14	21
	21	391.99	403.76	406.78	411.41	416.92	439.79	4.2	22
	21	459.5	461.5	465.7				2.2	20
	21	442.26	459.79	461.71	465.91			14	21
	21	441.90	443.19	458.61	461.28	465.38		4.2	22
$^5I_6$, $^5F_1$	22	086.3	114.8	116.9	119.5	121.3	123.5	2.2	20
	22	150.8	179.0	181.7	235	284	298	2.2	20
	22	314	328	332.5	342.2	349.5	392.3	2.2	20
$^5G_5$	23	928.5	975.73	980	988	013*	016	2.2	20
	23	049	058	097				2.2	20
$^5G_4$	25	847.12	852.84	877.62	879.32	886.38	899.8	2.2	20
	25	846.90	852.71	879.08	885.91	899.73	923.64	4.2	22
	25	924.0	952.4	956.9	963.6			2.2	20
	25	952.31	956.55	963.16				4.2	22
$^3K_7$	26	175.31	177.28	190.80	193.06	206.54	207.94	2.2	20
	26	212.81	213.91	215.55				2.2	20
$^3H_5$	27	563.38	564.82	632.33	634.71	641.24	659.02	2.2	20
	27	668.28	677.05	684.0	692	698.9		2.2	20
$^5G_2$	28	265.35	281.40	283.80	341.00	370.75		4.2	22
$^3D_2$	30	784.32	838.35	848.53	852.63	875.5		4.2	22

$ErCl_3 \cdot 6H_2O$

Term	Prefix	Energy (cm^{-1})						T	Ref.
$^4I_{15/2}$	-	0	16.8	36.7	125.0	179.0	214.6	77	23
	-	0	16.91	37.07				14	24
	-	297.1	308.9					77	23
$^4I_{11/2}$	10	199.4	238.9	254.1	263.6	286.3	296.0	4.2	23
$^4I_{9/2}$	12	392.4	429.3	489.8	563.4	607.4		4.2	23
$^4F_{9/2}$	15	266.0	283.9	331.4	342.6	423.9		4.2	23
	15	266.19	283.96	331.28	342.12	418.56	422.76	14	24

$ErCl_3 \cdot 6H_2O$ (continued)

Term	Prefix	Energy (cm^{-1})						T	Ref.
$^4S_{3/2}$	18	396.0	466.8					4.2	23
	18	396.35	465.93					14	24
$^2H_{11/2}$	19	115.3	155.3	195.8	229.0	246.7	277.2	4.2	23
	19	115.87	154.89	195.94	229.12	245.26	276.08	14	24
$^4F_{7/2}$	20	508.4	545.9	575.6	664.6			4.2	23
	20	509.17	546.30	575.51	644.50	646.96		14	24
$^4F_{5/2}$	22	207.4	220.4	248.6				4.2	23
$^4F_{3/2}$	22	558.4	609.0					4.2	23
$^2H_{9/2}$	24	528.9	551.2	618.0	668.2	691.4		4.2	23
$^4G_{11/2}$	26	357.3	374.8	423.5	471.5	493.4	548.4	4.2	23
$^2G_{9/2}$	27	407.1	411.9	431.2	441.5	470.2		4.2	23
$^2K_{15/2}$	27	482.3	747.4	816.5	819.5	852.5	857.1	4.2	23
	27	883.9	912.1					4.2	23
$^2G_{7/2}$	28	064.0	071.1	098.6				4.2	23
$^2P_{3/2}$	31	517	602					4	25
$^2K_{13/2}$	32	690	750	768	000*	044	081	4	25
	32	148						4	25
$^4G_{5/2}$	33	180	196	224				4	25
$^2P_{1/2}$	33	396						4	25
$^4G_{7/2}$	33	977	009*	038	129			4	25
$^2D_{5/2}$	34	828	865	901				4	25
$^2H_{9/2}$	36	381	415	520	611	621		4	25
$^4D_{5/2}$	38	569	579	584				4	25
$^4D_{7/2}$	38	920	252*					4	25
$^2I_{11/2}$	41	039	072	089	140	157	242	4	25
$^2L_{17/2}$	41	325	497	611	658	713	813	4	25
	41	900	992	172*				4	25
$^4D_{3/2}$	42	263	310					4	25
$^2I_{13/2}$	43	401	490	529	609	716	754	4	25
	43	837						4	25
$^2L_{15/2}$, $^2H_{9/2}$	47	828	928	967	106*	201		4	25
$^2D_{5/2}$	48	908	078*					4	25

$TmCl_3 \cdot 6H_2O$

Term	Prefix	Energy (cm^{-1})						T	Ref.
$^3H_6$	-	0	1.12	272	275	290	310	4.2	26
	-	334	365	398	400	415	442	4.2	26
	-	460						4.2	26
$^3F_4$	12	633.5	652.3	738.3	767.4	781.4	829.6	4.2	26
	12	841.8	905.7	917.8				4.2	26
$^3F_3$	14	522.0	585.1	587.1	591.3	620.6	647.8	4.2	26
	14	651.2						4.2	26
$^3F_2$	15	137.1	184.7	232.3	300.2	309.1		4.2	26
$^1G_4$	21	178.7	194.9	225.0	355.2	364.7	501.7	4.2	26
	21	518.3	554.5	597.4				4.2	26
$^1D_2$	27	958.2	003.5*	033.5	107.4	123.7		4.2	26
$^3P_1$	36	396.6	436.4	568.3				4.2	26
$^3P_2$	38	065.0	126.0	277.7	369.2	397.9		4.2	26

$YbCl_3 \cdot 6H_2O$

Term	Prefix	Energy (cm^{-1})		T	Ref.
$^2F_{7/2}$	-	0	132.8	4.2	28
$^2F_{5/2}$	10	282.32	297.13	4.2	28

References for 5.7. $RCl_3 \cdot 6H_2O$

1. Ivanov, V.I., 1969, Sov. Phys. Crystallogr. **13**, 786.
2. Graeber, E.J., G.H. Conrad and S.F. Duliere, 1966, Acta Cryst. **21**, 1012.
3. Bel'skii, N.K. and Yu.T. Struchkov, 1965, Sov. Phys. Crystallogr. **10**, 15.
4. Marezio, M., H.A. Plettinger and W.H. Zachariasen, 1961, Acta Cryst. **14**, 234.
5. Ugro, J.V., Jr., 1967, Ph.D. Thesis, Iowa State University (University Microfilms 67-13 008).
6. Stöhr, J., D.N. Olsen and J.B. Gruber, 1971, J. Chem. Phys. **55**, 4463.
7. Harrop, I.H., 1965, J. Chem. Phys. **42**, 4000.
8. Olsen, D.N., J. Stöhr and J.B. Gruber, 1971, J. Chem. Phys. **55**, 4471.
9. Dieke, G.H., 1968, Spectra and Energy Levels of Rare Earth Ions in Crystals (Interscience, New York), pp. 213 ff.
10. Voloshin, V.A., N.A. Kulagin, L.N. Ovander and A.M. Prudnikov, 1976, Opt. Spectrosc. **39**, 334.
11. Lammermann, H., 1958, Z. Phys. **150**, 551.
12. Hellwege, K.H. and H.G. Kahle, 1951, Z. Phys. **129**, 62.
13. Carnall, W.T., P.R. Fields and R. Sarup, 1971, J. Chem. Phys. **54**, 1476.
14. Hellwege, K.H., S. Hüfner and H. Schmidt, 1963, Z. Phys. **172**, 460.
15. Dieke, G.H. and L. Leopold, 1957, J. Opt. Soc. Am. **47**, 944.

16. Antic, E., M. Lemaitre-Blaise and P. Caro, 1975, C. R. Acad. Sci. Paris **280**, C407.
17. Ref. 9., pp. 258 ff.
18. Ref. 9, pp. 272 ff.
19. Dieke, G.H. and S. Singh, 1956, J. Opt. Soc. Am. **46**, 495.
20. Ref. 9., pp. 287 ff.
21. Kahle, H.G., 1956, Z. Phys. **145**, 347.
22. Stöhr, J. and J.B. Gruber, 1971, J. Chem. Phys. **55**, 4457.
23. Ref. 9, pp. 298 ff.
24. Kahle, H.G., 1956, Z. Phys. **145**, 361.
25. Carnall, W.T., P.R. Fields and R. Sarup, 1972, J. Chem. Phys. **57**, 43.
26. Olsen, D.N. and J.B. Gruber, 1971, J. Chem. Phys. **54**, 2077.
27. Dieke, G.H. and H.M. Crosswhite, 1956, J. Opt. Soc. Am. **46**, 885.

5.8. $Y(OH)_3$

Interest in the optical spectra of rare-earth doped $Y(OH)_3$ crystals stems from observation that some of the $R(OH)_3$ series magnetically order (Cone, 1972) at low temperature. Also, because the rare-earth sites have the same symmetry (C_{3h}) in both compounds, a comparison with the spectra of rare earths in $LaCl_3$ and $Y(OH)_3$ is useful. Knowledge of the energy levels of the lowest multiplets allows a comparison of the calculated and measured magnetic susceptibility (Kumar et al., 1973). Relaxation studies of Yb:$Y(OH)_3$ have been performed by Lichti and Stapleton (1973). Attempts have been made to derive the observed crystal-field parameters by the superposition model with little success (Kumar et al., 1976). Apparently the growth of $Y(OH)_3$ is relatively easy, at least for crystals large enough for experimental purposes (Mroczkowski et al., 1970). The indices of refraction of $Y(OH)_3$ are $n_o = 1.676$ and $n_e = 1.714$ (Winchell and Winchell, 1964).

5.8.1 Crystallographic data for $Y(OH)_3$

Hexagonal $P6_3/m$, #176, Z = 2

Ion	Pos.	Symm.	x	y	z
Y	2(c)	C_{3h}	1/3	2/3	1/4
O	6(h)	C_s	x	y	1/4
H	6(h)	C_s	x	y	1/4

Crystallographic data for $Y(OH)_3$ (continued)

X-ray data

		O		H		
a	c	x	y	x	y	Ref.
6.261	3.544	0.3958	0.3116	0.28	0.17	1
6.241	3.539	0.3957	0.3115	0.279	0.142	2
6.24	3.53	-	-	-	-	3

5.8.2 Crystal-field parameters for R:$Y(OH)_3$(cm^{-1})

R	B_{20}	B_{40}	B_{60}	B_{66}	Ref.
Gd	350	-624	-576	684	4
Tb	378	-552	-736	638	5
Ho	492	-456	-640	573	6
Er	382	-552	-624	562	7

5.8.3 Energy levels for R:$Y(OH)_3$

Gd:$Y(OH)_3$

Term	Prefix	Energy (cm^{-1})						T	Ref.
$^8S_{7/2}$	-	0						1.5	4
$^6P_{7/2}$	31	999.94	031.90*	053.91	060.83			1.5	4
$^6P_{5/2}$	32	590.59	639.64	653.05				1.5	4
$^6I_{7/2}$	35	750.63	765.45	774.03	776.68			1.5	4
$^6I_{9/2}$	36	090.60	110.57	111.93	117.33	127.79		1.5	4
$^6I_{17/2}$	36	169.85	169.85	172.08	172.24	173.09	175.74	1.5	4
	36	172.26	178.23	178.54				1.5	4
$^6I_{11/2}$	36	365.23	381.98	390.28	390.69	397.17	408.36	1.5	4
$^6I_{15/2}$	36	489.35	496.67	502.72	510.16	517.00	523.28	1.5	4
	36	525.71	528.62					1.5	4
$^6I_{13/2}$	36	537.94	543.36	550.08	550.08	552.66	558.34	1.5	4
	36	564.66						1.5	4

$Tb:Y(OH)_3$

Term	Prefix	Energy (cm^{-1})						T	Ref.
$^7F_6$	-	0	0	111.1	196.0	202.7	213.1	70	5
	-	23/.0						70	5
$^7F_5$	2	065.9	129.7	161.9	215.4	311.1		70	5
$^7F_4$	3	463.0	470.2	527.1	591.0			70	5
$^7F_3$	4	417.6	463.0	476.0	472.1	527.3		70	5

$Ho:Y(OH)_3$

Term	Prefix	Energy (cm^{-1})					T	Ref.
$^5I_8$	-	0	11.32	72.76	102.14		77	6
$^5F_5$	15	491.32	504.43	507.99	526.53	535.25	77	6
$^5F_4$, $^5S_2$	18	554.35	604.70	634.02	672.98		77	6
$^5F_3$	20	618.17	640.86	689.76	713.26		77	6

$Er:Y(OH)_3$

Term	Prefix	Energy (cm^{-1})						T	Ref.
$^4I_{15/2}$	-	0	61.0	136.5	152.6			77	7
$^4I_{11/2}$	10	277.62	282.28	320.42				77	7
$^4I_{9/2}$	12	431.90	583.30					77	7
$^4F_{9/2}$	15	297.45	337.0	357.88	396.44			77	7
$^4S_{3/2}$	18	447.05	493.77					77	7
$^2H_{11/2}$	19	208.9	216.5	224.60	255.27	280.31		77	7
$^4F_{7/2}$	20	520.5	580.1	657.1				77	7
$^4F_{5/2}$	22	239.8	248.4	268.5				77	7
$^4F_{3/2}$	22	622						77	7
$^2H_{9/2}$	24	571.8	664.5	700.3				77	7
$^2G_{11/2}$	26	400.1	435.1	449.8	458.7	489.76	519.21	77	7

References for 5.8. $Y(OH)_3$

1. Beall, G.W., W.O. Milligan and H.A. Wolcott, 1977, J. Inorg. Nucl. Chem. **39**, 65.
2. Christensen, A.N., R.G. Hazell and A. Nilsson, 1967, Acta Chem. Scand. **21**, 481.
3. Wyckoff, R.W.G., 1964, Crystal Structures, Vol. 2, 2nd Ed. (Interscience, New York), pp. 77 ff.
4. Schwiesow, R. and H.M. Crosswhite, 1969, J. Opt. Soc. Am. **59**, 592.
5. Scott, P.D., H.E. Meissner and H.M. Crosswhite, 1969, Phys. Lett. **28A**, 489.
6. Scott, P.D., 1970, Ph.D. Thesis, Yale University (University Microfilms 70-25 119).
7. Cone, R.L., 1972, J. Chem. Phys. **57**, 4893.

5.9. $R(OH)_3$

Most of the interest in the lanthanide trihydroxides, $R(OH)_3$, has focused on attempts to understand the interaction of triply ionized lanthanides with the crystal lattice. The possibility of pursuing a systematic study of the lanthanide series is encouraged by the fact that single crystals of $R(OH)_3$ can be grown with the same structure for almost all the lanthanides including yttrium (Mroczkowski et al., 1970). Several lanthanides having either an accidental or a Kramers degeneracy in the ground state become ferromagnetic or antiferromagnetic at low temperatures (Scott et al., 1969). This feature allows the study of self-induced splitting (internal Zeeman effect) of the energy levels of rare-earth ions at temperatures below the Curie point. The theory of this effect has been considered by Leavitt and Morrison (1978). Further, the character of the internal field in these ferromagnetic systems can be probed by observing the optical spectra of an impurity rare earth R′ in $R(OH)_3$ both above and below the Curie point. Such experiments have been performed by Cone (1972) on Er:$Tb(OH)_3$ and by Scott and Wolf (1969) on Tb:$Tb(OH)_3$. A transition to the antiferromagnetic phase has been reported by Folinsbee et al. (1977) at 1.25 K in $Pr(OH)_3$. The Raman spectra of eight rare-earth compounds $R(OH)_3$, have been determined by Swanson et al. (1978), in which the frequencies and the mode types were determined. Two infrared active modes in $Dy(OH)_3$ were found at 250 and 370 cm^{-1}. The indices of refraction for $La(OH)_3$, $Nd(OH)_3$, and $Sm(OH)_3$ have all been reported as $n_o = 1.740$ and $n_e = 1.768$ (Winchell and Winchell, 1964).

Technological uses of $R(OH)_3$ have undoubtedly been hindered by the difficulty of growing single crystals large enough for applications. At present, the crystals that are grown under high static pressures are quite small (a typical dimension is 1 mm). If a new technique is found to grow large crystals, the material should certainly find applications because of the tremendous variety of compositions that can be formed.

5.9.1 Crystallographic data for $R(OH)_3$

Hexagonal $P6_3/m$, #176, Z = 2

Ion	Pos.	Symm.	x	y	z
R	2(c)	C_{3h}	1/3	2/3	1/4
O	6(h)	C_s	x	y	1/4
H	6(h)	C_s	x	y	1/4

X-ray data

			O		H		
R	a	c	x	y	x	y	Ref.
La	6.523	3.849	-	-	-	-	1
La	6.547	3.854	0.3916	0.3095	0.225	0.152	2
Ce	6.4890	3.8061	0.389	0.308	-	-	3
Pr	-	-	0.390	0.309	0.281	0.143	4
Pr	6.456	3.769	0.392	0.310	-	-	5
Nd	6.422	3.742	-	-	-	-	6
Nd	6.418	3.743	0.3924	0.3108	-	-	2
Nd	6.421	3.74	-	-	-	-	7
Sm	6.371	3.679	-	-	-	-	1
Sm	6.368	3.683	0.3938	0.3113	-	-	2
Eu	6.352	3.653	0.396	0.312	-	-	5
Gd	6.33	3.63	-	-	-	-	1
Gd	6.329	3.631	0.3935	0.3107	0.26	0.13	2
Tb	6.308	3.600	-	-	-	-	1
Tb	6.270	3.560	0.3952	0.3096	0.278	0.143	8
Tb	6.315	3.603	0.3953	0.3120	0.28	0.14	2
Tb	6.308	3.600	0.3946	0.3117	0.2754	0.1426	9
Dy	6.287	3.575	-	-	-	-	1
Dy	6.286	3.577	0.3947	0.3109	0.29	0.15	2
Ho	6.268	3.551	-	-	-	-	1
Ho	6.266	3.553	0.3951	0.3112	0.30	0.17	2
Er	6.250	3.527	-	-	-	-	1
Er	6.243	3.527	0.3945	0.3101	0.23	0.14	2
Tm	6.221	3.503	0.393	0.309	-	-	5

5.9.2 Crystal-field parameters for $R:R(OH)_3$ (cm^{-1})

R	B_{20}	B_{40}	B_{60}	B_{66}	Ref.
Pr	480	-704	-848	663	10
Eu	422	-568	-864	649	11
Gd	366	-456	-1360	884	12
Tb	416	-552	-720	616	13
Dy	418	-608	-640	571	14
Er	384	-512	-640	548	15

5.9.3 Energy levels for $R:R(OH)_3$

$Pr:Pr(OH)_3$

Term	Prefix	Energy (cm^{-1})						T	Ref.
$^3H_4$	-	0	11	120	175	270	380	95	10
$^3F_4$	6	865	935	(985)	035*			95	10
$^3G_4$	9	778	848	964				95	10
$^1D_2$	16	825	098*	174				95	10
$^3P_0$	20	501						95	10
$^3P_1$	21	147	292					95	10
$^3P_2$	22	261	340	481				95	10

$Eu:Eu(OH)_3$

Term	Prefix	Energy (cm^{-1})				T	Ref.
$^7F_0$	-	0				4.2	11
$^7F_1$	-	334.98	435.81			4.2	11
$^7F_2$	1	012.19				4.2	11
$^7F_3$	1	884.96				4.2	11
$^7F_4$	2	745.77	868.79	895.36		4.2	11
$^7F_5$	3	853.06	919.27	(024.61)*		4.2	11
$^7F_6$	4	898.80	921.64	966.45	994.72	4.2	11

Eu:$Eu(OH)_3$ (continued)

Term	Prefix	Energy (cm^{-1})					T	Ref.
$^5D_0$	17	224.99					4.2	11
$^5D_1$	18	977.70	996.13				4.2	11
$^5D_2$	21	455.30					4.2	11
$^5D_3$	24	311.67	333.09	363.61			4.2	11
$^5L_8$	27	074.47	127.82	171.00	174.72		4.2	11
$^5D_4$	27	542.04	569.64	580.08	636.57		4.2	11
$^5L_9$	27	817.93	823.62	835.95	859.55	871.00	4.2	11

Gd:$Gd(OH)_3$

Term	Prefix	Energy (cm^{-1})					T	Ref.
$^8S_{7/2}$	-	0					1.5	12
$^6P_{7/2}$	32	018.35	050.37	077.20	077.56		1.5	12
$^6P_{5/2}$	32	610.44	658.99	671.93			1.5	12
$^6P_{3/2}$	33	207.3	236.7				1.5	12
$^6I_{7/2}$	35	766.8	781.6	790.3	792.7		1.5	12
$^6I_{9/2}$	36	106.7	125.0	125.0	134.0	143.0	1.5	12
$^6I_{17/2}$	36	185.6	195.6				1.5	12
$^6I_{11/2}$	36	381.5	394.0	416.3	422.5		1.5	12
$^6I_{15/2}$	36	503.4	544.9				1.5	12
$^6I_{13/2}$	36	552.4	574.0	580.7	580.7		1.5	12
$^6D_{9/2}$	39	472.78	486.92	499.51	513.02	537.68	1.5	12
$^6D_{1/2}$	40	421.56					1.5	12
$^6D_{7/2}$	40	525.15	525.15	535.56	538.90		1.5	12
$^6D_{3/2}$	40	655.8	705.1				1.5	12
$^6D_{5/2}$	40	776.0	789.7	852.3			1.5	12

$Tb:Tb(OH)_3$

Term	Prefix	Energy (cm^{-1})						T	Ref.
$^7F_6$	-	0	0	118.2	206.0	224.4	233.7	77	13
	-	252.3						77	13
$^7F_5$	2	082.0	143.9	170.9	229.1	323.9		77	13
$^7F_4$	3	473.1	476.1	483.4	539.2	600.7		77	13
$^7F_3$	4	428.6	478.8	484.3	485.2	540.5		77	13

$Dy:Dy(OH)_3$

Term	Prefix	Energy (cm^{-1})					T	Ref.
$^6H_{15/2}$	-	0	7.8	21.5	27.0	54.7	77	14
$^6F_{5/2}$	12	356.50	365.20	393.40			77	14
$^6F_{3/2}$	13	160.30	166.20				77	14
$^4F_{9/2}$	20	932.39	066.50*	078.60	130.55	179.05	77	14
$^4G_{11/2}$	23	320.93	382.46	383.18	426.58	443.52	77	14

$Er:Er(OH)_3$

Term	Prefix	Energy (cm^{-1})						T	Ref.
$^4I_{15/2}$	-	0	61.9	137.8	154.3			77	15
$^4I_{11/2}$	10	278.8	279.9	283.1	306.2	321.3	341.8	77	15
$^4I_{9/2}$	12	431.5	566.5	584.0				77	15
$^4F_{9/2}$	15	296.1	336.1	357.0	396.5			77	15
$^4S_{3/2}$	18	446.4	493.5					77	15
$^2H_{11/2}$	19	151.0	207.7	214.9	221.5	255.4	279.6	77	15
$^4F_{7/2}$	20	518.3	578.3	624.4	656.1			77	15
$^4F_{5/2}$	22	238.4	247.2	266.9				77	15
$^4F_{3/2}$	22	560.1	619.6					77	15
$^2H_{9/2}$	24	553.7	663.6	699.0				77	15

References for 5.9. $R(OH)_3$

1. Dillon, D.R. and W.O. Milligan, 1973, J. Appl. Cryst. **6**, 492.
2. Beall, G.W., W.O. Milligan and H.A. Wolcott, 1977, J. Inorg. Nucl. Chem. **39**, 65.
3. Mullica, D.F., J.D. Oliver and W.O. Milligan, 1979, Acta Cryst. **B35**, 2668.
4. Atoji, A. and D.E. William, 1959, J. Chem. Phys. **31**, 329.
5. Mullica, D.F., W.O. Milligan and G.W. Beall, 1979, J. Inorg. Nucl. Chem. **41**, 525.
6. Milligan, W.O., M.L. Beesley, M.H. Lloyd and R.G. Haire, 1968, Acta Cryst. **B24**, 979.
7. Roy, R. and H.A. McKinstry, 1953, Acta Cryst. **6**, 365.
8. Landers, G.H. and T.O. Brun, 1973, Acta Cryst. **A29**, 684.
9. Beall, G.W., W.O. Milligan, J. Korp and I. Bernal, 1977, Acta Cryst. **B33**, 3134.
10. Chirico, R.D., E.F. Westrum, J.B. Gruber and J. Warmkessel, 1979, J. Chem. Thermodyn. **11**, 835.
11. Cone, R.L. and R. Faulhaber, 1971, J. Chem. Phys. **55**, 5198.
12. Schwiesow, R.L. and H.M. Crosswhite, 1969, J. Opt. Soc. Am. **59**, 592.
13. Scott, P.D., H.E. Meissner and H.M. Crosswhite, 1969, Phys. Lett. **28A**, 489.
14. Scott, P.D., 1970, Ph.D. Thesis, Yale University (University Microfilms 70-25 119).
15. Cone, R.L., 1972, J. Chem. Phys. **57**, 4893.

5.10. Y_2O_3

The optical properties of rare-earth doped yttrium oxide and other rare-earth oxides have been studied extensively for several years, since the oxides are excellent laser host materials. Laser action of $Eu:Y_2O_3$ has been observed at 0.6113 μm (Chang, 1963); $Nd^{3+}:Y_2O_3$ has also been studied as a laser crystal (Hoskins and Soffer, 1964; Holloway et al., 1966). Recently, a $Nd^{3+}:Y_2O_3$ crystal was used as a room-temperature frequency converter; laser output was observed at 1.07 μm and at 1.31 μm when the crystal was pumped by a Kr c.w. laser (Stone and Burrus, 1978). The possibility of an X-ray pumped laser using various rare-earth ions in Y_2O_3 has also been discussed (Ratinen, 1971). Other applications of Y_2O_3 such as thermionic emission (Kul'varskaya, 1976) and electroluminescence (Tanaka et al., 1976) have also been described.

The index of refraction of Y_2O_3 has been measured as $n = 1.915$ at $\lambda = 0.569$ μm (Wickersheim and Lefever, 1961). Other measurements (Dulepov et al., 1972) give $n = 1.930$ at $\lambda = 0.589$ μm and $n = 1.917$ at $\lambda = 0.656$ μm. Krupke (1966a) has determined the coefficients in the Cauchy equation, $n(\lambda) = a + b/\lambda^2$, to be $a = 1.780$ and $b = 0.0598$ $(\mu m)^2$.

Yttrium oxide crystallizes in the Bixbyite (C) structure, with two inequivalent types of yttrium sites in the unit cell; these sites have C_2 and C_{3i} symmetry. As electric-dipole transitions are forbidden in C_{3i} sites (with an inversion symmetry), data on the energy levels and other optical properties of these sites are sparse and do not cover a wide range in energy. For this reason, our tabulation of data concentrates on the C_2 sites. In particular, all the crystal-field parameters and energy levels given here are those appropriate for C_2 sites. The C_{3i} sites (and their interaction with C_2 sites) have been studied primarily by means of far-infrared spectroscopy (Bloor and Dean, 1972), electron paramagnetic resonance (Schafer, 1969), energy-transfer studies (Heber et al., 1970), and similar methods.

5.10.1 Crystallographic data for Y_2O_3

Cubic Ia3, #206, Z = 16

Ion	Pos.	Symm.	x	y	z
Y_1	8(b)	C_{3i}	1/4	1/4	1/4
Y_2	24(d)	C_2	x	0	1/4
O	48(e)	C_1	x	y	z

X-ray data

	Y_2	O			
a	x	x	y	z	Ref.
-	-0.0327	0.3907	0.1520	0.3804	1
10.604	-0.0333	0.3889	0.1551	0.3789	2
-	-0.0326	0.3911	0.1519	0.3806	3
10.6073	-0.0323	0.3912	0.1515	0.3800	4

5.10.2 Crystal-field parameters for R:Y_2O_3 (cm^{-1})

R	B_{20}	B_{22}	B_{40}	RB_{42}	IB_{42}	RB_{44}	IB_{44}	Ref.
Nd	171.2	-793.1	-2705.6	-1721.9	-16.9	1463.5	12.2	5
Nd	-106	-831	-1564	-1772	14	753	-1006	6
Sm	-312	-773	-1436	-1228	381	682	-776	6
Eu	-1255	-396	-1145	-528	185	1226	406	7
Dy	-278	-669	-1190	-1409	270	799	-902	6
Er	-154	-608	-1216	-1496	3	774	18	8
Er	-150	-678	-1389	-1061	239	712	-852	6
Tm	-164	-519	-800	-1353	149	800	-65	8

Crystal-field parameters for $R:Y_2O_3$ (cm^{-1}) (continued)

R	B_{60}	RB_{62}	IB_{62}	RB_{64}	IB_{64}	RB_{66}	IB_{66}	Ref.
Nd	102.4	149.3	61.8	637.6	-452.3	152.0	-6.6	5
Nd	133	255	-115	784	-512	-132	-73	6
Sm	348	277	-88	690	-600	-113	-44	6
Eu	312	551	-35	703	-485	413	175	7
Dy	58	281	-40	385	-319	-97	-7	6
Er	-112	333	-25	212	-140	-14	56	8
Er	252	271	119	180	-218	-24	-42	6
Tm	48	130	3	324	-450	1	162	8

5.10.3 Intensity parameters for $R:Y_2O_3$ (10^{-20} cm^2)

R	Ω_2	Ω_4	Ω_6	Ref.
Pr	17.21	19.8	4.88	9
Nd	8.55	5.25	2.89	9
Eu	6.31	0.66	0.48	9
Eu	9.86	2.23	0.32	10
Eu	6.3	0.7	0.5	11
Er	4.6	1.2	0.5	9
Tm	4.0	1.5	0.6	9

5.10.4 Energy levels for $R:Y_2O_3$

$Ce:Y_2O_3$

Term	Prefix	Energy (cm^{-1})				T	Ref.
$^2F_{5/2}$	-	0				80	6
$^2F_{7/2}$	2	182	750	061*	880	80	6

$Nd:Y_2O_3$

Term	Prefix	Energy (cm^{-1})						T	Ref.
$^4I_{9/2}$	-	0	29	267	447	643		4.2	5
	-	0	28	267	447	643		77	12
$^4I_{11/2}$	1	897	935	147*	271	331	359	4.2	5
	1	896	933	144*	263	325	357	77	12
$^4I_{13/2}$	3	814	840	093*	200	280	305	4.2	5
	3	329						4.2	5
$^4I_{15/2}$	5	709	726	060*	162	315	401	4.2	5
	5	443	479					4.2	5
$^4F_{3/2}$	11	208.3	403.9					4.2	5
	11	210	408					77	12
$^4F_{5/2}$, $^2H_{9/2}$	12	137.6	321.4	395.6	436.4	492.3	553.6	4.2	5
	12	641.9	716.0					4.2	5
$^4F_{7/2}$, $^4S_{3/2}$	13	181.2	310.1	392.2	414.8	421.3	501.4	4.2	5
$^4F_{9/2}$	14	425.6	534.0	573.2	722.6			4.2	5
$^2H_{11/2}$	15	708.87	727.3	756.3	869.6	944.3	023.8*	4.2	5
$^4G_{5/2}$, $^2G_{7/2}$	16	589.9	767.1	902.7	030.3*	114.3	215.0	4.2	5
	16	309.1						4.2	5
$^4G_{7/2}$	18	464.4	592.0	717.8	793.7			4.2	5
$^4G_{9/2}$	19	177.2	192.9	210.6	271.0	286.4		4.2	5
$^2D_{5/2}$	23	330.7	526.7					4.2	5
$^2P_{3/2}$	25	697.0	912.8					4.2	5

$Sm:Y_2O_3$

Term	Prefix	Energy (cm^{-1})						T	Ref.
$^6H_{5/2}$	-	0	200	456				4.2	6
$^6H_{7/2}$	1	101	339	361	528			4.2	6
$^6H_{9/2}$	2	306	447	536	596	748		4.2	6
$^6H_{11/2}$	3	630	731	780	818	964	077*	4.2	6
$^6H_{13/2}$	5	012	054	079	169	246	448	4.2	6
	5	561						4.2	6
$^6F_{1/2}$, $^6H_{15/2}$, $^6F_{3/2}$	6	214	482	539	753	823	844	4.2	6
	6	921						4.2	6
$^6F_{5/2}$	7	283	345	422				4.2	6

$Sm:Y_2O_3$ (continued)

Term	Prefix	Energy (cm^{-1})						T	Ref.
$^6F_{7/2}$	8	142	169	174	294			4.2	6
$^6F_{9/2}$	9	283	313	354	383	427		4.2	6
$^6F_{11/2}$	10	568	663	692	750	775	877	4.2	6
$^4F_{5/2}$	17	557	698	837				4.2	6
$^4F_{3/2}$	18	826	839					4.2	6
$^4G_{7/2}$	19	771	957	941	076			4.2	6

$Eu:Y_2O_3$

Term	Prefix	Energy (cm^{-1})						T	Ref.
$^7F_0$	-	0						4.2	7,13-15
$^7F_1$	-	203	369	546				77	13
	-	199.4	359.5	543.3				77	14
	-	202	361	546				4.2	15
$^7F_2$	-	861	919	955				77	13
	-	858.9	906.4	380.0*				77	14
	-	859	907	949	378*			4.2	15
$^7F_3$	1	846	867	907	997	017*	129	77	13
	1	847	867	907	008*	021	130	77	14
	1	843	864	904	018*	124	157	4.2	15
	1	160						77	14
$^7F_4$	2	672	802	846	960	014*	080	77	13
	2	669	800	846	015*	080	119	77	14
	2	663	793	006*	073	113	172	4.2	15
	2	117	181					77	13
	2	163	178	190				77	14
	2	184						4.2	15
$^7F_5$	3	634	755	825	905	941	016*	77	13
	3	755	825	904	938	015*	063	77	14
	3	062	128	286				77	13
	3	127	158	227	286			77	14
$^7F_6$	4	589	611	791	812	925	960	77	13
	4	791	812	915	960	032*	045	77	14
	4	032*	045	271	314	459	636	77	13
	4	271	314	459	636			77	14

Eu:Y_2O_3 (continued)

Term	Pre-Fix	Energy (cm^{-1})						T	Ref.
$^5D_0$	17	221						77	13
	17	215.84						77	14
	17	224						4.2	7
$^5D_1$	18	945	968	005*	021	095		77	13
	18	930.50	953.57	991.50	008.14*	080.31		77	14
	18	937	961					4.2	7
$^5D_2$	21	362	373	404	497	514		77	13
	21	355.35	366.81	394.00	487.32	503.44		77	14
	21	361	373	402				4.2	7
$^5D_3$	24	195.96	222.10	258.31	267.07	284.17	330.37	77	14
	24	223	262	271	288	359		4.2	7
$^5L_6$	24	613.31	644.40	689.15	716.50	769.17	932.19	77	14
	24	116.23*	194.47	248.91	304.97	405.74	420.19	77	14
?	25	721.17	728.42	748.60	805.45	814.49	934.48	77	14
	25	947.60	958.52	982.06				77	14
?	26	064.98	090.52	091.09	141.73	155.89	208.00	77	14
	26	214.94	227.60	304.92	345.47	356.92	397.33	77	14
	26	404.72	426.49	448.17	457.97	490.78	521.28	77	14
	26	590.34	616.53	716.18	851.24	890.81	908.48	77	14
?	27	022.14	046.92	144.15	285.69	373.69	383.66	77	14
$^5D_4$	27	420.70	461.32	467.96	494.63	509.09	520.68	77	14
	27	543.27	552.30	625.16				77	14
$^5H_3$	30	382.40	437.31	499.66	531.73	579.90	629.31	77	14
	30	812.88	873.39	895.26	942.91	977.74		77	14
?	31	004.25	014.66	049.35	059.41	081.09	094.75	77	14
	31	163.53	204.42	228.86	245.28	269.97	295.34	77	14
	31	415.77	505.56	558.08	621.27	650.34		77	14
?	32	572.73	592.81	643.78	677.45	701.02	720.92	77	14
	32	803.47	825.18	847.29	876.32	895.01	932.89	77	14
?	33	172.94	195.11	209.69	230.10	278.92	309.72	77	14
	33	336.89	353.36	610.20	682.87	742.20	793.15	77	14
	33	789.50	855.03	879.30	921.45	963.99		77	14
?	34	003.40	062.48	273.58	346.47	363.03	449.03	77	14
	34	469.37	484.46	603.04	636.23	655.51	684.85	77	14
	34	804.75	862.67	875.52	911.20	925.11		77	14
?	35	059.45	274.22	363.91	792.54	816.67	826.30	77	14
	35	857.40	871.00	995.33				77	14
?	36	013.32	922.56	947.27	984.43	024.58*	159.68	77	14

$Dy:Y_2O_3$

Term	Prefix	Energy (cm^{-1})						T	Ref.
$^6H_{15/2}$	-	0	75	267	376	518	627	77	16
	-	0	73	262	370	501	608	4.2	6
	-	750	847					77	16
	-	727	833					4.2	6
$^6H_{13/2}$	3	589	674	847	888	955	012*	77	16
	3	595	684	854	893	963	020*	4.2	6
	3	035						77	16
	3	046						4.2	6
$^6H_{11/2}$	5	948	090*	186	213	237	370	4.2	6
$^6F_{11/2}$, $^6H_{9/2}$	7	758	829	847	930	949	008*	4.2	6
	7	015	048	209	248	393		4.2	6
$^6F_{9/2}$, $^6H_{7/2}$	9	090	195	315	381	403	447	4.2	6
	9	490	590	627				4.2	6
$^6H_{5/2}$	10	336	509	624				4.2	6
$^6F_{7/2}$	11	236	292	331	383			4.2	6
$^6F_{5/2}$	12	586	669	738				4.2	6
$^6F_{3/2}$	13	455	468					4.2	6
$^6F_{1/2}$	14	005						4.2	6
$^4F_{9/2}$	21	038	063	130	337	485		77	16
	21	039	064	132	340	489		4.2	6
$^4I_{15/2}$	21	911	952	010*	085	391	399	4.2	6
	21	406	471					4.2	6
$^4G_{11/2}$	23	405	547	616	661	697	780	4.2	6

$Er:Y_2O_3$

Term	Prefix	Energy (cm^{-1})						T	Ref.
$^4I_{15/2}$	-	0	38.9	76.5	89.3			20	17
	-	0	39	76	89	158	258	4.2	18
	-	490	510					4.2	18
$^4I_{13/2}$	6	510	542	588	594	684	840	4.2	18
	6	867						4.2	18
$^4I_{11/2}$	10	193	214	244	264	361	379	4.2	18
$^4I_{9/2}$	12	324	436	512	576	604		4.2	18
$^4F_{9/2}$	15	123.5	202.7	283.7	336.5	439.5		20	17
	15	120	199	280	333	436		4.2	18

$Er:Y_2O_3$ (continued)

Term	Prefix	Energy (cm^{-1})						T	Ref.
$^4S_{3/2}$	18	235.5	321.3					20	17
	18	220	329					4.2	18
$^2H_{11/2}$	19	042.6	050.3	075.7	191.7	222.4	246.3	20	17
	19	038	045	072	187	218	243	4.2	18
$^4F_{7/2}$	20	347.1	445.3	513.4	580.2			20	17
	20	346	442	511	575			4.2	18
$^4F_{5/2}$	22	056.2	082.8	182.2				20	17
	22	046	072	172				4.2	18
$^4F_{3/2}$	22	327	493					4.2	18
$^2H_{9/2}$	24	369.4	490.3	527.9	560.5	613.8		20	17
	24	364	485	522	554	608		4.2	18
$^4G_{11/2}$	26	091	115	207	388	399	459	4.2	18
$^2P_{3/2}$	31	289	488					4.2	18
$^4G_{7/2}$	33	769	879	930	052*			4.2	18

$Tm:Y_2O_3$

Term	Prefix	Energy (cm^{-1})						T	Ref.
$^3H_6$	-	0	30.7	89.3	219.0	230.3	340.0	4.2	8
	-	382.4	435.7	488.4	692.3	788.5	796.9	4.2	8
$^3H_4$	5	615.0	673.6	780.4	005.3*	018.4	114.1	4.2	8
	5	144.1	189.0					4.2	8
$^3H_5$	8	258.1	300.6	330.6	464.8	475.1	543.4	4.2	8
	8	569.0	756.6	916.6				4.2	8
$^3F_4$	12	555.9	634.5	696.6	812.9	842.5	871.8	4.2	8
	12	016.9*	047.7					4.2	8
$^3F_3$	14	566.9	571.6	626.9	657.7	662.1	690.1	4.2	8
	14	725.8						4.2	8
$^3F_2$	15	062.3	185.5	240.6	361.6			4.2	8
$^1G_4$	20	901.8	015.0*	060.5	526.9	595.3	618.3	4.2	8
	20	778.5						4.2	8
$^1D_2$	27	691.0	726.5	874.3	933.1			4.2	8
$^1I_6$	33	876.6	884.3	368.0	397.7	520.1		4.2	8
$^3P_0$	35	267.7						4.2	8
$^3P_1$	35	920.8	158.7*	231.3				4.2	8
$^3P_2$	37	556.9	753.9	847.2	194.3			4.2	8

$Yb:Y_2O_3$

Term	Prefix	Energy (cm^{-1})			T	Ref.
$^2F_{7/2}$	-	0			80	6
$^2F_{5/2}$	10	219	640	044*	80	6

References for 5.10. Y_2O_3

1. Paton, M.G. and E.N. Maslen, 1965, Acta Cryst. **19**, 307.
2. O'Connor, B.H. and T.M. Valentine, 1969, Acta Cryst. **B25**, 2140.
3. Bonnet, M., A. Delapalme and H. Fuess, 1975, Acta Cryst. **A31**, 264.
4. Faucher, M. and J. Pannetier, 1980, Acta Cryst. **B36**, 3209.
5. Chang, N.C., 1966, J. Chem. Phys. **44**, 4044.
6. Chang, N.C., J.B. Gruber, R.P. Leavitt and C.A. Morrison, 1982, J. Chem. Phys. **76**, 3877.
7. Dexpert-Ghys, J., 1979, Thesis, Université de Paris-Sud.
8. Gruber, J.B., W.F. Krupke and J.M. Poindexter, 1964, J. Chem. Phys. **41**, 3363.
9. Krupke, W.F., 1966, Phys. Rev. **145**, 325.
10. Weber, M.J., 1968, Phys. Rev. **171**, 283.
11. Krupke, W.F., 1974, Proc. IEEE Region VI Conf., p. 17.
12. Zverev, G.M., G.Ya. Kolodnyi and A.I. Smirnov, 1967, Opt. Spectrosc. **23**, 325.
13. Chang, N.C., 1963, J. Appl. Phys. **34**, 3500.
14. Chang, N.C. and J.B. Gruber, 1964, J. Chem. Phys. **41**, 3227.
15. Dexpert-Ghys, J. and M. Faucher, 1979, Phys. Rev. **B20**, 10.
16. Levshin, V.L., I.K. Lyubavskaya and N.D. Maksimov, 1973, in: Spektroskopiya Kristallov (Nauka, Moscow), p. 173.
17. Rosenberger, D., 1962, Z. Physik **167**, 360.
18. Kisliuk, P., W.F. Krupke and J.B. Gruber, 1964, J. Chem. Phys. **40**, 3606.

5.11. R_2O_3

Rare-earth sesquioxides are of interest as laser host materials in addition to other practical applications. Neodymium is known to exhibit laser action in several rare-earth oxides including La_2O_3 (Hoskins and Soffer, 1965) and Gd_2O_3 (Soffer and Hoskins, 1964). Laser action in crystals of the form $R':R_2O_3$ has also been observed, particularly $Ho:Er_2O_3$ (Soffer and Hoskins, 1966) and $Tm:Er_2O_3$ (Soffer and Hoskins, 1965). The possibility of obtaining stimulated emission from crystals of the latter form has spurred much of the fundamental spectroscopic research on the sesquioxides.

The rare-earth sesquioxides are known to crystallize in three distinct structures at room temperature, designated as A, B, and C. The A-type sesquioxides are triclinic and the space group is generally accepted as $P\bar{3}ml$, although some controversy exists with regard to this in the literature (Müller–Buschbaum and Schnering, 1965). The light rare-earth oxides (R = La, Ce, Pr, Nd) exist in the A-type structure at room temperature, with the rare-earth ions occupying sites of C_{3v} symmetry. The B-type structure, on the other hand, is monoclinic (space group C2/m) with three inequivalent rare-earth sites of C_s symmetry and is known to exist for all rare earths heavier than Pm. The C-type structure is cubic

with two inequivalent rare earth sites, one with C_2 symmetry and the other with C_{3i} symmetry; the space group is Ia3 (see, however, Zav'yalova et al., 1976). This structure exists for all the rare earths except Ce. In addition to the above forms, others exist at elevated temperatures. Also, for many rare earths, several other oxides of the form R_nO_{2n-2} exist (Kunzmann and Eyring, 1975). For a review of the structure and properties of the rare-earth oxides, see Chapter 27, Volume 3 (Eyring, 1979) of this series.

The phonon spectrum and ground-term splittings for both C_2 and C_{3i} sites of various R_2O_3 in the C-type structure have been determined by far-infrared spectroscopy (Bloor and Dean, 1972; Dean and Bloor, 1972) and electronic Raman spectroscopy (Schaak and Koningstein, 1970). Results of these measurements are reinforced by heat capacity studies (Justice and Westrum, 1963; Westrum and Justice, 1963; Gruber et al., 1981). Crystal-field analyses of Nd_2O_3 have been undertaken based on both the optical spectrum and the magnetic susceptibility (Caro et al., 1979). In addition, theoretical calculations of crystal-field parameters based on an electrostatic model including dipoles in a self-consistent manner have been performed (Faucher et al., 1980).

Magnetic ordering properties of several rare-earth sesquioxides have been studied, both theoretically (Angelov, 1979) and experimentally. The magnetic susceptibility of several oxides including Pr_2O_3 (Kern, 1964) has been measured over a wide range in temperature. Heavy rare-earth oxides of the C-type order antiferromagnetically at low temperatures (MacChesney et al., 1966; Bonrath et al., 1966a, b; Moon et al., 1968). Splittings due to internal fields of the Stark levels in the antiferromagnetic state have been measured for Er_2O_3 (Dean and Bloor, 1972). Electrical properties of the rare-earth oxides have also been measured (Bogoroditskii et al., 1965).

5.11.1 Crystallographic data for R_2O_3

A-type structure

Trigonal $P\bar{3}m1$, #164, Z = 1

Ion	Pos.	Symm.	x	y	z
R	2(d)	C_{3v}	1/3	2/3	z
O_1	2(d)	C_{3v}	1/3	2/3	z
O_2	1(a)	D_{3d}	0	0	0

Crystallographic data for R_2O_3 (continued)

X-ray data

			R	O_1	
R	a	c	z	z	Ref.
La	3.9373	6.1299	0.245	0.645	1
La	3.938	6.128	-	-	2
Ce	3.888	6.069	-	-	1
Pr	3.851	5.996	-	-	1
Pr	3.857	6.016	-	-	2
Nd	3.831	5.991	-	-	1
Nd	3.829	6.002	-	-	2
Nd	-	-	0.2462	0.6466	3

B-type structure

Monoclinic C2/m, #12, Z = 6 (second setting)

Ion	Pos.	Symm.	x	y	z
R_1	4(i)	C_s	x	0	z
R_2	4(i)	C_s	x	0	z
R_3	4(i)	C_s	x	0	z
O_1	4(i)	C_s	x	0	z
O_2	4(i)	C_s	x	0	z
O_3	4(i)	C_s	x	0	z
O_4	4(i)	C_s	x	0	z
O_5	2(a)	C_{2h}	0	0	0

Crystallographic data for R_2O_3 (continued)

X-ray data

					R_1		
R	a	b	c	β	x	z	Ref.
Sm	14.177	3.633	8.847	99.96	-0.3660	0.4912	4,5
Sm	14.18	3.636	8.841	99.92	-	-	2
Eu	14.12	3.600	8.801	99.98	-	-	2
Eu	14.1105	3.6021	8.8080	100.037	-0.36260	0.4897	6
Gd	14.061	3.566	8.760	100.10	-	-	4
Gd	14.08	3.571	8.764	100.03	-	-	2
Tb	14.04	3.541	8.725	100.06	-	-	2
Tb	13.92	3.536	8.646	100.58	-	-	7
Dy	13.97	3.549	8.661	100.00	-	-	2
Ho	13.90	3.492	8.592	99.98	-	-	2
Er	13.87	3.470	8.555	100.17	-	-	2
Tm	13.81	3.447	8.505	100.20	-	-	2
Yb	13.73	3.425	8.452	100.17	-	-	2
Lu	13.70	3.410	8.425	100.22	-	-	2

	R_2		R_3		O_1		
R	x	z	x	z	x	z	Ref.
Sm	-0.3100	0.1376	-0.0324	0.1860	0.130	0.290	4,5
Eu	-0.31028	0.13760	-0.03365	0.18763	0.1291	0.2855	6

	O_2		O_3		O_4		
R	x	z	x	z	x	z	Ref.
Sm	-0.180	0.020	-0.210	0.370	0.490	0.340	4,5
Eu	-0.1752	0.0267	-0.2039	0.3732	0.4734	0.3431	6

Crystallographic data for R_2O_3 (continued)

C-type structure

Cubic Ia3, #206, Z = 16

Ion	Pos.	Symm.	x	y	z
R_1	8(b)	C_{3i}	1/4	1/4	1/4
R_2	24(d)	C_2	x	0	1/4
O	48(e)	C_1	x	y	z

X-ray data

		R_2	O			
R	a	x	x	y	z	Ref.
La	11.38	-	-	-	-	8
Pr	11.136	-0.0290	0.385	0.155	0.382	8
Pr	11.152	-	-	-	-	9
Nd	11.048	-	-	-	-	8
Sm	10.932	-	-	-	-	8
Eu	10.866	-	-	-	-	8
Gd	10.813	-	-	-	-	8
Tb	10.728	-	-	-	-	8
Tb	10.7281	-	-	-	-	10
Dy	10.667	-	-	-	-	8
Ho	10.607	-0.0270	0.388	0.152	0.382	8
Ho	-	-0.0323	0.3907	0.1520	0.3797	11
Er	10.547	-0.0330	0.394	0.149	0.380	8
Er	10.5484	-	-	-	-	12
Tm	10.488	-	-	-	-	8
Yb	10.439	-0.0336	0.391	0.151	0.380	8
Lu	10.391	-	-	-	-	8

5.11.2 Index of refraction for R_2O_3

R	Structure	n(λ=0.589μm)	n(λ=0.656μm)	Ref.
La	A	2.03	-	13
Pr	A	2.13	-	13
Pr	C	1.943	1.930	14
Nd	A	2.10	-	13
Nd	C	1.920	1.907	14
Sm	B	2.09	-	13
Eu	C	1.969	1.955	14
Gd	C	1.965	1.951	14
Tb	C	1.964	1.950	14
Dy	C	1.963	1.949	14
Ho	C	1.960	1.946	14
Er	C	1.956	1.942	14
Tm	C	1.950	1.936	14
Yb	C	1.942	1.929	14
Lu	C	1.930	1.917	14

5.11.3 Crystal-field parameters for $R:R_2O_3$ (cm^{-1})

A-type structure

R	B_{20}	B_{40}	B_{43}	B_{60}	B_{63}	B_{66}	Ref.
Nd	-836	634	1606	752	-237	672	15

C-type structure, C_{3i} sites

R	B_{20}	B_{40}	B_{43}	B_{60}	B_{63}	B_{66}	Ref.
Er	-316	760	198	464	427	810	16

5.11.4 Energy levels for $R':R_2O_3$

$Nd:La_2O_3$ (A-type structure)

Term	Prefix	Energy (cm^{-1})						T	Ref.
$^4I_{9/2}$	-	0	23	82	242	487		10	17
$^4F_{3/2}$	11	175	322					10	17
$^4F_{5/2}$	12	195	267	319				10	17
$^2H_{9/2}$	12	358	391	408	550			10	17
$^4F_{7/2}$	13	141	150	252	272			10	17
$^4S_{3/2}$	13	336	349					10	17
$^4F_{9/2}$	14	398	406	472	568	613		10	17
$^2H_{11/2}$	15	613	665	800	895			10	17
$^2G_{7/2}$	16	666	690	739	778			10	17
$^4G_{5/2}$	17	021	039	186				10	17
$^2K_{13/2}$, $^4G_{7/2}$	18	581	603	644	652	695	719	10	17
$^2G_{9/2}$	19	106	144	178	223	265		10	17
$^4G_{9/2}$	20	599	645	668	795			10	17
$^2(P,D)_{3/2}$	20	903	923					10	17
$^4G_{11/2}$	21	379						10	17
$^2P_{1/2}$	22	884						10	17
$^2P_{3/2}$	25	720						10	17
$^4D_{3/2}$	27	361	409					10	17
$^4D_{5/2}$	27	741	760					10	17
$^2I_{11/2}$	27	807	049*					10	17
$^4D_{1/2}$	28	409						10	17
$^2I_{13/2}$	29	404	582	636				10	17

$Nd:Nd_2O_3$ (A-type structure)

Term	Prefix	Energy (cm^{-1})					T	Ref.
$^4I_{9/2}$	-	0	23	84	253	496	10	17
$^4F_{3/2}$	11	165	318				10	17
$^4F_{5/2}$	12	177	267	329			10	17
$^2H_{9/2}$	12	352	389	399	543	565	10	17

Nd:Nd_2O_3 (continued)

Term	Prefix	Energy (cm^{-1})						T	Ref.
$^4F_{7/2}$	13	127	179	248	272			10	17
$^4S_{3/2}$	13	342	359					10	17
$^4F_{9/2}$	14	384	425	458	561	618		10	17
$^2H_{11/2}$	15	617	640	687	791	887	897	10	17
$^2G_{7/2}$	16	654	707	728	785			10	17
$^4G_{5/2}$	17	004	027	196				10	17
$^2K_{13/2}$, $^4G_{7/2}$	18	558	583	607	672	695	716	10	17
	18	879	935	004*				10	17
$^2G_{9/2}$	19	080	138	181	207	259		10	17
$^4G_{9/2}$	20	555	595	603	619	766		10	17
$^2(P,D)_{3/2}$	20	913	935					10	17
$^4G_{11/2}$	21	211	258	305	343	367	376	10	17
$^2P_{1/2}$	22	862						10	17
$^2D_{5/2}$	23	225	256	558				10	17
$^2P_{3/2}$	25	687	846					10	17
$^4D_{3/2}$	27	307	356					10	17
$^4D_{5/2}$	27	668	742	765				10	17
$^2I_{11/2}$	27	811	020*	321				10	17
$^4D_{1/2}$	28	400						10	17
$^2I_{13/2}$	29	318	378	509	531	597	628	10	17
	29	667						10	17
$^2H_{9/2}$	32	067	129	161	548	589		10	17
$^2D_{3/2}$	33	309	459					10	17

Nd:Gd_2O_3, site 1 (B-type structure)

Term	Prefix	Energy (cm^{-1})						T	Ref.
$^4I_{9/2}$	-	0						4.2	18
$^4F_{5/2}$	12	139	283	369				4.2	18
$^4F_{7/2}$, $^4S_{3/2}$	13	146	245	303	344	358	413	4.2	18
$^4F_{9/2}$	14	413	467	514	592	656		4.2	18
$^2P_{1/2}$	22	853						4.2	18

Nd:Gd_2O_3, site 2 (B-type structure)

Term	Prefix	Energy (cm^{-1})						T	Ref.
$^4I_{9/2}$	-	0						4.2	18
$^4F_{5/2}$	12	068	294	386				4.2	18
$^4F_{7/2}$, $^4S_{3/2}$	13	176	267	327	415	430	432	4.2	18
$^4F_{9/2}$	14	442	485	526	690			4.2	18
$^2P_{1/2}$	22	895						4.2	18

Nd:Gd_2O_3, site 3 (B-type structure)

Term	Prefix	Energy (cm^{-1})						T	Ref.
$^4I_{9/2}$	-	0						4.2	18
$^4F_{5/2}$	12	196	353	401				4.2	18
$^4F_{7/2}$, $^4S_{3/2}$	13	220	289	366	428	445	446	4.2	18
$^4F_{9/2}$	14	448	495	548	630	696		4.2	18
$^2P_{1/2}$	22	934						4.2	18

Eu:Gd_2O_3 all sites (B-type structure)

Term	Prefix	Energy (cm^{-1})						T	Ref.
$^7F_0$	-	0						20	19
$^5D_0$	17	172.5	177.6					20	19
$^5D_1$	18	909.1	923.4	925.2	930.2	935.8	947.4	20	19
$^5D_2$	21	333.3	347.2	356.3	382.9	412.9	417.9	20	19
	21	438.2	445.0					20	19

Eu:Gd_2O_3, site A (B-type structure)

Term	Prefix	Energy (cm^{-1})						T	Ref.
$^7F_0$	-	0						4	20
$^7F_1$	-	154	345	644				4	20
$^7F_2$	-	849	062*	245	344			4	20
$^7F_3$	1	808	863	870	986	126*	177	4	20
	1	233						4	20
$^7F_4$	2	748	845	129*	163	168	262	4	20
	2	277						4	20
$^5D_0$	17	283						4	20

Eu:Gd_2O_3, site B (B-type structure)

Term	Prefix	Energy (cm^{-1})						T	Ref.
$^7F_0$	-	0						4	20
$^7F_1$	-	256	400	424				4	20
$^7F_2$	-	916	930	131*	309			4	20
$^7F_3$	1	833	874	882	927	964	055*	4	20
$^7F_4$	2	627	781	802	816	942	008*	4	20
	2	011	039	085				4	20
$^5D_0$	17	176						4	20

Eu:Gd_2O_3, site C (B-type structure)

Term	Prefix	Energy (cm^{-1})						T	Ref.
$^7F_0$	-	0						4	20
$^7F_1$	-	334	351	363				4	20
$^7F_2$	-	887	984	134*	144			4	20
$^7F_3$	1	832	865	890	928	946	032*	4	20
$^7F_4$	2	556	765	819	886	928	020*	4	20
	2	034	048	077				4	20
$^5D_0$	17	172						4	20

Dy:Dy_2O_3 (C-type structure, C_2 sites)

Term	Prefix	Energy (cm^{-1})						T	Ref.
$^6H_{15/2}$	-	0	74	261	355	505	602	10	21
	-	0	67	258				298	22
	-	746	080*					10	21
$^6H_{13/2}$	3	325	520	589	669	759	815	10	21
	3	946						10	21
$^6H_{11/2}$	5	691	941	088*	143	204	284	10	21
$^6H_{9/2}$, $^6F_{11/2}$	7	402	508	579	696	880	880	10	21
	7	011*	029	141	234	391		10	21
$^6H_{7/2}$, $^6F_{9/2}$	8	832	024*	087	122	184	376	10	21
	8	389	480	610				10	21
$^6H_{5/2}$	10	136	338	425				10	21
$^6F_{7/2}$	11	233	291	327	378			10	21

Dy:Dy_2O_3 (continued)

Term	Prefix	Energy (cm^{-1})						T	Ref.
$^6F_{5/2}$	12	586	666	735				10	21
$^6F_{3/2}$	13	453	465					10	21
$^6F_{1/2}$	14	004						10	21
$^4F_{9/2}$	21	040	064	131	339	485		10	21
	21	038	061	124	326			298	22
$^4I_{15/2}$	21	909	954	086*	324	385	400	10	21
	21	467	514					10	21
$^4G_{11/2}$	23	404	543	612	656	691	776	10	21
$^4I_{13/2}$	24	847	859	007*	097	245	367	10	21
	24	495						10	21
$^4F_{7/2}$	25	634	731	813	857			10	21
$^4M_{15/2}$, $^4I_{11/2}$	26	057	123	191	217	409	433	10	21
	26	617	645	678	694	055*	129	10	21
	26	263	338					10	21
$^4P_{3/2}$	27	499						10	21
$^6P_{5/2}$, $^4I_{9/2}$	28	310	017*					10	21
$^6P_{7/2}$,$^4F_{5/2}$,$^4G_{9/2}$	29	515	582	653	689	753	820	10	21
	29	862	907	923	947	963	977	10	21
$^4K_{15/2}$	30	129	248	328	368	457	556	10	21
	30	629	779					10	21
$^4G_{7/2}$	31	012	150	259	345			10	21
$^6P_{3/2}$	31	671	734					10	21
$^4D_{1/2}$	31	770						10	21
$^4H_{11/2}$	33	155	175	204	392	442	458	10	21
$^4F_{3/2}$	33	618	633					10	21
$^4D_{7/2}$	33	836	904	094*	102			10	21
$^4F_{5/2}$	34	163	189	234				10	21
$^4G_{9/2}$	34	251	263	277	295	355		10	21
$^4K_{11/2}$	34	389	432	445	470	480	492	10	21
$^4(G,K)_{11/2}$	34	679	719	864	995	059*	132	10	21
$^4H_{7/2}$	35	758	812	895	921			10	21
$^4G_{9/2}$	36	113	335	456	497	563		10	21
$^4G_{5/2}$	36	734	765	790				10	21

Er:Er_2O_3 (C-type structure, C_2 sites)

Term	Prefix	Energy (cm^{-1})						T	Ref.
$^4I_{15/2}$	-	0	38	75	88	159	265	10	23
	-	490	505					10	23
$^4I_{13/2}$	6	510	542	588	594	684	840	10	23
	6	867						10	23
$^4I_{11/2}$	10	202	222	252	273	370	390	10	23
$^4I_{9/2}$	12	317	430	467	570	599		10	23
	12	320	434	510	574	605		4.2	16
$^4F_{9/2}$	15	115	188	273	321	430		10	23
$^4S_{3/2}$	18	222	308					10	23
$(^2H,^4G)_{11/2}$	19	033	040	067	182	213	235	10	23
$^4F_{7/2}$	20	336	435	500	561			10	23
$^4F_{5/2}$	22	042	069	169				10	23
$^4F_{3/2}$	22	401	572					10	23
$^2H_{9/2}$	24	354	475	512	546	600		10	23
$^4G_{11/2}$	26	076	104	195	378	397	444	10	23
$^4G_{9/2}$	27	078	126	164	227	252		10	23
$^2K_{15/2}$	27	278	290	316	324	391	432	10	23
	27	546	682					10	23
$(^2G,^4G)_{7/2}$	27	741	875	916	132*			10	23
$(^2P,^2D,^4F)_{3/2}$	31	279	483					10	23
$^2K_{13/2}$	32	480	556	645	770	806	821	10	23
	32	873						10	23
$^4G_{5/2}$	32	982	035*	200				10	23
$^2P_{1/2}$	33	354						10	23
$^4G_{7/2}$	33	758	841	920	046*			10	23
$^2D_{5/2}$	34	526	612	690				10	23
$^2(G,H)_{9/2}$	36	193	229	381	462	549		10	23
$^4D_{5/2}$	38	124	215	236				10	23
$^4D_{7/2}$	38	605	680	910	204*			10	23
$^2I_{11/2}$	40	571	629	644	668	683	720	10	23
$^2L_{17/2}$	40	756	798	865	902	945	026*	10	23
	40	108	175	268				10	23
$^4D_{3/2}$	41	942	028*					10	23
$(^2P,^2D)_{3/2}$	42	464	605					10	23
$^2I_{13/2}$	42	935	101*	120	141	252	295	10	23
	42	349						10	23

References for 5.11. R_2O_3

1. Wyckoff, R.W.G., 1964, Crystal Structures, Vol. 2 (Interscience, New York), pp. 1 ff.
2. Hoekstra, H.R., 1966, Inorg. Chem. **5**, 754.
3. Boucherle, J.X. and J. Schweizer, 1975, Acta Cryst. **B31**, 2745.
4. Wyckoff, R.W.G., Ref. 1, pp. 11 ff.
5. Cromer, D.T., 1957, J. Phys. Chem. **61**, 753.
6. Yakel, H.L., 1979, Acta Cryst. **B35**, 564.
7. MacChesney, J.B., H.J. Williams, R.C. Sherwood and J.F. Potter, 1966, J. Chem. Phys. **44**, 596.
8. Wyckoff, R.W.G., Ref. 1, pp. 4 ff.
9. Kunzmann, P. and L. Eyring, 1975, J. Solid State Chem. **14**, 229.
10. Baenziger, N.C., H.A. Eick, H.S. Schuldt and L. Eyring, 1961, J. Am. Chem. Soc. **83**, 2219.
11. Boucherle, J.X., S. Quezel, J. Schweizer and F. Tcheou, 1979, Acta Cryst. **A35**, 818.
12. Hatibarua, J. and P.C. Mahanta, 1975, Indian J. Pure Appl. Phys. **13**, 479.
13. Batsanov, S.S. and E.V. Dulepov, 1973, Zh. Strukt. Khimii **14**, 541.
14. Dulepov, E.V., S.S. Batsanov and G.N. Kustova, 1972, Zh. Strukt. Khimii **13**, 935.
15. Caro, P., J. Derouet, L. Beaury and E. Soulie, 1979, J. Chem. Phys. **70**, 2542.
16. Dean, J.R. and D. Bloor, 1972, J. Phys. **C5**, 2921.
17. Henderson, J.R., M. Muramoto and J.B. Gruber, 1967, J. Chem. Phys. **46**, 2515.
18. Gruber, J.B., private communication.
19. Rosenberger, D., 1962, Z. Phys. **167**, 360.
20. Dexpert-Ghys, J., M. Faucher and P. Caro, 1981, Phys. Rev. **B23**, 607.
21. Henderson, J.R., M. Muramoto, T.M. Henderson and J.B. Gruber, 1967, J. Chem. Phys. **47**, 5097.
22. Tam, A.C. and C.K.N. Patel, 1979, Appl. Phys. Lett. **35**, 843.
23. Gruber, J.B., J.R. Henderson, M. Muramoto, K. Rajnak and J.G. Conway, 1966, J. Chem. Phys. **45**, 477.

5.12. Y_2O_2S

Rare-earth doped yttrium oxysulfide and the isomorphic rare-earth oxysulfides (R_2O_2S) have been of interest for several years because of their applicability as phosphor materials. Europium-doped Y_2O_2S has been widely used as a red-emitting phosphor in picture tubes for color television (Royce, 1968). High-efficiency luminescence has also been observed for several other rare-earth ions in rare-earth oxysulfides, the most notable being Pr:Y_2O_2S (Ozawa and Jaffe, 1970), Tb:La_2O_2S, and Tb:Gd_2O_2S (Wickersheim et al., 1970). Additional studies of phosphor-related properties of rare-earth doped oxysulfides have been performed (Koskenlinna et al., 1976; Amiryan et al., 1977). All rare-earth oxysulfides possess the same crystallographic structure regardless of the size of the rare-earth ion (Flauhaut, 1968); this property makes possible the study of the dependence of crystal-field splittings on host cation size in a series of isostructural crystals (Sovers and Yoshioka, 1969). Crystal growth, optical transmission range, hardness, indices of refraction, thermal expansion coefficient, and thermal conductivity of single crystals of La_2O_2S, Y_2O_2S, and Gd_2O_2S have been reported (Sobon et al., 1971). Laser action has been observed in Nd:La_2O_2S at 1.075 μm (Alves et al., 1971). The optical spectrum of pure Nd_2O_2S has been reported (Souillat et al., 1972); in this section we report the optical data on doped Y_2O_2S only.

5.12.1 Crystallographic data for Y_2O_2S

Trigonal $P\bar{3}m1$, #164, Z = 1

Ion	Pos.	Symm.	x	y	z
Y	2(d)	C_{3v}	1/3	2/3	z
O	2(d)	C_{3v}	1/3	2/3	z
S	1(a)	D_{3d}	0	0	0

X-ray data

		Y	O	
a	c	z	z	Ref.
3.780	6.563	-	-	1
3.7910	6.5959	-	-	2
4.0509	6.943	0.29	0.64	1 (La_2O_2S)

5.12.2 Crystal-field parameters for R:Y_2O_2S (cm^{-1})

R	B_{20}	B_{40}	B_{43}	B_{60}	B_{63}	B_{66}	Ref.
Sm	132	376	825	592	-103	554	3
Eu	124	1344	823	286	-362	554	4
Eu	101	1232	894	326	-353	548	5
Eu	114	642	1159	600	-238	475	6
Tb	208	544	865	256	-169	224	7
Tb	182.4	729.6	1060.6	408.0	-162.4	277.4	8
Dy	124	704	1082	368	-242	421	9
Ho	60	608	828	280	-137	211	9
Er	180	1400	800	8	-160	189	10

5.12.3 Intensity parameters for R:Y_2O_2S (10^{-20} cm^2)

R	Ω_2	Ω_4	Ω_6	Ref.
Eu	13.0	10.2	-	6

5.12.4 Energy levels for R:Y_2O_2S

$Sm:Y_2O_2S$

Term	Prefix	Energy (cm^{-1})						T	Ref.
$^6H_{5/2}$	-	0	12	98				4.2	3
$^6H_{7/2}$	1	004	042	135	172			4.2	3
$^6H_{9/2}$	2	214	252	282	356	369		4.2	3
$^4G_{5/2}$	17	544	750	819				4.2	3

$Eu:Y_2O_2S$

Term	Prefix	Energy (cm^{-1})						T	Ref.
$^7F_0$	-	0						77	4
$^7F_1$	-	346.9	384.5					77	4
$^7F_2$	-	911.5	940.5	187.0*				77	4
$^7F_3$	1	858.0	873.6	917.0	923.9	022.2*		77	4
$^7F_4$	2	583.1	794.5	848.3	963.7	997.5	016.9*	77	4
$^7F_5$	3	758.9	777.8	860.2	880.2	024.6*	052.1	77	4
$^7F_6$	4	847.2	869.6	897.5	903.5	933.7	109.0*	77	4
$^5D_0$	17	143.3						77	4
$^5D_1$	18	894.0	901.7					77	4
$^5D_2$	21	315.5	381.3	394.4				77	4
$^5D_3$	24	189.3	202.0	211.7	245.4	261.7		77	4

$Tb:Y_2O_2S$

Term	Prefix	Energy (cm^{-1})						T	Ref.
$^7F_6$	-	0	6	15	26	106	157	1.7	7
	-	188	220	250				1.7	7
$^7F_5$	2	026	037	057	207	212	240	1.7	7
$^7F_4$	3	249.5	257.5	268.5	385	441	473	1.7	7
$^7F_3$	4	288	330	333	380	412		1.7	7
$^7F_2$	4	920	115*	151				1.7	7
$^7F_1$	5	449	515					1.7	7

Dy:Y_2O_2S

Term	Prefix	Energy (cm^{-1})				T	Ref.
$^6H_{15/2}$	-	0	21	76	94	1.7	9
$^6F_{5/2}$	12	308	316	410		10	9
$^6F_{3/2}$	13	127	136			10	9
$^4F_{9/2}$	20	866				10	9

Ho:Y_2O_2S

Term	Prefix	Energy (cm^{-1})						T	Ref.
$^5I_8$	-	0	8	13	17	23	171	1.7	9
	-	176	183	193	203	218		1.7	9

Er:Y_2O_2S

Term	Prefix	Energy (cm^{-1})						T	Ref.
$^4I_{15/2}$	-	0	23	46	102	174	220	77	11
	-	0	22	43	110	172	218	77	10
	-	262	419					77	11
	-	256						77	10
$^4I_{13/2}$	6	478	497	520	587	637	665	77	10
	6	692						77	10
$^4I_{11/2}$	10	095	103	129	157	172	200	77	10
$^4I_{9/2}$	12	300	415	468	500			77	11
$^4F_{9/2}$	15	141	147	150	244	260		77	11
$^4S_{3/2}$	18	236	250					77	11
$^2H_{11/2}$	18	930	941	959	082*	104	119	77	11
$^4F_{7/2}$	20	320	382	392	404			77	11
$^4F_{5/2}$	21	950	986	025*				77	11

References for 5.12. Y_2O_2S

1. Wyckoff, R.W.G., 1964, Crystal Structures, Vol. 2 (Wiley, New York), pp. 2 ff.
2. Koskenlinna, M., M. Leskelä and L. Niinistö, 1976, J. Electrochem. Soc. **123**, 75.
3. Babkina, T.V., M.I. Gaiduk, L.N. Zorina and N.P. Soshchin, 1974, Opt. Spectrosc. **37**, 401.
4. Sovers, O.J. and T. Yoshioka, 1968, J. Chem. Phys. **49**, 4945.
5. Sovers, O.J. and T. Yoshioka, 1969, J. Chem. Phys. **51**, 5330.

6. Sovers, O.J. M. Ogawa and T. Yoshioka, 1979, J. Lumin. **18/19**, 336.
7. Rossat-Mignod, J., J.C. Souillat and G. Quezel, 1974, Phys. Stat. Sol. (b) **62**, 223.
8. Morozov, N.N., T.V. Babkina, M.I. Gaiduk, V.F. Zolin, C.I. Naryshkina and N.P. Soshchin, 1975, in: Spektroskopiya Kristallov (Nauka, Moscow), p. 308.
9. Rossat-Mignod, J., J.C. Souillat and G. Quezel, 1974, Phys. Stat. Sol. (b) **62**, 519.
10. Rossat-Mignod, J., J.C. Souillat and C. Linares, 1973, J. Phys. Chem. Solids **34**, 371.
11. Linares, C. and J.C. Souillat, 1970, C. R. Acad. Sc. Paris **271**, 861.

5.13. $LiNbO_3$

Ferroelectric lithium niobate ($LiNbO_3$) has been of considerable interest because of its nonlinear optical properties. Conversion of infrared into visible radiation in $LiNbO_3$ crystals has been observed (Midwinter and Warner, 1967; Arutyunyan and Mkrtchyan, 1975). Electro-optic coefficients of $LiNbO_3$ have been determined for a wide range of frequencies ranging from the visible (Smakula and Claspy, 1967) to the millimeter-wave portion of the spectrum (Vinogradov et al., 1970). Other nonlinear optical properties such as photovoltaic effects (Kratzig and Kurz, 1977) and optically induced refractive index changes (Ashkin et al., 1966; Chen, 1969) have also been observed.

Laser action has been observed in Nd:$LiNbO_3$ (Erlanova et al., 1967). In an attempt to produce nonlinear optical effects within a laser medium, Johnson and Ballman (1969) studied laser characteristics of $LiNbO_3$ doped with Nd, Ho, and Tm and observed second-harmonic generation in Tm:$LiNbO_3$. $LiNbO_3$ can be doped with both rare earths and transition metals (Burns et al., 1966), and indeed such co-doping is desirable and necessary to obtain high rare-earth concentrations for high-power lasers (Belabaev et al., 1975). Substitution of rare-earth impurity ions takes place at both Li sites and Nb sites, as revealed by electron paramagnetic resonance studies (Dischler et al., 1973); both these sites have C_3 symmetry. As a result, crystal-field analyses of the optical spectra are difficult, and we have found none reported.

5.13.1 Crystallographic data for $LiNbO_3$

Trigonal R3c, #161, Z = 6 (hexagonal axes)

Ion	Pos.	Symm.	x	y	z
Li	6(a)	C_3	0	0	z
Nb	6(a)	C_3	0	0	z*
O	18(b)	C_1	x	y	z

Crystallographic data for $LiNbO_3$ (continued)

X-ray data

		Li	O			
a	c	z	x	y	z	Ref.
5.14829	13.8631	0.2829	0.0492	0.3446	0.0647	1
-	-	0.2802	0.0477	0.3435	0.0633	2

* z - coordinate arbitrarily chosen as zero in both Refs. 1 and 2.

5.13.2 Index of refraction for $LiNbO_3$ (Ref. 3)

λ(μm)	n_o	n_e	(Ref. 3)
0.42	2.4144	2.3638	
0.45	2.3814	2.2765	
0.50	2.3444	2.2446	
0.55	2.3188	2.2241	
0.60	2.3002	2.2083	
0.70	2.2862	2.1964	
0.80	2.2756	2.1874	
0.90	2.2598	2.1741	
1.00	2.2487	2.1647	
1.20	2.2407	2.1580	
1.40	2.2291	2.1481	
1.60	2.2208	2.1410	
1.80	2.2139	2.1351	
2.00	2.2074	2.1297	
2.20	2.2015	2.1244	
2.40	2.1948	2.1187	
2.60	2.1882	2.1138	
2.80	2.1814	2.1080	

Index of refraction for $LiNbO_3$ (continued)

λ(μm)	n_o	n_e	(Ref. 3)
3.00	2.1741	2.1020	
3.20	2.1663	2.0955	
3.40	2.1580	2.0886	
3.60	2.1493	2.0814	
3.80	2.1398	2.0735	
4.00	2.1299	2.0652	
4.20	2.1193	2.0564	

Temperature-dependent dispersion equation (Ref. 4)

$$n_o^2 - 1 = 3.9130 + \frac{1.173 \times 10^5 + 1.65 \times 10^{-2} T^2}{\lambda^2 - (2.12 \times 10^2 + 2.7 \times 10^{-5} T^2)^2} - 2.78 \times 10^{-8} \lambda^2$$

$$n_e^2 - 1 = 3.357 + 2.605 \times 10^{-7} T^2 + \frac{0.970 \times 10^5 + 1.70 \times 10^{-2} T^2}{\lambda^2 - (2.01 \times 10^2 + 5.4 \times 10^{-5} T^2)^2} - 2.24 \times 10^{-8} \lambda^2$$

(λ in μm, T in K)

5.13.3 Energy levels for $LiNbO_3$

Nd:$LiNbO_3$

Term	Pre-fix	Energy (cm^{-1})						T	Ref.
$^4I_{9/2}$	-	0	82	154	434	481		77	5
	-	0	156	170	440	486		77	6
	-	0	156	250	450	492		77	7
	-	0	151	167	443	487		4	9
$^4I_{11/2}$	1	986	033*	106	189	227	262	77	5
	1	987	033*	107	190	228	263	77	6
	1	986.5	032.6*	106				4	9

$Nd:LiNbO_3$ (continued)

Term	Prefix	Energy (cm^{-1})						T	Ref.
$^4I_{13/2}$	3	918	973	035*	118	140	184	77	6
	3	917.5	973.6	035.5*	115	139	181	4	9
	3	211						77	6
	3	210						4	9
$^4I_{15/2}$	5	777	916	005*	087	105	217	77	6
	5	290	449					77	6
$^4F_{3/2}$	11	249	417					77	5
	11	250	409					77	6
	11	245	404					77	7
	11	250	408					4	9
$^4F_{5/2}$, $^2H_{9/2}$	12	(133)	291	396	421	449	463	77	6
	12	276	351	385	407	447	553	4.2	8
	12	574	(692)					77	6
$^4F_{7/2}$, $^4S_{3/2}$	13	199	291	(398)	437			77	6
	13	189	277	380	419			4.2	8
$^4F_{9/2}$	14	498	567	620	664	685		77	6
$^2H_{11/2}$	15	748	803	873	888	911	926	77	6
$^4G_{5/2}$	16	753	852	909				77	6
$(^4G,^2G)_{7/2}$	16	(949)	071*	135	176			77	6
$(^4G,^2G)_{7/2}$	18	719	786	836				77	6
	18	693	700	778	824			4.2	8
$^4G_{9/2}$	19	135	260	331				77	6
	19	075	119	223	311			4.2	8
$^2G_{9/2}$	20	682	764	799	868	938		77	6
	20	650	741	771	841	910	002*	4.2	8
$^4G_{11/2}$, $^2K_{15/2}$, $^2(P,D)_{3/2}$	20	973	022*	039	213	372	631	77	6
	20	357*						4.2	8
	21	696						77	6
$^2P_{1/2}$	22	923						77	5
	22	914						77	6
	22	914						77	7
	22	904	961					4.2	8
$^2D_{5/2}$	23	348	554	608				77	6
	23	331						4.2	8
$^2(P,D)_{3/2}$	25	745	882					77	6
$^4D_{3/2}$	27	365	469					77	6
$^2D_{1/2}$	28	031						77	6

$Ho:LiNbO_3$

Term	Prefix	Energy (cm^{-1})						T	Ref.
$^5I_8$	-	0	8	18	41	48	76	4.2	9
	-	0	27					300	10
	-	201	240	266	310	328	386	4.2	9
	-	404						4.2	9
$^5I_7$	5	121	130	148	155	162	170	4.2	9
	5	102	182	263	290	391	479	300	10
	5	241	271.5	291	304	(310)		4.2	9
$^5I_6$	8	648	734	807				300	10
$^5F_5$	15	151	385	504				300	10
$^5F_4$, $^5S_2$	18	050	315	416	518			300	10
$^5F_3$	20	325	408	492				300	10
$^5F_2$	20	926						300	10
$^3K_8$	21	231	367.5					300	10
$^5F_1$, $^5G_6$	21	645	858	026*	321	624	988	300	10
$^5G_5$	23	529	753	923				300	10
$^5G_4$	25	641						300	10
$^3K_7$	26	110						300	10
$^5G_5$	27	100						300	10
$^3H_6$	27	322	472	576	624	740	816	300	10
$^5G_2$	28	641	694					300	10
$^5G_3$	29	028	070	112	189	325	412	300	10

$Er:LiNbO_3$

Term	Prefix	Energy (cm^{-1})						T	Ref.
$^4I_{15/2}$	-	0	63	132	(156)	182	278	77	6
	-	0	54					300	10
	-	353	414					77	6
$^4I_{13/2}$	6	524	586	611	631	759	778	77	6
	6	410	502	557	601	654	703	300	10
	6	804						77	6
	6	757	803					300	10

$Er:LiNbO_3$ (continued)

Term	Prefix	Energy (cm^{-1})						T	Ref.
$^4I_{11/2}$	10	207	(260)	270	303	316	338	77	6
	10	050	152	204	256	309		300	10
$^4I_{9/2}$	12	381	410	453	603	612		77	6
	12	422	500	558				300	10
$^4F_{9/2}$	15	151	(174)	255	344			77	6
	14	925	106*	221	274			300	10
$^4S_{3/2}$	18	265	354					77	6
	18	083	182	248				300	10
$^2H_{11/2}$	19	(043)	(061)	(152)	(177)	(188)	(199)	77	6
	18	662	837	886	957	975	011*	300	10
	18	084	531	646				300	10
$^4F_{7/2}$	20	370	(407)	538	557			77	6
	20	000	228	284	437	492		300	10
$^4F_{5/2}$	22	395	526					77	6
	21	930	021*	075	124			300	10
$^4F_{3/2}$	22	395	526					77	6
	22	222	316	371				300	10
$^2H_{9/2}$	24	(371)	417	444	500	594		77	6
	24	390	570	624	731			300	10
$^4G_{11/2}$	26	(185)	197	300	349	380	398	77	6
	25	907	316*					300	10
$^4G_{9/2}$	26	954	137*	248	300			300	10
$^2K_{15/2}$	27	548						300	10
$^2G_{7/2}$	27	738	878	933	011*			300	10

$Tm:LiNbO_3$

Term	Prefix	Energy (cm^{-1})						T	Ref.
$^3H_6$	-	0	10	147	271	359	504	4.2	9
$^3H_4$	5	667	679	694	730	901	009*	4.2	9
	5	026	(053)	076				4.2	9

References for 5.13. $LiNbO_3$

1. Abrahams, S.C., J.M. Reddy and J.L. Bernstein, 1966, J. Phys. Chem. Solids **27**, 997.
2. Abrahams, S.C., W.C. Hamilton and J.M. Reddy, 1966, J. Phys. Chem. Solids **27**, 1013.
3. Boyd, G.D., W.L. Bond, and H.L. Carter, 1967, J. Appl. Phys. **38**, 1941.

4. Hobden, M.V. and J. Warner, 1966, Phys. Lett. **22**, 243.
5. Ivaleva, L.I., A.A. Kaminskii, Yu.S. Kuz'minov and V.N. Shpakov, 1969, Sov. Phys. Dokl. **13**, 1185.
6. Gabrielyan, V.T., A.A. Kaminskii and L. Li, 1970, Phys. Stat. Sol. (a) **3**, K37.
7. Kovaleva, L.V., Yu.S. Kuz'minov and B.S. Skorobogatov, 1970, in: Spektroskopiya Kristallov (Nauka, Moscow), p. 196.
8. Valyashko, E.G., L.N. Rashkovich, R.K. Sviridova and V.A. Timoshenkov, 1970, in: Spektroskopiya Kristallov (Nauka, Moscow), p. 188.
9. Johnston, L.F. and A.A. Ballman, 1969, J. Appl. Phys. **40**, 297.
10. Antonov, V.A. and P.A. Arsen'ev, 1975, Z. Prikl. Spektrosk. **22**, 341.

5.14. $YAlO_3$

The host material $YAlO_3$ is, at present, the second most successful rare-earth laser host material, being surpassed only by $Y_3Al_5O_{12}$ (YAG) (Kaminskii, 1981, lists 38 lasers with $YAlO_3$). In view of this popularity, one would assume that the energy levels of all the rare-earth ions in $YAlO_3$ would be thoroughly documented. Such is not the case. The two sets of reported data on Pr^{3+}:$YAlO_3$ are so different that the data could have been taken on two different host materials. No data at all were found on Sm^{3+} or Gd^{3+} in $YAlO_3$, and for a few other R^{3+} ions the reported data will require considerable interpretation before a meaningful, consistent analysis can be made.

Historically, lasers using $YAlO_3$ as a host material were discovered simultaneously in the United States (Weber et al., 1969) and in Russia (Bagdasarov et al., 1969; Bagdasarov and Kaminskii, 1969). The subsequent progress of the growth of good optical quality $YAlO_3$ was such as to warrant a brief but concise review of this material after only 2 years (Weber and Bass, 1971). Since then a number of review articles on solid-state lasers have included $YAlO_3$ (Kaminskii, 1978; Weber, 1979b; as well as Chapter 35, Volume 4 [Weber, 1979a] of this series).

5.14.1 Crystallographic data for $YAlO_3$

Monoclinic Pnma, #62, Z = 4

Ion	Pos.	Symm.	x	y	z
Y	4(c)	C_s	x	1/4	z
Al	4(b)	C_i	0	0	1/2
O_1	4(c)	C_s	x	1/4	z
O_2	8(d)	C_1	x	y	z

X-ray data

			Y		O_1		O_2			
a	b	c	x	z	x	z	x	y	z	Ref.
5.330	7.375	5.180	0.0526	0.9896	0.475	0.086	0.293	0.044	0.703	1
5.325	7.356	5.177	0.0530	0.9882	0.4739	0.0822	0.2944	0.0441	0.7047	2

5.14.2 Index of refraction for $YAlO_3$

Transparent for 0.3 μm ≤ λ ≤ 5.8 μm (Ref. 3)

Absorption edge approximately at 0.19 μm (Ref. 3)

Index of refraction, Sellmeier equations:

$$n^2 = 1 + \frac{A\lambda^2}{\lambda^2 - B} \qquad (\lambda \text{ in } \mu m,\ B \text{ in } (\mu m)^2)$$

	n_a	n_b	n_c	Ref.
A	2.70892	2.67792	2.63468	3,4
B	0.012607	0.012282	0.011592	
A	2.70381	2.67171	2.61960	5
B	0.012903	0.012605	0.012338	
A	2.70852	2.67542	2.62507	5 (1.14% Nd)
B	0.013017	0.012805	0.012322	

5.14.3 Crystal-field parameters for R:$YAlO_3$ (cm^{-1})

R	B_{20}	B_{22}	B_{40}	RB_{42}	IB_{42}	RB_{44}	IB_{44}	Ref.
Nd	814	-18	-1345	-521	525	-214	-575	6,7
Tb	567	-233	-1060	-217	497	-398	-82	6,7
Dy	653	-163	-882	-616	300	151	-405	6,7
Ho	716	-248	-838	-544	384	-63	-360	6,7
Er	431	-170	-839	-346	365	-218	-709	6,7
Tm	675	-76	-784	-480	367	-54	-445	6,7

R	B_{60}	RB_{62}	IB_{62}	RB_{64}	IB_{64}	RB_{66}	IB_{66}	Ref.
Nd	-1110	-348	-155	1214	221	-82	370	6,7
Tb	-751	-317	-425	740	-508	-230	91	6,7
Dy	-888	156	-203	649	-97	-440	48	6,7
Ho	-963	211	-214	-41	593	-750	19	6,7
Er	-742	-241	-180	534	17	23	224	6,7
Tm	-752	-72	-154	601	59	-218	115	6,7

5.14.4 Intensity parameters for R:$YAlO_3$ (10^{-20} cm^2)

R	Ω_2	Ω_4	Ω_6	Ref.
Nd	1.24	4.68	5.85	8
Eu	2.66	6.32	0.80	8
Tb	3.25	7.13	2.00	8
Ho	1.82	2.38	1.53	8
Er	1.06	2.63	0.78	8
Tm	0.67	2.30	0.74	8

5.14.5 Energy levels for R:$YAlO_3$

Ce:$YAlO_3$

Term	Prefix	Energy (cm^{-1})				T	Ref.
$^2F_{5/2}$	-	0				300	9
$^2F_{7/2}$	2	085	485	695	250*	300	9

Pr:$YAlO_3$

Term	Prefix	Energy (cm^{-1})						T	Ref.
$^3H_4$	-	0	25	62	83	98	224	77	10
	-	0	51	146	155	227	405	10	11
	-	308	337	335				77	10
	-	481	657	825				10	11
$^3H_5$	1	953	996	036*	079	112	143	77	10
	1	180	236	315	319			77	10
$^3F_2$	5	045	101	161	219	265		77	10
$^3F_4$	6	794	825	889	901	964	006*	77	10
	6	042	104	143				77	10
$^1G_4$	9	675	690	762	803	941	039*	77	10
	9	100	129	175				77	10
$^1D_2$	16	731	776	846	932	224*		77	10
	16	375	649	716	788	029*		10	11
$^3P_0$, $^3P_1$	20	713	816	820	899			77	10
$^1I_6$	21	026	079	213	240	277	322	77	10
	21	566						77	10

$Nd:YAlO_3$

Term	Prefix	Energy (cm^{-1})						T	Ref.
$^4I_{9/2}$	-	0	117	211	499	670		300	12
	-	0	118	212	500	671		77	13
$^4I_{11/2}$	2	023	098	157	269	320	368	300	12
	2	023	097	158	264	323	378	77	13
$^4I_{13/2}$	3	953	017*	087	190	285	324	300	12
	3	953	021*	092	200	291	328	77	13
	3	955	020*	090	200	292	323	300	14
	3	439						300	12
	3	446						77	13
	3	471						300	14
$^4I_{15/2}$	5	760	896	011*	199	242	311	300	12
	5	757	893	011*	240	307	402	77	13
	5	404	748					300	12
	5	687	743					77	13
$^4F_{3/2}$	11	419	542					300	12
	11	421	550					77	13
	11	421	545					300	14
$^4F_{5/2}$, $^2H_{9/2}$	12	302	413	450	513	561	715	300	12
	12	411	447	511	561	593	713	77	13
	12	745	887					300	12
	12	742	883					77	13
$^4F_{7/2}$, $^4S_{3/2}$	13	332	455	566	590	608	652	300	12
	13	323	452	565	589	607	651	77	13
$^4F_{9/2}$	14	680	730	746	795	925		300	12
	14	665	723	740	793	928		77	13
$^2H_{11/2}$	15	865	906	992	095*			300	12
	15	858	893	903	995	095*		77	13
$^4G_{5/2}$, $^2G_{7/2}$	16	849	964	027*	114	310	367	300	12
	16	963	023*	116	295	313	364	77	13
	16	458						300	12
	16	456						77	13
$^4G_{7/2}$	18	850	896	972	073*			300	12
	18	846	893	975	077*			77	13
$^2G_{9/2}$	19	234	301	342	547			300	12
	19	245	309	350	425	546		77	13
$^2K_{13/2}$	19	(637)	(652)	747	806	873	924	77	13
$^4G_{9/2}$	20	774	832	887	946	034*		300	12
	20	865	894	955	041*	110		77	13
$^4G_{11/2}$, $^2K_{15/2}$, $^2D_{3/2}$	21	103	232	288	525	745	835	300	12
	21	231	276	(294)	367	464	536	77	13
	21	924						300	12
	21	580	(630)	654	(718)	748	834	77	13
	21	(906)	930					77	13

Nd:$YAlO_3$ (continued)

Term	Prefix	Energy (cm^{-1})						T	Ref.
$^2P_{1/2}$	23	154						300	12
	23	164						77	13
$^2D_{5/2}$	23	463	635	759				77	13
$^2P_{3/2}$	25	981	123*					77	13

Eu:$YAlO_3$

Term	Prefix	Energy (cm^{-1})						T	Ref.
$^7F_0$	-	0						?	15
$^7F_6$	4	822	828	999	006*	027	032	?	15
	4	063	085	091	219	225	230	?	15
	4	414						?	15
$^5D_3$	24	715	753	818	973	006*	129	?	15
	24	262						?	15

Tb:$YAlO_3$

Term	Prefix	Energy (cm^{-1})						T	Ref.
$^7F_6$	-	0	36	61	96	134	164	77	17
	-	0	207.9	273.4	280.3	303.1	323.8	4.2	16
	-	229	250	297	328	447	505	77	17
	-	336.4	351.2	359.7	370.7	397.4	555.4	4.2	16
	-	641						77	17
	-	654.6						4.2	16
$^7F_5$	2	127	164	204	258	273	315	77	17
	2	126.3	165.1	182.5	214.5	243.9	245.5	4.2	16
	2	354	418	511	583	617		77	17
	2	270.5	326.7	332.2	494.5	530.9		4.2	16
$^7F_4$	3	407	444	490	573	621	651	77	17
	3	421.0	469.2	487.1	537.5	650.4	662.8	4.2	16
	3	696	747	845				77	17
	3	705.5	753.0	892.0				4.2	16
$^7F_3$	4	442	497	532	549	580	636	77	17
	4	389.0	405.7	503.7	544.8	573.2	684.5	4.2	16
	4	695						77	17
	4	692.2						4.2	16

Tb:$YAlO_3$ (continued)

Term	Prefix	Energy (cm^{-1})						T	Ref.
$^7F_2$	5	090	178	240	295			77	17
	4	977.7	085.2*	312.0	372.1	437.8		4.2	16
$^7F_1$	5	639	705	771				77	17
	5	497.9	535.6	576.9				4.2	16
$^7F_0$	5	873						77	17
	5	765.5						4.2	16
$^5D_4$	20	522	528	551	578	590	602	77	17
	20	563.2	571.9	590.5	603.5	641.2	(698.1)	4.2	16
	20	617	621	650				77	17
	20	681.4	686.8	701.9				4.2	16
$^5D_3$, $^5G_6$	26	301	359					77	17
	26	210.7	267.9	306.8	317.0	321.6	336.9	4.2	16
	26	347.2	380.5	385.5	404.8	432.9	438.4	4.2	16
	26	469.2	482.5	513.8	527.1	537.3	540.3	4.2	16
$^5G_5$	27	732.3	784.6	793.8	834.3	871.8	875.5	4.2	16
	27	897.6	912.9	018.7*	023.2			4.2	16
$^5D_1$	30	750.5	812.5	851.0				4.2	16
$^5H_7$	31	307.9	311.3	379.9	394.0	411.8	441.2	4.2	16
	31	492.3	499.6	525.8	529.2	562.8		4.2	16
$^5H_6$	32	821.9	836.2	861.3	865.3	910.6	951.9	4.2	16
	32	989.8	004.9*	009.9	044.7	103.3	147.7	4.2	16
$^5H_5$	33	750.4	760.9	800.2	826.7	852.3	874.9	4.2	16
	33	909.6						4.2	16
$^5F_3$	36	402.0	405.3	422.7	470.7	485.9	503.0	4.2	16
	36	539.5						4.2	16

Dy:$YAlO_3$

Term	Prefix	Energy (cm^{-1})						T	Ref.
$^6H_{15/2}$	-	0	65	142	226	286	305	77	18
	-	484	558					77	18
$^6H_{13/2}$	3	530	587	664	741	806	833	77	18
	3	881						77	18
$^6H_{11/2}$	5	865	952	043*	071	080	173	77	18
$^6H_{9/2}$, $^6F_{11/2}$	7	557	624	635	701	767	819	77	18
	7	843	862	954	004*	170		77	18
$^6H_{7/2}$, $^6F_{9/2}$	8	989	091*	147	189	221	268	77	18
	8	354	456	506				77	18

Dy:$YAlO_3$ (continued)

Term	Prefix	Energy (cm^{-1})						T	Ref.
$^6H_{5/2}$	10	235	337	504				77	18
$^6F_{7/2}$	11	074	123	165	203			77	18
$^6F_{5/2}$	12	469	508	558				77	18
$^6F_{3/2}$	13	293	304					77	18
$^4F_{9/2}$	21	002	036	121	231	378		77	18
$^4I_{15/2}$	21	945	009*	053	086	151	251	77	18
	21	269	401					77	18
$^4G_{11/2}$	23	317	447	485	512	538	605	77	18

Ho:$YAlO_3$

Term	Prefix	Energy (cm^{-1})						T	Ref.
$^5I_8$	-	0	44	65	97	118	129	77	18
	-	0	6	37	48	58	71	2	19
	-	140	155	196	234	291	312	77	18
	-	100	126	137	193	211	222	2	19
	-	330	380	405				77	18
	-	289	327	425	474	499		2	19
$^5I_7$	5	106	137	189	204	225	246	77	18
	5	186	187	222	253	255	264	2	19
	5	256	269	285	307	323	328	77	18
	5	266	268	280	288	318	326	2	19
	5	343	359	376				77	18
	5	337	346	357				2	19
$^5I_6$	8	606	626	647	690	708	730	77	18
	8	736	760	772	800	807	837	77	18
	8	867						77	18
$^5I_5$	11	163	229	247	252	274	303	77	18
	11	312	329	364	370	402		77	18
$^5F_5$	15	308	374	393	418	434	492	77	18
	15	512	520	556	596	661		77	18
$^5F_3$	20	522	553	587	607	646	712	77	18
	20	737						77	18

$Er:YAlO_3$

Term	Prefix	Energy (cm^{-1})						T	Ref.
$^4I_{15/2}$	-	0	50.7	170.7	217.6	265.9	388.0	4.2	20
	-	0	47	171	214	257	386	296	21
	-	443.1	516.4					4.2	20
	-	446	522					296	21
$^4I_{13/2}$	6	602.1	640.7	668.8	714.7	772.9	813.9	4.2	20
	6	607	645	671	718	777	817	296	21
	6	867.6						4.2	20
	6	872						296	21
$^4I_{11/2}$	10	281.9	292.8	322.4	347.0	382.0	402.4	4.2	20
	10	241	289	301	390	411		296	21
$^4I_{9/2}$	12	393.2	445.6	623.5	647.9	732.0		4.2	20
	12	399	453	623	650	730		296	21
$^4F_{9/2}$	15	262.7	343.6	373.7	396.3	480.7		4.2	20
	15	215	260	373	384	475		296	21
$^4S_{3/2}$	18	406.2	486.7					4.2	20
	18	404	483					296	21
$^2H_{11/2}$	19	118.7	162.1	189.6	239.9	275.1	303.1	4.2	20
$^4F_{7/2}$	20	481.5	554.5	616.8	685.0			4.2	20
$^4F_{5/2}$	22	195.8	227.0	259.3				4.2	20
$^4F_{3/2}$	22	516.4	536.4					4.2	20
$^2G_{9/2}$	24	478.8	525.9	666.0	697.9	765.5		4.2	20
$^4G_{11/2}$	26	307.5	322.0	380.5	458.5	476.4	525.9	4.2	20
$^4G_{9/2}$	27	352.2	381.2	410.5	544.2	670.3		4.2	20
$^2K_{15/2}$, $^2G_{7/2}$	27	398.6	445.1	486.7	682.7	732.1	760.6	4.2	20
	27	775.0	913.0	997.1	043.6*	065.1	077.0	4.2	20
$^2P_{3/2}$	31	449.0	585.2					4.2	20
$^2K_{13/2}$	32	773.3	822.6	983.4	061.3*	162.2	301.5	4.2	20
	32	375.5						4.2	20
$^4G_{7/2}$	33	865.7	962.4	038.1*	088.8			4.2	20
$^2D_{5/2}$	34	738.9	774.7	827.0				4.2	20
$^2H_{9/2}$	36	315.0	389.0	462.7	630.5	662.5		4.2	20
$^4D_{5/2}$	38	394.8	425.2	448.9				4.2	20
$^4D_{7/2}$	38	840.5	004.8*	076.0	312.4			4.2	20

$Tm:YAlO_3$

Term	Prefix	Energy (cm^{-1})						T	Ref.
$^3H_6$	-	0	70	144	214	243	288	77	18
	-	319	409	445	(472)	574	(596)	77	18
	-	628						77	18
$^3H_4$	5	631	719	729	825	894	919	77	18
	5	940	968	988				77	18
$^3H_5$	8	263	323	344	(377)	463	485	77	18
	8	535	553	562	(596)	696		77	18
$^3F_4$	12	510	572	662	739	780	881	77	18
	12	(909)	938	947				77	18
$^3F_3$	14	454	483	518	556	595	609	77	18
	14	623						77	18
$^3F_2$	15	030	096	195	292	(309)		77	18
$^1G_4$	21	028	108	204	300	329	463	77	18
	21	495	628					77	18
$^1D_2$	27	(700)	848	(902)	(007)*	(179)		77	18

$Yb:YAlO_3$

Term	Prefix	Energy (cm^{-1})				T	Ref.
$^2F_{3/2}$	-	0	209	341	590	77	22
	-	0	100	(154)	(234)	77	18
$^2F_{5/2}$	10	220	410	730		77	22
	10	107	324	519		77	18

References for 5.14. $YAlO_3$

1. Diehl, R. and G. Brandt, 1975, Mat. Res. Bull. **10**, 85.
2. Matsuyama, S., H. Morikawa, F. Marumo and S. Iwai, 1977, Report of Res. Lab. Eng. Mater. (Tokyo Inst. Technol.), p. 63.
3. Weber, M.J., B.H. Matsinger, V.L. Donlan and G.T. Surratt, 1972, J. Chem. Phys. **57**, 562.
4. Bass, M. and M.J. Weber, 1971, Laser Focus **1**, 34 (Sept. Issue).
5. Martin, K.W. and L.G. DeShazer, 1973, Appl. Opt. **12**, 941.
6. Karayianis, N., D.E. Wortman and C.A. Morrison, 1976, Solid State Comm. **18**, 1299.
7. Morrison, C.A., N. Karayianis and D.E. Wortman, 1977, Harry Diamond Laboratories Report TR-1788 (NTIS #038 050).
8. Weber, M.J., T.E. Varitimos and B.H. Matsinger, 1973, Phys. Rev. **B8**, 47.
9. Weber, M.J., 1973, J. Appl. Phys. **44**, 3205.
10. Arsenev, P.A., K.E. Bienert and A.V. Potemkin, 1974, Phys. Stat. Sol (a) **26**, K113.
11. Erickson, L.E., 1979, Phys. Rev. **B19**, 4412.
12. Weber, M.J. and T.E. Varitimos, 1971, J. Appl. Phys. **42**, 4996.
13. Kaminskii, A.A., 1981, Laser Crystals (Springer-Verlag, New York) p. 128.

14. Kaminskii, A.A., N.B. Karlov, S.E. Sarkisov, O.M. Stel'makh and V.E. Tukish, 1976, Sov. J. Quantum Electron. **6**, 1371.
15. Antonov, V.A., P.A. Arsenev, K.E. Bienert and A.V. Potemkin, 1975, in: Spektroskopiya Kristallov (Nauka, Moscow), p. 270.
16. Berg, J.L., 1973, M. S. Thesis, Air Force Institute of Technology, Wright Patterson Air Force Base, Ohio (NTIS #766 881).
17. Arsenev, P.A., K.E. Bienert and A.V. Potemkin, 1974, Phys. Stat. Sol. (a) **26**, K71.
18. Antonov, V.A., P.A. Arsenev, K.E. Bienert and A.V. Potemkin, 1973, Phys. Stat. Sol. (a) **19**, 289.
19. Weber, M.J., M. Bass, T.E. Varitimos and D.P. Bua, 1973, IEEE J. Quantum Electron. **QE-9**, 1079.
20. Donlan, V.L. and A.A. Santiago, 1972, J. Chem. Phys. **57**, 4717.
21. Weber, M.J., M. Bass and G.A. de Mars, 1971, J. Appl. Phys. **42**, 301.
22. Weber, M.J., 1971, Phys. Rev. **B4**, 3153.

5.15. YVO_4

The earliest investigations of neodymium-doped yttrium orthovanadate, YVO_4, as a laser material (O'Connor, 1966) were hampered by difficulties in crystal growth. Since then, many improvements in the growth techniques (McKnight and Rothrock, 1973) have provided good-quality crystals with recommendations for further improvement (Bass et al., 1976). Another difficulty in the use of rare-earth doped YVO_4 as a laser crystal is the creation of color centers in the crystal when exposed to conventional flash lamp radiation used in pumping (Kaminskii et al., 1969); appropriate filters remove this problem. Recently, however, it has been found that unfiltered flash lamps can be used at elevated temperatures (greater than 200°C) (Kaminskii, 1970) as the color centers anneal out rapidly enough for pulsed operation. Increases in temperature lower the threshold further, indicating rapid annealing at elevated temperatures. Possibly interrelated with the color centers are the trapping centers in R:YVO_4 studied at low temperatures (100–200 K) (Khodos et al., 1974) by thermoluminescence. The trapping centers are filled at low temperatures, and two peaks in the luminescence intensity were observed: one near 120 K and a second near 160 K for all the compounds investigated.

Since many of the rare-earth orthovanadates undergo a crystallographic phase transition or become ferromagnetic at low temperatures, the spectra of some R′:RVO_4 have been investigated for the purpose of comparison. Examples of this occurring are Ho:$GdVO_4$ (Kasten and Becker, 1977) and pure $HoVO_4$ (Battison et al., 1977). In $GdVO_4$ the crystal becomes antiferromagnetic at 2.46 K, and Ho was used as a probe by observing the internal Zeeman effect. The optical spectrum of Ho:YVO_4 was compared as a standard to rule out the possibility of a crystallographic transition. The spectrum of Ho^{3+} in $HoVO_4$ at low temperatures indicates a lower symmetry than the room-temperature D_{2d} (the spectrum of Ho:YVO_4 was used for comparison).

The electron spin-resonance parameters $g_\parallel$, $g_\perp$, A, B, and one P for a number of rare earths in YVO_4 have been reported (Ranon, 1968a, b). The Schottky specific heat, paramagnetic susceptibility, and quadrupole splitting have been calculated for Tm:YVO_4 using results from optical measurements and sub-

sequent crystal-field analysis based on these measurements (Kumar et al., 1977). A similar analysis has been performed (Kumar et al., 1980) on Nd:YVO_4 using the crystal-field parameters obtained from an analysis of the optical spectrum of Nd:YVO_4.

The infrared and Raman spectra of YVO_4 have been experimentally investigated (Miller et al., 1968), with only a few of the active modes missing. These data are important for understanding the nonradiative decay of rare earth ions in YVO_4. A thorough experimental and theoretical analysis of nonradiative decay of rare earth ions in YVO_4, $YAsO_4$ and YPO_4 has been given by Reed and Moos (1973a, b).

5.15.1 Crystallographic data for YVO_4

Tetragonal $I4_1/amd$, #141, Z = 4 (1st setting)

Ion	Pos.	Symm.	x	y	z
Y	4(a)	D_{2d}	0	0	0
V	4(b)	D_{2d}	0	0	1/2
O	16(h)	C_s	0	x	z

X-ray data

		O		
a	c	x	z	Ref.
7.123	6.291	-	-	1
7.120	6.289	0.1852	0.3251	2
7.123	6.292	0.1846	0.3273	3,4

5.15.2 Index of refraction for YVO_4

λ(μm)	n_o	n_e	(Ref. 5)
0.4000	2.0777	2.3402	
0.4500	2.0458	2.2932	
0.5000	2.0242	2.2618	
0.5500	2.0088	2.2396	
0.6000	1.9974	2.2233	
0.6500	1.9888	2.2109	
0.7000	1.9820	2.2013	
0.7500	1.9766	2.1936	
0.8000	1.9723	2.1875	

Index of refraction for YVO_4 (continued)

$$n_o^2 = 1 + \frac{2.7710\,\lambda^2}{\lambda^2 - 0.026336}, \qquad 0.4000 < \lambda < 0.8000 \ (\lambda \text{ in } \mu m) \text{ (Ref. 5)}$$

$$n_e^2 = 1 + \frac{3.5996\,\lambda^2}{\lambda^2 - 0.031346},$$

$$n_o^2 = 1 + \frac{2.7665\,\lambda^2}{\lambda^2 - 0.026884}, \qquad 0.488 < \lambda < 3.39 \ (\lambda \text{ in } \mu m) \text{ (Ref. 6)}$$

$$n_e^2 = 1 + \frac{3.5930\,\lambda^2}{\lambda^2 - 0.032103}.$$

5.15.3 Crystal-field parameters for R:YVO_4 (cm^{-1})

R	B_{20}	B_{40}	B_{44}	B_{60}	B_{64}	Ref.
Nd	-136	626	1024	-1170	-251	7
Nd	-122	632	1048	-1181	-268	8
Nd	-116	605	1105	-1191	-246	8
Eu	-109	380	704	-877	-19	9
Eu	-122	403	701	-962	-40	10
Er	-218	322	917	-702	10	8
Er	-206	364	926	-688	31.5	11
Tm	-175	337	832	-612	-50.2	12
Tm	-132	377	898	-521	-52.4	13

5.15.4 Intensity parameters for R:YVO_4 (10^{-20} cm^2)

R	Ω_2	Ω_4	Ω_6	Ref.
Nd	5.88	4.08	5.11	6

5.15.5 Energy levels for R:YVO_4

Nd:YVO_4

Term	Prefix	Energy (cm^{-1})						T	Ref.
$^4I_{9/2}$	-	0	108	173	226	433		77	14
	-	0	108	173	211	440		4.2	15
	-	0	112	174	201	437		85	16
$^4I_{11/2}$	1	966	988	047*	062	154	182	77	14
	1	966	988	047	062	154	181	4.2	15
	1	968	988	046*	(062.3)	151	180	85	16
$^4I_{13/2}$	3	910	931	980	042*	088	158	77	14,7
	3	170						77	14,7
$^4I_{15/2}$	5	834	871	917	065*	260	264	77	14,7
	5	318						77	14,7
$^4F_{3/2}$	11	366	384					77	14
	11	365	383					25	7
	11	365	380					85	16
$^4F_{5/2}$	12	366	(401)	(405)				77	14
	12	362	404					4.2	15
$^2H_{9/2}$	12	497	542	599	692			77	14
	12	473	494	686				4.2	15
$^4F_{7/2}$, $^4S_{3/2}$	13	319	340	392	(461)	(461)	(465)	77	14
	13	318	339	385	385	456		4.2	15
$^4F_{9/2}$	14	579	598	635	719	730		77	14
	14	567	589	626	710	734		4.2	15
$^2H_{11/2}$	15	765	853					77	14
	15	924	957					4.2	15
$^4G_{5/2}$	16	824	(951)	(970)				77	14
	16	812	966	972				4.2	15
$^2G_{7/2}$	17	215	244	268				77	14
	17	161	253					4.2	15
$^4G_{7/2}$	18	772	832	861	925			77	14
	18	758	843	907				4.2	15
$^2G_{9/2}$, $^2K_{13/2}$	19	055	109	172	216	257	298	77	14
	19	305	327	361	429			77	14
$^4G_{7/2}$, $^4G_{11/2}$, $^2K_{15/2}$	20	794	842	872	912	013*	101	77	14
	20	204	236	482	561			77	14
$^2D_{3/2}$	21	935						77	14
$^2P_{1/2}$	23	041						77	14
$^2D_{5/2}$	23	596	613	641				77	14
$^4D_{3/2}$	27	632	640					77	14
$^4D_{1/2}$	27	746						77	14

$Pm:YVO_4$

Term	Prefix	Energy (cm^{-1})			T	Ref.
$^5I_4$	-	0	147	298	?	17
$^5I_5$	1	707	929		?	17
$^5I_6$	3	340			?	17
$^5F_1$	12	346			?	17
$^5F_2$	12	850			?	17
$^5F_3$	14	136			?	17

$Eu:YVO_4$

Term	Prefix	Energy (cm^{-1})						T	Ref.
$^7F_0$	-	0						93	10
$^7F_1$	-	333.7	375.6					93	10
	-	360	404.5					100	18
$^7F_2$	-	936.4	975.4	038.7*	116.1			93	10
	-	970	995	018*	067			100	18
$^7F_3$	1	854.8	873.0	903.0	904.0	957.0		93	10
$^7F_4$	2	700.0	830.0	867.7	879.0	923.0	988.4	93	10
	2	063.0*						93	10
$^7F_5$	3	750	800	870	870	915	928	93	10
	3	949	065*					93	10
$^7F_6$	4	867	916	947	050*	053	071	93	10
$^5D_0$	17	183.2						93	10
	17	202.5						100	18
$^5D_1$	18	932	941					93	10
$^5D_2$	21	359	396	419	455			93	10

$Gd:YVO_4$

Term	Prefix	Energy (cm^{-1})				T	Ref.
$^8S_{7/2}$	-	0	0.0856	0.1759	0.2658	300	19

Ho:YVO_4

Term	Prefix	Energy (cm^{-1})						T	Ref.
$^5I_8$	-	0	12	21	40	48	105	77	20
	-	0	20.70	46.54	46.58	117.06	132.34	85	21
	-	124	226	264	288			77	20
$^5I_7$	5	117	127	130	137	203	213	77	20
	5	217	235	242				77	20
$^5I_5$	11	211.62	213.10	226.94	241.78	243.64	259.02	85	21
	11	271.05	290.54					85	21
$^5I_4$	13	229.0	316.52	337.03				85	21
$^5F_5$	15	401.06	410.86	414.67	437.99	485.97	519.40	85	21
	15	523.24	532.67					85	21
$^5S_2$	18	385	393	413				4.2	20
	18	394.67	394.13	413.11	428.46			85	21
$^5F_4$	18	487	537	572	624			4.2	20
	18	486.38	498.35	418.75	535.52	538.10	557.94	85	21
	18	571.39						85	21
$^5F_3$	20	519.92	526.11	537.87	563.33	600.57		85	21
$^5F_2$	21	030.46	059.00	082.27	095.04			85	21
$^3K_8$	21	294.05	301.41	314.52	322.09	1343.90	359.97	85	21
	21	361.51	383.53	401.51	406.67	410.32		85	21
$^5G_6$	21	924.14	927.51	939.00	970.28	012.02*	018.49	85	21
	21	091.76	154.10	165.36	166.14			85	21
$^5F_1$	22	209.07	264.68					85	21
$^5G_5$	23	828.20	833.09	848.94	889.33	896.02	974.06	85	21
$^5G_4$	25	712.54	719.80	746.03	751.45	767.88	811.22	85	21
	25	823.10						85	21

Er:YVO_4

Term	Prefix	Energy (cm^{-1})						T	Ref.
$^4I_{15/2}$	-	0	42.21	43.06	64.84	143.05	249.60	85	11
$^4F_{9/2}$	15	199.92	227.14	272.65	315.65	320.31		85	11
$^4S_{3/2}$	18	347.21	353.54					85	11
$^2H_{11/2}$	19	044.18	072.16	100.92	147.62	161.60	202.75	85	11
$^4F_{7/2}$	20	430.19	474.88	513.42	520.88			85	11
$^4F_{5/2}$	22	113.55	133.82	169.77				85	11
$^4F_{3/2}$	22	468.95	512.17					85	11
$^2H_{9/2}$	24	443.40	504.47	532.35	590.86	621.71		85	11
$^4G_{11/2}$	26	223.07	242.02	279.79	352.25	395.34	428.61	85	11

$Tm:YVO_4$

Term	Prefix	Energy (cm^{-1})						T	Ref.
$^3H_6$	-	0	53.80	119.13	137.62	158.42	192.27	4.2	13
	-	207.75	332.40					4.2	13
$^3H_4$	5	550.4	655.2	723.1	774.7	824.5	859.7	85	13
	5	878.6						85	13
$^3H_5$	8	204.0	231.9	268.1	295.9	338.3	440.1	85	13
	8	490.8						85	13
$^3F_4$	12	523.37	563.36	632.85	661.88	704.14	705.60	85	13
	12	774.06						85	13
$^3F_3$	14	411.18	452.90	453.39	458.78	475.43		85	13
$^3F_2$	15	007.21	017.61	068.55	146.71			85	13
$^1G_4$	20	937.63	102.19*	166.89	234.4	306.4	459.4	85	13
$^1D_2$	27	735.01	736.34	753.26	788.52			85	13

References for 5.15. YVO_4

1. Schwarz, H., 1963, Z. Anorg. Allgem. Chem. **323**, 44.
2. Lohmuller, G., G. Schmidt, B. Deppish, V. Gramlich and C. Scheringer, 1973, Acta Cryst. **B29**, 141.
3. Swanson, H.E., M.C. Morris and E.H. Evans, 1967, Standard X-ray Diffraction Patterns, Nat. Bur. Stand. (U.S.) Monogr. **25**, Sect. 5.
4. Baglio, J.A. and O.J. Sovers, 1971, J. Solid State Chem. **3**, 458.
5. McKnight, H.G. and L.R. Rothrock, 1973, U.S. Army ECOM Technical Report ECOM 0022F (NTIS #761 094).
6. Lomheim, T.S. and L.G. DeShazer, 1978, J. Appl. Phys. **49**, 5517.
7. Karayianis, N., C.A. Morrison and D.E. Wortman, 1975, J. Chem. Phys. **62**, 4125.
8. Karayianis, N., D.E. Wortman and C.A. Morrison, 1976, Harry Diamond Laboratories Report TR-1775 (NTIS #040 905).
9. Linares, C., A. Louat and M. Blanchard, 1977, Struct. Bonding **33**, 179.
10. Brecher, C., H. Samelson, A. Lempicki, R. Riley and T. Peters, 1967, Phys. Rev. **155**, 178.
11. Kuse, D., 1967, Z. Phys. **203**, 49.
12. Wortman, D.E., R.P. Leavitt and C.A. Morrison, 1974, J. Phys. Chem. Solids **35**, 591.
13. Knoll, K.D., 1971, Phys. Stat. Sol. (b) **45**, 553.
14. Kaminskii, A.A., 1981, Laser Crystals (Springer-Verlag, New York), p. 130.
15. Jenssen, H.P., 1974, private communication.
16. Yaney, P.P. and L.G. DeShazer, 1976, J. Opt. Soc. Am. **66**, 1405.
17. Loriers, J., P. Caro, P. Brun and A. Babusiaux, 1972, C.R. Acad. Sci. Paris **C275**, 977.
18. Koningstein, J.A. and O.S. Mortensen, 1967, Phys. Rev. Lett. **18**, 831.
19. Kahle, H.G., V. Koch, J. Plamper and W. Urban, 1968, J. Chem. Phys. **49**, 2702.
20. Wunderlich, J.A., 1977, Ph.D. Thesis, University of Southern California.
21. Schlaphof, W., 1970, Diplomarbeit, Universität Karlsruhe.

5.16. YPO_4

The host material YPO_4, xenotime, does not seem to have been used as a successful laser host material for any rare-earth ion. However, in view of resistance of this material to particle radiation (Ewing, 1975), this situation may change if radiation-hardened lasers become more fashionable. Many of the studies of rare earths in xenotime have been of pure RPO_4, where R is a rare earth heavier than Gd. Such compounds have interesting properties at low temperature; $DyPO_4$ is antiferromagnetic below 3.4 K (Wright et al., 1971; Schibuya et al., 1975), while $TbPO_4$ is antiferromagnetic below 2.28 K with a more complicated transition at 2.15 K (Nagele et al., 1980). Several studies of the Raman and infrared lattice vibrations have been done (Yurchenko et al., 1978; Lazarev et al., 1978; Richman, 1966; Mooney and Toma, 1967). Infrared reflection data have been analyzed (Armbruster, 1976) using a classical damped-oscillator model.

Studies of doping of Nd^{3+} in YPO_4 have shown that for a concentration of Nd^{3+} greater than 8.2 wt% the structure changes to the lower symmetry monazite form (Kireeva et al., 1973; Zverev et al., 1973). Concentration effects have been studied by electron spin resonance for a number of rare-earth ions in YPO_4 (Hillmer, 1973).

5.16.1 Crystallographic data for YPO_4

Tetragonal $I4_1/amd$, #141, Z = 4 (1st setting)

Ion	Pos.	Symm.	x	y	z
Y	4(a)	D_{2d}	0	0	0
P	4(b)	D_{2d}	0	0	1/2
O	16(h)	C_s	0	x	z

X-ray data

		O		
a	c	x	z	Ref.
6.885	5.982	0.178	0.312	1
6.878	6.036	0.064	0.234	2
6.875	6.031	-	-	3

5.16.2 Crystal-field parameters for R:YPO_4 (cm^{-1})

R	B_{20}	B_{40}	B_{44}	B_{60}	B_{64}	Ref.
Nd	475	-100	1088	-983	71	4
Eu	362	125	757	-785	-67	4
Eu	293	400	707	-525	559	5
Ho	341	-38	751	-713	50	4
Ho	344	-6	770	-718	58	4
Er	256	19	817	-699	55	4
Er	271	55	731	-698	76	4
Er	283	145	801	-646	126	6
Er	370	144	800	-646	88	7
Tm	275	6	692	-644	55	4

5.16.3 Energy levels for R:YPO_4

Ce:YPO_4

Term	Prefix	Energy (cm^{-1})			T	Ref.
$^2F_{5/2}$	-	0			300	8
	-	0	411		4.2	9
	-	0	403		7	10
$^2F_{7/2}$	2	157			300	8
	2	194	232	599	4.2	9
	2	200	236	598	7	10

Nd:YPO_4

Term	Prefix	Energy (cm^{-1})						T	Ref.
$^4I_{9/2}$	-	0	116	214	242	397		4.2	11
$^4I_{11/2}$	1	974	009*	036	044	125	161	4.2	11
$^4F_{3/2}$	11	413	466					4.2	11

Eu:YPO_4

Term	Prefix	Energy (cm^{-1})						T	Ref.
$^7F_0$	-	0						?	12
$^7F_1$	-	339	436					?	12
	-	339.4	435.6					300	5
$^7F_2$	-	910	020*	065	088			?	12
	-	909.6	020.4*	065.2	088.3			300	5
$^7F_3$	1	831.8	880.4	911.3	941.1	960.2		300	5
$^7F_4$	2	751.8	801.0	810.2	847.5	910.6	996.7	300	5
	2	126.7*						300	5
$^7F_5$	3	842	(865)	900	971	036*	063	300	5
$^7F_6$	4	856	875	(031)*	043	061	(077)	300	5
	4	126						300	5
$^5D_0$	17	211						?	12
	17	211.2						300	5
$^5D_1$	18	964.5	986.1					300	5
$^5D_2$	21	445	482	537	586			300	5

Tb:YPO_4

Term	Prefix	Energy (cm^{-1})				T	Ref.
$^7F_2$	5	062	083	147	259	?	12
$^7F_1$	5	506	593			?	12
$^7F_0$	5	801				?	12
$^5D_4$	20	496	516	561	581	?	12

Ho:YPO_4

Term	Prefix	Energy (cm^{-1})						T	Ref.
$^5I_8$	-	0	66.58	71.73	80.86	89.21	160.42	85	13
	-	188.09	250.21	279.26				85	13
$^5F_5$	15	432.11	452.27	463.68	532.79	536.26	539.05	85	13
	15	557.01	567.29					85	13
$^5S_2$	18	437.29	443.84	446.29	461.95			85	13
$^5F_4$	18	518.89	545.88	571.50	593.33	619.70	620.11	85	13
	18	625.01						85	13

Ho:YPO_4 (continued)

Term	Prefix	Energy (cm^{-1})						T	Ref.
$^5F_3$	20	584.04	601.85	644.30	668.71	675.57		85	13
$^5F_2$	21	049.43	077.99	083.44	139.71			85	13
$^3K_8$	21	331.45	332.69	347.65	355.93	355.93	358.67	85	13
	21	373.19	377.94	408.19	409.69	411.46	417.78	85	13
	21	445.31						85	13
$^3K_6$	22	043.76	043.85	075.18	121.47	148.33	157.96	85	13
	22	173.23	253.52	262.04	286.62			85	13
$^5F_1$	22	295.85	334.35					85	13
$^5G_5$	23	898.95	907.76	925.64	988.09	996.56	008.52*	85	13
	23	030.16	057.27					85	13
$^5G_4$	25	790.69	802.29	848.74	849.26	851.00	897.60	85	13
	25	907.83						85	13
$^3K_7$	26	143.35	146.94	152.17	161.93	176.02	181.47	85	13
$^3H_5$	27	566.23	566.48	580.87	618.23	620.88	626.09	85	13
	27	656.66	663.15					85	13
$^5G_6$	27	657.21	720.24	738.35	740.80	748.42	762.50	85	13
	27	836.88	843.73	860.47	872.41			85	13
$^5G_2$	28	219.31	254.90	254.99	344.11			85	13
$^5G_3$	28	783.76	784.35					85	13
$^3L_9$	28	792.34	825.50	860.54	913.35	920.81	968.30	85	13
	28	979.32	055.21*					85	13

Er:YPO_4

Term	Prefix	Energy (cm^{-1})						T	Ref.
$^4I_{15/2}$	-	0	32.01	52.50	107.94	143.34		85	6
$^4F_{9/2}$	15	241.51	270.88	279.37	324.98	367.78		85	6
$^4S_{3/2}$	18	367.14	416.34					85	6
$^2H_{11/2}$	19	087.12	119.67	145.84	183.42	201.78	235.27	85	6
$^4F_{7/2}$	20	484.73	496.28	557.61	573.54			85	6
$^4F_{5/2}$	22	162.08	191.58	195.49				85	6
$^4F_{3/2}$	22	517.03	550.67					85	6
$^2H_{9/2}$	24	502.72	538.98	541.38	623.33	656.15		85	6
$^4G_{11/2}$	26	310.34	332.48	353.29	405.43	466.59	485.49	85	6

$Tm:YPO_4$

Term	Prefix	Energy (cm^{-1})				T	Ref.
$^3H_6$	-	0	30.7	76.2	144.8	4.2	14
$^3F_4$	12	551.81	662.50	780.81		4.2	14
$^3F_3$	14	409.19	453.98	467.18		4.2	14
$^3F_2$	14	970.08	106.74*			4.2	14
$^1G_4$	21	260.15	291.88	404.52		4.2	14
$^1D_2$	27	799.31				4.2	14

References for 5.16. YPO_4

1. Schwarz, H., 1963, Z. Anorg. Allgem. Chem. **323**, 44.
2. Krstanovic, I., 1965, Z. Kristallogr. **121**, 315.
3. Tananaev, I.V., V.P. Repko, V.P. Orlovskii, G.M. Safronov, Kh.M. Kurbanov and A.G. Khaimova, 1971, Inorg. Mater. (USSR) **7**, 1579.
4. Karayianis, N., C.A. Morrison and D.E. Wortman, 1976, Harry Diamond Laboratories Report TR-1776 (NTIS #030 849).
5. Brecher, C., H. Samelson, R. Riley and A. Lempicki, 1968, J. Chem. Phys. **49**, 3303.
6. Kuse, D., 1967, Z. Phys. **203**, 49.
7. Vishwamittar and S.P. Puri, 1974, Phys. Rev. **B9**, 4673.
8. Briffaut, J.P. and J.P. Denis, 1970, Phys. Stat. Sol. **41**, 781.
9. Nakazawa, E. and S. Shianoya, 1974, J. Phys. Soc. Japan **36**, 504.
10. Hoshina, T. and S. Kuboniwa, 1971, J. Phys. Soc. Japan **31**, 828.
11. Zverev, G.M., A.M. Onishchenko, A.A. Semenov and A.I. Smirnov, 1972, Sov. Phys. Solid State **13**, 1817.
12. Ionkina, E.A., N.N. Morozov, E.N. Murav'ev, V.P. Orlovskii and V.P. Repko, 1973, Inorg. Mater. (USSR) **9**, 1130.
13. Becker, P.J., H.G. Kahle and D. Kuse, 1969, Phys. Stat. Sol. **36**, 695.
14. Knoll, K.D., 1971, Phys. Stat. Sol. (b) **45**, 553.

5.17. $CaWO_4$

Calcium tungstate diluted with a small amount of neodymium was the first continuous wave laser (Johnson et al., 1962). Since then a number of lasers have been built using the triply ionized rare earth ions Pr, Nd, Ho, Er, and Tm (Chesler and Geusic, 1972).

When rare earth ions are introduced into $CaWO_4$, the triply ionized rare earth ion replaces Ca^{2+}, leaving a charge imbalance. The most studied method of charge compensation in $CaWO_4$ has been by Nassau (1963) who carefully determined the correct amount of sodium to be added to the melt to minimize the number of "extra" lines appearing in the optical spectra.

Point-charge calculations of the crystal-field parameters for $R^{3+}:CaWO_4$ have been performed (Beiderbick et al., 1978; Brown et al., 1970); induced point dipole contributions to the crystal-field parameters have also been determined

(Eremin et al., 1970). A generalization of the point-charge model including shielding factors, radial wave function expansion, and effective charges on the covalent complexes (WO_4^{-2}) has been given for $CaWO_4$ by Leavitt et al. (1975). Although the theory was developed using data on R^{3+} in $CaWO_4$, the results are general enough to give crystal-field parameters for many different host materials that, when used in calculations of energy levels, agree well with the experimental data. Crystal-field parameters have also been derived using the angular overlap method (Urland, 1979). Some of the early work on the analysis of R^{3+} spectra by means of magnetic circular dichroism was done using Nd^{3+} in $CaWO_4$ (Boccara and Briat, 1969). Extensive electron spin-resonance studies of several scheelite crystals doped with Yb^{3+} were performed by Sattler and Nemarich (1970a). The infrared optical phonon spectrum of $CaWO_4$ has been analyzed by a number of workers (Barker, 1964; Porto and Scott, 1967; Russell and Loudon, 1965; Kanamori et al., 1974). These results are useful in detecting vibronic lines in rare-earth optical spectra and in determining the nonradiative decay rates of R^{3+} levels in $CaWO_4$ (Miyakawa and Dexter, 1970). Double resonance studies of Tm^{3+}:$CaWO_4$ have also been performed (Esterowitz and Chicklis, 1968).

5.17.1 Crystallographic data for $CaWO_4$

Tetragonal $I4_1/a$, #88, Z = 4 (1st setting)

Ion	Pos.	Symm.	x	y	z
Ca	4(b)	S_4	0	0	1/2
W	4(a)	S_4	0	0	0
O	16(f)	C_1	x	y	z

X-ray data

		O			
a	c	x	y	z	Ref.
5.243	11.376	0.2413	0.1511	0.0861	1,2
5.243	11.376	0.2415	0.1504	0.0861	3,4
5.24	11.381	0.25	0.15	0.075	5
5.2437	11.3754	-	-	-	6

5.17.2 Index of refraction for $CaWO_4$ (Ref. 7)

$\lambda(\mu m)$	n_o	n_e
0.4358	1.9543	1.9724
0.4861	1.9389	1.9560
0.5461	1.9267	1.9428
0.5876	1.9206	1.9362
0.5892	1.9203	1.9358
0.6563	1.9129	1.9280

5.17.3 Crystal-field parameters for R:$CaWO_4$ (cm^{-1})

R	B_{20}	B_{40}	B_{44}	B_{60}	RB_{64}	IB_{64}	Ref.
Pr	442	-951	1095	17.8	966	303	8
Pr	445	-943	1111	10.9	979	0	9
Nd	549	-942	1005	-17.1	947	1.34	10
Nd	509	-866	1042	-5.09	903	243	8
Nd	514.2	-1040.0	1071.6	24.0	980.0	13.1	11
Nd	448	-808	1568	275	714	0	12
Tb	478	-681	863	3.00	636	219	13
Dy	428	-825	972	-6.60	448	2.50	14
Ho	436	-664	779	-33.0	558	196	15
Er	433	-655	809	-2.56	546	156	8
Er	462	-720	815	-9.6	564	107	16
Tm	418	-688	754	17.1	504	359	17
Yb	431	-371	847	145	137	1003	18
Yb	446	-538	776	-11	452	518	19

5.17.4 Energy levels for R:$CaWO_4$

Pr:$CaWO_4$

Term	Prefix	Energy (cm^{-1})						T	Ref.
$^3H_4$	-	0	55					25	20,9
	-	0	42	59	81	93	293	77	21
$^3H_5$	2	235	241	282				25	20,9
	2	012	129	249	285	525	583	77	21
$^3H_6$	4	308	364	380	408	446	832	25	20,9
	4	350	387	409	448	593		77	21
$^3F_2$	5	080	093					25	20,9
	5	090	140	222	260			77	21
$^3F_3$	6	389	426	473	553	559		25	20,9
	6	333	428	488	507	579		77	21
$^3F_4$	6	835	843	871	999	026*	102	25	20,9
	6	887	916	999	068*			77	21
$^1G_4$	9	640	748	005*				25	20,9
$^1D_2$	16	578	841	111*				25	20,9
	16	598	649	873	083*			77	21
$^3P_0$	20	488						25	20,9
	20	528						77	21
$^3P_1$, $^1I_6$	20	945	945	039*	184	245	255	25	20,9
	20	983	136*	272	482	795		77	21
	20	455	801	815				25	20,9
$^3P_2$	22	150	267	282				25	20,9
	22	142	280					77	21

Nd:$CaWO_4$

Term	Prefix	Energy (cm^{-1})						T	Ref.
$^4I_{9/2}$	-	0	95	165	230	472		77	22
	-	0	121	159	229	473		4.2	23
	-	0	114	161	230	471		4.2	10
$^4I_{11/2}$	1	976	016*	056	189	226		77	22
	1	976	016*	019	055	191	226	4.2	23
	1	977	016*	(025)	057	189	227	4.2	10
$^4I_{13/2}$	3	929	953	979	008*	087	161	77	22
	3	928	954	971	004*	166	196	4.2	23,10
	3	205						77	22
	3	(207)						4.2	23,10
$^4I_{15/2}$	5	848	903	935	277*	305	377	77	22
	5	854	910	935	006*	277	301	4.2	23
	5	326	374					4.2	23

Nd:$CaWO_4$ (continued)

Term	Prefix	Energy (cm^{-1})						T	Ref.
$^4F_{3/2}$	11	406	469					77	22
	11	407	471					4.2	23,24
$^4F_{5/2}$, $^2H_{9/2}$	12	422	451	515	535	549	620	4.2	24,25
	12	689	726					4.2	24,25
$^4F_{7/2}$	13	375	400	503	525			4.2	24,25
$^4S_{3/2}$	13	530	538					4.2	25
$^4F_{9/2}$	14	633	663	756	761	827		4.2	25
$^2H_{11/2}$	15	829	871	892	948	017*	025	4.2	25
	15	033						4.2	25
$^4G_{5/2}$, $^2G_{7/2}$	16	981	055*	089	238	250	290	4.2	25
	16	420						4.2	25
$^4G_{7/2}$	18	887	900	989	020*			4.2	25
$^2G_{9/2}$	19	364	400	481	509	538		4.2	25

Gd:$CaWO_4$

Term	Prefix	Energy (cm^{-1})				T	Ref.
$^8S_{7/2}$	-	0				77	26
$^6P_{7/2}$	31	967.7	016.2*	042.4	(042.4)	77	26
$^6P_{5/2}$	32	569.3	621.7	639.7		77	26
$^6P_{3/2}$	33	170.3	205.3			77	26

Tb:$CaWO_4$

Term	Prefix	Energy (cm^{-1})						T	Ref.
$^7F_6$	-	0	0.27	135	152	180	202	77	27
	-	235	359	380	388			4.2	27
$^7F_5$	2	161	171	188	188	221	378	4.2	27
	2	404	414					4.2	27
$^7F_4$	3	382	417	443	529	541	607	4.2	27
	3	777						4.2	27
$^7F_3$	4	419	444	499	556	580		4.2	27
$^7F_2$	5	039	098	247	308			4.2	27
$^7F_1$	5	585	702					4.2	27
$^7F_0$	5	890						4.2	27

Dy:$CaWO_4$

Term	Prefix	Energy (cm^{-1})						T	Ref.
$^6H_{15/2}$	-	0	5	18	63	84	118	25	14
	-	381	388					25	14
$^6H_{13/2}$	3	476	476	512	564	619	697	25	14
	3	711						25	14
$^6H_{11/2}$	5	777	814	849	900	920	961	2	14
$^6F_{11/2}$, $^6H_{9/2}$	7	565	630	652	683	698	716	2	14
	7	733	774	827	905	970		2	14
$^6F_{9/2}$, $^6H_{7/2}$	8	930	995	013*	099	112	128	2	14
	8	152	176	340				2	14
$^6H_{5/2}$	10	105	267	329				2	14
$^4F_{9/2}$	20	907	922	972	060*	311		2	14

Ho:$CaWO_4$

Term	Prefix	Energy (cm^{-1})						T	Ref.
$^5I_8$	-	0	8	22	40	46	70	20	15
	-	200	248	254	262	284	300	20	15
	-	325						20	15
$^5I_7$	5	138	145	145	156	162	188	2	15
	5	209	218	271	275			2	15
$^5I_6$	8	653	661	661	662	674	677	2	15
	8	683	753	766	776			2	15
$^5I_5$	11	213	215	215	229	232	288	2	15
	11	310	313					2	15
$^5I_4$	13	180	253	308	388	499		2	15
$^5F_4$, $^5S_2$	18	415	442	452	514	524	552	2	15
	18	601	611	634	656			2	15

Er:$CaWO_4$

Term	Prefix	Energy (cm^{-1})						T	Ref.
$^4I_{15/2}$	-	0	20	26	53	233	269	4.2	28
	-	0	19.2	24.9	51.1	227.9	265.9	4.2	16
	-	278	318					4.2	28
	-	319.4						4.2	16
$^4I_{13/2}$	6	527	535	574	656	684	703	4.2	28
	6	375.8	383.9	424.3	505.4	534.4	551.8	4.2	16
	6	721						4.2	28
	6	569.2						4.2	16

Er:$CaWO_4$ (continued)

Term	Prefix	Energy (cm^{-1})						T	Ref.
$^4I_{11/2}$	10	191	218	256	276	295		4.2	28
	10	045.9	062.0	100.1	118.9	137.9	142.5	4.2	16
$^4I_{9/2}$	12	347	454	497	532	610		4.2	28
	12	190.5	323.4	355.3	374.1	451.5		4.2	16
$^4F_{9/2}$	15	237	276	287	353	386		4.2	8
	15	074.3	114.3	126.4	190.4	241.6		4.2	16
$^4S_{3/2}$	18	365	433					4.2	8
	18	206.6	272.2					4.2	16
$^2H_{11/2}$	18	933.1	948.4	979.5	032.7*	038.2	071.4	4.2	16
$^4F_{7/2}$	20	481	504	588	602			4.2	8
	20	316.5	327.4	420.1	432.4			4.2	16
$^4F_{5/2}$	22	180	195	225				4.2	8
	22	008.1	023.8	053.3				4.2	16
$^4F_{3/2}$	22	324.8	394.7					4.2	16
$^2H_{9/2}$	24	305.7	413.3	429.6	463.4	511.4		4.2	16
$^4G_{11/2}$	26	304.9						4.2	16
$^2K_{15/2}$	27	297.5						4.2	16
$^4G_{9/2}$	27	586.1						4.2	16
$^4G_{7/2}$	28	857.9						4.2	16

Tm:$CaWO_4$

Term	Prefix	Energy (cm^{-1})						T	Ref.
$^3H_6$	-	0	26	53	(245)	(328)	(338)	25	17
	-	(370)	(384)					25	17
$^3F_4$	5	594	733	745	811	926	927	25	17
	5	936						25	17
$^3H_5$	8	279	288	299	486	499	531	25	17
	8	535	550					25	17
$^3H_4$	12	583	600	628	759	832	835	25	17
$^3F_3$	14	481	509	563	572	575		25	17
$^3F_2$	15	039	(152)	156				25	17
$^1G_4$	20	986	180*	275	292	476	492	25	17
	20	520						25	17
$^1D_2$	27	808	(855)	929	(940)			25	17

Yb: $CaWO_4$

Term	Pre-fix	Energy (cm^{-1})				T	Ref.
$^2F_{7/2}$	-	0	(220)	366	492	4.2	18
$^2F_{5/2}$	10	278	366	665		4.2	18

References for 5.17. *$CaWO_4$*

1. Kay, M.I., B.C. Frazer and I. Almodovar, 1964, J. Chem. Phys. **40**, 504.
2. Swanson, H.E., H.F. McMurdie, M.C. Morris and E.H. Evans, 1962, Standard X-ray Diffraction Patterns, Nat. Bur. Std. (U.S.) Monogr. **25**, Sect. 1.
3. Zalkin, A. and D.H. Templeton, 1964, J. Chem. Phys. **40**, 501.
4. Gürmen, E., E. Daniels and J.S. King, 1971, J. Chem. Phys. **55**, 1093.
5. Sillen, L.G. and A. Nylander, 1943, Arkiv. Kemi, Mineral. Geol. **17A**, No 4.
6. Deshpande, V.T. and S.V. Suryanarayana, 1972, J. Mater. Sci. **7**, 255.
7. Bakhshieva, G.F. and A.M. Morozov, 1977, Sov. J. Opt. Tech. **44**, 542.
8. Wortman, D.E., C.A. Morrison and N. Karayianis, 1977, Harry Diamond Laboratories Report TR-1794 (NTIS #042 210).
9. Wortman, D.E., C.A. Morrison and R.P. Leavitt, 1975, Harry Diamond Laboratories Report TR-1726 (NTIS #020 721).
10. Karayianis, N. and R.T. Farrar, 1970, J. Chem. Phys. **53**, 3436.
11. Sengupta, D., 1971, Ph.D. Thesis, Carnegie-Mellon Univ. (Univ. Microfilms 71-24, 114).
12. Onopko, D.E., 1969, in: Spektroskopiya Tverdogo Tela, Vol. IV (Nauka, Moscow), p. 15.
13. Leavitt, R.P., C.A. Morrison and D.E. Wortman, 1974, J. Chem. Phys. **61**, 1250.
14. Wortman, D.E. and D. Sanders, 1971, J. Chem. Phys. **55**, 3212.
15. Wortman, D.E. and D. Sanders, 1970, J. Chem. Phys. **53**, 1247.
16. Bernal G., E., 1971, J. Chem. Phys. **55**, 2583.
17. Wortman, D.E., C.A. Morrison and R.P. Leavitt, 1975, Phys. Rev. **B12**, 4780. See also Wortman, D.E., C.A. Morrison and R.P. Leavitt, 1974, Harry Diamond Laboratories Report TR-1663 (NTIS #008 968).
18. Jones, G.R., 1967, J. Chem. Phys. **47**, 4347.
19. Brown, E.A., J. Nemarich, N. Karayianis and C.A. Morrison, 1970, Phys. Lett. **33A**, 375.
20. Low, W., 1964, US Air Force Contract Report 61(052)-549 (NTIS #610 504).
21. Aizenberg, I.B., F.Z. Gil'fanov and A.L. Stolov, 1966, Sov. Phys. J. **9**, 29.
22. Kariss, Ya.E., A.M. Morozov and P.P. Feofilov, 1964, Opt. Spectrosc. **17**, 481.
23. Farrar, R.T., W. Viehmann and C.A. Morrison, 1968 (unpublished results).
24. Morrison, C.A. and R.T. Farrar, 1964, Harry Diamond Laboratories Report TR-1265 (NTIS #457 608).
25. Farrar, R.T., 1965, Harry Diamond Laboratories Report TR-1309 (NTIS #625 923).
26. Gilfanov, F.Z., A.M. Levshin and A.L. Stolov, 1967, Opt. Spectrosc. **23**, 323.
27. Wortman, D.E., 1968, Phys. Rev. **175**, 488.
28. Wortman, D.E., 1971, J. Chem. Phys. **54**, 314.

5.18. *$PbMoO_4$*

Lead molybdate, $PbMoO_4$, has the scheelite structure typified by calcium tungstate. Discussions of the growth and physical properties of $PbMoO_4$ are included in papers on $CaWO_4$ (Ranon and Volterra, 1964). The R^{3+} ion in $PbMoO_4$ replaces the Pb^{2+} ion, and some method of charge compensation must

be used (Nassau and Broyer, 1962; Nassau and Loiacono, 1963). The optical spectra of rare earth ions in $PbMoO_4$ are similar to those of $CaWO_4$. A laser using Nd^{3+} operating under pulsed conditions has been reported by Johnson (1963). Much of the data on R^{3+}:$PbMoO_4$ has been reported by the Soviet workers (Morozov et al., 1966). Unfortunately, for some rare-earth ions reported lines have not been analyzed into a consistent energy-level diagram (Natadze et al., 1969). The magnetic and thermal properties of Nd^{3+} in $PbMoO_4$ have been investigated (Fakioglu and Erkoc, 1978). Crystal-field point-charge lattice sums have been reported (Biederbick et al., 1978; Karayianis and Morrison, 1973) for $PbMoO_4$ and a number of other scheelite structures. The infrared and Raman spectra of $PbMoO_4$, $CaWO_4$, $CaMoO_4$, and $PbWO_4$ have been reported by Khanna and Lippincott (1968). Electron paramagnetic resonance of Yb^{3+} in $PbMoO_4$ and in other scheelites has been reported (Sattler and Nemarich, 1970b).

5.18.1 Crystallographic data for $PbMoO_4$

Tetragonal $I4_1/a$, #88, Z = 4 (1st setting)

Ion	Pos.	Symm.	x	y	z
Pb	4(b)	S_4	0	0	1/2
Mo	4(a)	S_4	0	0	0
O	16(f)	C_1	x	y	z

X-ray data

		O			
a	c	x	y	z	Ref.
5.435	12.10	0.25	0.13	0.075	1
5.4312	12.0165	0.2352	0.1366	0.08110	2
5.47	12.18	0.247	0.092	0.085	3

5.18.2 Index of refraction for $PbMoO_4$

$\lambda(\mu m)$	n_o	n_e	Ref.
0.4358	2.6045	2.3854	4
0.4861	2.5043	2.3355	4
0.5461	2.4388	2.2960	4
0.5876	2.4095	2.2772	4
0.5892	2.4084	2.2764	4
0.6563	2.3758	2.2547	4
0.7	2.363	2.247	5
0.85	2.331	2.221	5
1.06	2.305	2.206	5
1.5	2.282	2.189	5
2	2.273	2.182	5
2.5	2.264	2.174	5
3.33	2.244	2.158	5
4	2.229	2.145	5
5	2.195	2.117	5

5.18.3 Crystal-field parameters for $R:PbMoO_4(cm^{-1})$

R	B_{20}	B_{40}	B_{44}	B_{60}	RB_{64}	IB_{64}	Ref.
Pr	370	-532	1061	149	871	0	6
Nd	352	-494	1329	137	469	0	7
Nd	600	-720	823	-112	684	0	8
Nd	428	-592	915	-104	692	0	9
Nd	663	-669	984	-84	600	14.6	10,11
Ho	470	720	736	0	-363	0	12

5.18.4 Energy levels for R:$PbMoO_4$

$Pr:PbMoO_4$

Term	Prefix	Energy (cm^{-1})				T	Ref.
$^3H_4$	-	0	62	131		4.2	13
$^3H_6$	4	320	367	410		4.2	13
$^3F_2$	5	038	049	062		4.2	13
$^3F_3$	6	388	418	511		4.2	13
$^3F_4$	6	815	840	986	041*	4.2	13
$^1G_4$	9	658	747	968		4.2	13
$^1D_2$	16	583	633	821	099*	4.2	13
$^3P_0$	20	500				4.2	13
$^3P_1$	21	054				4.2	13
$^3P_2$	22	174	258			4.2	13

$Nd:PbMoO_4$

Term	Prefix	Energy (cm^{-1})						T	Ref.
$^4I_{9/2}$	-	0	92	151	216	363		4.2	14
$^4I_{11/2}$	1	962	992	002*	035	134	161	4.2	14
$^4I_{13/2}$	3	918	945	960	993	032*	096	4.2	14
	3	920	947	962	993	032*	096	77	15
	3	918	945	960	993	063*	139	4.2	9
	3	139						4.2	14
	3	140						77	15
	3	139						4.2	9
$^4I_{15/2}$	5	865	910	946	010*	196	227	4.2	14
	5	860	910	946	010*	175	196	4.2	9
	5	273						4.2	14
	5	227	273					4.2	9
$^4F_{3/2}$	11	397	454					4.2	14
	11	374	450					4.2	9
	11	398	456					4.2	16
$^4F_{5/2}$	12	416.	447	496				4.2	9
	12	419	499	501				4.2	16
$^2H_{9/2}$	12	510	554	620	653	685		4.2	9
	12	513	557	623	660	694		4.2	16
$^4F_{7/2}$	13	369	393	466	492			4.2	9
	13	372	397	471	498			4.2	16
$^4S_{3/2}$	13	511	517					4.2	9
	13	515	519					4.2	16

Nd:$PbMoO_4$ (continued)

Term	Prefix	Energy (cm^{-1})						T	Ref.
$^4F_{9/2}$	14	624	646	735	745	789		4.2	9
	14	628	651	735	747	791		4.2	16
$^2H_{11/2}$	15	834	864	893	935	983	993	4.2	9
$^2G_{7/2}$	16	979	048*	067	107			4.2	9
$^4G_{5/2}$	17	222	286	383				4.2	9
$^4G_{7/2}$	18	904	909	980	030*			4.2	9
$^2G_{9/2}$	19	371	406	463	495	518		4.2	9
$^2P_{1/2}$	23	166						4.2	9
$^2D_{5/2}$	23	668	712	801				4.2	9

Ho:$PbMoO_4$

Term	Prefix	Energy (cm^{-1})						T	Ref.
$^5I_8$	-	0						4.2	12
$^5F_5$	15	407	434	477	511	526	542	4.2	12
$^5S_2$	18	408	411	429	439			4.2	12
$^5F_4$	18	519	573	582	590	605		4.2	12

References for 5.18. *$PbMoO_4$*

1. Sillen, L.G. and A.L. Nylander, 1943, Arkiv Kemi, Mineral. Geol. **17A**, No. 4.
2. Leciejewicz, J., 1965, Z. Krist. **121**, 158.
3. Araki, T., 1957, Mem. Coll. Sci. Univ. Kyoto, Ser. **B24**, 155.
4. Bakhshieva, G.F. and A.M. Morozov, 1977, Sov. J. Opt. Tech. **44**, 542.
5. Berny, J.G., J.P. Bourgoin and B. Ayrault, 1972, Opt. Comm. **6**, 383.
6. Onopko, D.E., 1970, in: Spektroskopiya Kristallov (Nauka, Moscow), p. 181.
7. Onopko, D.E., 1969, in: Spektroskopiya Tverdoga Tela, Vol. IV (Nauka, Moscow), p. 15.
8. Eremin, M.V., I.N. Kurkin, O.I. Mar'yakhina and L.Ya. Shekun, 1970, Sov. Phys. Solid State **11**, 1697.
9. Minhas, I.S., K.K. Sharma and J.B. Gruber, 1973, Phys. Rev. **B8**, 385.
10. Sengupta, D., 1971, Ph.D. Thesis, Carnegie-Mellon Univ. (Univ. Microfilms 71-24 114).
11. Sengupta, D., K.K. Sharma and J.O. Artman, 1969, J. Chem. Phys. **51**, 1652.
12. Kanskaya, L.M., A.I. Ryskin and A.M. Tkachuk, 1967, Opt. Spectrosc. **22**, 177.
13. Morozov, A.M., E.G. Reut and A.I. Ryskin, 1966, Opt. Spectrosc. **21**, 314.
14. Kariss, Ya.E. and P.P. Feofilov, 1964, Opt. Spectrosc. **17**, 387.
15. Kaminskii, A.A. and S.E. Sarkisov, 1973, Sov. J. Quantum. Electron. **3**, 248.
16. Farrar, R.T., W. Viehmann and C.A. Morrison, 1968 (unpublished results).

5.19. $LiYF_4$

Lithium yttrium fluoride, $LiYF_4$ (YLF), is one of the most versatile laser host materials thus far investigated. In his recent book Kaminskii (1981) lists 36 different wavelength lasers for R:$LiYF_4$; the shortest and longest wavelength lasers listed by Kaminskii are in R:$LiYF_4$, with R = Ce^{3+} and Ho^{3+}, respectively. The high efficiency of Nd:$LiYF_4$ lasers is emphasized by Sharp et al. (1973) and by Chicklis et al. (1971). The shortest wavelength (325 nm) optically pumped solid state laser listed by Kaminskii, Ce^{3+}:$LiYF_4$, has been reported by Ehrlich et al. (1979). The longest wavelength lasers, using holmium doping in $LiYF_4$, have been reported by Remski et al. (1969) and by Chicklis et al. (1972). The properties of $LiYF_4$ for high-power lasers are reported by Fricke (1973), who used discs of $LiYF_4$ separated so that coolant could be circulated through the laser structure. The analysis of a possible laser using Pm^{3+} in $LiYF_4$ has been given by Wortman and Morrison (1973). The early growth of experimental-size crystals and the investigation of the phase diagrams was carried out by Thoma et al. (1961, 1970). Larger crystals for optical experiments and better optical quality have been developed by Shand (1969) and Gabbe and Harmer (1968).

As early as 1971, long-wavelength solid-state lasers were being built using holmium-doped $LiYF_4$ (Chicklis et al., 1971) and multiple rare-earth doping (Chicklis et al., 1972). Efficient neodymium lasers have been made using $LiYF_4$ (Sharp et al., 1973). The crystal growth of $LiYF_4$ for lasers in the 2 μm region has been investigated by Devor et al. (1974), with Ho^{3+} as the particular dopant. They also report many of the physical properties and the thermal conductivity. A thorough investigation of practically all the aspects of R:$LiYF_4$ affecting the laser features of this host has been presented by Chicklis et al. (1973a). The ultraviolet absorption, linear, and nonlinear optical properties of $LiYF_4$ have been reported by Pollak et al. (1980); the optical properties in the ultraviolet have also been reported by Rehn et al. (1977).

The elastic properties and acoustic symmetry of $LiYF_4$ have recently been investigated (Blanchfield and Saunders, 1979). The use of R:$LiYF_4$ as quantum counters has been investigated by Brown et al. (1969) and Brown and Shand (1969). The general properties of quantum counters have been presented by Esterowitz and Chicklis (1968), and a discussion of related energy transfer of rare-earth ions in $LiYF_4$ with an application to Ho doping (Chicklis et al., 1973b) has been given. An investigation (both experimental and theoretical) of the optical spectrum and line-to-line intensities of Pr:$LiYF_4$ has been reported by Esterowitz et al. (1979b).

Electron spin resonance of the ground state of R:$LiYF_4$ for R = Nd, Dy, Er and Yb has been reported by Sattler and Nemarich (1971), and the first reported optically detected excited-state electron paramagnetic resonance of Er:$LiYF_4$ has been given by Kulpa and Nemarich (1975). A study of the second and third order Zeeman effect of Er^{3+} in $LiYF_4$ has been reported by Korableva (1978).

5.19.1 Crystallographic data for $LiYF_4$

Tetragonal $I4_1/a$, #88, Z = 4 (1st setting)

Ion	Pos.	Symm.	x	y	z
Y	4(b)	S_4	0	0	1/2
Li	4(a)	S_4	0	0	0
F	16(f)	C_1	x	y	z

X-ray data

		F			
a	c	x	y	z	Ref.
5.1668	10.7330	0.2820	0.1642	0.0815	1
5.175	10.74	-	-	-	2

5.19.2 Index of refraction for $LiYF_4$ (Ref. 3)

λ(μm)	n_e	n_o	λ(μm)	n_e	n_o
2.600	1.4602	1.4381	0.800	1.4726	1.4502
2.400	1.4617	1.4397	0.700	1.4741	1.4516
2.200	1.4632	1.4411	0.600	1.4762	1.4535
2.000	1.4645	1.4424	0.500	1.4796	1.4567
1.800	1.4658	1.4437	0.450	1.4822	1.4590
1.600	1.4670	1.4449	0.400	1.4858	1.4624
1.400	1.4681	1.4460	0.350	1.4913	1.4674
1.200	1.4693	1.4471	0.300	1.5001	1.4754
1.000	1.4708	1.4485	0.250	1.5156	1.4895
0.900	1.4716	1.4492	0.225	1.5287	1.5014

5.19.3 Crystal-field parameters for R:$LiYF_4$ (cm^{-1})

R	B_{20}	B_{40}	B_{44}	B_{60}	RB_{64}	IB_{64}	Ref.
Pr	489	-1043	1242	-42	1213	22.5	4
Pr	485	-1061	1296	-57.5	1186	0	5
Nd	441	-906	1115	-26.3	1073	20.6	6
Nd	480	-973	1119	-60.6	1051	49.0	7
Nd	502	-964	1105	-27.4	1019	35	8
Nd	401	-1008	1230	30	1074	0	9
Dy	330	-704	937	-70.4	609	92.7	10
Ho	410	-615	819	-27.9	677	32.8	11
Er	400	-692	925	-21.3	610	149	6
Er	314	-625	982	-32.4	584	171	12
Er	190	-1184	858	-44.8	295	0	13
Er	380	-640	975	-36.8	599	99.8	10
Tm	359	-608	844	-173	629	0	14
Tm	333	-648	876	-141	623	3	4
Yb	281	-556	569	-106	840	953	15

5.19.4 Energy levels for R:$LiYF_4$

Pr:$LiYF_4$

Term	Prefix	Energy (cm^{-1})						T	Ref.
$^3H_4$	-	0	79	220	496			10	4
	-	0	78					4.2	16
$^3H_5$	2	253	272	280	297	341	549	10	4
	2	255	274	279	299	(306)	341	4.2	16
$^3H_6$	4	314	394	454	486	557	907	10	4
	4	316	393	455	767	903	907	4.2	16
	4	945						10	4
	4	947						4.2	16
$^3F_2$	5	201	221	342				10	4
	5	202	219	(223)	345			4.2	16
$^3F_3$	6	481	521	586	671	686		10	4
	6	264	449	484	515	613	676	4.2	16
$^3F_4$	6	920	942	983	105*	116	142	10	4
	6	926	947	155*	226	481		4.2	16
	6	220						10	4

Pr:$LiYF_4$(continued)

Term	Prefix	Energy (cm^{-1})						T	Ref.
$^1G_4$	9	699	832	930	011*	112	217	10	4
	9	313						10	4
$^1D_2$	16	740	810	083*	406	860		10	4
	16	742	809	907	085*			4.2	16
$^3P_0$	20	860						10	4
	20	861						4.2	16
$^3P_1$	21	409	470					4.2	16
$^3P_2$	22	498	645					10	4
	22	498	(509)	637	645			4.2	16

Nd:$LiYF_4$

Term	Prefix	Energy (cm^{-1})						T	Ref.
$^4I_{9/2}$	-	0	132	182	249	528		77	17,7
	-	0	132	182	249	523		10	9
$^4I_{11/2}$	1	998	042*	079	220	264		77	17
	1	998	042*	042	079	228	264	77	7
$^4I_{13/2}$	3	948	976	995	026*	205	228	77	7
	3	948	976	995	026*	202	238	10	9
	3	238						77	7
$^4I_{15/2}$	5	851	912	947	026*	315	347	77	7
	5	851	911	947	026*	315	348	10	9
	5	388	432					77	7
	5	432						10	9
$^4F_{3/2}$	11	538	597					77	17
	11	541	598					10	9
$^4F_{5/2}$	12	528	558	635				10	9
$^2H_{9/2}$	12	677	742	817	857	933		10	9
$^4F_{7/2}$, $^4S_{3/2}$	13	504	532	642	652	659	675	10	9
$^4F_{9/2}$	14	769	795	814	894	966		10	9
$^2H_{11/2}$	15	941	987	013*	077	158		10	9
$^4G_{5/2}$	17	182	292	322				10	9
$^2G_{7/2}$	17	431	443	498	674			10	9
$^4G_{7/2}$	19	055	102	172	201			10	9
$^4G_{9/2}$, $^2K_{13/2}$	19	569	627	685	732	771	833	10	9
	19	990	040*					10	9

Nd:$LiYF_4$ (continued)

Term	Prefix	Energy (cm^{-1})						T	Ref.
$^2G_{9/2}$	21	066	079	084	119			10	9
$^2D_{3/2}$	21	295	358					10	9
$^4G_{11/2}$, $^2K_{15/2}$	21	459	565	729	768	834	858	10	9
	21	920	968	012*				10	9
$^2P_{1/2}$	23	420						10	9
$^2D_{5/2}$	23	923	952	056*				10	9
$^2P_{3/2}$	26	295	385					10	9
$^4D_{3/2}$	28	137	249					10	9
$^4D_{5/2}$	28	409	563	612				10	9
$^4D_{1/2}$	28	835						10	9
$^2I_{11/2}$	29	240	326	412	771			10	9
$^2L_{15/2}$, $^4D_{7/2}$	30	248	395	590	684			10	9
$^2I_{13/2}$, $^2L_{17/2}$	30	769	921	807*	827	878	959	10	9
	30	066*	113					10	9
$^2H_{9/2}$	33	014	124					10	9
$^2D_{3/2}$	33	456	546					10	9
$^2H_{11/2}$, $^2D_{5/2}$	34	258	317	376	447	554		10	9
$^2F_{5/2}$	38	491	700	789				10	9
$^2F_{7/2}$	39	936	096*	193				10	9

Tb:$LiYF_4$

Term	Prefix	Energy (cm^{-1})						T	Ref.
$^7F_6$	-	0	90.9	97.1	115.8	152.3	158.1	4.2	18
	-	207	353.1	354.3				4.2	18
$^7F_5$	2	108.5	124.3	124.3	169.3	169.6	179.4	4.2	18
	2	196.7	197.0					4.2	18
$^5D_4$	20	554.7	560.4	568.7	628.1	645.6		4.2	18
$^5D_3$	26	338.1	440.5	454.5				4.2	18

$Dy:LiYF_4$

Term	Prefix	Energy (cm^{-1})						T	Ref.
$^6H_{15/2}$	-	0	14.2	41.1	61.9	70.2	110.4	77	10
	-	344	375					77	10
$^6H_{13/2}$	3	507.1	(516.5)	534.2	579.1	632.9	717.7	77	10
	3	726.1						77	10
$^6H_{11/2}$	5	819.5	875.8	925.0	935.5	977.2	987.3	77	10
$^4F_{9/2}$	20	938.6	014.5*	115.3	414.7			77	10

$Ho:LiYF_4$

Term	Prefix	Energy (cm^{-1})						T	Ref.
$^5I_8$	-	0	7	23	48	56	72	4	11
	-	0	6.8	23.8				4.2	19
	-	217	(270)	(276)	(283)	(290)	303	4	11
	-	315						4	11
$^5I_7$	5	153	157	164	185	207	229	4	11
	5	233	291	293	293			4	11
$^5I_6$	8	670	(670)	680	686	687	696	4	11
	8	701	768	783	796			4	11
$^5I_5$	11	240	(240)	248	245	252	298	4	11
	11	327	333					4	11
$^5I_4$	13	184	266	337	405	532		4	11
$^5F_5$	15	485	491	508	555	620	627	4	11
	15	632	654					4	11
$^5S_2$	18	(478)	481	513	524			4	11
$^5F_4$	18	599	605	609	679	681	695	4	11
	18	707						4	11
$^5F_3$	20	629	648	700	743	755		4	11
$^5F_2$	21	(118)	122	162	213			4	11

$Er:LiYF_4$

Term	Prefix	Energy (cm^{-1})						T	Ref.
$^4I_{15/2}$	-	0	16	26	55	250	289	4.2	20
	-	0	17.25	28.97	55.70	252	291	2	21
	-	326	354					4.2	20
	-	320	347					2	21
$^4I_{13/2}$	6	536	540	580	672	696	724	4.2	20
	6	534.65	538.58	578.98	673.93	697.24	723.60	2	21
	6	738						4.2	20
	6	737.55						2	21

Er:$LiYF_4$ (continued)

Term	Prefix	Energy (cm^{-1})						T*	Ref.
$^4I_{11/2}$	10	222	239	285	303	320	355	4.2	20
	10	217.85	235	283	289	315		2	21
$^4I_{9/2}$	12	369	546	572	667			4.2	20
	12	360	534	565	660			2	21
$^4F_{9/2}$	15	314	333	349	425	477		4.2	20
	15	302.08						2	21
$^4S_{3/2}$	18	438	497					4.2	20
	18	432.44						2	21
$^2H_{11/2}$	19	157	176	228	313	330	346	4.2	20
	19	154	177	224	307	322	338	77	13
$^4F_{7/2}$	20	576	666	674				4.2	20
	20	565	657	665				77	13

Tm:$LiYF_4$

Term	Prefix	Energy (cm^{-1})						T	Ref.
$^3H_6$	-	0	31	56	282	310		5	14
$^3F_4$	5	605	760	757	827	944	967	5	14
	5	977						5	14
$^3H_5$	8	285	285	295	(500)	497	(500)	5	14
	8	508	532					5	14
$^3H_4$	12	621	644	741	825	831		5	14
$^3F_3$	14	531	561	605	605	616		5	14
$^3F_2$	15	104	218					5	14
$^1G_4$	20	981	195*	279	322	561	561	5	14
$^1D_2$	27	932	963	019*				5	14
$^1I_6$	34	728	928	(063)*				5	14
$^3P_1$	36	443	530					5	14
$^3P_2$	38	219						5	14

Yb:$LiYF_4$

Term	Prefix	Energy (cm^{-1})				T	Ref.
$^2F_{7/2}$	-	0	216	371	479	77	15
$^2F_{5/2}$	10	288	409	547		77	15

References for 5.19. $LiYF_4$

1. Teng, W.H. and J.S. King, 1973, private communication.
2. Keller, C. and H. Schmutz, 1965, J. Inorg. Nucl. Chem. **27**, 900.
3. Castleberry, D.E. and A. Linz, 1975, Appl. Opt. **14**, 2056.
4. Esterowitz, L., F.J. Bartoli, R.E. Allen, D.E. Wortman, C.A. Morrison and R.P. Leavitt, 1979, Phys. Rev. **B19**, 6442.
5. Esterowitz, L., F.J. Bartoli, R.E. Allen, D.E. Wortman, C.A. Morrison and R.P. Leavitt, 1979, Harry Diamond Laboratories Report TR-1875 (NTIS #067 845).
6. Wortman, D.E., N. Karayianis and C.A. Morrison, 1976, Harry Diamond Laboratories Report TR-1770 (NTIS #033 902).
7. Wortman, D.E., 1972, J. Phys. Chem. Solids **33**, 311.
8. Karayianis, N., 1971, J. Phys. Chem. Solids **32**, 2385.
9. deGama, A.A.S., G.F. de Sa, P. Porcher and P. Caro, 1981, J. Chem. Phys. **75**, 2583.
10. Davydova, M.P., S.B. Zdanovich, B.N. Kazakov, S.L. Korableva and A.L. Stolov, 1977, Opt. Spectrosc. **42**, 327.
11. Karayianis, N., D.E. Wortman and H.P. Jenssen, 1976, J. Phys. Chem. Solids **37**, 675.
12. Leavitt, R.P. and N. Karayianis (unpublished results).
13. Brown, M.R., K.G. Roots and W.A. Shand, 1969, J. Phys. **C2**, 593.
14. Jenssen, H.P., A. Linz, R.P. Leavitt, C.A. Morrison and D.E. Wortman, 1975, Phys. Rev. **B11**, 92.
15. Brown, E.A., 1980, Harry Diamond Laboratories Reports TR-1932 and TR-1934 (NTIS #091 252 and 090 976).
16. Caspers, H.H. and H.E. Rast, 1975, J. Lumin. **10**, 347.
17. Harmer, A.L., A. Linz and D.R. Gabbe, 1969, J. Phys. Chem. Solids **30**, 1483.
18. Castleberry, D.E., 1972, private communication.
19. Magarino, J., J. Tuchendler, J.P. D'Haenens and A. Linz, 1976, Phys. Rev. **B13**, 2805.
20. Petrov, M.V. and A.M. Tkachuk, 1978, Opt. Spectrosc. **45**, 81.
21. Kulpa, S.M., 1975, J. Phys. Chem. Solids **36**, 1317.

5.20. $Y_3Al_5O_{12}$

Most of the interest in $Y_3Al_5O_{12}$ (YAG) has been in its application as a host material for rare-earth ion lasers. As of 1981, Kaminskii, in his book *Laser Crystals*, lists 45 rare-earth ion lasers with YAG as the host material. The neodymium YAG laser is, beyond a doubt, the most popular solid-state laser in existence today (of the 45 lasers listed by Kaminskii, 23 are with neodymium).

Despite all the technological applications and investigations of rare-earth YAG lasers, the optical spectra of some of the rare-earth ions in this host are of questionable quality and in some cases nonexistent. Only two rare-earth ions in YAG, neodymium and erbium, have been thoroughly investigated and reported. This is rather surprising when compared to lanthanum trifluoride (LaF_3), for which Kaminskii reports only 16 lasers, although abundant excellent data exist (Carnall et al., 1977) for all of the rare-earth ions in LaF_3 except terbium.

It has long been recognized that the crystal-field parameters, B_{km}, can all be chosen real for D_2 symmetry, which is the symmetry of the Y site in $Y_3Al_5O_{12}$. The fact that the B_{km} are real does not in itself uniquely specify the situation, since there are six ways of choosing B_{km} real. Thus, the reported crystal-field parameters can appear to be completely different yet give identical crystalline Stark splittings. An example of this is the six sets of crystal-field parameters for Nd:$Y_3Al_5O_{12}$ given by Morrison et al. (1976), which are given in table 6. The

various sets in table 6 are related by simple rotations. To obtain the set of B'_{km} in the second row from the B_{km} of row 1, we use

$$B'_{20} = -\tfrac{1}{2}B_{20} + \tfrac{1}{2}\sqrt{6}B_{22},$$

$$B'_{22} = -\tfrac{1}{4}\sqrt{6}B_{20} + \tfrac{1}{2}B_{22}$$

for the twofold fields,

$$B'_{40} = \tfrac{3}{8}B_{40} - \frac{\sqrt{10}}{4}B_{42} + \frac{\sqrt{70}}{8}B_{44},$$

$$B'_{42} = -\frac{\sqrt{10}}{8}B_{40} + \tfrac{1}{2}B_{42} + \frac{\sqrt{7}}{4}B_{44},$$

$$B'_{44} = \frac{\sqrt{70}}{16}B_{40} + \frac{\sqrt{7}}{4}B_{42} + \tfrac{1}{8}B_{44}$$

for the fourfold fields, and

$$B'_{60} = -\tfrac{5}{16}B_{60} + \frac{\sqrt{105}}{16}B_{62} - \frac{3\sqrt{14}}{16}B_{64} + \frac{\sqrt{231}}{16}B_{66},$$

$$B'_{62} = \frac{\sqrt{105}}{32}B_{60} - \tfrac{17}{32}B_{62} + \frac{\sqrt{30}}{32}B_{64} + \frac{3\sqrt{55}}{32}B_{66},$$

$$B'_{64} = -\frac{3\sqrt{14}}{32}B_{60} + \frac{\sqrt{30}}{32}B_{62} + \tfrac{26}{32}B_{64} + \frac{\sqrt{66}}{32}B_{66},$$

$$B'_{66} = \frac{\sqrt{231}}{32}B_{60} + \frac{3\sqrt{55}}{32}B_{62} + \frac{\sqrt{66}}{32}B_{64} + \tfrac{1}{32}B_{66}$$

TABLE 6
Equivalent sets of B_{km} for Nd:$Y_3Al_5O_{12}$.

Set	B_{20}	B_{22}	B_{40}	B_{42}	B_{44}	B_{60}	B_{62}	B_{64}	B_{66}
1	514	±129	−363	∓2005	−950	−1702	∓763	837	∓718
2	−99	±379	455	∓1487	−1635	−1226	∓496	964	∓1149
3	−415	±250	−2715	±518	1018	1115	∓308	1590	∓43

for the sixfold fields. To obtain the third row of table 6 we change the sign of B'_{k2} and B'_{k6} (second row) and use these in the right side of the above equations. This procedure gives three sets of crystal-field parameters and, to obtain three more sets, we multiply the B_{k2} and B_{k6} of each set by -1. This latter procedure is compactly represented in table 6 by the presence of (±) or (∓). These equations can be used to relate any given set of B_{km} to other reported values of crystal-field parameters for comparison. It should be emphasized that the above equations only hold for crystal-field parameters B_{km} and $\bar{B}_{km}$ (the $A_{km}\langle r^k\rangle$ do not transform as spherical tensors). The reported crystal-field parameters have arbitrarily been converted to set 1 in our tables for this section and the next three sections on garnets.

The index of refraction of $Y_3Al_5O_{12}$ has been reported by Lomheim and De Shazer (1979) as

$$n^2(\lambda) = 1 + 2.2779\lambda^2/(\lambda^2 - 0.01142)$$

with λ measured in μm. A number of physical and thermal properties of $Y_3Al_5O_{12}$ have been given by Weber (1979b) and some thermo-optic properties are reported by Wilson and DeShazer (1980). The thermal expansion properties of several garnets have been given by Geller et al. (1969).

5.20.1 Crystallographic data for $Y_3Al_5O_{12}$

Cubic Ia3d, #230, Z = 8

Ion	Pos.	Symm.	x	y	z
Y	24(c)	D_2	0	1/4	1/8
Al_1	16(a)	C_{3i}	0	0	0
Al_2	24(d)	S_4	3/8	0	1/4
O	96(h)	C_1	x	y	z

X-ray data

	O			
a	x	y	z	Ref.
12.000	-0.0306	0.0512	0.1500	1
-	-0.0290	0.0530	0.1510	2

5.20.2 Crystal-field parameters for R:$Y_3Al_5O_{12}$ (cm^{-1})

R	B_{20}	B_{22}	B_{40}	B_{42}	B_{44}	B_{60}	B_{62}	B_{64}	B_{66}	Ref.
Nd	514	129	-363	-2005	-950	-1702	-763	837	-718	3
Nd	424	101	-191	-2108	-1082	-1784	-681	868	-641	4
Sm	502	95	800	-1542	-1003	-1386	-650	917	-541	5
Sm	599	-356	394	-1464	-212	-315	-481	684	-633	5
Eu	627	56	-344	-1611	-817	-1437	-608	600	-632	3
Tb	461	165	-169	-1720	-900	-1324	-621	599	-561	3
Dy	492	89	-60	-1743	-852	-1140	-434	557	-462	3
Dy	504	72	-71	-1737	-895	-1171	-454	576	-425	6
Dy	502	73	-77	-1771	-906	-1164	-446	552	-432	7
Er	424	82	-288	-1522	-899	-1122	-303	492	-322	3
Er	401	53	-107	-1591	-717	-1021	-349	538	-404	8

5.20.3 Intensity parameters for R:$Y_3Al_5O_{12}$(10^{-20} cm^2)

R	Ω_2	Ω_4	Ω_6	Ref.
Nd	0.2	2.7	5.0	9
Nd	0.37	2.29	5.97	10
Ho	1.2	5.29	1.48	11
Er	0.66	0.81	0.71	11
Tm	0.90	0.70	0.85	11
Tm	0.89	1.08	0.68	11
Tm	0.7	1.2	0.5	12

5.20.4 Energy levels for R:$Y_3Al_5O_{12}$

$Pr:Y_3Al_5O_{12}$

Term	Prefix	Energy (cm^{-1})						T	Ref.
$^3H_4$	-	0	19	50	573			77	13
	-	0	19.1	50.4				90	14
$^3H_5$	2	(250)	(560)	(910)				77	13
$^3H_6$	4	304	318	341	358	393	408	77	13
	4	567	046*	143	(366)	434	536	77	13
$^1G_4$	9	718	781	829	121*	275		77	13
$^1D_2$	16	418	889	042*	221			77	13
$^3P_0$	20	533						77	13
	20	533.2						90	14

$Nd:Y_3Al_5O_{12}$

Term	Prefix	Energy (cm^{-1})						T	Ref.
$^4I_{9/2}$	-	0	130	199	308	857		77	15
	-	0	134	197	311	848		4.2	16,17
	-	0	131	195	317	857		77	18
$^4I_{11/2}$	2	002	029	110	147	468	521	77	15
	2	(001)	(029)	111	146	473	526	4.2	16,17
	2	002	026	114	152	461	519	77	18

Nd:$Y_3Al_5O_{12}$ (continued)

Term	Prefix	Energy (cm^{-1})						T	Ref.
$^4I_{13/2}$	3	922	930	038*	052	442	507	77	15
	3	875	985	010*	032	490	560	4.2	16,17
	3	922	932	037*	052	434	447	77	18
	3	497						77	18
$^4I_{15/2}$	5	757	812	933	963	570*	585	77	15
	5	770	824	948	978	585*	645	4.2	16,17
	5	764	780	942	579*	638	728	77	18
	5	640	732					77	15
	5	645	755					4.2	16,17
$^4F_{3/2}$	11	427	512					77	15
	11	419	511					4.2	16,17
	11	425	509					77	18
$^4F_{5/2}$, $^2H_{9/2}$	12	370	432	519	575	607	623	77	15
	12	369	427	517	572	605	621	4.2	16,17
	12	369	873					77	18
	12	819	840					77	15
	12	820	873					4.2	16,17
$^4F_{7/2}$, $^4S_{3/2}$	13	363	433	563	572	596	633	77	15
	13	371	435	563	570	594	633	4.2	16,17
	13	371	432	563	570	594	633	77	18
$^4F_{9/2}$	14	626	678	793	819	916		77	15
	14	638	689	797	826	919		4.2	16,17
	14	638	689	797	826	919		77	18
$^2H_{11/2}$	15	743	838	870	957	103*	119	77	15
	15	745	833	867	952	091*	105	4.2	16,17
$^2G_{7/2}$, $^4G_{5/2}$	16	849	992	047*	241	268	322	77	15
	16	852	989	044*	241	263	322	4.2	16,17
	16	575						77	15
	16	570						4.2	16,17
$^4G_{7/2}$	18	723	822	843	986			77	15
	18	784	823	839	985			4.2	16,17
$^2K_{13/2}$, $^2G_{9/2}$	19	154	194	294	470	543	596	77	15
	19	139	271	305	470	526	549	4.2	16
	19	620	651	814	048*			77	15
	19	597	637	800	029*			4.2	16
$^4G_{9/2}$, $^4G_{11/2}$	20	730	773	790	803	962	029*	77	15
	20	705	748	768	780	952	019*	4.2	16
	20	718	761	783				4.2	17
	20	080	110	159	162			77	15
	20	067	098	142	149			4.2	16
$^2K_{15/2}$	21	522	593	661	697	767	791	77	15
	21	537	590	657	683	754	779	4.2	16
	21	872	906					77	15
	21	852	892					4.2	16

Nd:$Y_3Al_5O_{12}$ (continued)

Term	Prefix	Energy (cm^{-1})			T	Ref.
$^2D_{3/2}$, $^2P_{1/2}$	22 036	155*			77	15
	22 019	139*			4.2	16
$^2D_{5/2}$	23 874	764	849		77	15
	23 860	764	(791)		4.2	16
$^2P_{3/2}$	25 994				77	15
	25 957	970			4.2	16
$^4D_{3/2}$	27 571	670			77	15
$^4D_{1/2}$	27 809				77	15

Sm:$Y_3Al_5O_{12}$

Term	Prefix	Energy (cm^{-1})						T	Ref.
$^6H_{5/2}$	-	0	141.9	251.1				77	5
$^6H_{7/2}$	1	017.3	238.2	368.5	412.1			77	5
$^6H_{9/2}$	2	251.0	396.6	460.6	564.2	610.2		77	5
$^6H_{11/2}$	3	554.2	639.5	754.3	822.4	870.7	944.7	77	5
$^6H_{13/2}$	4	862.8	979.7	059.4*	173.9	222.7	227	77	5
	4	364.6						77	5
$^6H_{15/2}$, $^6F_{1/2}$,	6	142	297	346	(363)	565	695	77	5
$^6F_{3/2}$	6	754	840	907	940	988		77	5
$^6F_{5/2}$	7	271	375					77	5
$^6F_{7/2}$	8	115	151	164	254			77	5
$^6F_{9/2}$	9	257	287	308	349	369		77	5
$^6F_{11/2}$	10	547	559	582	643	680	(718)	77	5
	10	750						77	5

$Eu:Y_3Al_5O_{12}$

Term	Prefix	Energy (cm^{-1})						T	Ref.
$^7F_0$	-	0						77	19
	-	0						4.2	20
$^7F_1$	-	286	307	455				77	19
	-	281	305	455				4.2	20
$^7F_2$	-	819	902	010*	022	358		77	19
	-	(709)	820	(167)*	(186)	(241)	361	4.2	20
$^7F_3$	1	832	842	915	959	000*	008	77	19
	1	825	831	914	964	999	(051)*	4.2	20
	1	221						77	19
	1	(103)	(139)	210				4.2	20
$^7F_4$	2	856	865	957	137*	147	248	77	19
	2	847	854	947	130*	139	199	4.2	20
	2	242						4.2	20
$^7F_5$	3	787	791	946	097*	226		77	19
	3	775	829	842	982	037*	(191)	4.2	20
	3	205	256					4.2	20
$^7F_6$	4	976	983	028*	062	151	319	77	19
	4	977	024*	058	164	334		4.2	20
	4	358	445					77	19
$^5D_0$	17	220						77	19
$^5D_1$	18	952	991					77	19
$^5D_2$	21	356	448	473				77	19
$^5D_3$	24	639	678	683	697			77	19

$Gd:Y_3Al_5O_{12}$

Term	Prefix	Energy (cm^{-1})					T	Ref.
$^8S_{7/2}$	-	0					300	21
$^6P_{7/2}$	31	785	832	872	909		300	21
$^6P_{5/2}$	32	404	441	464			300	21
$^6P_{3/2}$	32	995	028*				300	21
$^6I_{7/2}$	35	521	568	586	683		300	21
$^6I_{9/2}$	35	866	891	914	953	969	300	21

$Tb:Y_3Al_5O_{12}$

Term	Prefix	Energy (cm^{-1})						T	Ref.
$^7F_6$	-	0	5	61	70	116	207	77	19
	-	270	432	443				77	19
$^7F_5$	2	128	138	161	189	335	350	77	19
	2	387	601	612				77	19
$^7F_4$	3	364	383	417	489	603	697	77	19
	3	721						77	19
$^7F_3$	4	394	535	577	590	682	707	77	19
$^7F_2$	5	010	446					77	19
$^7F_1$	5	612	632					77	19
$^7F_0$	5	882						77	19
$^5D_4$	20	513	548	588	601	646	659	77	19

$Dy:Y_3Al_5O_{12}$

Term	Prefix	Energy (cm^{-1})						T	Ref.
$^6H_{15/2}$	-	0	60.8	101.3	175.2	234.0	741.0	4.2	22
	-	0	59.4	101.3	174.7	233.0	741.0	77	23
$^6H_{13/2}$	3	564.3	590.6	698.0	720.1	778.2	821.3	4.2	22
	3	564.4	590.4	697.7	720.2	777.1	821.3	77	23
	3	948.3						4.2	22
	3	950.6						77	23
$^6H_{11/2}$	5	926.1	953.4	043.6*	088.3	102.3	315.0	4.2	22
	5	926.2	953.8	042.8*	087.0	101.7	105.8	77	23
$^6F_{11/2}$, $^6H_{9/2}$	7	640.8	672.8	742.2	760.2	802.1	909.3	77	23
	7	941.8	963.8	994	218*	285		77	23
$^6F_{9/2}$, $^6H_{7/2}$	9	007	040	074	308	315	334	77	23
	9	367	380	656				77	23
$^6H_{5/2}$	10	252	354	503				77	23
$^6F_{7/2}$	11	050.2	239.1	269.4	312.7			4.2	22
	11	053	235	265	310			77	23
$^6F_{5/2}$	12	495.1	523.8	674.2				4.2	22
	12	493.9	523.0	673.7				77	23
$^6F_{3/2}$	13	359.6	366.6					4.2	22
	13	358.6	366.0					77	23
?	20	859.5	896.9	060.8*	126.3			4.2	22
?	21	901.3	962.4					4.2	22
?	22	346.6	374.2					4.2	22

$Dy:Y_3Al_5O_{12}$ (continued)

Term	Prefix	Energy (cm^{-1})						T	Ref.
?	23	348.8	394.8					4.2	22
?	24	768.3	779.2	833.1	854.3			4.2	22
?	25	329.8	403.2	447.5	486.5			4.2	22
	25	930.8	956.1	070.8*				4.2	22
?	27	295.9	333.5	378.2	415.0	463.4	848.7	4.2	22
	27	927.7	940.7					4.2	22
?	28	349.8	401.8	410.0	418.3	436.2	483.8	4.2	22
	28	509.3	834.4	889.5				4.2	22
?	29	378.7	428.2	517.3	543.7	666.2	724.6	4.2	22
?	30	667.8	734.5	918.0	972.7	009.7*	045.2	4.2	22
	30	089.8						4.2	22
?	33	039.3	069.7	082.6	102.3	127.4	155.5	4.2	22
	33	353.7	388.8	412.5	460.4	467.3	536.8	4.2	22
	33	547.5	570.1	859.8	888.3	919.7	003.0*	4.2	22

$Ho:Y_3Al_5O_{12}$

Term	Prefix	Energy (cm^{-1})						T	Ref.
$^5I_8$	-	0	36	50	137	158	414	77	24
	-	0	38.5	50	138	156	415.5	4.2	25
	-	0	42	54	141	161	418	4.2	26
	-	448	465	495	523	594		77	24
	-	437	444	462	494	518	532	4.2	25
	-	448	464	494	519			4.2	26
$^5I_7$	5	229	231	244	269	302	318	77	24
	5	229	231					4.2	25
	5	228	230	244	251	304	312	4.2	26
	5	376	404	450				77	24
	5	318	338	350	371	377	406	4.2	26
	5	416	455					4.2	26
$^5I_6$	8	733	737	742	763	768	771	4.2	26
	8	817	839	851	869	936	940	4.2	26
	8	951						4.2	26
$^5I_5$	11	320	352	358	387	391	424	4.2	26
	11	428	472	476				4.2	26
$^5I_4$	13	281	339	343	362	366	380	4.2	26
	13	385	405	563				4.2	26
$^5F_5$	15	457	474	491	513	655	665	4.2	26
	15	670	697	739	744			4.2	26
$^5F_4$, $^5S_2$	18	451	462	530	539	542	547	4.2	26
	18	582	592	728	743			4.2	26

$Er:Y_3Al_5O_{12}$

Term	Prefix	Energy (cm^{-1})						T	Ref.
$^4I_{15/2}$	-	0	24	72	116	412	426	4.2	27
	-	0	23	60	78	426	433	77	24
	-	0	22	61	79	417	430	77	28
	-	468	564					4.2	27
	-	527	572					77	24
	-	526	573					77	28
$^4I_{13/2}$	6	549	598	603	788	807	887	77	24
	6	549	599	606	786	805	885	77	28
	6	766	858	949				4.2	27
$^4I_{11/2}$	10	252	281	360	370	411		4.2	27
	10	256	287	362	373	414	419	77	28
$^4I_{9/2}$	12	298	524	573	719	765		4.2	27
	12	303	527	577	719	765		77	28
$^4F_{9/2}$	15	290	319	364	485	530		4.2	27
	15	290	315	359	475	520		77	28
$^4S_{3/2}$	18	406	470					4.2	27
	18	397	461					77	28
$^2H_{11/2}$	19	100	124	161	328	350	367	4.2	27
	19	093	114	151	(310)	347	365	77	28
$^4F_{7/2}$	20	520	574	659	709			4.2	27
	20	513	569	648	700			77	28
$^4F_{5/2}$	22	230	250	299				4.2	27
	22	219	238	285				77	28
$^4F_{3/2}$	22	601	672					4.2	27
	22	585	659					77	28
$^2H_{9/2}$	24	422	576	591	765	784		77	27
$^4G_{11/2}$	26	218	280	327	569	577	607	77	27

$Tm:Y_3Al_5O_{12}$

Term	Prefix	Energy (cm^{-1})						T	Ref.
$^3H_6$	-	0	27	215	241	245	448	77	24
	-	547	588	610				77	24
$^3F_4$	5	557	737	809	875	907	046*	77	24
	5	148	177					77	24

$Yb:Y_3Al_5O_{12}$

Term	Prefix	Energy (cm^{-1})				T	Ref.
$^2F_{7/2}$	-	0	565	612	785	77	30
	-	0	140	490	620	77	31
$^2F_{5/2}$	10	140	490	620		77	29
	10	327	624	679		77	30

References for 5.20. $Y_3Al_5O_{12}$

1. Euler, F. and J.A. Bruce, 1965, Acta Cryst. **19**, 971.
2. Prince, E., 1957, Acta Cryst. **10**, 787.
3. Morrison, C.A., D.E. Wortman and N. Karayianis, 1976, J. Phys. **C9**, L191; Wortman, D.E., C.A. Morrison and N. Karayianis, Harry Diamond Laboratories Report TR-1773 (NTIS #033 884).
4. Nekvasil, V., 1978, Phys. Stat. Sol. (b) **87**, 317.
5. Grünberg, P., 1969, Z. Phys. **225**, 376.
6. Grünberg, P., S. Hüfner, E. Orlich and J. Schmitt, 1969, J. Appl. Phys. **40**, 1501.
7. Wadsack, R.L., J.L. Lewis, B.E. Argyle and R.K. Chang, 1971, Phys. Rev. **B3**, 4342.
8. Newman, D.J. and A. Edgar, 1976, J. Phys. **C9**, 103.
9. Krupke, W.F., 1971, IEEE J. Quantum Electron. **QE-7**, 153.
10. Kaminskii, A.A. and L. Li, 1974, Phys. Stat. Sol. (a) **26**, K21.
11. Antipenko, B.M. and Yu.V. Tomashevich, 1978, Opt. Spectrosc. **44**, 157.
12. Caird, J.A., 1973, Hughes Aircraft Tech. Report AFAL-TR-73-323 (NTIS #914 193).
13. Hooge, F.N., 1966, J. Chem. Phys. **45**, 4504.
14. Gourley, J.T., 1972, Phys. Rev. **B5**, 22.
15. Kaminskii, A.A., 1981, Laser Crystals (Springer-Verlag, New York), p. 129.
16. Koningstein, J.A., 1966, J. Chem. Phys. **44**, 3957.
17. Koningstein, J.A. and J.E. Geusic, 1964, Phys. Rev. **136**, A711.
18. Tofield, B.C., H.P. Weber, T.C. Damen and P.F. Liao, 1975, J. Solid State Chem. **12**, 207.
19. Koningstein, J.A., 1964, Phys. Rev. **136**, A717.
20. Asano, M. and J.A. Koningstein, 1979, Chem. Phys. **42**, 369.
21. Kaminskii, A.A., 1975, Lazernye Kristalli (Nauka, Moscow), p. 104.
22. Gehring, K.A., M.J.M. Leask and J.H.M. Thornley, 1969, J. Phys. **C2**, 484.
23. Grünberg, P., S. Hüfner, E. Orlich and J. Schmitt, 1969, Phys. Rev. **184**, 285.
24. Zverev, G.M., G.Ya. Kolodnyi and A.M. Onischenko, 1970, Sov. Phys. JETP **30**, 435.
25. Johnson, L.F., J.E. Geusic and L.G. Van Uitert, 1966, Appl. Phys. Lett. **8**, 200.
26. Ashurov, M.Kh., Yu.K. Voron'ko, E.V. Zharikov, A.A. Kaminskii, V.V. Osiko, A.A. Sobol', M.I. Timoshechkin, V.A. Federov and A.A. Shabaltal, 1979, Inorg. Mater. (USSR) **15**, 979.
27. Koningstein, J.A. and G.E. Geusic, 1964, Phys. Rev. **136**, A726.
28. Kaminskii, A.A., T.I. Butaeva, V.A. Fedorov, Kh.S. Bagdasarov and A.G. Petrosyan, 1977, Phys. Stat. Sol. (a) **39**, 541.
29. Koningstein, J.A., 1965, Theo. Chim. Acta (Berlin) **3**, 271.
30. Bogomolova, G.A., D.N. Vylegzhanin and A.A. Kaminskii, 1976, Sov. Phys. JETP **42**, 440.
31. Wood, D.L., 1963, J. Chem. Phys. **39**, 1671.

5.21. $Y_3Ga_5O_{12}$

Yttrium gallium garnet, YGaG, has been used as a host material for a number of rare earth ions for optical (Kaminskii, 1981), electron spin-resonance (Wolf et al., 1962), and electronic Raman spectroscopic studies (Koningstein, 1967). The Raman spectrum of YGaG has been reported by Song et al. (1973), and the elastic constants and Debye temperature have been measured (Nagaiah et al., 1979). The excitation of the 4f to 5d transitions of Tb^{3+} in YGaG and a number of other compounds has been investigated (Hoshina, 1969). Faraday rotation as a function of applied magnetic field and frequency has been studied for Nd^{3+} and Er^{3+} in YGaG by Lung (1971).

The superposition model of crystal fields has been used by Nekvasil et al. (1978) to calculate the crystal-field parameters except for B_{20} and B_{22} for Nd^{3+}, Sm^{3+}, and Er^{3+} in YGaG. A general derivation of the crystal-field parameters for Nd^{3+} in YGaG has been given by Bogomolova et al. (1977). In their calculation, these authors included contributions from point charges, induced point dipoles, and exchange interactions. They show that the polarizability of the oxygen ion is considerably reduced in the solid from the free-ion value. A theoretical analysis of the crystal field using a molecular orbital method with ligand overlap has been applied to Dy^{3+} in YGaG (Korolkov and Makhanek, 1977) with considerable success. The material $Y_3(Al_{1-x}Ga_x)_5O_{12}$ doped with Nd^{3+} has been investigated as a possible laser host (Watts and Holton, 1974), and the refined X-ray data for this material have been reported (Marezio et al., 1968). Nonradiative losses of Er^{3+} in YGaG have been studied (Ashurov et al., 1978) for the $^4I_{11/2} \rightarrow {}^4I_{13/2}$ transitions.

5.21.1 Crystallographic data for $Y_3Ga_5O_{12}$

Cubic Ia3d, #230, Z = 8

Ion	Pos.	Symm.	x	y	z
Y	24(c)	D_2	0	1/4	1/8
Ga_1	16(a)	C_{3i}	0	0	0
Ga_2	24(d)	S_4	3/8	0	1/4
O	96(h)	C_1	x	y	z

X-ray data

	O			
a	x	y	z	Ref.
12.280	-0.0272	0.0558	0.1501	1

5.21.2 Index of refraction for $Y_3Ga_5O_{12}$

λ(μm)	n	Ref.
0.3962	1.987	3
0.4970	1.955	3
0.546	1.925	2
0.5954	1.940	3
0.6961	1.931	3
0.7980	1.924	3
0.8952	1.921	3
0.9876	1.918	3
1.0867	1.916	3

5.21.3 Crystal-field parameters for $R:Y_3Ga_5O_{12}$ (cm^{-1})

R	B_{20}	B_{22}	B_{40}	B_{42}	B_{44}	B_{60}	B_{62}	B_{64}	B_{66}	Ref.
Ce	205	1	-364	-1887	-1097	-2992	-994	1391	-1074	4
Nd	131	-108	-202	-1757	-1149	-1539	-489	929	-845	5
Nd	115	-81	-26	-1839	-1115	-1632	-595	913	-660	6
Nd	52	-412	521	-1553	-1331	-1789	-677	704	-1277	7
Nd	424	101	-192	-2109	-1083	-1530	-866	936	-648	8
Sm	178	12	544	-1571	-775	-1161	-601	802	-749	9
Sm	-61	-60	-54	-1109	-588	-974	-82	581	-424	9
Eu	210	78	-1360	-127	-813	800	234	-1347	-	10
Dy	-157	-24	76	-1737	-847	-1031	-374	570	-407	5
Dy	163	-31	13	-1664	-904	-1019	-447	607	-418	11
Dy	226	-37	-32	-1613	-865	-1062	-373	528	-412	12
Ho	41	-211	84	-940	-651	-227	-104	19	-172	13
Er	46	-70	-110	-1518	-761	-959	-279	503	-390	5
Er	103	-19	-45	-1499	-671	-822	-227	558	-545	14
Yb	358	-32	-131	-1093	-481	-1761	-664	491	-160	15

5.21.4 Energy levels for R:$Y_3Ga_5O_{12}$

Ce:$Y_3Ga_5O_{12}$

Term	Prefix	Energy (cm^{-1})				T	Ref.
$^2F_{5/2}$	-	0	139	402		?	4
$^2F_{7/2}$	2	161	176	373	670	?	4

Pr:$Y_3Ga_5O_{12}$

Term	Prefix	Energy (cm^{-1})						T	Ref.
$^3H_4$	-	0	23	39	538			77	16
$^3H_5$	2	(180)	285	316	356	(540)	576	77	16
	2	(610)	647	727	800	(870)		77	16
$^3H_6$	4	285	346	381	448	530	534	77	16
	4	945	078*	106				77	16
$^3F_2$	5	353	404	425	459			77	16
$^3F_3$, $^3F_4$	6	492	507	538	(768)	805	993	77	16
	6	082*	104	232	289	389	(440)	77	16
	6	(645)						77	16
$^1G_4$	9	741	806	884	134*	240		77	16
$^1D_2$	16	405	533	995	078*	209		77	16
$^3P_0$	20	594						77	16
$^1I_6$, $^3P_1$	20	925	986	992	025*	048	139	77	16
	20	173	200	825	881	935	988	77	16
	20	114*	262	507				77	16

Nd:$Y_3Ga_5O_{12}$

Term	Prefix	Energy (cm^{-1})						T	Ref.
$^4I_{9/2}$	-	0	80	174	240			4.2	17
	-	0	79	179	246	784		77	18
	-	0	80	173	242	775		300	19
$^4I_{11/2}$	2	011	024	070	107	438	453	4.2	17
	1	994	077*	056	086	420	435	77	18
	1	995	006*	058	092	417	432	300	19
$^4I_{13/2}$	3	768	888	940	439*	437		4.2	17
	3	921	985	996	(030)*	381	414	77	18
$^4I_{15/2}$	5	826	877	961	564*	621	741	4.2	17
	5	765	810	900	920	520*	565	77	18
	5	675						77	18

$Nd:Y_3Ga_5O_{12}$ (continued)

Term	Prefix	Energy (cm^{-1})						T	Ref.
$^4F_{3/2}$	11	459	496					4.2	17
	11	443	478					77	18
	11	435	471					300	19
$^4F_{5/2}$	12	386	422	516				4.2	17
	12	283	384	418				77	18
$^2H_{9/2}$	12	568	594	607	810	828		4.2	17
	12	514	563	587	811	830		77	18
$^4F_{7/2}$, $^4S_{3/2}$	13	370	407	(566)	599	613		4.2	17
	13	373	412	556	603			77	18
$^4F_{9/2}$	14	643	763	815	868			4.2	17
	14	643	650	773	795	877		77	18
$^2H_{11/2}$	15	744	828	858	942	073*	083	4.2	17
	15	751	833	873	952	082*	093	77	18
$^4G_{5/2}$	16	859	985	042*				4.2	17
	16	866	988	047*				77	18
$^2G_{7/2}$	17	256	308	382	551			4.2	17
	17	250	313	553				77	18
$^4G_{7/2}$	18	753	816	852	984			4.2	17
	18	755	822	854	975			77	18
$^2G_{9/2}$, $^2K_{13/2}$	19	170	303	(318)	438	522	549	4.2	17
	19	246	309	327	436	516	558	77	18
	19	591	637	855	970			4.2	17
	19	577	635	980	000*			77	18
$^4G_{9/2}$	20	741	780	797				4.2	17
	20	713	760	786	867			77	18
$^4G_{11/2}$	20	985	029*	104	158	167		4.2	17
	20	929	004*	044	106	177	182	77	18
$^2K_{15/2}$	21	611	690	738	766	871	943	4.2	17
	21	612	697	(737)	763	877	949	77	18
$^2P_{1/2}$	23	150						4.2	17
	23	166						77	18
$^2D_{5/2}$	23	707	740	753				4.2	17
$^2P_{3/2}$	26	(019)	049					4.2	17

$Sm:Y_3Ga_5O_{12}$

Term	Prefix	Energy (cm^{-1})						T	Ref.
$^6H_{5/2}$	-	0	46.6	135.5				77	9
$^6H_{7/2}$	-	975.1	140.4*	287.3	316.9			77	9
$^6H_{9/2}$	2	198.2	328	359	455	509		77	9
$^6H_{11/2}$	3	530.5	542.0	701.2	740.9	748.6	852.8	77	9
$^6H_{13/2}$	4	869.1	881.2	971.5	135.0*	154.1	(173.0)	77	9
	4	237.1						77	9
$^6F_{7/2}$	7	956	972	983	079*			77	9
$^6F_{9/2}$	9	211	237	258	297	305		77	9
$^6F_{11/2}$	10	558	566	577	646	655	668	77	9

$Eu:Y_3Ga_5O_{12}$

Term	Prefix	Energy (cm^{-1})						T	Ref.
$^7F_0$	-	0						4.2	10,20
$^7F_1$	-	309	345	390				77	20
$^7F_2$	-	829	868	083*	113			77	20
$^7F_3$	1	882	896	950	982	004*		4.2	10,20
$^7F_4$	2	846	855	935	083*	108	202	4.2	10,20
	2	833	846	855	935	073*	083	77	20
	2	108	202					77	20
$^7F_5$	3	758	788	984	026*	042	150	77	20
	3	170						77	20
$^7F_6$	5	000	019	053	097	199	236	77	20
$^5D_0$	17	233						77	20
$^5D_1$	18	948	968					77	20

$Tb:Y_3Ga_5O_{12}$

Term	Prefix	Energy (cm^{-1})						T	Ref.
$^7F_6$	-	0	4	15	42	76	98	77	21
	-	273						77	21
$^7F_5$	2	045	055	066	091	099	112	4.2	21
	2	120	139	186	255	279		4.2	21
$^7F_4$	3	295	315	238	362	373	399	4.2	21
	3	511	609					4.2	21
$^7F_3$	4	349	468	492	520	551	600	4.2	21
$^7F_1$	5	338	437	497				4.2	21
$^7F_0$	5	781						4.2	21
$^5D_4$	20	450	473	512	519	526	574	4.2	21
$^5D_3$	26	109	117	121	146	167	177	4.2	21

$Dy:Y_3Ga_5O_{12}$

Term	Prefix	Energy (cm^{-1})						T	Ref.
$^6H_{15/2}$	-	0	20.4	71.1	117.6	149	(515)	4.2	11
	-	579.3						4.2	11
$^6H_{13/2}$	3	566.7	582.8	632.2	644.7	751.8	793.5	4.2	11
	3	823.4						4.2	11
$^6H_{11/2}$	5	944.6	954.6	984.8	014.1*	023.1	034.3	4.2	11
$^6F_{11/2}$, $^6H_{9/2}$	7	629.9	648.4	700.0	723.8	747.9	868.1	4.2	11
	7	888.6	911.6	927.0	134.0*	161.0		4.2	11
$^6F_{9/2}$, $^6H_{7/2}$	8	983	021*	023	254	262	287	4.2	11
	8	310	333	563				4.2	11
$^6H_{5/2}$	10	225	343	391				4.2	11
$^6F_{7/2}$	11	006	194	211	242			4.2	11
$^6F_{5/2}$	12	451.4	474.5	622.0				4.2	11
$^6F_{3/2}$	13	310	319					4.2	11

$Ho:Y_3Ga_5O_{12}$

Term	Prefix	Energy (cm^{-1})						T	Ref.
$^5I_8$	-	0	5.1	8.2	30	42.6	93.6	2	22,23
	-	110.6	113	380	418	427.5	432	2	22,23
	-	447	481					2	22,23
$^5I_7$	5	211	215	218	231	237	269	2	22,23
	5	282	289	324	345	348	365	2	22,23
	5	381	386	391				2	22,23

$Er:Y_3Ga_5O_{12}$

Term	Prefix	Energy (cm^{-1})						T	Ref.
$^4I_{15/2}$	-	0	44	49	76	423	433	4.2	24
	-	0	44	49	76	422	431	?	25
	-	488	526					4.2	24
	-	490	527					?	25
$^4I_{13/2}$	6	570	578	596	785	802	850	4.2	24
	6	572	579	597	788	805	853	?	25
	6	857						?	25
$^4I_{11/2}$	10	272	279	367	378	396	402	4.2	24
	10	267	274	363	374	392	397	?	25
$^4I_{9/2}$	12	323	544	575	726	755		4.2	24
	12	311	535	566	716	746		?	25
$^4F_{9/2}$	15	303	330	342	474	477		?	25
	15	314	408					4.2	26
$^4S_{3/2}$	18	427	455					4.2	24
	18	400	433					4.2	26
$^2H_{11/2}$	19	099	120	157	347	359	364	?	25
	19	113	164	267	368	500	700	4.2	26
$^4F_{7/2}$	20	542	589	665	898			4.2	26
$^4F_{5/2}$	22	237	291					4.2	26
$^4F_{3/2}$	22	634						4.2	26
$^2H_{9/2}$	24	461	618	818				4.2	26
$^4G_{11/2}$	26	267	652	940				4.2	26
$^2G_{9/2}$	27	359	548	917	145*			4.2	26

$Tm:Y_3Ga_5O_{12}$

Term	Prefix	Energy (cm^{-1})						T	Ref.
$^3H_6$	-	0	68	87	100	188		77	27
	-	0	64	82	95	145	377	77	28
	-	0	64	87	99			77	29
	-	425	435	447	482	495	515	77	28
	-	538						77	28
$^3F_4$	5	465	718	790	827	966	043*	77	28
	5	465	719	790	827	968	043*	4.2	29
	5	078	091	099				77	28
	5	079	089	097				4.2	29

$Yb:Y_3Ga_5O_{12}$

Term	Prefix	Energy (cm^{-1})				T	Ref.
$^2F_{7/2}$	-	0	544.2			4.2	30
	-	0	546	610	624	80	31
	-	0	550	900		?	4
$^2F_{5/2}$	10	312.76	586.7	739.3		4.2	30
	10	312	592	743		?	4

References for 5.21. $Y_3Ga_5O_{12}$

1. Euler, F. and J.A. Bruce, 1965, Acta Cryst. **19**, 971.
2. Scott, G.B., D.E. Lacklison and J.L. Page, 1974, Phys. Rev. **B10**, 971.
3. Holton, W.C., D.W. Bellavance, F.J. Bruni, M. de Wit and R.K. Watts, 1974, Texas Instruments Technical Report AFML-TR-74-126 (NTIS #783 842).
4. Herrmann, G.F., J.J. Pearson, K.A. Wickersheim and R.A. Buchanan, 1966, J. Appl. Phys. **37**, 1312.
5. Karayianis, N., D.E. Wortman and C.A. Morrison, 1977, Harry Diamond Laboratories Report TR-1793 (NTIS #042 205).
6. Nekvasil, V., 1978, Phys. Stat. Sol. (b) **87**, 317.
7. Stedman, G.E. and N.A. Cade, 1973, J. Phys. **C6**, 474.
8. Nekvasil, V., 1974, J. Phys. **C7**, L246.
9. Grünberg, P., 1969, Z. Phys. **225**, 376.
10. Koningstein, J.A., 1967, in: Crosswhite, H.M. and H.W. Moos, Eds., Optical Properties of Ions in Crystals (Interscience, New York), p. 105.
11. Grünberg, P., S. Hüfner, E. Orlich and J. Schmitt, 1969, Phys. Rev. **184**, 285.
12. Wadsack, R.L., J.L. Lewis, B.E. Argyle and R.K. Chang, 1971, Phys. Rev. **B3**, 4342.
13. Kamimura, H. and T. Yamaguchi, 1970, Phys. Rev. **B1**, 2902.
14. Dieke, G.H., 1968, Spectra and Energy Levels of Rare Earth Ions in Crystals (Interscience, New York), p. 162.
15. Buchanan, R.A., K.A. Wickerscheim, J.J. Pearson and G.F. Herrmann, 1967, Phys. Rev. **159**, 245 (two consecutive papers).
16. Hooge, F.N., 1966, J. Chem. Phys. **45**, 4504.
17. Koningstein, J.A. and J.E. Geusic, 1964, Phys. Rev. **136**, A711.
18. Kaminskii, A.A., G.A. Bogomolova, D.N. Vylegzhanin, Kh.S. Bagdasarov, A.M. Kevorkov and M.M. Gritsenko, 1976, Phys. Stat. Sol. (a) **38**, 409.
19. Watts, R.K. and W.C. Holton, 1974, J. Appl. Phys. **45**, 873.
20. Koningstein, J.A., 1965, J. Chem. Phys. **42**, 3195.
21. Joshi, B.D. and A.G. Page, 1977, J. Lumin. **15**, 29.
22. Johnson, L.F., J.F. Dillon and J.P. Remeika, 1969, J. Appl. Phys. **40**, 1499.
23. Johnson, L.F., J.F. Dillon and J.P. Remeika, 1970, Phys. Rev. **B1**, 1935.
24. Ashurov, M.Kh., Yu.K. Voronko, V.V. Osiko, A.A. Sobol, B.P. Starikov, M.I. Timoshechkin and A.Ya. Yablonskii, 1976, Phys. Stat. Sol. (a) **35**, 645.
25. Ref. 14, p. 298.
26. Pappalardo, R., 1963, Z. Phys. **173**, 374.
27. Pearson, J.J., G.F. Herrmann and R.A. Buchanan, 1968, J. Appl. Phys. **39**, 980.
28. Ralph, J.E., 1969, Solid State Commun. **7**, 1065.
29. Buchanan, R.A., J.J. Pearson and G.F. Herrmann, 1969, Solid State Commun. **7**, 195.
30. Ref. 14, p. 313.
31. Argyle, B.F., R.L. Wadsack and R.K. Chang, 1971, J. Appl. Phys. **42**, 1478.

5.22. $R_3Al_5O_{12}$

A good discussion of the crystal structure of $R_3Al_5O_{12}$ and numerous other garnet compounds is given by Geller (1978). Much of his discussion centers on ferrimagnetic garnets, but the discussion of $R_3Al_5O_{12}$ garnets is clear and precise, with many references to earlier work. Lasers have been built using Ho^{3+} in $Ho_3Al_5O_{12}$ by Kaminskii et al. (1976) and by Ivanov et al. (1975). A laser using Ho^{3+} in $Yb_3Al_5O_{12}$ has been built by Arsenev (1970), and Prokhorov et al. (1977) have built a laser using Er^{3+} in $Er_3Al_5O_{12}$. Laser emission from Ho^{3+} in a thin film of $R_3Al_5O_{12}$, where R is a mixture of rare earths and yttrium, has been reported by Van der Ziel et al. (1972). The thin films used were grown by liquid phase epitaxy; this method of growing thin-film garnets is covered in more detail by Stein and Kestigian (1975). The mechanical and thermal properties and Debye temperature of several $R_3Al_5O_{12}$ compounds have been investigated by Oliver (1967).

Energy transfer of Er^{3+} to Ho^{3+} and Tm^{3+} has been reported (Pacheco and Di Bartolo, 1978) in $Er_3Al_5O_{12}$ along with the temperature dependence of the fluorescence lifetimes of those ions in this host. The early work on $Dy_3Al_5O_{12}$ showed that the compound undergoes a magnetic phase transition at 2.49 K. The effective magnetic field, 4350 Oe, and exchange field, 9250 Oe, have been measured (Hellwege et al., 1964). The internal field below the transition temperature was reinvestigated by Blanc et al. (1970) and was found to be 4600 Oe with a linewidth larger at 77 K than at 4.2 K. This behavior of the linewidth has been explained by Cooke et al. (1965) in terms of short-range order. Further anomalous low-temperature behavior of $Dy_3Al_5O_{12}$ is discussed by Wyatt (1968) in terms of a two-phase mixture theory.

A number of different theoretical models have been used in the analysis and explanation of the Stark crystal field splitting in $R_3Al_5O_{12}$ compounds. The electrostatic theory was used to calculate the electric field gradient in $R_3Al_5O_{12}$ for four rare earths by Wojcik (1980), with excellent agreement with experiment. The superposition model of crystal fields has been applied by Newman and Stedman (1969) for $Er_3Al_5O_{12}$, with good agreement for the $A_{km}\langle r^k\rangle$ with $k \geq 4$. The crystal-field parameters for R = Tb and Dy were analyzed by an overlap-local coordination model by Korolkov and Makhanek (1977) with limited success. A detailed analysis of the crystal field in garnets using the exchange-charge model has been given by Bogomolova et al. (1977). This theory includes the point-charge and point-dipole contributions to the crystal field. The point-dipole contributions are handled in a self-consistent manner, and the crystal-field parameters calculated for Yb^{3+} in $Yb_3Al_5O_{12}$ are in good agreement with experiment.

An analysis of the crystal field of garnets and a number of other materials has been given by Kustov et al. (1980) using the rotational invariants A_k formed by $A_k = (2k+1)^{-1}\Sigma_m |B_{km}|^2$. Molecular orbital theory has been applied to the $5d^5$ Ru^{3+} ion in C_{3i} site symmetry in aluminum garnets by O'Reilly and Offenbacher (1971). A general evaluation of the spectroscopic factors affecting the laser properties of garnet crystals has been given by Kaminskii et al. (1975).

The magneto-optical properties of $Tb_3Al_5O_{12}$ have been investigated by De Sorbo (1967); the Verdet constant is quite large at 4.2 K, with wavelengths in the visible. Over an extended wavelength region, the inverse of the Verdet constant is proportional to the square of the reciprocal wavelength. Previous to De Sorbo's work, Rubenstein et al. (1964) had reported a large Verdet constant for $Tb_3Al_5O_{12}$ and suggested its use as an optical Faraday device. More recently, a compact optical isolator has been reported by Sansalone (1971) using $Tb_3Al_5O_{12}$ that has 26 dB isolation with 0.4 dB forward loss. The optical range of the device is from 4880 Å to 5145 Å.

5.22.1 Crystallographic data for $R_3Al_5O_{12}$

Cubic Ia3d, #230, Z = 8

Ion	Pos.	Symm.	x	y	z
R	24(c)	D_2	0	1/4	1/8
Al_1	16(a)	C_{3i}	0	0	0
Al_2	24(d)	S_4	3/8	0	1/4
O	96(h)	C_1	x	y	z

X-ray data

		O			
R	a	x	y	z	Ref.
Gd	12.113	-0.0311	0.0509	0.1490	1
Gd	12.111	-	-	-	2
Tb	12.00	-0.0314	0.0502	0.148	3
Dy	-	-0.032	0.056	0.151	4
Dy	12.0381	-	-	-	5
Dy	12.041	-	-	-	2
Ho	12.00	-0.0311	0.0513	0.1503	3
Ho	12.011	-	-	-	2
Er	11.964	-	-	-	2
Tm	11.96	-	-	-	6
Tm	11.957	-	-	-	2
Yb	11.931	-0.0296	0.0529	0.1504	1
Yb	11.9295	-	-	-	5
Lu	11.906	-0.0294	0.0537	0.1509	1

5.22.2 Index of refraction for $R_3Al_5O_{12}$

R	n	λ(μm)	Ref.	R	n	λ(μm)	Ref.
Gd	1.879	?	2	Er	1.857	?	2
Gd	1.866	0.5890	7	Er	1.853	0.5890	7
Tb	1.873	0.5890	7	Tm	1.854	?	2
Dy	1.868	?	2	Tm	1.854	0.5890	7
Dy	1.855	0.5890	5	Yb	1.842	0.5890	5
Dy	1.868	0.5890	7	Yb	1.848	0.5890	7
Ho	1.863	?	2	Lu	1.842	0.5890	7
Ho	1.863	0.5890	7				

5.22.3 Crystal-field parameters for $R:R_3Al_5O_{12}$ (cm^{-1})

R	B_{20}	B_{22}	B_{40}	B_{42}	B_{44}	B_{60}	B_{62}	B_{64}	B_{66}	Ref.
Tb	551	36	-156	-1651	-922	-1288	-432	541	-426	8
Dy	465	108	-72	-1779	-904	-1170	-423	464	-414	9
Dy	492	98	-8	-1807	-964	-1178	-432	478	-415	10
Er	398	55	-98	-1440	-751	-1196	-268	464	-404	9
Er	320	82	-1280	-177	-1721	480	63	-998	-84	11
Er	428	82	121	-1585	-628	-1044	-371	516	-394	12

5.22.4 Energy levels for $R:R_3Al_5O_{12}$

$Tb:Tb_3Al_5O_{12}$

Term	Prefix	Energy (cm^{-1})						T	Ref.
$^7F_6$	-	0	2	74	84	263	460	10	8
	-	0	5	75	82	262	322	4.2	13
	-	470						10	8
	-	373						4.2	13
$^7F_5$	2	134	147	177	209	349	375	10	8
	2	127	135	148	179	210	348	4.2	13
	2	402	478	618				10	8
	2	376	403	463	485			4.2	13

Tb:$Tb_3Al_5O_{12}$ (continued)

Term	Prefix	Energy (cm^{-1})						T	Ref.
$^7F_4$	3	388	399	411	448	517	621	10	8
	3	703	732	004*				10	8
$^7F_3$	4	368	501	519	554	617	677	10	8
	4	688						10	8
$^7F_2$	5	062	550	593	625			10	8
$^7F_1$	5	738	868	874				10	8

Dy:$Dy_3Al_5O_{12}$

Term	Prefix	Energy (cm^{-1})						T	Ref.
$^6H_{15/2}$	-	0	70	117				77	14
	-	0	63.5	71.3	74.2	94.2		2	15
	-	0	70.1	115.8	196.6	256.4		77	16
	-	0	70.3	115.6	191	251		77	17
	-	0	69	114	186			80	10
$^6H_{13/2}$	3	567	596	790	(953)			77	18
	3	565	594	673	719	786	832	80	10
	3	968						80	10
$^6H_{11/2}$	5	928	965	040*	062	113	132	4.2	14
	5	965	064*	114				1.2	15
	5	930	964	036*	059	109	127	4.2	17
$^6H_{9/2}$, $^6F_{11/2}$	7	651	684	760	780	823	927	4.2	14
	7	651	690	758	821			1.2	15
	7	657	687	762	783	824	926	4.2	17
	7	958	983	009*	223	292		4.2	14
	7	(955)	(979)	009*	224	295		4.2	17
$^6F_{9/2}$, $^6H_{7/2}$	9	022	057	092	329	349	385	4.2	14
	9	019	062	097	(331)	(381)	666	4.2	17
	9	662						4.2	14
$^6H_{5/2}$	10	247	363	515				4.2	14
	10	517						1.2	15
	10	258.7	365.4	515.1				20.4	16
	10	262.4	368.2	514.7				4.2	17
$^6F_{7/2}$	11	063	247	279	321			4.2	14
	11	060.4	249.5	282.9	323.4			1.2	15
	11	064.9	248.0	280.2	322.0			20.4	16
	11	062.6	247.8	280.1	322.2			4.2	17
$^6F_{5/2}$	12	503	538	683				4.2	14
	12	511.3	542.6	688.0				1.2	15
	12	507.7	538.5	684.1				20.4	16
	12	507.7	538.8	684.3				4.2	17

Dy:$Dy_3Al_5O_{12}$ (continued)

Term	Prefix	Energy (cm^{-1})						T	Ref.
$^6F_{3/2}$	13	359.5	366.4					4.2	14
	13	375.4	383.0					1.2	15
	13	372.4	379.6					20.4	16
	13	372.6	380.4					4.2	17
$^6F_{1/2}$	13	481.3						4.2	15
$^4F_{9/2}$	20	887.2	926.0	082.1*	148.9			1.2	15
	20	881.2	921.9	079.0*	146.3			20.4	16
?	21	911.9	973.2					20.4	16
?	22	353.3	386.9					20.4	16
?	23	357.9	411.0	498.8	538.8			20.4	16
?	24	787.1	799.4	851.6	872.5			20.4	16
?	25	011.1	140.2	180.7	350.6	418.6	464.6	20.4	16
	25	506.3	966.8	080.6*				20.4	16
?	27	302.5	340.8	394.4	438.5	484.8	860.1	20.4	16
	27	950.7						20.4	16
?	28	358.7	416.9	424.0	438.1	455.2	504.9	20.4	16
	28	534.4	900.1	961.8				20.4	16
?	29	397.4	450.6	532.6	562.1	683.4	745.0	20.4	16
	29	997.4	092.3*					20.4	16
?	30	680.3	755.4	936.0	990.2	027.7*	061.4	20.4	16
	30	109.5						20.4	16
?	33	056.5	083.9	097.5	118.1	131.7	142.6	20.4	16
	33	171.9	365.4	404.6	426.0	475.4	481.5	20.4	16
	33	552.6	563.8	585.7	874.3	904.0	936.7	20.4	16

Ho:$Ho_3Al_5O_{12}$

Term	Prefix	Energy (cm^{-1})						T	Ref.
$^5I_8$	-	0	16	41	62	89	104	4.2	19
	-	0	42.0	53.5	62.5	94.5		2	20
	-	0	42	54	141	161	418	4.2	21
	-	123	162	270	316	335	378	4.2	19
	-	448	464	494	519			4.2	21
	-	413	452	488	520	551		4.2	19
$^5I_7$	5	230	242	252	305	313	321	4.2	19
	5	228	230	244	251	304	312	4.2	21
	5	339	349	373	397	405	456	4.2	19
	5	318	338	350	371	377	406	4.2	21
	5	416	455					4.2	21

Ho:$Ho_3Al_5O_{12}$ (continued)

Term	Prefix	Energy (cm^{-1})						T	Ref.
$^5I_6$	8	733	737	742	763	768	771	4.2	21
	8	817	839	851	869	936	940	4.2	21
	8	951						4.2	21
$^5I_5$	11	320	352	358	387	391	424	4.2	21
	11	428	472	476				4.2	21
$^5I_4$	13	281	339	343	362	366	380	4.2	21
	13	385	405	563				4.2	21
$^5F_5$	15	457	474	491	513	655	665	4.2	21
	15	670	697	739	744			4.2	21
$^5F_4$, $^5S_2$	18	451	462	530	539	542	547	4.2	21
	18	582	592	728	743			4.2	21

Er:$Er_3Al_5O_{12}$

Term	Prefix	Energy (cm^{-1})						T	Ref.
$^4I_{15/2}$	-	0	26.6	58.4	78.8	422.8	436.1	4.2	11
	-	0	24	56	76	426	444	4.2	18
	-	530.1	574.3					4.2	11
$^4I_{9/2}$	12	301.3	528.7	575.8	721.9	766.3		4.2	11
$^4F_{9/2}$	15	291.2	314.7	355.3	474.0	518.4		4.2	11
$^4S_{3/2}$	18	395.2	455.5					4.2	11
$^2H_{11/2}$	19	091.2	112.6	149.2	347.6	365.6	370.6	4.2	11
$^4F_{7/2}$	20	516.4	568.2	649.3	697.5			4.2	11
$^4F_{5/2}$	22	217.8	238.8	284.2				4.2	11
$^4F_{3/2}$	22	587.9	660.9					4.2	11
$^2G_{9/2}$	24	417.3	572.8	589.3	763.7	784.8		4.2	11
$^4G_{11/2}$	26	206.8	269.6	314.9	461.4	469.7	500.7	4.2	11

Tm:$Tm_3Al_5O_{12}$

Term	Prefix	Energy (cm^{-1})				T	Ref.
$^3H_6$	-	0	32.4	35.6	39.3	2	20
	-	0	228			4.2	18

$Yb:Yb_3Al_5O_{12}$

Term	Prefix	Energy (cm^{-1})				T	Ref.
$^2F_{7/2}$	-	0	586	610	750	4.2	18
	-	0	618	701	766	77	22
$^2F_{5/2}$	10	328	640	680		77	22

References for 5.22. $R_3Al_5O_{12}$

1. Euler, F. and J.A. Bruce, 1965, Acta Cryst. **19**, 971.
2. Akhmetov, S.F., G.L. Akhmetova, G.A. Gazizova, V.S. Kovalenko and T.F. Mirenkova, 1977, Russ. J. Inorg. Chem. **22**, 1613.
3. Hammann, J., 1969, Acta Cryst. **B25**, 1853.
4. Herpin, A. and P. Meriel, 1964, C. R. Acad. Sc. Paris, **259**, 2416.
5. Keester, K. and G.G. Johnson, 1971, J. Appl. Cryst. **4**, 178.
6. Rimai, L. and R.W. Bierig, 1964, Phys. Rev. Lett. **12**, 284.
7. Rubinstein, C.B. and R.L. Barns, 1965, Am. Mineral. **50**, 782.
8. Boal, D., P. Grünberg and J.A. Koningstein, 1973, Phys. Rev. **B7**, 4757.
9. Wortman, D.E., C.A. Morrison and N. Karayianis, 1976, Harry Diamond Laboratories Report TR-1773 (NTIS #033 884).
10. Wadsack, R.L., J.L. Lewis, B.E. Argyle and R.K. Chang, 1971, Phys. Rev. **B3**, 4342.
11. Hellwege, K.H., S. Hüfner, M. Schinkmann and H. Schmidt, 1966, Phys. Kondens. Materie **4**, 397.
12. Orlich, E. and S. Hüfner, 1969, J. Appl. Phys. **40**, 1503.
13. Koningstein, J.A. and G. Schaack, 1970, Phys. Rev. **B2**, 1242.
14. Grünberg, P., K.H. Hellwege and S. Hüfner, 1967, Phys. Kondens. Materie **6**, 95.
15. Faulhaber, R. and S. Hüfner, 1969, Z. Physik **228**, 235.
16. Gehring, K.A., M.J.M. Leask and J.H.M. Thornley, 1969, J. Phys. **C2**, 484.
17. Aoyagi, K., K. Tsushima and M. Uesugi, 1969, J. Phys. Soc. Japan **27**, 49.
18. Koningstein, J.A. and P. Agunberg, 1971, Can. J. Chem. **49**, 2336.
19. Ivanov, A.O., I.V. Mochalov, A.M. Tkachuk, V.A. Federov and P.P. Feofilov, 1975, Sov. J. Quantum Electron. **5**, 115.
20. Milward, R.C., 1967, Phys. Lett. **25A**, 19.
21. Ashurov, M.Kh., Yu. K. Voron'ko, E.V. Zharikov, A.A. Kaminskii, V.V. Osiko, A.A. Sobol, M.I. Timoshechkin, V.A. Federov and A.A. Shabaltai, 1979, Inorg. Mater. (USSR) **15**, 979.
22. Buchanan, R.A., K.A. Wickersheim, J.J. Pearson and G.F. Herrmann, 1967, Phys. Rev. **159**, 245.

5.23. $R_3Ga_5O_{12}$

The growth of good quality rare earth gallium garnets has been discussed by Brandle et al. (1972); the control of the growth-atmosphere composition is stressed. The effects of growth conditions under which some of the rare-earth ions occupy the octahedral site in $R_3Ga_5O_{12}$ have also been investigated (Brandle and Barns, 1974); the number of rare-earth ions occupying the octahedral sites increased from Nd to Ho monotonically. An excellent discussion of the gallium garnet strutures is given by Geller (1978), with a thorough discussion of the site symmetry of each constituent ion. Accurate measurements of the lattice con-

stant of $Gd_3Ga_5O_{12}$ by the X-ray divergent-beam anomalous-transmission method has been made (Glass and Moudy, 1974). By slicing thin sections from a single boule of a gadolinium gallium garnet crystal, these workers showed that the lattice constant varied from 12.3807 to 12.3831 Å. Variations in the lattice constant of $Gd_3Ga_5O_{12}$ have also been noted by Makino et al. (1976), caused by crystal growth along various crystallographic axis. The low-temperature structure and antiferromagnetic properties of $Er_3Ga_5O_{12}$ have been investigated by Hammann (1968a) with T_N found to be 0.789 K. A similar study was made on $Nd_3Ga_5O_{12}$ (Hammann, 1968b) where the antiferromagnetic phase-transition temperature was found to be 0.516 K. Low-temperature ordering has been observed in $Ho_3Ga_5O_{12}$ at 0.25 K and 0.19 K (Hammann and Manneville, 1973) and was further investigated at low temperatures for this garnet and $Tb_3Ga_5O_{12}$ (with an ordering temperature of 0.24 K) by Hammann and Ocio (1977). Recently it has been shown that a uniform magnetic field can induce a staggered internal magnetic field in $Dy_3Ga_5O_{12}$ at temperatures much greater than the Neel temperature (Steiner et al., 1979).

The Judd–Ofelt intensity parameters $\Omega_2 = 0.0$, $\Omega_4 = 3.3$ and $\Omega_6 = 3.7$ (in units 10^{-20} cm^2) for Nd:$Gd_3Ga_5O_{12}$ have been measured by Krupke (1974). The line strengths and branching ratios were also measured by Krupke for this host–ion combination. The elastic constants and Debye temperatures have been measured for R = Gd, Nd and Sm in $R_3Ga_5O_{12}$ by Nagaiah et al. (1979). The elastic and thermoelastic constants of $Gd_3Ga_5O_{12}$ has been reported (Haussühl and Mateika, 1972). The nonradiative decay of the $^4I_{11/2}$ state of Er^{3+} in $Gd_3Ga_5O_{12}$ has been measured by Ashurov et al. (1978) and found to be less rapid than in several other garnets. A method of measurement of thickness and index of refraction of thin films of garnets has been presented by Henry and SooHoo (1977), with detailed results given for $Gd_3Ga_5O_{12}$ films. The spectroscopic properties of the mixed garnet film $Er_3Al_{5-x}Ga_xO_{12}$ ($x = 0.4$, 0.55, 0.7) have been reported by Dmitruk et al. (1979). The thin films were grown by liquid-phase epitaxy and the lifetimes of the $^4I_{11/2}$ level of Er^{3+} were reported.

An interesting modification of the sharp transitions $^7F_0$ to $^5D_0$ of Eu^{3+} in $Eu_3Ga_5O_{12}$ has been reported by Van der Ziel (1973) and analyzed in more detail by Van der Ziel and Van Uitert (1973). The transition-line modification is assumed to be caused by an overlap with the broad-band impurity absorption of Pt^{4+}; their analysis convincingly supports this assumption. Such interactions could have significant impact on possible laser applications using rare-earth ions and selected impurities. The existence of inequivalent sites of Er^{3+} in $Gd_3Ga_5O_{12}$ and other garnets and their identification has been reported by Ashurov et al. (1976); possible applications of these new centers are discussed.

Electron spin resonance has been reported on Yb^{3+} and Nd^{3+} impurities in $Eu_3Ga_5O_{12}$ (Hodges, 1975). The particular interest in this host is that the Eu^{3+} ion has a singlet ground state and the lines are not broadened by the host. Microwave losses of $Gd_3Ga_5O_{12}$ have been measured at 30 GHz, X-band, and 2 GHz by Adam et al. (1975). These measurements in this host are important in technological applications, as it is used as a nonreciprocal thin film substrate.

The crystal fields in $R_3Ga_5O_{12}$ for R = Nd, Eu, Gd, Er and Lu have been analyzed by Nekvasil et al. (1978) and Nekvasil (1979) using the superposition theory of Bradbury and Newman (1967).

The Raman spectra of $R_3Ga_5O_{12}$ (and other garnets) for R = Yb and Lu has been reported by Song et al. (1973). Previous investigations of the Raman spectra of garnets have been reported by Koningstein and Mortensen (1968), Koningstein (1968), and Koningstein and T.-N. Ng (1968).

5.23.1 Crystallographic data for $R_3Ga_5O_{12}$

Cubic Ia3d, #230, Z = 8

Ion	Pos.	Symm.	x	y	z
R	24(c)	D_2	0	1/4	1/8
Ga_1	16(a)	C_{3i}	0	0	0
Ga_2	24(d)	S_4	3/8	0	1/4
O	96(h)	C_1	x	y	z

X-ray data

		O			
R	a	x	y	z	Ref.
Pr	-	-0.0329	0.0503	0.1472	1
Nd	12.506	-	-	-	2
Nd	12.5065	-	-	-	3
Nd	-	-0.0317	0.0513	0.1478	1
Sm	12.437	-	-	-	3
Sm	12.432	-	-	-	4
Sm	12.433	-0.0295	0.0537	0.1488	5,6
Eu	-	-0.0298	0.0538	0.1489	1
Eu	12.401	-	-	-	7
Gd	12.376	-	-	-	8
Gd	12.379	-	-	-	3
Gd	12.377	-0.0284	0.0549	0.1497	5,6
Tb	-	-0.0290	0.0551	0.1494	1
Dy	-	-0.0284	0.0556	0.1497	1

Crystallographic data for $R_3Ga_5O_{12}$ (continued)

		O			
R	a	x	y	z	Ref.
Dy	12.307	-	-	-	9
Ho	-	-0.0269	0.0554	0.1505	1
Ho	12.2813	-	-	-	10
Er	12.255	-	-	-	11
Er	12.254	-0.0266	0.0567	0.1511	5,6
Tm	-	-0.0257	0.0564	0.1512	1
Tm	12.23	-	-	-	12
Yb	12.204	-0.0259	0.0563	0.1519	13
Yb	12.200	-	-	-	14
Lu	12.188	-0.0252	0.0570	0.1506	13
Lu	12.183	-	-	-	15

5.23.2 Index of refraction for $R_3Ga_5O_{12}$

$Gd_3Ga_5O_{12}$ $n^2 = 1 + 2.7382\lambda^2/(\lambda^2 - 0.01755)$ (λ in μm) Ref. 16

$Gd_3Ga_5O_{12}$ $\lambda = 1.152$ μm: $n = 1.945$ Ref. 17

$Gd_3Ga_5O_{12}$ Ref. 18

λ(μm)	n
.509	1.980
.546	1.974
.589	1.966
.633	1.960

$Ho_3Ga_5O_{12}$ $n = 1.965$ Ref. 10

5.23.3 Crystal-field parameters for R:$R_3Ga_5O_{12}$ (cm^{-1})

R	B_{20}	B_{22}	B_{40}	B_{42}	B_{44}	B_{60}	B_{62}	B_{64}	B_{66}	Ref.
Sm	152	162	-436	-1222	-730	-1534	-224	655	-492	19
Eu	318	1	3	-1586	-814	-1472	-448	718	-636	20
Dy	104	-158	102	-1575	-865	-1140	-320	527	-387	21
Dy	222	-23	-17	-1590	-805	-1033	-350	518	-417	19
Dy	45	-75	49	-1638	-791	-1226	-288	571	-313	22
Er	124	34	69	-1473	-602	-1057	-437	519	-271	23
Tm	170	126	55	-1474	-611	-1001	-464	317	-602	24

5.23.4 Energy levels for R:$R_3Ga_5O_{12}$

Nd:$Nd_3Ga_5O_{12}$

Term	Prefix	Energy (cm^{-1})						T	Ref.
$^4I_{9/2}$	-	0	115	187	(380)			10	25
$^4I_{11/2}$	1	489	507	573	612	884	929	10	25
$^4I_{13/2}$	3	353	439	455	788	841		10	25
$^4I_{15/2}$	5	474	538	640	655	189*	155	10	25
	5	246	333					10	25
$^4F_{3/2}$	11	430	504					10	25
$^4F_{5/2}$, $^2H_{9/2}$	12	383	443	540	588	728	814	10	25
	12	935						10	25
$^4F_{7/2}$, $^4S_{3/2}$	13	308	330	373	424	435	480	10	25
	13	574	593	657	720			10	25
$^4F_{9/2}$	14	642	678	778	794	821	904	10	25
$^2H_{11/2}$	15	774	850	884	960	083*	090	10	25
$^2P_{1/2}$	23	178	284					10	25
$^2D_{5/2}$	23	532	702	762	831			10	25
$^2P_{3/2}$	26	032						10	25

Sm:$Sm_3Ga_5O_{12}$

Term	Prefix	Energy (cm^{-1})						T	Ref.
$^6H_{5/2}$	-	0						4.2	26
$^6H_{7/2}$	1	000	163	309	326			4.2	26
$^6H_{9/2}$	2	227	(300)	395	516	534		4.2	26
$^6H_{11/2}$	3	538	580	698	748	771	851	4.2	26
$^6H_{13/2}$	4	879	930	011*	133	163	170	4.2	26
$^6F_{1/2}$, $^6H_{15/2}$	6	490	870					4.2	26
$^6F_{5/2}$	7	189	274	292				4.2	26
$^6F_{7/2}$	8	036	064	072	159			4.2	26
$^6F_{9/2}$	9	184	209	226	266	290		4.2	26

Eu:$Eu_3Ga_5O_{12}$

Term	Prefix	Energy (cm^{-1})						T	Ref.
$^7F_0$	-	0						10	20
$^7F_1$	-	306	328	409				10	20
	-	306	329	411				4.2	27
$^7F_2$	-	819	832	857	323*	342		10	20
	-	819	824	857	324*	341		4.2	27
$^7F_3$	1	830	853	896	924	974	983	10	20
	1	146*						10	20
$^7F_4$	2	448	830	925	070*	088	097	10	20
	2	834	927	077*	089	103		4.2	27
	2	142	199					10	20
$^7F_5$	3	766	823	956	012*	018	155	10	20
	3	165	183	215	232			10	20
$^7F_6$	4	939	958	990	009*	089	101	10	20
	4	204	240	282				10	20

Tb:$Tb_3Ga_5O_{12}$

Term	Prefix	Energy (cm^{-1})					T	Ref.
$^7F_6$	-	0	34	43	50	53	?	24

Dy:$Dy_3Ga_5O_{12}$

Term	Prefix	Energy (cm^{-1})						T	Ref.
$^6H_{15/2}$	-	0	20.3	72				77	28,29
	-	0	21.0	70.0	137.0			80	21
	-	0	21.5	71				4.2	30
$^6H_{13/2}$	3	559.0	576.0	635.0	647.0	747.0	784.0	80	21
	3	556	571	628	639	735	775	4.2	26
	3	824.0						80	21
	3	817						4.2	26
$^6H_{11/2}$	5	938	952	997	018*	033	042	4.2	28,29
	5	941	953	993	015*	031	040	4.2	26
$^6F_{11/2}$, $^6H_{9/2}$	7	626	646	697	724	751	875	4.2	28,29
	7	640	659	709	734	758	874	4.2	26
	7	896	918	934	134*	161		4.2	28,29
	7	896	918	938	167*	200		4.2	26
$^6H_{7/2}$, $^6F_{9/2}$	8	986	026*	255	264	287	310	4.2	29
	9	009	050	287	327	355	(597)	4.2	26
	8	996	026*	264	287	310	333	4.2	28
	8	333	563					4.2	29
	8	563						4.2	28
$^6H_{5/2}$	10	225	343	391				4.2	28,29
	10	238	359	406				4.2	26
$^6F_{7/2}$	11	008	191	210	241			4.2	28,29
	11	025	211	227	258			4.2	26
$^6F_{5/2}$	12	451.8	475.5	619.8				4.2	28,29
	12	460	480	630				4.2	26
$^6F_{3/2}$	13	308.5	318.7					4.2	28,29
	13	317	328					4.2	26

Ho:$Ho_3Ga_5O_{12}$

Term	Prefix	Energy (cm^{-1})						T	Ref.
$^5I_8$	-	0	5.9	30.3	39	44.2	86	1.3	31,32
	-	111						1.3	31,32
$^5F_5$	15	450	455	466	491	498	630	1.3	31
	15	636	669					1.3	31

Er:$Er_3Ga_5O_{12}$

Term	Prefix	Energy (cm^{-1})					T	Ref.
$^4I_{15/2}$	-	0	44	55	75	436	4.2	27

$Tm:Tm_3Ga_5O_{12}$

Term	Prefix	Energy (cm^{-1})					T	Ref.
$^3H_6$	-	0	85	113	123	184	4.2	33
	-	0	185	189	192	245	5	24

$Yb:Yb_3Ga_5O_{12}$

Term	Prefix	Energy (cm^{-1})				T	Ref.
$^2F_{7/2}$	-	0	546	610	624	80	34
	-	0	546	624		77	35
	-	0	539	554		?	36
$^2F_{5/2}$	10	313	619	747		77	35

References for 5.23. $R_3Ga_5O_{12}$

1. Dukhovskaya, E.L. and Yu.G. Saksonov, 1977, Sov. Phys. Crystallogr. **22**, 622.
2. Swanson, H.E., H.F. McMurdie, M.C. Morris and E.H. Evans, 1962, Standard X-ray Diffraction Patterns, Nat. Bur. Stds. (U.S.) Monogr. 25, Sect. 1, p. 34.
3. Nagaiah, B., M.R. Babu and D.B. Sirdeshmukh, 1979, Indian J. Pure Appl. Phys. **17**, 838.
4. Ref. 2, p. 42.
5. Dukhovskaya, E.L., A.P. Erastova, B.E. Rubinstein, Yu.G. Saksonov and L.A. Vorob'eve, 1973, Inorg. Mater. (USSR) **9**, 1074.
6. Dukhovskaya, E.L., Yu.G. Saksonov and A.G. Titova, 1973, Inorg. Mater. (USSR) **9**, 724.
7. Swanson, H.E., H.F. McMurdie, M.C. Morris and E.H. Evans, 1963, Standard X-ray Diffraction Patterns, Nat. Bur. Stds. (U.S.) Monogr. 25, Sect. 2, p. 17.
8. Ref. 7, p. 18.
9. Ref. 7, p. 15.
10. Keester, K.L. and G.G. Johnson, 1971, J. Appl. Cryst. **4**, 178.
11. Ref. 2, p. 12.
12. Rimai, L. and R.W. Bierig, 1964, Phys. Rev. Lett. **12**, 284.
13. Euler, F. and J.A. Bruce, 1965, Acta Cryst. **19**, 971.
14. Ref. 2, p. 49.
15. Ref. 7, p. 22.
16. Lomheim, T.S. and L.G. DeShazer, 1979, Phys. Rev. **B20**, 4343.
17. Warner, J., 1974, Mat. Res. Bull. **9**, 507.
18. McCollum, B.C., W.R. Bekebrede, M. Kestigian and A.B. Smith, 1973, Appl. Phys. Lett. **23**, 702.
19. Karayianis, N., D.E. Wortman and C.A. Morrison, 1977, Harry Diamond Laboratories Report TR-1793 (NTIS #042 205).
20. Boal, D., P. Grünberg and J.A. Koningstein, 1973, Phys. Rev. **B7**, 4757.
21. Wadsack, R.L., J.L. Lewis, B.E. Argyle and R.K. Chang, 1971, Phys. Rev. **B3**, 4342.
22. Filippi, J., F. Tcheou and J. Rossat-Mignod, 1980, Solid State Commun. **33**, 827.
23. Orlich, E. and S. Hüfner, 1969, J. Appl. Phys. **40**, 1503.
24. Koningstein, J.A. and C.J. Kane-Maguire, 1974, Can. J. Chem. **52**, 3445.
25. Nutter, P.B. and M.L. Harrison, 1963, Raytheon Company, Progress Report No. 1 (NTIS #475 607).
26. Veyssie, M. and B. Dreyfus, 1967, J. Phys. Chem. Solids **28**, 499.
27. Koningstein, J.A. and P. Grünberg, 1971, Can. J. Chem. **49**, 2336.
28. Grünberg, P. K.H. Hellwege and S. Hüfner, 1967, Phys. Kondens. Mater. **6**, 95.

29. Grünberg, P., S. Hüfner, E. Orlich and J. Schmitt, 1969, Phys. Rev. **184**, 285.
30. Blanc, J., D. Brochier and A. Ribeyron, 1970, Phys. Lett. **33A**, 201.
31. Belyaeva, A.I., V.N. Pavlov and A.V. Antonov, 1969, Opt. Spectrosc. **27**, 151.
32. Sievers, A.J. and M. Tinkham, 1963, J. Appl. Phys. **34**, 1235.
33. Pearson, J.J., G.F. Herrmann and R.A. Buchanan, 1968, J. Appl. Phys. **39**, 980.
34. Argyle, B.F., R.L. Wadsack and R.K. Chang, 1971, J. Appl. Phys. **42**, 1478.
35. Buchanan, R.A., K.A. Wickersheim, J.J. Pearson and G.F. Herrmann, 1967, Phys. Rev. **159**, 245.
36. Koningstein, J.A., 1968, Appl. Spectrosc. **22**, 438.

5.24. KY_3F_{10}

Several crystalline phases of the KF–YF_3 system have been reported (Borzenkova et al., 1971); among these, the compound KY_3F_{10} has several attractive properties as a potential laser host material. KY_3F_{10} is a congruent melting solid; it crystallizes in a face-centered cubic structure in which Y^{3+} ions occupy sites of C_{4v} symmetry (Pierce and Hong, 1973). Laser-quality single crystals have been grown and some of the physical properties of the crystals have been discussed (Pollack et al., 1980). The possibility of using Pr^{3+}:KY_3F_{10} as an efficient four-level blue-green laser has been discussed based on detailed line-to-line intensity calculations (Morrison et al., 1980b). Radiative and non-radiative decay processes of Eu^{3+}:KY_3F_{10} have also been investigated (Porcher and Caro, 1978).

5.24.1 Crystallographic data for KY_3F_{10}

Cubic Fm3m, #225, Z = 8

Ion	Pos.	Symm.	x	y	z
Y	24(e)	C_{4v}	x	0	0
K	8(c)	T_d	1/4	1/4	1/4
F_1	48(i)	C_{2v}	1/2	x	x
F_2	32(f)	C_{3v}	x	x	x

X-ray data

	Y	F_1	F_2	
a	x	x	x	Ref.
11.542	0.2401	0.3353	0.1081	1

5.24.2 Index of refraction for KY_3F_{10} (Ref. 2)

λ(μm)	n	λ(μm)	n
0.250	1.5265	0.900	1.4810
0.275	1.5169	1.000	1.4802
0.300	1.5102	1.2	1.4790
0.350	1.5011	1.4	1.4780
0.400	1.4955	1.6	1.4769
0.450	1.4917	1.8	1.4759
0.500	1.4890	2.0	1.4748
0.600	1.4856	2.2	1.4736
0.700	1.4834	2.4	1.4724
0.800	1.4820	2.6	1.4712

5.24.3 Crystal-field parameters for R:KY_3F_{10} (cm^{-1})

R	B_{20}	B_{40}	B_{44}	B_{60}	B_{64}	Ref.
Pr	-589.0	-1711	518.9	656.9	-195.9	3
Nd	-621.1	-1566	252.2	366.7	-366.6	3
Eu	-551	-1360	345	394	-234	4
Eu	-552	-1332	512	366	-41	5
Eu	-528	-1358	368	479	-41	6
Eu	-517.6	-1337	359.6	400.1	-271.7	3

5.24.4 Intensity parameters for R:KY_3F_{10} (10^{-20} cm^2)

R	Ω_2	Ω_4	Ω_6	Ref.
Eu	1.22	1.26	8.55	7

5.24.5 Energy levels for R:KY_3F_{10}

$Pr:KY_3F_{10}$

Term	Prefix	Energy (cm^{-1})						T	Ref.
$^3H_4$	-	0	166	175	217			4.2	3
$^3H_5$	2	184	211	684				4.2	3
$^3H_6$, $^3F_2$	4	283	347	418	477	041*	075	4.2	3
	4	229						4.2	3
$^3F_3$	6	433	441	496	573			4.2	3
$^3F_4$	6	829	895	006*	055			4.2	3
$^1G_4$	9	622						4.2	3
$^1D_2$	16	654	890	237*				4.2	3
$^3P_0$, $^1I_6$, $^3P_1$	20	728	794	204*	358	692		4.2	3
$^3P_2$	22	355	380	557	587			4.2	3

$Nd:KY_3F_{10}$

Term	Prefix	Energy (cm^{-1})						T	Ref.
$^4I_{9/2}$	-	0	120	131	182	320		4.2	3
$^4I_{11/2}$	1	979	986	049*	053	104		4.2	3
$^4I_{13/2}$	3	928	956	967	063*	078	193	4.2	3
$^4I_{15/2}$	5	886	988	165*	165	250		4.2	3
$^4F_{3/2}$	11	450	547					4.2	3

$Eu:KY_3F_{10}$

Term	Prefix	Energy (cm^{-1})						T	Ref.
$^7F_0$	-	0						4.2	4
$^7F_1$	-	278	411					4.2	4
$^7F_2$	-	933	030*	148	159			4.2	4
$^7F_3$	1	858	895	903	002*	012		4.2	4
$^7F_4$	2	748	778	800	845	014*	052	4.2	4
$^7F_5$	3	739	929	014*				4.2	4
$^5D_0$	17	269						4.2	4
$^5D_1$	19	007	039					4.2	4
$^5D_2$	21	458	478	514	530			4.2	4

References for 5.24. KY_3F_{10}

1. Pierce, J.W. and H.Y.-P. Hong, 1973, in: Proc. 10th Rare Earth Res. Conf., p. 527.
2. Folweiler, R.C., 1977, Sanders Assoc., Inc., Report (NTIS #COO-2921-1).
3. Morrison, C.A., D.E. Wortman, R.P. Leavitt and H.P. Jenssen, 1980, Harry Diamond Laboratories Report TR-1897 (NTIS #082 982).
4. Porcher, P. and P. Caro, 1976, J. Chem. Phys. **65**, 89.
5. Grenet, G. and M.R. Kibler, 1978, J. Solid State Chem. **23**, 1.
6. Porcher, P. and P. Caro, 1978, J. Chem. Phys. **68**, 4176.
7. Porcher, P. and P. Caro, 1980, J. Lumin. **21**, 207.

5.25. Cs_2NaRCl_6

The discovery of a sequence of elpasolite hexachlorides of the form Cs_2NaRCl_6 (Morss et al., 1970) opened up the possibility of several practical applications, most of which have only begun to be realized (Cresswell et al., 1978). These applications are based on the fact that rare earth ions occupy sites of perfect octahedral symmetry in these compounds, and induced electric dipole transitions are forbidden. Magnetic susceptibility studies have been performed on several of the compounds (Karraker, 1971; Hoehn and Karraker, 1974), and results of these studies were used to establish crystal-field parameters (Dunlap and Shenoy, 1975), complementing later optical studies. Electron paramagnetic resonance studies of several Kramers ions in Cs_2NaYCl_6 have been performed (Schwartz and Hill, 1974; O'Connor et al., 1977), confirming the octahedral nature of the rare-earth ion site. Electron-nuclear double resonance (Devaney and Stapleton, 1975) and electron spin-lattice relaxation measurements (North and Stapleton, 1977) have also been performed. Optical studies (Schwartz and Hill, 1974) have given the positions of some levels of the 5d configuration of $Ce:Cs_2NaYCl_6$. Evidence for a phase transition $O_h^5 \rightarrow C_{4h}^5$ at low temperature for several of the Cs_2NaRCl_6 compounds (Schwartz et al., 1976; Nevald et al., 1979) has been obtained from optical, electron spin resonance, nuclear magnetic resonance, and magnetization results.

5.25.1 Crystallographic data for Cs_2NaRCl_6

Cubic Fm3m, #225, Z = 4

Ion	Pos.	Symm.	x	y	z
Cs	8(c)	T_d	1/4	1/4	1/4
Na	4(a)	O_h	0	0	0
R	4(b)	O_h	1/2	1/2	1/2
Cl	24(e)	C_{4v}	x	0	0

Crystallographic data for Cs_2NaRCl_6 (continued)

X-ray data

		Cl	
R	a	x	Ref.
La	10.9923	-	1
Ce	10.9458	-	1
Pr	10.9118	-	1
Nd	10.8894	-	1
Sm	10.8341	-	1
Eu	10.8095	-	1
Gd	10.7918	-	1
Dy	10.7426	-	1
Y	10.7315	-	1
Er	10.7043	-	1
Er	9.061	0.26	2 (Cs_2NaErF_6)
Tm	10.6860	-	1
Lu	10.6550	-	1

5.25.2 Crystal-field parameters for R:Cs_2NaRCl_6 (cm^{-1})

R	B_{40}	B_{60}	Ref.	R	B_{40}	B_{60}	Ref.
Ce	1984	38	3	Eu	1360	51	10
Ce	2130	252.3	4	Eu	2103	279.4	4
Pr	2175	269	5	Tb	1684	157	11,12
Pr	2168	272	6	Tb	1659	168.8	4
Pr	2309	634	7	Dy	1392	62	9
Pr	2659	235	8	Ho	1596	133	13
Pr	2326	247.0	4	Er	1384	32	9
Nd	1792	286	9	Er	1368	32	14
Nd	1983	233.1	4	Tm	2325	493	15
Sm	1439	-	9	Yb	1368	27	16

5.25.3 Energy levels for R:Cs_2NaRCl_6

Ce:$Cs_2NaCeCl_6$

Term	Prefix	Energy (cm^{-1})			T	Ref.
$^2F_{5/2}$	-	0	562	577	35	3
$^2F_{7/2}$	2	160	661	048*	35	3

Pr:$Cs_2NaPrCl_6$

Term	Prefix	Energy (cm^{-1})						T	Ref.
$^3H_4$	-	0	236	250	417	427	703	10	6
	-	0	241	422	703			12	5
$^3H_5$	2	330	402					12	5
$^3H_6$	4	976	005*					10	6
	4	884	976	005*				12	5
$^3F_2$	5	204	297					10	6
	5	207	296					4.2	7
$^3F_3$	6	620						10	6
	6	620	631					12	5
	6	617						4.2	7
	6	620	631	651				4.2	4
$^3F_4$	7	009						4.2	7
	6	961	007*	049				4.2	4
$^1G_4$	9	897						4.2	7
	9	786	898					4.2	4
$^1D_2$	16	662	238*					4.2	7
	16	664	253*					4.2	4
	16	665	256*					4.2	8
$^3P_0$	20	621						4.2	7
	20	623						4.2	4
$^3P_1$, $^1I_6$	21	165						4.2	7
	21	056	166	180	218	960	075*	4.2	4
	20	750	127*	244	382	942	229*	4.2	8
	20	361						4.2	8
$^3P_2$	22	358	622					4.2	7
	22	361	494					4.2	4
	21	955	053*					4.2	8

Nd:$Cs_2NaNdCl_6$

Term	Prefix	Energy (cm^{-1})				T	Ref.
$^4I_{9/2}$	-	0	97	338		30	9
	-	0	75	338		1.8	17
$^4I_{11/2}$	1	918	959	982	129*	1.8	17
$^4F_{3/2}$	11	348				1.8	17

Sm:$Cs_2NaSmCl_6$

Term	Prefix	Energy (cm^{-1})		T	Ref.
$^6H_{5/2}$	-	0	162	4.2	9
$^6H_{7/2}$	1	044		4.2	9

Eu:$Cs_2NaEuCl_6$

Term	Prefix	Energy (cm^{-1})			T	Ref.
$^7F_0$	-	0			35	10
	-	0			4.2	18
$^7F_1$	-	360			35	10
	-	360			300	18
$^7F_2$	-	879	095*		35	10
	-	882	094*		4.2	4
$^7F_3$	1	903	964		35	10
	1	808	903	964	4.2	4
$^7F_4$	2	674	988	053*	77	19
$^5D_0$	17	220			300	18
	17	209			4.2	4
$^5D_1$	18	963			4.2	18
$^5D_2$	21	410	520		4.2	18
	21	389	500		4.2	4
$^5D_3$	24	277	310		77	19

Tb:$Cs_2NaTbCl_6$

Term	Prefix	Energy (cm^{-1})						T	Ref.
$^7F_6$	-	0	39	83	289	352	375	20	4
$^7F_5$	2	087	249	319	354			20	4
$^7F_4$	3	331	378	427	670			20	4
$^7F_3$	4	414	444	565				20	4
$^7F_2$	5	108	295					20	4
$^7F_1$	5	617						20	4
$^5D_4$	20	474	488	501	551			20	4
$^5D_3$	26	223	267	290				20	4

Dy:$Cs_2NaDyCl_6$

Term	Prefix	Energy (cm^{-1})			T	Ref.
$^6H_{15/2}$	-	0	183	346	45	9

Ho:$Cs_2NaHoCl_6$

Term	Prefix	Energy (cm^{-1})						T	Ref.
$^5I_8$	-	0	10	40	200	242	268	4.2	13
$^5I_7$	5	118	118	225	245	268		4.2	13
$^5F_5$	15	357	401	528	556			4.2	13
$^5F_4$, $^5S_2$	18	501	516	521	556			4.2	13

Er:$Cs_2NaErCl_6$

Term	Prefix	Energy (cm^{-1})				T	Ref.
$^4I_{15/2}$	-	0	56			35	9
$^4I_{13/2}$	6	462	491	517	627	5	14
$^4I_{11/2}$	10	160				5	14
$^4F_{9/2}$	15	200	326			5	14
$^2H_{11/2}$	18	968	011*	188	248	5	14
$^4F_{7/2}$	20	387				5	14

Tm: $Cs_2NaTmCl_6$

Term	Prefix	Energy (cm^{-1})			T	Ref.
$^3H_6$	-	0	108	147	30	9
	-	0	55	110	4.2	15
$^3F_4$	12	505	575	860	4.2	15
$^3F_3$	14	423	449		4.2	15
$^3F_2$	15	122			4.2	15
$^1G_4$	20	840	348*	500	4.2	15
$^1D_2$	27	700			4.2	15

Yb: $Cs_2NaYbCl_6$

Term	Prefix	Energy (cm^{-1})			T	Ref.
$^2F_{7/2}$	-	0	225	573	55	9
$^2F_{5/2}$	10	243	708		4.2	20

References for 5.25. Ca_2NaRCl_6

1. Morss, L.R., M. Siegel, L. Stenger and N. Edelstein, 1970, Inorg. Chem. **9**, 1771.
2. Aleonard, P.S. and C. Pouzet, 1968, J. Appl. Cryst. **1**, 113.
3. Amberger, H.-D., G.G. Rosenbauer and R.D. Fischer, 1976, Mol. Phys. **32**, 1291.
4. Morrison, C.A., R.P. Leavitt and D.E. Wortman, 1980, J. Chem. Phys. **73**, 2580, and references therein.
5. Amberger, H.-D., 1978, Z. Anorg. Allg. Chem. **439**, 48.
6. Amberger, H.-D., R.D. Fischer and G.G. Rosenbauer, 1975, Ber. Bunsenges Physik. Chem. **79**, 1226.
7. Cheng, C. and P.B. Dorain, 1976, J. Chem. Phys. **65**, 785.
8. Schwartz, R.W., 1976, Mol. Phys. **31**, 1909.
9. Amberger, H.-D., G.G. Rosenbauer and R.D. Fischer, 1977, J. Phys. Chem. Solids, **38**, 379.
10. Amberger, H.-D., R.D. Fischer and G.G. Rosenbauer, 1976, Z. Phys. Chem. N. F. **102**, 279.
11. Schwartz, R.W., H.G. Brittain, J.P. Riehl, W. Yeakel and F.S. Richardson, 1977, Mol. Phys. **34**, 361.
12. Thompson, L.C., O.A. Serra, J.P. Riehl, F.S. Richardson and R.W. Schwartz, 1977, Chem. Phys. **26**, 393.
13. Morley, J.P., T.R. Faulkner, F.S. Richardson and R.W. Schwartz, 1981, J. Chem. Phys. **75**, 539.
14. Jezowska-Trzebiatowska, B., W. Ryba-Romanowski, Z. Mazurak and J. Hanuza, 1980, Chem. Phys. **50**, 209.
15. Schwartz, R.W., T.R. Faulkner and F.S. Richardson, 1979, Mol. Phys. **38**, 1767.
16. Kanellakopulos, B., H.-D. Amberger, G.G. Rosenbauer and R.D. Fischer, 1977, J. Inorg. Nucl. Chem. **39**, 607.
17. Tofield, B.C. and H.P. Weber, 1974, Phys. Rev. **B10**, 4560.
18. Schwartz, R.W., 1975, Mol. Phys. **30**, 81.
19. Amberger, H.-D., 1978, Z. Phys. Chem. N.F. **109**, 125.
20. Schwartz, R.W., 1977, Inorg. Chem. **16**, 1694.

5.26. $R(C_2H_5SO_4)_3 \cdot 9H_2O$

The optical spectra of rare-earth ethyl sulfates are among the most thoroughly studied of those of any host material. Yttrium ethyl sulfate (YES) has been used as an important host for rare-earth ions and as a hydrogen ion polarization refrigerator (Jeffries, 1963; Abragam, 1963). The theory of hydrogen spin polarization refrigerators using R:YES has been given by McColl and Jeffries (1970), and more recent experimental results have achieved as high as 65% polarization with only 0.02 at% Yb (Button-Shafer et al., 1977).

The first resolved hyperfine structure in a solid was obtained for Ho^{3+} in HoES by Grohmann et al. (1961). A detailed analysis of this hyperfine structure was given by Hüfner (1963). The now more conventional method of measuring the hyperfine structure has been reported by Seidel et al. (1967) on Er in ErES. The laser excited fluorescence of Er^{3+} in ErES has been reported by Kato et al. (1979); they find a consistent shift of the fluorescence and absorption-line positions. The Zeeman effect has been measured on a large number of rare-earth ethyl sulfates; examples of the results of these measurements are given by Friederich et al. (1960) and Wheeler and Hill (1966). The change in the covalency of R with the surrounding ions has been measured by Wong et al. (1963) by comparing the optical spectra for Pr^{3+} in LaES, Pr^{3+} in $Y_3Al_5O_{12}$ and Pr^{3+} in LaF_3. The index of refraction for EuES was measured by LaFrance (1970); his result is given in terms of a Sellmeier equation:

$$n_{e,o}^2 = 1 + D_{e,o}\lambda^2/(\lambda^2 - B_{e,o})$$

with $D_{e,o} = 1.1489$, 1.1846 and $B_{e,o} = 0.010090$, 0.010115 for the extraordinary and ordinary rays, respectively, and λ is in μm.

Optical techniques have been used by Moore (1976) to measure the relaxation rates of Nd^{3+}, Sm^{3+}, and Er^{3+} in the corresponding RES. Moore also gives a detailed theoretical analysis of his result. Optical methods have also been used to measure the cross relaxation of Pr:ErES, Ce:NdES, and Pr:SmES by Moore and Satten (1973).

A rather complete analysis of the magnetic susceptibility and specific heat for Kramers rare-earth ions and Pr in RES has been given by Meijer (1978). In his calculation, Meijer uses the Luttinger-Tisza (1946) approximation and predicts that all the compounds will be antiferromagnetic at low temperatures.

An exhaustive survey of the results of electron spin resonance on RES up through the year 1969 has been given by Abragam and Bleaney (1970), so we shall only present a sample of the more recent work. The zero field splitting of Gd^{3+} in RES has been given for the entire rare-earth series (with the exception of Pm) by Viswanathan and Wong (1968); a similar measurement has been reported for a number of rare-earth ions by Smith et al. (1977). Accurate electron spin-resonance measurements have been made on Gd^{3+} in rare-earth ethyl sulfates by Gerkin et al. (1977) and Gerkin and Rogers (1979). One of the outstanding features of these workers' results is the explicit presentation of the zero field energy levels. The spin–lattice relaxation of Er^{3+} in ErES has been

reported by Tromp and Van Duyneveldt (1969). An excellent application of the Judd–Ofelt theory of transition probabilities for EuES has been given by Axe (1963); both magnetic and electric dipole transitions are taken into account. A similar analysis of the optical spectra of Tm^{3+} in TmES has been given by Krupke (1966b).

5.26.1 Crystallographic data for RES

Hexagonal $P6_3/m$, #176, Z = 2

Ion	Pos.	Symm.	x	y	z
R	2(c)	C_{3h}	1/3	2/3	1/4
S	6(h)	C_s	x	y	3/4
O_1	6(h)	C_s	x	y	3/4
O_2	6(h)	C_s	x	y	3/4
O_3	12(i)	C_1	x	y	z
O_4	6(h)	C_s	x	y	1/4
O_5	12(i)	C_1	x	y	z
C_1	6(h)	C_s	x	y	3/4
C_2	6(h)	C_s	x	y	3/4
H_{1A}	6(h)	C_s	x	y	3/4
H_{1B}	12(i)	C_1	x	y	z
H_2	12(i)	C_1	x	y	z
H_4	12(i)	C_1	x	y	z
H_{5A}	12(i)	C_1	x	y	z
H_{5B}	12(i)	C_1	x	y	z

X-ray data

R	a	c	Ref.
La	14.080	7.11	1
Ce	14.048	7.11	1
Pr	14.007	7.09	1

Crystallographic data for RES (continued)

R	a	c	Ref.
Nd	13.992	7.07	1
Sm	13.961	7.08	1
Gd	13.931	7.06	1
Dy	13.906	7.04	1
Er	13.915	7.11	1
Yb	13.924	7.057	1
Y	13.871	7.007	2

	S		O_1		O_2		O_3			
R	x	y	x	y	x	y	x	y	z	Ref.
Y	0.3163	0.3682	0.2464	0.4185	0.2293	0.2407	0.3827	0.3918	0.5777	2

	O_4		O_5			C_1		C_2		
R	x	y	x	y	z	x	y	x	y	Ref.
Y	0.3525	0.4955	0.2130	0.5457	0.4891	0.1807	0.0489	0.2738	0.1656	2

	H_{1A}		H_{1B}			H_2			
R	x	y	x	y	z	x	y	z	Ref.
Y	0.0088	0.2208	0.1303	0.0324	0.6299	0.3232	0.1821	0.6251	2

	H_4			H_{5A}			H_{5B}			
R	x	y	z	x	y	z	x	y	z	Ref.
Y	0.3638	0.4610	0.1397	0.1354	0.4965	0.4662	0.2367	0.5079	0.5763	2

5.26.2 Crystal-field parameters for R:RES (cm^{-1})

R	B_{20}	B_{40}	B_{60}	B_{66}	Ref.
Ce	18	-336	-720	716	3
Pr	46	-640	-704	732	4
Pr	31	-706	-778	578	5
Nd	120	-552	-800	632	4
Nd	117	-568	-683	626	6
Sm	156	-424	-	-	4
Sm	120	-509	-640	605	7
Sm	154	-385	-624	580	8
Eu	160	-505	-617	537	9
Gd	200	-552	-544	523	10
Tb	220	-598	-544	490	4
Dy	248	-632	-496	518	4
Dy	288	-681	-531	564	7
Dy	238	-210	-500	498	8
Ho	250	-630	-478	412	4
Er	252	-650	-496	407	11
Er	237.6	-591	-486	396	7
Tm	26	-640	-512	316	12
Tm	260	-568	-457	456	13
Yb	310	-464	-416	498	14

5.26.3 Intensity parameters for R:RES (10^{-20} cm^2)

R	Ω_2	Ω_4	Ω_6	Ref.
Eu	0.147	0.210	-	15
Tm	0.593	2.248	1.251	16

5.26.4 Energy levels for R:RES

PrES

Term	Prefix	Energy (cm^{-1})				T	Ref.
$^3H_4$	-	0	12.2	(175)	(181)	77	5
		0	11.91			4.2	17
$^3F_3$	6	310.4	330.7	382.6		77	5
$^3F_4$	6	830.8	862.8	872.0	896.0	77	5
$^1G_4$	9	793.6	811.0	862.8		77	5
$^1D_2$	16	709.3	857.7	955.0		4.2	17
$^3P_0$	20	687.0				4.2	17
$^3P_1$	21	281.1	290.6			77	5
	21	276.05	289.55			4.2	17
$^1I_6$	21	398.5	407.6	447.4	456.2	4.2	17
$^3P_2$	22	424.8	440.5	447.6		4.2	17

NdES

Term	Prefix	Energy (cm^{-1})						T	Ref.
$^4I_{9/2}$	-	0	149.64	154	279	311		4.2	18,6
$^4F_{3/2}$	11	534.40	553.61					4.2	18
	11	536.3	555.9					4.2	4
$^4F_{5/2}$, $^2H_{9/2}$	12	566.20	592.42	609.60	756.15	763.81		4.2	18
$^4F_{7/2}$	13	492.18	502.51	582.55	599.40			4.2	18
$^4S_{3/2}$	13	631.99	635.53					4.2	18
$^4F_{9/2}$	14	791.0	816.21	832.99	857.0			4.2	18
$^2H_{11/2}$	15	954.27	030.74*	052.79*				4.2	18
$^4G_{5/2}$	17	249.94	385.62	392.60				4.2	18
$^2G_{7/2}$	17	429.83	447.97					4.2	18
$^4G_{7/2}$	19	125.06	184.85	221.20				4.2	18
$^2G_{9/2}$	19	567.15	590.21	606.19	655.12	662.17	673.89	4.2	18
	19	685.84						4.2	18
$^4G_{9/2}$, $^2D_{3/2}$, $^4G_{11/2}$	21	135.04	164.47	273.55	289.80	300.27	390.26	4.2	18
	21	402.41	442.98	514.08	640.38	661.90	751.37	4.2	18
$^2P_{1/2}$, $^2D_{5/2}$	23	359.71	892.44	910.69				4.2	18
$^2P_{3/2}$	26	268.75	293.64					4.2	18
$^4D_{3/2}$	28	224.15	231.04					4.2	18

SmES

Term	Prefix	Energy (cm^{-1})						T	Ref.
$^6H_{5/2}$	-	0	53.8	63.6				80	19
$^6F_{9/2}$	9	104.28	112.56	153.67	178.75			4.2	20
$^6F_{11/2}$	10	505.8	515.74	531.83	534.2	540.17	545.94	4.2	21
$^4G_{5/2}$	17	877.03	878.77					4.2	19
$^4G_{7/2}$	20	018.70	025.59	039.17	101.90			4.2	19
$^6P_{5/2}$	23	990.9	026.7*	039.2				4.2	19
$^6P_{3/2}$, $^4L_{13/2}$	24	546.7	557	561.4	566	571.8	590.6	4.2	19
$^4F_{9/2}$	24	875.4	881.6	888.4	916.4	930.6		4.2	19
$^4K_{11/2}$	26	629.2	644	648.5	651.4	667	672.9	4.2	19
	26	675.1	718.0	725.2	737.0	746.3		4.2	19

EuES

Term	Prefix	Energy (cm^{-1})						T	Ref.
$^7F_0$	-	0						294	22
$^7F_1$	-	361.38	394.06					294	22
$^5D_0$	17	264.64						294	22
$^5D_1$	19	024.58	028.47					294	22
$^5D_2$	21	501.46	518.20					294	22
$^5L_6$	25	156	161	189	198	217	270	?	18
	25	295	321	334	354	366	399	?	18
	25	405	430	445				?	18
$^5L_7$, $^5G_2$	26	173	537	611	623	646	660	?	18
	26	687	690	701	706	759		?	18
$^5L_8$	27	111	212					?	18
$^5D_4$	27	593	617	617	650			?	18
$^5L_9$	27	860	892	924				?	18
$^5L_{10}$	28	370	388	510				?	18
$^5H_3$, $^5H_7$	31	091	251	277	301			?	18
$^5H_4$	31	454	461	491	498	514	516	?	18
	31	527	542					?	18
?	33	067	119	183	393	410	419	?	18
	33	454	461	498				?	18

EuES (continued)

Term	Prefix	Energy (cm^{-1})						T	Ref.
?	33	522	531	527	566	608		?	18
?	33	964	025*	028	051	088	104	?	18
	33	140						?	18
?	34	382	397	433				?	18
?	34	921	985	004*	012	036		?	18
?	36	153						?	18
?	37	350.48	354.76	395.93				100	23
?	38	028.61	037.27					100	23
?	38	632.90	723.27					100	23
?	38	921.95	994.73	010.67*				100	23

GdES

Term	Prefix	Energy (cm^{-1})					T	Ref.
$^8S_{7/2}$	-	0					1.7	18
$^6P_{7/2}$	32	136.07	153.85	163.63	164.56		1.7	18
$^6P_{5/2}$	32	727.73	757.85	760.18			1.7	18
$^6I_{7/2}$	35	873.99	881.34	897.87	901.00		1.7	18

TbES

Term	Prefix	Energy (cm^{-1})						T	Ref.
$^7F_6$	-	0	88.20	94.73	98.35	101.43	111.59	?	18
	-	121.95	126.44	131.48				?	18
$^5D_4$	20	507.03	507.83	521.05	523.06	525.37	547.09	4.2	18,24
$^5D_3$	26	309.93	316.28	327.05				?	18
$^5L_{10}$	26	426.96	435.84	462.39	464.85	467.15	470.96	?	18
	26	483.03	541.86	565.89	997.07	033.34*	060.30	?	18
	26	128.03	131.74	166.69	175.10	834.97	845.28	?	18
	26	851.20	884.91	897.35				4.2	18,24
$^5D_2$	28	212.07						?	18

TbES (continued)

Term	Prefix	Energy (cm^{-1})						T	Ref.
?	28	341.23	368.56	483.85	501.74	544.40	560.47	?	18
	28	594.41	035.55*					?	18
?	29	234.66	246.97	324.56	330.08	361.32	460.60	?	18
	29	472.99	553.81					?	18
?	31	447.03	468.00	532.73	540.00			?	18
?	32	956.90	974.64	981.97	038.45*	079.55		?	18

DyES

Term	Prefix	Energy (cm^{-1})						T	Ref.
$^6H_{15/2}$	-	0	16.03	21.20	58.9	68.1		4.2	18,20
$^6F_{9/2}$, $^6H_{7/2}$	8	955.94	007.47*	024.32	036.73	099.13		4.2	20
$^6H_{5/2}$	10	160.02	182.51					4.2	20
$^6F_{7/2}$	10	976.36	030.92					4.2	20
$^6F_{5/2}$	12	365.61	374.56	408.43				4.2	20
$^6F_{3/2}$	13	175.44	180.25					4.2	20
$^6F_{1/2}$	13	729.26						4.2	20
$^4F_{9/2}$	20	969.7	119.0*	122.2	128.0	135.0	205.2	58	25
$^4I_{15/2}$	22	035.5	062.9	106.3	122.2	159	175	4.2	25
	22	203	237					4.2	25
$^4G_{11/2}$	23	391.04	429.20	439.45	461.77	467.54	485.49	4.2	25
?	24	982.1	986.7	996.5	053.3*	055.4	138.3	58	25
	24	158.3	302					58	25
?	25	644.9	658.9	666.0	684.8	687.2	698.2	58	18
	25	708.4	714.7	731.0	748.7	778.4		58	18

HoES

Term	Prefix	Energy (cm^{-1})						T	Ref.
$^5I_8$	-	0	6.01	47.04	76.4	101.3	117.6	58	26,27
$^5I_5$	11	230.9	233	234	235.2	260.2	282.7	58	27
	11	295						58	27
$^5I_4$	13	292.5	298.7	314.7	392			58	27
$^5F_5$	15	517.61	530.14	534.08	550.38	559.23	606.59	4.2	26

HoES (continued)

Term	Prefix	Energy (cm^{-1})						T	Ref.
$^5S_2$	18	497.68	501.85					4.2	26
$^5F_4$	18	590.78	610.71	631.79	653.08	683.02		4.2	26
$^5F_3$	20	657.17	666.29	669	719.41	719.68		4.2	26
$^5F_2$	21	145.61	153.25	160.2				4.2	26
$^3K_8$	21	362.45	373.53	391.71	397.63	403.17	424.71	4.2	26
	21	434.09	440.34	443.32	465.49	465.79		4.2	26
$^5G_6$	22	193.85						4.2	26
$^5G_5$	24	020.4	037.7	044.0	063.7	085.0	108.8	4.2	18
$^5G_4$	25	883.0	934.2	940.6	961.4	026.4*		4.2	18
$^3K_7$	26	193.6	194.8	200.7	203.6	210.9	212.9	4.2	18
	26	215.1	224.0	230.3				4.2	18
$^3H_5$	27	688.0	717.5	726.5	731.5	733.5	757.7	4.2	18
$^5G_2$	27	817.2	823.1					4.2	18
$^5G_3$, $^3L_9$, $^3H_6$	28	292.5	319.4	898.1	913.9	933.5	950.5	4.2	18
	28	976.5	979.8	987.6	991.8	014.8*	021.9	4.2	18
	28	039.5	046.1	053.7	058.7	083.5		4.2	18
$^3K_6$	29	970.3	990.3	996.1	028.2*	059.2	078.0	4.2	18
$^3F_4$	30	135.1	138.8	141.0				4.2	18
$^3D_2$	30	868.8						4.2	18

ErES

Term	Prefix	Energy (cm^{-1})						T	Ref.
$^4I_{15/2}$	-	0	43.8	74.6	110.7	173.0		85	28
	-	0	44.0	74.7	110.7	172.5	215.0	77	11
	-	255.2	304.0					77	11
$^4I_{11/2}$	10	099.08	099.98	101.01	102.71	125.35	150.07	77	11
$^4I_{9/2}$	12	426.2	439.9	525.0	540.2	637.7		77	11
$^4F_{9/2}$	15	307.24	339.83	346.9	377.70	402.1		4.2	28
	15	306.0	339.4	348.5	377.2	401.6		77	11
$^4S_{3/2}$	18	460.72	488.34					4.2	28
	18	461.1	487.1					77	11
$^2H_{11/2}$	19	169.0	199.4	218.56	245.75	258.23	288.90	4.2	28
	19	169.3	217.1	226.7	245.7	258.4	289.3	77	11

ErES (continued)

Term	Prefix	Energy (cm^{-1})						T	Ref.
$^4F_{7/2}$	20	555.6	586.91	596.4	650.32			4.2	28
	20	556.4	588.1	623.0	651.1			77	11
$^4F_{5/2}$	22	256.04	268.7	280.35				4.2	28
	22	255.8	270.7	280.1				77	11
$^4F_{3/2}$	22	586.06	635.77					4.2	28
	22	584.8	631.6					77	11
$^2G_{9/2}$	24	573.05	581.82	658.5	688.93			4.2	28
	24	581.9	604.1	661.1	687.1	779.3		77	11
$^4G_{11/2}$	26	436.5	472.4	481.7	512.1	517.9	553.1	77	11

TmES

Term	Prefix	Energy (cm^{-1})						T	Ref.
$^3H_6$	-	0.0	32.0	(101)	(108)	111.5	134	?	18
	-	176.31	273.4	304				?	18
$^3F_4$	12	(561)	586	649	704	720	763	77	18,12
	12	585.77	648.67	704.44	720.00	763.32		4.2	29
$^3F_3$	14	407	466	486	487	(491)		77	18,12
	14	406.58	466.00	485.74	487.37			4.2	29
$^3F_2$	15	079	106	(144)				77	18,12
	15	078.80	106.14					4.2	29
$^1G_4$	21	168	191	255	279	341	379	77	18,12
	21	170.62	194.00	279.45	343.46	381.34		4.2	29
$^1D_2$	27	876	900	971				77	18,12
$^1I_6$	34	843.6	870.0	899.7				?	18
$^3P_0$	35	436.9						?	18
$^3P_1$	36	400.9						?	18
$^3P_2$	38	060	144.9	184.9				77	18,12

YbES

Term	Prefix	Energy (cm^{-1})				T	Ref.
$^2F_{7/2}$	-	0	42			77	18,30
	-	0	44	108	265	?	14
$^2F_{5/2}$	10	202.5	260.6			77	18,30
	10	200.9	258.3			?	14

References for 5.26. $R(C_2H_5SO_4)_3 \cdot 9H_2O$

1. Wyckoff, R.W.G., 1966, Crystal Structures, Vol. 5 (Wiley, New York) pp. 290 ff.
2. Broach, R.W., J.M. Williams, G.P. Felcher and D.G. Hinks, 1979, Acta Cryst. **B35**, 2317.
3. Birgenau, R.J., 1967, Phys. Rev. Lett. **19**, 160.
4. Hüfner, S., 1962, Z. Phys. **169**, 417.
5. Gruber, J.B., 1963, J. Chem. Phys. **38**, 946.
6. Gruber, J.B. and R.A. Satten, 1963, J. Chem. Phys. **39**, 1455.
7. Hill, J.C. and R.G. Wheeler, 1966, Phys. Rev. **152**, 482.
8. Powell, M.J.D. and R. Orbach, 1961, Proc. Phys. Soc. (London) **78**, 753 (as reported by Dieke, Ref. 18, p. 149).
9. Judd, B.R., 1959, Mol. Phys. **2**, 407.
10. Wybourne, B.G., 1966, Phys. Rev. **148**, 317.
11. Erath, E.H., 1961, J. Chem. Phys. **34**, 1985.
12. Gruber, J.B., and J.G. Conway, 1960, J. Chem. Phys. **32**, 1531; **32**, 1178.
13. Wong, E.Y. and I. Richman, 1961, J. Chem. Phys. **34**, 1182.
14. Wheeler, R.G., F.M. Reames and E.J. Wachtel, 1968, J. Appl. Phys. **39**, 915.
15. Axe, J.D., Jr., 1963, J. Chem. Phys. **39**, 1154.
16. Krupke, W.F., 1966, Ph.D. Thesis, University of California, Los Angeles (Univ. Microfilms 66-11 930).
17. Hellwege, K.H., G. Hess and H.G. Kahle, 1960, Z. Phys. **159**, 333.
18. Dieke, G.H., 1968, Spectra and Energy Levels of Rare Earth Ions in Crystals (Interscience, New York) pp. 202, 243, 250, 254, 269, 280, 310, 313.
19. Lämmermann, H., 1958, Z. Phys. **150**, 551.
20. Hellwege, K.H., G. Horstik, S. Hüfner and H. Lämmermann, 1961, Z. Phys. **165**, 253, 259 (two consecutive papers).
21. Lämmermann, H., 1960, Z. Phys. **160**, 355.
22. Hellwege, K.H., U. Johnsen, H.G. Kahle and G. Schaack, 1957, Z. Phys. **148**, 112.
23. Hellwege, K.H., S. Hüfner and A. Pöcker, 1963, Z. Phys. **172**, 453.
24. Kahle, H.G. and H. Kalbfleisch, 1962, Z. Phys. **166**, 184.
25. Gramberg, G., 1960, Z. Phys. **159**, 125.
26. Grohmann, I., K.H. Hellwege and H.G. Kahle, 1960, Z. Phys. **160**, 149.
27. Hellwege, K.H., S. Hüfner and D. Kuse, 1961, Z. Phys. **164**, 243.
28. Hellwege, K.H., S. Hüfner and H.G. Kahle, 1960, Z. Phys. **160**, 149.
29. Johnsen, U., 1958, Z. Phys. **152**, 454.
30. Wong, E.Y., 1963, J. Chem. Phys. **39**, 2781.

Acknowledgements

We owe special thanks to J.B. Gruber, who provided us continual guidance from the conception of this chapter and who also provided us with a great deal of unpublished data on several of the host materials considered here. We thank B.R. Judd and the Physics Department of the Johns Hopkins University for their hospitality, for several stimulating discussions, and for giving us access to much of the early unpublished data recorded by G.H. Dieke and his graduate students at Johns Hopkins. The following individuals provided us with a substantial amount of unpublished data, results prior to publication, and useful information: W.T. Carnall, P. Caro, L.G. DeShazer, and H.P. Jenssen. We also received unpublished data and results prior to publication from H.-D. Amberger, N.C. Chang, H.P. Christiansen, J. Dexpert-Ghys, K.H. Hellwege, H.G. Kahle, V. Nekvasil, P. Porcher, F.S. Richardson, and F.H. Spedding. This work was

influenced to a great extent by discussions and correspondence with H. Crosswhite, L. Esterowitz, F. Gaume, C.K. Jørgensen, M. Kibler, R. Reisfeld, and W. Urland, as well as with our colleagues at Harry Diamond Laboratories (past and present), including E.A. Brown, F.J. Crowne, R.T. Farrar, S.M. Kulpa, J. Nemarich, J.P. Sattler, and W. Viehmann. This chapter would have been impossible without our fruitful collaborations over the years, in particular with D.E. Wortman and N. Karayianis at HDL, and also with R.E. Allen, F.J. Bartoli, N.C. Chang, L. Esterowitz, J.B. Gruber, H.P. Jenssen, and A. Linz. We have received much support in this work (both financial and moral) from Harry Diamond Laboratories (W.W. Carter and H. Sommer), Night Vision and Electro-Optics Laboratories (R.G. Buser), and the Office of Naval Research (V. Nicolai). Finally we thank Jessica Putnam for her excellent typing of the manuscript, and J. Soln for a critical reading and useful comments.

References

Abragam, A., 1963, Cryogenics **3**, 42.
Abragam, A. and B. Bleaney, 1970, Electron Paramagnetic Resonance of Transition Ions (Oxford University).
Adam, J.D., J.H. Collins and D.B. Cruikshank 1975, in: Magnetism and Magnetic Materials (AIP Conference Proceedings No. 29), p. 643.
Afanasiev, M.L., S.P. Habuda and A.G. Lundin, 1972, Acta Cryst. **B28**, 2903.
Al'tshuler, S.A., F.L. Aukhadeev, I.I. Valeev, I.S. Konov, B.Z. Malkin and M.A. Teplov, 1972, JETP Lett. **16**, 164.
Alves, R.V., R.A. Buchanan, K.A. Wickersheim and E.A.C. Yates, 1971, J. Appl. Phys. **42**, 3043.
Amiryan, A.M., A.M. Gurvich, R.V. Katomina, I.Yu. Petrova, N.P. Soshchin and M.I. Tombak, 1977, J. Appl. Spectrosc. **27**, 1159.
Angelov, B.M., 1979, J. Phys. **C12**, L691.
Armbruster, A., 1976, J. Phys. Chem. Solids **37**, 321.
Arsenev, P.A., 1970, Ukr. Fiz. Zh. (Russ. Ed.) **15**, 689.
Arutyunyan, E.A. and V.S. Mkrtchyan, 1975, Sov. J. Quantum Electron. **5**, 450.
Ashkin, A., G.D. Boyd, J.M. Dziedzic, R.G. Smith, A.A. Ballman, H.J. Levinstein and K. Nassau, 1966, Appl. Phys. Lett. **9**, 72.
Ashurov, M.Kh., Yu.K. Voronko, V.V. Osiko, A.A. Sobol, B.P. Starikov, M.I. Timoshechkin and A.Ya. Yablonskii, 1976, Phys. Stat. Sol. (a) **35**, 645.
Ashurov, M.Kh., T.T. Basiev, Yu.K. Voronko, E.V. Zharikov, V.I. Zhekov, T.M. Murina, V.V. Osiko, M.I. Timoshechkin and I.A. Scherbakov, 1978, Sov. J. Quantum Electron. **8**, 588.
Axe, J.D., Jr., 1963, J. Chem. Phys. **39**, 1154.
Bagdasarov, Kh.S. and A.A. Kaminskii, 1969, JETP Lett. **9**, 303.
Bagdasarov, Kh.S., A.A. Kaminskii and G.I. Rogov, 1969, Sov. Phys. Dokl. **14**, 346.
Ball, M., M.J.M. Leask, W.P. Wolf and A.F.G. Wyatt, 1963, J. Appl. Phys. **34**, 1104.
Barker, A.S., 1964, Phys. Rev. **135**, A742.
Barnes, R.G. 1979, in: Gschneidner, K.A., Jr. and L. Eyring, Eds., Handbook on the Physics and Chemistry of Rare Earths (North-Holland, Amsterdam), Vol. 2, p. 387.
Bass, M., L.G. DeShazer and P.P. Yaney, 1976, University of Southern California Technical Report ECOM-74-0104-F (NTIS #029 916).
Battison, J.E., A. Kasten, M.J.M. Leask and J.B. Lowry, 1977, J. Phys. **C10**, 323.
Bauman, R.P. and S.P.S. Porto, 1967, Phys. Rev. **161**, 842.
Becquerel, J., 1906, C. R. Acad. Sci. **142**, 775.
Becquerel, J., 1908, Phys. Z. **8**, 632.
Belabaev, K.G., A.A. Kaminskii and S.E. Sarkisov, 1975, Phys. Stat. Sol. (a) **28**, K17.
Bethe, H., 1929, Ann. Phys. (Leipzig) **3**, 133.
Bethe, H., 1930, Z. Phys. **60**, 218.
Biederbick, R., A. Hofstaetter and A. Scharmann, 1978, J. Phys. **C11**, L593.
Bishton, S.S. and D.J. Newman, 1970, J. Phys. **C3**, L753.
Blanc, J., D. Brochier and A. Ribeyron, 1970, Phys. Lett. **33A**, 201.
Blanchfield, P. and G.A. Saunders, 1972, J. Phys. **C12**, 4673.
Bloor, D. and J.R. Dean, 1972, J. Phys. **C5**, 1237.
Boccara, A.C. and B. Briat, 1969, J. Phys. (Paris) **30**, 445.
Bogomolova, G.A., L.A. Bumagina, A.A. Kaminskii and B.Z. Malkin, 1977, Sov. Phys. Solid State **19**, 1428.
Bogoroditskii, N.P., V.V. Pasynkov, R.R. Basili and Yu.M. Volokobinskii, 1965, Sov. Phys. Dokl. **10**, 85.

Bonrath, H., K.H. Hellwege, K. Nicolay and G. Weber, 1966a, Phys. Kondens. Materie **4**, 382.
Bonrath, H., K.H. Hellwege, S. Hüfner, M. Schinkmann, H. Schuchert and G. Weber, 1966b, Phys. Kondens. Materie **4**, 391.
Borzenkova, M.P., G.N. Kuznetsova and A.V. Novoselova, 1971, Izv. Acad. Nauk SSSR, Neorg. Mater. **7**, 242.
Bradbury, M.I. and D.J. Newman, 1967, Chem. Phys. Lett. **1**, 44.
Brandle, C.D. and R.L. Barns, 1974, J. Crystal Growth **26**, 169.
Brandle, C.D., D.C. Miller and J.W. Nielsen, 1972, J. Crystal Growth **12**, 195.
Breit, G., 1930, Phys. Rev. **36**, 383.
Brown, E.A., J. Nemarich, N. Karayianis and C.A. Morrison, 1970, Phys. Lett. **33A**, 375.
Brown, M.R. and W.A. Shand, 1969, J. Phys. **C2**, 1908.
Brown, M.R., K.J. Roots and W.A. Shand, 1969, Signals Research and Development Establishment Ministry of Technology Report No. 69027 (NTIS #702 008).
Burns, G., 1962, Phys. Rev. **128**, 2121.
Burns, G., 1965, J. Chem. Phys. **42**, 377.
Burns, G., 1977, Introduction to Group Theory with Applications (Academic Press, New York), pp. 264 ff.
Burns, G., D.F. O'Kane and R.S. Title, 1966, Phys. Lett. **23**, 56.
Button-Schafer, J., R.L. Lichti and W.H. Potter, 1977, Phys. Rev. Lett. **39**, 677.
Carlson, B.C. and G.S. Rushbrooke, 1950, Proc. Cambridge Phil. Soc. **46**, 626.
Carnall, W.T., 1979, in: Gschneidner, K.A., Jr. and L. Eyring, Eds., Handbook on the Physics and Chemistry of Rare Earths, Vol. 3 (North-Holland, Amsterdam) p. 171.
Carnall, W.T., H. Crosswhite, H.M. Crosswhite and J.G. Conway, 1976, J. Chem. Phys. **64**, 3582.
Carnall, W.T., H. Crosswhite and H.M. Crosswhite, 1978, Argonne National Laboratory Report ANL-78-XX-95.
Carnall, W.T., H. Crosswhite, H.M. Crosswhite, J.P. Hessler, N. Edelstein, J.G. Conway, G.V. Shalimoff and R. Sarup, 1980, J. Chem. Phys. **72**, 5089.
Caro, P., J. Derouet, L. Beaury and E. Soulie, 1979, J. Chem. Phys. **70**, 2542.
Chakrabarti, S.K., S.K. Sarkar and S. Sengupta, 1976, Phys. Stat. Sol. (b) **77**, 329.
Chang, N.C., 1963, J. Appl. Phys. **34**, 3500.
Cheetham, A.K., B.E.F. Fender, H. Fuess and A.F. Wright, 1976, Acta Cryst. **B32**, 94.
Chen, F.S., 1969, J. Appl. Phys. **40**, 3389.
Chesler, R.B. and J.E. Geusic, 1972, in: Arecchi, F.T. and E.O. Schultz-Dubois, Eds., Laser Handbook, Vol. 1 (North-Holland, Amsterdam) p. 395.
Chicklis, E.P., C.S. Naiman, R.C. Folweiler, D.R. Gabbe, H.P. Jenssen and A. Linz, 1971, Appl. Phys. Lett. **19**, 119.
Chicklis, E.P., C.S. Naiman, R.C. Folweiler and J.C. Doherty, 1972, IEEE J. Quantum Electron. **QE-8**, 225.
Chicklis, E.P., R.C. Folweiler, C.S. Naiman, A. Linz, H.P. Jenssen and D.R. Gabbe, 1973a, Sanders Associates Technical Report ECOM-0013-F (NTIS #755 530).
Chicklis, E.P., C.S. Naiman and I.D. Abella, 1973b, Sanders Associates Technical Report AFOSR-TR-73-1588 (NTIS #766 843).
Condon, E.U. and G.H. Shortley, 1959, The Theory of Atomic Spectra (Cambridge University Press, England).
Cone, R.L., 1972, J. Chem. Phys. **57**, 4893.
Cooke, A.H., K.A. Gehring, M.J.M. Leask, D. Smith and J.H.M. Thornley, 1965, Phys. Rev. Lett. **14**, 685.
Cresswell, P.J., D.J. Robbins and A.J. Thomson, 1978, J. Lumin. **17**, 311.
Crosswhite, H., H.M. Crosswhite and B.R. Judd, 1968, Phys. Rev. **174**, 89.
Crosswhite, H.M., 1977, Colloques Internationaux C.N.R.S. No. 255, p. 65.
Crosswhite, H.M., H. Crosswhite, F.W. Kaseta and R. Sarup, 1976, J. Chem. Phys. **64**, 1981.
Crosswhite, H.M., H. Crosswhite, N. Edelstein and K. Rajnak, 1977, J. Chem. Phys. **67**, 3002.
Dean, J.R. and D. Bloor, 1972, J. Phys. **C5**, 2921.
Delsart, C., N. Pelletier-Allard and R. Pelletier, 1977, Phys. Rev. **B16**, 154.
De Rango, C., G. Tsoucaris and C. Zelwer, 1966, C. R. Acad. Sci. Paris **C263**, 64.
De Sorbo, W., 1967, Phys. Rev. **158**, 839.
Devaney, P. and H.J. Stapleton, 1975, J. Chem. Phys. **63**, 5459.
Devor, D.P., B.H. Soffer and M. Robinson, 1971, Appl. Phys. Lett. **18**, 122.
Devor, D.P., R.C. Pastor, M. Robinson, W.M. Akutagawa and K. Arita, 1974, Hughes Research Laboratories Technical Report ECOM-74-0034-F (NTIS #001 557).
Dieke, G.H., 1968, Spectra and Energy Levels of Rare Earth Ions in Crystals (Interscience, New York).
Dieke, G.H. and H.M. Crosswhite, 1963, Appl. Opt. **2**, 675.
Dieke, G.H. and L. Heroux, 1956, Phys. Rev. **103**, 1227.
Dieke, G.H. and S. Singh, 1961, J. Chem. Phys. **35**, 555.
Dischler, B., J.R. Herrington, A. Räuber, J. Schneider and W. Urban, 1973, Solid State Commun. **12**, 737.
Dmitruk, M.V., V.I. Zhekov, A.M. Prokhorov and M.I. Timoshechkin, 1979, Inorg. Mater. (USSR) **15**, 976.
Dulepov, E.V., S.S. Batsanov and G.N. Kustova, 1972, Zh. Strukt. Khimii **13**, 935.
Dulepov, E.V., E.G., Ippolitov, S.S. Batsanov, N.S. Nikolaev and V.K. Chimirev, 1976, Russ. J. Inorg. Chem. **21**, 1780.
Dunlap, B.D. and G.K. Shenoy, 1975, Phys. Rev. **B12**, 2716.
Ehrlich, D.J., P.F. Moulton and R.M. Osgood, Jr., 1979, Opt. Lett. **4**, 184.
Ehrlich, D.J., P.F. Moulton and R.M. Osgood, Jr., 1980, Opt. Lett. **5**, 339.
Eisenstein, J.C., 1961, J. Chem. Phys. **35**, 2097.

Elliot, R.J. and K.W.H. Stevens, 1953, Proc. Phys. Soc. (London) **A218**, 553.
Erdös, P. and H. Kang, 1972, Phys. Rev. **B6**, 3393.
Eremin, M.V., I.N. Kurkin, O.I. Mar'yakhina and L.Ya. Shekun, 1970, Sov. Phys. Solid State **11**, 1697.
Erickson, L.E., 1977, Phys. Rev. **B16**, 4731.
Esterowitz, L. and E. Chicklis, 1968, Phys. Rev. **174**, 463.
Esterowitz, L., F.J. Bartoli, R.E. Allen, D.E. Wortman, C.A. Morrison and R.P. Leavitt, 1979a, Phys. Rev. **B19**, 6442.
Esterowitz, L., F.J. Bartoli, R.E. Allen, D.E. Wortman, C.A. Morrison and R.P. Leavitt, 1979b, Harry Diamond Laboratories Report TR-1875 (NTIS #067 845).
Ettinger, D.C. and T.M. Niemczyk, 1978, J. Chem. Phys. **68**, 872..
Evlanova, N.F., A.S. Kovalev, V.A. Koptsik, L.S. Kornienko, A.M. Prokhorov and L.N. Rashkovich, 1967, JETP Lett. **5**, 291.
Ewing, R.C., 1975, Amer. Mineral. **60**, 728.
Eyring, L., 1979, in: Gschneidner, K.A., Jr., and L. Eyring, Eds., Handbook on the Physics and Chemistry of Rare Earths, Vol. 3 (North-Holland, Amsterdam), p. 377.
Fakioglu, S. and S. Erkoc, 1978, Phys. Stat. Sol. (b) **89**, 289.
Faucher, M. and P. Caro, 1977, J. Chem. Phys. **66**, 1273.
Faucher, M., J. Dexpert-Ghys and P. Caro, 1980, Phys. Rev. **B21**, 3689.
Feldman, K., K. Hennig, I. Natkaniec, B.N. Sawenko and K. Tempelhoff, 1971, Phys. Stat. Sol. (b) **45**, K105.
Feldmann, K., K. Hennig, L.P. Kaun, B. Lippold, S. Matthies, W. Matz, B.N. Savenko and D. Welsch, 1975, Phys. Stat. Sol. (b) **70**, 71.
Felsteiner, J., 1970, J. Phys. **C3**, L174.
Flauhaut, I., 1968, in: Progress in the Technology of the Rare Earths, Vol. 3 (Pergamon, Oxford) p. 267.
Folinsbee, J.T., P.R. Tapster, D.R. Taylor, S. Mroczkowski and W.P. Wolf, 1977, Solid State Commun. **24**, 499.
Freed, S. and F.H. Spedding, 1929a, Nature **123**, 525.
Freed, S. and F.H. Spedding, 1929b, Phys. Rev. **34**, 1929.
Freed, S. and F.H. Spedding, 1931, Phys. Rev. **38**, 670.
Freeman, A.J. and R.E. Watson, 1962, Phys. Rev. **127**, 2058.
Fricke, W.C., 1973, Sanders Associates Final Report (NTIS #760 019).
Friederich, A., K.H. Hellwege and H. Lämmermann, 1960, Z. Phys. **158**, 251.
Furrer, R., J. Pelzl and S. Hüfner, 1971, Z. Phys. **247**, 267.
Gabbe, D. and A.L. Harmer, 1968, J. Crystal Growth **3**, 4, 544.
Gandrud, W.B. and H.W. Moos, 1968, J. Chem. Phys. **49**, 2170.
Garashina, L.S. and Yu.S. Vishnyakov, 1977, Sov. Phys. Crystallogr. **22**, 313.
Garton, G. and P.J. Walker, 1978, Mat. Res. Bull. **13**, 129.
Geller, S., 1978, Proc. Int. Sch. Phys. "Enrico Fermi" **70**, 1.
Geller, S., G.P. Espinosa and P.B. Crandall, 1969, J. Appl. Cryst. **2**, 86.
Gerkin, R.E. and W.J. Rogers, 1979, J. Chem. Phys. **70**, 3764.
Gerkin, R.E., W.J. Rogers and W.J. Tourek, 1977, J. Chem. Phys. **66**, 4166.
German, K.R., A. Kiel and H. Guggenheim, 1975, Phys. Rev. **B11**, 2436.
Glass, H.L. and L.A. Moudy, 1974, J. Appl. Cryst. **7**, 22.
Goldschmidt, Z.B., 1978, in: Gschneidner, K.A., Jr. and L.Eyring, Eds., Handbook on the Physics and Chemistry of Rare Earths, Vol. 1 (North-Holland, Amsterdam), p. 1.
Goldschmidt, Z.B., A. Pasternak and Z.H. Goldschmidt, 1970, Phys. Lett. **28A**, 265.
Grohmann, I., K.H. Hellwege and H.G. Kahle, 1961, Z. Phys. **164**, 243.
Gruber, J.B., E.A. Karlow, O.N. Olsen and U. Ranon, 1970, Phys. Rev. **B2**, 49.
Gruber, J.B., R.D. Chirico and E.F. Westrum, 1982, J. Chem. Phys. **76**, 4600.
Habenschuss, A. and F.H. Spedding, 1979, J. Chem. Phys. **70**, 2797.
Hamermesh, M., 1962, Group Theory and its Applications to Physical Problems (Addison-Wesley, Reading, Mass.).
Hammann, J., 1968a, J. Phys. (Paris) **29**, 495.
Hammann, J., 1968b, Phys. Lett. **26A**, 263.
Hammann, J. and P. Manneville, 1973, J. Phys. (Paris) **34**, 615.
Hammann, J. and M. Ocio, 1977, Physica **86–88B**, 1153.
Hansen, P.E., R. Nevald and H.G. Guggenheim, 1978, Phys. Rev. **B17**, 2866.
Haussühl, S. and D. Mateika, 1972, Z. Naturforsch. **27a**, 1522.
Heber, J., 1967, Phys. Kondens. Materie **6**, 381.
Heber, J., K.H. Hellwege, U. Kobler and H. Murmann, 1970, Z. Phys. **237**, 189.
Hegarty, J. and W.M. Yen, 1980, J. Appl. Phys. **51**, 3545.
Hellwege, K.H., 1949, Ann. Phys. (Leipzig) **4**, 95–160 (five consecutive papers); **4**, 357.
Hellwege, K.H., S. Hüfner, M. Schinkmann and H. Schmidt, 1964, Phys. Lett. **12**, 107.
Hellwege, K.H., J. Kötzler and G. Weber, 1968, Z. Phys. **217**, 373.
Hennig, K., S. Matthies and D.G. Welsch, 1974, Phys. Lett. **49A**, 447.
Henry, N.F.M. and K. Lonsdale, Eds., 1969, International Tables for X-Ray Crystallography, Vol. I. Symmetry Groups (Kynoch, Birmingham, England).
Henry, R.D. and J. SooHoo, 1977, Mat. Res. Bull. **12**, 727.
Hill, P. and S. Hüfner, 1970, Z. Phys. **240**, 168.
Hillmer, W., 1973, Phys. Stat. Sol. (b) **55**, 305.
Hodges, J.A., 1975, Phys. Stat. Sol. (b) **68**, K73.
Hoehn, M.V. and D.G. Karraker, 1974, J. Chem. Phys. **60**, 393.

Holloway, W.W., M. Kestigian, F.F.Y. Wang and G.F. Sullivan, 1966, J. Opt. Soc. Am. **56**, 1409.
Hoshina, T., 1969, J. Chem. Phys. **50**, 5158.
Hoskins, R.H. and B.H. Soffer, 1964, Appl. Phys. Lett. **4**, 22.
Hoskins, R.H. and B.H. Soffer, 1965, J. Appl. Phys. **36**, 323.
Hudson, P.R.W., 1976, J. Phys. **C9**, L39.
Hüfner, S., 1963, Z. Phys. **172**, 512.
Hüfner, S., 1978, Optical Spectra of Transparent Rare Earth Compounds (Academic, New York).
Hutchings, M.T. and D.K. Ray, 1963, Proc. Phys. Soc. (London) **81**, 663.
Hutchison, C.A. and S.S. Kim, 1979, Phys. Rev. **B19**, 4454.
Imbusch, G.F., W.M. Yen, A.L. Schawlow, D.E. McCumber and M.D. Sturge, 1964, Phys. Rev. **133**, A1029.
Ivanov, A.O., I.V. Mochalov, A.M. Tkachuk, V.A. Fedorov and P.P. Feofilov, 1974, Sov. J. Quantum Electron. **5**, 115.
Jeffries, C.D., 1963, Cryogenics **3**, 41.
Johnson, L.F., 1963, J. Appl. Phys. **34**, 897.
Johnson, L.F. and A.A. Ballman, 1969, J. Appl. Phys. **40**, 297.
Johnson, L.F., G.D. Boyd, K. Nassau and R.R. Soden, 1962, Proc. IRE **50**, 213.
Jones, H.D. and B.R. Judd, 1970, Phys. Rev. **B2**, 2319.
Judd, B.R., 1955, Proc. Phys. Soc. (London) **A227**, 552.
Judd, B.R., 1962, Phys. Rev. **127**, 750.
Judd, B.R., 1963, Operator Techniques in Atomic Spectroscopy (McGraw-Hill, New York).
Judd, B.R., 1966, Phys. Rev. **141**, 4.
Judd, B.R., 1969, Advan. Chem. Phys. **14**, 91.
Judd, B.R., 1976, Math. Proc. Camb. Phil. Soc. **80**, 535.
Judd, B.R., 1977, Phys. Rev. Lett. **39**, 242.
Judd, B.R., 1979, J. Lumin. **18/19**, 604.
Judd, B.R., 1980, J. Phys. **C13**, 2695.
Judd, B.R., H.M. Crosswhite and H. Crosswhite, 1968, Phys. Rev. **169**, 130.
Justice, B.H. and E.F. Westrum, Jr., 1963, J. Phys. Chem. **67**, 339.
Kaminskii, A.A., 1970, Phys. Stat. Sol. (a) **1**, 573.
Kaminskii, A.A., 1978, in: DiBartoli, B., Ed., Luminescence of Inorganic Solids (Plenum, New York), p. 511.
Kaminskii, A.A., 1981, Laser Crystals (Springer-Verlag, New York).
Kaminskii, A.A., G.A. Bogomolova and L. Li, 1969, Neorg. Mater. **5**, 673.
Kaminskii, A.A., G.A. Bogomolova and A.M. Kevorkov, 1975, Inorg. Mater. (USSR) **11**, 757.
Kaminskii, A.A., T.I. Butaeva, A.M. Kevorkov, V.A., Federov, A.G. Petrosyan and M.M. Gritsenko, 1976, Inorg. Mater. (USSR) **12**, 1238.
Kanamori, H., S. Hayashi and Y. Ikeda, 1974, J. Phys. Soc. Japan **36**, 511.
Karayianis, N., 1970, J. Chem. Phys. **53**, 2460.
Karayianis, N., 1972, J. Chem. Phys. **56**, 3734.
Karayianis, N. and C.A. Morrison, 1973, Harry Diamond Laboratories Report TR-1648 (NTIS #776 330).
Karayianis, N. and C.A. Morrison, 1975, Harry Diamond Laboratories Report TR-1682 (NTIS #011 252).
Karayianis, N., D.E. Wortman and C.A. Morrison, 1976, Solid State Commun. **18**, 1299.
Karraker, D.G., 1968, Inorg. Chem. **7**, 473.
Karraker, D.G., 1971, J. Chem. Phys. **55**, 1084.
Kasten, A. and P.J. Becker, 1977, Phys. Stat. Sol. (b) **84**, 551.
Kato, Y., K. Okada, S. Hayashi and T. Takenaka, 1979, Chem. Phys. Lett. **61**, 266.
Kern, S., 1964, J. Chem. Phys. **40**, 208.
Katelaar, J.A.A., C.H. MacGillavry and P.A. Renes, 1947, Rec. Trav. Chim. Pays-Bas **66**, 501.
Khanna, R.K. and E.R. Lippincott, 1968, Spectrochim. Acta **24A**, 905.
Kharzeeva, S.E. and V.V. Serehrennikov, 1973, Tr. Tomsk. Gos. Univ. **237**, 158.
Khodos, M.Ya., A.A. Fotiev and B.V. Shul'gin, 1974, Inorg. Mater. (USSR) **10**, 1427.
Kireeva, I.K., V.P. Repko, V.P. Orlovskii, G.M. Safronov and I.V. Tananaev, 1973, Inorg. Mater. (USSR) **12**, 1915.
Koningstein, J.A., 1967, J. Chem. Phys. **46**, 2811.
Koningstein, J.A., 1968, Appl. Spectrosc. **22**, 438.
Koningstein, J.A. and O.S. Mortensen, 1968, J. Mol. Spectrosc. **27**, 343.
Koningstein, J.A. and T.-N. Ng, 1968, J. Opt. Soc. Am. **58**, 1462.
Korableva, S.L., 1978, Sov. Phys. Solid State **20**, 2139.
Korolkov, V.S. and A.G. Makhanek, 1977, Phys. Stat. Sol. (b) **81**, 387.
Koskenlinna, M., M. Leskalä and L. Niinistö, 1976, J. Electrochem. Soc. **123**, 75.
Koster, G.F., J.O. Dimmock, R.G. Wheeler and H. Statz, 1963, Properties of the Thirty-Two Point Groups (MIT, Cambridge, Mass.).
Kramers, H.A., 1930, Proc. Acad. Amsterdam **33**, 959.
Krätzig, E. and H. Kurz, 1977, J. Electrochem. Soc. **124**, 131.
Krupke, W.F., 1966a, Phys. Rev. **145**, 325.
Krupke, W.F., 1966b, Ph.D. Thesis (University of California, Los Angeles).
Krupke, W.F., 1974, Opt. Commun. **12**, 210.
Krupke, W.F. and J.B. Gruber, 1964, J. Chem. Phys. **41**, 1225.
Kulpa, S.M. and J. Nemarich, 1975, Phys. Lett. **50A**, 461.
Kul'varskaya, B.S., 1976, Sov. Phys. Tech. Phys. **21**, 855.
Kumar, V., G.K. Gupta, N. Dass and K. Chandra, 1973, Phys. Stat. Sol. (b) **59**, 607.
Kumar, V., Vishwamittar and K. Chandra, 1976, Chem. Phys. Lett. **42**, 561.
Kumar, V., Vishwamittar and K. Chandra, 1977, J. Phys. **C10**, 267.

Kumar, V., R. Kumar and K. Sen, 1980, Phys. Stat. Sol. (b) **99**, K17.
Kunzmann, P. and L. Eyring, 1975, J. Solid State Chem. **14**, 229.
Kuroda, H., S. Shionaya and T. Kushida, 1972, J. Phys. Soc. Japan **33**, 125.
Kustov, E.F., T.K. Maketov, G. Steczko and A.K. Prgevudsky, 1980, Phys. Stat. Sol. (a) **60**, 225.
LaFrance, T.S., 1970, Ph.D. Thesis (University of Southern California).
Lagendijk, E., R.F. Wielinga and W.J. Huiskamp, 1970, Phys. Lett. **31A**, 375.
Lazarev, A.N., N.A. Mazhenov and A.P. Mirgorodskii, 1978, Inorg. Mater. (USSR) **14**, 1641.
Lea, R.R., M.J.M. Leask and W.P. Wolf, 1962, J. Phys. Chem. Solids **23**, 1381.
Leavitt, R.P., 1980, J. Chem. Phys. **72**, 3472.
Leavitt, R.P. and C.A. Morrison, 1978, Harry Diamond Laboratories Report TR-1852 (NTIS #054 747).
Leavitt, R.P. and C.A. Morrison, 1980, J. Chem. Phys. **73**, 749.
Leavitt, R.P., C.A. Morrison and D.E. Wortman, 1975, Harry Diamond Laboratories Report TR-1673 (NTIS #017 849).
Lesiecki, M., J.W. Nibler and C.W. DeKock, 1972, J. Chem. Phys. **57**, 1352.
Levinstein, H.J., G.M. Loiacono and K. Nassau, 1963, J. Appl. Phys. **34**, 3603.
Lichti, R.L. and H.J. Stapleton, 1973, Phys. Rev. **B8**, 4134.
Lomheim, T.S. and L.G. DeShazer, 1979, Phys. Rev. **B20**, 4343.
Lung, P.W.Y., 1971, J. Phys. **C4**, 820.
Luttinger, J.M. and L. Tisza, 1946, Phys. Rev. **70**, 954.
MacChesney, J.B., H.J. Williams, R.C. Sherwood and J.F. Potter, 1966, J. Chem. Phys. **44**, 596.
Macfarlane, R.M., R.M. Shelby and R.L. Shoemaker, 1979, Phys. Rev. Lett. **43**, 1726.
Makino, H., S. Nakamura and K. Matsumi, 1976, Jpn. J. Appl. Phys. **15**, 415.
Malli, G. and K.M.S. Saxena, 1969, Can. J. Phys. **47**, 1397.
Marezio, M., J.P. Remeika and P.D. Dernier, 1968, Acta Cryst. **B24**, 1670.
Marvin, H.H., 1947, Phys. Rev. **71**, 102.
McColl, J.R. and C.D. Jeffries, 1970, Phys. Rev. **B1**, 2917.
McKnight, H.G. and L.R. Rothrock, 1973, U.S. Army ECOM Technical Report ECOM 0022F(NTIS #761 094).
Meijer, P.H.E., 1978, Physica **95B**, 287.
Midwinter, J.E. and J. Warner, 1967, J. Appl. Phys. **38**, 519.
Miller, S.A., H.H. Caspers and H.E. Rast, 1968, Phys. Rev. **168**, 964.
Misra, S.K. and P. Mikolajczak, 1979, J. Magn. Resonance **35**, 87.
Miyakawa, T. and D.L. Dexter, 1970, Phys. Rev. **B1**, 2961.
Monemar, B. and H. Titze, 1971, Physica Scripta **4**, 83.
Moon, R.M., W.C. Koehler, H.R. Child and L.J. Raubenheimer, 1968, Phys. Rev. **176**, 722.
Mooney, R.W. and S.Z. Toma, 1967, J. Chem. Phys. **46**, 3364.
Moore, C.A., 1976, Phys. Rev. **B13**, 1925.
Moore, C.A. and R.A. Satten, 1973, Phys. Rev. **B7**, 1753.
Morozov, A.M., D.E. Onopko, E.G. Reut, A.I. Ryskin, M.N. Tolstoy and P.P. Feofilov, 1966, in: Proc. Int. Conf. Luminescence, p. 1621.
Morrison, C.A., 1968, Ph.D. Thesis, University of Michigan (Univ. Microfilms 69-2361).
Morrison, C.A., 1970, Harry Diamond Laboratories Report TR-1482 (NTIS #705 564).
Morrison, C.A., 1976, Solid State Commun. **18**, 153.
Morrison, C.A., 1980, J. Chem. Phys. **72**, 1001.
Morrison, C.A. and R.T. Farrar, 1964, Harry Diamond Laboratories Report TR-1265 (NTIS #457 608).
Morrison, C.A. and R.P. Leavitt, 1979, J. Chem. Phys. **71**, 2366.
Morrison, C.A., D.E. Wortman and N. Karayianis, 1976, J. Phys. **C9**, L191.
Morrison, C.A., N. Karayianis and D.E. Wortman, 1977a, Harry Diamond Laboratories Report TR-1816 (NTIS #042 447).
Morrison, C.A., N. Karayianis and D.E. Wortman, 1977b, Harry Diamond Laboratories Report TR-1814 (NTIS #042 557).
Morrison, C.A., R.P. Leavitt and D.E. Wortman, 1980a, J. Chem. Phys. **73**, 2580.
Morrison, C.A., D.E. Wortman, R.P. Leavitt and H.P. Jenssen, 1980b, Harry Diamond Laboratories Report TR-1897 (NTIS #082 982).
Morrison, J.C., P.R. Fields and W.T. Carnall, 1970, Phys. Rev. **B2**, 3526.
Morss, L.R., M. Siegal, L. Stenger and N. Edelstein, 1970, Inorg. Chem. **9**, 1771.
Mroczykowski, S., J. Eckert, H. Meissner and J.C. Doran, 1970, J. Cryst. Growth **7**, 333.
Müller-Buschbaum, H. and H.G. Schnering, 1965, Z. Anorg. Allg. Chem. **340**, 232.
Nagaiah, B., M.R. Babu and D.B. Sirdeshmukh, 1979, Indian J. Pure Appl. Phys. **17**, 838.
Nägele, W., D. Hohlwein and G. Domann, 1980, Z. Phys. **B39**, 305.
Nassau, K., 1963, J. Phys. Chem. Solids **24**, 1511.
Nassau, K. and A.M. Broyer, 1962, J. Appl. Phys. **33**, 3064.
Nassau, K. and G.M. Loiacono, 1963, J. Phys. Chem. Solids **24**, 1503.
Natadze, A.L., A.I. Ryskin and A.M. Tkachuk, 1969, in: Solid State Spectroscopy, Vol. IV (Nauka, Moscow), p. 106.
Nekvasil, V., 1979, Czech, J. Phys. **B29**, 785.
Nekvasil, V., V. Roskovec and F. Zounova, 1978, J. Appl. Phys. **49**, 1471.
Nevald, R., F.W. Voss, O.V. Nielsen, H.-D. Amberger and R.D. Fischer, 1979, Solid State Commun. **32**, 1223.
Newman, D.J., 1970, Chem. Phys. Lett. **6**, 288.
Newman, D.J., 1971, Adv. Phys. **20**, 197.

Newman, D.J., 1977a, J. Phys. **C10**, L617.
Newman, D.J., 1977b, J. Phys. **C10**, 4753.
Newman, D.J. and G.E. Stedman, 1969, J. Chem. Phys. **51**, 3013.
Nielson, C.W. and G.F. Koster, 1963, Spectroscopic Coefficients for p^n, d^n, and f^n Configurations (MIT, Cambridge, Mass.).
Nordmann, H., 1970, Phys. Stat. Sol. (a) **2**, 475.
North, M.H. and H.J. Stapleton, 1977, J. Chem. Phys. **66**, 4133.
O'Connor, C.J., R.L. Carlin and R.W. Schwartz, 1977, J. Chem. Soc. Faraday Trans. 2 **73**, 361.
O'Connor, J.R., 1966, Appl. Phys. Lett. **9**, 407.
O'Connor, J.R. and W.A. Hargreaves, 1964, Appl. Phys. Lett. **4**, 208.
Ofelt, G.S., 1962, J. Chem. Phys. **37**, 511.
Oliver, D.W., 1967, General Electric Report (NTIS #AD 821 503).
O'Reilly, T.J. and E.L. Offenbacher, 1971, J. Chem. Phys. **54**, 3065.
Ostermayer, F.W., Jr. and L.G. Van Uitert, 1970, Phys. Rev. **B1**, 4208.
Ostermayer, F.W., Jr., J.P. van der Ziel, H.M. Marcos, L.G. Van Uitert and J.E. Geusic, 1971, Phys. Rev. **B3**, 2698.
Ovsyankin, V.V. and P.P. Feofilov, 1971, Opt. Spectrosc. **31**, 510.
Ozawa, L. and P.M. Jaffe, 1970, J. Electrochem. Soc. **117**, 1297.
Pacheco, D. and B. DiBartolo, 1978, J. Lumin. **16**, 1.
Peacock, R.D., 1975, Struct. Bonding **22**, 83.
Pierce, J.W. and H.Y.P. Hong, 1973, in: Proc. 10th Rare Earth Res. Conf., p. 527.
Piotrowski, M. and A. Murasik, 1980, Phys. Stat. Sol. (a) **60**, K195.
Piper, W.W., J.A. DeLuca and F.S. Ham, 1974, J. Lumin. **8**, 344.
Pollak, T.M., R.C. Folweiler, E.P. Chicklis, J.W. Baer, A. Linz and D. Gabbe, 1980, in: Proc. Symp. on Optical Materials for High Power Lasers (Nat. Bur. Stds. (US) Spec. Publ. 568), p. 127.
Porcher, P. and P. Caro, 1978, J. Chem. Phys. **68**, 4183.
Porto, S.P.S. and J.F. Scott, 1967, Phys. Rev. **157**, 716.
Pouradier, J.F. and F.E. Auzel, 1978, J. Phys. (Paris) **39**, 833.
Prinz, G.A., 1966, Phys. Rev. **152**, 474.
Prokhorov, A.M., A.A. Kaminskii, V.V. Osiko, M.I. Timoshechkin, E.V. Zharikov, T.I. Butaeva, S.E. Sarkisov, A.G. Petrosyan and V.A. Fedorov, 1977, Phys. Stat. Sol. (a) **40**, K69.
Racah, G., 1942a, Phys. Rev. **61**, 186.
Racah, G., 1942b, Phys. Rev. **62**, 438.
Racah, G., 1943, Phys. Rev. **63**, 367.
Racah, G., 1949, Phys. Rev. **76**, 1352.
Rajnak, K., 1965, J. Chem. Phys. **43**, 847.
Rajnak, K. and B.G. Wybourne, 1963, Phys. Rev. **132**, 280.
Rajnak, K. and B.G. Wybourne, 1964, J. Chem. Phys. **41**, 565.
Ranon, U., 1968a, Bull. Am. Phys. Soc. **13**, 164.
Ranon, U., 1968b, Phys. Lett. **28A**, 228.
Ranon, U. and V. Volterra, 1964, Phys. Rev. **134**, A 1483.
Rast, H.E., H.H. Caspers and S.A. Miller, 1969, Phys. Rev. **180**, 890.
Ratinen, H., 1971, Acta Polytech. Scand., Chem. Incl. Met. Ser. No. 107.
Reed, E.D. and H.W. Moos, 1973a, Phys. Rev. **B8**, 980.
Reed, E.D. and H.W. Moos, 1973b, Phys. Rev. **B8**, 988.
Rehn, V., D.L. Burdick and V.O. Jones, 1977, Nat. Bur. Stds. (US) Special Publication 509, p. 132.
Reisfeld, R. and C.K. Jørgensen, 1977, Lasers and Excited States of Rare Earths (Springer-Verlag, Berlin).
Remski, R.L., L.T. James, K.H. Gooen, B. DiBartolo and A. Linz, 1969, IEEE J. Quantum Electron. **QE-5**, 214.
Reuveni, A. and B.R. McGarvey, 1978, J. Magn. Res. **29**, 21.
Richman, I., 1966, J. Opt. Soc. Am. **56**, 1589.
Rose, M.E., 1957, Elementary Theory of Angular Momentum (Wiley, New York).
Rotenberg, M., R. Bivins, N. Metropolis and J.K. Wooten, Jr., 1969, The 3-*j* and 6-*j* Symbols (Technology, Cambridge, Mass.).
Royce, M.R., 1968, U.S. Pat. 3 418 246.
Rubenstein, C.B., L.G. Van Uitert and W.H. Grodkiewicz, 1964, J. Appl. Phys. **35**, 3069.
Russell, J.P. and R. Loudon, 1965, Proc. Phys. Soc. (London) **85**, 1029.
Sansalone, F.J., 1971, Appl. Optics **10**, 2329.
Sattler, J.P. and J. Nemarich, 1970a, Phys. Rev. **B1**, 4249.
Sattler, J.P. and J. Nemarich, 1970b, Phys. Rev. **B1**, 4256.
Sattler, J.P. and J. Nemarich, 1971, Phys. Rev. **B4**, 1.
Schaack, G. and J.A. Koningstein, 1970, J. Opt. Soc. Am. **60**, 1110.
Schäfer, G., 1969, Phys. Kondens. Materie **9**, 359.
Schibuya, N., K. Knorr, H. Dachs, M. Steiner and B.M. Wanklyn, 1975, Solid State Commun. **17**, 1305.
Schwartz, R.W. and N. Hill, 1974, J. Chem. Soc. Faraday Trans. 2 **70**, 124.
Schwartz, R.W. and P.N. Schatz, 1973, Phys. Rev. **B8**, 3229.
Schwartz, R.W., S.F. Watkins, C.J. O'Connor and R.L. Carlin, 1976, J. Chem. Soc. Faraday Trans. 2 **72**, 565.
Scott, P.D. and W.P. Wolf, 1969, J. Appl. Phys. **40**, 1031.
Scott, P.D., H.E. Meissner and H.M. Crosswhite, 1969, Phys. Lett. **28A**, 489.
Seidel, E.R., G. Kaindl, M.J. Clauser and R.L. Mössbauer, 1967, Phys. Lett. **25A**, 328.
Sengupta, D. and J.O. Artman, 1970, Phys. Rev. **B1**, 2986.
Shand, W.A., 1969, J. Crystal Growth **5**, 143.
Sharp, E.J., D.J. Horowitz and J.E. Miller, 1973, J. Appl. Phys. **44**, 5399.
Slater, J.C., 1929, Phys. Rev. **34**, 1293.

Smakula, P.H. and P.C. Claspy, 1967, Trans. AIME **239**, 421.
Smith, M.R., Y.H. Shing, R. Chatterjee and H.A. Buckmaster, 1977, J. Magn. Res. **26**, 351.
Sobolev, B.P. and P.P. Fedorov, 1973, Sov. Phys. Crystallogr. **18**, 392.
Sobon, L.E., K.A. Wickersheim, R.A. Buchanan and R.V. Alves, 1971, J. Appl. Phys. **42**, 3049.
Soffer, B.H. and R.H. Hoskins, 1966, IEEE J. Quantum Electron. **QE-2**, 253.
Suffer, B.H. and R.H. Hoskins, 1965, Appl. Phys. Lett. **6**, 200.
Soffer, B.H. and R.H. Hoskins, 1966, IEEE J. Quantum Electron. **QE-2**, 253.
Solomon, R. and L. Mueller, 1963, Appl. Phys. Lett. **3**, 135.
Sommerdijk, J.L., A. Bril and A.W. deJager, 1974, J. Lumin. **9**, 288.
Song, J.J., P.B. Klein, R.L. Wadsack, M. Selders, S. Mroczkowski and R.K. Chang, 1973, J. Opt. Soc. Am. **63**, 1135.
Souillat, J.C., J. Rossat-Mignod and C. Linares, 1972, Phys. Stat. Sol. (b) **52**, 601.
Sovers, O.J. and T. Yoshioka, 1969, J. Chem. Phys. **51**, 5330.
Sovers, O.J., M. Ogawa and T. Yoshioka, 1976, in: Proc. 12th Rare Earth Res. Conf. **2**, 728.
Spedding, F.H., 1931, Phys. Rev. **38**, 2080.
Spedding, F.H., 1933, J. Chem. Phys. **1**, 144.
Spedding, F.H. and A.H. Daane, 1961, The Rare Earths (Wiley, New York).
Spedding, F.H. and G.C. Nutting, 1931, Phys. Rev. **38**, 2294.
Spedding, F.H., C.C. Moss and R.C. Waller, 1940, J. Chem. Phys. **8**, 908.
Stein, B.F. and M. Kestigian, 1975, J. Cryst. Growth **31**, 366.
Steiner, M., L.M. Corliss, J.M. Hastings, M. Blume, N. Giordano and W.P. Wolf, 1979, Proc. Conf. Magnetism, Munich, Germany.
Sternheimer, R.M., M. Blume and R.F. Peierls, 1968, Phys. Rev. **173**, 376.
Stevens, K.W.H., 1952, Proc. Phys. Soc. (London) **A65**, 209.
Stone, J. and C.P. Burrus, 1978, J. Appl. Phys. **49**, 2281.
Swanson, B.I., C. Machell, G.W. Beall and W.O. Milligan, 1978, J. Inorg. Nucl. Chem. **40**, 694.
Tanaka, S., Y. Maruyama, H. Kobayashi and H. Sasakura, 1976, J. Lumin. **12/13**, 911.
Templeton, D.H. and G.F. Carter, 1954, J. Phys. Chem. **58**, 940.
Thoma, R.E., C.F. Weaver, H.A. Friedman, H. Insley, L.A. Harris and H.A. Yakel, 1961, J. Phys. Chem. **65**, 1096.
Thoma, R.E., G.D. Brunton, R.A. Penneman and T.K. Keenan, 1970, Inorg. Chem. **9**, 1096.
Thomas, K.S., S. Singh and G.H. Dieke, 1963, J. Chem. Phys. **38**, 2180.
Tinkham, M., 1964, Group Theory and Quantum Mechanics (McGraw-Hill, New York).
Tromp, H.R.C. and A.J. Van Duyneveldt, 1969, Physica **45**, 445.
Urland, W., 1979, Chem. Phys. **38**, 407.
Van der Ziel, J.P., 1973, Solid State Commun. **13**, 273.
Van der Ziel, J.P. and L.G. Van Uitert, 1973, Phys. Rev. **B8**, 1835.
Van der Ziel, J.P., W.A. Bonner, L. Kopf and L.G. Van Uitert, 1972, Phys. Lett. **42A**, 105.
Van Siclen, C.B., 1981, J. Phys. **C14**, 4611.
Van Vleck, J.H. 1937, J. Phys. Chem. **41**, 67.
Vinogradov, E.A., N.A. Prisova and G.V. Kozlov, 1970, Sov. Phys. Solid State **12**, 605.
Viswanathan, C.R. and E.Y. Wong, 1968, J. Chem. Phys. **49**, 966.
Voloshin, V.A., N.A. Kulagin, L.N. Ovander and A.M. Prudnikov, 1976, Opt. Spectrosc. **39**, 334.
Watts, R.K. and W.C. Holton, 1974, J. Appl. Phys. **45**, 873.
Weber, M.J., 1979a, in: Gschneidner, K.A., Jr. and L. Eyring, Eds., Handbook on the Physics and Chemistry of Rare Earths, Vol. 4 (North-Holland, Amsterdam) p. 275.
Weber, M.J., 1979b, in: Tang, C.L., Ed., Methods of Experimental Physics, Vol. 15A (Academic, New York), p. 167.
Weber, M.J. and M. Bass, 1971, Laser Focus (September), p. 34.
Weber, M.J., M. Bass, K. Andringa, R.R. Monchamp and E. Comperchio, 1969, Appl. Phys. Lett. **15**, 342.
Wensky, D.A. and W.G. Moulton, 1970, J. Chem. Phys. **53**, 3957.
Wesley, R.D. and C.W. DeKock, 1971, J. Chem. Phys. **55**, 3866.
Westrum, E.F., Jr. and B.H. Justice, 1963, J. Phys. Chem. **67**, 659.
Wheeler, R.G. and J.C. Hill, 1966, Phys. Lett. **20**, 496.
Wickersheim, K.A. and R. Lefever, 1961, J. Opt. Soc. Am. **51**, 1147.
Wickersheim, K.A., R.V. Alves and R.A. Buchanan, 1970, IEEE Trans. Nucl. Sci. **NS-17**, 57.
Wilson, K.E. and L.G. DeShazer, 1980, Proc. Topical Conference on Basic Optical Properties of Materials (Nat. Bur. Stds. (US) Spec. Publ. 574), p. 221.
Winchell, A.N. and H. Winchell, 1964, The Microscopic Characters of Artificial Inorganic Solid Substances, Optical Properties of Artificial Minerals (Academic Press, New York).
Wojcik, M., 1980, J. Magn. Magn. Mater. **15**, 21.
Wolf, W.P., M. Ball, M.T. Hutchings, M.J.M. Leask and A.F.G. Wyatt, 1962, J. Phys. Soc. Japan **17**, Suppl. B1, p. 443.
Wong, E.Y., O.M. Stafsudd and D.R. Johnston, 1963, J. Chem. Phys. **39**, 786.
Wortman, D.E. and C.A. Morrison, 1973, IEEE J. Quantum. Electron. **QE-9**, 956.
Wright, J.C., H.W. Moos, J.H. Colwell, B.W. Mangum and D.D. Thornton, 1971, Phys. Rev. **B3**, 843.
Wyatt, A.F.G., 1968, J. Phys. **C1**, 684.
Wybourne, B.G., 1965, Spectroscopic Properties of Rare Earths (Interscience, New York).

Wyckoff, R.W.G., 1964, Crystal Structures, Vol. 2 (Interscience, New York).
Yang, K.H. and J.A. DeLuca, 1976, Appl. Phys. Lett. **29**, 499.
Yen, W.M., W.C. Scott and A.L. Schawlow, 1964, Phys. Rev. **136**, A271.
Yurchenko, E.N., E.B. Burgina, V.I. Bugakov, E.N. Murav'ev, V.P. Orlovskii and T.V. Belyaevskaya, 1978, Inorg. Mater. (USSR) **14**, 1586.
Zalkin, A., D.H. Templeton and T.E. Hopkins, 1966, Inorg. Chem. **5**, 1466.
Zav'yalova, A.A., R.M. Imanov, N.A. Ragimli and S.A. Semiletov, 1976, Sov. Phys. Crystallogr. **21**, 411.
Zverev, G.M., A.M. Onishchencko, V.P. Orlovskii, V.P. Repko and A.A. Semenov, 1973, Inorg. Mater. (USSR) **9**, 370.

SUBJECT INDEX